IMWS-AMP 2026

IEEE MTT-S International Microwave Workshop Cairns, Australia

Proceedings

2026 IEEE MTT-S International Microwave Workshop Series on Advanced Materials and Processes for RF and THz Applications (IMWS-AMP)

July 22-24, 2026

Cairns, Australia



IEEE Advancing Technology for Humanity

THE UNIVERSITY OF SYDNEY

JAMES COOK UNIVERSITY AUSTRALIA

UTS UNIVERSITY OF TECHNOLOGY, SYDNEY

MTT-S MHz To THz Community

QWED

MICROWAVE AT 鑫太

KEYSIGHT TECHNOLOGIES

APPVISION

MILLIBEAM

2026 IEEE MTT-S International Microwave Workshop Series on Advanced Materials and Processes for RF and THz Applications (IMWS-AMP) took place 22-24 July 2026 in Cairns QLD, Australia.

IEEE MTT-S International Microwave Workshop Series on Advanced Materials and Processes for RF and THz Applications (IMWS-AMP 2026) is organized by the University of Technology Sydney (UTS), The University of Sydney and James Cook University.

IMWS-AMP 2026 is a continuation of a series of annual international events held in Suzhou, China (2015), Chengdu, China (2016), Pavia, Italy (2017), Michigan, USA (2018), Bochum, Germany (2019), Suzhou, China (2020), Chongqing, China (2021), Guangzhou, China (2022), Chengdu, China (2023), Nanjing, China (2024) and Wuxi, China (2025).

The purpose of this platform is to boost technical and educational activities as well as exchanges and collaborations within the international microwave community. IMWS-AMP 2026 will be held in Cairns, Australia on July 22- 24, 2026. IMWS-AMP 2026 will feature both invited and contributed papers. Distinguished researchers will be invited to deliver keynote speeches on technology trends and significant advances in relevant topics.

Conference Program	
Author Index	Paper Index
General Chair Welcome Message	TPC Chairs Welcome Message
Organising Committee	Technical Program Committee
Additional Reviewers	

Time (Brisbane)	Michaelmus A	Michaelmus B	Reef	Urchins 2
Wednesday, July 22				
08:50 am-09:05 am	*Opening Ceremony*			
09:05 am-09:55 am	K1: *Keynote: MHz to THz Technologies Addressing Fundamental Science Questions - Goutam Chattopadhyay*			
10:00 am-11:00 am	P1: *Semi-Plenary 1*	P2: *Semi-Plenary 2*		
11:00 am-11:30 am	*Break*			
11:30 am-12:45 pm	W1: *Workshop: Recent Advancement in Emerging Materials and Processing Technologies*	S1: *CMOS and BiCMOS Power Amplifiers I*	S10: *Metamaterials and Metasurfaces I*	S19: *Biomedical and Wearable Sensing II*
12:45 pm-02:00 pm	L1: *Lunch*			
02:00 pm-03:15 pm	W2: *Workshop: Recent Advancement in Emerging Materials and Processing Technologies*	S2: *CMOS and BiCMOS Power Amplifiers II*	S11: *Terahertz Technologies and Systems IV*	S20: *Metamaterials and Metasurfaces III*
03:15 pm-03:45 pm	*Break*			
03:45 pm-05:00 pm	W3: *Workshop: Recent Advancement in Emerging Materials and Processing Technologies*	S3: *Terahertz Technologies and Systems I*	S12: *Biomedical and Wearable Sensing I*	S21: *Antenna Arrays and Beamforming II*
05:00 pm-06:30 pm	*Welcome Reception @ Roof Top Pool Deck*			
Thursday, July 23				
09:00 am-09:45 am	K2: *Keynote: Reconfigurable Microwave and Millimeter-Wave Devices Enabled by Phase-Change Materials, BST and Liquid Crystal Technologies - Raafat Mansour*			
09:45 am-10:45 am	P3: *Semi-Plenary 3*	P4: *Semi-Plenary 4*		

Time (Brisbane)	Michaelmus A	Michaelmus B	Reef	Urchins 2
10:45 am-11:15 am	*Break*			
11:15 am-12:30 pm	*BPC: Ask Us Anything*	S4: *Terahertz Technologies and Systems II*	S13: *Metamaterials and Metasurfaces II*	S22: *Antenna Arrays and Beamforming I*
12:30 pm-01:45 pm	L2: *Lunch*			
01:45 pm-03:00 pm	*ISTP: Meet the Editors*	S5: *CMOS and BiCMOS Power Amplifiers III*	S14: *Machine Learning in RF and Microwave Applications*	S23: *Terahertz Technologies and Systems V*
03:00 pm-03:30 pm	*Break*			
03:30 pm-05:00 pm	*Panel Discussion*	S6: *GaN and Compound Semiconductor Devices*	S15: *Dielectric and Magnetic Materials*	S24: *Antenna Arrays and Beamforming III*
06:00 pm-10:30 pm	*Conference Banquet @ Urchins*			

Friday, July 24

09:00 am-09:45 am	K3: *Keynote: The Evolution of Guided-Wave Technologies: Driving the Future of Integrated Circuits and Systems - Ke Wu*			
09:45 am-10:45 am	P5: *Semi-Plenary 5*	P6: *Semi-Plenary 6*		
10:45 am-11:15 am	*Break*			
11:15 am-12:30 pm	*YP Session*	S7: *Low Noise Amplifiers and Receivers*	S16: *Millimeter-Wave and Terahertz Passives II*	S25: *Antenna Arrays and Beamforming IV*
12:30 pm-01:45 pm	L3: *Lunch*			
01:45 pm-03:00 pm	*WIM Session*	S8: *Terahertz Technologies and Systems III*	S17: *CMOS and BiCMOS Power Amplifiers IV*	S26: *Microwave Filters and Resonators I*

Time (Brisbane)	Michaelmus A	Michaelmus B	Reef	Urchins 2
03:00 pm-03:30 pm	*Break*			
03:30 pm-04:45 pm	S27: *Online*	S9: *Microwave Filters and Devices*	S18: *Dielectric Characterisation*	*BPC (Debabani-Mentoring Session)*
04:45 pm-05:00 pm		*Awards & Closing Ceremony*		

Wednesday, July 22

Wednesday, July 22 8:50 - 9:05

Opening Ceremony

Room: Michaelmus A, Michaelmus B

Wednesday, July 22 9:05 - 9:55

K1: Keynote: MHz to THz Technologies Addressing Fundamental Science Questions - Goutam Chattopadhyay

Goutam Chattopadhyay, Senior Research Scientist
Room: Michaelmus A
Chair: Yang Yang (University of Technology Sydney, Australia)
Space exploration has long served as a powerful catalyst for inspiring the imagination of the next generation. The sight of rovers on Mars, images from distant galaxies, and the dream of humans returning to the Moon or reaching Mars ignite curiosity and a spirit of discovery in young minds. These missions are not just feats of engineering - they are stories that capture the human desire to explore the unknown and push beyond boundaries. By engaging students, educators, and the public in the wonders of space, exploration fosters STEM education, fuels innovation, and builds a generation that dreams bigger and reaches further.

Beyond its inspirational value, space exploration offers a unique lens through which we can better understand ourselves and our place in the cosmos. As we study other planets and moons, we gain valuable insight into planetary evolution, atmospheric behavior, and the potential for life beyond Earth. Observing Earth from space also provides critical data on climate change, environmental degradation, and the fragile systems that sustain life. In this way, space science not only fuels our search for extraterrestrial life but also deepens our understanding of Earth's past, present, and future. Ultimately, exploring the universe is a journey inward as much as outward - it challenges us to think about our shared humanity, our responsibility to protect our planet, and our collective future among the stars.

In this lecture, we will explore the technological innovations in the MHz to THz frequency domain driving the next generation of instruments and highlight specific instrument developments along with the fundamental science questions they aim to address.

This work was carried out at the Jet Propulsion Laboratory, California Institute of Technology, under a contract with National Aeronautics and Space Administration (NASA).

Goutam Chattopadhyay Biography

Goutam Chattopadhyay is a Senior Scientist at NASA's Jet Propulsion Laboratory (JPL), California Institute of Technology (Caltech), and a Visiting Professor at Caltech in Pasadena, USA. He previously served as the BEL Distinguished Visiting Chair Professor at the Indian Institute of Science, Bangalore, and as an Adjunct Professor at the Indian Institute of Technology, Kharagpur. Dr. Chattopadhyay received his Ph.D. in Electrical Engineering from Caltech in 2000. He is a Fellow of the IEEE (USA), National Academy of Inventors (NAI), and the IETE (India); an Associate Fellow of the AIAA, the 2025 President of the IEEE Microwave Theory and Technology Society (MTT-S), a Track Editor for the IEEE Transactions on Antennas and Propagation, and an IEEE Distinguished Lecturer. His research focuses on microwave, millimeter-wave, and terahertz receiver systems and radars, as well as space instrumentation for the search for life beyond Earth.

Dr. Chattopadhyay has authored over 450 publications in international journals and conferences and holds more than 25 patents. He has received over 35 NASA Technical Achievement and New Technology Invention Awards. In 2026, he received NASA's Group Achievement Medal. In 2025, he received the NASA-JPL North Star Award, the highest honor bestowed upon a NASA-JPL scientist. In 2024, he was awarded the prestigious Armstrong Medal by the Radio Club of America (RCA) in recognition of his outstanding contributions to radio science. He also received the NASA-JPL People Leadership Award in 2023. Among other honors, he was named IEEE Region 6 Engineer of the Year in 2018 and received the Distinguished Alumni Award from the Indian Institute of Engineering Science and Technology (IIEST), India, in 2017. He is a two-time recipient of the Best Journal Paper Award from IEEE Transactions on Terahertz Science and Technology (2020 and 2013), and also received the Best Paper Award for Antenna Design and Applications at EuCAP in 2017. Additional accolades include the IETE Biman Bihari Sen Memorial Award (2022) and the IETE Prof. S. N. Mitra Memorial Award (2014).

Wednesday, July 22 10:00 - 11:00

P1: Semi-Plenary 1

Room: Michaelmus A

Chair: Konstanty S Bialkowski (The University of Queensland, Australia)

10:00 ***Printed VO_2 Tiles for Tunable Holographic Metasurface***

Kamran Ghorbani (RMIT University, Australia)

Metasurfaces, as two-dimensional arrays of subwavelength engineered meta-atoms, provide powerful control over electromagnetic waves through spatial modulation of amplitude, phase, polarisation, and surface impedance. Compared with conventional bulk metamaterials, metasurfaces offer a lower-profile, more fabrication-friendly platform while retaining strong wavefront-engineering capabilities, enabling applications such as beam steering, focusing, polarisation control, holography, and antenna miniaturisation. In antenna applications, metasurfaces have progressed from reflectarray or lens structures to radiating apertures, forming metasurface antennas capable of guiding, modulating, and radiating electromagnetic waves with high design flexibility. However, passive metasurfaces are inherently limited to fixed responses after fabrication, motivating extensive research into tunable and reconfigurable metasurfaces based on electrical, optical, mechanical, liquidcrystal, semiconductor, and phase-change-material tuning mechanisms. Although these approaches have enabled dynamic electromagnetic control, scalable implementation remains constrained by biasing complexity, fabrication cost, power consumption, and the need to individually address large numbers of unit cells.

pg. 1

10:30 ***Novel Design Strategies for Wideband Millimeter-Wave Switched-Type MMIC Phase Shifters with Low Amplitude and Phase Errors***

Wenquan Che (South China University of Technology, China)

In 5G and beyond 5G era, the growing demands for high data transmission rates in communication systems and high resolution in radar imaging pose strict requirements on millimeter-wave phase shifters. Specifically, wide bandwidth, precise phase control, and high amplitude consistency are essential for ensuring excellent beamforming quality and scanning accuracy. In this way, passive switched-type MMIC phase shifters have emerged as a promising solution, featuring zero DC power consumption and low-cost calibration. However, in the conventional direct-cascading architecture for multi-bit designs, inter-stage mismatch and load-pulling effects severely restrict the operational bandwidth and degrade the phase and amplitude accuracy. In this talk, some recent research on new phase-control theories and path-switching mechanisms for mmW switched-type

phase shifters in our group will be presented. These strategies are expected to provide an architecture-level solution for mmW multi-bit phase shifters in wireless communication.

pp. 2-3

P2: Semi-Plenary 2

Room: Michaelmus B
Chair: Maral Ansari (CSIRO, Australia)

10:00 ***A Wide-Coverage End-Fire High-Gain Circularly Polarized Mobile Phone Antenna for Satellite Communication***

Li-Bo Jia and Qing-Xin Chu (South China University of Technology, China)

To address the 3 dB polarization mismatch loss of linearly polarized antennas when receiving circularly polarized satellite signals, this work proposes an end-fire, high-gain circularly polarized mobile phone antenna with wide beamwidth. The antenna comprises three elements: a patch antenna integrated with the camera decoration (Deco), a frame antenna located at the top of the phone, and choke structures embedded in the side frames. The patch and frame antennas generate parallel electric and magnetic currents, respectively, whose combination produces end-fire left-handed circular polarization (LHCP). The antenna operates at a center frequency of 1.7 GHz with a bandwidth of 20 MHz. It features high gain and wide beamwidth, achieving a minimum LHCP gain higher than −5 dBic within a beam range exceeding a 90° cone angle across the operating band.

pp. 4-6

Wednesday, July 22 11:30 - 12:45

S1: CMOS and BiCMOS Power Amplifiers I

Room: Michaelmus B

11:30 ***Wave-Based Triple-Band CMOS Voltage-Controlled Oscillator***

Wen Cheng Lai (National Taiwan University of Science and Technology, Taiwan)

By exploiting the intrinsic multiple resonant modes of a 6th-order LC resonator, a triple-band wave-based oscillator is designed. The LC resonator consists of two units of left-handed transmission LC network ended with parallel-tuned LC resonator, and a cross-coupled switching transistor pair is used to start up the oscillation. Two pairs of varactors are used for band tuning and switching. The proposed oscillator has been implemented with the tsmc 0.18 μm 1P6M CMOS technology and the core power consumption is 3.735 mW at the dc drain-source bias of 0.75 V. The VCO can generate differential signals in the frequency range of 8.04 - 8.68 GHz, 5.82 - 6.15 GHz, and 3.68 - 4.08 GHz. The die area of the triple-band oscillator is 0.568 × 1.189 mm2.

Presenter bio: Dr. Wen-Cheng Lai has been working in the field of radio-frequency circuits, analog IC integrated design, computer and communication for more than 20 years. He received the Ph.D. degree from National Taiwan University of Science and Technology. He is Assistant Professor in Department of Electronic Engineering National Yunlin University of Science and Technology, Taiwan.

pp. 7-9

11:45 ***Bandwidth Reconfigurable Low-Noise Amplifier Based on Magnetic Coupling Effect***

Guangbao Shan, Pan Zhang, Yanwen Zheng, Ruixin Wang and Wang Fangqian (Xidian University, China)

This paper presents a band-reconfigurable low-noise amplifier (LNA) that utilizing transformer-based magnetic coupling technique. It consists of source-degenerated cascode amplifier integrated with a tunable magnetic

coupling network. By manipulating the amplitude and phase of the voltage ratio(β), the position of the transmission zero can be dynamically adjusted, enabling flexible tuning of bandwidth. Simulation results demonstrate that the 3-dB bandwidths range from 15.64 to 23.55 GHz and from 18.35 to 31.38 GHz, with corresponding gains of 16.84 dB and 16.98 dB, respectively.

pp. 10-12

12:00 ***Exploiting LDMOS-PA for kW SSPA Applications***

Xin Tong, Shiyang Luo, Xidi Hu, Hao Zhang and He Guan (Northwestern Polytechnical University, China)

This paper presents the design and implementation of a 250-W S-band Class-B solid-state power amplifier (SSPA) module based on the Ampleon BLC2425M10LS250 laterally diffused metal-oxide-semiconductor (LDMOS) transistor. Stepped-impedance microstrip matching networks are employed to achieve broadband impedance matching over 2.4-2.6 GHz. The amplifier is measured under pulsed operation with a 10% duty cycle and a 100-μs pulse period. Measured results demonstrate that the proposed module delivers 53.69-53.98 dBm (233-250 W) output power, 14.0-14.4 dB power gain, 66.5%-75.8% drain efficiency, and 63.6%-72.5% power-added efficiency across the operating band. In addition, a high-efficiency power-combining scheme is proposed to facilitate future kW-class industrial microwave systems.

pp. 13-15

12:15 ***An Energy-Efficient Reconfigurable BLE RF Receiving Front-End Based on Mixer-First Architecture for IoT Applications***

Yan Zhao, Jiawen Zhang, Tongde Huang, Wenhua Gu and Wen Wu (Nanjing University of Science and Technology, China)

This paper presents an energy-efficient reconfigurable Bluetooth Low Energy (BLE) RF receiver front-end based on a mixer-first architecture for Internet-of Things (IoT) applications. To eliminate the hardware redundancy and high cost associated with conventional designs using separate wake-up receiver (WuRX) and main receiver (RX) front-ends, the proposed architecture enables full hardware reuse between two parallel operating modes by reconfiguring the core transimpedance amplifier (TIA) to operate either as a linear amplifier or as a nonlinear active rectifier. The mixer-first architecture facilitates on-chip channel selection while reducing power consumption. Fabricated in a TSMC 28-nm CMOS process, the prototype consumes 0.2 mW in RX mode and achieves a minimum power consumption of 30 μW in non-duty-cycled WuRX mode. The measured input reflection coefficient, S11, is below -10 dB in both modes across the target frequency band. In WuRX mode, the front-end achieves a noise figure of approximately 21 dB over the signal bandwidth of interest. Based on the classical RF sensitivity calculation, the overall WuRX system is expected to achieve a receiving sensitivity better than -90 dBm at a data rate of 100 kbps. This work provides a low-cost, highly integrated RF front-end solution for BLE IoT terminals.

pp. 16-18

S10: Metamaterials and Metasurfaces I

Room: Reef

Chair: Yuanxi Cao (Xi'an Jiaotong University, China)

11:30 ***Space-Time Metasurface Antennas: Concept, Design, and Applications***

Geng-Bo Wu (City University of Hong Kong, Hong Kong)

While the global commercialization of the fifth-generation (5G) wireless communications is gradually taking off, there is already significant interest in the next generation of wireless communications. 6G scheduled to be launched in 2030, will provide a Tbps data rate, microsecond latency, and almost unlimited bandwidth to the

connectivity of numerous mobile and intelligent networks. Antennas and metasurfaces are ubiquitous and indispensable components for generating and manipulating electromagnetic (EM) waves. In this talk, I will share the development and design of the space-time metasurface antenna that can control all fundamental properties of EM waves. The space-time metasurface antenna can further facilitate information manipulation, which can fundamentally simplify the architecture of information transmitter systems. The unparalleled wave and information manipulation capabilities of the metasurface antenna will spark a surge of applications from next-generation wireless systems, cognitive sensing, to imaging.

pg. 19

11:45 ***Broadband Phase-Dispersive Conformal Metamaterial for EM Backscattering Enhancement***

Weizhi Chen (South China University of Technology, China); Xin Xiu (South China University of Technology & Nanjing University of Science and Technology, China); Yixi Tang (Nanjing University of Posts and Telecommunications, China); Kun Tang, Wenjie Feng and Wenquan Che (South China University of Technology, China)

A phase-dispersive conformal metamaterial for broadband electromagnetic (EM) backscattering enhancement is presented. The metamaterial comprises two layers of LC resonant structures to achieve broadband phase-dispersive characteristics. To enable a conformal design, the first layer employs a low-profile dielectric substrate with excellent flexibility, while the second layer is conformally attached to the target surface using an insertion-based method. The metamaterial is designed for backscattering enhancement, and a prototype was fabricated for experimental validation. The results demonstrate significant backscattering enhancement over a broadband from 4.0 to 7.0 GHz (54.5%) for dual polarizations. With respect to a bare metal target without the metamaterial, the y-polarized backscattering is enhanced to 97.5% over a metal plate of identical projected area, and the x-polarized backscattering reaches 74.5%.

pp. 20-22

12:00 ***Semantics-Guided End-to-End Intelligent Design Framework for Metasurface Absorbers***

Yongqi Lv, Wenhua Gu and Yanghui Wu (Nanjing University of Science and Technology, China)

Metasurface absorbers, as a type of two-dimensional metamaterial, control electromagnetic waves by adjusting the phase, amplitude, and polarization response of the units. Traditional design methods face challenges with high computational costs and low optimization efficiency. This paper proposes a semantic-guided, cross-modal end-to-end intelligent design framework, combining natural language processing and deep learning. A SigLIP-based visual-language alignment module connects natural language descriptions with target spectra, while a forward modeling method based on the SV-MC-FNO addresses the multi-solution problem in inverse design using a mixture density network (MDN). The introduction of cyclical consistency training with physical constraints enhances model reliability. Experimental results show significant improvements in design efficiency and accuracy.

pp. 23-25

12:15 ***Absorptivity Evaluation of Broadband FSS Absorbers Considering Higher-Order Floquet Modes***

Chonghuan Zhang, Liping Yan, Yanping Zhou and Changjun Liu (Sichuan University, China)

Frequency selective surface (FSS) absorbers are inherently periodic electromagnetic structures whose scattering characteristics are governed by the superposition of Floquet modes. When the structural period satisfies specific conditions, higher-order Floquet modes (i.e., grating lobes) become propagation and carrying additional scattering power. This energy is not captured by conventional fundamental-mode S-parameters, which may lead to inaccuracies in conventional absorptivity evaluation based on |S11| and |S21|. In this work, the modal composition of the scattered fields of an FSS absorber is analyzed using Floquet theory. A broadband resistive-sheet FSS absorber is employed as an example to compare reflection characteristics and

absorptivity with fundamental-mode-only and full-mode considerations. The results demonstrate that, when higher-order propagating modes are included, the 90% absorption bandwidth shrinks from 6.6 - 27.4 GHz to 6.6 - 20 GHz.

pp. 26-28

12:30 ***A Highly-Selective 3-D FSS with Exceptional Precision for Liquid Dielectric Constant Detection***

Xiaojing Lv (University of Technology Sydney, Australia); Zhichao Sun (University of Technology Sydeny, Australia); Jiexin Lai and Yang Yang (University of Technology Sydney, Australia)

This paper presents a novel 3-D FSS sensor for the high-accuracy dielectric characterization of liquid materials across a wide dynamic range. Featuring a miniaturized honeycomb lattice and an ultrathin profile, the proposed architecture uniquely leverages surface tension for stable liquid retention. To interpret the spectral response, a systematic two-step analytical framework is developed, mapping specific higher-order harmonic resonance peaks to low, medium, and high dielectric constants. Furthermore, the sensor's high frequency selectivity and multiple harmonic resonances are intuitively elucidated via Smith chart impedance trajectories, providing profound physical insight into the underlying matching mechanisms.

pp. 29-31

S19: Biomedical and Wearable Sensing II

Room: Urchins 2

Chair: Amir Ebrahimi (RMIT University, Australia)

11:30 ***Materials-Aware Design Strategies for Wearable Antenna Design***

Shengjian Jammy Chen (Flinders University, Australia & The University of Adelaide, Australia)

This review synthesises recent advances that co-optimise materials and electromagnetics for robust wearable antennas. It adopts a materials-aware design mindset that treats the substrate, radiator, and ground as coupled variables. In practice, one can shape dielectric loss and effective permittivity only where they matter; form the operating spectrum through interpretable modal control rather than add-on resonators; manage non-ideal conductors via coordinated radiator-ground co-design; miniaturise through ground-mediated propagation control; and embed biosymbiotic mechanics using additive manufacturing. Together, these strategies provide practical, material-oriented, application-focused guidance for future WBAN platforms.

Presenter bio: Shengjian Jammy Chen received M.E and Ph.D degrees in electrical and electronic engineering from the University of Adelaide, Australia. From 2017 to 2021, he was a lecturer and a postdoctoral researcher at the School of Electrical and Electronic Engineering of the University of Adelaide. Since 2022, he is a lecturer with College of Science and Engineering at Finders University. His current research interests include wearable and reconfigurable electromagnetic structures based on novel conductive materials such as conductive polymers and conductive fabrics, RFID-based wearable applications and leaky wave antennas. Dr. Chen was the recipient of the Young Scientist Best Paper Award at ICEAA 2015 & ICEAA 2016, and Travel Bursary Award in ICEAA 2016. He also received the Honorable Mention in APS/URSI 2017, the CST University Publication Award 2017, and Best Paper Award at IEEE APMC 2021.

pg. 32

11:45 ***Dosimetric Assessment of a Birdcage-Coil Wireless Power Transfer at 6.78 MHz for Capsule Robots***

Valerio De Santis, Riccardo Olivieri and Wassim Boumerdassi (University of L'Aquila, Italy); Tommaso Campi (Sapienza University of Rome, Italy); Francescaromana Maradei (University of Rome La Sapienza, Italy); Mauro Feliziani (Roma, Italy)

This work addresses the electromagnetic field (EMF) safety of a capsule robot moving inside the human body during wireless power transfer (WPT) operations. The WPT system consists of an innovative birdcage coil capable of generating a nearly uniform rotating magnetic field with non-zero components along all three spatial axes. This solution is wearable, enabling comfortable and efficient power transfer to any patient.

However, for obese human body models (HBMs), the current needed to transfer a reasonable power to the capsule battery could pose several EMF exposure risks due to the deeper colon tract and larger body cross-sections. A dosimetric analysis is therefore performed to assess compliance of the proposed WPT system with EMF safety standards. Different frequencies and HBMs are investigated to find the worst-case scenarios.

Presenter bio: Prof. De Santis is an Associate Professor at the University of L'Aquila, Italy. He serves as Secretary of IEEE-ICES-TC95-SC6 and expert member of IEC TC-106. His current research interests include biological effects of electromagnetic fields (EMFs), electromagnetic compatibility (EMC), and compliance assessment of EMF exposures.

pp. 33-35

12:00 ***2006-2026: Two Decades of Innovation with Metamaterial and Metasurfaces for an Array of Applications***

Chinmoy Saha (Indian Institute of Space Science and Technology, India & Royal Military College of Canada, Canada)

Over the past two decades, metamaterials and metasurfaces have revolutionized the field of electromagnetics by enabling unprecedented control over electromagnetic waves through engineered subwavelength structures. This invited talk presents a comprehensive overview of the research contributions in our group from 2006 to 2026, highlighting innovative developments in metamaterial and metasurface-inspired technologies for a wide spectrum of wireless and sensing applications.

The talk will cover the evolution of compact and multifunctional antennas, high-selectivity microwave filters, and advanced metasurface-enabled systems addressing the growing demands of modern wireless communications. Special emphasis will be given to the development of antennas for 4G/5G and beyond systems, cognitive radio platforms with frequency-reconfigurable and spectrum-sensing capabilities, and compact wideband radiators employing artificial electromagnetic structures for enhanced performance. Furthermore, the presentation will discuss recent advances in RF energy harvesting and rectenna technologies, including metasurface-assisted wireless power transfer and ambient energy-scavenging systems aimed at sustainable and self-powered wireless networks.

The talk will also highlight the translation of theoretical concepts into experimentally validated prototypes and practical systems, demonstrating how metamaterials and metasurfaces have evolved from scientific curiosities into enabling technologies for next-generation communication, sensing, and energy applications. Finally, future research directions involving intelligent metasurfaces, integrated wireless power and communication systems, and sub-THz platforms for 6G applications will be outlined.

pp. 36-37

12:15 ***Design of Millimeter Wave Ultra Wideband Solid-State LNA Module Based on Metal Cavity Packaging***

Hui Peng (Kashi University, China); Zhongqian Niu (University of Electronic Science and Technology of China & School of Electronic Science and Engineering, China); Jincai Qiao (Chongqing Institute of Microelectronics Industry Technology, UESTC, China); Ya Fei Wu (UESTC, China); Bo Zhang and Zuqiang Ou (University of Electronic Science and Technology of China, China)

This paper presents a 67-110 GHz low-noise amplifier (LNA) module designed to suppress harmful resonances within a metallic packaging cavity, which can otherwise lead to self-oscillation and performance degradation. By optimizing the cavity dimensions and incorporating specifically designed perturbation structures, the proposed approach effectively eliminates unwanted resonant modes. The viability of the design is experimentally verified, with measurement results confirming stable LNA operation across the full frequency band.

pp. 38-40

W1: Workshop: Recent Advancement in Emerging Materials and Processing Technologies

Room: Michaelmus A

Chairs: Chenhao Chu (ETH Zurich, Switzerland), He Zhu (Charles Darwin University, Australia)

11:30 ***Additive Manufacturing of High-Performance Filters with Unconventional Geometries***

Cristiano Tomassoni (University of Perugia, Italy)

Additive Manufacturing (AM) offers exciting capabilities for microwave engineering, enabling rapid prototyping, geometric flexibility, and easily customizable products. However, applying 3D printing to high-performance filters is not immediate, as these technologies are not originally tailored for high-frequency hardware. To meet strict electrical specifications, specific design adaptations and targeted post-processing steps are often required. This presentation highlights how AM can be effectively leveraged to build advanced microwave filters. Using selected hardware examples, we will discuss some of the most common 3D printing techniques adopted in this field and the practical actions needed to ensure optimal component performance. Finally, the talk will demonstrate how the geometric freedom of AM unlocks unconventional 3D topologies, allowing the development of a new class of filters that are highly optimized in terms of compactness, weight, and insertion losses.

Presenter bio: Cristiano Tomassoni received the Ph.D. degree in electronics engineering from the University of Perugia, Italy, in 1999. Since 2007, he has been an Assistant Professor with the University of Perugia. His main area of research concerns the modeling and design of waveguide devices and antennas. He is a member of the MTT-8 Filters and Passive Components Technical Committee of the IEEE Microwave Theory and Technique Society (MTT-S). Prof. Tomassoni was the recipient of the 2012 Microwave Prize presented by the IEEE Microwave Theory and Technique Society.

pg. 41

11:55 ***Additively Manufactured Microwave Devices and Antennas***

Yang Yang (University of Technology Sydney, Australia)

The race to develop next-generation wireless electronics is accelerating at a rapid pace. Thanks to advanced additive manufacturing technology, fast prototyping, low-entry-cost, and in-house short-run manufacturing empower millions of start-ups and companies with demanding confidentiality and accelerated innovation. We aim to build a new class of high-performance metamaterials and metasurfaces to advance the knowledge for future wireless devices. Compact and low-cost 3D-printed metasurfaces and metamaterials will be delivered to circumvent the limitations of traditional manufacturing technologies. The proposed 3D metadevices should be easily integrated into high-speed wireless systems in a dynamic environment. The cutting-edge additive manufacturing technologies advance 3D Radio frequency circuits with exceptional performance for emerging intelligent and immersive technologies, which will critically impact 5G/6G high-speed wireless devices in the millimetre-wave and terahertz applications. The 3D-printed radio frequency electronics will immediately benefit biomedical engineering, defence, space and telecommunication industries.

Presenter bio: Dr Yang received PhD in Electrical and Computer System Engineering in 2013 from Monash University and currently is working as a research assistant at Monash University Clayton Campus. Dr Yang has published 2 book chapters 5 international journals and 6 international conference papers during the past 4 years. His major reserach interests are microwave and electronics active and passive component and system level designs.

pg. 42

12:20 ***Reconfigurable and Tunable Millimeter-Waves Devices Based on Functional Materials***

Aurelian Crunteanu (XLIM, CNRS/ University of Limoges, France)

The increasing complexity of high-frequency transmission and reception front-ends resulting from the addition of new frequency bands and frequency diversification, requires reconfigurable topologies throughout the

entire telecommunication chain (antennas, phase shifters, filters, amplifiers, etc.) for reducing fabrication costs, system size, and overall power consumption. Most reported reconfiguration solutions in RF circuits are based on the integration of localized tunable devices and commonly rely on semiconductor-based devices, RF-MEMS, liquid crystals or functional materials. We are presenting the performances of a selection of reconfigurable devices (switches, tunable capacitors, agile filters, frequency- and polarization- reconfigurable antennas) designed for millimeter-waves operation and built upon a variety of constituent functional materials with controlled and tuned permittivity or conductivity (ferroelectrics, phase transition and phase change materials). We discuss the requirements for materials integration and emphasize the advantages of specific reconfiguration schemes enabling devices with on-demand agile functionalities.

pg. 43

Wednesday, July 22 12:45 - 2:00

Wednesday, July 22 2:00 - 3:15

S11: Terahertz Technologies and Systems IV

Room: Reef

Chair: Zong-Rui Xu (City University of Hong Kong, Hong Kong)

2:00 ***A Terahertz Scattering-Type Scanning near-Field Optical Microscopy for Single Cell Imaging***

Zhaomin Peng and Jun Shi (National Space Science Center Chinese Academy of Sciences, China); Dehai Zhang (National Space Science Center, China)

Imaging biological cells at sub-terahertz (sub-THz) frequencies is difficult because cellular structures often exhibit weak scattering and low dielectric contrast. We report a 100-GHz scattering-type scanning near-field optical microscopy (s-SNOM) platform designed to improve sensitivity for label-free cellular measurements. The system combines a zero-intermediate frequency (Zero-IF) detection architecture with strong transmitter-receiver isolation and a custom probe with an approximately 100-nm tip radius. As a proof of concept, we image semi-dry SKOV3 ovarian cancer cells on a Au-coated substrate and distinguish two morphological states: a rounded, poorly differentiated state and an elongated state. Measurable near-field contrast is retrieved via first- and second-harmonic demodulation, yielding stable 1st-2nd order near-field signals at 100 GHz.

pg. 44

2:15 ***Terahertz near-Field Scanning Microscopy for Nanoscale Imaging of Ovarian Cancer Cells***

Dehai Zhang (National Space Science Center, China); Zhaomin Peng (National Space Science Center Chinese Academy of Sciences, China); Jin Meng (National Space Science Center, Chinese Academy of Sciences, China)

Terahertz scanning type near-field optical microscopy, as high-resolution imaging platforms with nanometer-scale resolution, have been extensively utilized in materials science, physics, and biological research. Central to this imaging mechanism is the use of nanoscale probe tip vibration to modulate incident electromagnetic waves. By selectively detecting the scattered signals arising from tip-sample interactions and extracting near-field information from both the fundamental vibration frequency components (termed first-order signals) and their harmonic frequency components (e.g., second-order signals or higher-order signals), these systems achieve nanometric spatial resolution.

pg. 45

2:30 ***Research on Beam Steering Rectenna Array for Drone Microwave Wireless Power Supply***

Liwei Song (Xidian University, China)

To address the issue of unstable power supply caused by the difficulty in maintaining continuous beam alignment between transmitting and receiving antennas due to the dynamic changes in drone flight attitude, this study proposes a design for a beam-steering rectenna array. First, a pattern-reconfigurable receiving antenna element was designed by integrating a PIN diode switching network into the antenna parasitic layer. Second, a rectifier circuit suitable for wide input power ranges was designed using a dual-parallel Schottky diode topology. Finally, the designed antenna element and rectifier circuit were integrated into a rectenna element using a bent structure and a shared ground plane via the antenna's metal ground. The impact of the DC bias circuit structure on antenna performance was analyzed, and a 2×2 beam-steering rectenna array was constructed. Test results of the rectenna array at different power transmission distances show that the array can electrically adjust the receiving antenna beam direction. When the array is rotated to the aforementioned three angles, the maximum DC power received is 1.6 W, 1.2 W, and 1.3 W, respectively.

pp. 46-48

2:45 ***Microwave Beam-Steering Using near-Field Metasurfaces***

Maira Islam Nabeel and Karu Esselle (University of Technology Sydney, Australia); Khushboo Singh (University of Technology Sydney, Australia & Macquarie University, Australia); Purna B. Samal and Dush Thalakotuna (University of Technology Sydney, Australia)

Near-field meta-steering (NFMS) antennas have emerged as an effective class of beam-steering antennas for applications such as high-power microwave systems and are increasingly extending into the terahertz domain since their first introduction in 2017. These antennas have gained significant interest in both academia and industry due to their low profile, ease of implementation, and excellent performance. This manuscript presents several emerging implementations of NFMS antennas in high-power microwave and THz applications. As an example case study, a simple one-dimensional beam-steering antenna system is demonstrated to illustrate the operating principle. The proposed antenna employs a short horn feed, whose gain is enhanced by 11 dB while the beam is tilted to 19° using a dual-purpose near-field phase transformation metasurface. The proposed design is capable of steering the beam in the azimuth plane from 0° to 360°.

pp. 49-51

3:00 ***A Single Substrate Pancharatnam-Berry (PB) Phase Huygens' Metasurface for Dynamic Steering of Vortex Beams***

Jiechen Wang (Tianjin University, China); Yuxi Hu (Hebei University of Technology, China); Xiaoxuan Guo and Yang Yang (University of Technology Sydney, Australia)

This article presents a single-substrate Pancharatnam-Berry (PB) phase metasurface capable of dynamically steering vortex beams carrying orbital angular momentum (OAM). Based on the Huygens' resonance principle, the proposed metasurface achieves an overall thickness of only $0.125\lambda_0$ and a maximum transmission coefficient of −0.29 dB at 37.4 GHz. By spatially translating a left-hand circularly polarized (LHCP) patch antenna, high-purity OAM beams with a scanning range of ±10° are realized. The proposed design provides a compact and efficient solution for generating steerable vortex waves, showing significant potential for high-capacity wireless communication and sensing applications.

pp. 52-54

S2: CMOS and BiCMOS Power Amplifiers II

Room: Michaelmus B

2:00 ***Photo-Tunable Chip Scale THz Ring Modulator***

Dingxuan Gu, Xuecou Tu, Yunjie Rui, Bingnan Yan, Zhanzhang Mai, Huilin Zhang, Zeyu Xu, Cheng Liang, Heng Tang and Xiaoqing Jia (Nanjing University, China); Jian Chen (Nanjing University & Research Institute of Superconductor Electronics, China); Lin Kang and Peiheng Wu (Nanjing University, China)

This paper reports a low-loss on-chip optically tunable terahertz (THz) ring modulator (TRM) based on an all-silicon platform. Optical pumping technology enables the device to achieve active tunable resonant response with a minimum through-insertion loss of just 2 dB, dynamically controlling the coupling state from the overcoupled region to the critical region and then to the undercoupled region. At 458.75 GHz, modulation depth reaches 22.7 dB with an optical control speed exceeding 150 kHz, demonstrating practical value for high-speed switching and modulation. These findings represent a significant step forward in THz photonics by introducing a tunable ring resonator that combines electromagnetic field manipulation, reconfigurable coupling states, and on-chip compatibility, opening opportunities for applications in nonlinear optics, microcavity optics, and photonic integrated circuits (PICs).

pp. 55-57

2:15 ***A 110-150 GHz OOK Receiver for High-Speed Wireless Communication in 65-nm CMOS***

Wangmin Liao and Shuang Song (South China University of Technology, China); Taotao Xu (Anhui University, China); Quan Xue and Pei Qin (South China University of Technology, China)

This paper presents a fully integrated 110-150 GHz on-off keying (OOK) receiver implemented in 65-nm CMOS technology. To enable high-speed transmission despite parasitic limitations in the D-band, the proposed design features a wideband low-noise amplifier (LNA) with parasitic-aware layout optimization, a gain-boosted envelope detector (ED), and a bandwidth-extended baseband amplifier. The LNA achieves a peak gain of 20.3 dB with a 3-dB bandwidth of 40 GHz. The complete receiver occupies an area of 0.49 mm^2 and consumes 62.6 mW from a 1.2 V supply. At a carrier frequency of 130 GHz, the receiver supports data rates exceeding 25 Gb/s with an energy efficiency of 2.5 pJ/bit.

pp. 58-60

2:30 ***A 105 dBΩ High Gain, 1.5 mW Low Power Muti-Stage NRZ CMOS-TIA for Optical Receiver Systems***

Umar Mohammad (Nanjing University of Posts and Telecommunications, China)

This work proposes a multistage transimpedance amplifier (TIA) with multiple bandwidth and gain extension techniques. The TIA exhibits a high transimpedance gain of 105 dBΩ, a sensitivity of −8.2 dBm, and a data rate of 20 Gbps for non-return-to-zero (NRZ) scheme. The demonstrated results validate the proposed TIA for high-speed and low-noise intelligent optical communication systems. Bandwidth extension is achieved through techniques such as parasitic shunt capacitance splitting and inductive peaking are applied across various stages. To maximize gain, the TIA incorporates a single-input-to-differential circuit implemented using a simple RL shunt feedback inverter. Additionally, a differential amplifier followed by a buffer circuit contributes an additional gain of 16 dB. The design achieves an input-referred noise current density of 2.5 pA/√Hz and consumes a total power of 1.5 mW. The proposed TIA is implemented in a 65-nm TSMC technology node, operating at a nominal supply voltage of 1.2 V. The complete chip, including I/O pads, occupies a compact area of 1 mm2.

pp. 61-63

2:45 ***An Isolated Ultra-Low Power Modulator for OOK/BPSK Backscatter Communication***

Luchen Shen (Nanjing University of Science and Technology ,Nanjing China & The University of Hong Kong, Hong Kong SAR China); Hao Zhang (Nanjing University of Science and Technology)

To meet the growing ultra-low power demand in backscatter sensing networks, switching modulation (e.g., OOK/BPSK) is widely adopted. Yet existing backscatter modulators confront the challenges of inherent static power consumption with SPDT switches and signal crosstalk. To address these issues, this paper proposes an

ultra-low power modulator employing near-zero static power failsafe SPST switches for backscatter communication supporting OOK and BPSK with the quiescent power lower than 1 μW.

pp. 64-66

3:00 ***A Compact 24-to-30-GHz GaAs Series Doherty Power Amplifier Using a Three-Coupled-Line Balun***

Xin He, Haoshen Zhu, Dingyuan Zeng, Zeqi Liu, Dayan Yuan and Quan Xue (South China University of Technology, China)

This paper presents a millimeter-wave (mm-wave) Doherty power amplifier (PA) monolithic microwave integrated circuit (MMIC) fabricated in a 0.1-μm gallium arsenide (GaAs) process for 5G-NR FR2 applications. To extend bandwidth, a series voltage combining architecture is adopted for output power synthesis. A compact three-coupled-line balun is implemented to realize low-loss differential-to-single-ended combining. In addition, an adaptive bias technique is applied to the peak amplifier output stage to improve AM-AM linearity. The proposed PA operates at 24-30 GHz. Simulation results show a small-signal gain of 13.5 dB and a large-signal gain of 14 dB. The saturated output power is 27.6-28.3 dBm. A peak power-added efficiency (PAE) above 35% is achieved, with PAE exceeding 30% at 6-dB back-off and 25% at 8-dB back-off. The AM-AM distortion is within ±1.2 and the AM-PM variation is less than 18°. The chip area is 2.2 mm × 1.6 mm.

pp. 67-69

S20: Metamaterials and Metasurfaces III

Room: Urchins 2

Chair: Zhichao Sun (University of Technology Sydeny, Australia)

2:00 ***W-Band Wide-Angle Coverage Pillbox Multibeam Antenna Based on Bifocal Phase Compensation***

Yuanxi Cao, Cheng Guo, Jianxing Li, Juan Chen and Sen Yan (Xi'an Jiaotong University, China)

A pillbox beamforming network (BFN) based W-band multibeam antenna is proposed in the paper. The antenna is composed of a BFN, several phase delay lines, and a ridged waveguide (RWG) slot array. The phase delay lines convert the rectangular waveguide output ports of the pillbox BFN to the RWG, thus reducing the element space between the adjacent radiation slots and increasing the beam scanning range. Additional phase compensation is used to optimize the SLL and gain of beams, which is realized by the taper width of the RWG. The simulated results show that the antenna can achieve the beam scanning range of ±45°, and the gain variation of the beam switching is below 2.3 dB.

pp. 70-72

2:15 ***Non-Volatile Reflective Intelligent Surface Based on 2D Material Switches for 6G Wireless Communications***

Xiaoyu Xiao (University of Manchester, United Kingdom (Great Britain)); Zixing Peng (The University of Manchester, United Kingdom (Great Britain)); Xuzhao Liu, Jiaqiu He, Yifan Zhang, Cinzia Casiraghi and Zhirun Hu (University of Manchester, United Kingdom (Great Britain))

Currently reflective intelligent surface (RIS) implementations typically rely on semiconductor switches (e.g., PIN diodes or transistors) hence require continuous biasing, leading to non-negligible static power consumption that scales with the number of unit cells. Here we present an highly energy-efficient, efficient, intelligent surface enabled by non-volatile 2D-material-enabled RF switches. The switch is consisting of sandwiched Ag/MoS_2/Ag structure and exhibits stable non-volatile resistive switching and favorable RF characteristics, enabling two persistent states without DC holding power. By integrating these switches into a 1-bit reflective unit cell, a 6×6 RIS prototype operating at 3.5 GHz is demonstrated with programmable reflection patterns under different coding sequences, validating its capability for beam steering and wavefront control. Furthermore. system-level energy benefit of eliminating static bias power, which becomes increasingly

significant for large-scale RIS and sensing arrays is presented. These results indicate that non-volatile 2D-material switches provide a practical pathway toward low-power pro-grammable metasurfaces for 6G wireless communications.

pp. 73-75

2:30 ***A Curved Broadside-Coupled Stripline Phase Shifter and Its Application to Metasurface Designs***

Jiexin Lai and Xiaojing Lv (University of Technology Sydney, Australia); Zhichao Sun (University of Technology Sydeny, Australia); Yang Yang (University of Technology Sydney, Australia)

In this paper, a metasurface based on a compact curved broadside-coupled stripline (BCS) phase shifter is proposed for gain enhancement applications. The unit cell consists of a receiving antenna, a BCS phase shifter, and a transmitting antenna, all fabricated using standard printed circuit board (PCB) technology. The proposed metasurface exhibits stable radiation performance with a boresight gain of approximately 19 dBi and cross-polarization levels below -20 dB, and a 3-dB gain bandwidth of 18% (25 - 30 GHz).

pp. 76-78

2:45 ***High-Frequency Narrowband to Low-Frequency Broadband Transition in an SMA-Actuated Bandpass Frequency-Selective Surface***

Xiaojing Lv and Zhenlin Dai (University of Technology Sydney, Australia); Zhichao Sun (University of Technology Sydeny, Australia); Zhiwei Yin and Yang Yang (University of Technology Sydney, Australia)

This study presents a thermally actuated, dynamically reconfigurable FSS utilizing laser-cut Ni-Ti SMA elements. By exploiting a bistable SMA architecture, the unit-cell topology is physically reconfigured via temperature-triggered deformation, thereby re-routing the surface current paths without the need for complex voltage-biasing networks or bulky mechanical assemblies. The proposed FSS seamlessly transitions between two distinct spectral states: a highly selective high-frequency narrowband response when the SMA branches are engaged and a broadband response in the lower-frequency regime when the branches are disengaged. Correspondingly, the fractional bandwidth dynamically expands from 5.66% to 51.72%. The underlying electromagnetic mechanisms and bandwidth transition are further elucidated through Babinet's principle and Smith-chart impedance trajectories.

pp. 79-81

3:00 ***Liquid Crystal Tunable Phase Shifter Using Post-Wall Coplanar Waveguide***

Haoyu Zhou and Lei Guo (The University of Queensland, Australia)

A continuously tunable phase shifter based on liquid crystal from 10 GHz to 60 GHz is presented. In this design, most of the waves travel through the LC mixture via a post-wall coplanar waveguide, rather than the traditionally employed inverted microstrip line, maximizing the liquid crystal's tunability. Additionally, the proposed design offers straightforward fabrication and improved mechanical stability compared to the stripline designs. To validate the effectiveness of the proposed design, three delay line phase shifters employing inverted microstrip line, stripline, and post-wall coplanar waveguide are designed and simulated. The results show that, while all the structures have reflection coefficients less than -18 dB, the suggested structure demonstrates figure of merit values between 89.6 Degree/dB and 124.9 Degree/dB, which is, on average, 35 % greater than those attained by stripline designs. The enhanced FoM and decreased fabrication complexity make the proposed structure a promising candidate for applications in millimeter-wave beamforming.

pp. 82-84

W2: Workshop: Recent Advancement in Emerging Materials and Processing Technologies

Room: Michaelmus A

Chairs: Chenhao Chu (ETH Zurich, Switzerland), He Zhu (Charles Darwin University, Australia)

2:00 ***Liquid Metal Enabled Reconfigurable Microwave Devices and Antennas***

Yi Wang (University of Birmingham, United Kingdom (Great Britain))

The terahertz (THz) frequency band (0.1-10 THz) offers immense potential for advanced imaging applications due to its non-ionizing nature, ability to penetrate non-polar materials, and distinctive spectral signatures. A critical component of THz systems is the THz lens, which facilitates high-resolution biosensing, biological imaging, and the detection of concealed details. However, traditional dielectric refractive lenses are bulky, suffer from significant aberrations, and often fail to achieve the high imaging resolution required for emerging applications. To overcome these limitations, metasurfaces have been widely employed in the design of THz metalenses. Metasurfaces provide a compact and versatile alternative to traditional lenses. In this talk, we will present various THz metalens designs, including achromatic metalenses, hyper-dispersive metalenses, and super-oscillatory metalenses, all fabricated using advanced dielectric 3D printing technology. We will also highlight their transformative applications, such as THz super-resolution imaging, axial-scan-free 3D object imaging, and resilient wireless communications. These 3D-printed metalenses, with their unique characteristics, pave the way for next-generation compact, high-resolution, and in vivo THz imaging systems.

Presenter bio: Yi Wang is Professor of Microwave Engineering with the University of Birmingham. He leads the Emerging Device Technology (EDT) Research Lab, specializing in the application of new materials and advanced manufacturing techniques to high frequency devices. He is also the Academic Lead of the Engineering Cleanroom and the Terahertz Measurement Facility at Birmingham. He served the TPC Chair of 2021 European Microwave Conference. His current research interests include: 3D printed microwave and mm-wave devices, waveguide antenna technology, multiport filtering networks, filter-antenna integration, millimeter-wave and sub-terahertz antennas and devices for metrology, communication, and sensing.

pg. 85

2:25 ***3-D Printed Metalenses for Terahertz Imaging***

Geng-Bo Wu (City University of Hong Kong, Hong Kong)

The terahertz (THz) frequency band (0.1-10 THz) offers immense potential for advanced imaging applications due to its non-ionizing nature, ability to penetrate non-polar materials, and distinctive spectral signatures. A critical component of THz systems is the THz lens, which facilitates high-resolution biosensing, biological imaging, and the detection of concealed details. However, traditional dielectric refractive lenses are bulky, suffer from significant aberrations, and often fail to achieve the high imaging resolution required for emerging applications. To overcome these limitations, metasurfaces have been widely employed in the design of THz metalenses. Metasurfaces provide a compact and versatile alternative to traditional lenses. In this talk, we will present various THz metalens designs, including achromatic metalenses, hyper-dispersive metalenses, and super-oscillatory metalenses, all fabricated using advanced dielectric 3D printing technology. We will also highlight their transformative applications, such as THz super-resolution imaging, axial-scan-free 3D object imaging, and resilient wireless communications. These 3D-printed metalenses, with their unique characteristics, pave the way for next-generation compact, high-resolution, and in vivo THz imaging systems.

pg. 86

2:50 ***General-Purpose Terahertz Quasi-Optics and Mechanical Beamformers Enabled by 3D-Printing***

Daniel Headland (The University of Adelaide, Australia)

Owing to their short wavelength and light-like propagation behavior, terahertz waves require quasi-optical components to control the flow of radiation. To meet this need, 3D-printing has evolved over the past decade

from a niche technique to a highly customizable, general-purpose methodology to produce terahertz quasi-optics, using consumer-grade hardware.

pg. 87

Wednesday, July 22 3:45 - 5:00

S12: Biomedical and Wearable Sensing I

Room: Reef

Chair: Shengjian Jammy Chen (Flinders University, Australia & The University of Adelaide, Australia)

3:45 ***Integrated Microwave Photonics for Signal Processing and Sensing***

Xiaoke Yi (University of Sydney, Australia)

The field of microwave photonics has evolved significantly over the last decade, ushered by the breakthroughs in integrated photonics in realizing integrated microwave photonic devices with an array of functionalities packed on a nanoscale footprint. The combination of photonic integration with microwave photonics, enables the realization of reproducible, compact, lightweight, low-power consumption and low-cost microwave photonic systems that are physically and economically competitive against their electronic counterparts. Microwave photonics techniques have attracted dramatically increased attention. In this paper, we present recent advances across three interconnected themes: adaptive RF signal processing, high performance sensing, and photonic neural computing.

We first discuss adaptive microwave photonic interference mitigation for dynamic RF environments. By combining photonic amplitude and phase control, the system can suppress unknown and time-varying interference. Experimental results demonstrate robust recovery of signals of interest under continuous-wave, phase-modulated and multi-interference conditions. We then present machine-learning-enhanced microwave photonic sensing, where integrated photonic sensors convert optical responses into rich RF spectral signatures that can be interpreted by machine/deep learning (ML/DL) models. In our recent work, ML/DL-assisted microwave photonic sensors have enabled athermal operation, noise resilience, multi-parameter detection and extended sensing range. Finally, we discuss our recent photonic neural network accelerators based on inverse-designed nanophotonic structures. The photonic neural network perform classification within ultra-compact silicon photonic devices. The demonstrated photonic neural networks achieve a computational density of approximately 400 million parameters per mm^2, providing a scalable pathway towards energy-efficient analog photonic computing.

pg. 88

4:00 ***A Communication Signal Based Vital-Sign Sensing Method for Consumer Electronic Devices***

Chenming Li, Xingqi Xuan, Junhao Zhang, Yulin Zhou, Shilie Zheng, Xiaonan Hui and Xianmin Zhang (Zhejiang University, China)

In the information society, consumer electronic devices naturally possess wearable and portable characteristics. In light of this, we introduce a vital-sign detecting system for consumer electronic devices that utilizes wireless communication signals. Given the proximity of these devices to the human body, radio frequency energy is directed into a confined internal region, thereby facilitating the modulation of backscattered signals with pronounced bodily vibrations. Consequently, the received signals exhibit variations corresponding to the vital signs. After simply filtering out the high-speed modulated digital information, target signals can be obtained without complicated demodulation. The theoretical framework, numerical computations, and experimental results demonstrate congruence, thereby validating the efficacy of the proposed methodology for achieving stable, long-term monitoring across diverse wearing scenarios. The

average heart rate aligned with the established gold standard, and the root-mean-square error (RMSE) for instantaneous heart rate was 1.02 bpm.

pp. 89-91

4:15 ***Characterization of Knitted Textiles for Wearable Antennas***

David Mitchell (University of Illinois at Urbana-Champaign, USA); Jennifer T. Bernhard (University of Illinois at Urbana-Champaign & Electromagnetics Laboratory, USA)

Textile-integrated antennas have been the subject of much investigation due in part to their easy integration into everyday life. There are several methods that have been established for creating textile-integrated antennas. Two such methods are embroidery and knitting. Both employ the use of existing textile manufacturing methods and conductive threads and yarns. Embroidered antennas have been studied extensively and have made use of high precision, computer controlled embroidery machines (A. Kiourti, C. Lee, and J. L. Volakis, "Fabrication of Textile Antennas and Circuits With 0.1 mm Precision," IEEE Antennas and Wireless Propagation Letters, vol. 15, pp. 151-153, 2016). Knitted antennas, on the other hand, have not been as extensively studied. Some work has been done in characterizing the effective sheet impedance of knitted antennas and transmission lines, however this was only done for a single knit pattern (M. A. S. Tajin, C. E. Amanatides, G. Dion and K. R. Dandekar, "Passive UHF RFID-Based Knitted Wearable Compression Sensor," in IEEE Internet of Things Journal, vol. 8, no. 17, pp. 13763-13773, 1 Sept.1, 2021). A major advantage of knitted textiles is the ability to design and program different mechanical properties of the textile based on the knit pattern (Singal, K., Dimitriyev, M.S., Gonzalez, S.E. et al. "Programming mechanics in knitted materials, stitch by stitch". Nature Communications 15, 2622, 2024). This work will examine and characterize a variety of textiles with differing knit patterns and will attempt to establish a relationship between their mechanical and electrical properties. This will be done using techniques from metasurface design, where a knit stitch will be treated as the unit cell and the bulk surface impedance properties will be extracted from HFSS simulations (A. M. Patel and A. Grbic, "A Printed Leaky-Wave Antenna Based on a Sinusoidally-Modulated Reactance Surface," in IEEE Transactions on Antennas and Propagation, vol. 59, no. 6, pp. 2087-2096, June 2011). Those metasurface simulations will then be used to design a pattern on a textile, which will be manufactured and compared against the simulated results. This research was supported by an appointment to the Intelligence Community Postdoctoral Research Fellowship Program at The University of Illinois Urbana-Champaign administered by Oak Ridge Institute for Science and Education (ORISE) through an interagency agreement between the U.S. Department of Energy and the Office of the Director of National Intelligence (ODNI)

pg. 92

4:30 ***Ultra-Wideband Multi-Channel Millimeter-Wave Receiver for Solar Sensing***

Jun Shi (National Space Science Center Chinese Academy of Sciences, China); Dehai Zhang (National Space Science Center, China); Zhaomin Peng (National Space Science Center Chinese Academy of Sciences, China)

Solar radio emissions provide critical insights into dynamic solar atmospheric processes, including coronal heating, solar eruptions, and solar wind acceleration. We present a high-sensitivity, multi-channel receiver system operating across the 15-36 GHz range, specifically engineered to bridge observational gaps in capturing non-thermal phenomena, such as small-scale microwave bursts in the solar transition region. The system architecture employs low-noise amplifiers (LNAs) in the initial stage to minimize the overall noise figure, followed by multi-band filters and power dividers that split the signal into three primary sub-bands-15-22 GHz, 22-29 GHz, and 29-36 GHz-supporting dual-polarization observations. By integrating frequency down-conversion with high-speed digital spectroscopy, the system achieves the temporal and spectral resolution requisite for characterizing rapid frequency drift and transient burst dynamics in real-time. Currently, the system is deployed at the Lenghu Station on the Qinghai-Tibet Plateau at an altitude of 4,100 meters for pilot observations. Comparative measurements of solar and the cold sky demonstrate that the system possesses high observational sensitivity. This successful deployment validates the system's efficacy for comprehensive

solar monitoring and establishes a robust foundation for future observations aimed at advancing solar physics and space weather research.

pg. 93

4:45 ***PDMS-MWCNT Composite Material Properties, Preparation and Role in Wearable Antennas***

Musa Hussain (Griffith University, Queensland, Australia); Hajra Khan (Comsats University Islamabad Abbottabad Campus, Pakistan); Syed Muzahir Abbas (Macquarie University, Australia)

In this paper, the properties, preparation and applications of PDMS-MWCNT composite is discussed. The main focus of the paper remains on the applications of flexible antennas used in wearable electronic devices. The flow diagram of making of the PDMS and PDMS-MWCNT composite is given. Moreover, the detailed analysis of both materials in terms of scanning electron microscope (SEM) is analyzed. Later, some examples are given from the literature, which shows the role of these materials in the antenna designing applications.

pp. 94-96

S21: Antenna Arrays and Beamforming II

Room: Urchins 2

Chair: Muhammad Ali Babar Abbasi (Queen's University Belfast & Centre for Wireless Innovation (CWI), United Kingdom (Great Britain))

3:45 ***Power-Based Direction-Finding Enabled by a Null-Scanning Space-Time Leaky-Wave Antenna***

Yiqing Sun, Geng-Bo Wu and Chi Hou Chan (City University of Hong Kong, Hong Kong)

This paper presents a power-based direction-finding (DF) scheme based on a space-time leaky-wave antenna (STLWA) with fixed-frequency radiation null scanning capability. The direction of arrival (DoA) can be estimated by identifying the power-minimum angle between two lobes in the spatial power spectrum. To be specific, by programming the 1-bit phase-control unit cells with distinct time-periodic signals, the amplitude of the aperture field at the fundamental frequency can be flexibly controlled. By leveraging space-time modulation, the STLWA provides steerable radiation nulls at the fundamental frequency. DF experiments are conducted to validate the system's performance. The proposed approach offers a compact, phase-shifter-free, fixed-frequency solution for sensing and localization.

Presenter bio: SUN Yiqing received the B.Eng. degree in electronic engineering from Nanjing University of Science and Technology, Nanjing, China, in 2019, and received the M.Sc. degree in electronic science and technology from Beijing Institute of Technology, Beijing, China, in 2022. Currently, she is pursuing the Ph.D. degree in electrical engineering at the City University of Hong Kong (CityU), Hong Kong. Her current research interests include antenna design and spacetime-coding technology

pp. 97-99

4:00 ***Planar EBG Monostatic Antenna with Wideband Interport Isolation Characteristics for 5G in-Band Full Duplex Applications***

Haq Nawaz (Military Technological College, Oman); Hajra Khan (Comsats University Islamabad Abbottabad Campus, Pakistan); Syed Muzahir Abbas (Macquarie University, Australia)

This work presents a dual port, dual polarized shared-aperture (monostatic) based planar antenna with wideband interport isolation characteristics for sub-6 GHz simultaneous transmit and receive (STAR) or in band full duplex (IBFD) wireless applications. The presented compact metasurfaces antenna offers wider impedance bandwidth and excellent interport isolation levels across its entire operating bandwidth. The wideband impedance bandwidth characteristics have been achieved through combination of parasitic feeding and electromagnetic band gap (EBG) radiator excited through proximity feeding from modified four-pointed star shaped driven patch. The high interport isolation levels across entire operational bandwidth of the antenna

have been established through balanced transmit and receive modes operation. The presented EBG antenna with unidirectional radiation characteristics resonates at center operating frequency of 3.75 GHz with -10 dB impedance bandwidth of 1.5 GHz (40%) spanning over 3 GHz to 4.5 GHz. The isolation between transmit and receive ports of presented antenna is better than 62 dB across the entire operating bandwidth of 1.5 GHz. The presented dual port, dual polarized antenna offers superior gain performance for each port excitation attributed to the differential excitation of EBG patch. The proposed unidirectional antenna offers wider impedance bandwidth and high port to port isolation levels across wider impedance bandwidth compared to the earlier reported unidirectional antennas intended for IBFD or STAR applications.

Presenter bio: Syed Muzahir Abbas received his B.Sc. degree in Electrical (Telecommunication) Engineering from COMSATS Institute of Information Technology, Islamabad, Pakistan and his M.Sc. degree in Computer Engineering from the Center for Advanced Studies in Engineering (CASE), Islamabad, Pakistan in 2006 and 2009 respectively. He completed his Ph.D. degree in Electronics Engineering at Macquarie University, Sydney, Australia. He has served as RF Engineer (R & D, Mobility soultions) at Commscope, Australia, and as Transmission Engineer for Alcatel-Lucent Pakistan. He has also served as academic at various universities University of Sydney, Western Sydney University, Macquarie University and COMSATS. His research interests include high impedance surfaces, carbon nanotube (CNT) yarns and the development of antennas for ultra-wideband (UWB) and wireless body area network (WBAN) applications.

pp. 100-102

4:15 ***Low-Profile Broadband Beam-Scanning Antenna***

Shuo Sun (Beijing University of Posts and Telecommunications, China); Xiuping Li (Beijing University of Post and Telecommunications, China); Zihang Qi (Beijing University of Posts and Telecommunications, China); Wenyu Zhao (Beijing University of Posts and Telecommunications, China & EE, China); Jianxun Su (Beijing University of Posts and Telecommunications, China)

This paper presents a low-profile beam-scanning antenna, where the monopole antenna and metasurface are integrated on the same plane for ultra-compact configuration. A 7-mm-tall monopole antenna serves as the feed to excite surface waves (SW), while the metasurface generates Pancharatnam-Berry (PB) phase and propagation (PG) phase to regulate SW radiation. Specifically, the PB phase is fixed as a preset component, and the PG phase features 1-bit reconfigurable phase resolution. The broadband phase responses of both phases endow the antenna with excellent broadband radiation capability. At the boresight direction (0 °), the antenna achieves a 16.6% 3-dB gain bandwidth spanning 10.5-12.4 GHz. Furthermore, two-dimensional beam scanning over a range of ± 60 ° is realized within the operating band, with a scanning loss of less than 3 dB. Owing to its advantages of low profile, high integration, and broadband radiation performance, the proposed design is expected to be a promising candidate for mobile communication applications.

pp. 103-105

4:30 ***Generation of Scanning Self-Accelerating Beam by Manipulating Phase Distribution***

Qing You (University of Macau, Macao); Shi-Tong Wang (City University of Hong Kong, Hong Kong); Pui-In Mak, Rui P. Martins and Jun Yin (University of Macau, Macao)

This paper presents a method for achieving scanning of self-accelerating beams by simply reversing the phase from 0 degree to 180 degree. Building upon conventional approaches, this method leverages both gradient amplitude and abrupt phase profiles, requiring only phase manipulation to achieve beam scanning. A waveguide slot antenna array is designed based on this principle, and simulated results demonstrate its effectiveness and feasibility

pp. 106-108

4:45 ***Compact High-Gain 300 GHz Metasurface Antenna for Future 6G Terahertz Communications***

Mohammad Nasrat Zaqumi, Syed Muzahir Abbas and Subhas Chandra Mukhopadhyay (Macquarie University, Australia)

This paper presents a compact resonant cavity antenna (RCA) enhanced by a single-layer negative-epsilon surface (NEPS) metasurface operating at 300 GHz for terahertz communication systems. The proposed metasurface is composed of periodic circular patch resonators engineered to exhibit a stable reflection magnitude together with an effective negative permittivity (ε<0) around the target frequency. These electromagnetic characteristics enable efficient manipulation of the reflection phase and control of the electromagnetic wave propagation inside the Fabry-Perot cavity. By regulating the reflection phase distribution, the metasurface improves the near-field phase uniformity and promotes constructive interference at the partially reflective aperture, resulting in enhanced radiation collimation and power radiation efficiency. Full-wave numerical simulations demonstrate that the proposed antenna achieves a maximum directivity of approximately 20 dBi with an aperture efficiency of about 40% while maintaining a compact and low-profile structure. The proposed NEPS-assisted RCA provides a promising high-gain antenna platform for terahertz and future 6G communication applications.

Presenter bio: Syed Muzahir Abbas received his B.Sc. degree in Electrical (Telecommunication) Engineering from COMSATS Institute of Information Technology, Islamabad, Pakistan and his M.Sc. degree in Computer Engineering from the Center for Advanced Studies in Engineering (CASE), Islamabad, Pakistan in 2006 and 2009 respectively. He completed his Ph.D. degree in Electronics Engineering at Macquarie University, Sydney, Australia. He has served as RF Engineer (R & D, Mobility soultions) at Commscope, Australia, and as Transmission Engineer for Alcatel-Lucent Pakistan. He has also served as academic at various universities University of Sydney, Western Sydney University, Macquarie University and COMSATS. His research interests include high impedance surfaces, carbon nanotube (CNT) yarns and the development of antennas for ultra-wideband (UWB) and wireless body area network (WBAN) applications.

pp. 109-111

S3: Terahertz Technologies and Systems I

Room: Michaelmus B

Chair: Safumi Suzuki (Institute of Science Tokyo, Japan)

3:45 ***Terahertz Microsystems Front-End Integration Technologies and Communication Application***

Peng Wu (Chinese Academy of Sciences, China & University of Chinese Academy of Sciences, China)

Terahertz wave possesses wide available high frequency spectrum bandwidth and thus has potential applications in high-resolution imaging sensing and high-speed communication. Due to limitations in terahertz integration technologies and MMIC manufacturing processes, terahertz radar and communication systems still face bottlenecks such as low power output, high noise, and difficulties in array integration. The front-end SiP integration is still one of the key terahertz microsystem technologies. In the session, the newly proposed integration solutions, such as the planner transmission line and waveguide interconnection, 3D multilayer module, and multi-channel integration, will be presented, and terahertz SiP arrays will be further introduced for the high-speed communication.

Presenter bio: Peng Wu is a Research Fellow and the Deputy Director of Research Department with Aerospace Information Research Institute, Chinese Academy of Sciences, Beijing, China. At the same time, he is also currently a Professor and PhD supervisor with University of Chinese Academy of Sciences, Beijing, China. He is a member of the Satellite Communication Committee, China Institute of Communications. His current research interests include millimeter-wave/terahertz microsystems and their applications. He has led science and technology innovation projects, e.g., antenna systems for satellite communications, terahertz integration, and reconfigurable radar systems. His research outcomes have been applied in fields such as satellite communication and radar sensing.

pg. 112

4:00 ***Metatronics for High-Performance Terahertz Integrated Circuits***

Mohammad Samizadeh Nikoo (NTU Singapore, Singapore)

Approaching the terahertz band from the electronics side is of great technological importance, with the promise of advancing next-generation wireless communication systems toward 6G and beyond [1]. However, inherent limitations of high-speed transistors, the primary building blocks of monolithically integrated high-

frequency circuits, have hindered the realization of high-performance terahertz electronics [2], [3]. Electrical metastructures offer an alternative paradigm, in which electrical control of the conductivity of a semiconducting layer manipulates collective quasi-electrostatic responses within a device layout, enabling electronic functionalities such as switching, mixing, and parametric amplification. Compared with conventional transistors, electrical metastructures enable ultra-low contact resistances, leading to record-high switching cutoff frequencies beyond 10 THz in a compact device platform, referred to as electronic metadevices [4]-[7]. The first part of this talk highlights recent advances in III-nitride electronic metadevices operating up to 1 THz and introduces a new generation based on quasi-one-dimensional electrical metastructures with enhanced electrical performance [8]. We present theoretical insights into the collective responses governing the operation of electronic metadevices and elucidate their ultimate performance limits. In the second part, we introduce a metastructure-based paradigm for directly realizing high-performance millimeter-wave and terahertz components with ultracompact footprints, demonstrated the compatibility of metatronic devices with commercial silicon processes [9].

References [1] S. Dang, O. Amin, B. Shihada, and M.-S. Alouini, "What should 6G be?" Nat. Electron., vol. 3, pp. 20-29, 2020. [2] K. Sengupta, T. Nagatsuma, and D. M. Mittleman, "Terahertz integrated electronic and hybrid electronic-photonic systems," Nat. Electron., vol. 1, pp. 622-635, 2018. [3] W. Cao, H. Bu, M. Vinet, M. Cao, S. Takagi, S. Hwang, T. Ghani, and K. Banerjee, "The future transistors," Nature, vol. 620, pp. 501-515, 2023. [4] M. Samizadeh Nikoo and E. Matioli, "Electronic metadevices for terahertz applications," Nature, vol. 614, pp. 451-455, 2023. [5] M. Samizadeh Nikoo and H. Wang, "Theoretical foundation of electronic metadevices," IEEE Electron Device Lett., vol. 45, no. 3, pp. 456-459, Aug. 2023. [6] M. Samizadeh Nikoo, C. Chu, B. Lin, Y. Liu, Y. Kim, and H. Wang, "Active and integrated electronic metadevices for future telecommunication circuits," Commun. Eng., vol. 4, Art. no. 49, 2025. [7] A. Abushawish, Z. Huang, and M. Samizadeh Nikoo, "Strong collective responses in quasi-1D metadevices for millimeter-wave electronics," IEEE J. of Microw., Early Access, 2026. [8] A. Abushawish, Z. Huang, and M. Samizadeh Nikoo, "Quasi-1D Electronic Metadevices With Enhanced Electrical Properties," IEEE Electron Device Lett., vol. 46, no. 11, pp. 2169- 2172, Nov. 2025. [9] M. Samizadeh Nikoo, M. Eleraky, B. A. Abdelmagid, D. Lee, F. Jazaeri, A. Wang, B. Lin, and H. Wang, "High-power millimetre-wave switches on silicon using displacement fields and tunnelling currents," Nat. Electron., vol. 9, pp. 84-92, 2026.

4:15 ***Design of a High-Performance Terahertz Multiplier Based on Thin-Film Technology***

Li Wang (National Space Science Center, China); Jin Meng (National Space Science Center, Chinese Academy of Sciences, China); Dehai Zhang (National Space Science Center, China)

This paper presents a high-performance 510 GHz monolithic GaAs Schottky barrier diode (SBD) frequency tripler for terahertz local oscillator (LO) applications. As the operating frequency extends into the sub-millimeter-wave regime, traditional multipliers are often limited by inaccurate parasitic modeling and significant substrate-induced dielectric losses. To address the parasitic modeling issue, a deterministic two-port, four-structure parasitic extraction method is proposed. Compared with conventional equivalent-circuit modeling or empirical fitting methods, it enables clearer separation of extrinsic parasitics and supports more accurate parasitic modeling and Schottky diode structure optimization. Four specifically designed test structures-Single Pad (SP), Pin-Open (PO), Diode-Short (DS), and Diode-Open (DO)-are employed to systematically extract pad-related parasitics (Lpad, Cpad), finger-related components (Lf, Rf), and inter-electrode coupling effects (Cpp). By de-embedding these extrinsic parasitics from Y-parameters, a more accurate parasitic model of the SBD can be established, which helps reduce the adverse impact of overall parasitic effects on multiplier performance and provides a basis for optimizing the Schottky diode structure. The tripler is implemented using a 3-μm-thick GaAs membrane process with backside substrate etching, which removes the bulk GaAs to form a thin-film structure and effectively reduces substrate-induced dielectric loss and suppresses parasitic substrate modes at 510 GHz. A balanced topology is also adopted to suppress even-order harmonics. Experimental characterization was performed using a frequency multiplier chain and an

Erickson power meter. The fabricated MMIC demonstrates robust performance across the 490-530 GHz band. Under an input drive power ranging from 63 to 104 mW, the tripler achieves a peak output power of 3.72 mW at 508 GHz, with a maximum conversion efficiency of 4.2%. Milliwatt-level output power is maintained across the entire measured bandwidth, although the upper end of the band approaches the operating limit of the test equipment. These results demonstrate that the proposed four-structure extraction method and 3-μm thin-film technology together provide an effective means of improving the output performance of terahertz frequency triplers.

pg. 114

4:30 ***Design and Analysis of Circular Hollow Polymer Waveguide at THz Frequency Band***

Shengjie Zhou (Shanghai Jiaotong University, China); Changsheng Sun, Xiaochun LI and Junfa Mao (Shanghai Jiao Tong University, China)

This paper presents the design and analysis of a circular hollow polymer waveguide (CHPW) operating at W-band (75-110 GHz). The proposed structure consists of an air core surrounded by a polymer cladding, which effectively reduces dielectric loss compared to solid polymer waveguides. Mode analysis reveals that the designed CHPW supports single-mode propagation throughout the entire W-band, with the fundamental HE11 mode and higher-order TM01 mode identified. Parametric studies show that increasing the inner radius or polymer thickness raises both the phase and attenuation constants, with polymer thickness exhibiting a more significant influence. Material comparison indicates that PTFE offers lower loss and wider single-mode bandwidth than HDPE and PMMA, making it a promising candidate for terahertz (THz) applications. Compared with circular solid polymer waveguides (CSPW), the CHPW demonstrates lower attenuation and broader single-mode bandwidth but suffers from weaker field confinement. This work provides a useful guidance for the development of polymer waveguides at THz frequencies.

pp. 115-117

4:45 ***Hybrid Modeling Method of FT-Transformer and XGBoost for TFsurface***

Yihao Li (Nanjing University of Science and Technology. China); Shijie Wang (National University of Singapore, Singapore); Wen Lyu (Nanjing University of Science and Technology, China)

Terahertz field-effect transistors integrated with metasurfaces (TFsurfaces) hold significant promise for high-sensitivity chemical detection and imaging. However, optimizing the asymmetric interdigitated grating gate (AIGG) structure remains challenging due to complex near-field coupling effects and a high-dimensional parameter space spanning periodicity, gate number, asymmetry coefficient, and structural dimensions. Conventional empirical design methods are inefficient and struggle to globally optimize these detectors. This paper proposes a hybrid intelligent modeling framework that combines a Feature Tokenizer Transformer (FT-Transformer) with Extreme Gradient Boosting (XGBoost) to accurately predict the electromagnetic spectral response of TFsurfaces from structural parameters. Structure-frequency joint inputs are encoded by the FT-Transformer to capture complex nonlinear feature interactions; the resulting deep embeddings are then concatenated with original structural parameters and fed into XGBoost for regression. Evaluated on an independent test set, the proposed model achieves an (R^{2}) of 0.9985 and an MSE of (1.8 \times 10^{-5}), outperforming single-model baselines. This data-driven framework significantly accelerates the design of high-sensitivity THz detectors and offers a scalable solution for complex metasurface optimization.

pp. 118-120

W3: Workshop: Recent Advancement in Emerging Materials and Processing Technologies

Room: Michaelmus A

Chairs: Chenhao Chu (ETH Zurich, Switzerland), He Zhu (Charles Darwin University, Australia)

3:45 ***High-Tc Superconducting Monolithic Microwave Integrated Circuits (MMICs) for High-Sensitivity RF Receivers***

He Zhu (Charles Darwin University, Australia)

High-temperature superconducting (HTS) technologies have many potential applications, such as power transmission, medical imaging, quantum computing, military and aerospace, etc., due to their significant advantages of high energy efficiency, easy cooling as well as high reliability and stability. High-temperature superconducting technologies also play a critical role in wireless communications as they offer unique advantages for applications in high-frequency electromagnetic domains. High-sensitivity and broadband nature of superconducting devices can be applied for high-speed wireless communication systems, especially the heterodyne mixers are highly desirable for high-gain and low-noise RF receivers. This talk will introduce a series of monolithic microwave integrated circuits (MMICs), mainly heterodyne mixers and on-chip antennas, which are used in microwave and millimeter-wave RF receivers. The MMIC mixers are developed based on the quantum tunnelling effect of Josephson junctions and will significantly reduce power consumption and enhance the sensitivity of RF receivers. Besides, advanced antenna technologies, including the packaging techniques of a high-gain waveguide antenna with MMICs and a frequency-scanning leaky-wave antenna, will also be touched in this talk.

Presenter bio: He Zhu is a currently a Lecturer in Charles Darwin University, Australia. He served as a Research Scientist in the Electromagnetic Systems and Devices Group of CSIRO, Australia, from 2023 to April 2026. He was a Postdoctoral Research Fellow and then a Chancellor's Research Fellow with the Global Big Data Technologies Centre at the University of Technology Sydney from 2017 to 2023. Dr Zhu is now a Senior Member of IEEE and serving as an Associate Editor for Microwave and Optical Technology Letter (MOTL) and a reviewer for multiple prestigious journals.

pg. 121

4:10 ***Multi-Function Multi-Band Reconfigurable High-Q Filters***

Raafat R. Mansour (University of Waterloo, Canada)

Reconfigurable filters are key components in the development of agile multi-standard receivers.. This talk starts by addressing the needs for using multi-band and tunable filters in wireless communication systems and in flexible satellite payloads. It then addresses existing tuning technologies, providing a comparison between piezoelectric, Semiconductor, MEMS and PCM tuning elements in terms of linearity, insertion loss, suitability for use at millimeter-wave frequencies and ease of integration with high-Q filters. It outlines major design considerations for tunable filters presenting techniques to realize tunable filters with an absolute constant absolute bandwidth and a constant frequency spacing between transmission zeros, over a wide tuning range. The talk also illustrates examples of tunable filters and diplexers tuned only a by single tuning element, while exhibiting a constant absolute bandwidth. It then addresses approaches for realizing multi-band filters including dual-band and triple-band filters. Finally, it presents techniques for realizing multi-band filters where the various bands are tunable in both center frequency and bandwidth. Very recent work on realizing reconfigurable acoustic filters is also presented.

Presenter bio: Raafat Mansour is a Professor of Electrical and Computer Engineering at the University of Waterloo and holds Tier 1 - Canada Research Chair (CRC) in Micro-Nano Integrated RF Systems. He held an NSERC Industrial Research Chair (IRC) for two terms (2001-2005) and (2006-2010). Prior to joining the University of Waterloo in January 2000, Dr. Mansour was with COM DEV Cambridge, Ontario, over the period 1986-1999, where he held various technical and management positions in COM DEV's Corporate R&D Department. Professor Mansour holds 43 US and Canadian patents and more than 420 refereed IEEE publications to his credit. He is a co-author of a 23-chapter Book published by Wiley and has contributed 7 chapters to five other books. Professor Mansour founded the Centre for Integrated RF Engineering (CIRFE) at the University of Waterloo. It houses a clean room and a state-of-the-art RF test and characterization laboratory. He was as the Technical Program Chair of the 2012 IEEE International Microwave Symposium (IMS). Professor Mansour is a Fellow of the IEEE, a Fellow of the Canadian Academy of Engineering (CAE).

pg. 122

Wednesday, July 22 5:00 - 6:30

Welcome Reception @ Roof Top Pool Deck

Room: Michaelmus A, Michaelmus B, Reef, Urchins 2

Thursday, July 23

Thursday, July 23 9:00 - 9:45

K2: Keynote: Reconfigurable Microwave and Millimeter-Wave Devices Enabled by Phase-Change Materials, BST and Liquid Crystal Technologies - Raafat Mansour

Raafat Mansour
Room: Michaelmus A
Chair: Yang Yang (University of Technology Sydney, Australia)
The ability to dynamically reconfigure RF front ends allows a single hardware platform to accommodate multiple operating bands, communication protocols, adaptive beamforming, and efficient spectrum utilization. This multifunctional approach minimizes hardware complexity while reducing size, weight, power, and cost. The successful implementation of such systems depends on the availability of advanced switching and tuning technologies. The presentation will address the applications of Phase Change Material (PCM) switches to the realization of switch matrices, phase shifters, variable attenuators, and reflective intelligent surfaces (RISs). The presentation will further highlight the complementary capabilities of barium strontium titanate (BST) and liquid crystal (LC) technologies for realizing continuously tunable microwave and millimeter-wave components. Recent results on chip-scale millimeter-wave phase shifters employing BST and LC will be presented, illustrating how these technologies provide low-power analog tuning that complements the discrete, non-volatile reconfiguration offered by the PCM technology.

Thursday, July 23 9:45 - 10:45

P3: Semi-Plenary 3

Room: Michaelmus A
Chair: Amir Ebrahimi (RMIT University, Australia)

9:45 ***Semiconductor Electronics for High Power/High Speed Reconfigurable RF and Microwave Electronics***
Robert Caverly (Villanova University, USA)
Microwave and RF design engineers always seek to develop a design that will meet specifications the first time that the circuit is fabricated. To do so requires that as many elements and phenomenon as possible associated with the control devices and circuit be accurately modeled. In the case of the microwave and RF semiconductor control circuits, accurate modeling of the solid-state control components over frequency, voltage, current and power is key to successful control system design. This talk will cover material that will provide the RF and microwave design engineer insight into the physical operation and modeling of semiconductor devices for high-speed reconfigurability: PIN diodes and field-effect transistors (FETs) as control components and their use in microwave and RF control circuits. The talk will briefly cover basic RF and microwave control circuits for reconfigurable electronics, and then focus on linear and nonlinear models for PIN diode, MESFET and MOSFET control elements to implement these circuits. The talk will conclude with control circuit examples using these models for use in reconfigurable RF and microwave electronics.

Presenter bio: Dr. Robert H. Caverly received his Ph.D. degree in electrical engineering from The Johns Hopkins University, Baltimore, MD, in 1983. He is currently with the Department of Electrical and Computer Engineering since 1997 and is a Professor Emeritus. r. Caverly's research interests are focused on the characterization of semiconductor devices such as PIN diodes and FETs in the microwave and RF control environment for communication and biomedical applications. He has published more than 200 journal, conference and editorial papers, and is the author of the books Microwave and RF Semiconductor Control Device Modeling and CMOS RFIC Design Principles, both from Artech House. An IEEE Life Fellow, Dr. Caverly is currently the Editor in Chief of the IEEE Microwave Magazine.

pg. 123

10:15 ***Filters for Space Applications: CNC Milling and Additive Manufacturing Perspectives***

Cristiano Tomassoni (University of Perugia, Italy)

High-performance waveguide filters are critical components in space communications, where mass reduction and signal integrity are paramount. This presentation explores the design and realization of these devices, comparing traditional high-precision CNC milling with emerging Additive Manufacturing techniques. By evaluating experimental results, we analyze how different fabrication perspectives influence design flexibility, surface roughness, and overall RF performance in demanding space environments.

Presenter bio: Cristiano Tomassoni received the Ph.D. degree in electronics engineering from the University of Perugia, Italy, in 1999. Since 2007, he has been an Assistant Professor with the University of Perugia. His main area of research concerns the modeling and design of waveguide devices and antennas. He is a member of the MTT-8 Filters and Passive Components Technical Committee of the IEEE Microwave Theory and Technique Society (MTT-S). Prof. Tomassoni was the recipient of the 2012 Microwave Prize presented by the IEEE Microwave Theory and Technique Society.

pg. 124

P4: Semi-Plenary 4

Room: Michaelmus B

Chair: He Zhu (Charles Darwin University, Australia)

9:45 ***A Review of Microwave Beam-Steering Using near-Field Metasurfaces***

Karu Esselle (University of Technology Sydney, Australia)

Since its seminal publication in 2017, The Near Field Meta-Steering (NFMS) technology, which is also known as Near-Field Phase Transformation or Risley Prism Method, has become popular worldwide to find solutions to beam-steering challenges from microwaves through millimeter-wave to Terahertz, in both academia and industry. Especially it has significant advantages over alternatives at millimeter-wave, sub-Terahertz and Terahertz frequencies in which alternative methods for steering narrow beams have significant challenges. Another advantage is its very high radio-frequency efficiency relative to alternatives when steering high power microwave beams. This invited semi-plenary speech will review the progress of this technology since its invention, and outline what can be expected in the future.

pg. 125

10:15 ***Printable Nonlinear Tags and Handheld Devices for Clutter-Resilient Contactless Monitoring and Tracking***

Changzhi Li and Leya Zeng (Texas Tech University, USA)

This talk presents the development of printable nonlinear passive tags and portable harmonic radar systems for clutter-resilient contactless monitoring and tracking across object localization and biomedical sensing applications. The research integrates compact nonlinear tag design, scalable fabrication strategies, and high-linearity harmonic radar architectures operating at 4-8 GHz and 8-16 GHz. By exploiting second-order harmonic generation from passive diode-based tags, the system selectively detects nonlinear responses while inherently rejecting linear environmental reflections, enabling reliable operation in electromagnetically complex and motion-rich environments.

At the tag level, lightweight, battery-less nonlinear transponders were designed using Schottky diodes embedded within dipole-based and multi-element antenna geometries optimized for harmonic radiation. Early prototypes were fabricated using laser-cut masks and conductive coatings, enabling rapid, low-cost implementation of passive tags capable of meter-scale detection without onboard power. Multi-element configurations increased effective aperture and enhanced harmonic signal strength, significantly improving signal-to-noise ratio. Subsequent implementations advanced toward inkjet-printed and materials-dispensed structures on flexible substrates such as paper and PET, producing compact millimeter-scale tags suitable for conformal attachment to curved surfaces, including the human chest. Full-wave electromagnetic simulations were employed to optimize impedance matching, radiation characteristics, and antenna-diode integration at both fundamental and harmonic frequencies, ensuring efficient nonlinear conversion and stable backscatter performance.

At the system level, two harmonic radar platforms were developed. The 4-8 GHz harmonic radar system transmits a 4 GHz fundamental tone and receives the 8 GHz second harmonic generated by the nonlinear tag. The architecture incorporates frequency multiplication, cascaded filtering, and carefully distributed amplification stages to maintain transmit-receive isolation and suppress harmonic leakage. The 8-16 GHz harmonic radar system follows the same nonlinear detection principle, transmitting at 8 GHz and receiving at 16 GHz. Implemented on a multilayer PCB platform, this configuration employs high-linearity gain stages, low-pass and high-pass filtering networks, and coherent down-conversion to baseband for signal processing. Both systems operate in continuous-wave mode and emphasize spectral purity and harmonic isolation to ensure robust detection of weak nonlinear returns.

For biomedical applications, battery-free wearable tags attached beneath clothing enabled accurate, noninvasive respiratory monitoring with strong agreement with ground-truth measurements, even in the presence of nearby moving subjects and high radar cross-section reflectors. Beyond healthcare, the same nonlinear tagging principle supports lightweight object localization and tracking without onboard power.

Collectively, this presentation establishes a scalable framework that combines printable nonlinear tags with compact harmonic radar devices, enabling selective clutter-resilient detection for healthcare monitoring, asset tracking, search applications, and emerging nonlinear IoT sensing systems.

Presenter bio: Changzhi Li received the B.S. degree in electrical engineering from Zhejiang University, China, in 2004, and the Ph.D. degree in electrical engineering from the University of Florida, Gainesville, FL, in 2009. He is a Professor at Texas Tech University. His research interest is microwave/millimeter-wave sensing for healthcare, security, energy efficiency, structural monitoring, and human-machine interface. Dr. Li is an IEEE Microwave Theory and Techniques Society (MTT-S) Distinguished Microwave Lecturer, in the Tatsuo Itoh class of 2022-2024. He was a recipient of the IEEE MTT-S Outstanding Young Engineer Award, the IEEE Sensors Council Early Career Technical Achievement Award, the ASEE Frederick Emmons Terman Award, the IEEE-HKN Outstanding Young Professional Award, and the NSF Faculty Early CAREER Award. He is a Fellow of the National Academy of Inventors.

pg. 126

Thursday, July 23 11:15 - 12:30

BPC: Ask Us Anything

Broadening Participation Committee: Ask Us Anything
Room: Michaelmus A
Chair: Sulekha Chattopadhyay (Chattopadhyay, USA)

S13: Metamaterials and Metasurfaces II

Room: Reef
Chair: Geng-Bo Wu (City University of Hong Kong, Hong Kong)

11:15 ***Terminating Magnetostatic Surface Waves with Metallic Patterns***

Zequn Zeng (National University of Singapore, Singapore); Si-Ping Gao (Nanjing University of Aeronautics and Astronautics, China); Yongxin Guo (City University of Hong Kong, Hong Kong)

Magnetostatic surface waves (MSSWs) have been widely utilized in microwave ferrite devices due to their nonreciprocal propagation and ease of excitation. Conventional MSSW-based devices typically employ a single propagation channel. However, as microwave ferrite devices move toward higher integration density and multi-channel operation, unwanted reflections within a single MSSW channel and coupling between adjacent channels can lead to signal interference and performance degradation. Therefore, effective suppression of MSSW reflections and isolation between channels become crucial. In this paper, MSSW termination using metallic patterns is proposed to achieve both reflection suppression and inter-channel isolation. The termination mechanism is analyzed based on the dispersion relation of MSSWs. Bowtie- and zigzag-shaped metallic patterns are introduced to redirect waves and achieve MSSW termination. A test device incorporating two MSSW channels is designed and fabricated for validation. Measurement results confirm that the proposed structures effectively suppress reflections within a channel and reduce coupling between adjacent MSSW channels.

pp. 127-129

11:30 ***Ultra-Wideband Energy Selective Surface Based on Symmetrical Bow-Tie Topology for High-Power Electromagnetic Protection***

Tianyu Shi, Shaobin Liu and Meng Xing (Nanjing University of Aeronautics and Astronautics, China)

This paper presents an ultra-wideband (UWB) millimeter-wave energy selective surface (ESS) designed for adaptive electromagnetic protection in complex environments. The core innovation lies in the utilization of a symmetrical bow-tie topology that achieves an exceptionally broad transmission window. By loading adaptive GaAs PIN diodes at the center of the resonators, the surface dynamically reconfigures its impedance based on the incident power level. Simulation results demonstrate that the ESS provides a low-insertion-loss (IL < 1 dB) transparent window from 4 GHz to 16.7 GHz. Under high-power microwave (HPM) incidence, the surface provides robust shielding effectiveness (SE) exceeding 10 dB from 4 GHz to 12 GHz. The proposed ESS effectively balances the requirements of wideband communication and high-intensity interference mitigation.

pp. 130-132

11:45 ***Reflection-Type TTD Phase Shifter Based on Propagation-Controlled Reflective Loading***

Yang Xu (University of Technology Sydney, Australia); He Zhu (Charles Darwin University, Australia); Yang Yang (University of Technology Sydney, Australia)

This paper presents a reflection-type true time-delay (TTD) phase shifter based on propagation-controlled reflective loading, combining the compactness of conventional reflection-type phase shifters with frequency-linear phase response. By switching the electrical length of short-circuited reflective transmission lines, the proposed architecture achieves a constant group delay, satisfying the fundamental TTD condition. Simulated results across 3GHz-8 GHz demonstrate maximum phase range exceeding 360 deg, group delay variation within 20 ps, insertion loss below 0.3 dB, and return loss exceeding 10 dB.

Presenter bio: He Zhu is a currently a Lecturer in Charles Darwin University, Australia. He served as a Research Scientist in the Electromagnetic Systems and Devices Group of CSIRO, Australia, from 2023 to April 2026. He was a Postdoctoral Research Fellow and then a Chancellor's Research Fellow with the Global Big Data Technologies Centre at the University of Technology Sydney from 2017 to 2023. Dr Zhu is now a Senior Member of IEEE and serving as an Associate Editor for Microwave and Optical Technology Letter (MOTL) and a reviewer for multiple prestigious journals.

Presenter bio: Dr Yang received PhD in Electrical and Computer System Engineering in 2013 from Monash University and currently is working as a research assistant at Monash University Clayton Campus. Dr Yang has published 2 book chapters 5 international journals and 6 international conference papers during the past 4 years. His major reserach interests are microwave and electronics active and passive component and system level designs.

pg. 133

12:00 ***A Wideband Ultra-Large-Angle Dual-Polarized Bandpass Frequency Selective Surface***

Jiaxin Wang and Xin Xiu (South China University of Technology, China); Ye Han (Nanjing University of Posts and Telecommunications, China); Bao Wang (AVIC Research Institute for Special Structures of Aeronautical Composites, China); Mengzhu Yan and Wenquan Che (South China University of Technology, China)

This work proposes a wideband dual-polarized bandpass frequency selective surface (FSS) with ultra-large-angle stability for application scenarios under large-angle incidence. To overcome the inherent TE-TM wave impedance mismatch at large incident angles, a polarization-decoupling design methodology is employed. Based on this strategy, individual TE- and TM-polarized FSSs are developed, featuring stable wideband performance across 0-75° incidence and low cross-polarization interference. The desired dual-polarized FSS is then obtained by orthogonally combining the two types of FSSs, and further dimensional adjustment ensures an excellent polarization consistency in both transmission magnitude and phase. Simulation results show that across 45-75° incidence, the proposed FSS achieves a dual-polarization −3-dB passband of 7-13 GHz (60%), with a transmission phase difference of less than 25° between TE and TM polarizations. These simulations effectively validate the feasibility and superiority of the proposed design strategy.

pp. 134-136

12:15 ***Design of 3-D Frequency Selective Surface Based on Spatial Coupling***

Jun Ma, Kai-Ran Xiang, Zhihong Tu and Fu-Chang Chen (South China University of Technology, China)

In this paper, spatial coupling is introduced in the design of a three-dimensional (3-D) bandpass frequency selective surface (FSS). The 3-D configuration naturally establishes additional spatial coupling paths among the ports and resonators. As a result, both the source and load are coupled to each resonator as well as to each other, allowing an N-th-order FSS to generate N transmission zeros (TZs). This behavior enhances the TZ generation capability compared with conventional filter synthesis theory. To demonstrate this concept, a third-order 3-D FSS is designed, which exhibits three TZs. The resonant elements are realized using microstrip resonators, leading to a compact implementation with structural simplicity. The simulated results confirm the feasibility of incorporating spatial coupling into the design of 3-D bandpass FSSs

Presenter bio: Jun Ma was born in Shuangyashan, Heilongjiang, China. He received the B.S. degree from the South China University of Technology, Guangzhou, China, in 2022, where he is currently pursuing the Ph.D. degree with the School of Electronic and Information Engineering.His research interests include the synthesis theory, reflectionless antenna, and filtering antenna.

pp. 137-139

S22: Antenna Arrays and Beamforming I

Room: Urchins 2

Chairs: Xiaoxuan Guo (University of Technology Sydney, Australia), Qing You (University of Macau, Macao)

11:15 ***Invited Talk: Plasma-Based Reconfigurable FSS for Adaptive High-Power Microwave Shielding***

Krushna Kanth Varikuntla (Queen's University Belfast, United Kingdom (Great Britain) & Queens's University Belfast, United Kingdom (Great Britain)); Okan Yurduseven (Queen's University Belfast, United Kingdom (Great Britain)); Muhammad Ali Babar Abbasi (Queen's University Belfast & Centre for Wireless Innovation (CWI), United Kingdom (Great Britain))

This invited talk provides a focused overview of plasma-based reconfigurable frequency selective surfaces (FSS) for adaptive high-power microwave (HPM) shielding. Unlike conventional metallic FSS, plasma elements exhibit inherently power-dependent behaviour, enabling self-actuated reconfiguration without dedicated DC bias networks. We outline how plasma confined in commercially available gas-discharge tubes (GDTs) can be modelled as a dispersive medium, and highlight the key design levers: collision frequency primarily governs

loss and reflectivity (with reduced pressure improving selectivity), while electron density drives tunability toward a highly conductive state.

Building on these fundamentals, two experimentally validated FSS architectures are presented, supported by equivalent-circuit modelling and full-wave simulations. A double-layer GDT-loaded FSS provides a wide, flat-top bandpass centred at 4 GHz with low insertion loss in the low-power state, then transitions to strong isolation at high power due to resonance-driven field enhancement and plasma ignition. A second, cross-topology energy-selective surface autonomously shifts its stopband from 6 GHz (OFF) to 3 GHz (ON) without external bias. Waveguide measurements up to 50 dBm confirm robust high-power handling, alongside stable performance under oblique incidence and pressure-dependent quality factor. These results position plasma-FSS as a practical route to adaptive electromagnetic protection for satellite and aeronautical platforms, telecom infrastructure, and high-power medical and industrial environments.

pg. 140

11:30 ***A Reconfigurable Transmit-Reflect-Array Antenna Based on Tightly Coupled Dipole***

Shangsen Huang, Wei Hu, Yuchen Gao and Zhaoling Wang (Xidian University, China)

This paper presents a reconfigurable tightly coupled transmit-reflect-array (TRA) antenna for broadband wireless communication applications. The antenna features an active unit cell comprising tightly coupled dipole elements interconnected by PIN diodes and a polarizer grid for polarization selection, facilitating 1-bit phase reconfiguration. The reflection layer operates in reflection mode for x-polarized waves, while the transmission layer operates in transmission mode for y-polarized waves. By employing different coding sequences to control the ON and OFF states of the PIN diodes, the reflection and transmission phases can be precisely configured, enabling accurate independent beam steering at desired angles. With an F/D ratio of 0.8 and a 16×16 element array, the antenna achieves high gain and low sidelobe levels for both polarization modes. This reconfigurable TRA antenna is ideally suited for advanced wireless communication systems requiring simultaneous dual-mode operation.

Presenter bio: Wei Hu received the Ph.D. degree in electromagnetic fields and microwave technology from Xidian University, China, in 2013. From 2018 to 2019, he was an Academic Visitor with the School of Engineering from the University of Kent, U.K. He is currently a Full Professor with the National Key Laboratory of Radar Detection and Sensing, Xidian University. His research interests include broadband/multiband antennas, terminal antennas, conformal arrays, and wideband wide-scanning phased arrays.

pp. 141-143

11:45 ***Reconfigurable Bandpass Ultrathin Angular-Selective Surfaces***

Hao Jiang (City University of Hong Kong, Hong Kong); Mei Qian (South China University of Technology, China)

This work proposes an ultrathin bandpass angularselective surface (ASS). Unlike most previously reported structures relying on multilayer configurations, the proposed design employs a metallic pattern printed on a single substrate, resulting in a significantly reduced profile. The operating mechanism is interpreted using an equivalent circuit model in which the incident angle is treated as the independent variable to realize the desired angular-domain bandpass response. Full-wave simulations demonstrate that the passive ASS achieves angularselective filtering over a wide incidence range within the operating band. Moreover, a reconfigurable ASS is realized by integrating PIN diodes into the metallic-slot structure, enabling dynamic switching between bandpass and stopband states.

Presenter bio: Hao Jiang (Graduate Student Member, IEEE) was born in Macheng, Hubei, China. He received his M.S. degree from the University of Electronic Science and Technology of China (UESTC), Chengdu, China, in 2021. Since 2022, he has been pursuing his Ph.D. degree at the South China University of Technology (SCUT), Guangzhou, China. Since 2025, he has been a Visiting Ph.D. Student at the National University of Singapore (NUS), Singapore. He has authored or co-authored over 30 peer-reviewed journal and conference papers. His research interests

include RF front-end circuits and systems, satellite communication (SATCOM) phased-array transceivers, and metamaterials. Mr. Jiang served as an IEEE MTT-S Student Ambassador in 2023. He has received numerous awards and scholarships, including the Honorable Mention Award at the 2022 IEEE MTT-S IMWS-AMP, the First Prize in the Best Student Paper Award at the IEEE RFIT 2024, three consecutive recipients of the Chinese National Scholarship for Doctoral Students (from 2023 to 2025), three consecutive recipients of the SCUT Principal Scholarships (from 2023 to 2025), an IEEE MTT-S Graduate Fellowship for 2025, and the Best Applied Antenna Technology Paper

pp. 144-146

12:00 ***Modal Expansion Analysis and Inverse-Design of Reconfigurable AIS-Loaded Antennas***

Mengyuan Bie and Zhi Hao Jiang (Southeast University, China)

This paper presents two reconfigurable antennas loaded with anisotropic impedance surfaces. The first one achieves reconfigurable frequency and bandwidth with a 76.6% tuning range in the narrowband mode and 82.9% bandwidth in the wideband mode. The second antenna features 360° beam scanning with a step of 11.25° in the S-band. A semi-analytical mode expansion method is developed for the inverse-design of these two antennas by predicting accurate impedance bandwidth and radiation patterns.

pg. 147

12:15 ***A Data-Efficient and Physics-Constrained Deep Learning Framework for Reflectarray Antenna Inverse Design***

Qinghua Liu and Xue Ren (Shenzhen University, China)

A physics-guided Conditional Variational Autoencoder (cVAE) framework for the rapid inverse design of high-aperture-efficiency reflectarray antennas is proposed in this paper. Addressing the ill-posed nature of mapping electromagnetic responses to complex topologies, we incorporate structural symmetry, manufacturability constraints, and morphological filtering as prior rules to regularize the unit topology and enhance dataset quality. A high-precision Residual Network (ResNet), is embedded into the cVAE loop to enforce physical consistency, is trained as a forward proxy to replace time-consuming full-wave simulations. In this way, model efficiency enhancement is achieved through the regularized unit design, while antenna efficiency is ensured by the accurate proxy-constrained generative model. To validate the method, an 18×18 element reflectarray operating at 10 GHz is designed. Full-wave simulations demonstrate a realized gain of 23.9 dB, a sidelobe level of −19.6 dB, and an aperture efficiency of 60.4%. The proposed approach accelerates design iterations while maintaining engineering feasibility, providing a practical tool for advanced metasurface systems.

pp. 148-150

S4: Terahertz Technologies and Systems II

Room: Michaelmus B

Chair: Zhaomin Peng (National Space Science Center Chinese Academy of Sciences, China)

11:15 ***Semiconductor-grade Dry Nano-Island Coating Technology: Translating Advanced Materials from Lab Scale to Next-Gen 6G mm-Wave Substrates***

Hung-Wei Wu, Shuai Sun and Muhammad Waqas (Institute of Semiconductors, Guangdong Academy of Sciences, China); Deniz Eren Erisen (Laboratory for New Materials in Nano and Millimeter Waves Institute of Semicondu, China)

This invited paper presents our recent progress in translating semiconductor-grade nano-island-coating technology into high-value functional materials for 6G millimeter-wave substrates. The core concept is to engineer silica-based carrier powder with PVD-based nanoscale Al-nanoparticle island coating, followed by controlled conversion into AlN/Al_2O_3 nanoparticle-island-coated fillers. These engineered fillers are integrated into a non-fluorinated thermoset composite system to achieve low dielectric constant, low loss tangent, and improved thermal/mechanical reliability for high-frequency substrate applications. By combining powder surface modification, vacuum mixing, tape casting, and vacuum hot pressing, the proposed platform provides

a practical pathway from nano-engineered particles to the fabrication of 250 mm × 250 mm panel-scale substrates with thicknesses ranging from 100 μm to 100 mm. The target performance of the developed materials is Dk = 1.6-2.4 and Df < 0.0009 at 10 GHz, making them attractive for advanced RF packaging, satellite communications, radar sensing, and future THz devices. This work highlights how a coating-centered materials platform can bridge advanced processing, scalable manufacturing, and next-generation microwave system requirements.

pg. 151

11:30 ***D Band Terahertz Driving Source Based on GaN Monolithic Integrated Frequency Multiplier***

YH Li, S Jun and XM Zheng (National Space Science Center Chinese Academy of Sciences, China); Dehai Zhang (National Space Science Center, China); Jin Meng (National Space Science Center, Chinese Academy of Sciences, China)

Terahertz technology, characterized by its extensive development potential and broad application prospects, has emerged as a significant trend in future technological development. The radio-frequency (RF) front - end of a terahertz superheterodyne receiver is predominantly comprised of a mixer and a local oscillator (LO). Consequently, the LO, serving as the core component of the RF front-end, is critical for ensuring the proper operation of the entire superheterodyne system. The solid-state terahertz LO, which typically utilizes a Schottky diode-based multiplier as its core component, offers notable advantages such as high reliability, room-temperature operation, simple architecture, and low cost. These characteristics have led to its application in various fields such as meteorological detection, radio astronomy, and security inspection, solidifying its status as a vital branch of terahertz source research. The architecture of a solid-state terahertz LO typically comprises a pre-stage driver source and a final-stage multiplier. Given that the driver source, as the initial part of the entire LO chain, mainly functions to supply input power to the final - stage multiplier in the chain, effectively enhancing its output power is of great significance. To enhance power-handling capacity and thermal-dissipation performance, a 120 GHz driver source based on a GaN monolithic integrated multiplier is developed. Due to the advantages of GaN material, such as high thermal conductivity, high voltage withstand capability and high electron saturation rate, when utilized in Schottky diodes for frequency doublers, its defect in electron mobility is avoided. For the research on the 120 GHz driver source based on GaN monolithic integrated frequency doubler, a reasonable overall link composition scheme is proposed. The overall frequency - generation chain adopts a frequency multiplication scheme of 10 GHz microwave signals through a x6x2 cascade. Through an analysis of GaN material properties and their applicability to doubler design, a novel GaN Schottky diode design is conceived. The Schottky barrier diodes applied to terahertz frequency doublers usually have a relatively high input power, and the internal self-heating effect is quite obvious. Under actual operating conditions, material properties such as electrical conductivity, thermal conductivity, and heat capacity for each diode layer will change with temperature. Meanwhile, the internal temperature and parameters such as current, parasitic capacitance and parasitic resistance will affect each other. Therefore, the saturation current and series resistance parameters in the commonly used SPICE model of Schottky diodes are not constant, but should be temperature-related variables. The intrinsic and extrinsic parameters of Schottky barrier diodes related to temperature change with the working state, which will have a significant impact on the I-V characteristics of the diode. Therefore, the study of the thermal effect of Schottky barrier diodes cannot be ignored, which is crucial for improving the accuracy of the Schottky barrier diode model. To this end, a thermal resistance matrix is integrated into the diode model. The physical electrothermal model is composed of the drift-diffusion equation and the heat conduction equation. Furthermore, analyze the impact of adjacent metallized components in the matching structure on heat dissipation. The design of the 120 GHz monolithic doubler adopts a balanced circuit structure, mainly consists of WR15 input waveguide, WR8 RF waveguide, GaN Schottky diode, DC bias filter and matching circuit structure. For the fundamental frequency matching network, matching performance is optimized by tuning the lengths of the reduced-height and reduced-width waveguide sections and the position of the input short-circuit termination. The optimal output impedance value extracted from the chip is substituted into the lumped port of the diode. For the design of the output end

model, the bias circuit adopts an improved compact microstrip resonator (CMRC) filter, which has a more compact structure compared to the high and low impedance filters. This design effectively confines the second-harmonic signal to the output waveguide port while preventing it from leaking from the DC bias circuit, thus meeting the design requirements. The measured results demonstrate that incorporating the thermal resistance matrix into the core diode model significantly reduced the discrepancy between simulated and experimental results. Within the frequency range of 109-129 GHz, the maximum output power of the driver source measured is 35.56 mW. This research provides beneficial ideas for the manufacturing and design of Schottky diodes, and also lays a model foundation for the subsequent realization of high-performance terahertz frequency conversion devices.

pp. 152-153

11:45 ***Resonant Tunneling Diodes for Terahertz Sensing***

Safumi Suzuki (Institute of Science Tokyo, Japan)

Resonant tunneling diodes (RTDs) can oscillate at frequencies exceeding 2 THz at room temperature and generate milliwatt-level output power above 800 GHz. In the frequency range above 300 GHz, RTDs have demonstrated relatively high DC-to-RF conversion efficiency compared with other electronic devices. RTDs also exhibit unique functionalities, such as frequency-comb generation and signal detection, which are useful for terahertz sensing applications. This paper reviews recent developments in RTD oscillators.

Presenter bio: Safumi Suzuki received the B.E. degree in Electrical and Electronic Engineering and the M.E. and D.E. degrees in Electronics and Applied Physics from the Tokyo Institute of Technology, Japan, in 2005, 2007, and 2009, respectively. From 2009 to 2014, he was an Assistant Professor with the Department of Electronics and Applied Physics, from 2014 to 2016, an Associate Professor with the Department of Physical Electronics, and from 2016 to 2024, an Associate Professor with the Department of Electrical and Electronic Engineering, Tokyo Institute of Technology, respectively. Since 2024, he has been a Professor with the Institute of Integrated Research, Institute of Science Tokyo. His research interests include terahertz electronic devices and applications.

pg. 154

12:00 ***Dual-Wideband Antenna Decoupling via Hybrid Conduction-Radiation Mitigation***

Meng Xing, Shaobin Liu and Tianyu Shi (Nanjing University of Aeronautics and Astronautics, China)

This paper presents a hybrid decoupling strategy that synergistically integrates defected ground structures and metallic reflectors to address the strong long-distance mutual coupling problem in dual-antenna systems sharing a common ground plane over the 0.8-2.0 GHz band, where surface creeping waves dominate. Through full-wave simulations, we first characterize the surface current propagation on the metallic ground plane, identifying the central region between the two antennas as the critical coupling path. Based on this analysis, we design a transverse slotted defected ground structure (Mode 1) that perturbs the surface current distribution to effectively suppress low-frequency coupling. Concurrently, we introduce a folded metallic reflector (Mode 2) that modifies the propagation paths of high-frequency spatial waves, enhancing energy dissipation through reflection and phase manipulation. The synergistic integration of both mechanisms (Mode 3) is rigorously validated through full-wave simulations, demonstrating an average isolation enhancement exceeding 17 dB across the entire 0.8-2.0 GHz band. Our results reveal the complementary nature of the proposed approach: the defected ground structure outperforms the reflector at lower frequencies, while the reflector exhibits superior decoupling at higher frequencies. The combined strategy achieves broadband synergistic decoupling, offering a structurally simple and cost-effective engineering solution for high-isolation integration of multi-antenna systems on metallic platforms.

pp. 155-157

Thursday, July 23 12:30 - 1:45

Thursday, July 23 1:45 - 3:00

ISTP: Meet the Editors

Intersociety Technology Panel: Meet the Editors
Room: Michaelmus A
Chairs: Robert Caverly (Villanova University, USA), Imran Mehdi (Jet Propulsion Laboratory, California Institute of Technology, USA)

S14: Machine Learning in RF and Microwave Applications

Room: Reef
Chair: Qing You (University of Macau, Macao)

1:45 ***Surface Mount Radiator - Intelligent AiP for Physical AI and Edge Eevices***

Yifan Wang (Millibeam, Australia)

The rapid growth of 5G/6G, satellite communications, and AI-enabled edge devices is driving strong demand for compact, high-efficiency, and scalable antenna platforms. This presentation presents recent developments in surface-mounted Antenna-in-Package (AiP) technologies at MILLIBEAM, focusing on antenna radiation engineering, low-profile array architectures, RF materials, and integrated packaging approaches. The presentation highlights how advanced surface-mounted AiP platforms can enable intelligent RF systems for next-generation wireless infrastructure, sensing, Physical AI, and edge applications through vertically integrated "Silicon to Intelligent RF Systems" design strategies.

pg. 158

2:00 ***A Classification of Scattering Characteristics for Typical Artificial Structures via Attention-Augmented Dual-Branch Convolutional Neural Network***

Shuxin Wu, Yancheng Li, Meijun Qu and Jianxun Su (Communication University of China, China)

This paper presents a novel attention-augmented dual-branch convolutional neural network (DBA-Net) for classifying monostatic radar cross-section (RCS) characteristics of six typical artificial structures. A large-scale dataset is generated by computing full-azimuth RCS distribution and converting them into 2D heatmaps. The DBA-Net employs dual branches to extract multi-scale features and a dual-attention mechanism to focus on discriminative patterns. Experiments show the model achieves perfect classification accuracy with rapid convergence, demonstrating strong robustness and generalizability for intelligent electromagnetic target recognition.

pp. 159-161

2:15 ***Improved Hybrid Quantum Models for More Accurate Phase Prediction of Expansion Coefficients in Large Finite Periodic Structures***

Bingbing Song, Zhuoyue Zhao and Tian Liu (Southeast University, China); Fei Guo (Southeaset University, China); Zijun Hu, Wu Yang and Wei Bing Lu (Southeast University, China)

Accurately and efficiently analyzing the electromagnetic characteristics of large finite periodic structures (LFPSs) has always been a challenging problem in computational electromagnetics. In the past decade, several artificial neural networks (ANNs) based studies have been proposed to alleviate this challenge. However, with the rapid development of quantum technologies, the performance of ANN-based predictive models still exhibits significant potential for further improvement. In this paper, the hybrid quantum model proposed in previous work is enhanced by incorporating the residual architecture, enabling more accurate prediction for the phase of the expansion coefficients in sub-entire domain basis functions. Numerical experiments

demonstrate that the improved hybrid quantum model exhibits faster learning capability and higher prediction accuracy.

pp. 162-164

S23: Terahertz Technologies and Systems V

Room: Urchins 2
Chair: Zong-Rui Xu (City University of Hong Kong, Hong Kong)

1:45 ***High Q Terahertz Detector in Hybrid Metal–Optical Tamm State Cavity***

Zhanzhang Mai, Xuecou Tu, Bingnan Yan, Hongshan Jing, Dingxuan Gu, Yunjie Rui, Zeyu Xu, Cheng Liang, Baoran Lai, Xiaoqing Jia and Lin Kang (Nanjing University, China); Jian Chen (Nanjing University & Research Institute of Superconductor Electronics, China); Peiheng Wu (Nanjing University, China)

Terahertz optical cavity is one of the major elements to enhance and control the weak interaction between the atom-thick layer and normal incident terahertz light. Here we present a hybrid metal-optical Tamm state cavity with a Nb5N6 microbolometer detector embed, exhibiting a Q value of 1529 for direct detection. The cavity is formed by sandwiching a silicon substrate with the detector between two Si/air distributed Bragg reflectors (DBR), one of which is capped with an Au layer. The resonant frequency can be flexibly tuned by adjusting the substrate's thickness. The substrate and DBRs can be fabricated separately and assemble easily, which paves the way to effectively realize versatile high performance terahertz devices and strong interaction between terahertz light and matter.

pp. 165-166

2:00 ***A High-Performance Hybrid FBAR Chip Based on TGV Technology***

Keyan Li and Yongle Wu (Beijing University of Posts and Telecommunications, China); Zhiguo Lai and Qinghua Yang (HunterSun Electronics Company Ltd., China); Weimin Wang (Beijing University of Posts and Telecommunications, China)

In this paper, a hybrid chip combining a film bulk acoustic resonator (FBAR) chip and a glass-based integrated passive device (IPD) chip is proposed. The inductors in the hybrid circuit are implemented using through-glass via (TGV) as vertical spiral inductors. Such implementation can provide a high-Q inductor compared to a conventional planar spiral inductor, but also decrease the influence between the vertically stacked chips. Compared with the filter chip based on the same circuit implemented by conventional Si-based IPD technology, the insertion loss of the hybrid chip is lower while showing higher integration.

pp. 167-169

2:15 ***Geometry Scalable Model of on-Chip Multilayer Interdigital Capacitors***

Yiwen Liu, Huanpeng Wang, Yunqiu Wu, Jie Liu, Huihua Liu, Yiming Yu, Chenxi Zhao, Qingfeng Zhang and Kai Kang (University of Electronic Science and Technology of China, China)

Interdigital capacitors, composed of multiple metal layers, exhibit superior performance in compact form due to their high integration. In this paper, a scalable equivalent circuit model tailored for multilayer interdigital capacitors is proposed. The circuit parameters are accurately derived and the characteristics can be predicted based on the finger dimensions. The accuracy of the scalable model has been validated with an accuracy exceeding 92% across a frequency range of up to 40 GHz. This makes it highly significant for the modeling of on-chip passive devices.

pp. 170-172

2:30 ***High-Tc Superconducting Josephson Mixers from X- to Sub-THz Band***

He Zhu (Charles Darwin University, Australia)

This talk presents a unified approach to the design and integration of high-temperature superconducting (HTS) Josephson mixers across microwave, millimetre-wave, and sub-terahertz frequencies. A systematic design methodology is developed, combining circuit modelling, impedance matching, harmonic mixing techniques, and experimental validation to ensure predictable and scalable performance. The study emphasizes the importance of optimising Josephson junction parameters and demonstrates how accurate modelling can bridge the gap between simulation and measurement. Beyond circuit design, the work introduces advanced integration strategies, including compact waveguide transitions and antenna-coupled architectures, enabling efficient coupling between superconducting devices and radiating structures. By combining harmonic mixing concepts with frequency-scanning antenna technologies, the research establishes a pathway toward compact, low-noise, and energy-efficient superconducting receiver systems. The results provide a foundation for scalable HTS mixer technologies suitable for high-sensitivity communication, sensing, and imaging applications from microwave to sub-terahertz regimes.

Presenter bio: He Zhu is a currently a Lecturer in Charles Darwin University, Australia. He served as a Research Scientist in the Electromagnetic Systems and Devices Group of CSIRO, Australia, from 2023 to April 2026. He was a Postdoctoral Research Fellow and then a Chancellor's Research Fellow with the Global Big Data Technologies Centre at the University of Technology Sydney from 2017 to 2023. Dr Zhu is now a Senior Member of IEEE and serving as an Associate Editor for Microwave and Optical Technology Letter (MOTL) and a reviewer for multiple prestigious journals.

pg. 173

2:45 ***Metasurface Antenna Applied in Millimeter-Wave Imaging Systems***

Panpan Zuo, Lan Longpeng, Keyan Wei and Bin Gao (Civil Aviation University of China, China); Xiaoxuan Guo (University of Technology Sydney, Australia); Lei Yang (Civil Aviation University of China, China)

This paper presents the design of a Ku-band metasurface antenna for near-field millimeter-wave radar imaging. The proposed antenna features a three-layer structure. The slot-coupling feeding network integrating a Wilkinson power divider is employed to ensure amplitude and phase consistency across all radiating elements. Simulation results demonstrate that the antenna achieves a compact profile with an average gain exceeding 11 dBi and a 3-dB beamwidth confined within 35° across the Ku-band, fully satisfying the requirements for high-precision near-field millimeter-wave imaging, and the proposed digital imaging system based on metasurface antenna is expected to play a greater role as a key solution in next-generation personnel security screening and non-destructive testing.

pp. 174-176

S5: CMOS and BiCMOS Power Amplifiers III

Room: Michaelmus B

Chair: Fatemeh Norouzian (University of Birmingham, United Kingdom (Great Britain))

1:45 ***A 30-W Tri-Mode GaN Power Amplifier Based on Reconfigurable Multi-Network Architecture***

Tang Bowen, Chi Chen, Zhan Zhao and Yuehang Xu (University of Electronic Science and Technology of China, China)

This paper presents a fully integrated 30-W tri-mode gallium nitride (GaN) high power amplifier (HPA) supporting ultra-wideband (0.03-6.5 GHz), single-narrowband (SNB) (2.7-3.3 GHz), and concurrent dual-narrowband (DNB) operation. A dual-path single-transistor-driven distributed architecture with a shared-drain artificial transmission line enables broadband power combination. Frequency reconfiguration is achieved through gate artificial transmission lines, while switchable harmonic tuning enhances narrowband efficiency. The PA achieves over 44.8 dBm saturated output power across UWB and up to 53% peak power-added-

efficiency (PAE) in SNB mode. Fabricated in 0.25-μm GaN-on-silicon carbide (SiC) process, the design maintains high efficiency under continuous-wave operation.

pp. 177-179

2:00 ***A Fully Integrated Low-Cost 5-GHz Doherty Power Amplifier Using Compact Triple-Coil Splitter-Combiner in 180-nm CMOS***

Zhuoyin Chen, Yongle Wu, Shuchen Zhen, Zhixuan Gong, Xiaopan Chen and Weimin Wang (Beijing University of Posts and Telecommunications, China)

This paper presents a 5-GHz Doherty power amplifier (PA) implemented in a cost-effective 180-nm 1P6M CMOS technology with only one ultra thick metal (UTM) layer. To enable practical integration in legacy nodes with limited passive quality factors, an integrated transformer-based triple-coil network is adopted to realize signal splitting and load combining within a unified passive structure, reducing interconnection complexity and layout parasitics. The PA employs a differential cascode architecture with double neutralization to enhance gain and stability. Designed for 5-GHz applications, the simulated results show a small-signal gain of 12.7 dB, a PSAT of 21.4 dBm, a PAEmax of 23.0%, and a PAE6dB of 13.8%. The core circuit area is 1.42 mm2.

pp. 180-182

2:15 ***A Compact Wideband Filtering Power Dividers Using D-CRLH Resonators***

Xueyu Huang, Wenjie Feng, Wenquan Che, Kun Tang and Haoshen Zhu (South China University of Technology, China)

A design method for realizing a wideband filtering power divider (FPD) by adjusting the line-width of the resonators is proposed in this paper. Due to the slow-wave characteristic of the D-CRLH resonator, a compact circuit size is achieved. In addition, a stopband rejection exceeding 10f0 with a suppression level of better than 20 dB is realized by cascading a low-pass structure with the D-CRLH resonator. A wideband FPD with center frequency of 0.66 GHz and the fractional bandwidth of 44.2% is designed, fabricated and measured. The measured insertion loss is less than 4.05 dB and the isolation between two output ports is better than 21.5 dB from DC to 4.42 GHz (6.7f0). Simulated and measured results are in good agreement, validating the proposed approach

pg. 183

2:30 ***Optimized Design of Compact Multi-Coil Arrays for Misalignment-Tolerant Wireless Power Transfer***

Zihang Huang and Jingchen Wang (Xi'an Jiaotong-Liverpool University, China); Zhao Wang (Xi'an Jiaotong Liverpool University & University of Liverpool, China); Rui Pei (Xi'an Jiaotong-Liverpool University, China); Bintao Hu (University of Liverpool, United Kingdom (Great Britain)); Wenzhang Zhang (Xi'an Jiaotong-Liverpool University, China & University of Liverpool, United Kingdom (Great Britain)); Qian Dong and Eng Gee Lim (Xi'an Jiaotong-Liverpool University, China)

While magnetic resonant wireless power transfer (WPT) offers significant convenience, its performance typically degrades under misalignments. To address this, an optimized hybrid multi-coil transmitter array was designed for enhanced robustness. The proposed approach optimizes the array topology by removing redundant, weakly coupled elements and incorporating auxiliary gap coils to bridge magnetic nulls. This structural refinement not only intensifies the magnetic field but also achieves a more uniform field distribution. Simulation results indicate that the proposed WPT link delivers a power transfer efficiency of 81% at a transfer distance of 30 mm, exhibiting high tolerance to lateral and angular offsets. This compact transmitter configuration provides a practical solution for maintaining high-efficiency power delivery in misalignment-prone near-field charging scenarios.

pp. 184-186

2:45 ***Study on the Design of 50-75GHz Up-Conversion Module***

Hui Peng (Kashi University, China); Jincai Qiao (Chongqing Institute of Microelectronics Industry Technology, UESTC, China); Zuqiang Ou, Zhongqian Niu and Bo Zhang (University of Electronic Science and Technology of China, China); Ya Fei Wu (UESTC, China)

The up-conversion spread spectrum module, which can shift low-frequency signals to extremely high frequencies within the usable bandwidth, is a critical hardware component for enabling next-generation high-capacity communications, high-rate sensing, and other cutting-edge applications, and is of great significance to modern communication. As the application frequency of electromagnetic waves extends into the millimeter-wave and even terahertz bands, the requirements for signal sources as signal testing instruments are also gradually increasing. There is an urgent need to extend measurement frequencies to higher bands, which can be achieved by integrating an up-converter at the front end of the system. This paper conducts research based on up-conversion technology for 50GHz to 75GHz broadband signals. Several key devices in the frequency conversion system were developed, including a wide-stopband waveguide filter for splitting the 50GHz to 110GHz signal and suppressing image frequency signals, and a local oscillator based on a frequency multiplier and amplifier module. A 50GHz to 75GHz broadband signal up-conversion system was also constructed to down-convert a 28.95GHz to 30.15GHz broadband signal to the 50GHz to 75GHz range. Experiments show that the output power of the up-converted signal is not less than 13 dBm, the link gain is not less than 20 dB, and the output spurious suppression is greater than 40 dBc, meeting the system specifications.

pp. 187-189

Thursday, July 23 3:30 - 5:00

Panel Discussion

Room: Michaelmus A

The 2026 IEEE MTT-S International Microwave Workshop Series on Advanced Materials and Processes for RF and THz Applications (IMWS-AMP) includes a dedicated panel discussion featuring nine recognized researchers in electromagnetic engineering.

This panel convenes IEEE Fellows, MTT-S leadership, journal Editors-in-Chief, and specialized researchers to discuss current technical parameters and future implementations in the field. The participating panelists are: Prof. Kamran Ghorbani, Prof. Ke Wu, Prof. Quan Xue, Prof. Anding Zhu, Prof. Almudena Suárez Rodriguez, Prof. Qiaowei Yuan, Prof. Wenquan (Cherry) Che, Prof. Rodica Ramer, and Prof. Malgorzata Celuch.

Collectively, these panelists possess extensive empirical and theoretical backgrounds across multiple relevant disciplines. Their technical expertise encompasses microwave and millimeter-wave circuits, terahertz integration, non-linear modeling of RF systems, wireless power transfer, adaptive array antennas, and numerical methods for computational electromagnetics. Their research output directly supports application areas such as 5G/6G mobile communications, radar systems, microwave photonics, and substrate-integrated waveguides.

This session is designed to provide attendees with a structured, objective analysis of the practical development and physical realization of advanced RF and THz systems directly from the individuals guiding current research, system integration, and publication standards.

S15: Dielectric and Magnetic Materials

Room: Reef

Chair: David Mitchell (University of Illinois at Urbana-Champaign, USA)

3:30 ***Formula-Based Design of Bias Tees with Wide DC-Path Bandwidth and Transmission Zeros***

Keebaek Lee, Jongheun Lee and Juseop Lee (Korea University, Korea (South))

This paper presents a formula-based synthesis and design method for bias tees capable of superimposing low-frequency AC signals onto DC path while maintaining sharp frequency selectivity. By modeling the bias tee as a parallel connection of lowpass and highpass sections, closed-form expressions are derived to directly relate the element values of the RF path highpass section to those of the DC path lowpass section, allowing systematic circuit synthesis with reduced design complexity. The proposed approach enables the introduction of finite-frequency transmission zeros, resulting in a steep skirt response beyond those of conventional first-order bias tees. The fabricated prototype demonstrates an RF insertion loss better than 1 dB above 2.7 GHz and maintains acceptable matching.

pp. 190-192

3:45 ***Electromagnetic-Thermal-Fluid Multiphysics Coupling Simulation of Electronic Packaging Based on the FDTD Method***

Yan Peng, Guo Song, Tiancheng Zhang, Huaguang Bao and Dazhi Ding (Nanjing University of Science and Technology, China)

This paper focuses on the transient electromagnetic-thermal-fluid coupling analysis of microchannel cooling in electronic packages using the finite difference method. Complex geometric models are comprehensively modeled and analyzed, with numerical discretization and iterative computation implemented through the finite difference scheme. The effectiveness and efficiency of the proposed method are validated through case studies and comparisons with the commercial software COMSOL.

pp. 193-195

4:00 ***Rapid Analysis of Scattering Problem for LFPSs with Physics-Informed Attention Network***

Tian Liu (Southeast University, China); Fei Guo (Southeaset University, China); Wenzhe Song (Southeast University, China); Yanzhe Luo (Southeaset University, China); Wu Yang and Wei Bing Lu (Southeast University, China)

In this work, a physics-informed attention network (PIAN) is proposed for the rapid analysis of scattering problems in large-scale finite periodic structures (LFPSs). The encoder captures the relationship between array features and global coupling with self-attention mechanism, which guides the decoder to generate the final current coefficients of LFPSs based on the NASED initial current coefficients with cross-attention mechanism. The introduction of initial current coefficients enables the characterization of cell structure for different cells. The well-trained network can generalize to various cell structures, which significantly reduces the cost of dataset generation. Numerical experiments validate the accuracy, generalization capability, and efficiency of the proposed method.

pp. 196-198

4:15 ***Characteristic Mode-Based Efficient Analysis Method for Electromagnetic Scattering of Complex Electromagnetic Structures with Lossy Dielectric Materials***

Yutong Qiu, Jihong Gu, Zhaoyuan Wang and Zhou Cong (Nanjing University of Science and Technology, China); Chao-Fu Wang (National University of Singapore, Singapore); Dazhi Ding (Nanjing University of Science and Technology, China)

This paper proposes a fast solution method to analysis the electromagnetic scattering characteristics of the complex electromagnetic structures with lossy dielectric materials. In this method, the characteristic mode (CM) formulation for complex electromagnetic structures with lossy dielectric materials is first established based on the energy theory and the surface integral equation. Utilizing the modal reconstruction property of the theory of characteristic mode (TCM), the surface induced electromagnetic currents of individual array

elements are accurately solved, and the scattering fields are obtained. The scattering field of the array is then rapidly acquired through phase superposition, enabling the calculation of RCS. Numerical examples demonstrate that the proposed method significantly reduces computation time and memory overhead while maintaining accuracy.

pp. 199-201

4:30 ***Background Separation and Cancellation in Complex Indoor Testing Environments Based on the TTP Algorithm***

Wei Gao, Wen Jiang, Tao Hong, Wei Hu, Kun Wei and Yuchen Gao (Xidian University, China)

In indoor Radar Cross Section (RCS) test ranges, multipath signals generated by reflections from fixed structures such as walls and ceilings severely contaminate the true measured values of targets. This is particularly prominent in low-frequency band measurements and for low-RCS targets. Traditional background subtraction or time-gating methods often fail to isolate interference that is coherent or closely spaced with the target echo. To effectively suppress background clutter in indoor testing environments, this paper conducts an in-depth study on background separation and cancellation techniques. A target-background coupling model based on the Target Translation Processing (TTP) method is proposed. By utilizing a single translation of the target between two measurements, the phase of the multipath signal is actively altered, thereby achieving the separation of the target echo from the background multipath at the signal level. Simulation analysis determines that the optimal translation range is between 0.2λ and 0.3λ to minimize the ill-conditioning of the solution matrix. Experimental results on a flat plate demonstrate that the proposed algorithm can effectively suppress significant false interference peaks introduced by fixed wall reflections in the expected multipath directions, significantly improving the accuracy of target measurements and recovering the true RCS characteristics.

Presenter bio: Tao Hong, born in 1983, associate profressor of Xidian University, interests on ultra wide band antennas, frequenccy selective surfaces and metameterials.

pp. 202-204

S24: Antenna Arrays and Beamforming III

Room: Urchins 2
Chair: Zhichao Sun (University of Technology Sydeny, Australia)

3:30 ***S Parameters Matrix Estimation for E-MIMO-Based Beamforming***

Qiaowei Yuan (Tohoku Institute of Technology, Japan)

The Efficiency Maximum Multiple-Input Multiple-Output (E-MIMO) approach has recently been proposed as an effective beamforming technique for array antennas [1]. Practical implementation of E-MIMO requires accurate knowledge of the coupling matrix between transmitting and receiving elements, typically represented by the S-parameter or Z-parameter matrix. In realistic environments, however, direct measurement of the full multi-port matrix is time-consuming and often difficult, particularly when the receiving antennas are located far from the transmitting antennas. This paper proposes a method for estimating the coupling matrix using pilot signals. In the proposed approach, the mutual admittance or impedance matrix between the transmitting and receiving ports is derived from measured port voltages under known termination conditions at the transmitting side induced by pilot signal excitation. Numerical simulations are conducted to validate the proposed estimation method.

pp. 205-207

3:45 ***Modelling Clock Stability to Enabling Synchronisation for Multi-Static Passive Radar***

Konstanty S Bialkowski (The University of Queensland, Australia)

Passive radar is a type of radar system that offers several advantages over traditional active radar systems. Unlike active radar, passive radar does not require a dedicated transmitter and instead uses existing signals from the environment, like radio or television signals as a source of illumination, making it low cost, low power and portable. With advancements in receiver technology and computational power, passive radar has become an increasingly attractive option in many applications where active radar would have been used. However, the detection range and accuracy of passive radar are limited by the geometry of a single receiver scenario and the signal-to-noise ratio of the received signal. One way to overcome these limitations is to use multiple receivers to triangulate the position of a target, which provides increased coverage and the ability to detect smaller targets. To fully make use of the signals, coherent detection provides the opportunity to maximally combine the signals from all of the receivers. However, this depends on accurate synchronisation between receivers. In practice, this is challenging, as differences in receivers caused by both manufacturing defects as well as temperature fluctuations, can degrade the level of synchronisation. This work investigates the effect of synchronisation through experimental modelling of RF receivers and then looks at how these effect radar signal processing in terms of localisation performance in a virtual radar environment. Using the Generalised Canonical Correlation Analysis (GCCA) detector, a high-performance coherent detector is used. The key output of this work demonstrates that synchronization errors significantly affect localization performance, particularly where the detection performance is relying on coherent detection. However, when conditions, particularly temperature, remain stable, a calibration process can be used to mitigate most of the error. Understanding the impact of synchronization errors is crucial for improving and developing future multi-receiver passive radar and distributed beamforming systems.

pg. 208

4:00 ***Multi-Template Differential Correction for Subarray-Based Pattern Reconstruction of Large Phased Arrays***

Yuqing Yang, Weimin Wang and Yongle Wu (Beijing University of Posts and Telecommunications, China); Yuanan Liu (Beijing University of Posts and Telecom, China)

Electrically large phased arrays for satellite communications often exceed anechoic-chamber (AC) test-zone dimensions, motivating subarray-based pattern reconstruction realized through subarray stitching for OTA characterization. However, conventional stitching tiles an isolated-subarray pattern and implicitly assumes identical embedded behavior across the aperture. This assumption produces systematic boundary-induced errors that accumulate in the reconstructed pattern, particularly at wide zenith angles. This paper proposes a multi-template differential correction method that uses one isolated subarray and four representative embedded templates (middle, two edges, and one corner). The method models template deviations as differential fields, propagates them across the aperture via symmetry mapping, and applies an angle-dependent least-squares weight for direction-selective compensation. Numerical simulations show up to a 53% reduction in full-angle gain MSE and a 65% reduction in wide-zenith MSE, validating improved wide-angle reconstruction under test-zone constraints.

pp. 209-211

4:15 ***Multi-Material Additively Manufactured Wideband Dual-Linear Polarized Antenna with High Isolation***

Zhichao Sun (University of Technology Sydeny, Australia); Xiaojing Lv, Jiexin Lai and Yang Yang (University of Technology Sydney, Australia)

A multi-material additively manufactured wideband dual-linear polarized (dual-LP) antenna with high isolation is proposed in this paper. The structure integrates a magnetoelectric-dipole (ME-dipole) and a quasi-Yagi antenna. The ME-dipole utilizes a slot-coupled feed to produce horizontal polarization (HP), while the quasi-Yagi features two pairs of symmetrical dipoles with obliquely angled feed lines to realize vertical polarization (VP). The antenna is realized using multi-material additive manufacturing in a single integrated process, resulting in a highly compact design. Simulation results demonstrate that the antenna achieves a shared

impedance bandwidth (IMBW) of 48.71% in the millimeter-wave (mm-wave) band, while maintaining an isolation level below −34.5 dB. Owing to its compact configuration, wide bandwidth, and high isolation, the proposed antenna is well-suited for a variety of modern communication and sensing applications.

pp. 212-214

4:30 ***General-Purpose Terahertz Quasi-Optics and Mechanical Beamformers Enabled by 3D-Printing***

Bryce Chung, Daniel Headland and Withawat Withayachumnankul (Terahertz Engineering Laboratory, Adelaide University, Australia)

Owing to their short wavelength and light-like propagation behavior, terahertz waves require quasi-optical components to control the flow of radiation. To meet this need, 3D-printing has evolved over the past decade from a niche technique to a highly customizable, general-purpose methodology to produce terahertz quasi-optics, using consumer-grade hardware.

pg. 215

S6: GaN and Compound Semiconductor Devices

Room: Michaelmus B

Chair: Yuehang Xu (University of Electronic Science and Technology of China, China)

3:30 ***Phase-Tapered Bus-Bar Combiner for Efficiency Enhancement in C-Band GaN MMIC Power Amplifier***

Nupur Sood (Defence Research and Development Organization, India); Pinaki Sen (Defence Electronics Applications Laboratory & DRDO, India); Karun Rawat (Indian Institute of Technology Roorkee, India)

This work presents a layout-only phase-tapered bus bar combiner for Gallium Nitride (GaN) MMIC power amplifiers (PAs) in foundry compatible form. The approach improves power-added efficiency (PAE) by introducing asymmetry in drain-feed without increasing circuit complexity or addition of extra components. A graded drain feed taper is used to introduce controlled phase delays of 18.2° for the edge devices, 7.1° for second-edge devices and less than 1° for center devices at 4.65 GHz. This results in 12.5 percent reduction in DC current while maintaining excellent vector combining efficiency (ηcomb= 99.2 percent). Second, a single output-per-four-transistor topology reduces the required impedance transformation thus lowering the matching loss as well as avoiding closed metal loops. EM co-simulations carried out using UMS GaN technology (0.25 μm) with eight GH25-10 HEMTs (total periphery of 20 mm) results in a PAE of (44.5-46.3) percent in CW mode (improved by 5-points over conventional bus-bar), an output power of 47.6W and (21-22.7) dB of gain with a negligible linearity degradation over (4.35-4.97) GHz.

pp. 216-218

3:45 ***Design of Titanium SAW Phononic Crystal on Lithium Niobate LiNbO3/Si Structure***

Bao Jingfu, Mohammed Awad Ahmed Mohammed, Zijiang Yang, Taiyu Jiang and Ken-Ya Hashimoto (University of Electronic Science and Technology of China, China)

This study explores the use of surface acoustic wave (SAW) phononic crystals (PnCs), specifically square pillar-based PnCs reflectors in SAW resonators. The PnC generate acoustic band gap that reflects the wave to the resonator body, which enhances the stored energy and Bode Q in comparison to a traditional reflector. In this work, we propose a square-shaped titanium PnC implemented on a 15 ° Y-X $LiNbO_3/SiO_2/Si$ layered substrate. The proposed design generates a wide acoustic bandgap that. To evaluate the practical impact of PnCs in SAW devices, two SAW resonators employing PnC and reflector designs are compared and analyzed. From the simulated frequency responses, we find that using the Square-PnC as the reflector reduces resonator energy loss and enhances the stored energy

pp. 219-221

4:00 ***High-Efficiency Broadband S-Shaped Thin-Film Lithium Niobate Electro-Optic Modulator***

Xupeng Gu (University of Electronic Science and Technology of China, China); Ya Fei Wu (UESTC, China)

In this work, we propose and demonstrate an S-shaped Mach-Zehnder modulator (MZM) on a silicon substrate. As global data traffic demands surge, thin-film lithium niobate on silicon has emerged as a premier platform due to its high electro-optic coefficient and seamless integration with CMOS-compatible processes. However, conventional straight-path traveling-wave electrodes are often limited by severe conductor losses and velocity mismatch at millimeter-wave frequencies. By utilizing an innovative S-shaped topological layout, we effectively mitigate microwave transmission loss by alleviating high-frequency current crowding at the electrode edges. This geometry also provides the added benefit of increasing the optical group index, thereby enhancing both velocity matching and modulation efficiency. We fabricated a prototype with a 5 mm interaction length, and experimental results-which align well with numerical simulations-show a 1 dB reduction in electrode loss compared to traditional straight-path designs of the same length. Consequently, the device achieves a record EO bandwidth exceeding 110 GHz. This silicon-based S-shaped MZM offers a high-performance and scalable solution for the next generation of ultra-broadband photonic integrated circuits.

pp. 222-224

4:15 ***Characterisation of Dynamic Particulate Media Using Broadband FMCW Spectrometry***

James Elgy (University of Birmingham, United Kingdom (Great Britain)); Stephan Reschke (Toptica Photonics SE, Germany); Edward Hoare (University of Birmingham, United Kingdom (Great Britain)); Marina S. Gashinova (University of Birmngham, United Kingdom (Great Britain)); Fatemeh Norouzian (University of Birmingham, United Kingdom (Great Britain))

There is a growing interest in spectrometer-based techniques to measure and characterise particulate media across diverse fields, including medicine, environmental monitoring, and manufacturing. Spectrometers provide broadband measurements in a non-destructive manner, potentially enabling the extraction of rich spectral information that can enhance the characterisation of the medium. In this paper, we present a new dataset of transmission measurements through dynamic dust clouds acquired using an optoelectronic frequency-modulated continuous-wave (FMCW) spectrometer. The experimental results demonstrate that simultaneous broadband magnitude and phase measurements enable the estimation of the effective refractive index of the particulate air-dust mixture. These findings highlight the potential of FMCW spectrometry for quantitative characterisation of dynamic mediums.

pp. 225-227

4:30 ***From Language to Structure: Semantic-Guided Cross-Modal End-to-End Intelligent Design of High-Performance Metasurface Absorbers***

Yihao Li (Nanjing University of Science and Technology, China); Shijie Wang (National University of Singapore, Singapore); Wen Lyu, Yanghui Wu and Huanyu Yang (Nanjing University of Science and Technology, China)

Metasurface inverse design usually relies on numerical targets and therefore cannot directly use natural-language requirements. The inverse mapping from spectra to structural parameters is also non-unique. To address these issues, we propose a semantics-guided cross-modal framework for intelligent design of high-performance metasurface absorbers. The framework combines vision-language alignment, forward surrogate modeling, and probabilistic inverse design in a unified pipeline built on a four-modal dataset. Specifically, we use a CLIP-based module for text-spectrum alignment, a spatially varying multi-channel attention Fourier neural operator for forward prediction, and a mixture density network for inverse design. The forward model achieves (R^{2}=0.9954) on the test set and (R^{2}=0.9939) on the validation set. The inverse model achieves

MAE = 0.024855, RMSE = 0.046434, and (R^{2}=0.960359), while the semantic alignment module reaches (88.24%) Top-1 accuracy and (100.00%) Top-5 accuracy.

pp. 228-230

4:45 ***Towards Fully Integrated Terahertz Frontends: Silicon Photonics Meets Resonant Tunneling Diodes***

Weijie Gao and Nguyen Hoai Ngo (Osaka University, Japan); Daiki Ichikawa (The University of Osaka, Japan); Yuta Inose and Masayuki Fujita (Osaka University, Japan)

The terahertz frequency band offers great potential for ultrahigh-speed wireless communications and high-resolution sensing in 6G and beyond systems. However, compact and scalable terahertz frontends are still limited by the lack of a unified integration platform that supports both low-loss propagation and efficient active devices. In this work, we present a photonic-electronic co-integration framework combining effective medium silicon waveguides with resonant tunneling diodes. The platform enables low-loss, broadband propagation and compact nonlinear functionalities, including oscillation, detection, and phase control. Integrated transceivers and beam-steerable antennas at the 300-GHz band are demonstrated. This approach can be expected to promise fully integrated, reconfigurable terahertz frontends for next-generation communication and sensing systems.

Presenter bio: Postdoctoral Researcher at Osaka University with research interest focused on terahertz components, communications, and microwave reconfigurable antennas.

pg. 231

Thursday, July 23 6:00 - 10:30

Conference Banquet @ Urchins

Room: Michaelmus A, Michaelmus B, Reef, Urchins 2

Friday, July 24

Friday, July 24 9:00 - 9:45

K3: Keynote: The Evolution of Guided-Wave Technologies: Driving the Future of Integrated Circuits and Systems - Ke Wu

Ke Wu

Room: Michaelmus A

Chair: Yang Yang (University of Technology Sydney, Australia)

The development of advanced materials and innovative fabrication processes has been a key driver of progress in integrated circuits and systems. In parallel, guided-wave technologies have undergone remarkable evolution, enabling increasingly compact, high-performance, and multifunctional implementations. In particular, the three-dimensional, high-density integration of transmission lines supporting diverse propagation modes is reshaping the future of circuit and system integration. This talk presents an overview of transmission lines and guided-wave structures whose evolution has been driven by continuous advances in materials and fabrication technologies, followed by a discussion of emerging high-density integration techniques. State-of-the-art substrate integration approaches, encompassing both metallic and dielectric topologies, are reviewed with an emphasis on minimizing transmission loss while maximizing integration density. Emerging waveguide architectures and heterogeneous integration strategies are then introduced, enabling unified platforms that support both TEM and non-TEM propagation for highly integrated circuits and interconnects. Finally, mode composition and mode selectivity are explored for DC-to-THz systems targeting ultrafast, ultra-broadband, and truly all-pass operation. The presentation

concludes by proposing a unified all-pass transmission architecture for future DC-to-THz systems, laying the foundation for the convergence of electronic and photonic technologies.

Biography

Dr. Ke Wu is Industrial Research Chair in Future Wireless Technologies and Professor of Electrical Engineering with Polytechnique Montréal (University of Montreal). He is the Founding Director of the Institute for Wireless Intelligence (IWI). He was the Canada Research Chair in RF and millimeter-wave engineering and the Founding Director of the Center for Radiofrequency Electronics Research of Quebec, and the Director of Poly-Grames Research Center. He has authored/co-authored over 1500 technical papers, and 26 books/book chapters and filed more than 95 patents. Dr. Wu was the organizer of numerous conferences and events including the General Chair of the 2012 IEEE MTT-S International Microwave Symposium (IMS2012) and General Co-Chair of the 2025 IEEE International Symposium on Antennas and Propagation (APS). He was the 2016 President of the IEEE Microwave Theory and Technology Society (MTT-S). He also served as the two-terms inaugural representative of North America in the General Assembly of the European Microwave Association (EuMA). He was the recipient of many awards and prizes including the 2019 IEEE MTT-S Microwave Prize, the 2021 EIC Julian C. Smith Medal, 2022 IEEE MTT-S Outstanding Educator Award, 2022 IEEE AP-S John Kraus Antenna Award, and the 2025 IEEE MTT-S Pioneer Award. He was an IEEE MTT-S Distinguished Microwave Lecturer. Dr. Ke Wu is a Fellow of the IEEE, the Canadian Academy of Engineering, the Academy of Science of the Royal Society of Canada, and the German National Academy of Science and Engineering (acatech).

Friday, July 24 9:45 - 10:45

P5: Semi-Plenary 5

Room: Michaelmus A
Chair: Withawat Withayachumnankul (The University of Adelaide, Australia)

9:45 ***Sources and Detectors for Space THz Communication Systems***

Imran Mehdi (Jet Propulsion Laboratory, California Institute of Technology, USA)

THz applications have been increasing over the years. These applications include both space-based remote sensing as well as ground-based industrial applications such wireless communications. For communication systems, the THz frequency range is attractive as it provides larger bandwidth and smaller apertures. This talk will focus on the recent advancement in the development of room-temperature based wideband, compact sources and detectors in the THz range for space communication systems.

pp. 232-233

10:15 ***High-Sensitivity Terahertz Sensing with Quadrature Self-Homodyne Detection***

Bryce Chung, Nontiwat Amnuayphol, Harrison N Lees and Withawat Withayachumnankul (The University of Adelaide, Australia)

Terahertz sensing is often cited as a transformative solution for non-destructive evaluation, offering millimeter-scale spatial resolution and unique see-through capabilities. Despite the availability of various photonic and electronic systems, significant challenges remain. Photonic-based systems are often hampered by inherent laser drift and phase noise, while electronic systems suffer from phase noise amplification through high-order frequency multiplier chains. These issues compromise sensitivity, which is typically improved through temporal averaging at the expense of measurement speed. Furthermore, high-performance components remain costly and delicate, whilst their limited output power often restricts the effective sensing range. Sensitivity can be dramatically enhanced by comparing the probe signal with a reference of the original carrier, a technique known as self-homodyning. In this presentation, we discuss two quadrature (I/Q) self-

homodyne detection systems operating around 300 GHz, a strategic band for extended-range sensing due to minimal atmospheric absorption. One architecture utilizes I/Q interferometry, while the other employs I/Q mixing. Both systems achieve nanometer-scale vibration sensitivity with a theoretical measurement bandwidth reaching gigahertz rates. This detection scheme suppresses both external noise and source phase noise, enabling the use of high-power terahertz oscillators to further extend sensing range. We will demonstrate successful applications in acoustic eavesdropping, non-contact chip sensing, and vital-sign detection. assumption.

pg. 234

P6: Semi-Plenary 6

Room: Michaelmus B
Chair: Shengjian Jammy Chen (Flinders University, Australia & The University of Adelaide, Australia)

9:45 ***Diverse Semiconductor Integrated Microelectronics in the Application-Oriented AI Era***

Debabani Choudhury (SeraTech, LLC, USA)

Energy efficient materials, devices, technologies and systems will play a major role with the evolution of sensing and communication network architectures in the AI era. The progress in compound semiconductor devices combined with silicon technologies and 3D heterogeneous integration (3DHI) are defining the microelectronics future in the industry.

This talk will present the recent advancements in semiconductor and microelectronics integration technologies. The challenges and opportunities of the system-oriented compound semiconductor-based microelectronics in the Agentic AI era will also be discussed.

pp. 235-236

Friday, July 24 11:15 - 12:30

YP Session

Room: Michaelmus A
Chair: Syed Muzahir Abbas (Macquarie University, Australia)

S16: Millimeter-Wave and Terahertz Passives II

Room: Reef
Chair: Xiaojing Lv (University of Technology Sydney, Australia)

11:15 ***Millimeter-Wave and Sub-Terahertz Antenna and Metasurface Applications Using Screen Printed Vanadium Dioxide Switches***

Junghyeon Kim, Minjae Lee and Hyunwoo Koo (Chung-Ang University, Korea (South)); Duc Anh Pham (University of Illinois at Chicago, USA); Eiyong Park and Sungjoon Lim (Chung-Ang University, Korea (South))

Millimeter-wave (mm-wave) and sub-terahertz (sub-THz) frequencies are key technologies for future wireless systems such as 6G, enabling ultra-high data rates and massive connectivity. However, implementing reconfigurable RF components at these frequencies remains challenging because conventional semiconductor switches suffer from parasitic effects and performance degradation. Phase-change materials such as vanadium dioxide (VO_2) offer a promising alternative due to their reversible insulator-metal transition and large resistance change.

This work explores screen-printed VO_2 switches as a scalable platform for reconfigurable antenna and metasurface applications across microwave, mm-wave, and sub-THz frequencies.

First, a frequency-reconfigurable metasurface absorber is proposed using a large-area VO_2 layer integrated with a resistive metasurface pattern. Unlike conventional designs that require discrete RF components, the proposed structure achieves dynamic switching of absorption bands by modulating the sheet resistance of VO_2, demonstrating a simple and scalable approach for reconfigurable metasurfaces.

Second, a screen-printed VO_2-based intelligent reflective surface (IRS) operating at 100 GHz is demonstrated for sub-THz wireless communication. The IRS employs high phase-changing-ratio VO_2 switches to control the reflection phase and beam direction, enabling large-area beam steering while avoiding the parasitic limitations of conventional semiconductor switching devices.

Third, a VO_2-switched leaky-wave antenna operating in the V-band is presented to realize reconfigurable beam steering in mm-wave antenna systems. By switching the VO_2 elements between insulating and metallic states, the antenna dynamically alters its phase constant and radiation characteristics, enabling distinct beam-scanning behaviors within the operating band.

These three demonstrations collectively show that screen-printed VO_2 switches enable low-cost, large-area, and parasitic-free reconfigurable electromagnetic structures, highlighting their strong potential for adaptive antennas and metasurfaces in future mm-wave and sub-THz communication systems.

Presenter bio: Sungjoon Lim received the B.S. degree in electronic engineering from Yonsei University, Seoul, Korea, in 2002, and the M.S. and Ph.D. degrees in electrical engineering from the University of California at Los Angeles (UCLA), in 2004 and 2006, respectively. After a postdoctoral position at the Integrated Nanosystem Research Facility (INRF), the University of California at Irvine, he joined the School of Electrical and Electronics Engineering, Chung-Ang University, Seoul, Korea, in 2007, where he is currently a Professor. He has authored and coauthored more than 100 technical conference, letter and journal papers. His research interests include engineered electromagnetic structures (metamaterials, electromagnetic bandgap materials, and frequency selective surfaces), printed antennas, and RF MEMS applications. He is also interested in the modeling and design of microwave circuits and systems. Dr. Lim received the Institution of Engineering and Technology (IET) Premium Award in 2009.

pg. 237

11:30 ***Meta-Screen: Full-Space EM Environment Reconfiguration for mmWave Communications***

Jiatong Wu (Xi'an Jiaotong Liverpool University, China); Rui Pei (Xi'an Jiaotong-Liverpool University, China); Zhao Wang (Xi'an Jiaotong Liverpool University & University of Liverpool, China); Jingchen Wang, Mark Leach and Eng Gee Lim (Xi'an Jiaotong-Liverpool University, China)

This paper presents the Meta-Screen, a novel reconfigurable indoor partition for full-space millimeter-wave environment control. Utilizing a highly integrated Rx-Gnd-Tx unit cell with only two PIN diodes, the proposed architecture achieves 1-bit phase quantization for both transmission and bi-directional reflection modes. Simulations show wide fractional bandwidths of 27.1%, 23.8%, and 8.3% for transmissive, +z-reflective, and -z-reflective modes, respectively, with a common operational bandwidth of 4.1%. System-level validation of a 14×14 array at 24 GHz confirms robust beam-scanning up to 60° and peak gains of 17.94 dBi. This design offers a low-complexity, high-efficiency solution for 360° coverage in future 6G smart radio environments.

pp. 238-240

11:45 ***A Low-Rate Digital Predistortion with Single Real Undersampling Feedback Using Switch-Estimated Method Excited by 400 MHz Sub-6 GHz Signals***

Xiaoyu Lu and Jianfeng Zhai (Southeast University, China); Zuofeng Zhang, Dongfang Ning and Yanru Cao (ZTE Corporation, China); Peng Chen and Chao Yu (Southeast University, China)

This paper proposes a low-rate digital predistortion (DPD) technique. In this DPD technique, a switch-estimated method is applied to estimate the power amplifier (PA) output signal with low-complexity model extraction iteratively by a single real undersampling feedback signal. Furthermore, the band-limited DPD model is used to reduce the sampling rate of digital-to-analog converters (DACs). A 400 MHz 5G NR signal at the center frequency of 3.6 GHz is used to verify the proposed technique. The measurement results show that the proposed DPD technique can effectively reduce the hardware resources consumed during the model extraction process while maintain good linearization performance.

pp. 241-243

12:00 ***Ultra-Broadband 3D-Printed Metalens Using Height-Controlled Meta-Atoms***

Xuyi Zhu and Bing Zhang (Sichuan University, China)

This work presents a 15-40 GHz ultra-broadband metalens based on height-controlled meta-atoms and compatible with hybrid-material 3D printing fabrication. The proposed three-dimensional meta-atom introduces an additional vertical degree of freedom that governs multi-order mode evolution within the unit cell. By tuning the structural height, the evolution and interaction of higher-order modes are controlled, enabling effective phase control over a broad frequency range. Unlike conventional planar phase-shifting elements that rely primarily on two-dimensional geometric variations, the proposed 3D configuration leverages vertical structural modulation to extend the operational bandwidth while maintaining phase tunability. A prototype is fabricated and experimentally validated. Measured results demonstrate broadband operation from 15 to 40 GHz with a peak gain of 25.3 dBi at 25 GHz, corresponding to approximately 90% relative bandwidth. The proposed design provides a manufacturable route toward ultra-broadband metalenses.

pg. 244

12:15 ***A Switchable Dual CP Array System for CubeSat Communications Based on Collocated RHCP/LHCP 4×4 Patch Arrays***

Zi-Huan Lu (University of Technology Sydney, Australia); Zhichao Sun (University of Technology Sydeny, Australia); Xiaojing Lv and Yang Yang (University of Technology Sydney, Australia)

This paper presents a switchable dual circularly polarized (CP) 4×4 patch array system for CubeSat communications. The CP element uses a slot-coupled feed to achieve wideband matching and a low axial ratio (AR). A mirror transformed element is employed to realize right-hand circular polarization (RHCP) and left-hand circular polarization (LHCP) with similar performance. A sequential rotation feeding (SRF) network is used in the 4×4 arrays to improve the impedance and AR bandwidths. Simulation results show that the 4×4 RHCP and LHCP arrays achieve an overlapped bandwidth (|S11| < −10 dB, AR < 3 dB) of 48.7% (28.4-46.2 GHz), with realized peak gains above 16.6 dBic. Finally, the RHCP and LHCP arrays are collocated on the CubeSat top panel, providing a compact switchable dual CP antenna system for polarization diversity and reduced polarization mismatch.

pp. 245-247

S25: Antenna Arrays and Beamforming IV

Room: Urchins 2

Chair: Maral Ansari (CSIRO, Australia)

11:15 ***Pattern-Reconfigurable Metasurface for Dynamic Switching Between OAM Beam and Dual-Beam***

Xiaoxuan Guo (University of Technology Sydney, Australia); Yue Shi (Beijing Chenzhong Technology, China); Yang Yang (University of Technology Sydney, Australia)

A pattern-reconfigurable metasurface is proposed, which enables dynamic switching between Orbital Angular Momentum (OAM) vortex beams and dual-beam radiation patterns. The proposed metasurface is constructed using a multi-layer Printed Circuit Board (PCB), with its aperture phase distribution determining the radiation characteristics. The phase distribution for x-polarization consists of focusing phase and vortex OAM phase, while that for y-polarization comprises focusing phase and a periodically alternating phase of 0° and 180°. Simulation results demonstrate that the proposed metasurface can efficiently achieve dynamic switching between an OAM beam with a topological charge of 1 and dual-beam patterns.

pp. 248-250

11:30 ***A Textile Antenna for ON-/off-Body Communication***

Yu-Fei Wang, Zhe Chen, Shuai Gao, Yu-Xiang Sun and Tao Yuan (Shenzhen University, China)

A textile antenna with dual-band dual-mode operation is proposed for on- and off-body communications. An omnidirectional radiation pattern is achieved by loading shorting pins to excite the TM00 mode at the 2.45-GHz band for on-body communication, while a broadside radiation pattern with high gain is realized by etching slots to modify the TM30 mode at the 5.8-GHz band for off-body communication. Both bands can be tuned independently. A prototype was fabricated using textile materials, allowing it to conform to the human body. The measured results indicate that the antenna can fully cover the 2.45- and 5.8-GHz WBAN bands, achieving measured peak gains of 1.31 dBi in free space and -1.09 dBi on a three-layer human tissue model for the 2.45-GHz band, as well as 9.97 dBi in free space and 9.62 dBi on the phantom for the 5.8-GHz band. The demonstrated properties confirm that the proposed antenna is suitable for wearable applications.

pp. 251-253

11:45 ***A Compact Wideband Dual-Circularly Polarized Millimeter-Wave Antenna with Isolation Enhancement***

Zhichao Sun (University of Technology Sydeny, Australia); Xiaojing Lv, Jiexin Lai and Yang Yang (University of Technology Sydney, Australia)

A compact wideband dual-circularly polarized (dual-CP) antenna with isolation enhancement is proposed in this paper. First, a compact antenna element is designed, exhibiting a 27.66% dual-CP bandwidth in the Ka-band. By employing a downward-folded electric-dipole (E-dipole), the footprint of the antenna is significantly reduced, leading to a highly compact structure. However, the isolation between the two ports is low, reaching only 6.5 dB across the operating bandwidth. To address this issue, two dielectric layers are introduced above the radiator, with a cavity etched in the center of the lower dielectric layer. With the cavity-loaded structure, the port isolation is improved by up to 15 dB. Owing to its wideband dual-CP, compact configuration, and high port isolation, the proposed antenna element is well suited for satellite communication antenna arrays.

pp. 254-256

12:00 ***Broadband Circularly Polarized Glass Antenna with Surface Wave Suppression***

Xiaofeng Hou, Keying Huang, Zhipeng Zhang, Wenhai Zhang and Yilin Zheng (Soochow University, China); Chi-Hou Chio and Kam-weng Tam (University of Macau, Macao); ZhiXing Chen (Fuyao Glass Industry Group CO., LTD, China)

This paper presents a novel circularly polarized coplanar waveguide (CPW)-fed antenna designed for integration into vehicle roof glass for satellite navigation applications. The antenna utilizes an asymmetric ground plane to achieve broadband circular polarization. A key feature is the seamless integration of a coplanar frame structure within the blackout border region of the roof glass, which effectively suppresses surface wave propagation. Measurement results demonstrate that the prototype achieves an impedance bandwidth of 36.04% (1.16-1.67 GHz) and a 3-dB axial ratio (AR) bandwidth of 34.29% (1.16-1.64 GHz). Furthermore, the antenna exhibits a boresight right-hand circularly polarized (RHCP) gain exceeding 2 dBic across the B3 and L1 navigation bands. These characteristics satisfy the stringent requirements for modern

automotive Global Navigation Satellite System (GNSS) antennas. Keywords-Broadband, circular polarization, CPW feed, surface wave suppression, GNSS application

pp. 257-258

12:15 ***A Low Profile and High Front-to-Back Ratio Millimeter-Wave Array Based on Electromagnetic Band Gap Ground***

Yu-Qi Ma, Zhihong Tu, Huan-Bin Wang and Fu-Chang Chen (South China University of Technology, China)

This paper proposes a low profile and high front-to-back ratio millimeter-wave array based on electromagnetic bandgap ground (EBGG). The proposed array consists of two SIW slot antenna elements operating in the 24 GHz ISM band. In order to enhance gain and the front-to-back ratio (FBR), a π-shape EBGG is introduced on both sides of the array, while maintaining an ultra-low profile of only 0.04λ0. Compared with the original array, the peak realized gain of the proposed array is enhanced from 8.0 dBi to 9.0 dBi at 24.0 GHz, a reduction in the 3-dB beamwidth from 105° to 91°, and a significant enhancement in FBR from 17.34 dB to 30.17 dB. These results demonstrate that the proposed π-shape EBGG is an effective solution for achieving gain and FBR enhancement in low-profile millimeter-wave antenna arrays.

pp. 259-261

S7: Low Noise Amplifiers and Receivers

Room: Michaelmus B

Chair: Xupeng Gu (University of Electronic Science and Technology of China, China)

11:15 ***A 19.3-23.7-GHz RTWO with Common-Mode Resonance and Distributed Varactors***

Yuan Tian, Xiaosi Zhu, Pei Qin and Quan Xue (South China University of Technology, China)

This paper presents a millimeter-wave (mmW) rotary traveling-wave oscillator (RTWO) integrating distributed varactors and common-mode high-impedance techniques to mitigate dispersion-induced flicker noise upconversion. Fabricated in TSMC 65nm CMOS, the 16-phase RTWO achieves a tuning range from 19.3 GHz to 23.7 GHz with phase noise of −130.2 dBc/Hz at 10-MHz offset. With a power consumption of 9.6mW, peak Figure-of-Merit (FoM), FoMT and FoMP reach 187.8, 193.9, and 199.9 dBc/Hz, respectively.

pp. 262-264

11:30 ***A 8.8-12.5 GHz Dual-Core Series Resonance VCO with 201.3-dBc/Hz FoMT in 28-nm CMOS Technology***

Shuai Huang, Li Gao and Xiu Yin Zhang (South China University of Technology, China)

This paper proposes a dual-core series resonance voltage-controlled oscillator (SRVCO) designed for wideband communication applications. The dual-core SRVCO topology is utilized to achieve a wide tuning range (TR), significantly lower the power consumption of SRVCO while still maintaining a decent PN and FoM performance. By manipulating the coupling coefficient between the primary and secondary coils of the transformer, mode ambiguity is eliminated. Implemented in TSMC 28-nm bulk CMOS process, the VCO achieves a simulated continuous oscillation frequency range of 8.8 to 12.5 GHz (tuning range of 34.7%). This SRVCO operates at a 0.7 V supply with a power consumption of 13.1 mW. The simulated results demonstrate a best phase noise of -137.8 dBc/Hz at 10-MHz offset, corresponding to a figure-of-merit (FoM) of 190.5 dBc/Hz and a FOM of tuning range (FoMT) of 201.3 dBc/Hz.

pp. 265-267

11:45 ***Super-Mode-Group Based Reduced-Order Analysis of Multi-Mode Antenna Decoupling***

Yuqi Wang (South China University of Technology, China); Hao Jiang (City University of Hong Kong, Hong Kong); Yinglu Wan (Guangxi University, China)

Broadband and multiband antenna decoupling is often associated with the joint contribution of multiple characteristic modes. This paper presents a super-mode-group (SMG) framework for reduced-order analysis of symmetric multi-mode antennas. Starting from the characteristic-mode expansion of the port admittance matrix, the relevant modes are grouped into odd and even groups according to structural symmetry. Two grouped descriptors, namely the total excitation weight and the weighted modal eigenvalue, are introduced to describe the overall contribution of each group. The formulation shows that decoupling is favored when the odd and even groups remain balanced in grouped-power/conductance contribution and synchronized in near-resonant behavior. Numerical parametric results support this interpretation. The framework provides a reduced-order view for symmetric multi-mode antenna analysis.

pp. 268-270

12:00 ***A V-Band LNA with Pole-Tuning and Gm-Boosting Technique in 40-nm CMOS***

Xiangjie Li, Hetai Zhang, Pei Qin and Quan Xue (South China University of Technology, China)

For millimeter-wave applications in short-range wireless communication, this paper proposes an LNA based on a three-stage cascode. To expand the input-matching bandwidth, the input-matching network introduces another pole at a higher frequency, thereby achieving a wider S11 bandwidth. Moreover, two transformers were used to connect the transistor drain in the previous stage to the transistor source in the subsequent stage. This enables the transistor to exhibit enhanced conductivity in the latter stage, thereby increasing its gain. The increase in gain suppresses noise. Under a 1V power supply, the power consumption is 17.6mW. This low-noise amplifier has a peak gain of 21.1 dB at 61.1 GHz within a 3-dB bandwidth of 45.7-68.9GHz and achieves the lowest noise of 3.67dB at 55.9GHz. Meanwhile, this LNA is unconditionally stable across the entire frequency range. The area of this LNA is 0.17mm2.

pp. 271-273

12:15 ***A High-Sensitivity Rectifier Employing a Low-ESR Distributed Spiral Inductor***

Pai-Dong Lin (South China University of Technology); Jun-Hui Ou (South China University of Technology, China); Zhi-Xia Du (Guangdong University of Technology, China)

As the input power of rectifiers decreases to below -30 dBm, the rectifier exhibits a highly capacitive complex impedance, leading to a dramatic increase in power loss within the impedance matching network during energy transmission. To minimize the equivalent series resistance (ESR) of the matching structure, this paper proposes a low-ESR distributed spiral inductor, which is synergistically integrated with a T-junction microstrip structure to construct the matching network. Compared to the conventional impedance matching networks, this structure effectively minimizes parasitic ohmic losses within the matching network, achieving higher power conversion efficiency. Simulation results demonstrate that at an operating frequency of 900 MHz and an input power of -35 dBm, the rectifier circuit utilizing the proposed matching network achieves a power conversion efficiency (PCE) of approximately 10.97%.

pp. 274-276

Friday, July 24 12:30 - 1:45

Friday, July 24 1:45 - 3:00

WIM Session

Room: Michaelmus A

Chair: Wenquan Che (South China University of Technology, China)

S17: CMOS and BiCMOS Power Amplifiers IV

Room: Reef
Chair: Jingchen Wang (Xi'an Jiaotong-Liverpool University, China)

1:45 ***A Continuously Tunable Silicon-Based 3D Matching Network for Heterogeneous RF Transceiver***

Yanwen Zheng, Guangbao Shan and Xiang Fan (Xidian University, China); Chunyu Yang (Xidian university, China); Pan Zhang (Xidian University, China)

The wideband impedance mismatch is main critical challenge to improve the efficiency. This paper presents a multi-mode tunable matching network. The matching performance can be improved with the flexible combination of tuning excitation modulus and phase. Across the 0.1-10 GHz range, the return loss is less than 10 dB. The prototype occupies an area of only 200×140μm².

Presenter bio: He is a doctoral candidate at the School of Microelectronics, Xidian University. His main research direction is chiplet-based radio frequency system integration technology.

pp. 277-279

2:00 ***A Broadband Tunable Matching Network Based on Magnetic Coupling***

Wang Fangqian, Guangbao Shan and Yanwen Zheng (Xidian University, China)

To address the limitations of conventional lumped element matching networks in broadband applications, this paper investigates the broadband mechanism and tuning characteristics of magnetically coupled matching networks. Based on a tunable transformer structure, a matching network with adjustable bandwidth and ripple is proposed. The frequency and impedance tuning mechanisms of in-phase and out-of-phase configurations are systematically analyzed, thereby extending the theoretical framework of magnetically coupled matching networks.

pp. 280-282

2:15 ***Wideband High-Precision Resonator-Based Phase Shifters via Lossy Electric and Magnetic Coupling***

Ji Na (South China University of Technology, China); Guangxu Shen (Nanjing University of Posts and Telecommunications, China); Wenquan Che (South China University of Technology, China)

This paper presents a novel wideband phase shifter (PS) architecture featuring a dual-state multi-resonator response, where both states integrate an admittance inverter (J-inverter) model with lossy coupling. In addition, the transistors are not only used as switches but also reused to form the resonators. Implemented in a 0.25-μm GaAs IPD process, a representative 90° PS is designed for the 22-32 GHz band. Post-layout electromagnetic simulations demonstrate a phase shift of 91.5° ± 1.5°, a maximum insertion loss of 3 dB in both states, and an amplitude imbalance below 1 dB. The proposed architecture provides a compact and robust solution for millimeter-wave phased-array systems.

pp. 283-285

2:30 ***Ultra-Wideband RCS Reduction Metasurface with Tunable Transmission Window***

Cong Zhang, Yuchen Gao, Hui Xin and Tao Hong (Xidian University, China)

This paper presents a metasurface design that integrates polarization conversion and reconfigurable frequency selective surface (FSS) technologies to achieve ultra-wideband radar cross section (RCS) reduction with a continuously tunable transmission window. The structure comprises a tunable low-frequency polarization conversion metasurface (PCM) loaded with varactors and resistors, a high-frequency PCM orthogonally stacked to avoid Fano resonance, and a reconfigurable FSS. By adjusting varactor capacitance, the transmission window can be tuned from 4.6 GHz to 7.1 GHz with insertion loss <1 dB, while maintaining polarization conversion absorption ratio (PCAR) >0.9 in stopbands. A checkerboard array achieves >10 dB RCS

reduction from 5 GHz to 26 GHz (135.5% bandwidth). This design offers unique flexibility for adaptive stealth antennas.

pp. 286-288

S26: Microwave Filters and Resonators I

Room: Urchins 2
Chair: Jing-Yu Lin (University of Birmingham, United Kingdom (Great Britain))

1:45 ***3D-Printed Copper Waveguide Bandpass Filter for Q-Band Ground Station Application***

Lu Qian (University of Birmingham, United Kingdom (Great Britain)); John Robinson and Arun Arjunan (University of Wolverhampton, United Kingdom (Great Britain)); Yi Wang (University of Birmingham, United Kingdom (Great Britain))

Metal additive manufacturing has emerged as a transformative fabrication technique for microwave and millimetre-wave waveguide components, yet challenges persist due to degrading surface conductivity from high surface roughness, particularly in low-conductivity metals and alloys. Copper is one of the most electrically conductive metals. Its nominal bulk conductivity is 53% higher than aluminium. However, copper printing is not as well developed and utilised due to process difficulties that arise from the poor absorption of infrared laser commonly used in Laser Powder Bed Fusion (L-PBF) Additive Manufacturing (AM). This work investigates the application of pure copper printing to waveguide devices. A monolithic copper waveguide bandpass filter is fabricated using L-PBF technology, leveraging copper's superior electrical and thermal properties for high-power microwave applications. This filter employs a step-impedance low-pass design and exploits waveguide cut-off characteristics for passband frequency selectivity. The filter is designed for Q-band ground segment network applications, with a passband from 37.5 to 42.5 GHz. Optimized L-PBF processing parameters overcome copper's high reflectivity to infrared laser. RF measurements show excellent agreement with simulations, yielding a 0.45 dB insertion loss and an 18 dB worst-case return loss, with minimal frequency shift confirming high manufacturing accuracy. This study demonstrates the potential of copper 3D printing for waveguide filters.

Presenter bio: Yi Wang is Professor of Microwave Engineering with the University of Birmingham. He leads the Emerging Device Technology (EDT) Research Lab, specializing in the application of new materials and advanced manufacturing techniques to high frequency devices. He is also the Academic Lead of the Engineering Cleanroom and the Terahertz Measurement Facility at Birmingham. He served the TPC Chair of 2021 European Microwave Conference. His current research interests include: 3D printed microwave and mm-wave devices, waveguide antenna technology, multiport filtering networks, filter-antenna integration, millimeter-wave and sub-terahertz antennas and devices for metrology, communication, and sensing.

pp. 289-291

2:00 ***A Broadband Unequal Power Divider Based on an H-Plane Height-Reduced Waveguide T-Junction***

Bo Li (Chengdu Polaris Information and Communication Technology, China)

This paper presents a method for designing a broadband unequal power divider to achieve an arbitrary power-dividing ratio. The divider is realized by reducing the height of the narrow edge of a waveguide, without affecting the phase consistency between the two output ports. Formulas for determining the power ratio and a design methodology to compensate for discontinuities in the waveguide-using irises, a septum, and a matching section-are introduced. Moreover, a 2:1 unequal power divider operating in the frequency range of 25-31 GHz is designed and fabricated. The measured bandwidth is approximately 21%, featuring an input return loss exceeding 25 dB, an insertion loss below 0.15 dB, and a phase difference between the output ports of less than 5°.

pp. 292-294

2:15 ***Low-Loss Millimeter-Wave Wideband Bandpass Filter in InP Technology with Cryogenic Performance Analysis***

Hongliang Tian (Shenzhen University, China); Haiwen Liu (Dalian University, China); Junfa Mao (Shanghai Jiao Tong University, China)

This paper presents the design and cryogenic characterization of on-chip millimeter-wave ultra-wideband (UWB) bandpass filters (BPFs) optimized using advanced algorithms. First, an on-chip mm-wave UWB BPF is designed, which demonstrates a 0.12 dB insertion loss improvement and a 0.3 GHz frequency shift when cooled from 300 K to 77 K. Based on this design, a flip-chip InP-based balanced UWB BPF utilizing electromagnetic-circuit co-optimization with the grey wolf optimization (GWO) algorithm is designed. The filter is fabricated with spiral inductors and metal-insulator-metal capacitors on an alumina substrate, and maintains stable differential mode performance (center frequency: 15.45 GHz, bandwidth: 101.9%, common mode rejection: 20 dB over 0-24.5 GHz) across 300 K, 70 K, and 5 K. Notably, the minimum insertion loss decreases from 1.02 dB to 0.72 dB when cooled from 300 K to 70 K, with 0.3-0.8 dB improvements across the passband. Analysis reveals that enhanced gold conductivity at cryogenic temperatures is the primary mechanism for insertion loss reduction, significantly exceeding the adverse effects of dielectric loss and structural deformation. The GWO algorithm successfully extracts equivalent circuit parameters, enabling temperature-dependent performance prediction for cryogenic mm-wave applications.

pg. 295

2:30 ***A Broadband High-Selectivity Bandpass Filter Branch-Line Coupler Operating in the C-Band***

Yiyang Han, Kun Wei, Wei Hu and Wen Jiang (Xidian University, China)

This paper proposes a design scheme for a broadband highly selective bandpass filter branch line coupler (BHFC) applicable to the C-band. By integrating a broadband coupling structure-comprising parallel coupling lines, high-impedance transmission lines, and parallel open-circuit branch lines-at each port of a single-section branch line coupler, it achieves bandpass filtering characteristics with excellent selectivity and a wide operating bandwidth. The circuit design has been validated through electromagnetic simulation. Experimental results demonstrate an operating frequency range of 4.02 GHz to 7.88 GHz, with a relative bandwidth reaching 64.9%. The power imbalance is ±0.6 dB, return loss exceeds 13 dB, phase imbalance is ±6.6° and selectivity exceeding 73.2%.

pp. 296-298

2:45 ***Ultrahigh-Sensitivity Microwave Biosensor Based on a CPW Loaded with a Modified Complementary Electric-LC Resonator***

Shaghayegh Chamani and Xiaojing Lv (University of Technology Sydney, Australia); Trevor S. Bird (Antengenuity, Australia & University of Technology, Sydney, Australia); Yang Yang (University of Technology Sydney, Australia)

This paper presents an ultra-high-sensitivity microwave planar sensor for biological permittivity sensing based on a conductor-backed coplanar waveguide (CPW) integrated with a modified complementary electric-LC (CELC) resonator. The proposed structure incorporates meandered frames and an interdigital capacitor (IDC) into the CELC resonator etched on the bottom ground plane to enhance the effective inductance and capacitance of the resonant structure. The proposed sensor achieves peak and average sensitivities of 3.58% and 2.58%, respectively, demonstrating its potential for biological permittivity sensing applications.

pp. 299-301

S8: Terahertz Technologies and Systems III

Room: Michaelmus B

Chair: Daniel Headland (The University of Adelaide, Australia)

1:45 ***Reconfigurable Millimetre-Waves and Terahertz Devices Using Phase Change Materials***

Aurelian Crunteanu (XLIM, CNRS/ University of Limoges, France); Wilfrid Renkanga Mbatchi (XLIM, France); Eduard-Nicolae Sirjita (XLIM Research Institute, CNRS- University of Limoges, France); Cyril Decroze (XLIM, France); Georges Humbert (Xlim, France); Alexandre Boulle (Institute of Ceramic Research IRCER, France); Jean-Christophe Orlianges (XLIM, CNRS/ Université de Limoges, France)

We present the integration of phase transition materials -PTM (e.g. VO2) with volatile metal-insulator transition (MIT) and of chalcogenides (GeTe, Ge2Sb2Te5...) phase change materials (PCM)- showing a non-volatile, reversible structural and electrical state changes, as agile elements for switching, frequency reconfiguration and amplitude modulation of devices operating at millimeter-waves and THz frequencies.

pg. 302

2:00 ***Design of a Pattern Reconfigurable Amplifier Antenna with Gain Amplification Using Transistors***

Minghuan Wang (Nanjing University of Science and Technology, China); Hao Wang (Nanjing University of Science & Technology, China); Yan Wang and Jianyin Cao (Nanjing University of Science and Technology, China)

This letter proposes an amplifier antenna that integrates gain amplification and pattern reconfigurability. Using two transistors not only amplifies the antenna gain but also enables pattern switching among three states. The antenna and the microstrip-to-slotline transition serve as the input and output matching networks of the amplifier, respectively, which reduces the circuit size. This design achieves the highly efficient integration of the antenna and the amplifier. Two integrated antenna elements placed on the same dielectric substrate form a pattern reconfigurable antenna. Simulation results show that the designed pattern reconfigurable amplifier antenna operates over the frequency band 5.8 GHz to 10.3 GHz. The gain varies from 11.38 dBi to 16.88 dBi. The gain amplification over a wide operating frequency band and the radiation patterns in three states demonstrate the feasibility of the integrated design.

pp. 303-305

2:15 ***Characterization of 32 GT/s UCIe-Compatible Package Interconnects for Reconfigurable RF Chiplet Integration***

Baoping Meng, Guangbao Shan, Guoliang Li, Yanwen Zheng, Wenbin Wei and Jiaxu Cao (Xidian University, China)

To address the critical need for modular and flexible integration in reconfigurable RF integrated systems, a substrate interconnect model based on standard packaging is designed and validated for the 32 GT/s Universal Chiplet Interconnect Express (UCIe) standard. In reconfigurable architectures, the bandwidth consistency and electromagnetic isolation of the underlying interconnects are essential for enabling dynamic functional scheduling. This work establishes a full-link model incorporating pillars, vias, and traces on an organic substrate. Frequency response simulations demonstrate that at the 16 GHz Nyquist frequency, Voltage Transfer Function (VTF) loss remains above -7.5 dB and crosstalk is suppressed below -26 dB, satisfying UCIe specifications for standard packages. Furthermore, system robustness is verified via statistical eye diagram analysis, achieving an eye width of 0.925 UI at a low Bit Error Rate (BER). This study validates the feasibility of utilizing mature standard packaging processes to build high-performance, cost-effective communication platforms for reconfigurable RF chiplet integration.

pp. 306-308

2:30 ***A Sub-THz Conductive-Bridging Memristive Switch for Reconfigurable RF Front-Ends***

Zong-Rui Xu and Yongxin Guo (City University of Hong Kong, Hong Kong)

This paper proposes a sub-THz conductive-bridging memristive switch implemented on high-resistivity silicon for reconfigurable RF front-end applications. Driven by the increasing demand for low-power, compact, and non-volatile reconfigurable hardware in beyond-5G/6G systems, the proposed device explores the feasibility of extending conductive-bridging memristive switching mechanisms toward the sub-THz frequency range. The switch is developed based on a parasitic-aware compact model, in which the ON/OFF-state resistance transition is jointly considered with the intrinsic shunt capacitance and series inductance introduced by the device geometry and interconnect layout. To suppress high-frequency degradation, the structural design is optimized to minimize OFF-state capacitive coupling and parasitic inductive effects while maintaining a compact footprint compatible with high-density integration on silicon platforms. Compared with conventional semiconductor or volatile switching technologies, the proposed conductive-bridging memristive switch is expected to offer near-zero static power consumption, non-volatile state retention, and enhanced scalability for large-scale reconfigurable front-ends. The proposed concept provides a promising device-level solution for future sub-THz switches, switch matrices, and programmable passive networks in reconfigurable transceivers and intelligent RF systems.

pg. 309

2:45 ***On-Body Characterization of a Planar Horseshoe-Slot MXene Microstrip Antenna with an Elevated Ground Plane for Wearable Applications***

Purna B. Samal (University of Technology Sydney, Australia); Shengjian Jammy Chen (Flinders University, Australia & The University of Adelaide, Australia); Christophe Fumeaux (University of Queensland, Australia)

This paper presents the on-body characterization of a horseshoe-slot microstrip antenna with an elevated ground plane fabricated using flexible MXene conductors and a PDMS substrate. The design incorporates two previously developed efficiency-enhancement techniques: radiator optimization to reduce conductor loss and an elevated ground plane to mitigate dielectric loss. These methods improve radiation efficiency by approximately 14% without altering the antenna size or bandwidth. In this work, the optimized antenna is evaluated under on-body conditions to assess its suitability for wearable applications. The results show close agreement between simulation and measurement, with stable impedance characteristics, preserved broadside radiation patterns, and minimal gain degradation when placed on the body. These findings confirm the robustness of the efficiency-driven design for wearable applications.

Presenter bio: Shengjian Jammy Chen received M.E and Ph.D degrees in electrical and electronic engineering from the University of Adelaide, Australia. From 2017 to 2021, he was a lecturer and a postdoctoral researcher at the School of Electrical and Electronic Engineering of the University of Adelaide. Since 2022, he is a lecturer with College of Science and Engineering at Finders University. His current research interests include wearable and reconfigurable electromagnetic structures based on novel conductive materials such as conductive polymers and conductive fabrics, RFID-based wearable applications and leaky wave antennas. Dr. Chen was the recipient of the Young Scientist Best Paper Award at ICEAA 2015 & ICEAA 2016, and Travel Bursary Award in ICEAA 2016. He also received the Honorable Mention in APS/URSI 2017, the CST University Publication Award 2017, and Best Paper Award at IEEE APMC 2021.

pp. 310-312

Friday, July 24 3:30 - 4:45

BPC (Debabani-Mentoring Session)

Room: Urchins 2

Chair: Debabani Choudhury (SeraTech, LLC, USA)

S18: Dielectric Characterisation

Room: Reef

Chair: Aurelian Crunteanu (XLIM, CNRS/ University of Limoges, France)

3:30 ***THz Material Characterization of Rough Samples***

Miguel Navarro-Cía (University of Birmingham, United Kingdom (Great Britain))

The accurate extraction of material properties from free-space methods is dependent on several assumptions, including that the sample has parallel, flat surfaces, and constant thickness, and that the material is homogeneous. In reality, none of these are satisfied for standard samples probed with THz due to the usual non-negligible surface roughness in the range of tens of microns. This invited talk will give an overview on the work done at the University of Birmingham to develop methodologies that pivot around quasi-optical time- and frequency-domain spectroscopy systems to deal with rough samples

Presenter bio: Miguel Navarro-Cía received the M.Sci. and Ph.D. degrees in Telecommunication Engineering, and M.Res. degree in Introduction to Research in Communications from Universidad Pública de Navarra, in 2006, 2010 and 2007, respectively. From September 2006 to March 2011, he worked as a FPI fellow and a Research & Teaching Assistant at UPNA. He was a Research Associate at Imperial College London and University College London in 2011 and 2012, respectively, and a Junior Research Fellow at Imperial College London from December 2012 until November 2015. Currently he is Birmingham Fellow at University of Birmingham. He worked as Visiting Researcher at University of Pennsylvania for 3 months in 2010, at Imperial College London in 2008, 2009 and 2010 for 4, 6 and 3 months, respectively, and at Valencia Nanophotonics Technology Center for 2 months in 2008. His current research interests are focused on plasmonics, THz near-field time-domain spectroscopy, metamaterials and antennas.

pg. 313

3:45 ***A Branch-Independent Computational Method for Dielectric Material Characterization***

Yunhao Fu (The University of New South Wales, Australia); Rodica Ramer (University of New South Wales, Australia)

A branch-independent computational method is proposed, permitting dielectric material characterization by extracting its real relative permittivity εr from a propagation factor. The propagation factor, which describes the interaction between a dielectric and an electromagnetic wave, is widely employed in material characterization. However, εr extracted from the propagation factor suffers from phase ambiguity due to the multi-valued nature of the logarithm operation. The resulting multiple phase branches correspond to different εr, making it difficult to determine the correct value. A computational method based on the first derivative of the phase branch is developed with closed-form formulas, producing the correct εr. Simulation validation in the 12-18 GHz band is conducted to demonstrate the method under ideal conditions; an experimental measurement on PTFE samples follows. Unlike traditional wideband characterization methods, which focus solely on a single frequency, the branch-independent method considers the propagation factor's overall behavior in wideband dielectric material characterization.

pp. 314-316

4:00 ***Application of Q-Chokes for Enhanced Characterization of Materials in FR3 Band***

Malgorzata Celuch (QWED, Poland); Wojciech Gwarek (QWED Sp. z O. O., Poland); Lukasz Nowicki (Warsaw University of Technology, Poland & QWED, Poland); Marzena Olszewska-Placha (QWED Sp. z o. o, Poland)

This contribution concerns resonator-based characterization of materials. First, the relevant physical principles are discussed and illustrated with EM modeling. Then, industrial round-robin results are summarized, assessing the commercially available techniques from the viewpoint of 5G/mmWave applications. The presentation then focuses on the novel Q-Choked resonators and their advantages for materials' characterization in the forthcoming FR3 frequency band.

pg. 317

4:15 ***Microwave Probe with Enhanced Sensitivity for Wideband Dielectric Characterizations***

Amir Ebrahimi (RMIT University, Australia); Syed Akbar Raza Naqvi and Amin Abbosh (The University of Queensland, Australia)

This paper presents a high-sensitivity microwave probe for broadband dielectric characterization, achieving improved accuracy compared to conventional open-ended coaxial probes based on RG405 coaxial cable. The proposed design employs a series inductive loading at the probe tip, implemented using a via-connected circular patch structure, to enhance electromagnetic interaction with the material under test. An analytical circuit model is developed to quantify amplitude and phase sensitivities, confirming significant improvement over standard probes. A fabricated prototype demonstrates superior performance across 1-7 GHz, validated through measurements of water-ethanol mixtures with up to 15% water content.

pg. 318

4:30 ***A High-Sensitivity Dielectric Characterization Method for Thin-Film Materials Using Ridge Gap Waveguide Resonator***

Jiamin He (University of Electronic Science and Technology of China, China)

This paper presents a high-sensitivity dielectric characterization method for thin-film materials using a ridge gap waveguide resonator. The ridge structure enhances the electric field interaction with the material under test (MUT), achieving a 20.5% improvement in sensitivity. The method requires no vias or metal plating, offering reusability and broadband operation. It is verified in Ka-band with RO4350B and in W-band with quartz film, showing good agreement with manufacturer data and simulations.

pp. 319-320

S27: Online

Room: Michaelmus A

3:30 ***Radiative Wireless Power Transfer with Advanced Materials***

Naoki Shinohara (Kyoto University, Japan)

Radiative wireless power transfer (WPT) via microwaves and millimeter waves is considered a promising technology to expand the application of electricity. A lot of historical excellent research and development of the WPT via microwaves were carried out in 1960s and in 1970s. Recently, advanced WPT business has started in the world based on the WPT radio wave regulations. Especially in Japan, new legal WPT radio wave regulations at 920MHz, at 2.4GHz, and at 5.8GHz was published in 2022. After the 2022, over 800 WPT base stations has already installed and are working in Japanese buildings mainly for battery-free Billing Energy Management System (BEMS). In Japan in 2026, we will update the Japanese WPT regulation for more conveniency. In 2026 in IEEE, discussion for new IEEE WPT regulation has already started as IEEE Standard WG3735 originally supported by MTT-S. Current WPT business is based on the wide beam WPT technology, in which wireless power is provided widely to multi-users without beam forming like conventional wireless communication system. Key technology in the wide beam WPT is a high efficiency rectenna, rectifying antenna with diode or CMOS. For the wide beam WPT, advanced diode or SMOS with high efficiency is required. In the next step of the WPT, novel beam forming technology with a phased array antenna is expected. In this talk, current R&D and business of the WPT via microwaves and millimeter waves are introduced. The expectation for the advanced materials for next step WPT is also explained in this talk.

pg. 321

3:42 ***Microwave Sensors Exploiting Nonlinear Dynamics***

Almudena Suarez (Universidad de Cantabria, Spain)

Oscillator-based sensing offers compact implementations, with autonomous operation, simple readout mechanisms, and the possibility of exploiting nonlinear dynamical phenomena. These phenomena can significantly enhance sensitivity and provide new sensing modalities that go beyond conventional frequency-shift measurements. The central idea is to deliberately operate oscillators in specific nonlinear regimes in which measurable quantities-such as oscillation frequency, locking bandwidth, beat frequency, spectral structure, or switching thresholds-exhibit a strong dependence on the properties of the material under test. The presentation will first provide an insightful study of how the sensing behavior of a resonant structure is affected when it is incorporated into a loop containing an active nonlinear block. We then address oscillator sensors based on injection locking, using the boundaries of the locking band as the sensing observables. We additionally investigate the high sensitivity of the beat frequency near the locking edges, which is compared with that of the original free-running oscillator. In a different configuration, we synthesize a low-frequency self-oscillation that, through its coupling to the main one, enables sensing based on multiple spectral lines. Using self-injected configurations, we demonstrate extremely sensitive operation near the hysteresis limit, as well as the deliberate use of hysteresis to trigger a state change only when the measurand crosses specific thresholds. A key aspect is the use of rigorous nonlinear analysis and design methodologies that combine analytical modeling, bifurcation theory, describing-function techniques, and harmonic-balance simulations, enabling a systematic understanding of the various dynamical behaviors on which these sensors are based. Experimental implementations based on transistor oscillators operating in the microwave range demonstrate the practical feasibility of these concepts. They illustrate how nonlinear dynamical phenomena, often regarded as undesired effects, can instead provide powerful sensing mechanisms and open new opportunities for the design of compact, highly sensitive microwave sensors.

pg. 322

3:55 ***Design of Filtering Power Amplifier Based on TGV-IPD Filtering Matching Network***

Shiyu Zhu (South China University of Technology, China); Jin-Xu Xu (Pazhou Lab, China); Xiu Yin Zhang (South China University of Technology, China)

This paper presents a 6.425-7.125 GHz filtering power amplifier (FPA) implemented using a 0.1-um GaAs pHEMT process integrated with glass-substrate inte-grated passive device (IPD) technology. A two-stage architecture is adopted, where multiple transmission zeros are introduced to realize a bandpass filtering response. To minimize insertion loss, the output match-ing network (OMN) is fabricated using high-Q through glass via (TGV) IPD technology. Simulation results show that the proposed PA achieves a gain of 20.5-21 dB over the frequency range of 6.425-7.125 GHz with a strong out-of-band rejection. The output power reaches 32.2-32.9 dBm with a saturated power-added efficiency (PAE) of 46.5-49.5%.

pp. 323-325

4:07 ***Machine Learning-Assisted End-to-End Synthesis of RF Transformer-Based Matching Networks***

Tao Wang, Li Gao, Yao Fo Chen and Xiuyin Zhang (South China University of Technology, China)

This paper proposes a learning-driven synthesis framework for RF transformer-based matching networks with three-dimensional electromagnetic (EM) structures. Unlike conventional methods that derive EM structures from target circuit element values and topologies, the proposed method directly synthesizes passive networks from desired performance metrics and given topologies. Using on-chip transformer impedance matching networks as a case study, the model first extracts key features from input impedance and load capacitance via neural networks to predict initial geometric parameters of the transformer's 3D EM structure in 28-nm TSMC CMOS technology. Subsequently, Bayesian optimization (BO) refines these geometric parameters for precise performance tuning. The resulting structures achieve arbitrary impedance matching while simultaneously accommodating two load capacitances. As a proof of concept, multiple transformer designs were synthesized

and validated by Cadence simulations, confirming their compliance with the targeted impedance characteristics.

pp. 326-328

4:22 ***A Wideband Terahertz Interconnection Between Microstrip Line and Waveguide Using Novel Short-Circuited Stub***

Juncheng Min (Aerospace Information Research Institute, Chinese Academy of Sciences, China); Peng Wu (Chinese Academy of Sciences, China & University of Chinese Academy of Sciences, China); Kaiyuan Du and Chao Xue (Institute of Electronics, Chinese Academy of Sciences, China)

A novel wideband terahertz interconnection between microstrip line and waveguide is proposed for full-band applications, addressing the requirements of high-frequency test equipment, radar modules, and communication systems. A short-circuited stub is newly introduced to enhance the performance of the microstrip-to-waveguide transition. The short-circuited stub adjacent to the probe provides additional inductive loading, generating multiple resonant matching frequencies and thereby improving impedance matching across a wider bandwidth. With the proposed interconnection scheme, the D band is entirely covered, and in the frequency range from 95 GHz to 200 GHz, the simulated return loss and insertion loss are better than -15 dB and -0.75 dB. To experimentally validate the design, a back-to-back probe transition is fabricated. The measured return loss and insertion loss are better than -13 dB and -1.1 dB, respectively, from 103 GHz to 177 GHz, demonstrating excellent wideband performance. The proposed interconnection exhibits not only broad operational bandwidth but also strong potential for compact integration in high-frequency systems.

pp. 329-331

4:35 ***A 300-GHz Broadband Power-Reconfigurable Load-Modulated Balanced Amplifier***

Kaiyuan Du (Institute of Electronics, Chinese Academy of Sciences, China); Peng Wu (Chinese Academy of Sciences, China & University of Chinese Academy of Sciences, China); Juncheng Min (Aerospace Information Research Institute, Chinese Academy of Sciences, China); Zhongjun Yu (Aerospace Information Research Institute Chinese Academy of Sciences, China)

This paper presents a 300 GHz broadband power-reconfigurable load-modulated balanced amplifier (PR-LMBA) for broadband sub-terahertz applications. The proposed architecture leverages intrinsic load modulation within a balanced topology to realize dual-mode power operation without employing RF switches or reconfigurable matching networks. Implemented in a 0.13-um SiGe BiCMOS technology, the PR-LMBA achieves a peak small-signal gain of 19.4 dB with a 3-dB bandwidth of 62 GHz (246-308 GHz). In high-power mode, a maximum output power of 11.4 dBm and a peak power-added efficiency (PAE) of 2.3% are obtained. In low-power mode, the amplifier provides 4.7 dBm output power with 1.89% PAE, corresponding to a 6.3 dB reconfigurable power range.

pp. 332-334

S9: Microwave Filters and Devices

Room: Michaelmus B

Chair: Bo Li (Chengdu Polaris Information and Communication Technology, China)

3:30 ***A Low-Loss Tunable Bandpass Filter Based on Boundary-Reconfigurable Patch Resonators***

Huihui Fei, Ren Rong Zhao, Peng Chen and Chao Yu (Southeast University, China)

This paper presents a low-loss tunable bandpass filter (BPF) based on a boundary-reconfigurable patch resonator. Frequency tuning is realized by reconfiguring the resonator boundary conditions without using

conventional lumped elements such as varactor diodes, thereby maintaining low insertion loss. The fabricated filter demonstrates a center-frequency tuning range from 0.45 to 1.15 GHz, corresponding to a tuning ratio of 2.56. Across the entire CF tuning range, the measured minimal insertion loss is maintained below 1.35 dB. In addition, bandwidth reconfigurability is realized, with the fractional bandwidth adjustable from 20.5% to 32.0%. Moreover, transmission zeros are generated at both sides of the passband which enhance the BPF's selectivity. Therefore, the proposed filter provides a practical solution for low-loss tunable filtering applications.

pp. 335-337

3:45 ***A Multi-Mode Tunable Bandpass Filter with the Continuous Transmission Zero***

Guangbao Shan, Chunyu Yang and Yanwen Zheng (Xidian University, China)

This paper presents a compact tunable bandpass filter (TBPF) realized using Through-Silicon Via (TSV) technology. The controlled tunable transmission zeros (TZs) are introduced to achieve bandwidth tuning. The area of the filter is 720×510um2. The result demonstrates a wide continuous bandwidth tuning range from 10 GHz to 14.92 GHz, with a minimum insertion loss of 0.113 dB. Index terms: Tunable, BPF, RF front-end, 3d integration

pp. 338-340

4:00 ***Wideband Phased-Array Meta-Antenna Without Air Cavity for Ku-Band Satellite Communication***

Qing You (University of Macau, Macao); Dianxin Luan (University of Edinburgh, United Kingdom (Great Britain)); Pui-In Mak, Rui P. Martins and Jun Yin (University of Macau, Macao)

This paper presents a wideband dual-linear polarization Ku-Band phased-array meta-antenna that eliminates the need for an air cavity. By incorporating a metasurface, the proposed antenna achieves a broad operational bandwidth from 10.7 GHz to 14.5 GHz with a realized gain exceeding 1.7 dBi. The wideband performance is realized without an air cavity, thereby simplifying the fabrication process. By leveraging this antenna design, a method for achieving both dual-linear and dual-circular polarization is demonstrated. Implemented on a cost-effective PCB platform, the proposed phased array offers a low-cost solution well-suited for satellite communication applications.

pp. 341-343

4:15 ***A Hexagonal Six-Port Hybrid Coupler for Beamforming Applications***

Zhiwei Yin (University of Technology Sydney, Australia); He Zhu (Charles Darwin University, Australia); Xiaojing Lv and Yang Yang (University of Technology Sydney, Australia)

Multibeam scanning capabilities are essential for modern wireless communication systems, including 5G/6G MIMO and satellite technology. This paper presents a novel approach to implementing a 3-beam feeding network using a compact planar six-port regular hexagonal hybrid coupler. Compared to conventional Nolen matrix (NM) designs that rely on a cascaded arrangement of multiple couplers and phase shifters, the proposed design integrates these functionalities into a single planar component. This approach achieves a significant size reduction of over 70% while maintaining excellent RF performance. To verify the concept, a prototype operating at 2.45 GHz was designed and fabricated. The measured results demonstrate an equal power division of 5±0.9 dB and phase differences of ±120 deg and ±0 deg across the 2.28--2.61 GHz band. The simplicity and effectiveness of this approach make it highly suitable for compact, scalable beamforming systems.

pp. 344-346

4:30 ***Short-Circuit Ring Patch Bandpass Filter on Glass Substrate with MLP-Based Optimization***

Jing-Yu Lin (University of Birmingham)

This paper presents a novel design framework for 3rd-order on-chip bandpass filters (BPFs) based on short-circuited ring patch (SCRP) resonators fabricated using through-glass via (TGV) technology on fused silica substrates. The filter units are implemented using 1/n-mode SCRP resonators. To achieve efficient and precise structural optimization, a multilayer perceptron (MLP)-based model is employed, trained on electromagnetic simulation data to map geometric parameters to S-parameter responses. The optimized design, targeting 5G n257/n258 bands, and filter prototypes were designed, fabricated, and experimentally characterized. Both filters exhibit excellent performance, with measured insertion loss (IL) below 1.5 dB and return loss (RL) exceeding 15 dB. The measured results show strong agreement with simulations, validating the effectiveness of the proposed MLP-assisted design methodology.

pp. 347-349

Friday, July 24 4:45 - 5:00

Awards & Closing Ceremony

Room: Michaelmus B

Technical Program Committee

Syed Muzahir Abbas	Macquarie University	Australia
Muhammad Ali Babar Abbasi	Queen's University Belfast & Centre for Wireless Innovation (CWI)	United Kingdom (Great Britain)
Ali Abdulateef Abdulbari	University of Technology	Iraq
Huaguang Bao	Nanjing University of Science and Technology	China
Xiue Bao	Beijing Institute of Technology & KU Leuven	China
H. W. Peter Beadle	Academic Event Services	Australia
Konstanty S Bialkowski	The University of Queensland	Australia
Yuanxi Cao	Xi'an Jiaotong University	China
Robert Caverly	Villanova University	USA
Jian Chen	Nanjing University & Research Institute of Superconductor Electronics	China
Peng Chen	Southeast University	China
Shengjian Jammy Chen	Flinders University & The University of Adelaide	Australia
Aurelian Crunteanu	XLIM, CNRS/ University of Limoges	France
Valerio De Santis	University of L'Aquila	Italy
Cyril Decroze	XLIM	France
Shuvashis Dey	North Dakota State University	USA
Qian Dong	Xi'an Jiaotong-Liverpool University	China
Zhi-Xia Du	Guangdong University of Technology	China
Amir Ebrahimi	RMIT University	Australia
Wang Fangqian	Xidian University	China
Mauro Feliziani	Roma	Italy
Yunhao Fu	The University of New South Wales	Australia
Shuai Gao	Shenzhen University	China
Si-Ping Gao	Nanjing University of Aeronautics and Astronautics	China
Dingxuan Gu	Nanjing University	China
Jihong Gu	Nanjing University of Science and Technology	China
Wenhua Gu	Nanjing University of Science and Technology	China
Xiaoxuan Guo	University of Technology Sydney	Australia
Daniel Headland	The University of Adelaide	Australia
Zhirun Hu	University of Manchester	United Kingdom (Great Britain)
Muhammad Inam Abbasi	Universiti Teknikal Malaysia Melaka (UTeM)	Malaysia
Hao Jiang	City University of Hong Kong	Hong Kong

Bao Jingfu	University of Electronic Science and Technology of China	China
Debabrata K. Karmokar	Adelaide University	Australia
Thirupathaiah Kola	Koneru Lakshmaiah Education Foundation Hyderabad & Abu Dhabi University	India
Juseop Lee	Korea University	Korea (South)
Harrison N Lees	The University of Adelaide	Australia
Bo Li	Chengdu Polaris Information and Communication Technology	China
Guoliang Li	Xidian University	China
Jianxing Li	Xi'an Jiaotong University	China
Xiaochun LI	Shanghai Jiao Tong University	China
Xiuping Li	Beijing University of Post and Telecommunications	China
YH Li	National Space Science Center Chinese Academy of Sciences	China
Sungjoon Lim	Chung-Ang University	Korea (South)
Jing-Yu Lin	University of Birmingham	United Kingdom (Great Britain)
Changjun Liu	Sichuan University	China
Xi Sung Loo	Nanyang Technological University	Singapore
Dianxin Luan	University of Edinburgh	United Kingdom (Great Britain)
Xiaojing Lv	University of Technology Sydney	Australia
David Mitchell	University of Illinois at Urbana-Champaign	USA
Umar Mohammad	Nanjing University of Posts and Telecommunications	China
Maira Islam Nabeel	University of Technology Sydney	Australia
Miguel Navarro-Cía	University of Birmingham	United Kingdom (Great Britain)
Haq Nawaz	Military Technological College	Oman
Zhongqian Niu	University of Electronic Science and Technology of China	China
Rui Pei	Xi'an Jiaotong-Liverpool University	China
Zhaomin Peng	National Space Science Center Chinese Academy of Sciences	China
Duc Anh Pham	University of Illinois at Chicago	USA
Lu Qian	University of Birmingham	United Kingdom (Great Britain)
Pei Qin	South China University of Technology	China
Xue Ren	Shenzhen University	China
Purna B. Samal	University of Technology Sydney	Australia

Mohammad Samizadeh Nikoo	NTU Singapore	Singapore
Guangbao Shan	Xidian University	China
Jun Shi	National Space Science Center Chinese Academy of Sciences	China
Naoki Shinohara	Kyoto University	Japan
Liming Si	Beijing Institute of Technology	China
Jianxun Su	Communication University of China	China
Houjun Sun	Beijing Institute of Technology	China
Shuo Sun	Beijing University of Posts and Telecommunications	China
Zhichao Sun	University of Technology Sydeny	Australia
Safumi Suzuki	Institute of Science Tokyo	Japan
Kun Tang	South China University of Technology	China
Dush Thalakotuna	University of Technology Sydney	Australia
Cristiano Tomassoni	University of Perugia	Italy
Xuecou Tu	Nanjing University	China
Krushna Kanth Varikuntla	Queen's University Belfast & Queens's University Belfast	United Kingdom (Great Britain)
Yinglu Wan	Guangxi University	China
Chao-Fu Wang	National University of Singapore	Singapore
Hong Bin Wang	UESTC	China
Jingchen Wang	Xi'an Jiaotong-Liverpool University	China
Shi-Tong Wang	City University of Hong Kong	Hong Kong
Yi Wang	University of Birmingham	United Kingdom (Great Britain)
Withawat Withayachumnankul	The University of Adelaide	Australia
Geng-Bo Wu	City University of Hong Kong	Hong Kong
Hung-Wei Wu	Institute of Semiconductors, Guangdong Academy of Sciences	China
Peng Wu	Chinese Academy of Sciences & University of Chinese Academy of Sciences	China
Shuxin Wu	Communication University of China	China
Ya Fei Wu	UESTC	China
Kai-Ran Xiang	South China University of Technology	China
Xin Xiu	South China University of Technology	China
Yuehang Xu	University of Electronic Science and Technology of China	China
Zong-Rui Xu	City University of Hong Kong	Hong Kong
Wu Yang	Southeast University	China

Yang Yang	SiChuan University	China
Yang Yang	University of Technology Sydney	Australia
Qing You	University of Macau	Macao
Qiaowei Yuan	Tohoku Institute of Technology	Japan
Tao Yuan	Shenzhen University	China
Bing Zhang	Sichuan University	China
Qingfeng Zhang	University of Electronic Science and Technology of China	China
Tiancheng Zhang	Nanjing University of Science and Technology	China
Wenhai Zhang	Soochow University	China
Wenzhang Zhang	Xi'an Jiaotong-Liverpool University & University of Liverpool	China
Wenyu Zhao	Beijing University of Posts and Telecommunications & EE	China
Yan Zhao	Nanjing University of Science and Technology	China
Kuisong Zheng	Northwestern Polytechnical University	China
Yanwen Zheng	Xidian University	China
Yilin Zheng	Soochow University	China
Hao-Ran Zhu	Anhui University	China
Haoshen Zhu	South China University of Technology	China
He Zhu	Charles Darwin University	Australia
Jiejie Zhu	Xidian University	China
Panpan Zuo	Civil Aviation University of China	China

Additional Reviewers

Roktim Barua	North Dakota State University	USA
Hanlin Cai	University of Cambridge	United Kingdom (Great Britain)
Haoyu Chen	Huaqin Technology Co., Ltd.	China
Egecan Guler	The University of Edinburgh	United Kingdom (Great Britain)
Harshwardhan Kamble	University of Birmingham	United Kingdom (Great Britain)
Md Ashif Islam Oni	North Dakota State University	USA
Md Mirazur Rahman	North Dakota State University	USA
Yang You	Ningbo University	China

Organising Committee

General Chair

Yang Yang (University of Technology Sydney, Australia)

General Co-Chair

Tao Huang (James Cook University, Australia)

TPC Chair

Withawat Withayachumnankul (The University of Adelaide, Australia)

TPC Co-Chair

Konstanty S Bialkowski (The University of Queensland, Australia)
Amir Ebrahimi (RMIT University, Australia)
Si-Ping Gao (Nanjing University of Aeronautics and Astronautics, China)
Zhi Hao Jiang (Southeast University, China)

A B C D E F G H I J K L M N O P Q R S T V W X Y Z

Author	Session	Start page	Title
A A B C D E F G H I J K L M N O P Q R S T V W X Y Z			
	S12.5	94	*PDMS-MWCNT Composite Material Properties, Preparation and Role in Wearable Antennas*
Abbas, Syed Muzahir	S21.2	100	*Planar EBG Monostatic Antenna with Wideband Interport Isolation Characteristics for 5G in-Band Full Duplex Applications*
	S21.5	109	*Compact High-Gain 300 GHz Metasurface Antenna for Future 6G Terahertz Communications*
Abbasi, Muhammad Ali Babar	S22.1	140	*Invited Talk: Plasma-Based Reconfigurable FSS for Adaptive High-Power Microwave Shielding*
Abbosh, Amin	S18.4	318	*Microwave Probe with Enhanced Sensitivity for Wideband Dielectric Characterizations*
Amnuayphol, Nontiwat	P5.2	234	*High-Sensitivity Terahertz Sensing with Quadrature Self-Homodyne Detection*
Arjunan, Arun	S26.1	289	*3D-Printed Copper Waveguide Bandpass Filter for Q-Band Ground Station Application*
B A B C D E F G H I J K L M N O P Q R S T V W X Y Z			
Bao, Huaguang	S15.2	193	*Electromagnetic-Thermal-Fluid Multiphysics Coupling Simulation of Electronic Packaging Based on the FDTD Method*
Bernhard, Jennifer	S12.3	92	*Characterization of Knitted Textiles for Wearable Antennas*
Bialkowski, Konstanty	S24.2	208	*Modelling Clock Stability to Enabling Synchronisation for Multi-Static Passive Radar*
Bie, Mengyuan	S22.5	147	*Modal Expansion Analysis and Inverse-Design of Reconfigurable AIS-Loaded Antennas*
Bird, Trevor	S26.5	299	*Ultrahigh-Sensitivity Microwave Biosensor Based on a CPW Loaded with a Modified Complementary Electric-LC Resonator*
Boulle, Alexandre	S8.1	302	*Reconfigurable Millimetre-Waves and Terahertz Devices Using Phase Change Materials*
Boumerdassi, Wassim	S19.2	33	*Dosimetric Assessment of a Birdcage-Coil Wireless Power Transfer at 6.78 MHz for Capsule Robots*
Bowen, Tang	S5.1	177	*A 30-W Tri-Mode GaN Power Amplifier Based on Reconfigurable Multi-Network Architecture*
C A B C D E F G H I J K L M N O P Q R S T V W X Y Z			
Campi, Tommaso	S19.2	33	*Dosimetric Assessment of a Birdcage-Coil Wireless Power Transfer at 6.78 MHz for Capsule Robots*
Cao, Jianyin	S8.2	303	*Design of a Pattern Reconfigurable Amplifier Antenna with Gain Amplification Using Transistors*
Cao, Jiaxu	S8.3	306	*Characterization of 32 GT/s UCIe-Compatible Package Interconnects for Reconfigurable RF Chiplet Integration*

Cao, Yanru	S16.4	241	*A Low-Rate Digital Predistortion with Single Real Undersampling Feedback Using Switch-Estimated Method Excited by 400 MHz Sub-6 GHz Signals*
Cao, Yuanxi	S20.1	70	*W-Band Wide-Angle Coverage Pillbox Multibeam Antenna Based on Bifocal Phase Compensation*
Casiraghi, Cinzia	S20.2	73	*Non-Volatile Reflective Intelligent Surface Based on 2D Material Switches for 6G Wireless Communications*
Caverly, Robert	P3.1	123	*Semiconductor Electronics for High Power/High Speed Reconfigurable RF and Microwave Electronics*
Celuch, Malgorzata	S18.3	317	*Application of Q-Chokes for Enhanced Characterization of Materials in FR3 Band*
Chamani, Shaghayegh	S26.5	299	*Ultrahigh-Sensitivity Microwave Biosensor Based on a CPW Loaded with a Modified Complementary Electric-LC Resonator*
Chan, Chi Hou	S21.1	97	*Power-Based Direction-Finding Enabled by a Null-Scanning Space-Time Leaky-Wave Antenna*
	P1.2	2	*Novel Design Strategies for Wideband Millimeter-Wave Switched-Type MMIC Phase Shifters with Low Amplitude and Phase Errors*
	S10.2	20	*Broadband Phase-Dispersive Conformal Metamaterial for EM Backscattering Enhancement*
Che, Wenquan	S13.4	134	*A Wideband Ultra-Large-Angle Dual-Polarized Bandpass Frequency Selective Surface*
	S5.3	183	*A Compact Wideband Filtering Power Dividers Using D-CRLH Resonators*
	S17.3	283	*Wideband High-Precision Resonator-Based Phase Shifters via Lossy Electric and Magnetic Coupling*
Chen, Chi	S5.1	177	*A 30-W Tri-Mode GaN Power Amplifier Based on Reconfigurable Multi-Network Architecture*
Chen, Fu-Chang	S13.5	137	*Design of 3-D Frequency Selective Surface Based on Spatial Coupling*
	S25.5	259	*A Low Profile and High Front-to-Back Ratio Millimeter-Wave Array Based on Electromagnetic Band Gap Ground*
Chen, Jian	S2.1	55	*Photo-Tunable Chip Scale THz Ring Modulator*
	S23.1	165	*High Q Terahertz Detector in Hybrid Metal−Optical Tamm State Cavity*
Chen, Juan	S20.1	70	*W-Band Wide-Angle Coverage Pillbox Multibeam Antenna Based on Bifocal Phase Compensation*
Chen, Peng	S16.4	241	*A Low-Rate Digital Predistortion with Single Real Undersampling Feedback Using Switch-Estimated Method Excited by 400 MHz Sub-6 GHz Signals*
	S9.1	335	*A Low-Loss Tunable Bandpass Filter Based on Boundary-Reconfigurable Patch Resonators*
Chen, Shengjian	S19.1	32	*Materials-Aware Design Strategies for Wearable Antenna Design*

	S8.5	310	*On-Body Characterization of a Planar Horseshoe-Slot MXene Microstrip Antenna with an Elevated Ground Plane for Wearable Applications*
Chen, Weizhi	S10.2	20	*Broadband Phase-Dispersive Conformal Metamaterial for EM Backscattering Enhancement*
Chen, Xiaopan	S5.2	180	*A Fully Integrated Low-Cost 5-GHz Doherty Power Amplifier Using Compact Triple-Coil Splitter-Combiner in 180-nm CMOS*
Chen, Yao	S27.4	326	*Machine Learning-Assisted End-to-End Synthesis of RF Transformer-Based Matching Networks*
Chen, Zhe	S25.2	251	*A Textile Antenna for ON-/off-Body Communication*
Chen, ZhiXing	S25.4	257	*Broadband Circularly Polarized Glass Antenna with Surface Wave Suppression*
Chen, Zhuoyin	S5.2	180	*A Fully Integrated Low-Cost 5-GHz Doherty Power Amplifier Using Compact Triple-Coil Splitter-Combiner in 180-nm CMOS*
Chio, Chi-Hou	S25.4	257	*Broadband Circularly Polarized Glass Antenna with Surface Wave Suppression*
Choudhury, Debabani	P6.1	235	*Diverse Semiconductor Integrated Microelectronics in the Application-Oriented AI Era*
Chu, Qing-Xin	P2.1	4	*A Wide-Coverage End-Fire High-Gain Circularly Polarized Mobile Phone Antenna for Satellite Communication*
Chung, Bryce	S24.5	215	*General-Purpose Terahertz Quasi-Optics and Mechanical Beamformers Enabled by 3D-Printing*
	P5.2	234	*High-Sensitivity Terahertz Sensing with Quadrature Self-Homodyne Detection*
Cong, Zhou	S15.4	199	*Characteristic Mode-Based Efficient Analysis Method for Electromagnetic Scattering of Complex Electromagnetic Structures with Lossy Dielectric Materials*
Crunteanu, Aurelian	W1.3	43	*Reconfigurable and Tunable Millimeter-Waves Devices Based on Functional Materials*
	S8.1	302	*Reconfigurable Millimetre-Waves and Terahertz Devices Using Phase Change Materials*

D A B C D E F G H I J K L M N O P Q R S T V W X Y Z

Dai, Zhenlin	S20.4	79	*High-Frequency Narrowband to Low-Frequency Broadband Transition in an SMA-Actuated Bandpass Frequency-Selective Surface*
De Santis, Valerio	S19.2	33	*Dosimetric Assessment of a Birdcage-Coil Wireless Power Transfer at 6.78 MHz for Capsule Robots*
Decroze, Cyril	S8.1	302	*Reconfigurable Millimetre-Waves and Terahertz Devices Using Phase Change Materials*
Ding, Dazhi	S15.2	193	*Electromagnetic-Thermal-Fluid Multiphysics Coupling Simulation of Electronic Packaging Based on the FDTD Method*
	S15.4	199	*Characteristic Mode-Based Efficient Analysis Method for Electromagnetic Scattering of Complex Electromagnetic*

			Structures with Lossy Dielectric Materials
Dong, Qian	S5.4	184	*Optimized Design of Compact Multi-Coil Arrays for Misalignment-Tolerant Wireless Power Transfer*
Du, Kaiyuan	S27.5	329	*A Wideband Terahertz Interconnection Between Microstrip Line and Waveguide Using Novel Short-Circuited Stub*
	S27.6	332	*A 300-GHz Broadband Power-Reconfigurable Load-Modulated Balanced Amplifier*
Du, Zhi-Xia	S7.6	274	*A High-Sensitivity Rectifier Employing a Low-ESR Distributed Spiral Inductor*

E A B C D E F G H I J K L M N O P Q R S T V W X Y Z

Ebrahimi, Amir	S18.4	318	*Microwave Probe with Enhanced Sensitivity for Wideband Dielectric Characterizations*
Elgy, James	S6.4	225	*Characterisation of Dynamic Particulate Media Using Broadband FMCW Spectrometry*
Erisen, Deniz Eren	S4.1	151	*Semiconductor-grade Dry Nano-Island Coating Technology: Translating Advanced Materials from Lab Scale to Next-Gen 6G mm-Wave Substrates*
Esselle, Karu	S11.4	49	*Microwave Beam-Steering Using near-Field Metasurfaces*
	P4.1	125	*A Review of Microwave Beam-Steering Using near-Field Metasurfaces*

F A B C D E F G H I J K L M N O P Q R S T V W X Y Z

Fan, Xiang	S17.1	277	*A Continuously Tunable Silicon-Based 3D Matching Network for Heterogeneous RF Transceiver*
Fangqian, Wang	S1.2	10	*Bandwidth Reconfigurable Low-Noise Amplifier Based on Magnetic Coupling Effect*
	S17.2	280	*A Broadband Tunable Matching Network Based on Magnetic Coupling*
Fei, Huihui	S9.1	335	*A Low-Loss Tunable Bandpass Filter Based on Boundary-Reconfigurable Patch Resonators*
Feliziani, Mauro	S19.2	33	*Dosimetric Assessment of a Birdcage-Coil Wireless Power Transfer at 6.78 MHz for Capsule Robots*
Feng, Wenjie	S10.2	20	*Broadband Phase-Dispersive Conformal Metamaterial for EM Backscattering Enhancement*
	S5.3	183	*A Compact Wideband Filtering Power Dividers Using D-CRLH Resonators*
Fu, Yunhao	S18.2	314	*A Branch-Independent Computational Method for Dielectric Material Characterization*
Fujita, Masayuki	S6.6	231	*Towards Fully Integrated Terahertz Frontends: Silicon Photonics Meets Resonant Tunneling Diodes*
Fumeaux, Christophe	S8.5	310	*On-Body Characterization of a Planar Horseshoe-Slot MXene Microstrip Antenna with an Elevated Ground Plane for Wearable Applications*

Gao, Bin	S23.6	174	*Metasurface Antenna Applied in Millimeter-Wave Imaging Systems*
Gao, Li	S7.2	265	*A 8.8-12.5 GHz Dual-Core Series Resonance VCO with 201.3-dBc/Hz FoMT in 28-nm CMOS Technology*
	S27.4	326	*Machine Learning-Assisted End-to-End Synthesis of RF Transformer-Based Matching Networks*
Gao, Shuai	S25.2	251	*A Textile Antenna for ON-/off-Body Communication*
Gao, Si-Ping	S13.1	127	*Terminating Magnetostatic Surface Waves with Metallic Patterns*
Gao, Wei	S15.5	202	*Background Separation and Cancellation in Complex Indoor Testing Environments Based on the TTP Algorithm*
Gao, Weijie	S6.6	231	*Towards Fully Integrated Terahertz Frontends: Silicon Photonics Meets Resonant Tunneling Diodes*
	S22.2	141	*A Reconfigurable Transmit-Reflect-Array Antenna Based on Tightly Coupled Dipole*
Gao, Yuchen	S15.5	202	*Background Separation and Cancellation in Complex Indoor Testing Environments Based on the TTP Algorithm*
	S17.4	286	*Ultra-Wideband RCS Reduction Metasurface with Tunable Transmission Window*
Gashinova, Marina	S6.4	225	*Characterisation of Dynamic Particulate Media Using Broadband FMCW Spectrometry*
Ghorbani, Kamran	P1.1	1	*Printed VO_2 Tiles for Tunable Holographic Metasurface*
Gong, Zhixuan	S5.2	180	*A Fully Integrated Low-Cost 5-GHz Doherty Power Amplifier Using Compact Triple-Coil Splitter-Combiner in 180-nm CMOS*
Gu, Dingxuan	S2.1	55	*Photo-Tunable Chip Scale THz Ring Modulator*
	S23.1	165	*High Q Terahertz Detector in Hybrid Metal−Optical Tamm State Cavity*
Gu, Jihong	S15.4	199	*Characteristic Mode-Based Efficient Analysis Method for Electromagnetic Scattering of Complex Electromagnetic Structures with Lossy Dielectric Materials*
Gu, Wenhua	S1.4	16	*An Energy-Efficient Reconfigurable BLE RF Receiving Front-End Based on Mixer-First Architecture for IoT Applications*
	S10.3	23	*Semantics-Guided End-to-End Intelligent Design Framework for Metasurface Absorbers*
Gu, Xupeng	S6.3	222	*High-Efficiency Broadband S-Shaped Thin-Film Lithium Niobate Electro-Optic Modulator*
Guan, He	S1.3	13	*Exploiting LDMOS-PA for kW SSPA Applications*
Guo, Cheng	S20.1	70	*W-Band Wide-Angle Coverage Pillbox Multibeam Antenna Based on Bifocal Phase Compensation*
Guo, Fei	S14.3	162	*Improved Hybrid Quantum Models for More Accurate Phase Prediction of Expansion Coefficients in Large Finite Periodic Structures*

	S15.3	196	*Rapid Analysis of Scattering Problem for LFPSs with Physics-Informed Attention Network*
Guo, Lei	S20.5	82	*Liquid Crystal Tunable Phase Shifter Using Post-Wall Coplanar Waveguide*
	S11.5	52	*A Single Substrate Pancharatnam-Berry (PB) Phase Huygens' Metasurface for Dynamic Steering of Vortex Beams*
Guo, Xiaoxuan	S23.6	174	*Metasurface Antenna Applied in Millimeter-Wave Imaging Systems*
	S25.1	248	*Pattern-Reconfigurable Metasurface for Dynamic Switching Between OAM Beam and Dual-Beam*
Guo, Yongxin	S13.1	127	*Terminating Magnetostatic Surface Waves with Metallic Patterns*
	S8.4	309	*A Sub-THz Conductive-Bridging Memristive Switch for Reconfigurable RF Front-Ends*
Gwarek, Wojciech	S18.3	317	*Application of Q-Chokes for Enhanced Characterization of Materials in FR3 Band*
Han, Ye	S13.4	134	*A Wideband Ultra-Large-Angle Dual-Polarized Bandpass Frequency Selective Surface*
Han, Yiyang	S26.4	296	*A Broadband High-Selectivity Bandpass Filter Branch-Line Coupler Operating in the C-Band*
Hashimoto, Ken-Ya	S6.2	219	*Design of Titanium SAW Phononic Crystal on Lithium Niobate LiNbO3/Si Structure*
He, Jiamin	S18.5	319	*A High-Sensitivity Dielectric Characterization Method for Thin-Film Materials Using Ridge Gap Waveguide Resonator*
He, Jiaqiu	S20.2	73	*Non-Volatile Reflective Intelligent Surface Based on 2D Material Switches for 6G Wireless Communications*
He, Xin	S2.5	67	*A Compact 24-to-30-GHz GaAs Series Doherty Power Amplifier Using a Three-Coupled-Line Balun*
Headland, Daniel	W2.3	87	*General-Purpose Terahertz Quasi-Optics and Mechanical Beamformers Enabled by 3D-Printing*
	S24.5	215	*General-Purpose Terahertz Quasi-Optics and Mechanical Beamformers Enabled by 3D-Printing*
Hoare, Edward	S6.4	225	*Characterisation of Dynamic Particulate Media Using Broadband FMCW Spectrometry*
Hong, Tao	S15.5	202	*Background Separation and Cancellation in Complex Indoor Testing Environments Based on the TTP Algorithm*
	S17.4	286	*Ultra-Wideband RCS Reduction Metasurface with Tunable Transmission Window*
Hou, Xiaofeng	S25.4	257	*Broadband Circularly Polarized Glass Antenna with Surface Wave Suppression*
Hu, Bintao	S5.4	184	*Optimized Design of Compact Multi-Coil Arrays for Misalignment-Tolerant Wireless Power Transfer*

H A B C D E F G H I J K L M N O P Q R S T V W X Y Z

	S22.2	141	*A Reconfigurable Transmit-Reflect-Array Antenna Based on Tightly Coupled Dipole*
Hu, Wei	S15.5	202	*Background Separation and Cancellation in Complex Indoor Testing Environments Based on the TTP Algorithm*
	S26.4	296	*A Broadband High-Selectivity Bandpass Filter Branch-Line Coupler Operating in the C-Band*
Hu, Xidi	S1.3	13	*Exploiting LDMOS-PA for kW SSPA Applications*
Hu, Yuxi	S11.5	52	*A Single Substrate Pancharatnam-Berry (PB) Phase Huygens' Metasurface for Dynamic Steering of Vortex Beams*
Hu, Zhirun	S20.2	73	*Non-Volatile Reflective Intelligent Surface Based on 2D Material Switches for 6G Wireless Communications*
Hu, Zijun	S14.3	162	*Improved Hybrid Quantum Models for More Accurate Phase Prediction of Expansion Coefficients in Large Finite Periodic Structures*
Huang, Keying	S25.4	257	*Broadband Circularly Polarized Glass Antenna with Surface Wave Suppression*
Huang, Shangsen	S22.2	141	*A Reconfigurable Transmit-Reflect-Array Antenna Based on Tightly Coupled Dipole*
Huang, Shuai	S7.2	265	*A 8.8-12.5 GHz Dual-Core Series Resonance VCO with 201.3-dBc/Hz FoMT in 28-nm CMOS Technology*
Huang, Tongde	S1.4	16	*An Energy-Efficient Reconfigurable BLE RF Receiving Front-End Based on Mixer-First Architecture for IoT Applications*
Huang, Xueyu	S5.3	183	*A Compact Wideband Filtering Power Dividers Using D-CRLH Resonators*
Huang, Zihang	S5.4	184	*Optimized Design of Compact Multi-Coil Arrays for Misalignment-Tolerant Wireless Power Transfer*
Hui, Xiaonan	S12.2	89	*A Communication Signal Based Vital-Sign Sensing Method for Consumer Electronic Devices*
Humbert, Georges	S8.1	302	*Reconfigurable Millimetre-Waves and Terahertz Devices Using Phase Change Materials*
Hussain, Musa	S12.5	94	*PDMS-MWCNT Composite Material Properties, Preparation and Role in Wearable Antennas*

I A B C D E F G H I J K L M N O P Q R S T V W X Y Z

Ichikawa, Daiki	S6.6	231	*Towards Fully Integrated Terahertz Frontends: Silicon Photonics Meets Resonant Tunneling Diodes*
Inose, Yuta	S6.6	231	*Towards Fully Integrated Terahertz Frontends: Silicon Photonics Meets Resonant Tunneling Diodes*

J A B C D E F G H I J K L M N O P Q R S T V W X Y Z

Jia, Li-Bo	P2.1	4	*A Wide-Coverage End-Fire High-Gain Circularly Polarized Mobile Phone Antenna for Satellite Communication*
Jia, Xiaoqing	S2.1	55	*Photo-Tunable Chip Scale THz Ring Modulator*
	S23.1	165	*High Q Terahertz Detector in Hybrid Metal−Optical Tamm State Cavity*

Jiang, Hao	S22.3	144	*Reconfigurable Bandpass Ultrathin Angular-Selective Surfaces*
	S7.3	268	*Super-Mode-Group Based Reduced-Order Analysis of Multi-Mode Antenna Decoupling*
Jiang, Taiyu	S6.2	219	*Design of Titanium SAW Phononic Crystal on Lithium Niobate LiNbO3/Si Structure*
Jiang, Wen	S15.5	202	*Background Separation and Cancellation in Complex Indoor Testing Environments Based on the TTP Algorithm*
	S26.4	296	*A Broadband High-Selectivity Bandpass Filter Branch-Line Coupler Operating in the C-Band*
Jiang, Zhi Hao	S22.5	147	*Modal Expansion Analysis and Inverse-Design of Reconfigurable AIS-Loaded Antennas*
Jing, Hongshan	S23.1	165	*High Q Terahertz Detector in Hybrid Metal−Optical Tamm State Cavity*
Jingfu, Bao	S6.2	219	*Design of Titanium SAW Phononic Crystal on Lithium Niobate LiNbO3/Si Structure*
Jun, S	S4.2	152	*D Band Terahertz Driving Source Based on GaN Monolithic Integrated Frequency Multiplier*

K A B C D E F G H I J K L M N O P Q R S T V W X Y Z

Kang, Kai	S23.3	170	*Geometry Scalable Model of on-Chip Multilayer Interdigital Capacitors*
Kang, Lin	S2.1	55	*Photo-Tunable Chip Scale THz Ring Modulator*
	S23.1	165	*High Q Terahertz Detector in Hybrid Metal−Optical Tamm State Cavity*
Khan, Hajra	S12.5	94	*PDMS-MWCNT Composite Material Properties, Preparation and Role in Wearable Antennas*
	S21.2	100	*Planar EBG Monostatic Antenna with Wideband Interport Isolation Characteristics for 5G in-Band Full Duplex Applications*
Kim, Junghyeon	S16.1	237	*Millimeter-Wave and Sub-Terahertz Antenna and Metasurface Applications Using Screen Printed Vanadium Dioxide Switches*
Koo, Hyunwoo	S16.1	237	*Millimeter-Wave and Sub-Terahertz Antenna and Metasurface Applications Using Screen Printed Vanadium Dioxide Switches*

L A B C D E F G H I J K L M N O P Q R S T V W X Y Z

Lai, Baoran	S23.1	165	*High Q Terahertz Detector in Hybrid Metal−Optical Tamm State Cavity*
Lai, Jiexin	S10.6	29	*A Highly-Selective 3-D FSS with Exceptional Precision for Liquid Dielectric Constant Detection*
	S20.3	76	*A Curved Broadside-Coupled Stripline Phase Shifter and Its Application to Metasurface Designs*
	S24.4	212	*Multi-Material Additively Manufactured Wideband Dual-Linear Polarized Antenna with High Isolation*
	S25.3	254	*A Compact Wideband Dual-Circularly Polarized Millimeter-Wave Antenna with Isolation Enhancement*

Lai, Wen Cheng	S1.1	7	*Wave-Based Triple-Band CMOS Voltage-Controlled Oscillator*
Lai, Zhiguo	S23.2	167	*A High-Performance Hybrid FBAR Chip Based on TGV Technology*
Leach, Mark	S16.2	238	*Meta-Screen: Full-Space EM Environment Reconfiguration for mmWave Communications*
Lee, Jongheun	S15.1	190	*Formula-Based Design of Bias Tees with Wide DC-Path Bandwidth and Transmission Zeros*
Lee, Juseop	S15.1	190	*Formula-Based Design of Bias Tees with Wide DC-Path Bandwidth and Transmission Zeros*
Lee, Keebaek	S15.1	190	*Formula-Based Design of Bias Tees with Wide DC-Path Bandwidth and Transmission Zeros*
Lee, Minjae	S16.1	237	*Millimeter-Wave and Sub-Terahertz Antenna and Metasurface Applications Using Screen Printed Vanadium Dioxide Switches*
Lees, Harrison	P5.2	234	*High-Sensitivity Terahertz Sensing with Quadrature Self-Homodyne Detection*
Li, Bo	S26.2	292	*A Broadband Unequal Power Divider Based on an H-Plane Height-Reduced Waveguide T-Junction*
Li, Changzhi	P4.2	126	*Printable Nonlinear Tags and Handheld Devices for Clutter-Resilient Contactless Monitoring and Tracking*
Li, Chenming	S12.2	89	*A Communication Signal Based Vital-Sign Sensing Method for Consumer Electronic Devices*
Li, Guoliang	S8.3	306	*Characterization of 32 GT/s UCIe-Compatible Package Interconnects for Reconfigurable RF Chiplet Integration*
Li, Jianxing	S20.1	70	*W-Band Wide-Angle Coverage Pillbox Multibeam Antenna Based on Bifocal Phase Compensation*
Li, Keyan	S23.2	167	*A High-Performance Hybrid FBAR Chip Based on TGV Technology*
Li, Xiangjie	S7.5	271	*A V-Band LNA with Pole-Tuning and Gm-Boosting Technique in 40-nm CMOS*
LI, Xiaochun	S3.5	115	*Design and Analysis of Circular Hollow Polymer Waveguide at THz Frequency Band*
Li, Xiuping	S21.3	103	*Low-Profile Broadband Beam-Scanning Antenna*
Li, Yancheng	S14.2	159	*A Classification of Scattering Characteristics for Typical Artificial Structures via Attention-Augmented Dual-Branch Convolutional Neural Network*
Li, YH	S4.2	152	*D Band Terahertz Driving Source Based on GaN Monolithic Integrated Frequency Multiplier*
Li, Yihao	S3.6	118	*Hybrid Modeling Method of FT-Transformer and XGBoost for TFsurface*
	S6.5	228	*From Language to Structure: Semantic-Guided Cross-Modal End-to-End Intelligent Design of High-Performance Metasurface Absorbers*
Liang, Cheng	S2.1	55	*Photo-Tunable Chip Scale THz Ring Modulator*

	S23.1	165	*High Q Terahertz Detector in Hybrid Metal−Optical Tamm State Cavity*
Liao, Wangmin	S2.2	58	*A 110-150 GHz OOK Receiver for High-Speed Wireless Communication in 65-nm CMOS*
Lim, Eng	S5.4	184	*Optimized Design of Compact Multi-Coil Arrays for Misalignment-Tolerant Wireless Power Transfer*
	S16.2	238	*Meta-Screen: Full-Space EM Environment Reconfiguration for mmWave Communications*
Lim, Sungjoon	S16.1	237	*Millimeter-Wave and Sub-Terahertz Antenna and Metasurface Applications Using Screen Printed Vanadium Dioxide Switches*
Lin, Jing-Yu	S9.5	347	*Short-Circuit Ring Patch Bandpass Filter on Glass Substrate with MLP-Based Optimization*
Lin, Pai-Dong	S7.6	274	*A High-Sensitivity Rectifier Employing a Low-ESR Distributed Spiral Inductor*
Liu, Changjun	S10.5	26	*Absorptivity Evaluation of Broadband FSS Absorbers Considering Higher-Order Floquet Modes*
Liu, Haiwen	S26.3	295	*Low-Loss Millimeter-Wave Wideband Bandpass Filter in InP Technology with Cryogenic Performance Analysis*
Liu, Huihua	S23.3	170	*Geometry Scalable Model of on-Chip Multilayer Interdigital Capacitors*
Liu, Jie	S23.3	170	*Geometry Scalable Model of on-Chip Multilayer Interdigital Capacitors*
Liu, Qinghua	S22.6	148	*A Data-Efficient and Physics-Constrained Deep Learning Framework for Reflectarray Antenna Inverse Design*
Liu, Shaobin	S13.2	130	*Ultra-Wideband Energy Selective Surface Based on Symmetrical Bow-Tie Topology for High-Power Electromagnetic Protection*
	S4.4	155	*Dual-Wideband Antenna Decoupling via Hybrid Conduction-Radiation Mitigation*
Liu, Tian	S14.3	162	*Improved Hybrid Quantum Models for More Accurate Phase Prediction of Expansion Coefficients in Large Finite Periodic Structures*
	S15.3	196	*Rapid Analysis of Scattering Problem for LFPSs with Physics-Informed Attention Network*
Liu, Xuzhao	S20.2	73	*Non-Volatile Reflective Intelligent Surface Based on 2D Material Switches for 6G Wireless Communications*
Liu, Yiwen	S23.3	170	*Geometry Scalable Model of on-Chip Multilayer Interdigital Capacitors*
Liu, Yuanan	S24.3	209	*Multi-Template Differential Correction for Subarray-Based Pattern Reconstruction of Large Phased Arrays*
Liu, Zeqi	S2.5	67	*A Compact 24-to-30-GHz GaAs Series Doherty Power Amplifier Using a Three-Coupled-Line Balun*
Longpeng, Lan	S23.6	174	*Metasurface Antenna Applied in Millimeter-Wave Imaging Systems*

Lu, Wei Bing	S14.3	162	*Improved Hybrid Quantum Models for More Accurate Phase Prediction of Expansion Coefficients in Large Finite Periodic Structures*
	S15.3	196	*Rapid Analysis of Scattering Problem for LFPSs with Physics-Informed Attention Network*
Lu, Xiaoyu	S16.4	241	*A Low-Rate Digital Predistortion with Single Real Undersampling Feedback Using Switch-Estimated Method Excited by 400 MHz Sub-6 GHz Signals*
Lu, Zi-Huan	S16.6	245	*A Switchable Dual CP Array System for CubeSat Communications Based on Collocated RHCP/LHCP 4×4 Patch Arrays*
Luan, Dianxin	S9.3	341	*Wideband Phased-Array Meta-Antenna Without Air Cavity for Ku-Band Satellite Communication*
Luo, Shiyang	S1.3	13	*Exploiting LDMOS-PA for kW SSPA Applications*
Luo, Yanzhe	S15.3	196	*Rapid Analysis of Scattering Problem for LFPSs with Physics-Informed Attention Network*
	S10.6	29	*A Highly-Selective 3-D FSS with Exceptional Precision for Liquid Dielectric Constant Detection*
	S20.3	76	*A Curved Broadside-Coupled Stripline Phase Shifter and Its Application to Metasurface Designs*
	S20.4	79	*High-Frequency Narrowband to Low-Frequency Broadband Transition in an SMA-Actuated Bandpass Frequency-Selective Surface*
Lv, Xiaojing	S24.4	212	*Multi-Material Additively Manufactured Wideband Dual-Linear Polarized Antenna with High Isolation*
	S16.6	245	*A Switchable Dual CP Array System for CubeSat Communications Based on Collocated RHCP/LHCP 4×4 Patch Arrays*
	S25.3	254	*A Compact Wideband Dual-Circularly Polarized Millimeter-Wave Antenna with Isolation Enhancement*
	S26.5	299	*Ultrahigh-Sensitivity Microwave Biosensor Based on a CPW Loaded with a Modified Complementary Electric-LC Resonator*
	S9.4	344	*A Hexagonal Six-Port Hybrid Coupler for Beamforming Applications*
Lv, Yongqi	S10.3	23	*Semantics-Guided End-to-End Intelligent Design Framework for Metasurface Absorbers*
Lyu, Wen	S3.6	118	*Hybrid Modeling Method of FT-Transformer and XGBoost for TFsurface*
	S6.5	228	*From Language to Structure: Semantic-Guided Cross-Modal End-to-End Intelligent Design of High-Performance Metasurface Absorbers*

M A B C D E F G H I J K L M N O P Q R S T V W X Y Z

Ma, Jun	S13.5	137	*Design of 3-D Frequency Selective Surface Based on Spatial Coupling*

Ma, Yu-Qi	S25.5	259	*A Low Profile and High Front-to-Back Ratio Millimeter-Wave Array Based on Electromagnetic Band Gap Ground*
Mai, Zhanzhang	S2.1	55	*Photo-Tunable Chip Scale THz Ring Modulator*
	S23.1	165	*High Q Terahertz Detector in Hybrid Metal−Optical Tamm State Cavity*
Mak, Pui-In	S21.4	106	*Generation of Scanning Self-Accelerating Beam by Manipulating Phase Distribution*
	S9.3	341	*Wideband Phased-Array Meta-Antenna Without Air Cavity for Ku-Band Satellite Communication*
Mansour, Raafat	W3.2	122	*Multi-Function Multi-Band Reconfigurable High-Q Filters*
Mao, Junfa	S3.5	115	*Design and Analysis of Circular Hollow Polymer Waveguide at THz Frequency Band*
	S26.3	295	*Low-Loss Millimeter-Wave Wideband Bandpass Filter in InP Technology with Cryogenic Performance Analysis*
Maradei, Francescaromana	S19.2	33	*Dosimetric Assessment of a Birdcage-Coil Wireless Power Transfer at 6.78 MHz for Capsule Robots*
Martins, Rui P.	S21.4	106	*Generation of Scanning Self-Accelerating Beam by Manipulating Phase Distribution*
	S9.3	341	*Wideband Phased-Array Meta-Antenna Without Air Cavity for Ku-Band Satellite Communication*
Mehdi, Imran	P5.1	232	*Sources and Detectors for Space THz Communication Systems*
Meng, Baoping	S8.3	306	*Characterization of 32 GT/s UCIe-Compatible Package Interconnects for Reconfigurable RF Chiplet Integration*
	S11.2	45	*Terahertz near-Field Scanning Microscopy for Nanoscale Imaging of Ovarian Cancer Cells*
Meng, Jin	S3.4	114	*Design of a High-Performance Terahertz Multiplier Based on Thin-Film Technology*
	S4.2	152	*D Band Terahertz Driving Source Based on GaN Monolithic Integrated Frequency Multiplier*
Min, Juncheng	S27.5	329	*A Wideband Terahertz Interconnection Between Microstrip Line and Waveguide Using Novel Short-Circuited Stub*
	S27.6	332	*A 300-GHz Broadband Power-Reconfigurable Load-Modulated Balanced Amplifier*
Mitchell, David	S12.3	92	*Characterization of Knitted Textiles for Wearable Antennas*
Mohammad, Umar	S2.3	61	*A 105 dBΩ High Gain, 1.5 mW Low Power Muti-Stage NRZ CMOS-TIA for Optical Receiver Systems*
Mohammed, Mohammed	S6.2	219	*Design of Titanium SAW Phononic Crystal on Lithium Niobate LiNbO3/Si Structure*
Mukhopadhyay, Subhas	S21.5	109	*Compact High-Gain 300 GHz Metasurface Antenna for Future 6G Terahertz Communications*

N A B C D E F G H I J K L M N O P Q R S T V W X Y Z

Na, Ji	S17.3	283	*Wideband High-Precision Resonator-Based Phase Shifters via Lossy Electric and Magnetic Coupling*
Nabeel, Maira	S11.4	49	*Microwave Beam-Steering Using near-Field Metasurfaces*
Naqvi, Syed Akbar Raza	S18.4	318	*Microwave Probe with Enhanced Sensitivity for Wideband Dielectric Characterizations*
Navarro-Cía, Miguel	S18.1	313	*THz Material Characterization of Rough Samples*
Nawaz, Haq	S21.2	100	*Planar EBG Monostatic Antenna with Wideband Interport Isolation Characteristics for 5G in-Band Full Duplex Applications*
Ngo, Nguyen	S6.6	231	*Towards Fully Integrated Terahertz Frontends: Silicon Photonics Meets Resonant Tunneling Diodes*
Ning, Dongfang	S16.4	241	*A Low-Rate Digital Predistortion with Single Real Undersampling Feedback Using Switch-Estimated Method Excited by 400 MHz Sub-6 GHz Signals*
Niu, Zhongqian	S19.4	38	*Design of Millimeter Wave Ultra Wideband Solid-State LNA Module Based on Metal Cavity Packaging*
Niu, Zhongqian	S5.5	187	*Study on the Design of 50-75GHz Up-Conversion Module*
Norouzian, Fatemeh	S6.4	225	*Characterisation of Dynamic Particulate Media Using Broadband FMCW Spectrometry*
Nowicki, Lukasz	S18.3	317	*Application of Q-Chokes for Enhanced Characterization of Materials in FR3 Band*

O A B C D E F G H I J K L M N O P Q R S T V W X Y Z

Olivieri, Riccardo	S19.2	33	*Dosimetric Assessment of a Birdcage-Coil Wireless Power Transfer at 6.78 MHz for Capsule Robots*
Olszewska-Placha, Marzena	S18.3	317	*Application of Q-Chokes for Enhanced Characterization of Materials in FR3 Band*
Orlianges, Jean-Christophe	S8.1	302	*Reconfigurable Millimetre-Waves and Terahertz Devices Using Phase Change Materials*
Ou, Jun-Hui	S7.6	274	*A High-Sensitivity Rectifier Employing a Low-ESR Distributed Spiral Inductor*
Ou, Zuqiang	S19.4	38	*Design of Millimeter Wave Ultra Wideband Solid-State LNA Module Based on Metal Cavity Packaging*
	S5.5	187	*Study on the Design of 50-75GHz Up-Conversion Module*

P A B C D E F G H I J K L M N O P Q R S T V W X Y Z

Park, Eiyong	S16.1	237	*Millimeter-Wave and Sub-Terahertz Antenna and Metasurface Applications Using Screen Printed Vanadium Dioxide Switches*
Pei, Rui	S5.4	184	*Optimized Design of Compact Multi-Coil Arrays for Misalignment-Tolerant Wireless Power Transfer*
	S16.2	238	*Meta-Screen: Full-Space EM Environment Reconfiguration for mmWave Communications*
Peng, Hui	S19.4	38	*Design of Millimeter Wave Ultra Wideband Solid-State LNA Module Based on Metal Cavity Packaging*
	S5.5	187	*Study on the Design of 50-75GHz Up-Conversion Module*

Peng, Yan	S15.2	193	*Electromagnetic-Thermal-Fluid Multiphysics Coupling Simulation of Electronic Packaging Based on the FDTD Method*
Peng, Zhaomin	S11.1	44	*A Terahertz Scattering-Type Scanning near-Field Optical Microscopy for Single Cell Imaging*
	S11.2	45	*Terahertz near-Field Scanning Microscopy for Nanoscale Imaging of Ovarian Cancer Cells*
	S12.4	93	*Ultra-Wideband Multi-Channel Millimeter-Wave Receiver for Solar Sensing*
Peng, Zixing	S20.2	73	*Non-Volatile Reflective Intelligent Surface Based on 2D Material Switches for 6G Wireless Communications*
Pham, Duc	S16.1	237	*Millimeter-Wave and Sub-Terahertz Antenna and Metasurface Applications Using Screen Printed Vanadium Dioxide Switches*

Q A B C D E F G H I J K L M N O P Q R S T V W X Y Z

Qi, Zihang	S21.3	103	*Low-Profile Broadband Beam-Scanning Antenna*
Qian, Lu	S26.1	289	*3D-Printed Copper Waveguide Bandpass Filter for Q-Band Ground Station Application*
Qian, Mei	S22.3	144	*Reconfigurable Bandpass Ultrathin Angular-Selective Surfaces*
Qiao, Jincai	S19.4	38	*Design of Millimeter Wave Ultra Wideband Solid-State LNA Module Based on Metal Cavity Packaging*
	S5.5	187	*Study on the Design of 50-75GHz Up-Conversion Module*
	S2.2	58	*A 110-150 GHz OOK Receiver for High-Speed Wireless Communication in 65-nm CMOS*
Qin, Pei	S7.1	262	*A 19.3-23.7-GHz RTWO with Common-Mode Resonance and Distributed Varactors*
	S7.5	271	*A V-Band LNA with Pole-Tuning and Gm-Boosting Technique in 40-nm CMOS*
Qiu, Yutong	S15.4	199	*Characteristic Mode-Based Efficient Analysis Method for Electromagnetic Scattering of Complex Electromagnetic Structures with Lossy Dielectric Materials*
Qu, Meijun	S14.2	159	*A Classification of Scattering Characteristics for Typical Artificial Structures via Attention-Augmented Dual-Branch Convolutional Neural Network*

R A B C D E F G H I J K L M N O P Q R S T V W X Y Z

Ramer, Rodica	S18.2	314	*A Branch-Independent Computational Method for Dielectric Material Characterization*
Rawat, Karun	S6.1	216	*Phase-Tapered Bus-Bar Combiner for Efficiency Enhancement in C-Band GaN MMIC Power Amplifier*
Ren, Xue	S22.6	148	*A Data-Efficient and Physics-Constrained Deep Learning Framework for Reflectarray Antenna Inverse Design*
Renkanga Mbatchi, Wilfrid	S8.1	302	*Reconfigurable Millimetre-Waves and Terahertz Devices Using Phase Change Materials*
Reschke, Stephan	S6.4	225	*Characterisation of Dynamic Particulate Media Using Broadband FMCW Spectrometry*

Robinson, John	S26.1	289	*3D-Printed Copper Waveguide Bandpass Filter for Q-Band Ground Station Application*
Rui, Yunjie	S2.1	55	*Photo-Tunable Chip Scale THz Ring Modulator*
	S23.1	165	*High Q Terahertz Detector in Hybrid Metal−Optical Tamm State Cavity*

S A B C D E F G H I J K L M N O P Q R S T V W X Y Z

Saha, Chinmoy	S19.3	36	*2006-2026: Two Decades of Innovation with Metamaterial and Metasurfaces for an Array of Applications*
	S11.4	49	*Microwave Beam-Steering Using near-Field Metasurfaces*
Samal, Purna	S8.5	310	*On-Body Characterization of a Planar Horseshoe-Slot MXene Microstrip Antenna with an Elevated Ground Plane for Wearable Applications*
Samizadeh Nikoo, Mohammad	S3.3	113	*Metatronics for High-Performance Terahertz Integrated Circuits*
Sen, Pinaki	S6.1	216	*Phase-Tapered Bus-Bar Combiner for Efficiency Enhancement in C-Band GaN MMIC Power Amplifier*
Shan, Guangbao	S1.2	10	*Bandwidth Reconfigurable Low-Noise Amplifier Based on Magnetic Coupling Effect*
	S17.1	277	*A Continuously Tunable Silicon-Based 3D Matching Network for Heterogeneous RF Transceiver*
	S17.2	280	*A Broadband Tunable Matching Network Based on Magnetic Coupling*
	S8.3	306	*Characterization of 32 GT/s UCIe-Compatible Package Interconnects for Reconfigurable RF Chiplet Integration*
	S9.2	338	*A Multi-Mode Tunable Bandpass Filter with the Continuous Transmission Zero*
Shen, Guangxu	S17.3	283	*Wideband High-Precision Resonator-Based Phase Shifters via Lossy Electric and Magnetic Coupling*
Shen, Luchen	S2.4	64	*An Isolated Ultra-Low Power Modulator for OOK/BPSK Backscatter Communication*
Shi, Jun	S11.1	44	*A Terahertz Scattering-Type Scanning near-Field Optical Microscopy for Single Cell Imaging*
	S12.4	93	*Ultra-Wideband Multi-Channel Millimeter-Wave Receiver for Solar Sensing*
Shi, Tianyu	S13.2	130	*Ultra-Wideband Energy Selective Surface Based on Symmetrical Bow-Tie Topology for High-Power Electromagnetic Protection*
	S4.4	155	*Dual-Wideband Antenna Decoupling via Hybrid Conduction-Radiation Mitigation*
Shi, Yue	S25.1	248	*Pattern-Reconfigurable Metasurface for Dynamic Switching Between OAM Beam and Dual-Beam*
Shinohara, Naoki	S27.1	321	*Radiative Wireless Power Transfer with Advanced Materials*
Singh, Khushboo	S11.4	49	*Microwave Beam-Steering Using near-Field Metasurfaces*

Sirjita, Eduard-Nicolae	S8.1	302	*Reconfigurable Millimetre-Waves and Terahertz Devices Using Phase Change Materials*
Song, Bingbing	S14.3	162	*Improved Hybrid Quantum Models for More Accurate Phase Prediction of Expansion Coefficients in Large Finite Periodic Structures*
Song, Guo	S15.2	193	*Electromagnetic-Thermal-Fluid Multiphysics Coupling Simulation of Electronic Packaging Based on the FDTD Method*
Song, Liwei	S11.3	46	*Research on Beam Steering Rectenna Array for Drone Microwave Wireless Power Supply*
Song, Shuang	S2.2	58	*A 110-150 GHz OOK Receiver for High-Speed Wireless Communication in 65-nm CMOS*
Song, Wenzhe	S15.3	196	*Rapid Analysis of Scattering Problem for LFPSs with Physics-Informed Attention Network*
Sood, Nupur	S6.1	216	*Phase-Tapered Bus-Bar Combiner for Efficiency Enhancement in C-Band GaN MMIC Power Amplifier*
	S21.3	103	*Low-Profile Broadband Beam-Scanning Antenna*
Su, Jianxun	S14.2	159	*A Classification of Scattering Characteristics for Typical Artificial Structures via Attention-Augmented Dual-Branch Convolutional Neural Network*
Suarez, Almudena	S27.2	322	*Microwave Sensors Exploiting Nonlinear Dynamics*
Sun, Changsheng	S3.5	115	*Design and Analysis of Circular Hollow Polymer Waveguide at THz Frequency Band*
Sun, Shuai	S4.1	151	*Semiconductor-grade Dry Nano-Island Coating Technology: Translating Advanced Materials from Lab Scale to Next-Gen 6G mm-Wave Substrates*
Sun, Shuo	S21.3	103	*Low-Profile Broadband Beam-Scanning Antenna*
Sun, Yiqing	S21.1	97	*Power-Based Direction-Finding Enabled by a Null-Scanning Space-Time Leaky-Wave Antenna*
Sun, Yu-Xiang	S25.2	251	*A Textile Antenna for ON-/off-Body Communication*
Sun, Zhichao	S10.6	29	*A Highly-Selective 3-D FSS with Exceptional Precision for Liquid Dielectric Constant Detection*
	S20.3	76	*A Curved Broadside-Coupled Stripline Phase Shifter and Its Application to Metasurface Designs*
	S20.4	79	*High-Frequency Narrowband to Low-Frequency Broadband Transition in an SMA-Actuated Bandpass Frequency-Selective Surface*
	S24.4	212	*Multi-Material Additively Manufactured Wideband Dual-Linear Polarized Antenna with High Isolation*
	S16.6	245	*A Switchable Dual CP Array System for CubeSat Communications Based on Collocated RHCP/LHCP 4×4 Patch Arrays*
	S25.3	254	*A Compact Wideband Dual-Circularly Polarized Millimeter-Wave Antenna with Isolation Enhancement*
Suzuki, Safumi	S4.3	154	*Resonant Tunneling Diodes for Terahertz Sensing*

Tam, Kam-weng	S25.4	257	*Broadband Circularly Polarized Glass Antenna with Surface Wave Suppression*
Tang, Heng	S2.1	55	*Photo-Tunable Chip Scale THz Ring Modulator*
Tang, Kun	S10.2	20	*Broadband Phase-Dispersive Conformal Metamaterial for EM Backscattering Enhancement*
	S5.3	183	*A Compact Wideband Filtering Power Dividers Using D-CRLH Resonators*
Tang, Yixi	S10.2	20	*Broadband Phase-Dispersive Conformal Metamaterial for EM Backscattering Enhancement*
Thalakotuna, Dush	S11.4	49	*Microwave Beam-Steering Using near-Field Metasurfaces*
Tian, Hongliang	S26.3	295	*Low-Loss Millimeter-Wave Wideband Bandpass Filter in InP Technology with Cryogenic Performance Analysis*
Tian, Yuan	S7.1	262	*A 19.3-23.7-GHz RTWO with Common-Mode Resonance and Distributed Varactors*
Tomassoni, Cristiano	W1.1	41	*Additive Manufacturing of High-Performance Filters with Unconventional Geometries*
	P3.2	124	*Filters for Space Applications: CNC Milling and Additive Manufacturing Perspectives*
Tong, Xin	S1.3	13	*Exploiting LDMOS-PA for kW SSPA Applications*
Tu, Xuecou	S2.1	55	*Photo-Tunable Chip Scale THz Ring Modulator*
	S23.1	165	*High Q Terahertz Detector in Hybrid Metal−Optical Tamm State Cavity*
Tu, Zhihong	S13.5	137	*Design of 3-D Frequency Selective Surface Based on Spatial Coupling*
	S25.5	259	*A Low Profile and High Front-to-Back Ratio Millimeter-Wave Array Based on Electromagnetic Band Gap Ground*

Varikuntla, Krushna Kanth	S22.1	140	*Invited Talk: Plasma-Based Reconfigurable FSS for Adaptive High-Power Microwave Shielding*

Wan, Yinglu	S7.3	268	*Super-Mode-Group Based Reduced-Order Analysis of Multi-Mode Antenna Decoupling*
Wang, Bao	S13.4	134	*A Wideband Ultra-Large-Angle Dual-Polarized Bandpass Frequency Selective Surface*
Wang, Chao-Fu	S15.4	199	*Characteristic Mode-Based Efficient Analysis Method for Electromagnetic Scattering of Complex Electromagnetic Structures with Lossy Dielectric Materials*
Wang, Hao	S8.2	303	*Design of a Pattern Reconfigurable Amplifier Antenna with Gain Amplification Using Transistors*
Wang, Huan-Bin	S25.5	259	*A Low Profile and High Front-to-Back Ratio Millimeter-Wave Array Based on Electromagnetic Band Gap Ground*

Wang, Huanpeng	S23.3	170	*Geometry Scalable Model of on-Chip Multilayer Interdigital Capacitors*
Wang, Jiaxin	S13.4	134	*A Wideband Ultra-Large-Angle Dual-Polarized Bandpass Frequency Selective Surface*
Wang, Jiechen	S11.5	52	*A Single Substrate Pancharatnam-Berry (PB) Phase Huygens' Metasurface for Dynamic Steering of Vortex Beams*
Wang, Jingchen	S5.4	184	*Optimized Design of Compact Multi-Coil Arrays for Misalignment-Tolerant Wireless Power Transfer*
	S16.2	238	*Meta-Screen: Full-Space EM Environment Reconfiguration for mmWave Communications*
Wang, Li	S3.4	114	*Design of a High-Performance Terahertz Multiplier Based on Thin-Film Technology*
Wang, Minghuan	S8.2	303	*Design of a Pattern Reconfigurable Amplifier Antenna with Gain Amplification Using Transistors*
Wang, Ruixin	S1.2	10	*Bandwidth Reconfigurable Low-Noise Amplifier Based on Magnetic Coupling Effect*
Wang, Shi-Tong	S21.4	106	*Generation of Scanning Self-Accelerating Beam by Manipulating Phase Distribution*
Wang, Shijie	S3.6	118	*Hybrid Modeling Method of FT-Transformer and XGBoost for TFsurface*
	S6.5	228	*From Language to Structure: Semantic-Guided Cross-Modal End-to-End Intelligent Design of High-Performance Metasurface Absorbers*
Wang, Tao	S27.4	326	*Machine Learning-Assisted End-to-End Synthesis of RF Transformer-Based Matching Networks*
	S23.2	167	*A High-Performance Hybrid FBAR Chip Based on TGV Technology*
Wang, Weimin	S5.2	180	*A Fully Integrated Low-Cost 5-GHz Doherty Power Amplifier Using Compact Triple-Coil Splitter-Combiner in 180-nm CMOS*
	S24.3	209	*Multi-Template Differential Correction for Subarray-Based Pattern Reconstruction of Large Phased Arrays*
Wang, Yan	S8.2	303	*Design of a Pattern Reconfigurable Amplifier Antenna with Gain Amplification Using Transistors*
Wang, Yi	W2.1	85	*Liquid Metal Enabled Reconfigurable Microwave Devices and Antennas*
	S26.1	289	*3D-Printed Copper Waveguide Bandpass Filter for Q-Band Ground Station Application*
Wang, Yifan	S14.1	158	*Surface Mount Radiator - Intelligent AiP for Physical AI and Edge Eevices*
Wang, Yu-Fei	S25.2	251	*A Textile Antenna for ON-/off-Body Communication*
Wang, Yuqi	S7.3	268	*Super-Mode-Group Based Reduced-Order Analysis of Multi-Mode Antenna Decoupling*

Wang, Zhao	S5.4	184	*Optimized Design of Compact Multi-Coil Arrays for Misalignment-Tolerant Wireless Power Transfer*
	S16.2	238	*Meta-Screen: Full-Space EM Environment Reconfiguration for mmWave Communications*
Wang, Zhaoling	S22.2	141	*A Reconfigurable Transmit-Reflect-Array Antenna Based on Tightly Coupled Dipole*
Wang, Zhaoyuan	S15.4	199	*Characteristic Mode-Based Efficient Analysis Method for Electromagnetic Scattering of Complex Electromagnetic Structures with Lossy Dielectric Materials*
Waqas, Muhammad	S4.1	151	*Semiconductor-grade Dry Nano-Island Coating Technology: Translating Advanced Materials from Lab Scale to Next-Gen 6G mm-Wave Substrates*
Wei, Keyan	S23.6	174	*Metasurface Antenna Applied in Millimeter-Wave Imaging Systems*
Wei, Kun	S15.5	202	*Background Separation and Cancellation in Complex Indoor Testing Environments Based on the TTP Algorithm*
	S26.4	296	*A Broadband High-Selectivity Bandpass Filter Branch-Line Coupler Operating in the C-Band*
Wei, Wenbin	S8.3	306	*Characterization of 32 GT/s UCIe-Compatible Package Interconnects for Reconfigurable RF Chiplet Integration*
Withayachumnankul, Withawat	S24.5	215	*General-Purpose Terahertz Quasi-Optics and Mechanical Beamformers Enabled by 3D-Printing*
	P5.2	234	*High-Sensitivity Terahertz Sensing with Quadrature Self-Homodyne Detection*
Wu, Geng-Bo	S10.1	19	*Space-Time Metasurface Antennas: Concept, Design, and Applications*
	W2.2	86	*3-D Printed Metalenses for Terahertz Imaging*
	S21.1	97	*Power-Based Direction-Finding Enabled by a Null-Scanning Space-Time Leaky-Wave Antenna*
Wu, Hung-Wei	S4.1	151	*Semiconductor-grade Dry Nano-Island Coating Technology: Translating Advanced Materials from Lab Scale to Next-Gen 6G mm-Wave Substrates*
Wu, Jiatong	S16.2	238	*Meta-Screen: Full-Space EM Environment Reconfiguration for mmWave Communications*
Wu, Peiheng	S2.1	55	*Photo-Tunable Chip Scale THz Ring Modulator*
	S23.1	165	*High Q Terahertz Detector in Hybrid Metal−Optical Tamm State Cavity*
	S3.2	112	*Terahertz Microsystems Front-End Integration Technologies and Communication Application*
Wu, Peng	S27.5	329	*A Wideband Terahertz Interconnection Between Microstrip Line and Waveguide Using Novel Short-Circuited Stub*
	S27.6	332	*A 300-GHz Broadband Power-Reconfigurable Load-Modulated Balanced Amplifier*

Wu, Shuxin	S14.2	159	A Classification of Scattering Characteristics for Typical Artificial Structures via Attention-Augmented Dual-Branch Convolutional Neural Network
Wu, Wen	S1.4	16	An Energy-Efficient Reconfigurable BLE RF Receiving Front-End Based on Mixer-First Architecture for IoT Applications
	S19.4	38	Design of Millimeter Wave Ultra Wideband Solid-State LNA Module Based on Metal Cavity Packaging
Wu, Ya Fei	S5.5	187	Study on the Design of 50-75GHz Up-Conversion Module
Wu, Yanghui	S6.3	222	High-Efficiency Broadband S-Shaped Thin-Film Lithium Niobate Electro-Optic Modulator
	S10.3	23	Semantics-Guided End-to-End Intelligent Design Framework for Metasurface Absorbers
	S6.5	228	From Language to Structure: Semantic-Guided Cross-Modal End-to-End Intelligent Design of High-Performance Metasurface Absorbers
	S23.2	167	A High-Performance Hybrid FBAR Chip Based on TGV Technology
Wu, Yongle	S5.2	180	A Fully Integrated Low-Cost 5-GHz Doherty Power Amplifier Using Compact Triple-Coil Splitter-Combiner in 180-nm CMOS
	S24.3	209	Multi-Template Differential Correction for Subarray-Based Pattern Reconstruction of Large Phased Arrays
Wu, Yunqiu	S23.3	170	Geometry Scalable Model of on-Chip Multilayer Interdigital Capacitors

X A B C D E F G H I J K L M N O P Q R S T V W X Y Z

Xiang, Kai-Ran	S13.5	137	Design of 3-D Frequency Selective Surface Based on Spatial Coupling
Xiao, Xiaoyu	S20.2	73	Non-Volatile Reflective Intelligent Surface Based on 2D Material Switches for 6G Wireless Communications
Xin, Hui	S17.4	286	Ultra-Wideband RCS Reduction Metasurface with Tunable Transmission Window
Xing, Meng	S13.2	130	Ultra-Wideband Energy Selective Surface Based on Symmetrical Bow-Tie Topology for High-Power Electromagnetic Protection
	S4.4	155	Dual-Wideband Antenna Decoupling via Hybrid Conduction-Radiation Mitigation
Xiu, Xin	S10.2	20	Broadband Phase-Dispersive Conformal Metamaterial for EM Backscattering Enhancement
Xiu, Xin	S13.4	134	A Wideband Ultra-Large-Angle Dual-Polarized Bandpass Frequency Selective Surface
Xu, Jin-Xu	S27.3	323	Design of Filtering Power Amplifier Based on TGV-IPD Filtering Matching Network
Xu, Taotao	S2.2	58	A 110-150 GHz OOK Receiver for High-Speed Wireless Communication in 65-nm CMOS

Xu, Yang	S13.3	133	*Reflection-Type TTD Phase Shifter Based on Propagation-Controlled Reflective Loading*
Xu, Yuehang	S5.1	177	*A 30-W Tri-Mode GaN Power Amplifier Based on Reconfigurable Multi-Network Architecture*
Xu, Zeyu	S2.1	55	*Photo-Tunable Chip Scale THz Ring Modulator*
	S23.1	165	*High Q Terahertz Detector in Hybrid Metal−Optical Tamm State Cavity*
Xu, Zong-Rui	S8.4	309	*A Sub-THz Conductive-Bridging Memristive Switch for Reconfigurable RF Front-Ends*
Xuan, Xingqi	S12.2	89	*A Communication Signal Based Vital-Sign Sensing Method for Consumer Electronic Devices*
Xue, Chao	S27.5	329	*A Wideband Terahertz Interconnection Between Microstrip Line and Waveguide Using Novel Short-Circuited Stub*
Xue, Quan	S2.2	58	*A 110-150 GHz OOK Receiver for High-Speed Wireless Communication in 65-nm CMOS*
	S2.5	67	*A Compact 24-to-30-GHz GaAs Series Doherty Power Amplifier Using a Three-Coupled-Line Balun*
	S7.1	262	*A 19.3-23.7-GHz RTWO with Common-Mode Resonance and Distributed Varactors*
	S7.5	271	*A V-Band LNA with Pole-Tuning and Gm-Boosting Technique in 40-nm CMOS*

Y A B C D E F G H I J K L M N O P Q R S T V W X Y Z

Yan, Bingnan	S2.1	55	*Photo-Tunable Chip Scale THz Ring Modulator*
	S23.1	165	*High Q Terahertz Detector in Hybrid Metal−Optical Tamm State Cavity*
Yan, Liping	S10.5	26	*Absorptivity Evaluation of Broadband FSS Absorbers Considering Higher-Order Floquet Modes*
Yan, Mengzhu	S13.4	134	*A Wideband Ultra-Large-Angle Dual-Polarized Bandpass Frequency Selective Surface*
Yan, Sen	S20.1	70	*W-Band Wide-Angle Coverage Pillbox Multibeam Antenna Based on Bifocal Phase Compensation*
Yang, Chunyu	S17.1	277	*A Continuously Tunable Silicon-Based 3D Matching Network for Heterogeneous RF Transceiver*
	S9.2	338	*A Multi-Mode Tunable Bandpass Filter with the Continuous Transmission Zero*
Yang, Huanyu	S6.5	228	*From Language to Structure: Semantic-Guided Cross-Modal End-to-End Intelligent Design of High-Performance Metasurface Absorbers*
Yang, Lei	S23.6	174	*Metasurface Antenna Applied in Millimeter-Wave Imaging Systems*
Yang, Qinghua	S23.2	167	*A High-Performance Hybrid FBAR Chip Based on TGV Technology*

Yang, Wu	S14.3	162	*Improved Hybrid Quantum Models for More Accurate Phase Prediction of Expansion Coefficients in Large Finite Periodic Structures*
	S15.3	196	*Rapid Analysis of Scattering Problem for LFPSs with Physics-Informed Attention Network*
	S10.6	29	*A Highly-Selective 3-D FSS with Exceptional Precision for Liquid Dielectric Constant Detection*
	W1.2	42	*Additively Manufactured Microwave Devices and Antennas*
	S11.5	52	*A Single Substrate Pancharatnam-Berry (PB) Phase Huygens' Metasurface for Dynamic Steering of Vortex Beams*
	S20.3	76	*A Curved Broadside-Coupled Stripline Phase Shifter and Its Application to Metasurface Designs*
	S20.4	79	*High-Frequency Narrowband to Low-Frequency Broadband Transition in an SMA-Actuated Bandpass Frequency-Selective Surface*
Yang, Yang	S13.3	133	*Reflection-Type TTD Phase Shifter Based on Propagation-Controlled Reflective Loading*
	S24.4	212	*Multi-Material Additively Manufactured Wideband Dual-Linear Polarized Antenna with High Isolation*
	S16.6	245	*A Switchable Dual CP Array System for CubeSat Communications Based on Collocated RHCP/LHCP 4×4 Patch Arrays*
	S25.1	248	*Pattern-Reconfigurable Metasurface for Dynamic Switching Between OAM Beam and Dual-Beam*
	S25.3	254	*A Compact Wideband Dual-Circularly Polarized Millimeter-Wave Antenna with Isolation Enhancement*
	S26.5	299	*Ultrahigh-Sensitivity Microwave Biosensor Based on a CPW Loaded with a Modified Complementary Electric-LC Resonator*
	S9.4	344	*A Hexagonal Six-Port Hybrid Coupler for Beamforming Applications*
Yang, Yuqing	S24.3	209	*Multi-Template Differential Correction for Subarray-Based Pattern Reconstruction of Large Phased Arrays*
Yang, Zijiang	S6.2	219	*Design of Titanium SAW Phononic Crystal on Lithium Niobate LiNbO3/Si Structure*
Yi, Xiaoke	S12.1	88	*Integrated Microwave Photonics for Signal Processing and Sensing*
Yin, Jun	S21.4	106	*Generation of Scanning Self-Accelerating Beam by Manipulating Phase Distribution*
	S9.3	341	*Wideband Phased-Array Meta-Antenna Without Air Cavity for Ku-Band Satellite Communication*
Yin, Zhiwei	S20.4	79	*High-Frequency Narrowband to Low-Frequency Broadband Transition in an SMA-Actuated Bandpass Frequency-Selective Surface*

You, Qing	S9.4	344	*A Hexagonal Six-Port Hybrid Coupler for Beamforming Applications*
	S21.4	106	*Generation of Scanning Self-Accelerating Beam by Manipulating Phase Distribution*
	S9.3	341	*Wideband Phased-Array Meta-Antenna Without Air Cavity for Ku-Band Satellite Communication*
Yu, Chao	S16.4	241	*A Low-Rate Digital Predistortion with Single Real Undersampling Feedback Using Switch-Estimated Method Excited by 400 MHz Sub-6 GHz Signals*
	S9.1	335	*A Low-Loss Tunable Bandpass Filter Based on Boundary-Reconfigurable Patch Resonators*
Yu, Yiming	S23.3	170	*Geometry Scalable Model of on-Chip Multilayer Interdigital Capacitors*
Yu, Zhongjun	S27.6	332	*A 300-GHz Broadband Power-Reconfigurable Load-Modulated Balanced Amplifier*
Yuan, Dayan	S2.5	67	*A Compact 24-to-30-GHz GaAs Series Doherty Power Amplifier Using a Three-Coupled-Line Balun*
Yuan, Qiaowei	S24.1	205	*S Parameters Matrix Estimation for E-MIMO-Based Beamforming*
Yuan, Tao	S25.2	251	*A Textile Antenna for ON-/off-Body Communication*
Yurduseven, Okan	S22.1	140	*Invited Talk: Plasma-Based Reconfigurable FSS for Adaptive High-Power Microwave Shielding*

Z A B C D E F G H I J K L M N O P Q R S T V W X Y Z

Zaqumi, Mohammad Nasrat	S21.5	109	*Compact High-Gain 300 GHz Metasurface Antenna for Future 6G Terahertz Communications*
Zeng, Dingyuan	S2.5	67	*A Compact 24-to-30-GHz GaAs Series Doherty Power Amplifier Using a Three-Coupled-Line Balun*
Zeng, Leya	P4.2	126	*Printable Nonlinear Tags and Handheld Devices for Clutter-Resilient Contactless Monitoring and Tracking*
Zeng, Zequn	S13.1	127	*Terminating Magnetostatic Surface Waves with Metallic Patterns*
Zhai, Jianfeng	S16.4	241	*A Low-Rate Digital Predistortion with Single Real Undersampling Feedback Using Switch-Estimated Method Excited by 400 MHz Sub-6 GHz Signals*
Zhang, Bing	S16.5	244	*Ultra-Broadband 3D-Printed Metalens Using Height-Controlled Meta-Atoms*
Zhang, Bo	S19.4	38	*Design of Millimeter Wave Ultra Wideband Solid-State LNA Module Based on Metal Cavity Packaging*
	S5.5	187	*Study on the Design of 50-75GHz Up-Conversion Module*
Zhang, Chonghuan	S10.5	26	*Absorptivity Evaluation of Broadband FSS Absorbers Considering Higher-Order Floquet Modes*
Zhang, Cong	S17.4	286	*Ultra-Wideband RCS Reduction Metasurface with Tunable Transmission Window*

	S11.1	44	*A Terahertz Scattering-Type Scanning near-Field Optical Microscopy for Single Cell Imaging*
	S11.2	45	*Terahertz near-Field Scanning Microscopy for Nanoscale Imaging of Ovarian Cancer Cells*
Zhang, Dehai	S12.4	93	*Ultra-Wideband Multi-Channel Millimeter-Wave Receiver for Solar Sensing*
	S3.4	114	*Design of a High-Performance Terahertz Multiplier Based on Thin-Film Technology*
	S4.2	152	*D Band Terahertz Driving Source Based on GaN Monolithic Integrated Frequency Multiplier*
	S1.3	13	*Exploiting LDMOS-PA for kW SSPA Applications*
Zhang, Hao	S2.4	64	*An Isolated Ultra-Low Power Modulator for OOK/BPSK Backscatter Communication*
Zhang, Hetai	S7.5	271	*A V-Band LNA with Pole-Tuning and Gm-Boosting Technique in 40-nm CMOS*
Zhang, Huilin	S2.1	55	*Photo-Tunable Chip Scale THz Ring Modulator*
Zhang, Jiawen	S1.4	16	*An Energy-Efficient Reconfigurable BLE RF Receiving Front-End Based on Mixer-First Architecture for IoT Applications*
Zhang, Junhao	S12.2	89	*A Communication Signal Based Vital-Sign Sensing Method for Consumer Electronic Devices*
Zhang, Pan	S1.2	10	*Bandwidth Reconfigurable Low-Noise Amplifier Based on Magnetic Coupling Effect*
	S17.1	277	*A Continuously Tunable Silicon-Based 3D Matching Network for Heterogeneous RF Transceiver*
Zhang, Qingfeng	S23.3	170	*Geometry Scalable Model of on-Chip Multilayer Interdigital Capacitors*
Zhang, Tiancheng	S15.2	193	*Electromagnetic-Thermal-Fluid Multiphysics Coupling Simulation of Electronic Packaging Based on the FDTD Method*
Zhang, Wenhai	S25.4	257	*Broadband Circularly Polarized Glass Antenna with Surface Wave Suppression*
Zhang, Wenzhang	S5.4	184	*Optimized Design of Compact Multi-Coil Arrays for Misalignment-Tolerant Wireless Power Transfer*
Zhang, Xianmin	S12.2	89	*A Communication Signal Based Vital-Sign Sensing Method for Consumer Electronic Devices*
Zhang, Xiu Yin	S7.2	265	*A 8.8-12.5 GHz Dual-Core Series Resonance VCO with 201.3-dBc/Hz FoMT in 28-nm CMOS Technology*
	S27.3	323	*Design of Filtering Power Amplifier Based on TGV-IPD Filtering Matching Network*
Zhang, Xiuyin	S27.4	326	*Machine Learning-Assisted End-to-End Synthesis of RF Transformer-Based Matching Networks*
Zhang, Yifan	S20.2	73	*Non-Volatile Reflective Intelligent Surface Based on 2D Material Switches for 6G Wireless Communications*

Zhang, Zhipeng	S25.4	257	*Broadband Circularly Polarized Glass Antenna with Surface Wave Suppression*
Zhang, Zuofeng	S16.4	241	*A Low-Rate Digital Predistortion with Single Real Undersampling Feedback Using Switch-Estimated Method Excited by 400 MHz Sub-6 GHz Signals*
Zhao, Chenxi	S23.3	170	*Geometry Scalable Model of on-Chip Multilayer Interdigital Capacitors*
Zhao, Ren Rong	S9.1	335	*A Low-Loss Tunable Bandpass Filter Based on Boundary-Reconfigurable Patch Resonators*
Zhao, Wenyu	S21.3	103	*Low-Profile Broadband Beam-Scanning Antenna*
Zhao, Yan	S1.4	16	*An Energy-Efficient Reconfigurable BLE RF Receiving Front-End Based on Mixer-First Architecture for IoT Applications*
Zhao, Zhan	S5.1	177	*A 30-W Tri-Mode GaN Power Amplifier Based on Reconfigurable Multi-Network Architecture*
Zhao, Zhuoyue	S14.3	162	*Improved Hybrid Quantum Models for More Accurate Phase Prediction of Expansion Coefficients in Large Finite Periodic Structures*
Zhen, Shuchen	S5.2	180	*A Fully Integrated Low-Cost 5-GHz Doherty Power Amplifier Using Compact Triple-Coil Splitter-Combiner in 180-nm CMOS*
Zheng, Shilie	S12.2	89	*A Communication Signal Based Vital-Sign Sensing Method for Consumer Electronic Devices*
Zheng, XM	S4.2	152	*D Band Terahertz Driving Source Based on GaN Monolithic Integrated Frequency Multiplier*
	S1.2	10	*Bandwidth Reconfigurable Low-Noise Amplifier Based on Magnetic Coupling Effect*
Zheng, Yanwen	S17.1	277	*A Continuously Tunable Silicon-Based 3D Matching Network for Heterogeneous RF Transceiver*
	S17.2	280	*A Broadband Tunable Matching Network Based on Magnetic Coupling*
Zheng, Yanwen	S8.3	306	*Characterization of 32 GT/s UCIe-Compatible Package Interconnects for Reconfigurable RF Chiplet Integration*
	S9.2	338	*A Multi-Mode Tunable Bandpass Filter with the Continuous Transmission Zero*
Zheng, Yilin	S25.4	257	*Broadband Circularly Polarized Glass Antenna with Surface Wave Suppression*
Zhou, Haoyu	S20.5	82	*Liquid Crystal Tunable Phase Shifter Using Post-Wall Coplanar Waveguide*
Zhou, Shengjie	S3.5	115	*Design and Analysis of Circular Hollow Polymer Waveguide at THz Frequency Band*
Zhou, Yanping	S10.5	26	*Absorptivity Evaluation of Broadband FSS Absorbers Considering Higher-Order Floquet Modes*
Zhou, Yulin	S12.2	89	*A Communication Signal Based Vital-Sign Sensing Method for Consumer Electronic Devices*

Zhu, Haoshen	S2.5	67	*A Compact 24-to-30-GHz GaAs Series Doherty Power Amplifier Using a Three-Coupled-Line Balun*
	S5.3	183	*A Compact Wideband Filtering Power Dividers Using D-CRLH Resonators*
	W3.1	121	*High-Tc Superconducting Monolithic Microwave Integrated Circuits (MMICs) for High-Sensitivity RF Receivers*
Zhu, He	S13.3	133	*Reflection-Type TTD Phase Shifter Based on Propagation-Controlled Reflective Loading*
	S23.5	173	*High-Tc Superconducting Josephson Mixers from X- to Sub-THz Band*
	S9.4	344	*A Hexagonal Six-Port Hybrid Coupler for Beamforming Applications*
Zhu, Shiyu	S27.3	323	*Design of Filtering Power Amplifier Based on TGV-IPD Filtering Matching Network*
Zhu, Xiaosi	S7.1	262	*A 19.3-23.7-GHz RTWO with Common-Mode Resonance and Distributed Varactors*
Zhu, Xuyi	S16.5	244	*Ultra-Broadband 3D-Printed Metalens Using Height-Controlled Meta-Atoms*
Zuo, Panpan	S23.6	174	*Metasurface Antenna Applied in Millimeter-Wave Imaging Systems*

Welcome Message from the General Chairs

On behalf of the Organising Committee, it is our great pleasure to welcome you to the 2026 IEEE MTT-S International Microwave Workshop Series on Advanced Materials and Processes for RF and THz Applications (IEEE MTT-S IMWS-AMP 2026), held in Cairns, Australia, from 22-24 July 2026.

IEEE MTT-S IMWS-AMP is a premier international forum for researchers, engineers, industry professionals, and students to exchange the latest advances in advanced materials, manufacturing technologies, and RF, millimetre-wave, and terahertz systems. The workshop promotes technical innovation, interdisciplinary collaboration, and international engagement while supporting the educational mission of the IEEE Microwave Theory and Technology Society (MTT-S). IEEE MTT-S IMWS-AMP 2026 is financially sponsored by the IEEE MTT-S and jointly organised by The University of Sydney, The University of Technology Sydney, James Cook University, Adelaide University, The University of Queensland, RMIT University, and the Commonwealth Scientific and Industrial Research Organisation (CSIRO).

We sincerely thank our sponsors, organising institutions, Technical Program Committee, reviewers, volunteers, and all contributors for their invaluable support. This year's workshop features an exciting technical program of keynote addresses, invited presentations, contributed papers, and poster sessions covering the latest developments in advanced materials and processes for RF and THz applications. We are honoured to welcome distinguished experts from academia and industry, whose presentations will inspire new ideas, foster collaboration, and help shape future research directions.

Beyond the conference, we encourage you to experience the natural beauty of Cairns, the gateway to the UNESCO World Heritage-listed Great Barrier Reef and Daintree Rainforest. We also invite you to learn about the rich cultures and traditions of Australia's Aboriginal and Torres Strait Islander peoples, whose continuous cultural heritage spans more than 65,000 years.

We wish you a productive and enjoyable conference and hope that your time at IEEE MTT-S IMWS-AMP 2026 will be both professionally rewarding and personally memorable. We look forward to welcoming you to Cairns.

General Chair Prof. Yang Yang The University of Sydney

General Co-Chair Dr Tao Huang James Cook University

Welcome Message from the Technical Program Committee Chairs

On behalf of the Technical Program Committee (TPC), it is our great pleasure to welcome you to the 2026 IEEE MTT-S International Microwave Workshop Series on Advanced Materials and Processes for RF and Terahertz Applications (IMWS-AMP) in the beautiful city of Cairns, Australia.

Acknowledgements and Appreciation We sincerely thank all authors for submitting their high-quality work to this year's workshop. The technical depth of your submissions is the foundation of this event. We also extend our deepest appreciation to our dedicated reviewers and committee members for meticulously vetting the papers and maintaining the high standards of the IEEE MTT-S community.

Acceptance and Global Diversity IMWS-AMP 2026 has drawn a strong response from the global scientific community. Out of 168 submissions, 146 papers were accepted for the final Program after a rigorous peer-review process. To ensure a comprehensive and dynamic technical exchange, these accepted papers have been carefully curated into the following categories:

- 104 Regular Session Papers, showcasing the latest peer-reviewed advancements across our core technical tracks.
- 22 Invited Papers, featuring insights from distinguished experts in the field.
- 12 Semi-Plenary Papers, offering broad, impactful perspectives on critical microwave and terahertz challenges delivered by IEEE Fellows.
- 8 TC-17 Workshop Papers, providing specialised, in-depth discussions on targeted technologies and applications.

The program is strengthened by 3 Keynotes from leading figures in the field. We are proud to welcome authors from 26 different countries and regions, representing a truly international bridge for knowledge sharing across the Asia/Pacific, Europe, the Americas, the Middle East, and Africa.

Technical Program Excellence This year's Program smoothly weaves together materials science with practical circuit and antenna architectures. The core MTT disciplines are excellently represented:

- Advanced Materials & Manufacturing: Breakthroughs in 2D materials, flexible substrates, 3D printing, and advanced packaging.
- Intelligent Wave Engineering: Comprehensive sessions on programmable metasurfaces, metamaterials, and antennas.
- Integrated Front-Ends & Systems: Cutting-edge research in CMOS/BiCMOS power amplifiers, wireless power transfer, biomedical sensing, and terahertz communications.

We hope you find the Keynote Speeches, Semi-Plenary talks, and Special Sessions highly inspiring, and that you take time to network, forge new partnerships, and experience the magnificent natural wonders of Cairns.

With warm regards,

Technical Program Committee Chair

Withawat Withayachumnankul, The University of Adelaide

Technical Program Committee Co-Chairs

Konstanty Bialkowski, The University of Queensland, Australia Si-Ping Gao, Nanjing University of Aeronautics and Astronautics, China Zhihao Jiang, Southeast University, China Amir Ebrahimi, RMIT, Australia Naixing Feng, Anhui University, China Wenjie Feng, South China University of Technology, China He Zhu, Commonwealth Scientific and Industrial Research Organisation (CSIRO), Australia

2 3 A B C D E F G H I L M N O P R S T U W
2 2 3 A B C D E F G H I L M N O P R S T U W

2006-2026: Two Decades of Innovation with Metamaterial and Metasurfaces for an Array of Applications

3 2 3 A B C D E F G H I L M N O P R S T U W

3-D Printed Metalenses for Terahertz Imaging

3D-Printed Copper Waveguide Bandpass Filter for Q-Band Ground Station Application

A 2 3 A B C D E F G H I L M N O P R S T U W

A 105 dBΩ High Gain, 1.5 mW Low Power Muti-Stage NRZ CMOS-TIA for Optical Receiver Systems

A 110-150 GHz OOK Receiver for High-Speed Wireless Communication in 65-nm CMOS

A 19.3-23.7-GHz RTWO with Common-Mode Resonance and Distributed Varactors

A 30-W Tri-Mode GaN Power Amplifier Based on Reconfigurable Multi-Network Architecture

A 300-GHz Broadband Power-Reconfigurable Load-Modulated Balanced Amplifier

A 8.8-12.5 GHz Dual-Core Series Resonance VCO with 201.3-dBc/Hz FoMT in 28-nm CMOS Technology

A Branch-Independent Computational Method for Dielectric Material Characterization

A Broadband High-Selectivity Bandpass Filter Branch-Line Coupler Operating in the C-Band

A Broadband Tunable Matching Network Based on Magnetic Coupling

A Broadband Unequal Power Divider Based on an H-Plane Height-Reduced Waveguide T-Junction

A Classification of Scattering Characteristics for Typical Artificial Structures via Attention-Augmented Dual-Branch Convolutional Neural Network

A Communication Signal Based Vital-Sign Sensing Method for Consumer Electronic Devices

A Compact 24-to-30-GHz GaAs Series Doherty Power Amplifier Using a Three-Coupled-Line Balun

A Compact Wideband Dual-Circularly Polarized Millimeter-Wave Antenna with Isolation Enhancement

A Compact Wideband Filtering Power Dividers Using D-CRLH Resonators

A Continuously Tunable Silicon-Based 3D Matching Network for Heterogeneous RF Transceiver

A Curved Broadside-Coupled Stripline Phase Shifter and Its Application to Metasurface Designs

A Data-Efficient and Physics-Constrained Deep Learning Framework for Reflectarray Antenna Inverse Design

A Fully Integrated Low-Cost 5-GHz Doherty Power Amplifier Using Compact Triple-Coil Splitter-Combiner in 180-nm CMOS

A Hexagonal Six-Port Hybrid Coupler for Beamforming Applications

A High-Performance Hybrid FBAR Chip Based on TGV Technology

A High-Sensitivity Dielectric Characterization Method for Thin-Film Materials Using Ridge Gap Waveguide Resonator

A High-Sensitivity Rectifier Employing a Low-ESR Distributed Spiral Inductor

A Highly-Selective 3-D FSS with Exceptional Precision for Liquid Dielectric Constant Detection

A Low Profile and High Front-to-Back Ratio Millimeter-Wave Array Based on Electromagnetic Band Gap Ground

A Low-Loss Tunable Bandpass Filter Based on Boundary-Reconfigurable Patch Resonators

A Low-Rate Digital Predistortion with Single Real Undersampling Feedback Using Switch-Estimated Method Excited by 400 MHz Sub-6 GHz Signals

A Multi-Mode Tunable Bandpass Filter with the Continuous Transmission Zero

A Reconfigurable Transmit-Reflect-Array Antenna Based on Tightly Coupled Dipole

A Review of Microwave Beam-Steering Using near-Field Metasurfaces

A Single Substrate Pancharatnam-Berry (PB) Phase Huygens' Metasurface for Dynamic Steering of Vortex Beams

A Sub-THz Conductive-Bridging Memristive Switch for Reconfigurable RF Front-Ends

A Switchable Dual CP Array System for CubeSat Communications Based on Collocated RHCP/LHCP 4×4 Patch Arrays

A Terahertz Scattering-Type Scanning near-Field Optical Microscopy for Single Cell Imaging

A Textile Antenna for ON-/off-Body Communication

A V-Band LNA with Pole-Tuning and Gm-Boosting Technique in 40-nm CMOS

A Wide-Coverage End-Fire High-Gain Circularly Polarized Mobile Phone Antenna for Satellite Communication

A Wideband Terahertz Interconnection Between Microstrip Line and Waveguide Using Novel Short-Circuited Stub

A Wideband Ultra-Large-Angle Dual-Polarized Bandpass Frequency Selective Surface

Absorptivity Evaluation of Broadband FSS Absorbers Considering Higher-Order Floquet Modes

Additive Manufacturing of High-Performance Filters with Unconventional Geometries

Additively Manufactured Microwave Devices and Antennas

An Energy-Efficient Reconfigurable BLE RF Receiving Front-End Based on Mixer-First Architecture for IoT Applications

An Isolated Ultra-Low Power Modulator for OOK/BPSK Backscatter Communication

Application of Q-Chokes for Enhanced Characterization of Materials in FR3 Band

B 2 3 A B C D E F G H I L M N O P R S T U W

Background Separation and Cancellation in Complex Indoor Testing Environments Based on the TTP Algorithm

Bandwidth Reconfigurable Low-Noise Amplifier Based on Magnetic Coupling Effect

Broadband Circularly Polarized Glass Antenna with Surface Wave Suppression

Broadband Phase-Dispersive Conformal Metamaterial for EM Backscattering Enhancement

C 2 3 A B C D E F G H I L M N O P R S T U W

Characterisation of Dynamic Particulate Media Using Broadband FMCW Spectrometry

Characteristic Mode-Based Efficient Analysis Method for Electromagnetic Scattering of Complex Electromagnetic Structures with Lossy Dielectric Materials

Characterization of 32 GT/s UCIe-Compatible Package Interconnects for Reconfigurable RF Chiplet Integration

Characterization of Knitted Textiles for Wearable Antennas

Compact High-Gain 300 GHz Metasurface Antenna for Future 6G Terahertz Communications

D 2 3 A B C D E F G H I L M N O P R S T U W

D Band Terahertz Driving Source Based on GaN Monolithic Integrated Frequency Multiplier

Design and Analysis of Circular Hollow Polymer Waveguide at THz Frequency Band

Design of 3-D Frequency Selective Surface Based on Spatial Coupling

Design of a High-Performance Terahertz Multiplier Based on Thin-Film Technology

Design of a Pattern Reconfigurable Amplifier Antenna with Gain Amplification Using Transistors

Design of Filtering Power Amplifier Based on TGV-IPD Filtering Matching Network

Design of Millimeter Wave Ultra Wideband Solid-State LNA Module Based on Metal Cavity Packaging

Design of Titanium SAW Phononic Crystal on Lithium Niobate LiNbO3/Si Structure

Diverse Semiconductor Integrated Microelectronics in the Application-Oriented AI Era

Dosimetric Assessment of a Birdcage-Coil Wireless Power Transfer at 6.78 MHz for Capsule Robots

Dual-Wideband Antenna Decoupling via Hybrid Conduction-Radiation Mitigation

E 2 3 A B C D E F G H I L M N O P R S T U W

Electromagnetic-Thermal-Fluid Multiphysics Coupling Simulation of Electronic Packaging Based on the FDTD Method

Exploiting LDMOS-PA for kW SSPA Applications

F 2 3 A B C D E F G H I L M N O P R S T U W

Filters for Space Applications: CNC Milling and Additive Manufacturing Perspectives

Formula-Based Design of Bias Tees with Wide DC-Path Bandwidth and Transmission Zeros

From Language to Structure: Semantic-Guided Cross-Modal End-to-End Intelligent Design of High-Performance Metasurface Absorbers

G 2 3 A B C D E F G H I L M N O P R S T U W

General-Purpose Terahertz Quasi-Optics and Mechanical Beamformers Enabled by 3D-Printing

General-Purpose Terahertz Quasi-Optics and Mechanical Beamformers Enabled by 3D-Printing

Generation of Scanning Self-Accelerating Beam by Manipulating Phase Distribution

Geometry Scalable Model of on-Chip Multilayer Interdigital Capacitors

H 2 3 A B C D E F G H I L M N O P R S T U W

High Q Terahertz Detector in Hybrid Metal−Optical Tamm State Cavity

High-Efficiency Broadband S-Shaped Thin-Film Lithium Niobate Electro-Optic Modulator

High-Frequency Narrowband to Low-Frequency Broadband Transition in an SMA-Actuated Bandpass Frequency-Selective Surface

High-Sensitivity Terahertz Sensing with Quadrature Self-Homodyne Detection

High-Tc Superconducting Josephson Mixers from X- to Sub-THz Band

High-Tc Superconducting Monolithic Microwave Integrated Circuits (MMICs) for High-Sensitivity RF Receivers

Hybrid Modeling Method of FT-Transformer and XGBoost for TFsurface

I 2 3 A B C D E F G H I L M N O P R S T U W

Improved Hybrid Quantum Models for More Accurate Phase Prediction of Expansion Coefficients in Large Finite Periodic Structures

Integrated Microwave Photonics for Signal Processing and Sensing

Invited Talk: Plasma-Based Reconfigurable FSS for Adaptive High-Power Microwave Shielding

L 2 3 A B C D E F G H I L M N O P R S T U W

Liquid Crystal Tunable Phase Shifter Using Post-Wall Coplanar Waveguide

Liquid Metal Enabled Reconfigurable Microwave Devices and Antennas

Low-Loss Millimeter-Wave Wideband Bandpass Filter in InP Technology with Cryogenic Performance Analysis

Low-Profile Broadband Beam-Scanning Antenna

M 2 3 A B C D E F G H I L M N O P R S T U W

Machine Learning-Assisted End-to-End Synthesis of RF Transformer-Based Matching Networks

Materials-Aware Design Strategies for Wearable Antenna Design

Meta-Screen: Full-Space EM Environment Reconfiguration for mmWave Communications

Metasurface Antenna Applied in Millimeter-Wave Imaging Systems

Metatronics for High-Performance Terahertz Integrated Circuits

Microwave Beam-Steering Using near-Field Metasurfaces

Microwave Probe with Enhanced Sensitivity for Wideband Dielectric Characterizations

Microwave Sensors Exploiting Nonlinear Dynamics

Millimeter-Wave and Sub-Terahertz Antenna and Metasurface Applications Using Screen Printed Vanadium Dioxide Switches

Modal Expansion Analysis and Inverse-Design of Reconfigurable AIS-Loaded Antennas

Modelling Clock Stability to Enabling Synchronisation for Multi-Static Passive Radar

Multi-Function Multi-Band Reconfigurable High-Q Filters

Multi-Material Additively Manufactured Wideband Dual-Linear Polarized Antenna with High Isolation

Multi-Template Differential Correction for Subarray-Based Pattern Reconstruction of Large Phased Arrays

N 2 3 A B C D E F G H I L M N O P R S T U W

Non-Volatile Reflective Intelligent Surface Based on 2D Material Switches for 6G Wireless Communications

Novel Design Strategies for Wideband Millimeter-Wave Switched-Type MMIC Phase Shifters with Low Amplitude and Phase Errors

O 2 3 A B C D E F G H I L M N O P R S T U W

On-Body Characterization of a Planar Horseshoe-Slot MXene Microstrip Antenna with an Elevated Ground Plane for Wearable Applications

Optimized Design of Compact Multi-Coil Arrays for Misalignment-Tolerant Wireless Power Transfer

P 2 3 A B C D E F G H I L M N O P R S T U W

Pattern-Reconfigurable Metasurface for Dynamic Switching Between OAM Beam and Dual-Beam

PDMS-MWCNT Composite Material Properties, Preparation and Role in Wearable Antennas

Phase-Tapered Bus-Bar Combiner for Efficiency Enhancement in C-Band GaN MMIC Power Amplifier

Photo-Tunable Chip Scale THz Ring Modulator

Planar EBG Monostatic Antenna with Wideband Interport Isolation Characteristics for 5G in-Band Full Duplex Applications

Power-Based Direction-Finding Enabled by a Null-Scanning Space-Time Leaky-Wave Antenna

Printable Nonlinear Tags and Handheld Devices for Clutter-Resilient Contactless Monitoring and Tracking

Printed VO_2 Tiles for Tunable Holographic Metasurface

R 2 3 A B C D E F G H I L M N O P R S T U W

Radiative Wireless Power Transfer with Advanced Materials

Rapid Analysis of Scattering Problem for LFPSs with Physics-Informed Attention Network

Reconfigurable and Tunable Millimeter-Waves Devices Based on Functional Materials

Reconfigurable Bandpass Ultrathin Angular-Selective Surfaces

Reconfigurable Millimetre-Waves and Terahertz Devices Using Phase Change Materials

Reflection-Type TTD Phase Shifter Based on Propagation-Controlled Reflective Loading

Research on Beam Steering Rectenna Array for Drone Microwave Wireless Power Supply

Resonant Tunneling Diodes for Terahertz Sensing

S 2 3 A B C D E F G H I L M N O P R S T U W

S Parameters Matrix Estimation for E-MIMO-Based Beamforming

Semantics-Guided End-to-End Intelligent Design Framework for Metasurface Absorbers

Semiconductor Electronics for High Power/High Speed Reconfigurable RF and Microwave Electronics

Semiconductor-grade Dry Nano-Island Coating Technology: Translating Advanced Materials from Lab Scale to Next-Gen 6G mm-Wave Substrates

Short-Circuit Ring Patch Bandpass Filter on Glass Substrate with MLP-Based Optimization

Sources and Detectors for Space THz Communication Systems

Space-Time Metasurface Antennas: Concept, Design, and Applications

Study on the Design of 50-75GHz Up-Conversion Module

Super-Mode-Group Based Reduced-Order Analysis of Multi-Mode Antenna Decoupling

Surface Mount Radiator - Intelligent AiP for Physical AI and Edge Eevices

T 2 3 A B C D E F G H I L M N O P R S T U W

Terahertz Microsystems Front-End Integration Technologies and Communication Application

Terahertz near-Field Scanning Microscopy for Nanoscale Imaging of Ovarian Cancer Cells

Terminating Magnetostatic Surface Waves with Metallic Patterns

THz Material Characterization of Rough Samples

Towards Fully Integrated Terahertz Frontends: Silicon Photonics Meets Resonant Tunneling Diodes

U 2 3 A B C D E F G H I L M N O P R S T U W

Ultra-Broadband 3D-Printed Metalens Using Height-Controlled Meta-Atoms

Ultra-Wideband Energy Selective Surface Based on Symmetrical Bow-Tie Topology for High-Power Electromagnetic Protection

Ultra-Wideband Multi-Channel Millimeter-Wave Receiver for Solar Sensing

Ultra-Wideband RCS Reduction Metasurface with Tunable Transmission Window

Ultrahigh-Sensitivity Microwave Biosensor Based on a CPW Loaded with a Modified Complementary Electric-LC Resonator

W-Band Wide-Angle Coverage Pillbox Multibeam Antenna Based on Bifocal Phase Compensation

Wave-Based Triple-Band CMOS Voltage-Controlled Oscillator

Wideband High-Precision Resonator-Based Phase Shifters via Lossy Electric and Magnetic Coupling

Wideband Phased-Array Meta-Antenna Without Air Cavity for Ku-Band Satellite Communication

Printed VO_2 Tiles for Tunable Holographic Metasurface

Kamran Ghorbani, RMIT University,
Melbourne, Australia
kamran.ghorbani@rmit.edu.au

I. Introduction

Metasurfaces, as two-dimensional arrays of subwavelength engineered meta-atoms, provide powerful control over electromagnetic waves through spatial modulation of amplitude, phase, polarisation, and surface impedance. Compared with conventional bulk metamaterials, metasurfaces offer a lower-profile, more fabrication-friendly platform while retaining strong wavefront-engineering capabilities, enabling applications such as beam steering, focusing, polarisation control, holography, and antenna miniaturisation. In antenna applications, metasurfaces have progressed from reflectarray or lens structures to radiating apertures, forming metasurface antennas capable of guiding, modulating, and radiating electromagnetic waves with high design flexibility. However, passive metasurfaces are inherently limited to fixed responses after fabrication, motivating extensive research into tunable and reconfigurable metasurfaces based on electrical, optical, mechanical, liquid-crystal, semiconductor, and phase-change-material tuning mechanisms. Although these approaches have enabled dynamic electromagnetic control, scalable implementation remains constrained by biasing complexity, fabrication cost, power consumption, and the need to individually address large numbers of unit cells.

II. Previous works

Our previous work addressed this challenge by demonstrating an optically programmable digital impedance surface (DIS) using a binary 1-bit triangular unit-cell topology. The surface integrated RF switches, phototransistors, optical fibres, and a low-cost AMOLED display to generate programmable impedance patterns without dense electrical wiring. The same fabricated DIS was experimentally validated as both a holographic antenna and a reflectarray, demonstrating beam steering over approximately ±45° in two principal planes. Among its main contributions, the work is the first demonstration of a fully optical control pathway for holographic antennas, showing that optical pattern projection can replace complex electronic routing for surface reconfiguration. It also introduced a novel triangular unit-cell geometry developed with future compound conformal surfaces in mind through Voronoi-based patterning. However, the approach remained limited by relatively low radiation efficiency, mainly due to the small electrical aperture and RF switch loss, as well as manufacturing complexity associated with the large number of optical fibres and manually assembled vias.

III. Our new project

This motivates the use of VO_2 based surface impedance tuning as a compact and scalable route toward reconfigurable holographic metasurface antennas. In our new work, two complementary VO_2 based unit cells are developed to provide bidirectional reactance control: Design I uses four square metal patches with a central VO_2 island and exhibits a positive reactance shift when heated above 68°C, while Design II, inspired by Booker's complementary principle, uses a VO_2 filled cross-slot within a single metal patch and exhibits a negative reactance shift under the same thermal stimulus. This complementary response enables overlapping holographic impedance patterns, where different tiles must increase, decrease, or maintain their reactance to achieve beam steering.

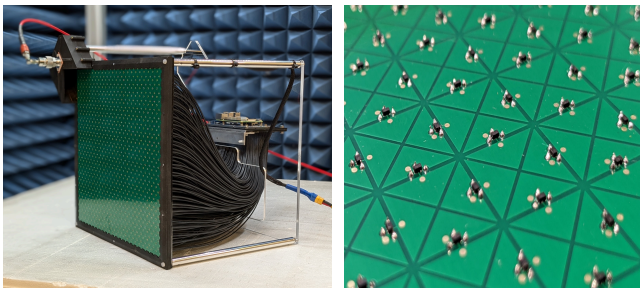


Fig. 1. Views of the assembled DIS.

A full metasurface is designed using these unit cells and will be fabricated on a quartz substrate by aerosol jet printing with silver and VO_2 inks. In the cold state, where VO_2 remains insulating, the antenna beam is directed toward 30° at 10 GHz. When the substrate is heated above 68°C, VO_2 undergoes its metal–insulator transition, reconfiguring the reactance distribution and steering the beam to 60°. This approach avoids costly microelectronic processing and complex per-element wiring, while enabling simple on-chip thermal control via Joule heating and cost-effective printed fabrication.

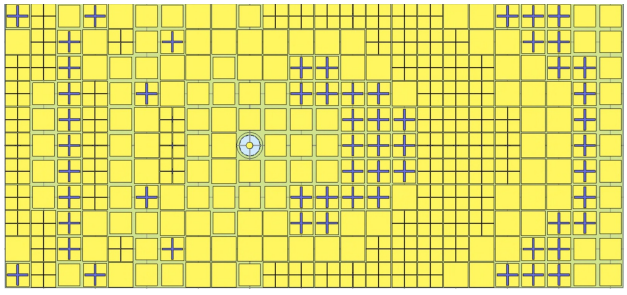


Fig. 2. Simulated layout of the proposed metasurface antenna.

References

[1] H.-T. Chen, A. J. Taylor, and N. Yu, "A review of metasurfaces: Physics and applications," Rep. Prog. Phys., vol. 79, no. 7, Art. no. 076401, Jun. 2016, doi: 10.1088/0034-4885/79/7/076401.

[2] J G. Beziuk et al., "Evaluation of an Optically Programmable Digital Impedance Surface (DIS) for Antenna and Reflect Array Applications," in IEEE Transactions on Antennas and Propagation, vol. 74, no. 2, pp. 1692-1706, Feb. 2026.

979-8-3315-4544-4/26/$31.00 ©2026 IEEE

Novel Design Strategies for Wideband Millimeter-wave Switched-type MMIC Phase Shifters with Low Amplitude and Phase Errors

Dr. Wenquan Che

School of Electronic and Information Engineering, South China University of Technology, 510641 Guangzhou, China
Email*: eewqche@scut.edu.cn*

Abstract

In 5G and beyond 5G era, the growing demands for high data transmission rates in communication systems and high resolution in radar imaging pose strict requirements on millimeter-wave phase shifters. Specifically, wide bandwidth, precise phase control, and high amplitude consistency are essential for ensuring excellent beamforming quality and scanning accuracy. In this way, passive switched-type MMIC phase shifters have emerged as a promising solution, featuring zero DC power consumption and low-cost calibration. However, in the conventional direct-cascading architecture for multi-bit designs, inter-stage mismatch and load-pulling effects severely restrict the operational bandwidth and degrade the phase and amplitude accuracy. In this talk, some recent research on new phase-control theories and path-switching mechanisms for mmW switched-type phase shifters in our group will be presented. These strategies are expected to provide an architecture-level solution for mmW multi-bit phase shifters in wireless communication.

Bio of the speaker

Dr. Wenquan Che received the PhD degree from the City University of Hong Kong (CITYU), Hong Kong, China, in 2003. From 2007 to 2008, she conducted academic research as one Humboldt Fellow with the Institute of High Frequency Technology, Technische Universität München, Munich, Germany. She had been with Nanjing University of Science and Technology as one lecturer, associate professor and professor since 1995. In Oct. 2018, she joined South China University of Technology as one full professor. She has authored or coauthored over 350 internationally referred

979-8-3315-4544-4/26/$31.00 ©2026 IEEE

journal papers and over 150 international conference papers. Her current research interests include microwave and millimeter-wave circuits and systems, antenna technologies etc.

Dr. Che has been one IEEE Fellow since 2022, and has been an Elected Member of the IEEE MTT-S AdCom (2018-2026). She was a recipient of the 2007 Humboldt Research Fellowship presented by the Alexander von Humboldt Foundation of Germany, the 5th China Young Female Scientists Award in 2008, and also the Distinguished Young Scientist awarded by the National Natural Science Foundation Committee of China in 2012. She had been the Editor-in-Chief of Microwave and Optical Technology Letters (2019-2025), and reviewer for several IEEE Transactions and journals. She is currently one associate editor of IEEE Journal on Wireless Power Technologies.



A Wide-Coverage End-Fire High-Gain Circularly Polarized Mobile Phone Antenna for Satellite Communication

（Invited paper）
Li-Bo Jia, Qing-Xin Chu, *Fellow, IEEE*
South China University of Technology, Guangzhou 510000, China

***Abstract*—To address the 3 dB polarization mismatch loss of linearly polarized antennas when receiving circularly polarized satellite signals, this work proposes an end-fire, high-gain circularly polarized mobile phone antenna with wide beamwidth. The antenna comprises three elements: a patch antenna integrated with the camera decoration (Deco), a frame antenna located at the top of the phone, and choke structures embedded in the side frames. The patch and frame antennas generate parallel electric and magnetic currents, respectively, whose combination produces end-fire left-handed circular polarization (LHCP). The antenna operates at a center frequency of 1.7 GHz with a bandwidth of 20 MHz. It features high gain and wide beamwidth, achieving a minimum LHCP gain higher than −5 dBic within a beam range exceeding a 90° cone angle across the operating band.**

Keywords—mobile phone antenna, circular polarized (CP), LHCP, end-fire radiation, wide beamwidth

I. INTRODUCTION

Satellite communication requires circularly polarized (CP) antennas for ionospheric penetration, but mobile terminals use linearly polarized (LP) antennas due to compact structures. When LP antennas receive satellite signals, a 3 dB polarization mismatch loss occurs, hindering high-gain performance. Since LP gain enhancement has reached its limits, CP offers a promising alternative. During voice calls, the phone top faces the sky, necessitating end-fire radiation and wide angular coverage.

Three main approaches exist for achieving CP on mobile phones. The first uses orthogonal dipoles [4]–[7], but this is difficult to implement in metal-frame phones and to achieve end-fire radiation under low-profile constraints. The second employs microstrip patch antennas [8], [9], which suffer from large size and cannot realize end-fire CP. A better approach generates parallel electric and magnetic currents using cavities on the phone back combined with the frame antenna to achieve end-fire CP radiation [10]–[12].

This paper presents a CP antenna for metal-frame smartphones. A patch antenna integrated with the camera Deco generates magnetic field radiation, while the frame antenna provides electric current radiation. When operating together, they achieve end-fire LHCP radiation with wide-angle coverage, and the optimal axial ratio reaches 0.56 dB. The antenna operates in the TX band (centered at 1.7 GHz with 20 MHz bandwidth). By loading inductive or capacitive components, the operating band can be switched to the RX band (centered at 1.5 GHz with 20 MHz bandwidth) without changing aperture size. Across the operating band, the minimum LHCP gain exceeds −5 dBic within a beam range of over 90° cone angle.

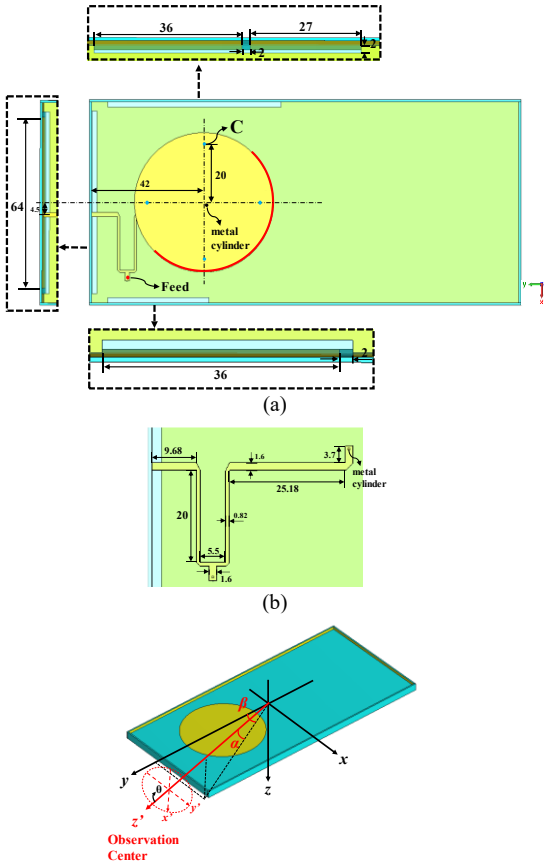


Fig. 1. Geometry of the proposed antenna. (a) 3-D view. (b) Feeding network. (c) Coordinate setting.

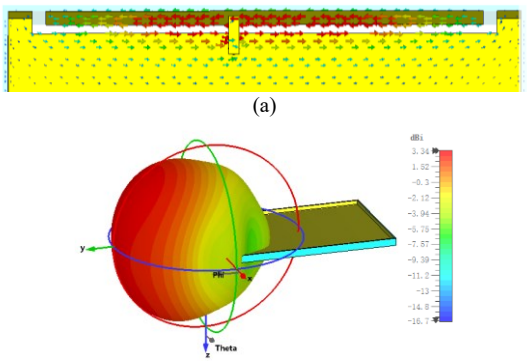


Fig. 2. Frame antenna. (a) Current distribution. (b) Pattern.

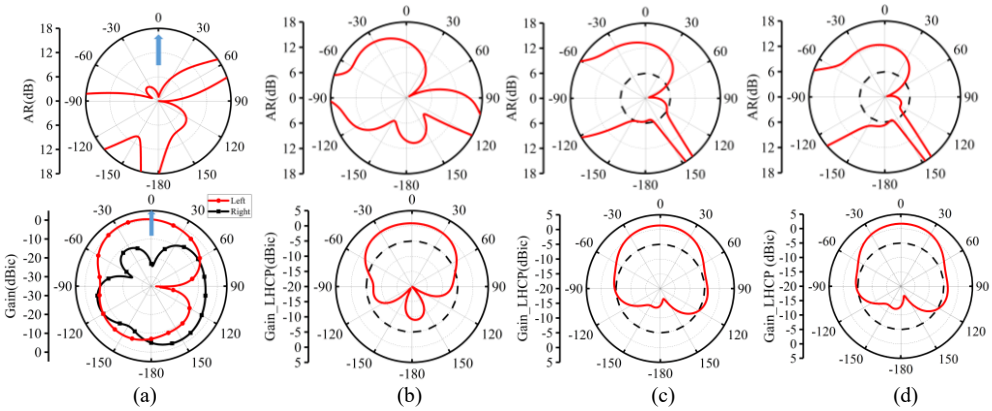


Fig. 3. The gain and AR of the antennas on y 'oz '-plane at 1.7 GHz. (a) CASE 1 (b) CASE 2 (c) CASE 3 (d) CASE 4

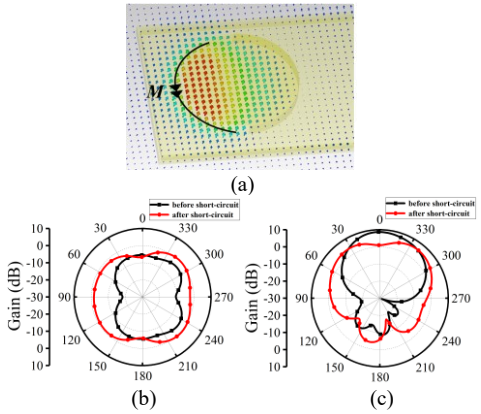


Fig. 4. (a) Equivalent magnetic current distribution; Comparison of pattern before and after half-patch shorting on the (b) xoy-plane and (c) yoz-plane.

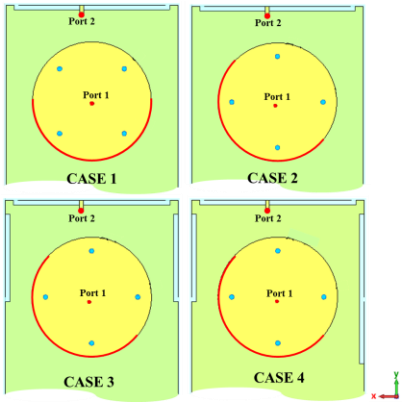


Fig. 5. Structural optimization steps of the proposed antenna.

II. ANTENNA DESIGN

Fig. 1 shows the proposed antenna geometry. The phone dimensions are 161.6 mm × 76.6 mm. The periphery uses a 0.8 mm thick FR-4 substrate with inner copper forming a 5 mm high metal frame. The ground is printed on the bottom surface, 2.7 mm below the upper edge of the frame. The camera Deco forms a circular patch antenna positioned 5 mm above ground, with half its edge shorted as shown in Fig. 1. A 50 Ω coaxial line feeds a T-shaped power divider on the substrate, outputting two equal-amplitude signals: one feeds the frame antenna; the other feeds the patch with a 1 mm offset from center. To evaluate LHCP coverage, a coordinate system (x', y', z') is introduced in Fig. 1(c), where z' is denoted as [α, β]. Here, β is the azimuth deviation from the y-axis, and α is

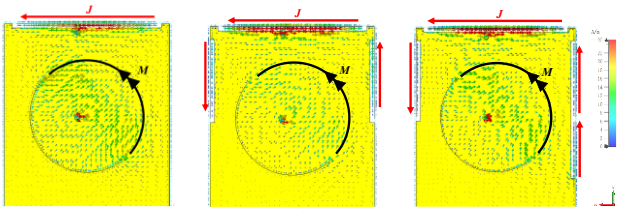


Fig. 6. Current distribution at 1.7 GHz of (a) CASE 2, (b) CASE 3, and (c) CASE 4.

the elevation deviation from the xoy-plane. Both parameters are selectable within a small range for practical use.

A T-shaped frame antenna on the top of the phone radiates as an electric current, providing a horizontally polarized electric field component as shown in Fig. 2. The circular patch antenna operates in the fundamental TM11 mode with the lower half edge is shorted to ground and the opening aperture acts as a magnetic current as shown in Fig. 4. The partially enclosed structure concentrates more energy toward the top of the phone.

To achieve end-fire CP radiation, the two antennas are adjusted and excited simultaneously, as shown in Fig. 5. In Case 1, the patch and frame antennas are excited with port phases of [90°, 0°] and the observation center is set to [0°, 6°] to maximize LHCP gain coverage. As shown in Fig. 3(a), left-hand circular polarization with good axial ratio is achieved toward the top of the phone. However, the maximum LHCP radiation direction exhibits a certain elevation angle relative to the phone plane and leans slightly to the left. Significant backward radiation toward the bottom is also observed. In Case 2, the patch is rotated 45° clockwise, with feed phases of [0°, 85°] and observation center [11.3°, 0°]. As shown in Fig. 7, the displacement of the equivalent current maxima enhances beam-edge LHCP gain, increasing the −5 dBic coverage angle from 64° to 72°. However, as shown in Fig. 3(b), the minimum axial ratio shifts to the beam edge, while broadside AR deteriorates to 12 dB. In Case 3, λ/4 chokes are loaded on both sides to suppress side-frame current, with feed phases of [0°, 80°] and observation center [19.3°, 0°]. Backward radiation is suppressed, and as shown in Fig. 3(c), the beam-edge AR reaches 0.89 dB. In Case 4, the right-side choke clearance is extended downward. As shown in Fig. 6, the extended branches carry current in the same direction as the frame current, elongating the radiating structure. The beam-edge AR further improves to 0.56 dB, and the LHCP beam is further widened.

Maintaining the same aperture size as the model in Fig. 1,

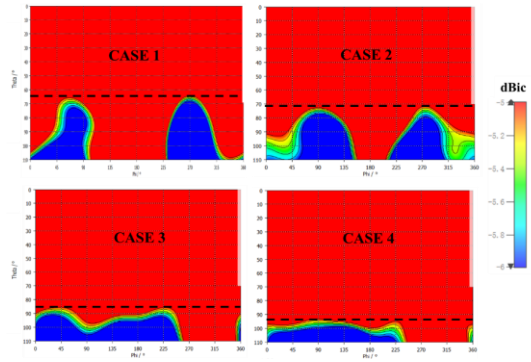


Fig. 7. The evolution of the LHCP gain coverage angle.

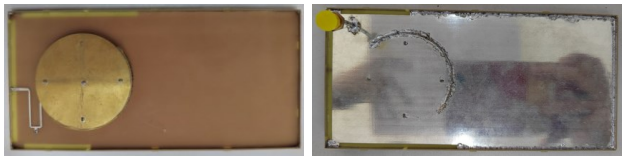


Fig. 8. Prototype of the proposed antenna.

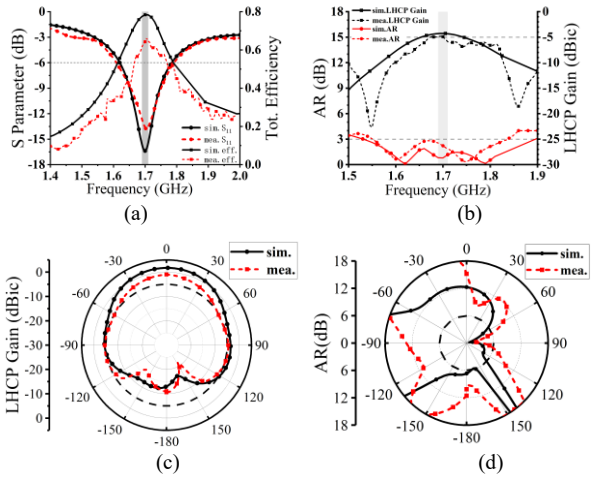


Fig. 9. Comparison of measured and simulation results. (a) S_{11} and efficiency. (b) Minimum AR and LHCP gain at beam edge (θ = 80°). (c) LHCP gain on y'oz'-plane at 1.7 GHz. (d) AR on y'oz'-plane at 1.7 GHz.

the antenna can be tuned to operate in the RX band by loading parallel capacitors at appropriate positions on the frame and patch antenna, as shown in Fig. 11. With all other parameters unchanged, the antenna maintains a −5 dBic LHCP gain coverage of over 80° within the RX band.

III. Simulated And Measured Results

Since the RX and TX band models differ only in the loaded reactive components, prototype fabrication and measurement were performed only for the TX band. The patch is a copper sheet with radius R = 26 mm. The shorted edge is formed by a 5 mm wide rectangular strip of length π×R, bent into an arc and welded between the patch and ground. The prototype is shown in Fig. 8. Fig. 9 compares the measured and simulated results. The measured −6 dB impedance bandwidth is 182 MHz (1.610–1.792 GHz), covering the TX band. At 1.7 GHz, the measured efficiency is 66.2%, lower than the simulated 78.4% due to welding losses during assembly. As a result, the measured LHCP gain coverage is also reduced noticeably near 1.71 GHz. Nevertheless, the radiation pattern remains end-fire with wide coverage. The measured AR distribution agrees well with simulation, achieving a beam-edge AR of 1.94 dB.

IV. Conclusion

This paper proposes an end-fire high-gain circularly polarized mobile phone antenna with wide angular coverage. By integrating a patch antenna with the camera Deco and combining it with the frame antenna, end-fire LHCP radiation is achieved. The antenna exhibits high gain and wide coverage, with a minimum LHCP gain exceeding −5 dBic within a cone angle of over 80° across the operating band. In-band efficiency is greater than 78%, and frequency band switching is realized through circuit switching. The feasibility of the design is validated by prototype measurements, demonstrating significant application potential for satellite communication terminals.

Acknowledgment

This work is supported by the National Key Research and Development Program of China under Grant 2021YFA1003404 and Honor Terminal Co., Ltd.

References

[1] Xu Z Q, Zhou Q Q, Ban Y L, et al. Hepta-band coupled-fed loop antenna for LTE/WWAN unbroken metal-rimmed smartphone applications[J]. IEEE Antennas and Wireless Propagation Letters, 2018, 17(2): 311-314.

[2] Serghiou D, Khalily M, Singh V, et al. Sub-6 GHz dual-band 8×8 MIMO antenna for 5G smartphones[J]. IEEE Antennas and Wireless Propagation Letters, 2020, 19(9): 1546-1550.

[3] Deng Q, Dong S X, Xiao Y, et al. A Low-SAR Frame-Antenna for Mobile Phone Based on Tangential Fields Cancellation[C]//2024 IEEE International Workshop on Antenna Technology. Piscataway, N.J.: IEEE, 2024: 345-347.

[4] Rao S, Wang Y, Xu F, et al. Dual-Band Circularly Polarized Antenna With Circular Polarization in the Endfire Direction in Metal-Bezel Smartphones for n256-Band Direct Phone to-Satellite Communication[J]. IEEE Transactions on Antennas and Propagation, 2025, 73(4): 2385-2394.

[5] Cao Z, Chang L, Li Y, et al. Compact Mobile Terminal Antenna With Endfire Circularly Polarized Beam for Satellite Communications[J]. IEEE Transactions on Antennas and Propagation, 2023, 71(12): 9980-9985.

[6] Zhang X, Wei K, Li Y, et al. A Polarization Reconfigurable Antenna for Satellite Communication in Foldable Smartphone[J]. IEEE Transactions on Antennas and Propagation, 2023, 71(12): 9938-9943.

[7] Zhang X, Wei K, Li Y, Zhang Z. A Circularly Polarized Antenna Based on Narrowed Crossed Dipole for Smartphone Satellite Communication[J]. IEEE Antennas and Wireless Propagation Letters, 2024, 23(8): 2511-2515.

[8] Zhang Y, Li Y, Hu M, et al. Dual-Band Circular-Polarized Microstrip Antenna for Ultrawideband Positioning in Smartphones With Flexible Liquid Crystal Polymer Process[J]. IEEE Transactions on Antennas and Propagation, 2023, 71(4): 3155-3163.

[9] Mak K M, Lai H W, Luk K M, et al. Circularly Polarized Patch Antenna for Future 5G Mobile Phones[J]. IEEE Access, 2014, 2: 1521-1529.

[10] Zhu H, Zhou D, Ma N, et al. Endfire Circularly Polarized Antenna for Satellite Communication in Metal-Rimmed Mobile Phones[C]//2024 14th International Symposium on Antennas, Propagation and EM Theory. Piscataway, N.J.: IEEE, 2024: 01-04.

[11] Tan H, Deng C, Zhang Y, et al. An Endfire Circularly Polarized Antenna for GNSS Mobile Phone Application[C]//2024 IEEE International Workshop on Radio Frequency and Antenna Technologies. Piscataway, N.J.: IEEE, 2024: 77-79.

[12] Sun L, Wang H. Circularly-Polarized Antenna Design in Mobile Phones by the Combination of Common and Differential Modes[C]//2024 IEEE MTT-S International Wireless Symposium (IWS). Piscataway, N.J.: IEEE, 2024: 1-3.

Wave-Based Triple-Band CMOS Voltage-Controlled Oscillator

Wen-Cheng Lai
Dept. of Electrical Eng., Ming Chi Univ. of Techn., Taiwan, R.O.C.
wenlai@mail.mcut.edu.tw;
wenlai@mail.ntust.edu.tw

Sheng-Lyang Jang
Dept. of Electrical Eng., Ming Chi Univ. of Techn., Taiwan*; Dept. of Electronic Eng., National Taiwan Univ. of Sci. and Techn.,* Taiwan, R.O.C.

Jen-Hsiang Hsieh
Dept. of Electronic Eng., National Taiwan Univ. of Sci. and Techn., Taipei City, Taiwan, R.O.C.

***Abstract*—By exploiting the intrinsic multiple resonant modes of a 6th-order *LC* resonator, a triple-band wave-based oscillator is designed. The *LC* resonator consists of two units of left-handed transmission *LC* network ended with parallel-tuned *LC* resonator, and a cross-coupled switching transistor pair is used to start up the oscillation. Two pairs of varactors are used for band tuning and switching. The proposed oscillator has been implemented with the *tsmc* 0.18 µm 1P6M CMOS technology and the core power consumption is 3.735 mW at the dc drain-source bias of 0.75 V. The VCO can generate differential signals in the frequency range of 8.04 - 8.68 GHz, 5.82 - 6.15 GHz, and 3.68 - 4.08 GHz. The die area of the triple-band oscillator is 0.568 × 1.189 mm².**

Keywords—CMOS, left-handed LC resonator, triple-band, differential VCO.

I. Introduction

Fully-integrated reconfigurable radio for multi-band/multi-mode/multi-function operation has been a long term goal for consumer applications. The multiple functional requirements demand flexible, low power, and frequency-agile RF transceivers, in which multi-band voltage-controlled-oscillators (VCOs) play a crucial role. The objective of this paper is to address the design of a triple-band oscillator implemented in the *tsmc* 0.18 µm 1P6M CMOS process. A triple-band oscillator can be designed with three-independent sub-oscillators, or it can be designed with a dual-band oscillator and a single-band oscillator. Finally it can be designed with a single oscillator with selectable frequency bands. The first method uses one oscillator and it forces two oscillators idle at a time. The last triple-band oscillator can be designed using by inductive or capacitive switching with MOS switches as conventional dual-band oscillators. The MOSFET switch degrades the *Q*-factor and phase noise. In the past, Buadana and Socher [1] use an oscillator to drive an output buffer, a push-push buffer and a quad-push to generate three harmonic-related frequency signals. Itoh and Tanaka [2] use the heterojunction transistor (HBT) as the band-selective switch for realizing a triple band oscillator and the resonator consists of a parallel resonant *LC* and a series-resonant *LC* network, the VCO can only provide two unbalanced outputs due to asymmetric *LC* resonator. Recently Jang, Chen, Chang and Juang [3] uses symmetric *LC* network consisted of a tuned resonator in shunt with a parallel-tuned *LC* resonator and uses the MOS varactors to switch the frequency band. In [4], a triple-mode VCO uses a sixth-order resonator based on three coupled inductors, and switchable current sources are used to excite different resonant frequency. The oscillators [3, 4] were designed using the lumped *LC* circuit model. Low-phase noise voltage-controlled oscillators (VCOs) are categorized into two distinct types by their physical mechanism: *LC*-based VCOs, and wave-based VCOs. The latter has not been used to design a triple band VCO. In this paper, we propose a new switch MOSFET-less triple-band oscillator, which is designed using the concept of distributed wave-oscillator. The band-selection is accomplished by varying varactor bias.

XXX-X-XXXX-XXXX-X/XX/$XX.00 ©20XX IEEE

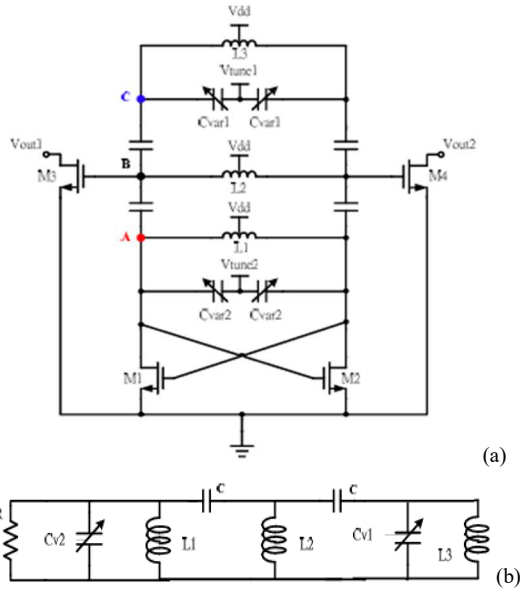


Fig. 1. (a) Schematic of the proposed triple-band VCO circuit. (b) The small-signal equivalent circuit of the 6th order *LC* resonator. R is the loss due to the passives.

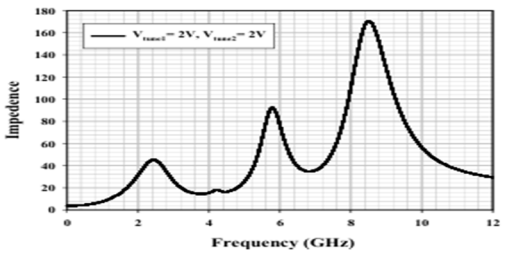


Fig. 2. Simulated impedances seen at node A. V_{DD} = 0.8 V. Disconnecting the drains of M_1 and M_2. V_{tune1} = 2.0V. V_{tune2} = 2.0V.

II. Circuit Design

Figure 1 shows the implemented triple-band VCO composed of a resonator and a cross-coupled pair (M_1, M_2) to generate negative resistance to compensate for the resistive *LC*-tank loss. The center-tapped inductor L_3, and accumulation-mode varactors (C_{var1}, C_{var1}) forms a parallel-

tuned LC resonator. The bias V_{tune1} is the control voltage used for selecting the resonant frequency of the parallel-tuned LC resonator. The MIM capacitors (C_1~C_4) and the inductors (L_1, L_2) forms a left-handed transmission LC network. The accumulation-mode varactors (C_{var2}, C_{var2}) are used for switching bands by using the bias V_{tune2}. Two common-source amplifiers (M_3, M_4) are used for measurement purpose. The input impedance of the circuit shown in Fig. 1(b) is

$$Z_{in} = \frac{num}{deno} \tag{1}$$

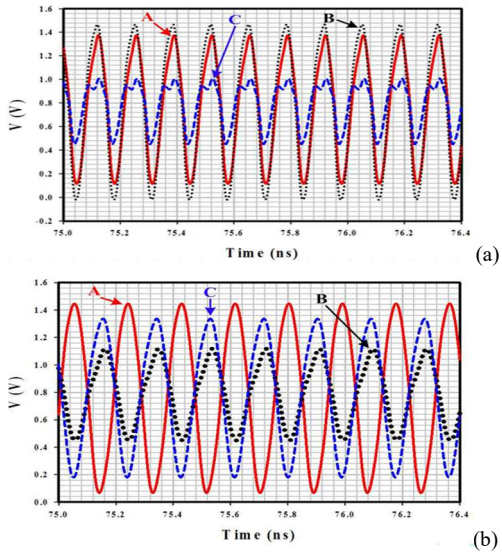
$$num = sL_2\{1-\omega^2(L_3C_{v1}+L_3C+2L_2C)+\omega^4(2L_2CL_3C_{v1}+L_2CL_3C)\} \tag{2a}$$

$$\begin{aligned} deno = {} & \{1-\omega^2(L_3C_{v1}+L_3C+3L_2C+C_{v1}L_2) \\ & +\omega^4[3L_2CL_3C_{v1}+2L_2CL_3C+L_2CL_2C+C_{v1}L_2(L_3C_{v1}+L_3C+2L_2C)] \\ & -\omega^6[L_2CL_2CL_3C_{v1}+C_{v1}L_2(2L_2CL_3C_{v1}+L_2CL_3C)]\} \\ & +gsL_2\{1-\omega^2(L_3C_{v1}+L_3C+2L_2C)+\omega^4(2L_2CL_3C_{v1}+L_2CL_3C)\} \end{aligned} \tag{2b}$$

The resonant frequencies are determined by Zin=R, from (2b) we can get

$$\begin{aligned} & 1-\omega^2(L_3C_{v1}+L_3C+3L_2C+C_{v1}L_2) \\ & +\omega^4[3L_2CL_3C_{v1}+2L_2CL_3C+L_2CL_2C+C_{v1}L_2(L_3C_{v1}+L_3C+2L_2C)] \\ & -\omega^6[L_2CL_2CL_3C_{v1}+C_{v1}L_2(2L_2CL_3C_{v1}+L_2CL_3C)]=0 \end{aligned} \tag{3}$$

Eq. (3) yields three resonant frequencies. Fig. 2 shows the simulated impedance of the passive LC resonator used in Fig. 1 and it has three impedance peaks with the resonant frequencies at 2.32GHz, 5.69GHz and 8.49GHz because of three inductors and other capacitors. And this indicates that the passive can be used to design a triple-band oscillator when it is used with a negative resistor circuit and an external resonant frequency excitation method is required because the wave-based oscillator tends to operate at the high-frequency mode. And this is achieved by varactor switching. The wave-based concept of the circuit operation can be seen from the time domain analysis. Fig. 3(a) shows that the simulated output voltages at the nodes A, B and C for the circuit operated at the high-frequency (f_H) band, which is denoted as the fundamental mode. The voltage amplitude exhibits monotonic variations as a function of the position.



The voltages at the nodes A, B and C are almost in-phase. Fig. 3(b) shows that the simulated output voltages at the nodes A, B and C for the circuit operated at the middle-frequency (f_M) band. At this mode, the voltages at the nodes A and C are out-of-phase. Fig. 3(c) shows that the simulated output voltages at the nodes A, B and C for the circuit operated at the low-frequency (f_L) band. At this harmonic mode, the voltages at the nodes A and B are also out-of-phase. The intuitive understanding of the VCO operation principle is as follows: At high V_{tune2}, the capacitance of (C_{var2}, C_{var2}) is small, and we can neglect the effect of (C_{var2}, C_{var2}); the VCO can operate at two frequency bands (high band, middle-frequency band) by tuning the voltage V_{tune1}. At low V_{tune1}, the capacitance of (C_{var1}, C_{var1}) is large, and the effect of (C_{var1}, C_{var1}) is equivalent to short-circuit, therefore we can neglect the presence of the center-tapped inductor L_3. The VCO operates at the high frequency band [6]. At high V_{tune1}, the capacitance of (C_{var1}, C_{var1}) is small, the presence of inductor L_3 decreases the oscillation frequency and the VCO operates at the middle frequency band. At low V_{tune2}, the capacitance of (C_{var2}, C_{var2}) is large, the capacitance of (C_{var2}, C_{var2}) decreases the oscillation frequency, and the VCO operates at the low frequency band.

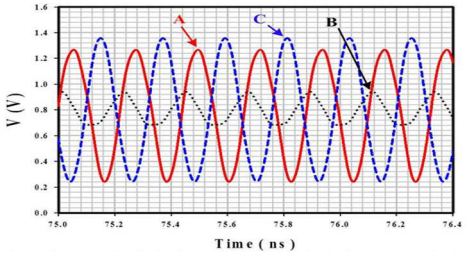


Fig. 3. Simulated voltage waveforms. (a) High-band, V_{tune1} = 0 V, V_{tune2} = 2 V. (b) middle-band, V_{tune1} = 2 V, V_{tune2} = 2 V. (c) Low-band, V_{tune1} = 2 V, V_{tune2} = 0 V. V_{DD} = 0.8 V.

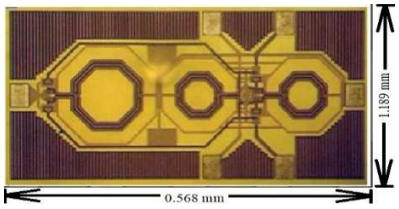


Fig. 4. Chip photograph of the proposed triple band (TB) VCO.

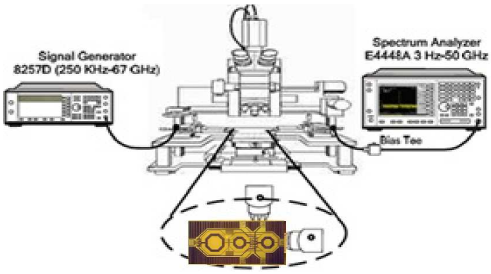


Fig. 5. Measurement on wafer probing setup.

III. Experimental Results and Discussion

The triple-band VCOs were designed and fabricated in the *tsmc* 0.18 µm 1P6M CMOS technology. Figure 4 shows the

micrograph of the proposed triple-band VCO with a chip area of 0.568 × 1.189 mm^2 including all test pads and dummy metal. Figure 5 proposes triple-band VCO measurement with spectrum analyzer EA4448A and signal generator 8257D on wafer probing [7]-[9]. To measure the phase noise performance of the VCO, the Agilent spectrum analyzer was used. With the supply voltage of V_{DD} = 0.75 V, the current and power consumption of the core VCO are 4.98 mA and 3.735 mW, respectively.

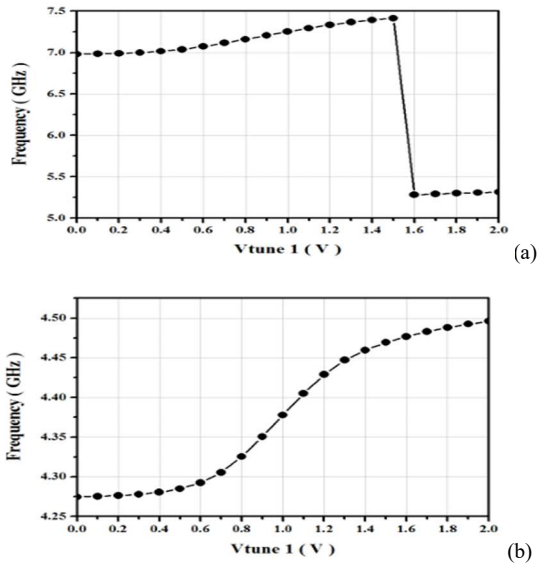


Fig. 6. Measured tuning range by varying V_{tune1} of varactor. V_{DD} = 0.75 V. (a) V_{tune2} = 2V, (b) V_{tune2} = 0.

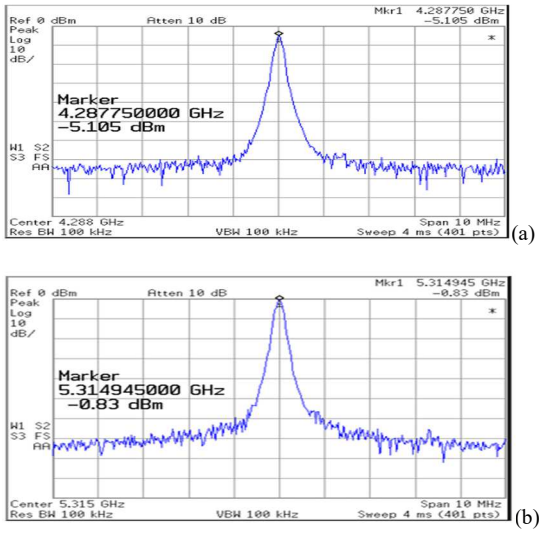


Fig. 6 shows the tuning ranges of the oscillation frequency as varying V_{tune1} and V_{tune2}. As shown in Fig. 6(a), at V_{tune2} = 2V, the triple-band VCO operates between 6.98-7.41GHz at high band as the control voltage V_{tune1} is tuned from 0 V to 1.5 V; the tuning range is 5.28-5.31GHz at middle band as the control voltage V_{tune1} is tuned from 1.6 V to 2 V. As shown in Fig. 6(b), at V_{tune2} = 0V, the triple-band VCO operates between 4.27-4.49GHz at low band as the control voltage V_{tune1} is tuned from 0 V to 2 V.

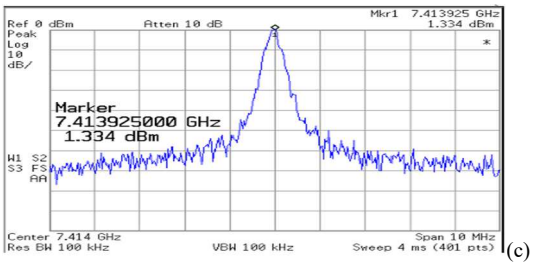


Fig. 7. Measured spectra of (a) the low-band VCO at V_{tune2} = 0 V, V_{tune1} = 0.55 V, (b) the middle-band VCO. V_{tune2} = 2 V, V_{tune1} = 2 V, and (c) the high-band VCO. V_{tune2} = 2 V, V_{tune1} = 1.5 V, V_{DD} = 0.75 V.

Fig. 7(a) shows the output spectrum at 4.27 GHz, with -3.95dBm output power. Fig. 7(b) shows the output spectrum at 5.31 GHz, with -0.83dBm output power. Fig. 7(c) shows the output spectrum at 7.41GHz, with 1.33 dBm output power. The measured low-band phase noise and the phase noise is -123.40 dBc/Hz at 1MHz offset frequency from the center frequency of 4.287 GHz. The high (middle, low)-band VCO FOM is -190.3(-183.77, -181.67) dBc/Hz.

IV. Conclusion

A novel triple-band cross-coupled voltage-controlled oscillator using varactor-switching technique has been proposed and successfully implemented in the 0.18 µm CMOS process. To our best knowledge, this is the first reported wave-based triple-band VCO to date. The high band is at 7.41 GHz, the middle-band is at 5.31 GHz, and the low-band is at 4.27 GHz. The new triple-band VCO uses the concept of varactor bias switching to excite three bands of oscillation frequency and has potential for RF application.

References

[1] N. Buadana and E. Socher, "A triple band travelling wave VCO using digitally controlled artificial dielectric transmission lines," *IEEE Radio Frequency Integrated Circuits Conf. (RFIC 2011)*, Jun. 2011.

[2] Y. Itoh and S. Tanaka, "A triple-band SiGe HBT differential VCO using a reconfigurable multi-band resonator", *Proceed. of the 40th European Microwave Conf.*, pp. 456-459, Sept. 2010.

[3] S.-L. Jang, *et al.,* "Triple-band CMOS voltage-controlled oscillator," *Microw. Opt. Technol. Lett.,* vol. 55, 4, pp.737-740, Apr. 2013.

[4] Z. Safarian and H. Hashemi, "Wideband multi-mode CMOS VCO design using coupled inductors," *IEEE Trans. Circuits Syst. I, Reg. Papers*, vol. 56, no. 8, pp. 1830–1843, Aug. 2009.

[5] W. F. Andress and D. Ham, "Standing wave oscillators utilizing wave adaptive tapered transmission lines," *IEEE J. Solid-State Circuits,* vol. 40, no. 3, pp. 638–651, Mar. 2005.

[6] S.-L. Jang, *et al.,* "Fully-integrated standing wave oscillator using composite right/left-handed LC network," *Microw. Opt. Technol. Lett.,* vol. 55, 5, pp.985-988, May. 2013

[7] W. -C. Lai, *et al., "*A Triple-Band Voltage-Controlled Oscillator Using Two Shunt Right-Handed 4th- Order Resonators," *Journal of Semiconductor Technology and Science,* 16(4), pp. 506-510, Aug. 2016.

[8] W. -C. Lai, *et al., "*An X-Band GaN HEMT Oscillator with Four-Path Inductors," *Applied Computational Electromagnetics Society Journal*, vol. 35, no. 9, Sept., 2020.

[9] J. -C. Wang , *et al.,* "Editorial for the Special Issue on Recent Advances in Microwave Components and Devices," *Micromachines*, 15(2), 180 , Jan. 2024.

Bandwidth reconfigurable low-noise Amplifier Based on magnetic coupling effect

Guangbao Shan, Pan Zhang, Yanwen Zheng*, Ruixin Wang, Fangqian Wang
Faculty of Integrated Circuit
Xidian University
Xi'an,China
Email: zhengyanwen@xidian.edu.cn

***Abstract*—This paper presents a band-reconfigurable low-noise amplifier (LNA) that utilizing transformer-based magnetic coupling technique. It consists of source-degenerated cascode amplifier integrated with a tunable magnetic coupling network. By manipulating the amplitude and phase of the voltage ratio(β), the position of the transmission zero can be dynamically adjusted, enabling flexible tuning of bandwidth. Simulation results demonstrate that the 3-dB bandwidths range from 15.64 to 23.55 GHz and from 18.35 to 31.38 GHz, with corresponding gains of 16.84 dB and 16.98 dB, respectively.**

Keywords—Magnetic coupling effect, Low-noise amplifier (LNA), Reconfigurable

I. INTRODUCTION

Applications such as the Internet of Things, mobile devices, and satellite communications are propelling the advancement of RF front-end systems toward multiple frequency bands, diverse standards, miniaturization, and integration. However, the LNA faces limitations in its frequency band reconstruction capability, which has emerged as a critical bottleneck for the RF front-end system. Varactor-based reconfigurable LNA suffer from limited range and high-frequency loss[1], while switch-based path selection significantly increases die area and degrades the NF due to switch resistance[2], [3], [4]. Although active inductors offer an alternative, they require high power consumption to achieve an adequate Q factor[5]. To overcome these limitations, we propose a reconfigurable LNA architecture that leverages an active magnetic coupling technique[6], [7], enabling wide-range frequency tuning without compromising area or noise performance.

II. Reconfigurable Low-Noise Amplifier Design

A. Circuit Design

Fig. 1 illustrates the complete schematic of the proposed circuit. It features a two-stage cascode topology incorporating an integrated transformer-based tuning technique. Module 1 serves as the input matching network and comprises inductor L_1 and L_2, as well as capacitors C_1 and C_2. The core amplification and frequency-reconstruction capabilities are driven by Modules 2 and 4. Module 2 employs a two-stage cascode topology with source-degeneration inductors L3 and L8 to optimize noise and linearity. Specifically, the first stage is designed for bandwidth tuning, while the second stage is utilized for gain compensation to counteract high-frequency roll-off. Module 4 acts as an adjustable control unit. By tuning *Vc*, the magnitude and phase of the voltage ratio β are modulated, thereby enabling regulation the bandwidth of the amplifier. Module 3 is a source follower configured for output matching.

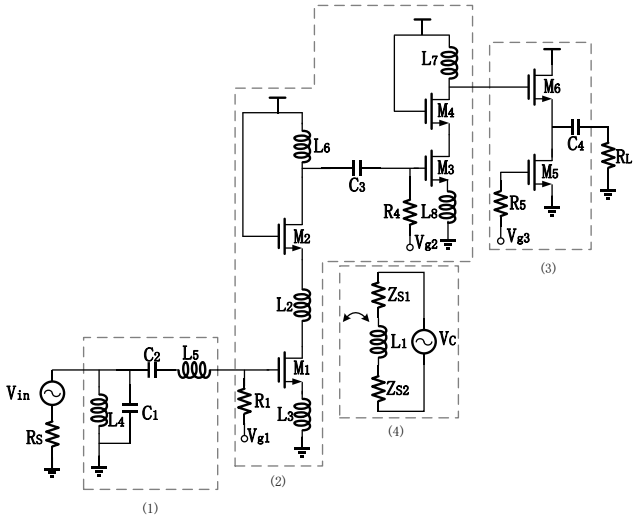


Fig. 1. Circuit schematic diagram

B. Principle Analysis

The initial stage of the LNA is illustrated in Fig. 2. Based on Thevenin's equivalent, the open-circuit voltage of the common-source stage is $-g_m r_o v_{in}$, and the corresponding equivalent resistance is r_o. The equivalent circuit for the common-gate transistor is presented in Fig. 3. Isolate the capacitors and calculate the equivalent impedance solely for the branch containing i_R. The equivalent impedance values can be derived using (1).

$$Z_{eq} = \frac{r_o + sL_6}{1 + g_m r_o + g_{mb} r_o} \tag{1}$$

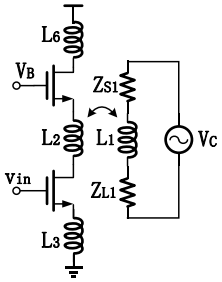


Fig. 2. Schematic of the primary gain stage

This work was supported in part by the National Key Research and Development Program of China under Grant 2022YFB4401303, and in part by the National Natural Science Foundation of China under Grant 61934006, Grant 62090040, and Grant 62090043. (Corresponding author: Yanwen Zheng.)

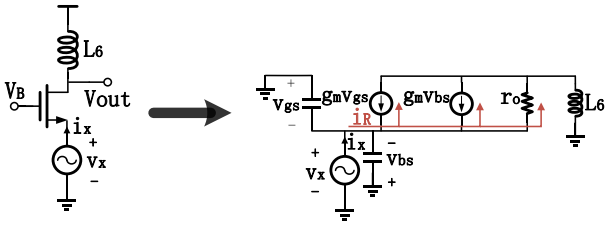


Fig. 3. Equivalent circuit of the common-gate transistor

Based on the above information, Fig. 2 can be equivalently represented as shown in Fig. 4, and the key parameters for the model in Fig. 4 can be derived as (2), (3), (4) and (5).

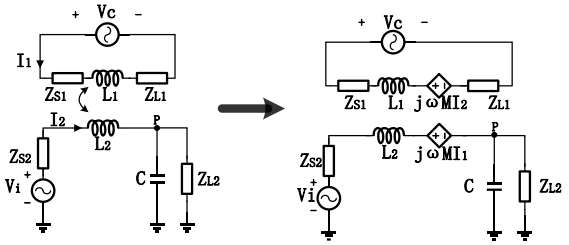


Fig. 4 Single-stage equivalent circuit diagram

$$V_i = -g_{m1} r_{o1} v_{in} \tag{2}$$

$$Z_{s2} = r_{o1} \tag{3}$$

$$Z_{L2} = \frac{r_{o2} + sL_6}{1 + g_{m2} r_{o2} + g_{mb2} r_{o2}} \tag{4}$$

$$C = C_{gs2} + C_{sb2} \tag{5}$$

When Z_{S1}=Z_{L1}=R, according to Kirchhoff's voltage law, it can obtain:

$$V_c = (2R + j\omega L_1) I_1 + j\omega M I_2 \tag{6}$$

$$V_i = j\omega M I_1 + \left(Z_{S2} + j\omega L_2 + \frac{Z_{L2} \cdot \frac{1}{j\omega C}}{Z_{L2} + \frac{1}{j\omega C}} \right) I_2 \tag{7}$$

The solution of I_1, I_2 is as (8) and (9).

$$I_1 = \frac{\left(Z_{S2} + j\omega L_2 + \frac{Z_{L2}}{1 + j\omega C Z_{L2}} \right) V_c - j\omega M V_i}{\left(Z_{S2} + j\omega L_2 + \frac{Z_{L2}}{1 + j\omega C Z_{L2}} \right)(2R + j\omega L_1) + \omega^2 M^2} \tag{8}$$

$$I_2 = \frac{(2R + j\omega L_1) V_i - j\omega M V_c}{\left(Z_{S2} + j\omega L_2 + \frac{Z_{L2}}{1 + j\omega C Z_{L2}} \right)(2R + j\omega L_1) + \omega^2 M^2} \tag{9}$$

α is defining as the current ratio, it can be expressed as shown in (10).

$$\alpha = \frac{I_1}{I_2} = \frac{\left(Z_{S2} + j\omega L_2 + \frac{Z_{L2}}{1 + j\omega C Z_{L2}} \right) V_c - j\omega M V_i}{(2R + j\omega L_1) V_i - j\omega M V_c} = \alpha_r + j\alpha_i \tag{10}$$

To simplify the analysis, given V_i=-$g_{m1} r_{o1} v_{in}$, let β be defined as the voltage ratio, where φ_c and φ_{in} represent the phases of Vc and v_{in}, respectively.

$$\beta = \frac{V_c}{v_{in}} = \frac{|V_c|}{|V_{in}|} \angle(\varphi_c - \varphi_{in}) \tag{11}$$

α can be written as (12) by substituting (11) into (10):

$$\alpha = \frac{\left(Z_{S2} + j\omega L_2 + \frac{Z_{L2}}{1 + j\omega C Z_{L2}} \right) \beta + j\omega M g_{m1} r_{o1}}{-(2R + j\omega L_1) g_{m1} r_{o1} - j\omega M \beta} \tag{12}$$

Then, V_i can be expressed as (13):

$$V_i = \left(Z_{S2} + j\omega (L_2 + M\alpha) + \frac{Z_{L2}}{1 + j\omega C Z_{L2}} \right) I_2 \tag{13}$$

The equivalent inductance of the filter circuit can be represented as (14):

$$L_{eq} = L_2 + M\alpha_r \tag{14}$$

In the filter circuit, the relationship between the source voltage and the node voltage at the load end can be expressed as (15):

$$V_i = (Z_{S2} + j\omega L_{eq}) I_2 + V_P \tag{15}$$

The values of node voltages are given by (16).

$$V_P = \frac{\frac{Z_{L2}}{1 + j\omega C Z_{L2}} \left((2R + j\omega L_1) V_i - j\omega M V_c \right)}{\left(Z_{S2} + j\omega L_2 + \frac{Z_{L2}}{1 + j\omega C Z_{L2}} \right)(2R + j\omega L_1) + \omega^2 M^2} \tag{16}$$

Furthermore, it has:

$$I_{Z_{L2}} = \frac{I_2}{1 + sCZ_{L2}} \tag{17}$$

Based on the equations above and the analysis in Fig. 3 and Fig. 4, the output voltage is derived as (18):

$$V_o = I_{Z_{L2}} \cdot sL_6 = \frac{\frac{j\omega L_6}{1 + j\omega C Z_{L2}} \left((2R + j\omega L_1) V_i - j\omega M V_c \right)}{\left(Z_{S2} + j\omega L_2 + \frac{Z_{L2}}{1 + j\omega C Z_{L2}} \right)(2R + j\omega L_1) + \omega^2 M^2} \tag{18}$$

We can derive the gain as presented in (19).

$$\frac{V_o}{V_i} = \frac{\frac{j\omega L_6}{1 + j\omega C Z_{L2}} \left[(2R + j\omega L_1) + \frac{j\omega M \beta}{g_m r_{o1}} \right]}{\left(Z_{S2} + j\omega L_2 + \frac{Z_{L2}}{1 + j\omega C Z_{L2}} \right)(2R + j\omega L_1) + \omega^2 M^2} \tag{19}$$

By substituting (2), (3), (4) and (5) into (19), The final gain is given by (20):

$$\frac{V_o}{v_{in}} = -\frac{\frac{j\omega L_6 \cdot (1 + g_{m2} r_{o2} + g_{mb2} r_{o2})}{\Phi} \cdot \left[(2R + j\omega L_1) g_{m1} r_{o1} + j\omega M \beta \right]}{\left(r_{o1} + j\omega L_2 + \frac{r_{o2} + j\omega L_6}{\Phi} \right)(2R + j\omega L_1) + \omega^2 M^2} \tag{20}$$

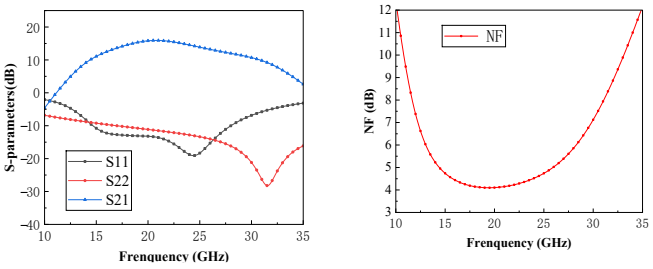
where $\Phi = 1 + g_{m2} r_{o2} + g_{mb2} r_{o2} + j\omega (C_{gs2} + C_{sb2})(r_{o2} + j\omega L_6)$.

The transfer zero is located at $s_z = \frac{-2R \cdot g_{m1} r_{o1}}{L_1 g_{m1} r_{o1} + M\beta}$.

By manipulating the amplitude and phase of the voltage ratio β , the zero point can be driven to shift toward either low or high frequencies. The location of the inherent roll-off of the circuit can be modified. This mechanism facilitates large-scale continuous reconstruction of the passband edge flatness and 3 dB bandwidth while maintaining stable frequency gain associated with the main pole.

III. Results and Discussion

As illustrated in Fig. 5, in the absence of transformer-based tuning, the LNA achieves a minimum noise figure of 4.1 dB. The forward gain S21 at 20.8 GHz is 15.92 dB, with a 3-dB bandwidth ranging from 16.35 GHz to 26.46 GHz.



（a）S-parameters (b) NF

Fig. 5. S parameters and NF

To validate the reconfiguration capability of the proposed multi-band reconfigurable LNA, the layout was designed in Cadence. Self-designed 65-nm inductors with EM-extracted models were employed to ensure realistic Q-factors in simulations. The total area of the layout is 0.79×0.73 mm^2.

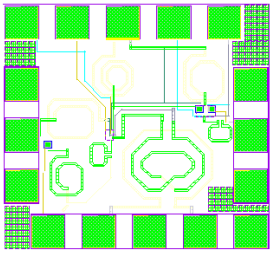


Fig. 6. Layout of LNA

A 1V sinusoidal input v_{in} was applied. The sinusoidal control voltage Vc varies in magnitude (0 - 6 V) and phase (-180° - 180°). Fig. 7 presents some representative gain and bandwidth under different magnitudes and phases of β. It shows that the maximum and minimum bandwidth values range from 15.64 to 23.55 GHz and from 18.35 to 31.38 GHz, with corresponding gains of 16.84 dB and 16.98 dB, respectively.

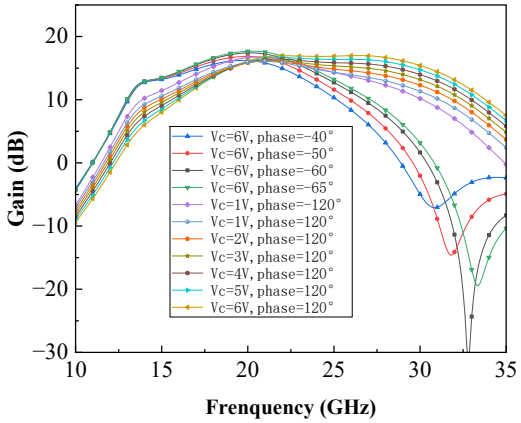


Fig. 7. Gain under different modulation voltages

A comparative summary of the proposed LNA is provided in Table I. In contrast to other advanced designs, this LNA demonstrates a low noise figure and power dissipation, while maintaining a small footprint than previously reported implementations.

TABLE I. PERFORMANCE SUMMARY AND COMPARISON

	[1]	[2]	[4]	This Work
Process	0.1μm GaAs	65nm CMOS	45nm SOI	65nm CMOS
Freq(GHz)	26.5~41	28/39	24/28/39	15.64~31.38
Gain(dB)	24~27.7	16.8/15	9.5/12/15.5	16~17.5
NF(dB)	2.4~2.8	4.06/4.46	4.5/4.5/5.5	4.1
Pdc(mW)	74	20.4	20.68	13.45
Chip Area(mm^2)	1.6	0.35	0.69	0.577

IV. Conclusion

This paper proposes a reconfigurable LNA architecture based on transformer coupling. The design adopts a systematic approach, spanning from small-signal analytical modeling to full-circuit simulation verification. It details the position shift of transmission zeros in relation to variations in the voltage ratio β. By introducing controlled transmission zeros, the LNA successfully achieves bandwidth reconfiguration. This methodology offers broad application potential for multi-band and multi-mode reconfigurable configurations in future millimeter-wave (mm-wave) RF microsystems.

References

[1] Z. Wang et al., "A Ka-Band Switchable LNA With 2.4-dB NF Employing a Varactor-Based Tunable Network," in IEEE Microwave and Wireless Components Letters, vol. 31, no. 4, pp. 385-388, April 2021

[2] D. Cheng, X. Chen, Q. Chen, X. Ma and L. Li, "A Reconfigurable LNA With Compact Magnetic-Capacitive Coupling Transformer Networks for 5G 28-/39-GHz Applications," in IEEE Microwave and Wireless Technology Letters, vol. 34, no. 7, pp. 915-918, July 2024.

[3] B. Liu, F. Meng, Z. Ma, K. S. Yeo and K. Ma, "A 28/39 GHz Tri-Mode Frequency-Reconfigurable LNA for Multiband 5G Communications," in IEEE Transactions on Circuits and Systems II: Express Briefs, vol. 71, no. 9, pp. 4036-4040, Sept. 2024.

[4] R. A. Shaheen, T. Rahkonen and A. Pärssinen, "Millimeter-wave Frequency Reconfigurable Low Noise Amplifiers for 5G," in IEEE Transactions on Circuits and Systems II: Express Briefs, vol. 68, no. 2, pp. 642-646, Feb. 2021.

[5] Y. Luo and T. Xia, "Design of Reconfigurable Low Noise Amplifier Based on Active Inductor," 2020 IEEE International Conference on Artificial Intelligence and Computer Applications (ICAICA), Dalian, China, 2020, pp. 977-982.

[6] Y. Zheng, G. Shan, X. Fan, Z. Yang and G. Li, "An 0.04–10.32 nH Ultracompact Tunable Inductor Based on Flexible Magnetic Coupling Tuning Technique," in IEEE Transactions on Electron Devices, vol. 71, no. 8, pp. 4945-4951, Aug. 2024, doi: 10.1109/TED.2024.3418298.

[7] G. Shan et al., "A Broadband Tunable On-Chip Transformer Based on Magnetic Coupling Technique," in IEEE Transactions on Microwave Theory and Techniques.

Exploiting LDMOS-PA for kW SSPA Applications

Xin Tong
School of Integrated Circuits and Microelectronics
Northwestern Polytechnical University (NPU)
Xi'an, 710072, China
xin.tong@mail.nwpu.edu.cn

Shiyang Luo
School of Integrated Circuits and Microelectronics
Northwestern Polytechnical University (NPU)
Xi'an, 710072, China
oceanr@mail.nwpu.edu.cn

Xidi Hu
School of Integrated Circuits and Microelectronics
Northwestern Polytechnical University (NPU)
Xi'an, 710072, China
huxd@mail.nwpu.edu.cn

Hao Zhang*
School of Microelectronics
Nanjing University of Science and Technology (NJUST)
Nanjing, 210094, China
zhang.hao@nwpu.edu.cn

He Guan*
School of Integrated Circuits and Microelectronics
Northwestern Polytechnical University (NPU)
Xi'an, 710072, China
he.guan@nwpu.edu.cn

***Abstract*—This paper presents the design and implementation of a 250-W S-band Class-B solid-state power amplifier (SSPA) module based on the Ampleon BLC2425M10LS250 laterally diffused metal–oxide–semiconductor (LDMOS) transistor. Stepped-impedance microstrip matching networks are employed to achieve broadband impedance matching over 2.4–2.6 GHz. The amplifier is measured under pulsed operation with a 10% duty cycle and a 100-µs pulse period. Measured results demonstrate that the proposed module delivers 53.69–53.98 dBm (233–250 W) output power, 14.0–14.4 dB power gain, 66.5%–75.8% drain efficiency, and 63.6%–72.5% power-added efficiency across the operating band. In addition, a high-efficiency power-combining scheme is proposed to facilitate future kW-class industrial microwave systems.**

Keywords—Solid-state power amplifier (SSPA), LDMOS, S-band, kW-class, power combining.

I. Introduction

Industrial microwave sources for applications such as plasma excitation, particle accelerators, microwave heating, and material processing require increasingly higher output power levels. With the rapid development of semiconductor technologies, solid-state power amplifiers (SSPAs) have gradually replaced vacuum-tube-based solutions in high-power radio-frequency (RF) systems due to their superior stability, flexible power scalability, extended lifetime, and reduced maintenance cost [1], [2].

The advancement of gallium nitride (GaN) technology has significantly expanded the achievable frequency and power ranges of SSPAs. Owing to its high breakdown voltage and high power density, GaN devices can operate at elevated voltage and current levels within a compact physical footprint. However, the reduced parasitic capacitance associated with high power density typically leads to lower optimum load impedances, increasing impedance-matching complexity and sensitivity to layout and assembly tolerances [3].

In the S-band, laterally diffused metal–oxide–semiconductor (LDMOS) devices remain attractive for high-power industrial applications. As summarized in Table I, the selected LDMOS (BLC2425M10LS250) and GaN (CLF24H4LS300P) devices are compared at 2.45 GHz. The LDMOS device offers lower cost and requires a moderate supply voltage compared with the GaN counterpart. Furthermore, as shown in Table II, the LDMOS transistor exhibits a significantly larger optimum load impedance. This relatively higher load impedance allows impedance matching to be realized using only microstrip transmission lines, thereby reducing matching-network complexity and assembly sensitivity.

TABLE I
Device Characteristics of the Selected LDMOS and GaN Devices

Parameter	LDMOS (BLC2425M10LS250)	GaN (CLF24H4LS300P)
V_{DS} (V)	32	50
P_L (W)	260 (CW), 260 (Pulsed)[1]	320 (CW), 350 (Pulsed)[1]
η_D (%)	68.5 (CW), 68.8 (Pulsed)[1]	74.0 (CW), 75.0 (Pulsed)[1]
G_p (dB)	15.2	14.0
Unit Price[2] (USD)	95	250

[1] Pulsed condition: 100-µs pulse width, 10% duty cycle.
[2] Price based on a quotation for quantities above 20 units.

TABLE II
Load-Pull Impedances of the Selected LDMOS and GaN Devices

f (GHz)	LDMOS (BLC2425M10LS250)		GaN (CLF24H4LS300P)	
	Z_S (Ω)	Z_L (Ω)	Z_S (Ω)	Z_L (Ω)
2.40	3.43−j6.80	**2.31−j2.00**	3.82−j8.04	**0.79+j0.13**
2.45	3.31−j6.57	**2.14−j1.70**	3.29–j7.75	**0.77+j0.14**
2.50	3.20−j6.29	**1.98−j1.43**	2.85–j7.43	**0.71+j0.18**

For kilowatt-class industrial RF systems, the required output power is typically achieved by combining multiple SSPA modules through power-combining networks [1], [2], [4]. Therefore, the development of a high-efficiency, compact, and cost-effective S-band SSPA module is of practical importance for scalable industrial microwave systems.

This work presents a 250-W Class-B LDMOS SSPA operating from 2.4 to 2.6 GHz using stepped-impedance matching networks at both the input and output ports. Under pulsed operation, the fabricated prototype achieves high output power and high efficiency with a compact layout and reliable thermal design. Moreover, a high-efficiency power-combining scheme based on spatial or radial combiners is proposed for future kilowatt-class implementation, aiming to ensure high combining efficiency, strong port isolation, and improved amplitude and phase consistency. The proposed approach demonstrates the feasibility of a compact and scalable solution for high-power industrial microwave systems.

979-8-3315-4544-4/26/$31.00 ©2026 IEEE

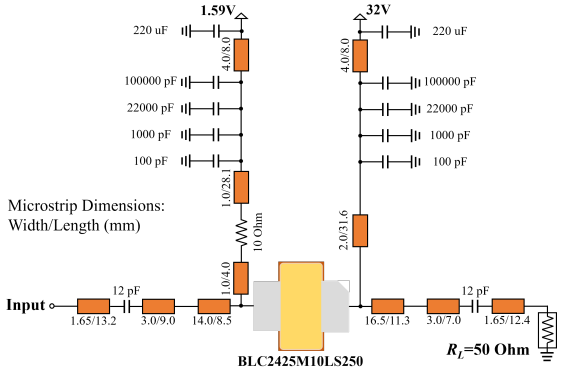


Fig. 1. Complete schematic of the designed SSPA module.

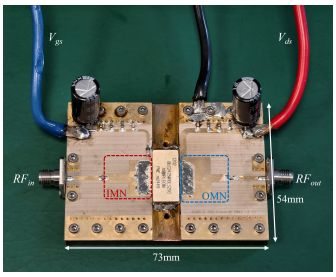
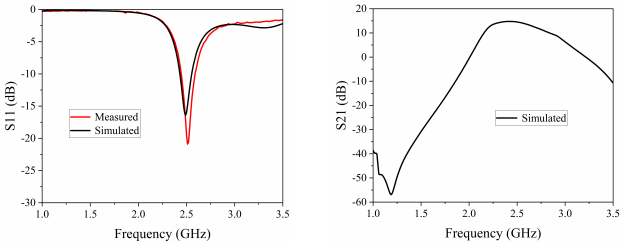


Fig. 2. Photograph of the fabricated SSPA module.



(a) (b)

Fig. 3. Simulated and measured S-parameters of the designed PA. (a) S_{11}. (b) S_{21}.

II. SSPA Module Design and Measurement

The proposed SSPA module employs the Ampleon BLC2425M10LS250 LDMOS transistor. The gate and drain supply voltages are set to 1.59 V and 32 V, respectively, resulting in a quiescent drain current I_{DQ} of 10 mA. The printed circuit board (PCB) is fabricated on a Rogers TC350 substrate with a thickness of 30 mil and a relative permittivity of 3.5.

A. Matching Network Design

The measured load-pull data provided by the manufacturer, as listed in Table I, are used as initial design targets. The optimal source impedance Z_S and load impedance Z_L are adopted for the matching network design. A stepped-impedance transformation approach is employed, in which two cascaded microstrip sections with different characteristic impedances are used to transform the device impedance to 50 Ω at both ports.

B. Large-Signal Optimization

Based on the large-signal device model, circuit simulations are performed in Advanced Design System (ADS) with an input power of 40 dBm. The stepped-impedance matching networks at both the input and output ports are further optimized using harmonic-balance simulation. The complete schematic of the designed SSPA module, together with the microstrip dimensions, is shown in Fig. 1. A 100-Ω shunt resistor is connected at the gate to ensure unconditional stability, and a 12-pF Murata capacitor is employed as a dc-blocking capacitor.

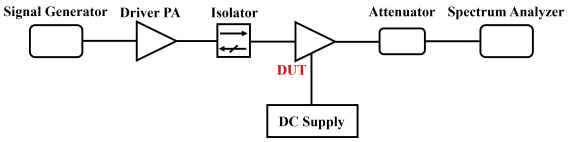
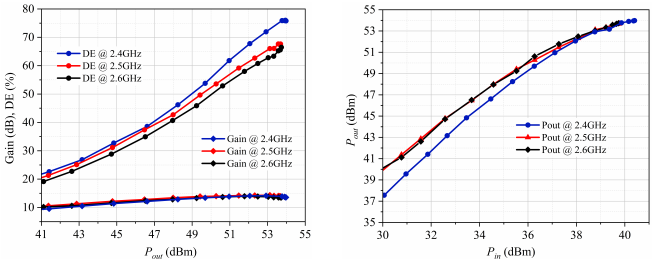


Fig. 4. Test bench of the designed circuit.



(a) (b)

Fig. 5. Measured performance at 2.4, 2.5 and 2.6 GHz. (a) power gain and DE versus P_{out}. (b) P_{out} versus P_{in}.

C. Implementation and Measurement

The proposed SSPA module is fabricated according to the design procedure described above. A photograph of the fabricated circuit is shown in Fig. 2, where the input and output matching networks are highlighted. The module exhibits a compact size of 73 × 54 mm², corresponding to an area of 39.42 cm². To ensure adequate thermal dissipation and mitigate device self-heating, the amplifier is mounted on a copper heat sink.

The simulated and measured S-parameters are presented in Fig. 3. Good agreement is observed for the input reflection coefficient S_{11}. The small-signal gain S_{21} is obtained from large-signal S-parameter (LSSP) simulation in ADS, since the Class-B amplifier is biased near cutoff and the available vector network analyzer (Keysight E5071C) cannot provide sufficient RF drive power for reliable small-signal gain characterization.

The large-signal measurement setup is shown in Fig. 4. A Ceyear 1441B signal generator operating in pulsed mode with a 10% duty cycle and a 100-µs pulse period is connected to a driver amplifier (TLPA0.5G6G-4040-S) to provide the input drive. The pulsed performance is measured using a Baluelec SA2052 spectrum analyzer, with a 50-dB attenuator inserted to protect the instrument. Due to limitations of the test setup, the maximum available input power is 40 dBm, and the SSPA module is not driven into deep saturation.

Fig. 5 (a) shows the measured power gain and drain efficiency versus output power at 2.4, 2.5, and 2.6 GHz, while Fig. 5 (b) presents the measured output power versus input power. Fig. 6 summarizes the measured performance at an input power of approximately 40 dBm across the target band.

The proposed SSPA module achieves an output power of 53.69–53.98 dBm (233–250 W), a drain efficiency of 66.5%–75.8%, and a power-added efficiency of 63.6%–72.5% from 2.4 to 2.6 GHz. In addition, the measured power gain ranges from 14.0 to 14.4 dB. These results demonstrate good agreement between simulation and measurement, confirming the effectiveness of the proposed design.

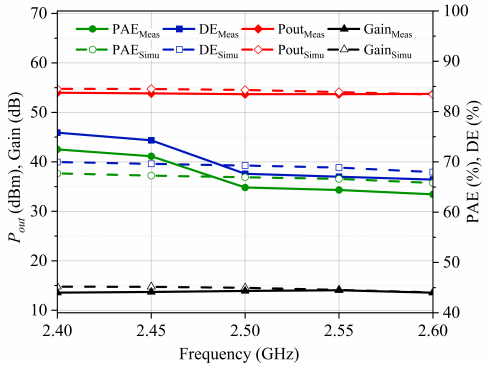


Fig. 6. Measured performance versus frequency at P_{in} ≈ 40dBm.

TABLE III
STATE-OF-THE-ART LDMOS SSPAS IN S-BAND

Ref.	Freq (GHz)	P_{out} (W)	P_{out} (dBm)	Gain (dB)	DE (%)
[5]	2.11–2.17	426	56.30	~18.3	~49.2
[6]	1.805–2.2	400	56.02	15.3–16.5	40.0–43.0
[7]	2.7–2.9	329	55.17	13.4–14.1	57.8–60.9
[8]	2.4–2.5	250	53.49	19.3–20.0	~58.3
[9]	1.8–2.2	230	53.61	16.1–17.6	~30.0
This work	**2.4–2.6**	**250**	**53.98**	**14.0–14.4**	**66.5–75.8**

A comparison with recently reported S-band LDMOS SSPAs is summarized in Table III. The proposed design achieves competitive output power while maintaining high efficiency, indicating its suitability for further power combining toward kilowatt-class microwave sources.

III. HIGH-EFFICIENCY POWER COMBINING SCHEME FOR KILOWATT-CLASS SYSTEMS

As illustrated in Fig. 7, spatial power combiners can be employed to combine multiple 250-W SSPA modules, thereby forming a kilowatt-class microwave source. For high-power multi-way combining, the combiner is required to exhibit low insertion loss, high inter-channel amplitude and phase balance, sufficient power-handling capability, strong port isolation, and effective thermal management, since any imbalance or loss directly degrades the overall efficiency and reliability of the combined system. Owing to their distributed-field structure and inherent geometrical symmetry, spatial and radial combiners are well suited to satisfy these requirements and can provide balanced power distribution with robust high-power performance [10], [11]. The practical implementation and experimental validation of the proposed combining architecture will be investigated in future work.

IV. CONCLUSION

A 250-W S-band Class-B LDMOS SSPA module employing stepped-impedance matching networks has been demonstrated. Under pulsed operation, the fabricated prototype delivers an output power of 53.69–53.98 dBm, a power gain of 14.0–14.4 dB, a drain efficiency of 66.5%–75.8%, and a power-added efficiency of 63.6%–72.5% over 2.4–2.6 GHz. In addition to the validated single-module performance, a spatial and radial power-combining architecture has been proposed to enable scalable multi-way integration toward kW-class microwave sources. The demonstrated efficiency and compact implementation of the unit amplifier establish a reliable foundation for high-power multi-module combining. These results confirm the feasibility of the proposed approach for practical and scalable kW-class industrial microwave SSPAs.

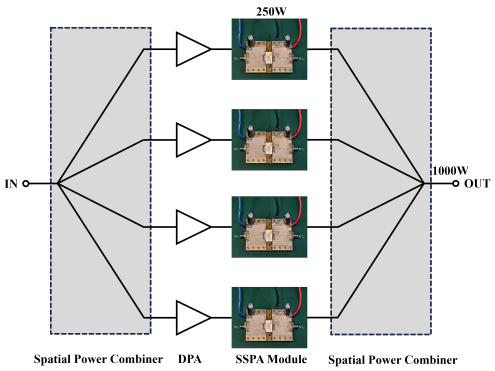


Fig. 7. Power combining scheme for kilowatt-class microwave source.

REFERENCES

[1] R. Tong, O. Bengtsson, J. Olsson, A. Bäcklund and D. Dancila, "Kilowatt Power Amplifier With Improved Power Back-Off Efficiency for Cyclotron Application," in *IEEE Transactions on Microwave Theory and Techniques*, vol. 70, no. 2, pp. 1401-1409, Feb. 2022.

[2] C. Majumder, B. Majumder and B. Ghosh, "A kW-range Solid-State Power Amplifier Design for OTH Radar's Transmitter Application.," *2023 IEEE Microwaves, Antennas, and Propagation Conference (MAPCON)*, Ahmedabad, India, 2023, pp. 1-6.

[3] J. J. Komiak, "GaN HEMT: Dominant Force in High-Frequency Solid-State Power Amplifiers," in *IEEE Microwave Magazine*, vol. 16, no. 3, pp. 97-105, April 2015.

[4] K. H. Kim *et al.*, "2.7 - 3.1 GHz, 1.5 kW Pulsed Solid-State Power Amplifier with Automatic Gain Equalization Circuit for Radar Application," *2007 IEEE Radar Conference*, Waltham, MA, USA, 2007, pp. 1044-1048.

[5] L. Wang, H. Rueda, W. Brakensiek, C. Dragon and K. Foxx, "A half-kW capable 28-V LDMOS RF power transistor in a small-footprint package," *2013 IEEE MTT-S International Microwave Symposium Digest (MTT)*, Seattle, WA, USA, 2013, pp. 1-3.

[6] N. Zhu, R. McLaren, D. G. Holmes, J. L. Holt, P. Rashev and J. K. Jones, "An integrated RF match and baseband termination supporting 395 MHz instantaneous bandwidth for high power amplifier applications," *2017 IEEE MTT-S International Microwave Symposium (IMS)*, Honolulu, HI, USA, 2017, pp. 1114-1117.

[7] H. R. Dhanyal, W. Hu, H. Feroz, H. Nawaz, A. Samad and U. Farooq, "Miniaturized High-Efficiency Pulsed-Power Amplifier for Surveillance and Tracking Radar," *2020 5th International Conference on Computer and Communication Systems (ICCCS)*, Shanghai, China, 2020, pp. 840-843.

[8] Z. Li, D. Zhang, Y. Sun, B. Bian, Y. Juan and H. Li, "A Studyon the Design of a High-Efficiency 2.45GHz RFPower Amplifier Using LDMOS Technology," *2025 IEEE 8th International Symposium on Electromagnetic Compatibility (ISEMC)*, Hefei, China, 2025, pp. 1-3.

[9] L. Zhao, M. Watts, B. Noori and J. Jones, "A 230 W, 1.8 to 2.2 GHz broadband LDMOS power amplifier utilizing multi-section integrated passive device input matching," *2015 European Microwave Conference (EuMC)*, Paris, France, 2015, pp. 227-230.

[10] H. Theveneau, C. Gaquière, R. Lenglet, M. Werquin, J. -C. Joly and S. Tortel, "Spatial Power Combiner With Low-Impedance Inputs and Increased Isolation," in *IEEE Microwave and Wireless Components Letters*, vol. 27, no. 11, pp. 956-958, Nov. 2017.

[11] M. M. Fahmi, J. A. Ruiz-Cruz and R. R. Mansour, "Modular Design of Pyramidal Radial Combiners Based on Nonuniform Parallel Plate Waveguide Sections With Constant Impedance," in *IEEE Transactions on Microwave Theory and Techniques*, vol. 71, no. 2, pp. 727-736, Feb. 2023.

An Energy-Efficient Reconfigurable BLE RF Receiving Front-End Based on Mixer-First Architecture for IoT Applications

Yan Zhao, Jiawen Zhang, Tongde Huang, Wenhua Gu, Wen Wu
Key Laboratory of Short-Range RF Sensing Chip and Microsystem, Ministry of Education
Nanjing University of Science and Technology
Nanjing ,China
y.zhao@njust.edu.cn, zhangjiawen@njust.edu.cn, tongdeh@njust.edu.cn, guwenhua@njust.edu.cn, wuwen@njust.edu.cn

***Abstract*—This paper presents an energy-efficient reconfigurable Bluetooth Low Energy (BLE) RF receiver front-end based on a mixer-first architecture for Internet-of-Things (IoT) applications. To eliminate the hardware redundancy and high cost associated with conventional designs using separate wake-up receiver (WuRX) and main receiver (RX) front-ends, the proposed architecture enables full hardware reuse between two parallel operating modes by reconfiguring the core transimpedance amplifier (TIA) to operate either as a linear amplifier or as a nonlinear active rectifier. The mixer-first architecture facilitates on-chip channel selection while reducing power consumption. Fabricated in a TSMC 28-nm CMOS process, the prototype consumes 0.2 mW in RX mode and achieves a minimum power consumption of 30 µW in non-duty-cycled WuRX mode. The measured input reflection coefficient, S11, is below -10 dB in both modes across the target frequency band. In WuRX mode, the front-end achieves a noise figure of approximately 21 dB over the signal bandwidth of interest. Based on the classical RF sensitivity calculation, the overall WuRX system is expected to achieve a receiving sensitivity better than -90 dBm at a data rate of 100 kbps. This work provides a low-cost, highly integrated RF front-end solution for BLE IoT terminals.**

Keywords—reconfigurable RF front-end, wake-up receiver, mixer-first architecture, bluetooth low energy.

I. INTRODUCTION

With the large-scale deployment of the Internet of Things (IoT), Bluetooth Low Energy (BLE) has become the mainstream short-range wireless communication standard for consumer electronics, smart home devices, and industrial sensing terminals, owing to its ultra-low power consumption, high compatibility, and mature protocol stack [1]–[3]. For short-range BLE communication, the standard specification mandates a minimum receiver sensitivity of −70 dBm, while commercial applications increasingly demand lower cost, longer battery life, and reliable performance. As the core module of BLE receivers, the RF front-end architecture directly affects chip cost, power consumption, and receiver performance [4].

In conventional BLE RF front-end designs, a dedicated wake-up receiver (WuRX) is commonly employed to extend battery life, but its always-on channel monitoring dominates the receiving-link power consumption [5]. Traditional solutions use independent WuRX and RX front-ends, causing hardware redundancy, increased chip area, and higher bill-of-materials (BOM) cost. Additionally, mainstream RX front-ends rely on a dedicated low-noise amplifier (LNA) input stage, which introduces extra static power consumption [6]. To overcome these limitations, this paper proposes an energy-efficient reconfigurable BLE RF receiver front-end with two parallel operating modes, WuRX and RX, based on a unified mixer-first architecture, enabling full hardware reuse and WuRX function integration. The mixer-first architecture eliminates the power-hungry LNA, thereby reducing RF-link power consumption. In WuRX mode, the proposed design overcomes the power–latency trade-off inherent in traditional duty-cycled receivers, reduces standby power consumption [7], and achieves a lower on-off keying (OOK) demodulation threshold for extended detection range. In RX mode, the same hardware enables ultra-low-power BLE communication [8]. Compared with discrete dual-front-end architectures, the proposed design reduces redundant circuitry and chip area while enabling dynamic power–performance optimization.

The proposed reconfigurable RF front-end meets the requirements of both regular BLE communication and ultra-low-power standby wake-up operation. It offers a low-cost, highly integrated front-end solution for large-scale BLE IoT terminals and shows potential for practical engineering deployment and commercial applications

II. CIRCUIT ARCHITECTURE AND DESIGN

A. Reconfigurable Mixer-First RF Front-End Architecture

There are inherent discrepancies between the WuRX and the RX in terms of circuit topology, performance requirements, and signal-processing methodologies. Specifically, the WuRX RF front-end leverages nonlinear rectification to demodulate OOK-modulated RF carriers, whereas the RX requires the RF front-end to perform linear processing on the incoming RF signals. This fundamental functional incompatibility imposes a critical constraint on the reconfiguration of these two circuit modules with distinct functionalities. To address this challenge, this work presents a reconfigurable design based on the mixer-first circuit architecture. In RX mode, a transimpedance amplifier (TIA) is employed for linear signal processing, whereas in WuRX mode, part of the TIA circuit is reconfigured as a nonlinear active rectifier. This design integrates the WuRX function into the RF receiver, thereby achieving highly efficient receiver integration. The mixer-first architecture directly down-converts the RF carrier signals, eliminates the RF amplifier module to reduce RF power consumption, and enhances out-of-band interference suppression, making it well suited for RX-mode applications.

979-8-3315-4544-4/26/$31.00 ©2026 IEEE

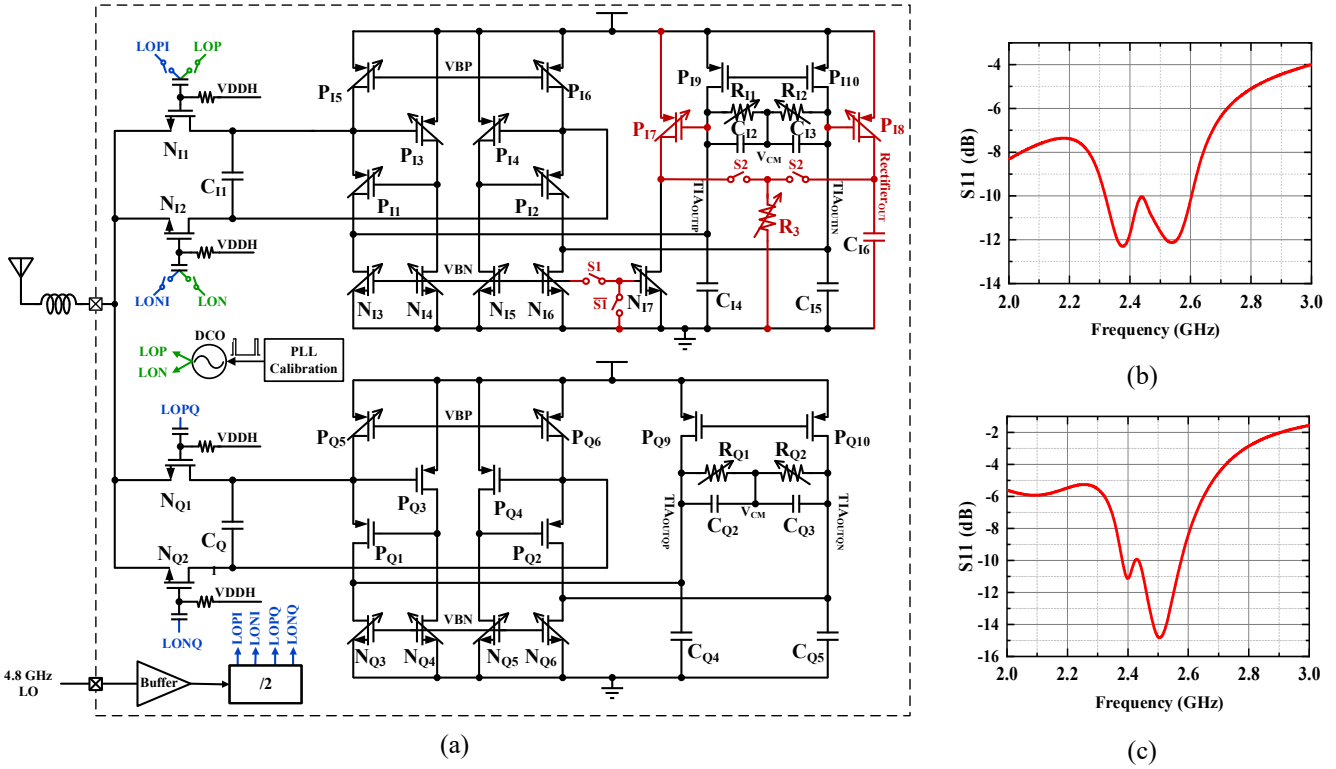


Figure.1 (a)Mixer-first reconfigurable RF front-end circuit schematic, Measured S11 curves for two receiving modes: (b)RX;(c)WuRX

As illustrated in Fig. 1(a), the reconfigurable operation between the rectifier and TIA is realized through mode switching and corresponding transistor tuning. In WuRX mode, differential local oscillator (LO) signals LOP and LON, generated by an on-chip digitally controlled oscillator (DCO), are supplied to process the OOK modulated RF carriers. Switches S1 and S2 are used to reconfigure the circuit between rectifier and TIA modes. When S1 and S2 are closed, the current mirror N_{I7} is activated to provide bias current for the rectifying transistors, and the RF front-end circuit is switched to active rectifier mode to demodulate the OOK RF carriers, with $Rectifier_{OUT}$ as the corresponding output node. In RX mode, on-chip generated quadrature I/Q LO signals (LOPI, LONI, LOPQ, and LONQ) are employed, and the circuit is configured into differential I/Q paths via a four-channel passive mixer. When S1 and S2 are open, the rectifying transistors are disconnected from the signal path, and the circuit switches to a folded resistive-output TIA mode identical to that of the Q path, with TIA_{OUT} as the output. Both operation modes share a single off-chip inductor, which provides the required impedance matching for its mixer-first architecture, increases the source impedance of the mixer-first structure, and delivers passive gain without additional power consumption.

B.Active Envelope Detector Design

This work proposes an active envelope detector based on the mixer-first architecture. As illustrated in the upper signal path of Fig. 1(a), the mixer-first architecture eliminates the power-hungry RF LNA, significantly reducing overall power consumption. The OOK signal modulated on a 2.4-GHz carrier is down-converted to an uncertain intermediate frequency (U-IF) through a two-channel passive mixer composed of transistors N_1 and N_2, enabling on-chip channel selection prior to envelope detection. The down-converted U-IF current signal is fed into the source terminals of common-gate transistors P_{I1} and P_{I2}. A feedforward path is constructed by the common-source amplifier formed by transistors P_{I3}, P_{I4}, N_{I4} and N_{I5}, which boosts the equivalent transconductance (g_m) of the common-gate input stage to $(1+A)g_m$, where A denotes the voltage gain of the common-source amplifier. This design effectively reduces the input impedance of the stage, and enables accurate impedance matching with ultra-low power consumption. A tunable dimension scheme is implemented for transistors P_{I1}, P_{I2}, P_{I3} and P_{I4}. In active rectifier mode, increasing the dimensions of P_{I1}-P_{I4} pushs the devices into the deep subthreshold region, which provides higher transconductance for impedance matching while enhancing nonlinearity to improve rectification efficiency In addition, the dimensions of current mirror transistors N_{I3}–N_{I6}, N_{Q3}–N_{Q6}, P_{I5}–P_{I6} and P_{Q5}–P_{Q6} are also tunable for co-optimization of power consumption and noise figure. The rectifying transistors P_{I7} and P_{I8}, as well as load resistors R_1, R_2 and R_3 are all designed as 3-bit binary-weighted tuning arrays. Fine tuning of the rectifying transistors is implemented to mitigate the impact of process-voltage-temperature (PVT) variations, while the load resistors enable gain tuning, thereby further improving the sensitivity of the WuRX.

Benefiting from the proposed mixer-first reconfigurable RF front-end, the OOK-modulated WuRX outperforms the Gaussian Frequency Shift Keying (GFSK) scheme used in conventional BLE receivers in low-SNR scenarios, achieving a lower demodulation threshold and a comparable communication range. Meanwhile, the RX mode achieves ultra-low-power operation for BLE short-range communication. This reconfigurable design eliminates redundant circuit modules in traditional schemes, improves hardware utilization, and reduces overall chip area.

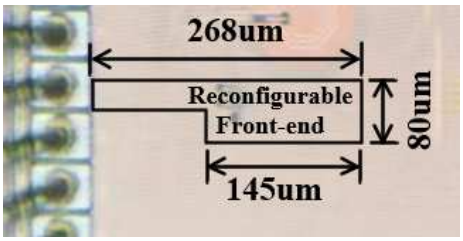


Figure 2. Micrograph of fabricated chip

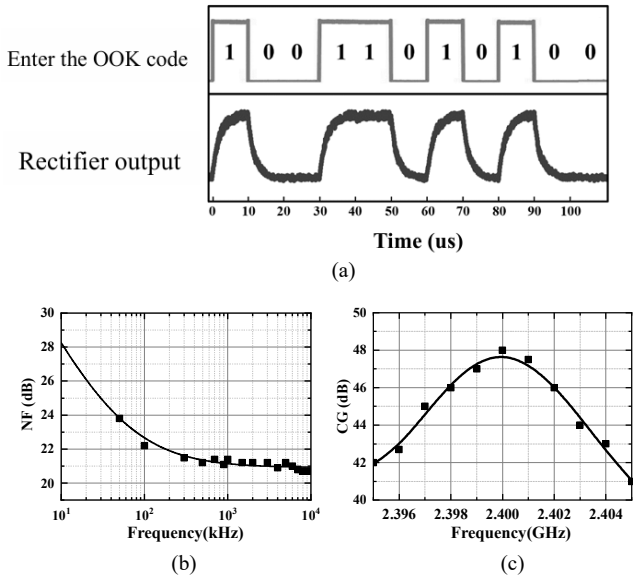


Figure 3.Measurement Results of the WuRX: (a) Time-Domain Data Stream of the WuRX; (b) Measured Noise Figure; (c) Measured Conversion Gain

III. MEASUREMENT RESULTS

The proposed energy-efficient reconfigurable BLE RF receiver front-end is fabricated and verified using the TSMC 28-nm CMOS process, with the die micrograph shown in Fig. 2. The measured S11 curves of the RX and WuRX modes are plotted in Fig. 1(b) and 1(c) respectively, both achieving an S11 better than −10 dB within the target BLE frequency band. In RX mode, which supports short-range communication, the RF power consumption is significantly reduced, and the total power consumption is lowered to 0.2 mW. For the proposed WuRX in non-duty-cycled mode, the power consumption ranges from 30 μW to 37.8 μW, depending on the sensitivity requirement. The designed WuRX circuit supports duty-cycled operation mode, and the power consumption can be further reduced by duty-cycling optimization in subsequent implementations.

The detailed measurement results of the WuRX are shown in Fig. 3. Fig. 3(a) depicts the transient response characteristics of the WuRX, where the input OOK data are configured with a baseband data rate of 100 kbps, an RF carrier frequency of 2.4 GHz, and an input signal power of −80 dBm. The measurement results show that, after receiving the OOK-modulated signal through the RF front-end, the envelope detection module successfully demodulates the OOK carrier through nonlinear rectification, with no bit errors observed during the demodulation process. This verifies the reliable demodulation capability of the proposed WuRX under weak-signal conditions. Fig. 3(b) shows the measured noise figure curve of the WuRX, which is approximately 21 dB within the signal bandwidth of interest. With the LO frequency set to 2.4 GHz, the measured RF conversion gain curve is plotted in Fig. 3(c). The WuRX exhibits a peak conversion gain of 48 dB, a −3-dB bandwidth of approximately 3 MHz, and a gain attenuation of around 6 dB at a 5-MHz frequency offset. This performance meets the bandwidth requirement of the intermediate frequency and effectively suppresses noise from the baseband circuit, thereby ensuring that the impact of the baseband circuit on the overall sensitivity is negligible. Based on the classical sensitivity calculation formula, the proposed WuRX is expected to achieve a receiving sensitivity better than −90 dBm at a data rate of 100 kbps.

IV. CONCLUSION

This work presents the design, implementation, and measurement verification of an energy-efficient reconfigurable BLE RF receiver front-end based on a mixer-first architecture. First, the circuit design of the mixer-first reconfigurable RF front-end is analyzed in detail. This architecture integrates the WuRX mode into the receiver system through TIA circuit reconfiguration and enables the RX mode to achieve short-range BLE communication with ultra-low power consumption.

The measurement results demonstrate that the prototype achieves a power consumption of 0.2 mW in RX mode and a minimum power consumption of 30 μW in non-duty-cycled WuRX mode. Based on the measured front-end performance and classical sensitivity calculation theory, the proposed design provides core performance support for the overall WuRX system to achieve a receiving sensitivity better than −90 dBm at 100 kbps. This design alleviates the inherent trade-off among power consumption, sensitivity, and cost in conventional BLE front-ends, and provides a low-cost, highly integrated solution for battery-powered BLE IoT terminals.

REFERENCES

[1] Ma Z, Xiao M, Xiao Y, et al. High-Reliability and Low-Latency Wireless Communication for Internet of Things: Challenges, Fundamentals, and Enabling Technologies[J]. IEEE Internet of Things Journal. 2019, 6(5): 7946-7970.

[2] Purushothaman V K, Klumperink E A M, Clavera B T, et al. A Fully Passive RF Front End With 13-dB Gain Exploiting Implicit Capacitive Stacking in a Bottom-Plate N-Path Filter/Mixer[J]. IEEE Journal of Solid-State Circuits, 2019, 55(5): 1139–1150.

[3] Feng L Q, Ji X S; Liao Q X, et al. A 0.5V 0.55mm^2 Bias-Current-Free BLE Transceiver with 1-Bit Delay-Based Demodulation for Energy-Harvesting IoT applications[C]. 2025 IEEE Custom Integrated Circuits Conference (CICC). Boston, MA, USA, 2025, 1-3.

[4] Bidabadi F S, Nagarajan M, Kumar T B, et al. An Ultra-Low Power Low-IF BLE Receiver for IoT Applications[C]. 2024 IEEE International Conference on IC Design and Technology (ICICDT). Singapore, Singapore, 2024, 1-4.

[5] Wang P H P, Mercier P P. A Dual-Mode Wi-Fi/BLE Wake-Up Receiver[J]. IEEE Journal of Solid-State Circuits. 2021, 56(4):1288-1298.

[6] Pletcher N M, Gambini S, Rabaey J. A 52 μW wake-up receiver with -72 dBm sensitivity using an uncertain-IF architecture[J]. IEEE Journal of Solid-State Circuits. 2009, 44(1): 269-280.

[7] Salazar C, Cathelin A, Kaiser A, et al. A 2.4 GHz Interferer-Resilient Wake-Up Receiver Using a Dual-IF Multi-Stage N-Path Architecture[J]. IEEE Journal of Solid-State Circuits, 2016, 51(9): 2091-2105.

[8] Wang P H P, Mercier P P. An Interference-Resilient BLE-Compatible Wake-Up Receiver Employing Single-Die Multi-Channel FBAR-Based Filtering and a 4-D Wake-Up Signature[J]. IEEE Journal of Solid-State Circuits. 2020, 56(2): 416-426.

Space-Time Metasurface Antennas: Concept, Design, and Applications

Geng-Bo Wu
Department of Electrical Engineering
State Key Laboratory of Terahertz and Millimeter Waves, City University of Hong Kong
Hong Kong, China
bogwu2@cityu.edu.hk

***Abstract*—While the global commercialization of the fifth-generation (5G) wireless communications is gradually taking off, there is already significant interest in the next generation of wireless communications. 6G scheduled to be launched in 2030, will provide a Tbps data rate, microsecond latency, and almost unlimited bandwidth to the connectivity of numerous mobile and intelligent networks. Antennas and metasurfaces are ubiquitous and indispensable components to generate and manipulate electromagnetic (EM) waves. In this talk, I will share the development and design of the space-time metasurface antenna that can control all fundamental properties of EM waves. The space-time metasurface antenna can further facilitate information manipulation, which can fundamentally simplify the architecture of information transmitter systems. The unparalleled wave and information manipulation capabilities of the metasurface antenna will spark a surge of applications from next-generation wireless systems, cognitive sensing to imaging.**

XXX-X-XXXX-XXXX-X/XX/$XX.00 ©20XX IEEE

979-8-3315-4544-4/26/$31.00 ©2026 IEEE

Broadband Phase-Dispersive Conformal Metamaterial for EM Backscattering Enhancement

Weizhi Chen
School of Electronic and Information Engineering
South China University of Technology
Guangzhou 510641, China
cwz1710@139.com

Xin Xiu
School of Electronic and Optical Engineering
Nanjing University of Posts and Telecommunications
Nanjing 210023, China
xiuxin33@126.com

Yixi Tang
School of Electronic and Optical Engineering
Nanjing University of Posts and Telecommunications
Nanjing 210023, China
yxitang@163.com

Kun Tang
School of Electronic and Information Engineering
South China University of Technology
Guangzhou 510641, China
tangkun@scut.edu.cn

Wenjie Feng
School of Electronic and Information Engineering
South China University of Technology
Guangzhou 510641, China
eewjfeng@scut.edu.cn

Wenquan Che*
School of Electronic and Information Engineering
South China University of Technology
Guangzhou 510641, China
eewqche@scut.edu.cn

***Abstract*—A phase-dispersive conformal metamaterial for broadband electromagnetic (EM) backscattering enhancement is presented. The metamaterial comprises two layers of *LC* resonant structures to achieve broadband phase-dispersive characteristics. To enable a conformal design, the first layer employs a low-profile dielectric substrate with excellent flexibility, while the second layer is conformally attached to the target surface using an insertion-based method. The metamaterial is designed for backscattering enhancement, and a prototype was fabricated for experimental validation. The results demonstrate significant backscattering enhancement over a broadband from 4.0 to 7.0 GHz (54.5%) for dual polarizations. With respect to a bare metal target without the metamaterial, the *y*-polarized backscattering is enhanced to 97.5% over a metal plate of identical projected area, and the *x*-polarized backscattering reaches 74.5%.**

***Keywords*—Conformal metamaterial, phase manipulation, electromagnetic (EM) backscattering enhancement.**

I. Introduction

Backscattering enhancement plays a key role in various civilian applications by increasing the electromagnetic (EM) responses of relevant objects. For example, improving the backscattering of lifeboats, dinghies, or buoys greatly enhances their detectability, which in turn facilitates timely rescue and ensures safer navigation. Furthermore, enhancing backscattering is essential in scattering experiments and remote sensing, where stronger echoes facilitate more precise target detection and characterization.

Conventional approaches for backscattering enhancement typically rely on EM mechanisms, including multiple reflections and refractions. Techniques such as geometric shaping, corner reflectors, or Luneburg lenses are used to direct scattered energy toward specific directions, achieving localized enhancement. Nevertheless, these methods are often bulky and structurally complex, which limits their close integration with target platforms and flexible deployment.

With the advancement of artificial EM structural modulation techniques [1], EM structures based on metamaterials or metasurfaces have emerged as a major research focus for backscattering enhancement [2]–[5]. By carefully designing the unit cell geometry, effective EM parameters, and spatial arrangement, scattering can be precisely manipulated, enabling the desired backscattering enhancement at detection systems. Conformal gradient metasurfaces have been proposed for this purpose, enabling targets to generate enhanced echoes, but their operational bandwidth is limited [2]. To achieve a broader operational bandwidth, planar broadband retro-reflective metasurfaces have been realized by combining multiple narrowband designs [3]. Nevertheless, they remain highly sensitive to the angle of incidence, and their retro-reflection efficiency is relatively low. Meanwhile, origami metasurfaces have been introduced to achieve broadband, high-efficiency backscattering enhancement [5]. However, their performance is highly contingent on accurate folding geometry and phase coordination, and conformal integration with target platforms remains a significant challenge.

In this work, a phase-dispersive conformal metamaterial is proposed for broadband backscattering enhancement. By employing a two-layer *LC* resonant structure, broadband phase-dispersive characteristics are achieved. Benefiting from its broadband performance, the proposed metamaterial indicates great potential for applications in enhancing target detectability and remote sensing.

II. Phase-Dispersive Metamaterial Design

In practical backscattering enhancement scenarios, targets often have curved or non-planar geometries. This work investigates the fundamental principles of backscattering enhancement for such structures, highlights the role of the phase compensation mechanism, and proposes a metamaterial based on a two-layer *LC* resonator design.

A. Phase Compensation Principle

For the sake of clarity in illustrating the phase compensation principle of curved structures, a cylindrical geometry is used as an example and one phase-inversion method is proposed based on the generalized Snell's law.

As shown in Fig. 1, consider a cylinder with radius R and its axis aligned along the x-direction. The curved surface in the y–z plane forms a semicircular arc, which can be parameterized by the polar angle φ, with φ in $[-\pi/2, \pi/2]$. The coordinates of a point on the surface are given by:

$$r(\varphi) = (y, z) = (R\cos\varphi, R\cos\varphi) \tag{1}$$

This work was supported in part by the National Natural Science Foundation of China under Grant 62321002.

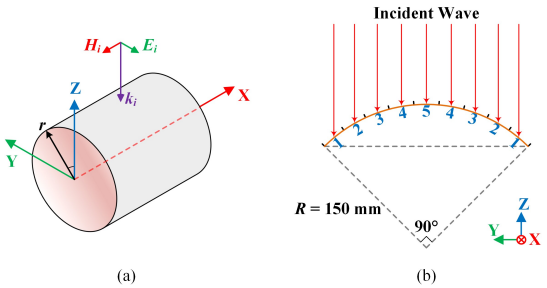


Fig. 1. Schematic of phase compensation on the cylindrical surface. (a) Perspective view. (b) Side view.

Assume a plane wave incident normally on the curved surface along the $-z$ direction. The unit vector of the incident direction is given by:

$$\vec{s}_i = (0,0,-1) \tag{2}$$

The reflected wave is required to propagate vertically upward, and the unit vector of the reflected direction is:

$$\vec{s}_r = (0,0,+1) \tag{3}$$

For a surface with a phase discontinuity ϕ, the generalized Snell's law along the tangential vector $\vec{t}$ of the surface is given by:

$$k_0(\vec{s}_r - \vec{s}_i)\cdot\vec{t} = \frac{\partial\phi}{\partial s} \tag{4}$$

where, s denotes the arc length along the surface, and $\partial\phi/\partial s$ indicates the phase gradient along the tangential direction.

The unit tangent vector of the cylindrical surface at polar angle φ is expressed as:

$$\vec{t}(\varphi) = \frac{d\vec{r}}{ds} = \frac{1}{R}\cdot\frac{d\vec{r}}{d\varphi} = (-\sin\varphi, 0, \cos\varphi) \tag{5}$$

Note that the arc length $s = R\cdot\varphi$, so that $\partial/\partial s = (1/R)\cdot\partial/\partial\varphi$. Substituting this into the generalized Snell's law yields:

$$\frac{\partial\phi}{\partial\varphi} = 2k_0R\cos\varphi \tag{6}$$

Integrating with respect to φ:

$$\phi(\varphi) = \int 2k_0R\cos\varphi d\varphi = 2k_0R\sin\varphi + C \tag{7}$$

where, C is the phase constant. Expressing (7) in Cartesian coordinates gives:

$$\phi(y,z) = 2k_0z + C \tag{8}$$

It can be seen that, to reflect all points in the opposite direction, the required phase varies linearly with height z, i.e., $\phi = 2k_0z$. Consequently, each unit must compensate for twice the vertical phase difference relative to the reference plane, ensuring that all reflected waves coherently combine along the $+z$ direction above the surface without lateral spreading.

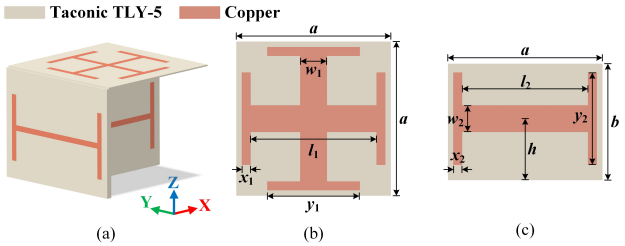


Fig. 2. Schematic of the unit cell of the broadband phase-dispersive metamaterial. (a) Perspective view. (b) Top view of the first layer. (c) Side view of the second layer.

TABLE I. PHYSICAL PARAMETERS OF UNIT CELLS

Unit	l_1 (mm)	y_1 (mm)	w_1 (mm)	l_2 (mm)	y_2 (mm)	w_2 (mm)	Incident Angle
1	0.0	0.0	0.0	0.0	0.0	0.0	40.0°
2	11.2	4.8	0.2	8.0	4.5	1.4	30.0°
3	8.0	5.5	0.3	11.3	8.5	1.2	20.0°
4	8.2	7.8	0.3	11.3	8.5	0.4	10.0°
5	8.3	8.0	0.2	11.2	8.8	0.2	0.0°

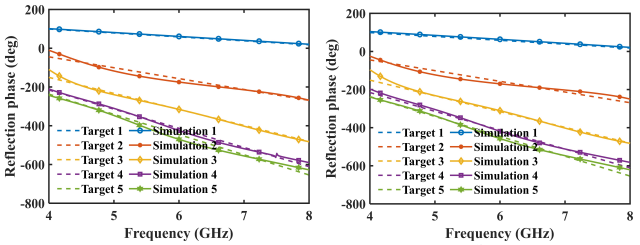


Fig. 3. Simulated reflection phase of each unit cell. (a) y-polarization. (b) x-polarization.

B. Unit Cell Design

Unlike conventional phase-coded metamaterials based on single-layer LC resonators, this work proposes a two-layer LC resonator design to realize phase gradients with broadband phase-dispersive characteristics [6]. To reduce coupling between the two layers and facilitate conformal design, this work adopts a two-layer orthogonally arranged structure, as shown in Fig. 2, with the first layer parallel to the ground plane and the second layer perpendicular to it.

In this design, the substrate is Taconic TLY-5, with the first and second dielectric layers having thicknesses of 0.128 mm and 0.508 mm, respectively, a relative permittivity of 2.2, and a loss tangent of 0.0009. To minimize phase errors caused by coupling between adjacent units, two units are arranged side by side along the y-direction of the basic unit cell shown in Fig. 1(b). Each unit cell has a period of a = 12.38 mm, a total height of 10.0 mm (b = 9.872 mm), and a second-layer patch located h = 4.6 mm above the ground plane. Parameters x_1 and x_2 have negligible impact on EM performance and are therefore set to 0.2 mm.

Based on the configuration shown in Fig. 1(b), the physical parameters of the unit cell are listed in Table I. These parameters were used in CST full-wave simulations for numerical verification, and the resulting reflection phases are shown in Fig. 3. The results indicate that the reflection phases for both x- and y-polarizations are in good agreement with the target phase across the 4.0–7.0 GHz frequency range, confirming the effectiveness of the proposed method.

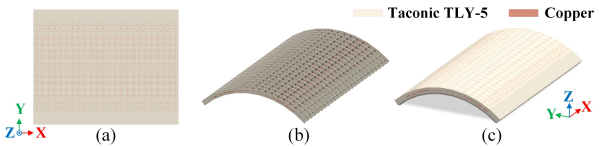


Fig. 4. Conformal structure for backscattering enhancement. (a) First-layer array. (b) Second-layer array. (c) Overall array.

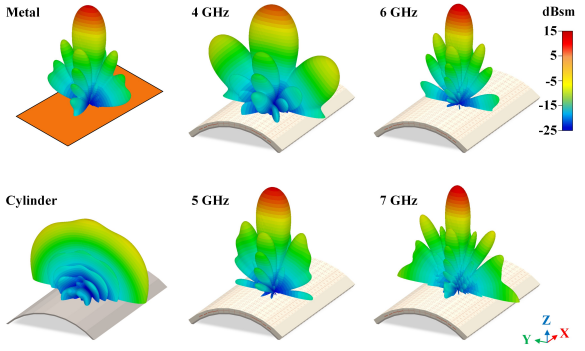


Fig. 5. Far-field scattering simulation results.

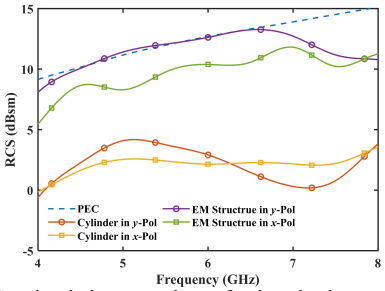


Fig. 6. RCS simulation results of the backscattering-enhanced metamaterial.

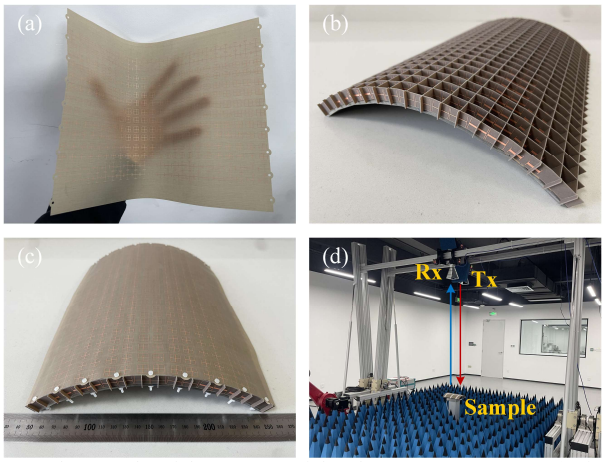


Fig. 7. Photographs of the metamaterial and measurement setup. (a) First-layer structure. (b) Second-layer structure. (c) Assembled array. (d) Measurement setup.

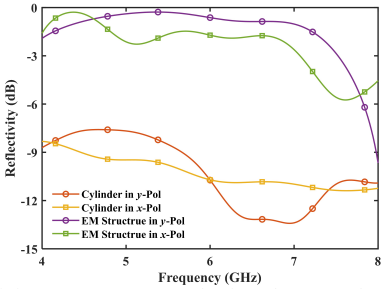


Fig. 8. Reflectivity measurement results for a bare metal cylinder and the proposed metamaterial.

III. Backscattering Enhancement Verification

To validate the backscattering enhancement of the designed unit, a conformal metamaterial array was fabricated on a cylindrical surface, measuring approximately 297.6 mm × 203.2 mm and comprising 24 × 18 units, as shown in Fig. 4.

Fig. 5 presents the far-field scattering simulation results of the metamaterial array. For simplicity, only the *y*-polarized responses are shown. It can be seen that the far-field scattering pattern of the conformal array closely resembles that of a metal plate, with the scattered energy primarily concentrated along the +*z* direction. Fig. 6 illustrates the monostatic RCS simulation results of the array under normal incidence, demonstrating its backscattering behavior. Compared with a metal plate of the same projected area, the conformal metamaterial on the curved substrate achieves an average *y*-polarized backscattering enhancement of 97.5% over the 4.0–7.0 GHz range, approaching the ideal enhancement peak. The *x*-polarized RCS is also improved, showing an average enhancement of 74.5%.

For further validation, the metamaterial was fabricated and measured, as shown in Fig. 7. Reflectivity measurements were carried out in a microwave anechoic chamber using a bow-tie antenna setup. As shown in Fig. 8, over the 4.0–7.0 GHz frequency range, the average *y*-polarized reflectivity exceeds −1 dB, while the *x*-polarized reflectivity remains above −2 dB, demonstrating excellent backscattering enhancement.

IV. Conclusion

This work proposes a broadband phase-dispersive metamaterial for backscattering enhancement on conformal structures. To address the limited phase-dispersive range of conventional phase-coded EM structures, a two-layer *LC* resonator design is employed. A conformal metamaterial array was designed, fabricated, and measured on a cylindrical surface to validate the approach. Simulation and experimental results show that, over 4.0–7.0 GHz and for dual polarizations, the array achieves backscattering enhancement with *y*-polarized reflectivity above −1 dB and *x*-polarized reflectivity above −2 dB, confirming the effectiveness of the design. With its efficient design and excellent broadband performance, the approach demonstrates potential applications in EM decoys, target detection, and related fields.

References

[1] N. Yu et al., "Light propagation with phase discontinuities: generalized laws of reflection and refraction," *Science*, vol. 334, no. 6054, pp. 333–337, Oct. 2011.

[2] Y. Shang and Z. Shen, "Polarization-independent backscattering enhancement of cylinders based on conformal gradient metasurfaces," *IEEE Trans. Antennas Propag.*, vol. 65, no. 5, pp. 2386–2396, May 2017.

[3] Y. Jia et al., "Wideband planar retro-reflective metasurfaces for backscattering enhancement under oblique incidence," *J. Phys. D: Appl. Phys.*, vol. 51, no. 33, p. 335103, Aug. 2018.

[4] M. Li et al., "Angular-adaptive spin-locked retroreflector based on reconfigurable magnetic metagrating," *Adv. Opt. Mater.*, vol. 7, no. 13, p. 1900151, Jul. 2019.

[5] Q. Zhang et al., "Wideband and high-efficiency backscattering enhancement based on origami metasurface retroreflector," *IEEE Trans. Microw. Theory Techn.*, vol. 73, no. 9, pp. 6847–6854, Sep. 2025.

[6] W. Chen, X. Xiu, J. Liu, and W. Che, "Design approach of broadband phase-dispersive metasurface for EM illusion using deep learning-based method," *IEEE Trans. Microw. Theory Techn.*, vol. 74, no. 3, pp. 2888–2900, Mar. 2026.

Semantics-Guided End-to-End Intelligent Design Framework for Metasurface Absorbers

1st Yongqi Lv
School of Microelectronics (School of Integrated Circuits)
Nanjing University of Science and Technology
Nanjing, China
124132011732@njust.edu.cn

2nd Wenhua Gu
School of Microelectronics (School of Integrated Circuits)
Nanjing University of Science and Technology
Nanjing, China
guwenhua@njust.edu.cn

Yanghui Wu*
School of Microelectronics (School of Integrated Circuits)
Nanjing University of Science and Technology
Nanjing, China
316104002471@njust.edu.cn

***Abstract*—Metasurface absorbers, as a type of two-dimensional metamaterial, control electromagnetic waves by adjusting the phase, amplitude, and polarization response of the units. Traditional design methods face challenges with high computational costs and low optimization efficiency. This paper proposes a semantic-guided, cross-modal end-to-end intelligent design framework, combining natural language processing and deep learning. A SigLIP-based visual-language alignment module connects natural language descriptions with target spectra, while a forward modeling method based on the SV-MC-FNO addresses the multi-solution problem in inverse design using a mixture density network (MDN). The introduction of cyclical consistency training with physical constraints enhances model reliability. Experimental results show significant improvements in design efficiency and accuracy.**

Keywords—Metasurface absorber, deep learning, semantic guidance, cross-modal learning, neural networks, inverse design, physical constraints, cyclical consistency, Fourier neural operator

I. Introduction

Metasurfaces, two-dimensional metamaterials composed of sub-wavelength units, offer precise control over electromagnetic waves, with applications in radar stealth, electromagnetic compatibility, and wireless communication[1]. Metasurface absorbers achieve perfect absorption by designing phase, amplitude, and polarization responses[2]. However, traditional design methods like equivalent circuit models and transmission line theory suffer from high computational costs and low optimization efficiency.

Recent advancements in deep learning have facilitated metasurface design through neural networks, which model nonlinear relationships between geometric parameters and electromagnetic responses, improving design efficiency[3]. However, current methods lack physical understanding and struggle with multi-modal information, particularly bridging the gap between semantic design and physical feasibility.

To address these limitations, we propose an intelligent design framework combining natural language processing, deep learning, and generative design[7]. This framework uses a SigLIP-based semantic alignment module, a spatially variable multi-channel attention Fourier neural operator (SV-MC-FNO) for forward modeling, and a mixture density network (MDN) for inverse design. Incorporating physical constraints and cyclical consistency training enhances model reliability and design accuracy.

II. Methodology

A. Semantic Alignment via Vision-Language Contrastive Learning

To establish a connection between natural language design descriptions and physical spectral responses, we have developed a semantic alignment module based on the SigLIP (Sigmoid Loss for Language Image Pre-training) architecture. Unlike traditional inverse design methods that solely rely on numerical objectives, this module creates a bidirectional mapping between the natural language space T and the spectral feature space V.

The module employs a dual-encoder architecture — one for text and one for images. The input consists of paired data, where the text describes the performance requirements in natural language, and the spectral images represent the corresponding absorption curves visually. The text encoder processes the tokenized input sequence to generate textual embedding features, while the absorption image encoder extracts visual embedding features from the spectral images. The embedding features of both modalities are mapped into a shared latent space through a linear projection head, enabling metric-based calculations.

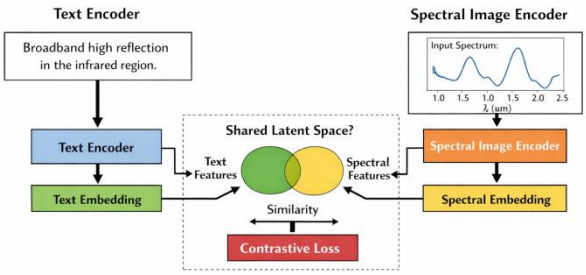


Fig.1. dual-encoder architecture

To achieve the alignment between semantic and physical representations, we adopt a contrastive learning paradigm optimized by the AdamW optimizer. The core objective is to maximize the feature similarity between matching "text-spectrum" pairs (positive samples) within a mini-batch while minimizing the similarity between non-matching pairs (negative samples).

The cosine similarity between the i-th spectral image and the j-th text description is computed as follows:

$$S_{ij} = \frac{f_{text}(T_i) \cdot f_{spectra}(I_j)}{\|f_{text}(T_i)\| \|f_{spectra}(I_j)\|} \quad (1)$$

where $f_{text}(T_i)$ and $f_{spectra}(I_j)$ are the feature vectors output by the text encoder and spectral image encoder, respectively. The overall training objective is the average of

the "image-to-text loss" $L_{img\to txt}$ and "text-to-image loss" $L_{txt\to img}$:

$$L_{total} = \frac{1}{2}(L_{img\to txt} + L_{txt\to img}) \quad (2)$$

The "image-to-text loss" and "text-to-image loss" are represented as follows:

$$L_{img\to txt} = -\frac{1}{B}\sum_{i=1}^{B} log\frac{exp(S_{ii})}{\sum_{j=1}^{B} exp(S_{ij})} \quad (3)$$

$$L_{txt\to img} = -\frac{1}{B}\sum_{i=1}^{B} log\frac{exp(S_{ii})}{\sum_{i=1}^{B} exp(S_{ji})} \quad (4)$$

By minimizing L_{total}, the model learns to cluster semantically consistent spectral responses around their corresponding natural language instructions in the latent space.

B. Forward Modeling Based on SV-MC-FNO

The forward design problem can be described as learning a surrogate operator that maps geometric structure parameters to their corresponding electromagnetic spectral responses. Traditional numerical solvers incur high computational costs, and standard deep learning models (such as CNNs) are often limited by receptive fields and grid dependencies. To address these issues, we propose the SV-MC-FNO (Spatially Variable Multi-Channel Fourier Neural Operator) for forward modeling[4].

The backbone of our predictor is based on the Fourier Neural Operator (FNO), which learns kernel integral operators in the frequency domain. For the input function at the k-th layer, the update rule is defined as:

$$\mathcal{Y} = \mathcal{F}^{-1}(\mathcal{W} \cdot \mathcal{F}(\mathcal{X})) \quad (5)$$

where $\mathcal{F}$ represents the Fast Fourier Transform (FFT), $\mathcal{W}$ is the learnable complex spectral weight matrix, and $\mathcal{F}^{-1}$ denotes the inverse Fourier transform.

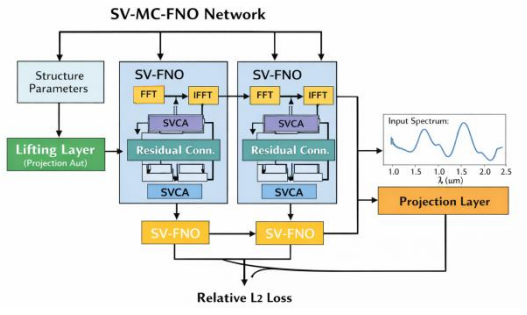


Fig.2. SV-MC-FNO network

The standard FNO performs the same computation for all frequency components and spatial locations after spectral convolution. However, metasurface spectra often exhibit sharp resonance peaks, requiring highly sensitive processing of high-frequency details. To address this, we introduce the Spatially Variable Channel Attention (SVCA) module. Unlike the global average pooling used in SE-Net, our attention module computes an adaptive attention map that varies in the spectral domain:

$$\mathcal{A} = \sigma(\mathcal{W}_a \cdot \mathcal{F}(x)) \quad (6)$$

where $\mathcal{W}_a$ is the attention weight matrix, and σ is the activation function.

C. Probabilistic Inverse Design Based on Mixture Density Networks

The inverse mapping from spectral targets S to structural parameters suffers from non-uniqueness. Different metasurface geometries may produce identical or nearly indistinguishable spectral responses. To address this, we model the inverse design as a probabilistic task using a Mixture Density Network (MDN)[5].

We use a deep convolutional neural network (CNN) as the backbone network to extract high-level features from the input spectral data[8]. The network consists of three cascaded 1D convolutional layers with progressively smaller kernel sizes (15, 11, and 7), and a stride of 4. After the convolutional layers, the spectral data is processed through an adaptive average pooling layer to ensure robustness to varying spectral lengths.Rather than predicting a single deterministic vector, the network outputs parameters for a Gaussian Mixture Model (GMM) representing the conditional probability density. The probability density for the k-th component of the mixture model is defined as:

$$P(x|\theta) = \sum_{k=1}^{K} \pi_k N(x|\mu_k, \Sigma_k) \quad (7)$$

where π_k, μ_k, and Σ_k represent the mixture coefficient, mean, and variance for the k-th component, respectively.

The optimization objective of the network is to minimize the negative log-likelihood (NLL) of the true parameters given the input spectral data:

$$L_{NLL} = -\sum_{k=1}^{K} \pi_k log(x_k|\theta) \quad (8)$$

D. Cyclical Consistency Training with Physical Constraints

To enforce strict physical validity and improve the generalization capability of the inverse model, we introduce a cyclical consistency training strategy with physical constraints[6].We construct a closed-loop system by cascading the inverse network (MDN) with the pre-trained forward network (SV-MC-FNO). In this stage, the forward network serves as a differentiable surrogate for the electromagnetic solver, with its parameters $\theta_{forward}$ frozen, and gradients are only backpropagated to update the parameters $\theta_{inverse}$ of the inverse network.Given the target spectrum S_{target}, the inverse model first predicts the GMM parameters. To allow the gradients to flow through the cycle, we deterministically select the structural candidate corresponding to the Gaussian component with the highest probability. The predicted structure is then fed into the frozen forward model to generate the reconstructed spectrum $S_{reconstructed}$.

We design a composite physical constraint loss function consisting of two parts: the spectrum reconstruction loss L_{recon}, which penalizes the magnitude deviation over the

entire frequency band; and the gradient consistency loss L_{grad}, which minimizes the distance between the first-order derivatives of the target and reconstructed spectra. This explicitly constrains the consistency of the resonance peak positions and sharpness:

$$L_{recon} = \frac{\left\| S_{reconstructed} - S_{target} \right\|_2}{\left\| S_{target} \right\|_2 + \epsilon} \tag{9}$$

$$L_{grad} = \left\| \nabla S_{target} - \nabla S_{reconstructed} \right\| \tag{10}$$

The final objective function of the inverse design network combines the probabilistic NLL loss with the cyclical constraints from physical information:

$$L_{total} = L_{NLL} + \lambda_{recon}(L_{recon} + \alpha L_{grad}) \tag{11}$$

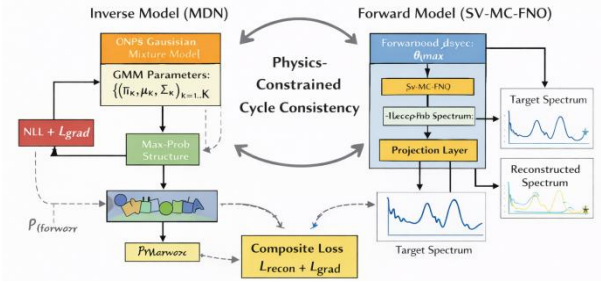


Fig.3. Physics-Constrained Cycle Consistency Flowchart

III. Results

In this section, we present a comparison between the predicted absorption rates of the absorber, obtained using the neural network model, and those obtained through full-wave simulations. First, we predicted the absorption rate of the metasurface absorber using the neural network model and compared the results with the full-wave simulation. The results show a high consistency between the predicted absorption rates and the full-wave simulation results across different frequency bands, with minimal prediction errors, validating the effectiveness and accuracy of the neural network model in predicting the absorption rate.

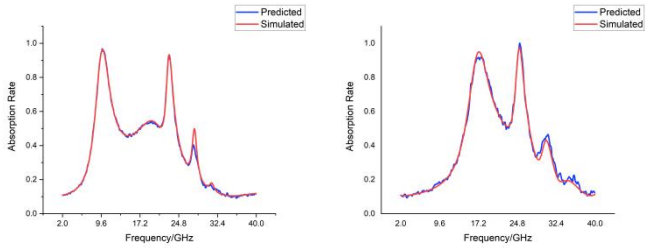


Fig.4.Comparison of Predicted and Full-Wave Simulated Absorption Rates

Next, we present the absorption rates of the metasurface absorbers obtained via inverse design and compare them with the full-wave simulation results. During the inverse design process, the neural network inferred the structural parameters based on the target spectrum, and the resulting absorption rates were verified through full-wave simulations. The results indicate that the absorption rates of the inverse-designed absorbers closely match those obtained from full-wave simulations, demonstrating the feasibility and accuracy of the inverse design method in practical applications.

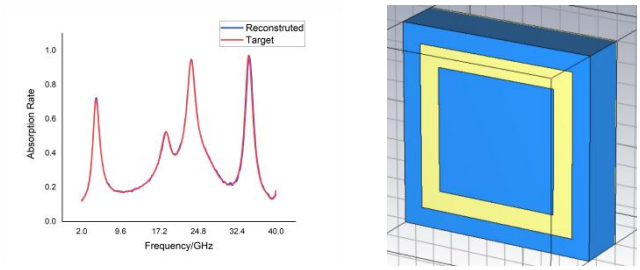


Fig.5.Comparison of Target and Reconstructed Absorption Rates with Structural Design

These comparative results show that the neural network-based design approach significantly improves the design efficiency of metasurface absorbers, while maintaining high design accuracy and considerably reducing the design and optimization time.

IV. Discussion

We proposed a deep learning-based design method for metasurface absorbers, experimentally validating its effectiveness in predicting absorption rates and inverse design. The model achieved high accuracy, with predicted absorption rates closely matching full-wave simulation results. The inverse design framework also demonstrated feasibility, inferring structural parameters from target spectra and yielding results consistent with simulations.

The neural network model accelerated metasurface absorber design, offering performance comparable to traditional methods. However, challenges remain, including the model's reliance on extensive simulation data and its limited ability to handle complex multi-objective optimization tasks. Future work should focus on reducing dependence on simulation data and improving the model's handling of multi-modal information and physical constraints.

References

[1] D. R. Smith, J. B. Pendry, and M. C. K. Wiltshire, "Metamaterials and metasurfaces," Science, vol. 305, no. 5685, pp. 788-792, Aug. 2004.

[2] N. I. Landy, S. Sajuyigbe, J. J. Mock, D. R. Smith, and W. J. Padilla, "Perfect metamaterials and optical metasurfaces," Phys. Rev. Lett., vol. 100, no. 20, pp. 207402, May 2008.

[3] Z. Zhao, Y. Yang, J. Zhai, and X. Zhang, "High-efficiency metasurfaces for electromagnetic wave manipulation," IEEE Trans. Antennas Propag., vol. 66, no. 10, pp. 5511-5522, Oct. 2018.

[4] X. Li, W. Li, Z. Zhu, and Q. Zhang, "Fourier neural operator for parametric partial differential equations," Proc. 37th Int. Conf. Machine Learning (ICML), 2020.

[5] C. M. Bishop, "Mixture density networks," Neural Comput., vol. 6, no. 2, pp. 256-261, Mar. 1994.

[6] J. Y. Zhu, T. Park, P. Isola, and A. A. Efros, "Unpaired image-to-image translation using cycle-consistent adversarial networks," Proc. IEEE Int. Conf. Comput. Vision (ICCV), pp. 2228-2236, Oct. 2017.

[7] F. Yang, H. Liu, J. Sun, and X. Zhang, "Inverse design of metasurfaces based on deep learning," IEEE Trans. Antennas Propag., vol. 68, no. 1, pp. 307-314, Jan. 2020.

[8] J. P. G. Mattheeuw, A. S. P. S. S. S. Alouini, and D. J. M. R. F. Liao, "Optimizing electromagnetic metamaterials with neural networks," IEEE J. Electromagn. Waves Appl., vol. 34, no. 10, pp. 1390-1399, Oct. 2020.

Absorptivity Evaluation of Broadband FSS Absorbers Considering Higher-Order Floquet Modes

Chonghuan Zhang
College of Electronics and Information Engineering
Sichuan University
Chengdu, China
zhangchonghuan@stu.scu.edu.cn

Liping Yan
College of Electronics and Information Engineering
Sichuan University
Chengdu, China
liping_yan@scu.edu.cn

Yanping Zhou
College of Electronics and Information Engineering
Sichuan University
Chengdu, China
ypzhou11@scu.edu.cn

Changjun Liu
College of Electronics and Information Engineering
Sichuan University
Chengdu, China
cjliu@scu.edu.cn

***Abstract*- FSS absorbers are inherently periodic electromagnetic structures whose scattering characteristics are governed by the superposition of Floquet modes. When the structural period satisfies specific conditions, higher-order Floquet modes become propagating (i.e., grating lobes) and carrying additional scattering power. This energy is not captured by conventional fundamental-mode S-parameters, which may lead to inaccuracies in conventional absorptivity evaluation based on $|S_{11}|$ and $|S_{21}|$. In this work, the modal composition of the scattered fields of an FSS absorber is analyzed using Floquet theory. A broadband resistive-sheet FSS absorber is employed as an example to compare reflection characteristics and absorptivity with fundamental-mode-only and full-mode considerations. The results demonstrate that, when higher-order propagating modes are included, the 90% absorption bandwidth shrinks from 6.6 - 27.4 GHz to 6.6 - 20 GHz.**

***Index Terms*- Absorptivity, broadband, frequency selective surface, grating lobes.**

I. Introduction

Compared with conventional microwave absorbers, frequency selective surface (FSS) absorbers have been widely adopted in electromagnetic interference (EMI) suppression, radar cross section (RCS) reduction, and electromagnetic stealth applications [1], owing to their low profile, broadband response, and high design flexibility. In both design and characterization, absorptivity serves as a primary performance metric.

From the perspective of energy conservation, the absorptivity is rigorously defined as $A(\omega) = 1 - R(\omega) - T(\omega)$, where $A(\omega)$, $R(\omega)$, and $T(\omega)$ denote absorptivity, reflectivity, and transmissivity, respectively [2]. The reflectivity and transmissivity are commonly approximated as $R(\omega) = |S_{11}|^2$ and $T(\omega) = |S_{21}|^2$, leading to the widely used expression: $A(\omega) = 1 - |S_{11}|^2 - |S_{21}|^2$, where $|S_{11}|$ and $|S_{21}|$ are the reflection and transmission coefficients of the fundamental mode [3], [4].

However, an FSS absorber is intrinsically a periodic electromagnetic structure, whose scattered fields are, in general, composed of multiple Floquet modes [5]. When the unit cell period is less than half a wavelength, higher-order modes are evanescent and do not contribute to the far field radiation. In this case, the fundamental-mode approximation is valid. Nevertheless, for broadband and ultra-wideband FSS absorbers operating at high frequencies, the unit cell period is often comparable to or even larger than one wavelength to provide enough space for multi-resonant pattern design [4], [6], [7]. Under such conditions, higher-order Floquet modes may become propagating, forming grating lobes that radiate energy toward undesired directions.

The scattered power carried by these higher-order propagating modes is not included in the fundamental-mode S-parameters $|S_{11}|$ and $|S_{21}|$. As a result, absorptivity calculated solely from fundamental mode scattering parameters neglect the power redistributed into grating lobes, potentially leading to overestimated absorption performance. Moreover, the presence of grating lobes increases the RCS and may introduce unintended electromagnetic interference to nearby systems.

In this work, the modal composition of the scattered fields of FSS absorbers is analyzed based on Floquet theory. A broadband resistive-sheet FSS absorber is investigated as a representative example. Full-wave simulations are conducted to compare (i) reflection characteristics of individual Floquet modes and (ii) absorptivity calculated under fundamental-mode-only and full propagating mode considerations. It is shown that inclusion of higher-order propagating modes reduces the 90% absorption bandwidth from 6.6–27.4 GHz to 6.6–20 GHz. These results re-examine the conventional absorptivity formulation that relies solely on fundamental-mode scattering and establish a more rigorous and physically consistent approach for evaluating the absorption performance of FSS absorbers.

II. Floquet Theory-Based Analysis

The electromagnetic field distributions of periodic structures, such as FSS, have been systematically derived in the literature [5]. For such structures, the solution to the scalar wave equation can be expressed in the form of a Floquet expansion,

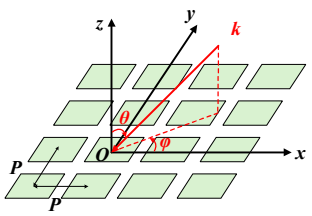


Fig. 1. Schematic of the two-dimensional periodic structure.

This work was supported in part by National Natural Science Foundation of China (NSFC) under Grant U22A2015 and in part by Sichuan Science and Technology Program under Grant 24GJHZ0386.

in which each term represents a distinct Floquet mode.

As illustrated in Fig. 1, a plane wave with wavenumber k is incident upon the FSS absorber from the direction (θ, φ), where θ and φ denote the elevation and azimuthal angle, respectively. The unit cell periodicity along both the x- and y-direction is denoted by P. Under these conditions, the scalar field can be expressed as:

$$\psi_{mn} = \sum_{m=-\infty}^{+\infty} \sum_{n=-\infty}^{+\infty} e^{-j(u_{mn}x + v_{mn}y \pm \gamma_{mn}z)} \tag{1}$$

where m and n denote the spatial harmonic indices of the Floquet modes along the x- and y-directions, respectively. Accordingly, the transverse propagation constants along the x- and y-directions, u_{mn} and v_{mn} are given by:

$$\begin{cases} u_{mn} = k\sin\theta\cos\varphi + 2\pi m / P \\ v_{mn} = k\sin\theta\sin\varphi + 2\pi n / P \end{cases} \tag{2}$$

Enforcing the Helmholtz equation yields the longitudinal propagation constant:

$$\gamma_{mn} = \begin{cases} \sqrt{k^2 - u_{mn}^2 - v_{mn}^2}, & if\ k^2 > u_{mn}^2 + v_{mn}^2 \\ -j\sqrt{u_{mn}^2 + v_{mn}^2 - k^2}, & if\ k^2 < u_{mn}^2 + v_{mn}^2 \end{cases} \tag{3}$$

When γ_{mn} is real and positive, the corresponding mode is propagating; otherwise, it is evanescent. The mode with $m = n = 0$ corresponds to the fundamental Floquet mode, while all the other propagating modes constitute grating lobes.

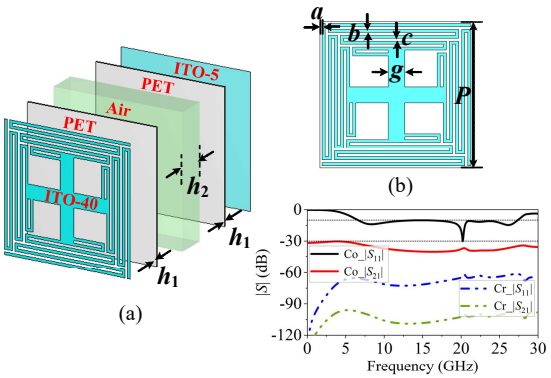


Fig. 2. Unit cell topology of the proposed example FSS absorber: (a) 3-D perspective view, (b) top view of the FSS layer, and (c) corresponding S-parameters of absorber. (P = 15, h_1 = 0.175, h_2 = 3.5, a = 0.2, b = 0.3, c = 0.3, g = 1.6. Unit: mm)

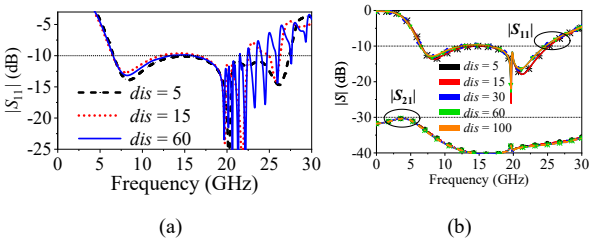


Fig. 3. S-parameters of the absorber versus *dis*: (a) without higher-order modes and (b) with higher-order modes.

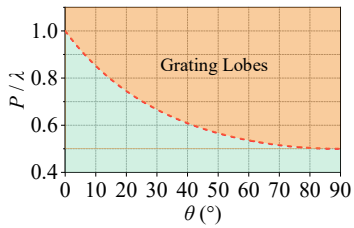


Fig. 4. Grating-lobe onset conditions.

III. Wideband FSS Absorber Example

A. Fundamental-Mode-Only S-Parameter Evaluation

The unit cell of an example FSS absorber is illustrated in Fig. 2(a). The structure consists of three vertically stacked layers: a ground plane, a dielectric spacer, and a patterned FSS layer. The FSS layer and the ground plane are fabricated using indium tin oxide (ITO) films with sheet resistances of 40 Ω/sq and 5 Ω/sq, respectively, both deposite on polyethylene terephthalate (PET) substrates (ε_r = 3, tgδ = 0.06).

Owing to the rotational symmetry of the geometry, only TE-polarized incidence is considered. When the port modal setting includes only the fundamental mode, and the port reference place is placed at a distance *dis* equal to a quarter wavelength at the center frequency (a typical default in full-wave solvers), the simulated co- and cross-polarized $|S_{11}|$ and $|S_{21}|$ under normal incidence are shown in Fig. 2(c). The absorption exceeds 90% is observed across 6.6 - 27.4 GHz.

To examine the robustness of the result, the port distance *dis* is increased while keeping all other parameters unchanged. As shown in Fig. 3(a), the $|S_{11}|$ at low frequencies remains nearly unchanged, whereas noticeable oscillations appear at higher frequencies. This behavior is mainly due to the higher-order Floquet modes that become propagating at higher frequencies but are not included in the port modal setting. Consequently, the interaction between the fundamental and higher-order modes is not fully captured, leading to artificial oscillatory variations in the reflection coefficient. This observation indicates that inclusion of higher-order propagating modes is essential for obtaining accurate S-parameters. .

B. Inclusion of Higher-Order Floquet Modes

For a given the periodicity P, the onset frequencies of grating lobes can be directly determined from (2) and (3). Without loss of generality, φ = 0° is assumed and the period is normalized to the wavelength. The grating lobe conditions are summarized in Fig. 4. It is observed that, to completely suppress grating lobes over the entire operational bandwidth, the unit cell period must be less than half of the wavelength corresponding to the highest operating frequency. However, in many practical broadband FSS designs, the period is often chosen to be approximately half of the wavelength at the center frequency to provide sufficient physical space for multiple resonant elements required for broadband operation.

Consequently, higher-order propagating modes near the upper end of the operating band are excited.

For the example structure shown in Fig. 2, the first grating-lobe onset under normal incidence occurs at 20 GHz. Within the considered operating band, 10 propagating modes exist above this frequency, including two fundamental modes and eight grating-lobes. To rigorously evaluate the absorption performance, all propagating modes must be included in the port modal expansion of the full wave simulation.

Fig. 3(b) shows the fundamental-mode $|S_{11}|$ and $|S_{21}|$ as a function of *dis* when higher-order modes are incorporated in the simulation. In contrast to Fig. 3(a), both curves exhibit negligible dependence on the port distance *dis*. This confirm that the multimode simulation properly accounts for all for modal coupling and eliminates spurious port-position sensitivity.

Fig. 5 presents the $|S_{11}|$ and $|S_{21}|$ for the eight higher-order propagating modes. Below 20 GHz, these modes decay rapidly with increasing *dis*, indicating evanescent behavior. Above 20 GHz, however, the response becomes insensitive to *dis*, demonstrating their transition to propagating modes.

Notably, several higher-order modes, such as TE_{10}, $TE_{(-1)0}$, TM_{01} and $TM_{0(-1)}$, exhibit reflection levels higher than -20 dB. Therefore, the scattered power carried by these modes is non-neglectable and must be included in absorptivity calculation.

C. *Absorptivity Calculation*

When only the fundamental mode is considered, with *dis* = 5 mm (quarter wavelength at the center frequency), the absorptivity calculated using $A(\omega) = 1 - |S_{11}|^2 - |S_{21}|^2$ exceeding 90% over 6.6 to 27.4 GHz, as is shown in Fig. 6. However, when higher-order propagating modes are taken into account, the absorptivity must be redefined as

$$A = 1 - \sum_{p} (|S_{11}^{(p)}|^2 + |S_{21}^{(p)}|^2), \tag{4}$$

where p denotes all propagating Floquet modes.

As progressively more higher-order modes are included, a pronounced degradation of absorptivity is observed at high frequencies. When all propagating modes are accounted for, the upper bound of the 90% absorption bandwidth shrinks from 27.4 GHz to 20 GHz. This reduction quantitatively demonstrates that power redistributed into grating lobes leads to overestimation of absorption performance when only the fundamental mode is considered.

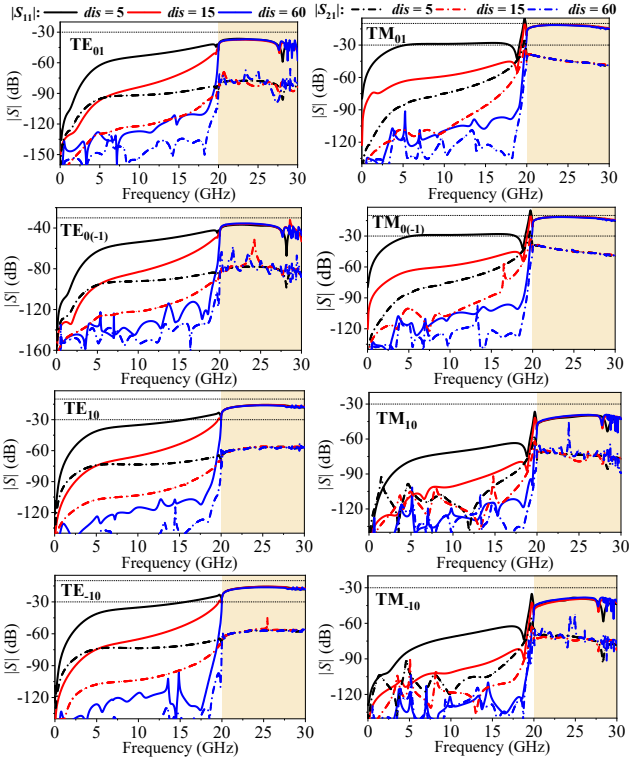


Fig. 5. $|S_{11}|$ and $|S_{21}|$ of eight higher-order Floquet modes.

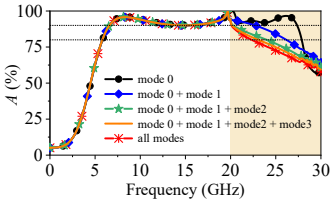


Fig. 6. Absorptivity considering different higher-order modes.

IV. Conclusion

This work has investigated the absorptivity evaluation of FSS absorbers from a Floquet modal perspective. It is shown that when higher-order propagating modes (grating lobes) are excited, absorptivity calculated solely from fundamental-mode S-parameters may be overestimated. By incorporating all propagating Floquet modes into the S-parameter formulation, a physically consistent and port-independent evaluation method is established. The results highlight the necessity of multimode analysis for accurate characterization of broadband FSS absorbers, particularly when the unit-cell period exceeds the half-wavelength at high frequencies.

References

[1] R. Wu et al., "An Optically Transparent Broadband Metamaterial Absorber for Passive Radiation Jamming," *IEEE Trans. Microw. Theory Tech.*, vol. 73, pp. 8607-8618, Nov. 2025.

[2] N.I. Landy, S. Sajuyigbe, J.J. Mock, D.R. Smith and W.J. Padilla, "Perfect Metamaterial Absorber," *Phys. Rev. Lett.*, vol. 100, pp. 207402, May. 2008.

[3] Y. Li *et al*., "An Ultra-Wideband Multilayer Absorber Using an Equivalent Circuit-Based Approach," *IEEE Trans. Antennas Propag.*, vol. 70, pp. 11911-11921, Dec. 2022.

[4] E. Celenk, C. Lynch and M. M. Tentzeris, "An Ultrawideband All-Textile Metamaterial Absorber for Ku-, K-, and Ka-Band Applications," *IEEE Antennas Wirel. Propag. Lett.*, vol. 23, pp. 1789-1793, June 2024.

[5] B. A. Munk, Frequency Selective Surfaces: Theory and Design. New York, NY, USA: Wiley, 2000.

[6] S. P. Mishra and S. Maity, "Screen-Printed Flexible Wideband Microwave Absorber," *IEEE Antennas Wirel. Propag. Lett.*, vol. 25, pp. 621-625, Feb. 2026.

[7] C. J. Hodgkinson, D. E. Anagnostou and S. K. Podilchak, "Phase Gradient Metasurface Radome Offering Beam Angle Translation and Wideband Absorption," *IEEE Antennas Wirel. Propag. Lett.*, vol. 23, pp. 2974-2978, Oct. 2024.

A Highly-Selective 3-D FSS with Exceptional Precision for Liquid Dielectric Constant Detection

Xiaojing Lv
School of Electrical and Data Engineering
University of Technology Sydney
Sydney, Australia
xiaojing.lv@uts.edu.au

Zhichao Sun
School of Electrical and Data Engineering
University of Technology Sydney
Sydney, Australia
bryan.sun@uts.edu.au

Jiexin Lai
School of Electrical and Data Engineering
University of Technology Sydney
Sydney, Australia
jiexin.lai@student.uts.edu.au

Yang Yang
School of Electrical and Data Engineering
University of Technology Sydney
Sydney, Australia
yang.yang-1@uts.edu.au

***Abstract*—This paper presents a novel 3-D FSS sensor for the high-accuracy dielectric characterization of liquid materials across a wide dynamic range. Featuring a miniaturized honeycomb lattice and an ultrathin profile, the proposed architecture uniquely leverages surface tension for stable liquid retention. To interpret the spectral response, a systematic two-step analytical framework is developed, mapping specific higher-order harmonic resonance peaks to low, medium, and high dielectric constants. Furthermore, the sensor's high frequency selectivity and multiple harmonic resonances are intuitively elucidated via Smith chart impedance trajectories, providing profound physical insight into the underlying matching mechanisms.**

***Keywords*—FSS, 3-D printing, sensor, Smith chart.**

I. Introduction

Frequency-selective surfaces (FSSs), composed of periodic unit-cell geometries [1], have been extensively employed in a wide range of wireless communication technologies, including advanced spatial filtering, antenna performance enhancement, and electromagnetic compatibility (EMC) improvement. FSSs respectively featured with ultra-wide operating bandwidth, high selectivity, or multiple passband/stopband divisions cater to specific demands in applications such as radar dome, terahertz (THz) imaging, and 5G channel multiplexing [2]–[4].

The design and fabrication of FSSs have predominantly relied on printed circuit board (PCB)-based processes, wherein dielectric spacers are alternately layered with metallic claddings patterned via laser or chemical etching techniques. Despite the commendable precision in patterning, the design of 2-D FSSs is inherently constrained by limited spatial degrees of freedom (DoFs), which poses substantial challenges in miniaturizing unit-cell size, reducing overall thickness profile, and tailoring frequency response. These limitations often necessitate reliance on increasingly intricate geometric shapes, which, despite requiring exponentially greater computational resources, yield diminishing returns in globally optimized performance. To prevent the FSS from becoming a bottleneck in communication systems integrated with other rapidly evolving electromagnetic components, metallic vias and through-holes have been incorporated into dielectric spacers for additional DoFs in the orthogonal dimension, often referred to as 2.5-D or quasi-3-D FSSs.

Among the commonly utilized techniques for measuring liquid dielectric constants, the capacitive sensing approach is notable for its simplicity and cost-effectiveness [5]; however, it is highly susceptible to environmental disturbances and fringing effect. The resonant cavity approach achieves enhanced precision but is hindered by the design complexity and fabrication cost [6]. The coaxial probe approach is straightforward to operate; however, its reliability heavily depends on the accuracy of full-wave modeling and the quality of the probe-liquid interface [7]. The microfluidic sensor approach requires minimal sample volume but is restricted by complex fabrication processes and a limited dynamic range [8].

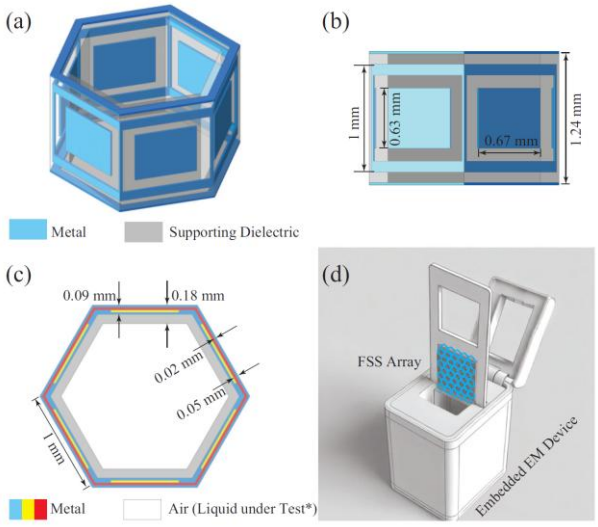


Fig. 1. Proposed multi-material additive-manufactured FSS structure. (a) Overview of the 3-D lattice design; (b) Side view highlighting the geometries in the orthogonal direction; (c) Top view indicating the hollowed section; (d) Conceptual prototype of a slip-in integrated waveguiding device.

This conference paper presents an FSS design adopting 3-D honeycomb lattice, which can be realized using multi-material additive manufacturing techniques as demonstrated in [2]. By fully leveraging the spatial DoFs to exhaust its unit-cell potential, this FSS delivers high frequency-selectivity precision and an ultra-wide measurable dynamic range of dielectric constants, spanning from 5 to 80, thereby encompassing the most frequently encountered liquid materials. This FSS also features miniaturized unit cells size with an edge length of 1 mm and an overall thickness profile of 1.24 mm. Additionally, the proposed design boasts low

979-8-3315-4544-4/26/$31.00 ©2026 IEEE

XXX-X-XXXX-XXXX-X/XX/$XX.00 ©20XX IEEE

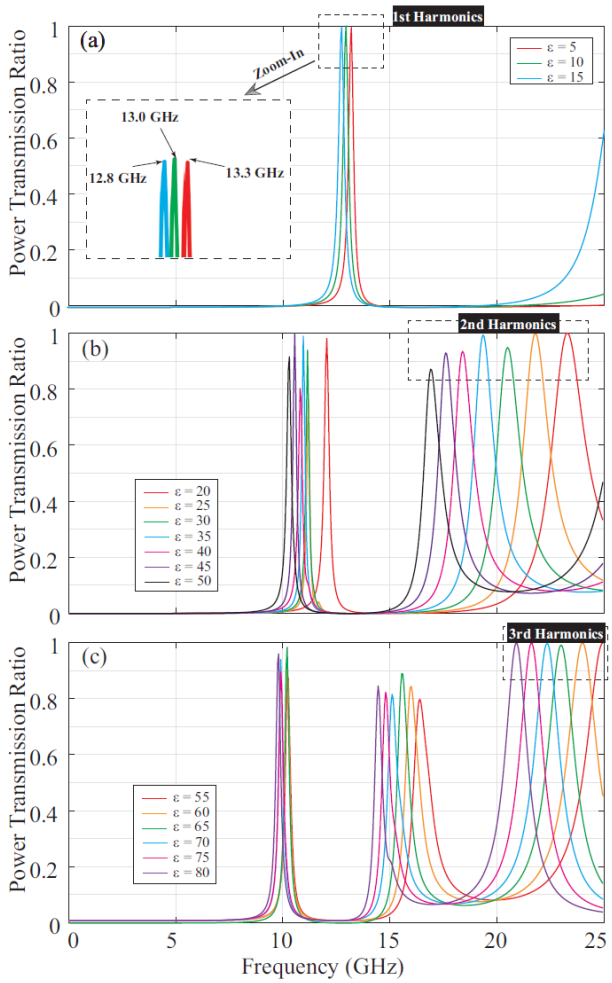


Fig. 2. The highly-selective transmission curves of the proposed 3-D FSS infiltrated with chemical liquids, with dielectric constants ranging from 5 to 80 in increments of 5. (a) Low-dielectric-constant liquids featured by fundamental harmonics; (b) Medium-dielectric-constant liquids featured by second-order harmonics; (c) High-dielectric-constant liquids featured by third-order harmonics.

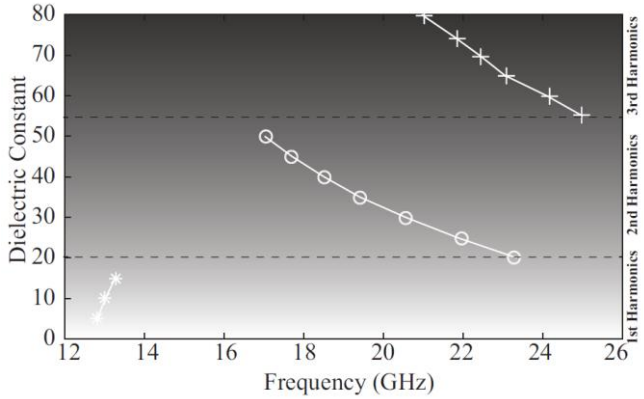


Fig. 3. Piece-wise regression curves mapping harmonic peak frequency to liquid dielectric constant.

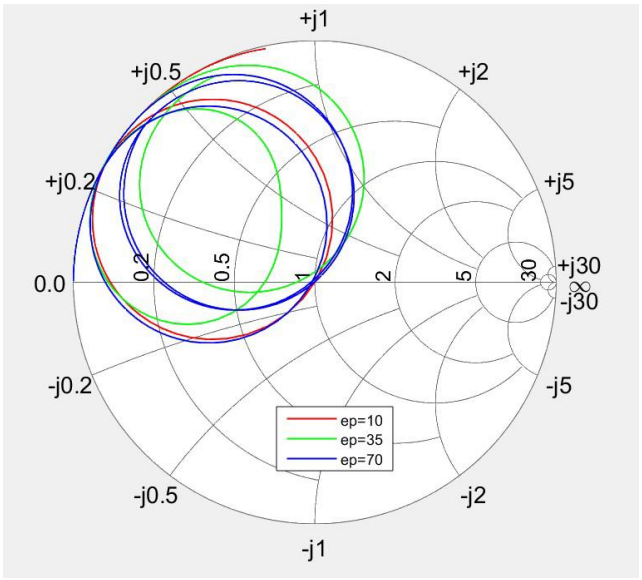


Fig. 4. Smith chart showcasing the high-Q transmission coefficients and harmonic counts for liquid materials with low (ϵ = 10), medium (ϵ = 35) and high (ϵ = 70) dielectric constants.

fabrication costs, minimal sample volume requirements, and ease of operation, offering promising applications in medical and chemical industries.

II. A TWO-STEP METHOD FOR DIELECTRIC CONSTANT MEASUREMENT

At 20 degrees Celsius, the dielectric constants of commonly encountered liquids range from approximately 5 (e.g., chloroform) to 80 (e.g., water). When the hollowed sections of the proposed FSS, as illustrated in Fig. 1(c), have been filled with a specific liquid material driven by surface tension after full immersion, the dielectric constant of this liquid can be inferred by locating the FSS's transmission peak frequency, facilitating rapid identification of the substance. The fabrication process of the DragonFly® IV printer has been referenced for modeling [2], where the metallic geometries utilize silver ink cured by infrared light, while the dielectric material employed acrylate ink ($\epsilon_{DF} = 2.78$) cured by ultraviolet light. The thicknesses of the patches and meshes are standardized to 0.02 mm for consistency.

Within the X – K frequency spectrum, as shown in Fig. 2, liquid materials with low (ϵ = 5−15), medium (ϵ = 20−50), and high (ϵ = 55−80) dielectric constants exhibit transmission curves qualitatively characterized by single, double, and triple peaks, respectively. On such a basis, the dielectric constants of liquids can be strategically measured using a two-step approach by firstly identifying the number of harmonics inthe operating frequency range, and then accordingly determine the peak frequency of the fundamental, secondary, or tertiary harmonic.

The piece-wise fitted curves in Fig. 3 further specifies the relationship between the selected harmonic peak frequency and the corresponding liquid dielectric constant. The highly-selective transmission curves and the number of harmonics up-to 25 GHz can also be explained from the perspective of impedance matching. As illustrated in the Smith chart in Fig.4, taking three dielectric constants (e.g., 10, 35, 70) within the low, medium, and high ranges as examples, all loci pass quickly through the center that corresponds to perfect impedance matching with the number of crossings is one, two, and three, respectively.

III. SUMMARY

This paper presents a highly-selective 3-D FSS sensor for detecting liquid dielectric constant, which can be developed using the accessible advanced multi-material additive manufacturing technology. Leveraging surface tension, the miniaturized and ultra-thin honeycomb mesh effectively retains the liquid-under-test and achieves exceptional accuracy over a wide dielectric constant range from 5 to 80. This innovative design with the two-step analysis approach holds significant promise for applications in chemical, agricultural, and biomedical detection.

REFERENCES

[1] B. A. Munk, *Frequency Selective Surfaces: Theory and Design*, John Wiley & Sons, 2000.

[2] X. Lv, Y. Yang, Z. Luo and J. S. Tyo, "Multimaterial 3-D-Printed FSSs for Ultrawide and Dual Passbands in the K-Ka Spectra," in *IEEE Transactions on Microwave Theory and Techniques*, vol. 73, no. 1, pp. 75–86, Jan. 2025.

[3] X. Lv, R. T. Ako, M. Bhaskaran, S. Sriram, C. Fumeaux and W. Withayachumnankul, "Frequency-Selective-Surface-Based Mechanically Reconfigurable Terahertz Bandpass Filter," in *IEEE Transactions on Terahertz Science and Technology*, vol. 12, no. 3, pp. 257–266, May. 2022.

[4] X. Lv, Z. Luo and Y. Yang, "3D-Printed Multi-Band FSS with Near-Equal Fractional Pass-/Stop-Band Divisions," in *European Conference on Antennas and Propagation (EuCAP)*, Stockholm, Sweden, 2025, pp. 1-3.

[5] D. Yang, X. Zhang, Z. Hu and Y. Yang, "Oil Contamination Monitoring Based on Dielectric Constant Measurement," in *International Conference on Measuring Technology and Mechatronics Automation*, Zhangjiajie, China, 2009, pp. 249–252.

[6] C. Li, S. Mousavi, R. Asadi, S. Mousavi, R. Vahdani and X. Ye, "Dk and Df Characterization of Low-loss Dielectric Liquid by Cylindrical Cavity Resonator," in *IEEE International Symposium on Electromagnetic Compatibility, Signal & Power Integrity (EMC+SIPI)*, Phoenix, AZ, USA, 2024, pp. 119–124.

[7] T. T. Khan, "A Method for Measuring Dielectric Properties of Non-Magnetic Liquids and Predicting Their Contamination Level," in *International Conference on Informatics, Electronics & Vision (ICIEV)*, Dhaka, Bangladesh, 2012, pp. 445–450.

[8] J. W. Kim, P. Pasupathy, S. Zhang and D. P. Neikirk, "Measurement of Liquid Complex Dielectric Constants Using Non-Contact Sensors," in *IEEE SENSORS*, Christchurch, New Zealand, 2009, pp. 2017–2020.

Materials-Aware Design Strategies for Wearable Antenna Design

Shengjian Jammy Chen
College of Science and Engineering, Flinders University, Tonsley, SA, Australia
shengjian.chen@flinders.edu.au

***Abstract*—This review synthesises recent advances that co-optimise materials and electromagnetics for robust wearable antennas. It adopts a materials-aware design mindset that treats the substrate, radiator, and ground as coupled variables. In practice, one can shape dielectric loss and effective permittivity only where they matter; form the operating spectrum through interpretable modal control rather than add-on resonators; manage non-ideal conductors via coordinated radiator–ground co-design; miniaturise through ground-mediated propagation control; and embed biosymbiotic mechanics using additive manufacturing. Together, these strategies provide practical, material-oriented, application-focused guidance for future WBAN platforms.**

***Index Terms*—wearable antennas; WBAN; PDMS; PF4 foam; MXene; conductive textiles; 3-D printing; NinjaFlex TPU; CMA; SAR; miniaturization**

I. Introduction

Wearable body-area networks demand antennas that sustain performance near lossy tissue, tolerate bending, meet radiation-safety limits, and remain comfortable over time. Addressing these requirements benefits from a materials-aware mindset that treats substrate, radiator, and ground as coupled variables, enabling joint control of permittivity/loss and topology (grounding, feeding, modal behaviour) [1]–[5].

II. Materials-Aware Design Strategies

A. Hybrid PDMS–PF4 Loss Shaping

A dual-band/dual-mode microstrip is mapped for dielectric loss, and only PDMS hotspots are replaced by ultra-low-loss PF4, improving average efficiency while preserving geometry, bandwidth, patterns, and compliant SAR on both $2.45\,\mathrm{GHz}$ and $5.8\,\mathrm{GHz}$ bands [1].

B. CMA-Guided Multiband/UWB Textile Structure

On a textile platform with a full ground, a slot is placed in a CMA-identified low-current region to merge with existing modes, widening the $2.45\,\mathrm{GHz}$ match while retaining the $5\,\mathrm{GHz}$ and UWB high-band operation; patterns remain stable on-body and under practical bending [2].

C. Efficiency-Driven Design with Lossy Conductors

For MXene-on-PDMS patches, radiator reshaping lowers peak surface current (ohmic loss) and an elevated ground reduces substrate field density (dielectric loss), raising average efficiency without sacrificing the wide bandwidth around $5\,\mathrm{GHz}$ [3].

D. 3-D Corrugated Ground Miniaturisation

Locally raising the ground beneath the radiating edges adds reactive loading and slows the guided wave, yielding substantial size reduction with modest bandwidth impact and reduced cross-polarisation; an optimal gap avoids Q-factor-driven bandwidth collapse [4].

E. Biosymbiotic 3D-printed Serpentine-Mesh PIFA

At $915\,\mathrm{MHz}$, a serpentine copper mesh over a sparse TPU pillar substrate delivers flexibility, stretchability, breathability, and permeability with a grounded layout for isolation; impedance is tunable for $50\ \Omega$ or rectifier conjugate match, with comparable on/off-body bandwidth and robust bending performance [5].

III. Summary

Across these strategies, the material–field interaction is deliberately shaped rather than accepted as a constraint. Practical guidance follows: hybridise PDMS with PF4 only where loss mapping demands; form bands by modal reasoning rather than add-on resonators; co-design radiator and ground to share losses when conductors are non-ideal; miniaturise from the ground side using slow-wave corrugations while protecting bandwidth; and embed biosymbiotic mechanics with meshed conductors and pillar substrates, validating SAR, on-body detuning, and bending for WBAN use.

References

[1] P. B. Samal, S. J. Chen, and C. Fumeaux, "Flexible hybrid-substrate dual-band dual-mode wearable antenna," *IEEE Trans. Antennas Propag.*, vol. 72, no. 2, pp. 1286–1296, Feb. 2024.

[2] P. B. Samal, S. J. Chen, and C. Fumeaux, "Wearable textile multiband antenna for WBAN applications," *IEEE Trans. Antennas Propag.*, vol. 71, no. 2, pp. 1391–1402, Feb. 2023.

[3] P. B. Samal, S. J. Chen, T. T. Tung, D. Losic, and C. Fumeaux, "Efficiency-driven design for planar antennas with lossy materials," *IEEE Open J. Antennas Propag.*, vol. 4, pp. 23–33, Jan. 2023.

[4] P. B. Samal, S. J. Chen, and C. Fumeaux, "3-D-Corrugated Ground Structure: A microstrip antenna miniaturization technique," *IEEE Trans. Antennas Propag.*, vol. 72, no. 5, pp. 4010–4022, May 2024.

[5] X. Yin, T. Stuart, S. J. Chen, M. Farley, P. Gutruf, and C. Fumeaux, "Biosymbiotic 3-D-printed planar inverted-F antenna," *IEEE Trans. Antennas Propag.*, vol. 72, no. 1, pp. 412–423, Jan. 2024.

979-8-3315-4544-4/26/$31.00 ©2026 IEEE

Dosimetric Assessment of a Birdcage-Coil Wireless Power Transfer at 6.78 MHz for Capsule Robots

V. De Santis*[1], R. Olivieri[1], W. Boumerdassi[1], T. Campi[2], F. Maradei[2], and M. Feliziani[1]

[1]University of L'Aquila, L'Aquila, Italy *valerio.desantis@univaq.it
[2]Sapienza University of Rome, Rome, Italy

***Abstract*—This work addresses the electromagnetic field (EMF) safety of a capsule robot moving inside the human body during wireless power transfer (WPT) operations. The WPT system consists of an innovative birdcage coil capable of generating a nearly uniform rotating magnetic field with non-zero components along all three spatial axes. This solution is wearable, enabling comfortable and efficient power transfer to any patient. However, for obese human body models (HBMs), the current needed to transfer a reasonable power to the capsule battery could pose several EMF exposure risks due to the deeper colon tract and larger body cross-sections. A dosimetric analysis is therefore performed to assess compliance of the proposed WPT system with EMF safety standards. Different frequencies and HBMs are investigated to find the worst-case scenarios.**

Keywords—Birdcage coil, endoscopic capsule, numerical dosimetry, wearable devices, wireless power transfer (WPT).

I. Introduction

The functionality of endoscopic capsule robots is strongly constrained by the limited availability of electrical energy. Traditionally, power is supplied by small integrated batteries. However, in many applications, the battery operating time remains limited, and several device functionalities must be restricted to reduce power consumption [1].

Wireless power transfer (WPT) based on magnetic resonant coupling represents a promising solution to extend the operating lifetime of ingestible capsules [2]-[6], either by recharging onboard batteries or by directly supplying power. In conventional WPT systems, a transmitting coil placed outside the body transfers energy to a receiving coil integrated into the capsule robot. The primary goal is to maximize the power transfer efficiency (PTE) while maintaining compliance with electromagnetic field (EMF) safety regulations despite the arbitrary position and orientation of the capsule within the human trunk.

Though many existing approaches rely on single-axis transmitting coils [3]-[4], often requiring multi-axis receivers that increase device size and weight, the system investigated here combines an optimized monoaxial receiving coil with an innovative transmitting coil capable of generating a rotating magnetic field that is nearly uniform in magnitude but varies in direction, with non-zero components along all three spatial axes. This innovative configuration, proposed in [6] at 300 kHz, enables continuous power delivery to the capsule.

However, previous work mainly focused on the feasibility of the birdcage-based WPT concept at 300 kHz, without investigating its EMF safety in realistic human body models (HBMs). In particular, the influence of different HBM shape, including obese subjects, and inhomogeneous tissues, as well as the operation at higher industrial science and medicine (ISM) frequencies, has not yet been analyzed. Therefore, the main contribution of this work is a comprehensive dosimetric assessment of the proposed wearable birdcage WPT system using realistic HBMs and multiple operating frequencies up to 6.78 MHz, in order to identify safe and effective operating conditions compliant with international EMF exposure guidelines [7]-[9]. In this work, we therefore present a numerical dosimetric investigation using several HBMs with different sizes, ages, and sexes with the aim of identifying the most suitable operating frequency for this application between 300 kHz and 6.78 MHz. At frequencies higher than 6.78 MHz, absorption loss in biological tissues becomes significant; therefore, such frequencies are not suitable for powering mobile capsules located deep within the body [10].

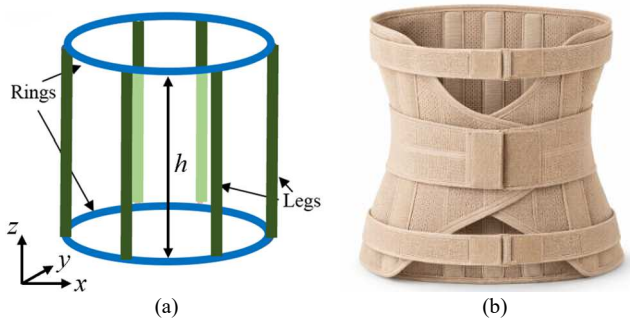
II. Models and Methods

A. Birdcage transmitting coil

A particularly effective coil configuration to achieve a nearly uniform magnetic field within a large volume is the birdcage structure. A birdcage coil is composed of two circular conductive rings, known as end rings, which are interconnected by an even number of longitudinal conductive elements called legs, as shown in Fig. 1(a). This configuration is commonly employed in magnetic resonance imaging systems for radio-frequency (RF) excitation [11]. Each leg carries a sinusoidal current, and the currents are sequentially phase-shifted along the circumference of the cage. The phase difference between neighboring legs is equal to $360°/M$, where M represents an even number of legs. According to EMF theory, this arrangement generates a rotating, spatially uniform magnetic field within the inner region of the birdcage. Such a magnetic field is particularly advantageous for the wireless powering of edible capsules located deep within the body. When a birdcage coil with a vertical z-axis is considered, the legs are parallel to the z-axis and the end rings lie in the xy-plane; thus, the resulting magnetic field inside the cage exhibits a negligible B_z component. This condition is not ideal for the intended application, since the monoaxial capsule may align itself parallel to the z-axis during its movement. Hence, it becomes necessary to generate a magnetic field with a non-zero B_z component. A nearly uniform B_z field can be produced using a Helmholtz-like coil configuration [6].

The proposed transmitting coil design integrates the birdcage structure with a Helmholtz pair, formed by two loops positioned in the xy-plane near the end rings of the birdcage coil and placed at a distance h that encloses the colon tract. Moreover, a rigid birdcage structure with a circular cross-section is not optimal in terms of patient comfort. For this reason, the proposed approach is to reshape the cage bars so that the structure better conforms to the patient's body. An example of a possible elastic jacket-like configuration is shown in Fig. 1(b). In this case, the birdcage structure is deformed. However, the magnetic field distribution inside the cage is not significantly affected.

979-8-3315-4544-4/26/$31.00 ©2026 IEEE



(a) (b)

Fig. 1. Birdcage coil configuration system (a), and a possible example with the deformed birdcage coil embedded within a wearable jacket (b).

B. Coil current evaluation

According to the Faraday's law, the maximum induced electromotive force $e \approx 2\pi f NBS$ in a solenoidal monoaxial coil grows with the frequency f, the number of turns N, the magnetic flux density B, and the coil area S. The operating frequency f is a crucial design parameter for WPT systems. A study on WPT medical applications has demonstrated efficient operation in the MHz range [12], while another work has also reported very good performance at 300 kHz [10]. This study aims to investigate the most suitable operating frequency between 300 kHz and 6.78 MHz for a birdcage coil intended for wireless powering of a capsule robot.

The voltage required by a capsule robot can be assumed $e \approx 1\,\mathrm{V}$. This value is therefore adopted as the minimum reference voltage that must be ensured at the terminals of the receiving coil embedded in the capsule at any location within the human body. From this requirement, the minimum magnetic flux density can be expressed by Faraday's law as

$$B_{\min} = \frac{e}{2\pi f N S} \tag{1}$$

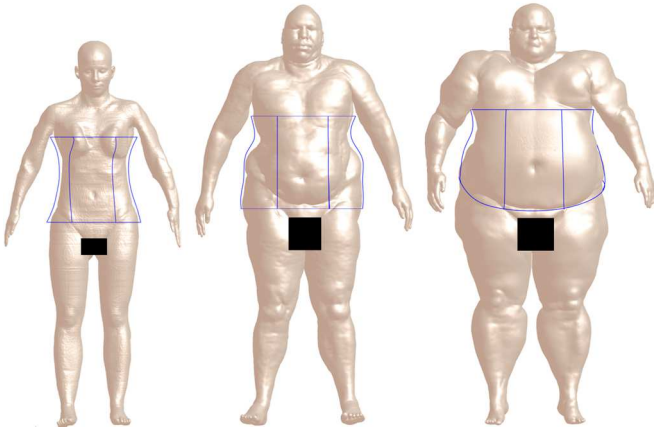
Assuming for example $e = 1\,\mathrm{V}$, $S = 0.8\,\mathrm{cm}^2$, and $N = 100$, the resulting minimum magnetic flux density is

$$B_{\min}(f) = \frac{20}{f}\ [\mathrm{T}] \tag{2}$$

The current I in the birdcage coil can then be adjusted so that this value of $B_{\min}$ is achieved.

C. Dosimetric analysis

The dosimetric simulations are carried out by the magneto quasi-static (MQS) solver implemented in the commercial software tool Sim4Life [13]. The selected HBMs (see Fig. 2), namely Ella prone, Eddie with a body mass index (BMI) of 46, and Fats with a BMI of 70, represent a female during a magnetic resonance imaging (MRI) scan in a prone position, and two obese males, supposed to be the worst-case scenarios for their large size. The HBMs were discretized with a uniform grid resolution of 1 mm. The IT'IS database was used for the tissue dielectric properties at the considered frequencies [14], with the exception of the skin, where a higher conductivity value has been assigned according to the work proposed in [15].



(a) (b) (c)

Fig. 2. Considered HBMs wearing a flexible birdcage with M = 6 legs. (a) Ella prone, (b) Eddie BMI-46, and (c) Fats BMI-70.

III. Numerical Results

A. HBM analysis

First, the dosimetric analysis has been assessed for the three considered HBMs at 300 kHz and 6.78 MHz. In particular, a unitary current of 1 A has been assigned to the Helmholtz coils (in-phase) and to the M = 6 legs (with $360°/M = 60°$ shift-phase) at the frequency of 300 kHz [6]. In this way, the results can be scaled up to the basic restrictions provided by international safety standards [7]-[9].

Figure 3 shows the induced electric field distributions at 300 kHz in the *xy*-plane with the peak field values, whereas Table I reports the dosimetric quantities (volume averaging and 99-th percentile) as specified by [7]. As expected, the obese HBMs lead to the highest induced fields due to their larger cross-section, in accordance with Faraday's Law.

Although Fats BMI-70 represents the largest HBM, the highest induced electric field is observed for Eddie BMI-46. This suggests that the induced field distribution is not only related to body size, but also to anatomical shape and current path distribution within the exposed tissues. It should be noted that the specific absorption rate (SAR) is not reported at frequencies below 1 MHz, as it is not the dominant dosimetric quantity [16]. Thus, the Eddie BMI-46 model is considered later on.

B. Frequency analysis

Once the worst HBM has been obtained, the ISM frequency of $f = 6.78$ MHz is selected. Fig. 4 illustrates the B-field, induced electric field, and SAR distributions showing that the $B_{\min}$ is within 2 µT in the stomach and colon tissues, assuming 1 A excitation. Thus, to achieve the required target, a current of 1.45 A is required. Instead, from an EMF safety point of view, the best frequency is 300 kHz, based on the results summarized in Table II. Indeed, the ICNIRP-2010 limit at 300 kHz is 40.5 V/m and 915.3 V/m at 6.78 MHz [7], while the SAR specified by ICNIRP-2020 and IEEE-C95.1 is 2 W/kg [8]-[9]. Hence, the current needed to meet these limits is 9.67 A at 300 kHz and 8.04 at 6.78 MHz.

These results highlight the trade-off between WPT performance and EMF exposure: increasing the operational frequency significantly increases the induced electric fields and SAR within tissues.

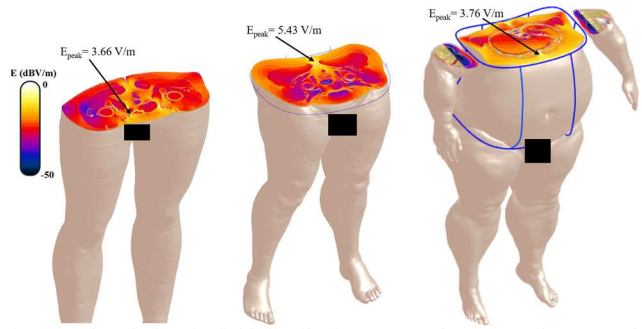


Fig. 3. Induced electric field distributions at 300 kHz. (a) Ella prone, (b) Eddie BMI-46, and (c) Fats BMI-70.

TABLE I. INDUCED ELECTRIC FIELDS AT 300 KHZ FOR DIFFERENT HBMS

HBM	E_{peak} (V/m)	E_{avg} (V/m)	E_{99} (V/m)
Ella prone	3.66	2.24	0.69
Eddie BMI-46	5.43	4.19	0.92
Fats BMI-70	3.76	3.57	0.84

TABLE II. INDUCED ELECTRIC FIELD AND SAR AT DIFFERENT FREQUENCIES

Frequency (MHz)	E_{peak} (V/m)	E_{avg} (V/m)	E_{99} (V/m)	SAR (W/kg)	SAR_{10g} (W/kg)
0.30	5.43	4.19	0.92	-	-
1.00	17.38	16.95	3.27	0.034	2.14×10^{-4}
6.78	146.01	113.80	22.84	2.16	0.012

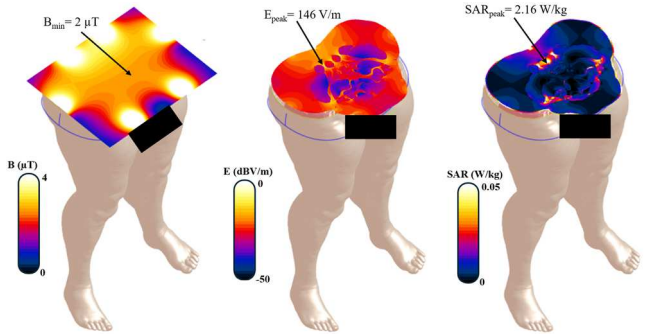


Fig. 4. Magnetic flux density (a), induced electric field (b) and SAR (c) distributions for the Eddie BMI-46 at f = 6.78 MHz.

IV. DISCUSSION AND CONCLUSIONS

The proposed transmitting system based on a birdcage coil represents a promising solution for the wireless powering of capsule robots. In this work, the system has been envisioned in an innovative wearable configuration, integrated into a jacket-like structure that can be comfortably worn by the patient. This approach could enable practical and flexible use of this technology in clinical scenarios while maintaining an adequate magnetic field distribution within the body.

A study was conducted to identify the most suitable operating frequency for the transmitting birdcage coil between 300 kHz and 6.78 MHz. The results indicate that 6.78 MHz, which lies within the ISM band, represents an appropriate compromise between EMF safety constraints and the induced voltage on the receiving coil. However, in practical WPT applications, the actual power delivered to the capsule must also be considered. This depends on several factors, including power losses in the electronics and windings, as well as the load impedance, all of which vary with frequency. Nevertheless, this study provides a useful guideline for identifying an appropriate operating frequency from a dosimetric perspective.

The dosimetric analysis was performed using different human body models. The results show that the most critical conditions occur for obese individuals with respect to the induced electric field levels. However, the evaluated specific absorption rate values remain well below the relevant safety limits and therefore do not raise significant concerns. Overall, the obtained results support the feasibility of the proposed system and highlight its potential for the wireless powering of capsule robots. Compared to previous studies on birdcage-based WPT systems, this work provides, for the first time, a dosimetric investigation on realistic heterogeneous HBMs with different body sizes and operating frequencies. In future works, the trade-off between induced voltage and EMF exposure will be better clarified, providing practical design guidelines for wearable WPT systems intended for capsule robotics.

REFERENCES

[1] Q. Cao *et al.*, "Robotic wireless capsule endoscopy: recent advances and upcoming technologies," *Nature Commun.*, vol. 15, p. 4597, 2024.

[2] R. Carta, J. Thon, and R. Puers, "A wireless power supply system for robotic capsular endoscopes," *Sens. Actuators A Phys.*, vol. 162, no. 2, pp. 177–183, Aug. 2010.

[3] M. Basar, M. Ahmad, J. Cho, and F. Ibrahim, "Application of wireless power transmission systems in wireless capsule endoscopy: An Overview," *Sensors*, vol. 14, no. 6, pp. 10929–10951, Jun. 2014.

[4] H. Zhuang, W. Wang, K. Zhao, Q. Fei, and G. Yan, "Design and analysis of a wireless power transfer system for capsule robot using an optimised planar square spiral transmitting coil pair," *Int J Med Robot.*, vol. 18, e2399, 2022.

[5] J. Gao *et al.*, "Design and optimization of a novel double-layer Helmholtz coil for wirelessly powering a capsule robot," *IEEE Trans. Power Electron.*, vol. 39, no. 1, pp. 1826-1839, Jan. 2024,

[6] T. Campi, S. Cruciani, F. Maradei and M. Feliziani, "Innovative wireless charging system for implantable capsule robots," *IEEE Trans. Electromagn. Compat.*, vol. 63, no. 5, pp. 1726-1734, Oct. 2021.

[7] ICNIRP "Guidelines for limiting exposure to time-varying electric and magnetic fields for low frequencies (1 Hz - 100 kHz)," *Health Phys.*, vol. 99, pp. 818-836, 2010.

[8] ICNIRP "Guidelines for limiting exposure to time-varying electric, magnetic, and electromagnetic fields (up to 300 GHz)," *Health Phys.*, vol. 118, no.5, pp. 483–524, 2020.

[9] IEEE-C95.1, *IEEE Standard for Safety Levels with Respect to Human Exposure to Electric, Magnetic and Electromagnetic Fields, 0 Hz to 300 GHz*. NY, USA, 2019.

[10] T. Campi, S. Cruciani, V. De Santis, F. Maradei, and M. Feliziani, "Near field wireless powering of deep medical implants," *Energies*, vol. 12, no. 14, p. 2720, Jul. 2019.

[11] C. E. Hayes, W. A. Edelstein, J. F. Schenck, O. M. Mueller, and M. Eash, "An efficient, highly homogeneous radiofrequency coil for whole-body NMR imaging at 1.5 T," *J. Magnetic Resonance* (1969), vol. 63, no. 3, pp. 622–628, Jul. 1985.

[12] N. O. Elazab, A. Lamkaddem, K. A. Abdalmalak, and D. S. Vargas, "Miniature triple-band capsule antenna with reverse current technique for biomedical implants with optimized SAR performance," *IEEE Ant. Wireless Propag. Lett.*, (Early Access), doi: 10.1109/LAWP.2026.3655211.

[13] Sim4Life. SIMulation 4 LIFE science platform. [Online]. Available: https://www.zurichmedtech.com/sim4life.

[14] C. Baumgartner *et al.*, "IT'IS database for thermal and electromagnetic parameters of biological tissues, version 5.0," Aug. 21, 2025 [Online]. Available: www.itis.swiss/database.

[15] V. De Santis, X. L. Chen, I. Laakso, and A. Hirata, "An equivalent skin conductivity model for low-frequency magnetic field dosimetry," *Biomed. Phys. Eng. Express*, vol. 1, no. 1, p. 015201, 2015.

[16] X. L. Chen, A. E. Umenei, D. W. Baarman, N. Chavannes, V. De Santis, J. R. Mosig, and N. Kuster, "Human exposure to close-range Wireless Power Transfer systems as a function of design parameters," *IEEE Trans. Electromag. Compat.*, vol. 56, no. 5, pp. 1027-1034, 2014.

2006-2026: Two Decades of Innovation with Metamaterial and Metasurfaces for an Array of Applications

Dr. Chinmoy Saha

Professor
Department of Avionics
Indian Institute of Space Science and Technology,
Department of Space, Government of India
Thiruvananthapuram, Kerala 695547, India,
csaha@ieee.org, chinmoysaha@iist.ac.in

Abstract: Over the past two decades, metamaterials and metasurfaces have revolutionized the field of electromagnetics by enabling unprecedented control over electromagnetic waves through engineered subwavelength structures. This invited talk presents a comprehensive overview of the research contributions in our group from 2006 to 2026, highlighting innovative developments in metamaterial and metasurface-inspired technologies for a wide spectrum of wireless and sensing applications.

The talk will cover the evolution of compact and multifunctional antennas, high-selectivity microwave filters, and advanced metasurface-enabled systems addressing the growing demands of modern wireless communications. Special emphasis will be given to the development of antennas for 4G/5G and beyond systems, cognitive radio platforms with frequency-reconfigurable and spectrum-sensing capabilities, and compact wideband radiators employing artificial electromagnetic structures for enhanced performance. Furthermore, the presentation will discuss recent advances in RF energy harvesting and rectenna technologies, including metasurface-assisted wireless power transfer and ambient energy-scavenging systems aimed at sustainable and self-powered wireless networks.

The talk will also highlight the translation of theoretical concepts into experimentally validated prototypes and practical systems, demonstrating how metamaterials and metasurfaces have evolved from scientific curiosities into enabling technologies for next-generation communication, sensing, and energy applications. Finally, future research directions involving intelligent metasurfaces, integrated wireless power and communication systems, and sub-THz platforms for 6G applications will be outlined.



Chinmoy Saha (MIEEE'06–SMIEEE'15, SM URSI) received his B.Tech, M.Tech. and PhD degrees in Radio Physics and Electronics, University of Calcutta, Kolkata, India in 2002, 2005 and 2012 respectively. He is the current Vice Chair of MTT-S MGA committee, chair of IEEE MTT-S SIGHT committee and region-10 (Asia and pacific) coordinator of IEEE MTT-S since 2023. He is currently working as a full Professor in the Department of Avionics, Indian Institute of Space Science and Technology, Department of Space, Government of India. He has visited several International Universities of repute and has strong research collaboration with several International Universities in North America and Europe. He visited Royal Military College of Canada and Queens University, Canada as visiting professor/post-doctoral fellow in 2015 and 2017-2018. He is a senior Member of the IEEE, senior member of International Union of Radio Science and a Fellow of IETE. He served as the Rregion-10 coordinator of IEEE Antennas and Propagation Society during 2021-2022. He founded the IEEE MTT-S Kerala chapter in 2019 and served as the chairperson of the chapter during 2019-2021. He also has served as the Chairman of Antennas and Propagation Chapter of IEEE Kerala section during 2018-2019. Dr. Saha was also involved as the Chairman of the award committee of IEEE Kerala Section (2025-presnet), chairman of Conference Activity board of IEEE Kerala Section during 2022-2023. Recently, in September 2024, Dr. Saha

979-8-3315-4544-4/26/$31.00 ©2026 IEEE

has founded Electromagnetic Compatibility (EMC) society Chapter of IEEE Kerala section in which he is the current chair. Dr. Saha has received several prestigious awards which includes National Award "*AICTE Visvesvaraya Best Teacher Award 2021*" received form Union Education minister, Government of India, "*IETE Prof. SN Mitra Memorial Award 2021*", "Outstanding researcher award 2024" from IEEE Kerala Section, "*Outstanding Teacher Award*" in 2019 from Department of Avionics, IIST, "*National Scholarship from Ministry of Human Resource Development"* from Government of India, "*Outstanding Contribution Award* from the AP-MTT Kolkata chapter, "*Best Contribution Award for Notable Services and Significant Contributions towards the Advancements of IEEE and the Engineering Profession*" from IEEE Kolkata Section and several best paper awards in various International conferences. His current research interest includes microwave Wireless Power Transfer (WPT) and Energy Harvesting, Microwave Circuits, Metamaterial/metasurface & applications, multi-functional antennas for modern wireless applications, mm-wave THz systems, and antennas and components for space applications. He has more than 250 publications in International Journals and conference Proceedings including 63 journal papers. Prof. Saha has authored three books with Cambridge University Press, UK and Taylor and Francis, USA. He served as the guest editor-in-chief for a special issue of International Journal of RF and Microwave Computer Aided Engineering during 2018-2019 and currently working as editor-in-chief for an ongoing special issue of EPJ Applied Metamaterials. He has guided /currently guiding 15 Ph.D. thesis and 30+ M.Tech. thesis.

Design of Millimeter Wave Ultra Wideband Solid-State LNA Module Based on Metal Cavity Packaging

Hui Peng[1], Zhongqian Niu[2], Jincai Qiao[4], Yafei Wu[2], Bo Zhang[3], Zuqiang Ou[4*]
[1] School of Physics and Electrical Engineering, Kashi University, Kashi, China.
[2] School of Electronic Science and Engineering, University of Electronic Science and Technology of China, Chengdu, China.
[3] Yangtze Delta Region Institute (Quzhou), University of Electronic Science and Technology of China, Quzhou, China.
[4] Chongqing Institute of Microelectronics Industry Technology, University of Electronic Science and Technology of China, Chongqing, China.
zuqiang.ou@hotmail.com

***Abstract*—This paper presents a 75 GHz~110 GHz low-noise amplifier (LNA) module designed to suppress harmful resonances within a metallic packaging cavity, which can otherwise lead to self-oscillation and performance degradation. By optimizing the cavity dimensions and incorporating specifically designed perturbation structures, the proposed approach effectively eliminates unwanted resonant modes. The viability of the design is experimentally verified, with measurement results confirming stable LNA operation across the full frequency band.**

***Keywords*—Low noise amplifier, resonance suppression, millimeter wave, ultra wideband.**

I. Introduction

In millimeter-wave spectrum analysis instruments, the transceiver front-end circuit enables frequency translation of millimeter-wave signals, thereby directly converting signals that are challenging for ADCs to process down to microwave low-frequency bands. Consequently, a wideband receiver front-end is highly desirable to achieve an extensive measurement range for the spectrum analyzer, necessitating an exceptionally low noise figure. The incorporation of a low-noise amplifier (LNA) in the receiver system can significantly enhance the noise figure performance. Furthermore, wideband operation is crucial, as it eliminates the need for numerous band-switching switches, thereby simplifying the front-end chain and reducing overall losses.

In MMIC packaging technology, waveguide-to-microstrip transitions are often designed within enclosed metal cavities, with gold wire bonding employed for signal input and output from the bare chip pads. When electromagnetic waves reach millimeter-scale wavelengths, the physical dimensions of the vacant cavity surrounding the bare chip significantly impact module performance. If the cavity volume is excessively large, it may satisfy resonance conditions, generating harmonics and their higher-order frequencies that could fall within the target frequency band, potentially leading to device self-oscillation or degraded isolation. A common engineering practice uses utilizing microwave absorbing materials inside the cavity [1]. These materials typically feature high dielectric constants, high magnetic permeability, and high loss tangents, concentrating the electromagnetic field within the cavity and dissipating it. However, microwave absorbing materials introduce significant power and gain losses, adversely affecting the in-band gain flatness of the module. Furthermore, there is no optimal criterion for absorber placement, resulting in poor consistency. In recent years, numerous scholars have investigated methods to suppress detrimental cavity resonances, such as employing Artificial Magnetic Conductor (AMC) structures [2]. Nevertheless, these structures are complex, and at higher operating frequencies, their physical dimensions decrease, making fabrication challenging. Therefore, a simple metal cavity packaging method with effective resonance suppression is highly sought after in engineering applications. This paper will present the design methodology and demonstrate the fabricated performance of a 75 GHz~110 GHz LNA module as an example.

II. Overall Structure of Metal Cavity Packaged LNA Module

The overall block diagram of the LNA module is shown in Fig. 1. The input signal within the 75 GHz~110 GHz frequency range is fed into the module via a waveguide. Since the LNA DIE uses pads as its input and output ports, microstrip lines are required to interface with these pads. The top view of the LNA module structure is illustrated in Fig. 2. The waveguide-microstrip conversion structure at both the input and output ports consists of a microstrip probe extending into the sidewall of the waveguide. This structure converts the TE mode propagating in the waveguide into the TEM mode (or Quasi-TEM mode) of the planar transmission line (microstrip), and vice versa. Matching networks are employed to optimize the broadband voltage standing wave ratio (VSWR), thereby achieving ultra-wideband transmission characteristics. The design methodology and optimization procedure of the cavity-based packaging approach for the solid-state module are detailed in [3], aiming for a seamless integration that preserves the intrinsic low-noise performance of the MMIC across the entire waveguide band.

979-8-3315-4544-4/26/$31.00 ©2026 IEEE

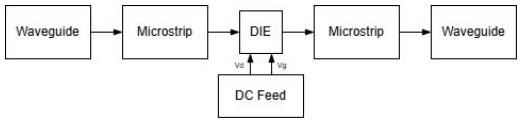


Fig. 1. The overall block diagram of the LNA module

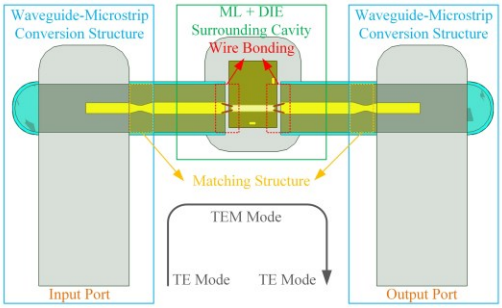


Fig. 2. The top view of the LNA module structure

III. Design of Resonance Suppression Structure for the Die Cavity

In the LNA module, the cavity surrounding the DIE is the most critical area prone to resonance. However, because the chip is enclosed within a metal housing, a sufficiently large cavity must be reserved to accommodate essential components such as chip capacitors, feedthrough insulators, and bonding wires. At millimeter wave frequencies, the physical dimensions of this cavity become electrically large relative to the wavelength, making it highly susceptible to satisfying resonance conditions. Consequently, electromagnetic waves within the millimeter-wave band can resonate inside the cavity. For active amplification circuits, such parasitic resonances pose a significant risk, as they can lead to severe performance degradation, including unwanted self-oscillation and instability.

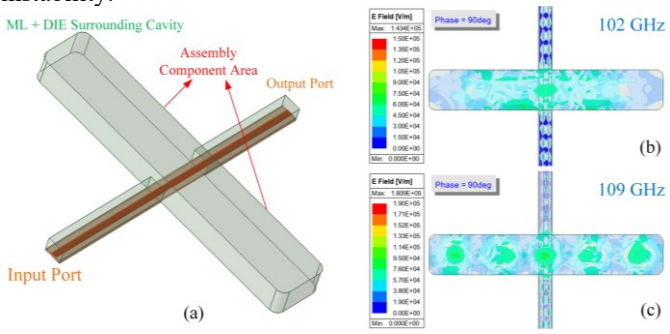


Fig. 3. Resonance simulation of the cavity containing the microstrip line and the DIE surrounding cavity. (a) Simulation model; (b) Electric field distribution at 102 GHz; (c) Electric field distribution at 109 GHz

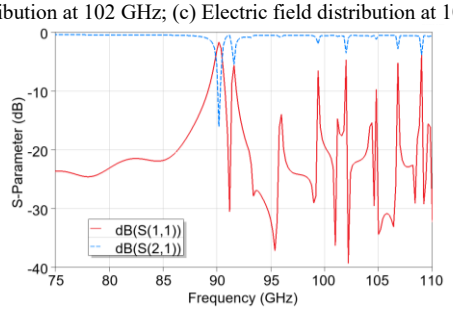


Fig. 4. Simulation results of the cavity containing the microstrip line and the DIE surrounding cavity

To characterize the aforementioned phenomenon, a simulation model was established, as shown in Fig. 3(a). The cavity resonance observed in the simulation is illustrated in Fig. 3(b) and 3(c). Specifically, Fig. 3(b) depicts the TE10 mode at a resonant frequency of 102 GHz, while Fig. 3(c) shows the TE50 mode at a resonant frequency of 109 GHz. These resonant modes, if not properly suppressed, can couple to the active circuit and lead to instability or performance degradation within the operating band.

To investigate the resonance characteristics, the cavity region surrounding the die, along with the input and output microstrip lines-highlighted by the green dashed rectangle in Fig. 2, was isolated for dedicated analysis. In this work, a perturbation method is employed to suppress unwanted resonances. Specifically, a cross-shaped perturbation structure is placed on the ceiling of the cavity above the die area to disrupt the propagation of higher-order transverse electric (TE) modes. The conceptual model of this perturbation structure is depicted in Fig. 5(a). The implemented design, shown in Fig. 5(b), incorporates two cross-shaped elements strategically positioned to effectively break up the high-order TE resonant modes within the cavity. It is important to note that simulating the complex electromagnetic fields inside the active die region is highly challenging; therefore, the simulation model and its results do not account for the Quasi-TEM mode propagating on the chip surface. The simulation results are presented in Fig. 6. Compared to the original cavity response, the resonant spikes in the S21 curve have been successfully eliminated. The residual trend of the S21 response has been shifted to higher frequencies, specifically above 110 GHz, which lies outside the operational bandwidth of the module. From the simulation results, this structure meets the packaging requirements without resonance from 75GHz to 110GHz.

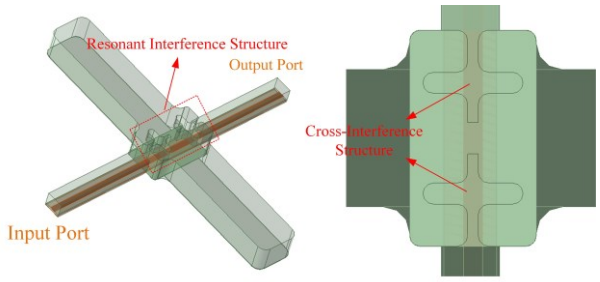


Fig. 5. Simulation model with the cross-shaped perturbation structure. (a) Overall architecture; (b) Top view of the implemented perturbation structure

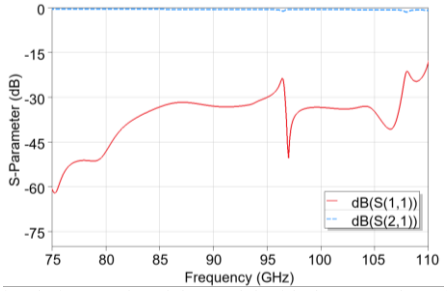


Fig. 6. Simulation results of the model with the cross-shaped perturbation structure

IV. Processing and Measurement

To evaluate the effectiveness of the proposed perturbation structure, a reference LNA module without the perturbation elements was also fabricated for comparison. During measurement, a 30 dB attenuator was connected at the input of the device under test to protect the vector network analyzer from potential damage caused by self-oscillation. The measured performance of this reference module is shown in Fig. 7, where significant self-oscillation can be observed within the operating band.

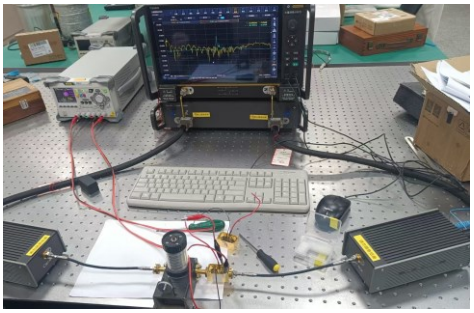


Fig. 7. Test setup of the LNA module without the perturbation structure

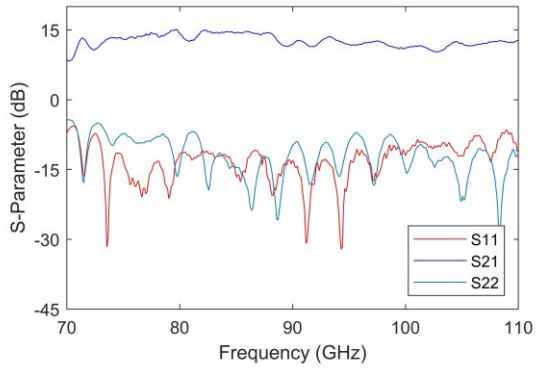


Fig. 8. Measurement results of the LNA module with the perturbation structure

Based on the design methodology described above, an LNA module incorporating the cross-shaped perturbation structure was designed, fabricated, and characterized. The measurement results, presented in Fig. 8, demonstrate that the module operates stably across the 75 GHz~110 GHz frequency range, achieving a gain of greater than 12 dB. In contrast to the module without perturbation structures, the self-oscillation is effectively suppressed, successfully fulfilling the design objective.

Conclusion

This paper presents a cross-shaped perturbation structure to suppress parasitic cavity resonances in millimeter-wave LNA modules. By disrupting higher-order TE modes within the die cavity, the proposed method eliminates resonant spikes. Experimental results for a 75 GHz~110 GHz LNA module demonstrate stable operation with over 12 dB gain across the entire band, effectively eliminating self-oscillation observed in unperturbed designs. This simple, fabrication-friendly technique provides effective resonance suppression without compromising gain performance, and can be readily extended to other millimeter-wave and sub-terahertz packaged modules.

Acknowledgment

This work is supported by the National Key Research and Development Program of China under Grant No. 2024YFE0200403. This work is supported by Zhejiang Provincial Natural Science Foundation LD25F040007. This work is supported by the Fundamental Research Funds for the Central Universities No. ZYGX2024Z012, No. ZYGX2024XJ009, ZYGX2024J006. This work is supported by the Xinjiang Talent Development Fund Project No. XJRC-2025-KJ-YJ-CXPT-183. This work is also supported by the Key Scientific Research Project of Kashi University, No. 20242882.

References

[1] A. Khoshniat and R. Abhari, "Metamaterial Absorbers for Lining System Shield Box and Packaging: Cavity Analysis and Equivalent Material Design," in *IEEE Transactions on Electromagnetic Compatibility*, vol. 63, no. 4, pp. 1007-1014, Aug. 2021.

[2] J. Sun, J. Xu, H. Cheng, Q. Zhu, X. Han. "Research on Ka-band Solid-state Power Amplifier Module Packages Using a Lid of Nails," in *Journal of Electronics & Information Technology*, vol 42, no. 12, pp. 3074-3080, 2020.

[3] Z. Ou, Y. Zhong, J. Qiao, Z. Niu and H. Peng, "Design and Optimization of Metallic Cavity Packaging for Millimeter-Wave RF Chips," *2025 IEEE MTT-S International Microwave Workshop Series On Advanced Materials and Processes for RF and THz Applications (IMWS-AMP)*, Wuxi, China, 2025, pp. 1-3

Additive Manufacturing of High-Performance Filters with Unconventional Geometries

Cristiano Tomassoni
University of Perugia, Italy
cristiano.tomassoni@unipg.it

Additive Manufacturing (AM) offers exciting capabilities for microwave engineering, enabling rapid prototyping, geometric flexibility, and easily customizable products. However, applying 3D printing to high-performance filters is not immediate, as these technologies are not originally tailored for high-frequency hardware. To meet strict electrical specifications, specific design adaptations and targeted post-processing steps are often required. This presentation highlights how AM can be effectively leveraged to build advanced microwave filters. Using selected hardware examples, we will discuss some of the most common 3D printing techniques adopted in this field and the practical actions needed to ensure optimal component performance. Finally, the talk will demonstrate how the geometric freedom of AM unlocks unconventional 3D topologies, allowing the development of a new class of filters that are highly optimized in terms of compactness, weight, and insertion losses.

979-8-3315-4544-4/26/$31.00 ©2026 IEEE

Additively Manufactured Microwave Devices and Antennas

Yang Yang
University of Technology Sydney, Australia
yang.yang.au@ieee.org

The race to develop next-generation wireless electronics is accelerating at a rapid pace. Thanks to advanced additive manufacturing technology, fast prototyping, low-entry-cost, and in-house short-run manufacturing empower millions of start-ups and companies with demanding confidentiality and accelerated innovation. We aim to build a new class of high-performance metamaterials and metasurfaces to advance the knowledge for future wireless devices. Compact and low-cost 3D-printed metasurfaces and metamaterials will be delivered to circumvent the limitations of traditional manufacturing technologies. The proposed 3D metadevices should be easily integrated into high-speed wireless systems in a dynamic environment. The cutting-edge additive manufacturing technologies advance 3D Radio frequency circuits with exceptional performance for emerging intelligent and immersive technologies, which will critically impact 5G/6G high-speed wireless devices in the millimetre-wave and terahertz applications. The 3D-printed radio frequency electronics will immediately benefit biomedical engineering, defence, space and telecommunication industries.

979-8-3315-4544-4/26/$31.00 ©2026 IEEE

Reconfigurable and Tunable Millimeter-Waves Devices Based on Functional Materials

Aurelian Crunteanu
XLIM, CNRS/ University of Limoges, France
aurelian.crunteanu@xlim.fr

The increasing complexity of high-frequency transmission and reception front-ends resulting from the addition of new frequency bands and frequency diversification, requires reconfigurable topologies throughout the entire telecommunication chain (antennas, phase shifters, filters, amplifiers, etc.) for reducing fabrication costs, system size, and overall power consumption. Most reported reconfiguration solutions in RF circuits are based on the integration of localized tunable devices and commonly rely on semiconductor-based devices, RF-MEMS, liquid crystals or functional materials. We are presenting the performances of a selection of reconfigurable devices (switches, tunable capacitors, agile filters, frequency- and polarization- reconfigurable antennas) designed for millimeter-waves operation and built upon a variety of constituent functional materials with controlled and tuned permittivity or conductivity (ferroelectrics, phase transition and phase change materials). We discuss the requirements for materials integration and emphasize the advantages of specific reconfiguration schemes enabling devices with on-demand agile functionalities.

979-8-3315-4544-4/26/$31.00 ©2026 IEEE

A Terahertz scattering-type scanning near-field optical microscopy for single cell imaging

Zhaomin Peng
Key Laboratory of Microwave Remote Sensing, National Space Science Center Chinese Academy of Sciences
Beijing,China
Pengzhaomin@nssc.ac.cn

Jun Shi
Key Laboratory of Microwave Remote Sensing, National Space Science Center Chinese Academy of Sciences
Beijing,China
Shijun@nssc.ac.cn

Dehai Zhang
Key Laboratory of Microwave Remote Sensing, National Space Science Center Chinese Academy of Sciences
Beijing,China
Zhangdehai@mirslab.cn

I. Abstract

Biological cell imaging in the sub-terahertz (sub-THz) regime is exceptionally challenging because eukaryotic cells are weak scatterers with intrinsically low dielectric contrast. While scattering-type scanning near-field optical microscopy (s-SNOM) can bypass the diffraction limit by confining the interaction to the AFM tip apex, reliable cellular imaging in the lower-THz window (below ~200 GHz) remains difficult due to reduced near-field signal levels and increased susceptibility to leakage and background. S-SNOM is a probe-based technique that overcomes the diffraction limit by confining light–matter interaction to the nanometric region underneath a tapping AFM tip. The tip acts as a nanoscale scatterer that converts localized near-field information into detectable far-field radiation, while interferometric (coherent) detection and harmonic demodulation suppress the far-field background[1]. As a result, the achievable lateral resolution is governed primarily by the tip apex radius rather than the free space wavelength, enabling nanoscale imaging from the infrared down to the terahertz and sub-terahertz bands.

We developed a 100 GHz s-SNOM platform engineered for weakly scattering biological specimens. The instrument integrates a zero intermediate frequency (Zero-IF) coherent receiver to retain the tapping-modulated scattering signal at baseband, achieves 39.95 dB transmitter-receiver isolation to mitigate leakage dominated backgrounds, and uses a custom probe with an ~100 nm apex radius to enhance sub-THz scattering efficiency[2]. A low-frequency RF source is frequency-multiplied to 100 GHz and split into an illumination branch and a local-oscillator branch for coherent mixing. A directional coupler routes the back-scattered signal into the receiver; its isolated port is terminated with a matched load to suppress reflections and improve isolation. After low-noise amplification, Zero-IF mixing converts the signal to baseband, a DC block removes offsets and drifts, and phase-locked demodulation extracts s1 and s2 (demodulation orders n=1 and n=2) for imaging.

We demonstrate label-free cellular imaging using semi-dry SKOV3 ovarian cancer cells on a gold substrate. Measurements are acquired over a 40 $\mu m \times 40\ \mu m$ field of view with a tapping amplitude of approximately A $\approx$ 200 nm. Near-field maps at s1 and s2 consistently resolve two representative morphologies: a compact rounded phenotype and an elongated phenotype (As shown in Fig. 1). Within each cellular footprint, the near-field response shows localized nonuniformity that is not fully explained by height contrast alone, suggesting subcellular-scale dielectric heterogeneity (e.g., local hydration or compositional variations). Future work will pursue controlled hydration studies and multi-frequency sub-THz measurements for improved dielectric specificity.

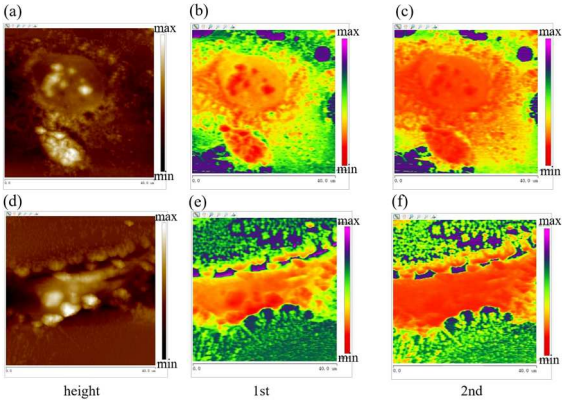


Fig. 1. Representative 100-GHz s-SNOM imaging of semi-dry SKOV3 ovarian cancer cells on a gold substrate. (a–c) Sample A with a rounded phenotype: (a) AFM topography, (b) demodulated near-field amplitude at the 1st harmonic (n = 1), and (c) demodulated near-field amplitude at the 2nd harmonic (n = 2). (d–f) Sample B with an elongated phenotype: (d) AFM topography, (e) n = 1 near-field map, and (f) n = 2 near-field map. The harmonic near-field channels provide morphology-consistent contrast, with the 2nd harmonic exhibiting enhanced near-field selectivity.

References

[1] F. Keilmann and R. Hillenbrand, "Near-field microscopy by elastic light scattering from a tip," Philos Trans A Math Phys Eng Sci, vol. 362, no. 1817, pp. 787-805, Apr 15 2004, doi: 10.1098/rsta.2003.1347

[2] Z. Peng, S. Ge, J. Meng, Z. Liu, and D. Zhang, "Advancing Nanoscale Imaging: A 100-GHz Ultramicroscopy System Based on Nonfocusing Zero-Intermediate Frequency Radar Technology," IEEE Transactions on Instrumentation and Measurement, vol. 73, pp. 1-9, 2024, doi: 10.1109/TIM.2024.3449942.

979-8-3315-4544-4/26/$31.00 ©2026 IEEE

Terahertz Near-Field Scanning Microscopy for Nanoscale Imaging of Ovarian Cancer Cells

Dehai Zhang
Key Laboratory of Microwave Remote Sensing, National Space Science Center Chinese Academy of Sciences
Beijing,China
Zhangdehai@mirslab.cn

Zhaomin Peng
Key Laboratory of Microwave Remote Sensing, National Space Science Center Chinese Academy of Sciences
Beijing,China
Shijun@nssc.ac.cn

Jin Meng
Key Laboratory of Microwave Remote Sensing, National Space Science Center Chinese Academy of Sciences
Beijing,China
Mengjin@mirslab.cn

I. Abstract

Terahertz scanning type near-field optical microscopy, as high-resolution imaging platforms with nanometer-scale resolution, has been extensively utilized in materials science, physics, and biological research. Central to this imaging mechanism is the use of nanoscale probe tip vibration to modulate incident electromagnetic waves. By selectively detecting the scattered signals arising from tip-sample interactions and extracting near-field information from both the fundamental vibration frequency components (termed first-order signals) and their harmonic frequency components (e.g., second- harmonicr signals or higher- harmonics signals), these systems achieve nanometric spatial resolution. In biological imaging, numerous research teams have conducted imaging investigations on biological microstructures such as small protein molecules and Staphylococcus aureus[1]. However, due to inherent limitations including weak scattering signals from biological specimens and low dielectric contrast, applications of this system for thicker cellular-level biological samples remain relatively underexplored. In this study, we implemented systematic optimizations through three key improvements: development of a high-isolation directional coupler integrated with specially designed antennas to achieve effective signal transceiver separation; adoption of a non-focusing configuration that replaces conventional optical paths with near-field radiation zones for both signal excitation and collection, thereby enhancing the collection efficiency of near-field scattered signals; implementation of low-noise amplifiers at the primary receiver stage to optimize the overall noise figure. These comprehensive optimizations enable effective detection of weak near-field scattering signals typical in biological specimens. The overall system architecture and the actual experimental setup[2] are illustrated in the accompanying fig. 1(a)(b). The self-developed system was employed to image ovarian cancer cell samples prepared via cell-embedded sectioning, with the overall thickness of the sample sections ranging from 1 to 2 μm. The resulting surface topography map and first and second-order near-field signal amplitude maps are illustrated in the fig. 1(c).

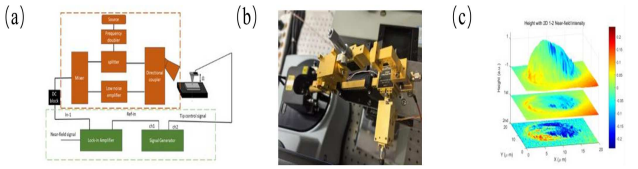


Fig. 1(a)the architecture of THz scanning type near-field optical microscopy (b) the actual experimental system (c) The resulting surface topography map and first and second-order near-field signal amplitude maps.

The 3D height map is pseudo-colored using first-order near-field signal amplitudes, with spatial projections of first and second-order signals corresponding to their respective positions. These findings serve as a critical reference for subsequent investigations into cellular dynamics analysis and clinical cell-level diagnostics for cancer pathology, particularly in resolving subcellular dielectric heterogeneity and biomechanical properties.

References

[1] X. Hu, G. Zhang, "Terahertz s-SNOM Imaging of a Single Cell with Nanoscale Resolution," Nano Letters, vol. 24, no. 25, pp. 7757-7763, 2024, doi: 10.1021/acs.nanolett.4c01868.

[2] Z. Peng, D. Zhang, "Advancing Nanoscale Imaging: A 100-GHz Ultramicroscopy System Based on Nonfocusing Zero-Intermediate Frequency Radar Technology," IEEE Transactions on Instrumentation and Measurement, vol. 73, pp. 1-9, 2024, doi: 10.1109/TIM.2024.3449942.

979-8-3315-4544-4/26/$31.00 ©2026 IEEE

Research on Beam Steering Rectenna Array for Drone Microwave Wireless Power Supply

Liwei Song, Song Li
State Key Laboratory of Electromechanical Integrated Manufacturing of High-performance Electronic Equipment,
Xidian University
Xi'an, China
lwsong@xidian.edu.cn

***Abstract*—To address the unstable power supply caused by beam misalignment between transmitting and receiving antennas due to dynamic changes in UAV flight attitude, a beam-tunable rectenna array is proposed. First, a pattern-reconfigurable receiving antenna element is designed by integrating a PIN-diode switching network into the parasitic layer. Measurements show that the main beam can be steered to 0° and ±20° at 5.8 GHz, with gains above 6.5 dBi. Second, a rectifying circuit based on a dual-parallel Schottky diode topology is developed for wide input power operation. The measured peak rectification efficiency reaches 60.7% at an input power of 31 dBm, and remains above 50% over the input power range of 18–35 dBm. Finally, the antenna element and rectifying circuit are integrated into a rectenna element using a folded structure and a shared antenna ground. The influence of the DC bias circuit on antenna performance is analyzed, and a 2 × 2 beam-tunable rectenna array is fabricated. Measurements at different power transmission distances show that the array can electrically steer the receiving beam. When the array is rotated to the three beam directions, the maximum received DC powers are 1.6 W, 1.2 W, and 1.3 W, respectively. These results demonstrate that the proposed array can effectively maintain stable power reception in dynamic microwave power transfer scenarios, providing a feasible solution for UAV microwave wireless power supply.**

Keywords—microwave power transmission, drone power supply, rectenna, pattern reconfiguration, wide input power, beam steering.

I. Introduction

With the development of technology, drones are widely used, but their endurance is limited by long charging time and low battery capacity. Microwave wireless power transmission (MWPT) offers long range, high power, high efficiency, and low susceptibility to weather, making it a promising power supply method to extend drone endurance.

References [1] presented lightweight rectennas and arrays for MWPT experiments. However, these experiments were static, whereas in actual drone flight, the position and orientation of the receiving antenna relative to the transmitting antenna change dynamically, making fixed-beam receiving antennas unsuitable. Phased arrays or mechanical steering are costly and heavy for drones. In contrast, pattern-reconfigurable technology features fast response, light weight, and low cost, making it more suitable for drone platforms.

Most existing pattern-reconfigurable antennas focus on increasing the number of states or achieving multi-parameter reconfigurability, whereas MWPT scenarios emphasize gain characteristics in each state. Furthermore, rectifying circuits are sensitive to input power; efficiency drops sharply when deviating from the optimal point. Studies [2]-[5] proposed wide-input-power rectifiers, but their power levels are mostly below the watt level, insufficient for drone needs.Meanwhile, a single rectenna provides limited DC output, requiring large arrays [6], [7], but these arrays have fixed beams and cannot solve the beam alignment problem during dynamic flight.

To address these issues, this paper proposes a beam-reconfigurable rectenna array design. First, a pattern-reconfigurable antenna with beam-steering capability and high gain (controlled by PIN diodes) and a watt-level rectifier based on an impedance compression network are designed. Then, an integrated rectenna element and array are constructed. Finally, a prototype is fabricated and tested. Experiments show that when the transmitting and receiving antennas are misaligned, reconfiguring the array beam direction maintains high DC output power, verifying the feasibility and effectiveness of the proposed design.

II. Rectenna Element Design

A. Receiving Antenna Element Design

The detailed structure of the receiving antenna element is shown in Fig. 1.

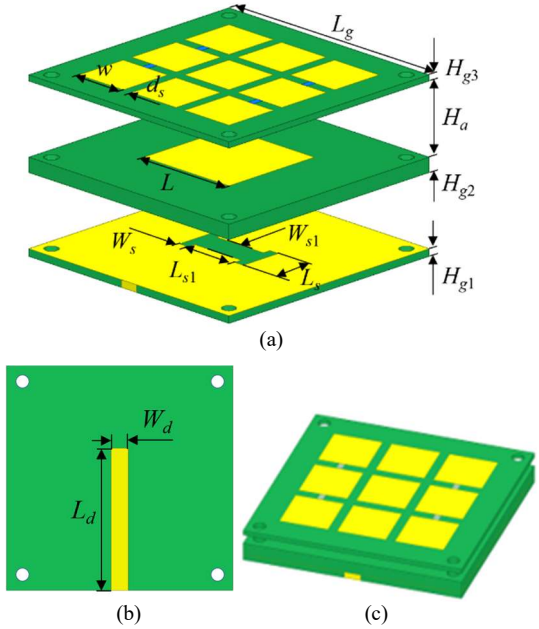


Fig. 1. (a) Overall structure, (b) Feeder line, (c) Antenna model.

As shown in Fig. 1, the receiving antenna consists of three layers: the parasitic layer, air layer, and driven antenna layer from top to bottom. Four mounting holes with a diameter of 2 mm are placed at the corners of the dielectric substrate. The parasitic layer is fabricated on an F4B substrate with a relative permittivity of 3.5 and a loss tangent of 0.0013. It is composed of metal patches, with four SMP-1340-079LF PIN diodes loaded across the patch gaps. In the OFF state, each diode is modeled as a 5 kΩ resistor in parallel with a 0.21 pF capacitor, in series with a 0.7 nH inductor. In the ON state, it is modeled as a 0.85 Ω resistor in series with a 0.7 nH inductor. The driven antenna layer is a slot-coupled microstrip antenna fabricated

on an F4B substrate with a relative permittivity of 2.65 and a loss tangent of 0.0013. The detailed structural parameters are listed in TABLE I.

TABLE I. RECEIVING ANTENNA DIMENSIONS

Parameters	Dimension	Parameters	Dimension
L	15 mm	W_s	3.9 mm
L_g	35.2 mm	L_{s1}	6.2 mm
H_{g1}	1 mm	W_{s1}	1.5 mm
H_{g2}	2 mm	W	7.8 mm
H_{g3}	0.8 mm	d_s	1.5 mm
H_a	1.5 mm	L_d	21.7 mm
L_s	8.2 mm	W_d	2.6 mm

The receiving antenna element has three switch states. In State 1, all PIN diodes are OFF. In State 2, PIN diodes 1 and 2 are ON, while diodes 3 and 4 are OFF. In State 3, PIN diodes 1 and 2 are OFF, while diodes 3 and 4 are ON.

The measured S_{11} results of the pattern-reconfigurable receiving antenna element are shown in Fig. 2.

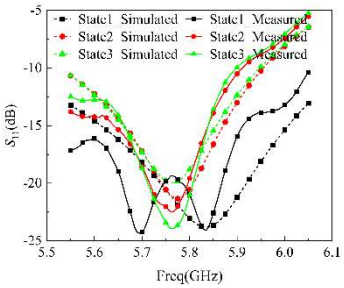


Fig. 2. Measured S_{11} of the receiving antenna element.

As shown in Fig. 2, at the resonant frequency of 5.8 GHz, the measured S_{11} values are −21.04 dB in State 1, −19.6 dB in State 2, and −21.03 dB in State 3.

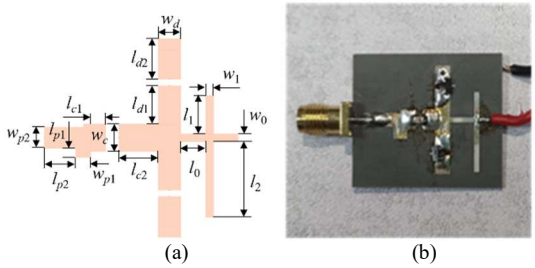
The measured gain and pattern-reconfigurable characteristics of the receiving antenna element are listed in TABLE II. During the measurement, a horn antenna with a gain of 9.4 dBi and an aperture of 55 mm was used as the transmitting antenna. In the H-plane radiation pattern, left beam deflection is defined as negative, while right deflection is defined as positive.

TABLE II. TEST RESULTS OF THE RECEIVING ANTENNA ELEMENT

Position	S_{21}			Gain			Degree	
	State 1	*State 2*	*State 3*	*State 1*	*State 2*	*State 3*	*State 2*	*State 3*
200 mm	-16.44 dB	-16.84 dB	-17.52 dB	7.9 dBi	7.5 dBi	6.8 dBi	20°	-20°
220 mm	-17.31 dB	-18.80 dB	-18.57 dB	7.9 dBi	6.4 dBi	6.6 dBi	20°	-24°
240 mm	-17.62 dB	-19.18 dB	-19.73 dB	8.3 dBi	6.7 dBi	6.2 dBi	20°	-20°
260 mm	-18.51 dB	-20.01 dB	-20.59 dB	8.1 dBi	6.6 dBi	6.0 dBi	20°	-20°
280 mm	-19.34 dB	-20.24 dB	-20.32 dB	7.9 dBi	7.0 dBi	6.9 dBi	20°	-20°

B. *Rectifier Circuit Design*

In a rectifier circuit, the nonlinear characteristics of the rectifier diode cause its input impedance to vary with input power. Once impedance mismatch occurs, the rectification efficiency drops sharply. The structure of the rectifier circuit is shown in Fig. 3, consisting of a matching circuit, a capacitor, a diode, an impedance compression network, and a harmonic suppression network. The circuit uses a Murata capacitor with the model number GQM1875C2E620FB12. Here, an HSMS2822 Schottky diode is used, which features a high reverse breakdown voltage, low turn-on voltage, low parasitic resistance, and fast response speed. The rectifier circuit uses the same F4B dielectric substrate as the antenna element. The specific circuit parameters are listed in TABLE III.



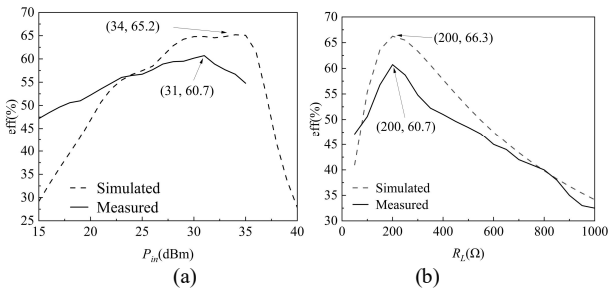
(a) (b)

Fig. 3. (a) Schematic diagram, (b) Fabricated prototype.

TABLE III. RECTIFIER CIRCUIT DIMENSIONS

Parameters	Dimension	Parameters	Dimension
w_{p2}	2.6 mm	l_{d1}	3.8 mm
l_{p2}	5.5 mm	l_{d2}	2.2 mm
w_{p1}	2.6 mm	w_0	1 mm
l_{p1}	1.6 mm	w_1	1 mm
w_c	3.9 mm	l_0	4.4 mm
l_{c1}	1.6 mm	l_1	4.7 mm
l_{c2}	2.3 mm	l_2	9.2 mm
w_d	2.8 mm		

The simulated and measured rectification efficiencies of the rectifier circuit at 5.8 GHz are shown in Fig. 4.



(a) (b)

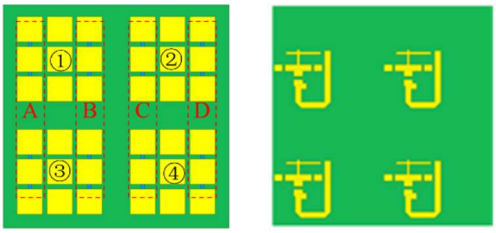
Fig. 4. (a) Rectification efficiency vs. input power, (b) Rectification efficiency vs. load.

As shown in Fig. 4, the optimal input power of the rectifier is 31 dBm, with a peak rectification efficiency of 60.7%. The efficiency remains above 50% over the input power range of 18–35 dBm, and the optimal load is 200 Ω.

III. Rectenna Array Design

A. Rectenna Array Design

The rectifier circuit is placed on the back side of the receiving antenna element at the feed line and connected via a metal bent structure, forming an integrated rectenna unit. The integrated rectenna units are then arranged into a 2×2 rectenna array with an element spacing d_x of 0.3 mm, and each unit is numbered. The PIN diodes in the array are divided into four groups: A, B, C, and D. The array has three states: State 1 – all PIN diodes are off; State 2 – A and C are on, B and D are off; State 3 – A and C are off, B and D are on, as shown in Fig. 5.

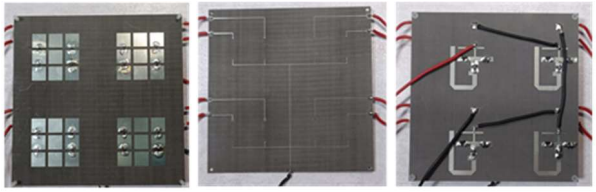


(a) (b)

Fig. 5. (a) Parasitic layer of rectenna array, (b) Rectifier.

B. Experimental Measurement

The fabricated rectenna array is shown in Fig. 6. The DC output terminals of the array elements are connected in series. The overall size is 94.7 mm × 94.7 mm × 5.3 mm.



(a) (b) (c)

Fig. 6. (a) Rectenna element, (b) DC bias circuit, (c) Rectifier.

During the test, the power amplifier output was fixed at 50 W. At a transmission distance of 190 mm, the received power of a single receiving antenna reached 31 dBm, matching the optimal input power of the rectifier prototype. Therefore, the rectenna array was tested at this distance. The DC output power versus load under the three reconfigurable states is shown in Fig. 7. In the H-plane pattern, left beam deflection is defined as negative and right deflection as positive.

As shown in Fig. 7, the rectenna array achieves a maximum DC output power of 1.6 W in State 1 with a load of 2800 Ω, where the beam points to 0°. In State 2, the maximum output power is 1.2 W with a load of 2400 Ω, and the H-plane beam is deflected by 20°. Compared with the case of only rotating the array without bias voltage, the maximum power difference is 0.3 W. In State 3, the maximum output power is 1.3 W with a load of 1800 Ω, and the H-plane beam is deflected by −24°. Compared with the unbiased case, the maximum power difference is 0.5 W.

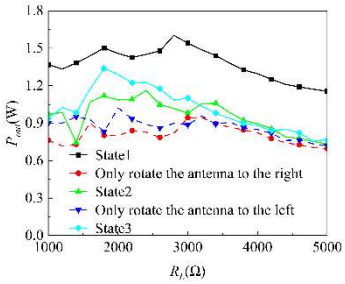


Fig. 7. Experimental results.

IV. Conclusion

This paper proposes a beam-reconfigurable rectenna array for UAV microwave wireless power supply. A receiving antenna element with three reconfigurable states is designed using an independently controlled parasitic layer, enabling H-plane beam directions of 0° and ±20°. A watt-level rectifier based on an impedance compression network is also developed, achieving a peak efficiency of 60.7% at 31 dBm and maintaining over 50% efficiency from 18 dBm to 35 dBm.

A 5.8-GHz beam-reconfigurable rectenna array is then fabricated and tested. The measured results show that the array can steer its H-plane beam to 0° and ±20°, with maximum DC output powers of 1.6 W, 1.3 W, and 1.2 W, respectively. The proposed design can improve power reception under antenna misalignment and provides a feasible solution for UAV microwave wireless power supply.

Acknowledgment

This work was supported in part by the National Natural Science Foundation of China under Grant U2241205 and in part by Shaanxi Provincial Outstanding Youth Science Fund Project under Grant 2025JC-JCQN-025.

References

[1] N. Hasegawa, Y. Nakamoto, T. Fujiwara and Y. Ohta, "Lightweight rectenna array for demonstration of microwave power transfer to flying-objects," 2021 IEEE Asia-Pacific Microwave Conference (APMC), Brisbane, Australia, 2021, pp. 446-448.

[2] M. Yang, Q. Wang, L. Yang and Y. Zhang, "Design of a two-stage rectifier with wide input power range," 2022 International Applied Computational Electromagnetics Society Symposium (ACES-China), Xuzhou, China, 2022, pp. 1-3.

[3] J. Liu, J. F. Chen, J. Y. Li, Z. -X. Du, Y. Liu and X. Q. He, "A broadband rectifier with wide input power dynamic range based on quadrature coupler for rf energy harvesting," in IEEE Transactions on Circuits and Systems II: Express Briefs, vol. 71, no. 9, pp. 4301-4305, Sept. 2024.

[4] Z. Yue, X. Xu, S. H. Wu and X. Q. Lin, "High-efficiency and wide-dynamic-range rectifier based on power reflection for wireless power transfer in sensor networks," in IEEE Journal of Microwaves, vol. 5, no. 3, pp. 666-676, May 2025.

[5] D. -A. Nguyen, K. Woo, G. T. Bui, H. Nam and C. Seo, "Wide dynamic-range and high-efficiency shunt-diode rectifier based on class-r harmonic control and resistance compression network," in IEEE Transactions on Circuits and Systems II: Express Briefs, vol. 71, no. 4, pp. 2359-2363, April 2024.

[6] M. Passafiume, M. Righini, G. Collodi and A. Cidronali, "Low-directivity high-gain rectenna array for improving power-harvesting efficiency on 5.8 ghz batteryless transponder," 2022 IEEE/MTT-S International Microwave Symposium - IMS 2022, Denver, CO, USA, 2022, pp. 348-351.

[7] S. Bansal, V. K. Malav and A. Sharma, "Battery-less reconfigurable intelligent surface powered by energy harvesting rectenna array," 2024 IEEE Microwaves, Antennas, and Propagation Conference (MAPCON), Hyderabad, India, 2024, pp. 1-5.

Microwave Beam-Steering using Near-Field Metasurfaces

Maira I. Nabeel, Karu P. Esselle, Khushboo Singh, Purna B. Samal and Dushmantha N. Thalakotuna
School of Electrical and Data Engineering
University of Technology Sydney, NSW, Australia
maira.nabeel@uts.edu, karu.esselle@uts.edu.au, khushboo.singh@uts.edu.au,

***Abstract*—Near-field meta-steering (NFMS) antennas have emerged as an effective class of beam-steering antennas for applications such as wireless communications and high-power microwave systems and, since their first introduction in 2017, have been increasingly extended into the terahertz domain. These antennas have gained significant interest in both academia and industry due to their low profile, ease of implementation, and excellent performance. This manuscript presents several emerging implementations of NFMS antennas in high-power microwave and THz applications. As an example case study, a simple one-dimensional beam-steering antenna system is demonstrated to illustrate the operating principle. The proposed antenna employs a short horn antenna as a base antenna, whose gain is enhanced by 11 dB while the beam is tilted to 19° using a dual-purpose near-field phase transformation metasurface. The proposed design is capable of steering the beam in the azimuth plane from 0° to 360°.**

***Index Terms*—Risley prism, metasteering, metasurface, metalens, metascreen, terahertz, high power microwave, near-field metasteering, phase transformation, phase gradient, phase correction, transmitarray, millimetre-wave, mmW.**

I. Introduction

Modern wireless communication systems place stringent requirements on antenna performance, particularly the need for high gain within tight Size, Weight, and Power (SWaP) limitations [1]. Beam-steering antennas are widely employed in SATCOM, Communication on the Move (COTM), and Communication on the Pause (COTP), defence and military systems, as well as in applications such as target tracking and various Internet of Things (IoT) systems [1].

Beam steering can be mechanical, electronic, or hybrid. Conventional mechanically steered antennas use parabolic dishes or other such fixed-beam antennas and tilt and rotate them using heavy-duty motors, making them bulky and unsuitable for mobile or aerodynamically sensitive platforms. Electronically steered phased arrays offer a planar profile and faster steering, but require a large number (often thousands) of beamformer ICs, which are not readily available for small companies in most countries. Due to their poor RF efficiency at microwave and millimetre-wave (mmW) frequencies, thermal management of dissipated heat across the antenna aperture is challenging. Such ICs are extremely rare at mmW frequencies and are unlikely to be commercially available at sub-terahertz or terahertz frequencies in the foreseeable future.

A recently invented method – generally called Near-Field Phase Transformation (NFPT) – has led to antenna beam-steering solutions that do not suffer from the above-mentioned limitations of electronic and conventional mechanical systems [2]. These systems require only the mechanical rotation of two thin metasurfaces. Their advantages over electronic beam-steering methods are even more convincing at mmW and THz frequencies. Since its introduction in 2017 [2], this method has become popular within a few years and has been adopted by a large number of researchers in academia, industry, and governments to develop new beam-steering antenna solutions. In addition to its original name, it is now known by other names such as Near-Field Meta-Steering (NFMS) and Near-Field Risley Prism method.

A key advantage of NFMS is that it eliminates the need for mechanical tilting. In its original topology, only the rotational motion of two metasurfaces is required to achieve complete 2D beam steering. This allows for the design of compact, high-performance antenna systems in which the overall volume remains fixed during beam steering, as no tilting mechanism is required. NFMS systems can be concealed easily and require low-power stepper motors to rotate the metasurfaces, which are often thin and light. It should be noted that power is required only when rotating the metasurfaces to change the beam direction; when the beam is pointing at a fixed location, no power is consumed. Since NFMS antenna systems incorporate passive metasurfaces, they avoid the challenges associated with active RF components. The metasurfaces are placed in the near field of the base antenna (typically at a sub-wavelength distance from the base antenna), resulting in much lower profile compared to far-field Risley Prism systems, which are many wavelengths tall.

II. Configuration of NFMS Antenna System

A typical NFMS antenna configuration, as shown in Fig. 1, consists of a fixed-beam base antenna with planar one or two metasurfaces placed in its near-field region, usually within a fraction of a wavelength from the base antenna. The metasurfaces transform the near-field phase distribution at the aperture of the base antenna into a desired 2D phase profile. Such a surface is commonly referred to as a phase transformation or phase correction metasurface (PCS).

If the near-field phase of the base antenna is non-uniform, the metasurface can be designed to convert it into a nearly uniform phase distribution, thereby improving the antenna gain. An NFPT metasurface can also introduce a linear phase

979-8-3315-4544-4/26/$31.00 ©2026 IEEE

gradient to the input phase, enabling beam tilting at a desired angle. This type of surface is known as a phase gradient metasurface (PGM).

For base antennas with non-uniform near-field phase, NFPT metasurfaces can correct the phase and add a gradient, either separately or combined (PCS-PGM). If the phase is uniform, only a PGM is needed for beam steering.

A single PGM placed above the base antenna can steer the beam in one dimension (the ϕ-plane) by rotating it about the antenna axis. Using two PGMs enables two-dimensional beam steering in both azimuth (ϕ) and elevation (θ) planes through independent rotation of the metasurfaces.

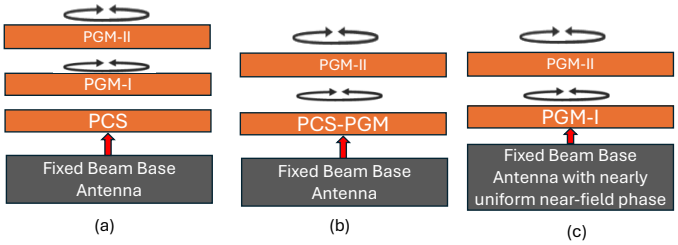


Fig. 1. Near-field meta-steering antenna system topologies. (a) separate phase correction (PCS), and two phase gradient metasurfaces (PGM-I and PGM-II) placed above a base antenna with non-uniform near-field phase distribution, (b) dual-purpose phase correction and phase gradient metasurface combined as one and a separate PGM only, and (c) two PGMs placed above the base antenna with nearly uniform near-field phase distribution.

III. Research and Developments in NFMS

Initially, the concept of Near-field phase correction using an all-dielectric structure was proposed in [3]. Planar metasurfaces were then proposed in [4], to enhance the gain of an antenna system, further decreasing the antenna height. Later, the concept was extended to 1D and 2D beam steering, where [2] presented beam steering of a linearly polarised base antenna within a conical region of $\pm 51^{\circ}$. Since then, significant advancements have been made in the field of NFMS, with the approach being adopted by industry, academia, and defense for designing high-power antennas as well as antennas operating in the terahertz (THz) band.

A. High-Power Microwave Systems Using NFMS

Beam-steering antennas for High Power Microwave (HPM) systems have gained considerable attention due to rapid advancements in HPM technology. Key challenges include stable radiation performance, compact planar structures, and high power-handling capability. Conventional electrical beam-steering methods are not suitable for HPM due to limited power handling, leading high-power systems to rely on bulky mechanical steering with multiple motors. The NFMS concept was demonstrated for HPM beam steering in [5], using all-metal metasurfaces to achieve X-band steering with 4-GW power handling. Another similar Ku-band circularly polarised lens antenna, for beam steering high-power microwave beams, was presented in [6]. The measured peak gain and aperture efficiency of the antenna was 38.1 dBi and 80.5% respectively with steering range of 91.2°. The power handling capability of the antenna is estimated to be 1 GW.

B. Terahertz Focusing Antenna Systems using NFMS

Terahertz antenna systems benefit from the wide bandwidth and high penetration of this frequency range. One such near-field focusing lens antenna was proposed in [7], where beam-steering in a conical region of 72° was achieved at 300 GHz, suitable for applications in 3-D THz imaging. Another NFMS antenna consisting of a rotatable concave and a convex-like lens was presented in [8], with a scanning range of $\pm 50^{\circ}$, and a gain of 20.6 dBi with a wider 3 dB gain bandwidth of $33.5\ \%$. Due to the wider bandwidth, the antenna is suitable for application in automotive radars for intelligent transportation. In addition, other avenues where NFMS antenna systems have been successfully employed include wideband mmW communications, ultra-wide beam scanning ranges and industrial applications [1].

As an example, in this paper, we simulated a $2\lambda_o$ short horn antenna with a near-field metasurface to achieve one-dimensional beam steering and demonstrate the basic working principle of NFMS.

IV. Implementation of a One-Dimensional NFMS Antenna

Fig. 2 shows the configuration of the short horn antenna and the metasurface placed above the antenna aperture. The horn antenna has a conical flare fed by a rectangular waveguide (WR-159) operating in the band of 4.90 GHz to 7.05 GHz. The conical flare has a diameter of $5\lambda_o$ at 5.8 GHz.

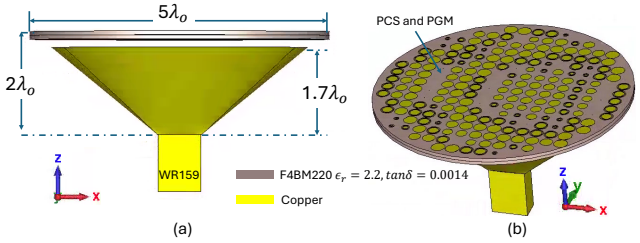


Fig. 2. Configuration of horn antenna with dual-purpose phase correction and phase gradient metasurface placed above the horn antenna. (a) Side view of the antenna system, and (b) perspective view of the antenna system.

The PCS-PGM is placed above the antenna at a spacing of $\lambda_o/6$ from the base antenna. For this steering design, the PGM is implemented using a 4 mm thick F4BM220 ($\epsilon_r = 2.2$, $tan\delta = 0.0014$) substrate with a copper thickness of 0.035μm. The cell used to implement the PGM is shown in Fig. 3. It consists of two types of elements: a simple circular patch on three layers, with identical radius on the outer layers, and a circular patch with a slot on the outer layers, while a patch on the inner layer. A parametric sweep is performed on the radius of the circular patches, and the resulting transmission phase and magnitude are recorded using CST MWS. Cells that provide the required phase response with high transmission magnitude ($|S_{21}| \geq -1$dB) are selected from the database

and placed at the appropriate locations to implement the PCS-PGM.

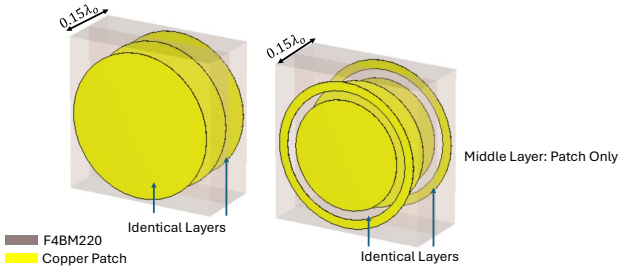


Fig. 3. The two types of cells used to implement the PCS-PGM with circular patches (left) and circular slots and patches (right).

A. Beam Steering Simulation Results

The maximum gain that can be achieved using a $2\lambda_o$ horn antenna is around 16.5 dBi. To further increase the gain, the height of the antenna has to be increased, which is not always possible in height-constrained systems. A short-length horn has a non-uniform near-field phase distribution, which can be converted to a nearly uniform phase distribution, thus enhancing the antenna gain. In our simulated design example, when the combined PCS-PGM is placed above the horn antenna, keeping the combined height of antenna and metasurface constrained to $2\lambda_o$, a gain improvement from 9.35 dBi to 21 dBi is achieved. Furthermore, due to the implementation of an additional linear phase gradient, the beam is tilted to 19 degrees as shown in Fig. 4. By rotating the PCS-PGM

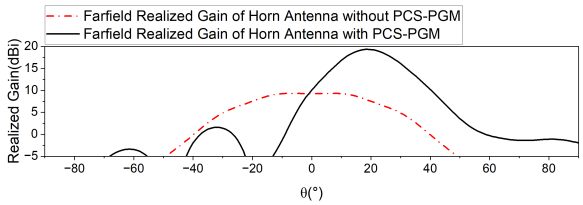


Fig. 4. Farfield realized gain predicted via simulations with and without PCS-PGM.

about its axis in the azimuth plane, one-dimensional beam steering is achieved. This can be extended to 2D beam steering by introducing a second metasurface as shown in Fig. 1(b). The resultant UV-plots for different PCS-PGM orientations are shown in Fig. 5.

V. Conclusion

Near-field Metasteering offers a compact beam-steering solution for various applications. The method is well accepted by both industry and academia, and has been effectively employed to design various antennas. In this paper, we have presented a brief overview of the avenues where the technique has been tested and already implemented to steer the beam of an antenna. We have also presented a new one-dimensional beam steering antenna system. Simulation results indicate a

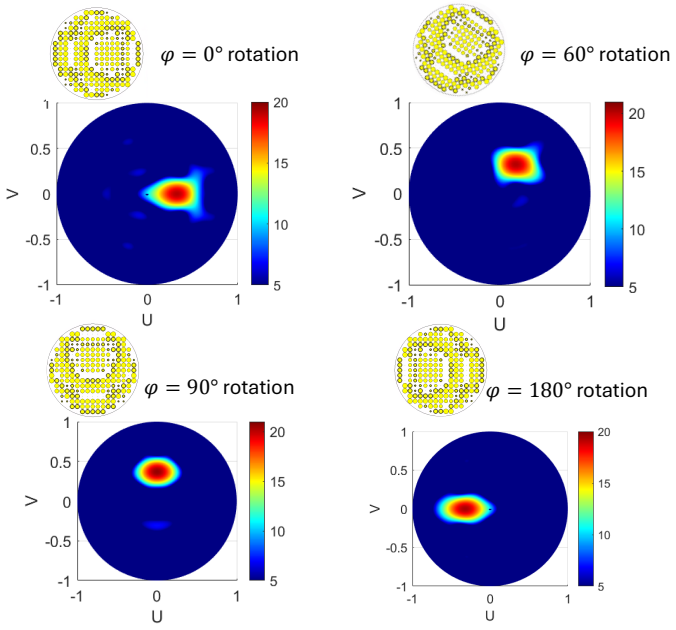


Fig. 5. UV-projections to show one-dimensional beam steering with the rotation of PCS-PGM.

gain enhancement of around 11 dB and tilting the beam to 19° in the elevation plane. The beam can be steered in the azimuth plane from 0° to 360° by rotating the metasurface about its axis.

VI. Acknowledgements

This research was funded by the Australian Government through the Office of National Intelligence.

References

[1] K. Esselle, P. Samal, K. Singh, and D. Thalakotuna, "A method to continuously steer the beam of almost any antenna: A review of the near-field phase transformation or the risley prism," *Authorea Preprints*, 2026.

[2] M. U. Afzal and K. P. Esselle, "Steering the beam of medium-to-high gain antennas using near-field phase transformation," *IEEE Transactions on Antennas and Propagation*, vol. 65, no. 4, pp. 1680–1690, 2017.

[3] M. U. Afzal, K. P. Esselle, and B. A. Zeb, "Dielectric phase-correcting structures for electromagnetic band gap resonator antennas," *IEEE Transactions on Antennas and Propagation*, vol. 63, no. 8, pp. 3390–3399, 2015.

[4] M. U. Afzal and K. P. Esselle, "A low-profile printed planar phase correcting surface to improve directive radiation characteristics of electromagnetic band gap resonator antennas," *IEEE Transactions on Antennas and Propagation*, vol. 64, no. 1, pp. 276–280, 2015.

[5] X. Zhao, C. Yuan, L. Liu, S. Peng, Q. Zhang, L. Yu, and Y. Sun, "All-metal beam steering lens antenna for high power microwave applications," *IEEE Transactions on Antennas and Propagation*, vol. 65, no. 12, pp. 7340–7344, 2017.

[6] Y. Sun, F. Dang, C. Yuan, J. He, Q. Zhang, and X. Zhao, "A beam-steerable lens antenna for ku-band high-power microwave applications," *IEEE Transactions on Antennas and Propagation*, vol. 68, no. 11, pp. 7580–7583, 2020.

[7] G.-B. Wu, Y.-S. Zeng, K. F. Chan, S.-W. Qu, J. Shaw, and C. H. Chan, "3-d printed 3-d near-field focus-scanning lens for terahertz applications," *IEEE Transactions on Antennas and Propagation*, vol. 70, no. 11, pp. 10 007–10 016, 2022.

[8] X.-Y. Zhang, G.-B. Wu, Y.-X. Xie, G.-L. Huang, and S.-Y. Zhu, "A risley-prism based achromatic beam-steering metalens antenna with wide bandwidth," *IEEE Antennas and Wireless Propagation Letters*, 2025.

A Single Substrate Pancharatnam–Berry (PB) phase Huygens' Metasurface for Dynamic Steering of Vortex Beams

Jiechen Wang
School of Electrical and Data, Engineering, Tech Lab
University of Technology Sydney
Sydney, Australia
wjc200627@163.com

Yuxi Hu
School of Mechanical Engineering,
Hebei University of Technology
Tianjin, China
Huyuxi_2024@163.com

Xiaoxuan Guo
School of Electrical and Data, Engineering, Tech Lab
University of Technology Sydney
Sydney, Australia
xiaoxuanguo02@hotmail.com

Yang Yang
School of Electrical and Data, Engineering, Tech Lab
University of Technology Sydney
Sydney, Australia
yang.yang-1@uts.edu.au

***Abstract*-This paper presents a Pancharatnam–Berry (PB) phase metasurface constructed on a single dielectric layer, specifically engineered for the dynamic steering of vortex beams carrying orbital angular momentum (OAM). By capitalizing on the Huygens' resonance mechanism, the proposed metasurface maintains an ultra-thin profile of merely 0.125λ_0 while achieving a minimal transmission loss of -0.29 dB at its operational frequency of 37.4 GHz. Dynamic beam steering across a ±10° range is accomplished through lateral displacement of a left-hand circularly polarized (LHCP) patch antenna feed, yielding vortex beams with high modal purity. This design presents a compact and effective platform for generating controllable vortex waves, holding promise for advanced wireless communication and sensing systems.**

I. Introduction

Multi-beam metasurface provide an effective solution to overcome the size and cost limitations of conventional antenna technologies [1]–[5]. Vortex waves carrying orbital angular momentum (OAM) offer distinct advantages for wireless sensing and communication systems. Specifically, multiple data streams can be multiplexed on the same frequency channel, thereby significantly improving spectral efficiency and channel capacity without requiring additional bandwidth [6]–[8]. However, conventional vortex wave generation techniques suffer from limited mode purity and restricted beam-steering capability. Addressing these challenges, this work introduces a dynamically steerable OAM beam generator founded on a single-substrate PB phase metasurface. The design, rooted in the principles of Huygens' resonance, achieves an ultra-thin form factor of 0.125λ_0 and a high transmission efficiency, characterized by a -0.29 dB loss at 37.4 GHz. High-purity OAM beams with a scanning range of ±10° are obtained by laterally translating an LHCP patch antenna feed.

II. Design and Analysis of the Transmission Unit Cell

The architecture of the proposed single-substrate metasurface element is depicted in Fig. 1. It comprises two metallic layers patterned on opposite sides of a substrate. The top layer, as shown in Fig. 1(b), features a pair of orthogonally oriented rectangular resonators. The bottom layer, illustrated in Fig. 1(c), is configured antisymmetrically relative to the top layer, achieved by rotating the top metallic pattern by 180° around the z-axis. The substrate material is F4B, characterized by a relative permittivity of 2.2 and a loss tangent of 0.001. Its thickness, h, is 1 mm. Key optimized geometrical dimensions include a period p = 4.8 mm, l_1 = 3 mm, w_1 = 0.2 mm, and d_1 = 1.4 mm. The counterclockwise rotation angle of the cross-shaped metal strips is denoted by α.

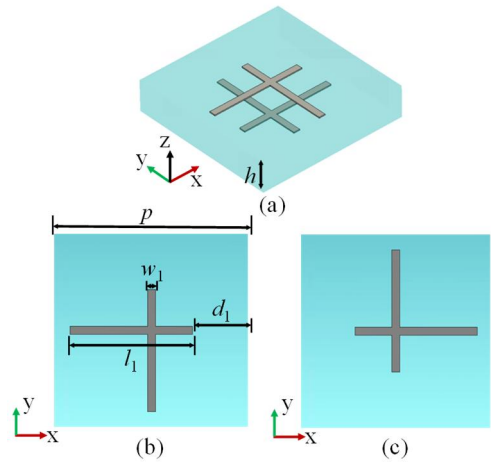


Fig. 1. Schematic of the single-substrate metasurface element. (a) 3-D view of the proposed element. (b) Top view of the proposed element. (c) Bottom view of the proposed element.

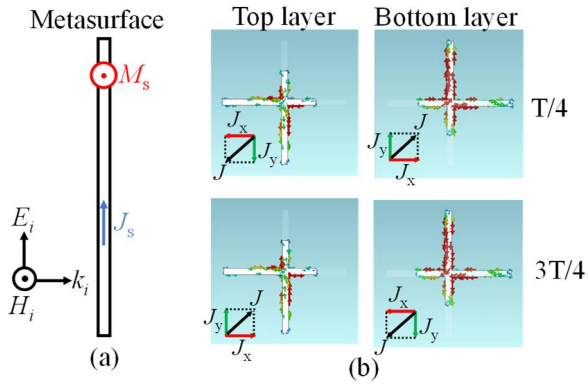


Fig. 2. (a) Field sketch of Huygens' surface. (b) Simulated surface currents of Cross-shaped resonator at the top and bottom layers at 37.4 GHz.

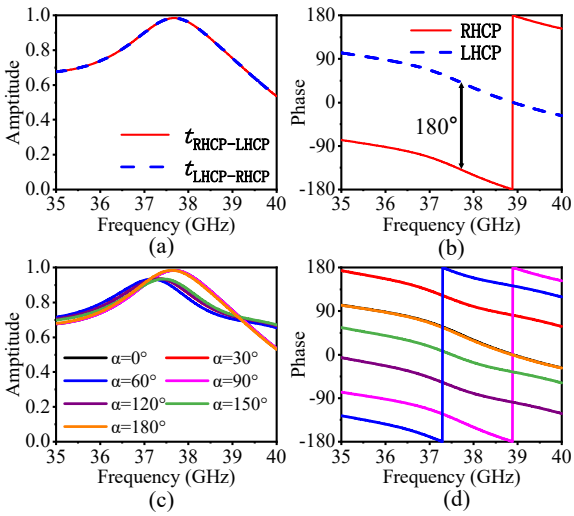


Fig. 3. (a) Transmission coefficients of the metasurface element. (b) Transmission phase under LHCP and RHCP incidence. (c)Simulated RHCP transmission amplitude and (d) phase responses of the element with different rotational angles of α for LHCP incidence.

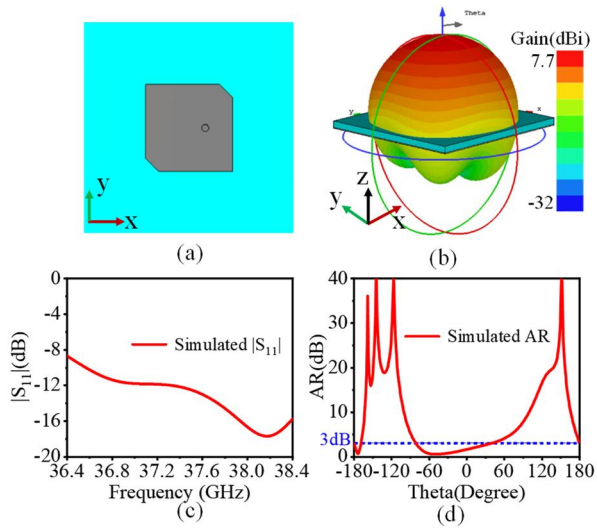


Fig. 4. Performances of the source feed. (a) Schematic of the LHCP microstrip antenna. (b) Simulated realized gain pattern at 37.4 GHz. Simulated (c) $|S_{11}|$ and (d) AR, respectively.

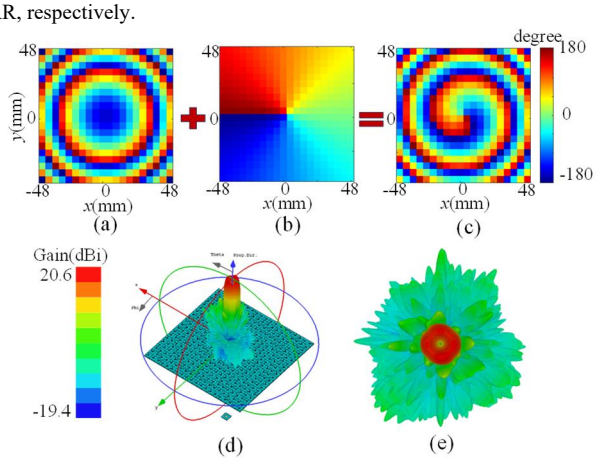


Fig. 5. (a)-(c) Phase distribution and calculation process for generating l = 1 OAM beam at 37.4 GHz. (d) Simulated 3D radiation pattern at 37.4 GHz. (e) Simulated the hollow OAM waves generated by PB phase Huygens' Metasurface under the normal incidence of LHCP plane wave.

A Huygens' metasurface is distinguished by its concurrent support for electric and magnetic dipolar responses, which can be analytically described using equivalent surface electric and magnetic currents (J_s and M_s) [9], [10]. As illustrated in Fig. 2(a), the realization of an efficient Huygens' metasurface relies on the excitation of tangential magnetic currents. Full-wave simulations are conducted to analyze the current distributions. Fig. 2(b) and (c) present the simulated surface currents on the upper and lower metallic resonators at t = T/4 and t = 3T/4 at 37.4 GHz, respectively. Due to the antisymmetric configuration, the upper and lower metallic layers exhibit equal current amplitudes with opposite phase distributions. As a result, the surface currents on both layers, together with the displacement currents in the substrate, form a closed current loop that behaves as a magnetic dipole. Meanwhile, the metallic resonators also support electric dipole moments. The balance between the induced electric and magnetic dipoles leads to the excitation of Huygens' resonance, enabling high transmission efficiency.

For a PB phase element, near-unity transmission efficiency is contingent upon fulfilling two primary criteria: (1) maintaining high transmission amplitudes for both orthogonal polarizations, and (2) securing a 180° phase disparity between the co-polarized transmission coefficients for orthogonal circular polarizations [11]. When these prerequisites are met, a complete 360° phase coverage for the cross-polarized transmitted wave can be conveniently attained by merely rotating the element. Fig. 3(a) and (b) confirm that at 37.4 GHz, the co-polarized transmission phases for LHCP and right-hand circularly polarized (RHCP) incident waves are separated by approximately 180°, all while preserving high transmission magnitudes. Under LHCP illumination, Fig. 3(c) illustrates the transmission amplitude of the converted RHCP wave as the rotation angle α is varied from 0° to 180° in 30° steps. The amplitude at 37.4 GHz remains consistently high, around 0.97. Moreover, Fig. 3(d) demonstrates a linear relationship between the transmission phase and the rotation angle.

III. Application in Metalens Antenna and OAM Wave Generation

A circularly polarized (CP) microstrip patch antenna serves as the feed source for generating the incident LHCP wave, selected for its structural simplicity and minimal footprint. The antenna's geometry is detailed in Fig. 4(a). It consists of a metallic patch, modified with two truncated corners to excite circular polarization, printed on a grounded dielectric substrate. This substrate has a thickness of 0.254 mm, a relative permittivity of 2.2, and a loss tangent of 0.001. The simulated 3D realized gain pattern at 37.4 GHz is presented in Fig. 4(b), while Fig. 4(c) and (d) show the simulated reflection coefficient ($|S_{11}|$) and axial ratio (AR), respectively.

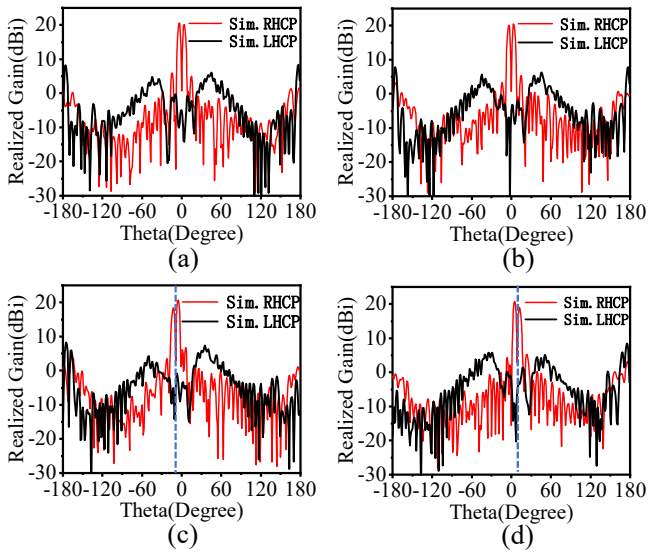


Fig. 6. The simulated 2-D RHCP and LHCP radiation patterns at (a) xoz and (b) yoz plane at 37.4 GHz, respectively. Simulated 2-D RHCP and LHCP radiation patterns at 37.4 GHz in the xoz plane at scan angles of (c) -10 degrees and (d) 10 degrees.

The metasurface itself has an aperture of 96 mm × 96 mm, comprising a 20 × 20 array of the designed unit cells. The focal distance, measured from the phase center of the CP feed to the metasurface's center, is set at F = 76.8 mm. To generate an OAM-carrying beam, the metasurface must impart a specific phase profile that first compensates for the spherical wavefront emanating from the feed and then superimposes the required azimuthal phase variation. As depicted in Fig. 5(a), the compensating phase distribution, φ_1, is designed to flatten the incident phase front. To create an OAM mode with a topological charge of l = 1, an additional phase term, φ_2, exhibiting a 2π helical progression around the azimuth, is introduced. The ultimate phase pattern applied to the metasurface, shown in Fig. 5(c), is the summation of φ_1 and φ_2, following the process illustrated in Fig. 5(a)-(b). The simulated 3D realized gain pattern for the resulting beam is shown in Fig. 5(d). A top-down view of this radiation pattern, Fig. 5(e), clearly reveals the characteristic donut-shaped intensity profile with a central null, confirming the successful generation of an OAM beam.

A key functionality of this design is the ability to steer the generated OAM beam by laterally displacing the feed antenna. The beam deflection angle, θ, is governed by the geometric relationship between the feed offset distance (d), the focal length (F), and the desired scan angle, as expressed in equation (1).

$$d = F \times \tan\theta \quad (1)$$

Fig. 6(a) and (b) present the simulated RHCP and LHCP radiation patterns in the principal xoz and yoz planes at 37.4 GHz when the feed is centered. A pronounced null along the boresight direction is evident, characteristic of an OAM beam with l=1. The beam-steering capability is demonstrated in Fig. 6(c) and (d), which show the radiation patterns in the xoz plane for feed offsets corresponding to beam deflection angles of -10° and +10°, respectively. Crucially, the deflected vortex beams retain their distinctive donut shape and high mode purity, underscoring the efficacy of this dynamic scanning approach.

IV. Conclusion

A thin and high-efficiency PB-phase metasurface for dynamic vortex beam steering has been presented. By leveraging Huygens' resonance, the unit cell achieves near-unity transmission and full 360° phase coverage through element rotation. A LHCP patch antenna is used as the feed to generate an OAM beam with mode l = 1 and a donut-shaped field distribution. Beam steering up to ±10° is achieved by laterally shifting the feed while maintaining high mode purity. The proposed design provides a compact and flexible platform for OAM-based beam-scanning systems in future high-capacity wireless communication applications.

References

[1] X. Guo, Y. Guo, Y. Luo and Y. Yang, "Full-Space Transmission–Reflection-Integrated Metasurface for Multibeam Generation on Orthogonal Planes," *IEEE Trans. Microw. Theory Techn.*, vol. 73, no. 10, pp. 8199-8209, Oct. 2025.

[2] X. Guo and Y. Yang, "Polarization-Multiplexed Metasurface for Dynamic Reconfiguration Between Orbital Angular Momentum and Focusing Beams," *IEEE Trans. Microw. Theory Techn.*, vol. 74, no. 4, pp. 3163-3173, April 2026.

[3] C. Zhang, Y. Luo, Y. He, N. Yan and K. Ma, "Multibeam Quad-Polarized Transmit-Array Antenna With Arbitrary Radiation Direction for Vehicle Communication via Generalized Phase Superposition," *IEEE Trans. Antennas Propag.*, vol. 73, no. 3, pp. 1414-1425, March 2025.

[4] X. Guo, Y. Luo, Z. N. Chen, N. Yan, W. An and K. Ma, "Multiple Tri-Beam Low Scanning Loss Metasurface Antenna for Wide-Angle Coverage by Superposing Focusing and Periodic Phases," *IEEE Trans. Microw. Theory Techn.*, vol. 71, no. 8, pp. 3466-3478, Aug. 2023.

[5] X. Guo, Y. Luo, N. Yan, W. An and K. Ma, "Multibeam Transmit-Reflect-Array Antenna Using Alternating Transmission and Reflection Elements for Space–Air–Ground–Sea Integrated Network," *IEEE Trans. Antennas Propag.*, vol. 71, no. 11, pp. 8668-8676, Nov. 2023.

[6] W. Geng, Q. Guo, J. Su and Z. Li, "Dartboard Metasurface for RCS Reduction and OAM Wave Generation," *IEEE Trans. Antennas Propag.*, vol. 73, no. 4, pp. 2497-2509, April 2025.

[7] F. Qin, X. Cao, C. Gu, J. Bi, S. Gao and W. Cheng, "Mode Conversion of Multimode OAM Waves Based on Transmitted Metasurface," *IEEE Antennas Wireless Propag. Lett.*, vol. 23, no. 12, pp. 4373-4377, Dec. 2024.

[8] X. Guo and Y. Yang, "Low-Profile Full-Space Transmission-Reflection-Integrated Multiple Focused and OAM Beams Metasurface for Indoor Communication," *IEEE Trans. Microw. Theory Techn.*, vol. 73, no. 6, pp. 3644-3654, June 2025.

[9] C. Xue, Q. Lou and Z. N. Chen, "Broadband Double-Layered Huygens' Metasurface Lens Antenna for 5G Millimeter-Wave Systems," *IEEE Trans. Antennas Propag.*, vol. 68, no. 3, pp. 1468-1476, March 2020.

[10] G. Zhai, Y. Chen, S. Wang, J. Gao and J. Ren, "High-Efficiency Wideband Single-Substrate Layer Linear-to-Circular Polarization Converter Based on Huygens' Metasurface," *IEEE Trans. Microw. Theory Techn.*, vol. 73, no. 8, pp. 4689-4698, Aug. 2025.

[11] G. Ding, S. Chen, X. -Y. Luo, S. -Y. Wang and K. Chen, "Ultrathin Single-Substrate Pancharatnam–Berry Phase Metasurface With High Transmission Efficiency," *IEEE Trans. Antennas Propag.*, vol. 71, no. 12, pp. 9571-9580, Dec. 202

Photo-Tunable Chip Scale THz Ring Modulator

Dingxuan Gu[1], Xuecou Tu[1,2*], Yunjie Rui[1], Bingnan Yan[1], Zhanzhang Mai[1], Huilin Zhang[1], Zeyu Xu[1], Cheng Liang[1], Heng Tang[1], Xiaoqing Jia[1,2], Jian Chen[1,3], Lin Kang[1,2] and Peiheng Wu[1,2]
[1]Research Institute of Superconductor Electronics (RISE), School of Electronic Science and Engineering, Nanjing University, Nanjing, Jiangsu 210023, China
[2]Hefei National Laboratory, Hefei 230088, China
[3]Purple Mountain Laboratories, Nanjing, Jiangsu 211111, China
*Corresponding author email: Xuecou Tu (tuxuecou@nju.edu.cn)

Abstract—This paper reports a low-loss on-chip optically tunable terahertz (THz) ring modulator (TRM) based on an all-silicon platform. Optical pumping technology enables the device to achieve active tunable resonant response with a minimum through-insertion loss of just 2 dB, dynamically controlling the coupling state from the overcoupled region to the critical region and then to the undercoupled region. At 458.75 GHz, modulation depth reaches 22.7 dB with an optical control speed exceeding 150 kHz, demonstrating practical value for high-speed switching and modulation. These findings represent a significant step forward in THz photonics by introducing a tunable ring resonator that combines electromagnetic field manipulation, reconfigurable coupling states, and on-chip compatibility, opening opportunities for applications in nonlinear optics, microcavity optics, and photonic integrated circuits (PICs).

I. Introduction

THz waveguides are the important components of integrated microsystems, and the study of waveguide-based micro-ring resonators is of great significance for THz communication technology. Micro-ring resonators have received much attention due to their simple structure, high quality factor, and potential for high-density integration on wafers. Silicon-based micro-ring resonators are well established for silicon photonics applications, including as modulators, multiplexers and so on [1-3]. With the rapidly growing demand for THz PICs, the precise control and dynamic tuning of chip-scale THz signals has emerged as a research hotspot [4-5]. In particular, high-speed dynamic modulation techniques have become increasingly critical for enabling large-capacity data processing. There is an urgent need to explore highly efficient and integration-compatible dynamic modulation techniques tailored for the THz spectrum [6-8].

This paper demonstrates a low-loss on-chip ring resonator with a minimum loss of only 2 dB across a 50 GHz bandwidth (450–500 GHz). By optically exciting carriers in silicon using a 655 nm pump laser, it achieves a modulation depth of 22.7 dB and a bandwidth exceeding 150 kHz, while enabling dynamic control of the coupled state, from overcoupling through critical coupling to undercoupling regions, demonstrating its practical value for high-speed switching and modulation applications.

II. Design and Simulation

A silicon-based ring resonator operating in the 0.45–0.5 THz frequency band, as shown in Figure 1(a). The device consists of a linear bus waveguide coupled to a side-coupled ring resonator, with a coupling gap g = 5 μm and ring radius R = 1940 μm. The waveguide cross-section employs a rectangular ridge structure: a high-resistivity silicon substrate is etched to form a waveguide trench with height h_2 = 140 μm and width W = 210 μm, supported by a substrate layer of thickness h_1 = 60 μm. This design enables TE single-mode propagation within the operating band while effectively suppressing substrate radiation loss. Parameters including W, h_1, and g were optimized through full-wave simulation to ensure the formation of a characteristic overcoupling notch in the transmission spectrum under intrinsic conditions. For a single degenerate mode operating near the angular frequency ω, the steady-state transmission coefficient $T(\omega)$ of the ring resonator is given by equation [9]:

$$T(\omega)=\frac{s_{\text{out}}}{s_{\text{in}}}=1-\frac{K}{i\Delta\omega+\frac{\gamma+K}{2}} \tag{1}$$

where $\Delta\omega=\omega-\omega_0$represents the detuning from the intrinsic resonance frequency ω_0, γ is the intrinsic decay rate of the cavity (which includes material absorption, scattering, etc.), K is the external coupling rate between the bus waveguide and the micro-ring, and s_{in} and s_{out} represent the field amplitudes at the input and output waveguides, $K=\gamma$ represents the critical coupling condition, where interference at the transmission end results in destructive interference. $K>\gamma$ indicates overcoupling, while $K<\gamma$ signifies undercoupling, both conditions involve energy leakage at the transmission end. Calculations indicate that under intrinsic conditions, due to the extremely small transient coupling gap, the resonance peak intensity of the TRM within its operational bandwidth falls below 10 dB, indicating a typical overcoupled state. It also exhibits extremely low through loss (below 2 dB) and low transmission reflection.

979-8-3315-4544-4/26/$31.00 ©2026 IEEE

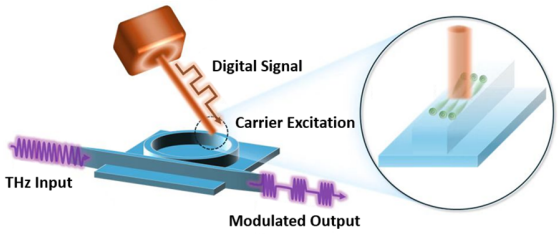


Fig.1. Schematic of the photo-tunable TRM concept. Modulated pump light induces time-varying carriers, outputting terahertz signals carrying modulated information.

At room temperature, silicon possesses a bandgap energy of 1.12 eV. When the energy of incident photons exceeds this bandgap, photo-excited carriers, namely, electron–hole pairs with equal concentrations are generated within the silicon substrate [10]. The concentration of these photo-generated carriers is directly dependent on both the wavelength and power density of the incident pump light. The excitation of electron-hole pairs causes a surge in silicon conductivity, increasing its imaginary refractive index (Imag(n)) and enhancing the absorption effect of THz waves [11].

To study the effect of light irradiation on the coupling state of silicon micro-ring resonators, we calculated the resonant transmission characteristics of silicon micro-rings with varying imaginary parts of the refractive index. Figure 2(a) displays the three-dimensional distribution of transmission amplitude as a function of frequency and Imag(n). It is evident that as the Imag(n) increases from small to large values, the resonance line smoothly transitions from overcoupling to undercoupling. In the small-Imag(n) region, the system exhibits strong coupling characteristics, with the transmission spectrum showing a narrow and shallow dip. At Imag(n) = 0.05, the notch reaches its deepest point, with transmission attenuation falling below -20 dB. At this point, the output is nearly completely suppressed at the resonance frequency, corresponding to the critical coupling condition $K = \gamma$. As the imaginary part of the refractive index increases further, the notch becomes shallower and the linewidth brodens, indicating the system has transitioned to an undercoupled state. Figures 2(b)(i) to (iii) compare the resonant field distributions under three different coupling states. The loss-induced resonant field exhibits significant energy dissipation, which suppresses reverse coupling energy and limits transmission modulation, thereby enabling port transmission control.

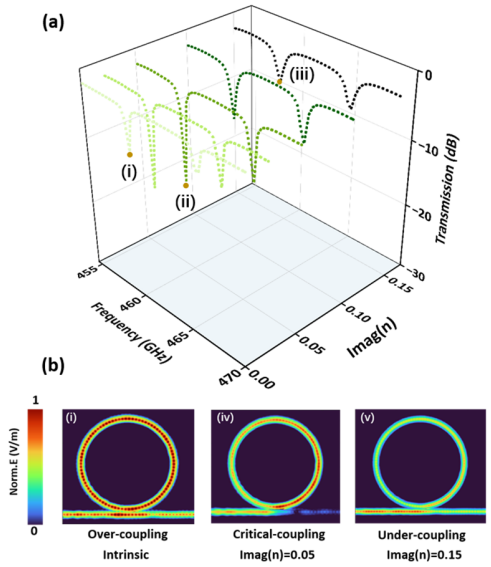


Fig.2. (a) Variation in transmission amplitude of the eigenstate under changes in the imaginary part of silicon's effective refractive index (Imag(n) = 0, 0.02, 0.05, 0.1, 0.15), with critical coupling achieved when the loss imaginary part is 0.05. (b) Resonant field distribution under three coupling states (i)–(iii).

III. Fabrication and Measurement.

The TRM chip was fabricated using a 4-inch commercial high-resistance silicon wafer (HR-Si, ρ > 10,000 Ω·cm) with a thickness of 200 μm. MEMS technology was employed to perform photolithography and deep etching on the wafer. Photoresist was spin-coated onto the wafer surface, followed by exposure to pattern the waveguide. Deep silicon etching was then conducted using an inductively coupled plasma (ICP) etching system, achieving an etch depth of 140 micrometers. Subsequently, photolithography and deep silicon etching were performed on the sample's backside to separate the device from the wafer substrate.

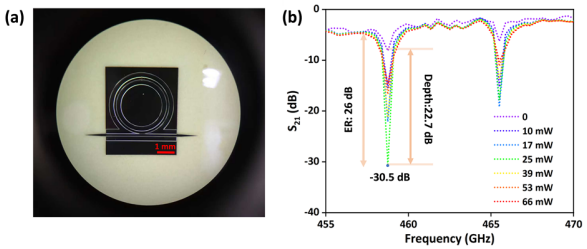


Fig.3. (a) Schematic optical micrograph of the TRM chip. (b) The measured transmission spectrum of the TRM chip was measured under laser power pumping ranging from 0 to 66 mW, achieving state switching and a modulation depth of 22.7 dB.

To verify the optical response characteristics of the chip, a continuous-wave laser with a wavelength of 655 nm was precisely focused onto one end of the ring waveguide, away from the bus waveguide, with a spot diameter of approximately 0.9 mm. Simultaneously, the packaged chip was connected to a vector network analyzer extension module for scattering parameter measurements. Figure 3(b) presents the measured transmission spectra as a function of pump power. The pump

laser excites the intrinsic silicon carriers, inducing controllable loss in the micro-ring waveguide. In an over-coupled resonator design, the resonance strength initially increases with the photodisintegration. At a pump power of 25 mW, the device reaches a critical coupling state, exhibiting a maximum resonance dip of 30.5 dB and an extinction ratio (ER) of 26 dB at a frequency of 458.75 GHz—corresponding to optimal filtering performance. As pump power further increases, the resonance effect gradually diminishes, transitioning the chip into an undercoupled state. Notably, the insertion loss introduced during modulation is extremely low. Even at the maximum pump power of 66 mW, the additional loss transmitted through the through port is only approximately 0.5 dB. It indicates that the depth of the dynamic modulation reaches 22.7 dB, demonstrating the application potential of light-controlled TRM chips for achieving THz communications.

IV. Response Rate Characterization

To demonstrate the performance of this TRM, we constructed a high-speed terahertz modulation test setup. A continuous-wave THz signal was generated by inputting the RF source into a cascaded frequency multiplier chain, which was then transmitted to the chip. A 655 nm laser source was configured, with a 50% duty cycle TTL modulation signal applied to the laser. In this setup, a high-level TTL signal (logic "1", >2.3V) activates the laser, while a low-level signal (logic "0", <0.7V) deactivates it. The modulated laser beam is precisely aligned with the ring waveguide on the chip. The final output is a THz wave carrying an amplitude-modulated (AM) envelope corresponding to the TTL signal. A Schottky barrier diode (SBD) is employed as the detector to capture this modulated THz signal, as shown in Fig 4(a).

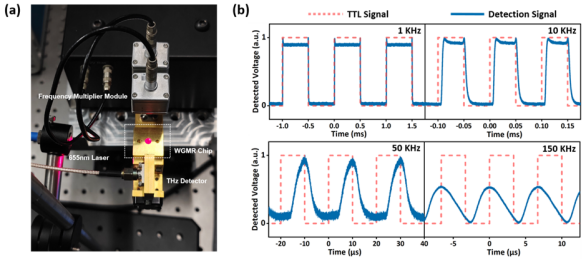


Fig.4. Terahertz amplitude modulation test results: (a) Overall experimental setup. (b) envelope-detected output waveforms under modulation frequencies of 1, 10, 50 and 150 kHz.

The output waveform is converted into a voltage signal and visualized in real-time via an oscilloscope. Initially, a 1 kHz TTL modulation signal was applied to the laser, with a period significantly longer than the carrier relaxation time. The pump laser power was set to approximately 10 mW. The modulated THz output exhibited an undistorted square-wave envelope, indicating clear and rapid switching transitions, as shown in Figure 4(b). To investigate the upper limit of modulation speed, the TTL signal frequency was incrementally increased. When the frequency reaches 10 kHz, the rising and falling edges of the output waveform gradually become clearly distinguishable. At a modulation frequency of 50 kHz, the laser's on/off cycle matches the characteristic time required for the carrier dynamics to reach equilibrium. Ultimately, fitting the peak amplitude of the envelope voltage yields a 3 dB modulation bandwidth of approximately 156.7 kHz for the chip, limited by the relaxation time of the photogenerated silicon carriers.

V. Conclusion

This work systematically demonstrates an all silicon, chip-scale, optically tunable waveguided THz modulator. The device combines low insertion loss, high modulation depth, and exceptional integration capability. The packaged chip achieves a minimum through-port insertion loss of just 2 dB and a return loss exceeding 15 dB. Within a pump power range of 0 to 66 mW, the chip demonstrates a dynamic modulation range of up to 22.7 dB and a measured 3 dB modulation bandwidth of approximately 156.7 kHz. Our research findings pave the way for developing THz microsystems with unprecedented performance and integration density.

Acknowledgements

The authors acknowledge the support from the National Natural Science Foundation of China (Grant Nos. 62271245), the Excellent Youth Natural Science Foundation of Jiangsu Province (Grant No. BK20240063), Quantum Science and Technology-National Science and Technology Major Project (No. 2021ZD0303401), Synergetic Innovation Center of Quantum Information and Quantum Physics, the Key Lab of Optoelectronic Devices and System with Extreme Performance and Jiangsu Key Laboratory of Advanced Techniques for Manipulating Electromagnetic Waves.

References

[1] Zhao Y., Jang J.K., Beals G.J. et al., "All-optical frequency division on-chip using a single laser," *Nature*, vol. 627, pp. 546–552, 2024.

[2] Sun S., Wang B., Liu K. et al., "Integrated optical frequency division for microwave and mmWave generation," *Nature*, vol. 627, pp. 540–545, 2024.

[3] Tao Z., Wang H., Feng H. et al., "Ultrabroadband on-chip photonics for full-spectrum wireless communications," *Nature*, vol. 645, pp. 80–87, 2025.

[4] Han R., Hu Z., Wang C., Holloway J., Yi X., Kim M. and Mawdesley J., "Filling the Gap: Silicon Terahertz Integrated Circuits Offer Our Best Bet," *IEEE Microw. Mag.*, vol. 20, no. 4, 2019.

[5] Ducournau G., "Silicon photonics targets terahertz region," *Nat. Photon.*, vol. 12, pp. 574–575, 2018.

[6] Zhang Y., Shu H., Guo Y. et al., "Integrated photonics enabling ultra-wideband fibre–wireless communication," *Nature*, pp. 1–8, 2026.

[7] Dechwechprasit P., Tam C. Y., Ako R. T., Boes A., Fumeaux C., Withayachumnanku W., "Terahertz photomodulator on intrinsic silicon platform," in *Proc. 50th Int. Conf. Infrared, Millimeter, and Terahertz Waves (IRMMW-THz)*, pp. 1–2, 2025.

[8] Zeng H., Liang H., Zhang Y. et al., "High-precision digital terahertz phase manipulation within a multichannel field perturbation coding chip," *Nat. Photon.*, vol. 15, pp. 751–757, 2021.

[9] Suh W., Wang Z. and Fan S. H., "Temporal coupled-mode theory and the presence of non-orthogonal modes in lossless multimode cavities," *IEEE J. Quantum Electron.*, vol. 40, pp. 1511–1518, 2004.

[10] Ulbricht R., Hendry E., Shan J. et al., "Carrier dynamics in semiconductors studied with time-resolved terahertz spectroscopy," *Rev. Mod. Phys.*, vol. 83, pp. 543–586, 2011.

[11] Jiang Z. G., Shams M. I. B., Cheng L.-J., Fay P., Hesler J. L., Tong C. E. and Liu L., "Investigation and demonstration of a WR-4.3 optically controlled waveguide attenuator," *IEEE Trans. Terahertz Sci. Technol.*, vol. 7, no. 1, pp. 20–26, 2017.

A 110-150 GHz OOK Receiver for High-Speed Wireless Communication in 65-nm CMOS

Wangmin Liao[1], Shuang Song[1], Taotao Xu[2], Quan Xue[1], Pei Qin[1*]
[1]*South China University of Technology, Guangzhou, 510641, China*
[2]*Anhui University, Hefei, 230039, China*
[*]qinpei7777@scut.edu.cn

***Abstract*—This paper presents a fully integrated 110–150 GHz on-off keying (OOK) receiver implemented in 65-nm CMOS technology. To enable high-speed transmission despite parasitic limitations in the D-band, the proposed design features a wideband low-noise amplifier (LNA) with parasitic-aware layout optimization, a gain-boosted envelope detector (ED), and a bandwidth-extended baseband amplifier. The LNA achieves a peak gain of 20.3 dB with a 3-dB bandwidth of 40 GHz. The complete receiver occupies an area of 0.49 mm² and consumes 62.6 mW from a 1.2 V supply. At a carrier frequency of 130 GHz, the receiver supports data rates exceeding 25 Gb/s with an energy efficiency of 2.5 pJ/bit.**

***Index Terms*—D-band receiver, on-off keying (OOK), LNA, envelope detector, broadband**

I. Introduction

In recent years, the sub-terahertz (sub-THz) frequency range has garnered considerable attention for high-speed wireless communication due to its abundant spectrum resources, especially in the D-band. Driven by this trend, silicon-based technologies have emerged as ideal choices for D-band transceiver systems, benefiting from their low cost, high integration density, and seamless compatibility with digital baseband circuits [1].

Compared to high-order modulation, non-coherent schemes such as On-Off Keying (OOK) benefit from architectural simplicity. Specifically, OOK eliminates the necessity for complex architectures, carrier synchronization, and high-performance ADC/DAC. Notably, the expansive bandwidth of the D-band effectively compensates for the lower spectral efficiency of OOK, positioning it as a promising solution for energy-efficient and high-speed transmission.

Recent studies have reported high-performance of silicon-based D-band transceiver front-ends and broadband amplifiers. However, to further increase the system data rate, the receiver front-end requires even wider RF bandwidths. This poses significant challenges for high-speed receiver designs, particularly for broadband low-noise amplifiers (LNA). Constrained by parasitic effects, traditional gain-enhancement techniques are difficult to implement efficiently in the D-band. Furthermore, limited transistor model accuracy complicates the design of a broadband frequency response as well in this frequency range.

To address these challenges, this paper presents a fully integrated 110–150 GHz OOK receiver implemented in 65-nm CMOS technology. Fig. 1 illustrates the system architecture of the proposed OOK receiver, which comprises an LNA, an

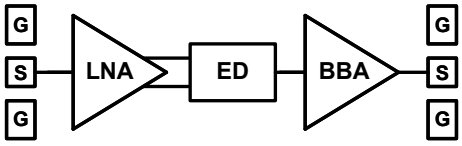


Fig. 1. Block diagram of the proposed receiver.

OOK envelope detector, and a Baseband Amplifier (BBA). Through circuit topology optimization, this work overcomes the broadband matching limitation in the D-band, achieving a flat gain response and high-quality demodulation while maintaining low noise performance, thereby providing a highly energy-efficient solution for short-range high-speed wireless interconnects.

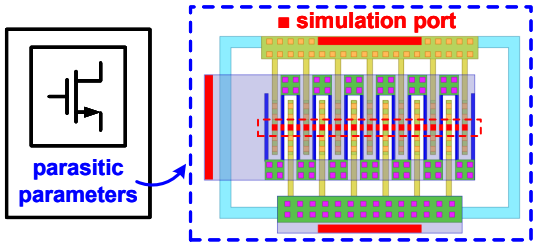


Fig. 2. Block diagram of the proposed receiver.

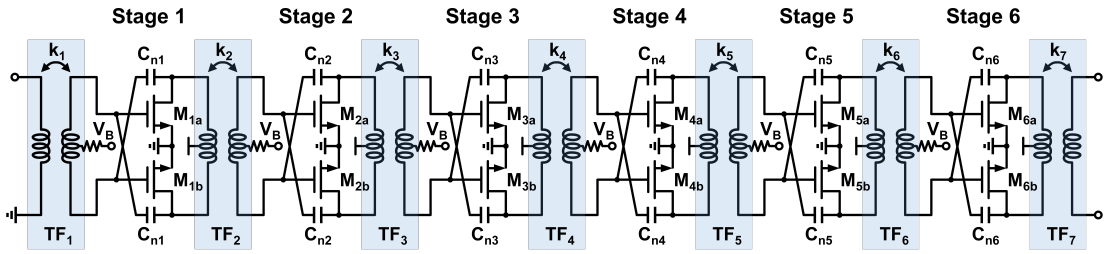
II. Circuit Design And Implementation

A. Wideband Low Noise Amplifier

The schematic of the Wideband LNA is shown in Fig. 3. It comprises six differential common-source (CS) stages. The first stage employs relatively large transistors to achieve an optimal trade-off between noise figure and gain. Considering the relaxed input signal power requirement of the envelope detector (ED), the following five stages utilize smaller transistors to minimize power consumption. Capacitive neutralization is applied in all differential CS stages to enhance both gain and stability. Furthermore, compact coupled transformers are employed for all matching networks. The pole positions of the transimpedance (Z_{21}) in the inter-stage transformers are carefully designed to extend the overall bandwidth.

In the sub-THz frequency range, the parasitic effects of CMOS technology become increasingly significant. Therefore, the layout design of the metal lines and vias surrounding the transistors should be carefully considered. In addition, the

979-8-3315-4544-4/26/$31.00 ©2026 IEEE



M_1	$M_{2\sim6}$	C_{n1}	$C_{n2\sim6}$	k_2	k_3	k_4	k_5	k_6
1um x 16 / 60nm	1um x 12 / 60nm	6.8 fF	5.2 fF	0.44	0.36	0.3	0.4	0.4

Fig. 3. Schematic of the LNA.

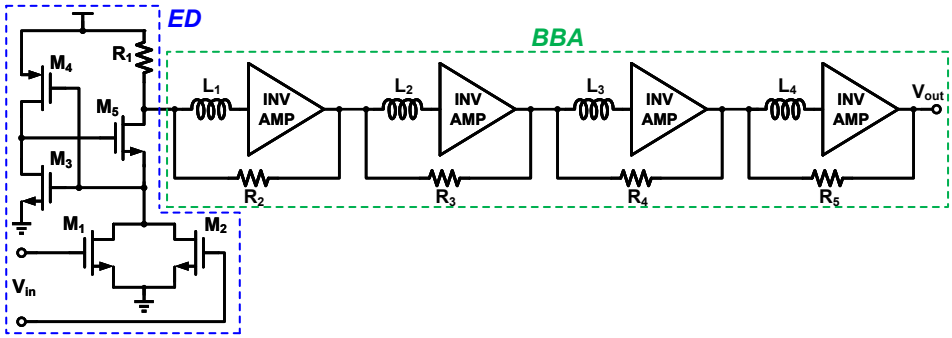


Fig. 4. Schematic of the ED and BBA.

accuracy of the transistor model is also a critical issue. In this work, the transistor layout is optimized to precisely extract the parasitic parameters around the transistor using EMX. As shown in Fig. 2, each gate is connected to the sixth metal layer (M6) through four vias, which reduces the gate resistance and minimizes the overlap area between the lower-level metal and the source/drain regions. Compared with a conventional RF transistor layout, the used layout reduces parasitic resistance and capacitance, resulting in an improvement of approximately 50 GHz in the transistor-gain corner frequency [2].

B. OOK Envelope Detector

The schematic of the proposed OOK ED is shown in Fig. 4. The module employs a source-coupled NMOS differential pair as the main detection unit, integrated with the preceding LNA via a transformer to achieve impedance matching. The differential pair is biased in the subthreshold region, leveraging its nonlinearity for efficient envelope detection. However, while Class-AB biasing provides substantial nonlinearity, the inherently low transconductance g_m limits the conversion gain [3]. Therefore, a gain-boosting technique is implemented to increase the output load impedance Z_L, thereby compensating for the gain loss and improving the circuit sensitivity [4]. Additionally, a current mirror biasing structure is employed to provide precise and robust DC operating points, thereby ensuring the stability against voltage variations.

C. Baseband Amplifier

Fig. 4 illustrates the schematic of the proposed BBA, which consists of four cascaded self-biased inverter stages. The main amplification unit is essentially a current-reuse inverter-based amplifier, employing a feedback resistor connected between the input and output to achieve self-biasing. By optimizing the aspect ratios of the NMOS and PMOS transistors, the DC operating point of each stage is stabilized at approximately $V_{DD}/2$, thereby improving the signal dynamic range without coupling capacitors. Additionally, in order to meet the data rate requirements of the system, series inductive peaking is introduced between stages to extend the high-frequency bandwidth. Furthermore, an open-drain buffer is integrated at the output stage to match the $50\,\Omega$ impedance of the measurement equipment. The DC supply for this buffer is provided through a bias-tee.

III. Simulation Results

Fig. 5 shows the layout of the proposed OOK receiver, which occupies an area of $0.98 \times 0.5\,\mathrm{mm}^2$ including pads. The design consumes 62.6 mW of DC power under a 1.2 V supply. As illustrated in Fig. 6, the LNA achieves a peak gain of 20.3 dB, with a 3-dB bandwidth from 110.3 to 150.8 GHz.

Following demodulation by the ED, the baseband amplifier achieves a gain of 40 dB across a 35-GHz bandwidth. The output signal quality is demonstrated by the eye diagram shown in Fig. 7. At a carrier frequency of 130 GHz, the proposed receiver supports a data rate exceeding 25 Gb/s. The output voltage swing is tunable via the DC supply provided through the bias-tee, reaching a maximum of 1.2 V. The clear eye opening indicates excellent demodulation performance. Furthermore, by varying the bias voltage of the ED, the output

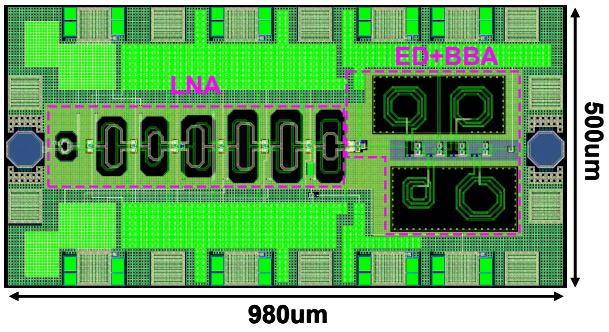


Fig. 5. Layout of the proposed OOK receiver.

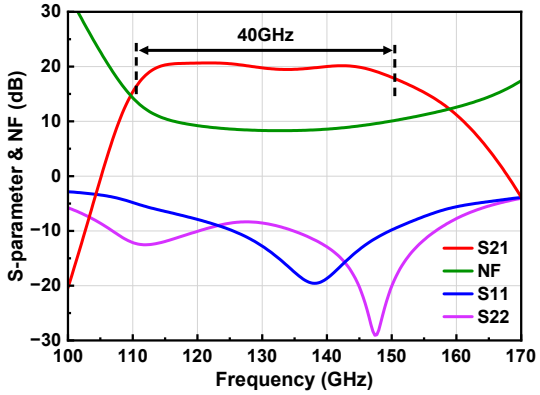


Fig. 6. Simulated results of LNA.

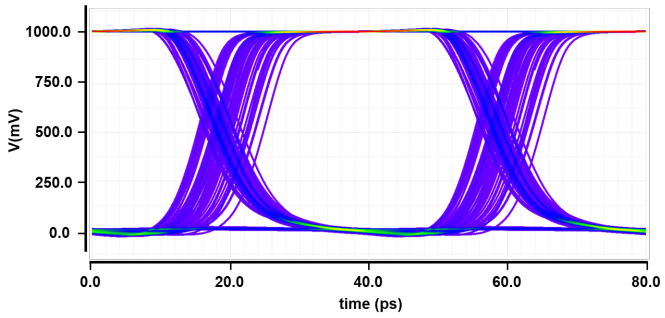


Fig. 7. Simulated eye diagram.

signal can be dynamically optimized, thereby extending the input power dynamic range.

Table I compares the proposed OOK receiver with recently published state-of-the-art designs. Benefiting from the wide bandwidth and high gain of the LNA and BBA, this work achieves a high data rate while maintaining low power consumption and a compact footprint. With a data rate of 25 Gb/s, the proposed design achieved the energy efficiency of 2.5 pJ/bit.

IV. Conclusion

In this paper, a 110–150 GHz OOK receiver implemented in 65-nm CMOS technology is presented, incorporating a parasitic-optimized LNA, a gain-boosted envelope detector, and a bandwidth-extended baseband amplifier to address broadband matching and modeling constraints in the D-band. The proposed LNA achieves a peak gain of 20.3 dB with a 3-dB bandwidth from 110.3 to 150.8 GHz. The receiver occupies an area of 0.49 mm^2, consumes 62.6 mW from a 1.2 V supply, and supports data rates exceeding 25 Gb/s at 130 GHz, resulting in an energy efficiency of 2.5 pJ/bit.

TABLE I
Performance Comparison of D-Band Receivers

Ref.	JSSC 2019 [5]	ESSCIRC 2021 [6]	ASSCC 2023 [7]	JSSC 2025 [3]	This Work*
Tech.	65nm	28nm	28nm	28nm	**65nm**
Freq. (GHz)	127	135	110-160	140	**110-150**
Mod.	PAM4	ASK	OOK	OOK	**OOK**
LNA Gain (dB)	10	35	22	30	**20.3**
LNA BW (GHz)	20	30.6	50	27	**40**
BBA BW (GHz)	N.A.	10.5	35	N.A.	**35**
Data Rate (Gb/s)	20	27	>16	26	**>25**
Power (mW)	79.5	130	160	162	**62.6**

* Post-layout simulation results

Acknowledgement

This work was supported in part by the National Natural Science Foundationof China under Grant U23A20288, 62271210, 62301224, and by the Natural Science Foundation of Guangdong Province under Grant 2023B0303000008, 2024A1515011982. (Corresponding author: Pei Qin)

References

[1] B. Suh, H. Lee, S. Kim, and S. Jeon, "A D-Band Multiplier-Based OOK Transceiver With Supplementary Transistor Modeling in 65-nm Bulk CMOS Technology," *IEEE Access*, vol. 7, pp. 7783–7793, 2019.

[2] C. Wang *et al.*, "24.3 A 236-to-266GHz 4-Element Amplifier-Last Phased-Array Transmitter in 65nm CMOS," in *IEEE Int. Solid-State Circuits Conf. (ISSCC) Dig. Tech. Papers*, Feb. 2024, pp. 415–417.

[3] Q. Peng *et al.*, "A 26-Gb/s 140-GHz OOK CMOS Transmitter and Receiver Chipset for High-Speed Wireless and Dielectric Waveguide Communication," *IEEE J. Solid-State Circuits*, vol. 60, no. 6, pp. 1985–1996, Jun. 2025.

[4] H.-J. Lee *et al.*, "An 20-Gb/s W-Band OOK CMOS Receiver for High-Speed Wireless Interconnect," *IEEE Microw. Wirel. Technol. Lett.*, vol. 26, no. 10, pp. 840–842, Oct. 2016.

[5] Y. Kim *et al.*, "A Millimeter-Wave CMOS Transceiver With Digitally Pre-Distorted PAM-4 Modulation for Contactless Communications," *IEEE J. Solid-State Circuits*, vol. 54, no. 6, pp. 1600–1612, Jun. 2019.

[6] K. Dens *et al.*, "A PAM4 Dielectric Waveguide Link in 28 nm CMOS," in *IEEE 47th Eur. Solid State Circuits Conf. (ESSCIRC)*, Sep. 2021, pp. 479–482.

[7] D. Tang *et al.*, "A 110-160 GHz ASK Receiver with Isomorphic Low Noise Power Amplifier and Multi-Mode Interface in 28-nm CMOS," in *IEEE Asian Solid-State Circuits Conf. (A-SSCC)*, Nov. 2023, pp. 1–3.

A 105 dBΩ High Gain, 1.5 mW Low Power Multi-Stage NRZ CMOS-TIA for Optical Receiver Systems

Umar Mohammad
College of Industry Education Integration
Nanjing Uni. of Posts and Tel. University
Nanjing, China
410682@njupt.edu.cn

Ying Zhang
College of Industry Education Integration
Nanjing Uni. of Posts and Tel. University
Nanjing, China
zhangying@njupt.edu.cn

Yufeng GUO
School of Integrated Circuits
NJUPT,
Nanjing, China
yfguo@njupt.edu.cn

***Abstract*—This work proposes a multistage transimpedance amplifier (TIA) with multiple bandwidth and gain extension techniques. The TIA exhibits a high transimpedance gain of 105 dBΩ, a sensitivity of −8.2 dBm, and a data rate of 20 Gbps for the non-return-to-zero (NRZ) scheme. The demonstrated results validate the proposed TIA for high-speed and low-noise intelligent optical communication systems. Bandwidth extension is achieved through techniques such as parasitic-shunt capacitance splitting and inductive peaking applied across various stages. To maximize gain, the TIA incorporates a single-input-to-differential circuit implemented using a simple RL shunt feedback inverter. Additionally, a differential amplifier followed by a buffer circuit contributes an additional gain of 16 dB. The design achieves an input-referred noise current density of 2.5 pA/$\sqrt{\text{Hz}}$ and consumes a total power of 1.5 mW. The proposed TIA is implemented in a 65-nm TSMC technology node, operating at a nominal supply voltage of 1.2 V. The complete chip, including I/O pads, occupies a compact area of 1 mm^2.**

***Index Terms*—Low Power TIA Design, Optical Receiver Systems, High Gain Transimpedance Amplifier, Single-ended Converter Circuits.**

I. Introduction

In recent years, designers have explored energy-efficient TIAs using CMOS, BiCMOS, SiGe-BiCMOS, and FinFET technology nodes [1], [2]. Past studies have proposed various techniques to optimize CMOS optical receivers, including linear TIAs in BiCMOS [3], linear TIAs in 45-nm SOI CMOS [4], and linear TIAs co-packaged with photodiodes (PD) [5]. Since photodiodes play a critical role in determining the performance of optical receivers, their design for high responsivity, low noise, and higher bandwidth is crucial [6]. While techniques such as CG-TIA, CS-TIA, and other amplifier topologies have addressed some challenges, they often lag in achieving an optimal FoM and trade-offs [7].

This work addresses these challenges by proposing a novel multistage TIA architecture that employs basic common-source structures enhanced with capacitive coupling, shunting, and inductive peaking techniques. The corresponding transistor-level circuit diagram is presented in Fig. 1 of this work.

II. Design Implementation

Fig. 1 shows the proposed TIA architecture and its transistor-level implementation. The design employs a multi-

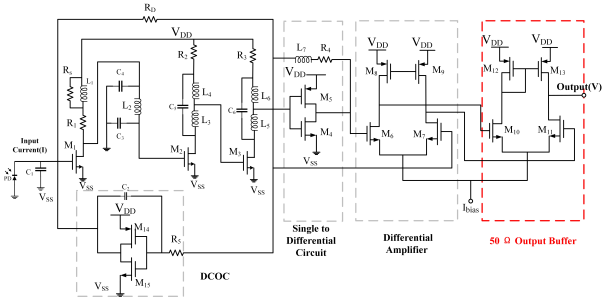


Fig. 1. Proposed multi-stage circuit designed for Optical Receiving Systems.

stage hybrid topology: a shunt-peaked CS input stage for bandwidth extension, followed by a π-filter (L_2, C_3, C_4) for high-frequency noise suppression. The filter components are dimensioned as $L = Z_0/(\pi f_c)$ and $C = 1/(Z_0 \pi f_c)$ based on the target cutoff frequency f_c and first-stage output impedance Z_0. Two cascaded T-coil stages ($L_3 = L_4 = L$) provide inductive peaking for further bandwidth enhancement and integrated ESD protection. A feedback resistor R_D boosts gain, while a DC offset cancellation loop (inverter with Miller capacitor C_{offset} and series resistor R_{offset}) stabilizes the DC operating point. In addition to, Single-to-differential conversion is achieved via a CMOS inverter with inductor L_7 and resistor R_6 in feedback. The signal path concludes with a differential amplifier and output buffer, collectively adding 16 dB gain. The complete TIA achieves 105 dBΩ transimpedance gain to our knowledge, the highest reported to date.

III. Results and Discussion

The proposed circuit is implemented using 65-nm CMOS technology in Cadence Virtuoso. The design integrates an off-chip photodiode with a ground-signal-ground (GSG) bonding structure. The core area of the chip is 1 mm^2, with a total power consumption of 1.5 mW. While the active circuit area occupies a relatively small portion, the capacitors and inductors contribute significantly to the overall area. Notably, the total design area also includes testing pads. Fig. 2 shows the transimpedance gain of the proposed design, showing a remarkable 105 dB gain. This gain represents the performance

of the entire design, not just the TIA block shown in Fig. 1. The post-simulated electrical bandwidth of the circuit is observed to be 12 GHz, which highlights its suitability for high-speed optical communication applications.

The IRN power spectrum is presented in Fig. 3. By optimizing the feedback resistor R_D and incorporating proper techniques, the design significantly mitigates high-frequency noise. The IRN results indicate an average noise level of 2.5 pA/$\sqrt{\text{Hz}}$, particularly demonstrating a reduction at higher frequencies.

Moreover, to evaluate bit-error-rate (BER) and sensitivity, simulations were conducted across various design stages, as shown in Fig. 4. The results demonstrate a BER less than 10^{-12} and a sensitivity of -8 dBm, meeting stringent performance criteria for optical receiver systems. In optical communication systems, the BER is determined using the equation: $p = \frac{QI_{in}}{R}$. Where Q represents the signal-to-noise ratio (SNR) required for the desired BER, I_{in} is the input-referred RMS noise, and R is the photodiode responsivity. For a BER of 10^{-12}, Q is 7. Additionally, critical factors such as junction capacitance C_d influence the receiver's bandwidth, while dark current I_d directly impacts sensitivity.

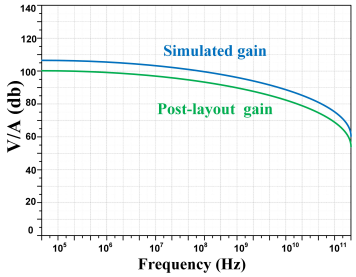


Fig. 2. Transimpedance gain of the proposed design.

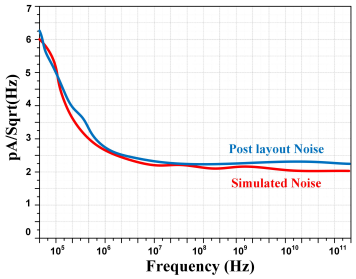


Fig. 3. Input-referred noise of the proposed design.

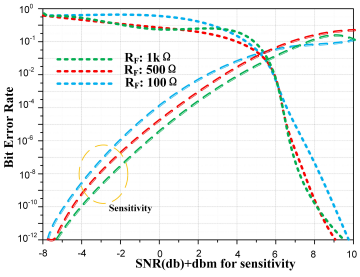


Fig. 4. BER and sensitivity analysis of the proposed design.

Furthermore, process-voltage-temperature (PVT) simulations were carried out to validate key design parameters, including TIA gain, bandwidth, IRN, and power consumption. As shown in Fig. 5, the simulated results align closely with experimental outcomes, confirming the robustness of the design. The power efficiency of the proposed design is inherently by the adoption of multiple peaking techniques and optimized current distribution across cascaded stages. In the first stage, a CS amplifier with M_1 has a transconductance g_m given by: $g_m = 2\pi C_{\text{tot}} \cdot \text{GBW} = 6.28\,\text{mS}$ (assuming $C_{\text{tot}} \approx 50\,\text{fF}$ and $\text{GBW} \approx 20\,\text{GHz}$). Assuming a power-performance tradeoff with $g_m/I_d = 10\,\text{V}^{-1}$, the bias current for this stage is $I_d = g_m/10 = 0.628\,\text{mA}$. With a supply voltage $V_{DD} = 1.2\,\text{V}$, the power consumption at this stage is $P = I_d \times V_{DD} = 0.75\,\text{mW}$. For the second stage, with a single-stage gain of $50\,\text{dB}$ and a $-3\,\text{dB}$ frequency of $15.5\,\text{GHz}$, the transconductance is approximately $9.8\,\text{mS}$, requiring $I_d = 0.98\,\text{mA}$ and consuming $P = 1.18\,\text{mW}$ of power. Through careful current reuse and biasing optimization, the combined first and second stages consume approximately $1.2\,\text{mW}$. Subsequent stages, including inductive peaking, differential amplification, and buffering, are designed with minimal headroom and current scaling, bringing the total power consumption to $1.5\,\text{mW}$. This represents a 70% reduction in incremental power between the first and subsequent stages through optimized transconductance efficiency and supply voltage utilization. Additionally, the proposed design effectively suppresses common-mode noise through single-to-differential (S2D) conversion and careful optimization of the feedback resistor R_D. The combination of noise mitigation and power efficiency ensures optimal system performance.

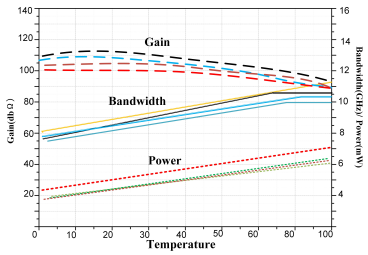


Fig. 5. PVT simulations of the proposed design.

Fig. 6 shows the eye diagram of the proposed design, from which a data rate of 20 Gbps can be observed. The design demonstrates a jitter of 1.2 ps, a critical metric for evaluating signal integrity. Both jitter and BER impact the maximum achievable communication distance. Fig. 6 presents the sharp and wide eye opening of the presented TIA design, indicating minimal jitter and excellent signal quality.

Table II summarizes the key parameters used in the implementation of the proposed design, whereas the chip micrograph of the presented circuit with highlighted inductors and other CMOS realizations is shown in Fig. 7 of this work.

IV. Comparative Results and Study Analysis

Table I presents a state-of-the-art comparison between the proposed work and previously published optical receiver designs. On comparing to the existing works, the proposed work

TABLE I
STATE-OF-THE-ART COMPARISON WITH PREVIOUS WORKS.

Reference	Proposed Work	TCAS-I-2025 [8]	TCAS-1 2023 [9]	JSSC-2023 [10]	IMWTL-1 2025 [11]	JSSC-2019 [12]
Technology	65nm CMOS	90nm biCMOS	45nm CMOS	16nm FinFET	28nm CMOS	28nm CMOS
Supply Voltage-V	1.2	3.3	–	0.9	1.2	–
Z_T Gain	105	75	53	63	66.4	47
Power (mW)	1.5	100	101	47	49	34.6
Bandwidth (GHz)	12	32	27	32	38.8	27
IRN (pA/$\sqrt{\text{Hz}}$)	2.5	5.48	31.1	16.9	16.3	–
Jitter (ps)	1.2	–	1.6	–	–	–
Topology	Hybrid	RC compensation	Hybrid SS-P	Hybrid	Inverter Based-UNT	Hybrid

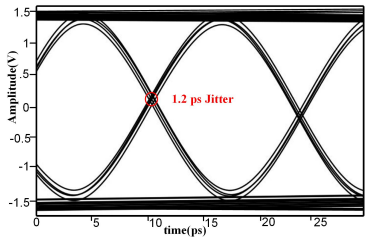


Fig. 6. Eye diagram of the implementation for jitter noise calculation.

TABLE II
DEVICE CONSIDERATIONS FOR THE PROPOSED CIRCUIT.

Circuit Parameters	Values
M_1, M_1, M_3	40/0.1 in W/L(μM)
$M_4 - M_15$	40/2.8 in W/L(μM)
R_D	108 Ω
R_s	10 Ω
$L_1 - L_7$	91.7 pH
General Considerations	$V_{DD}: 1.2V, I_b: 11mA, C_1: 9.4fF$

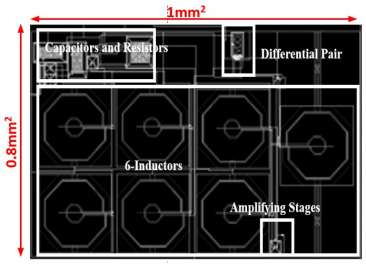


Fig. 7. Chip layout of the proposed design

demonstrates low power consumption, low jitter, and high gain without compromising data rate or bandwidth. The work in [8] delivers a well-performing circuit; however, it falls short in terms of gain and jitter compared to this work. The design presented in [9] achieves lower power consumption but at the cost of reduced bandwidth and higher INR. Additionally, the work in [10] represents one of the most advanced designs in the literature to date; however, it lags behind this work in terms of TIA gain and IRN. Similarly, designs reported in [11], [12] exhibit lower gain and comparatively low performance metrics compared to the proposed circuit shown in Fig. 1 of this work.

V. CONCLUSION

This work successfully addresses the requirements of low-power, low-jitter, and high-gain optical receiver systems for next-generation industrial applications operating at 20 Gbps data rates. Comprehensive testing and verification were conducted for an input supply current range of 10∼300 μA_{pp}, demonstrating the circuit's versatility and stability. The final design achieves a TIA gain of 105 dB, an input-referred noise (IRN) of 2.5 pA/$\sqrt{\text{Hz}}$, and power consumption of 1.5 mW. Furthermore, the bit error rate (BER) is reported to be less than 10^{-12} with a sensitivity of –8.2 dBm, highlighting the circuit's reliability for high-speed optical communications. The total chip area, including testing pads, is 1 mm^2.

REFERENCES

[1] Nakhkoob, B. and Hella, M.M., "A 5-Gb/s noise optimized receiver using a switched TIA for wireless optical communications," *IEEE Trans. Circuits Syst. I, Reg. Papers*, vol. 61, no. 4, pp. 1255-1268, April 2014.
[2] E. Säckinger, "Broadband Circuits for Optical Fiber Communication." Hoboken, NJ: Wiley, 2005.
[3] G. Silva Valdecasa et al., "High-Speed SiGe BiCMOS Detector Enabling a 28 Gbps Quasi-Coherent Optical Receiver," *IEEE Trans. Circuits Syst. II: Exp. Briefs*, vol. 69, no. 3, pp. 964-968, March 2022.
[4] Y. Xie et al., "Low-Noise High-Linearity 56Gb/s PAM-4 Optical Receiver in 45nm SOI CMOS," in *2018 IEEE International Symposium on Circuits and Systems (ISCAS), Florence, Italy*, 2018, pp. 1-4.
[5] D. Patel, A. Sharif-Bakhtiar and T. C. Carusone, "A 112-Gb/s −8.2-dBm Sensitivity 4-PAM Linear TIA in 16-nm CMOS With Co-Packaged Photodiodes," *IEEE J. Solid-State Circuits*, vol. 58, no. 3, pp. 771-784, March 2023.
[6] F. -P. Chouet al., "Silicon Photodiodes in Standard CMOS Technology," *IEEE J. Selected Topics in Quantum Electronics*, vol. 17, no. 3, pp. 730-740, May-June 2011.
[7] B. Razavi, "Design of Integrated Circuits for Optical Communications." New York, NY, USA: McGraw-Hill, 2003.
[8] M. B. Babar and G. W. Roberts, "A Multi-Stage RC Compensation Technique for Decoupling the Transimpedance and BW: Creating High Speed and Low Noise TIA Designs," in *IEEE Transactions on Circuits and Systems I: Regular Papers*, vol. 72, no. 8, pp. 3847-3860, Aug. 2025.
[9] S. Chen et al., "A 50Gb/s CMOS Optical Receiver With Si-Photonics PD for High-Speed Low-Latency Chiplet I/O," *IEEE Trans. Circuits Syst. I, Reg. Papers*, vol. 70, no. 11, pp. 4271-4282, Nov. 2023.
[10] D. Patel, A. Sharif-Bakhtiar and T. C. Carusone, "A 112-Gb/s -8.2-dBm Sensitivity 4-PAM Linear TIA in 16-nm CMOS With Co-Packaged Photodiodes," *IEEE J. Solid-State Circuits*, vol. 58, no. 3, pp. 771-784, March 2023.
[11] Z. Su et al., "A 38-GHz Differential Transimpedance Amplifier With Unbalanced Neutralizing Technique," in *IEEE Microwave and Wireless Technology Letters*, vol. 35, no. 8, pp. 1218-1221, Aug. 2025.
[12] L. Szilagyi et al., "A 53-Gbit/s Optical Receiver Frontend With 0.65 pJ/bit in 28-nm Bulk-CMOS," *IEEE J. Solid-State Circuits*, vol. 54, no. 3, pp. 845-855, March 2019.

An Isolated Ultra-low Power Modulator for OOK/BPSK Backscatter Communication

Luchen Shen
Nanjing University of Science and Technology
Nanjing, 210094, China
The University of Hong Kong
Hong Kong, SAR, China
Luchen.Shen@connect.hku.hk

Hao Zhang
Nanjing University of Science and Technology
Nanjing, 210094, China
State Laboratory of Millimeter Waves
Nanjing, 210096, China
Zhang.Hao@nwpu.edu.cn

***Abstract*—To meet the growing ultra-low power demand in backscatter sensing networks, switching modulation (e.g., OOK/BPSK) is widely adopted. Yet existing backscatter modulators confront the challenges of inherent static power consumption with SPDT switches and signal crosstalk. To address these issues, this paper proposes an ultra-low power modulator employing near-zero static pow$er failsafe SPST switches for backscatter communication supporting OOK and BPSK with the quiescent power lower than 1 µW.**

Keywords—backscatter communication, OOK, BPSK, SPST, SPDT, failsafe logic

I. Introduction

Wireless sensing networks are emerging as a popular application of internet of things (IoT) technology[1,2]. However, the energy constraints of sensor nodes remain a major constraint for large-scale deployment. With the ideas of sustainable 5G and 6G technology recently[3], backscatter communication has the potential to meet the requirement of ultra-low power consumption [4,5].

However, low-power OOK/BPSK backscatter in compact transceivers is still constrained by two circuit-level issues. First, since the backscattered OOK/BPSK signal remains at the carrier frequency, transmitter leakage and the desired modulated signal occupy the same frequency band. This in-band transmit-receive coupling cannot be suppressed by simple schemes and lead to degraded operating range and sensing accuracy [6,7]. Second, conventional load-switching modulators based on SPDT switches introduce static power consumption, which is undesirable for low-duty-cycle sensing nodes.

To mitigate transmit–receive crosstalk, TDD/FDD operation and space–time coding have been widely used to separate or manage simultaneous transmit and receive links [8–10]. In this work, RF-domain signal separation based on a 90° hybrid coupler is adopted as a compact alternative for carrier in-band frequency backscatter operation. However, the power consumption of such architectures is still strongly affected by the RF switches used to control the load states. RF switches used in backscatter modulators are commonly implemented with PIN-diodes, SOI/CMOS, GaAs MMIC, or MEMS technologies [11–16]. Although these technologies offer different tradeoffs among switching speed, insertion loss, isolation, and bias power, their static or control power consumption remains a concern for low-duty-cycle sensing nodes. PIN-diode switches require relatively high drive power, MEMS switches suffer from slow switching and high actuation voltage, and SOI/CMOS switches can introduce insertion loss that degrades the SNR and power efficiency. Commercial GaAs MMIC SPDT switches offer a better RF tradeoff, but still consume approximately 12–28.5 µW in representative implementations.

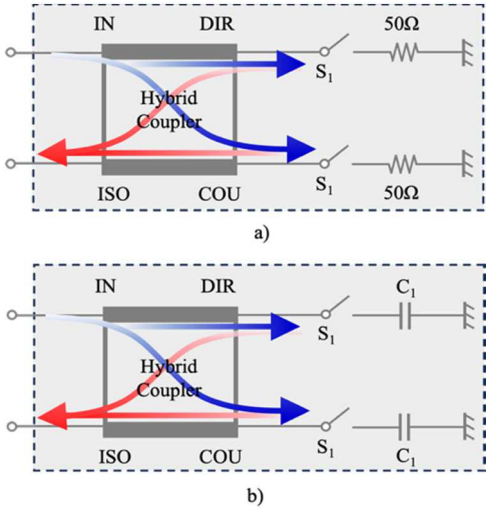


Fig. 1. Overall structure. Schematic diagrams of the proposed OOK/BPSK backscatter modulators based on a 90° hybrid coupler and failsafe SPST switches. (a) OOK modulator with 50-Ω loads. (b) BPSK modulator with capacitive loads C_1.

To address this limitation, this paper proposes a failsafe SPST-based OOK/BPSK modulator. The selected HMC550A GaAs failsafe SPST switch is normally on when unpowered and requires only very low on-state current. By integrating a 90° hybrid coupler with two failsafe SPST switches, the proposed modulator separates the carrier leakage from the modulated output in co-frequency operation and supports both OOK and BPSK modulation. The proposed architecture reduces the static power consumption to below 1 µW while maintaining a modulation isolation is 19.16 dB simulated and providing an isolated and ultra-low-power modulation approach for energy-constrained backscatter sensing nodes.

II. Mechanism

The modulator employs a 90 degree hybrid coupler which provides a balanced interface, and the reflection coherence is dynamically controlled by two SPST switches.

Fig 1a. shows an on-off keying (OOK) modulator with two zero-bias switches (S_1) that consume <1 µW in the shutdown state (e.g., the Analog Devices HMC550AE shutdown quiescent power consumption is 320 nW, since V_{dd}=1.6 V and I=200 mA).

TABLE I. PERFORMANCE COMPARISON OF DIFFERENT SWITCH

No	Type	Tech	Module/Ref.	Switch time	Static Power	Frequency (GHz)	IL(dB)	Isolation(dB)
1	SPDT-T/R	GaAs	HMC546MS8	21ns Rise/fall, 102ns ON, 32 ns OFF	-	0.2 - 2.2	0.4	-
2	SPDT	GaAs	NJG1818K75	200ns typ, 400ns max	~ 28.5uW	1.0-7.125	0.5	25
3	SPDT	GaAs	NJG1512HD3_E	8us typ	~ 12uW	0.1-3	0.6 typ. @f=1.0GHz 1.0dB typ. @f=2.0GHz	44
4	SP4T	MEMS	ADGM1304	75us (ON)	~ 8.25mW Low power mode: ~4mW	DC-14	0.26typ @f=2.5GHz	24 typ @f=2.5GHz
5	SPDT	FDSOI	[11]	-	~0.25mW	DC- 80	2.1 @60 GHz 2.6 @80 GHz	25 (60 GHz) 21 (80 GHz)
6	SPST	Pin	[12]	-	0.2W	3.03 57.8%bw	1.19	29.1
7	SPST	MEMS	[14]	26us/11us	-	10 - 30	<0.35 @DC~21.2GHz	> 30 @17.7~ 21.2GHz
8	SPST	GaAs	HMC550A (used in this work)	20ns Rise/fall, 30 ns Switch	480nW-1uW	DC - 6.0	0.7	25 (DC-2GHz) 12 (DC-6GHz)

When the RF switch is in the off-state (open-circuit condition), the carrier signal at the IN-port of the Hybrid coupler is v_S, which is transmitted through the Hybrid coupler's DIR/COU port[17], which can be calculated as:

$$v_{DIR} = -i\frac{v_S}{\sqrt{2}}; v_{COU} = -\frac{v_S}{\sqrt{2}} \quad (1)$$

When the RF switch (S_1) is turned on at zero bias, the matching load (50Ω) is fully absorbed by the carrier signal, no signal transmission to the Hybrid coupler ISO port. When the RF switch (S1) is turned off, v_S is fully reflected. The Hybrid coupler transmits to the ISO port, and the ISO/IN port has high isolation, which can be calculated as:

$$v_{ISO} = iv_S \quad (2)$$

When the RF switch (S_1) is shut down, S_1 fully reflects the carrier signal v_S and transmits it to the ISO port to meet the needs of on-off keying (OOK) modulation.

Fig. 1b illustrates the proposed BPSK architecture. The two RF switches (S1) toggle simultaneously between an open-circuit ($Z_L=\infty$) and a short-circuit (Z_L=0) state to achieve Binary Phase-Shift Keying (BPSK) modulation:

$$\Gamma = \frac{Z_L - Z_0}{Z_L + Z_0} \quad (3)$$

Therefore, in the on state, two phase-shifting capacitors are turned on, while in off state, v_S is fully reflected and transmitted to the ISO port via the Hybrid coupler, and the ISO/IN port has high isolation calculated as:

$$v_{ISO} = iv_S\Gamma_{C_1} \quad (4)$$

In Equation (4), $\Gamma_{C_1} = e^{j\theta_{C_1}}$ is reflection coherence of C_1, $\theta_{C_1} = -2\,arctan(\omega_0 C_1 Z_0)$ is shifting angle, ω_0 is the operating frequency, and Z_0 is the characteristic impedance (50Ω). The phase shift meets the requirement of the RF switch to phase shift 180° in the on/off state and the parasitic capacitor initial phase shift would not affect the phase shift in modulation.

However, Equation (4) provides a theoretical baseline, further optimization and fine-tuning are essential. This accounts for the insertion loss of the switch and the discrepant parasitic parameters between the turn on/off states.

III. VALIDATION

Based on theoretical analysis, the proposed design is simulated at the operation frequency 2.4 GHz using ADS, with its experimental validation conducted via the VNA-based measurement system shown in Fig. 2. The modulator consists of a hybrid coupler, two HMC550 SPST switches and load. The parameter of hybrid coupler and C_1 is tuned in the simulation. The S-parameter of HMC550 SPST switch at different working condition is given by the producer, so the S-parameter simulation for the modulator can be conducted.

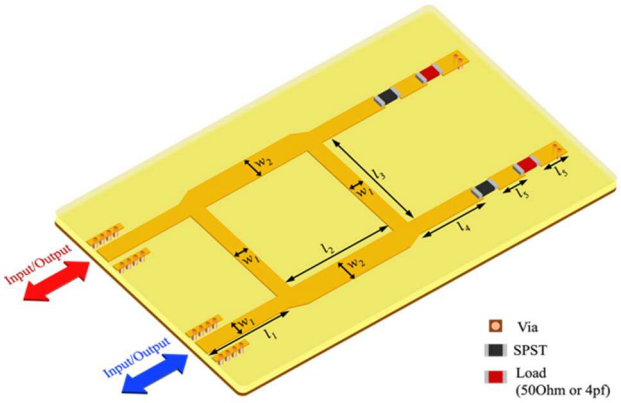


Fig. 2. Overall structure. The load is 50Ohm for OOK and 4pF for BPSK. The parameters are: l_1=17.2mm, l_2=17.48mm, l_3=17.141mm, l_4=17.2mm, l_5=2mm, w_1=1.17mm, w_2=1.873mm, h=0.508mm, Er=3.36.

A. On-off Keying (OOK)

Fig. 3 is the simulation and measurement result of OOK modulator. In On state (V_{dd} = 0, V_{crtl} = 0), signal from IN-port into the modulator is absorbed by the 50Ohm load, the simulated and measured S_{21} values in this state are -19.73 dB and −14.86 dB, respectively; In Off state (V_{dd} = 3V, V_{crtl} = 0), the signal is reflected and routed to the ISO port through the hybrid coupler. The corresponding on/off S_{21} difference, defined as the modulation isolation is 19.16 dB in simulation and 14.29 dB in measurement, it would work effectively in wireless sensing of communication applications.

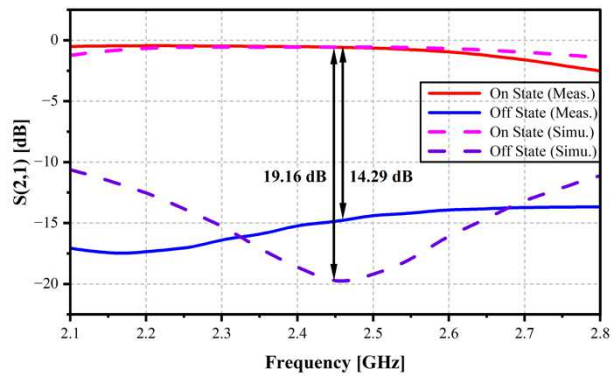


Fig. 3. S-Parameter magnitude of OOK modulator. a) Return loss (S_{11}) in On and Off state. b) S_{21} in On and Off state.

B. On-Binary Phase Shift Keying (BPSK)

Fig. 4 shows the simulation result of BPSK modulator with unwrap phase of reflection signal. In simulation, the phase of reflection signal is -133.15° and 46.90° in On state (V_{dd} = 0, V_{crtl} = 0) and Off state (V_{dd} = 3V, V_{crtl} = 0) individually, and the phase shift is 180.05°; the measured phase (unwrapped) of reflection signal in On and Off state are -68.36° and -241.67° individually, and the phase shift is 173.30°.

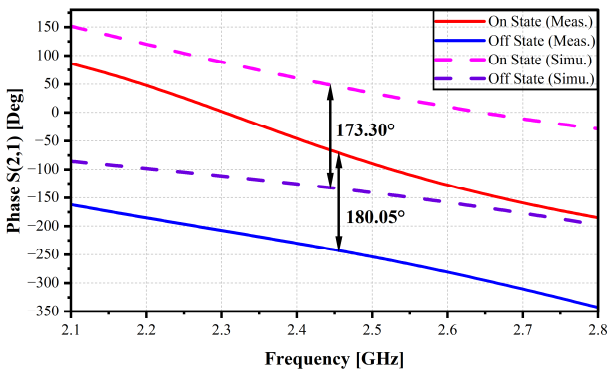


Fig. 4. Measured and simulated S_{21} phase responses in On and Off state of BPSK modulator.

IV. Conclusion

This study proposed an isolated ultra-low power modulator supporting OOK/BPSK. By integrating a hybrid coupler with two failsafe SPST switches, the design achieves a switching time of 20 ns and a static power consumption of less than 1μW. The prototype demonstrates a measured OOK modulation isolation of 14.29 dB at 2.45 GHz, compared with 19.16 dB in simulation. In BPSK mode, a measured phase difference of 173.30° is obtained, close to the simulated value of 180.05°. This work provides a modulation method for energy-constrained IoT applications.

Acknowledgment

This work was supported by the State Laboratory of Millimeter Waves under Grant K202525.

References

[1] J.-P. Niu and G. Y. Li, "An Overview on Backscatter Communications," Journal of Communications and Information Networks, vol. 4, no. 2, pp. 1 - 14, Jun. 2019, doi: 10.23919/jcin.2019.8917868.

[2] V. Talla, M. Buettner, D. Wetherall, and J. R. Smith, "Hybrid analog-digital backscatter platform for high data rate, battery-free sensing," in 2013 IEEE Topical Conference on Wireless Sensors and Sensor Networks (WiSNet), IEEE, Jan. 2013, pp. 1 - 3. doi: 10.1109/wisnet.2013.6488614.

[3] Nidhi and Shamsher Singh, "Green communication in 5G and next-generation networks: A comprehensive research study," International Journal of Science and Research Archive, vol. 16, no. 1, pp. 1854–1865, Jul. 2025, doi: 10.30574/ijsra.2025.16.1.2074.

[4] H. Jeong, N. Ha, A. Georgiadis, M. M. Tentzeris, and S. Kim, "Polarization Diversity and Transfer Learning-Based Modulation Optimization for High-Speed Dual Channel MIMO Backscatter Communication," IEEE Internet of Things Journal, vol. 11, no. 12, pp. 21857-21871, Jun. 2024, doi: 10.1109/jiot.2024.3379854.

[5] J. V. de Almeida, X. Gu, and K. Wu, "SWIPT Base Stations for Battery-Free, Wirelessly Powered IoT Networks: A Review on Architectures, Circuits and Technologies," IEEE Microwave Magazine, vol. 25, no. 6, pp. 22 - 40, Jun. 2024, doi: 10.1109/mmm.2024.3378610.

[6] Z. Wu, L. Li, Y. Xiao, and S. Xie, "A Simple Decoupling Method for Closely-Spaced Circular Patch Antennas," in 2024 IEEE MTT-S International Wireless Symposium (IWS), IEEE, May 2024, pp. 1-3. doi: 10.1109/iws61525.2024.10713804.

[7] J. D. Griffin and G. D. Durgin, "Gains For RF Tags Using Multiple Antennas," IEEE Transactions on Antennas and Propagation, vol. 56, no. 2, pp. 563-570, 2008, doi: 10.1109/tap.2007.915423.

[8] E. Olyaei Torshizi and W. Henkel, "Exploiting FDD Channel Reciprocity for Physical Layer Secret Key Generation in IoT Networks," IEEE Communications Letters, vol. 28, no. 6, pp. 1268-1272, Jun. 2024, doi: 10.1109/lcomm.2024.3388160.

[9] H. Tezuka, M. Moriyama, K. Takizawa, and F. Kojima, "Link-level Performance Evaluation of an ULNOMA system with TDD constructed by hardware," in 2020 IEEE 91st Vehicular Technology Conference (VTC2020-Spring), IEEE, May 2020, pp. 1 - 5. doi: 10.1109/vtc2020-spring48590.2020.9129122.

[10] C. Boyer and S. Roy, "Space Time Coding for Backscatter RFID," IEEE Transactions on Wireless Communications, vol. 12, no. 5, pp. 2272-2280, May 2013, doi: 10.1109/twc.2013.031313.120917.

[11] M. Rack, L. Nyssens, Q. Courte, D. Lederer, and J.-P. Raskin, "Impact of Device Shunt Loss on DC-80 GHz SPDT in 22 nm FD-SOI," in ESSDERC 2021 - IEEE 51st European Solid-State Device Research Conference (ESSDERC), IEEE, Sep. 2021, pp. 195–198. doi: 10.1109/essderc53440.2021.9631835.

[12] H. Wan, J. Xu, H. Zhang, and L. Zhu, "Wideband-Filtering Switches With Ultra-Wide Stopband Using P-I-N Diodes Loaded on Slotline," IEEE Transactions on Circuits and Systems I: Regular Papers, vol. 70, no. 2, pp. 931–939, Feb. 2023, doi: 10.1109/tcsi.2022.3225961.

[13] H. Uda et al., "A very high isolation GaAs SPDT switch IC sealed in an ultra compact plastic package," in GaAs IC Symposium IEEE Gallium Arsenide Integrated Circuit Symposium 17th Annual Technical Digest 1995, IEEE, pp. 132–135. doi: 10.1109/gaas.1995.528978.

[14] H. Wei and W. Han, "A MEMS SPDT Switching Networks Based on High Lifetime MEMS Switch," in 2025 2nd International Conference on Electronic Engineering and Information Systems (EEISS), IEEE, May 2025, pp. 1–5. doi: 10.1109/eeiss65394.2025.11085855.

[15] Wei Hongtao, Gao Xuebang, Wu Hongjiang, Wei Bihua, and Lu Yanan, "W-band GaAs PIN diode SPST switch MMIC," in 2012 International Conference on Computational Problem-Solving (ICCP), IEEE, Oct. 2012, pp. 93–95. doi: 10.1109/iccps.2012.6384329.

[16] C. F. Campbell, "A failsafe high power transmit-receive switch/limiter MMIC," in 2017 IEEE MTT-S International Microwave Symposium (IMS), IEEE, Jun. 2017, pp. 1122–1125. doi: 10.1109/mwsym.2017.8058795.

[17] H. Zhang, S. Gao, W. Wu, and Y.-X. Guo, "Uneven-to-even power distribution for maintaining high efficiency of dual-linearly polarized rectenna," IEEE Microw. Wireless Compon. Lett., vol. 28, no. 12, pp. 1119–1121, Dec. 2018, pp. 1119-1121.

A Compact 24-to-30-GHz GaAs Series Doherty Power Amplifier Using a Three-Coupled-Line Balun

Xin He*, Haoshen Zhu†‡, Dingyuan Zeng†, Zeqi Liu*, Dayan Yuan†, Quan Xue*†
*School of Microelectronics, South China University of Technology, Guangzhou, China
†School of Electronic and Information Engineering, South China University of Technology, Guangzhou, China
‡Email: zhuhs@scut.edu.cn

***Abstract*—This paper presents a millimeter-wave (mm-wave) Doherty power amplifier (PA) monolithic microwave integrated circuit (MMIC) fabricated in a 0.1-μm gallium arsenide (GaAs) process for 5G-NR FR2 applications. To extend bandwidth, a series voltage combining architecture is adopted for output power synthesis. A compact three-coupled-line balun is implemented to realize low-loss differential-to-single-ended combining. In addition, an adaptive bias technique is applied to the peak amplifier output stage to improve AM–AM linearity. The proposed PA operates at 24-30 GHz. Simulation results show a small-signal gain of 13.5 dB and a large-signal gain of 14 dB. The saturated output power is 27.6-28.3 dBm. A peak power-added efficiency (PAE) above 35% is achieved, with PAE exceeding 30% at 6-dB back-off and 25% at 8-dB back-off. The AM–AM distortion is within ±1.2 and the AM–PM variation is less than 18°. The chip area is 2.2 mm × 1.6 mm.**

***Index Terms*—Doherty Power Amplifier (DPA), mm-wave GaAs MMIC, series voltage combining, coupled-line balun.**

I. Introduction

5G-NR has adopted mm-wave bands to provide wider bandwidth, ultra-low latency and higher capacity. However, widely used high-order quadrature amplitude modulation (QAM) and orthogonal frequency division multiplexing (OFDM) lead to a high peak-to-average power ratio (PAPR). Conventional power amplifiers suffer sharp efficiency degradation under deep power back-off (PBO), resulting in higher power consumption, degraded system performance and serious thermal issues.

Among power amplifier architectures designed to enhance back-off efficiency, the Doherty power amplifier (DPA) has become one of the most widely adopted solutions due to its structural simplicity and reliable performance. Compared with silicon-based complementary metal–oxide–semiconductor (CMOS) technology and group III–V gallium nitride (GaN) technology, GaAs exhibits superior electron mobility and a highly mature fabrication process, enabling excellent high-frequency response in the mmWave band. Furthermore, with the deployment of mm-wave 5G massive multiple-input multiple-output (mMIMO) systems, the required output power per power amplifier is significantly reduced due to array-based power combining. This relaxation in power density requirements further enhances the cost-effectiveness of GaAs-based implementations [1].

In recent years, numerous mm-wave MMIC DPAs have been reported, primarily focusing on load modulation strategies, efficiency enhancement, and bandwidth extension [2] [3] [4].

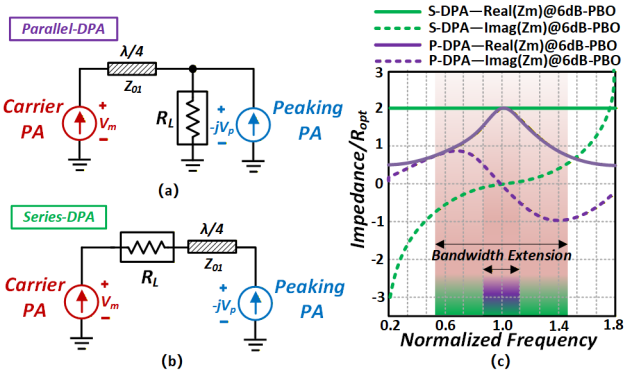


Fig. 1. Basic models of Doherty power amplifiers: (a) parallel current combining type and (b) series voltage combining type, as well as (c) theoretical carrier impedance bandwidth comparison at 6 dB back-off.

Broadband design approaches for MMIC DPAs have largely been based on parallel current-combining architectures, and several wideband design methodologies have been developed accordingly [5] [6] [7]. However, these approaches inevitably introduce additional insertion loss and increased chip area. Although the GaN-based series DPA (S-DPA) architecture was adopted in [8], the inherent bandwidth advantage of the S-DPA was not fully realized. Its performance is only demonstrated within a narrow frequency band of 19–20 GHz, and it occupies a large chip area of approximately 11.1 mm^2.

However, thanks to the multi-layer metal structure in CMOS processes, low-loss transformers can be effectively designed, and existing series DPAs are typically implemented in CMOS. Compound semiconductor processes, with only two metal layers, make it difficult to realize wideband, low-loss baluns. As a result, research on S-DPA in compound processes is extremely limited, and the few existing works have failed to demonstrate the bandwidth and area advantages of the S-DPA. This work, for the first time, combines a three-coupled-line balun with a series DPA featuring adaptive bias, and the designed S-DPA achieves excellent wideband performance and compact size.

II. Circuit Design

A. S-DPA Analysis

The series and parallel DPAs differ only in circuit architecture, while their operating principles are basically the same.

As shown in Fig.1(a), the parallel DPA (P-DPA) has a $\lambda/4$ impedance transformer in the main path. At power back-off, the impedance seen by the main path is $2R_{opt}$. However, when the frequency deviates from the center frequency, the impedance varies drastically, exhibiting narrowband characteristics in load modulation. In contrast, as shown in Fig.1(b), the S-DPA moves the $\lambda/4$ impedance transformer from the main path to the auxiliary path. Its characteristic impedance Z_{01} is set to the optimal load impedance R_{opt} of the peaking PA, and converting the high impedance of the turned-off auxiliary path into a low impedance. Therefore, As shown in Fig.1(c), at 6 dB power back-off, the real part of the drain impedance of the Carrier power amplifier remains constantly equal to $2R_{opt}$, and the frequency response is much flatter than that of the P-DPA.

B. Three-Coupled-Line Balun Design

Since the S-DPA delivers a differential signal to the load, an additional balun is required to convert the differential signal to single-ended. The conventional coupled-line Marchand balun can only achieve a limited coupling coefficient and requires two coupled lines with an electrical length of $\lambda/4$, resulting in a large size. Multi-conductor Marchand balun can extend the operating bandwidth and enhance the coupling coefficient to a certain extent, but multiple coupled lines are not easy to bend and occupy a very large area. Therefore, a three-coupled-line balun is proposed to mitigate the trade-off among operating bandwidth, coupling factor, and chip area occupied by the balun, as shown in Fig.2(a). By means of loading capacitors, the electrical length of the three-coupled-line balun can be effectively compensated. As shown in Fig.2(a) and (c), the adopted three-coupled-line balun exhibits an insertion loss of only approximately 0.6 dB within the 24–30 GHz operating bandwidth under the condition of 6 dB power back-off, where the auxiliary power amplifier is short-circuited and the impedance of the main power amplifier is $2R_{opt}$. Under saturation conditions, the insertion loss of the two branches is also only about 0.7 dB within the same bandwidth, and the phase difference is approximately 180° within a variation of 0.5° across the operating bandwidth.

C. Overall Circuit Design

The complete circuit schematic and layout are shown in Fig. 3. Both the carrier and peaking PAs adopt a two-stage cascade configuration. The final-stage transistors employ a symmetric 6×100 μm. The drain supply inductors $L1$ and $L2$ are used to resonate with the drain-source parasitic capacitance C_{ds} of the transistors. The output balun is a capacitor-loaded three-coupled-line balun, and the auxiliary $\lambda/4$ transmission line is implemented using a T-type equivalent circuit. The final-stage transistor of the auxiliary path adopts a diode-based adaptive bias. Through its rectification effect, the gate voltage is rapidly increased after the transistor is turned on, thereby improving the gain and AM-AM distortion. The detailed principle is elaborated in [9]. The input stage uses a 4×75 μm transistor to drive the power stage, and the gate voltage is adjusted to alleviate AM-PM distortion. A 1:1 Wilkinson power divider and phase-shift line are employed to ensure differential combining when the signal enters the balun.

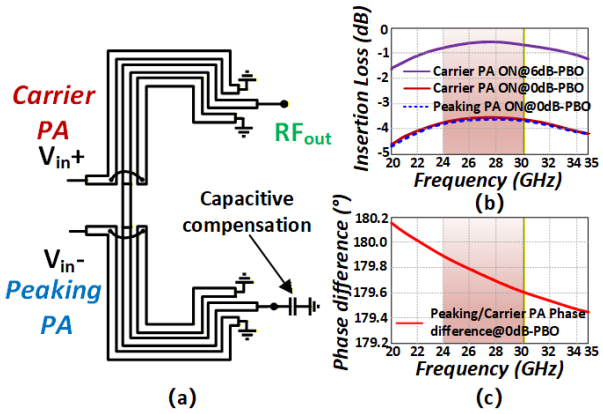


Fig. 2. (a) Layout of the three-coupled-line balun, (b) insertion loss of the balun at 6 dB power back-off and saturation, and (c) phase difference between the two input ports at saturation operation.

III. Simulation Results

The proposed S-DPA based on three-coupled-line balun is implemented using a 0.1-μm GaAs pseudomorphic high electron mobility transistor (pHEMT) process. The total chip area is 2.2×1.6 mm^2. The drain supply voltage V_d and gate voltages V_{g1}-V_{g4} are set to $4V$ and $-0.7V$ / $-0.7V$ / $-1.3V$ / $-1.4V$, respectively, with a quiescent current of $25.8mA$. As shown in Fig.4(a), the S-parameter performance is simulated across small-signal and large-signal operation by sweeping the input power. Within the operating band of 24–30 GHz, the small-signal gain is 13–14 dB, and the power gain is approximately 14–15.3 dB. Both small-signal and large-signal conditions achieve S_{11} < -10 dB, S_{22} < -7 dB, and reverse isolation better than 25 dB. Under large-signal operation, as illustrated in Fig.4(b) and Fig.5(a), at an input power P_{in} =14 dBm, the saturated output power is 27.6–28.3 dBm with a PAE of 35%. At 6/8 dB power back-off, the PAE is 30% / 25%. As shown in Fig. 5(b), due to the adoption of the adaptive bias network, the power gain curve is relatively flat from 24 GHz to 30 GHz. Meanwhile, excellent AM-AM and AM-PM characteristics are maintained over the entire input power range, with gain and phase distortion within ±1.2 dB and 0°-18°, respectively. Table I compares the proposed S-DPA with recently reported state-of-the-art DPAs. The proposed S-DPA achieves the widest operating bandwidth, maintains excellent performance at deep power back-off, and also offers a significant advantage in terms of chip area.

IV. Conclusion

In this paper, a S-DPA MMIC based on a three-coupled-line balun is proposed. In addition, an adaptive bias network is integrated into the auxiliary path, achieving good linearity and a compact layout with a chip area of only 2.2 mm × 1.6 mm. From 24 to 30 GHz, the simulation results show that the gain reaches 14 dB, the saturated output power exceeds

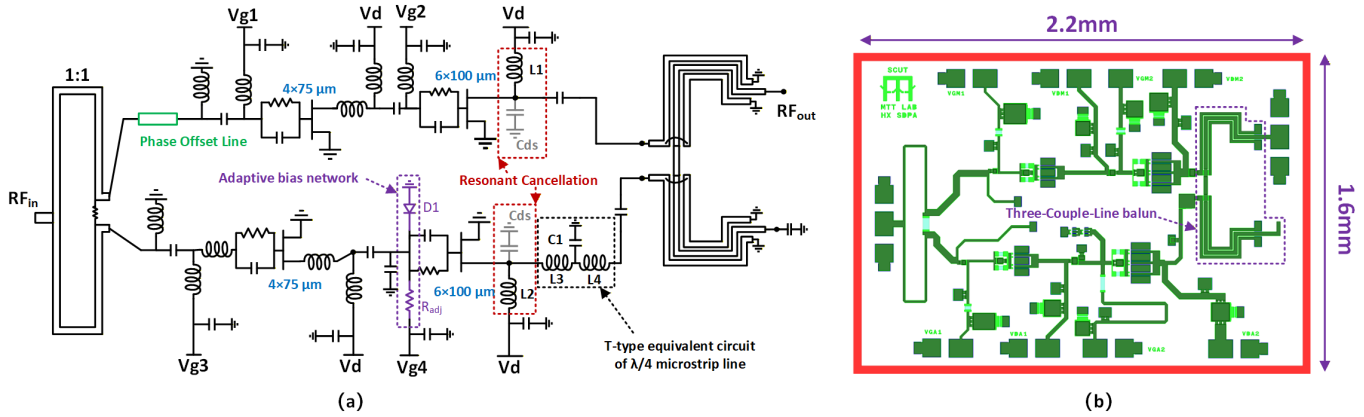


Fig. 3. (a) Schematic and (b) layout of the proposed S-DPA based on the three-coupled-line balun.

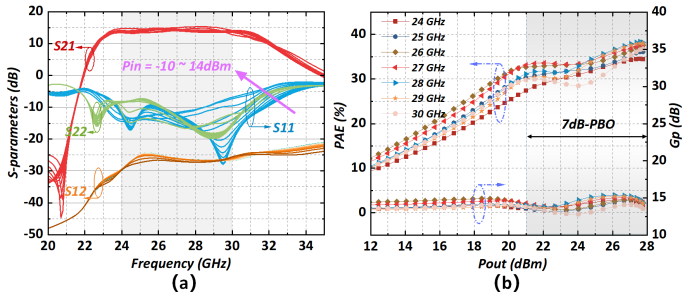


Fig. 4. (a) S-parameters versus input power, and (b) PAE and power gain versus output power under large-signal conditions.

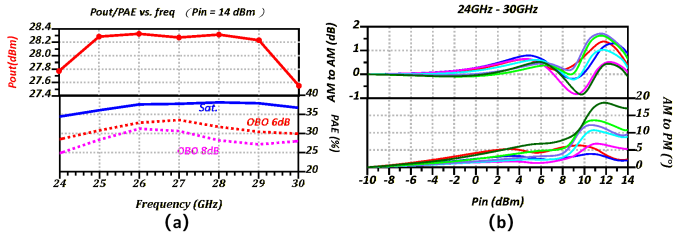


Fig. 5. (a) Output power, saturated PAE, and PAE performance at 6/8 dB power back-off at Pin = 14 dBm. (b) AM-AM distortion and AM-PM distortion.

27.6 dBm, and the PAE is approximately 36%. At 6-dB and 8-dB power back-off, the PAE can still reach 30% and 25%, respectively. The proposed design covers the 5G-NR n257, n258, and n261 bands, demonstrating its potential application merits for mm-wave communications.

TABLE I
PERFORMANCE COMPARISON WITH STATE-OF-THE-ART DPAS

Ref.	Tech. / Topol.	Freq. (GHz)	FBW (%)	Power Gain (dB)	Psat (dBm)	PAE(%) (PBO-0/6/8dB)	Size (mm^2)
[3]	90-nm GaAs P-DPA	26.5-30.5	14	17.7	30	38/30.2/20#	5.8
[7]	100-nm GaN P-DPA	22.5-27.5	20	12	31.1-32.2	23.6-38.8/ 22.8-29/ 20-23.2	6.88
[8]	150-nm GaN S-DPA	19-20	5	14	36	31/24/18#	11.1
[9]	150-nm GaN P-DPA	24-27.5/ 27.5-29	13.6/ 5.3	17.3-19.5/ 15.7-19.1	35.5-36.1/ 34.8-35.4	31.7/24.8/19# 28.6/24.4/16#	5.32
T.W. (Sim.)	100-nm GaAs S-DPA	24-30	22.2	13.5-14.3	27.6-28.3	35/30/25	3.52

#: read from graph.

ACKNOWLEDGMENT

This work is supported in part by the National Natural Science Foundation of China (NSFC) under Grant 62271216, 62271210, and 62321002, and in part by Guangzhou Basic and Applied Basic Research Funding under Grant 2025A0415379.

REFERENCES

[1] W. Chen, G. Lv, X. Liu, D. Wang and F. M. Ghannouchi, "Doherty PAs for 5G Massive MIMO: Energy-Efficient Integrated DPA MMICs for Sub-6-GHz and mm-Wave 5G Massive MIMO Systems," *IEEE Microwave Magazine*, vol. 21, no. 5, pp. 78–93, May 2020

[2] D. P. Nguyen, B. L. Pham and A. -V. Pham, "A Compact Ka-Band Integrated Doherty Amplifier With Reconfigurable Input Network," *IEEE Transactions on Microwave Theory and Techniques*, vol. 67, no. 1, pp. 205–215, Jan. 2019

[3] H. Xie, Y. Fan, W. Y. Li, L. Wang and Y. J. Cheng, "A Ka-Band Watt-Level High-Efficiency Doherty Amplifier MMIC in 90-nm GaAs Technology," *IEEE Microwave and Wireless Technology Letters*, vol. 33, no. 2, pp. 204–207, Feb. 2023

[4] R. Giofrè, A. Piacibello, V. Camarchia and P. Colantonio, "A Two-Way GaN Doherty Amplifier for 5G FR2 With Extended Back-Off Range," *IEEE Microwave and Wireless Technology Letters*, vol. 34, no. 3, pp. 314–317, March 2024

[5] S. Wan, W. Chen, G. Lv, Y. Zhang, X. Shi and Z. Feng, "Broadband GaN MMIC Doherty Power Amplifier Using Compact Short-Circuited Coupler," *IEEE Solid-State Circuits Letters*, vol. 7, pp. 307–310, 2024

[6] J. -H. Feng, T. -Y. Cheng, H. -T. Dong, L. -S. Wu and J. -F. Mao, "A 25-to-34-GHz Doherty Power Amplifier With Reconfigurable Output Network," *IEEE Microwave and Wireless Technology Letters*, vol. 35, no. 9, pp. 1352–1355, Sept. 2025

[7] M. S. Mugisho, C. Friesicke, M. Ayad, T. Maier and R. Quay, "A Ka-Band GaN Doherty Power Amplifier with High Efficiency Over a Fractional Bandwidth of 20.4%," *2025 IEEE International Microwave Symposium (IMS)*, San Francisco, CA, USA, 2025, pp. 651-654

[8] S. De Marzi, S. Furxhi, R. Giofrè, A. Alì and P. Colantonio, "A K-Band GaN MMIC Series-Connected Load Doherty Power Amplifier," *2022 International Workshop on Integrated Nonlinear Microwave and Millimetre-Wave Circuits (INMMiC)*, Cardiff, United Kingdom, pp. 1–3, 2022

[9] R. Liu, L. Qi and A. Zhu, "A Linearity-Improved 24–29-GHz GaN MMIC Doherty Power Amplifier With Reconfigurable Self-Adaptive Peaking Gate Bias Network," *IEEE Transactions on Microwave Theory and Techniques*, vol. 72, no. 12, pp. 6845–6856, Dec. 2024

W-Band Wide-Angle Coverage Pillbox Multibeam Antenna Based on Bifocal Phase Compensation

Yuanxi Cao
School of Information and Communications Engineering
Xi'an Jiaotong University
Xi'an, China
caoyx@xjtu.edu.cn

Cheng Guo
School of Information and Communications Engineering
Xi'an Jiaotong University
Xi'an, China
guocheng@xjtu.edu.cn

Jianxing Li
School of Information and Communications Engineering
Xi'an Jiaotong University
Xi'an, China
jianxingli.china@xjtu.edu.cn

Juan Chen
School of Information and Communications Engineering
Xi'an Jiaotong University
Xi'an, China
chen.juan.0201@mail.xjtu.edu.cn

Sen Yan
School of Information and Communications Engineering
Xi'an Jiaotong University
Xi'an, China
sen.yan@xjtu.edu.cn

***Abstract*—A pillbox beamforming network (BFN) based W-band multibeam antenna is proposed in the paper. The antenna is composed of a BFN, several phase delay lines, and a ridged waveguide (RWG) slot array. The phase delay lines convert the rectangular waveguide output ports of the pillbox BFN to the RWG, thus reducing the element space between the adjacent radiation slots and increasing the beam scanning range. Additional phase compensation is used to optimize the SLL and gain of beams, which is realized by the taper width of the RWG. The simulated results show that the antenna can achieve the beam scanning range of ±45°, and the gain variation of the beam switching is below 2.3 dB.**

Keywords—multibeam antenna, pillbox beamforming network, bifocal, styling, insert

I. Introduction

Multi-beam antennas have garnered extensive attention and deployment in wireless applications, primarily attributable to their economical passive beam-steering capabilities [1]-[5]. In the multibeam design, BFN serves as the pivotal element governing scanning performance. Various BFNs have been explored in prior literature, including quasi-optical lenses[6]-[9] and reflectors [10][12], and transmission line matrices [13]-[15], which have been coupled with diverse radiator arrays and feeding mechanisms to realize distinct radiation patterns. Nevertheless, unlike their active phased-array counterparts [16][17], passive multi-beam configurations lack the agility to dynamically adjust excitation amplitudes at individual radiating elements [18][19]. For the large-angle steered beams, the non-linear output phase gradients from the BFN cannot excite the beam with ideal gain and SLL. The phenomenon makes the multibeam antenna hard to provide the beams with a stable gain coverage range. It should be emphasized that the performance degradation is particularly evident in full-metal waveguide-based antenna designs, due to the fact that the cutoff characteristics make the radiator elements cannot have minor element space, leading to a large grating lobe.

This work was supported by the National Natural Science Foundation of China (No. 62401450) and the Fundamental Research Funds of Shaanxi Key Laboratory of Artificially-Structured Functional Materials and Devices (No. AFMD-KFJJ-24203).

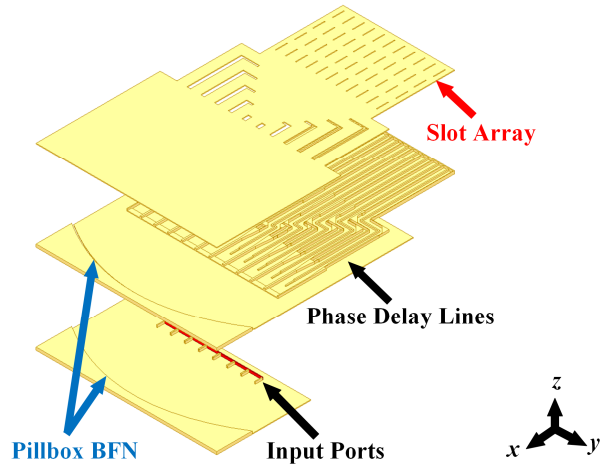


Fig. 1. Exploded view of the proposed antenna.

To address these constraints, several beam-scanning performance-optimized multi-beam antennas are designed and presented. In [20], a dual-source excited Rotman lens multibeam antenna is proposed. The dual-source excited field can achieve taper magnitude distributions, thus the SLL of the steer beams can be suppressed. This amplitude-optimization-based method requires a complex switching matrix for beam control, which will significantly degrade the antenna efficiency at W-band and terahertz frequencies. In [21], the output progressive phase differences among the feeding ports are inverted by the additional phase delay lines, achieving gain equalization. However, the asymmetrical phase delay lines induce amplitude imbalance in the array excitation, thereby hindering effective SLL control under large-angle beam scanning conditions.

Based on the above discussion, a bifocal phase-compensated pillbox multibeam antenna is proposed. The antenna is an air-filled full-metal design, which can achieve a relatively good efficiency in millimeter-wave and terahertz bands compared with the PCB-based designs. To optimize the beam scanning performance of the antenna, the output waveguide ports of the pillbox BFN are gradually tapered to RGW with a minor space between the adjacent channels.

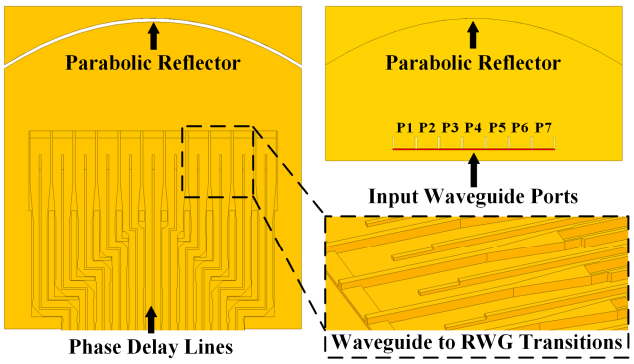


Fig. 2. Schematic diagram of the pillbox BFN and the phase delay lines.

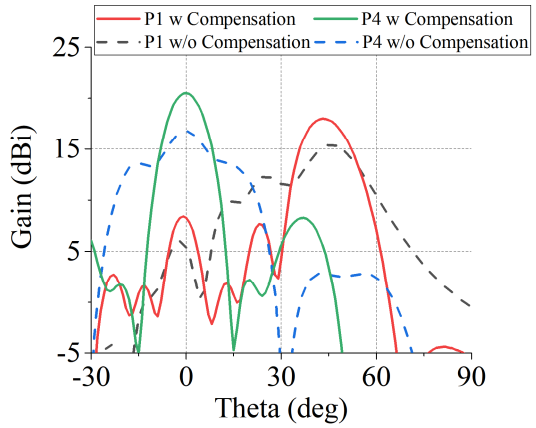


Fig. 3. Radiation patterns with/without phase compensated broadside and steered beams.

Hence, a wider beam scanning angle can be achieved with the same phase gradients.

II. Antenna Design Procedure

The schematic diagram of the proposed antenna is presented in Fig. 1. The antenna can mainly be divided into three components, i.e., a pillbox BFN, phase delay lines, and a slot array. The pillbox BFN is realized by two stacked parallel plate waveguides (PPWs). A cylindrical parabolic reflector is used to transform the field from the source in the bottom PPW to the top PPW. Then, the output waveguide ports of the pillbox BFN are converted to RWGs. Each RWG can provide different phase delays, thus it is able to achieve the bifocal phase compensation. The radiator of the antenna is a 4×11 slot array. The input ports switching of the pillbox BFN can achieve the beam scanning capability in the *y* direction.

A. Design of the Bifocal Phase Compensated Pillbox BFN

The schematic diagram of the pillbox BFN and the phase delay lines are shown in Fig. 2. The diameter and the focal distance of the parabolic reflector are 25.0 mm and 9.5 mm. The sources of the pillbox BFN are opened waveguides, which are located on the focal plane of the parabolic reflector. A parabolic-shaped slot is used to couple the field from the bottom PPW to the top PPW.

It should be emphasized that the output fields excited by defocus sources cannot be linearly distributed. Hence, the steer beams always suffer from the SLL and gain deteriorations. Moreover, the large width (over 0.5λ) of the air-filled output waveguides makes the array inevitably generate a beam with a grating lobe for large-angle scanning. Hence, the output waveguides are converted to RWG and then closely arranged to each other. The width RWG lines are modify optimized to achieve the bifocal phase compensation.

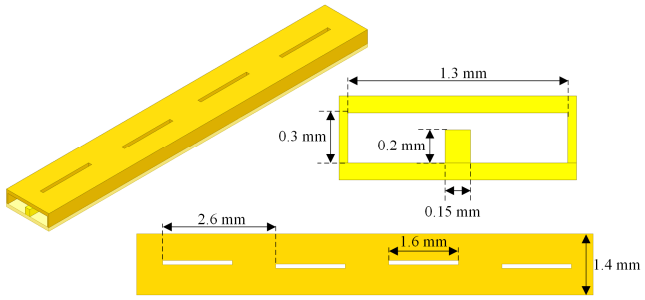


Fig. 4. Schematic diagram of the RWG slot array.

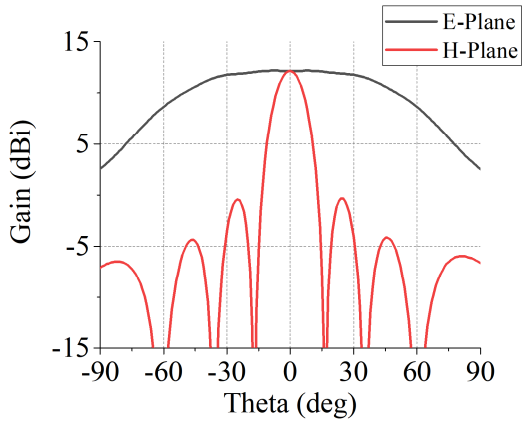


Fig. 5. E- and H-plane radiation pattern of the 1×4 slot array.

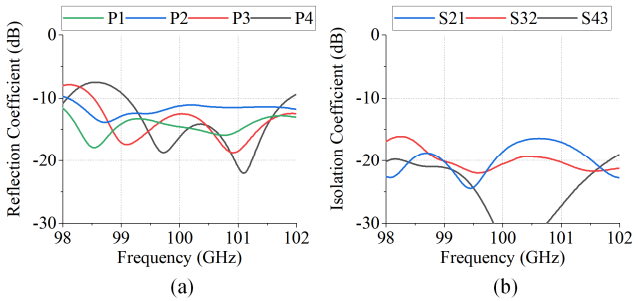


Fig. 6. (a) Reflection coefficients; (b) isolation coefficients of the antenna.

Fig. 3 compares the with/without phase compensation broadside and steered beams excited by P4 and P1. It can be observed that the gain of the beams can be significantly improved, and the SLL of the beams is also suppressed. The results prove the feasibility of the phase compensation technology.

B. Design of the Slot Array

The radiator of the proposed antenna is RWG based slot array, as shown in Fig. 4. Four longitudinal slots are alternately left and right arranged. The distance between the adjacent slots is 0.5 λ_g. The slot arrangement can introduce an additional 180° phase difference between the adjacent slots in the RWG direction, making the array not have a grating lobe in *x* direction.

The radiation patterns of the 1×4 slot array are shown in Fig. 5. The impedance matching bandwidth of the array is 98.3-105.0 GHz. The gain of the slot array is 12.3 dBi. The 3

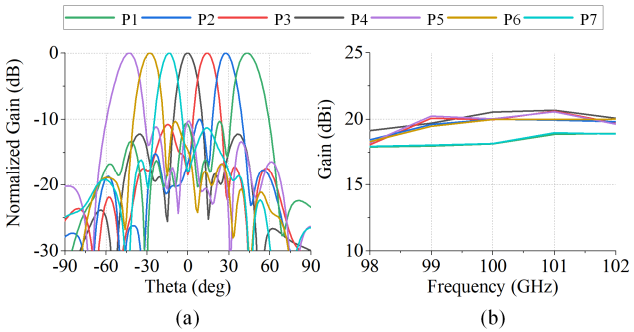


Fig. 7. (a) Normalized radiation patterns; (b) gain of the antenna.

dB beamwidth of the E-plane beam is 112°, which guarantees that the antenna exhibits minimal gain degradation during E-plane beam scanning.

III. Simulated Antenna Performance

To verify the feasibility of the design concept, full-wave simulations are done to present the performance of the antenna. The S-parameters are shown in Fig. 6. Due to its symmetrical structure, only half the results are presented. The -10 dB impedance matching bandwidth is 99.1 to 101.8 GHz. The isolations between the adjacent ports are below -15.9 dB.

The normalized radiation patterns of the antenna are shown in Fig. 7(a), the 7 beams can cover ±45° in the elevation plane. The SLLs of the beams are below -10.1 dB. Fig. 7(b) summarizes the gain of the beams. The maximum value is 20.9 dBi, and the maximum gain variation during the beam switching is 2.3 dB. The results prove that the antenna can achieve a relatively good beam scanning performance.

IV. Conclusion

This paper proposes a W-band multibeam antenna based on a bifocal phase compensated pillbox BFN. The phase delay lines play a key role in expanding the beam scanning range by converting the output ports of the pillbox BFN, while the taper width of the RWG effectively realizes phase compensation to optimize beam performance. Simulations verify that the antenna achieves a beam scanning range of ±45° and a gain variation of no more than 2.3 dB during beam switching. The low-cost beam scanning capability makes the design a feasible and reliable solution for W-band wireless sensing and communication applications.

References

[1] W. Hong et al., "Multibeam antenna technologies for 5G wireless communications," *IEEE Trans. Antennas Propag.,* vol. 65, no. 12, pp. 6231-6249, Dec. 2017.

[2] H. Zhu et al., "Ultrawideband compact magnetoelectric dipole antenna/array with dual-polarization," *IEEE Trans. Antennas Propag.*, vol. 71, no. 5, pp. 4504–4509, May 2023.

[3] J. C. Zhang, J. Yao, and D. P. Tsai, "Meta-lens based on multi-level phase-change," *J. Appl. Phys.*, vol. 136, no. 5, p. 053101, Aug. 2024.

[4] J. C. Zhang et al., "Electromagnetic wave tailoring: From one dimension to multiple dimensions," *Electromagn. Sci.*, vol. 1, no. 3, pp. 1–21, Sep. 2023, Art. no. 0030131.

[5] Y. J. Guo, M. Ansari, R. W. Ziolkowski and N. J. G. Fonseca, "Quasi-optical multi-beam antenna technologies for B5G and 6G mmwave and THz networks: A review," *IEEE Open J. Antennas Propag.,* vol. 2, pp. 807-830, 2021.

[6] X. Guo, Y. Guo, Y. Luo, and Y. Yang, "Full-space transmission–reflection-integrated metasurface for multibeam generation on orthogonal planes," *IEEE Trans. Microw. Theory Techn.*, vol. 73, no. 10, pp. 8199–8209, Oct. 2025.

[7] H. Lu, Z. Liu, J. Liu, G. Wu, Y. Liu, and X. Lv, "Fully metallic anisotropic lens crossover-in-antenna based on parallel plate waveguide loaded with uniform posts," *IEEE Trans. Antennas Propag.*, vol. 68, no. 7, pp. 5061–5070, Jul. 2020.

[8] P. Liu et al., "A novel E-plane-focused cylindrical Luneburg lens loaded with metal grids for sidelobe level reduction," *IEEE Trans. Antennas Propag.*, vol. 68, no. 2, pp. 736–744, Feb. 2020.

[9] X. Guo, Y. Luo, N. Yan, W. An, and K. Ma, "Multibeam transmit-reflect-array antenna using alternating transmission and reflection elements for space–air–ground–sea integrated network," *IEEE Trans. Antennas Propag.*, vol. 71, no. 11, pp. 8668–8676, Nov. 2023.

[10] Y. Cao, S. Yan, S. Wu, and J. Li, "3D printed multi-beam OAM antenna based on quasi-optical beamforming network," *J. Lightw. Technol.*, vol. 41, no. 7, pp. 2196–2204, Apr. 2023.

[11] Y. Cao, S. Yan, and J. Chen, "An SIW pillbox-based compact dual-polarized multibeam antenna with passive 2-D beam scanning capability," *IEEE Trans. Circuits Syst. II, Exp. Briefs*, vol. 70, no. 1, pp. 116–120, Jan. 2023.

[12] M. Del Mastro et al., "Ultra-low-profile continuous transverse stub array for SatCom applications," *IEEE Trans. Antennas Propag.*, vol. 70, no. 6, pp. 4459–4471, Jun. 2022.

[13] C. Wei, Y. Liu, J.-W. Lian, C. Geng, and D. Ding, "Millimeter-wave wide-angle ridge gap waveguide multibeam antenna fed by 3-D printing Butler matrix," *IEEE Trans. Microw. Theory Tech.*, vol. 73, no. 9, pp. 5791–5802, Sep. 2025.

[14] C. Geng, J.-W. Lian, and D. Ding, "Millimeter-wave highly efficient E-plane ridge gap waveguide Butler matrix for wide-angle endfire multibeam antenna applications," *IEEE Trans. Microw. Theory Tech.*, vol. 73, no. 8, pp. 5096–5107, Aug. 2025

[15] C. Geng, J.-W. Lian, Y. J. Guo, and D. Ding, "Millimeter-wave three-layer substrate-integrated 9 × 9 Butler matrix and its application to wide-angle endfire multibeam metasurface antenna," *IEEE Trans. Microw. Theory Tech.*, vol. 72, no. 4, pp. 2253–2266, Apr. 2024.

[16] J.-W. Lian, H.-N. Wu, C. Geng, W. Hong, and D. Ding, "Compact millimeter-wave orthogonal SIW multibeam antenna based on shared-cavity Rotman lens and shared-aperture array antenna," *IEEE Trans. Antennas Propag.*, vol. 73, no. 8, pp. 6169–6174, Aug. 2025

[17] J.-W. Lian, Y.-L. Ban, and Y. J. Guo, "Wideband dual-layer Huygens' metasurface for high-gain multibeam array antennas," *IEEE Trans. Antennas Propag.*, vol. 69, no. 11, pp. 7521–7531, Nov. 2021.

[18] W. Liu, Y. Cao, J. Chen and S. Yan, "Design of a Low-Profile Dual-Band Shared-Aperture Circularly Polarized Phased Array," in IEEE Antennas and Wireless Propagation Letters, vol. 23, no. 2, pp. 543-547, Feb. 2024.

[19] J. Xu et al., "A dual-polarized PUMA array with 8.1:1 bandwidth and 45° scanning off broadside using dual-layer dipoles," IEEE Trans. Antennas Propag., vol. 73, no. 9, pp. 6979–6984, Sept. 2025.

[20] Y. Cao, S. Wu, J. Zhang, J. Li, and S. Yan, "Compact 2-D passive beam-scanning multibeam antenna based on Rotman lens and mechanical sweeping phase gradient metasurface," *IEEE Trans. Antennas Propag.*, vol. 73, no. 7, pp. 4993–4998, Jul. 2025.

[21] J. Li, C. He, H. Fan, and R. Jin, "Gain-equalized multibeam antenna fed by a compact dual-layer Rotman lens at Ka-band," *IEEE Trans. Antennas Propag.*, vol. 70, no. 3, pp. 2307–2311, Mar. 2022.

Non-volatile Reflective Intelligent Surface Based on 2D Material Switches for 6G Wireless Communications

Xiaoyu Xiao[(1)],Zixing Peng[(2)], Xuzhao Liu[(3)], Jiaqiu He[(2)] ,Yifan Zhang[(1)],),Cinzia Casiraghi[(2)],Zhirun Hu[(1)]

(1) Department of Electrical and Electronic Engineering, School of Engineering, University of Manchester, Manchester, UK
(2) Department of Chemistry, University of Manchester, Manchester, UK
(3) Department of Materials and Henry Royce Institute, University of Manchester, UK

***Abstract*— Currently reflective intelligent surface (RIS) implementations typically rely on semiconductor switches (e.g., PIN diodes or transistors) hence require continuous biasing, leading to non-negligible static power consumption that scales with the number of unit cells. Here we present an highly energy-efficient, efficient, intelligent surface enabled by non-volatile 2D-material-enabled RF switches. The switch is consisting of sandwiched Ag/MoS_2/Ag structure and exhibits stable non-volatile resistive switching and favorable RF characteristics, enabling two persistent states without DC holding power. By integrating these switches into a 1-bit reflective unit cell, a 6×6 RIS prototype operating at 3.5 GHz is demonstrated with programmable reflection patterns under different coding sequences, validating its capability for beam steering and wavefront control. Furthermore. system-level energy benefit of eliminating static bias power, which becomes increasingly significant for large-scale RIS and sensing arrays is presented. These results indicate that non-volatile 2D-material switches provide a practical pathway toward low-power programmable metasurfaces for 6G wireless communications.**

***Index Terms*—Reconfigurable intelligent surface; metasurfaces; non-volatile switch; zero-static power; MoS_2; energy efficiency; wireless sensing.**

I. Introduction

Reflective intelligent surfaces (RIS), also known as intelligent reflecting/reflective surfaces, are being actively explored as a hardware layer for shaping wireless propagation by imposing programmable amplitude/phase responses on incident electromagnetic waves [1], [2], [3]. By tailoring the reflected wavefront, RIS can enhance link quality, mitigate blockage, and enable smart wireless channeling. In practice, RIS is realized by a large number of subwavelength unit cells whose electromagnetic response is reconfigured through embedded switches and a bias/control network. Although semiconductor switches (e.g., PIN diodes or FETs) offer mature, high-speed operation, their state is typically maintained by continuous DC biasing [4], [5]. As the aperture and element count scale from tens to hundreds or thousands, the required bias infrastructure and the cumulative static power dissipation become increasingly burdensome, particularly for battery-powered nodes, low-maintenance deployments, or energy-constrained wireless platforms.

Non-volatile (zero-static-power) switches provide a compelling alternative for RIS because the programmed state can be retained without consuming any static power [6], [7], [8]. At the array level, this brings paradigm shift in electrical reconfigurability, especially being advantageous for scenarios where large amount of switches are needed or sensing task changes slowly or only requires intermittent updates. Two-dimensional (2D) materials are attractive candidates for non-volatile RF switching due to their simple heterostructure stacks, compatibility with low-temperature and substrate-friendly processing, and potential for lightweight or conformal implementations. Importantly, incorporating non-volatile switching with RIS directly addresses the energy-efficiency while preserving the electrical reconfigurability [9], [10], [11], [12].

Here, an energy-efficient RIS enabled by non-volatile MoS_2-based RF switches is presented. The RIS is made of screen-printed graphene, and the non-volatile switches are directly inkjet-printed on the graphene patterns.

II. Inkjet-printed Non-volatile Switches and Screen-printed Graphene Metasurface

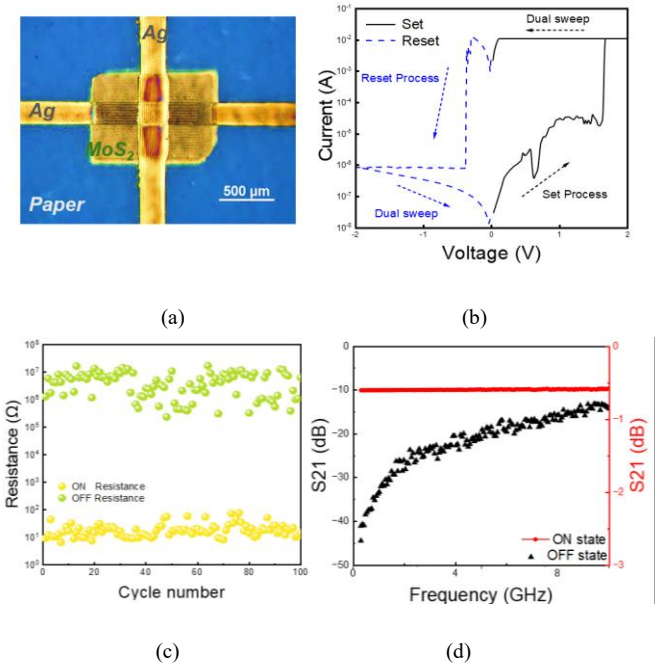


Fig. 1. (a) Schematic illustration of the Ag/MoS_2/Ag non-volatile RF switch fabricated on a paper substrate. (b) Representative I–V characteristics. (c) Endurance performance (ON/OFF ratio > 10^3). (d) Measured RF transmission (|S21|) of the switch in the ON and OFF states.

A. Non-volatile MoS_2 Switch

Fig. 1 summarizes the device concept and key electrical/RF metrics of the non-volatile MoS_2 RF switch used for zero-static-power state control. Fig. 1(a) illustrates the inkjet-printed Ag/MoS_2/Ag switch on a substrate with patterned Ag electrodes and a compact active region of 0.2 × 0.2 mm², suitable for integration into metasurface unit cells. Fig. 1(b) shows representative I-V characteristics, where the device is programmed at approximately +1.5 V (SET) and −0.5 V (RESET) over 100 cycles. Fig. 1(c) quantifies endurance, yielding ON resistance and OFF resistance (ON/OFF ratio $> 10^3$) across 100 manual switching cycles. Fig. 1(d) presents the measured |S21| from DC to 12 GHz, demonstrating <0.7 dB insertion loss in the ON state and >10 dB isolation in the OFF state

B. Metasurface Unit Cell Design and Prototype

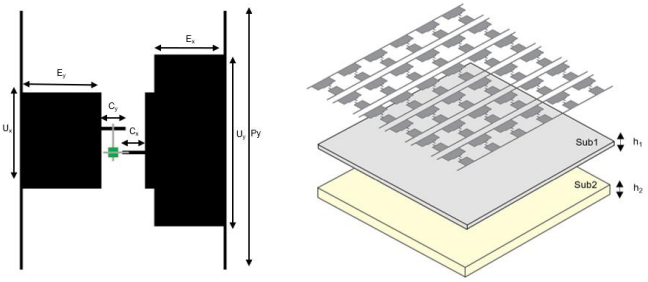
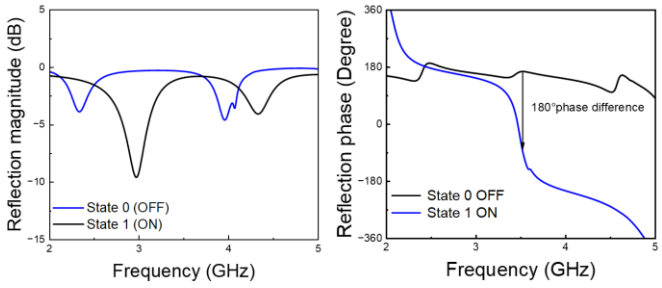


Fig. 2. Geometry and dimensions of the proposed reflective metasurface. Dimensions (mm): h_1=0.1, h_2=6.0， E_x=14.1， E_y=15.9， C_y=C_x=5.0， U_x=18， U_y=36.

The proposed structure is a reflective metasurface implemented on a dielectric substrate and backed by a continuous copper ground plane to enforce reflection-mode operation. The patterned top metallization forms the reconfigurable unit-cell network, while the switching function is provided by non-volatile MoS_2-based RF switches. By programming the MoS_2 switch between its conductive and insulating states, the current path within each unit cell is enabled or interrupted, producing two persistent reflection states. Once the states are established, no DC holding bias is needed any more. This zero-static-power switching mechanism is particularly attractive for large-area RIS, where eliminating continuous bias power supply can significantly reduce power consumption and improve overall energy efficiency for wireless communications .

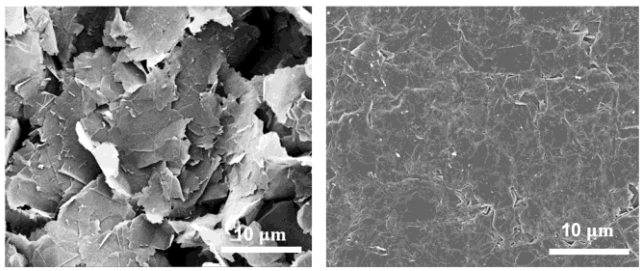


(a) (b)

Fig. 3 Simulated reflection response of the 1-bit RIS unit cell under two switch states. (a) Reflection magnitude versus frequency. (b) Reflection phase versus frequency, with the phase difference between the two states

Fig. 3 verifies the binary phase functionality of the proposed unit cell controlled by a non-volatile RF switch. When the switch is OFF (State 0, open circuit), the current path across the bridging region is interrupted, leading to one reflection-phase branch; when the switch is ON (State 1, closed circuit), the conductive connection modifies the effective resonance of the cell and produces a distinct phase branch. As a result, the two states provide a near-constant phase separation close to 180° in the operating band centered at 3.5 GHz, while maintaining comparable reflection magnitude. This 1-bit phase contrast enables straightforward coding of the reflective array for programmable wavefront control (e.g., beam steering) without requiring continuous DC holding power once the non-volatile switch state is programmed.

Fig. 4 compares the microstructure of the graphene pattern before and after densification. In the as-deposited state (Fig. 4(a)), the graphene flakes form a relatively porous and loosely packed network, which limits interflake contacts hence increases sheet resistance. After densification (Fig. 4(b)), the film becomes visibly more compact and interconnected, consistent with improved percolation pathways for in-plane conduction. Correspondingly, the sheet resistance is reduced from 80 Ω/sq to 1.2 Ω/sq, which is critical for minimizing ohmic loss when the graphene pattern is used as the conductive layer in the reflective metasurface.



(a) (b)

Fig. 4. SEM images of the graphene pattern (10 µm scale bar): (a) before densification and (b) after densification (sheet resistance reduced from 80 Ω/sq to 1.2 Ω/sq)

III. Simulated and Measured Results

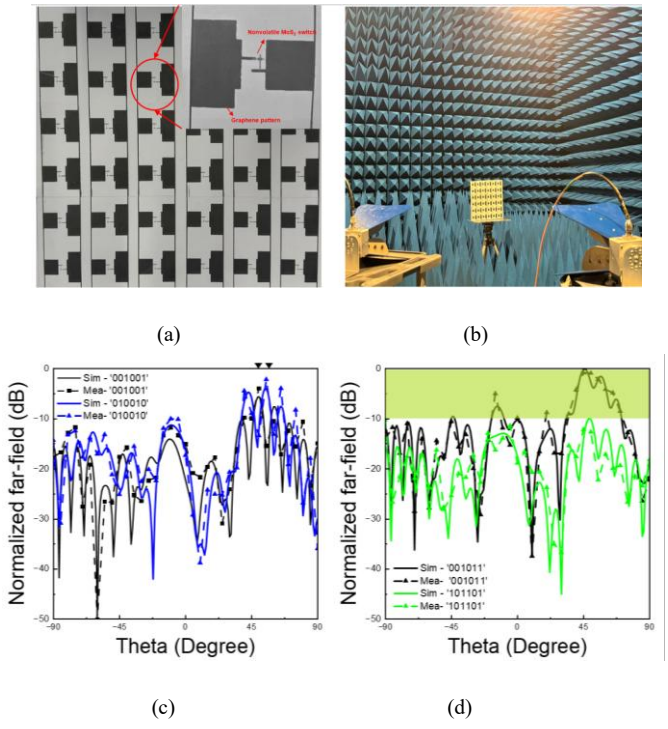


Fig. 5. (a) Anechoic-chamber measurement setup. (b) Unit-cell photograph showing the graphene pattern and the integrated non-volatile MoS_2 switch. (c) Simulated and measured normalized far-field patterns for

The simulated and measured results are given in Fig. 5, clearly indicating the beam-steering capability of the proposed phased array based on non-volatile MoS_2 switches and a good agreement between the two. The RIS is characterized in an anechoic chamber (Fig. 5(a)), and the unit-cell implementation (graphene conductive pattern plus a non-volatile MoS_2 switch) is shown in Fig. 5(b). By applying different binary coding sequences across the array, distinct scattering responses are obtained. Fig. 5(c) shows that switching the coding from "001001" to "010010" leads to an approximately 10° shift in the main-lobe direction, and the measured patterns follow the simulated trend. Fig. 5(d) illustrates that the coding "001011" produces a lower backscattered level compared with "101101", indicating a reduced effective radar cross section (RCS) for the 50° incidence case.

IV. Conclusion

This paper presented a 2D material enabled, energy-efficient RIS driven by non-volatile MoS_2-based RF switches and low-loss graphene conductors. By integrating the non-volatile switch into a 1-bit reflective unit cell, a near-180° reflection-phase contrast was achieved around 3.5 GHz while maintaining comparable reflection magnitude, enabling straightforward binary coding for wavefront control. A 6 × 6 prototype was experimentally validated under 50° oblique incidence, where different coding sequences produced distinct scattering responses, including an approximately 10° shift of the main-lobe direction and reduced backscattered level (RCS reduction) relative to the reference state, with good agreement between simulation and measurement. Overall, the combination of non-volatile MoS_2 switching and low-resistance graphene conductors provides a scalable pathway toward low-power RIS platforms for future wireless sensing and communications.

References

[1] C. Gao *et al.*, 'Multifunctional Intelligent Reconfigurable Metasurface', *ACS Appl. Mater. Interfaces*, p. acsami.4c09944, Oct. 2024, doi: 10.1021/acsami.4c09944.

[2] J. C. Liang *et al.*, 'An Angle-Insensitive 3-Bit Reconfigurable Intelligent Surface', *IEEE Transactions on Antennas and Propagation*, vol. 70, no. 10, pp. 8798–8808, Oct. 2022, doi: 10.1109/TAP.2021.3130108.

[3] B. Ren, C. Qi, P. Li, X. He, and A. M. H. Wong, 'A Self-Adaptive Reconfigurable Metasurface for Electromagnetic Wave Sensing and Dynamic Reflection Control', *Advanced Science*, vol. 12, no. 32, p. e05155, Aug. 2025, doi: 10.1002/advs.202505155.

[4] A. Rafique, A. Mehmood, N. U. Hassan, M. Q. Mehmood, and M. Zubair, 'Power Consumption Analysis of a Reconfigurable Intelligent Surface for Self-Sustained Operations', in *2024 IEEE 99th Vehicular Technology Conference (VTC2024-Spring)*, Jun. 2024, pp. 1–5. doi: 10.1109/VTC2024-Spring62846.2024.10683501.

[5] Y. Saifullah, Y. He, A. Boag, G.-M. Yang, and F. Xu, 'Recent Progress in Reconfigurable and Intelligent Metasurfaces: A Comprehensive Review of Tuning Mechanisms, Hardware Designs, and Applications', *Advanced Science*, vol. 9, no. 33, p. 2203747, 2022, doi: 10.1002/advs.202203747.

[6] Y. Shen *et al.*, 'A high speed response Nafion-based non-volatile RF switch', *Appl. Phys. Lett.*, vol. 126, no. 24, p. 242103, Jun. 2025, doi: 10.1063/5.0270011.

[7] D. Seo *et al.*, 'VOx-Based Non-Volatile Radio-Frequency Switches for Reconfigurable Filter', *Advanced Science*, vol. 12, no. 31, p. e01989, 2025, doi: 10.1002/advs.202501989.

[8] Y. Ning, X. Xiao, Z. Zhang, and Z. Hu, 'Non-volatile Pattern Reconfigurable Antenna Based on Even- and Odd-Mode Spoof Surface Plasmon Polaritons', in *2023 17th European Conference on Antennas and Propagation (EuCAP)*, Mar. 2023, pp. 1–5. doi: 10.23919/EuCAP57121.2023.10133367.

[9] M. Kim *et al.*, 'Zero-static power radio-frequency switches based on MoS_2 atomristors', *Nat Commun*, vol. 9, no. 1, p. 2524, Jun. 2018, doi: 10.1038/s41467-018-04934-x.

[10] X. Xiao *et al.*, 'Fully printed zero-static power MoS_2 switch coded reconfigurable graphene metasurface for RF/microwave electromagnetic wave manipulation and control', *Nat Commun*, vol. 15, no. 1, p. 10591, Dec. 2024, doi: 10.1038/s41467-024-54900-z.

[11] M. Wang *et al.*, 'Robust memristors based on layered two-dimensional materials', *Nat Electron*, vol. 1, no. 2, pp. 130–136, Feb. 2018, doi: 10.1038/s41928-018-0021-4.

[12] T. Wu *et al.*, 'Integrated two-dimensional microwave transmitters fabricated on the wafer scale', *Nat Electron*, vol. 8, no. 10, pp. 913–920, Oct. 2025, doi: 10.1038/s41928-025-01452-9.

A Curved Broadside-Coupled Stripline Phase Shifter and Its Application to Metasurface Designs

Jiexin Lai
School of School of Electrical and Data Engineering, University of Technology Sydney, Sydney, NSW 2019, Australia
Jiexin.Lai@student.uts.edu.au

Zhichao Sun
School of School of Electrical and Data Engineering, University of Technology Sydney, Sydney, NSW 2019, Australia
Bryan.Sun@uts.edu.au

Xiaojing Lv
School of School of Electrical and Data Engineering, University of Technology Sydney, Sydney, NSW 2019, Australia
xiaojing.lv@uts.edu.au

Yang Yang
School of School of Electrical and Data Engineering, University of Technology Sydney, Sydney, NSW 2019, Australia
yang.yang.au@ieee.org

***Abstract*—In this paper, a metasurface based on a compact curved broadside-coupled stripline (BCS) phase shifter is proposed for gain enhancement applications. The unit cell consists of a receiving antenna, a BCS phase shifter, and a transmitting antenna, all fabricated using standard printed circuit board (PCB) technology. The proposed metasurface exhibits stable radiation performance with a boresight gain of approximately 19 dBi and cross-polarization levels below –20 dB, and a 3-dB gain bandwidth of 18% (25 – 30 GHz).**

***Keywords*—Metasurface, broadside-coupled stripline, millimeter wave, gain enhancement.**

I. Introduction

Subwavelength unit cells (UCs) are an important part of the metasurfaces, and can be designed to modify the amplitude, phase, and polarization of electromagnetic (EM) waves. By arranging the UCs according to specific phase distribution, metasurfaces can realize various functionalities, including anomalous refraction [1], beamforming [2], orbital angular momentum (OAM) generation [3], holographic imaging [4], and so on. Therefore, the phase modulation capability is one of the key metrics for UCs.

The main challenge of the phase modulation capability is to confine the EM wave within a subwavelength scale. All-dielectric unit cells [5] realize phase delay because of the shorter wavelength in the dielectric medium. Fabry–Perot (FP) unit cells realize phase modulation through multiple reflections between polarization grids [1]. Multilayered unit cells [6] can be represented by an equivalent circuit or filter model, which has a linear phase response to realize the desired phase delay. The basic structure of a Huygens' unit cell (HUC) consists of an electric resonator and a magnetic resonator [7], and the phase modulation can be fulfilled by engineering the balance between electric and magnetic responses. The antenna-circuit-antenna (ACA) unit cells [8] rely on the phase shifter in the intermediate circuit to achieve phase modulation.

In this paper, we propose an ACA unit cell based on the curved broadside-coupled stripline (BCS) phase shifter for phase modulation. The receiving (Rx) and transmitting (Tx) antennas convert the incident EM wave into an electrical signal that propagates within the BCS phase shifter. With the capability of nearly 2π phase coverage, the BCS phase shifter has a compact footprint, less than a quarter wavelength, which shows the potential for achieving polarization multiplexed unit cells, which means a single UC can accommodate multiple phase

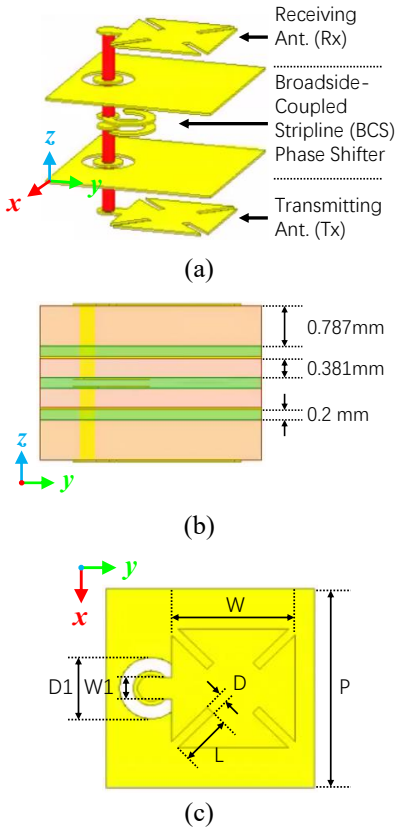


Fig. 1. Antenna-circuit-antenna (ACA) unit cell. (a) UC configuration without dielectric substrate. (b) Side view of the proposed UC. (c) Top view of the proposed UC. (P = 5 mm, W = 2.9 mm, W1 = 0.55 mm, L = 1.2 mm, D = 0.22 mm, D1 = 1.5 mm)

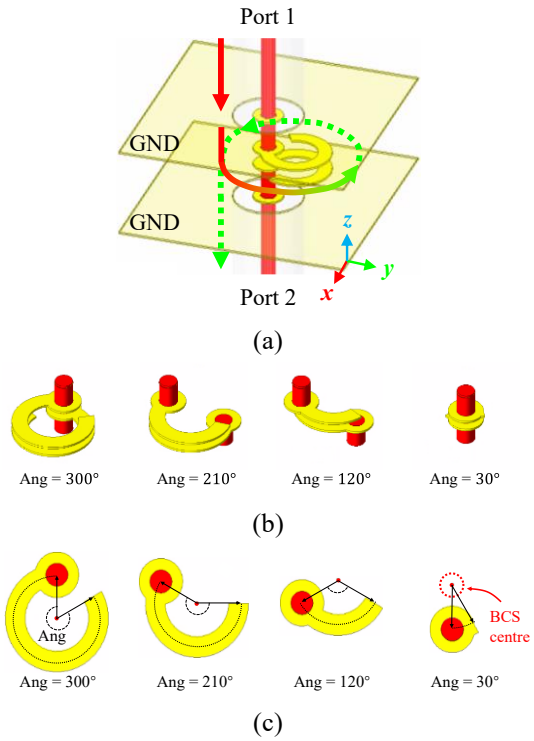


Fig. 2. (a) Structure of the proposed BCS phase shifter without the substrate. (b) Geometries of the BCS phase shifters with various "Ang" to achieve variable phase delays. (c) Top views of the upper striplines for different "Ang".

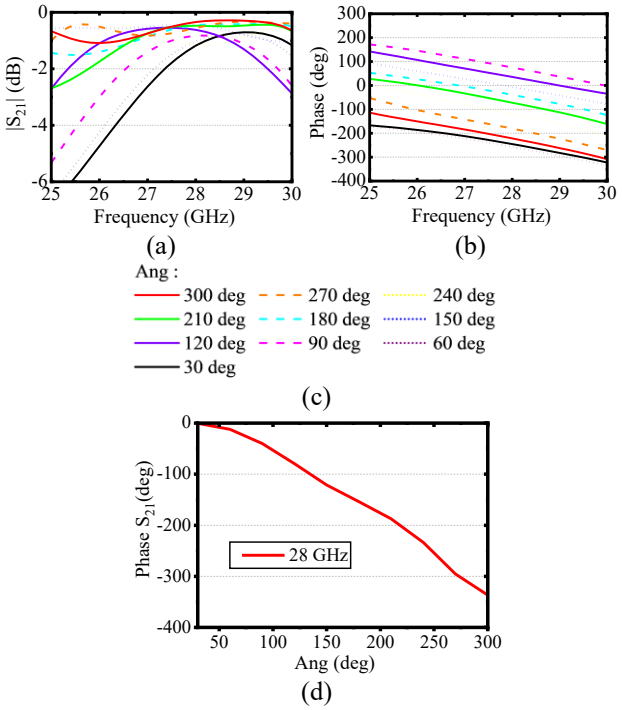


Fig. 3. Simulated performance of the proposed UC. (a) Transmission coefficients with various "Ang". (b) Transmission phase with various "Ang". (c) Definition of labels. (d) Normalized transmission phase versus "Ang" at 28 GHz.

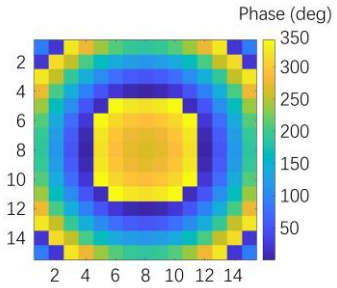


Fig. 4. Phase distribution of the proposed metasurface for gain enhancement.

shifters. In this case, each UC integrates a BCS phase shifter to verify the phase-shifting performance of the BCS, and the metasurface employs a spherical-wave compensation phase distribution to achieve gain enhancement. Simulations demonstrate the effectiveness of the proposed phase-shifting UC.

II. Unit Cell Design

As shown in Fig. 1 (a), the UC consists of a receiving antenna (Rx), a BCS phase shifter, and a transmitting antenna (Tx), and can be fabricated by the printed circuit board (PCB) technology. In Fig. 1 (b), the orange layers represent the Taconic TLY-5 substrate ($\varepsilon_r = 2.2, tan\delta = 0.0009$) with the thickness of 0.787 mm and 0.381 mm, while the green ones represent the RO4450T prepreg ($\varepsilon_r = 3.35, tan\delta = 0.004$) with the thickness of 0.2 mm. The ground plane resides on the upper surface of a 0.381 mm dielectric substrate. The BCS phase shifter stack-up includes two 0.381 mm dielectric layers and a single 0.2 mm prepreg layer. Fig. 1 (c) shows the top view of the UC with the dimension details.

Fig. 2 (a) illustrates the BCS phase shifter configuration with Ang = 300°. The upper and lower coaxial ports have an impedance of 50Ω. Primary–secondary boundary conditions are applied on the four sides of the unit cell. The structure is vertically stacked between two ground planes, with oppositely oriented C-shaped striplines connecting the inner conductors of the coaxial ports. The red-to-green arrow marks the signal path. Fig. 2 (b) shows the BCS phase shifter with various "Ang". The parameter "Ang" denotes the angular length of the curved stripline, measured in degrees. Among them, Ang = 300° corresponds to the deepest phase delay. The yellow lines represent the conductive layer, while the red ones indicate the metal vias. In Fig. 2 (c), as the length of the BCS increases, the transmission phase covers a nearly 2π phase cycle. Fig. 3 (a) and (b) show the performance of the UC under various "Ang", where the transmission coefficients are above -2 dB across the frequency band from 27.5 to 29.5 GHz (relative bandwidth of 7%). Fig. 3 (d) shows the normalized transmission phase versus "Ang" at 28 GHz. The maximum phase delay reaches −336° at Ang = 300°, which is enough for the 3-bit phase shift steps from 0° to 315°.

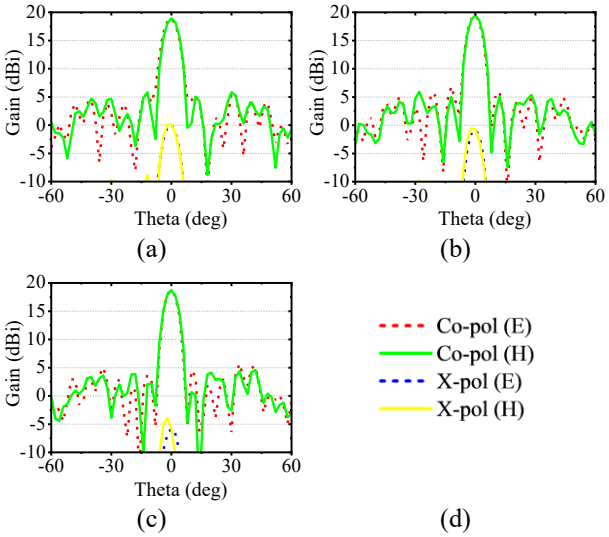


Fig. 5. Simulated radiation patterns at (a) 26.5 GHz, (b) 28 GHz, and (c) 29.5 GHz. (d) Definition of labels.

III. Metasurface Simulation

To demonstrate the phase-shifting capability of the BCS unit, a 15 × 15 array is simulated using Ansys Electronics Desktop. Based on the spatial phase delay from the feed source [9], the phase distribution for each UC can be given:

$$\varphi(x,y) = k_0\left(\sqrt{F^2+x^2+y^2}-F\right)+\varphi_0 \qquad (1)$$

where F is the focal length (80 mm), k_0 represent the wave number at 29 GHz, (x,y) is the position of the UC, and φ_0 represents the initial phase at the feed source. The calculated phase distribution is shown in Fig. 4.

Fed by a WR-28 waveguide probe, the radiation patterns of the proposed metasurface at 26.5 GHz, 28 GHz, and 29.5 GHz are shown in Fig. 5, and the boresight gains are 19 dBi, 19.5 dBi, and 18.2 dBi, respectively. The cross-polarization level is about -20 dB with a sidelobe level of approximately -15 dB. Stable radiation patterns are realized. The simulated gain versus frequency is shown in Fig. 6. The simulated 3-dB gain bandwidth is 18% (25 – 30 GHz).

IV. Conclusion

This paper presented a metasurface unit cell based on a compact BCS phase shifter for gain enhancement applications, characterized by nearly 360° phase coverage and a low-profile multilayer structure. The unit cell integrates a receiving antenna, a BCS phase shifter, and a transmitting antenna, all fabricated using standard PCB technology, ensuring low cost and ease of fabrication.

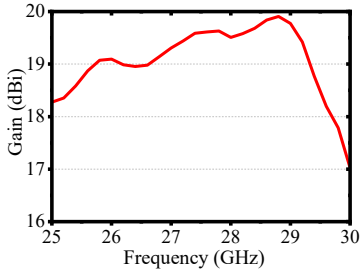


Fig. 6. Simulated gain of the proposed metasurface fed by a WR-28 waveguide probe.

Acknowledgment

This work was supported in part by the Australian Research Council (ARC) Linkage Infrastructure Equipment and Facilities under Grant LE220100035, Linkage Project LP210300004, and UTS ARC Future Fellowship (FT23) Near Miss Support.

References

[1] N. K. Grady, J. E. Heyes, D. R. Chowdhury, Y. Zeng, M. T. Reiten, A. K. Azad, A. J. Taylor, D. A. Dalvit, H. T. Chen, "Terahertz metamaterials for linear polarization conversion and anomalous refraction," in *Science*, vol. 340, no. 6138, pp. 1304-1307, Jun. 2013.

[2] X. Guo, Y. Luo, Z. N. Chen, N. Yan, W. An and K. Ma, "Multiple tri-beam low scanning loss metasurface antenna for wide-angle coverage by superposing focusing and periodic phases," in *IEEE Trans. Microw. Theory Techn.*, vol. 71, no. 8, pp. 3466-3478, Aug. 2023.

[3] X. Guo and Y. Yang, "Low-profile full-space transmission-reflection-integrated multiple focused and OAM beams metasurface for indoor communication," in *IEEE Trans. Microw. Theory Techn.*, vol. 73, no. 6, pp. 3644-3654, June 2025.

[4] Z. Wang, X. Ding, K. Zhang, B. Ratni, S. N. Burokur, X. Gu, Q. Wu, "Huygens metasurface holograms with the modulation of focal energy distribution," in *Adv. Opt. Mater.*, vol. 6, no. 12, pp. 1800121, Jun. 2018.

[5] H. Yi, S. W. Qu, K. -B. Ng, C. H. Chan and X. Bai, "3-D Printed millimeter wave and terahertz lenses with fixed and frequency scanned beam," in *IEEE Trans Antennas Propag.*, vol. 64, no. 2, pp. 442-449, Feb. 2016.

[6] M. Li and N. Behdad, "Wideband True-Time-Delay Microwave Lenses Based on Metallo-Dielectric and All-Dielectric Lowpass Frequency Selective Surfaces," in *IEEE Trans. Antennas Propag.*, vol. 61, no. 8, pp. 4109-4119, Aug. 2013.

[7] S. Wang et al., "Compact Dual-Band Independently Modulated Huygens' Metasurface for Full-Space EM Wave Manipulation," in *IEEE Trans. Microw. Theory and Techn.*, vol. 71, no. 12, pp. 5160-5170, Dec. 2023.

[8] J. Zhu, M. Li, J. Lai, Y. Yang, "Multimaterial additively manufactured transmissive spin-decoupled polarization-maintaining metasurfaces," in *Laser Photonics Rev.*, vol. 17, no. 12, pp. 2300433, Dec. 2023.

[9] J. Zhu, Y. Yang, Z. Hou, S. Liao and Q. Xue, "Dual-Band Aperture-Shared High Gain Antenna for Millimeter-Wave Multi-Beam and Sub-6 GHz Communication Applications," in *IEEE Trans. Antennas Propag.*, vol. 70, no. 6, pp. 4848-4853, June 2022.

High-Frequency Narrowband to Low-Frequency Broadband Transition in an SMA-Actuated Bandpass Frequency-Selective Surface

Xiaojing Lv
School of Electrical and Data Engineering
University of Technology Sydney
Sydney, Australia
xiaojing.lv@uts.edu.au

Zhenlin Dai
School of Electrical and Data Engineering
University of Technology Sydney
Sydney, Australia
zhenlin.dai@student.uts.edu.au

Zhiwei Yin
School of Electrical and Data Engineering
University of Technology Sydney
Sydney, Australia
zhiwei.yin@ student.uts.edu.au

Zhichao Sun
School of Electrical and Data Engineering
University of Technology Sydney
Sydney, Australia
bryan.sun@uts.edu.au

Yang Yang
School of Electrical and Data Engineering
University of Technology Sydney
Sydney, Australia
yang.yang-1@uts.edu.au

***Abstract*—This study presents a thermally actuated, dynamically reconfigurable FSS utilizing laser-cut Ni–Ti SMA elements. By exploiting a bistable SMA architecture, the unit-cell topology is physically reconfigured via temperature-triggered deformation, thereby re-routing the surface current paths without the need for complex voltage-biasing networks or bulky mechanical assemblies. The proposed FSS seamlessly transitions between two distinct spectral states: a highly selective high-frequency narrowband response when the SMA branches are engaged and a broadband response in the lower-frequency regime when the branches are disengaged. Correspondingly, the fractional bandwidth dynamically expands from 5.66% to 51.72%. The underlying electromagnetic mechanisms and bandwidth transition are further elucidated through Babinet's principle and Smith-chart impedance trajectories.**

***Keywords*—FSS, SMA, bandpass filter, reconfiguration, Smith chart.**

I. Introduction

Metasurfaces exploit planar arrays of subwavelength resonant elements to engineer electromagnetic (EM) responses unattainable with naturally occurring materials. By tailoring the topology of these constituent unit cells, artificial surfaces can realize exotic macroscopic properties, including anomalous reflection, anomalous refraction, and negative effective refractive indices. While metasurfaces typically emphasize spatially varying phase distributions for wavefront manipulation, their strictly periodic counterparts—comprising identical unit cells without local phase gradients—are classically defined as frequency-selective surfaces (FSSs) [1]-[2]. Leveraging their inherent spectral filtering characteristics, FSSs have been extensively employed as spatial filters and Fabry-Pérot (FP) cavity antennas. Furthermore, by introducing resistive loading to dissipate incident EM energy, these structures can be readily extended to function as high-performance absorbers and rasorbers [3]-[5].

FSS architectures serve as foundational building blocks in metasurface engineering. Their EM behavior is efficiently analyzed using equivalent circuit models (ECMs), which offer intuitive physical insights and enable rapid spectral prediction. Crucially, ECMs facilitate inverse design paradigms, where

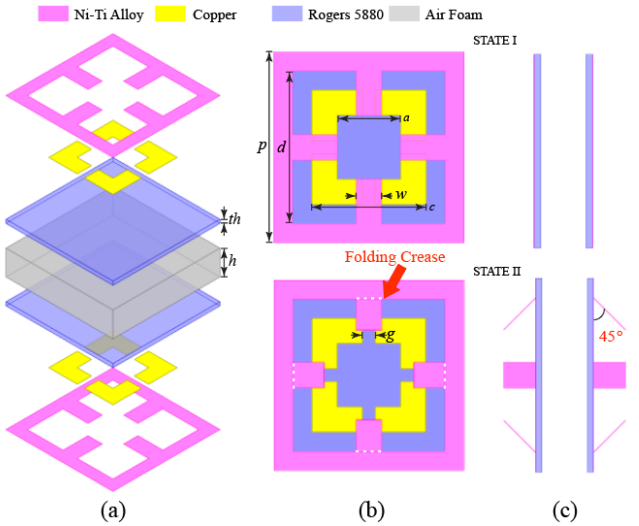


Fig. 1. Unit-cell geometry and switching mechanism of the proposed double-layer, mirror-symmetric, spectrally reconfigurable FSS. (a) Exploded view illustrating the stacked dielectric slabs and detailed metallic geometries of each layer. (b) Top view detailing the SMA actuation: the branches lie flat (0°) to contact the central copper open-square ring (ON state) and lift by 45° to disengage (OFF state). (c) Side view corresponding to the two operational states.

targeted frequency responses directly guide the synthesis and parameterization of unit-cell geometries. While conventional FSSs readily achieve diverse responses—such as bandpass, bandstop, broadband, highly selective narrowband, and multi-band filtering—recent efforts have focused on expanding structural degrees of freedom (DoFs) to push performance boundaries. Consequently, complex 2.5-D and 3-D metal-dielectric hybrid structures have emerged, delivering sharper roll-offs, superior out-of-band rejection, unit-cell miniaturization, and reduced profile thicknesses [6].

Beyond enhancing static spectral performance, the development of dynamically tunable FSSs has emerged as a critical research frontier. Conventional reconfiguration strategies predominantly rely on active electronic components integrated with voltage-biasing networks to achieve rapid band tuning. While effective, these approaches inevitably

979-8-3315-4544-4/26/$31.00 ©2026 IEEE

XXX-X-XXXX-XXXX-X/XX/$XX.00 ©20XX IEEE

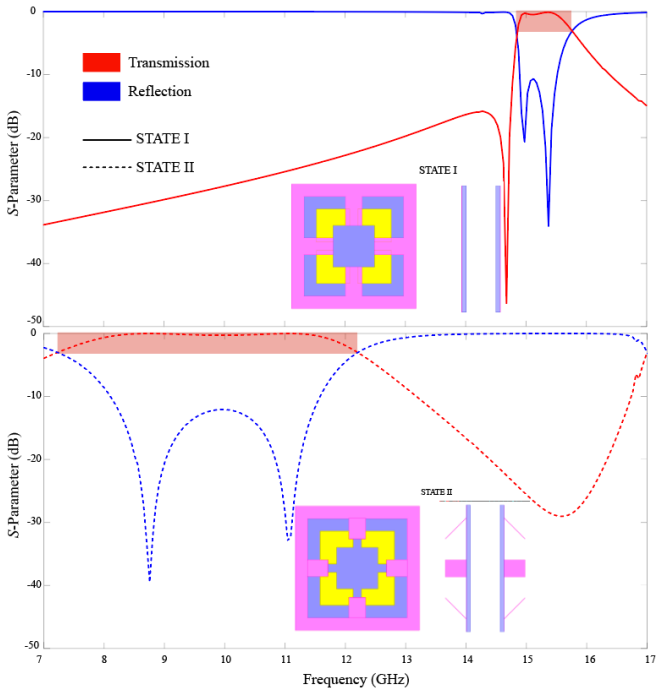


Fig. 2. Frequency responses of the proposed FSS under two switching states. (a) In State I, the −3 dB transmission band is confined to 14.77-15.63 GHz, giving a 5.66% fractional bandwidth. (b) In State II, the transmission region broadens to 7.21-12.24 GHz, corresponding to a fractional bandwidth of 51.72%.

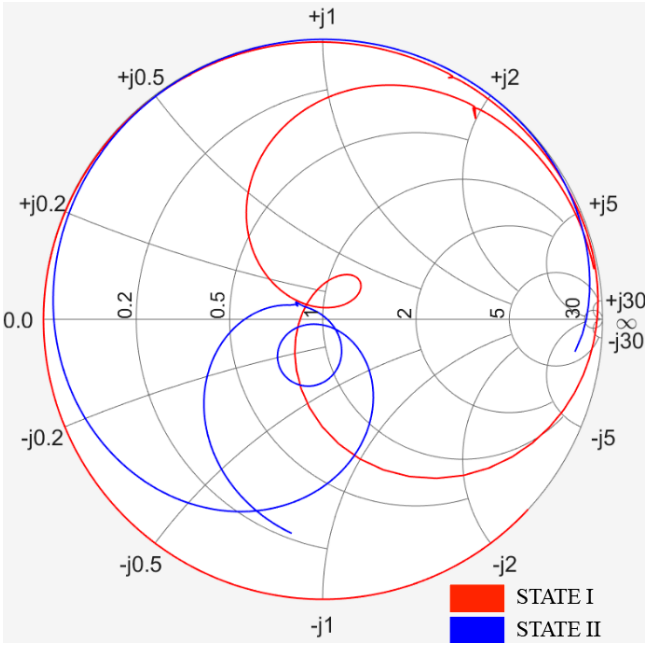


Fig. 3. Smith-chart trajectories qualitatively illustrating the impedance-matching evolution of the two operational states, corresponding to a broadband passband at lower frequencies (OFF) and a narrowband passband at higher frequencies (ON).

introduce additional circuit complexity and parasitic coupling effects, which may compromise the EM performance of the optimized unit cell [7]. As an alternative, mechanically adjustable designs have been proposed, where the spacing between multiple FSS layers is varied to alter the equivalent transmission-line length and thereby tune the resonance frequencies. However, such implementations typically require precision mechanical assemblies and bulky motor-driven actuators [8]. Consequently, there is a compelling need for novel reconfiguration paradigms that avoid both complex electrical biasing networks and cumbersome electromechanical mechanisms.

In this work, a thermally actuated, dynamically reconfigurable FSS has been proposed, which is driven by laser-cut Ni-Ti shape-memory alloy (SMA) elements. Utilizing a bistable SMA architecture, the design achieves a rapid and repeatable mechanical response triggered by temperature variations. This physical deformation directly modifies the resonant topology, fundamentally reconfiguring the surface current distribution within the unit cell to excite distinct resonant modes. Consequently, the FSS demonstrates a dynamic spectral transition, switching between a broad passband in the lower-frequency regime and a narrow passband at higher frequencies.

II. Unit-Cell Geometry and Reconfigured Frequency Response

As illustrated in Fig. 1, the proposed unit cell operates in two distinct configurations. The vertically stacked architecture comprises a pair of mirror-symmetric metallic arrays separated by an air-foam spacer ($\varepsilon_0 = 1$) with a thickness of h = 3.5 mm. To facilitate visual interpretation, the laser-patterned copper and SMA features—specifically, the inner open-square loop and the outer square loop with actuating branches—are color-coded yellow and pink, respectively, highlighting their topological differences. These conductive patterns are fabricated on a Rogers RT/Duroid 5880 dielectric substrate ($\varepsilon_r = 2.2$, $\tan\delta = 0.0009$) with a thickness of th = 0.5 mm. The optimized structural dimensions are p = 15 mm, d = 9 mm, c = 8 mm, a = 5 mm, g = 1 mm, and w = 2 mm. Crucially, the spectral behavior of the synthesized FSS is dynamically dictated by the mechanical state of the SMA branches, which either lie flat against the substrate plane (0° contact) at higher temperature or elevate out-of-plane at a 45° angle at lower temperature.

When the SMA switch is engaged (ON state), the proposed FSS operates as a highly selective bandpass filter in the upper-frequency regime. This behavior can be qualitatively understood through Babinet's principle, as its complementary screen exhibits a characteristic bandstop profile. The cascaded mirror-symmetric double-layer architecture further optimizes this response: strong inter-layer coupling broadens the inherently single resonance into a slightly wider passband while significantly steepening the roll-off rate between the transmission and rejection bands. Conversely, when the SMA branches are disengaged (OFF state), the surface current paths are fundamentally re-routed. The modified topology essentially functions as a classic centrally-loaded bandpass resonator [6]. In this state, the double-layer arrangement again facilitates effective inter-layer coupling, substantially expanding the operational bandwidth to yield a broad passband in the lower-frequency region.

To provide deeper physical insight, the input-impedance evolution of the two operating states is analyzed using a Smith chart. In this representation, the perimeter denotes perfect impedance mismatch, while the center corresponds to perfect matching with free space. For State I, the impedance locus primarily traverses the outer boundary, signifying dominant reflection. At higher frequencies, the trajectory abruptly converges toward the center, forming a tight resonance loop before rapidly diverging. This rapid transit through the

matched region manifests as a highly selective, narrowband transmission window. Conversely, the impedance locus for State II enters the central matched region at lower frequencies and forms a much broader loop encompassing the center. This extended containment within the matching zone dictates a significantly wider passband. Notably, the frequency dispersion along these trajectories is nonlinear; thus, the absolute path length does not strictly correspond to uniform frequency increments. Ultimately, these distinct impedance loci rigorously corroborate the observed bandwidth disparity between the two configurations.

III. Summary

This work presents a thermally responsive, dynamically reconfigurable frequency-selective surface (FSS) that leverages laser-patterned Ni–Ti shape-memory alloy (SMA) elements for unit-cell topology transformation. By exploiting the temperature-dependent bistability of the SMA branches, the design eliminates the need for complex electrical biasing and bulky motorized tuning. The FSS switches seamlessly between two distinct operational states: a highly selective high-frequency narrowband passband (SMA engaged) and a significantly broadened low-frequency passband (SMA disengaged). A mirror-symmetric double-layer architecture further enhances this transition, steepening the roll-off and expanding the bandwidth. Corroborated by Smith-chart impedance analyses, this SMA-driven approach offers a compact, bias-free, and mechanically simplified platform for adaptive electromagnetic filtering and multifunctional metasurfaces.

References

[1] B. A. Munk, Frequency Selective Surfaces: Theory and Design. *John Wiley & Sons*, 2000.

[2] Y. Yang et al., "A Review of Multimaterial Additively Manufactured Electronics and 4-D Printing/Origami Shape-Memory Devices: Design, Fabrication, and Implementation," in *Proc. IEEE*, vol. 112, no. 8, pp. 954-999, Aug. 2024.

[3] J. Zhu, Y. Yang, N. Hu, S. Liao, and J. Nulman, "Additively manufactured multi-material ultrathin metasurfaces for broadband circular polarization decoupled beams and orbital angular momentum generation," *ACS Appl. Mater. Interfaces*, vol. 13, no. 49, Dec. 2021.

[4] F. Costa, A. Monorchio, and G. Manara, "Analysis and design of ultrathin electromagnetic absorbers comprising resistively loaded high impedance surfaces," *IEEE Trans. Antennas Propag.*, vol. 58, no. 5, pp. 1551–1558, May. 2010.

[5] X. Lv, S. J. Chen, F. Babaeian, Z. Luo, and Y. Yang, "Metasurface absorbers revisited: Evaluation, design, fabrication and validation," *IEEE Microwave Magazine*, in press, 2026.

[6] X. Lv, Y. Yang, Z. Luo and J. S. Tyo, "Multimaterial 3-D-Printed FSSs for Ultrawide and Dual Passbands in the K-Ka Spectra," in *IEEE Transactions on Microwave Theory and Techniques*, vol. 73, no. 1, pp. 75–86, Jan. 2025.

[7] A. Ebrahimi, Z. Shen, W. Withayachumnankul, S. F. Al-Sarawi and D. Abbott, "Varactor-Tunable Second-Order Bandpass Frequency-Selective Surface With Embedded Bias Network," *IEEE Trans. Antennas Propag.*, vol. 64, no. 5, pp. 1672-1680, May. 2016.

[8] X. Lv, R.T. Ako, M. Bhaskaran, S. Sriram, C. Fumeaux and W. Withayachumnankul, "Frequency-selective surface based mechanically reconfigurable terahertz bandpass filter," *IEEE Trans. Terahertz Sci. Technol.*, vol. 12, no. 3, pp. 257-266, Feb. 2022.

Liquid Crystal Tunable Phase Shifter Using Post-Wall Coplanar Waveguide

Haoyu Zhou
School of Electrical Engineering and Computer Science
The University of Queensland
Brisbane, Australia
haoyu.zhou@uq.edu.au

Lei Guo
School of Electrical Engineering and Computer Science
The University of Queensland
Brisbane, Australia
l.guo3@uq.edu.au

***Abstract*—A continuously tunable phase shifter based on liquid crystal from $10\,\mathrm{GHz}$ to $60\,\mathrm{GHz}$ is presented. In this design, most of the waves travel through the LC mixture via a post-wall coplanar waveguide, rather than the traditionally employed inverted microstrip line, maximizing the liquid crystal's tunability. Additionally, the proposed design offers straightforward fabrication and improved mechanical stability compared to the stripline designs. To validate the effectiveness of the proposed design, three delay line phase shifters employing inverted microstrip line, stripline, and post-wall coplanar waveguide are designed and simulated. The results show that, while all the structures have reflection coefficients less than $-18\,\mathrm{dB}$, the suggested structure demonstrates figure of merit values between $89.6\,^\circ/\mathrm{dB}$ and $124.9\,^\circ/\mathrm{dB}$, which is, on average, $35\,\%$ greater than those attained by stripline designs. The enhanced FoM and decreased fabrication complexity make the proposed structure a promising candidate for applications in millimeter-wave beamforming.**

***Index Terms*—Post-wall coplanar waveguide; liquid crystal; delay line phase shifter; high figure of merit.**

I. Introduction

Modern communications systems are shifting towards the millimeter-wave frequency range, where the need for low-loss, compact, and affordable tunable phase shifters becomes more and more significant for creating reconfigurable and tunable antenna array systems [1].

Among all the tuning materials, liquid crystal (LC) can provide the required tuning capability due to its highly anisotropic properties, and it stands out for millimeter-wave applications because of its low dielectric loss in the millimeter-wave frequency range. The relative permittivity of LC can be adjusted by altering the orientation of its molecules through applying an external electric field [2]. In this way, LC can be utilized as the substrate layer for microwave circuit to alter various characteristics of the electromagnetic signals.

In [3], an LC-based delay lines phase shifter exhibits an insertion loss of $4.3\,\mathrm{dB}$ and provided a $90\,^\circ$ phase shift at $24\,\mathrm{GHz}$. However, a $50\,\mathrm{mm}$ long line is necessary to achieve the $90\,^\circ$ phase shift, resulting in increase circuit size. In addition, the phase shifter suffered from considerable insertion loss. Over the last twenty years, efforts have been made to address these challenges. For instance, meandered lines [4] have been implemented to create a more compact circuit. Additionally, in [5], [6], nanowire-filled membranes and defected ground structures have been employed to produce slow-wave effects to increase the achievable phase range. Nonetheless, these alterations still make used of the traditional inverted microstrip line shown in Fig. 1a, where some of the waves travel through the air or the supporting materials. As a result, the LC only affected a specific portion of the propagating waves, leading to limited performance.

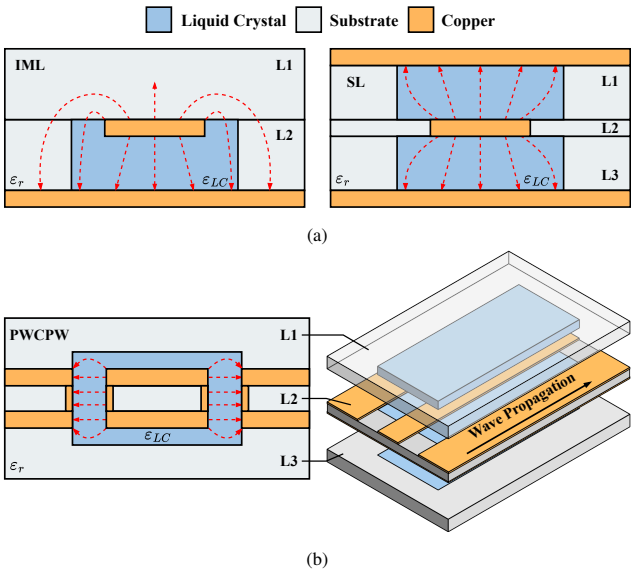


Fig. 1. Cross-sectional views of liquid crystal transmission lines based on (a) inverted microstrip line (IML) and stripline (SL); (b) cross-sectional view and exploded 3D view of the proposed post-wall coplanar waveguide (PWCPW) structure.

In [7], [8], the stripline (SL) structure depicted in Fig. 1a has been employed in the design of LC-based phase shifters. These designs enable most of the electromagnetic fields to remain confined within tunable LC materials, resulting in a greater phase shift range with reduced insertion loss. However, despite the enhancements in performance, the central layer (L2) of the stripline structure encounters considerable challenges in fabrication and is susceptible to mechanical instability due to the absence of supporting materials both above and below the copper core. Consequently, these designs have solely been explored through

979-8-3315-4544-4/26/$31.00 ©2026 IEEE

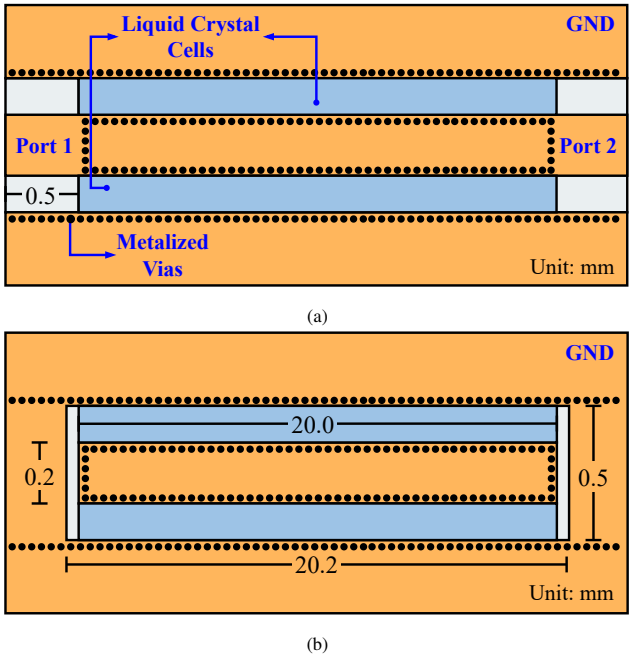


Fig. 2. (a) Top and (b) bottom views of the parametrized geometry of the central layer (L2) in the proposed phase shifter based on post-wall coplanar waveguide.

simulation tools, and their practical feasibility remains to be confirmed by measurement outcomes.

In this paper, post-wall coplanar waveguide (PWCPW) shown in Fig. 1b has been employed to create tunable phase shifters, addressing fabrication challenges while maintaining enhancements in phase shift range and insertion loss. As illustrated in Fig. 1b, compared to stripline in Fig. 1a, the electromagnetic fields in the proposed post-wall coplanar waveguide are primarily distributed between the central core and the adjacent ground planes. This allows the structure to more effectively confine electromagnetic waves within LC materials. Meanwhile, it also allows the biasing field to be more uniformly distributed. Consequently, the proposed structure can have potential improvement in the phase shift range compared to the inverted microstrip structure and stripline structure. Furthermore, the central layer (L2) of the proposed structure can be implemented on both sides of a substrate layer, resulting in notably reduced fabrication complexities and enhanced mechanical stability. To demonstrate the efficacy of the propsoed structure, delay line LC-based phase shifters utilizing inverted microstrip line, stripline, and post-wall coplanar waveguide have been designed and simulated. The results show that the proposed structure can achieve a greater phase range with reduced insertion loss across a broad frequency range.

II. Structural Design

Fig. 1 presents the cross-sectional views of all three designs for the LC-based phase shifter. Fig. 1a depicts the inverted microstrip line and stripline structures, respectively, while Fig. 1b illustrates the proposed post-wall coplanar waveguide design. The supporting substrate used is Rogers RO3003, which has a relative permittivity of 3 and a loss tangent of 0.0013. The thickness of the supporting substrate is chosen to be $0.13\,\mathrm{mm}$, ensuring that the majority of the waves will propagate within the anisotropic LC across all three designs [2].

The proposed LC delay line phase shifter's detailed geometry of the central layer (L2), based on a post-wall coplanar waveguide, is depicted in Fig. 2. It consists of a post-wall coplanar waveguide with a width of $0.2\,\mathrm{mm}$, which is surrounded by two LC-filled slots with $0.15\,\mathrm{mm}$ in width. At the input and output ports (Port1 & Port 2), the post-wall coplanar waveguide is converted into standard grounded coplanar waveguide feed lines. These dimensions are obtained through full-wave simulation to guarantee optimal matching at both the input and output ports. In addition, LC cells with a thickness of $50\,\mathrm{um}$ are attached on the top and bottom substrate as L1 and L3 shown in Fig. 1b to guarantee that any fringing fields will also travel inside the anisotropic LC materials. Between the top and bottom metal planes, metalized vias with a diameter of $50\,\mathrm{um}$ and a distance of $50\,\mathrm{um}$ between edges are employed to form an efficient post wall, guiding the propagation of electromagnetic waves. The length of the post-wall coplanar waveguide section is set to $20\,\mathrm{mm}$ and is kept the same for the phase shifter designs based on inverted microstrp line and stripline in the simulation. Consequently, its influence on the performance should be eliminated, allowing the simulated outcomes to demonstrate the effectiveness of the proposed design.

III. Simulated Results

All three structures are simulated using the full-wave simulation software - ANSYS Electronics Desktop. In simulation, the LC mixture GT7-29001 is employed, which is modelled as an anisotropic material with the complex permittivity tensor established according to the approach outlined in [2]. Without external biasing electric field, the relative permittivity is 2.46 with a loss tangent of 0.0116. Under fully biased condition with external electric field, the relative permittivity of this LC can be tuned to 3.53 with a loss tangent of 0.006. By taking into account both the maximum achievable phase range ($\Delta\Phi_{max}$) and the maximum insertion loss (IL_{max}), the overall performance of the LC-based phase shifter can be assessed based on its figure of merit (FoM) value at a specific frequency [2].

$$FoM = \frac{\Delta\Phi_{max}}{IL_{max}}(^\circ/dB) \tag{1}$$

The simulated transmission and reflection coefficients for the three phase shifter designs are presented in Fig. 3. Across the frequency range of $10\,\mathrm{GHz}$ to $60\,\mathrm{GHz}$, the reflection coefficients for all three structures remain below $-18\,\mathrm{dB}$, demonstrating effective impedance matching. However, within the frequency range of $10\,\mathrm{GHz}$ to $40\,\mathrm{GHz}$, the maximum insertion loss for both the proposed post-wall coplanar waveguide and the stripline design is

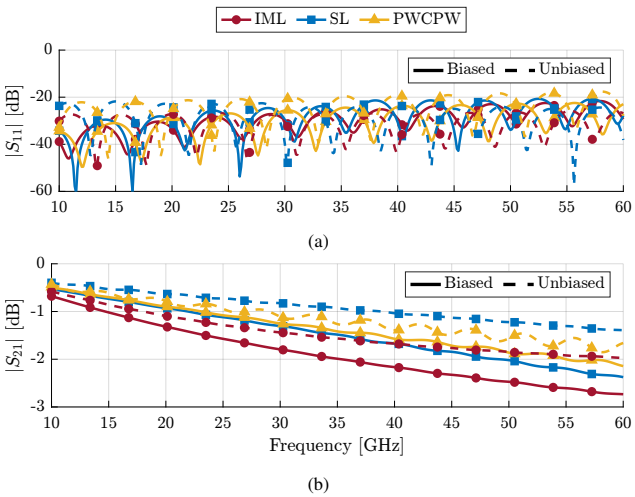


Fig. 3. Simulated (a) reflection and (b) transmission coefficients of the delay line phase shifters based on inverted microstrip line (IML), stripline (SL), and post-wall coplanar waveguide (PWCPW).

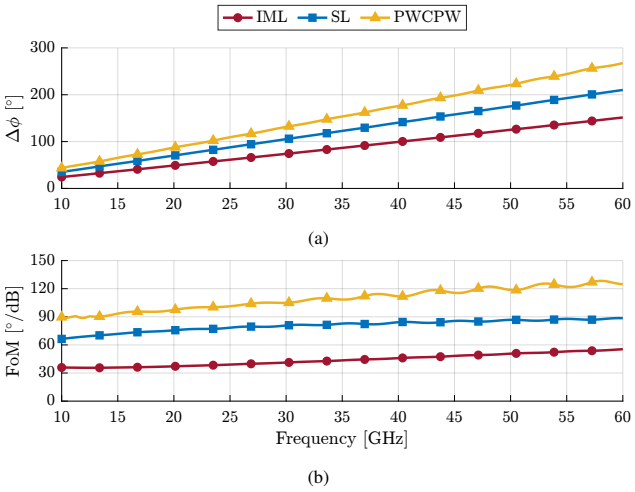


Fig. 4. Simulated (a) phase shift ranges and (b) Figure-of-Merits (FoM) of the delay line phase shifters based on inverted microstrip line (IML), stripline (SL), and post-wall coplanar waveguide (PWCPW).

similar and lower than that observed for the inverted microstrip line design. From 40 GHz to 60 GHz, the maximum insertion loss of the suggested structures is less than that of the other two designs when fully biased.

The simulated phase shift range and FoM of the three phase shifter designs are shown in Fig. 4. The suggested post-wall coplanar waveguide exhibits a larger phase shift range compared to the other two designs throughout the entire bandwidth from 10 GHz to 60 GHz. With the improved insertion loss and phase shift range, the proposed structure attains a superior FoM relative to the other two designs, varying from 89.6 °/dB at 10 GHz to 124.9 °/dB at 60 GHz (35 °/dB - 55 °/dB for inverted microstrip line and 75 °/dB - 90 °/dB for stripline across the same frequency range). This enhancement in performance validates the design concept of the proposed structure discussed earlier. A comparison among some up-to-date LC-based tunable phase shifters is summarized in Table I (only the simulation results are compared). It can be seen that the proposed structure has better FoM than the slow-wave structures presented in [5], [6] and the stripline design in [7].

TABLE I
PERFORMANCE COMPARISON OF STATE-OF-ART STRUCTURES

Frequency (GHz)	Phase Shift Range (°)	IL_{max} (dB)	FoM (°/dB)	Reference
56	100	1.5	66.7	[6]
67	537	9.7	55.4	[5]
60	210.6	2.38	88.5	[7]
60	267.3	2.14	124.9	**This Work**

IV. CONCLUSION

A post-wall coplanar waveguide design for LC-based tunable devices is introduced, which effectively utilizes the anisotropic properties of liquid crystals while ensuring a simple manufacturing process. Simulation results indicate that the proposed structure offers an FoM value ranging from 89.6 °/dB to 124.9 °/dB across frequencies from 10 GHz to 60 GHz. This represents a 35 % improvement over the stripline structure. Additionally, the proposed design shows reduced fabrication complexities and enhanced mechanical stability. Consequently, this structure has the potential to be used in a variety of applications in beam forming and beam switching within the millimeter-wave frequency range.

REFERENCES

[1] H. Zhou, L. Guo, C. Fumeaux, and A. Abbosh, "Dual-band phase shifter with independent phase control and diplexer functionality for K/ka-band LEO satellite systems," *IEEE Transactions on Circuits and Systems I: Regular Papers*, 10 Mar. 2026, early access, doi:10.1109/TCSI.2025.3645211. [Online]. Available: https://ieeexplore.ieee.org/document/11314166

[2] J. Rolf, G. Alexander, and W. Christian, "Microwave liquid crystal enabling technology for electronically steerable antennas in satcom and 5g millimeter-wave systems," *Crystals (Basel)*, vol. 10, no. 6, p. 514, 2020.

[3] S. Muller, P. Scheele, C. Weil, M. Wittek, C. Hock, and R. Jakoby, "Tunable passive phase shifter for microwave applications using highly anisotropic liquid crystals," in *2004 IEEE MTT-S International Microwave Symposium Digest (IEEE Cat. No.04CH37535)*, vol. 2, 2004, Conference Proceedings, pp. 1153–1156 Vol.2.

[4] O. H. Karabey, A. Gaebler, S. Strunck, and R. Jakoby, "A 2-d electronically steered phased-array antenna with 2 × 2 elements in lc display technology," *IEEE Transactions on Microwave Theory and Techniques*, vol. 60, no. 5, pp. 1297–1306, 2012.

[5] D. Wang, E. Polat, H. Tesmer, R. Jakoby, and H. Maune, "Highly miniaturized continuously tunable phase shifter based on liquid crystal and defected ground structures," *IEEE Microwave and Wireless Components Letters*, vol. 32, no. 6, pp. 519–522, 2022.

[6] D. Wang, E. Polat, C. Schuster, H. Tesmer, G. P. Rehder, A. L. C. Serrano, L. G. Gomes, P. Ferrari, H. Maune, and R. Jakoby, "Fast and miniaturized phase shifter with excellent figure of merit based on liquid crystal and nanowire-filled membrane technologies," *IEEE Journal of Microwaves*, vol. 2, no. 1, pp. 174–184, 2022.

[7] H. Zhou, L. Guo, and A. Abbosh, "Liquid crystal tunable stripline phase shifter," in *2023 5th Australian Microwave Symposium (AMS)*, Feb. 2023, pp. 3–4.

[8] J. Li and Y. Xiao, "180° differential phase shifting of 60 GHz signals using liquid crystal-filled strip-line designs with enhanced FoM performance and compact footprint," in *2025 27th International Conference on Digital Signal Processing and Its Applications (DSPA)*, Mar. 2025, pp. 1–5.

Reconfigurable and Tunable Millimeter-Waves Devices Based on Functional Materials

Yi Wang
University of Birmingham, United Kingdom (Great Britain)
y.wang.1@bham.ac.uk

Additive Manufacturing (AM) offers exciting capabilities for microwave engineering, enabling rapid prototyping, geometric flexibility, and easily customizable products. However, applying 3D printing to high-performance filters is not immediate, as these technologies are not originally tailored for high-frequency hardware. To meet strict electrical specifications, specific design adaptations and targeted post-processing steps are often required. This presentation highlights how AM can be effectively leveraged to build advanced microwave filters. Using selected hardware examples, we will discuss some of the most common 3D printing techniques adopted in this field and the practical actions needed to ensure optimal component performance. Finally, the talk will demonstrate how the geometric freedom of AM unlocks unconventional 3D topologies, allowing the development of a new class of filters that are highly optimized in terms of compactness, weight, and insertion losses.

979-8-3315-4544-4/26/$31.00 ©2026 IEEE

3-D Printed Metalenses for Terahertz Imaging

Geng-Bo Wu
City University of Hong Kong, Hong Kong
bogwu2@cityu.edu.hk

The terahertz (THz) frequency band (0.1-10 THz) offers immense potential for advanced imaging applications due to its non-ionizing nature, ability to penetrate non-polar materials, and distinctive spectral signatures. A critical component of THz systems is the THz lens, which facilitates high-resolution biosensing, biological imaging, and the detection of concealed details. However, traditional dielectric refractive lenses are bulky, suffer from significant aberrations, and often fail to achieve the high imaging resolution required for emerging applications. To overcome these limitations, metasurfaces have been widely employed in the design of THz metalenses. Metasurfaces provide a compact and versatile alternative to traditional lenses. In this talk, we will present various THz metalens designs, including achromatic metalenses, hyper-dispersive metalenses, and super-oscillatory metalenses, all fabricated using advanced dielectric 3D printing technology. We will also highlight their transformative applications, such as THz super-resolution imaging, axial-scan-free 3D object imaging, and resilient wireless communications. These 3D-printed metalenses, with their unique characteristics, pave the way for next-generation compact, high-resolution, and in vivo THz imaging systems.

979-8-3315-4544-4/26/$31.00 ©2026 IEEE

General-Purpose Terahertz Quasi-Optics and Mechanical Beamformers Enabled by 3D-Printing

Daniel Headland
The University of Adelaide, Australia
daniel.headland@adelaide.edu.au

Owing to their short wavelength and light-like propagation behavior, terahertz waves require quasi-optical components to control the flow of radiation. To meet this need, 3D-printing has evolved over the past decade from a niche technique to a highly customizable, general-purpose methodology to produce terahertz quasi-optics, using consumer-grade hardware..

979-8-3315-4544-4/26/$31.00 ©2026 IEEE

Integrated microwave photonics for signal processing and sensing

Invited Talk

Xiaoke Yi*, Liwei Li, Linh Nguyen and Robert Minasian

xiaoke.yi@sydney.edu.au

School of Electrical and Computer Engineering, The University of Sydney, NSW, 2006, Australia

Abstract – The field of microwave photonics has evolved significantly over the last decade, ushered by the breakthroughs in integrated photonics in realizing integrated microwave photonic devices with an array of functionalities packed on a nanoscale footprint. The combination of photonic integration with microwave photonics, enables the realization of reproducible, compact, lightweight, low-power consumption and low-cost microwave photonic systems that are physically and economically competitive against their electronic counterparts. Microwave photonics techniques have attracted dramatically increased attention. In this paper, we present recent advances across three interconnected themes: adaptive RF signal processing, high performance sensing, and photonic neural computing.

We first discuss adaptive microwave photonic interference mitigation for dynamic RF environments. By combining photonic amplitude and phase control, the system can suppress unknown and time-varying interference. Experimental results demonstrate robust recovery of signals of interest under continuous-wave, phase-modulated and multi-interference conditions. We then present machine-learning-enhanced microwave photonic sensing, where integrated photonic sensors convert optical responses into rich RF spectral signatures that can be interpreted by machine/deep learning (ML/DL) models. In our recent work, ML/DL-assisted microwave photonic sensors have enabled athermal operation, noise resilience, multi-parameter detection and extended sensing range. Finally, we discuss our recent photonic neural network accelerators based on inverse-designed nanophotonic structures. The photonic neural network perform classification within ultra-compact silicon photonic devices. The demonstrated photonic neural networks achieve a computational density of approximately 400 million parameters per mm², providing a scalable pathway towards energy-efficient analog photonic computing.

Keywords: Microwave photonics, photonic signal processing, sensing, neural networks.

979-8-3315-4544-4/26/$31.00 ©2026 IEEE

A Communication Signal based Vital-sign Sensing Method for Consumer Electronic Devices

Chenming Li, Xingqi Xuan, Junhao Zhang, Yulin Zhou, Shilie Zheng, Xiaonan Hui*, Xianmin Zhang
College of Information Science & Electronic Engineering,
Zhejiang University
Hangzhou, China
x.hui@zju.edu.cn

***Abstract*—In the information society, consumer electronic devices naturally possess wearable and portable characteristics. In light of this, we introduce a vital-sign detecting system for consumer electronic devices which utilizes wireless communication signals. Given the proximity of these devices to the human body, radio frequency energy is directed into a confined internal region, thereby facilitating the modulation of backscattered signals with pronounced bodily vibrations. Consequently, the received signals exhibit variations corresponding to the vital signs. After simply filtering out the high-speed modulated digital information, target signals can be obtained without complicated demodulation. The theoretical framework, numerical computations, and experimental results demonstrate congruence, thereby validating the efficacy of the proposed methodology for achieving stable, long-term monitoring across diverse wearing scenarios. The average heart rate aligned with the established gold standard, and the root-mean-square error (RMSE) for instantaneous heart rate was 1.02 bpm.**

Keywords—near-field electromagnetics, vital-sign detection, wireless communication systems, wearable devices

I. Introduction

With the rapid development of microwave technology and hardware capabilities, non-contact vital signs detection has been steadily evolving toward higher accuracy and higher levels of integration. At present, the relatively mature and widely adopted non-contact sensing approaches are radar-based systems [1], which transmit millimeter wave signals to capture the subtle vibrations generated by vital activities on the surface of the human, thereby extracting vital signs such as heart rate and respiration. The accuracy and effectiveness of radar-based systems have been widely validated in consumer, medical and other scenarios. Then, with the gradual opening of physical-layer information in Wi-Fi systems [2], non-contact vital sign detection can be more conveniently integrated into daily-life. Researchers can obtain Wi-Fi's channel state information (CSI) through open protocols and also separate vital signs like radar-based systems [3]. This approach provides a more universal solution for non-contact vital signs monitoring without additional hardware. From a system-level perspective, the core architecture of the aforementioned systems fundamentally relies on radio-frequency (RF) transceiver units. In modern information society, consumer electronic devices, such as smartphones, smart glasses, and earphones are commonly equipped with chips that have similar RF transceiver functionalities. If these devices can be used for sensing, they can naturally possess portability, wearability, etc.

Therefore, this article explores a communication signal based vital sign sensing method for consumer electronic devices. Since smart devices are typically in direct contact with the human body, a great number of RF energy can be efficiently coupled into target region [4]. And the energy of vital signs is concentrated within a narrow bandwidth. So, they will induce observable modulations in high-rate communication signals, which can be extracted through simple filtering without requiring demodulation. Experimental results showed that the proposed method achieved the root-mean-square error (RMSE) of approximately 1.02 bpm in long-term beat-to-beat heart rate monitoring under wearable scenarios, while the average heart rate was consistent with the electrocardiogram (ECG).

II. Signal Model and Detection Principle

Considering practical scenarios, the RF transceiver of consumer electronic devices is simplified as shown in Fig. 1. The RF transceiver unit generates RF signals modulated with communication information, which are then radiated by the transmitting antenna. From the perspective of sensing, Wi-Fi signals can be modeled as a superposition of multiple orthogonal subcarriers [5], which allows for continuous observation at the receiving end. For any subcarrier,

$$x_k(t) = \mathbf{B}_k e^{j(\omega_k t+\varphi_k)} \tag{1}$$

where $\mathbf{B}_k$ is a complex value determined by the baseband symbol modulation, affecting the amplitude and phase of the corresponding subcarrier. Due to the near-field effect, portable and wearable devices, often situated close to the human body, can efficiently couple substantial energy to a localized area within the body. Hence, the received signal consists of two parts:

$$S_1 = \alpha_1 x_k(t) e^{j\beta\varphi_1(t)} \tag{2}$$

$$S_2 = \alpha_2 x_k(t) e^{j\varphi_2} \tag{3}$$

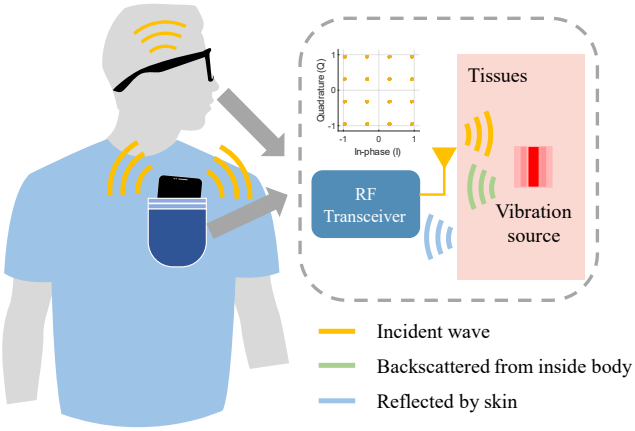


Fig. 1. Illustration of the system architecture and the signal propagation model.

where S_1 is the backscattered signals from inside the human body, which is modulated with the target vibrations. S_2 is the part directly reflected by the skin. α_1, α_2 are the attenuation factor. φ_1 demonstrates the movement of the target and β is modulation coefficient, which is defined as:

$$\beta = 4\pi \frac{d}{\lambda} \tag{4}$$

where d is the amplitude of the vibration source and λ denotes the wavelength in the media. φ_2 is the phase variation induced by the skin reflection. If directly extracting the phase of (2), the instantaneous phase will be affected by communication symbol modulation, which may overwhelm the target signals. Therefore, demodulation and phase unwrapping are commonly required to recover the usable phase information [6]. However, even for high-rate communication signals, the symbol duration is much longer than the round-trip electromagnetic propagation time [7]. The propagation process can be regarded as quasi-static within one symbol interval. So, S_1 and S_2 can be coherent [8]. Because the vibration inside the human body is stronger than the corresponding movement on the surface and the equivalent wavelength becomes shorter in high-permittivity media, the modulation in the received signal is mainly dominated by the vital signs inside the human body. As demonstrated in Fig. 2, a numerical calculation based on the above process was conducted. The transmitted signals were 16-QAM and the simulated vibration was 1.2 Hz. A slow variation envelope modulation on the received signals can be observed, which is consistent with the ground truth. Based on this, the target signals are easily obtained by filtering the high-speed signal without demodulation.

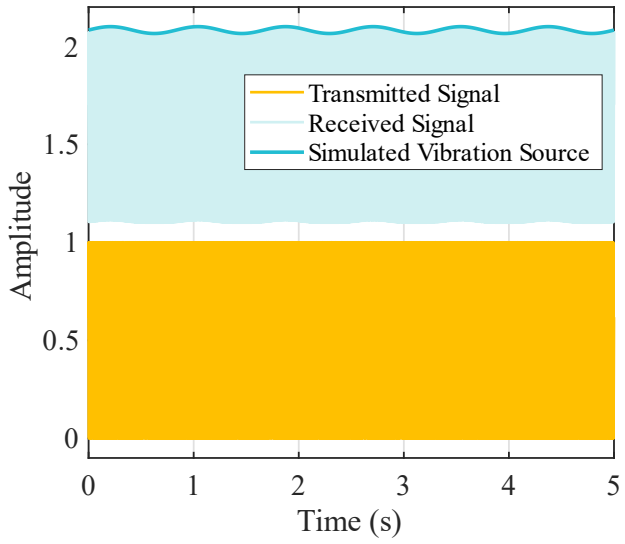


Fig. 2. Numerical calculation based on the proposed signal propagation model.

III. Experiments and Results

To verify the effectiveness and accuracy of the proposed method, as shown in Fig. 3(a), a standard software defined radio (SDR, B210) was employed to simulate consumer electronic devices. The transmitted signal was a random symbol sequence modulated using 16-QAM at a carrier frequency of 2.4 GHz. The receiving end acquired the signals without demodulation. Moreover, an ECG simultaneously collected the signals as a reference. Firstly, obtaining the cardiac dynamics from the heart is conducted and a flexible printed circuit (FPC) antenna was used to emulate the situation where consumer electronic devices were worn on the human body. As shown in Fig. 3(b), from the enlarged figure, it can be observed that the envelope of the received signals fluctuates with the heartbeat signal, which is consistent with theory and numerical calculation. Furthermore, the beat-to-beat heart rate (HR) is analyzed in Fig. 3(c). The instantaneous HR is almost identical to that obtained by ECG, with the RMSE of 1.02 bpm. It is able to provide a good foundation for more refined analysis of cardiac function, such as heart rate variability.

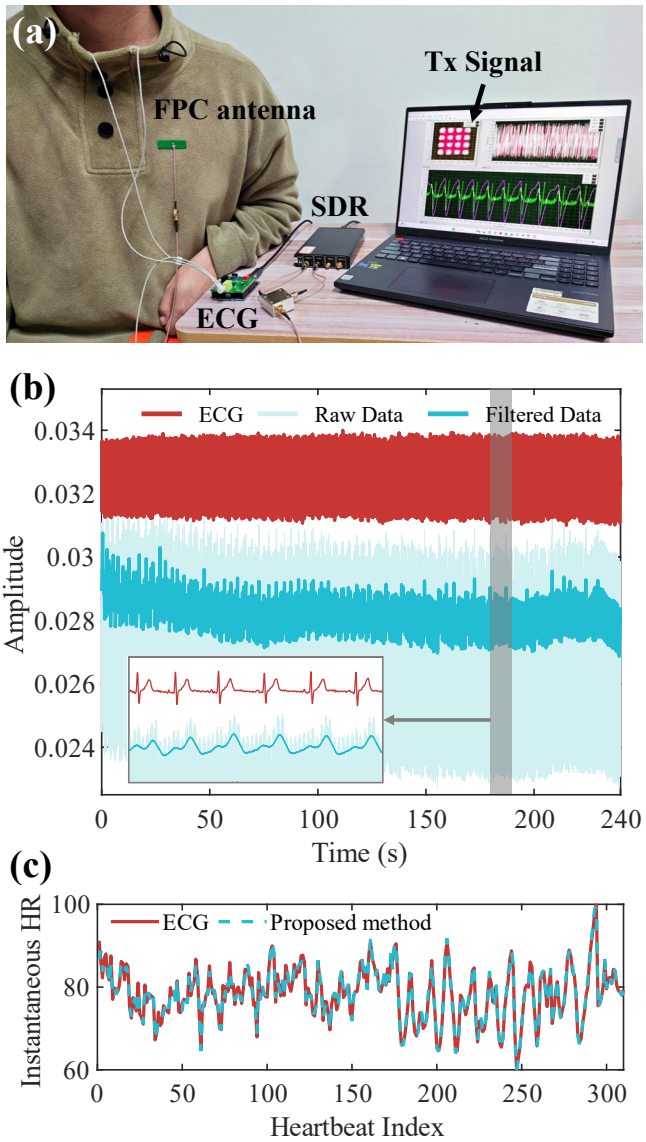


Fig. 3. Long-term heartbeat extraction experiment. (a) The experimental setup. (b) Experimental results. The light blue curve presents the raw data, and the dark blue curve denotes the signal after simple filtering. The red curve is the simultaneously collected ECG signal. (c) Comparison of beat-to-beat HR obtained from the proposed method and ECG.

In addition, the scene of wearing glasses was also conducted. As shown in Fig. 4(a) and (b), the proposed method achieved stable detection. A 60-seconds segment's spectrum are depicted in Fig. 4(c). The heartbeat spectrum is

very clear and consistent with the ECG method, which indicates the proposed method has the potential to be transferred to different consumer electronic devices and obtain stable detection.

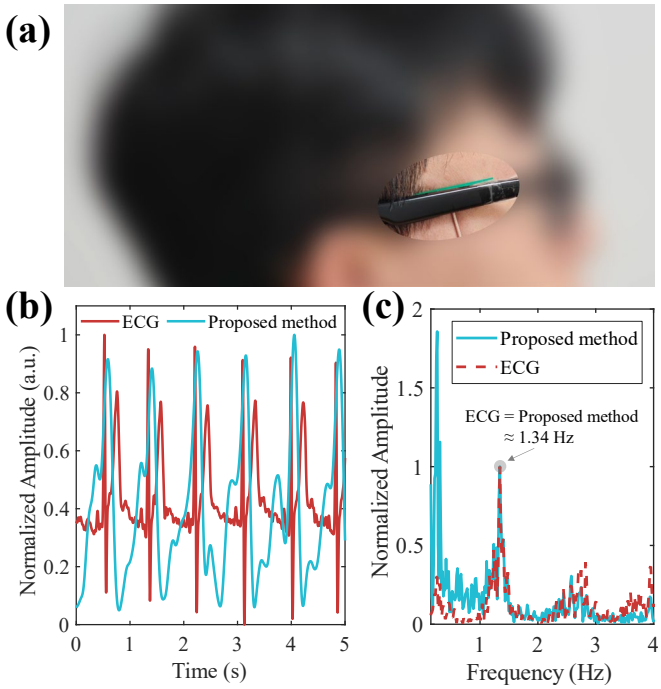


Fig. 4. Experiments and detection results in simulated smart glasses scene. (a) Illustration of wearing method. (b) Time-domain segment synchronously acquired by the proposed system and the ECG. (c) Comparison of frequency spectrum obtained from the 60 s measurement.

IV. Conclusions

In this article, we propose a communication signal based vital sign sensing method for consumer electronic devices. By establishing the signal propagation model, the vital signs can induce a slow variation envelope to the received signals. Therefore, the target signals are obtained by filtering. Experiments proved that the proposed method has high accuracy and long-term stability under different scenarios. Compared with ECG, the average HR is the same and the instantaneous HR RMSE is 1.02 bpm. This work provides a convenient vital sign detection method for consumer electronics devices with high accuracy and effectiveness.

Acknowledgment

The project is supported by the National Natural Science Foundation of China (Grant 62371419), the National Natural Science Fund for Excellent Young Scientists Fund Program (Overseas), Ningbo Natural Science Foundation (Grant 2024H008), the Key R&D Program of Zhejiang (2023C03160). The authors gratefully acknowledge the support of Zhejiang University Education Foundation Qizhen Scholar Foundation.

References

[1] E. Antolinos and J. Grajal, "Improving vital signs monitoring in real-world environments with W-band phased-array radars," *IEEE Trans. Microw. Theory Techn.*, vol. 73, no. 8, pp. 4363–4374, Aug. 2025.

[2] D. Zhang, L. Fang, X. Xie, S. Yang, J. Chen, and Y. Chen, "Enhancing CSI-based wireless sensing with open-source Linux 802.11ax CSI tool," *IEEE Sensors J.*, vol. 25, no. 10, pp. 18041–18052, May 2025.

[3] Q. Pu, J. Zhang, M. Zhou, and Y. Yi, "Robust respiratory and heartbeat rate estimation based on Wi-Fi beamforming feedback information," *IEEE Trans. Mobile Computing*, Early Access, pp. 1–18, 2025.

[4] C. Li, S. Zheng, X. Hui, and X. Zhang, "Electromagnetic effective coupling and high spatial resolution theory in near-field cardiac sensing," *IEEE Trans. Microw. Theory Techn.*, vol. 72, no. 4, pp. 2283–2297, Apr. 2024.

[5] J. He and W. Yang, "IMar: Multi-user continuous action recognition with WiFi signals," in *Proc. ACM Interact. Mob. Wearable Ubiquitous Technol.*, vol. 6, no. 3, p. 117:1-117:27, Sep. 2022.

[6] Y. Yang, L. Yuan, J. Zhao, and W. Gong, "Content-agnostic backscatter from thin air," in *Proc. ACM Mobile Sys. Appl. Services, in MobiSys '22*. New York, NY, USA: Association for Computing Machinery, Jun. 2022, pp. 343–356.

[7] Z. Liu, L. Chen, X. Zhou, Z. Jiao, G. Guo, and R. Chen, "Machine learning for time-of-arrival estimation with 5G signals in indoor positioning," *IEEE Internet Things J.*, vol. 10, no. 11, pp. 9782–9795, Jun. 2023.

[8] X. Hui and E. C. Kan, "Monitoring vital signs over multiplexed radio by near-field coherent sensing," *Nature Electron.*, vol. 1, no. 1, pp. 74–78, Nov. 2017.

Characterization of Knitted Textiles for Wearable Antennas

David S. Mitchell and Jennifer T. Bernhard
Electromagnetics Lab, University of Illinois at Urbana-Champaign, Urbana, IL, USA, 61801

Textile-integrated antennas have been the subject of much investigation due in part to their easy integration into everyday life. There are several methods that have been established for creating textile-integrated antennas. Two such methods are embroidery and knitting. Both employ the use of existing textile manufacturing methods and conductive threads and yarns. Embroidered antennas have been studied extensively and have made use of high precision, computer controlled embroidery machines (A. Kiourti, C. Lee, and J. L. Volakis, "Fabrication of Textile Antennas and Circuits With 0.1 mm Precision," *IEEE Antennas and Wireless Propagation Letters*, vol. 15, pp. 151–153, 2016). Knitted antennas, on the other hand, have not been as extensively studied. Some work has been done in characterizing the effective sheet impedance of knitted antennas and transmission lines, however this was only done for a single knit pattern (M. A. S. Tajin, C. E. Amanatides, G. Dion and K. R. Dandekar, "Passive UHF RFID-Based Knitted Wearable Compression Sensor," in *IEEE Internet of Things Journal*, vol. 8, no. 17, pp. 13763-13773, 1 Sept.1, 2021). A major advantage of knitted textiles is the ability to design and program different mechanical properties of the textile based on the knit pattern (Singal, K., Dimitriyev, M.S., Gonzalez, S.E. et al. "Programming mechanics in knitted materials, stitch by stitch". *Nature Communications* 15, 2622, 2024).

This work will examine and characterize a variety of textiles with differing knit patterns and will attempt to establish a relationship between their mechanical and electrical properties. This will be done using techniques from metasurface design, where a knit stitch will be treated as the unit cell and the bulk surface impedance properties will be extracted from HFSS simulations (A. M. Patel and A. Grbic, "A Printed Leaky-Wave Antenna Based on a Sinusoidally-Modulated Reactance Surface," in *IEEE Transactions on Antennas and Propagation*, vol. 59, no. 6, pp. 2087-2096, June 2011). Those metasurface simulations will then be used to design a pattern on a textile, which will be manufactured and compared against the simulated results.

This research was supported by an appointment to the Intelligence Community Postdoctoral Research Fellowship Program at The University of Illinois Urbana-Champaign administered by Oak Ridge Institute for Science and Education (ORISE) through an interagency agreement between the U.S. Department of Energy and the Office of the Director of National Intelligence (ODNI).

979-8-3315-4544-4/26/$31.00 ©2026 IEEE

Ultra-Wideband Multi-Channel Millimeter-Wave Receiver for Solar Sensing

Jun Shi
Key Laboratory of Microwave Remote Sensing, National Space Science Center, Chinese Academy of Sciences
Beijing, China
shijun@nssc.ac.cn

Zhaomin Peng Name Surname
Key Laboratory of Microwave Remote Sensing, National Space Science Center, Chinese Academy of Sciences
Beijing, China
pengzhaomin@nssc.ac.cn

Dehai Zhang
Key Laboratory of Microwave Remote Sensing, National Space Science Center, Chinese Academy of Sciences
Beijing, China
zhangdehai@mirslab.cn

I. Abstract

Solar radio emissions provide critical insights into dynamic solar atmospheric processes, including coronal heating, solar eruptions, and solar wind acceleration. We present a high-sensitivity, multi-channel receiver system operating across the 15–36 GHz range, specifically engineered to bridge observational gaps in capturing non-thermal phenomena, such as small-scale microwave bursts in the solar transition region. The system architecture employs low-noise amplifiers (LNAs) in the initial stage to minimize the overall noise figure, followed by multi-band filters and power dividers that split the signal into three primary sub-bands—15–22 GHz, 22–29 GHz, and 29–36 GHz—supporting dual-polarization observations. By integrating frequency down-conversion with high-speed digital spectroscopy, the system achieves the temporal and spectral resolution requisite for characterizing rapid frequency drift and transient burst dynamics in real-time.

Currently, the system is deployed at the Lenghu Station on the Qinghai-Tibet Plateau at an altitude of 4,100 meters for pilot observations. Comparative measurements of solar and the cold sky demonstrate that the system possesses high observational sensitivity. This successful deployment validates the system's efficacy for comprehensive solar monitoring and establishes a robust foundation for future observations aimed at advancing solar physics and space weather research.

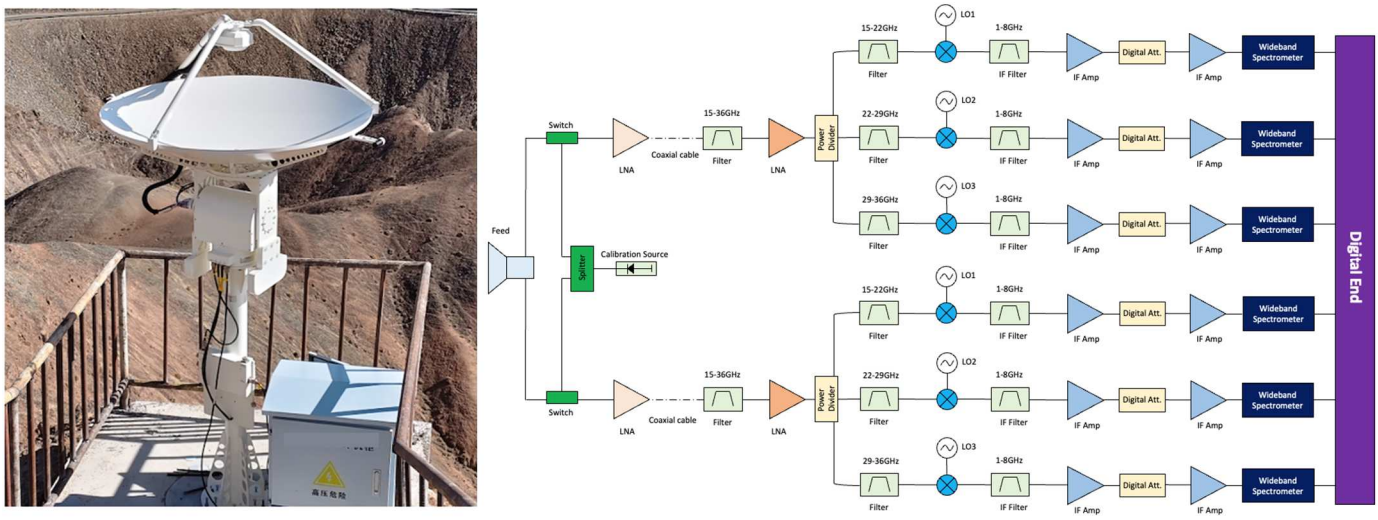


Fig. 1. Photo and diagram of the receiver.

PDMS-MWCNT Composite Material Properties, Preparation and Role in Wearable Antennas

Musa Hussain[1], Hajra Khan[2], Syed Muzahir Abbas[3]
[1]School of Engineering and Built Environment, Griffith University, Gold Coast Campus, QLD, 4215, Australia
[2]Department of Electrical and Computer Engineering, COMSATS University Islamabad, Abbottabad, Pakistan
[3]Faculty of Science and Engineering, Macquarie University, Sydney, NSW 2109, Australia

***Abstract*—In this paper, the properties, preparation and applications of PDMS-MWCNT composite is discussed. The main focus of the paper remains on the applications of flexible antennas used in wearable electronic devices. The flow diagram of making of the PDMS and PDMS-MWCNT composite is given. Moreover, the detailed analysis of both materials in terms of scanning electron microscope (SEM) is analyzed. Later, some examples are given from the literature, which shows the role of these materials in the antenna designing applications.**

Keywords—MWCNT, PDMS, SEM, Wearable Antenna.

I. Introduction

With the advancement and development in wireless communication system, the rapid change in requirement of wearable devices are observed [1]. The flexible wearable devices are required for wearable applications, which are made of polymer-based materials are made up of long molecular chains and are light, resistant to corrosion, and easy to work with. They are used in structural, insulating, and flexible electronic applications [2]. Polymers are used in electronics as substrates for flexible circuits, dielectric layers in capacitors, encapsulating materials, and parts of organic semiconductors. Multi-Walled Carbon Nanotubes (MWCNTs) are graphene layers that are arranged in concentric cylinders. They have a high electrical conductivity, a large aspect ratio, a high mechanical strength, and a strong electromagnetic interaction. When mixed into polymer matrices, MWCNTs create conductive networks with low percolation thresholds [3]. This greatly improves electrical conductivity and electromagnetic interference (EMI) shielding. MWCNT-polymer composites make it possible to make lightweight, flexible, and small antennas with better bandwidth, variable permittivity, and better radiation efficiency for RF and antenna applications [4]. Because they lose dielectric energy and are conductive, they are also utilized in absorbers, frequency-selective surfaces, and microwave shielding. In general, polymer/MWCNT composites offer both structural flexibility and customized electrical performance. This makes them promising for next-generation communication systems, flexible RF devices, and wearable electronics [5–6].

II. Material Properties, Preparation and Analysis

A. Properties of PDMS and MWNCT

Polydimethylsiloxane (PDMS) is a widely used silicon-based polymer for various electronic applications, especially in antennas [7]. It has simple production processes, excellent dielectric properties, and offers flexibility as well as low cost. Besides these properties, PDMS is lightweight, transparent, biocompatible with the human body and with conductive materials. It also has the advantage of being easy to mold and shape, which helps design the desired or required geometrical structure of the antenna [8].

MWCNT is one of the finest conductive fillers that offers a high dielectric constant. It is chemically stable, flexible, biocompatible, and has high tensile strength and high thermal conductivity. However, it has large van der Walls forces which make it easy to generate the leakage path in the polymer matrix [9].

As discussed above, MWCNTs are highly entangled by Van der Waals forces, and the presence of CNTs in large bundles or dense agglomerates can cause uncontrolled electronic alteration and poor performance. Therefore, making a homogenous distribution of MWCNT in PDMS is required to get high electrical performance for the electronic devices. MWCNT-PDMS offers excellent electrical conductivity, mechanical strength, flexibility, thermal stability, and biocompatibility [10].

B. Preparation of PDMS and PDMS MWCNT Composite

The PDMS used as a substrate material are prepared in the laboratory by the following steps. First, silicon elastomer base and curing agent are mixed well in a 1:10 ratio by string. Then, the mixture is placed in a vacuum pressure pump for 45–60 minutes to remove the trapped air bubbles. After that the PDMS solution is poured over a 3D mold. At this stage, a casting knife is used for an even surface of the substrate. Then it is placed in an oven for 3 to 4 hours at 60°C. After this stage, the sample is cured and solidified, then it is peeled out of the 3D mold. The step-by-step process of preparation of PDMS as a substrate is depicted in Figure 1(a).

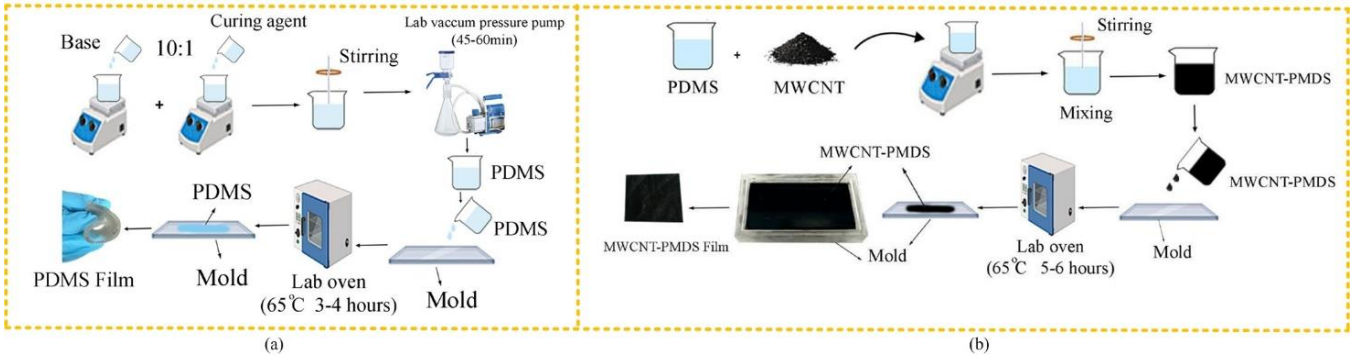


Figure 1. Schematic diagram of preparation of (a) PDMS layer (b) MWCNT-PDMS composite layer.

The preparation steps of the MWCNT-PDMS composite material, are given in Figure 1(b). It can be seen, that initially the MWCNT powder is mixed with PDMS solution. After that, the solution of MWCNT-PDMS is poured over the 3D mold which has the replica of the structure of the antenna. To make even surfaces, a casting knife is used. The sample is then placed in an oven at 60°C. After 5–6 hours, the sample is solidified and peeled out from the mold.

C. SEM Analysis of PDMS and PDMS-MWCNT Composite

The Field Emission Scanning Electron Microscopy (FE-SEM) images comparing the surface morphology of the pure PDMS and MWCNT/PDMS composite are given in Figure 2. The pure PDMS surface is continuous and relatively smooth, with only fine, closely spaced wrinkles from the crosslinked siloxane network. In contrast, the MWCNT/PDMS composite shows a much rougher and more uneven surface, with crumpled and raised regions generated by the embedded nanotubes. The increased surface roughness and good dispersion of MWCNTs in the PDMS matrix help improve the composite's electrical pathways and electromagnetic response, making it good for use in antenna.

To verify the elemental composition and chemical homogeneity of the PDMS surface, SEM–EDS analysis was performed. Figure 2 presents the SEM–EDS analysis of the pure PDMS sample. The composition (28.70 wt% C, 37.53 wt% Si and 24.49 wt% O) is consistent with the polysiloxane

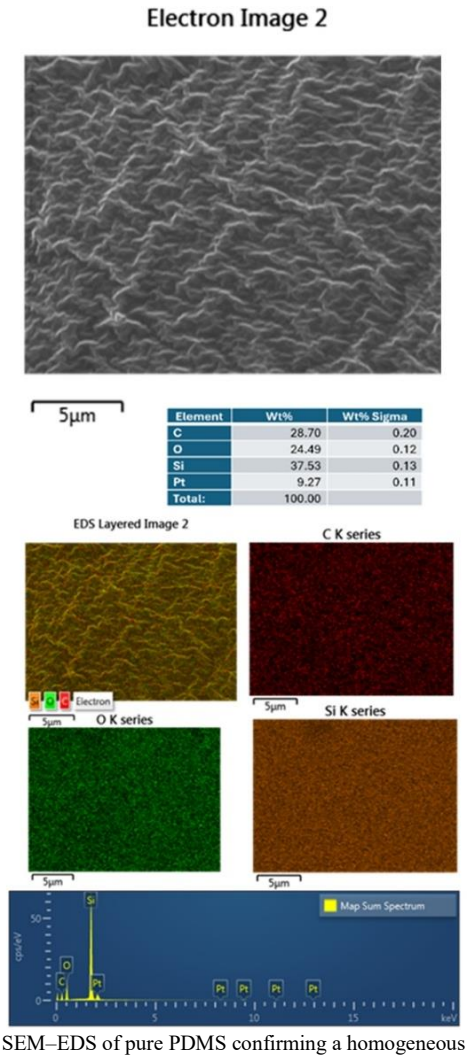


Figure 2. SEM–EDS of pure PDMS confirming a homogeneous Si–O–C polysiloxane matrix.

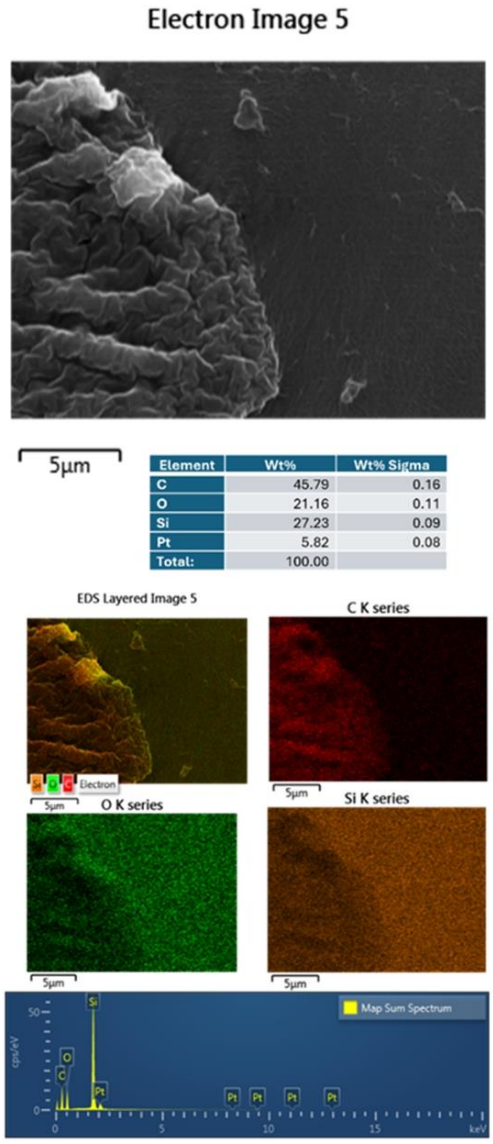


Figure 3. SEM–EDS of MWCNT/PDMS composite.

backbone of PDMS, with the high Si content and Si–O ratio confirming a silicone-rich matrix without additional carbonaceous reinforcement such as MWCNTs. The platinum (9.27 wt%) comes from the Pt-based material that was used to look at the SEM. The elemental maps show Si, O and C to be uniformly distributed, indicating a chemically homogeneous pure PDMS surface.

SEM–EDS characterization of the conductive MWCNT/PDMS antenna composite as shown in Figure 3, highlighting high carbon content (45.79 wt%) from embedded MWCNTs, with 27.23 wt% Si and 21.16 wt% O from the PDMS polysiloxane matrix. The elemental maps confirm a homogeneous distribution of C, Si and O, indicating well-dispersed nanotubes and a uniform composite structure suitable for flexible antenna applications.

III. PDMS-MWCNT Composite Role In Wearable Antennas

MWCNT–PDMS composites are great for designing flexible and stretchable antennas because they combine the flexibility and low dielectric constant of Polydimethylsiloxane (PDMS) with the excellent electrical conductivity and aspect ratio of MWCNTs. When MWCNTs are evenly spread out in

the PDMS matrix, they make conductive networks that let you change the conductivity and permittivity, which makes it easier to match impedance and make antennas smaller. These materials enable lightweight, conformal, and wearable antennas that maintain consistent RF performance while bending and stretching, while also enhancing electromagnetic interference (EMI) shielding and mechanical endurance. In Figure 4, the examples of various antenna are given [11–13]. It can be seen that these antenna offers simple geometrical structure, compact in size, light in weight and also offers flexibility. Moreover, these antenna are muti-functional, as it offers multiple frequency bands. The antenna prototype is also placed on human body to check the SAR performance and gain of the antenna. These detailed explanation shows that PDMS-MWCNT composite material is one of the potential material used for biomedical electronic devices.



Figure 4. Examples of wearable antenna design by using PDMS-MWCNT Composite [11–13].

IV. Conclusion

The paper focus on the PDMS and PDMS-MWCNT composite material used in antenna designing. Initially the properties of these materials are explained and after that the preparation is discussed along with flow diagram. After that the SEM analysis of these materials are performed and explained. In the last, some example from literature is given, where these materials are used in antenna designing. These examples shows that PDMS-MWCNT composite is potential material for antenna designing used for wearable and biomedical portable electronic devices.

References

[1] Zhao, Xin, et al. "Strain and pressure sensors based on MWCNT/PDMS for human motion/perception detection." *Polymers* 15.6 (2023): 1386.

[2] Song, K., Cho, N. K., Choi, Y., Connolly, S., & Nam, H. J. (2024). In-depth analysis of mechanical and electrical responses of PDMS/MWCNT micro-composite films under cyclic loading conditions. *Polymer*, *290*, 126552.

[3] Bora, P. J., Chandana, G., Mahanta, B., Doh, J., Ramamurthy, P. C., & Raghavan, N. (2023). Optimization of PDMS-MWCNT nanocomposites for strong Ku-band absorption by integrating microwave simulations and genetic algorithm. *Composites Communications*, *39*, 101568.

[4] Panda, S., & Acharya, B. (2019). PDMS/MWCNT nanocomposites as advanced electronic materials: mechanical, electrical and thermal studies. *Integrated Ferroelectrics*, *202*(1), 171-184.

[5] Shin, S. C., Hong, M., & Lee, S. E. (2025). Double-layered radar absorbing MWCNT/PDMS composites optimized by genetic algorithm using complex permittivity as a continuous variable. *Composites Part A: Applied Science and Manufacturing*, 109204.

[6] Karuppiah, P., Nambi Ramachary, R., Kulandai Samy, J. W., & Vadivel Murugan, P. V. (2024). A Theoretical Investigation of the Electrical and Dielectric Properties of PDMS-CNT. *Macromolecular Theory and Simulations*, *33*(3), 2300062.

[7] Sharma, P. K., & Chung, J. Y. (2023). Evaluation of polydimethylsiloxane (PDMS) as a substrate for the realization of flexible/wearable antennas and sensors. *Micromachines*, *14*(4), 735.

[8] Salleh, S. M., Ain, M. F., Ahmad, Z., Abidin, I. S. Z., Seng, L. Y., & Osman, M. N. (2023). Stretchable and bendable polydimethylsiloxane-silver composite antenna on PDMS/air gap substrate for 5G wearable applications. *IEEE Access*, *11*, 133623-133639.

[9] Alhashmi Alamer, F., & Almalki, G. A. (2022). Fabrication of conductive fabrics based on SWCNTs, MWCNTs and graphene and their applications: a review. *Polymers*, *14*(24), 5376.

[10] Islam, M. H., Afroj, S., Uddin, M. A., Andreeva, D. V., Novoselov, K. S., & Karim, N. (2022). Graphene and CNT-based smart fiber-reinforced composites: a review. *Advanced Functional Materials*, *32*(40), 2205723.

[11] Hussain, M., Awan, W. A., Abbas, S. M., & Zhu, Y. (2025). Compact Bendable Multiwalled Carbon Nanotube/PDMS Antenna for WLAN and Wi-Fi 6E Wearables in 5G/6G Networks. *Advanced Engineering Materials*, *27*(23), e202502127.

[12] Hussain, M., Awan, W. A., Zahra, H., Abbas, S. M., Al-Bawri, S. S., & Zhu, Y. (2025). Design and characterization of multiwall carbon nanotube/polydimethylsiloxane composite MIMO antenna for wearable and vehicular applications. *Scientific Reports*, *15*(1), 27925.

[13] Shi, Y., Duan, J., Zhang, B., Ma, J., & Meng, Q. (2024). Multi-frequency composite wearable antenna for wireless communications. *Smart Materials and Structures*, *33*(6), 067002.

Power-Based Direction-Finding Enabled by a Null-Scanning Space-Time Leaky-Wave Antenna

Yiqing Sun[1,2,3], Geng-Bo Wu[1,2,3], and Chi Hou Chan[1,2]

[1] Department of Electrical Engineering, City University of Hong Kong, Hong Kong, China (yiqingsun5-c@my.cityu.edu.hk)
[2] State Key Laboratory of Terahertz and Millimeter Waves (City University of Hong Kong), Hong Kong, China
[3] City University of Hong Kong Shenzhen Research Institute, Shenzhen, 518057, China (bogwu2@cityu.edu.hk)

***Abstract*—This paper presents a power-based direction-finding (DF) scheme based on a space-time leaky-wave antenna (STLWA) with fixed-frequency radiation null scanning capability. The direction of arrival (DoA) can be estimated by identifying the power-minimum angle between two lobes in the spatial power spectrum. To be specific, by programming the 1-bit phase-control unit cells with distinct time-periodic signals, the amplitude of the aperture field at the fundamental frequency can be flexibly controlled. By leveraging space-time modulation, the STLWA provides steerable radiation nulls at the fundamental frequency. DF experiments are conducted to validate the system's performance. The proposed approach offers a compact, phase-shifter-free, fixed-frequency solution for sensing and localization.**

Keywords—Beam scanning, direction-finding, radiation null, space-time leaky-wave antenna

I. Introduction

Direction finding (DF) is a technique for determining the direction of arrival (DoA) of electromagnetic (EM) waves. It plays a key role in applications including wireless communication, autonomous driving, radar, and navigation [1]-[3]. Among various DF methods, power-based DF is attractive as it relies solely on power acquisition, avoiding coherent receivers and phase calibration, thereby reducing hardware complexity and system costs. Power-based DF relies on beam-scanning antennas that scan across space to form a spatial power spectrum, and DoA can be estimated by analyzing the measured spatial power spectrum. Among various types of beam-scanning antennas, leaky-wave antennas (LWAs) have become an attractive choice due to their planar form factor, lightweight construction, and ease of fabrication. Several LWA-based DF systems have been reported over the past decade [4]-[6].

Most power-based DF systems rely on the conventional beam-scanning characteristics of the antennas, and DoA estimation is performed by identifying the power peak in the spatial spectrum. Therefore, achieving high accuracy in the power-peak paradigm demands highly directive narrow beams, which, in turn, require large apertures to reduce beamwidth. As an alternative, the power-null-based DF method has been proposed, enabled by LWAs with radiation null-scanning capability [7]-[9]. The power-null-based DF is appealing because radiation nulls exhibit much sharper angular selectivity than main lobes, enabling finer discrimination of arrival angles. However, existing null-scanning LWAs require dual-antenna configurations or a wide frequency band to allow scanning [9], thereby limiting their compactness and practical applicability.

This work addresses these gaps by presenting a compact, fixed-frequency, power-based DF system enabled by a null-scanning space-time leaky-wave antenna (STLWA). By incorporating temporal modulation, the STLWAs unlock advanced radiation-control capabilities that are difficult for space-only reconfigurable LWAs [10]-[14]. In this work, a null-pattern synthesis method based on a phase-controlled STLWA is first introduced, and DF experiments are conducted to verify the power-null-based DF method.

II. Null-Scanning STLWA Working Principle

A. STLWA Configuration

As shown in Fig. 1(a), the STLWA contains forty unit cells with 1-bit phase control capability. The STLWA uses a microstrip line sandwiched between two substrates as the guiding structure, with two transitions at its terminals to facilitate measurement [14]. As shown in Fig. 1(b), each unit cell contains two PIN diodes, which are controlled by the bias voltages from the FPGA. As shown in the inset of Fig. 1(a), the control signal for the unit cell at location x is a temporal periodic signal with a duty cycle of $\tau(x)$. When PIN-1 is on and PIN-2 is off, the unit cell operation state is denoted by "+1"; when PIN-1 is off and PIN-2 is on, the operation state is "-1". As shown in Fig. 1(c), under continuous-wave (CW) excitation of 1 W, the two operation states of the unit cell provide equal radiated power and a phase difference of around 180°. By applying spatiotemporal modulation, each unit cell is independently controlled and alternates between two states, leading to a space-varying, time-periodic coupling coefficient $C(x, t)$ between the microstrip line and free space.

B. STC Strategy for Null-pattern Synthesis

Assume a CW RF signal is injected into the STLWA with a fundamental frequency of f_0, and the frequency of the time-periodic modulation signals is $\Delta f << f_0$. In the time domain, the coupled E-field distribution just above the aperture is:

$$E(x,t) = E_0 e^{j2\pi f_0 t} e^{-j\beta_{gw} x} \Pi(x) C(x,t) \tag{1}$$

where E_0 is the field magnitude, $\beta_{gw} = 1.4k_0$ is the phase constant of the guided mode in the microstrip line, k_0 is the free-space wavenumber at f_0, and $\Pi(x)$ is a rectangular function defining the antenna aperture. Given the time-periodicity of $C(x, t)$, the electric field in the time domain can be expanded into a Fourier series in the frequency domain, and the corresponding Fourier coefficients are:

$$a_m(x) = \begin{cases} 2\tau(x) - 1, m = 0 \\ 2(-1)^m \frac{\sin(\pi m \tau(x))}{\pi m}, m = \pm 1, \pm 2.. \end{cases} \tag{2}$$

Equation (2) reveals that the field amplitude at the fundamental frequency can be controlled via the duty cycle $\tau(x)$, regardless of the specific coding. Thus, a time-domain

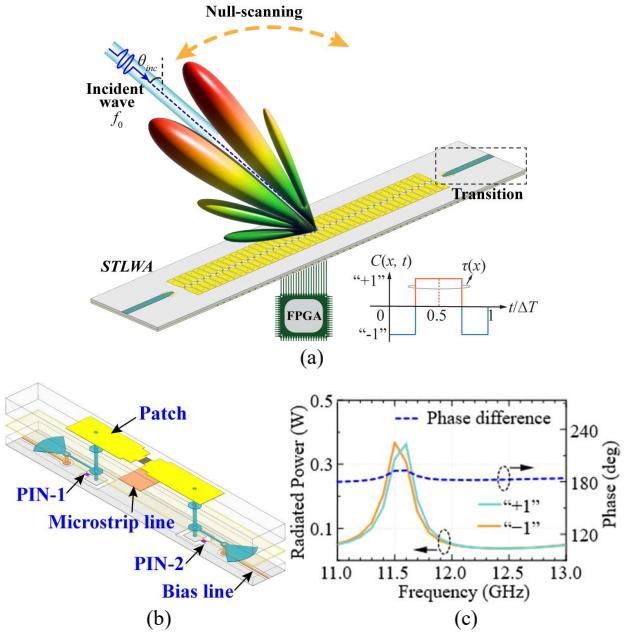


Fig. 1. (a) Configuration of the null-scanning STLWA operating at the fundamental frequency. (b) Unit-cell configuration (c) Simulated results of the unit cell.

randomization strategy can be adopted to disrupt the spatial periodicity and thereby suppress the sideband radiations [10].

This amplitude-control capability of the STC scheme can be leveraged to implement spatial amplitude modulation (AM) distribution. By forming a sinusoidal amplitude envelope across the antenna aperture, spatial AM generates the $n = -1$ space harmonic and converts it into a fast wave [15]. Therefore, the required duty cycle distribution $\tau(x)$ along the aperture should follow a sinusoidal function of:

$$\tau(x) = \frac{1}{2}\left(1 + M\cos\frac{2\pi x}{\Lambda}\right) \tag{3}$$

where $\Lambda = 2\pi/\left(\beta_{gw} - k_0 \sin\theta_r\right)$ is the spatial modulation period. Thus, the radiation angle θ_r can be flexibly controlled by changing the modulation period Λ [15]. Beam directions of ±4.6° are selected as examples. The overlapping angle of these two beams is the desired radiation null direction of $\theta_{null} = 0°$. The required envelope of duty cycle and the corresponding theoretical radiation patterns are shown in Figs. 2(a) and (b), respectively.

To generate a radiation pattern with a deep null at $\theta_{null} = 0°$, the two beams must be out of phase [9]. The required phase condition is expressed by:

$$\Delta\psi = (2n+1)\pi, n = 0, \pm1, \pm2.. \tag{4}$$

where $\Delta\psi = \left|\psi_1\left(\theta_{null}\right) - \psi_2\left(\theta_{null}\right)\right|$ is the difference between the radiation phases of the two constituent beams (ψ_1 and ψ_2) at θ_{null}. Therefore, the two duty cycle envelopes should be superimposed with a phase-compensation term, leading to a final duty cycle distribution for null-pattern synthesis as:

$$\tau(x) = \frac{1}{2}\left[1 + M_1\cos\frac{2\pi x}{\Lambda_1} + M_2\cos\left(\frac{2\pi x}{\Lambda_2} + \varphi_2\right)\right] \tag{5}$$

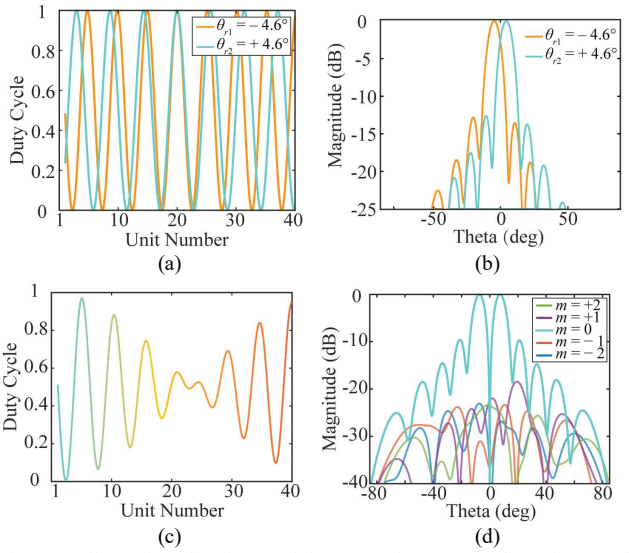


Fig. 2. Illustration for the spatial AM and corresponding duty cycle distributions. (a) Duty cycle distributions for $\theta_{r1} = -4.6°$, $\theta_{r2} = 4.6°$. (b) radiation patterns for $\theta_{r1} = -4.6°$, $\theta_{r2} = 4.6°$. (c) Required duty cycle distributions for null pattern with $\theta_{null} = 0°$. (d) Radiation patterns at different harmonic frequencies with $\theta_{null} = 0°$.

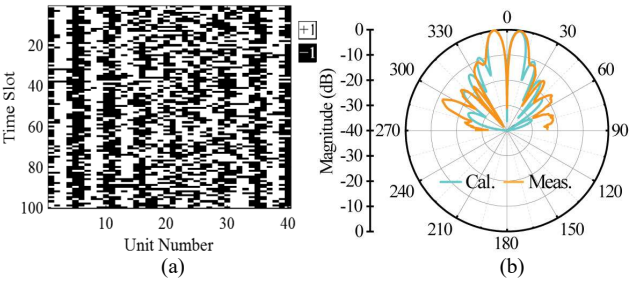


Fig. 3. STC matrix and null-scanning radiation patterns with θ_{null} set to 0°. (a) Calculated STC matrix. (b) Measured radiation pattern at $f_0 = 12$ GHz.

For the case of $\theta_{null} = 0°$, $\theta_{r1} = -4.6°$, $\theta_{r2} = 4.6°$, the condition in (4) is fulfilled when $\varphi_2 = 206°$, and the corresponding duty cycle distribution is presented in Fig. 2(c) with theoretical radiation pattern shown in Fig. 2(d).

III. Experimental Results

Based on the calculated duty cycle distribution shown in Fig. 2(c), we can obtain the STC matrix after randomization to eliminate spatial periodicity, as depicted in Fig. 3(a). The modulation frequency is set to $\Delta f = 20$ kHz. The corresponding radiation pattern is demonstrated in Fig. 3(b). We can observe that the measured result agrees well with the theoretical one, thereby validating the feasibility of the proposed null pattern synthesis method. Following the same synthesis process, a series of STC matrices corresponding to different radiation null directions can be obtained.

Based on this, a fixed-frequency DF system is established. A horn antenna is utilized to provide the incident wave at f_0, while the STLWA is connected to a vector network analyzer (VNA). Different STC matrices are sequentially loaded into the FPGA to generate dynamically scanning radiation nulls across space. We also conducted the DF experiment under the conventional power-peak-based DF method using main-lobe-scanning radiation patterns for comparison. The received powers are recorded by the VNA as a function of the scanning angles, leading to the spatial power spectra. For the null-

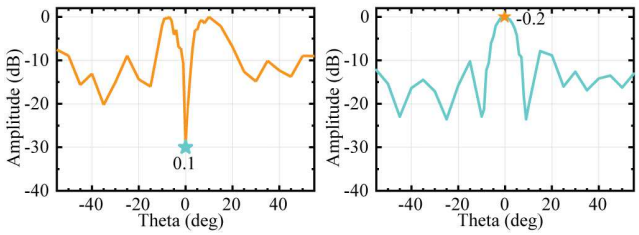


Fig. 4. DF performance of the proposed STLWA-based DF system. (a) Spatial power spectra obtained under null-scanning mode with incident angles of 0°. (b) Spatial power spectra obtained under the main lobe-scanning mode with incident angles of 0°.

scanning STCLWA, the DoA is estimated by searching for the angle of minimum received power between two adjacent peaks, i.e., the power null. In contrast, under the main lobe scanning mode, the DoA is estimated by locating the angle corresponding to the maximum received power, i.e., the power peak. Figs. 4(a) and (b) present the measured spatial power spectra by using the power-null and power-peak DF method, respectively, both under a representative incident angle of θ_{inc} = 0°. The power-null-based DF approach demonstrates superior angular resolution and estimation accuracy compared to the conventional power-peak-based method.

IV. Conclusion

In this work, a novel DF system based on an STLWA with fixed-frequency null-scanning capability has been proposed and experimentally validated. By tailoring the duty cycle of the STC sequences, dynamic beam control is achieved without requiring frequency variation or external phase-shifting components. Leveraging the null-scanning capability, the proposed system achieves accurate DoA estimation by analyzing the spatial power spectrum. Comparative experiments further demonstrate that the null-based DF method achieves superior accuracy compared to conventional peak-based approaches. As a compelling combination of fixed-frequency operation, high estimation precision, and low system complexity, the proposed DF system presents promising potential for next-generation sensing and localization applications.

Acknowledgement

This work was supported in part by the Hong Kong Research Grants Council of the Hong Kong SAR under Grant CityU 21207824 and in part by AoE/E-101/23-N, the National Natural Science Foundation of China 62401487.

References

[1] C. U. Bas *et al.*, "Real-time millimeter-wave MIMO channel sounder for dynamic directional measurements," *IEEE Trans. Veh. Technol.*, vol. 68, no. 9, pp. 8775–8789, Sep. 2019.

[2] M. Ibrahim *et al.*, "Design and analysis of compressive antenna arrays for direction of arrival estimation," *Signal Process.*, vol. 138, pp. 35–47, Sep. 2017.

[3] C. He *et al.*, "Direction finding by time-modulated linear array," *IEEE Trans. Antennas Propag.*, vol. 66, no. 7, pp. 3642–3652, Jul. 2018.

[4] A. Gil-Martínez, M. Poveda-García, J. García-Fernández, M. M. Campo-Valera, D. Cañete-Rebenaque, and J. L. G. Tornero, "Direction finding of RFID tags in UHF band using a passive beam-scanning leaky-wave antenna," *IEEE J. Radio Freq. Identif.*, vol. 6, pp. 552–563, Jun. 2022.

[5] D. Xu, Y. Wang, J. Sarrazin, B. Ma, and Q. Zhu, "DOA estimation of coherent signals based on EPUMA method with frequency beam scanning leaky-wave antennas," *IEEE Access*, vol. 11, pp. 88378–88387, Aug. 2023.

[6] R. S. Zakariyya *et al.*, "Joint DoA and CFO estimation scheme with received beam scanned leaky wave antenna for industrial internet of things (IIoT) systems," *IEEE Internet Things J.*, vol. 10, no. 15, pp. 13686–13696, Aug. 2023.

[7] M. Huang and J. Liu, "A null frequency scanning leaky-wave antenna," *IEEE Trans. Antennas Propag.*, vol. 70, no. 9, pp. 7625–7635, Sep. 2022.

[8] M. Huang and J. Liu, "An array of two periodic leaky-wave antennas with sum and difference beam scanning for application in target detection and tracking," *Front Inform. Technol. Electron Eng.*, vol. 24, no. 4, pp. 567–581, Apr. 2023.

[9] D. Zheng *et al.*, "On the synthesis of null-scanning leaky-wave antennas (NSLWAs) for millimeter-wave direction-finding applications," *IEEE Trans. Antennas Propag*, vol. 73, no. 4, pp. 2462-2474, Apr. 2025.

[10] G.-B. Wu *et al.*, "A universal metasurface antenna to manipulate all fundamental characteristics of electromagnetic waves," *Nat. Commun.*, vol. 14, no. 1, p. 5155, Aug. 2023.

[11] S.-X. Huang *et al.*, "Enabling real-time near-field focusing imaging with space-time-coding metasurface antenna," *IEEE Trans. Antennas Propag.*, vol. 72, no. 12, pp. 9082-9094, Dec. 2024.

[12] G.-B. Wu *et al.*, "A synthetic moving-envelope metasurface antenna for independent control of arbitrary harmonic orders," *Nat. Commun.*, vol. 15, no. 1, p. 7202, Aug. 2024.

[13] G.-B. Wu *et al.*, "A Space-time holographic metasurface antenna". *Sci. Adv.* vol. 11, no. 38, ,eadx7090, Sep, 2025.

[14] Y. Sun, G. -B. Wu, and C. Hou Chan, "A versatile shaped-beam space-time-coding metasurface antenna based on 1-bit phase control," *IEEE Trans. Antennas Propag.*, vol. 73, no. 11, pp. 8876-8887, Nov. 2025.

[15] G.-B. Wu, Q.-L. Zhang, K. F. Chan, B.-J. Chen, and C. H. Chan, "Amplitude-modulated leaky-wave antennas," *IEEE Trans. Antennas Propag.*, vol. 69, no. 7, pp. 3664–3676, Jul. 2021.

Planar EBG Monostatic Antenna with Wideband Interport Isolation Characteristics for 5G In-Band Full Duplex Applications

Haq Nawaz[1], *Senior Member IEEE,* Syed Muzahir Abbas[2], *Senior Member IEEE*

[1]Marine Engineering Department, Military Technological College (MTC), Muscat 111, Oman

[2]School of Engineering, Faculty of Science and Engineering, Macquarie University, Sydney, NSW 2109, Australia

haq.nawaz@mtc.edu.om

***Abstract*—This work presents a dual port, dual polarized shared-aperture (monostatic) based planar antenna with wideband interport isolation characteristics for sub-6 GHz simultaneous transmit and receive (STAR) or in band full duplex (IBFD) wireless applications. The presented compact metasurfaces antenna offers wider impedance bandwidth and excellent interport isolation levels across its entire operating bandwidth. The wideband impedance bandwidth characteristics have been achieved through combination of parasitic feeding and electromagnetic band gap (EBG) radiator excited through proximity feeding from modified four-pointed star shaped driven patch. The high interport isolation levels across entire operational bandwidth of the antenna have been established through balanced transmit and receive modes operation. The presented EBG antenna with unidirectional radiation characteristics resonates at center operating frequency of 3.75 GHz with -10 dB impedance bandwidth of 1.5 GHz (40%) spanning over 3 GHz to 4.5 GHz. The isolation between transmit and receive ports of presented antenna is better than 62 dB across the entire operating bandwidth of 1.5 GHz. The presented dual port, dual polarized antenna offers superior gain performance for each port excitation attributed to the differential excitation of EBG patch. The proposed unidirectional antenna offers wider impedance bandwidth and high port to port isolation levels across wider impedance bandwidth compared to the earlier reported unidirectional antennas intended for IBFD or STAR applications.**

***Index Terms*— EBG antenna, self interference cancellation, simultaneous transmit and receive antenna, in-band full duplex, high interport isolation, wider bandwidth**

I. INTRODUCTION

The frequency spectrum, or bandwidth, is a vital resource for wireless mobile applications. To support higher data rates and throughputs, modern wireless communication systems must utilize the available bandwidth effectively. This requires novel techniques to enable effective and efficient utilization of spectrum for full duplex wireless communication. The simultaneous transmission and reception (STAR) or in-band full duplex (IBFD) is one of these techniques to enhance spectral efficiency by allowing concurrent transmission and reception of radio signals within overlapping bandwidth [1-2]. This propagation domain technique or approach has the theoretical potential to double the spectral efficiency or throughput of wireless communications systems [1-3].

The primary challenge to achieving STAR or IBFD wireless functionality lies in managing the significant self-coupling that occurs between the transmitter and its co-located receiver within the same transceiver [1-3]. This in-band coupling is known as self-interference (SI). In practice, the SI arising from IBFD operations can be quite intricate, influenced by the transmitter's behavior and various other factors [1-3]. These high-power SI signals can easily overpower the signals of interest (SOI), leading to saturation of the receiver [3-4].

The successful implementation of STAR or IBFD wireless communication relies on effectively suppressing or mitigating these high levels of self-interference (SI) signals. This capability allows the receiver to accurately detect incoming signals from the remote transmitter [3]. The requirements for SI cancellation (SIC) are defined by the radiated or the transmit power and bandwidth specifications for the IBFD transceiver [3]. Achieving optimal SIC levels for a specific IBFD node often involves employing multistage and multi-domain SIC techniques [3-5]. These techniques can be classified broadly into RF (analog) and digital domain SIC strategies [2], [6]. However, a significant portion of SIC must occur at the antenna or frontend of the IBFD node to prevent the saturation of the receive chain and to ensure the efficacy of digital SIC techniques [3-6]. Moreover, the real IBFD wireless communication should be based on transceiver having single antenna for transmission and reception of radio signals. Consequently, a single or shared aperture (monostatic) based unidirectional antenna with minimal interport coupling or high interport isolation is considered as a fundamental component of the IBFD or STAR transceiver [6].

The interport isolation for the monostatic (shared-aperture), unidirectional IBFD antennas can be effectively improved through various RF-domain SIC techniques [2],[5], [7-13]. Among these isolation improvement techniques, the balanced feeding stands out as one of the most impactful approaches for achieving notable interport

979-8-3315-4544-4/26/$31.00 ©2026 IEEE

isolation levels for IBFD antennas [9-13]. While many existing unidirectional IBFD antennas are reported to have narrow impedance bandwidths and limited SIC or isolation bandwidths. However, the unidirectional, monostatic, low profile IBFD antenna presented here in this work offers a wider impedance bandwidth along with enhanced interport isolation levels throughout its entire operating bandwidth.

II. Proposed Unidirectional Monostatic Planar EBG Antenna

The structure of the proposed unidirectional monostatic electromagnetic band gap (EBG) antenna is shown in Fig. 1 along with its designated transmit (Tx) and receive (Rx) ports. The layout of the proposed planar EBG antenna is comprised of two RO4003 substate layers with 1.524 mm thickness of each layer as indicated in Fig.1. The radiating geometry is comprised of a four-pointed star driven patch and parasitic patch (splitted in to four sub-patches). The four-port driven patch is excited through 7 mm x 3.5 mm feed lines where two pairs of co-linear ports are used for transmitting and receive modes as indicated in Fig.1. The parasitic patch has four sub-cells with dimensions of 16.6 mm x 16.6 mm for each cell. The vertical and horizontal spacing between the cells is 1 mm. The parasitic EBG patch is electromagnetically excited through driven patch. The modified structure of driven patch and EBG nature of parasitic patch offer improved impedance bandwidths compared to their conventional square-shaped patches. The driven patch and parasitic EBG patch will resonate at different frequencies and the proposed structure achieves wider impedance bandwidth due to overlapping of these operating bands.

The orthogonal feeding ports of proposed EBG antenna will excite dual linear polarization for each pair of transmit and receive ports. Moreover, the symmetrical structure of the presented antenna will result in equal amounts of SI from transmit ports to both of receive ports. The resulting SI levels are reduced due to dual polarized ports resulting in initial levels of interport isolation for presented EBG antenna. The interport isolation can be further improved through balanced transmit and receive mode operation resulting in impressive levels of port-to-port decoupling as demonstrated in [10],[13].

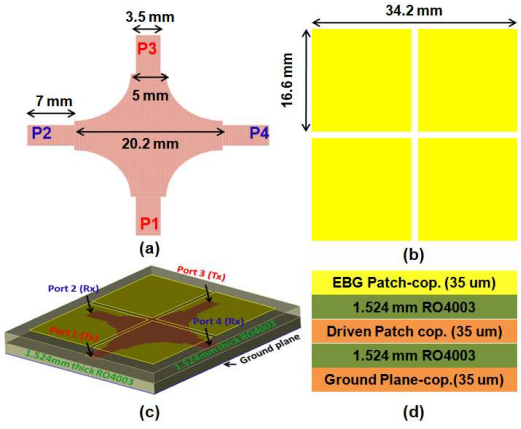


Fig. 1. The structure of the proposed antenna (a) driven patch (b) parasitic EBG patch (c) EM Model (d) PCB structure.

The simulated reflection co-efficients and interport coupling results for the proposed unidirectional dual polarized, EBG antenna are presented in Fig. 2. As clear from the simulated S_{11}, S_{22}, S_{33},S_{44}, results, the simulated -10 dB bandwidth spans across 3GHz to 4.5GHz for all ports i.e. port 1, 3 (transmit port), port 2 and port 4 (receive ports). The resulting bandwidth of 1.5 GHz (40% with respect to centre frequency of 3.75 GHz), emerges from modified driven patch and EBG paracitic patch.

Based on the dual polarization nature of each pair of transmit and receive ports, the SI or leakage of transmit signals to receive ports (S_{21}, S_{41}, S_{23}, S_{43}) will be suppressed to around 8 dB across entire bandwidth of 1.5 GHz. However, these isolation levels are not enough for successful IBFD operation. Consequently, additional RF domain SIC is required to meet the intended isolation or decoupling requirements at front-end of IBFD transceiver.

The balanced or differential excitation in the Tx and Rx modes through their respective ports can effectively reduce the interport coupling or self-interference (SI), enhancing isolation between ports [9-13]. In an ideal scenario, combining SI signals (S_{21}, S_{41}, S_{23}, S_{43}) through differential feeding can completely suppress the interport coupling for $S_{21} = S_{41} = S_{23} = S_{43}$. This operation will result in completely isolated ports i.e. infinite interport isolation levels. As shown in Fig. 2, such differential performance yields at least 62 dB of interport isolation across the entire operating bandwidth of 1.5 GHz. In this case, the simulated levels of port-to-port isolation are limited by the accuracy of simulations. In practice, very high interport isolation levels can be realized for the case of $S_{21} \approx S_{41} \approx S_{23} \approx S_{43}$ if the well-balanced differential circuits are used for Tx and Rx modes [9-13].

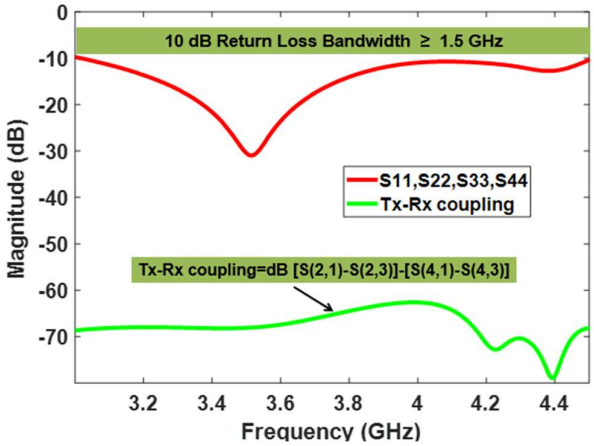


Fig. 2. The simulated reflection coefficients (S_{11}, S_{22}, S_{33} , S_{44}) and differetial mode Tx-Rx coupling performance for the proposed unidirectional, dual polarized, monostatic EBG antenna.

In practical case, the levels of interport isolation achieved within the desired bandwidth are influenced by the performance especially the magnitude and phase balance characteristics of the differential circuit used for the transmission (Tx) and reception (Rx) modes in the presented unidirectional, dual-polarized, monostatic EBG antenna. For instance, a differential circuit featuring a microstrip to slot-line transition, as referenced in [13], can be employed to effectively excite the presented antenna to

achieve remarkable interport isolation levels across its operational bandwidth of 1.5 GHz.

The simulated gains for the presented EBG antenna range from 5.4 dBi to 6.6 dBi for both transmission (Tx) and reception (Rx) modes. The differential or balanced feeding technique enhances gain performance compared to traditional unbalanced feeding methods.

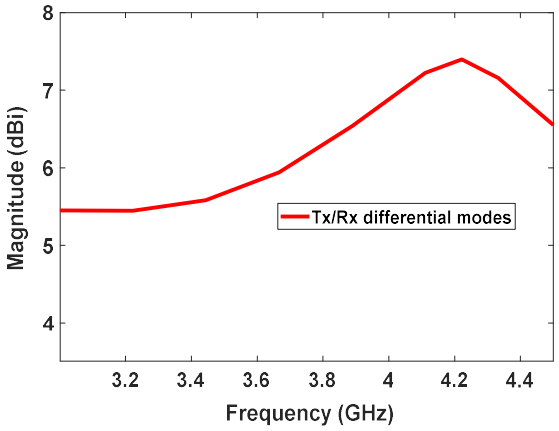


Fig. 3. The simulated gain versus frequency performance of differentially driven, dual-polarized, monostatic EBG antenna.

As outlined in table-I, the presented differentially driven, unidirectional, dual-polarized, monostatic EBG antenna features wider impedance bandwidth and high interport isolation over wide operational bandwidth surpassing the performance of previously reported, planar IBFD antennas [9-11], [14-17].

Table-I: The comparative performance analysis of presented unidirectional, monostatic EBG antenna

Ref. Designs	-10 dB Bandwidth	Isolation Levels	Radiation Patterns
[9]-I	50 MHz	62 dB	Unidirectional
[9]-II	50 MHz	70 dB	Unidirectional
[10]	90 MHz	60 dB	Unidirectional
[11]	50 MHz	43 dB	Unidirectional
[14]	90 MHz	25 dB	Unidirectional
[15]	4 GHz	15 dB	Bidirectional
[16]	50 MHz	55 dB	Unidirectional
[17]	90 MHz	50 dB	Unidirectional
EBG Ant.	1.5 GHz	60 dB	Unidirectional

III. Conclusion

A dual-port, dual linearly polarized antenna based on shared or single aperture has been introduced, specifically tailored for 5G in-band full duplex wireless applications. This antenna showcases unidirectional radiation and an extended impedance bandwidth, along with impressive interport isolation throughout its operational range of 1.5 GHz, spanning over 3 GHz to 4.5 GHz. The exceptional interport isolation is achieved by utilizing effective SIC operation in differentially driven transmit and receive modes. The presented antenna can be utilized for various IBFD applications within frequency range 1 (FR1) for 5G New Radio (5G NR). Its operational bandwidth accommodates multiple frequency bands including n48 (3.55 – 3.7 GHz), n77 (3.3 – 4.2 GHz), and n78 (3.3 – 3.8 GHz), for 5G NR to enable IBFD capabilities.

References

[1] B. Smida, et al., "In-Band Full-Duplex: The Physical Layer," *Proceedings of the IEEE*, vol. 112, no. 5, pp. 433-462, May 2024.

[2] K. E. Kolodziej, B. T. Perry and J. S. Herd, "In-Band Full-Duplex Technology: Techniques and Systems Survey," IEEE Transactions on Microwave Theory and Techniques, vol. 67, no. 7, pp. 3025-3041, July 2019.

[3] D. Korpi, et al., "Full-Duplex Transceiver System Calculations: Analysis of ADC and Linearity Challenges", IEEE Trans. Wireless Communication., vol. 13, no. 7, pp. 3821-36, July 2014.

[4] N. Reiskarimian, T. Dinc, J. Zhou *et al*., "One-Way Ramp to a Two-Way Highway: Integrated Magnetic-Free Nonreciprocal Antenna Interfaces for Full-Duplex Wireless," *IEEE Microwave Magazine*, vol. 20, no. 2, pp. 56-75, Feb. 2019.

[5] C. D. Nwankwo, L. Zhang, A. Quddus, et al.:, "A Survey of Self-Interference Management Techniques for Single Frequency Full Duplex Systems," IEEE Access, vol. 6, pp. 30242-30268, 2018.

[6] M. Yilan, H. Ayar, H. Nawaz, O. Gurbuz and I. Tekin, "Monostatic Antenna In-Band Full Duplex Radio: Performance Limits and Characterization," *IEEE Transactions on Vehicular Technology*, vol. 68, no. 5, pp. 4786-4799, May 2019.

[7] H. Nawaz, Ö. Gürbüz and I. Tekin, "2.4GHz dual polarized monostatic antenna with simple two-taps RF Self Interference Cancellation (RF-SIC) circuitry," *Electronics Letters*, vol. 55, no. 6, pp. 299–300, March, 21, 2019.

[8] H. Nawaz and I. Tekin, "Dual polarized patch antenna with high inter-port isolation for 1 GHz in-band full Duplex applications," *2016 IEEE International Symposium on Antennas and Propagation* , Fajardo, PR, USA, 2016, pp. 2153-2154.

[9] H. Nawaz and I. Tekin, "Dual-Polarized, Differential Fed Microstrip Patch Antennas With Very High Interport Isolation for Full-Duplex Communication," *IEEE Transactions on Antennas and Propagation*, vol. 65, no. 12, pp. 7355-7360, Dec. 2017.

[10] Nawaz H, Niazi A.U., "A compact proximity-fed 2.4 GHz monostatic antenna with wide-band SIC characteristics for in-band full duplex applications," *International Journal of RF and Microwave Computer-Aided Engineering,* 2020; 30:e22087.

[11] H. Nawaz and I. Tekin, "Three ports microstrip patch antenna with dual linear and linear co-polarization characteristics," in *Electronics Letters*, vol. 53, no. 8, pp. 518-520, 4 13 2017.

[12] H. Nawaz, A. U. Niazi, M. Abdul Basit and M. Usman, "Single Layer, Differentially Driven, LHCP Antenna With Improved Isolation for Full Duplex Wireless Applications," *IEEE Access*, vol. 7, pp. 169796-169806, 2019.

[13] H. Nawaz, "Unidirectional, Shared-Aperture Antenna with Wideband Interport Isolation Performance for 5G STAR Applications," *2025 IEEE 13th Asia-Pacific Conference on Antennas and Propagation (APCAP)*, Christchurch, New Zealand, 2025, pp. 231-233.

[14] S. Chakrabarti and A. Chakraborty, "Dual-band dual-polarised microstrip antenna with improved inter-port isolation," in *Electronics Letters*, vol. 55, no. 5, pp. 239-240, 7 3 2019.

[15] H. Nawaz, and Ibrahim Tekin, "Dual port disc monopole antenna for wide-band MIMO-based wireless applications," *Microwave and Optical Technology Letters*, vol. 59, no. 11, pp. 2942–2949, 2017.

[16] M. S. Amjad, H. Nawaz, K. Özsoy, Ö. Gürbüz and I. Tekin, "A Low-Complexity Full-Duplex Radio Implementation With a Single Antenna ," IEEE Transactions on Vehicular Technology, vol. 67, no. 3, pp. 2206-2218, March 2018.

[17] C. Goodbody, T. Karacolak and N. Tran, "Dual-polarized patch antenna for in-band full-duplex applications," in *Electronics Letters*, vol. 54, no. 22, pp. 1255-1256, 1 11 2018.

Low-profile broadband beam-scanning antenna

Shuo Sun, Xiuping Li, Zihang Qi, Wenyu Zhao, Jianxun Su
State Key Laboratory of Information Photonics and Optical Communications,
Key Laboratory of Universal Wireless Communications of Ministry of Education,
Beijing Key Laboratory of Work Safety Intelligent Monitoring,
School of Electronic Engineering, Beijing University of Posts and Telecommunications,
Beijing 100876, China
email: xpli@bupt.edu.cn

***Abstract* - This paper presents a low-profile beam-scanning antenna, where the monopole antenna and metasurface are integrated on the same plane for ultra-compact configuration. A 7-mm-tall monopole antenna serves as the feed to excite surface waves (SW), while the metasurface generates Pancharatnam-Berry (PB) phase and propagation (PG) phase to regulate SW radiation. Specifically, the PB phase is fixed as a preset component, and the PG phase features 1-bit reconfigurable phase resolution. The broadband phase responses of both phases endow the antenna with excellent broadband radiation capability. At the boresight direction (0 °), the antenna achieves a 16.6% 3-dB gain bandwidth spanning 10.5–12.4 GHz. Furthermore, two-dimensional beam scanning over a range of ± 60 ° is realized within the operating band, with a scanning loss of less than 3 dB. Owing to its advantages of low profile, high integration, and broadband radiation performance, the proposed design is expected to be a promising candidate for mobile communication applications.**

***Index Terms*—surface wave, metasurface, low-profile.**

I. INTRODUCTION

In recent years, electronic beam-scanning antennas have demonstrated tremendous application potential in fields such as mobile communications and radar detection. Relevant research has been extensively conducted, including phased arrays, transmissive or reflective metasurfaces, etc. However, these designs suffer from drawbacks such as complex feeding structures and relatively high profiles in practical deployment. Therefore, designing electronic beam-scanning antennas with low complexity and high integration remains challenging.

Notably, designs using surface wave (SW) as excitation have provided a new solution to this challenge. A representative example is the holographic metasurface antenna (HMA) [1]. This type of antenna adopts a quarter-wavelength monopole antenna as the surface wave feed, realizing leaky-wave radiation by regulating surface impedance, and exhibits the advantages of simple feeding and low profile. In the field of electronic beam scanning, existing studies have achieved beam agile functionality by adjusting surface impedance via PIN [2][3] or varactor diodes [4]. Nevertheless, limited by the strong dispersive characteristics of surface impedance, such designs generally lack broadband regulation capability, making it difficult to meet the practical application requirements of high-capacity communication scenarios.

To address the aforementioned issues, this paper proposes a broadband low-profile beam-scanning antenna, as shown in Figure 1. The antenna adopts the same architecture as HMA to ensure low-profile characteristics, but differs in radiation mechanism. Based on the generalized Snell's law, the design constructs gradient phases through the cooperative regulation of propagation (PG) phase and Pancharatnam–Berry (PB) phase, thereby achieving SW radiation. Specifically, metasurface unit cells with hybrid phase modulation are designed. The PB phase of the unit cell is fixed as a preset phase, while the PG phase achieves 1-bit reconfiguration via the on-off switching of PIN diodes. The hybrid regulation of these two phases enables dynamic beam scanning. Meanwhile, the broadband phase responses of both phases endow the antenna with broadband radiation capability.

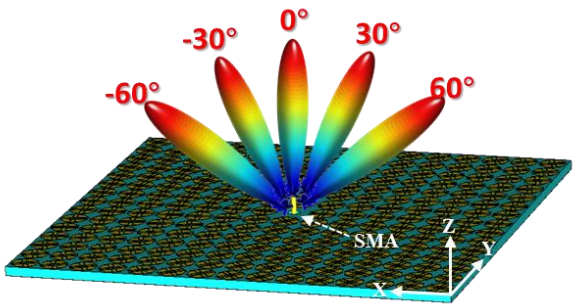


Figure 1. Antenna schematic diagram.

II. METHOD

Here, the electric field of the SW is expressed as $e^{-jk_{sw}\rho}$ (where ρ is the radial vector, $k_{sw}=n_{sub}k_0$, k_{sw} is the SW wave vector, k_0 is the free-space wave vector, and n_{sub} denotes the refractive index of the substrate). Based on the generalized Snell's law [5], to achieve the radiation of SW and control the pointing direction of the radiated beam, it is necessary to satisfy the gradient phase condition as expressed in (1):

$$\nabla\phi = k_{sw} - k_0 \sin\theta_{out} \cdot (\cos\phi_{out} x + \sin\phi_{out} y). \quad (1)$$

Where $\nabla\phi$ denotes the gradient phase of the derivative with respect to ρ, and θ_{out} and ϕ_{out} represent the pitch and azimuthal angle.

Metasurface achieves the gradient phase condition. For incident circularly polarized waves of different chiralities, its co-polarized reflective component carries the superposed PB phase and PG phase:

$$\phi_{\text{L-out}} = \phi_{\text{L-in}} + \phi_{\text{PG}} - \phi_{\text{PB}},$$
$$\phi_{\text{R-out}} = \phi_{\text{R-in}} + \phi_{\text{PG}} + \phi_{\text{PB}}. \quad (2)$$

In which, $\phi_{\text{L/R-out/in}}$ denotes the decomposed phase of the outgoing and incident circularly polarized basis. $\phi_{\text{PG}} = \phi_{\text{xx}}$ is the propagation phase. ϕ_{xx} is x-polarized reflection phase, generated by the phase accumulation of electromagnetic wave propagation. $\phi_{\text{PB}} = 2\beta$ is the geometric phase, produced by the unit rotation angle β, featuring a frequency-independent characteristic. Additionally, the energy distribution between the co-polarized and cross-polarized components of the reflected wave is regulated by $\Delta\phi = |\phi_{\text{xx}} - \phi_{\text{yy}}|$ in (3):

$$|r_{\text{LL/RR}}| = \sin\left(\frac{\Delta\phi}{2}\right), |r_{\text{LR/RL}}| = \cos\left(\frac{\Delta\phi}{2}\right). \quad (3)$$

To achieve efficient co-polarized manipulation, $\Delta\phi$ is set to π.

For chiral components of different handedness, the gradient phase condition expressed in (1) must be satisfied. Furthermore, the incident SW electric field can be decomposed into $\phi_{\text{L-in}} = \varphi$ and $\phi_{\text{R-in}} = -\varphi$, where φ is the azimuthal angle. By combining the above relationships, the expressions for the PG phase and PB phase are derived as shown in (4):

$$\phi_{\text{PG}} = \nabla\phi + (\phi_{\text{L-out}} + \phi_{\text{R-out}})/2,$$
$$\phi_{\text{PB}} = (\phi_{\text{L-out}} - \phi_{\text{R-out}})/2 + \varphi. \quad (4)$$

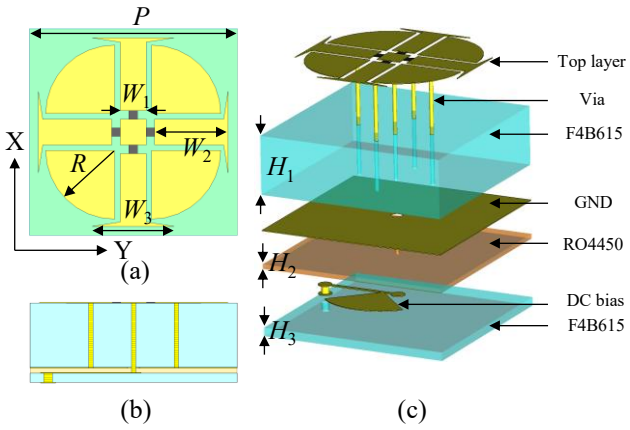


Figure 2. Structure of the unit cell. (a) Top view. (b) Side view. (c) Exploded view.

The structure of the metasurface is illustrated in Figure 2. In which, the top layer is composed of Jerusalem crosses and sector-shaped parasitic patches, which are utilized to extend the bandwidth of the reflective phase. MADP-000907-14020 diodes are embedded between the cross slots. In the ON state, each diode can be equivalent to a series combination of a 7.8 Ω resistor and a 30 pH inductor, while in the OFF state, it is equivalent to a series combination of a 0.025 pF capacitor and a 30 pH inductor. The diodes along the X and Y directions are reverse-connected, enabling state switching via positive and negative voltages. Both the unit and the DC layer substrate are fabricated using F4B615 material with a ε_r of 6.15 and a tanδ of 0.001. The DC layer is placed beneath the ground and connected to the diodes on the top layer through metallized vias. Etched sector-shaped stubs are employed to suppress the leakage of radio frequency energy. RO4450 is used for bonding between the unit cell and the DC layer. Detailed dimensions of the unit cell are listed in Table I.

TABLE I
UNIT-CELL DIMENSIONS (UNIT MM)

W_1	W_2	W_3	R
1.2	3.4	3.8	3.2
P	H_1	H_2	H_3
9.7	3	0.2	0.5

Figure 3 (a) illustrates the PG phase of the unit cell. It can be observed that within the frequency range of 10–12.5 GHz, the ON and OFF states achieve a phase difference of 180°±20°. This ensures that the unit cell can provide accurate phase compensation within the operating band. Meanwhile, as expressed in (3), a phase difference close to π guarantees a high magnitude of the cross-polarized component, thus ensuring the high efficiency of hybrid phase modulation. Figure 3 (b) illustrates the PB phase of the unit cell. It can be observed that rotating the spin angle β by 20° yields a phase difference of 40°.

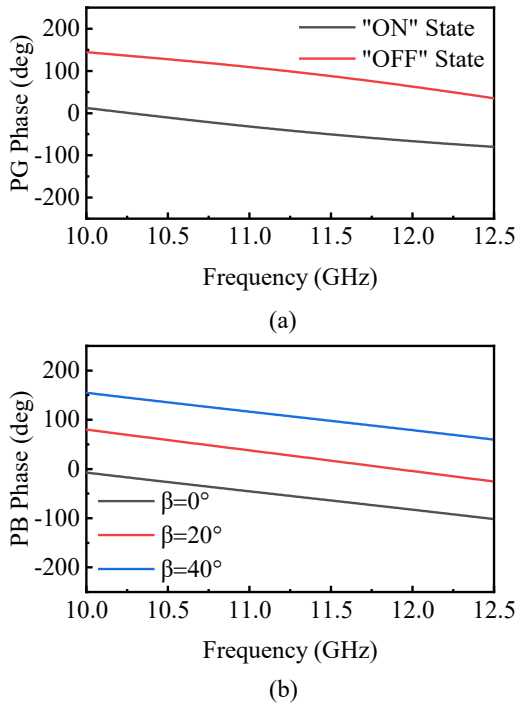


Figure 3. Phase response of the unit cell. (a) PG phase. (b) PB phase.

III. RESULTS AND DISCUSSION

The architecture of the proposed antenna is illustrated in Figure 1. A 7-mm-tall monopole antenna is integrated with a 15×15 unit-cells array, featuring a profile of approximately 0.26λ_0 (at 11 GHz). For validation, a horizontally polarized radiated beam is designed. The outgoing field can be decomposed into $\phi_{\text{L-out}} = \phi_{\text{R-out}} = 0$. By substituting into Eq. (4), the desired PG and PB phase distributions can be obtained. Figure 4 presents the reflection coefficient of the antenna. It can

be seen that the antenna achieves excellent impedance matching, which indicates that the designed metasurface can effectively guide the SW energy for sufficient radiation.

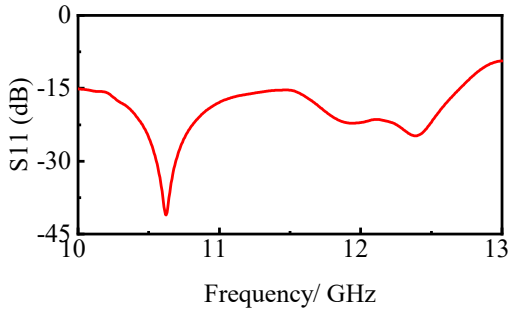


Figure 4. The S11 parameter of the antenna.

Fig. 5 demonstrates the beam scanning performance of the metasurface. Solid lines represent the radiation patterns at 11 GHz, while dashed lines correspond to those at 12 GHz. Specifically, Fig. 5(a) illustrates the radiation patterns in the φ=0° plane. It can be clearly observed that the beam achieves a beam scanning range of ±60°, with a gain loss within 3 dB. Meanwhile, Fig. 5(b) presents the radiation patterns in the φ=90° plane, where the beam scanning results are consistent with those in the φ=0° plane. This verifies the two-dimensional (2D) beam scanning capability of the proposed design.

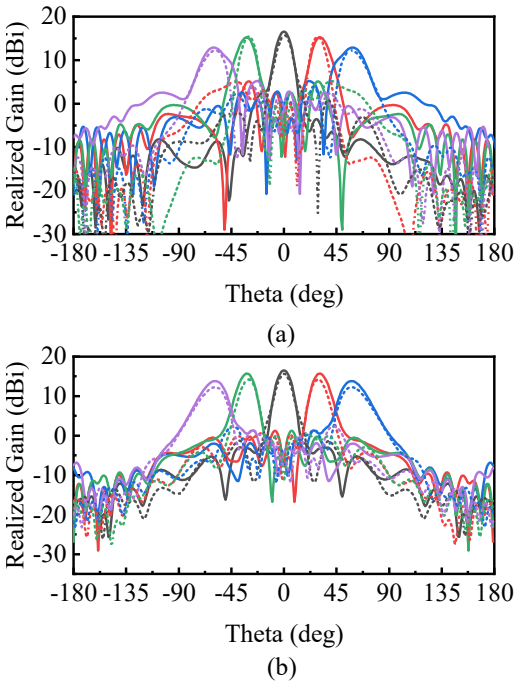


Figure 5. Antenna radiation patterns at 11 GHz and 12 GHz. (a) phi = 0° plane. (b) phi = 90° plane.

To further demonstrate the broadband radiation performance of the proposed antenna, Figure 6 presents the gain-frequency curve at the boresight direction. In which, within the frequency range of 10.5–12.4 GHz, the gain degradation of the antenna is less than 3 dB.

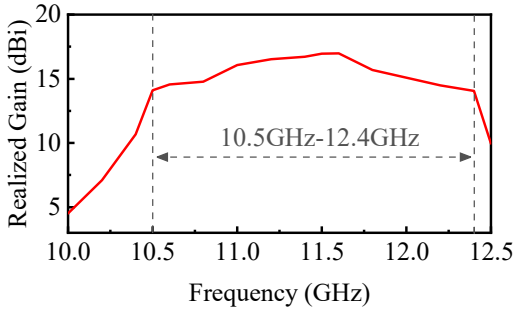


Figure 6. The gain bandwidth of the antenna.

IV. Conclusion

A low-profile wideband beam-scanning antenna is proposed in this paper. The monopole antenna and metasurface are integrated on the same plane, achieving an ultra-compact configuration. By leveraging metasurface elements with fixed PB phase and 1-bit reconfigurable PG phase, the surface waves excited by the monopole antenna enable wideband radiation. Simulation results demonstrate that the antenna achieves a 3-dB gain bandwidth covering 10.5–12.4 GHz. Furthermore, 2D beam scanning within the range of ±60° is realized across the entire operating band. With its prominent advantages of ultra-low profile, high integration, and excellent wideband radiation performance, the proposed antenna provides a promising solution for mobile communication applications and serves as a competitive candidate in related fields.

V. Acknowledgment

This work was supported by the National Natural Science Foundation of China under Grant (62321001) and BUPT Excellent Ph. D. Students Foundation (CX20241024).

References

[1] B. H. Fong, J. S. Colburn, J. J. Ottusch, J. L. Visher, and D. F. Sievenpiper, "Scalar and Tensor Holographic Artificial Impedance Surfaces," IEEE Transactions on Antennas and Propagation, vol. 58, no. 10, pp. 3212-3221, Oct 2010.

[2] Y. -D. Wang, D. Wang, J. Zhao, L. -Z. Yin, Y. -H. Tan and P. -K. Liu, "Active Holographic Metasurface for Electrically Controllable 2-D Beam Scanning," 2021 International Conference on Microwave and Millimeter Wave Technology (ICMMT), Nanjing, China, 2021, pp. 1-3.

[3] H. Zhao, Y. Pan and Y. Shen, "Low-Profile 2-D Beam-Scanning Antenna Based on Reconfigurable Modulated Metasurface," in IEEE Transactions on Antennas and Propagation, vol. 74, no. 1, pp. 75-85, Jan. 2026.

[4] X. Zhang et al., "Conformal reconfigurable holographic metasurface for multifunctional radiation and scattering modulation," Optics Express, vol. 33, no. 2, pp. 2047-2059, 2025/01/27 2025.

[5] T. Y. Zhang, H. F. Ma, H. L. Wang, Y. K. Zhang, Z. H. You, and T. J. Cui, "High-Efficiency Metasurface Emitters for Generating Arbitrarily Polarized Spatial Propagating Waves," ADVANCED MATERIALS TECHNOLOGIES, vol. 7, no. 11, NOV 2022, Art. no. 2200267.

Generation of Scanning Self-Accelerating Beam by Manipulating Phase Distribution

Qing You [1], Shi-Tong Wang [2], Pui-In Mak[1], Rui P. Martins[1], Jun Yin[1*]
[1] University of Macau, Macau, China
[2] City University of Hong Kong, Hong Kong, China
qingyou@ieee.org, *junyin@um.edu.mo

***Abstract*- This paper presents a method for achieving scanning of self-accelerating beams by simply reversing the phase from 0° to 180°. Building upon conventional approaches, this method leverages both gradient amplitude and abrupt phase profiles, requiring only phase manipulation to achieve beam scanning. A waveguide slot antenna array is designed based on this principle, and simulated results demonstrate its effectiveness and feasibility.**

I. Introduction

The nondiffracting and self-accelerating beams have sparked considerable interest due to their potential applications in the microwave, millimeter-wave, and terahertz bands. These characteristics address critical demands in these frequency ranges. [1] [2].

The Airy beam was among the first wave structures discovered to exhibit self-acceleration, enabling it to propagate along curved trajectories without the need for an external potential. In 2007, G. A. Siviloglou *et al.* reported the first experimental observation of an Airy beam, generated via Fourier transform using a Gaussian input beam and a cubic phase mask [3]. This approach illustrates that self-accelerating beams can be synthesized by introducing amplitude and phase gradients—specifically, a Gaussian amplitude profile and a cubic phase distribution in the Fourier domain. An alternative method generates the Airy beam by directly engineering the desired transverse intensity profile at the radiating aperture [4] [5]. Leveraging the precise control over amplitude and phase offered by metasurfaces and antenna arrays, researchers have also realized Airy beams with oscillatory amplitude and abrupt phase variations [6] [7] [8]. However, these methods are generally limited to generating self-accelerating beams with a fixed curvature.

To enable beam steering of self-accelerating beams, a phase-scanning method has been incorporated into Airy beam generation [9] [10]. In 2025, a phase-scanning self-accelerating beam was demonstrated in [10], where a gradient phase distribution is superimposed onto the abrupt phase mask of the Airy beam. By varying the operating frequency, the gradient phase distribution is dynamically tuned, thereby enabling beam scanning. While this approach achieves beam steering, it does so at the cost of frequency agility, which may severely limit communication data rates.

In this paper, we propose a method to achieve beam scanning of self-accelerating beams at a fixed frequency solely by manipulating the phase distribution. The proposed approach integrates the characteristic of existing techniques by generating a self-accelerating beam with both gradient amplitude and abrupt phase distribution. By tailoring the phase profile, the curvature of the beam can be dynamically controlled. To validate the concept, a slot antenna array is designed, and simulated results confirm the feasibility of the proposed method. This work demonstrates strong potential for applications in near-field high-speed communication and wireless power transmission.

II. Distribution of the Proposed Method

The proposed method combines the characterisitic of the existing methods and consists of gradient amplitude and abrupt phase distribution, as shown in Fig. 1.

The gradient amplitude distribution of the proposed method is

$$I(x) = \exp(kx) \tag{1}$$

where k is the constant that can control the gradient of the amplitude distribution.

The abrupt phase distribution of the proposed method is

$$P(x) = \begin{cases} p_0, & Ai\left(\dfrac{x}{x_0}\right)\exp\left(a_x\dfrac{x}{x_0}\right) \geq 0 \\ p_0+\pi, & Ai\left(\dfrac{x}{x_0}\right)\exp\left(a_x\dfrac{x}{x_0}\right) < 0 \end{cases} \tag{2}$$

in which $Ai(\cdot)$ is the Airy function, x_0 is the arbitrary scaling factor, a_x is the attenuation parameter, and p_0 is the initial phase of the abrupt phase.

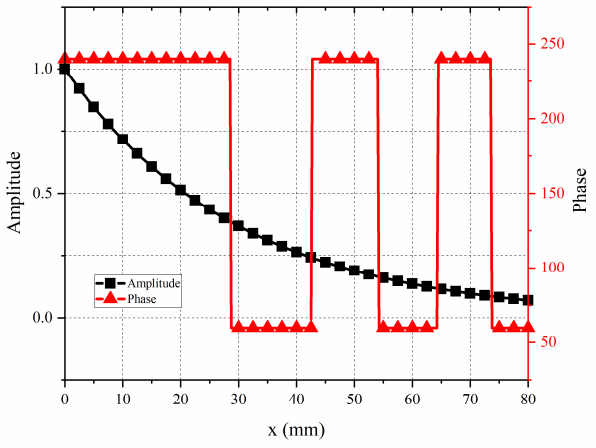


Fig. 1. Amplitude and phase distribution of the proposed method.

Fig. 2 represents the calculated normalized electric field of the proposed beam when $a_x = 0.1$, $x_0 = 0.1$, $p_0 = 60$ and $k = 0.03$. And Fig. 3 presents the normalized electric field in *xoy*-plane with different a_x. The results show that the location of the main beam can be manipulated by only adjusting the a_x, which will only affect the phase distribution.

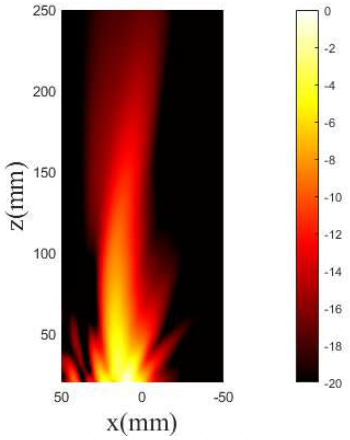
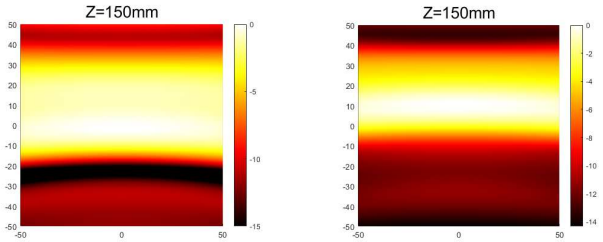


Fig. 2. Calculated normalized electric field of the proposed beam in the *xoz*-plane.



(a) (b)

Fig. 3. Calculated normalized electric field of the proposed beam in *xoy*-plane with different a_x. (a) $a_x = 0.125$, (b) $a_x = 0.1$.

III. Generation of the Proposed Beam

To verify the proposed method of achieving Airy beam scanning solely through phase control, a linear waveguide slot array is designed and simulated. The overall antenna geometry is illustrated in Fig. 4 (a) where a zoom-in view shows the details of feeding structure. It can be observed that the power is fed from the wave port, transmitted through waveguide, and radiated through multiple slots etched on the wave guide. The details of slots are shown in Fig. 4(b). There are 31 slots with the same length and width marked in the figure. It should be noted that the distance between slots and the central line of the waveguide determines the amplitude, while the phase is controlled by the relative position between slots and the central line of the waveguide. When the slot is switched to the other side of the central line, a 180° phase difference will be introduced.

To demonstrate the beam scanning capability, three cases with the same amplitude distribution and distinct phase distributions is designed. For intuitive demonstration, the phase distributions are illustrated in Fig. 5, where the two phases are represented by blocks of different colors.

The simulated electric fields of three designated cases are plotted in Fig. 6. Apparently, it can be seen that the maximized electric field region is different among three cases, which strongly verifies the proposed phase-only beam scanning method.

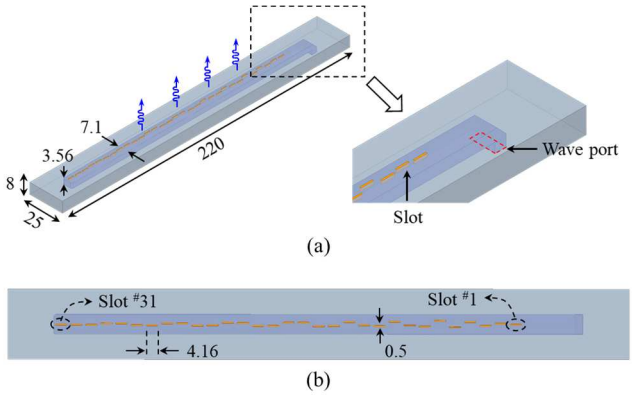


Fig. 4. Geometry of the proposed slot antenna array for generating airy beam. (a) 3-D structure. (b) Top view. Unit: mm.

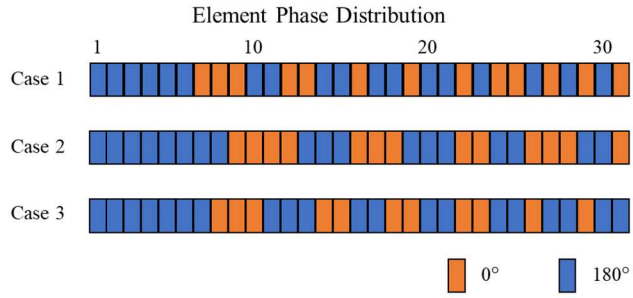


Fig. 5. Element phase distribution of three cases.

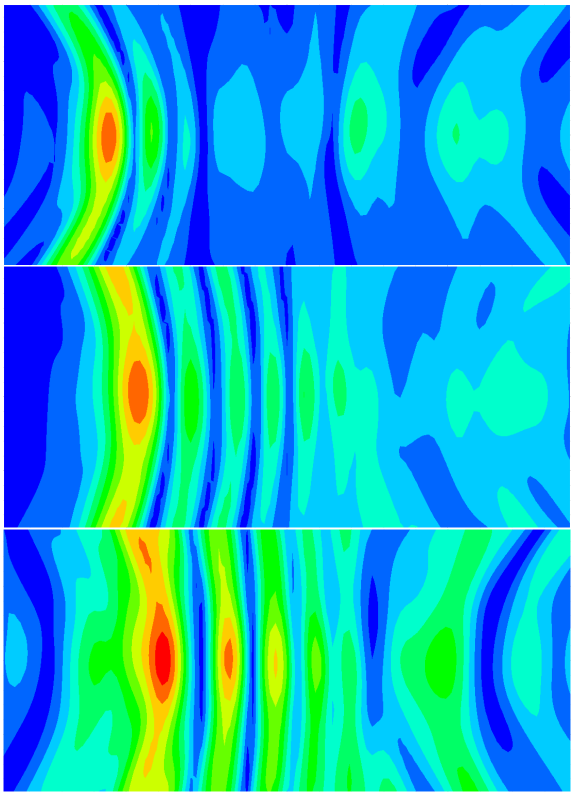


Fig. 6. Electric field distributions of three cases.

IV. Conclusion

A simple method for scanning self-accelerating beams is proposed by only reversing the abrupt phase from 0° to 180° while keeping the amplitude distribution unchanged. Compared with existing approaches, the proposed method can realize the scan of self-accelerating beam at fixed frequency. To verify this concept, a waveguide slot antenna array is designed based on the calculated amplitude and phase distributions. Simulated electric-field results for three different phase distributions show that the radiation pattern can be effectively manipulated, and the self-accelerating beam can be scanned as expected. These results demonstrate the feasibility and effectiveness of the proposed method, which provides a practical and low-complexity solution for beam control in advanced antenna and wireless communication systems.

Acknowledgement

The work is funded by the Macau Science and Technology Development Fund (FDCT) - 0109/2025/RIB2, - 0001/2025/NRP, and the University of Macau Research Fund - MYRG-GRG2024-00298-IME

References

[1] A. Mazzinghi, M. Balma, D. Devona, G. Guarnieri, G. Mauriello, M. Albani, and A. Freni, "Large depth of field pseudo-Bessel beam generation with a RLSA antenna," *IEEE Trans. Antennas Propag.*, vol. 62, no. 8, pp. 3911–3919, Aug. 2014.

[2] Y. F. Wu, Y. J. Cheng, and Y. C. Zhong, "Substrate integrated waveguide slot array antenna to generate Bessel beam with high transverse linearly-polarized purity," *IEEE Trans. Antennas Propag.*, vol. 70, no. 1, pp. 750-755, Jan. 2022.

[3] G. A. Siviloglou, J. Broky, A. Dogariu, and D. N. Christodoulides, "Observation of accelerating airy beams," *Phys. Rev. Lett.*, vol. 99, no. 21, Nov. 2007.

[4] R. Feng, B. Ratni, J. Yi, Z. Jiang, H. Zhang, A. Lustrac, and S. N. Burokur, "Flexible manipulation of Bessel-like beams with a reconfigurable metasurface," *Adv. Opt. Mater.*, vol. 8, no. 23, Dec. 2020.

[5] J. Wen, L. Chen, X. Vhen, S. Kanwai, L. Zhang, S. Zhuang, D. Zhang, and D. Lei "Use of dielectric metasurfaces to generate deep-subwavelength nondiffractive Bessel-like beams with arbitrary trajectories and ultralarge deflection," *Laser Photon. Rev.*, vol. 15, no. 5, May 2021.

[6] Y. Huang, J. Li, H. -X. Xu, H. Yu, Z. Yang, and P. Yu, "Experimental demonstration of microwave two-dimensional Airy beam generation based on single-layer metasurface," *IEEE Trans. Antennas Propag.*, vol. 68, no. 11, pp. 7507–7516, Nov. 2020.

[7] I. D. Chremmos, G. Fikioris, and N. K. Efremidis, "Accelerating and abruptly-autofocusing beam waves in the fresnel zone of antenna arrays," *IEEE Trans. Antennas Propag.*, vol. 61, no. 10, pp. 5048–5056, Oct. 2013.

[8] Q. You, Y. F. Wu, Y. Chai, and Y. J. Cheng, "A method of generating nondiffraction self-accelerating beam via Airy-Bessel fusion in two orthogonal directions", *IEEE Trans. Microw. Theory Tech.*, vol. 72, no. 5, pp. 2938-2948, May 2024.

[9] Y. T. Chen, X. Q. Lin, Y. Fan, and S. L. Liu, "Generation of Ka-Band accelerating and self-bending beam by series-fed patch array," *IEEE Antennas Wirel. Propag. Lett.*, vol. 20, no. 2, pp. 239-243, Feb. 2021.

[10] Q. You, Y. F. Wu, Y. Yang, Y. Chai, and Y. J. Cheng, "Near-field phase-scanning self-accelerating airy-Bessel beam for nonline-of-sight wireless communication," *IEEE Trans. Microw. Theory Techn*., vol. 73, no. 8, pp. 4717–4729, Aug. 2025.

Compact High-Gain 300 GHz Metasurface Antenna for Future 6G Terahertz Communications

Mohammad Nasrat Zaqumi, Syed Muzahir Abbas, Subhas Mukhopadhyay

School of Engineering, Faculty of Science and Engineering, Macquarie University, Sydney, NSW 2109, Australia

mohammadnasrat.zaqumi@mq.edu.au

***Abstract*— This paper presents a compact resonant cavity antenna (RCA) enhanced by a single-layer negative-epsilon surface (NEPS) metasurface operating at 300 GHz for terahertz communication systems. The proposed metasurface is composed of periodic circular patch resonators engineered to exhibit a stable reflection magnitude together with an effective negative permittivity ($\varepsilon<0$) around the target frequency. These electromagnetic characteristics enable efficient manipulation of the reflection phase and control of the electromagnetic wave propagation inside the Fabry–Perot cavity. By regulating the reflection phase distribution, the metasurface improves the near-field phase uniformity and promotes constructive interference at the partially reflective aperture, resulting in enhanced radiation collimation and power radiation efficiency. Full-wave numerical simulations demonstrate that the proposed antenna achieves a maximum directivity of approximately 20 dBi with an aperture efficiency of about 40% while maintaining a compact and low-profile structure. The proposed NEPS-assisted RCA provides a promising high-gain antenna platform for terahertz and future 6G communication applications.**

Keywords—Metasurface, Resonant cavity antenna, Terahertz antennas, 6G communications, Negative-epsilon materials.

I. Introduction

Artificial electromagnetic materials have significantly advanced antenna technology by enabling enhanced control over electromagnetic (EM) wave propagation and radiation characteristics. Metasurfaces provide powerful tools for manipulating wavefronts, phase responses, and electromagnetic field distributions at subwavelength scales. Among them, negative epsilon (NEP) metasurfaces have attracted considerable attention due to their unique capability to support minimal phase variation for propagating waves, which improves phase uniformity across the antenna aperture and enhances radiation performance [1,2].

Conventional high-directivity antennas, such as parabolic reflectors and large antenna arrays, can achieve high gain but often suffer from practical limitations including bulky geometries, complex feeding networks, and increased fabrication costs [3,4]. These challenges become more critical in emerging terahertz and 6G communication systems, where compact, lightweight, and highly directive antennas are required [5,7]. Resonant cavity antennas (RCAs) provide a promising compact alternative for high-directivity radiation. Typically, an RCA consists of a primary radiator enclosed between a fully reflective ground plane and a partially reflective surface (PRS), forming a cavity that supports constructive interference to enhance radiation. However, conventional RCA structures often exhibit non-uniform near-field phase distributions, which degrade aperture efficiency and limit achievable directivity [8,9].

In this work, a single-layer planar negative-epsilon metasurface is integrated with a 300 GHz resonant cavity antenna to improve near-field phase uniformity and enhance radiation characteristics. The proposed metasurface employs periodic circular patch resonators engineered to exhibit negative effective permittivity at the operating frequency, enabling improved wavefront control and enhanced antenna directivity for terahertz 6G communication applications.

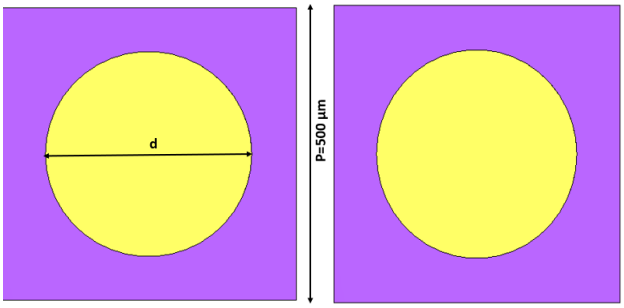


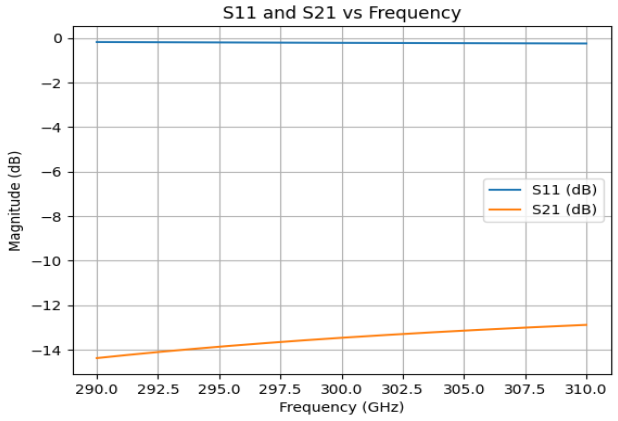
Fig. 1. Proposed circular resonator: (a) front view with dimensions (P= $\lambda_0/2$= 500 µm, d=700 µm), (b) back view.

The remainder of this paper is organized as follows. Section II presents the design methodology and electromagnetic characteristics of the proposed NEP metasurface. Section III discusses the simulated performance of the integrated resonant cavity antenna. Finally, Section IV concludes the paper and outlines future research directions.

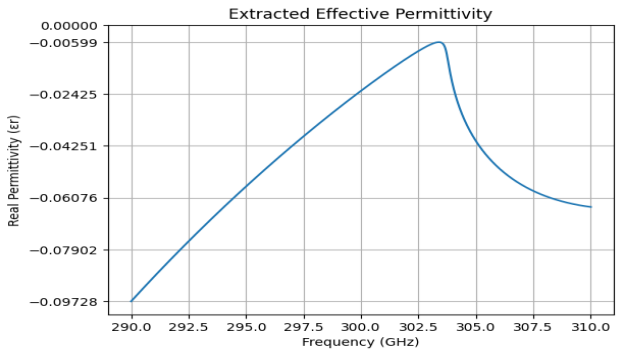
II. Design Methodology and Characteristics of the NEPS Metasurface

The resonant cavity antenna (RCA) was designed to mitigate near-field phase non-uniformity while enhancing the direct transmission of electromagnetic energy in the far-field. A classical RCA structure consists of a fully reflective surface

979-8-3315-4544-4/26/$31.00 ©2026 IEEE



(a)



(b)

Fig.2. Unit cell performance: (a) reflection and transmission coefficients, (b) permittivity.

(FRS) and a partially reflective surface (PRS) separated by approximately $\boldsymbol{\lambda_0/2}$, where $\boldsymbol{\lambda_0}$is the free-space wavelength at the resonance frequency (300 GHz). The PRS is designed using Quartz material ($\boldsymbol{\varepsilon_r = 3.75}$) with a thickness of $0.15\boldsymbol{\lambda_0}$ (150 µm). The antenna is excited through a waveguide-fed slot embedded in the ground plane, where the ground plane thickness is $0.05\boldsymbol{\lambda_0}$ (50 µm), while the lateral dimensions of both the PRS and FRS are $4\boldsymbol{\lambda_0} \times 4\boldsymbol{\lambda_0}$.

To address the near-field phase irregularities observed in conventional RCA structures, a negative epsilon surface (NEPS) is introduced. The NEPS unit cell consists of symmetric circular metallic patches printed on both sides of a Quartz substrate ($\boldsymbol{\varepsilon_r = 3.75}$), as shown in Fig. 1. The circular patch acts as a capacitive resonator, enabling bandpass transmission characteristics and producing negative effective permittivity around the operational frequency of 300 GHz. The unit cell parameters, including the patch radius (d=2r) and periodicity (p), were optimized to achieve the desired transmission response and negative epsilon behavior, as illustrated in Fig.2.The NEPS elements are arranged in an 8 × 8 periodic arrays with a periodicity of $P = \lambda_0/2$ on a Quartz substrate of thickness $0.1\lambda_0$ (100 µm) and overall dimension $4\lambda_0 \times 4\lambda_0$. The metasurface layer is placed at a height of $\lambda_0/4$ above the PRS, where it is depicted in Fig.3 The introduced NEPS effectively compensates for the near-field phase distortions, producing a more uniform phase distribution across the aperture, which improves beam collimation and enhances the far-field directivity of the RCA at 300 GHz.

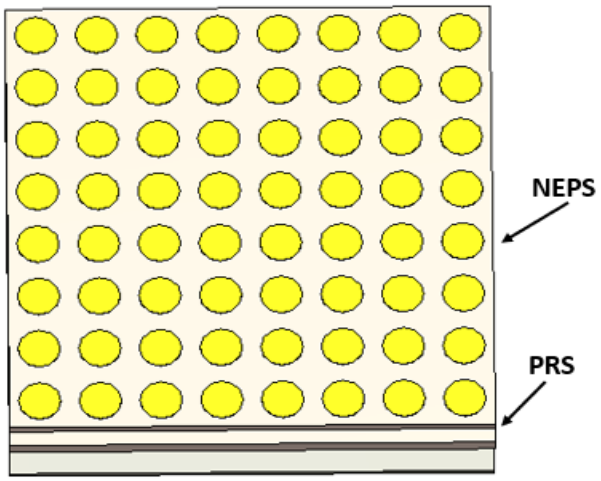


Fig.3. Perspective view of the RCA with NEPS.

III. PERFORMANCE EVALUATION OF THE PROPOSED ANTENNA SYSTEM

The integration of the negative epsilon metasurface (NEPS) with the resonant cavity antenna significantly enhances the electromagnetic performance of the system by improving the phase distribution across the antenna aperture. In the conventional cavity configuration, the radiated fields inside the cavity exhibit a non-uniform near-field phase profile, which leads to partial destructive interference and inefficient radiation. By introducing the NEPS within the cavity, the electromagnetic response of the structure is modified such that the near-field phase distribution becomes more uniform, enabling improved phase alignment of the radiated fields at the aperture. This phase equalization mechanism suppresses destructive interference within the cavity and promotes constructive interference in the broadside direction at the partially reflective surface (PRS). As a result, the radiated energy is effectively collimated toward the main beam direction while reducing power leakage into undesired directions.

This wavefront regulation mechanism directly improves the radiation characteristics of the antenna. The improved phase uniformity across the aperture enables stronger beam focusing and enhanced radiation directivity. As illustrated in Fig. 4, the inclusion of the NEPS significantly improves the aperture phase uniformity compared to the conventional RCA. Consequently, the antenna exhibits a directivity enhancement of approximately 7.5 dB, demonstrating the effectiveness of the metasurface in controlling the cavity fields. Furthermore, the far-field radiation patterns shown in Fig. 5 reveal a substantial reduction in the half-power beamwidth from 44° to 10°,

indicating strong wavefront collimation and improved beam focusing capability.

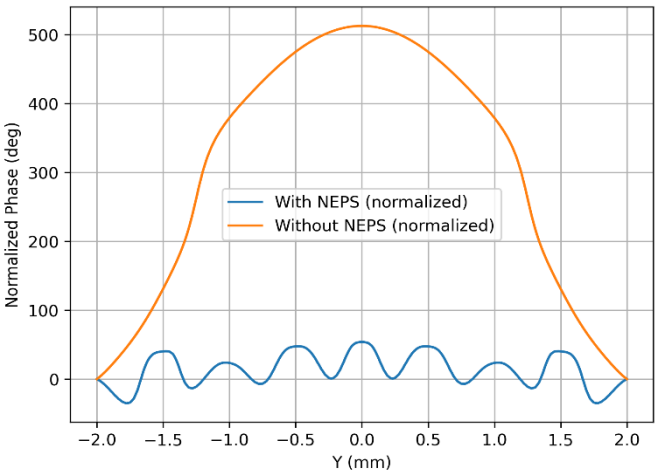


Fig. 4. Electric field phase distribution of the RCA with NEPS.

In addition to the radiation improvements, the metasurface also enhances the aperture utilization efficiency of the antenna. The improved field distribution allows a larger portion of the aperture to contribute constructively to radiation, leading to an aperture efficiency of approximately 40% at the operating frequency of 300 GHz. These results demonstrate that the proposed NEPS effectively regulates the electromagnetic field distribution inside the cavity, enabling improved phase control, energy collimation, and radiation efficiency, which ultimately results in a compact high-gain antenna suitable for terahertz and emerging 6G communication systems.

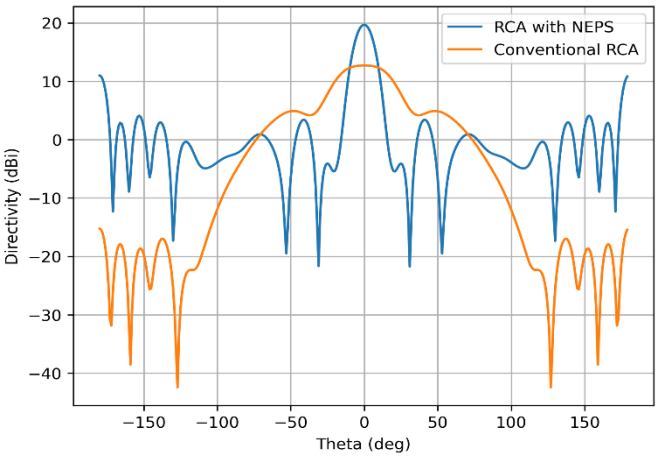


Fig. 5. Radiation pattern of the RCA with NEPS.

IV. Conclusion

This paper presented a compact resonant cavity antenna enhanced by a single-layer negative-epsilon metasurface operating at 300 GHz for terahertz communication applications. The proposed metasurface improves the near-field phase uniformity inside the Fabry–Perot cavity, enabling constructive interference at the antenna aperture and enhanced radiation collimation. Numerical simulations demonstrate that the proposed antenna achieves a maximum directivity of approximately 20 dBi with an aperture efficiency of about 40%, while maintaining a compact and low-profile structure. The improved field distribution across the aperture enables efficient energy utilization and strong beam focusing, making the proposed antenna suitable for high gain 6G terahertz communication systems. Future work will investigate metasurface phase engineering techniques to enable beam tilting and dynamic beam steering for adaptive coverage in emerging 6G terahertz communication networks.

References

[1] J. Wang et al., "Metantenna: When metasurface meets antenna again," IEEE Transactions on Antennas and Propagation, vol. 68, no. 3, pp. 1332-1347, 2020.

[2] Alu, Andrea, and Nader Engheta. "Pairing an epsilon-negative slab with a mu-negative slab: resonance, tunneling and transparency." IEEE Transactions on antennas and propagation 51, no. 10 (2003): 2558-2571.

[3] Y. Ge, Z. Sun, Z. Chen, and Y.-Y. Chen, "A high-gain wideband low-profile Fabry–Pérot resonator antenna with a conical short horn," IEEE Antennas and wireless propagation letters, vol. 15, pp. 1889-1892, 2016.

[4] S. J. Yang, Y. Yang, and X. Y. Zhang, "Low scattering element-based aperture-shared array for multiband base stations," IEEE Transactions on Antennas and Propagation, vol. 69, no. 12, pp. 8315-8324, 2021.

[5] Guo, Yingjie Jay, and Richard W. Ziolkowski. Advanced antenna array engineering for 6G and beyond wireless communications. John Wiley & Sons, 2021.

[6] Song, Ho-Jin, and Tadao Nagatsuma. "Present and future of terahertz communications." IEEE transactions on terahertz science and technology 1, no. 1 (2011): 256-263.

[7] M. U. Afzal, K. P. Esselle, and B. A. Zeb, "Dielectric phase-correcting structures for electromagnetic band gap resonator antennas," IEEE Transactions on Antennas and Propagation, vol. 63, no. 8, pp. 3390-3399, 2015.

[8] Ali, Md Yeakub, Khushboo Singh, Slawomir Koziel, Anna Pietrenko-Dabrowska, Mohammad Nasrat Zaqumi, and Subhas Mukhopadhyay. "A Low-Profile Printed Near-Field Metasurface for Enhanced Far-Field Radiation in Aperture-Type Antennas." IEEE Access 13 (2025): 196613-196621.

[9] Zaqumi, Mohammad Nasrat, Fatima Ghulam Kakepoto, Ali Lalbaksh, Syed Muzahir Abbas, Mohsen Asadnia, and Subhas Mukhopadhyay. "Metasurface-Driven Fabry-Perot Cavity Antenna for Next-Generation Point-To-Point Communication." In 2025 IEEE International Symposium on Antennas and Propagation and North American Radio Science Meeting (AP-S/CNC-USNC-URSI), pp. 2435-2437. IEEE, 2025.

Terahertz Microsystems Front-end Integration Technologies and Communication Application

Abstract

Terahertz wave possesses wide available high frequency spectrum bandwidth and thus has huge potential applications in high-resolution imaging sensing and high-speed communication. Due to limitations in terahertz integration technologies and MMIC manufacturing processes, terahertz radar and communication systems still face bottlenecks such as low power output, high noise, and difficulties in array integration. The front-end SiP integration is still one of the key terahertz microsystem technologies. In the session, the newly proposed integration solutions, such as the planner transmission line and waveguide interconnection, 3D multilayer module, and multi-channel integration, will be presented, and terahertz SiP arrays will be further introduced for the point-to-point high-speed communication.



Peng Wu is a Research Fellow and the Deputy Director of Aerospace Remote Sensing System Department of the Aerospace Information Research Institute, Chinese Academy of Sciences, Beijing, China. At the same time, he is also currently a Professor and PhD supervisor with University of Chinese Academy of Sciences, Beijing, China. He is a member of the Satellite Communication Committee, China Institute of Communications. His current research interests include millimeter-wave/terahertz microsystems and their applications. He has led national/CAS science and technology innovation projects, e.g., the antenna systems for satellite communications, and reconfigurable radar systems. His research outcomes have been applied in fields such as satellite communication and radar sensing.

979-8-3315-4544-4/26/$31.00 ©2026 IEEE

Metatronics for High-Performance Terahertz Integrated Circuits

Mohammad Samizadeh Nikoo

School of Electrical and Electronic Engineering,
Nanyang Technological University, Singapore 637457, Singapore
e-mail: mohammad.sn@ntu.edu.sg

Approaching the terahertz band from the electronics side is of great technological importance, with the promise of advancing next-generation wireless communication systems toward 6G and beyond [1]. However, inherent limitations of high-speed transistors, the primary building blocks of monolithically integrated high-frequency circuits, have hindered the realization of high-performance terahertz electronics [2], [3].

Electrical metastructures offer an alternative paradigm, in which electrical control of the conductivity of a semiconducting layer manipulates collective quasi-electrostatic responses within a device layout, enabling electronic functionalities such as switching, mixing, and parametric amplification. Compared with conventional transistors, electrical metastructures enable ultra-low contact resistances, leading to record-high switching cutoff frequencies beyond 10 THz in a compact device platform, referred to as electronic metadevices [4]-[7].

The first part of this talk highlights recent advances in III-nitride electronic metadevices operating up to 1 THz and introduces a new generation based on quasi-one-dimensional electrical metastructures with enhanced electrical performance [8]. We present theoretical insights into the collective responses governing the operation of electronic metadevices and elucidate their ultimate performance limits. In the second part, we introduce a metastructure-based paradigm for directly realizing high-performance millimeter-wave and terahertz components with ultracompact footprints, demonstrated the compatibility of metatronic devices with commercial silicon processes [9].

References

[1] S. Dang, O. Amin, B. Shihada, and M.-S. Alouini, “What should 6G be?” *Nat. Electron.*, vol. 3, pp. 20–29, 2020.
[2] K. Sengupta, T. Nagatsuma, and D. M. Mittleman, “Terahertz integrated electronic and hybrid electronic–photonic systems,” *Nat. Electron.*, vol. 1, pp. 622–635, 2018.
[3] W. Cao, H. Bu, M. Vinet, M. Cao, S. Takagi, S. Hwang, T. Ghani, and K. Banerjee, “The future transistors,” *Nature*, vol. 620, pp. 501–515, 2023.
[4] M. Samizadeh Nikoo and E. Matioli, “Electronic metadevices for terahertz applications,” *Nature*, vol. 614, pp. 451–455, 2023.
[5] M. Samizadeh Nikoo and H. Wang, “Theoretical foundation of electronic metadevices,” *IEEE Electron Device Lett.*, vol. 45, no. 3, pp. 456–459, Aug. 2023.
[6] M. Samizadeh Nikoo, C. Chu, B. Lin, Y. Liu, Y. Kim, and H. Wang, “Active and integrated electronic metadevices for future telecommunication circuits,” *Commun. Eng.*, vol. 4, Art. no. 49, 2025.
[7] A. Abushawish, Z. Huang, and M. Samizadeh Nikoo, “Strong collective responses in quasi-1D metadevices for millimeter-wave electronics,” *IEEE J. of Microw.*, Early Access, 2026.
[8] A. Abushawish, Z. Huang, and M. Samizadeh Nikoo, “Quasi-1D Electronic Metadevices With Enhanced Electrical Properties,” *IEEE Electron Device Lett.*, vol. 46, no. 11, pp. 2169– 2172, Nov. 2025.
[9] M. Samizadeh Nikoo, *et al.*, “High-power millimetre-wave switches on silicon using displacement fields and tunnelling currents,” *Nat. Electron.*, vol. 9, pp. 84–92, 2026.

979-8-3315-4544-4/26/$31.00 ©2026 IEEE

Design of a High-Performance Terahertz Multiplier Based on Thin-Film Technology

Li Wang
Key Laboratory of Microwave Remote Sensing, National Space Science Center Chinese Academy of Science
Beijing, China
wangli1@mirslab.cn

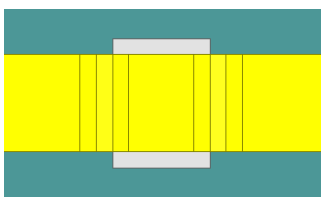
Jin Meng
Key Laboratory of Microwave Remote Sensing, National Space Science Center Chinese Academy of Science
Beijing, China
menjin@mirslab.cn

Dehai Zhang
Key Laboratory of Microwave Remote Sensing, National Space Science Center Chinese Academy of Science
Beijing, China
zhangdehai@mirslab.cn

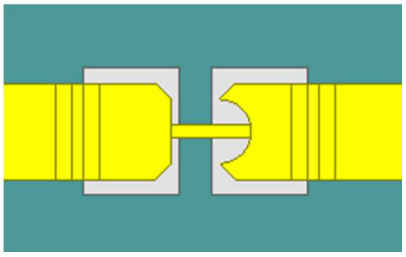
***Abstract*—This paper presents a high-performance 510 GHz monolithic GaAs Schottky barrier diode (SBD) frequency tripler for terahertz local oscillator (LO) applications. As the operating frequency extends into the sub-millimeter-wave regime, traditional multipliers are often limited by inaccurate parasitic modeling and significant substrate-induced dielectric losses. To address the parasitic modeling issue, a deterministic two-port, four-structure parasitic extraction method is proposed. Compared with conventional equivalent-circuit modeling or empirical fitting methods, it enables clearer separation of extrinsic parasitics and supports more accurate parasitic modeling and Schottky diode structure optimization.**

Four specifically designed test structures—Single Pad (SP), Pin-Open (PO), Diode-Short (DS), and Diode-Open (DO)—are employed to systematically extract pad-related parasitics (Lpad, Cpad), finger-related components (Lf, Rf), and inter-electrode coupling effects (Cpp). By de-embedding these extrinsic parasitics from Y-parameters, a more accurate parasitic model of the SBD can be established, which helps reduce the adverse impact of overall parasitic effects on multiplier performance and provides a basis for optimizing the Schottky diode structure. The tripler is implemented using a 3-μm-thick GaAs membrane process with backside substrate etching, which removes the bulk GaAs to form a thin-film structure and effectively reduces substrate-induced dielectric loss and suppresses parasitic substrate modes at 510 GHz. A balanced topology is also adopted to suppress even-order harmonics.

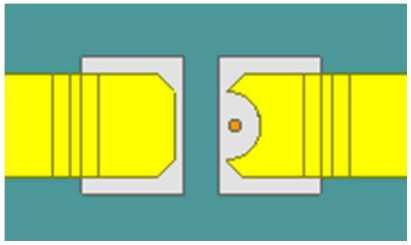
Experimental characterization was performed using a frequency multiplier chain and an Erickson power meter. The fabricated MMIC demonstrates robust performance across the 490–530 GHz band. Under an input drive power ranging from 63 to 104 mW, the tripler achieves a peak output power of 3.72 mW at 508 GHz, with a maximum conversion efficiency of 4.2%. Milliwatt-level output power is maintained across the entire measured bandwidth, although the upper end of the band approaches the operating limit of the test equipment. These results demonstrate that the proposed four-structure extraction method and 3-μm thin-film technology together provide an effective means of improving the output performance of terahertz frequency triplers.



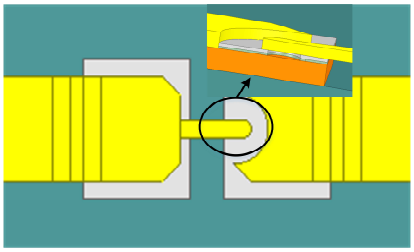
(a)



(b)



(c)



(d)

Fig. 1. The model of the test structure (a) single pad structure; (b) pin-open structure; (c) diode-short structure; (d) diode-open structure

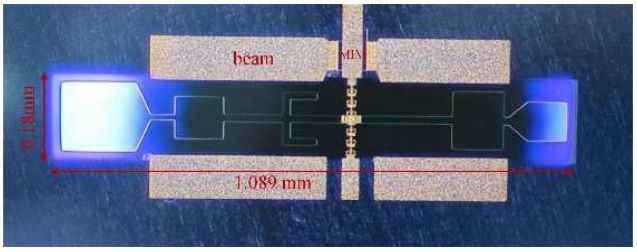


Fig. 2. A Balanced MMIC Tripler Based on Thin-Film Technolog

Design and Analysis of Circular Hollow Polymer Waveguide at THz Frequency Band

Sheng-Jie Zhou
School of Integrated Circuits
Shanghai Jiao Tong University
Shanghai, China
19532505397@sjtu.edu.cn

Chang-Sheng Sun
School of Integrated Circuits
Shanghai Jiao Tong University
Shanghai, China
sunchangsheng@sjtu.edu.cn

Xiao-Chun Li*
School of Integrated Circuits
Shanghai Jiao Tong University
Shanghai, China
Corresponding author*lixc@sjtu.edu.cn

Jun-Fa Mao
School of Integrated Circuits
Shanghai Jiao Tong University
Shanghai, China
jfmao@szu.edu.cn

***Abstract*—This paper presents the design and analysis of a circular hollow polymer waveguide (CHPW) operating at W-band (75–110 GHz). The proposed structure consists of an air core surrounded by a polymer cladding, which effectively reduces dielectric loss compared to solid polymer waveguides. Mode analysis reveals that the designed CHPW supports single-mode propagation throughout the entire W-band, with the fundamental HE_{11} mode and higher-order TM_{01} mode identified. Parametric studies show that increasing the inner radius or polymer thickness raises both the phase and attenuation constants, with polymer thickness exhibiting a more significant influence. Compared with circular solid polymer waveguides (CSPW), the CHPW demonstrates lower attenuation and broader single-mode bandwidth but suffers from weaker field confinement. The performance of CHPW with different materials shows that PTFE offers lower loss and wider single-mode bandwidth than HDPE and PMMA, making it a promising candidate for terahertz (THz) applications.**

Keywords—Circular hollow polymer waveguide, terahertz, W-band, mode analysis, normalized phase constant, HFSS.

I. Introduction

The advancement in the new generation of wireless communication technology has necessitated high-speed data transmission [1]. High-speed interconnections at millimeter-wave (mm-wave) and terahertz (THz) frequency band can provide a wider bandwidth and a lower latency compared with those at traditional low frequencies [2]. However, the conventional metallic interconnections (metallic waveguides and transmission lines) suffer from high conductor loss at THz band due to skin effect and surface roughness [1].

Polymer waveguides have gained widespread attention in academic field for their advantages such as low loss, broad bandwidth, low cost and light weight [3]-[5]. Polymer waveguides conduct the electromagnetic wave through the dielectric core with a surrounding clad (usually air), which eliminate the conductor loss but suffer from dielectric loss and radiation loss. According to the cross-section shape, the polymer waveguides can be mainly divided into rectangular solid polymer waveguides, circular solid polymer waveguides and hollow polymer waveguides. Rectangular solid polymer waveguides were extensively researched [5]-[7] for their ability to control mode polarization and compatibility with planar integration processes. Circular solid polymer waveguides feature wider bandwidth and lower loss [8], thus are widely used in optical fibers. Hollow polymer waveguides, also including rectangular [9] and circular shape [10], were proposed to further minimize the dielectric loss. However, the air core results in poor confinement to electromagnetic field and energy. Although hollow polymer waveguides have gained much attention by researchers, the parametric performance and analysis at THz frequencies are not fully studied.

In this paper, a circular hollow polymer waveguide (CHPW) at W-band (75-110 GHz) is investigated. First, the structure design is presented. The performance (modes, attenuation and phase constants) and its variation with dimension and materials are then analyzed. A performance comparison between the hollow and solid circular polymer waveguides is also conducted. Finally, a conclusion is drawn.

II. Structure Design

The structure of the CHPW in simulation is illustrated in Fig. 1. The default polymer material—high density poly-ethylene (HDPE) with a permittivity of 2.3 and a loss tangent of 0.0005 is selected. The CHPW has an inner air core with the radius r_{in} of 0.5 mm and a polymer clad with the thickness Δr of 0.5 mm. The dielectric length l is 8 mm, which is approximately 4λ for solid HDPE material at 90 GHz. The excitation end is designed as a circular port with the radius r_{port} of 5 mm to accommodate the mode field in the circular hollow polymer waveguide. This presented structure is simulated using the high-frequency structure simulator (HFSS).

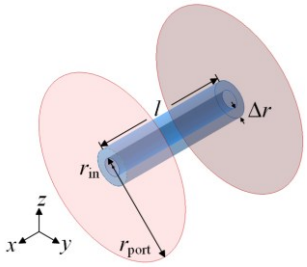


Fig. 1. Structure of the circular hollow polymer waveguide in simulation.

III. Peformance Analysis

A. Mode Analysis

The simulated normalized phase constant of the lowest three modes for the CHPW is shown in Fig. 2. The propagation condition of one mode is $\beta/k_0 > 1$, hence the intersection point of the normalized phase constant curve and $\beta/k_0 = 1$ line is the cutoff frequency of that mode [9]. It is demonstrated that the designed CHPW has a single-mode bandwidth of the whole W-band. The electric field patterns of the lowest three modes are depicted in Fig. 3. The first two modes are both HE_{11} mode but with orthogonal polarization directions—HE_{11}^{x} and HE_{11}^{y} as shown in Fig. 3(a) and (b), where x and y only denote two

perpendicular polarization directions and are unrelated to the coordinate system. Therefore, the normalized phase constant curves of the lowest two modes are identical in Fig. 2. The first higher order mode (the actual second mode) is TM_{01} or TE_{01} mode (with similar cutoff frequencies). The TM_{01} mode pattern is shown in Fig. 3(c), where the electric field orientates radially.

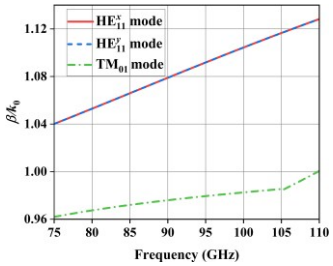


Fig. 2. Normalized phase constant of the lowest three modes for the CHPW.

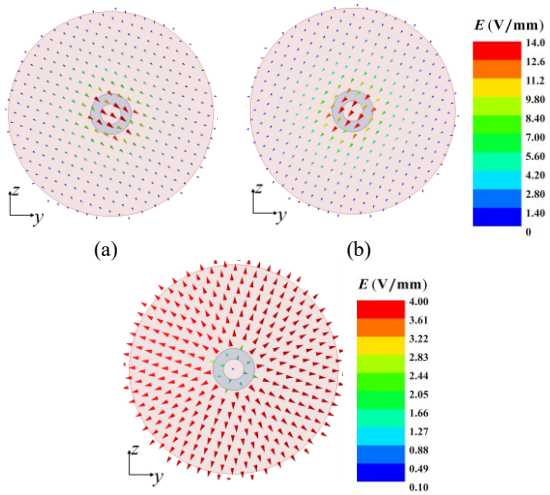
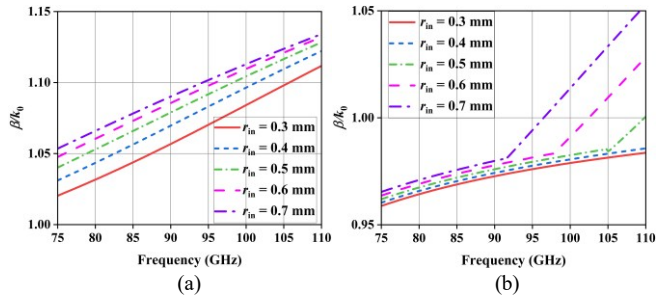


Fig. 3. Electric field patterns of the lowest three modes for the CHPW. (a) HE^x_{11} mode. (b) HE^y_{11} mode. (c) TM_{01} mode.

B. Dimension Analysis

The normalized phase constants and attenuation constant varying with parameters of r_{in} and Δr are shown in Fig. 4 and Fig. 5, respectively. It is evident that as r_{in} or Δr increases, the phase and attenuation constants both ascend. In high frequency range, the influence of r_{in} on attenuation constant appears to be insignificant. It is evident that Δr has a greater impact on the phase and attenuation constants than r_{in}. Therefore, a thinner polymer thickness is needed to achieve a wider single-mode bandwidth and lower loss. The single-mode (TM_{01} mode) cutoff frequencies when r_{in} = 0.5, 0.6 and 0.7 mm are 109.83, 102.46 and 96.48 GHz respectively. The single-mode cutoff frequencies when Δr = 0.6 and 0.7 mm are 98.40 and 89.46 GHz respectively.



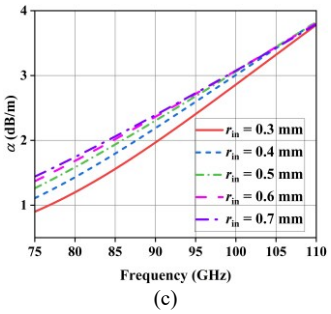


Fig. 4. Normalized phase constants of (a) HE_{11} mode, (b) TM_{01} mode and (c) attenuation constant of HE_{11} mode corresponding to different r_{in} values.

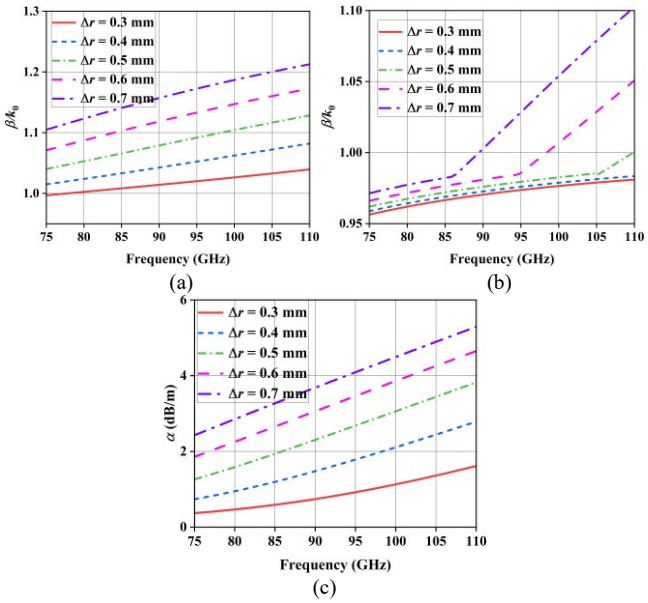


Fig. 5. Normalized phase constants of (a) HE_{11} mode, (b) TM_{01} mode and (c) attenuation constant of HE_{11} mode corresponding to different Δr values.

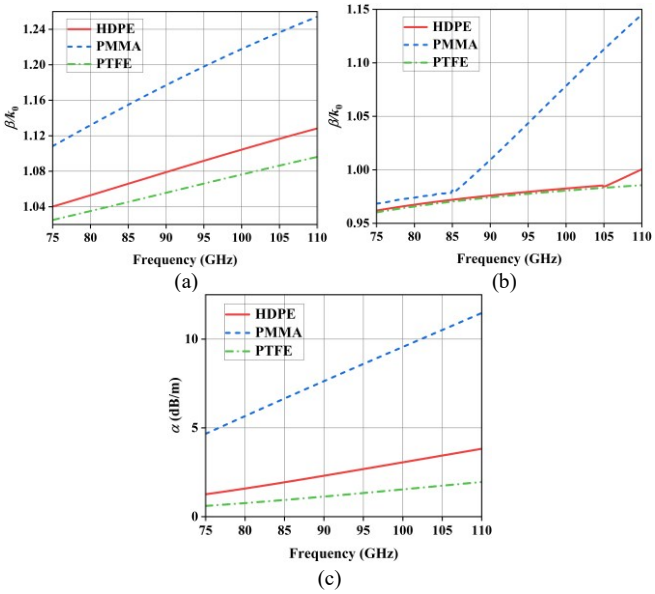


Fig. 6. Normalized phase constants of (a) HE_{11} mode, (b) TM_{01} mode and (c) attenuation constant of HE_{11} mode corresponding to different materials.

C. Material Analysis

The normalized phase constants and attenuation constant with different polymer materials are illustrated in Fig. 6. Optical fiber material polymethyl methacrylate (PMMA,

permittivity of 3.0 and loss tangent of 0.001) and dielectric material polytetrafluoroethylene (PTFE, permittivity of 2.1 and loss tangent of 0.0003) are studied. Compared with CHPW in HDPE, CHPW in PMMA has a higher phase constant but a greater attenuation. CHPW in PTFE features a smaller attenuation and a lower phase constant. Single-mode cutoff frequency of CHPW in PTFE is higher than 110 GHz, which indicates that it also has a single-mode bandwidth of the whole W-band. Therefore, PTFE appears to be an excellent alternative of the CHPW material at W-band. Although PMMA is widely used in optical fibers, it is unsuitable for CHPW at W-band due to its narrow single-mode bandwidth and high loss in this spectrum.

IV. Performance Comparison

CHPW and circular solid polymer waveguide (CSPW) [8] share similar propagation modes. For better comparison between CHPW and CSPW at W-band, a CSPW with the same outer radius ($r_{out} = r_{in} + \Delta r$) of the CHPW is also simulated. The normalized phase constants and attenuation constants of CHPW and CSPW are demonstrated in Fig. 7. CHPW has a higher single-mode cutoff frequency than CSPW, thus features a wider single-mode bandwidth. The single-mode cutoff frequency of CSPW is approximately 101.75 GHz. The attenuation of CHPW is lower than that of CSPW due to less dielectric loss. The longitudinal section electric field diagrams of CHPW and CSPW are depicted in Fig. 8. Obviously, the field in CHPW is less concentrated than CSPW. Moreover, the power confinement factor can be expressed as

$$\Gamma = \frac{\int_{r\le r_{out}} \boldsymbol{S}\cdot\boldsymbol{a}_x}{\int_{r\le r_{port}} \boldsymbol{S}\cdot\boldsymbol{a}_x} \quad (1)$$

where $\boldsymbol{a}_x$ is the unit vector in x-direction and $\boldsymbol{S}$ is the Poynting vector. The calculated Γ values of CHPW and CSPW are 52.02% and 76.02% respectively. Therefore, the capability of energy confinement for CHPW is worse than CSPW. It is found that CHPW is more suitable for long-distance signal transmission but suffers from proximity coupling, which requires larger distance between adjacent CHPWs.

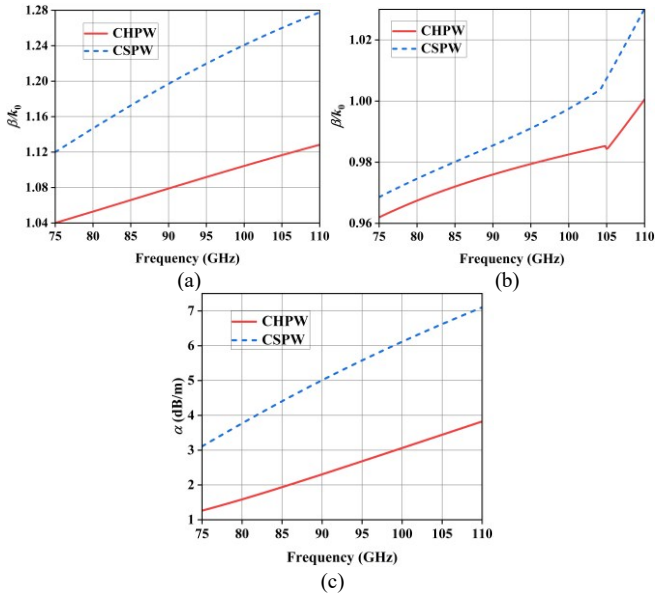


Fig. 7. Normalized phase constants of (a) HE_{11} mode, (b) TM_{01} mode and (c) attenuation constant of HE_{11} mode for CHPW and CSPW.

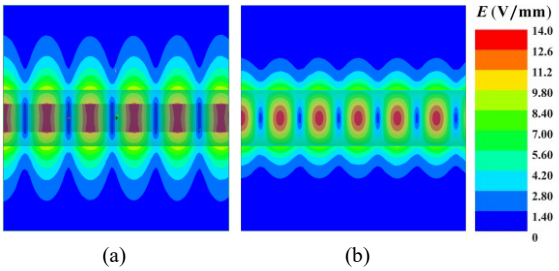


Fig. 8. Longitudinal section electric field diagrams. (a) CHPW. (b) CSPW.

V. Conclusion

In this paper, a CHPW operating at W-band is studied. The designed CHPW has a single-mode bandwidth of the whole W-band. Both the inner radius and polymer thickness influence the phase and attenuation constants of CHPW. However, the polymer thickness exerts a more significant effect. CHPWs made from different materials exhibit different performance characteristics, where PTFE is a great alternative to HDPE at W-band. This work provides a useful guidance for the development of polymer waveguides at THz frequencies.

Acknowledgment

This work was supported by the National Natural Science Foundation of China under Grant 62371284 and 62188102.

References

[1] H.-B. Zhan, X.-C. Li and C.-S. Sun, “Low-Loss Horizontal Transition Between Rectangular Dielectric Waveguide and Microstrip Line at WBand,” *IEEE Microwave and Wireless Technology Letters*, vol. 34, no. 4, pp. 371-374, 2024.

[2] L.-F. Gao, K. Ning and J.-F. Mao, “Novel Broadband Transition from Rectangular Dielectric Waveguide to Planar Circuit at W-Band,” in *2025 International Conference on Microwave and Millimeter Wave Technology (ICMMT)*, Xi’an, China, 2025, pp. 1-3.

[3] J. Richter, Y. Yazici, C. Ziegler and L.-P. Schmidt, “A Broadband Transition between Dielectric and Planar Waveguides at Millimeter-wave Frequencies,” in *2003 33rd European Microwave Conference*, Munich, Germany, 2003, pp. 947-950.

[4] C.-M. Liu, L.-P. Carignan and K. Wu, "Hybrid Metallo-Dielectric Waveguide Architecture for Compact Low-Loss THz Applications," *IEEE Microwave and Wireless Technology Letters*, vol. 34, no. 5, pp. 486-489, 2024.

[5] W.-L. Tsai, I. Ocket, J. Vaes, M. Cauwe, P. Reynaert and B. Nauwelaers, "Novel Broadband Transition for Rectangular Dielectric Waveguide to Planar Circuit Board at D Band," in *2018 IEEE/MTT-S International Microwave Symposium - IMS*, Philadelphia, PA, USA, 2018, pp. 386-389.

[6] L.-F. Gao, K. Ning and J.-F. Mao, "Novel Broadband Transition from Rectangular Dielectric Waveguide to Planar Circuit at W-Band," in *2025 International Conference on Microwave and Millimeter Wave Technology (ICMMT)*, Xi'an, China, 2025, pp. 1-3.

[7] J. S. Häseker and M. Schneider, "90 Degree Microstrip to Rectangular Dielectric Waveguide Transition in the W-Band," *IEEE Microwave and Wireless Components Letters*, vol. 26, no. 6, pp. 416-418, 2016.

[8] A. Meyer, S. Karau and M. Schneider, "Broadband Stacked-Patch Transition from Microstrip Line to Circular Dielectric Waveguide for Dual-Polarized Applications at W-Band Frequencies," in *2019 49th European Microwave Conference (EuMC)*, Paris, France, 2019, pp. 440-443.

[9] C.-S. Sun, X.-C. Li, H.-B. Zhang and J.-F. Mao, “A Low-Cost Hollow Rectangular Dielectric Waveguide,” in *2023 IEEE MTT-S International Wireless Symposium (IWS)*, Qingdao, China, 2023, pp. 1-3.

[10] C.-Y. Liu, H.-E. Ding, S.-H. Wu and T.-L. Wu, "Extremely Low-Loss Planar Transition From Hollow Dielectric Waveguide to Printed Circuit Board for Millimeter-Wave Interconnect," *IEEE Transactions on Microwave Theory and Techniques*, vol. 69, no. 9, pp. 4010-4020, 2021.

Hybrid Modeling Method of FT-Transformer and XGBoost for TFsurface

1st Yihao Li
School of Microelectronics
Nanjing University of Science & Technology
Nanjing, China
avopears@outlook.com

2nd Shijie Wang
Dept. of Biomedical Engineering
National University of Singapore
Singapore, Singapore
e1499409@u.nus.edu

3rd Wen Lyu
School of Microelectronics
Nanjing University of Science & Technology
Nanjing, China
lyuwen@njust.edu.cn

***Abstract*—Terahertz field-effect transistors integrated with metasurfaces (TFsurfaces) hold significant promise for high-sensitivity chemical detection and imaging. However, optimizing the asymmetric interdigitated grating gate (AIGG) structure remains challenging due to complex near-field coupling effects and a high-dimensional parameter space spanning periodicity, gate number, asymmetry coefficient, and structural dimensions. Conventional empirical design methods are inefficient and struggle to globally optimize these detectors. This paper proposes a hybrid intelligent modeling framework that combines a Feature Tokenizer Transformer (FT-Transformer) with Extreme Gradient Boosting (XGBoost) to accurately predict the electromagnetic spectral response of TFsurfaces from structural parameters. Structure-frequency joint inputs are encoded by the FT-Transformer to capture complex nonlinear feature interactions; the resulting deep embeddings are then concatenated with original structural parameters and fed into XGBoost for regression. Evaluated on an independent test set, the proposed model achieves an R^2 of 0.9985 and an MSE of 1.8×10^{-5}, outperforming single-model baselines. This data-driven framework significantly accelerates the design of high-sensitivity THz detectors and offers a scalable solution for complex metasurface optimization.**

***Index Terms*—HEMT, Deep Learning, Metasurface, THz Detection.**

I. Introduction

Terahertz (THz) technology has broad applications in trace chemical detection due to the vibrational and rotational energy levels of many chemicals in the THz frequency range [1]. Detectors play a critical role in imaging and chemical spectroscopy by capturing and analyzing signals. The terahertz field-effect transistor (TeraFET), a planar transistor detector compatible with standard semiconductor fabrication processes, has garnered significant attention in imaging and spectroscopy due to its advantages, including room-temperature operation, high environmental tolerance, and ease of array integration [2]–[4]. Furthermore, its planar transistor structure is well-matched with two-dimensional metasurfaces, enabling multi-dimensional detection and ultra-high sensitivity through resonance effects. These detectors, which integrate metasurfaces with TeraFETs, are referred to as TFsurfaces.

Despite these advantages, improving detector performance remains a significant challenge. Due to the substantial size mismatch between the transistor gate and the THz wavelength, individual transistors still suffer from low coupling efficiency. The design of TFsurfaces must consider both the meta-atom structure and the near-field enhancement characteristics beneath the transistor gate, resulting in a highly complex design process [5]. Traditional experience-based methods struggle to efficiently and accurately design high-sensitivity detectors for target frequency bands [6]. This challenge is particularly pronounced for cross-fingered TFsurfaces, which involve parameters such as periodicity N, gate number, asymmetry coefficient g_1, metasurface length L_{meta}, and width W_{meta}. The need to optimize near-field coupling efficiency across multiple gates further complicates the design process, limiting the global optimization of high-sensitivity TFsurfaces [7].

This study proposes a hybrid intelligent modeling framework tailored for the "structural parameters-to-spectrum" tabular data of metasurfaces. The framework integrates the deep feature extraction capabilities of the FT-Transformer with the efficient ensemble learning mechanism of XGBoost to achieve precise modeling and prediction of the electromagnetic responses of metasurfaces. The metasurface design involves geometric parameters such as periodicity N, gate number, asymmetry coefficient g_1, metasurface length L_{meta}, and width W_{meta}. The electromagnetic response is represented as spectral data, with frequency as the independent variable and electric field intensity as the dependent variable. The core objective of this research is to accurately predict the electromagnetic spectral response based on structural parameters.

II. TFsurface Structure and Neural Network Architecture

The schematic of the asymmetric interdigitated grating gate (AIGG) TFSurface structure is shown in Fig. 1. The structure has dimensions of $200 \times 200\mu m$, with gate region details characterized by parameters such as periodicity N, gate number, and asymmetry coefficient g_1. The multi-periodic design introduces multiple gate regions, extending the traditional TeraFET, which typically features a single self-mixing region, to a structure with multiple mixing regions. However, optimizing the design with five parameters remains a significant challenge.

To achieve high-precision and generalizable predictions of the electromagnetic response for this type of structure, this study proposes a hybrid modeling framework that combines a deep neural network with a gradient boosting decision

979-8-3315-4544-4/26/$31.00 ©2026 IEEE

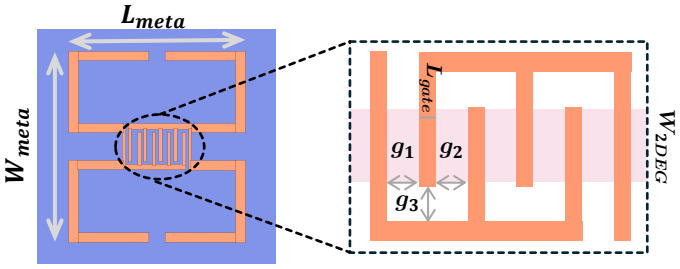


Fig. 1. Structure of the Meta-atom.

tree (XGBoost). As illustrated in Fig. 2, the framework consists of three main components. First, data preprocessing strategies, such as flattening and feature standardization, are applied to establish a robust foundation for subsequent modeling. Metasurface structural parameter vectors $\mathbf{x} = [N, g_{ate}, g_1, l_{meta}, w_{meta}]^\mathsf{T} \in \mathbb{R}^d$. Second, a Feature Tokenizer Transformer model is employed to extract deep semantic features from the structure-frequency joint inputs, enabling effective encoding of complex nonlinear relationships and physical interactions. Finally, the deeply embedded features are fused with the original parameters and input into the XGBoost model, where multi-objective hyperparameter optimization and regression training are performed to further enhance the model's predictive performance and interpretability. This end-to-end modeling framework achieves a well-balanced trade-off among accuracy, robustness, and scalability.

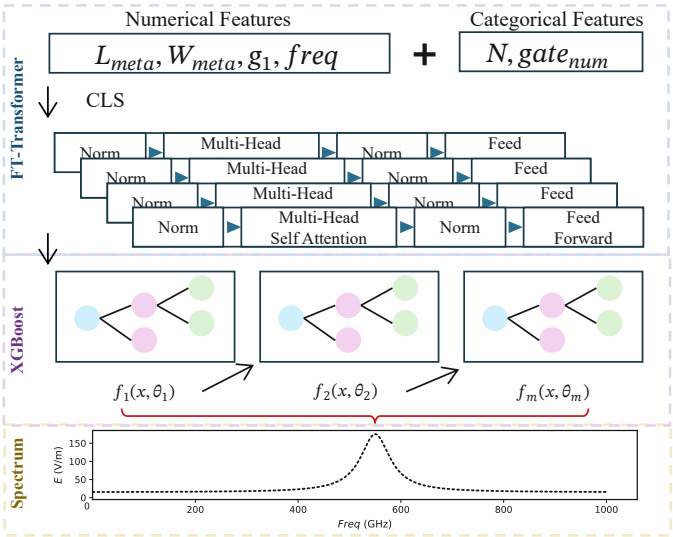


Fig. 2. Network architecture.

$$\hat{y} = \mathcal{H}_\Theta(\mathbf{x}, \omega) = G_\Phi(\mathbf{x}, \omega, T_\theta(\mathbf{x}, \omega)) \tag{1}$$

The overall objective of this hybrid network is to learn a mapping from the joint structural-frequency space to the electromagnetic response space: $y(\omega; \mathbf{x})$ denotes the electromagnetic response magnitude at frequency ω under structure $\mathbf{x}$. T_θ is the FT-Transformer encoder, G_Φ is the XGBoost-based fusion regressor.

$$\mathbf{A}_{ij}^{(\ell)}(\omega) = \frac{\exp\left(\frac{\left(\mathbf{W}_Q^{(\ell)}\tilde{\mathbf{e}}_i\right)^\mathsf{T}\left(\mathbf{W}_K^{(\ell)}\tilde{\mathbf{e}}_j\right)}{\sqrt{d_k}}\right)}{\sum_m \exp\left(\frac{\left(\mathbf{W}_Q^{(\ell)}\tilde{\mathbf{e}}_i\right)^\mathsf{T}\left(\mathbf{W}_K^{(\ell)}\tilde{\mathbf{e}}_m\right)}{\sqrt{d_k}}\right)} \tag{2}$$

$\mathbf{A}_{ij}^{(\ell)}(\omega)$ is the nonlocal dependency strength from feature j to feature i at layer ℓ, conditioned on frequency ω.

A. Data preprocessing

Before hybrid modeling, the raw data underwent systematic preprocessing. First, data flattening techniques were applied to transform the mapping between the original structural parameters and the entire spectral curve into an explicit combination of structural parameters and frequency as input features. This new data representation uses both structural parameters and frequency as input features to predict the electric field intensity (amplitude) at specific frequencies. For categorical structural parameters (e.g., periodicity N), an OrdinalEncoder was employed, fitted exclusively on the training data to prevent data leakage. The choice of OrdinalEncoder over One-Hot Encoder was based on two considerations: (1) it avoids the high-dimensional sparse feature matrix generated by one-hot encoding, which is more efficient for subsequent embedding layers; and (2) tree-based models like XGBoost inherently handle ordered integer encodings well, effectively learning optimal split points. For continuous numerical features (e.g., g_1, L_{meta}, W_{meta}), MinMaxScaler was used for normalization, with the scaler parameters fitted solely on the training set. This approach enhances the stability and convergence speed of model training. In addition, the target variable was normalized to further enhance the numerical stability of the model and mitigate potential issues such as gradient explosion or vanishing caused by differences in numerical scales. During the prediction phase, an inverse transformation was applied to restore the physical dimensions of the normalized results. These preprocessing strategies laid a solid foundation for subsequent model training and performance enhancement.

B. Deep learning feature extraction

In the feature extraction phase, a deep learning model specifically designed for structured tabular data, the Feature Tokenizer Transformer (FT-Transformer), was employed as the core architecture. This model builds upon the traditional Transformer encoder with structural adaptations and task-specific optimizations, demonstrating strong modeling capacity and interpretability.

Specifically, the FT-Transformer first tokenizes both categorical and numerical features in the input. These features are then transformed into a sequence of fixed-dimensional embedding vectors, enabling a unified encoding representation of the heterogeneous feature space. The resulting embedding sequence is subsequently fed into a standard Transformer encoder stack, which alternates between multi-head self-attention mechanisms and feed-forward network layers. This

architecture effectively captures complex feature interactions and global dependency patterns. The high-dimensional, dense embedding vector space learned by the FT-Transformer exhibits greater linear separability compared to the original sparse feature space. This provides the XGBoost model in the second stage with richer and more effective input features. After completing deep feature extraction, the high-dimensional semantic embeddings extracted by the FT-Transformer were concatenated with the original structural parameters to construct an enriched hybrid feature set. This feature set combines the physical interpretability of the original parameters with the high-order nonlinear features automatically extracted by the deep learning model. To fully exploit the information potential of this enhanced feature set, the gradient boosting tree model XGBoost was introduced as the second-stage regressor.

III. Results and Discussion

To validate the effectiveness and advancement of the hybrid modeling framework, a series of detailed comparative experiments were conducted. The experimental results demonstrated that the proposed hybrid model achieved significant advantages in prediction accuracy and exhibited excellent generalization performance. Notably, the model maintained stable predictive performance even under varying data volumes and increasing structural complexity, exhibiting strong robustness and adaptability.

The evaluation results on an independent test set further confirmed the model's superior performance in predicting spectral responses. On a normalized scale, the final model achieved a mean squared error (MSE) of (1.8×10^{-5}) and a coefficient of determination (R^2) of 0.9985, indicating exceptional fitting accuracy and error control. When restored to the original physical scale, the model still maintained outstanding performance, with an MSE of 1.5044 and an (R^2) of 0.9985, demonstrating its reliability in practical engineering applications.

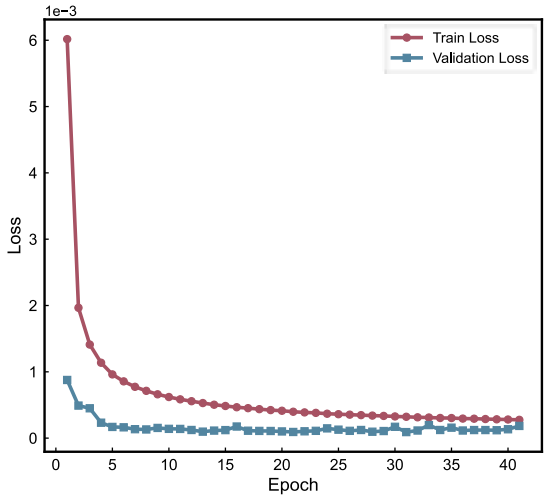


Fig. 3. Loss curves for training and validation.

IV. Summary

In this work, we proposed an innovative hybrid intelligent modeling framework that combines deep learning and ensemble learning to accurately predict the electromagnetic response of TFsurfaces. By integrating the FT-Transformer with XGBoost, we successfully captured the complex nonlinear relationships between structural parameters and frequency, achieving high-precision spectral predictions.

Experimental results demonstrated that the proposed model exhibited outstanding performance on an independent test set, significantly enhancing the efficiency and effectiveness of designing high-sensitivity THz detectors. In the future, we plan to further optimize the model architecture and explore its potential applications in the design of more complex electromagnetic systems.

V. Acknowledgment

We acknowledge funding by Key Technologies Research and Development Program (2023YFB3207800), Jiangsu Provincial Key Research and Development Program (No. BE2023818), the National Natural Science Foundation of China (Grant Nos.62271258, 62401261, 62404103), Basic Research Program of Jiangsu (Nos.BK20243046, BK20253062), Fundamental Research Funds for Central Universities (No. 30925010603), National Key Laboratory of Integrated Circuits and Microsystems (No: NICL2025KF2001).

References

[1] M. Tonouchi, "Cutting-edge terahertz technology," *Nature photonics*, vol. 1, no. 2, pp. 97–105, 2007.

[2] Y. Li, J. Sun, C. Qin, X. Deng, and X. Zheng, "A high-performance terahertz detector based on a graded channel gan high-electron-mobility transistor with a recessed gate," *Optical Materials*, vol. 150, p. 115233, 2024.

[3] Y. Zhu, Q. Ding, L. Xiang, J. Zhang, X. Li, L. Jin, Y. Shangguan, J. Sun, and H. Qin, "0.2-4.0 thz broadband terahertz detector based on antenna-coupled algan/gan hemts arrayed in a bow-tie pattern," *Optics Express*, vol. 31, no. 6, pp. 10 720–10 731, 2023.

[4] J. Sun, Y. Zhu, W. Feng, Q. Ding, H. Qin, Y. Sun, Z. Zhang, X. Li, J. Zhang, X. Li *et al.*, "Passive terahertz imaging detectors based on antenna-coupled high-electron-mobility transistors," *Optics express*, vol. 28, no. 4, pp. 4911–4920, 2020.

[5] A. V. Chernyadiev, D. B. But, Y. Ivonyak, K. Ikamas, and A. Lisauskas, "A cmos-integrated terahertz near-field sensor based on an ultra-strongly coupled meta-atom," *Scientific Reports*, vol. 14, no. 1, p. 11483, 2024.

[6] Y. Li, R. Chen, J. Sun, X. Deng, X. Li, Y. Xie, S. Wang, Z. You, C. Qin, and X. Zheng, "Deep-learning-driven design of multiplexed meta-array couplers for broadband hemt terahertz detection," *Photonics Research*, vol. 13, no. 5, pp. 1290–1301, 2025.

[7] Y. Li, S. Wang, Z. You, X. Deng, and X. Li, "Enhanced thz self-mixing detection in terafets via asymmetric interdigitated grating gates coupled to srr metasurface arrays," in *2025 50th International Conference on Infrared, Millimeter, and Terahertz Waves (IRMMW-THz)*. IEEE, 2025, pp. 1–2.

High-Tc Superconducting Monolithic Microwave Integrated Circuits (MMICs) for High-Sensitivity RF Receivers

He Zhu
[1] Charles Darwin University, Darwin, NT, Australia
email: he.zhu@cdu.edu.au

High-temperature superconducting (HTS) technologies have many potential applications, such as power transmission, medical imaging, quantum computing, military and aerospace, etc., due to their significant advantages of high energy efficiency, easy cooling as well as high reliability and stability. High-temperature superconducting technologies also play a critical role in wireless communications as they offer unique advantages for applications in high-frequency electromagnetic domains. High-sensitivity and broadband nature of superconducting devices can be applied for high-speed wireless communication systems, especially the heterodyne mixers are highly desirable for high-gain and low-noise RF receivers. This talk will introduce a series of monolithic microwave integrated circuits (MMICs), mainly heterodyne mixers and on-chip antennas, which are used in microwave and millimeter-wave RF receivers. The MMIC mixers are developed based on the quantum tunnelling effect of Josephson junctions and will significantly reduce power consumption and enhance the sensitivity of RF receivers. Besides, advanced antenna technologies, including the packaging techniques of a high-gain waveguide antenna with MMICs and a frequency-scanning leaky-wave antenna, will also be touched in this talk.

979-8-3315-4544-4/26/$31.00 ©2026 IEEE

Multi-Function Multi-Band Reconfigurable High-Q Filters

Raafat R. Mansour
University of Waterloo, Canada
rrmansour@uwaterloo.ca

Reconfigurable filters are key components in the development of agile multi-standard receivers.. This talk starts by addressing the needs for using multi-band and tunable filters in wireless communication systems and in flexible satellite payloads. It then addresses existing tuning technologies, providing a comparison between piezoelectric, Semiconductor, MEMS and PCM tuning elements in terms of linearity, insertion loss, suitability for use at millimeter-wave frequencies and ease of integration with high-Q filters. It outlines major design considerations for tunable filters presenting techniques to realize tunable filters with an absolute constant absolute bandwidth and a constant frequency spacing between transmission zeros, over a wide tuning range. The talk also illustrates examples of tunable filters and diplexers tuned only a by single tuning element, while exhibiting a constant absolute bandwidth. It then addresses approaches for realizing multi-band filters including dual-band and triple-band filters. Finally, it presents techniques for realizing multi-band filters where the various bands are tunable in both center frequency and bandwidth. Very recent work on realizing reconfigurable acoustic filters is also presented.

979-8-3315-4544-4/26/$31.00 ©2026 IEEE

Semiconductor Electronics for High Power/High Speed Reconfigurable RF and Microwave Electronics

Robert H Caverly
Department of Electrical and Computer Engineering
Villanova University
Villanova, PA 19085 USA
ORCID: 0000-0002-9212-7660

***Abstract*— Microwave and RF design engineers always seek to develop a design that will meet specifications the first time that the circuit is fabricated. To do so requires that as many elements and phenomena as possible associated with the control devices and circuit be accurately modeled. In the case of the microwave and RF semiconductor control circuits, accurate modeling of the solid-state control components over frequency, voltage, current, and power is key to successful control system design. This talk will cover material that will provide the RF and microwave design engineer insight into the physical operation and modeling of semiconductor devices for high-speed reconfigurability: PIN diodes and field-effect transistors (FETs) as control components and their use in microwave and RF control circuits. The talk will briefly cover basic RF and microwave control circuits for reconfigurable electronics and then focus on linear and nonlinear models for PIN diode, MESFET and MOSFET control elements to implement these circuits. The talk will conclude with control circuit examples using these models for use in reconfigurable RF and microwave electronics.**

Keywords—P-i-n diodes, field effect transistors, switching circuits, electronic switching systems, microwave circuits, microwave devices, semiconductor devices, semiconductor device modeling

979-8-3315-4544-4/26/$31.00 ©2026 IEEE

Filters for Space Applications: CNC Milling and Additive Manufacturing Perspectives

Cristiano Tomassoni
Dept. of Engineering
University of Perugia
Perugia, Italy
cristiano.tomassoni@unipgit

***Abstract*— High-performance waveguide filters are critical components in space communications, where mass reduction and signal integrity are paramount. This presentation explores the design and realization of these devices, comparing traditional high-precision CNC milling with emerging Additive Manufacturing techniques. By evaluating experimental results, we analyze how different fabrication perspectives influence design flexibility, surface roughness, and overall RF performance in demanding space environments.**

Keywords—filtes, space technologies, additive manufacturing

I. INTRODUCTION

The rapid evolution of modern satellite communication systems, particularly for LEO constellations and high-throughput satellites (HTS), is driving an unprecedented demand for microwave components that minimize Size, Weight, and Power (SWaP). In the space industry, miniaturization is no longer an option but a strict requirement; however, reducing the physical footprint of a filter typically leads to a degradation of the Quality Factor (Q) and power handling. This talk explores cutting-edge design strategies and manufacturing paradigms aimed at achieving extreme miniaturization without compromising technically sound RF performance, featuring several benchmark designs developed in collaboration with the European Space Agency (ESA). A significant focus is placed on the use of TM-mode d metallic resonators which, unlike traditional TE-mode solutions, allow for a drastic reduction in the filter's profile and overall volume[1][2]. To further enhance selectivity without increasing the filter order—which would add mass and insertion loss—the discussion delves into specialized techniques for introducing transmission zeros. Traditionally, these zeros require cross-couplings between non-adjacent resonators, often forcing the filter into a folded or U-shaped physical layout. However, in space payloads, in-line configurations are frequently preferred due to their easier integration within complex mechanical housings and more straightforward routing.

The analysis covers an innovative approach where transmission zeros are generated in a strictly in-line geometry by exploiting non-resonant modes [3][4], allowing for high selectivity and sharp rejection skirts while maintaining a compact, linear mechanical footprint. These advanced topologies are physically realized through traditional high-precision CNC machining. However innovative Additive Manufacturing (AM) offers new opportunities for microwave technology. Selective Laser Melting (SLM) is showcased for the creation of monolithic metallic structures; by printing the filter as a single, seamless piece, the need for screws and silver-plated joints is eliminated, significantly reducing the risk of Passive Intermodulation (PIM) and enhancing mechanical robustness against the extreme vibrations of a rocket launch [5]. Furthermore, the frontier of ceramic AM is examined through Lithography-based Ceramic Manufacturing (LCM) by Lithoz. The ability to 3D-print high-purity Alumina with micrometric precision enables the realization of dielectric-loaded filters with complex internal geometries[6][7], offering a new degree of freedom for achieving high-Q performance in extremely small volumes and effectively overcoming the geometric limitations of traditional ceramic processing. Experimental data and measured prototypes demonstrate how these combined strategies—advanced TM-mode design, non-resonant mode coupling, and AM fabrication—provide a comprehensive toolkit for the next generation of space-borne microwave hardware.

REFERENCES

[1] L. Pelliccia et al., "Very-compact Waveguide Bandpass Filter based on Dual-Mode TM Cavities for Satellite Applications in Ku-band," 2018 48th European Microwave Conference (EuMC), Madrid, Spain, 2018, pp. 93-96,

[2] C. Tomassoni et al., "Compact broadband waveguide filter with wide spurious-free range based on mixed TM and combline resonators," 2017 47th European Microwave Conference (EuMC), Nuremberg, Germany, 2017, pp. 985-988,

[3] S. Bastioli, C. Tomassoni and R. Sorrentino, "A New Class of Waveguide Dual-Mode Filters Using TM and Nonresonating Modes," in IEEE Transactions on Microwave Theory and Techniques, vol. 58, no. 12, pp. 3909-3917, Dec. 2010, doi: 10.1109/TMTT.2010.2086068.

[4] C. Tomassoni, S. Bastioli and R. Sorrentino, "Generalized TM Dual-Mode Cavity Filters," in IEEE Transactions on Microwave Theory and Techniques, vol. 59, no. 12, pp. 3338-3346, Dec. 2011, doi: 10.1109/TMTT.2011.2172622.

[5] E. López-Oliver et al., "Very High Q-Factor Bandpass Filter Using Additive Manufacturing," 2021 IEEE MTT-S International Microwave Filter Workshop (IMFW), Perugia, Italy, 2021, pp. 243-245.

[6] P. Vallerotonda, L. Pelliccia, F. Cacciamani, C. Tomassoni and O. Bouzekri, "Additive-Manufactured TM01δ Mode Dielectric Resonators for Compact On-Board Wideband Filters," 2023 53rd European Microwave Conference (EuMC), Berlin, Germany, 2023, pp. 388-391,

[7] P. Vallerotonda, F. Cacciamani, L. Pelliccia, C. Tomassoni, G. Cannone and V. T. di Crestvolant, "Compact Ultra-Wideband Cavity Filter Based on Suspended Ceramic Resonators in Additive Manufacturing," 2022 IEEE/MTT-S International Microwave Symposium - IMS 2022, Denver, CO, USA, 2022, pp. 92-95.

979-8-3315-4544-4/26/$31.00 ©2026 IEEE



Karu Esselle, *FRSN, FIEEE, FIEAust*, is Distinguished Professor in Electromagnetic and Antenna Engineering at University of Technology Sydney. A large collection of awards Karu recently received include *Academic Research Team of the Year* (Team Leader) at 2025 Australian Space Awards, 2024 *Premier's Prize* for Leadership in Innovation in New South Wales, Australia's national *2023 Eureka Prize* for Outstanding Science in Safeguarding Australia (Team Leader), Australia's national *2022 Professional Engineer of the Year*, both the most prestigious space award in Australia – the "Winner of Winners" *Excellence Award* – as well as the *Academic of Year* Award at the 2022 Australian Space Awards, 2022 UTS *Chancellor's Medal*, both the *Excellence Award* and the *Academic of the Year* Award at 2021 Australian Defence Industry Awards, and 2019 Motohisa Kanda Award (from IEEE USA) for the most cited paper in *IEEE Transactions on EMC* in the past five years.

Karu is a Fellow of the Royal Society of New South Wales, IEEE and Engineers Australia. He has authored over 750 research publications, and his papers have been cited over 18,000 times. His h-index is 66. Karu is among the top 0.3% of active researchers in the world in the research area of Networking and Telecommunications, according to a career-long research impact analysis published in Elsevier, which considered only actively publishing researchers in this field.

Since 2002, his research income is over 35 million dollars. Karu has provided expert assistance to more than a dozen companies in USA, Europe and Australia. At present, Karu is the Representative of the IEEE Antennas & Propagation Society (AP-S) for all Asia-Pacific countries excluding China and India. From 2018 to 2020, Karu chaired the prestigious Distinguished Lecturer Program Committee of the IEEE AP-S. He has served or is serving in 8 global committees of this IEEE society, including AdCom and Awards. In addition, Karu has been a Senior Editor of *IEEE Access* and has served as an Associate Editor for nearly all major journals in his fields including *IEEE Transactions on Antennas Propagation*, *IEEE Antennas and Propagation Magazine*, *IEEE Access* and *IET MAP*. Previously he was Director of WiMed Research Centre and Associate Dean – Higher Degree Research (HDR) at Macquarie University. He has also served as a member of the Dean's Advisory Council and the Division Executive. Karu is a Director of Innovations for Humanity Pty Ltd. Additional information can be found at https://www.uts.edu.au/staff/karu.esselle and https://en.wikipedia.org/wiki/Karu_Esselle .

Printable Nonlinear Tags and Handheld Devices for Clutter-Resilient Contactless Monitoring and Tracking

Changzhi Li and Leya Zeng
Texas Tech University, USA

This talk presents the development of printable nonlinear passive tags and portable harmonic radar systems for clutter-resilient contactless monitoring and tracking across object localization and biomedical sensing applications. The research integrates compact nonlinear tag design, scalable fabrication strategies, and high-linearity harmonic radar architectures operating at 4–8 GHz and 8–16 GHz. By exploiting second-order harmonic generation from passive diode-based tags, the system selectively detects nonlinear responses while inherently rejecting linear environmental reflections, enabling reliable operation in electromagnetically complex and motion-rich environments.

At the tag level, lightweight, battery-less nonlinear transponders were designed using Schottky diodes embedded within dipole-based and multi-element antenna geometries optimized for harmonic radiation. Early prototypes were fabricated using laser-cut masks and conductive coatings, enabling rapid, low-cost implementation of passive tags capable of meter-scale detection without onboard power. Multi-element configurations increased effective aperture and enhanced harmonic signal strength, significantly improving signal-to-noise ratio. Subsequent implementations advanced toward inkjet-printed and materials-dispensed structures on flexible substrates such as paper and PET, producing compact millimeter-scale tags suitable for conformal attachment to curved surfaces, including the human chest. Full-wave electromagnetic simulations were employed to optimize impedance matching, radiation characteristics, and antenna–diode integration at both fundamental and harmonic frequencies, ensuring efficient nonlinear conversion and stable backscatter performance.

At the system level, two harmonic radar platforms were developed. The 4–8 GHz harmonic radar system transmits a 4 GHz fundamental tone and receives the 8 GHz second harmonic generated by the nonlinear tag. The architecture incorporates frequency multiplication, cascaded filtering, and carefully distributed amplification stages to maintain transmit–receive isolation and suppress harmonic leakage. The 8–16 GHz harmonic radar system follows the same nonlinear detection principle, transmitting at 8 GHz and receiving at 16 GHz. Implemented on a multilayer PCB platform, this configuration employs high-linearity gain stages, low-pass and high-pass filtering networks, and coherent down-conversion to baseband for signal processing. Both systems operate in continuous-wave mode and emphasize spectral purity and harmonic isolation to ensure robust detection of weak nonlinear returns.

For biomedical applications, battery-free wearable tags attached beneath clothing enabled accurate, noninvasive respiratory monitoring with strong agreement with ground-truth measurements, even in the presence of nearby moving subjects and high radar cross-section reflectors. Beyond healthcare, the same nonlinear tagging principle supports lightweight object localization and tracking without onboard power.

Collectively, this presentation establishes a scalable framework that combines printable nonlinear tags with compact harmonic radar devices, enabling selective clutter-resilient detection for healthcare monitoring, asset tracking, search applications, and emerging nonlinear IoT sensing systems.

979-8-3315-4544-4/26/$31.00 ©2026 IEEE

Terminating Magnetostatic Surface Waves with Metallic Patterns

Zequn Zeng
Department of Electrical and Computer Engineering
National University of Singapore
Singapore
zequn.zeng@u.nus.edu

Si-Ping Gao
College of Integrated Circuits
Nanjing University of Aeronautics and Astronautics
Nanjing, China
gao.sp@nuaa.edu.cn

Yong-Xin Guo
Department of Electrical Engineering
City University of Hong Kong
Hong Kong, China
yongxin.guo@cityu.edu.hk

***Abstract*—Magnetostatic surface waves (MSSWs) have been widely utilized in microwave ferrite devices due to their nonreciprocal propagation and ease of excitation. Conventional MSSW-based devices typically employ a single propagation channel. However, as microwave ferrite devices move toward higher integration density and multi-channel operation, unwanted reflections within a single MSSW channel and coupling between adjacent channels can lead to signal interference and performance degradation. Therefore, effective suppression of MSSW reflections and isolation between channels become crucial. In this paper, MSSW termination using metallic patterns is proposed to achieve both reflection suppression and inter-channel isolation. The termination mechanism is analyzed based on the dispersion relation of MSSWs. Bowtie- and zigzag-shaped metallic patterns are introduced to redirect waves and achieve MSSW termination. A test device incorporating two MSSW channels is designed and fabricated for validation. Measurement results confirm that the proposed structures effectively suppress reflections within a channel and reduce coupling between adjacent MSSW channels.**

***Keywords*—Magnetostatic surface waves (MSSWs), microwave ferrite device, metallic pattern, yttrium iron garnet (YIG).**

I. Introduction

Ferrites have attracted considerable attention in microwave device applications [1], [2]. Microwave devices employing ferrites enable the manipulation of RF signals through a tunable magnetic bias, where the ferrite acts as a magnetically tunable dielectric medium [3]. When an electromagnetic (EM) wave propagates in a ferrite material, an interaction between the EM field and the magnetization occurs, allowing the excitation and propagation of magnetostatic waves (MSWs) [4]. MSWs in ferrites can be categorized into magnetostatic surface waves (MSSWs) and magnetostatic volume waves (MSVWs) [5].

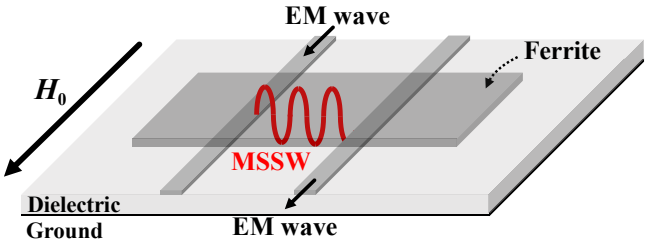


Fig. 1. Illustration of MSSW propagation channel.

Compared with MSVWs, MSSWs are often preferred in microwave ferrite devices due to their inherent nonreciprocity, lower propagation loss, and relatively simple excitation conditions [6]. Various microwave devices utilizing MSSWs have been demonstrated. For example, tunable filters based on MSSWs have achieved low insertion loss and wide tuning ranges [7]. In addition, frequency-selective limiters (FSLs) using MSSW propagation have been demonstrated with low threshold power [8], and nanoscale implementations have also been proposed [9].

Significant efforts have been devoted to improving the transmission efficiency of MSSWs [3]. Conventional MSSW-based devices typically employ a single propagation channel, as illustrated in Fig. 1, consisting of a ferrite film and two microstrip lines underneath that serve as transducers for EM-MSSW conversion and vice versa. In such structures, MSSW reflections within the channel can interfere with the signal. Furthermore, as MSSW-based devices move toward higher integration density and multifunctionality, multiple MSSW channels will be integrated on the same substrate, introducing potential crosstalk between adjacent channels. Therefore, both suppression of MSSW reflections and isolation between channels are crucial. Although MSSW reflections can be suppressed using a 45° ferrite-film edge [10], it requires additional material cutting, while the isolation between adjacent MSSW channels has not yet been investigated in the literature.

In this paper, MSSW termination structures based on metallic patterns are proposed to achieve both reflection suppression and inter-channel isolation. The underlying mechanism is analyzed based on the dispersion characteristics of MSSWs. An yttrium iron garnet (YIG)-based test device incorporating two MSSW channels is designed and fabricated for experimental validation. Measurement results demonstrate the effectiveness of the proposed approach in suppressing MSSW reflections and reducing coupling between adjacent channels.

II. MSSW Termination Mechanism

When a ferrite is saturated under an external magnetic field H_0, all the magnetic moments within the material are aligned with the direction of H_0, allowing for the propagation of

MSSWs. The excitation of MSSWs is commonly done by microwave excitation transducers (see Fig. 1).

The dispersion relation of MSSWs in a dielectric layered structure were reported in [11]:

$$e^{2|k|d} = \left(\frac{\mu_1 - \mu_2 s - 1}{\mu_1 + \mu_2 s + 1}\right)\left(\frac{\mu_1 + \mu_2 s + \tanh(-|k|t)}{\mu_1 - \mu_2 s - \tanh(-|k|t)}\right), \quad (1)$$

where $s = k/|k|$; d is the thickness of ferrite film; t is the dielectric thickness; $\mu_1 = 1 + \omega_0\omega_m/(\omega_0^2 - \omega^2)$; $\mu_2 = \omega\omega_m/(\omega_0^2 - \omega^2)$,where $\omega = 2\pi f$; $\omega_0 = 2\pi\gamma H_0$; $\omega_m = 2\pi\gamma(4\pi M_s)$; f is the frequency of RF signal; M_s is the saturation magnetization; γ is the gyromagnetic ratio. Consequently, when H_0 and ferrite parameters d and M_s are fixed, the MSSW wavenumber k becomes a function of t, which is approximated as the spacing between the ferrite film and the ground plane.

According to EM wave reflection and transmission theory, a boundary between two media with different propagation constants causes reflection due to discontinuity in propagation conditions. This principle also applies to MSSWs, which propagate in transverse-electric (TE) mode [12]. By introducing metallic patterns between adjacent MSSW channels, as illustrated in Fig. 2, t in the metallized region is reduced to nearly zero, leading to a significant change in k. When an MSSW encounters this region, the abrupt change in propagation conditions results in reflection. Bowtie- and zigzag-shaped metallic patterns are adopted to control the reflection direction. Reflections from the 45° edges propagate parallel to the bias field H_0, satisfying the magnetostatic backward volume wave (MSBVW) condition. Since MSBVWs shows strong attenuation within the MSSW band, the reflected waves rapidly decay along the propagation path, thereby suppressing unwanted reflections and achieving MSSW isolation. The same mechanism also applies to suppress MSSW reflections within a single channel using metallic pattern, as illustrated in Fig. 3.

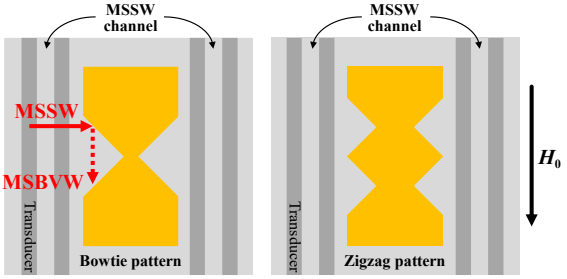


Fig. 2. Patterns of metallic isolation structure.

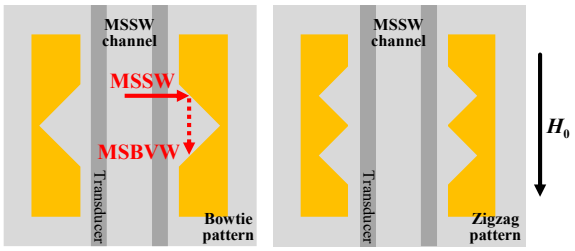


Fig. 3. Metallic patterns for reflection suppression.

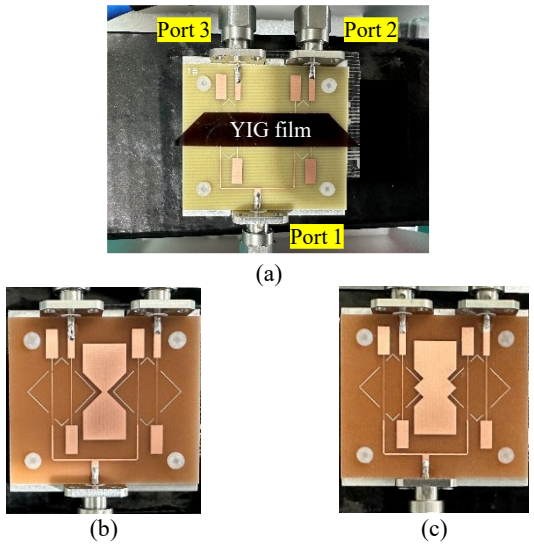


Fig. 4. (a) YIG-based test device with two MSSW channels. (b) Bowtie- and (c) zigzag-shaped isolation patterns.

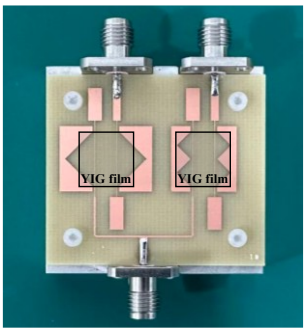


Fig. 5. Test device with two types of reflection suppression patterns.

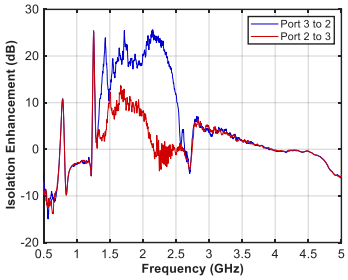
III. Measurement and Validation

To validate the MSSW termination effect of metallic patterns, a YIG-based test device incorporating two MSSW channels was designed and fabricated, as shown in Fig. 4(a). A T-junction power divider was used to split the input RF power into the two channels. For each channel, the transducer termination was optimized using an open-circuit 6×2.5-mm² stub to facilitate efficient MSSW propagation. A trapezoidal YIG film with a top-base length of 30 mm was placed over two pairs of transducers, forming two adjacent MSSW channels. Bowtie- and zigzag-shaped metallic patterns were introduced between the channels, as shown in Fig. 4(b) and Fig. 4(c). Using the same test device configuration, two metallic patterns for MSSW reflection suppression were designed and fabricated, as shown in Fig. 5. Two 10×10-mm² YIG films were placed over the two channels with different reflection-suppression patterns.

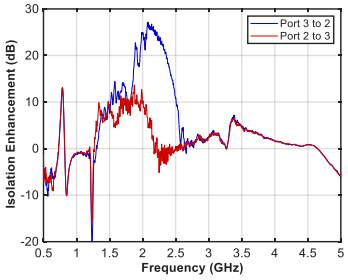
The isolation enhancement between the two MSSW channels was characterized by measuring the transmission between Port 2 and Port 3 and comparing it with the test device without any isolation pattern [see Fig. 4(a)]. The isolation performances of the bowtie- and zigzag-shaped patterns are presented in Fig. 6(a) and Fig. 6(b), respectively. As observed, both patterns improve

the isolation within the MSSW band, and the bowtie-shaped pattern exhibiting a wider isolation bandwidth. The difference between the transmission from Port 3 to Port 2 and from Port 2 to Port 3 indicates the nonreciprocity of MSSW propagation.

The MSSW reflection suppression within a single channel using the bowtie- and zigzag-shaped patterns is shown in Fig. 7(a) and Fig. 7(b), respectively. Compared with the device without any reflection-suppression pattern, both structures effectively reduce MSSW reflections. The bowtie-shaped pattern provides slightly weaker suppression because the pattern does not fully cover the edge of the YIG film, as illustrated in Fig. 5.

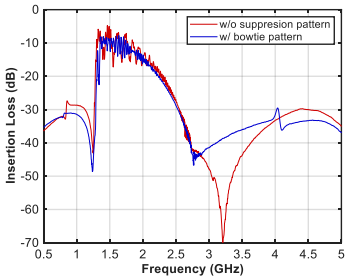


(a)

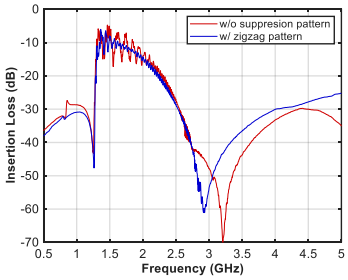


(b)

Fig. 6. Isolation enhancement between two MSSW channels based on (a) bowtie-shaped and (b) zigzag-shaped isolation patterns.



(a)



(b)

Fig. 7. Reflection suppression within a single MSSW channel based on (a) bowtie-shaped and (b) zigzag-shaped isolation patterns.

IV. Conclusion

In this paper, metallic patterns for MSSW isolation and reflection suppression are proposed and experimentally demonstrated. The underlying mechanism is analyzed based on the dispersion characteristics of MSSWs, where the metallized region alters the propagation conditions and induces MSSW reflection. Bowtie- and zigzag-shaped patterns are further introduced to redirect reflected waves and promote rapid attenuation, effectively suppressing unwanted reflections within a channel, and improving inter-channel isolation. A YIG-based test device incorporating two MSSW channels was designed and fabricated for validation. Measurement results confirm that the proposed metallic patterns effectively suppress reflections and reduces coupling between adjacent channels, demonstrating its potential for multi-channel integrated MSSW-based devices.

Acknowledgement

This work is supported by the National Natural Science Foundation of China under Grant 62571234.

References

[1] C. Devitt, R. Wang, S. Tiwari, and S. A. Bhave, “An edge-coupled magnetostatic bandpass filter,” *Nat. Commun.*, vol. 15, no. 1, p. 7764, Sep. 2024.

[2] Z. Zeng, S. -P. Gao and Y. -X. Guo, "Measurement-Based RLGC Extraction for Improving YIG-Based Frequency Selective Limiter Modelling," *2022 IEEE MTT-S International Microwave Workshop Series on Advanced Materials and Processes for RF and THz Applications (IMWS-AMP)*, Guangzhou, China, November 2022, pp. 1-3.

[3] Z. Zeng, S. -P. Gao and Y. Guo, "A Scalable Model for Efficiently Designing Magnetostatic Surface Wave Transmission Lines," *IEEE Trans. Microw. Theory Techn.*, vol. 73, no. 10, pp. 7132-7140, Oct. 2025.

[4] J. Adam, M. Daniel, P. Emtage, and S. Talisa, “Magnetostatic waves,” *Thin Films for Advanced Electronic Devices*, ser. Physics of Thin Films, M. H. Francombe and J. L. Vossen, Eds. Elsevier, 1991, vol. 15, pp. 1–141.

[5] R. Rafii-El-Idrissi, R. Marques, and F. Medina, “Comprehensive analysis of strip- and slot-line guided forward, backward, and complex magnetostatic waves,” *IEEE Trans. Microw. Theory Techn.*, vol. 49, no. 9, pp. 1599–1606, 2001.

[6] Z. Zeng, S. -P. Gao and Y. -X. Guo, "A Novel Design Methodology for MSSW Transmission Lines Without Iteratively Solving Maxwell-Landau-Lifshitz-Gilbert Equation," *2024 IEEE MTT-S International Wireless Symposium (IWS)*, Beijing, China, 2024, pp. 1-3.

[7] G.-M. Yang, J. Wu, J. Lou, M. Liu, and N. X. Sun, “Low-loss magnetically tunable bandpass filters with YIG films,” *IEEE Trans. Magn.*, vol. 49, no. 9, pp. 5063–5068, 2013.

[8] H. Lin, X. Shi, C. Dubs, M. Sanghadasa, and N. Sun, “Compact and passive thin-film frequency-selective limiters,” *IEEE Microw. Wireless Compon. Lett.*, vol. 33, no. 8, pp. 1155–1158, 2023.

[9] K. Dav´ıdkov´a, K. Levchenko, F. Bruckner, R. Verba, F. Majcen, Q. Wang, M. Lindner, C. Dubs, V. Vlaminck, J. Kl´ıma, M. Urb´anek, D. Suess, and A. Chumak, “Nanoscale spinwave frequency-selective limiter for 5G technology,” *Phys. Rev. Appl.*, vol. 23, p. 034026, Mar. 2025.

[10] J. Wu, X. Yang, S. Beguhn, J. Lou, and N. X. Sun, “Nonreciprocal tunable low-loss bandpass filters with ultra-wideband isolation based on magnetostatic surface wave,” *IEEE Trans. Microw. Theory Techn.*, vol. 60, no. 12, pp. 3959–3968, 2012.

[11] W. L. Bongianni, “Magnetostatic propagation in a dielectric layered structure,” *J. Appl. Phys.*, vol. 43, no. 6, pp. 2541–2548, Nov. 1972.

[12] A. Ganguly and D. Webb, “Microstrip excitation of magnetostatic surface waves: Theory and experiment,” *IEEE Trans. Microw. Theory Techn.*, vol. 23, no. 12, pp. 998–1006, 1975.

Ultra-wideband Energy Selective Surface Based on Symmetrical Bow-tie Topology for High-Power Electromagnetic Protection

Tianyu Shi
Nanjing University of Aeronautics and Astronautics
College of Electronic and Engineering
Nanjing, China
sty@nuaa.edu.cn

Shaobin Liu
Nanjing University of Aeronautics and Astronautics
College of Electronic and Engineering
Nanjing, China
lsb@nuaa.edu.cn

Meng Xing
Nanjing University of Aeronautics and Astronautics
College of Electronic and Engineering
Nanjing, China
2207825975@qq.com

***Abstract*—This paper presents an ultra-wideband (UWB) millimeter-wave energy selective surface (ESS) designed for adaptive electromagnetic protection in complex environments. The core innovation lies in the utilization of a symmetrical bow-tie topology that achieves an exceptionally broad transmission window. By loading adaptive GaAs PIN diodes at the center of the resonators, the surface dynamically reconfigures its impedance based on the incident power level. Simulation results demonstrate that the ESS provides a low-insertion-loss (IL < 1 dB) transparent window from 4 GHz to 16.7 GHz. Under high-power microwave (HPM) incidence, the surface provides robust shielding effectiveness (SE) exceeding 10 dB from 4 GHz to 12 GHz. The proposed ESS effectively balances the requirements of wideband communication and high-intensity interference mitigation.**

Keywords—ultra-wideband (UWB), energy selective surface (ESS), electromagnetic protection, PIN diode

I. INTRODUCTION

The rapid evolution of high-speed wireless communication and sophisticated radar systems has led to an increasingly congested electromagnetic environment. In such a landscape, electronic front-ends are frequently exposed to high-power microwave (HPM) pulses, which can originate from intentional interference or co-site high-intensity radiation [1] . These threats can lead to severe performance degradation, signal masking, or even catastrophic thermal failure of sensitive radio-frequency (RF) components. Traditional electromagnetic interference (EMI) mitigation strategies typically rely on frequency-selective surfaces (FSS) or passive limiters. However, conventional FSS structures are inherently static, failing to provide the dynamic adaptability required to distinguish between legitimate low-power signals and hazardous high-power pulses within the same operational frequency band.

Energy Selective Surfaces (ESS) have emerged as a revolutionary implementation of reconfigurable intelligent surface (RIS) technology to address these challenges [2] . By integrating nonlinear components—most notably PIN diodes—into periodic metallic arrays, an ESS can autonomously modulate its surface impedance based on the incident field intensity. In its linear state, the ESS functions as a transparent window with minimal insertion loss, allowing for high-fidelity communication. Conversely, upon sensing a high-intensity electric field that exceeds the diode's threshold, the surface undergoes a rapid nonlinear transition to a low-impedance state, effectively reflecting the incident energy and safeguarding the backend circuitry.

Despite their potential, contemporary ESS designs face a critical "bandwidth-protection" trade-off. Achieving an ultra-wideband (UWB) transparent window while maintaining deep shielding effectiveness across a broad protection band remains a significant engineering hurdle. Most traditional designs utilize narrowband dipole or loop resonators, which limit the operational spectrum and introduce significant phase distortion.

In this work, we propose a novel millimeter-wave UWB ESS utilizing a symmetrical four-arm bow-tie topology. By exploiting the frequency-independent-like characteristics of bow-tie geometries and incorporating them into a third-order filter synthesis, we achieve an unprecedented fractional bandwidth. This research provides a rigorous framework for synthesizing compact, wideband adaptive surfaces capable of surviving in the most intense electromagnetic environments..

II. DESIGN METHODOLOGY AND THEORETICAL FRAMEWORK

A. Design Principle

The fundamental operation of the Energy Selective Surface (ESS) is governed by its power-dependent surface impedance, which allows for an autonomous transition between high-transmissivity and high-reflectivity states. The transmission coefficient S_{21} of the surface can be analytically expressed as [3] :

$$S_{21}=20\lg\left(\frac{E_t}{E_i}\right)=-20\lg\left(1+\frac{Z_0}{2Z_{ESS}}\right) \quad (1)$$

where E_t and E_i represent the transmitted and incident electric field strengths, respectively. Z_0 is the characteristic impedance of free space (377 Ω), and Z_{ESS} denotes the equivalent surface impedance of the structure. To achieve ultra-wideband (UWB) performance, the design must fulfill dual criteria: in the low-power regime, Z_{ESS} must remain sufficiently high to minimize insertion loss across the intended band; conversely, under high-power illumination, the surface impedance must drop to a near-short-circuit state ($Z_{ESS} \approx 0$) to facilitate maximum reflection [4] .

B. Circuit Model Design

To realize the desired UWB response, the ESS is synthesized based on a third-order band-pass filter topology. This design can be accurately represented by an equivalent circuit model (ECM) where each metallic layer and dielectric substrate corresponds to a specific lumped or distributed element. The equivalent circuit diagram is shown in Fig. 1.

979-8-3315-4544-4/26/$31.00 ©2026 IEEE

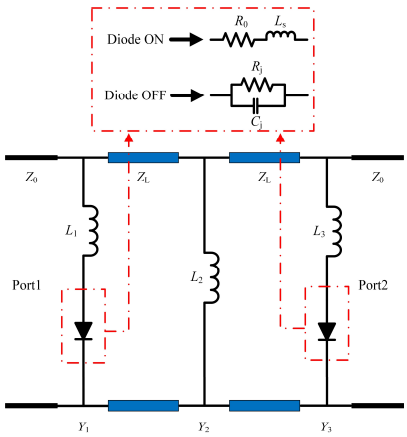


Fig. 1. ECM of third-order filter ESS

The nonlinear behavior of the surface is determined by the state of the integrated PIN diodes. In the low-power state (OFF), the diode is modeled as a parallel combination of a high cut-off resistance R_j and a minute junction capacitance C_j. In the high-power state (ON), it transitions into a series connection of a low forward resistance R_{on} and a parasitic inductance L_s [5]. The total transmission response is the result of the cascaded *ABCD* matrix interaction of these components .

$$M_{total} = M_{Y1} \cdot M_{line\,1} \cdot M_{Y2} \cdot M_{line\,2} \; M_{Y3} \qquad (2)$$

where $M_{Y1,3}$ represent the admittance of the top and bottom bow-tie layers, and M_{line} represents the dielectric substrates.

By optimizing the coupling between these stages, a three-pole Butterworth-like response is synthesized to cover the ultra-wide band spectrum [6] .

C. Unit Structure Design

The physical realization of the ESS unit cell utilizes a triple-metallic-layer configuration separated by two layers of dielectric substrate, as illustrated in Fig. 2. The structural parameters are meticulously optimized to align with the theoretical ECM requirements for ultra-wideband (UWB) performance [7] [8] .

Symmetrical Bow-tie Layers (Top and Bottom): These two layers employ a four-arm symmetrical bow-tie topology. The selection of this specific geometry is predicated on its inherently low quality factor (*Q*), which, compared to conventional narrowband resonators, facilitates a flatter impedance response across a broad spectrum, thereby supporting the ultra-wideband (UWB) transmission window. The periodic side length of the unit cell is denoted by *p*. The geometric parameters of the symmetrical arms are defined as follows: the base length is represented by *a* with a width of *b*; the neck width is denoted by *c*; and the internal aperture edges are characterized by a maximum width of *d* and a minimum width of *e*. To regulate the operational state of the periodic array, MACOM mest2g-10-20 PIN diodes are integrated at the central gaps of these resonant structures [9] .

Inductive Middle Layer: The intermediate metallic layer is composed of an "asterisk-shaped" patch featuring four central via-holes. This layer functions as the central shunt inductor (Y_2) within the third-order filter synthesis, providing the requisite phase compensation and mutual inductance to flatten the

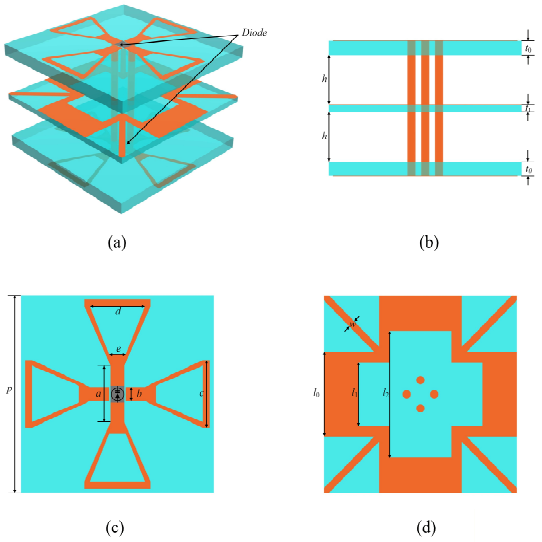


Fig. 2. ESS unit structure: (a) 3D view(b) Side view (c) Top/bottom layer (d) Middle layer

TABLE I. OPTIMIZED STRUCTURE PARAMETERS

Parameter	p	a	b	c	d	e	l_0
Value (mm)	14	4	1	4.8	4	1.2	6
Parameter	l_1	l_2	w	h	t_0	t_1	
Value (mm)	4.5	9	0.5	4	1	0.5	

passband across the X and Ku bands. The wide cross-patch component is defined by its outer width l0 and the side lengths of the central rectangular region, l_1 and l_2, while the width of the narrow diagonal patches is denoted by *w*. The via-holes, which electrically connect the top and bottom layers, effectively enhance the interlayer coupling.

Substrate Configuration: The 3D and side views show that the ESS is composed of three layers separated by two air gaps, each with a thickness of *h*. The dielectric substrates for the top and bottom layers have a thickness of t_0, while the intermediate substrate layer is characterized by a thickness of t_1. All substrate layers are composed of F4B material with a relative permittivity (ε_r) of 2.2. This multi-layered stack functions as an impedance matching network, strategically employed to further enhance the transparency and minimize the insertion loss of the ultra-wideband (UWB) window. The optimized structural parameters are summarized in Table I.

III. ESS CELL MODEL SIMULATION AND ANALYSIS

A. Low-Power Transmission State

Under the low-power incidence state, the ESS operates in its linear transparent mode. The PIN diodes remain in the high-impedance OFF state, represented in the equivalent circuit by the junction capacitance C_j. As illustrated in the simulation results (Fig. 3), the proposed ESS exhibits a stable and exceptionally wide passband. The insertion loss (IL) remains below 1 dB across the ultra-wide frequency range of 4 GHz to 16.7 GHz. This ultra-wideband transparency is achieved through the synergy of the low-*Q* symmetrical bow-tie topology and the third-order filter synthesis. The multi-layered dielectric stack, consisting of F4B substrates and air gaps, serves as a gradient impedance matching network that

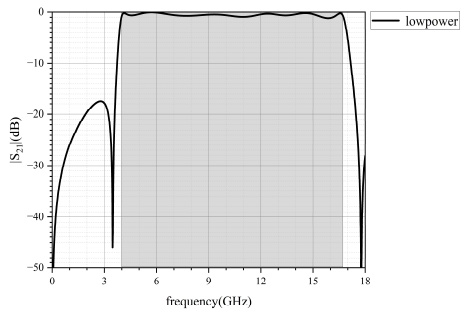


Fig. 3. Simulated transmission coefficient in the low-power state

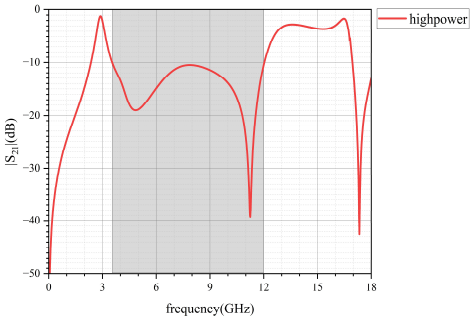


Fig. 4. Simulated shielding effectiveness in the high-power state

effectively suppresses out-of-band reflections and maintains a flat transmission profile across the X and Ku bands.

B. High-Power Shielding State

Upon the incidence of high-power microwave (HPM) signals, the ESS autonomously transitions into its nonlinear shielding mode. The elevated electric field intensity triggers the PIN diodes into the low-impedance ON state. This transition fundamentally reconfigures the surface impedance, converting the inductive-capacitive resonant network into a reflective inductive grid.

Notably, the proposed Energy Selective Surface (ESS) demonstrates a broad operational protection band. Simulation results indicate that the shielding effectiveness (SE) remains above 10 dB across the frequency range of 4 GHz to 12 GHz, achieving a fractional bandwidth of 100%. This wideband suppression capability effectively mitigates the risks posed by cross-band high-power electromagnetic pulse interference. Furthermore, at the resonance frequency of 11.2 GHz, the shielding depth reaches 39 dB, illustrating an exceptionally strong energy attenuation effect that ensures the survivability of backend electronic systems under intense field environments.

C. Discussion on Performance and Robustness

The simulated performance indicates a significant advancement in the fractional bandwidth of energy selective surfaces. By replacing traditional narrow-band dipoles with symmetrical bow-tie resonators, the design achieves a relative bandwidth exceeding 120% in the transparent state

.Furthermore, the integration of the asterisk-shaped middle layer with central via-holes ensures strong interlayer coupling, which stabilizes the transmission window and enhances the shielding depth in the high-frequency region. While providing an immediate, high-decibel safety margin when subjected to intentional or accidental high-power interference.

IV. Conclusion

In this research, a high-performance millimeter-wave energy selective surface has been synthesized using a symmetrical bow-tie topology and high-performance GaAs PIN diodes. By integrating the frequency-independent-like characteristics of bow-tie resonators with a third-order filter circuit model, the surface achieves a seamless 4–16.7 GHz transparent window in its linear state. Upon high-power excitation, the ESS demonstrates a rapid impedance reconstruction, providing a robust protection band across 4–12 GHz with a peak shielding effectiveness of 39 dB at 11.2 GHz. The fractional protection bandwidth of 100% marks a significant advancement over traditional narrowband designs.

Future work will focus on further extending the operational protection bandwidth to cover higher millimeter-wave frequencies. Research will explore the optimization of gradient dielectric layers and the implementation of fractal-based unit cell designs to enhance phase matching and suppression depth across an even wider spectral range.

References

[1] T. Shi, S. Liu, S. Tang, and Y. Liu, "Millimeter-wave ultra-wideband energy selective surface for 5G communications protection," 2025 IEEE MTT-S International Microwave Workshop Series On Advanced Materials and Processes for RF and THz Applications (IMWS-AMP), Wuxi, China, 2025, pp. 1-3.

[2] Z. Wu, Y. Xu, P. Liu, T. Tian, and M. Lin, "An ultra-broadband energy selective surface design method: From filter circuits to metamaterials," IEEE Trans. Antennas Propag., vol. 71, no. 7, pp. 5865–5873, July 2023.

[3] N. Hu et al., "Design of ultrawideband energy-selective surface for high-power microwave protection," IEEE Antennas Wireless Propag. Lett., vol. 18, no. 4, pp. 669–673, Apr. 2019.

[4] T. Zhou, P. Liu, C. Liu, H. Jiang, and T. Tian, "Multilayer energy selective surface with wide operational band and high shielding effectiveness based on second-order filter," IEEE Trans. Electromagn. Compat., vol. 67, no. 1, pp. 337–340, Feb. 2025.

[5] L. Zhou, L. Liu, and Z. Shen, "High-performance energy selective surface based on the double-resonance concept," IEEE Trans. Antennas Propag., vol. 69, no. 11, pp. 7658–7666, Nov. 2021.

[6] J. Zhang, M. Lin, Z. Wu, L. Ding, L. Bian, and P. Liu, "Energy selective surface with power-dependent transmission coefficient for high-power microwave protection in waveguide," IEEE Trans. Antennas Propag., vol. 67, no. 4, pp. 2494–2502, Apr. 2019..

[7] S. Zhong, M. Chen, G. Xu, and Y. Chen, "Dual-band energy-selective surface with enhanced independence based on two-layer diode-loaded FSS," IEEE Trans. Antennas Propag., vol. 72, no. 6, pp. 5011–5020, June 2024.

[8] C. Yang, P. G. Liu, and X.-J. Huang, "A novel method of energy selective surface for adaptive HPM/EMP protection," IEEE Antennas Wireless Propag. Lett., vol. 12, pp. 112–115, Jan. 2013.

[9] C. Zhang et al., "Millimeter-wave large-angle dual-polarization reconfigurable intelligent surface for 6G communication relay," IEEE Antennas Wireless Propag. Lett., vol. 23, no. 10, pp. 2900–2904, Oct. 2024.

[10] X. Mo, L. Gui, K. Ying, X. Sang, and X. Diao, "Reconfigurable intelligent surface deployment for wideband millimeter wave systems," IEEE Trans. Commun., vol. 72, no. 5, pp. 2989–3004, May 202

Reflection-Type TTD Phase Shifter Based on Propagation-Controlled Reflective Loading

Yang Xu
University of Technology Sydney
Sydney, Australia

He Zhu
Commonwealth Scientific and Industrial Research Organisation (CSIRO)
Sydney, Australia

Yang Yang
University of Technology Sydney
Sydney, Australia

Phase shifters are key building blocks in modern phased-array systems for 5G/6G wireless communications and radar applications [1]–[2]. Among various implementations, reflection-type phase shifters (RTPS) are widely adopted due to their compact size, large achievable phase range, and relatively simple structure. As discussed in prior studies [2], such reactive phase shifters inherently exhibit nonlinear phase–frequency characteristics and therefore cannot realize true time-delay (TTD) behavior, leading to beam squint in wideband phased-array systems. To overcome this limitation, TTD phase shifters have been developed to provide a frequency-linear phase response, thereby eliminating beam squint. Among these, switched-line type TTD phase shifters achieve TTD operation by directly controlling the propagation delay through discrete transmission-line segments. Although such structures effectively mitigate beam squint, they typically suffer from large footprint and increased insertion loss due to long transmission paths and switching networks.

In this work, a reflection-type true time-delay phase shifter (RT-TTD PS) is proposed, combining the compactness of RTPS with the linear phase characteristic of switched-line TTD structures. The schematic is shown in Fig. 1(a), where a 3-dB hybrid coupler is employed, and the reflective loads connected to the coupled and through ports are implemented using reconfigurable short-circuited transmission lines with switchable electrical lengths. Unlike conventional RTPS designs that change reactance values, the proposed architecture modifies the effective propagation length of the reflective transmission line. According to the operating principle of RTPS [3], the reflection phase ϕ can be expressed as:

$$\phi(\omega) = \angle\Gamma(\omega) = -\frac{\pi}{2} - 2arctan(\frac{X(\omega)}{Z_0}) \qquad (1)$$

where Z_0 is the characteristic impedance of the total system. When the load is implemented as a shorted transmission line with electrical length βl, the reactive load $X(\omega)$ is $jZ_0\tan(\beta l)$, thus $\phi(\omega)$ can be expressed with βl, and group delay τ can be expressed as:

$$\tau = -\frac{d\phi}{d\omega} = \frac{2l}{v_p} \qquad (2)$$

where v_p denotes the phase velocity of the transmission line. The reflection phase thus exhibits a strictly linear dependence on frequency, yielding a frequency-linear phase response and thus a constant group delay τ.

The derived formulation confirms that the proposed structure satisfies the fundamental condition for TTD operation. Broadband simulations across 3–8 GHz demonstrate a total phase range exceeding 360° at 8 GHz and a group delay variation within 20 ps, validating the wideband TTD behavior of the proposed architecture. The simulated insertion loss remains below 0.3 dB and the return loss exceeds 10 dB across the entire band. Furthermore, owing to the reflection-type configuration, the propagation path is traversed twice, resulting in a more compact footprint compared to conventional switched-line TTD implementations.

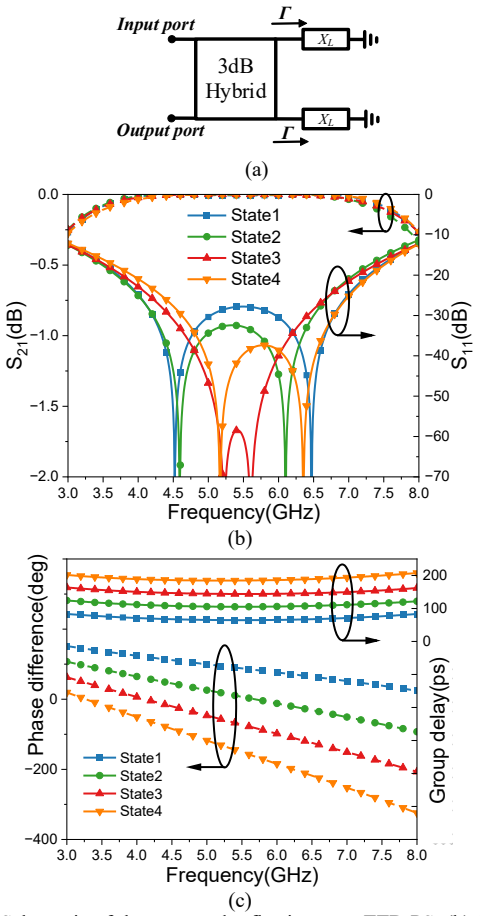


Fig. 1 (a) Schematic of the proposed reflection-type TTD PS. (b) Simulated S-parameters (S11 and S21) across 3–8 GHz. (c) Simulated phase difference and group delay of the proposed RT-TTD PS.

[1] T. K. Ho, Y. Yang, F. Zhu and N. C. Karmakar, "A Novel and Simplified Topology for Vector-Sum Phase Shifters," *2023 IEEE International Symposium on Radio-Frequency Integration Technology (RFIT), Cairns, Australia*, 2023, pp. 56-59.

[2] F. Lin and H. Deng, "Continuously Tunable True-Time-Delay Phase Shifter Based on Transmission Lines With Simultaneously Reconfigurable Impedance and Phase Constant," *IEEE Trans. Microw. Theory Techn.*, vol. 67, no. 12, pp. 4714-4723.

[3] H. Zhu, Y. Xu, T. Zhang, J. Du and Y. Jay Guo, "Reconfigurable Generalized Joined Coupler Matrices for Independent Control of Multiple Steerable Beams," *IEEE Trans. Antennas Propag.*, vol. 73, no. 3, pp. 1573-1584.

979-8-3315-4544-4/26/$31.00 ©2026 IEEE

A Wideband Ultra-Large-Angle Dual-Polarized Bandpass Frequency Selective Surface

Jiaxin Wang
School of Electronic and Information Engineering
South China University of Technology,
Guangzhou, China
wangjiaxinscut@163.com

Xin Xiu
School of Optical and Electronic Information
Nanjing University of Posts and Telecommunications
Nanjing, China
xiuxin33@126.com

Ye Han
School of Optical and Electronic Information
Nanjing University of Posts and Telecommunications
Nanjing, China
hanye_xa@163.com

Bao Wang
Innovation Center for Electromagnetic Functional Structure
AVIC Research Institute for Special Structures of Aeronautical Composites,
Jinan, China
15008473703@163.com

Mengzhu Yan
School of Electronic and Information Engineering
South China University of Technology,
Guangzhou, China
yanmengzhu526@163.com

Wenquan Che
School of Electronic and Information Engineering
South China University of Technology,
Guangzhou, China
eewqche@scut.edu.cn

***Abstract*—This work proposes a wideband dual-polarized bandpass frequency selective surface (FSS) with ultra-large-angle stability for application scenarios under large-angle incidence. To overcome the inherent TE-TM wave impedance mismatch at large incident angles, a polarization-decoupling design methodology is employed. Based on this strategy, individual TE- and TM-polarized FSSs are developed, featuring stable wideband performance across 0–75° incidence and low cross-polarization interference. The desired dual-polarized FSS is then obtained by orthogonally combining the two types of FSSs, and further dimensional adjustment ensures an excellent polarization consistency in both transmission magnitude and phase. Simulation results show that across 45–75° incidence, the proposed FSS achieves a dual-polarization −3-dB passband of 7–13 GHz (60%), with a transmission phase difference of less than 25° between TE and TM polarizations. These simulations effectively validate the feasibility and superiority of the proposed design strategy.**

Keywords—Frequency selective surface (FSS), wideband, ultra-large-angle incidence, polarization consistency.

I. Introduction

Frequency selective surfaces (FSSs) are periodic structures that provide spatial filtering responses for electromagnetic (EM) waves, which are widely used in wireless communication and radar systems [1]. In recent years, many studies have focused on bandwidth and selectivity enhancement of FSS, but most for scenarios with small incident angles ($\theta_i < 60°$). In the scenarios that involve large-angle incidence ($\theta_i > 60°$), such as aircraft nose radome [2], the significant divergence in wave impedance leads to severe impedance mismatch under TE and TM polarizations, as shown in Fig. 1, thus limiting practical applications of existing FSS.

To improve the angular stability of FSSs, reducing the unit cell period [3] is a common method. This can effectively suppress grating lobes and stabilize resonant frequencies but typically provides first-order responses and exhibits angular dependence in quality factors. Loading matching layers on both sides of the FSS can also improve the FSS angular stability, but at the cost of increasing the overall profile [4]. Recently, effective medium theory has also been employed to achieve the angular stability of FSS. By adjusting the equivalent EM parameters, the perfect matching conditions can theoretically be satisfied across the whole angular domain [5]. However, FSSs designed based on this concept usually suffer from mutual constraints among bandwidth, stable angular range, and dual-polarization performance [6]. In summary, the FSS performance using existing methods is limited when the incident angle exceeds 60°.

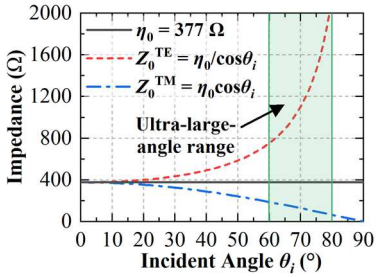


Fig. 1. TE- and TM-polarized wave impedances in free space versus incidence angle θ_i.

To address this limitation, this work presents a wideband ultra-large-angle dual-polarized FSS. First, a polarization-decoupling strategy is introduced to overcome the TE-TM wave impedance divergence at large angles, enabling effective matching for dual-polarization filtering performance. Then, aided by the angle insensitivity of dipoles and split-ring resonators (SRRs), TE- and TM-polarized FSSs with wide bandwidth, high selectivity, and good stopband suppression across 0–75° incidence are achieved. Next, by orthogonally combining the two types of FSS, the final dual-polarized FSS is obtained, whose response is highly similar to that of the corresponding single-polarized FSSs. Besides, excellent polarization consistency in transmission magnitude and phase within an ultra-large-angle range of 45–75° is also achieved, superior to previously reported FSSs with conventional methods.

II. Design and Analysis of the Wideband Ultra-Large-Angle Dual-Polarized Bandpass FSS

The proposed wideband ultra-wide-angle dual-polarized bandpass FSS is shown in Fig. 2(a). To address the impedance divergence between TE- and TM-polarized waves, a polarization-decoupling strategy is employed. Based on this strategy, the wideband TE- and TM-polarized FSSs with ultra-large-angle stability are first designed with extremely low

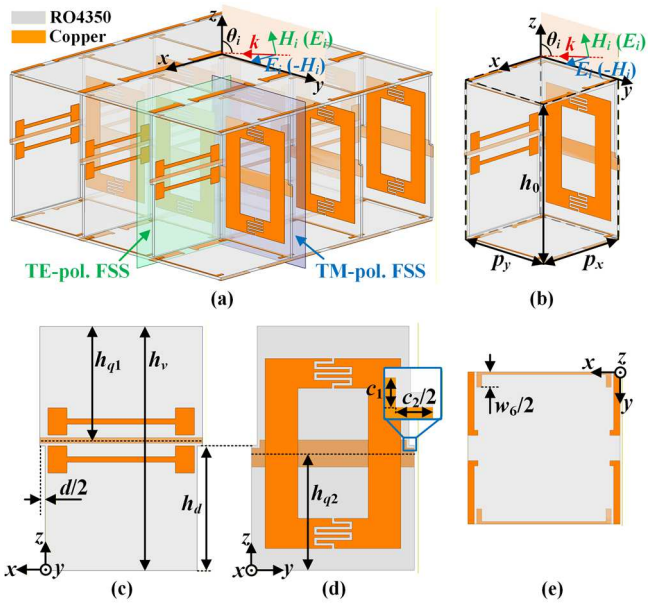


Fig. 2. Proposed dual-polarized FSS. (a) Periodic structure. (b) Perspective view, (c) view onto xoz-plane, (d) view onto yoz-plane, and (e) top view of the unit cell. (p_x = 6mm, p_y = 6mm, h_v = 9mm, h_d = 4.6 mm, d = 0.4 mm, h_{q1} = 4.1 mm, h_{q2} = 4.3 mm, c_1 = 0.3 mm, c_2 = 0.6 mm, w_6 = 1.1mm.)

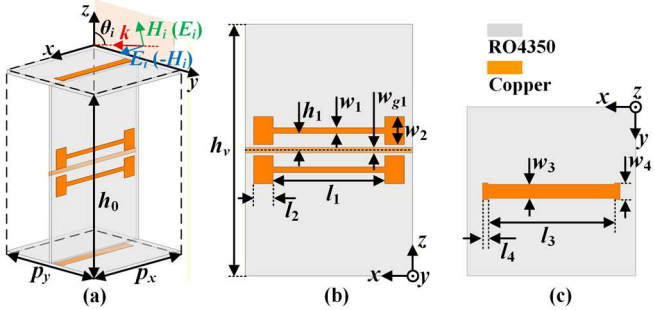


Fig. 3. Unit cell geometry of the TE-polarized FSS. (a) Perspective view. (b) Front view. (c) Top view. (p_x = 6mm, p_y = 6mm, h_v = 9mm, h_1 = 0.6mm, l_1 = 4mm, l_2 = 0.7mm, w_1 = 0.2mm, w_2 = 1mm, w_{g1} = 0.2mm, l_3 = 4.6mm, l_4 = 0.2mm, w_3 = 0.5mm, w_4 = 0.6mm.)

cross-polarization interference. Then, the two structures are combined in an orthogonal arrangement to obtain the desired dual-polarized response.

A. Wideband Ultra-Large-Angle TE-Polarized FSS

The unit cell configuration of the proposed wideband ultra-large-angle TE-polarized FSS is shown in Fig. 3, under the EM wave illumination from *yoz*-plane at an angle θ_i. The FSS consists of two horizontal substrates and a vertical substrate sandwiched between them. The major structure is a symmetrically arranged dipole pair and a backing metal strip, both printed on the vertical substrate, forming a second-order bandpass FSS. Since the dipoles and the strip respond only to the electric field parallel to *x*-axis, and the electric field of the TE-polarized wave remains parallel to the *x*-axis across different incident angles, the resonant frequency of the second-order FSS exhibits good angular stability. Furthermore, to overcome the severe passband ripple at large incident angles under TE polarization, an additional symmetric dipole pair is introduced and printed on the two horizontal substrates. All metallic patterns are fabricated on the 0.168-mm RO4350 substrate (ε_r = 3.66, tanδ = 0.0037), and the unit cell period is 6 mm×6 mm ($0.2\lambda_0 \times 0.2\lambda_0$).

Fig. 4 displays the simulated TE-polarized S-parameters of the second-order and the complete FSS at 70° incidence.

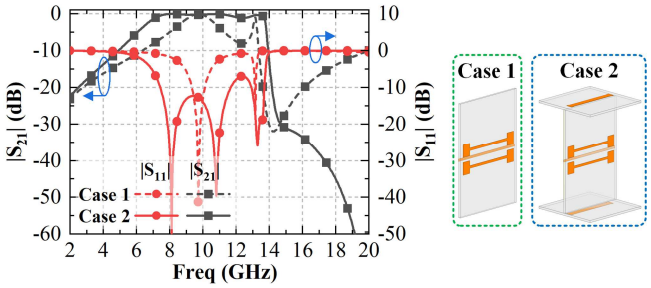


Fig. 4. Simulated S-parameters of the TE-polarized second-order and complete FSS at 70° incidence for TE polarization.

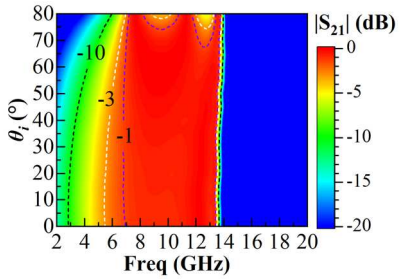


Fig. 5. Simulated transmission coefficient of the complete TE-polarized FSS varying with the frequency and incident angle.

Compared with the second-order FSS, the complete FSS introduces another two transmission poles via the added dipole pair, thereby reducing the passband ripple and achieving a wide 1-dB passband covering 7–13 GHz. Fig. 5 further illustrates the angular stability of the complete FSS. A suppression exceeding 20 dB is achieved from 14 GHz to 20 GHz, along with a sharp roll-off at the upper band edge. In the passband, ripples become noticeable at angles larger than 75°; nevertheless, a −3 dB passband of 7.2–13.3 GHz is maintained across 0–75°.

B. Wideband Ultra-Large-Angle TM-Polarized FSS

The unit cell configuration of the proposed TM-polarized FSS is shown in Fig. 6, which also consists of two horizontal and one vertical substrates. Differently, an SRR is adopted, and interdigital structures are incorporated into the SRR to increase the capacitance. The SRR can be regarded as a magnetic resonator, which is always perpendicular to the magnetic field direction (*x*-axis) of TM-polarized waves, thus enhancing the stability of the resonant frequency under TM polarization. The combination of the SRR and the backing metal strip forms an FSS with lower band-edge selectivity. Besides, a pair of dipoles is loaded on the horizontal substrates to improve the selectivity at the upper band edge. Moreover, the used substrate, overall profile (h_0), and unit cell period (p_x and p_y) are all the same as those of the TE-polarized FSS, thus facilitating integration for dual-polarization operation.

Fig. 7 compares the simulated S-parameters of the TM-polarized FSS with and without the dipole pair. Besides the transmission zero at lower frequency, the added dipole pair enhances the selectivity and stopband suppression at upper frequencies. Meanwhile, the passband is slightly extended to about 7–13 GHz. Fig. 8 shows the angular stability of the TM-polarized FSS. A sharp roll-off with a stable lower-stopband suppression exceeding 10 dB is observed across 0–80° incidence. Though the upper band edge shifts upward with increasing θ_i due to the angular dispersion of the dipoles, a −3 dB passband spanning 7–12.3 GHz over the 0–80° angular range is still obtained, along with stable upper stopband suppression.

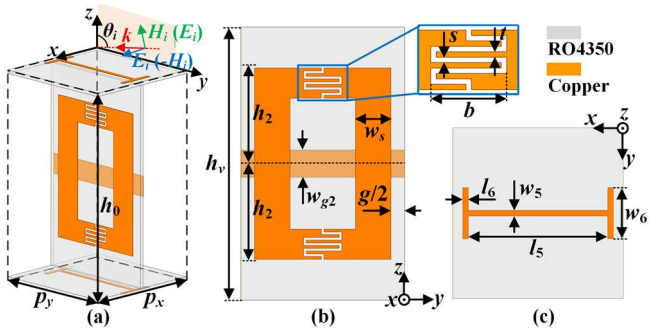


Fig. 6. Unit cell geometry of the TM-polarized FSS. (a) Perspective view. (b) Front view. (c) Top view. (p_x = 6 mm, p_y = 6 mm, h_v = 9 mm, h_2 = 3.5 mm, w_s = 1.3 mm, g = 1 mm, s = 0.1 mm, t = 0.1 mm, b = 1.4 mm, w_{g2} = 1 mm, l_5 = 4.9 mm, l_6 = 0.2 mm, w_5 = 0.2 mm, w_6 = 1.8 mm).

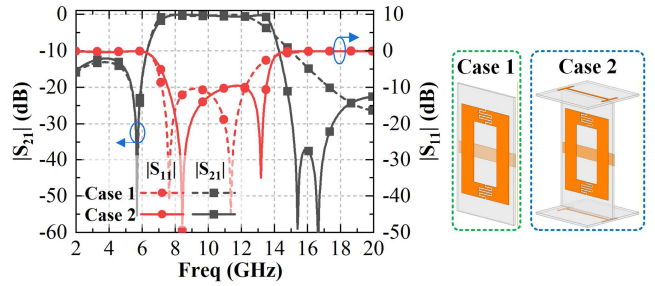


Fig. 7. Simulated S-parameters of the TM-polarized FSS with and without the dipole pair at 70° incidence for TM polarization.

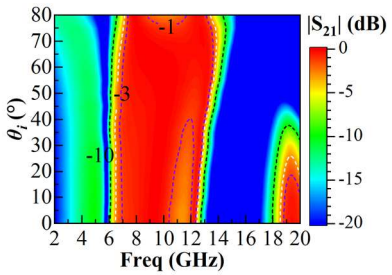


Fig. 8. Simulated transmission coefficient of the complete TM-polarized FSS varying with the frequency and incident angle.

C. *Wideband Ultra-Large-Angle Dual-Polarized FSS*

Based on the polarization-decoupling design approach, the two kinds of FSS are orthogonally combined to achieve dual-polarized spatial filtering at large angles. Fig. 2(b) shows the unit cell of the resulting FSS. As shown in Fig. 2(c) and (d), interlocking slots are etched into the substrates to facilitate assembly, accompanied by some minor adjustments of the metallic patterns to avoid the electrical connection. Furthermore, the interference between orthogonal dipoles on the horizontal substrate enhances the capacitive effect. Therefore, the dipoles of the TE-polarized FSS are shifted by half a period along y-axis, and w_6 is reduced to 1.1 mm.

Fig. 9 shows the frequency-angle transmission responses of the FSS under TE and TM polarization. As shown in Fig. 9(a), over a wide angular range of 45–75°, the FSS achieves an overlapping −3 dB-passband covering 7.0–13.0 GHz (60%) for both polarizations. Across the same angular range, the FSS maintains good stopband suppression and frequency selectivity under dual polarization: suppression exceeds 18 dB from 14.5 GHz to 20 GHz and is greater than 10 dB below 3.5 GHz. The high similarity between the results in Fig. 9(a) and those in Figs. 5 and 8 verifies the low cross-polarization interference. Moreover, Fig. 9(b) indicates that the transmission phase also shows good polarization

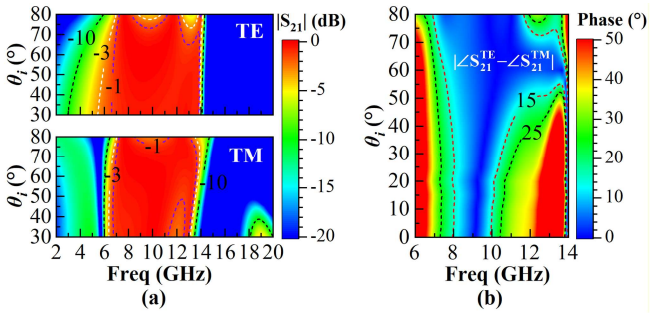


Fig. 9. Simulated transmission (a) magnitude and (b) phase difference of the dual-polarized FSS varying with the frequency and incident angle.

consistency. Within the passband, the TE-TM transmission phase difference ($|\angle S_{21}^{TE} - \angle S_{21}^{TM}|$) is less than 25° across 45–75° incidence, and less than 15° within 50–70°. The TE-TM phase difference degrades at small incident angles, but it remains below 25° over 7.2–10.5 GHz across 0–80°. Notably, although this work focuses on the performance under ultra-large-angle incidence, the target angular range can be flexibly adjusted only via parameter optimization.

III. Conclusion

In this work, a wideband ultra-large-angle dual-polarized FSS is proposed. First, the polarization-decoupling strategy is adopted to address the divergence of the dual-polarization wave impedance. Then, wideband angle-stable TE- and TM-polarized FSSs are respectively achieved, benefiting from the stability of dipoles and SRRs. Finally, the dual-polarized FSS is obtained by orthogonally combining the two FSSs with some dimensional adjustment, featuring excellent polarization consistency in transmission magnitude and phase. Compared with the reported works, the proposed FSS exhibits obvious advantages in bandwidth, selectivity, and polarization consistency under large-angle incidence, indicating its great potential for applications involving large-angle incidence. Due to the time limitation, the fabrication and measurement of the proposed FSS will be presented in future work.

Acknowledgment

This work was partly supported by Research Institute for Special Structures of Aeronautical Composites, AVIC, and the National Natural Science Foundation of China (62321002).

References

[1] B. A. Munk, *Frequency Selective Surfaces: Theory and Design*. Hoboken, NJ, USA: Wiley, 2000.

[2] X. Sheng, Y. Zhang, R. Shen, and N. Liu, "A Cylindrical Equivalent Source-Based Physical Optics Method for Rapid Analysis of Airborne Radomes," *IEEE Access*, vol. 10, pp. 99282–99289, 2022.

[3] T. Li et al., "A novel miniaturized strong-coupled FSS structure with excellent angular stability," IEEE Trans. Electromagn. Compat., vol. 63, no. 1, pp. 38–45, Feb. 2021.

[4] J. Ni et al., "A Fifth-Order X-Band Frequency-Selective Surface With High Selectivity and Angular Stability Based on 3-D Coupling Slot," *IEEE Trans. Antennas Propag.*, vol. 72, no. 7, pp. 5743–5753, Jul. 2024.

[5] Z. S. Sacks, D. M. Kingsland, R. Lee, and Jin-Fa Lee, "A perfectly matched anisotropic absorber for use as an absorbing boundary condition," *IEEE Trans. Antennas Propag.*, vol. 43, no. 12, pp. 1460–1463, Dec. 1995.

[6] Q. Lv et al., "Ultrawide-angle ultralow-reflection phenomenon for transverse electric mode in anisotropic metasurface," Adv. Opt. Mater., vol. 10, no. 12, Jun. 2022, Art. no. 2102400.

Design of 3-D Frequency Selective Surface Based on Spatial Coupling

Jun Ma
School of Electronic and Information Engineering
South China University of Technology
Guangzhou, China
eejma@mail.scut.edu.cn

Kairan Xiang
School of Electronic and Information Engineering
South China University of Technology
Guangzhou, China
eekrxiang@scut.edu.cn

Zhihong Tu
School of Electronic and Information Engineering
South China University of Technology
Guangzhou, China
zhtu@scut.edu.cn

Fuchang Chen
School of Electronic and Information Engineering
South China University of Technology
Guangzhou, China
chenfuchang@scut.edu.cn

***Abstract*—In this paper, spatial coupling is introduced in the design of a three-dimensional (3-D) bandpass frequency selective surface (FSS). The 3-D configuration naturally establishes additional spatial coupling paths among the ports and resonators. As a result, both the source and load are coupled to each resonator as well as to each other, allowing an *N*-th-order FSS to generate *N* transmission zeros (TZs). This behavior enhances the TZ generation capability compared with conventional filter synthesis theory. To demonstrate this concept, a third-order 3-D FSS is designed, which exhibits three TZs. The resonant elements are realized using microstrip resonators, leading to a compact implementation with structural simplicity. The simulated results confirm the feasibility of incorporating spatial coupling into the design of 3-D bandpass FSSs.**

Keywords—3-D FSS, high selectivity, spatial coupling, transmission zero.

I. Introduction

Frequency selective surface (FSS) has long been employed as spatial filtering structures, finding applications in radomes[1], electromagnetic shielding[2], absorbers[3], and so on. An FSS typically consists of periodically arranged unit cells in specific geometric configurations. In order to achieve enhanced frequency selectivity and out-of-band suppression, high-order responses are commonly achieved by cascading multiple single-layer FSSs[4-7]. In [4], meandering square slot resonators were utilized to realize a third-layer FSS. In [7], two metallic cross patterns and a metallic slot coupling aperture were introduced to design a FSS with two transmission zeros (TZs). Another strategy is based on antenna-filter-antenna [8] or filtenna-filtenna configurations [9]. By integrating filtering response in a receive–transmit antenna unit cell, the design of FSSs can be changed to design of filtering antennas with radiation nulls. This method features a simple design process and enhances adjustability in TZs position configuration.

Moreover, three-dimensional (3-D) FSSs have attracted increasing attention due to the additional design freedom enabled by their unique spatial configurations[10-13]. Vertically cascaded slotline structures[10] and square coaxial waveguide[11] have been reported to realize bandpass FSSs with multiple TZs. Introducing extra coupling paths through spatial arrangements makes the interactions between the source, load and resonators more complex, offering new possibilities for TZ generation without increasing structural complexity.

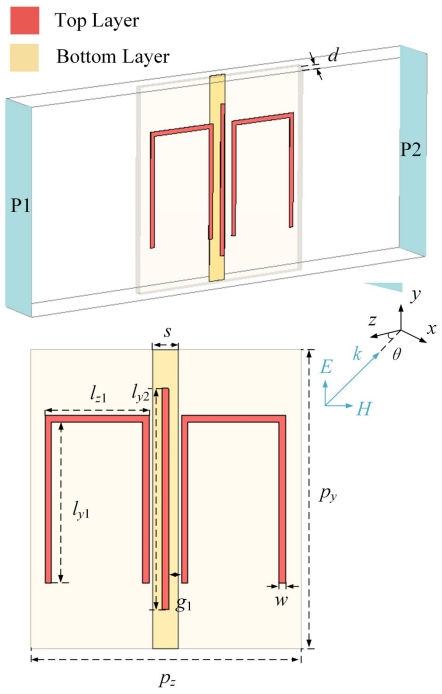


Fig. 1. Structure of the third-order 3-D FSS. (g_1=1.0, l_{y1}=12.8, l_{y2}=16.9, l_{z1}=8.0, w=0.5, s=2.0, d=5.0, p_y=22.8, p_z=21.0) Unit:mm.

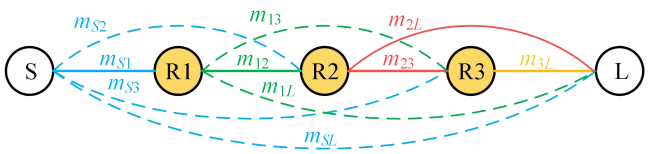


Fig. 2. Topology of the third-order 3-D FSS.

Motivated by this observation, this paper utilize the spatial coupling in the design of 3-D bandpass FSSs. It is shown that by properly arranging the coupling paths in a third-order FSS, three TZs can be generated. A compact 3-D FSS prototype is developed to demonstrate the feasibility of this approach, and the corresponding operating mechanism is analyzed in detail.

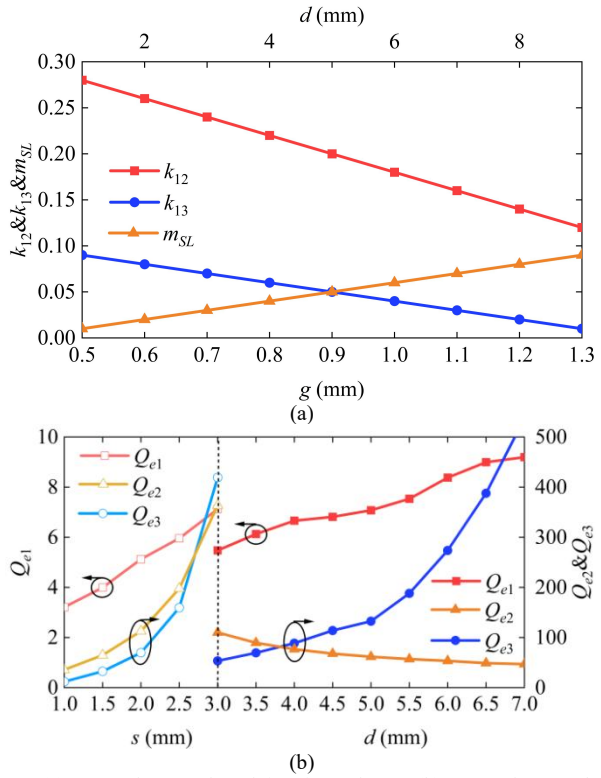


Fig. 3. (a) Extraction results of k_{12}, k_{13} and m_{SL}. (b) Extraction results of Q_{e1},Q_{e2} and Q_{e3}.

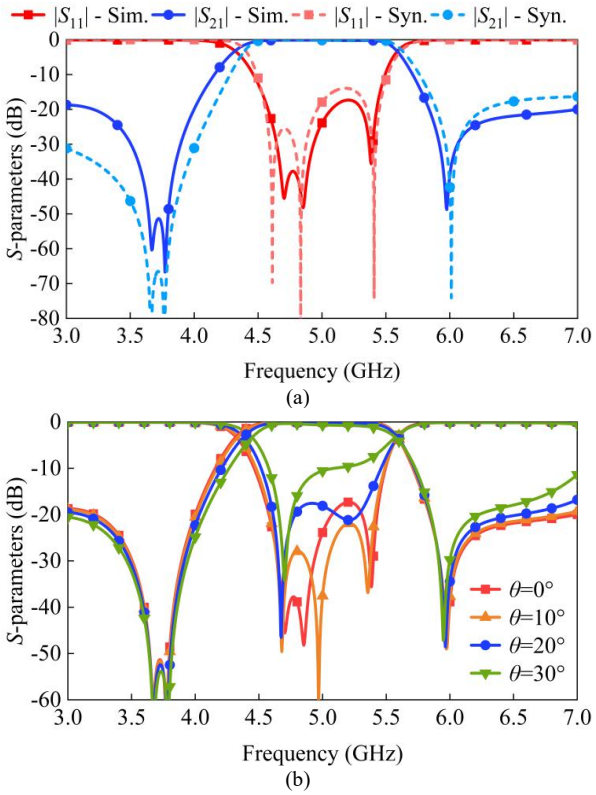


Fig. 4. Simulated results of the proposed 3-D FSS. (a) Under normal incident angle. (b) Under different incident angles.

II. Analysis and Design of Third-order 3-D FSS

A. Configuration

Fig. 1 depicts the configuration of the proposed third-order 3-D FSS. It is realized using a 1.0-mm-thick Rogers RO4350B substrate. A centrally positioned metal strip on the bottom layer acts as an effective ground plane. Two symmetry U-shaped microstrip resonators, together with a narrow metallic strip, are patterned on the top layer and serve as the resonating elements of the FSS. A plane wave is assumed to propagate along the z-axis while the electric field is polarized in the y-direction. The corresponding topology is presented in Fig. 2.

With the introduction of spatial coupling in the 3-D configuration, both the source (Port 1) and the load (Port 2) couple to all three resonators. Additional cancellation paths are formed for each resonator, allowing a third-order topology to generate three TZs. To quantitatively relate the synthesis results to the physical structure of the proposed FSS, the coupling coefficients k_{ij} and external quality factors Q_{ei} are calculated and extracted based on the synthesis design method.

B. Extraction

According to [14], coupling coefficients between resonators can be extracted under the weak coupling condition. As illustrated in Fig. 3(a), enlarging the gaps between the resonators reduces the coupling coefficients k_{12} and k_{13}. In contrast, increasing the distance between the substrates enhances the source-load coupling coefficient m_{SL}. Q_{ei} can be calculated from the group delay of the reflection coefficient under single-port excitation. The dominant geometrical parameters influencing Q_e are the width of the metallic strip (s) and the distance between the substrate (d). As shown in Fig. 3(b), increasing s weakens the coupling between the port and the resonators, leading to a higher Q_{ei}. With respect to the substrate distance, Q_{e1} and Q_{e3} increase as d becomes larger, whereas Q_{e2} varies in the opposite manner.

C. Simulated Results

An FSS prototype is designed based on the topology shown in Fig. 2. The target center frequency is 5 GHz with a fractional bandwidth of 20% The corresponding coupling coefficients are calculated as :

$$\begin{aligned} &m_{S1} = m_{3L} = 0.95, m_{S2} = m_{2L} = 0.05, m_{SL} = 0.02 \\ &m_{S3} = m_{1L} = -0.10, m_{12} = m_{23} = -0.85, \\ &m_{11} = m_{33} = -0.30, m_{22} = -0.20, m_{13} = 0.05 \end{aligned} \quad (1)$$

According to these parameters, the initial geometrical dimensions of the proposed FSS are obtained. After minor full-wave tuning, the simulated results are presented in Fig. 4(a). The passband insertion loss is below 0.5 dB, and three TZs are observed at 3.65, 3.75, and 6.0 GHz. The simulated response demonstrates consistency in bandwidth and TZ positions with the synthesis results, confirming the effectiveness of the proposed design approach. As shown in Fig. 4(b), the angular stability is validated through S21 under oblique incidence. Even at incident angles up to 30°, the passband maintains stable transmission characteristics with insertion loss below 2 dB.

III. Conclusion

This paper investigates the application of spatial coupling in the design of a 3-D bandpass FSS. By exploiting the additional coupling paths introduced by the 3-D configuration, a third-order FSS capable of generating three TZs is realized. The corresponding transmission response is validated through full-wave simulations. The simulated results demonstrate that spatial coupling provides an effective approach to achieving multiple TZs within a compact structure. The proposed configuration offers a feasible solution for the design of 3-D bandpass FSSs with enhanced frequency selectivity.

Acknowledgment

This work was supported in part by the National Natural Science Foundation of China under Grant 62471186, in part by the Guangdong Basic and Applied Basic Research Foundation under Grant 2025A1515012959, in part by the Science and Technology Planning Project of Guangzhou City under Grant 2024A04J6306, and in part by the Guangdong Provincial Key Laboratory of Short-Range Wireless Detection and Communication.

References

[1] A. A. Omar and Z. Shen, "Thin 3-D bandpass frequency-selective structure based on folded substrate for conformal radome applications," *IEEE Trans. Antennas Propag*., vol. 67, no. 1, pp. 282–290, Jan. 2019.

[2] M. L. Hakim, M. T. Islam, and T. Alam, "Incident angle stable broadband conformal mm-Wave FSS for 5G (n257, n258, n260, and n261) band EMI shielding application," *IEEE Antennas Wireless Propag. Lett*., vol. 23, no. 2, pp. 488–492, Feb. 2024.

[3] Y. Wu, H. Hu, J. Tian, S. Lei, B. Jiang, B. Chen, H. Jiang, and Q. Xue, "A polarization-independent wideband switchable rasorber with high roll-off characteristics utilizing third-order switchable FSS," *IEEE Antennas Wireless Propag. Lett*., vol. 24, no. 3, pp. 736−740, Mar. 2025.

[4] T. Zhang, Z. Xia, J. Zhu, X. Wang, J. Wang, Y. Guo, and W. Wu, "Design of a dual-polarized FSS with wide angular stability and high selectivity," *IEEE Antennas Wireless Propag. Lett*., vol. 23, no. 10, pp. 3208–3211, Oct. 2024.

[5] A. Lalbakhsh, M. U. Afzal, K. P. Esselle, and S. L. Smith, "All-metal wideband frequency-selective surface bandpass filter for TE and TM polarizations," *IEEE Trans. Antennas Propag*., vol. 70, no. 4, pp. 2790-2800, Apr. 2022.

[6] Z. Yang, W. Hu, W. Jiang, Q. Luo, and Q. Huang, "High-selectivity fss with wide stopbands for EMI suppression in wireless power transfer systems," *IEEE Antennas Wireless Propag. Lett*., vol. 23, no. 11, pp. 3832−3836, Nov. 2024

[7] B. Wu, H.-L. Li, Y.-T. Zhao, Y.-L. Wang, W.-B. Lu, and L. Chen, "Design and validation of flexible multilayer frequency selective surface with transmission zeros," *IEEE Antennas Wireless Propag. Lett*., vol. 18, no. 2, pp. 250–254, Feb. 2019.

[8] Y. Li et al., "Frequency selective surface with quasi-elliptic bandpass response using radiation null of patch antenna," *IEEE Antennas Wireless Propag. Lett*., vol. 20, no. 1, pp. 13-17, Jan. 2021.

[9] H. Lin, Y. Li, S.-W. Wong, K. W. Tam, B. Liu, and L. Zhu,"High-selectivity FA-FA-based frequency selective surfaces using magnetoelectronic dipole antennas," *IEEE Trans. Antennas Propag*., vol. 70, no. 11, pp. 10669-10677, Nov. 2022.

[10] W. Zhang, B. Li, L. Zhu, X. Zhao, Y.-P. Lyu, and C.-H. Cheng, "Synthesis design of bandpass frequency selective surface with multiple transmission zeros using slotline structures," *IEEE Trans. Antennas Propag.*, vol. 70, no. 10, pp. 9449–9459, Oct. 2022.

[11] J. Zhu, W. Tang, C. Wang, C. Huang, and Y. Shi, "Dual-polarized bandpass frequency-selective surface with quasi-elliptic response based on square coaxial waveguide," *IEEE Trans. Antennas Propag*., vol. 66, no. 3, pp. 1331–1339, Mar. 2018.

[12] W. Zhang, B. Li, L. Zhu, Y.-P. Lyu, and C.-H. Cheng, "Stacked slotline structure-based unit cell and its application for synthesis of 3-D bandpass frequency-selective surfaces," *IEEE Trans. Antennas Propag*., vol. 68, no. 12, pp. 7958–7968, Dec. 2020.

[13] J. Ni, W. Zhao, X. Pang, S. Zhao, K. Duan, J. Wang, X. Zhang, T. Jiang, K. Chen, J. Zhao, and Y. Feng, "A fifth-order X-band frequency-selective surface with high selectivity and angular stability based on 3-D coupling slot," *IEEE Trans. Antennas Propag*., vol. 72, no. 7, pp. 5743–5753, July.2024.

[14] J.-S. Hong, Microstrip Filters for RF Microwave Applications, 2nd Edition. Hoboken, New Jersey: John Wiley Sons, Inc, 2011.

Invited Talk: Plasma-Based Reconfigurable FSS for Adaptive High-Power Microwave Shielding

Krushna K. Varikuntla, Okan Yurduseven, M. Ali Babar Abbasi

May 11, 2026

Abstract

This invited talk provides a focused overview of plasma-based reconfigurable frequency selective surfaces (FSS) for adaptive high-power microwave (HPM) shielding. In contrast to conventional metallic FSS, plasma elements exhibit intrinsically power-dependent electromagnetic (EM) behaviour, enabling *self-actuated* reconfiguration without dedicated DC biasing networks. We first establish the EM description of plasma confined in commercially available gas-discharge tubes (GDTs), modelled as a dispersive medium under the Drude framework. The effective relative permittivity and conductivity are expressed as:

$$\epsilon_{rp}(\omega) = 1 - \frac{e^2 n_e}{\epsilon_0 m(\omega^2 + \nu_m^2)}, \qquad \sigma_p(\omega) = \frac{e^2 n_e \nu_m}{m(\omega^2 + \nu_m^2)},$$

where n_e is the electron density (m^{-3}) and ν_m is the electron–neutral collision frequency (Hz). This analysis clarifies the key design levers, i.e., ν_m governs loss and reflectivity (with reduced pressure improving selectivity), while n_e controls tunability by driving the plasma toward a highly conductive state.

Building on these fundamentals, two experimentally validated FSS architectures are presented, supported by equivalent-circuit modelling and full-wave simulations. The first is a double-layer, GDT-loaded reconfigurable FSS that delivers a wide, flat-top bandpass response centred at 4 GHz with ∼0.5 dB insertion loss in the low-power (OFF) state, and transitions to >10 dB isolation in the high-power (ON) state. Importantly, plasma ignition is shown to occur at resonance, where localised electric-field enhancement triggers ionisation, confirming power-selective operation. The second is a self-reconfigurable energy-selective surface based on a cross topology with integrated plasma cells, which autonomously shifts its stopband from 6 GHz (OFF) to 3 GHz (ON) without external bias circuitry. Waveguide measurements up to 50 dBm verify robust high-power handling, beyond the regime where semiconductor limiters are typically constrained by breakdown. With a compact unit cell of $0.15\lambda \times 0.15\lambda \times 0.012\lambda$, the prototype also demonstrates stable performance under oblique incidence and a pressure-dependent quality factor, with lower pressure yielding higher isolation. Collectively, these results establish plasma-FSS technology as a practical route to adaptive EM protection for satellite and aeronautical platforms, telecommunications infrastructure, and high-power medical and industrial environments.

Acknowledgement: This study was supported by the EME Hub, funded by Defence Science and Technology Laboratory, UK. The work was also partially supported by the Department for the Economy of Northern Ireland under the U.S. Ireland R&D Partnership under Grant USI 269 and Leverhulme Trust under the Research Leadership Award RL- 2019-019, respectively.

979-8-3315-4544-4/26/$31.00 ©2026 IEEE

A Reconfigurable Transmit-Reflect-Array Antenna Based on Tightly Coupled Dipole

1st Shangsen Huang
National Key Laboratory of Rader Detection and Sensing, Xidian University
Xi'an, China
24021211997@stu.xidian.edu.cn

2nd Wei Hu
National Key Laboratory of Rader Detection and Sensing, Xidian University
Xi'an, China
whu@mail.xidian.edu.cn

3rd Yuchen Gao
National Key Laboratory of Rader Detection and Sensing, Xidian University
Xi'an, China
gaoyuchen@xidian.edu.cn

4th Zhaoling Wang
National Key Laboratory of Rader Detection and Sensing, Xidian University
Xi'an, China
wangzhaolll@163.com

Abstract—This paper presents a reconfigurable tightly coupled transmit-reflect-array (TRA) antenna for broadband wireless communication applications. The antenna features an active unit cell comprising tightly coupled dipole elements interconnected by PIN diodes and a polarizer grid for polarization selection, facilitating 1-bit phase reconfiguration. The reflection layer operates in reflection mode for x-polarized waves, while the transmission layer operates in transmission mode for y-polarized waves. By employing different coding sequences to control the ON and OFF states of the PIN diodes, the reflection and transmission phases can be precisely configured, enabling accurate independent beam steering at desired angles. With an F/D ratio of 0.8 and a 16×16 element array, the antenna achieves high gain and low sidelobe levels for both polarization modes. This reconfigurable TRA antenna is ideally suited for advanced wireless communication systems requiring simultaneous dual-mode operation.

Keywords—Bidirectional, dual-polarization, tightly coupled d dipole, transmit-reflect-array (TRA)

I. INTRODUCTION

With the rapid advancement of wireless communication, navigation, and radar jamming technologies, the contemporary operational environment imposes increasingly stringent requirements on antenna structures within communication systems. To enhance signal coverage while reducing structural complexity and cost, antennas are required to exhibit multi-beam scanning capabilities and employ simplified feeding networks [1]. The transmit-reflect-array (TRA) antenna represents a novel type of high-gain antenna capable of simultaneously radiating bidirectional beams relative to the aperture [2], [3], [4]. This characteristic renders it highly promising for applications in multidirectional radiation scenarios, such as indoor communications. Furthermore, although traditional mechanically scanned antennas can achieve flexible and controllable beam steering, they are gradually being supplanted by electronically scanned antennas, which offer rapid switching times and straightforward implementation, largely due to the bulkiness of T/R modules associated with the former. The integrated transmitarray and reflectarray antenna, capable of radiating bidirectionally from the aperture with independent beam control for each side, holds significant importance for expanding signal coverage and enhancing the application potential of antennas in domains such as high-data-rate transmission and wireless network communications [5].

Consequently, the design of a reconfigurable transmit-reflect-array antenna can synergistically combine the advantages of both antenna types. On one hand, it can be integrated with Field Programmable Gate Array (FPGA)-controlled electronic components to achieve flexible beam manipulation [6], [7]. On the other hand, its bidirectional radiation characteristic broadens the signal coverage area. Additionally, given the inherent narrow operating bandwidth typical of transmit-array and reflect-array antennas, designing a broadband reconfigurable integrated antenna is of great

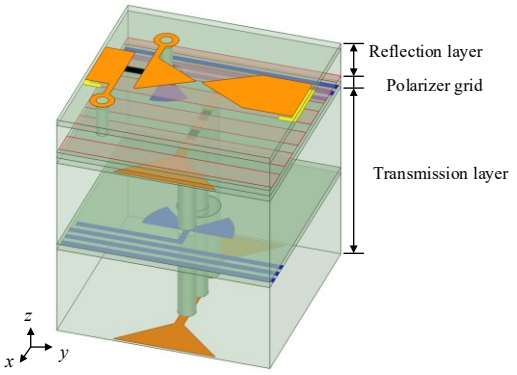


Fig. 1. Structure of TRA unit cell.

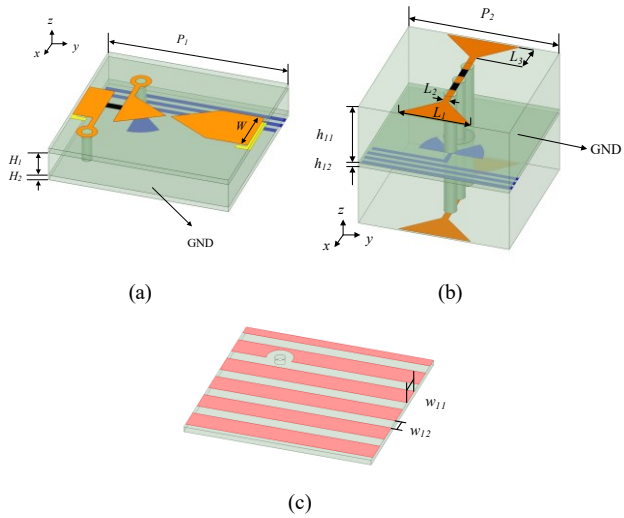


Fig. 2. Structure of the Triple-layer TRA element. (a)Reflection layer. (b)Transmission layer. (c)Polarizer grid.

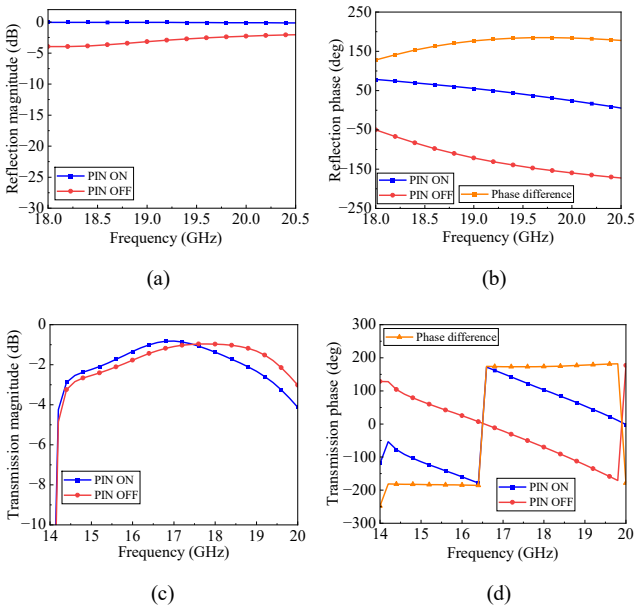


Fig. 3. (a) Reflection magnitude and (b) reflection phase. (c) Transmission magnitude and (d) transmission phase.

significance for improving wireless signal transmission efficiency. Tightly coupled elements can significantly broaden the operational bandwidth of the antenna due to their mutual coupling structure, and therefore are often employed in the design of transmitarray and reflectarray [8], [9]. Based on the above analysis, this paper integrates reconfigurable technology with the transmitarray and reflectarray antenna concept, grounded in the principles of tightly coupled array structures, to propose a reconfigurable transmit-reflect-array antenna featuring flexible beam control.

II. Unit-Cell Design

As shown in Fig.1, the overall unit cell adopts a "reflector-polarizer grid-transmission" layer arrangement. Fig.2 is the structural diagram of each layer. The reflection unit employs a tightly coupled structure, operating in reflection mode for x-polarized waves. Its specific parameters are as follows: P_1 = 7.1 mm, W = 2.4 mm, H_1 = 2 mm, H_2 = 1 mm. By switching the PIN diode on and off, the length of the dipole arms is altered, consequently changing the current path within the unit cell. This results in a phase difference of between the two switching states. The PIN diode used in the unit is the MACOM MADP-000907-14020. In the ON state, its equivalent circuit is a series combination of a R = 7.8 Ω resistor and an L = 30 pH inductor. In the OFF state, its equivalent circuit is a series combination of a C = 0.025pF capacitor and an L = 30 pH inductor. Owing to its polarization selective property, the polarizer grid serves two functions. On one hand, it acts as a ground plane for the reflection structure, reflecting incident y-polarized waves. On the other hand, it allows x-polarized waves to pass through, illuminating the transmission structure and enabling transmission. The polarizer grid is featuring a strip width of w_{11} = 0.8 mm and an inter-strip spacing of w_{12} = 0.5 mm.The radiating elements of the transmission layer are designed using tightly coupled dipole antennas, which are controlled by integrating PIN diodes. Its specific parameters are as follows: P_2 = 7.1 mm, L_1 = 3.4 mm, L_2 = 0.3 mm, L_3 = 1.45 mm, h_{11}=3mm, h_{12} = 0.2mm.

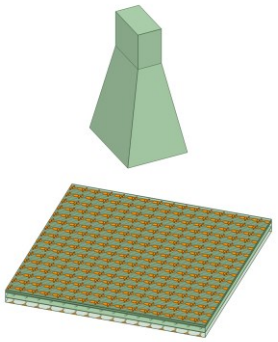


Fig. 4. Configuration of the 1-bit reconfigurable TRA.

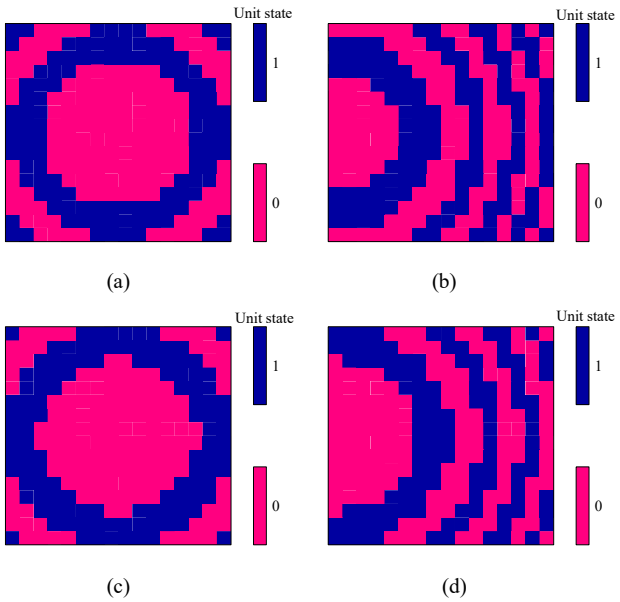


Fig. 5. Reflection phase for (a) 0° and (b) 30° . Transmission phase for (c) 0° and (d) 30° .

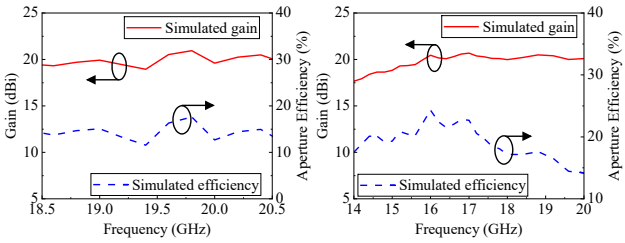
The unit cell was simulated in HFSS, and the results are shown in the Fig. 3. It can be observed that the unit cell reflects y-polarized incident waves while transmitting x-polarized incident waves, thereby achieving a transmission/reflection dual-polarization mode of operation. Furthermore, in both operational states, $180° \pm 20°$ phase tuning can be achieved via the PIN diode.

III. Results and Discussion

A TRA aperture is formed by a planar array of 16 × 16 elements with the F/D of 0.8, and the antenna aperture diameter is 113.6 mm. A standard gain horn is employed as the feed source, and the structure of the TRA is depicted in Fig.4. For any unit cell (x_i, y_i) on the array aperture, the phase compensation provided by the transmission or reflection unit cell is:

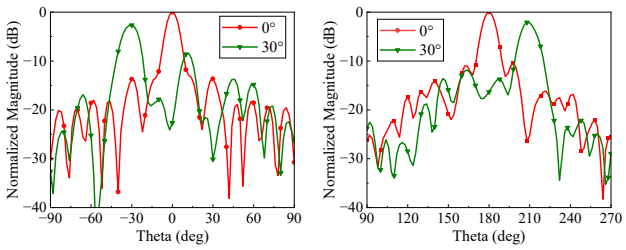
$$\phi_{RT}(x_i, y_i) = k_0(d_i - (x_i \cos\varphi_b + y_i \sin\varphi_b)\sin\theta_b) + \psi_0 \quad (1)$$

Where (θ_b, φ_b) represents the direction of the beam radiated from the array aperture, and k_0 is the wavenumber of the electromagnetic wave in free space. After calculating the reflection or transmission compensation phase using Equation (1), the normalized phase is classified into two phase states according to the following formula:



(a) (b)

Fig. 6. Simulated gain and efficiency in (a) reflection and (b) transmission mode.



(a) (b)

Fig. 7. Radiation pattern of the array simulated in (a) reflection and (b) transmission mode.

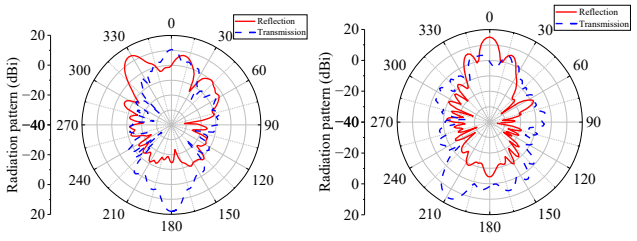
$$\varphi_{mn}=\begin{cases}\varphi_0, \varphi_0-\dfrac{\pi}{2}<\varphi_{mn}<\varphi_0+\dfrac{\pi}{2}\\ \varphi_1, \varphi_1-\dfrac{\pi}{2}<\varphi_{mn}<\varphi_1+\dfrac{\pi}{2}\end{cases} \tag{2}$$

Based on the two Equations (1) and (2), the quantized phase. for each unit cell can be obtained. The antenna unit cell with the PIN diode in the ON state is regarded as the "1" unit, with a phase of φ_1, while the antenna unit cell with the PIN diode in the OFF state is regarded as the "0" unit, with a phase of φ_0 ,and the relationship between the two variables is:

$$\varphi_1-\varphi_0=\pi \tag{3}$$

Consequently, the 1-bit phase distribution diagrams for the reflection and transmission phases of the unit cells are obtained, as shown in the Fig.5. The operating states of the PIN diodes for different unit cells are adjusted according to these phase diagrams. The operating frequency band for reflection is 18.5 – 20.5 GHz, and for transmission it is 14.5 – 19.5 GHz. As shown in Fig.6, the reflection gain maintains above 15 dBi across the entire operating frequency band, peaking at 20.9 dBi. The reflection efficiency remains above 10% throughout the operating band, with a maximum aperture efficiency of 17.6%. Similarly, the transmission gain exceeds 15 dBi over the whole operating frequency band, reaching a maximum of 20.7 dBi. The transmission efficiency is achieving a peak aperture efficiency of 24.3%.

The common operating frequency of 19 GHz was selected to observe the beams in both states. The normalized radiation patterns for the two states are shown in the Fig.7. As can be seen, the array antenna can achieve a 30° beam deflection in both reflection mode and transmission mode with this phase compensation distribution. It can be observed from the Fig.8 that when the reflected beam is steered, the transmitted beam direction remains unchanged. When the transmitted beam is



(a) (b)

Fig. 8. (a) Reflected beam steering to 30°, while transmitted beam maintains steering to 0°. (b) Transmitted beam steering to 30°, while reflected beam maintains steering to 0°.

steered, the reflected beam direction remains unchanged. Thus, the reflected and transmitted beams of this array antenna can operate independently, each undergoing reconfigurable modulation.

IV. Conclusion

This paper proposes and designs a reconfigurable tightly coupled transmit-array and reflect-array integrated antenna. By integrating PIN diodes into the tightly coupled dipole antenna elements, 1-bit phase control is achieved. The final designed antenna element reflects x-polarized waves within the 18.5 – 20.5 GHz frequency band and transmits y-polarized waves within the 14.5 – 19.5 GHz band. The overall antenna exhibits stable radiation patterns in both operational modes, which can function independently without mutual interference. Furthermore, it possesses independent reconfigurable control capability, enabling dual-polarization operation with a beam scanning angle. This makes it suitable for communication applications requiring versatile beam directions.

References

[1] OZPINAR H, AKSIMSEK S, TOKAN N T. A Novel Compact, Broadband, High Gain Millimeter-Wave Antenna for 5G Beam Steering Applications[J]. IEEE Transactions on Vehicular Technology, 2020, 69(3): 2389-2397.

[2] GAO Y, WANG Z, TANG H, et al. Ultrawideband Transmit-Reflect-Array Antenna for 6G Communication[J]. IEEE Antennas and Wireless Propagation Letters, 2024, 23(11): 3669-3673.

[3] WU L X, CHEN K, JIANG T, et al. Circular-Polarization-Selective Metasurface and Its Applications to Transmit-Reflect-Array Antenna and Bidirectional Antenna[J]. IEEE Transactions on Antennas and Propagation, 2022, 70(11): 10207-10217.

[4] YANG F, DENG R, XU S, et al. Design and Experiment of a Near-Zero-Thickness High-Gain Transmit-Reflect-Array Antenna Using Anisotropic Metasurface[J]. IEEE Transactions on Antennas and Propagation, 2018, 66(6): 2853-2861.

[5] REIS J R, VALA M, CALDEIRINHA R F S. Review Paper on Transmitarray Antennas[J]. IEEE Access, 2019, 7: 94171-94188.

[6] XUE L, XU S, WANG M, et al. Wideband Reconfigurable Transmitarray Antenna Using Tightly Coupling Effect With Wide-Angle Beam Scanning Capability[J]. IEEE Antennas and Wireless Propagation Letters, 2024, 23(12): 4358-4362

[7] YANG H, YANG F, XU S, et al. A 1-Bit 10 × 10 Reconfigurable Reflectarray Antenna: Design, Optimization, and Experiment[J]. IEEE Transactions on Antennas and Propagation, 2016, 64(6): 2246-2254.

[8] CAI Y M, LI W, LI K, et al. A Novel Ultrawideband Transmitarray Design Using Tightly Coupled Dipole Elements[J]. IEEE Transactions on Antennas and Propagation, 2019, 67(1): 242-250.

[9] HAMZA M, ZEKIOS C L, GEORGAKOPOULOS S V. A Low Profile Planar Dual-Polarized Tightly Coupled Dipole Reflectarray With 5:1 Bandwidth[J]. IEEE Open Journal of Antennas and Propagation, 2022, 3: 958-969.

Reconfigurable Bandpass Ultrathin Angular-Selective Surfaces

Hao Jiang*, Mei Qian†
*Department of Electrical Engineering, City University of Hong Kong, Hong Kong, China
†School of Electronic and Information Engineering, South China University of Technology, Guangzhou, China
Email: eehaojiang@ieee.org

***Abstract*—This work proposes an ultrathin bandpass angular-selective surface (ASS). Unlike most previously reported structures relying on multilayer configurations, the proposed design employs a metallic pattern printed on a single substrate, resulting in a significantly reduced profile. The operating mechanism is interpreted using an equivalent circuit model in which the incident angle is treated as the independent variable to realize the desired angular-domain bandpass response. Full-wave simulations demonstrate that the passive ASS achieves angular-selective filtering over a wide incidence range within the operating band. Moreover, a reconfigurable ASS is realized by integrating PIN diodes into the metallic-slot structure, enabling dynamic switching between bandpass and stopband states.**

***Index Terms*—Angular-selective surfaces (ASSs), circuit model, reconfigurable.**

I. Introduction

Angular-domain responses of metamaterial unit cells play a fundamental role in electromagnetic wave control for microwave systems. Angular-selective surfaces (ASSs), which tailor transmission responses according to the incident angle, have attracted increasing interest due to their potential applications in sidelobe suppression, directivity enhancement, and interference mitigation [1], [2]. Ultrathin ASSs can realize various angular-domain filtering characteristics, making them promising candidates for advanced RF front-end systems.

Angular selectivity has been extensively explored in optical regimes using planar optics, photonic crystals, and metamaterials [3], [4]. However, extending such concepts to microwave frequencies remains challenging due to practical material limitations and structural complexity. Existing microwave ASS implementations, including cascade transmission-line synthesis [5], [6], multilayer frequency-selective surfaces (FSS) configurations [7], and Brewster-angle-inspired designs [8], often suffer from excessive thickness and limited angular selectivity.

To address these challenges, this work proposes an ultrathin bandpass ASS realized using a metallic structure printed on a single standard substrate. The proposed design achieves the desired angular-domain filtering response while maintaining a compact profile. Moreover, a reconfigurable version is developed by integrating PIN diodes into the metallic structure, enabling dynamic switching of the angular transmission characteristics.

II. Operating Principle of the Bandpass ASS

The bandpass response of a conventional two-dimensional FSS is commonly realized by metallic resonators that can be modeled using a parallel LC circuit, where the resonant frequency is determined by the circuit parameters.

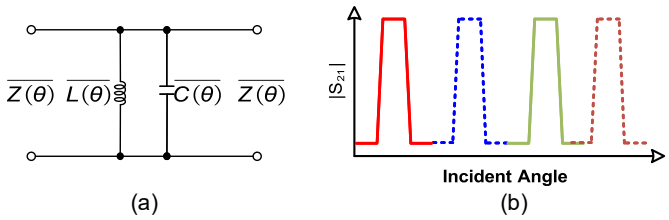


Fig. 1: Concept of the bandpass ASS: (a) equivalent circuit; (b) desired angular-domain response.

For a bandpass ASS, the resonant behavior can be interpreted in a similar circuit framework, as illustrated in Fig. 1(a). In this case, the incident angle (θ) is treated as the independent variable, and the structure can be described by an equivalent circuit consisting of a normalized inductance $\overline{L(\theta)}$ and capacitance $\overline{C(\theta)}$. Consequently, variations in the incident angle lead to corresponding changes in the equivalent circuit parameters, resulting in different transmission responses in the angular domain.

At a given frequency, the free-space wave impedance for a given polarization (TE or TM) is normalized to θ as $\overline{Z(\theta)} = 1$. The desired angular-domain bandpass characteristics are illustrated in Fig. 1(b), where distinct transmission behaviors are obtained at different incidence angles.

III. Modeling and Design

In this section, unlike previously reported ASSs, the proposed ASS design employs only a metallic structure printed on a single standard substrate, ensuring an ultrathin profile while achieving the desired angular-domain response. Moreover, the concept is extended to a reconfigurable implementation.

A. Modeling and Design of the ASS

Fig. 2(a) and (b) illustrates the unit-cell configuration of the proposed bandpass ASS (ASS I) and its reconfigurable extension (ASS II), respectively. The periodic unit cell adopts a rectangular lattice and mainly consists of two parallel metallic strips with an embedded split-ring resonator located at the center.

In the reconfigurable extension, two PIN diodes are inserted at designated positions within the metallic gaps between the

979-8-3315-4544-4/26/$31.00 ©2026 IEEE

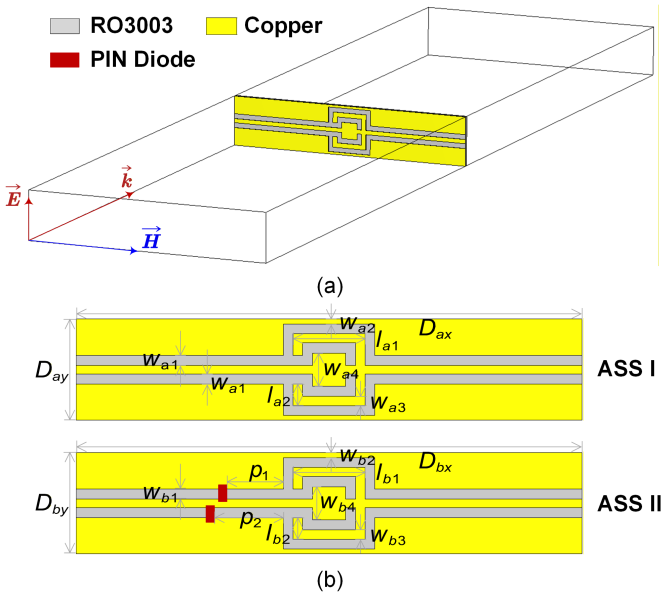


Fig. 2: Schematic of the bandpass ASS. (a) Simulation unit-cell layout. (b) Planar passive structure (ASS I) and its reconfigurable extension (ASS II) using PIN diodes.

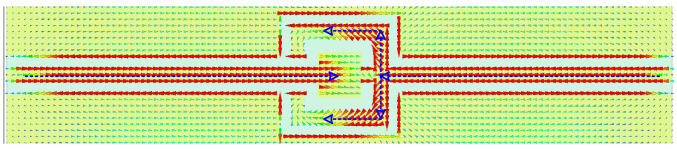


Fig. 3: Surface current distribution at the bandpass resonant frequency

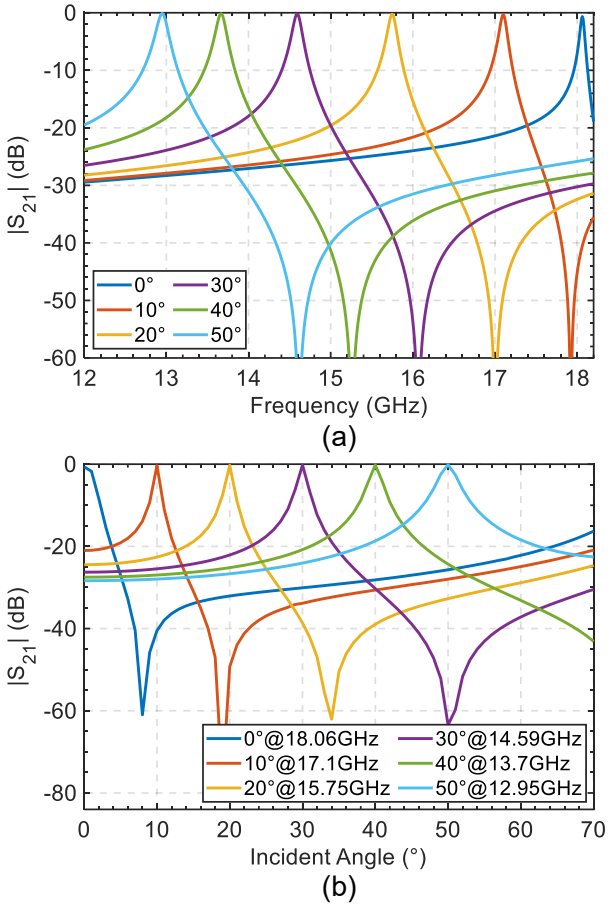


Fig. 4: Transmission responses of ASS I under TM polarization with a 10° angular step: (a) frequency-domain response; (b) angular-domain response.

strips, enabling switching of the surface current paths and thereby altering the resonant modes. The two electrically isolated metallic strips inherently form the biasing network of the reconfigurable ASS, eliminating the need for additional dc bias lines.

Fig. 3 shows the surface current distribution at the bandpass resonant frequency. The currents are primarily concentrated along the two parallel metallic strips and around the central split-ring resonator, forming a closed current loop. The metallic strips contribute an inductive response, whereas the gaps between adjacent conductors introduce capacitive coupling. This distributed inductive–capacitive interaction establishes the resonant mode that produces the bandpass transmission characteristic of the proposed ASS.

B. Simulation Results of The Passive ASS

Here, the transmission characteristics of ASS I under TM polarization are discussed. Fig. 4(a) and (b) shows the simulated frequency-domain responses at different incidence angles. A pronounced transmission passband is observed for all incidence angles, exhibiting good frequency selectivity. As the incidence angle increases, the center frequency of the passband gradually shifts toward lower frequencies.

Furthermore, from a frequency-domain perspective, within the operating frequency range of 12–18.2 GHz, the transmission band exhibits good angular selectivity within the range of $\theta = 10°\sim80°$. Specifically, the transmission magnitude is significantly enhanced (low insertion loss) around certain angles, while it is strongly suppressed at other angles.

C. Simulation Results of The Reconfigurable ASS

Fig. 5(a)–(f) present the transmission characteristics of the reconfigurable ASS II under TM polarization for different reference incident angles ($10°\sim50°$). When the PIN diodes are in the OFF state (blue solid lines), the structure exhibits a low-insertion-loss bandpass response for all incident angles, while the transmission frequency gradually shifts toward lower frequencies as the angle increases (from 6.7 GHz to 5.4 GHz). In contrast, when the diodes are turned ON (red dashed lines), the bandpass window nearly disappears, and the structure exhibits a stopband characteristic over a wide angular range.

Fig. 6(a) and (b) further demonstrate the wideband and wide-angle transmission responses of ASS II. The results demonstrate that by altering the bias state of the diodes, ASS II

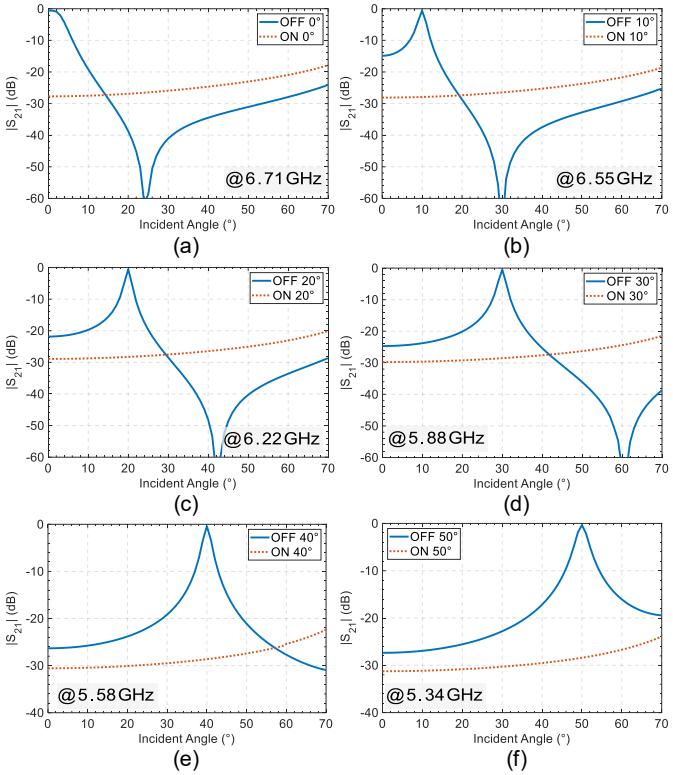


Fig. 5: Transmission response of ASS II under TM polarization at different incident angles: (a) θ = 0°; (b) θ = 10°; (c) θ = 20°; (d) θ = 30°; (e) θ = 40°; (f) θ = 50°.

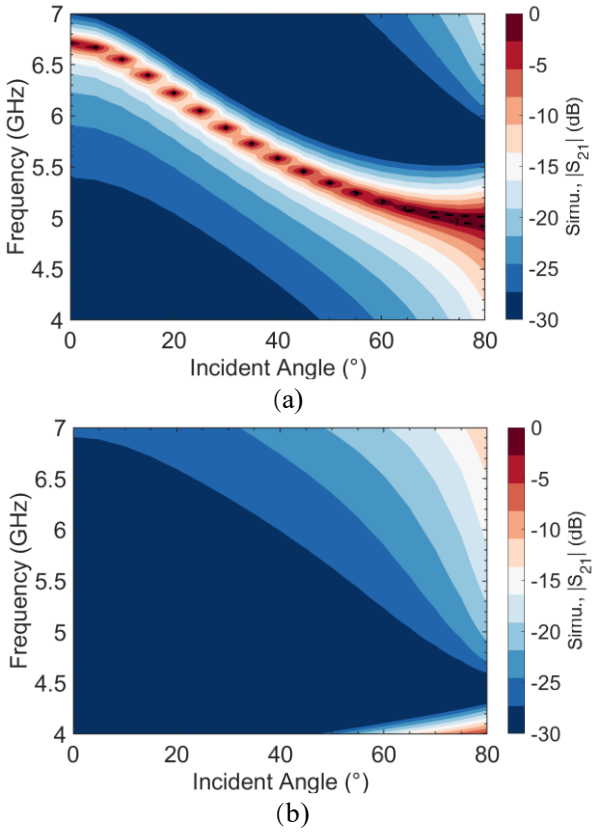


Fig. 6: Wideband and wide-angle responses of ASS II: (a) passband state; (b) stopband state. (Angle sampling step is 5°)

can switch between the bandpass and stopband states, thereby enabling reconfigurable functionality in the angular domain.

IV. Conclusion

This work presents bandpass ASSs with an ultrathin profile. By exploiting the angular-dependent equivalent circuit behavior of the unit-cell, the proposed structure realizes controllable transmission responses in the angular domain while maintaining a single-layer implementation. Simulation results verify their stable angular-selective filtering over a wide incidence range. The incorporation of PIN diodes in the structure further enables dynamic switching of the angular-domain response, providing a compact and flexible platform for adaptive microwave front-end systems.

References

[1] P. ranchi and R. Mailloux, "Theoretical and experimental study of metal grid angular filters for sidelobe suppression," *IEEE Trans. Antennas Propag.*, vol. AP-31, no. 3, pp. 445–450, May 1983.

[2] Y. Lee, S. Hun Jeong, W. Sang Park, J. Seung Yun, and S. Ik Jeon, "Multi-layer spatial angular filter with air gap tuner to suppress the grating lobes of microstrip patch arrays," *IEEE MTT-S Int. Microw. Symp. Dig.*, Jun. 2002, pp. 1329–1332.

[3] Y. Kuai *et al.*, "Planar photonic chips with tailored angular transmission for high-contrast-imaging devices," *Nat. Commun.*, vol. 12, p. 6835, Nov. 2021.

[4] C. Xu *et al.*, "Angular selection of incident waves by photonic crystals with position-varying Dirac points at the Brillouin zone boundary," *Phys. Rev. B, Condens. Matter*, vol. 93, no. 24, Jun. 2016, Art. no. 245116.

[5] T. Qin *et al.*, "Efficient synthesis of angular selective surfaces based on accurate equivalent circuit analysis," *IEEE Trans. Microw. Theory Techn.*, vol. 71, no. 6, pp. 2625–2638, Jun. 2023.

[6] H. Jiang, Y. Wu, Y. Zhang, Y. Lyu, Z. N. Chen, and Q. Xue, "Synthesis and Design of Ultrathin Angular-Selective Surfaces," *IEEE Trans. Microw. Theory Techn.*, vol. 73, no. 12, pp. 10058–10070, Dec. 2025.

[7] N. Kou and S. Yu, "Angular selectivity based on odd mode resonance of frequency selective surface," *IEEE Antennas Wireless Propag. Lett.*, vol. 21, no. 11, pp. 2151–2155, Nov. 2022.

[8] Y. Gao, B. Li, R. Wang, Q. Yan, J. Huangfu, and D. Ye, "Polarization independent broadband angular selectivity based on anisotropic diamagnetic metamaterial," *IEEE Trans. Antennas Propag.*, vol. 70, no. 8, pp. 7306–7310, Aug. 2022.

Modal Expansion Analysis and Inverse-Design of Reconfigurable AIS-Loaded Antennas

Mengyuan Bie and Zhi Hao Jiang*
State Key Laboratory of Millimeter-Waves, School of Information Science and Engineering
Southeast University
Nanjing, P.R. China
zhihao.jiang@seu.edu.cn

***Abstract*—This paper presents two reconfigurable antennas loaded with anisotropic impedance surfaces. The first one achieves reconfigurable frequency and bandwidth with a 76.6% tuning range in the narrowband mode and 82.9% bandwidth in the wideband mode. The second antenna features 360° beam scanning with a step of 11.25° in the *S*-band. A semi-analytical mode expansion method is developed for the inverse-design of these two antennas by predicting accurate impedance bandwidth and radiation patterns.**

Keywords—anisotropic impedance surface, mode expansion method, reconfigurable

I. Introduction

As a technique based on expansion of the orthogonal-mode series of electromagnetic fields and boundary conditions, the mode expansion method (MEM) is initially developed for the analysis of guiding structures [1], resonators [2], and has also been extended to the modeling and design of open structures such as antennas [3] and frequency selective surfaces [4]. Particularly in the context of antenna design, this method has been successfully applied to antennas loaded with passive artificial impedance surfaces (AIS) [5]. Compared to commercial full-wave simulators, the inverse-design enabled by the MEM is significantly accelerated, demonstrating its superior efficiency. However, studies on the MEM and inverse-design for antennas loaded with reconfigurable AISs remain limited and require further exploration.

This work presents the mode analysis and inverse-design of two exemplary antennas loaded with reconfigurable AISs. In the first design, by introducing two types of azimuth-homogeneous AISs, frequency and bandwidth reconfigurability is enabled in a monopole antenna. In the second design, by tuning the impedance of an azimuth-inhomogeneous AIS, 360° beam scanning is achieved for a monopole antenna.

II. Antenna Design and Expererimental Results

As shown in Fig. 1 and Fig. 2, two monopole antennas loaded with reconfigurable AIS are presented. The first one [see Fig. 1] consists of a top-hat monopole surrounded by three octagonal AISs. Among them, one AIS loaded with varactors enables continuous narrowband frequency tuning, while the other two AISs loaded with PIN diodes facilitate switching between narrowband and wideband operational modes. Measured results demonstrate a frequency tuning range of 76.6% in the narrowband mode and an impedance bandwidth of 82.9% in the wideband mode. The second antenna [see Fig. 2] comprises a monopole enclosed by a cylindrical AIS. The AIS is integrated with PIN diodes, allowing it to switch between inductive and capacitive impedance. This design achieves 360° beam scanning in the azimuth plane with an interval of 11.25°. In the inverse-design of these two antennas, the MEM serves as the computational engine, significantly reducing the design time.

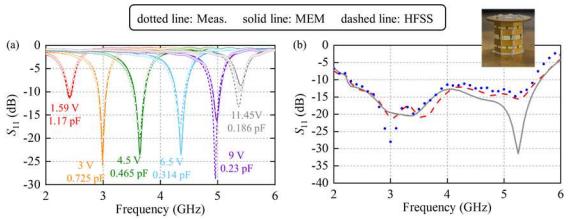


Fig. 1. Reflection coefficients of the frequency- and bandwidth-reconfigurable antenna in the (a) narrowband mode and (b) wideband mode.

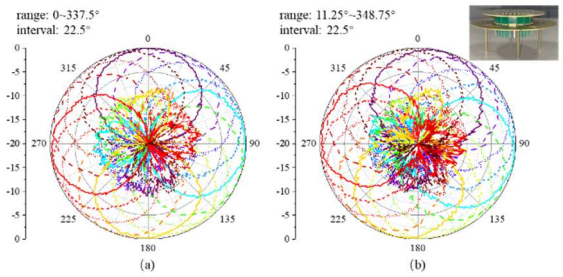


Fig. 2. Measured radiation patterns at 3.5 GHz scanning in the angular range of (a) 0°~337.5° and (b) 11.25°~348.75° for the beam-scanning antenna.

III. Conclusion

This paper presents two novel antennas loaded with reconfigurable AISs, demonstrating frequency/bandwidth and pattern reconfigurability, respectively. Furthermore, the MEM provides accurate predictions of the impedance bandwidth and radiation patterns for the inverse-design, offering a new design tool for reconfigurable AIS-loaded antennas.

References

[1] A. Wexler, "Solution of waveguide discontinuities by modal analysis," *IEEE Trans. Microw. Theory Techn.*, vol. 15, no. 9, pp. 508–517, Sep. 1967.

[2] D. M. Pozar, "Resonant frequency and Q of an open-ended rectangular cavity," *IEEE Trans. Microw. Theory Techn.*, vol. 25, no. 7, pp. 589–593, Jul. 1977.

[3] Z. Shen and R. H. MacPhie, "Rigorous evaluation of the input impedance of a sleeve monopole by modal-expansion method," *IEEE Trans. Antennas Propag.*, vol. 44, no. 12, pp. 1584–1591, Dec. 1996.

[4] S. M. Shamaei, S. R. Sarraf, and M. Gholamreza, "Modal analysis of frequency selective surface containing ring loops," *Appl. Comput. Electrom.*, vol. 30, no. 10, pp. 1074–1078, 2015.

[5] Z. H. Jiang and W. Hong, "Design and experiments of bandwidth-controllable broadband monopole antennas with conformal anisotropic impedance surface coatings," *IEEE Trans. Antennas Propag.*, vol. 66, no. 3, pp. 1133–1142, Mar. 2018.

979-8-3315-4544-4/26/$31.00 ©2026 IEEE

A Data-Efficient and Physics-Constrained Deep Learning Framework for Reflectarray Antenna Inverse Design

Qinghua Liu[1,2], Xue Ren[*1,2]

[1]The State Key Laboratory of Radio Frequency Heterogeneous Integration, Shenzhen University, Shenzhen, 518060, China

[2]College of Electronics and Information Engineering, Shenzhen University, Shenzhen 518060, China

eerenxue@szu.edu.cn

***Abstract*—A physics-guided Conditional Variational Autoencoder (cVAE) framework for the rapid inverse design of high-aperture-efficiency reflectarray antennas is proposed in this paper. Addressing the ill-posed nature of mapping electromagnetic responses to complex topologies, we incorporate structural symmetry, manufacturability constraints, and morphological filtering as prior rules to regularize the unit topology and enhance dataset quality. A high-precision Residual Network (ResNet), is embedded into the cVAE loop to enforce physical consistency, is trained as a forward proxy to replace time-consuming full-wave simulations. In this way, model efficiency enhancement is achieved through the regularized unit design, while antenna efficiency is ensured by the accurate proxy-constrained generative model. To validate the method, an 18×18 element reflectarray operating at 10 GHz is designed. Full-wave simulations demonstrate a realized gain of 23.9 dB, a sidelobe level of −19.6 dB, and an aperture efficiency of 60.4%. The proposed approach accelerates design iterations while maintaining engineering feasibility, providing a practical tool for advanced metasurface systems.**

***Keywords*—Reflectarray antenna, inverse design, deep learning, conditional variational autoencoder (cVAE).**

I. Introduction

Reflectarray antennas (RA) combine the low-profile and lightweight characteristics of planar arrays with the high-gain advantage of parabolic reflectors, and thus are widely used in satellite communications, radar imaging, and next-generation wireless systems [1][2][3]. Their design, however, requires solving a high-dimensional inverse mapping from target reflection phase or frequency responses to complex unit-cell geometries that meet stringent electromagnetic performance requirements.

Deep learning has recently been introduced to accelerate inverse design by learning mappings between unit-cell topology and electromagnetic (EM) responses [4][5][6]. Big-data strategies can reach high prediction accuracy, yet they often rely on tens of thousands of simulated samples, which are costly to generate. Generative adversarial networks (GANs) further attempt to produce unit geometries directly from target responses, but they are notoriously sensitive to data imbalance and rarely provide a physically interpretable latent space [7].

In this work, we propose a physics-guided Conditional Variational Autoencoder (cVAE) framework tailored to reflectarray elements. Model efficiency is achieved at the data level: by enforcing structural symmetry, manufacturability constraints, and morphological filtering, we regularize the 32×32 binary topology and dramatically reduce the effective design space, enabling robust training with only 4,500 simulated samples. Antenna efficiency is then ensured at the model level: a high-precision ResNet forward proxy, trained on the same dataset, is embedded into the cVAE loss to enforce consistency between generated geometries and their EM responses over the operating band.

II. Inverse Design of Metasurface Elements

The proposed framework consists of two core components: a high-precision forward proxy model, which effectively substitutes for full-wave simulation, and a cVAE-based inverse design model. The unit cell design and network architecture are detailed below.

A. Unit Structure Design and Dataset Generation

Fig. 1(a) illustrates the 3D view of the proposed reflectarray unit cell. It consists of three layers: a top metallic topological structure, a single dielectric substrate layer (Rogers RT/duroid 5880 with relative permittivity ε_r=2.2, loss tangent $\tan\delta = 0.0009$, and thickness h=1.575 mm), and a bottom copper ground plane. The unit cell periodicity is L=10 mm, corresponding to approximately one third of the wavelength at the center frequency of 10 GHz.

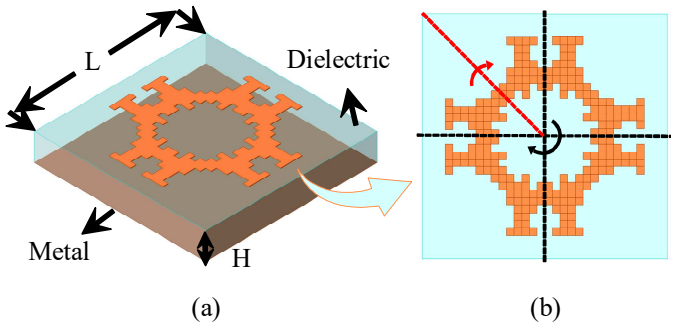


Fig. 1. Structure of the proposed RA element. (a) 3D view. (b) Discretization and coding of the metasurface pattern.

As shown in Fig. 1(b), the copper pattern is discretized into a 32×32 binary matrix, where "1" represents metal and "0" represents a vacuum. To prevent electrical continuity between adjacent unit cells, the outermost ring of the matrix is set to "0" by default. To reduce the design degrees of freedom and minimize cross-polarization levels, symmetry constraints are

applied. The topology is first generated as a 16×16 matrix, mirrored vertically (red dashed line), and then rotationally replicated to form the full 32×32 pattern. This reduces the design space from $2^{32\times32}$ to 2^{120}.

Furthermore, to ensure manufacturability and avoid isolated pixels or vertex-only connections, which contribute negligibly to the EM response but introduce noise during training, morphological filtering is applied during generation. A dataset containing 4,500 distinct metasurface structures was generated. The target frequency range was set to 8-12 GHz, discretized into 64 frequency points. Full-wave simulations were performed using CST Microwave Studio to obtain the reflection phase data, serving as the input-output pairs for the network.

B. Network Models

To establish a bidirectional mapping, a forward proxy model was first trained to predict the EM response from the binary topology. The dataset was split into training, validation, and testing sets in an 8:1:1 ratio. A deep ResNet architecture was adopted, taking the top-left 16×16 quadrant of the pixelated structure as input. The output is the normalized reflection phase across 64 frequency points. Since EM response prediction is a regression problem, the mean squared error (MSE) loss function is used:

$$L_{pre_mse} = \frac{1}{n}\sum_{i=1}^{n}(y_i - \hat{y}_i)^2 \quad (1)$$

where n is the total number of frequency sampling points, y_i is the ground-truth simulation value, and $\hat{y}_i$ is the predicted value.

Fig. 2 shows the statistical distribution of prediction errors on the test set, with an overall average MSE of only 1.93×10^{-4}. These results indicate that the ResNet proxy has good generalization and stability over the parameter space, providing a practical physical basis for subsequent inverse generation.

The architecture and workflow of the proposed inverse design framework are illustrated in Fig. 3. As shown in Fig. 3(a), the cVAE network is trained to learn the mapping between structures and EM responses. The input comprises the structure vector $x \in \{0,1\}^{16\times16}$ and the conditional vector c (normalized reflection phase at 10 GHz). The encoder maps (x, c) to parameters of a latent Gaussian distribution $\mu(x, c)$ and $\sigma^2(x, c)$. A latent vector z is then sampled and passed to the decoder to reconstruct the structure $\hat{x}$. The training loss for the cVAE is defined as $L_{cVAE} = \alpha_{rec}L_{rec} + \alpha_{KL}L_{KL} + \alpha_{FM}L_{FM}$, where L_{rec} is the reconstruction loss, L_{KL} represents the KL divergence term, and L_{FM} stands for the physics-aware forward model loss, which utilizes the pre-trained proxy to constrain the predicted phase of the generated structure and ensure physical consistency.

Fig. 3(b) illustrates the architecture of the forward proxy model. During the inverse generation process, given a target phase ϕ_{tar}, the decoder generates multiple candidate structures by sampling from the prior distribution $p(z)$. These candidates are then fed into the forward proxy model to predict their full-band EM responses. Subsequently, a rigorous screening strategy is applied to filter the results, prioritizing candidates that minimize the phase error at 10 GHz while maximizing spectral smoothness to suppress dispersion. Finally, a 4-bit quantization scheme is selected from the optimal candidates to form the phase library.

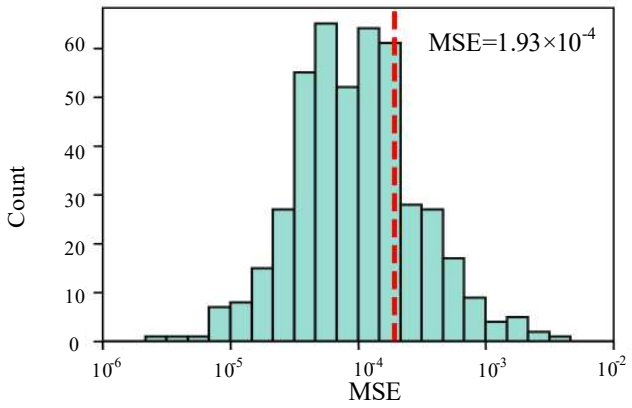


Fig. 2. Performance test and prediction error distribution of the predictor across the entire test samples.

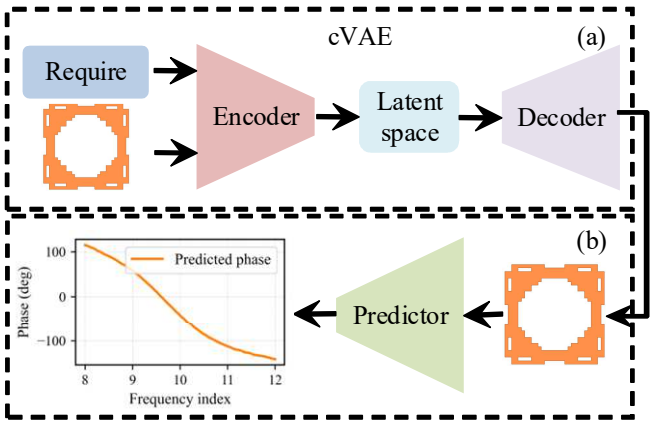


Fig. 3. Architecture of the proposed inverse design framework. (a)Training workflow of the cVAE network. (b)Architecture of the forward proxy model used for phase prediction.

III. EXPERIMENTAL RESULTS

To evaluate the effectiveness of the proposed method, a prototype reflectarray antenna was designed and simulated. As shown in Fig. 4, the RA consists of an 18×18 element array. It is fed by a linearly polarized horn antenna with a focal length-to-diameter ratio (F/D) of 0.85. The main beam direction was preset to Φ_{MAX}=20°, and aperture size P = 180 mm.

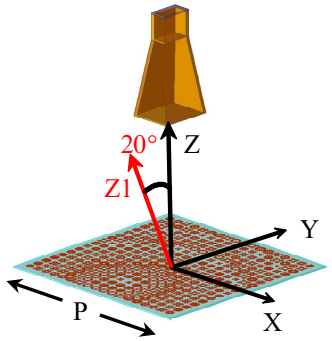


Fig. 4. Schematic of the normal-feed reflectarray.

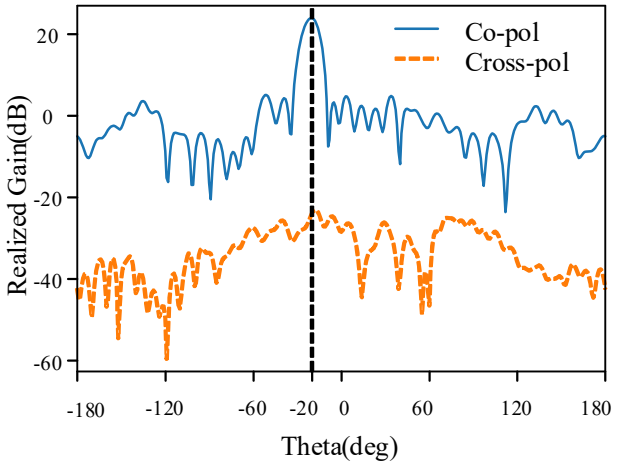


Fig. 5. Simulated radiation patterns of the reflectarray at 10 GHz.

Fig. 5 presents the simulated radiation pattern of the proposed antenna at 10 GHz. The simulated realized gain is 23.9 dB, with a first sidelobe level (SLL) of -19.6 dB and a cross-polarization level below -47 dB. The simulation results confirm accurate beam pointing at the preset 20° angle.

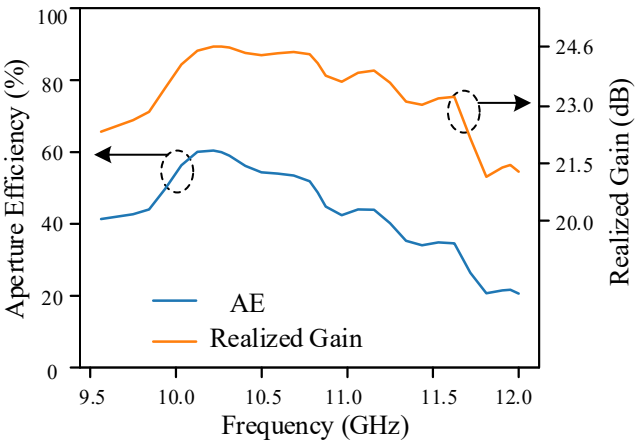


Fig. 6. Comparison of the simulated actual gains and aperture efficiencies of the proposed RA in the 9.5-12 GHz frequency range.

Fig. 6 illustrates the simulated gain and aperture efficiency across the 9.5-12 GHz frequency range. The maximum simulated gain is 24.6 dB, corresponding to a peak aperture efficiency of approximately 60.4%. The antenna exhibits a 3-dB gain bandwidth exceeding 21%, verifying the effectiveness of the optimization method over the considered band.

IV. Conclusion

This paper presented a physics-guided cVAE framework for the efficient inverse design of reflectarray antennas. By integrating a high-precision ResNet forward proxy into the generative model, we established a robust link between complex geometric topologies and electromagnetic responses. The approach successfully automated the generation of a 4-bit coding element library, which was utilized to design an 18×18 element reflectarray. Simulation results confirmed high gain, low sidelobes, and wide bandwidth.

Acknowledgment

This work was supported in part by the Guangdong Basic and Applied Basic Research Foundation under Grant 2024A1515010254, in part by Shenzhen Science and Technology Program under Grant SGDX20230821100459006, KJZD20240903100200001, and in part by the State Key Laboratory of Radio Frequency Heterogeneous Integration (Independent Scientific Research Program No. 2024005).

References

[1] G.-B. Wu, Y.-S. Zeng, K. F. Chan, B.-J. Chen, S.-W. Qu and C. H. Chan, "High-gain filtering reflectarray antenna for millimeter-wave applications", IEEE Trans. Antennas Propag., vol. 68, no. 2, pp. 805-812, Feb. 2020.

[2] J. A. Joy, S. K. Palaniswamy, S. Kumar, M. Kanagasabai, S. Bashyam and M. I. Hussein, “Modern Reflectarray Antennas: A Review of the Design, State-of-the-Art, and Research Challenges,” IEEE Access, vol. 12, pp. 46717–46740, 2024.

[3] Y. Bao, S. Liao, X. Ren, and K. Tang, “Millimeter-wave Wideband Wide-Angle Scanning Tightly Coupled Monopole Reflectarray with Simplified Structure,” in 2025 IEEE MTT-S Int. Wireless Symp. (IWS), 2025, pp. 1–3.

[4] X. -C. Zhu, P. -P. Zhang, Y. -X. Zhang, J. -X. Ge and Z. -H. Gao, "A highgain filtering antenna based on folded reflectarray antenna and polarization-sensitive frequency selective surface," IEEE Antennas Wirel. Propag. Lett, vol. 19, no. 8, pp. 1462-1465, Aug. 2020.

[5] D. E. Serup, G. F. Pedersen and S. Zhang, "Electromagnetically controlled beam-steerable reflectarray antenna," IEEE Trans. Antennas Propag., vol. 71, no. 5, pp. 4570-4575, May 2023.

[6] Y. Lyu, T. H. Gan, and Z. N. Chen, "TE–TM Balanced Wide-Angle Metacells for Low Scan-Loss Metalens Antenna Using Prior Knowledge-Guided Generative Deep Learning-Enabled Method," IEEE Trans. Antennas Propag., vol. 73, no. 5, pp. 2940-2949, May 2025.

[7] P. Liu and Z. N. Chen, "Full-Range Amplitude–Phase Metacells for Sidelobe Suppression of Metalens Antenna Using Prior-Knowledge-Guided Deep-Learning-Enabled Synthesis," IEEE Trans. Antennas Propag., vol. 71, no. 6, pp. 5036-5045, Jun. 2023.

Semiconductor-grade Dry Nano-Island Coating Technology: Translating Advanced Materials from Lab Scale to Next-Gen 6G mm-Wave Substrates

Hung-Wei Wu
Laboratory for New Materials in Nano and Millimeter Waves
Institute of Semiconductors, Guangdong Academy of Sciences
Guangzhou, China
hwwu@ieee.org

Shuai Sun
Laboratory for New Materials in Nano and Millimeter Waves
Institute of Semiconductors, Guangdong Academy of Sciences
Guangzhou, China
sunshuai@gdisit.com

Muhammad Waqas
Laboratory for New Materials in Nano and Millimeter Waves
Institute of Semiconductors, Guangdong Academy of Sciences
Guangzhou, China
muhammadwaqas@gdisit.com

Deniz Eren Erisen
Laboratory for New Materials in Nano and Millimeter Waves
Institute of Semiconductors, Guangdong Academy of Sciences
Guangzhou, China
dengren@gdisit.com

Abstract—The emerging 6G, satellite, and low-altitude communications landscape is increasingly limited not by antenna topology alone, but by the coupled behavior of filler surfaces, polymer interphases, conductor roughness, void populations, and three-dimensional part geometry. This invited talk introduces a semiconductor-grade dry nano-island coating platform intended to control that coupling from the powder surface upward.

The platform combines high-vacuum physical vapor deposition, gas-phase nanoparticle formation, and controlled electrostatic adsorption to populate carrier powders with discrete functional nano-islands rather than continuous films. The operation is dry: no solution-phase reducing agents, dispersants, surfactants, or solvent residues are introduced. Functional loading is controlled at the ppm level (typically 100-10,000 ppm), enabling surface-specific modification without indiscriminate bulk addition. Island morphology and coverage are assessed by SEM; WDXRF/XRF screening, ICP confirmation, and gravimetric mass balance provide a traceable loading-control framework.

The engineered powders are converted into low-polarity dielectric composites through vacuum mixing and degassing, B-stage film casting, and programmed vacuum hot pressing. The laboratory process is designed for coupon-to-panel builds up to 300 x 300 mm, with spacer-defined thickness flexibility appropriate to both planar substrates and thicker structural laminates. The central technical objective is not a single headline dielectric number; it is a defensible evidence chain linking surface morphology and loading to laminate microstructure, dielectric response, transmission-line behavior, and final antenna performance at the frequency of use.

Device-level validation will center on frequency-specific RF coupons, 28-GHz-class planar radiators, Ka-band and circularly polarized array concepts, and measurement protocols that report S-parameters, insertion loss, radiation pattern, and polarization behavior with the relevant specimen construction and fixture. An industry-facing low-altitude-economy pilot with Pure Base extends the same platform to lightweight conformal antenna windows, redone-like covers, and RF-transparent structural skins for unmanned aerial systems. These are materials and integration POC articles, not airworthy or flight-certified hardware, and will be assessed only against defined geometries, frequency bands, environmental conditions, and test methods.

The proposed collaboration model is deliberately application-led: antenna designers, satellite and UAV integrators, RF-packaging teams, and substrate manufacturers define the use case, geometry, stack-up, and qualification target; the laboratory contributes dry surface engineering, materials/forming design, and a measurement plan. The objective is not to sell a generic sheet, but to establish a disciplined route from nano-engineered powder to application-specific mm-wave hardware.

Keywords—Nano-island coating, 6G mmWave substrates, core–shell dielectric fillers, PVD composite materials, ultra-low loss dielectrics, phased array antennas, structurally integrated RF materials, vacuum annealing, electromagnetic functional composites

©2026 IEEE AWMS-AMP

D band Terahertz Driving Source Based on GaN Monolithic Integrated Frequency Multiplier

Yuhang Li
The CAS Key Laboratory of Microwave Remote Sensing, National Space Science Center
Beijing, China
liyuhang@nssc.ac.cn

Jun Shi
The CAS Key Laboratory of Microwave Remote Sensing, National Space Science Center
Beijing, China
shijun@mirslab.cn

Xiaomeng Zheng
The CAS Key Laboratory of Microwave Remote Sensing, National Space Science Center
Beijing, China
zhengxiaomeng@nssc.ac.cn

Jin Meng
The CAS Key Laboratory of Microwave Remote Sensing, National Space Science Center
Beijing, China
mengjin@mirslab.cn

Dehai Zhang
The CAS Key Laboratory of Microwave Remote Sensing, National Space Science Center
Beijing, China
zhangdehai@mirslab.cn

***Abstract*—**Terahertz technology, characterized by its extensive development potential and broad application prospects, has emerged as a significant trend in future technological development. The radio-frequency (RF) front - end of a terahertz superheterodyne receiver is primarily composed of a mixer and a local oscillator (LO). Consequently, as the core component of the RF front-end, the LO is critical to the proper operation of the entire superheterodyne system. The solid-state terahertz LO, which typically utilizes a Schottky diode-based multiplier as its core component, offers notable advantages such as high reliability, room-temperature operation, simple architecture, and low cost. These characteristics have led to its application in diverse fields , including meteorological detection, radio astronomy, and security inspection, thereby solidifying its status as a critical branch of terahertz source research.

The architecture of a solid-state terahertz LO consists of a pre-stage driver source and a final-stage multiplier. Given that the driver source, serving as the initial part of the entire LO chain, primarily supplies input power to the final-stage multiplier, enhancing its output power effectively is of great significance.

To enhance power-handling capacity and thermal-dissipation performance, a 120 GHz driver source based on a GaN monolithic integrated multiplier is developed. Due to the advantages of GaN material, such as high thermal conductivity, high voltage withstand capability and high electron saturation rate, when utilized in Schottky diodes for frequency doublers, its defect in electron mobility is avoided. For the evelopment f the 120 GHz driver source based on a GaN monolithic integrated frequency doubler, a uitable overall link composition scheme is proposed. The overall frequency generation chain adopts a frequency multiplication scheme of 10 GHz microwave signals through a ×6×2 cascade.

Through an analysis of GaN material properties and their applicability to doubler design, a novel GaN Schottky diode design is conceived. Schottky barrier diodes applied to terahertz frequency doublers typically operate under relatively high input power, making the internal self-heating effect non-negligible. Under actual operating conditions, material properties such as electrical conductivity, thermal conductivity, and heat capacity for each diode layer will change with temperature. Meanwhile, the internal temperature and parameters such as current, parasitic capacitance and parasitic resistance will affect each other. Therefore, the saturation current and series resistance parameters in the commonly used SPICE model of Schottky diodes are not constant but rather temperature-dependent variables. The intrinsic and extrinsic parameters that are temperature-dependent change with the operating state, significantly affecting the I-V characteristics of the diode. Therefore, the study of the thermal effect of Schottky barrier diodes cannot be ignored, as it is crucial for improving model accuracy. To this end, a thermal resistance matrix is integrated into the diode model. The physical electrothermal model is composed of the drift-diffusion equation and the heat conduction equation. Furthermore, the impact of adjacent metallized components in the matching structure on heat dissipation is analyzed. The physical electrothermal model is composed of the drift-diffusion equation and the heat conduction equation, as shown in Fig. 1(a), and the coupling solution process used is shown in Fig. (b).

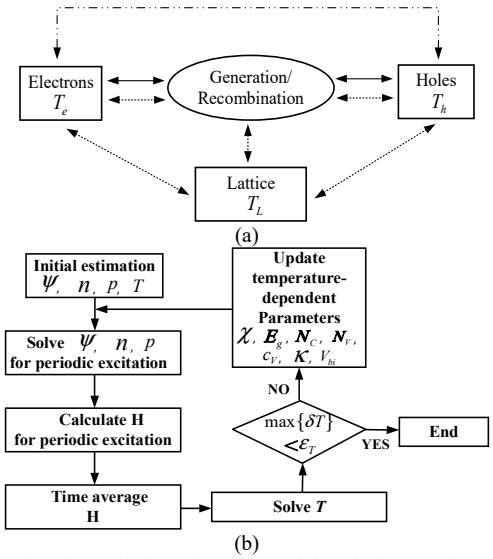


Fig. 1. The physical electrothermal model and the coupling solution process: (a) Interactions among the subsystems of carriers and lattice, (b) The decoupling process of solving the heat conduction equation and the electrical equation

n and p are the electron and hole concentrations, ψ is the electrostatic potential, χ is the electronic affinity, E_g is the energy gap, T is the temperature, N_C and N_V denote the

effective density of states for the conduction band and in the valence band, ε_T is the error bound, $\max\{\delta T\}$ is the maximum error of the temperature distribution achieved through the device in two successive iterations.

The design of the 120 GHz monolithic doubler adopts a balanced circuit structure, mainly consists of WR15 input waveguide, WR8 RF waveguide, GaN Schottky diode, DC bias filter and matching circuit structure, as shown in Fig. 2. For the fundamental frequency matching network, matching performance is optimized by tuning the lengths of the reduced-height and reduced-width waveguide sections, as well as the position of the input short-circuit termination. The optimal output impedance value extracted from the chip is substituted into the lumped port of the diode. For the design of the output end model, the bias circuit adopts an improved compact microstrip resonator (CMRC) filter, which offers a more compact structure than conventional high and low impedance filters. This design effectively confines the second-harmonic signal to the output waveguide port while preventing it from leaking from the DC bias circuit, thus meeting the design requirements.

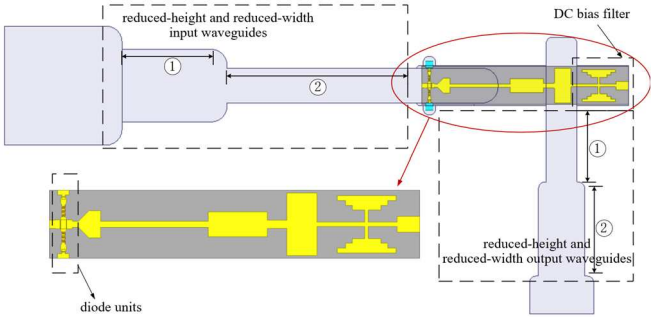


Fig. 2. Overall model of 120 GHz frequency doubler.

The measured results demonstrate that incorporating the thermal resistance matrix into the core diode model significantly reduces the discrepancy between simulated and experimental results. Within the frequency range of 109-129 GHz, the measured maximum output power of the driver source measured is 35.56 mW. This research provides beneficial ideas for the manufacturing and design of Schottky diodes, and further lays a model foundation for the subsequent realization of high-performance terahertz frequency conversion devices.

Keywords—Local oscillator source, Terahertz, GaN Schottky Diode, Frequency multiplier

Resonant Tunneling Diodes for Terahertz Sensing

Safumi Suzuki
Institute of Integrated Research,
Institute of Science Tokyo
Tokyo, Japan
safumi@first.iir.isct.ac.jp

***Abstract*— Resonant tunneling diodes (RTDs) can oscillate at frequencies exceeding 2 THz at room temperature and generate milliwatt-level output power above 800 GHz. In the frequency range above 300 GHz, RTDs have demonstrated relatively high DC-to-RF conversion efficiency compared with other electronic devices. RTDs also exhibit unique functionalities, such as frequency-comb generation and signal detection, which are useful for terahertz sensing applications. This paper reviews recent developments in RTD oscillators.**

Keywords—terahertz, resonant tunneling diode, oscillator

I. Introduction

Terahertz (THz) waves, typically defined in the frequency range from approximately 100 GHz to 10 THz, occupy the spectral region between microwaves and optical waves [1]. Since around 2000, research on the generation and detection of terahertz signals has expanded rapidly. Early development was largely driven by photonic technologies such as terahertz time-domain spectroscopy using femtosecond lasers, parametric sources, and difference-frequency generation. These approaches demonstrated the potential of terahertz waves for applications including spectroscopy, imaging, and sensing. However, practical deployment has remained limited because photonic terahertz systems are often large, complex, and expensive.

In recent years, electronic terahertz devices have attracted increasing attention as compact and cost-effective alternatives. Among them, resonant tunneling diodes (RTDs) are particularly promising for terahertz applications [2-5]. RTDs utilize quantum mechanical resonant tunneling through a double-barrier heterostructure, which results in a negative differential resistance (NDR) region in the current–voltage characteristics. This property enables high-frequency oscillation when the device is integrated with a resonant circuit.

II. Terahertz RTD Device

RTD oscillators have demonstrated oscillation frequencies exceeding 2 THz at room temperature [6]. In addition, they can generate milliwatt-level output power at frequencies above approximately 800 GHz [7, 8]. Compared with other electronic devices operating above 300 GHz, RTDs show relatively high DC-to-RF conversion efficiency [3]. These features make RTDs one of the most promising solid-state electronic sources in the terahertz frequency range.

Another important characteristic of RTDs is their multifunctionality. In addition to oscillation, RTDs can exhibit frequency-comb generation and signal detection capabilities [9-12]. These unique properties enable various sensing architectures using a single device platform. For example, RTD oscillators can be used as local oscillators, transmitters, and detectors in terahertz sensing systems. This versatility simplifies system configuration and allows compact implementations.

Based on these advantages, RTD devices have been explored for a variety of terahertz sensing applications. Examples include radar sensing, spectroscopy, imaging, and short-range wireless sensing systems. The small device size and relatively high output power enable highly integrated terahertz modules, which are suitable for portable or embedded sensing platforms.

In summary, resonant tunneling diodes provide a compact and efficient electronic platform for terahertz signal generation and detection. Their capability for high-frequency oscillation, relatively high conversion efficiency, and multifunctional operation makes them highly attractive for terahertz sensing systems. Continued progress in device design and system integration is expected to further advance RTD-based terahertz technologies and enable practical sensing applications in the near future.

Acknowledgment

This work was supported by a scientific grant-in-aid (24H00031) from JSPS, CREST (JPMJCR21C4) from JST, X-NICS (JPJ011438) and ARIM (JPMXP1224IT0018, JPMXP1224IT0019) from MEXT, ATLA (JPJ013268), and the ROHM Company.

References

[1] A. Leitenstorfer et al. J. Physics D: Applied Physics, 56 (2023) 223001.
[2] M. Asada and S. Suzuki, Sensors, 21, 4 (2021) 1384.
[3] S. Suzuki and M. Asada, Appl. Phys. Express, 17, 7 (2024) 070101.
[4] Y. Koyama, et al.. IEEE Transactions on Terahertz Science and Technology, 12, 5 (2022) 510–519.
[5] https://www.rohm.com/news-detail?news-title=2025-01-15_news_terahertz&defaultGroupId=false
[6] Y. Yoshida, T. Sato, M. Asada, and S. Suzuki, Proceedings of the International Conference on Infrared, Millimeter, and Terahertz Waves (IRMMW-THz), Perth (2024) pp.1–2.
[7] H. Tanaka, H. Fujikata, F. Han, T. Shimura and S. Suzuki, Appl. Phys. Express, 18 (2025) 111001.
[8] F. Han, T. Shimura, H. Tanaka and S. Suzuki, IEEE Transactions on Terahertz Science and Technology, in press.
[9] T. Hiraoka, Y. Inose, T. Arikawa et al., Nature Communications, 13 (2022) 3740.
[10] Y. Nishida, N. Nishigami, S. Diebold, J. Kim, M. Fujita and T. Nagatsuma, Scientific Reports, 9, 1 (2019) 18125.
[11] Y. Li, Y. Nishida, T. Sagisaka, R. Kaname, R. Mizuno, M. Fujita and T. Nagatsuma, Journal of Lightwave Technology, 39, 24 (2021) 7850–7861.
[12] M. Asada and S. Suzuki, Proceedings of the International Conference on Infrared, Millimeter, and Terahertz Waves (IRMMW-THz) (2024) pp.1–2.

XXX-X-XXXX-XXXX-X/XX/$XX.00 ©20XX IEEE

Dual-Wideband Antenna Decoupling via Hybrid Conduction-Radiation Mitigation

Meng Xing
College of Electronic Information Engineering
Nanjing University of Aeronautics and Astronautics
Nanjing, China
2207825975@qq.com

Shaobin Liu
College of Electronic Information Engineering
Nanjing University of Aeronautics and Astronautics
Nanjing, China
lsb@nuaa.edu.cn

Tianyu Shi
College of Electronic Information Engineering
Nanjing University of Aeronautics and Astronautics
Nanjing, China
sty196@nuaa.edu.cn

***Abstract*—This paper presents a hybrid decoupling strategy that synergistically integrates defected ground structures and metallic reflectors to address the strong long-distance mutual coupling problem in dual-antenna systems sharing a common ground plane over the 0.8-2.0 GHz band, where surface creeping waves dominate. Through full-wave simulations, we first characterize the surface current propagation on the metallic ground plane, identifying the central region between the two antennas as the critical coupling path. Based on this analysis, we design a transverse slotted defected ground structure (Mode 1) that perturbs the surface current distribution to effectively suppress low-frequency coupling. Concurrently, we introduce a folded metallic reflector (Mode 2) that modifies the propagation paths of high-frequency spatial waves, enhancing energy dissipation through reflection and phase manipulation. The synergistic integration of both mechanisms (Mode 3) is rigorously validated through full-wave simulations, demonstrating an average isolation enhancement exceeding 17 dB across the entire 0.8-2.0 GHz band. Our results reveal the complementary nature of the proposed approach: the defected ground structure outperforms the reflector at lower frequencies, while the reflector exhibits superior decoupling at higher frequencies. The combined strategy achieves broadband synergistic decoupling, offering a structurally simple and cost-effective engineering solution for high-isolation integration of multi-antenna systems on metallic platforms.**

Keywords—Antenna Decoupling, Surface Wave Suppression, Defected Ground Structure, Metallic Reflector, Hybrid Strategy

I. Introduction

The evolution of wireless communication systems toward multifunctionality and high integration has necessitated the colocation of multiple antennas on shared platforms. In typical platforms such as aircraft, ships, and vehicles, antennas often share a common metallic ground plane, leading to severe electromagnetic coupling that critically degrades system performance [1]. While direct spatial waves attenuate with increasing antenna separation, surface creeping waves propagating along the metallic ground plane maintain low-loss long-distance coupling, emerging as the dominant mechanism deteriorating isolation [2].

Substantial research efforts have been dedicated to decoupling co-ground antennas. Electromagnetic bandgap structures effectively suppress surface wave propagation through periodic resonant elements that create forbidden bands [3]; however, their characteristic dimensions often prove prohibitive for compact platform integration. Defected ground structures introduce patterned slots on the ground plane to perturb current distributions [4], effectively disrupting surface wave propagation paths. Metallic reflectors, as structurally simple passive devices, modify spatial wave propagation directions through reflective path control, achieving effective coupling suppression at higher frequencies. While each approach offers distinct advantages, single-structure solutions struggle to simultaneously address both conductive and radiative coupling across wide frequency bands.

This work systematically analyzes the coupling mechanisms in co-ground dual-antenna systems operating over 0.8-2.0 GHz, establishing that surface creeping waves dominate at lower frequencies while spatial radiation coupling prevails at higher frequencies. Building on this understanding, we propose a hybrid decoupling strategy centered on low-frequency blocking and high-frequency reflective control: a transverse slotted defected ground structure perturbs low-frequency surface current distributions, while a metallic reflector modifies high-frequency spatial wave propagation paths. Simulation results validate the efficacy of this approach and reveal the frequency-dependent dominance of each decoupling mechanism, providing a structurally simple yet innovative solution for high-isolation integration of multi-antenna systems on metallic platforms.

II. System Configuration

The dual-antenna system under investigation is configured as depicted in Figure 1. Two wideband dipole antennas are symmetrically positioned at opposite ends of an elongated metallic ground plane, measuring 60 cm (length) × 8 cm (width) × 0.3 cm (height), with a center-to-center spacing of 50 cm. This configuration yields an electrical separation of approximately 1.6λ at the lowest operating frequency of 0.8 GHz and 4λ at the highest frequency of 2.0 GHz, thereby effectively emulating the relatively large antenna spacing commonly encountered in practical engineering scenarios. The antennas operate across a 0.8-2.0 GHz band, achieving a substantial 85% relative bandwidth with a reflection coefficient (S11 < -10 dB) that satisfies the impedance matching prerequisites for broadband communication systems.

This setup is meticulously designed to replicate real-world antenna deployments on elongated metallic platforms, such as vehicular communication mounts, ship deck edges, aircraft fuselage surfaces, and equipment chassis. In these

979-8-3315-4544-4/26/$31.00 ©2026 IEEE

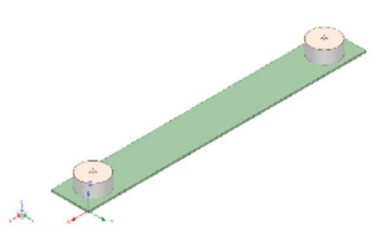


Figure 1. Schematic of the dual-antenna system configuration.

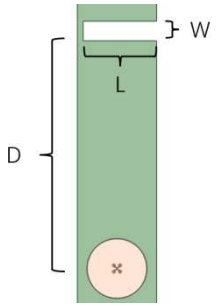


Figure 2. Parameter definition for the defected ground structure.

applications, antennas are frequently constrained to the periphery or extremities of the structure. Limited by platform dimensions, the antennas share a common ground plane with constrained separation, which inherently exacerbates surface-wave coupling. Consequently, this configuration serves as an engineering-representative testbed for investigating the dominant challenge of strong coupling over extended distances via surface waves and for validating effective decoupling methodologies.

III. Hybrid Decoupling Structure Design

A. *Defected Ground Structure for Low-Frequency Decoupling (Mode 1)*

Based on the preceding mechanism analysis, we propose a transverse slotted defected ground structure, hereafter denoted as Mode 1. This structure introduces patterned slots in the ground plane region between the transmitting and receiving antennas, extending inward from one long edge (60 cm side) of the ground plane. To maintain common ground characteristics, the slot depth remains less than the ground plane width (8 cm), with complete penetration through the plate thickness (3 mm). Key geometric parameters include slot length L, slot width W, and distance D from the transmitting antenna, as illustrated in Figure 2.

The decoupling mechanism of the defected ground structure operates through the introduction of slot patterns that deliberately alter surface current flow paths, increasing the electrical path length and thereby disrupting the in-phase superposition conditions of surface waves. This perturbation forces surface currents, originally concentrated along the direct inter-antenna path, to detour, with partial energy reflected or dissipated, consequently reducing coupled energy reaching the receiving antenna. Unlike physical current interruption, the defected ground structure more accurately achieves surface wave propagation suppression through impedance discontinuities [5].

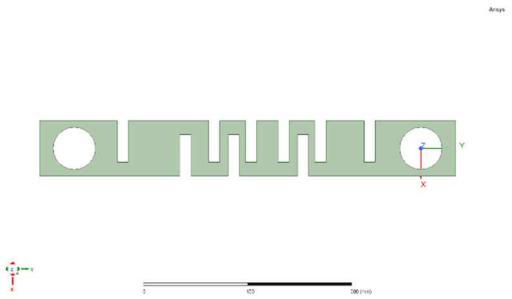


Figure 3. Optimized platform configuration with defected ground structure (Mode 1).



Figure 4. Metallic reflector installation configuration (Mode 2).

Following comprehensive optimization, the defected ground structure adopts a multi-slot configuration with the following parameters: L = 69.3 mm, W = 15.9 mm, with slot positions D distributed at 65.9 mm, 145.8 mm, 162.1 mm, 190.3 mm, 236.7 mm, 261.9 mm, 289.5 mm, 306.3 mm, 331.1 mm, and 522.5 mm. Simulation results demonstrate that Mode 1 achieves an average S21 reduction of approximately 14.5 dB in the low-frequency range, effectively suppressing low-frequency surface wave coupling. Notably, Mode 1 exhibits superior decoupling performance compared to the subsequently introduced reflector scheme in the low-frequency regime.

The final optimized platform configuration is presented in Figure 3.

B. *Metallic Reflector for High-Frequency Decoupling (Mode 2)*

To mitigate the dominant spatial radiation coupling in the high-frequency band, we introduce a folded metallic reflector (Mode 2). Fabricated from aluminum, identical to the ground plane material, the reflector employs a folded configuration to achieve a low-profile, dual-faceted structure (vertical and horizontal sections) measuring 80 mm × 40 mm × 1 mm. It is strategically mounted on the ground plane between the two antennas. The underlying decoupling mechanism is threefold: path modulation, which redirects the original propagation trajectory of high-frequency spatial waves, deflecting direct coupling energy along alternative paths; phase interference, which introduces a phase differential between the reflected and direct waves at the receiving antenna—when this differential approaches 180°, partial destructive interference ensues; and near-field redistribution, which restructures the reactive field distribution between the antennas, thereby attenuating field-strength concentrations that facilitate high-frequency coupling. The synergy of these mechanisms culminates in robust suppression of spatial radiation coupling in the high-frequency regime.

The reflector placement is illustrated in Figure 4.

C. *Hybrid Integration Strategy (Mode 3)*

The optimized defected ground structure and metallic reflector are synergistically integrated on the same metallic

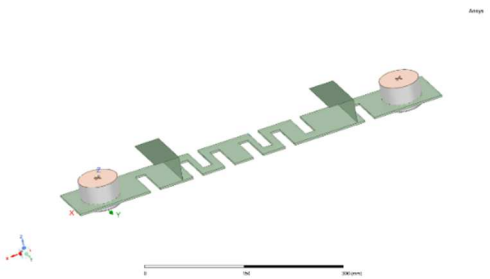


Figure 5. Hybrid decoupling structure integration (Mode 3).

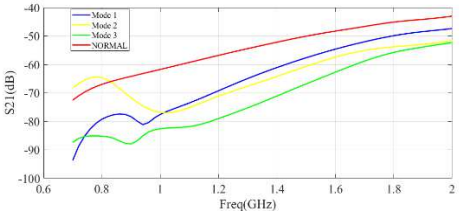


Figure 6. Simulated S21 comparison for different decoupling configurations.

platform, designated as the hybrid decoupling structure Mode 3, depicted in Figure 5. Building on the preceding analysis, the defected ground structure targets low-frequency surface wave suppression, while the metallic reflector mounted on the common ground platform addresses high-frequency spatial wave control. The two structures operate independently, forming a dual-mechanism decoupling framework of low-frequency blocking and high-frequency reflection.

IV. Simulation Validation and Results Analysis

A. Simulation Model and Configuration

To validate the proposed design, we established full-wave simulation models for numerical analysis. Simulations covered the 0.8-2.0 GHz frequency band, utilizing frequency-domain solvers for S-parameter computation. Adaptive tetrahedral meshing was employed with a convergence accuracy of 0.02. All simulations were performed in the HFSS environment.

B. Decoupling Performance Comparison

Figure 6 presents simulated S21 curves for different configurations, while Table 1 summarizes the performance improvements achieved by each scheme.

As evidenced by comparative simulations, the defected ground structure (Mode 1) achieves an isolation enhancement of up to 14.51 dB in the lower frequency band, whereas the metallic reflector (Mode 2) delivers an improvement of 11.34 dB in the upper band—revealing a distinct frequency-domain complementarity between the two mechanisms. By synergistically integrating their respective advantages, the hybrid configuration (Mode 3) attains a compelling 17.13 dB isolation enhancement across the entire operational bandwidth. These results conclusively validate the effective synergy of the proposed "low-band suppression, high-band reflection" strategy.

TABLE I. Performance Comparison of Different Decoupling Configurations

Structure Description	Avg. Isolation Improvement		
	0.8-1GHz	***1-2GHz***	***0.8-2GHz***
Mode 1	14.51 dB	8.46 dB	9.43 dB
Mode 2	7.02 dB	11.34 dB	10.49 dB
Mode 3	21.24 dB	16.31 dB	17.13 dB

V. Conclusion

Full-wave simulation results clearly demonstrate that the proposed hybrid decoupling strategy—combining low-frequency suppression and high-frequency reflection control—can effectively and robustly mitigate strong mutual coupling in a 0.8–2.0 GHz dual-antenna system sharing a common ground. Specifically, the defected ground structure (DGS) introduces an impedance perturbation mechanism that enhances isolation by approximately 14.5 dB in the lower frequency band, while a metallic reflector achieves around 11.3 dB isolation improvement in the upper band through a carefully tailored and optimized path regulation mechanism. These two distinct physical mechanisms exhibit mutually complementary advantages across the entire frequency domain of interest. When both mechanisms are fully integrated into a unified hybrid decoupling configuration, an average isolation enhancement exceeding 17 dB is reliably attained across the whole operating band, from 0.8 to 2.0 GHz, and all without compromising antenna impedance matching at any single frequency point. The proposed design, relying solely on simple metallic structures and thus completely avoiding any lumped components, offers the clear benefits of low fabrication cost and ease of practical implementation, thereby strongly and convincingly highlighting its practical engineering value for real-world applications. It thereby provides a highly effective and technically sound technical solution for achieving high-isolation integration of multi-antenna systems mounted on metallic platforms.

References

[1] F. Liu, J. Guo, L. Zhao, G. L. Huang, X. Li, and K. W. Leung, "Dual-band metasurface-based decoupling method for two closely packed dual-band antennas," IEEE Trans. Antennas Propag., vol. 68, no. 1, pp. 552-557, Jan. 2020.

[2] S. Zhang and G. F. Pedersen, "Mutual coupling reduction for UWB MIMO antennas with a wideband neutralization line," IEEE Antennas Wireless Propag. Lett., vol. 15, pp. 166-169, 2016.

[3] D. Lorente Catalan, M. Limbach, H. Esteban González, C. B. A. Musso, and P. de Maagt, "Novel multilayer electromagnetic bandgap structure with simultaneously surface-wave suppression in the L, S, C and X-bands," in Proc. IEEE Int. Workshop Antenna Technol. (iWAT), 2026.

[4] K. Wei, J. Y. Li, L. Wang, Z. J. Xing, and R. Xu, "Mutual coupling reduction by novel fractal defected ground structure for UWB MIMO antenna," IEEE Access, vol. 5, pp. 22281-22286, 2017.

[5] Y. Liu, L. Bian, K. Xu, L. Wang, Y. Zhang, and J. Shi, "A pattern-reversal wideband antenna integrating metal rings, diodes-loaded stubs and defective ground," IEEE Open J. Antennas Propag., vol. 3, pp. 722-731, 2022.

Surface Mount Radiator - Intelligent AiP for Physical AI and Edge Devices

Dr. Yifan Wang

Director, MILLIBEAM, Sydney, NSW, Australia
Visiting Professor, School of Electrical and Data Engineering, University of Technology Sydney, Australia

yifan.wang@millibeam.com

Abstract: The rapid growth of 5G/6G, satellite communications, and AI-enabled edge devices is driving strong demand for compact, high-efficiency, and scalable antenna platforms. This presentation presents recent developments in surface-mounted Antenna-in-Package (AiP) technologies at MILLIBEAM, focusing on antenna radiation engineering, low-profile array architectures, RF materials, and integrated packaging approaches. The presentation highlights how advanced surface-mounted AiP platforms can enable intelligent RF systems for next-generation wireless infrastructure, sensing, Physical AI, and edge applications through vertically integrated "Silicon to Intelligent RF Systems" design strategies.

Yifan Wang is an Electromagnetics Scientist and RF Engineer with hybrid experience in research and development. He has established himself as a prominent figure in the field, specialising in various facets of electromagnetics engineering and research. With a Doctor of Philosophy (PhD) in Electrical Engineering from the University of Queensland, Australia, Yifan's academic journey has been marked by groundbreaking research in microwave devices and techniques, particularly in the realm of Phased array antennas and Computational electromagnetics.

Yifan's professional trajectory spans academia and industry, showcasing his versatility and leadership in both domains. He has held roles such as Director (Antenna Engineering) at Millibeam Corp in Sydney, Australia, where he spearheaded R&D initiatives in the burgeoning 5G/6G antenna market. His contributions have been instrumental in defining new product lines and fostering technical innovation within RF/Antenna teams. Prior to his current role, Yifan served as a Principal Antenna/Packaging Engineer at Movandi Corp in Irvine, USA, where he led diverse R&D activities ranging from phased array antenna module (PAAM) design for 5G gNodeB applications to pioneering research in transformation optics and frequency selective surfaces. His tenure saw the successful commercialisation of cutting-edge antenna solutions, cementing his reputation as a visionary leader in the field. Before joining Movandi, he was a Lecturer and an Advanced Queensland Industry Fellow at the University of Queensland. Through these roles, he has contributed significantly to the academic community, supervising PhD candidates, teaching postgraduate courses, and spearheading research endeavours in computational electromagnetics and microwave engineering.

Throughout his career, Yifan has amassed a prolific publication record, with 60+ papers published in esteemed journals and presented at international conferences. His research has garnered widespread recognition, evidenced by his extensive list of patents and research grants as Chief Investigator.

979-8-3315-4544-4/26/$31.00 ©2026 IEEE

A Classification of Scattering Characteristics for Typical Artificial Structures via Attention-Augmented Dual-Branch Convolutional Neural Network

Shuxin Wu
School of Information and Communication Engineering
Communication University of China
Beijing, China
wushuxin@mails.cuc.edu.cn

Yancheng Li
School of Information and Communication Engineering
Communication University of China
Beijing, China
liyc18178297701@163.com

Meijun Qu
National Key Laboratory of Scattering and Radiation
Beijing, China
qumeijun@126.com

Jianxun Su
School of Electronic Engineering
Beijing University of Posts and Telecommunications
Beijing, China
sujianxun_jlgx@163.com

***Abstract*—This paper presents a novel attention-augmented dual-branch convolutional neural network (DBA-Net) for classifying monostatic radar cross-section (RCS) characteristics of six typical artificial structures. A large-scale dataset is generated by computing full-azimuth RCS distribution and converting them into 2D heatmaps. The DBA-Net employs dual branches to extract multi-scale features and a dual-attention mechanism to focus on discriminative patterns. Experiments show the model achieves satisfactory classification accuracy with rapid convergence, demonstrating strong robustness and generalizability for intelligent electromagnetic target recognition.**

Keywords—Radar Cross-Section (RCS), Artificial Structure, Scattering Characteristics, Convolutional Neural Network (CNN), Attention Mechanism, Classification.

I. Introduction

In modern electronic warfare, radar target recognition and electromagnetic characteristic management are of paramount importance. Canonical artificial structures, such as corner reflectors and basic geometric shapes, serve as fundamental scattering elements or decoys, and their distinct radar cross-section (RCS) characteristics are key to target identification and electronic countermeasures [1], [2]. Rapid and accurate classification of these structures from their RCS data is therefore crucial for situational awareness. However, traditional identification methods often rely on expert analysis or manual feature engineering, which can be time-consuming and lack the adaptability required for dynamic battlefield environments [3], [4]. The advancement of deep learning offers a promising data-driven pathway toward automatic and robust classification [5].

To address this need, this paper develops a specialized deep learning framework for the automatic classification of RCS characteristics from six types of canonical artificial structures: the top-hat, sphere, cylinder, dihedral, trihedral corner reflector (TCR), and pyramid corner reflector (PCR), shown in Fig. 1. This work involves constructing a large-scale, parameterized dataset by computing full-azimuth monostatic RCS patterns using validated analytical formulas and transforming them into 2D heatmaps. We propose a novel Dual-Branch Convolutional Neural Network with Attention Enhancement (DBA-Net), which utilizes parallel convolutional pathways to capture multi-scale scattering features and integrates a dual-attention mechanism to adaptively focus on the most discriminative patterns in the RCS characteristics. This tailored approach aims to achieve high-accuracy, real-time classification, providing a potent tool for intelligent electromagnetic target recognition.

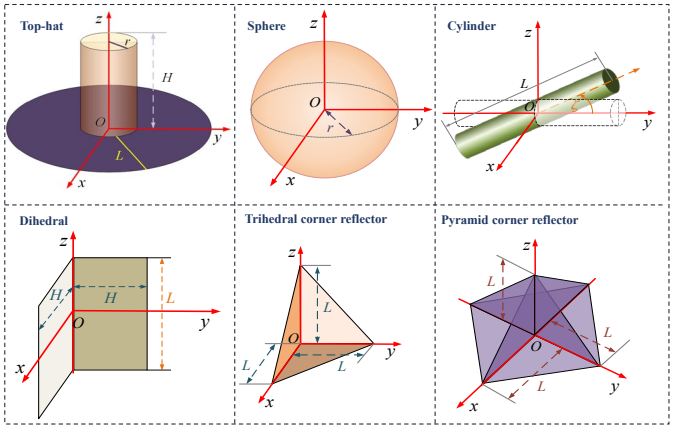


Fig. 1. Typical geometric configurations of man-made structures and definitions of structural parameters.

II. Methodology

A. Fast and Accurate Monostatic RCS Computation Based on PO/Equivalent Area Projection

To generate the large-scale, high-fidelity dataset required for deep learning, an efficient and accurate method for computing the monostatic RCS of the canonical structures is essential. This work employs a hybrid analytical-numerical approach based on Physical Optics (PO) and the Equivalent Area Projection method. This method provides a favorable trade-off between

TABLE I. HIGH-FREQUENCY APPROXIMATE ANALYTICAL FORMULAS AND CORRECTIONS FOR TYPICAL BODIES OF DIFFERENT TYPES

Type	Analytical Formula	Correction
Top-hat	$M=\begin{cases}2H\sqrt{jkr\sin\theta}, & \cot(\theta)\le H/L\\ 2L\cot\theta\sqrt{jkr\sin\theta}, & \cot(\theta)>H/L\end{cases}$ (1)	$M=\begin{cases}\sigma=H\sqrt{jkr}, & \theta=0\\ \sigma=2jk\sqrt{\pi}(r+L)^2, & \theta=\frac{\pi}{2}\end{cases}$ (2)
Sphere	$M=jk\sqrt{\pi}\sum_{n=1}^{\infty}(-1)^n(2n+1)(a_n-b_n)$, $a_n=-\frac{j_n(kr_0)}{h_n^{(1)}(kr_0)}, b_n=-\frac{[krj_n(kr_0)]'}{[krh_n^{(1)}(kr_0)]'}$ (3)	
Cylinder	$M=\sqrt{jk}A\sqrt{\cos\varphi}\,\mathrm{sinc}(kL\sin\varphi\cos\theta),\varphi\in\left[-\frac{\pi}{2},\frac{\pi}{2}\right]$ (4)	
Dihedral	$M_{Dihedral}=\frac{jk}{\sqrt{\pi}}\cdot\sqrt{2}LH\cdot\mathrm{sinc}(kL\lvert\cos\theta\rvert)\cdot\sin\theta\cdot\lvert\sin 2\varphi\rvert,\varphi=[0,\frac{\pi}{2}]$ (5)	
TCR	$M_{TCR}=\frac{jk}{\sqrt{\pi}}\begin{cases}l+m+n-2/(l+m+n) & l+m\ge n\\ 4lm/(l+m+n) & l+m<n\end{cases}$ (6) $([n,m,l]=[\max(\mathbf{r}),\mathrm{mid}(\mathbf{r}),\min(\mathbf{r})]$, $\mathbf{r}=[\sin\theta_0\cos\varphi_0,\sin\theta_0\sin\varphi_0,\cos\theta_0])$	$M_{TCR}=\frac{jk}{\sqrt{\pi}}L^2\begin{cases}1, & \theta=0\\ \min(\sin(\varphi),\cos(\varphi)), & \theta=\pi/2,0<\varphi<\pi/2\\ \min(\sin(\theta),\cos(\theta)), & \varphi=0,0<\theta<\pi/2\end{cases}$ (7)
PCR	The reflection mechanism is basically consistent with that of TCR.	$M_{PCR}=\frac{jk}{\sqrt{\pi}}L^2\begin{cases}4, & \theta=0\\ 2\min(\sin(\varphi),\cos(\varphi)), & \theta=\pi/2,\varphi\ne n\pi/2,n=0,1,2,3\\ 2\min(\sin(\theta),\cos(\theta)), & \varphi=n\pi/2,n=0,1,2,3,0<\theta<\pi/2\end{cases}$ (8)

TABLE II. TYPICAL ARTIFICIAL STRUCTURE DATASET CONFIGURATION

Category	Parameter	Configuration	Category	Parameter	Configuration
Angular Sampling	θ	0°: 2°: 90°	Structure-Specific Parameters	TOPHAT	[r, H, L]
	φ	0°: 0.5°: 360°		Sphere	[r]
Geometric Parameters	r	[0.2, 2] m		Cylinder	[r, L, ζ]
	H	[0.2, 2] m		Dihedral	[H, L, ζ]
	L	[0.2, 2] m		TCR	[r, H, L, ζ]
	ζ	[0, 2π] rad		PCR	[r, H, L, ζ]
Sample Scale	number of samples	2,000	Image Specification	Image Specification	46 × 721 × 3
	total number	12,000 (6×2000)		Color Map Range	-30 dB ~ 40 dB

computational speed and engineering accuracy, enabling the rapid generation of thousands of RCS patterns. The core of this method is an analytical formula derived for each of the six structures by leveraging their specific geometric characteristics and dominant scattering physics (e.g., specular reflection, cavity multiple reflections, edge diffraction). The key formulas are summarized in Table I.

B. Dataset Construction

A high-quality, large-scale dataset is essential for training a deep learning model. Shown in Table II, the dataset based on efficient and validated analytical formulas for the RCS of six structures are generated. For each structure type, 2,000 samples are generated by randomly sampling geometric parameters (radius r, height H, length L, and orientation angle ζ) within specified ranges to ensure diversity. The RCS is calculated across the full angular domain: θ from 0° to 90° with a 2° interval, and φ from 0° to 360° with a 0.5° interval. The resulting RCS matrix for each sample is normalized and converted into a 2D RGB heatmap with a fixed color mapping range of -30 dB to 40 dB. The final dataset comprises 12,000 images, each with a dimension of 46×721×3 and a corresponding class label. Fig. 2 shows sample heatmaps, where distinct patterns are observable.

C. Network Architecture: DBA-Net

The DBA-Net is proposed as illustrated in Fig. 3. The core design philosophy is divide-and-conquer, fuse-and-enhance. The architecture first processes the input RCS heatmap through two parallel convolutional branches: one using 3×3 kernels to capture fine-grained local patterns, and the other using 5×5 kernels to extract broader contextual features. The multi-scale feature maps from both branches are then concatenated. To focus on the most discriminative information, a dual-attention mechanism that comprises channel and spatial attention modules recalibrates the features by emphasizing important channels and spatial regions. These refined features are further processed by a convolutional refinement block, globally pooled, and finally passed through fully connected layers to produce the classification output over the six structure classes.

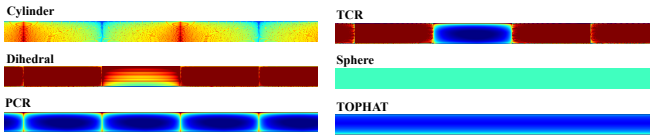


Fig. 2. Sample example of a heat map for typical artificial structures.

III. RESULTS AND ANALYSIS

The DBA-Net was trained for 200 epochs (13,000 iterations) on a single GPU, taking approximately 7 hours and 4 minutes. As shown in Fig. 4(a), both training and validation accuracy curves rose rapidly from the random-guess level (16.7%) to nearly 100% within the first 2,000 iterations and remained stable thereafter, indicating fast convergence and no overfitting. The loss curves in Fig. 4 (b) decreased smoothly and converged close to zero. A piecewise learning rate decay strategy was used,

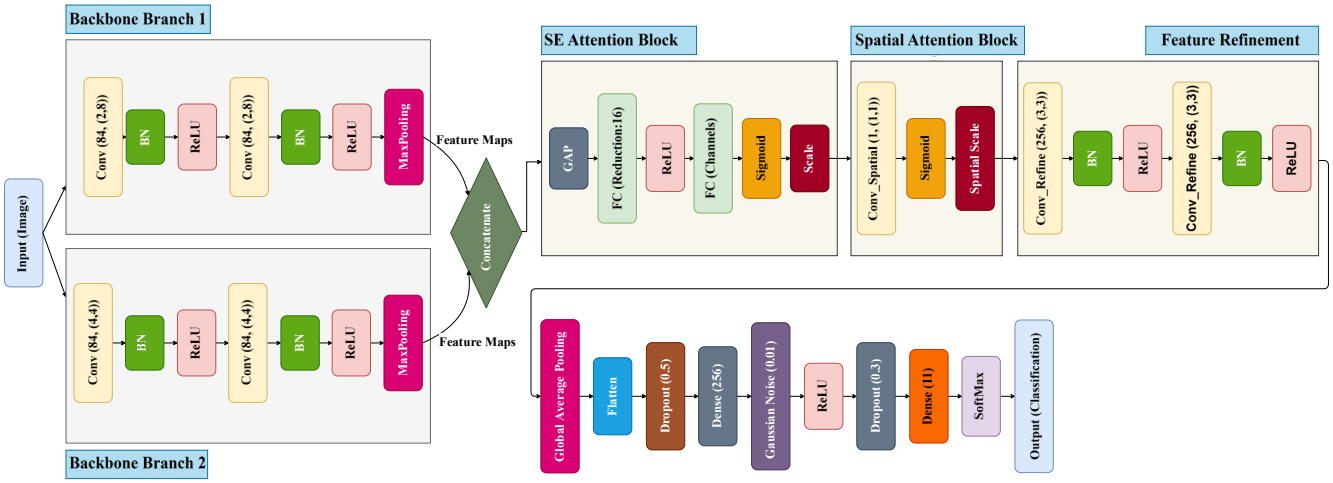
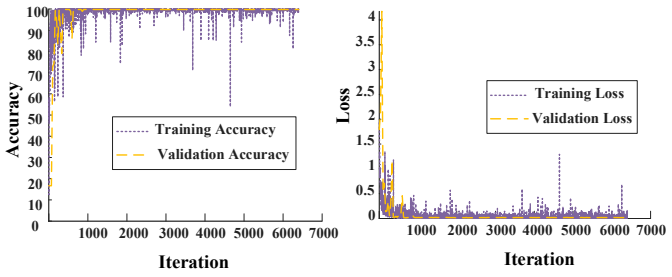


Fig. 3. DBA-Net architecture.



(a) (b)

Fig. 4. Training performance results of the DBA-Net network. (a) Accuracy, (b) Loss.

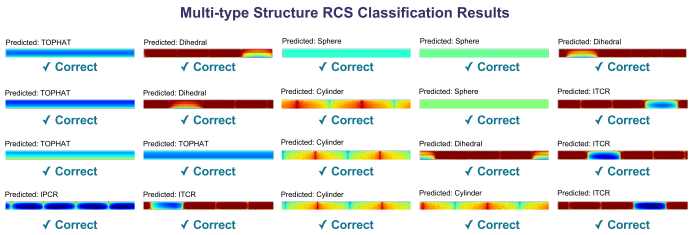
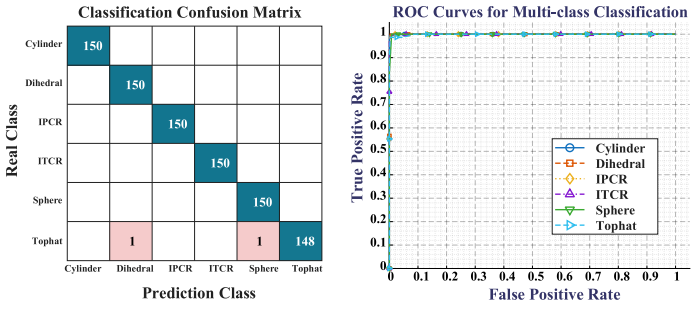


Fig. 5. Verification of DBA-Net Network Prediction Results.



(a) (b)

Fig. 6. Verification of DBA-Net Network Performance Indicators. (a) Confusion Matrix, (b) ROC.

with the final rate reaching 1.9073e-8, ensuring thorough convergence.

The model was evaluated on a held-out test set of 1,800 samples. As shown in Fig. 5, all 20 randomly selected test samples were correctly classified. Quantitatively, the confusion matrix (Fig. 6(a)) shows no misclassifications. The multiclass ROC curves (Fig. 6 (b)) for all classes reach the ideal top-left corner.

IV Conclusion

This paper proposes a novel deep learning framework for automatically classifying scattering characteristics of six canonical artificial structures. By constructing a large-scale parametric RCS dataset and designing the DBA-Net with dual-branch feature extraction and attention mechanisms, achieved satisfactory classification accuracy. The model demonstrates excellent robustness, fast convergence, and strong generalization. It provides a practical tool for intelligent electromagnetic target recognition and has promising applications in electronic warfare for rapid threat assessment. Future work may extend this method to more complex targets or challenging measurement scenarios.

Acknowledgment

This work was supported by National Natural Science Foundation of China (U2441236).

References

[1] P. K. Huang, H. C. Yin, and X. J. Xu, *Radar Target Characteristics*. Beijing, China: Publishing House of Electronics Industry, 2005.

[2] J. Wang, L. Guo, Y. Wei, S. Chai, K. Li, and A. Wang, "Physical mechanism analysis of complex target scattering center based on ISAR image," in *Proc. 13th Int. Symp. Antennas, Propag. EM Theory (ISAPE)*, Zhuhai, China, Dec. 2021, pp. 1–3.

[3] J. Jackson and R. Moses, "Feature extraction algorithm for 3D scene modeling and visualization using monostatic SAR," *Proc. SPIE*, vol. 6237, Jun. 2006.

[4] G. Sun, L. Zhu, S. Xing, J. Wang, D. Feng, and X. Wang, "SAR imaging modulation based on time-modulated corner reflector with wide-angle domain control," *IEEE Antennas Wireless Propag. Lett.*, vol. 22, no. 12, pp. 3157–3161, Dec. 2023.

[5] D. Xiao, L. Guo, W. Liu, and M. Hou, "Efficient RCS prediction of the conducting target based on physics-inspired machine learning and experimental design," *IEEE Trans. Antennas Propag.*, vol. 69, no. 4, pp. 2274–2289, Apr. 2021.

Improved Hybrid Quantum Models for More Accurate Phase Prediction of Expansion Coefficients in Large Finite Periodic Structures

Bingbing Song
State Key Laboratory of Millimeter Waves, School of Cyber Science and Engineering
Southeast University
Nanjing, China
230239719@seu.edu.cn

Zhuoyue Zhao
State Key Laboratory of Millimeter Waves, School of Information Science and Engineering
Southeast University
Nanjing, China
carleezhao@seu.edu.cn

Tian Liu
State Key Laboratory of Millimeter Waves, School of Information Science and Engineering
Southeast University
Nanjing, China
230258109@seu.edu.cn

Fei Guo
State Key Laboratory of Millimeter Waves, School of Information Science and Engineering
Southeast University
Nanjing, China
230248807@seu.edu.cn

Zijun Hu
State Key Laboratory of Millimeter Waves, School of Cyber Science and Engineering
Southeast University
Nanjing, China
230239718@seu.edu.cn

Wu Yang
State Key Laboratory of Millimeter Waves, School of Information Science and Engineering
Southeast University
Nanjing, China
yangwu@seu.edu.cn

Weibing Lu
Southeast University&Donghua University
Shanghai, P.R.China
wblu@seu.edu.cn

***Abstract*—Accurately and efficiently analyzing the electromagnetic characteristics of large finite periodic structures (LFPSs) has always been a challenging problem in computational electromagnetics. In the past decade, several artificial neural networks (ANNs) based studies have been proposed to alleviate this challenge. However, with the rapid development of quantum technologies, the performance of ANN-based predictive models still exhibits significant potential for further improvement. In this paper, the hybrid quantum model proposed in previous work is enhanced by incorporating the residual architecture, enabling more accurate prediction for the phase of the expansion coefficients in sub-entire domain basis functions. Numerical experiments demonstrate that the improved hybrid quantum model exhibits faster learning capability and higher prediction accuracy.**

Keywords—Hybrid quantum models, artificial neural networks, subentire-domain basis functions method, large finite periodic structures

I. INTRODUCTION

Large-scale finite periodic structures constitute the foundation of technologies such as phased-array antennas, absorbers, and meta-surfaces. Traditional numerical methods, such as the subentire-domain (SED) basis functions method [1], [2] can accurately analyze LFPSs, but they require substantial computational time and memory to calculate the mutual coupling among array cells. This bottleneck has recently been mitigated by the application of artificial neural networks (ANNs) [3], [4], which learn the mapping between array parameters and the expansion coefficients of the SED basis functions, thereby avoiding the construction and solution of reduced matrices.

Nevertheless, neural networks still rely heavily on large datasets and extensive training iterations, a limitation that may be alleviated by recent advances in quantum technologies. Unlike classical neural network approaches, quantum technologies provide a fundamentally different computational paradigm [5], [6], [7]. Recently, quantum technologies have been preliminarily explored in the field of electromagnetics. Zhang et al. [8] proposed a quantum computing framework based on the Harrow–Hassidim–Lloyd (HHL) algorithm to solve electromagnetic problems formulated by the finite element method. Colella et al. [9] employed a variational quantum eigensolver with shot-based measurements to simulate waveguide eigenmodes, demonstrating the feasibility of solving the discretized Helmholtz equation on noisy intermediate-scale quantum devices. Ewe et al. [10] developed a variational quantum algorithm (VQA) combined with the finite difference method to compute electromagnetic waveguide propagation modes by minimizing Hamiltonian expectation values on near-term quantum devices. Chen et al. [11], [12]initially applied the HHL quantum algorithm to solve EFIE matrix equations for 3D PEC scatterers and later extended this work by introducing a hybrid quantum-classical scheme that leverages both HHL and VQA algorithms to achieve improved accuracy and efficiency compared to conventional methods. Liu et al. [13] proposed a quantum neural network to estimate the coupling degree of airborne antennas, demonstrating well generalization ability and fast computational speed comparable to artificial neural networks.

In this work, the hybrid quantum model in previous studies [14] is improved to achieve more accurate predictions on the phase of the expansion coefficients of SED basis functions. Specifically, the residual structure is incorporated into the feature mapping module of the hybrid quantum model, enabling the reuse of shallow features to better capture the more challenging phase prediction task. In the proposed framework, the SED method is first employed to compute the SED basis functions for three position-based unit cells. Subsequently, hybrid quantum models with and without the residual structure are used to predict the phase and amplitude of the expansion coefficients, respectively. Finally, a quantum simulator is utilized to implement the proposed quantum framework, and its performance is compared with that of conventional ANNs and residual neural network models. The results demonstrate that the hybrid variational quantum model achieves higher learning efficiency and improved accuracy, particularly under conditions with limited training samples.

979-8-3315-4544-4/26/$31.00 ©2026 IEEE

II. Improved Hybrid Quantum Models

In this paper, the hybrid variational quantum algorithm (HVQA) proposed in previous studies is further improved by incorporating a residual architecture into the feature-mapping component. As illustrated in Figure. 1, the feature-mapping module composed of neural networks contains four hidden layers with 32, 32, 28, and 28 neurons, respectively. The output of the first hidden layer is added to the input of the third hidden layer, forming a residual connection, and the output of the third hidden layer is further added before the variational quantum circuit. Core formula of residual block can be written as follows:

$$x_l = f^l\left(w^l x_{l-1} + b^l\right), l \in \{1,2,4\}$$

$$x_m = x + f^m\left(w^m x_{m-1} + b^m\right), m \in \{3\}$$

$$f_l(\xi) = \max(0,\xi), l \in \{1,2\}$$

$$f_m(\eta) = \frac{e^{\eta} - e^{\eta}}{e^{\eta} + e^{\eta}}, m \in \{3,4\}$$

In addition, the input layer, the variational quantum circuit, and the output layer remain consistent with those in the previous work. By introducing additional hidden layers and residual connections, the model facilitates more effective feature propagation and mitigates the degradation problem in deeper architectures. The residual pathways allow shallow features to be preserved and reused during the mapping process, thereby improving the model's representation capability and enhancing its learning performance on challenging tasks. In addition to the model for phase, the model for predicting amplitude still uses the hybrid variational quantum model structure without residual structure.

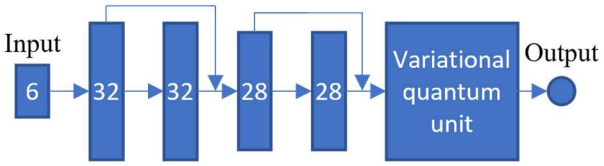


Fig. 1. Improved hybrid quantum models

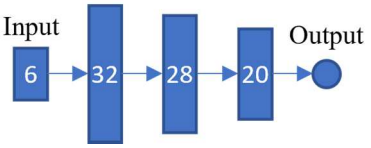
III. Experimental Results

In this chapter, we compared improved HVQA model with residual (HVQA-R) to adaptive ANN (AANN), residual network (ResNet), and HVQA on learning efficiency and accuracy. The HVQA and HVQA-R model is deployed through the quantum simulator PennyLane [15], while AANN and ResNet are implemented through Pytorch. All experiments are run on Intel(R) Core(TM) i9-14900KF 3.20 GHz Nvidia 4090 GPU.

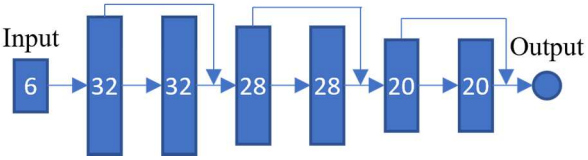
A. Advantages for predicting the phase

The structural diagrams of AANN and ResNet are shown in Figure 2. The hidden layer of ANN contains 6, 32, 28, and 20 neurons. The hidden layer of ResNet is twice the number of neurons in ANN. HVQA model can be referenced in our previous work [14], and it replaces the third hidden layer of AANN with a parameterized quantum circuit containing 20 variable parameters. In addition, the activation functions for configuring neurons in the three methods are the same.

Firstly, the convergence speed of four methods during the first 200 iterations was compared, and the results are shown in Figure 3. When training corner cells (CC) and edge cells (EC) phase, HVQA-R has 75.6% (0.0003 vs. 0.00124) and 62.5% (0.0006 vs. 0.0018) advantage compared to ANN, 72.7% (0.0003 vs. 0.0011) and 45.4% (0.0006 vs. 0.0011) advantage compared to ResNet, and 66.7% (0.0003 vs. 0.0009) and 25% (0.0006 vs. 0.0008) advantage compared to HVQA. When training interior cells (IC) data, HVQA-R showed an improvement of approximately 25% to another three methods, and it is more stable during the training process.

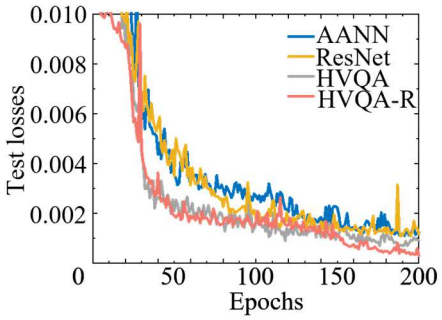


(a) The architecture of AANN.

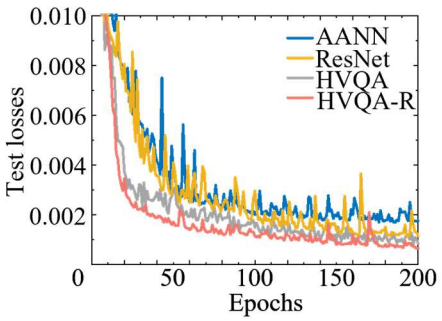


(b) The architecture of ResNet.

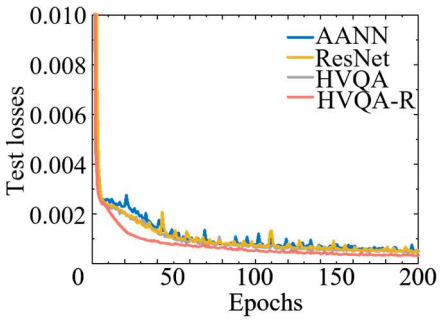
Fig 2. The architecture of the comparison model. (a) AANN (b) ResNet. In addition, the HVQA model can be referenced in our previous work [14].



(a)



(b)



(c)

Fig 3. Test losses of the first 200 training epochs. (a), (b), and (c) show the phase comparison for CC, EC, and IC, respectively.

There are two main reasons why HVQA-R can achieve optimal results. One is that compared to ANN and Resnet, hybrid quantum methods can map classical information to quantum Hilbert space, which can more fully extract potential knowledge from classical information. Another issue is that corner and edge units are affected by edge effects, making their current characteristics more difficult to capture than those of internal units. In addition, incorporating a residual structure into HVQA enables the model to better capture shallow features, thereby enhancing its representational capacity for predicting more challenging phase data. Therefore, HVQA-R can achieve optimal performance, and only a small number of parameters are needed.

B. The effectiveness on bistatic radar cross section

The effectiveness of HVQA-R is verified on the bistatic radar cross section (RCS) of the square-ring antenna array with the array size is 60×60 and the structure period is 0.8λ. The structure of the antenna is shown in Figure 4.

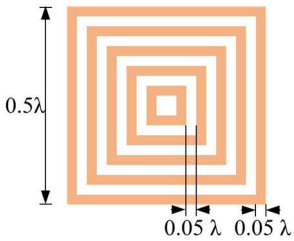


Fig 4. The structure of the square-ring antenna.

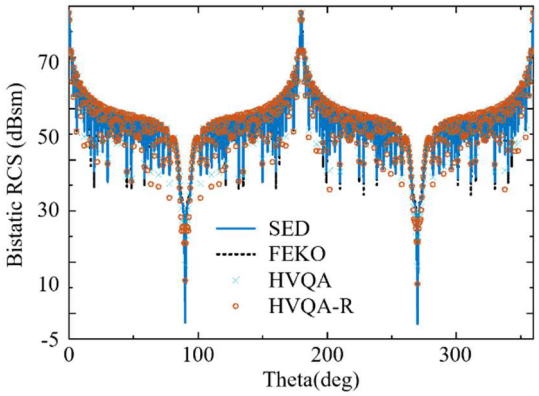


Fig 5. Comparison of RCS with two benchmark algorithms.

The mean absolute error (MAE) of prediction results of HVQA-R on the phase data of CC, EC, and IC is 0.049, 0.039, and 0.059, respectively, which has further improved compared to the accuracy of HVQA(0.08, 0.095, 0.11). The experimental results show that HVQA-R is able to closely match the predictions of the two benchmark algorithms. Furthermore, the errors of HVQA-R relative to SED basis functions method and FEKO are 1.16 dBsm and 1.36 dBsm, respectively, which are lower than the corresponding errors of HVQA, 1.33 dBsm and 1.56 dBsm.

IV. Conclusion

This study enhances the capability of a hybrid quantum model to predict phase data by incorporating a residual structure into the architecture. In future work, we will further investigate how structural improvements at the quantum level can be designed to enhance the model's predictive performance for both amplitude and phase data.

Acknowledgment

This work was supported in part by the Key Program of the National Natural Science Foundation of China under Grant 62231001, the Special Fund for Key Basic Research in Jiangsu Province No. BK20243015, the Fundamental Research Funds for the Central Universities under Grant 2242022k60004.

References

[1] W. B. Lu, T. J. Cui, Z. G. Qian, X. X. Yin, and W. Hong, "Accurate analysis of large-scale periodic structures using an efficient sub-entire-domain basis function method," IEEE Trans. Antennas Propag., vol. 52, no. 11, pp. 3078–3085, Nov. 2004.

[2] F. Guo, T. Liu, B. Song, W. Yang, and W. Lu, "Efficient Analysis of Electromagnetic Scattering in Large-Scale Finite Periodic Structures Using Characteristic Modes," IEEE Antennas Wireless Propag. Lett., vol. 24, no. 12, pp. 4970–4974, Dec. 2025.

[3] W. Xiang, Z. Zhang, W. Zheng, J. Li, W. Yang, and W. Lu, "Rapid subentire-domain basis functions method based on adaptive artificial neural networks," IEEE Trans. Antennas Propag., vol. 70, no. 8, pp. 6522–6532, Aug. 2022.

[4] T. Liu, F. Guo, B. Song, Z. Chen, H. Chen, W. Yang, J. Zhang, J. You, and W. Lu, "Efficient Analysis of Electromagnetic Scattering From Composite Finite Periodic Structures by Prior Physics-Driven Graph Neural Network," IEEE Antennas Wireless Propag. Lett., vol. 24, no. 12, pp. 319–323, Dec. 2025.

[5] J. Biamonte, P. Wittek, N. Pancotti, P. Rebentrost, N. Wiebe and S. Lloyd, "Quantum machine learning", Nature, vol. 549, no. 7671, pp. 195-202, Sep. 2017.

[6] V. Havlícek, A. D. Córcoles, K. Temme, A. W. Harrow, A. Kandala, J. M. Chow, and J. M. Gambetta, "Supervised learning with quantum-enhanced feature spaces", Nature, vol. 567, no. 7747, pp. 209-212, Mar. 2019.

[7] M. Cerezo, A. Arrasmith, R. Babbush, S. C. Benjamin, S. Endo, K. Fujii, J. R. McClean, K. Mitarai, X. Yuan, L. Cincio, and P. J. Coles, "Variational quantum algorithms", Nat. Rev. Phys., vol. 3, no. 9, pp. 625–644, Sep. 2021.

[8] J. Zhang, F. Feng, and Q.-J. Zhang, "Quantum computing method for solving electromagnetic problems based on the finite element method," IEEE Trans. Microw. Theory Tech., vol. 71, no. 11, pp. 4681–4696, Nov. 2023, doi: 10.1109/TMTT.2023.3297406.

[9] E. Colella, S. Beloin, L. Bastianelli, V. M. Primiani, F. Moglie, and G. Gradoni, "Variational quantum shot-based simulations for waveguide modes", IEEE Trans. Microw. Theory Tech., vol. 72, no. 4, pp. 2085–2091, Apr. 2024.

[10] W.-B. Ewe, D. E. Koh, S. T. Goh, H.-S. Chu, and C. E. Png, "Variational quantum-based simulation of waveguide modes", IEEE Trans. Microw. Theory Tech., vol. 70, no. 5, pp. 2517–2525, May 2022.

[11] R. Chen, T.-Y. Ma, M.-H. Dou, and C.-F. Wang, "Investigation of quantum algorithms for the solution of EFIE-based matrix equation system for 3D PEC scatterers", in *Proc. 2025 Photonics & Electromagnetics Research Symp. - Fall (PIERS - Fall)*, Chiba, Japan, Nov. 2025.

[12] R. Chen, T.-Y. Ma, M.-H. Dou, and C.-F. Wang, "Solution of the electric field integral equation using a hybrid quantum-classical scheme: Investigation of accuracy and efficiency", arXiv preprint arXiv:2512.03808, 2025.

[13] T. Liu, B. Song, F. Meng, W. Yang, J. Li, J. You, and W. Lu, "Rapid estimation method for coupling degree of airborne antenna based on quantum neural network," IEEE Antennas Wireless Propag. Lett., vol. 22, no. 12, pp. 2951–2955, Dec. 2023.

[14] B. Song, T. Liu, F. Meng, W. Yang, and W. Lu, "Hybrid variational quantum algorithm enhanced subentire-domain basis functions method with high learning efficiency and better robustness," IEEE Trans. Antennas Propag., vol. 73, no. 9, pp. 6709–6719, Sep. 2025.

[15] V. Bergholm, J. Izaac, M. Schuld, C. Gogolin, M. S. Alam, S. Ahmed, et al., "PennyLane: Automatic differentiation of hybrid quantum-classical computations", arXiv:1811.04968, 2018.

High Q Terahertz Detector in Hybrid Metal−Optical Tamm State Cavity

Zhanzhang Mai[1], Xuecou Tu[1,2*], Bingnan Yan[1], Hongshan Jing[1], Dingxuan Gu[1], Yunjie Rui[1], Zeyu Xu[1], Cheng Liang[1], Baoran Lai[1], Xiaoqing Jia[1,2], Jian Chen[1,3], Lin Kang[1,2] and Peiheng Wu[1,2]
[1]Research Institute of Superconductor Electronics (RISE), School of Electronic Science and Engineering, Nanjing University, Nanjing, Jiangsu 210023, China
[2]Hefei National Laboratory, Hefei 230088, China
[3]Purple Mountain Laboratories, Nanjing, Jiangsu 211111, China
*Corresponding author email: Xuecou Tu (tuxuecou@nju.edu.cn)

***Abstract*—Terahertz optical cavity is one of the major elements to enhance and control the weak interaction between the atom-thick layer and normal incident terahertz light. Here we present a hybrid metal-optical Tamm state cavity with a Nb_5N_6 microbolometer detector embed, exhibiting a Q value of 1529 for direct detection. The cavity is formed by sandwiching a silicon substrate with the detector between two Si/air distributed Bragg reflectors (DBR), one of which is capped with an Au layer. The resonant frequency can be flexibly tuned by adjusting the substrate's thickness. The substrate and DBRs can be fabricated separately and assemble easily, which paves the way to effectively realize versatile high performance terahertz devices and strong interaction between terahertz light and matter.**

I. INTRODUCTION

TERAHERTZ optical cavities have been a focus of intense research interest, providing experimental verification of cavity quantum electrodynamics and developing advanced terahertz devices such as sensors, narrow filters, lasers and sensitive detectors. For instance, Fabry-Perot cavity has been reported to achieve strong light-matter coupling between electron gas and terahertz photons [1]. Also, an asymmetric-coupled FP cavity is applied to form a tunable and sensitive terahertz detector [2]. For high quality factor application, optical Tamm state (OTS), a certain type of surface wave can be sustained at the interface between two reflectors, exhibiting a strong energy confinement. A class of OTS known as Tamm state can be excited at the interface of a dielectric layer adjacent to metallic film, resulting in efficient light absorption peak. Using this configuration, a terahertz Tamm cavity using Si/air DBR have been proposed, demonstrating Q value of 230, which is extracted through Fourier transform infrared (FTIR) spectrometer [3]. Furthermore, a record Q value of 1017 is present using a hybrid Tamm state cavity. This hybrid structure innovatively uses the detector substrate as the adjacent dielectric layer of Au reflector in Tamm state structure, which is directly characterized by a Nb_5N_6 microbolometer detector [4]. Still, the quality factor of these cavities is limited due to the large metallic and dielectric losses. Without the necessity of the metallic film to excite the Tamm state, the OTS structure using two dielectric DBRs may offer a possibility to improve the Q value even account for the dielectric losses.

In this work, we propose a hybrid metal-OTS cavity, consisting of a silicon substrate sandwiched between two Si/air distributed Bragg reflectors (DBR), one of which is capped with an Au layer (DBR_{bot}) as shown in Fig. 1(a). The light is confined to the surface of the substrate and bottom Au layer blocks the leaky light. The performance of the cavity is usually characterized by high resolution Fourier transform infrared (FTIR) spectrometer. Spencer [5] proposes a new concept of active Electro-optic cavities for in-situ measurement of cavity fields, but it requires electro-optic active medium within the cavity. Since we only concern about the electric filed intensity at the surface of terahertz devices, we use the same method in [4], directly measure electric filed intensity through a Nb_5N_6 microbolometer detector integrated on the silicon substrate. This method not only provides a direct insight in the cavity, but also reduces the complexity of design and fabrication since the DBRs and the detector can be fabricated separately.

II. RESULTS

As illustrated in Fig.1(a), the two DBRs sandwich the silicon substrate and the detector is integrated at the surface adjacent to the DBR_{top} and the Au reflector is placed on the bottom of the DBR_{bot}. The combination of HRFZ-Si and Air as the DBR layers offers a large refractive index contrast, forming a higher reflectivity DBRs with fewer layers in terahertz range. The thickness of each DBRs' layer is set to a quarter of the target frequency (0.65 THz). The refractive indices of Si and air are set as 3.4147-0.0008i and 1, leading to the layers' thicknesses are t_{Si} = 33 μm and t_{air} = 115 μm. Note that the Si is not lossless here since there is always a deviation in fabrication and the data is extracted from [4]. The thickness of the detector substrate is set as 510 μm, which support the resonant modes within the DBR stopband.

Using the electromagnetic wave transfer matrix method,

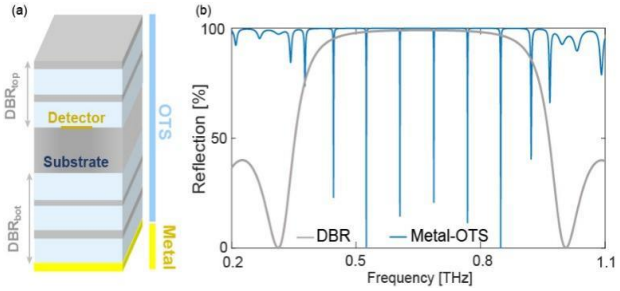


Fig.1. (a) Illustration of the hybrid metal−OTS structure with a Nb5N6 microbolometer detector. (b) Reflectance spectra of a bare two period Si/air DBR and a hybrid metal-OTS cavity at $t_{substrate}$ = 510 μm.

the reflection spectrum of 2 period Si/air DBR and the hybrid metal-OTS cavity are shown in Fig.1(b). The DBR has near unity reflection across 0.5 THz – 0.8 THz and there are multiple resonant modes in the stopband. Here we focus the resonant mode at 0.6056 THz, where the reflection reaches 0.2 and demonstrate over 50% improvement in quality factor of 1529 than previous work [4].

To further compare the resonant modes in the hybrid metal-OTS structure with the Tamm state and OTS, we investigate

979-8-3315-4544-4/26/$31.00 ©2026 IEEE

the optical performance of these modes with the same layers' thicknesses for incident light around 0.6 THz. We use finite-difference time domain (FDTD) method to calculate the normalized electric field (|E|/|E0|) distributions at the resonance frequency. As shown in Fig.2 (a), the hybrid - Tamm state exhibits a relatively weak standing wave pattern by using Au mirror to confine light. The extra metallic loss leads to relatively broad reflection peak and low Q. OTS and hybrid metal-OTS structure, on the other hand, utilize tow DBRs with less material losses, resulting in stronger light confinement observed as higher maximum values for the normalized electric field. Also, the reduced material loss helps increase the quality factor. The nonzero electric field intensity below the bottom DBR of the OTS structure indicates that light leaks through the bottom structure. In hybrid metal-OTS structure, the gold layer reduces the transmission loss and improve the energy confinement (stronger electric field distribution). Accordingly, the hybrid metal-OTS structure exhibits a higher Q value of 1529 than 1169 for OTS structure, near 50% improvement than that of the hybrid Tamm state (1041).

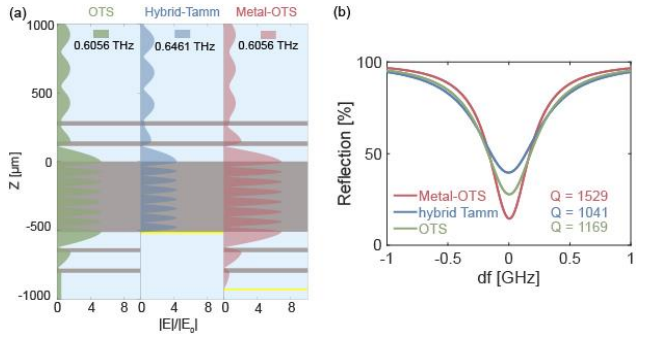


Fig.2. (a) The simulated normalized electric field magnitude (|E|/|E0|) distributions of the OTS, the hybrid-Tamm, and the hybrid metal−OTS structures at the resonance frequency (|E0| is the incident electric field magnitude) (b) The reflection spectra of the OTS, hybrid-Tamm and hybrid metal−OTS structures for normal incidence.

III. SUMMARY

In this work, we present a terahertz hybrid metal-OTS structure with a terahertz microbolometer detector embedded. The OTS features offer the cavity the capability to confine a large amount of energy, along with the metallic mirror to block the leaky light, resulting in a higher Q factor resonance (1529). The Q of this structure surpasses that of a hybrid Tamm cavity and a pure OTS cavity. Besides, this presented hybrid metal-OTS structure can be easily fabricated through straightforward MEMS processing, stacking and assembly, providing a great platform for versatile terahertz devices such as high-power sources, high-sensitivity detectors. Furthermore, its application holds promise for futher investigations into the strong coupling between 2D materials and terahertz photons.

Acknowledgements

The authors acknowledge the support from the National Natural Science Foundation of China (Grant Nos. 62271245), the Excellent Youth Natural Science Foundation of Jiangsu Province (Grant No. BK20240063), Quantum Science and Technology-National Science and Technology Major Project (No. 2021ZD0303401), Synergetic Innovation Center of Quantum Information and Quantum Physics, the Key Lab of Optoelectronic Devices and System with Extreme Performance and Jiangsu Key Laboratory of Advanced Techniques for Manipulating Electromagnetic Waves.

REFERENCES

[1]. Zhang Q., Lou M., Li X., Reno J. L., Pan W., Watson J. D., Manfra M. J. and Kono J, "Collective non-perturbative coupling of 2D electrons with high-quality-factor terahertz cavity photons," *Nat. Phys.*, vol.12, pp. 1005−1011, 2016.

[2]. Xuecou Tu, Chengtao Jiang, Peng Xiao, Shimin Zhai, Xiaoqing Jia, Yaqian Wu, Qingyu Meng, Boyan Chen, Lin Kang, Jian Chen, and Peiheng Wu, "Fabry–Pérot cavity-coupled microbolometer terahertz detector with a continuously tunable air spacer gap," *Opt. Lett.*, vol. 44, 1019-1022, 2019.

[3]. M. Simon, S. Clémentine, B. Joël, T. Jérôme, D. Sukhdeep, B. Jean-Blaise, R. Pascale, M. Juliette, "Tamm Cavity in the Terahertz Spectral Range", *ACS Photonics*, vol. 7, pp. 2906-2914, 2020.

[4]. Tu X., Zhang Y., Zhou S., Tang W., Yan X., Rui Y., Wang W., Yan B., Zhang C., Ye Z., Shi H., Su R., Wan C., Dong D., Xu R., Zhao Q., Wang H., Kang L., Chen J., Wu P., "Tamm-cavity terahertz detector," *Nat Commun*, vol. 15, pp. 5542, 2024.

[5]. M Spencer, J Urban, M Frenzel, N Mueller, O Minakova, M Wolf, A Paarmann, S Maehrlein, "Electro-optic cavities for in-situ measurement of cavity fields," *Light Sci Appl*, vol. 14, pp. 69, 2025.

A High-Performance Hybrid FBAR Chip Based on TGV Technology

Keyan Li
School of Integrated Circuits
Beijing University of Posts and Telecommunications
Beijing, China
lky990710@gmail.com

Yongle Wu
School of Integrated Circuits
Beijing University of Posts and Telecommunications
Beijing, China
wuyongle138@gmail.com

Zhiguo Lai
Design Department
HunterSun Electronics Company Ltd.
Suzhou, China
zhiguo.lai@huntersuntech.com

Qinghua Yang
Design Department
HunterSun Electronics Company Ltd.
Suzhou, China
yangqinghua@tsinghua.org.cn

Weimin Wang
School of Integrated Circuits
Beijing University of Posts and Telecommunications
Beijing, China
wangwm@bupt.edu.cn

***Abstract*—In this paper, a hybrid chip combining a film bulk acoustic resonator (FBAR) chip and a glass-based integrated passive device (IPD) chip is proposed. The inductors in the hybrid circuit are implemented using through-glass via (TGV) as vertical spiral inductors, which can provide a high-*Q* inductor compared to a conventional planar spiral inductor, while also reducing coupling between the vertically stacked chips. Compared with the filter chip based on the same circuit implemented by conventional Si-based IPD technology, the insertion loss of the hybrid chip is lower while showing higher integration.**

Keywords—FBAR, high-integration, hybrid chip, TGV-based inductors, vertically-stack packaging

I. INTRODUCTION

With spectrum resources becoming increasingly scarce, high-selectivity filtering devices are becoming more and more important. Hybrid film bulk acoustic resonator (FBAR) filters are suitable for communication needs due to their combination of high selectivity and wideband. For hybrid FBAR circuits, there are several limitations in their implementation:

1) If the lumped element resonator in the hybrid FBAR circuit is implemented using the traditional integrated passive device (IPD) process, the IPD chip can be used as a substrate to be directly packaged with the FBAR chip [1]. However, because the inductor of a traditional IPD chip is a horizontal spiral, the magnetic field it generates is mainly vertically distributed. The out-of-plane magnetic field generated by the planar spiral inductor couples with the metal ground, causing a decrease in the inductor's *Q* value. Bumps of the FBAR chip are on the redistribution layer (RDL) connected with resonators by through silicon via (TSV). Face-to-face metal layers of the IPD chips and the RDL introduce parasitic capacitances. These effects lead to significant and difficult-to-control parasitic coupling in the hybrid FBAR-IPD structure.

2) To avoid vertical stacking of the two types of chips, the IPD chip and FBAR chip can be placed side-by-side and co-packaged on an additional substrate [1], [2]. However, this packaging method not only results in an excessively large hybrid FBAR chip size after packaging, but also excessively long electrical interconnects between the chips. This means the equivalent inductor of the substrate traces cannot be ignored, causing a shift in the resonant frequency of the lumped element resonator or the generation of additional resonant points. On the other hand, to ensure that the final overall inductors remain constant, the inductors' value of the IPD chip must be appropriately reduced to allow for the equivalent inductance of the substrate traces. This involves allocating a portion of the high-*Q* inductors to the low-*Q* equivalent inductors, increasing the overall loss of the filter.

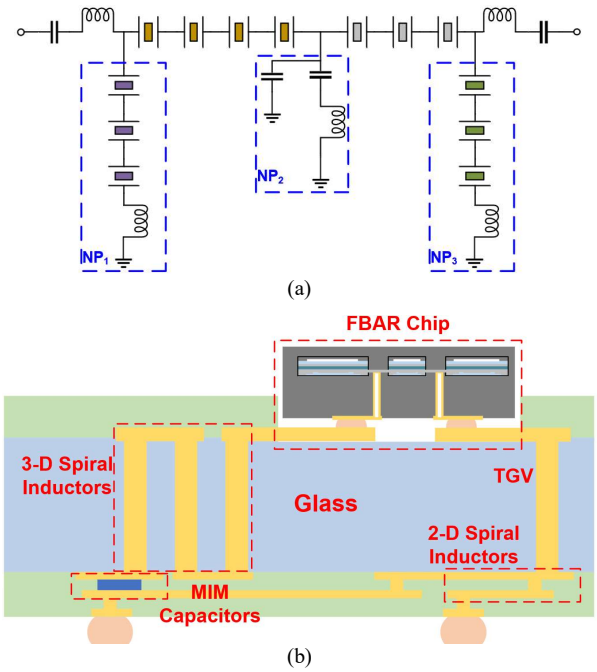


Fig. 1. (a) The hybrid FBAR circuit is used in both [2] and the proposed chip. (b) The proposed hybrid FBAR chip with a glass-based IPD chip.

3) To address the aforementioned issues simultaneously and to design a highly integrated hybrid FBAR chip with no parasitic response, the method of integrating capacitors within the FBAR chip is proposed [3], [4], [5] to implement the matching network. As for hybrid FBAR chips, inductors can be implemented through substrate traces, thus lumped component resonators can be realized after packaging FBAR chips (embedded with capacitors) and substrate, to provide wideband matching. The essence of this method is to implement two components on a single chip, which places extremely high demands on the materials and processes used

979-8-3315-4544-4/26/$31.00 ©2026 IEEE

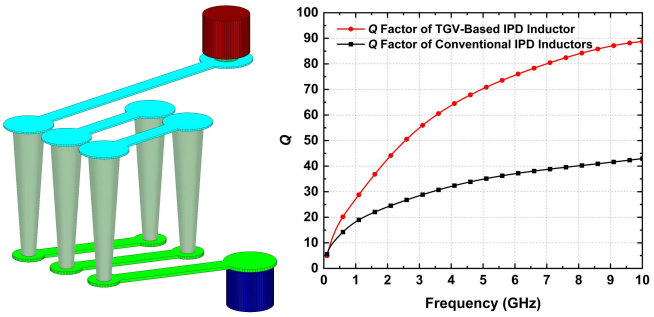


Fig. 2. (a) EM model of TGV-based inductors. (b) The Q factor of IPD inductors used in [2] and TGV-based inductors. (L = 1.2 nH)

in the chip. It requires consideration of the interplay between the FBAR fabrication and capacitor manufacturing processes. For example, whether the etchant used in the FBAR cavity releasing step will corrode the capacitor dielectric is a factor that needs to be considered beforehand. In other words, this method's process is not yet mature, and the final product yield will be very low. To summarize, the number of technologies used in hybrid chips needs to be controlled to realize a highly integrated and low-loss hybrid chip, but the vertical stacking of both chips will cause significant parasitic response. To reduce the parasitic response by replacing the vertically distributed magnetic field, adjustments need to be made to the inductors. In the latest IPD research, the chips based on glass are proposed [6], [7] and remembered due to their high-Q inductors. In this paper, a novel hybrid FBAR chip based on the same circuit as [2], as shown in Fig. 1(a), with a glass-based IPD chip is proposed to address the challenge of coexisting low parasitic response and low equivalent inductor in hybrid chips, as shown in Fig. 1(b). The simulated results of the proposed hybrid chip show much lower insertion loss and higher integration compared to the hybrid FBAR chip [2].

II. The Proposed Hybrid Chip

To see it from a higher view, hybrid FBAR chips can be seen as devices that assume three responsibilities: high selectivity, wideband impedance matching, and packaging. The hybrid chip proposed in [2] has obviously assigned these responsibilities to three technologies: the FBAR technology undertakes high-selectivity responsibility, the IPD technology undertakes wideband impedance matching responsibility, and the substrate technology undertakes packaging responsibility. Such an assignment requires multiple technologies and leads to an oversized chip. To increase the integration, fewer technologies need to be used. The idea of embedding capacitors in FBAR chips can release the wideband impedance matching responsibility from IPD technology and assign it to the other two technologies after packaging, but the tape-out process is challenging.

The two most obvious differences between glass-based IPD and conventional IPD technologies are the existence of through-glass via (TGV) and the degree of technology customization. The existence of TGV allows the inductors to spiral vertically, decreasing the influence on the vertically stacked chips. The high degree of technology customization allows glass-based IPD chips to have solder bumps on both top and bottom surfaces, making glass-based IPD chips much more suitable for undertaking both 'wideband impedance matching' and 'packaging' responsibilities. Thus, in this chip

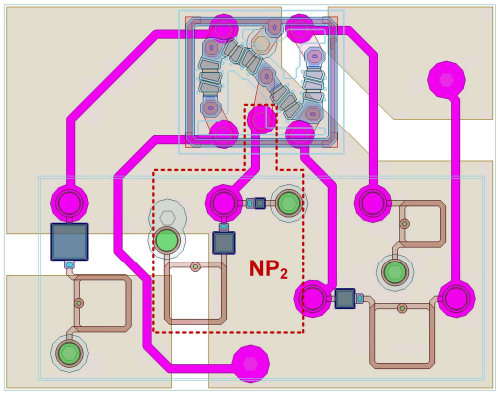


Fig. 3. The traces in the substrate in [2] used to connect two chips are too long and may change the original lumped components resonators.

design, a glass-based IPD chip is packaged directly with an FBAR chip via flip-chip (FC).

A. The Inductors Based on TGV

Due to the high degree of technology customization, the bottom metal layer of the glass-based IPD chip can be taped out as traces, thus the inductors can be spiraled vertically as 'Top Trace-TGV-Bottom Trace', as shown in Fig. 2(a). The Q factor of different types of inductors is simulated based on the finite element method (FEM). The Q factor of inductors is defined as [8]:

$$Q(f) = \frac{2\pi f L(f)}{R_S(f)}, \tag{1a}$$

$$L(f) = \frac{\mathrm{Im}(Z_{11})}{2\pi f}, \tag{1b}$$

$$R_S(f) = \mathrm{Re}(Z_{11}). \tag{1c}$$

It can be seen from Fig. 2(b) that, compared with the conventional IPD inductor (34 at 4.7 GHz), the TGV-based inductor has a much higher Q factor (68 at 4.7 GHz). In addition, the magnetic field it generates is mainly horizontally distributed, allowing the FBAR chip to be placed onto the IPD chip vertically for packaging.

B. The Proposed Hybrid FBAR Chip

Vertical stacking of the two chips has the advantage of reducing the equivalent inductors of the connecting traces. As shown in Fig. 3, the on-substrate traces used to connect two chips are too long to ignore their equivalent inductors [2]. The values of IPD inductors need to be decreased to leave room for the equivalent inductors, yet their Q factor is much lower than that of IPD inductors, which means the overall Q factor is lower than expected. In addition, under certain circumstances, the equivalent inductors may change the original resonators and generate unexpected resonant frequencies, as shown in NP_2 of Fig. 3.

The EM model of the proposed hybrid FBAR chip is shown in Fig. 4(a). The size of the proposed hybrid FBAR chip is 1590 × 1168 μm^2. Vertical stacking of the two chips can reduce the overall length of connecting traces from about 800 μm [2] to within 150 μm, as shown in Fig. 4(b). The connecting metal used for the conventional hybrid FBAR chip is 'TSV-RDL-bump-trace of substrate-bump', where the

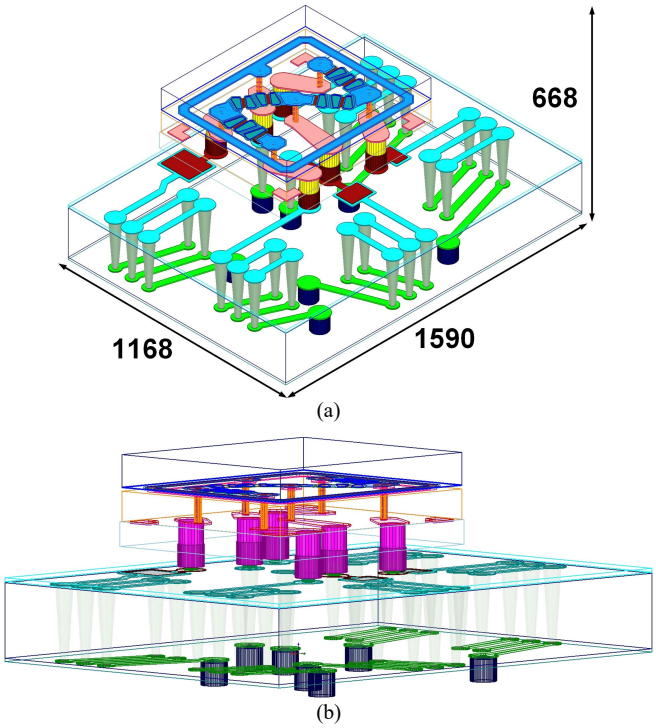


Fig. 4. (a) The EM model of the proposed hybrid chip. (b) The connecting length is within 150 μm.

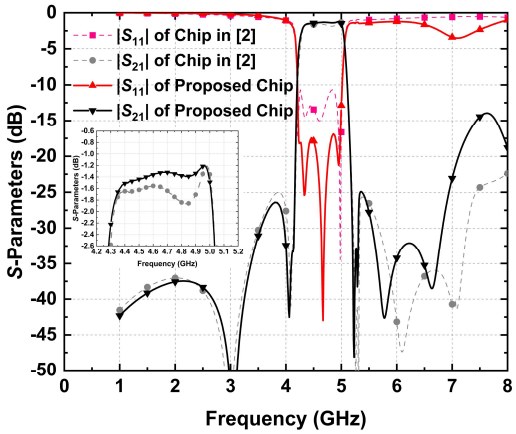


Fig. 5. The comparison of simulated results between the proposed chip and the hybrid chip proposed in [2].

'trace of substrate' is eliminated for the proposed hybrid chip.

The comparison between the simulation results of the hybrid chip in [2] and the proposed chip based on the same hybrid circuit is shown in Fig. 5. The minimum insertion loss is 1.35 dB, and the return loss is better than 13 dB in the passband. To be compared, the hybrid chip using the same packaging method of vertical stacking shows a significant parasitic response [1]. The hybrid chip proposed in [9] also uses the same packaging method, but it shows very little parasitic response, which may be because the inductors on the IPD chip are placed reasonably to reduce the overlapping area with traces on the FBAR chip. However, such design principles impose significant limitations on model design, leading to an insufficient number of lumped elements and inadequate filter performance, or excessively low chip integration density. The proposed chip uses the same packaging method and has no need for any additional arrangement of the inductors, but hardly shows any parasitic response, verifying the validity of the proposed method. It can be seen from **Table I** that with a much smaller size, the performance of the chip does not deteriorate. In addition, due to the higher *Q*-factor of the TGV-based inductors, the insertion loss of the proposed chip is better than that of the hybrid chip proposed in [2].

III. Conclusion

A novel hybrid FBAR filter chip with both TGV and TSV technologies is proposed, which addresses the challenge of coexisting low parasitic response, low equivalent inductor, and high integration in conventional hybrid chips. Compared with the hybrid FBAR chip combining three technologies, the proposed chip has higher integration with lower insertion loss without deteriorating in other performance.

TABLE I. Simulated Performances of the Hybrid Chip and the Proposed Chip

Ref.	*IL* [a] (dB)	*Rej.* [b] (dB)	*Technology*	*Area* (μm²)	*H* (μm)
[2]	1.86	35	FBAR+IPD +Substrate	1700 × 1900	470
This work	**1.51**	**32**	**FBAR+IPD (Glass-Based)**	**1590 × 1168**	**668**

[a] The worst insertion loss in the passband.

[b] The highest rejection at the upper stopband.

Acknowledgment

This work was supported by National Natural Science Foundations of China (No. U20A20203, No. 62320106002, No. U23A20291, and No. U22A2014). In addition, the corresponding Chinese patent (No. 202610507725.2) has been pending. (Corresponding author: Yongle Wu).

References

[1] K. Li, Y. Wu, Z. Lai, Q. Yang, W. Wang, and Y. Yang, "Design of Hybrid Bandpass Filter Chips with High Selectivity and Wideband Using IPD and FBAR Technology," *Int. J. RF Microw. Comput.-Aided Eng.*, vol. 2024, pp. 1–14, May 2024.

[2] K. Li, Y. Wu, Z. Lai, Q. Yang, and W. Wang, "An Iterative Extremely Accurate Generalized Design Methodology for TSV-Based Hybrid AlScN FBAR and IPD Filtering Chips," *IEEE Trans. Microw. Theory Techn.*, vol. 73, no. 9, pp. 5663–5674, Sep. 2025.

[3] A. Volatier, G. Fattinger, F. Dumont, P. Stoyanov, and R. Aigner, "Technology Enhancements for High Performance BAW Duplexer," in *Proc. IEEE Int. Ultrason. Symp. (IUS)*, Jul. 2013, pp. 761–764.

[4] A. Hosseini-Fahraji, M. Schaefer, and A. Gimenez, "Metal-Insulator-Metal Capacitor Integration in Bulk Acoustic Wave Filters," in *Proc. IEEE Int. Microw. Filter Workshop (IMFW)*, Feb. 2024, pp. 125–127.

[5] G. Fattinger, P. Stokes, V. Potdar, A. Volatier, F. Dumont, and R. Aigner, "Miniaturization of BAW Devices and the Impact of Wafer Level Packaging Technology," in *Proc. IEEE Int. Ultrason. Symp. (IUS)*, Jul. 2013, pp. 228–231.

[6] H. Ma, Z. Hu, and D. Yu, "A Low-Loss Bandpass Filter With Stacked Double-Layer Structure Using Glass-Based Integrated Passive Device Technology," *IEEE Electron Device Lett.*, vol. 44, no. 7, pp. 1216–1219, Jul. 2023.

[7] J. Zhang, J.-X. Xu, Y. Xia, and X. Yin Zhang, "Miniaturized High-Selectivity Bandpass Filter With Wide Stopband Based on Through-Glass-Via IPD Technology," *IEEE Electron Device Lett.*, vol. 45, no. 8, pp. 1536–1539, Aug. 2024.

[8] L. Zhu, S. Sun, and R. Li, *Microwave Bandpass Filters for Wideband Communications*. Hoboken, NJ, USA: Wiley, 2012, pp. 18–84.

[9] R. Ding et al., "Compact and High Steep Skirts Hybrid Heterogeneous Integrated N77 Full Band BAW Filter Based on Band-Stop Theory," *IEEE Electron Device Lett.*, vol. 45, no. 5, pp. 793–796, May 2024.

Geometry Scalable Model of on-Chip Multilayer Interdigital Capacitors

Yiwen Liu
School of Electronic Science and Engineering
University of Electronic Science and Technology of China
Chengdu, China
202321020720@std.uestc.edu.cn

Huanpeng Wang
Yangtze Delta Region Institute (Huzhou)
University of Electronic Science and Technology of China
Huzhou, China
whp@csj.uestc.edu.cn

Yunqiu Wu
School of Electronic Science and Engineering
University of Electronic Science and Technology of China
Chengdu, China
yqwu@uestc.edu.cn

Jie Liu
School of Electronic Science and Engineering
University of Electronic Science and Technology of China
Chengdu, China
ljragdoll@126.com

Huihua Liu
School of Electronic Science and Engineering
University of Electronic Science and Technology of China
Chengdu, China
lhhua@uestc.edu.cn

Yiming Yu
School of Electronic Science and Engineering
University of Electronic Science and Technology of China
Chengdu, China
ymyu@uestc.edu.cn

Chenxi Zhao
School of Electronic Science and Engineering
University of Electronic Science and Technology of China
Chengdu, China
cxzhao@uestc.edu.cn

Qingfeng Zhang
School of Electronic Science and Engineering
University of Electronic Science and Technology of China
Chengdu, China
qfzhang@uestc.edu.cn

Kai Kang*
School of Electronic Science and Engineering
University of Electronic Science and Technology of China
Chengdu, China
kangkai@uestc.edu.cn

***Abstract*—Interdigital capacitors, composed of multiple metal layers, exhibit superior performance in compact form due to their high integration. In this paper, a scalable equivalent circuit model tailored for multilayer interdigital capacitors is proposed. The circuit parameters are accurately derived and the characteristics can be predicted based on the finger dimensions. The accuracy of the scalable model has been validated with an accuracy exceeding 92% across a frequency range of up to 40 GHz. This makes it highly significant for the modeling of on-chip passive devices.**

Keywords—interdigital capacitor, equivalent circuit model, multilayer structure, integrated circuits

I. Introduction

The interdigital capacitor (IDC), characterized by interdigitated finger-shaped electrodes, is widely recognized for its excellent high-frequency performance and compact integration potential. It is widely used in impedance matching networks, RF filters, and many other integrated circuits. With increasing integration density of chips, the multilayer structure enables IDCs to achieve superior performance within a reduced area.

For modeling of IDCs, conventional approaches primarily extract circuit parameters from measured data [1], or apply calculations based on single-layer IDC formulation [2]. The coupling capacitances in IDCs can be computed by empirical formulas [3]. Recently, some research innovatively adopted neural network to construct a scalable model for single-layer IDCs as in [4]. However, limited computational methods are available for multilayer IDCs, which enables precise prediction of characteristics based on structural parameters.

This paper proposes a scalable equivalent circuit model for multilayer IDCs, establishing explicit dependencies of high-frequency characteristics on dimensional parameters. The accuracy of the model was verified at multiple sizes up to 40 GHz. The model's capability to efficiently predict on-chip IDC characteristics provides substantial value for RF integrated circuit design, particularly in early-stage design exploration and optimization.

II. Scalable Equivalent Circuit Model

A. Equivalent Circuit Model

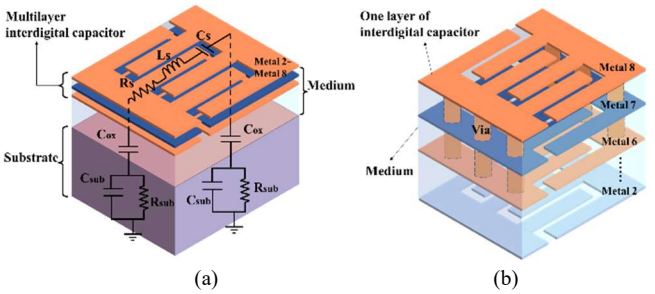


Fig. 1. Schematic of (a) multilayer interdigital capacitor and (b) connection details between multilayers

The structure of a multilayer IDC is shown in Fig. 1(a), as well as the equivalent circuit model. The component C_s characterizes equivalent capacitance of multilayer structure.

979-8-3315-4544-4/26/$31.00 ©2026 IEEE

The capacitor C_{ox} applied to both ports indicate the capacitive effect of vertical electric field in oxide layer below the metal IDC. The property of resistive loss R_s is similar to that of rectangular metals, which is proportional to length and inversely proportional to width. For a single finger, inductive loss L_s can be obtained using transmission line theory. Multi-finger inductances are treated as series-connected, while multi-layer inductances operate in parallel. The parallel branch composed of capacitor C_{sub} and resistor R_{sub} introduce effect of lossy substrate. In this paper, substrate parameters are fixed for same process.

The details of the vertical interconnect between layers are shown in Fig. 3(b). The vias connecting multiple layers are mainly distributed in the termination area.

B. Multilayer Equivalent Capacitance C_s

For single-layer interdigital capacitance, it can be calculated by the method proposed in [2]:

$$C_p = (\varepsilon_r + 1)L[A_1 \times (2N-3) + A_2] \quad (1)$$

The effective areas A_1 and A_2, introduced by interior and exterior fingers, depend on oxide thickness and finger width. The parameters L and N represent length and number of fingers, as ε_r is relative dielectric constant of oxide material.

However, for multilayer IDC, the underlying "ground plane" for each layer is non-ideal. Therefore, the regions between fingers will introduce lateral capacitance due to leakage of electric filed from edge to lower layer, which can be estimated using (2). The thickness of interlayer medium h_m and finger gap d_g greatly impact the capacitance, where the coefficient λ is to correct the leakage.

$$C_l = \frac{\lambda h_m (2N-1) L \varepsilon_0 \varepsilon_r}{d_g} \quad (2)$$

In addition, the calculation based on (1) only considers the capacitance of finger region, there is also capacitance exists at terminations for multilayer structure. This can be equivalent to parallel-plate capacitor based on (3). The W_t and d_t represents width and spacing of two terminations, where W_t is positively correlated with the width of finger, and d_t is positively correlated with the length of finger.

$$C_0 = \frac{\varepsilon_0 \varepsilon_r h W_t}{d_t} \quad (3)$$

$$C_s = C_p + C_l + C_0 \quad (4)$$

The capacitance for multilayer IDC can be obtained from those three components using (4).

C. Vertical Oxide Capacitance C_{ox}

This vertical capacitance is usually explained simply as a parallel-plate oxide capacitance produced by each electrode. However, this is inaccurate for multilayer IDCs, where the electric field caused by multilayer metals is much more complex. The vertical field will not be evenly distributed to both electrodes. In addition, interdigital structure also makes both ports jointly affected by same field effect. Therefore, in proposed model, the oxide capacitance is still estimated using parallel plate capacitance formula, where it is equivalently applied to both electrodes. It should be particularly noted that in the physical samples involved in this study, electrodes of interdigital capacitor have an extended structure similar to a transmission line. This part is interconnected to test pads on both sides, and the capacitive component of oxide layer introduced by the occupied area cannot be ignored.

Furthermore, the non-negligible sidewall thickness of multilayer IDCs generates additional capacitance through surrounding dielectrics, calculated by (5):

$$C_{fringe} = \varepsilon_0 \varepsilon_r W_{total} (\frac{4}{\pi}) \ln(1 + \frac{h_{top}}{h_{bottom}}) \alpha \quad (5)$$

The parameter W_{total} indicates the total sidewall width of multilayer IDC, the h_{top} and h_{bottom} represent the distance from substrate to top and bottom layer respectively. In addition, the coefficient α is applied to correct the edge effect. Based on the specific characteristics of IDC in this paper, coefficient α is taken as *(90/WN)*, which is inversely proportional to width and number of fingers.

III. Model Validation

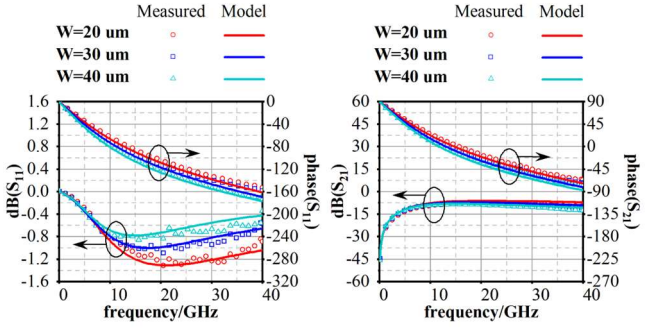
Utilizing the scalable modeling method, several multi-layer IDCs were characterized and validated by measured data within 40 GHz.

Three groups of samples with 100-μm finger length, 3 finger pairs, and 7 metal layers were selected. Only the width of fingers is changed, while other process and dimensional parameters remained consistent. The main parameters in the equivalent circuit model are calculated based on the scaling law proposed in this paper. The specific values and model accuracy are listed in the following table:

TABLE I. Parameter Values and Accuracy of Scalable Models with Different Width of Fingers

Sample	Finger width (μm)	R_s/Ω	L_s/pH	C_s/fF	C_{ox}/fF	Accuracy
W-1	20	2.85	13.23	89.5	111.6	96.4%
W-2	30	2.10	12.00	91.3	138.4	95.2%
W-3	40	1.42	13.26	93	167.1	92.6%

From the information shown in table above, it can be known that within the variation of finger width, the equivalent series resistance R_s is affected to a minor extent, but it still shows a decreasing trend as the width increases. This is mainly due to the increase in the cross-sectional area of metal. The inductance L_s, which characterizes inductive loss, is related to the characteristic impedance and should show a trend of first decreasing and then increasing with the



(a) (b)

Fig. 2. Comparison of (a) S_{11} parameters and (b) S_{21} parameters based on different width of fingers

increase of finger width. The data of the selected samples in the table can also reflect this rule.

The variation in finger width has the most significant impact on vertical oxide layer capacitor C_{ox}. The increasing finger width directly expands the parallel plate area of oxide layer and total width of side wall metal, thereby significantly affecting two main components of C_{ox}. Meanwhile, multilayer equivalent capacitance C_s also increases slowly while finger width increasing, as the single-layer interdigital capacitance C_p and structure capacitance C_0 that constitutes C_s are both positively correlated with the finger width.

Taking the S-parameter of circuit model as the reference for electrical characteristics, Fig. 2 shows the comparison between the measured data and the equivalent circuit model. The scalable equivalent circuit model proposed in this paper demonstrates excellent electrical property prediction capabilities for samples with different finger widths.

In addition to the above, three samples with a finger width of 30 μm, a finger pairs of 3, and composed of 5 layers of metal were selected to investigate the electrical influence of the finger length variation. Using the scalable modeling method proposed, the model parameters are calculated and presented in the following table:

TABLE II. PARAMETER VALUES AND ACCURACY OF SCALABLE MODELS WITH DIFFERENT LENGTH OF FINGERS

Sample	Finger length (μm)	R_s/Ω	L_s/pH	C_s/fF	C_{ox}/fF	Accuracy
L-1	50	0.93	9.23	45.9	34.9	95.7%
L-2	100	1.86	18.00	67.4	43.5	94.2%
L-3	150	2.79	27.69	91.5	52.1	94.5%

According to the data in Table II, a longer interdigital length significantly enhances the inductive effect and increases the equivalent resistance Rs due to the extension of total loss path. The multilayer equivalent capacitance C_s is mainly composed of the superposition of interdigital capacitance C_p and the edge leakage capacitance C_l. Both capacitive components are positively correlated with the finger length, and this rule is clearly reflected in the data shown in the table. In addition, the vertical oxide capacitance C_{ox} increases with the increasing finger length, as the finger length extends the parallel plate area of the oxide layer

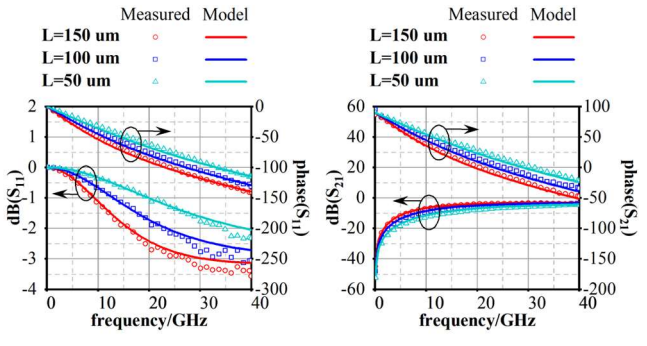


Fig. 3. Comparison of (a) S_{11} parameters and (b) S_{21} parameters based on different length of fingers

capacitance. In the scaling model proposed in this paper, the finger length does not affect the size of the side wall capacitance, so its overall influence on C_{ox} is weaker than that on the finger width.

Fig. 3 compares the S-parameter of measured data with the model fitting results. Within the range of 0 to 40 GHz, the model can accurately describe the electrical characteristics of multilayer interdigital capacitance under the variation of finger length.

Based on the verification results of the varied width and length of finger mentioned above, the multi-layer structure effectively reduces the resistive loss, keeping the parameter R_s of all samples at a relatively low value. Meanwhile, the inductive effect shows a higher sensitivity to changes in the length of finger.

The number of metal layers also has a significant impact on the characteristics of capacitors. Taking samples W-2 and L-2 as examples, the only difference between the two samples is the metal layer. The multilayer equivalent capacitance C_s in the 5-layer sample L-2 is significantly smaller than that in the 7-layer W-2 sample, which conforms to the physical expectation of multilayer capacitance superposition. In addition, the bottom metal of L-2 is further away from the substrate, resulting in a significant reduction in its vertical oxide layer capacitance C_{ox}.

The accuracy of all the models compared with the measured data within the range of 0 to 40 GHz reaches 92% to 97%, which is evident that the scalable model proposed can precisely predict the performance of IDCs based on size of fingers.

IV. CONCLUSION

A scalable equivalent circuit model applicable to multi-layer IDCs is proposed, while the scalable laws of finger width and length on its electrical characteristics is validated by measured data. The model has a prediction accuracy of over 92.6% within the frequency range of 0-40 GHz. This model and its scaling laws can achieve precise predictions of electronic characteristics based on the geometry parameters of fingers, providing a reliable analysis tool for circuit design and its early-stage optimization.

ACKNOWLEDGMENT

This work is supported by the National Natural Science Foundation of China (Grant No. W2541020).

REFERENCES

[1] K. Subramaniam, A. V. Kordesch and M. Esa, "Nine-element lumped metal finger capacitor model extraction method for RF applications," in *2006 4th Student Conference on Research and Development*, 2006, Shah Alam, Malaysia, pp. 25-28.

[2] G. D. Alley, "Interdigital capacitors and their application to lumped-element microwave integrated circuits," *IEEE Transactions on Microwave Theory and Techniques*, vol. 18, no. 12, pp. 1028-1033, Dec. 1970.

[3] S. Jeyaraman, V. N. R. Vanukuru, D. Nair and A. Chakravorty, "Modeling of high-Q conical inductors and MOM capacitors for millimeter-wave applications," *IEEE Transactions on Electron Devices*, vol. 67, no. 12, pp. 5646-5652, Dec. 2020.

[4] Y. Xiong, S. Guo, S. Hu, Y. Gu, Y. Fang and Y. Guo, "A scalable model for on-chip interdigital capacitor based on space-mapping neural network," in *2024 9th International Conference on Integrated Circuits and Microsystems (ICICM)*, 2024, Wuhan, China, pp. 93-97.

High-T_c Superconducting Josephson Mixers from X- to Sub-THz Band

He Zhu[1], Ting Zhang[1], and Jia Du[1]
[1] CSIRO Manufacturing, 36 Bradfield Rd, Lindfield West, 2070, NSW, Australia
email: he.zhu@csiro.au

High-temperature superconducting (HTS) Josephson mixers offer ultra-low noise, high sensitivity, and low local oscillator (LO) power requirements, making them strong candidates for next-generation microwave, millimetre-wave (mm-wave), and sub-terahertz (sub-THz) systems [1]-[4]. This talk will present a comprehensive investigation of HTS Josephson mixer design, modelling, and antenna integration across X-band, W-band, and sub-THz frequencies, establishing a scalable methodology from circuit-level optimisation to fully integrated imaging front-ends.

At X-band (9.5–10 GHz), a single-balanced HTS Josephson mixer implemented on a $YBa_2Cu_3O_{7-x}$ (YBCO)/MgO substrate is designed using a systematic circuit methodology. The topology incorporates a 3 dB branch-line hybrid coupler, a sixth-order impedance matching network tailored to a lumped-element Josephson junction model, compact low-pass filtering, and carefully engineered RF and IF grounding structures. The predicted conversion loss at 40 K is 3.24 dB with an exceptionally low optimal LO power of –50 dBm and strong linearity performance. Although measured results showed reduced performance due to non-ideal junction parameters (low R_n and R_nI_c), re-simulation using measured junction characteristics closely matched experimental data, validating the proposed design framework and highlighting the critical role of HTS junction parameter optimisation.

Extending to W-band (82–90 GHz), a third-harmonic HTS Josephson mixer is proposed to enable high-efficiency frequency conversion using a low-frequency LO source. The design integrates two Josephson junctions across a slotline and introduces a novel waveguide-to-slotline transition to address the integration challenges between bulky WR-10 waveguides and compact HTS monolithic microwave integrated circuits (MMICs). Simulations demonstrate less than 3 dB conversion loss, over 17 dBi antenna gain, transition loss below 2 dB, and port isolation exceeding 24–30 dB across a 10% bandwidth. The third-harmonic approach significantly improves compactness and LO power efficiency for mm-wave superconducting modules.

For sub-THz imaging applications, a YBCO step-edge Josephson mixer is monolithically integrated with a thin-film leaky-wave antenna (LWA) operating in dual bands of 175–205 GHz and 225–265 GHz. Fabricated on an MgO substrate and composed of 20 Y-shaped coplanar waveguide elements, the LWA enables wideband frequency-controlled beam scanning with excellent impedance matching (< –20 dB return loss) and low insertion loss (< –15 dB). When operated in a cryogenic environment (40–77 K), the system supports multi-frequency imaging with a wide IF bandwidth (0–20 GHz), enabling high-resolution sub-THz imaging through frequency-swept beam steering.

Collectively, these works establish a unified HTS mixer design methodology spanning circuit modelling, harmonic mixing techniques, advanced impedance matching, and innovative antenna integration. The results demonstrate that precise control of Josephson junction parameters, combined with optimized RF transitions and frequency-scanning antenna architectures, enables compact, low-LO-power, and high-performance superconducting receivers from microwave to sub-THz frequencies, paving the way for advanced sensing and imaging systems.

References

[1] J. Du, X. Gao, T. Zhang and H. Zhu, "High-Tc superconducting quantum devices for cutting-edge Terahertz technology," *Journal of Physics D: Applied Physics,* vol. 58, no. 31, p. 313001, 2025.
[2] H. Zhu, T. Zhang, and Jia Du, "Monolithic High-temperature Superconducting (HTS) K-band Sub-harmonic Mixer Based on Reverse-biased Josephson Junctions", *Superconductor Science and Technology*, 39 025001, Feb., 2026.
[3] T. Zhang, J. Du and Y. J. Guo, "An 8–10-GHz lowloss image-reject HTS mixer based on cascaded Josephson junctions," IEEE Microwave and Wireless Components Letters, vol. 31, no. 8, p. 945–948, 2021.
[4] X. Gao, T. Zhang, J. Du and Y. J. Guo, "340 GHz Double-Sideband Mixer Based on Antenna-Coupled High-Temperature Superconducting Josephson Junction," *IEEE Transactions on Terahertz Science and Technology,* vol. 10, no. 1, pp. 21-31, 2020.

979-8-3315-4544-4/26/$31.00 ©2026 IEEE

Metasurface Antenna Applied in Millimeter-Wave Imaging Systems

1st Panpan Zuo
School of Electronic Information and Automation
Civil Aviation University of China
Tianjin, China
ppzuo@cauc.edu.cn

2ndLongpeng Lan
School of Electronic Information and Automation
Civil Aviation University of China
Tianjin, China

3rd Keyan Wei
School of Electronic Information and Automation
Civil Aviation University of China
Tianjin, China

4thBin Gao
School of Electronic Information and Automation
Civil Aviation University of China
Tianjin, China

5thXiaoxuan Guo
School of Electrical and Data, Engineering, Tech Lab
University of Technology Sydney
Sydney, Australia

6th Lei Yang
School of Electronic Information and Automation
Civil Aviation University of China
Tianjin, China

***Abstract*—This paper presents a Ku-band metasurface antenna for mmWave near-field radar imaging. It features a compact three-layer stacked architecture comprising a 4 × 4 patch radiating array, a slotted grounded excitation layer, and a 1:16 equal-power Wilkinson power divider network. This feeding structure ensures rigorous amplitude and phase consistency among the array elements. Simulations confirm the design's compactness, demonstrating an average Ku-band gain above 11 dBi and a 3dB beamwidth constrained within 35°, which effectively satisfies the demands of high-precision near-field mmWave imaging.**

Keywords—metasurface antenna, millimeter-wave, imaging system

I. Introduction

In recent years, millimeter-wave technology has emerged as a pivotal solution for next-generation personnel security screening and non-destructive testing [1]. Operating within the 30–300 GHz band, mmWave radiation possesses unique electromagnetic characteristics suitable for imaging. Its short wavelength enables effective penetration through optically opaque materials, such as clothing, to generate reflections from the human skin, facilitating the detection of concealed contraband. Unlike ionizing X-rays, mmWave radiation poses negligible health risks, ensuring safety for high-frequency screening. Furthermore, its intrinsically short wavelength allows for millimeter-level spatial resolution, enabling the precise reconstruction of geometric details of hidden objects.

In near-field imaging architectures, the front-end antenna serve as the core sensor, with its radiation performance directly dictating system imaging quality. However, existing commercial systems predominantly rely on bulky mechanical scanning mechanisms, which limits their suitability for portability and cost-efficiency. Metasurfaces offer a robust platform for antenna design, demonstrating the capability to manipulate electromagnetic amplitude, phase, and polarization with high precision [2]. By utilizing periodic unit cells, metasurface achieves efficient radiation with a low physical profile, thereby reducing hardware costs and complexity compared to traditional RF systems.

Despite this potential, designing metasurface antennas for high-precision near-field imaging presents significant technical challenges. A critical hurdle is ensuring high amplitude and phase consistency across the aperture excitation to mitigate beam defocusing, while concurrently ensuring broadband impedance matching. To address these challenges, this work proposes a Ku-band metasurface antenna optimized for near-field security imaging. A compact three-layer stacked architecture is employed to optimize radiation efficiency and wavefront integrity through precise structural conrtol.

II. Metasurface Antenna Design and Millimeter-Wave Imaging System

A. Metasurface Antenna Design

In this paper, a Ku-band metasurface antenna is presented for radar imaging applications. As shown in Fig. 1, the antenna adopts a three-layered structure. Layer 1 is constructed by a 4×4 periodic patch array, with each patch element sized 5.15 mm × 5.15 mm. Layer 2 serves as the ground plane, with slotted structures to couple energy to layer 1. On Layer 3, a 1:16 equal-power Wilkinson power divider network—implemented using microstrip technology—is integrated within the feeding layer. Specifically, eight 200 Ω isolation resistors are embedded within the network configuration to achieve stable and uniform excitation for the radiating patch array. This feeding scheme ensures excellent amplitude and phase consistency among all antenna elements.

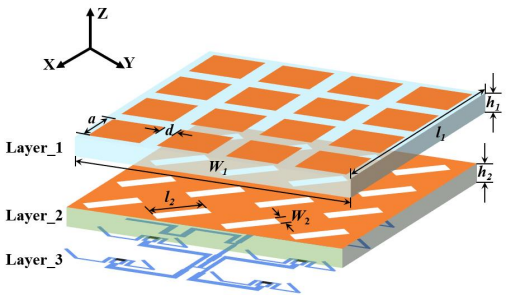


Fig. 1. Geometry of the proposed metasurface antenna

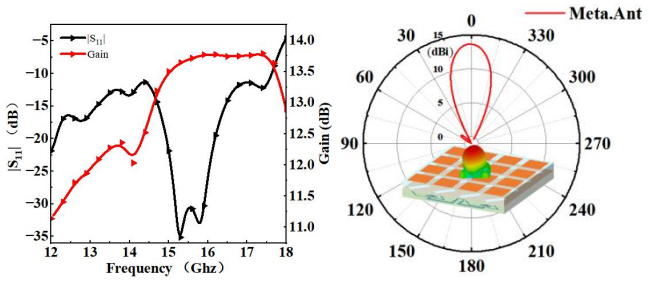
An air layer with a height of h_1 is employed to separate Layer 1 and Layer 2, while Layer 2 and Layer 3 are connected by a polyimide substrate (relative dielectric constant ε_r = 3.5, loss tangent tan δ = 0.0027). All substrate layers have the same dimensions of 35.2 mm × 37.2 mm. The specific dimensional parameters of the antenna are summarizedin Table I.

TABLE I. Geometrical Parameters of the Proposed Metasurface antenna (unit: mm)

Parameter	h_1	h_2	w_1	l_1
Value	2.2	0.3	35.2	37.2
Parameter	a_1	d	W_2	l_2
Value	5.15	3.65	1.72	6.78

The performance of the designed antenna is verified using the commercial full-wave simulation software CST. As shown in Fig.2 (a), the return loss of the proposed metasurface antenna remains consistently below −10 dB. The antenna also exhibits stable high-gain characteristic over the 12GHz-17.66GHz, with a minimum gain greater than 11 dBi and the peak of the gain can reach up to 14 dBi—achieving a higher aperture efficiency relative to the larger arrays typically utilized for achieving a similar gain level [3]. Furthermore, this excellent performance is realized using a low-profile planar configuration with a simple single-layer feeding network.

Across the Ku-band, the 3 dB beamwidth is confined within 35º, reaching 28.2º at the central frequency [4]. This narrow beamwidth is achieved without complex amplitude/phase networks [5] and features a narrower beamwidth than conventional dual-band designs, which typically exceed 30º [6]. These results demonstrate that the proposed antenna exhibits excellent beam alignment and directivity, satisfying the requirements of high-efficiency directional imaging in Ku-band.



(a) (b)

Fig. 2. (a) Return loss and Gain. (b) Antenna radiation patterns

B. *Millimeter-Wave Signal Acquisition System*

A prototype mmWave radar imaging system is implemented using the proposed metasurface antenna. Operating as a single-input single-output (SISO) frequency-modulated continuous-wave (FMCW) radar, the system synthesizes a large aperture through two-dimensional mechanical scanning, following the synthetic aperture radar (SAR) principle. In this configuration, the proposed metasurface antenna functions as the primary transmitting sensor. By integrating a Wilkinson power divider within its three-layer stacked architecture, the antenna generates a near-field wavefront with high amplitude and phase consistency. This ensures uniform target illumination, forming the physical foundation for high-resolution and low-artifact imaging.

The proposed system is organized into four primary functional modules: the Data Acquisition and Processing Unit, the RF Transceiver Subsystem, the High-Precision Mechanical Scanning platform, and the Metasurface Antenna Sensor Module [7]. The integrated architecture is depicted in Fig. 3, and the technical specifications of each module are provided in the following subsections:

- **Data Acquisition and Processing Unit:** Functioning as the system's computational core, this MATLAB-based unit employs the **Range Migration Algorithm (RMA)** for phase compensation and focusing to reconstruct high-resolution 2-D scattering images of concealed targets.
- **RF Transceiver Subsystem:** Serving as the primary signal source, this VNA-based subsystem operates in transmission mode to generate high-stability Ku-band wideband Continuous Wave excitation signals, delivering them to the front-end antenna via precision phase-stable cables.
- **High-Precision Mechanical Scanning Subsystem:** Serving as the primary motion control unit, this PLC-driven system utilizes a sliding rail and load platform to accurately position the metasurface antenna across the scanning scene, ensuring uniform spatial sampling of the scanning plane.
- **Metasurface Antenna Sensor Module:** Incorporating the proposed three-layer Ku-band metasurface antenna as the primary radiating element, this module utilizes an internal 1:16 Wilkinson power divider to produce a near-field wavefront with stable amplitude and phase distribution, enabling uniform target illumination. Its low-profile design minimizes system volume while optimized beamforming effectively suppresses phase distortion and defocusing, thereby improving the imaging dynamic range.

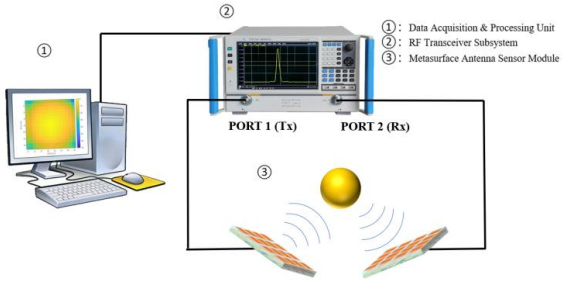


Fig. 3. Block diagram of the millimeter-wave signal acquisition system

Generated by the RF transceiver, the signal traverses the RF link to the antenna and is radiated toward the target surface. The backscattered signal is captured by the receiving antenna and routed to the receiver channel for dechirp processing with the reference signal to extract the baseband data, as illustrated in Fig.4. Finally, the baseband data is processed via imaging algorithms to reconstruct the target image.

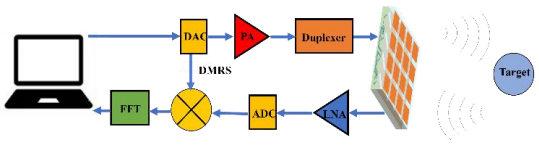


Fig. 4. Signal Chain

C. Digital Imaging System

The 3D image reconstruction methodology relies on the processing of backscattered signals through frequency-domain algorithms. Specificaly, the VNA functions as a transceiver to emit microwave signals and record the corresponding backscattered waves. Scattering parameters $S_{21}(f)$ acquired at each scanning position represent the target's electromagnetic and geometric characteristics and are organized into a 3D echo matrix.. This data undergoes a 2D FFT to the frequency domain, followed by Stolt interpolation for Range Migration Compensation to map the non-uniform data onto a uniform grid. Finally, a 2D IFFT transforms the signal back to the spatial domain, yielding the focused SAR image [8]. The reconstruction principle is formulated as:

$$\sigma(x,y,z) = \int [S_{21}(f)exp(j2\pi ft)]_{Stolt}df \qquad (1)$$

Simulation-based verification was conducted utilizing software CST. A spherical target modeled as a Perfect Electric Conductor (PEC) was configured, with the design parameters summarized in Table II. The reconstructed image (Fig.5) indicates that the target is resolvable with a high signal-to-background ratio. The effective recovery of the circular geometry fully validates the feasibility of the proposed imaging system.

TABLE II. Table of Experimental Parameters

Param	CF[1] (GHz)	BW[2] (GHz)	SF[3] (MHz)	NE[4]	IS[5]	SF[6] (mm)	Target Material
Value	15.3	40	40	25	100	100	PEC

1CF: Center Frequency. 2BW: Bandwidth.
3SF: Stepped Frequency. 4NE: Number Of Array Elements.
5IS: Imaging Area Size. 6DA: Center Distance of Imaging Area

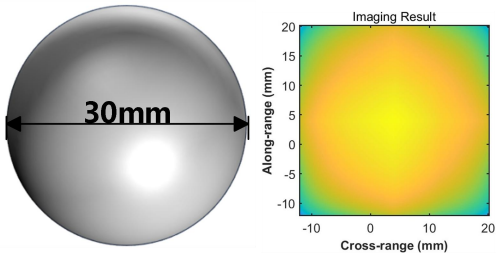


Fig. 5. Comparison between the simulated target model and the imaging results

D. Discussion

The simulation results demonstrate the performance of the proposed metasurface antenna and its suitability for millimeter-wave near-field imaging applications. However, the study also revealed certain limitations, which are outlined as follows:

- The current antenna dimensions exceed the center wavelength, leading to spatial undersampling and image blurring in array configurations. Future work will focus on structural optimization to achieve element miniaturization.
- To transition from the current mechanical scanning system, subsequent designs will integrate FPGA-controlled reconfigurable elements. This enhancement aims to enable electronic beamforming and expand the antenna's operational modes.

III. CONCLUSION

This paper presents a metasurface antenna designed for mmWave imaging, featuring a compact three-layer stacked architecture that optimizes both near-field radiation efficiency and system integration. The design comprises three functional layers: a top radiating layer consisting of a 4 × 4 patch array; a middle excitation layer incorporating precision-etched slots; and a bottom feeding layer that integrating a 1:16 equal-power Wilkinson power divider network. The proposed antenna exhibits radiation performance within the Ku-band, maintaining a reflection coefficient below -10 dB, achieving a minimum gain exceeding 11 dBi, and constraining the 3-dB beamwidth to within 35º. Furthermore, simulation-based studies confirmed the suitability of the proposed antenna for near-field mmWave scanning and imaging applications. Future work will focus on further structural optimization to expand its applicability to a broader range of operational environments.

ACKNOWLEDGEMENT

This work is supported by the Scientific Research Project of Tianjin Municipal Education Commission under Grant 2024KJ113, and the National Natural Science Foundation of China project under Grant 62271487.

REFERENCES

[1] Luukanen, A., Appleby, R., Kemp, M., Salmon, N. (2012). Millimeter-Wave and Terahertz Imaging in Security Applications. In: Peiponen, KE., Zeitler, A., Kuwata-Gonokami, M. (eds) Terahertz Spectroscopy and Imaging. Springer Series in Optical Sciences, vol 171. Springer, Berlin, Heidelberg.

[2] Cui, T., Qi, M., Wan, X. et al. Coding metamaterials, digital metamaterials and programmable metamaterials. Light Sci Appl 3, e218 (2014).

[3] P. N. Vummadisetty et al., "A metasurface-based cross-slot aperture coupled antenna array for Ku-band satellites in reception," in Proc. IEEE Int. Symp. Antennas Propag., 2024, pp. 1-5.

[4] Y. Jiang, Z. Zheng, S. S. A. Yuan, H. Xue, L. Li, and W. E. I. Sha, "Quantum-Inspired Optimization for 2-bit Quantized Phase-Only Metasurfaces With Near-Field Multiobjective Control," in IEEE Transactions on Microwave Theory and Techniques, vol. 73, no. 12, pp. 9886-9901

[5] Q. Liu, X.-W. Chen, W.-B. Niu, M.-Y. Xia, and W.-M. Zhang, "Low sidelobe dual-beam metasurface antenna based on Taylor distribution and digital filtering methods," IEEE Antennas Wireless Propag. Lett., vol. 22, no. 8, pp. 863-867, Aug. 2024.

[6] W. Zhu, J. Yu, H. Mi, L. Xiao, D. Zhang, and B. Xiao, "Dual-band high-gain metasurface antenna based on symmetry breaking effect for radar imaging," IEEE Antennas Wireless Propag. Lett., vol. 24, no. 3, pp. 1-4, Mar. 2025.

[7] S. Hamidi and M. Nezhad-Ahmadi, "High Resolution Millimeter Wave Imaging Based on FMCW Radar Systems at W-Band," *2025 IEEE 15th Annual Computing and Communication Workshop and Conference (CCWC)*, Las Vegas, NV, USA, 2025, pp. 00110-00116.

[8] V. Skouroliakou, A. M. Molaei, M. García-Fernández, G. Álvarez-Narciandi and O. Yurduseven, "Frequency Domain Image Reconstruction for Imaging With Multistatic Dynamic Metasurface Antennas," in IEEE Access, vol. 10, pp. 124728-124737, 2022.

A 30-W Tri-Mode GaN Power Amplifier Based on Reconfigurable Multi-Network Architecture

Bowen Tang
School of Electronic Science and Engineering University of Electronic Science and Technology of China
Chengdu, China
mr.tang007@foxmail.com

Chi Chen
School of Electronic Science and Engineering University of Electronic Science and Technology of China
Chengdu, China
2126560946@qq.com

Zhan Zhao
School of Electronic Science and Engineering University of Electronic Science and Technology of China
Chengdu, China
1373035426@qq.com

Yuehang Xu
School of Electronic Science and Engineering University of Electronic Science and Technology of China
Chengdu, China
yuehangxu@uestc.edu.cn

***Abstract*—This paper presents a fully integrated 30-W tri-mode gallium nitride (GaN) high power amplifier (HPA) supporting ultra-wideband (0.03–6.5 GHz), single-narrowband (SNB) (2.7–3.3 GHz), and concurrent dual-narrowband (DNB) operation. A dual-path single-transistor-driven distributed architecture with a shared-drain artificial transmission line enables broadband power combination. Frequency reconfiguration is achieved through gate artificial transmission lines, while switchable harmonic tuning enhances narrowband efficiency. The PA achieves over 44.8 dBm saturated output power across UWB and up to 53% peak power-added-efficiency (PAE) in SNB mode. Fabricated in 0.25-μm GaN-on-silicon carbide (SiC) process, the design maintains high efficiency under continuous-wave operation.**

Keywords—high efficiency, high power amplifier, tri-mode, ultra-wideband.

I. Introduction

Modern cognitive radio, electronic warfare and wideband communication systems increasingly require power amplifiers (PAs) that can provide both multi-octave coverage and high-efficiency, spectrally clean narrowband operation [1], [2]. However, existing reconfigurable PAs often rely on switchable matching networks or resonant blocks whose parasitics deteriorate wideband performance while still failing to match the efficiency and selectivity of standalone narrowband PAs [3], [4].

To overcome these limitations, this work presents a 30-W tri-mode gallium nitride (GaN) PA that supports ultra-wideband (UWB), single-narrowband (SNB), and concurrent dual-narrowband (DNB) operations. First, frequency reconfiguration is performed directly on the gate artificial transmission lines (ATLs), enabling narrowband tuning with minimal impact on the intrinsic wideband response. Second, narrowband efficiency is enhanced through switchable harmonic-tuning stubs that shape the second- and third-harmonic impedances under SNB and concurrent DNB conditions. Supporting networks—including switchable filter branches at the drive-stage input matching network, switching DC blocks (SDCBs), and a switchable drain-bias configuration—facilitate the transition among UWB, SNB, and concurrent DNB modes. Importantly, no switches are inserted in the high-current output path. All reconfigurable elements are placed either on the gate line or in the drive stage. The proposed architecture achieves UWB coverage with high-efficiency narrowband performance.

II. Tri-Mode PA Design

A. Tri-Mode Realization

Fig. 1 shows the block diagram of the proposed PA. Mode switching is primarily enabled by the frequency-reconfigurable networks (FRNs) embedded in the gate ATLs. The FRNs can introduce a band-pass response for SNB and concurrent DNB modes with minimal degradation to the UWB mode. Efficiency is further enhanced by a harmonic-tuning network (HTN) consisting of switchable second- and third-harmonic short-circuit stubs. Supporting elements—including four switchable filter branches at the drive-stage input matching network, SDCBs, and a switchable drain-bias network—modify low-frequency and out-of-band characteristics for each operating mode.

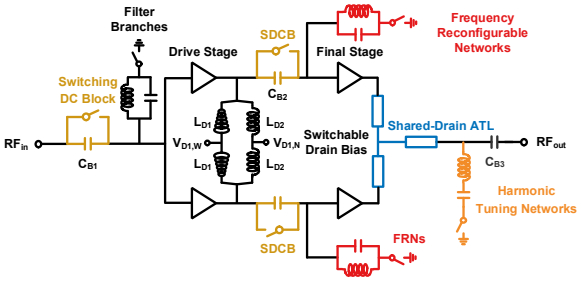


Fig. 1 Block diagram of the proposed PA.

Further, the band-pass network can be implemented by introducing either a series or a parallel LC tank into the ATL. The series LC approach requires an additional DC-feed path and couples its bandwidth strongly to the ATL inductor Lg, reducing both tunability and wideband matching. The parallel LC–C structure avoids these issues by interacting weakly with the original ATL and is therefore selected, as shown in Fig. 2(a). One section of the reconfigurable gate ATL is analyzed using the ideal equivalent circuit shown in Fig. 2(b). The input impedances of band-pass and low-pass modes are given by:

$$Z_{\text{in-bp}}(\omega)=\frac{j\omega C_{\text{bs}}\left(1-\omega^2 L_{\text{p}}C_{\text{p}}\right)+j\omega C_{\text{gs}}\cdot\left[1+j\omega R_{\text{on}}C_{\text{bs}}-\omega^2 L_{\text{p}}\left(C_{\text{p}}+C_{\text{bs}}+j\omega R_{\text{on}}C_{\text{p}}C_{\text{bs}}\right)\right]}{1+\text{j}\omega R_{\text{on}}C_{\text{bs}}-\omega^2 L_{\text{p}}\left(C_{\text{p}}+C_{\text{bs}}+j\omega R_{\text{on}}C_{\text{p}}C_{\text{bs}}\right)}, \tag{1}$$

$$Z_{\text{in-lp}}(\omega)=\frac{1-\omega^2 L_{\text{p}}\left(C_{\text{p}}+C_{\text{e}}\right)}{j\omega C_{\text{e}}\left(1-\omega^2 L_{\text{p}}C_{\text{p}}\right)+j\omega C_{\text{gs}}\left[1-\omega^2 L_{\text{p}}\left(C_{\text{p}}+C_{\text{e}}\right)\right]},\ C_{\text{e}}=\frac{C_{\text{bs}}C_{\text{off}}}{C_{\text{bs}}+C_{\text{off}}}. \tag{2}$$

Given their complexity, the impact of parameters on circuit performance is evaluated via simulation. The analysis identifies the gate-source parasitic capacitance C_{gs} as the dominant factor affecting S_{21} of the reconfigurable gate ATL. The simulated S_{21} with varying C_{gs} in low-pass and band-pass modes are presented in Fig. 3(a) and (b), and the values of other components are kept the same. The results demonstrate that minimizing C_{gs} reduces insertion loss in both modes, as a smaller C_{gs} will decrease the cutoff frequency of gate ATL.

979-8-3315-4544-4/26/$31.00 ©2026 IEEE

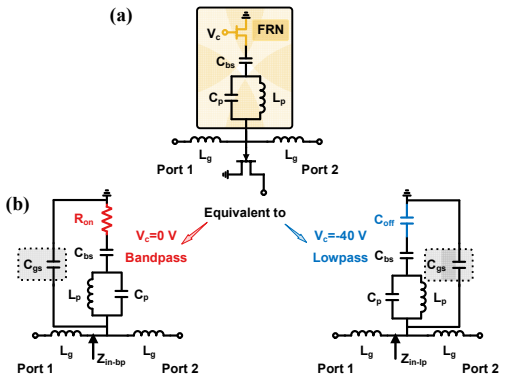


Fig. 2 (a) One section of the reconfigurable gate ATL. (b) The ideal band-pass and low-pass equivalent circuits of the reconfigurable gate ATL.

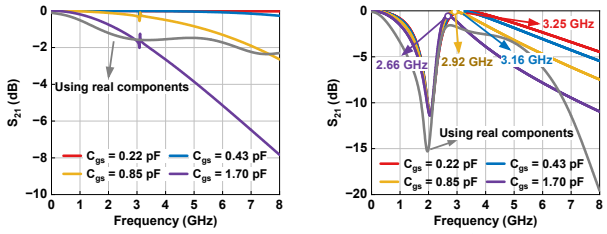


Fig. 3 Analysis of the modal parameters of reconfigurable gate ATL in (a) low-pass mode and (b) band-pass mode.

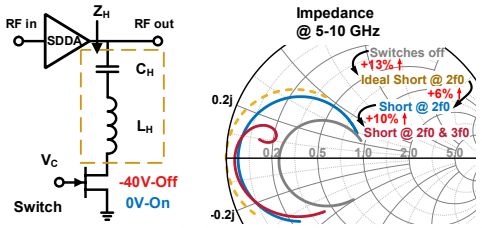


Fig. 4 Schematic of HTN with the simulated impedance at 2nd and 3rd harmonics (5–10 GHz).

Furthermore, simulations using real component models also are presented in Fig. 3(a) and (b) to validate the practical implementation.

SDCBs and switchable drain-bias network determine the low-frequency behavior. When SDCB is enabled, a large blocking capacitor and a large off-chip conical inductor preserve low-frequency gain for UWB and concurrent DNB operations. When disabled, the series combination of two blocking capacitors forms a small effective capacitance. Together with a small off-chip inductor, a high-pass response is introduced that enhances SNB out-of-band suppression. This network primarily supports mode switching through low-frequency cutoff control.

To enhance the efficiency in narrowband modes, switchable LC harmonic short-circuit stubs are tapped onto the shared-drain ATL, as shown in Fig. 4. The input impedance Z_H and resonant frequency f_c of the stub are given by:

$$Z_H(\omega) = \frac{1-\omega^2 L_H C_H}{j\omega C_H}, \tag{3}$$

$$f_c = \frac{1}{2\pi}\sqrt{\frac{1}{L_H C_H}}. \tag{4}$$

Switchable second- and third-harmonic short-circuit stubs are introduced to enhance narrowband efficiency. Series switch resistance limits ideal second-harmonic tuning; therefore, third-harmonic tuning is added for compensation. The SNB mode achieves up to 10% efficiency improvement while maintaining unaffected UWB performance when disabled.

B. Overall PA Design

The PA employs a dual-path SDDA structure. The final stage uses a three-stage distributed configuration with 3.2-mm gate width per path to achieve 30-W output power. The drains are combined through a shared-drain ATL. Switchable filter branches are implemented at the drive-stage input for narrowband suppression. Fig. 5 shows the complete schematic, and Table 1 summarizes the bias configurations.

III. Measurement and Discussion

Fig. 6 shows the photo of the PA with an area of 5.10 × 2.21 mm^2. The PA was fabricated using a 0.25-μm GaN-on-silicon carbide (SiC) process. Small signal measurements were conducted under the biases of V_{d1} = 12 V, I_{d1} = 20 mA, V_{d2} = 40 V, I_{d2} = 290 mA. The comparisons of the measured and simulated *S*-parameters are shown in Fig. 7(a), (b) and (c), showing good agreement. In UWB mode, the measured S_{21} is greater than 20 dB in 0.03-6.5 GHz. In SNB mode, the measured S_{21} is greater than 24 dB in 2.6-3.3 GHz. In concurrent DNB mode, the measured S_{21} is greater than 28 dB in 0.03-0.4 GHz and 2.7-3.3 GHz. The measured

Table 1. Bias Configuration for Different Operating Modes

voltage/drain bias / operating mode	V_{c1}	V_{c2}	drain bias
UWB	0 V	-40 V	L_{D1}
SNB	-40 V	0 V	L_{D2}
Concurrent DNB	0 V	0 V	L_{D1}

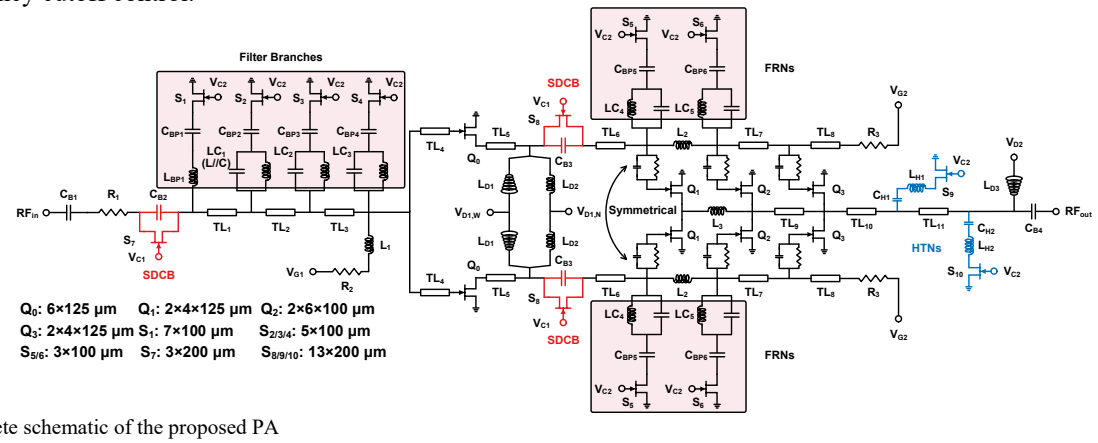


Fig. 5 Complete schematic of the proposed PA

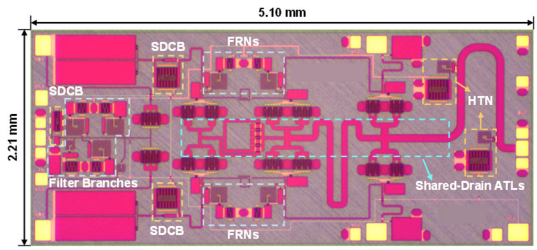


Fig. 6 Photo of the tri-mode PA.

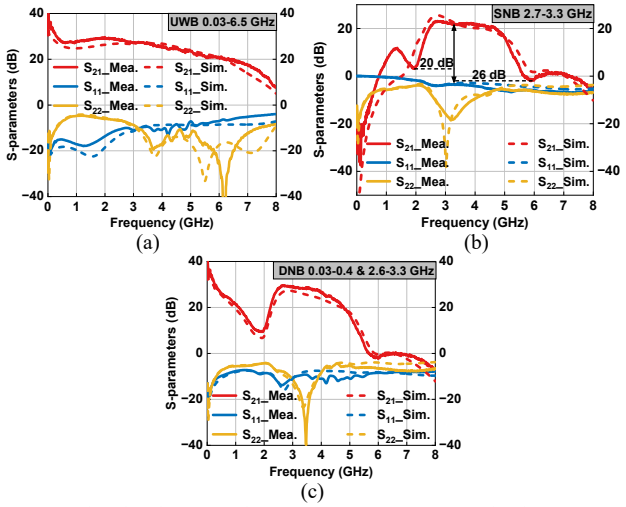


Fig. 7 Simulated and measured S-parameters. (a) UWB mode. (b) SNB mode. (c) Concurrent DNB mode.

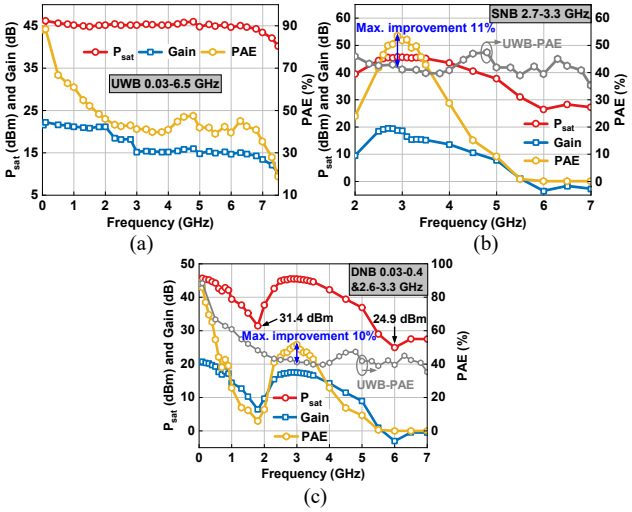


Fig. 8 Measured CW large-signal results. (a) UWB mode. (b) SNB mode. (c) Concurrent DNB mode.

continuous wave (CW) large-signal results are shown in Fig. 8. In UWB mode, the PA delivers a saturated output power (P_{sat}) exceeding 44.8 dBm within 0.03-6.5 GHz, with a power gain greater than 14.8 dB and a power added efficiency (PAE) greater than 39%. In SNB mode, the P_{sat} ranges from 45.4 to 45.7 dBm within 2.7-3.3 GHz. The PAE ranges from 49% to 53%, with a maximum improvement of 11% compared to UWB mode. In concurrent DNB mode, the P_{sat} exceeds 45.2 dBm in both 0.03–0.4 GHz and 2.6-3.3 GHz, and the corresponding PAE is greater than 67%/47%, with a maximum improvement of 10% compared to UWB mode in the upper band.

Table 2 and Table 3 compare the proposed PA with

Table 2. Comparison of UWB GaN PAs

Reference	BW (GHz)	P_{sat} (dBm)	PAE (%)	Gain (dB)	Area (mm×mm)
[2]	0.03-6	40.2	41	14.2	2.34×1.88
[5]	0.3-6	37.8	34	21.8	N/A
[6]	0.02-6	44.5*	29*	12.5*	3.99×2.40
This Work (CW)	**0.03-6.5**	**44.8**	**39**	**14.8**	**5.10×2.21**

* Pulse excitation.

Table 3. Comparison of S-band GaN PAs

Reference	BW (GHz)	P_{sat} (dBm)	PAE (%)	Gain (dB)	Area (mm×mm)
[8]	2.8-3.2	46.8*	58*	21.8*	N/A
[9]	2.7-3.5	44.8*	52*	25.8*	3.38×2.00
[10]	3.1-3.5	50.1*	53*	22.1*	5.80×3.30
This Work (CW)	**2.7-3.3**	**45.4**	**49**	**18.4**	**5.10×2.21**

* Pulse excitation.

reported UWB and S-band GaN PAs, respectively. In UWB mode, the design delivers a wide bandwidth with state-of-the-art P_{sat} and competitive PAE. In SNB mode, the PA maintains competitive performance under rigorous CW conditions. The results verify competitive reconfigurable performance.

IV. Conclusion

A 30-W tri-mode GaN PA is presented in this paper. Combining a shared-drain ATL-based SDDA topology with a reconfigurable multi-network architecture, the PA achieves high-efficiency UWB, SNB and concurrent DNB operations. The results demonstrate that a single multi-mode integrated chip, operating under rigorous CW conditions, can match the performance of single-mode components. This offers a compact, power-efficient, and thermally robust solution for next-generation multi-function systems.

References

[1] B. Kim, M. Greene and M. Osmus, "Broadband high efficiency GaN discrete and MMIC power amplifiers over 30 – 2700 MHz range," in *2014 IEEE MTT-S International Microwave Symposium (IMS2014)*, Tampa, FL, USA, 2014, pp. 1-3.

[2] B. Tang, H. Jin, Z. Zhang, et al., "A 0.03 to 6 ghz gallium nitride monolithic microwave integrated circuit power amplifier with improved oip3/pdc using nonlinear cancellation," *Chinese Journal of Electronics*, vol. 35, no. 1, pp. 1–15, 2026.

[3] A. Ghiotto, E. Kerhervé, N. Demirel, et al., "Dual-mode power amplifier module with in-band reconfigurable output power for multifunctional radar and radio communication systems," in *2014 International Radar Conference*, Lille, France, 2014, pp. 1-3

[4] S. Chen, F. Yan, Y. Liang et al., "A 1.5-to-17 GHz Non-uniform Distributed Power Amplifier Using Reconfigurable Modules in 0.25μm GaN HEMT," in *2023 IEEE/MTT-S International Microwave Symposium - IMS 2023*, San Diego, CA, USA, 2023, pp. 323-326.

[5] "ADPA1116, 0.3 GHz to 6 GHz, 39.5 dBm, GaN Power Amplifier," Analog Devices, Norwood, MA, USA.

[6] "CMPA0060025D, 25 W, DC-6.0 GHz, GaN MMIC Power Amplifier," MACOM, Lowell, MA, USA, 2022.

[7] "QPA1000, 2.8-3.2 GHz, 50 Watt GaN Power Amplifier," Qorvo, Greensboro, NC, USA.

[8] "CMPA2735030, 30 W, 2.7-3.5 GHz, GaN MMIC Power Amplifier," MACOM, Lowell, MA, USA.

[9] P. K. Singh, K. Suman, S. K. Gedela, et al., "100 W High Power Amplifier MMIC in 0.45 μm GaN Technology," *2019 14th European Microwave Integrated Circuits Conference (EuMIC)*, Paris, France, 2019, pp. 1-4

A Fully Integrated Low-Cost 5-GHz Doherty Power Amplifier Using Compact Triple-Coil Splitter-Combiner in 180-nm CMOS

Zhuoyin Chen
School of Integrated Circuits
Beijing University of Posts and Telecommunications
Beijing, China
chenzhuoyin001@gmail.com

Yongle Wu
School of Integrated Circuits
Beijing University of Posts and Telecommunications
Beijing, China
wuyongle138@gmail.com

Shuchen Zhen
School of Integrated Circuits
Beijing University of Posts and Telecommunications
Beijing, China
zhensc2024@bupt.edu.cn

Zhixuan Gong
School of Integrated Circuits
Beijing University of Posts and Telecommunications
Beijing, China
gongzhixuan0924@gmail.com

Xiaopan Chen
School of Integrated Circuits
Beijing University of Posts and Telecommunications
Beijing, China
chenxiaopan@bupt.edu.cn

Weimin Wang
School of Integrated Circuits
Beijing University of Posts and Telecommunications
Beijing, China
wangwm@bupt.edu.cn

***Abstract*—This paper presents a 5-GHz Doherty power amplifier (PA) implemented in a cost-effective 180-nm 1P6M CMOS technology with only one ultra-thick metal (UTM) layer. To enable practical integration in legacy nodes with limited passive quality factors, an integrated transformer-based triple-coil network is adopted to realize signal splitting and load combining within a unified passive structure, reducing interconnection complexity and layout parasitics. The PA employs a differential cascode architecture with double neutralization to enhance gain and stability. Designed for 5-GHz applications, the measured results show a small-signal gain of 12.7 dB, a P_{SAT} of 21.8 dBm, a PAE_{max} of 20.8%, and a PAE_{6dB} of 14.7%. For single-carrier 20-MHz 64-QAM signals, the measured P_{avg} of 12.7 dBm and ACLR of –25.1 dBc at 5 GHz are achieved at an EVM level of –25.1 dB. The core circuit area is 1.42 mm^2.**

***Index Terms*—CMOS, Doherty, impedance matching, power amplifier (PA), transformer.**

I. Introduction

The 5-GHz spectrum continues to gain strategic importance in next-generation wireless systems, including Wi-Fi 6/6E, private 5G networks, and emerging industrial IoT platforms operating in unlicensed bands. Compared with mm-wave solutions, sub-7-GHz transceivers offer relaxed link budgets, improved propagation robustness, and lower implementation costs, making them attractive for consumer and edge-device markets. In these applications, power efficiency under modulated signals with a high peak-to-average power ratio (PAPR) is a critical design consideration.

Although 3-D ICs based on through-silicon via (TSV) technology offer promising integration capabilities, GaAs and advanced CMOS nodes can provide superior output power and efficiency [1] [2], legacy CMOS technologies remain highly attractive for cost-sensitive and high-volume integration. However, implementing efficient Doherty power amplifiers (PAs) in low-cost CMOS is challenging due to limited passive quality factors and the constraint of only one ultra-thick metal (UTM) layer, which constrains design flexibility and layout efficiency [3] [4] [5] [6].

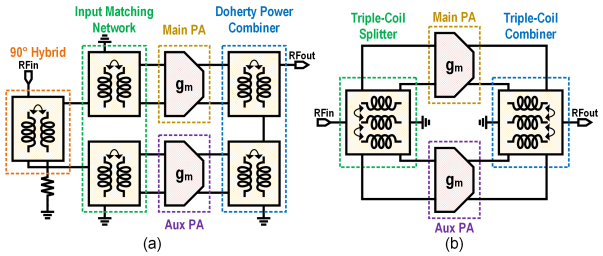


Fig. 1. (a) Basic structure of Doherty PA. (b) Proposed structure of compact Doherty PA.

To address these limitations, this work presents a fully integrated 5-GHz CMOS Doherty PA in 180-nm 1P6M 1-UTM technology. An integrated triple-coil transformer network is adopted to simultaneously realize signal splitting and load combining within a unified passive structure, reducing routing complexity and mitigating parasitic loss [7] [8]. Combined with a differential cascode architecture and double neutralization, the proposed design demonstrates a practical and area-efficient solution for low-cost sub-7-GHz CMOS transmitters.

II. Design of the Proposed Doherty PA

A conventional Doherty PA typically requires a 90° input hybrid, individual input matching networks for the main and

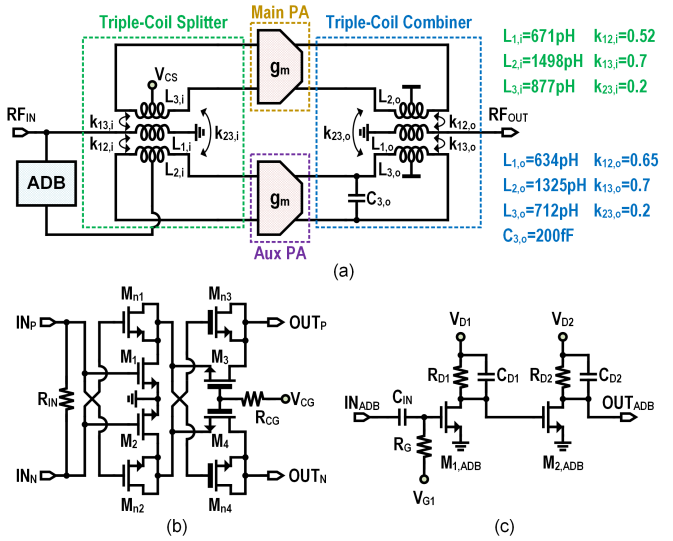


Fig. 2. (a) Schematic of the proposed compact Doherty PA. (b) Detailed circuit schematic of g_m stage. (c) Detailed circuit schematic of ADB.

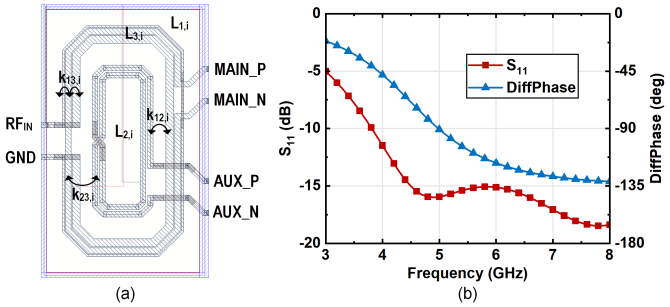


Fig. 3. (a) Layout of the triple-coil splitter. (b) Simulated S_{11} and output differential phase of the triple-coil splitter.

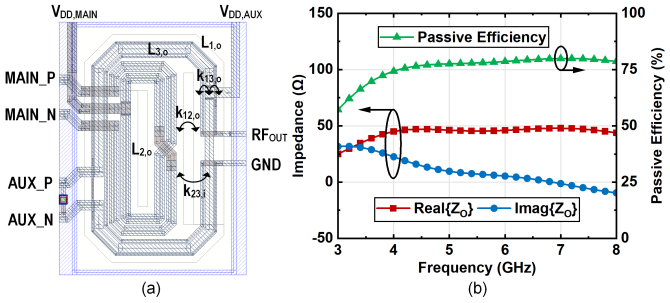


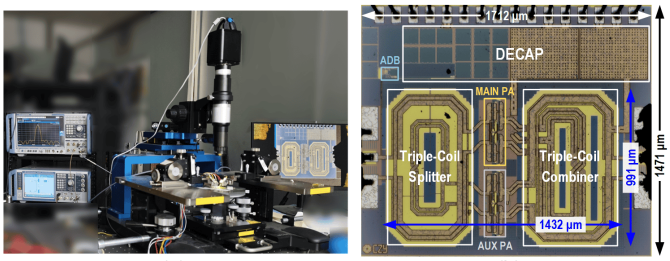
Fig. 4. (a) Layout of the triple-coil combiner. (b) Simulated output impedance and passive efficiency of the triple-coil combiner.

auxiliary amplifiers, and a transformer-based load combining network at the output, as illustrated in Fig. 1(a). In sub-7-GHz CMOS implementations, these passive networks are commonly realized using multiple transformers and routing interconnections, which significantly increase layout complexity and metal resource consumption. Such challenges become more critical in legacy 180-nm processes where only one UTM layer is available for high-Q passive implementation. To address these constraints, the proposed architecture, shown in Fig. 1(b), employs triple-coil transformer structures at both the input and output. The input triple-coil network simultaneously provides signal splitting with a 90° phase difference and impedance transformation, while the output triple-coil network realizes Doherty load combining within a compact passive structure [7] [8]. By integrating these functions, the overall passive network is simplified and better suited for single-UTM CMOS implementation.

Fig. 2(a) shows the schematic of the proposed compact Doherty PA. It consists of a main g_m stage, an auxiliary g_m stage, an adaptive-bias circuit (ADB), a triple-coil splitter, and a triple-coil combiner. The detailed circuit schematic of g_m stage is shown in Fig. 2(b). A differential cascode structure with double neutralization is adopted to enhance gain and improve stability. The main g_m stage is biased at Class-AB, while the auxiliary g_m stage operates in Class-C. To improve efficiency at power back-off (PBO), a two-stage ADB, shown in Fig. 2(c), is applied to dynamically control the auxiliary g_m stage. The layout of the proposed triple-coil splitter is shown in Fig. 3(a). Inductors $L_{1,i}$, $L_{2,i}$, and $L_{3,i}$ are all implemented using the UTM layer to reduce series resistance. The line widths of $L_{2,i}$ and $L_{3,i}$ are both 20 μm to balance quality factor and area constraints. To enhance magnetic coupling between the primary and one secondary while suppressing undesired coupling between the two secondary coils, $L_{1,i}$ is edge-coupled symmetrically to the two sides of $L_{3,i}$, which increases $k_{13,i}$ and reduces $k_{23,i}$. As shown in Fig. 3(b), the simulated input return loss is better than -15 dB over the target band. At 5 GHz, the differential outputs exhibit a 90° phase difference, enabling the splitter to simultaneously perform signal division and quadrature generation without requiring a conventional hybrid coupler. The layout of the triple-coil combiner is shown in Fig. 4(a). Similar to the splitter, inductors $L_{1,o}$, $L_{2,o}$, and $L_{3,o}$ are realized using the UTM layer to minimize conduction loss. The line widths of $L_{2,o}$ and $L_{3,o}$ are greater than 30 μm, to accommodate higher current density at the output side. The primary coil $L_{1,o}$ adopts symmetric edge coupling with $L_{3,o}$ to increase $k_{13,o}$ while suppressing $k_{23,o}$, improving power combining efficiency and port isolation. Fig. 4(b) presents the simulated real and imaginary parts of the output impedance seen by the PA, demonstrating the proper impedance transformation at 5 GHz. The simulated passive efficiency of the combiner reaches 78% at 5 GHz, corresponding to an insertion loss of 1.1 dB, validating its suitability for Doherty load modulation in a single-UTM CMOS implementation.

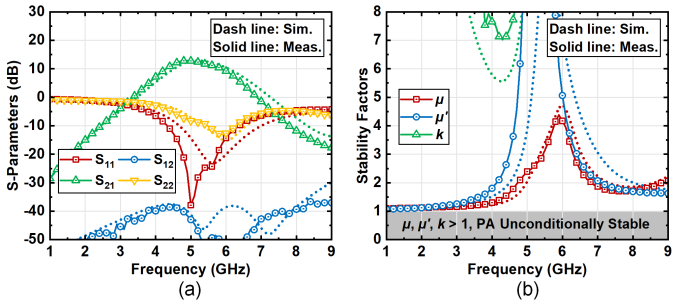
III. Measurement Results

The proposed compact Doherty PA is designed in a 180-nm CMOS process. Fig. 5 shows the measurement setup and chip micrograph. The core area of the chip is 1.42 mm^2. Fig. 6(a) shows the measured S-parameters at a supply voltage of 3.3 V. S_{21} of the PA achieves 12.9-dB peak gain and a 3-dB bandwidth from 4.2 to 6.1 GHz. The proposed triple-coil



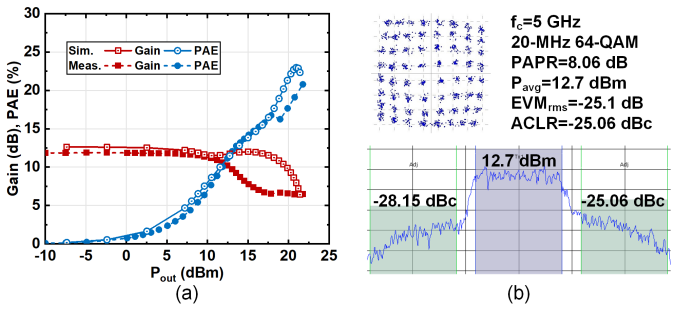
(a) (b)

Fig. 5. (a) Measurement setup. (b) Chip micrograph of the Doherty PA.



(a) (b)

Fig. 6. (a) Measured S-parameters. (b) Measured stability factors.



(a) (b)

Fig. 7. (a) Measured large-signal gain and PAE versus output power. (b) Measured 64-QAM constellation and signal spectrum.

splitter at the input ensures a wide S_{11} response, remaining below -10 dB from 4.3 to 6.4 GHz. Fig. 6(b) displays the measured stability factors, confirming unconditional stability in the operating band. The measured large-signal continuous-wave (CW) performance are shown in Fig. 7(a). The proposed PA achieves a P_{SAT} of 21.8 dBm and a PAE_{max} of 20.8% at 5 GHz. At PBO, the PAE_{6dB} is measured to be 14.7%, demonstrating PBO efficiency enhancement. Fig. 7(b) exhibits the measured results of single-carrier 20-MHz 64-QAM signals without digital predistortion (DPD). At 5 GHz, the proposed PA achieves 12.7 dBm P_{avg} with –25.1-dB EVM_{rms} and –25.1-dBc ACLR. TABLE I summarizes and compares the performance of the CMOS PAs.

IV. Conclusion

This paper presents a fully integrated 5-GHz Doherty PA implemented in a 180-nm 1P6M CMOS technology with only one UTM layer. An integrated triple-coil transformer network is employed to realize signal splitting and load combining within a unified passive structure, reducing routing complexity and parasitics. The PA adopts a differential cascode architecture with double neutralization to enhance gain and stability. The proposed design demonstrates a practical and low-cost CMOS solution for sub-7-GHz wireless transmitters.

TABLE I
Performance Comparison of CMOS PAs

Ref.	[3]	[9]	[4]	[10]	This Work
Technology	180-nm	180-nm	90-nm	90-nm	180-nm
UTM layers	1	1	2	1	1
Topology	Single-End Doherty	2nd-Trap Linear	Series-Combined Doherty	Dual-Power Mode	Triple-Coil Doherty
Freq. (GHz)	2.4	5	2.4	5.2	5
Gain (dB)	12	17.3	16.6	25.0*	12.7
P_{SAT} (dBm)	21.5	22.3	20.5	24.9	21.8
PAE_{max} (%)	14.5	28.3	26.7	25.6	20.8
PAE_{6dB} (%)	11.5	N.A.	15.5*	12.0	14.7
Area (mm^2)	2.76	1.05	1.92	2.9	1.42

*graphically estimated

Acknowledgment

This work was supported by National Natural Science Foundations of China (No. 62320106002, No. U21A20510, No. U23A20291, and No. U22A2014). The authors would like to thank Prof. Wenhua Chen from Tsinghua University for providing the test facilities and experimental support.

References

[1] J. Bachi et al., "A novel approach for Doherty PA design using a compact L-C combiner," *IEEE Trans. Circuits Syst. II, Exp. Briefs*, vol. 69, no. 10, pp. 4023-4027, Oct. 2022.

[2] S. Imai, K. Mukai, H. Okabe, and T. Wada, "Dual-adaptive bias scheme of condition-tolerant Doherty power amplifier for 5G handsets," *IEEE Trans. Microw. Theory Techn.*, vol. 73, no. 5, pp. 2695-2710, May 2025.

[3] L. Yang et al., "A 2.4 GHz fully integrated cascode-cascade CMOS Doherty power amplifier," *IEEE Microw. Wireless Comp. Letters*, vol. 18, no. 3, pp. 197-199, Mar. 2008.

[4] E. Kaymaksut and P. Reynaert, "Transformer-Based Uneven Doherty Power Amplifier in 90 nm CMOS for WLAN Applications," *IEEE J. Solid-State Circuits*, vol. 47, no. 7, pp. 1659-1671, Jul. 2012.

[5] Z. Chen et al., "A K-band CMOS high-selectivity power amplifier with compact asymmetrical filtering coupled resonator network," *IEEE Microw. Wireless Technol. Lett.*, vol. 36, no. 2, pp. 261-264, Feb. 2026.

[6] Z. Chen et al., "A Ku-/K-Band Switchless Reconfigurable Dual-Band Tri-Mode Filtering CMOS Power Amplifier," *IEEE Microw. Wireless Technol. Lett.*, early access, Feb. 9, 2026, doi: 10.1109/LMWT.2026.3658952.

[7] E. Liu and H. Wang, "A 28-GHz Extremely Compact Doherty Power Amplifier With a Single Transformer-Based Doherty Active Load Modulation Matching Network," *IEEE J. Solid-State Circuits*, early access, Nov. 4, 2025, doi: 10.1109/JSSC.2025.3626463.

[8] L. Liu, Y. Fang, Q. Zhou, T. Chi, and S. Li, "A mm-Wave Doherty Power Amplifier in a Single-Path Footprint Using Compact Reciprocal Doherty Networks," in *2026 IEEE Int. Solid-State Circuits Conf. (ISSCC)*, San Francisco, CA, USA, Feb. 2026.

[9] J. -H. Song et al., "CMOS Power Amplifiers with Symmetrical IMD3 Performance for 802.11ac 5G-band WiFi Applications," in *2024 IEEE Asia-Pacific Microw. Conf. (APMC)*, Nov. 2024, pp. 955-957.

[10] T.-S. Yang, W.-W. Wang, P.-Y. Hsu, and L.-H. Lu, "A 5.2-GHz area-efficient RF front-end with 2.79 x PAE enhancement at 7.7-dB power back-off," in *IEEE MTT-S Int. Microw. Symp. Dig.*, Jun. 2024, pp. 698-701.

A Compact Wideband Filtering Power Dividers Using D-CRLH Resonators

1st Xueyu Huang
School of Electronic and Information Engineering
South China University of Technology
Guangzhou 510640, China
202310182133@mail.scut.edu.cn

2nd Wenjie Feng
School of Electronic and Information Engineering
South China University of Technology
Guangzhou 510640, China
fengwenjie1985@163.com

3rd Wenquan Che
School of Electronic and Information Engineering
South China University of Technology
Guangzhou 510640, China
eewqche@scut.edu.cn

4th Kun Tang
School of Electronic and Information Engineering
South China University of Technology
Guangzhou 510640, China
tangkun@scut.edu.cn

5th Haoshen Zhu
School of Electronic and Information Engineering
South China University of Technology
Guangzhou 510640, China
zhuhs@scut.edu.cn

***Abstract*—A design method for realizing a wideband filtering power divider (FPD) by adjusting the line-width of the resonators is proposed in this paper. Due to the slow-wave characteristic of the D-CRLH resonator, a compact circuit size is achieved. In addition, a stopband rejection exceeding 10f_0 with a suppression level of better than 20 dB is realized by cascading a low-pass structure with the D-CRLH resonator. A wideband FPD with center frequency of 0.66 GHz and the fractional bandwidth of 44.2% is designed, fabricated and measured. The measured insertion loss is less than 4.05 dB and the isolation between two output ports is better than 21.5 dB from DC to 4.42 GHz (6.7f_0). Simulated and measured results are in good agreement, validating the proposed approach.**

***Keywords*—Compact size, dual composite right-/left-handed (D-CRLH), filtering power divider (FPD), high-isolation, ultra-wide stopband.**

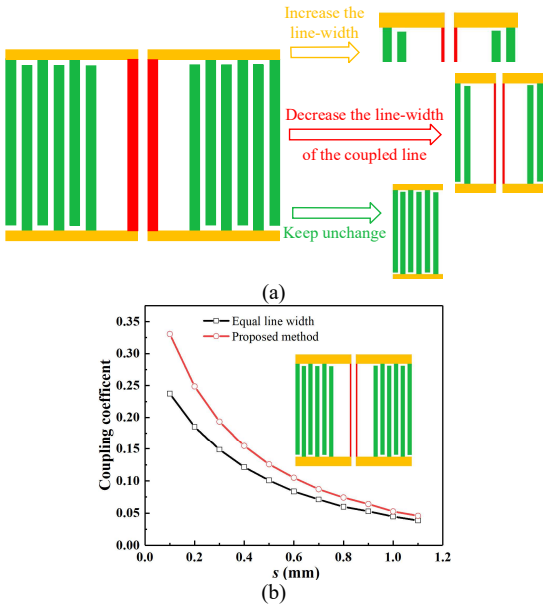


Fig. 1 (a) The structure of the proposed method to implement strong coupling, (b) Comparison of coupling coefficient between different resonators.

Optimized Design of Compact Multi-Coil Arrays for Misalignment-Tolerant Wireless Power Transfer

Zihang Huang[1], Jingchen Wang[1], Zhao Wang[1], Rui Pei[1], Bintao Hu[2], Wenzhang Zhang[2], Qian Dong[1], Eng Gee Lim[1],
[1]School of Advanced Technology, Xi'an Jiaotong-Liverpool University, Suzhou, China
[2]School of Internet of Things, Xi'an Jiaotong-Liverpool University, Suzhou, China

***Abstract*—While magnetic resonant wireless power transfer (WPT) offers significant convenience, its performance typically degrades under misalignments. To address this, an optimized 3×3 hybrid multi-coil transmitter array was designed for enhanced robustness. The proposed approach optimizes the array topology by removing redundant, weakly coupled elements and incorporating auxiliary gap coils to bridge magnetic nulls. This structural refinement not only intensifies the magnetic field but also achieves a more uniform field distribution. Simulation results indicate that the proposed WPT link delivers a power transfer efficiency of 81% at a transfer distance of 30 mm, exhibiting high tolerance to lateral and angular offsets. This compact transmitter configuration provides a practical solution for maintaining high-efficiency power delivery in misalignment-prone near-field charging scenarios.**

Keywords—wireless power transfer; magnetic resonance coupling; coil arrays; misalignment tolerance.

I. INTRODUCTION

Wireless power transfer (WPT) has recently attracted substantial research interest, driven by its inherent advantages in operational safety, convenience, and electrical insulation across diverse applications [1]. While near-field WPT utilizes resonate configurations (e.g., spirals and coils) to maintain high power transfer efficiency (PTE) over short distances [2], its performance remains highly sensitive to the relative positioning of the coupling elements. In practical scenarios, the PTE is often significantly compromised by intrinsic conductor losses and spatial misalignments, specifically lateral offset and angular rotation. Consequently, developing misalignment-tolerant architectures with robust coupling characteristics has become a primary objective for advancing near-field WPT technology.

To mitigate the adverse effects of misalignment, various methodologies have been investigated. One prominent strategy involves the deployment of multi-coil transmitter architectures, which are capable of homogenizing the near-field distribution and extending the effective charging volume. For instance, petal-shaped coil geometries have been reported to sustain high PTE under significant lateral offsets, providing an effective passive mechanism for enhancing misalignment robustness [3]. Additionally, dual-layer planar loop arrays have demonstrated superior spatial tolerance, yielding substantial efficiency gains over conventional single-layer configurations [4]. Beyond passive structures, reconfigurable coil arrays offer active compensation by dynamically steering the near-field distribution through impedance matching or capacitive tuning, thereby maintaining connectivity under severe misalignment [5]. Alternatively, metamaterial-based approaches have emerged as a sophisticated means of shaping magnetic flux. By tailoring the effective permeability—specifically through the use of negative or near-zero permeability (MNZ) inclusions—these materials can intensify magnetic coupling while simultaneously suppressing leakage fields [6].

However, despite these advancements, existing multi-coil structures often face a trade-off between structural complexity and misalignment robustness, or they require sophisticated active control systems that increase overall cost and volume. Building upon the hybrid coil-array concept [7], this paper presents a highly optimized, passively tuned transmitter architecture designed for robust WPT. Unlike idealized analyses, the proposed design is evaluated using realistic copper loss models to ensure practical fidelity. A pivotal contribution of this work lies in the strategic simplification of the array geometry, achieving an optimal balance between PTE and device footprint. Specifically, to enhance magnetic field intensity and homogeneity, the redundant center of the original array was replaced with a central square patch, while auxiliary circular sub-coils were integrated to bridge coupling gaps. By eliminating the need for complex active control, this compact architecture provides a cost-effective and robust solution for misalignment-tolerant near-field charging.

II. ARCHITECTURE OF THE PROPOSED WPT LINK

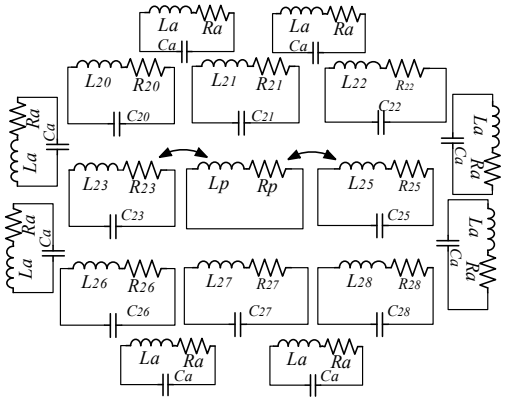


Fig. 1. Equivalent circuit model of the proposed coil-array transmitter.

This work is partially supported by the XJTLU AI University Research Centre, Jiangsu Province Engineering Research Centre of Data Science and Cognitive Computation at XJTLU and SIP AI innovation platform (YZCXPT2022103), and XJTLU Research Development Fund (RDF-24-01-079, RDF-22-02-099, RDF-22-02-047 and in part by the National Science Foundation of the Jiangsu Higher Educational Institution of China No. 25KJB510033).

XXX-X-XXXX-XXXX-X/XX/$XX.00 ©20XX IEEE

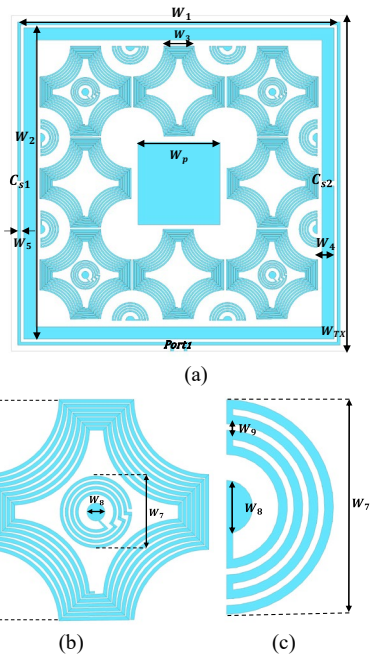


Fig. 2. Geometric configuration of the proposed Tx coil-array transmitter: (a) overall layout with a central square patch and series capacitor locations; (b) star-shaped unit element; (c) auxiliary circular sub-coil.

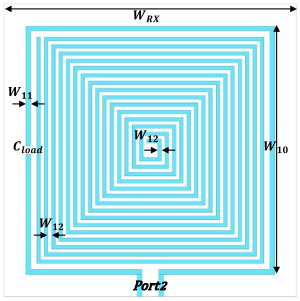


Fig. 3. The structure of the proposed Rx resonant coil.

TABLE I. PARAMETERS OF THE PROPOSED WPT LINK

Parameters	Value	Parameters	Value	Parameters	Value
w_1	141.33 mm	w_7	12.8 mm	w_{TX}	146 mm
w_2	136 mm	w_8	3.2 mm	w_p	36 mm
w_3	13.33 mm	w_9	0.47 mm	w_{RX}	120 mm
w_4	5.33 mm	w_{10}	102 mm	C_{s1}	47 pF
w_5	1.33 mm	w_{11}	2 mm	C_{s2}	363 pF
w_6	40 mm	w_{12}	1.5 mm	C_{load}	500 nF

Fig. 1 illustrates the equivalent lumped-element circuit of the proposed transmitter (Tx) structure. Each resonator within 3×3 array is characterized by its self-inductance (L_{ij}), intrinsic resistance (R_{ij}), and parasitic capacitance (C_{ij}). To further refine the magnetic coupling, eight auxiliary gap coils are incorporated into the model, represented by their respective parameters L_a, R_a and C_a. Distinct from conventional periodic arrays, the central metallic patch is treated as a lossy inductive element (L_p, R_p).

The geometric configurations of the proposed transmitter (Tx) and receiver (Rx) are illustrated in Fig. 2 and Fig. 3, respectively. These are deposited on an FR-4 dielectric substrate with a thickness of 1.0 mm and a relative permittivity of 4.4. The Rx resonator is implemented as a square planar spiral coil consisting of 15 turns.

III. PERFORMANCE OF THE PROPOSED WPT LINK

This section evaluates the performance of the proposed WPT link based on full-wave electromagnetic simulations in CST Studio Suite. As illustrated in Fig. 4(a), the transmission coefficient $|S_{21}|$ reaches -0.95 dB at the operating frequency of 13.56 MHz when the transfer distance is 30 mm. At a coil separation of 30 mm. Following the S-parameter-based efficiency derivation [8], the peak PTE is calculated as 81% at the operating frequency. Fig. 4(b) depicts the variation of $|S_{21}|$ and the estimated PTE as a function of the transfer distance. Remarkably, at an extended distance of 60 mm, the system maintains a robust efficiency of approximately 40%. This gradual roll-off characteristic underscores the link's capability for stable power delivery across an enhanced operating range.

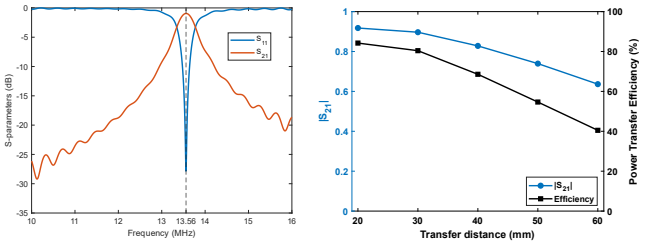


Fig. 4. (a)Simulated S_{11} and S_{21} of the proposed WPT link at a transfer disctance of 30; (b) Comparison of S_{21} and PTE against WPT transfer distance.

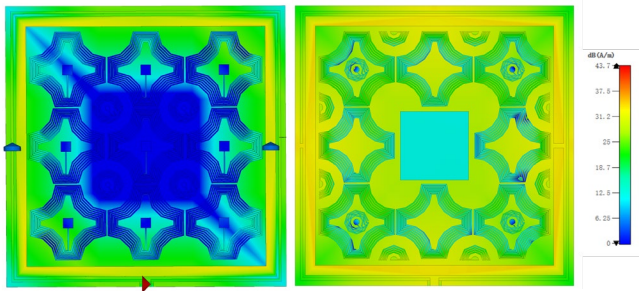


Fig. 5. Simulated magnetic field magnitude distribution of the transmitter array:(a) Enlarged 3×3 layout.; (b) Proposed Tx coil-array.

As illustrated in Fig. 5, the original 3×3 array architecture exhibits a distinct low-flux region near the center, indicating a diminished coupling zone. To mitigate it, a central square patch is integrated into the design, along with eight auxiliary gap coils incorporated at the edge. Compared to the 3×3 baseline, the average magnetic field intensity in the central region increases by 18.7 dB. The metallic patch facilitates magnetic coupling in the under-coupled zone by establishing a passive current path via induced eddy currents. This redistribution of magnetic flux homogenizes the near field, effectively bridging the central "cavity" to ensure robust power transfer.

IV. Misalignment Performance of the Proposed Link

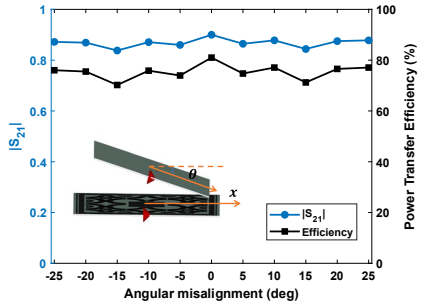


Fig. 6. Comparison of $|S_{21}|$ and PTE against WPT angular misalignment.

The proposed WPT link demonstrates exceptional robustness against angular tilt across the entire evaluation range of -25° to 25° as illustrated in Fig. 6. Due to the geometric symmetry of the structure, the transmission characteristics exhibit an approximately symmetric response with respect to positive and negative tilt angles, with only minor deviations caused by asymmetric field coupling and edge effects. Throughout the angular span, the PTE remains consistently above 70%, with the transmission coefficient $|S_{21}|$ staying above 0.84. This performance indicates that the hybrid coil array effectively mitigates the coupling loss typically associated with receiver inclination. A notable observation is the non-linear "recovery" characteristic between 15° and 25°. While the efficiency reaches a local minimum of approximately 71% at a tilt of 15°, it subsequently ascends to 77% as the angle further increases to 25°. As the Rx tilts, the reduced air gap on one side of the coil array effectively compensates for the reduction in the projected overlap area, thereby sustaining the PTE at steep angles.

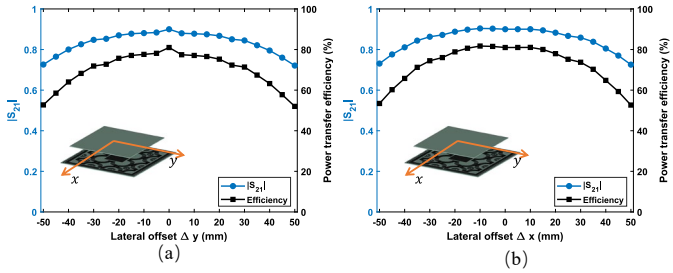


Fig. 7. Comparison of $|S_{21}|$ and power transfer efficiency under lateral misalignment. (a) Lateral offset along the x-direction (Δx). (b) Lateral offset along the y-direction (Δy).

Fig. 7 evaluates the proposed WPT link's robustness against lateral misalignments along the *x*- and *y*- axes. Lateral displacement induces variations in mutual inductance, which leads to a slight frequency detuning effect, shifting the resonant peak away from the operating frequency. Due to the symmetric configuration, the transmission characteristics exhibit nearly symmetric behavior with respect to positive and negative offsets along both axes. Across the entire evaluated lateral offset range from -50 mm to 50 mm, the PTE remains consistently above 50%. Even at the maximum tested offset of 50 mm, the system sustains a PTE of approximately 53%. Furthermore, at a moderate offset of 25 mm, the efficiency stays as high as approximately 75%, highlighting the effectiveness of the field-homogenizing patch and auxiliary coils. These results underscore the proposed WPT link's capability to provide stable and reliable power delivery, accommodating substantial positional uncertainties during practical charging scenarios.

V. Conclusion

This paper presented the systematic optimization of a compact hybrid coil-array transmitter designed to enhance magnetic field intensity and homogeneity for robust WPT. By strategically integrating a central metallic patch and auxiliary circular sub-coils, the proposed architecture efflectively eliminates "magnetic nulls" and bridges flux gaps between array elements. The proposed WPT link achieves a peak transmission coefficient $|S_{21}|$ of 0.9 at 13.56 MHz, corresponding to a peak PTE of approximately 81% at a 30 mm separation. Furthermore, the proposed hybrid array exhibits remarkable spatial robustness, maintaining a PTE above 70% across an angular tilts of up to 25° and staying above 50% throughout a lateral offset range of -50 to 50 mm. A unique coupling-path reconfiguration mechanism enables a non-linear efficiency recovery at steep angles, while the quasi-isotropic lateral tolerance ensures stable performance along both *x*- and *y*- axes. In summary, the proposed passively optimized hybrid array offers a high-performance, spatially robust solution for near-field charging, with future work focusing on dynamic frequency tracking to further mitigate detuning effects under extreme misalignments.

References

[1] X. Duan, W. Han, Y. Hu, H. Tian, J. Huang, and Z. Zhang,"Magnetic-field-editable wireless power transfer system with DD2 magnetic couplers for position detection and misalignment tolerance," IEEE Open Journal of Power Electronics, vol. 6, pp. 266–276, 2025.

[2] D. Kupreyev, K. Dautov, M. Hashmi, and M. A. Chaudhary, "High-performance planar hexagonal coil-type wireless power transfer system," in *Proc. IEEE MTT-S Latin America Microw. Conf. (LAMC)*, 2021, pp. 1–3, doi: 10.1109/LAMC50424.2021.9602805.

[3] Y. Ding, J. Wang, E. G. Lim, Z. Wang, R. Pei, and W. Zhang, "Enhancing Lateral Misalignment Tolerance in Wireless Power Transfer using Flower-shaped Coils," in *2024 IEEE 12th Asia-Pacific Conference on Antennas and Propagation (APCAP)*, 2024, doi: 10.1109/APCAP62011.2024.10881737.

[4] Y.-H. Nam and J.-H. Lee, "Efficient Near-Field Beamforming Using Two-Layer Planar Loop Array for Magnetic Resonance Wireless Power Transfer," *IEEE Microwave and Wireless Components Letters*, 2020, doi: 10.1109/LMWC.2020.3000768.

[5] T. Lim and Y. Lee, "Reconfigurable Coil Array for Near-Field Beamforming to Compensate for Misalignment in WPT Systems," *IEEE Transactions on Microwave Theory and Techniques*, vol. 69, no. 11, Nov. 2021, doi: 10.1109/TMTT.2021.3090066.

[6] C. Lu, X. Huang, C. Rong, X. Tao, Y. Zeng, and M. Liu, "A Dual-Band Negative Permeability and Near-Zero Permeability Metamaterials for Wireless Power Transfer System," *IEEE Transactions on Industrial Electronics*, vol. 68, no. 8, pp. 7072–7082, Aug. 2021, doi: 10.1109/TIE.2020.3009608.

[7] X. Zhang, J. Wang, E. G. Lim, Z. Wang, M. Leach, R. Pei, Z. Jiang, and W. Zhang, "Hybrid Circular-Polygon Coil Arrays for Robust Wireless Power Transfer in Dynamic Misalignment," in *2025 IEEE MTT-S International Microwave Workshop Series on Advanced Materials and Processes for RF and THz Applications (IMWS-AMP)*, 2025, doi: 10.1109/IMWS-AMP66175.2025.11136447.

[8] W. Zhao and S. Mai, "Design of High Efficiency Planar Spiral Coil for Implantable Wireless Power Transfer Systems," 2022 IEEE International Symposium on Circuits and Systems (ISCAS), Austin, TX, USA, 2022, pp. 147-151, doi: 10.1109/ISCAS48785.2022.993799

Study on the Design of 50-75GHz Up-conversion Module

Hui Peng[1], Zuqiang Ou[2], Zhongqian Niu[3], Yafei Wu[3], Bo Zhang[4], Jincai Qiao[2*]
[1] School of Physics and Electrical Engineering, Kashi University, Kashi, China
[2] Chongqing Institute of Microelectronics Industry Technology, University of Electronic Science and Technology of China, Chongqing, China
[3] School of Electronic Science and Engineering, University of Electronic Science and Technology of China, Chengdu, China.
[4] Yangtze Delta Region Institute (Quzhou), University of Electronic Science and Technology of China, Quzhou, China.
qiaojincai@uestc.cq.cn

***Abstract*—This paper presents a 50~75 GHz broadband up-conversion system for next-generation high-capacity communications and high-rate sensing. As electromagnetic waves extend to the millimeter-wave and terahertz bands, test instruments have an increasingly urgent demand for higher-frequency signal sources, which can be satisfied by adopting an up-conversion scheme at the system front-end. Key components are developed in this paper, including a wide-stopband waveguide filter for image rejection and a local oscillator based on frequency multiplication and amplification. The proposed up-conversion system converts a 29.5~30.5 GHz broadband signal to the 50~75 GHz band. The system is designed to achieve the following specifications: output power ⩾13 dBm, link gain ⩾20 dB, and spurious suppression >40 dBc.**

Keywords—up-converter, image frequency signals, spurious suppression.

I. INTRODUCTION

The up-conversion spread-spectrum module can shift low-frequency signals to extremely high frequencies within the available bandwidth. As key hardware for next-generation high-capacity communications and high-rate sensing, it is of great significance to modern communication systems. With the operating frequency of electromagnetic waves extending to the millimeter-wave and even terahertz bands, the requirements for signal sources in test instruments are continuously increasing, making it urgent to expand the measurement frequency to higher bands, which can be achieved by integrating an up-converter at the system front-end.

At present, domestic spread-spectrum modules have approached the international mainstream level in core indicators such as frequency range and output power. However, there is still room for improvement in refined indicators including full-band phase noise consistency, multi-channel phase coherence, and long-term frequency stability [1].

With the continuous breakthroughs in key domestic technologies such as high-frequency semiconductor processes, high-performance phase-locked loops, and intelligent calibration algorithms, domestic spread-spectrum modules will develop toward wider bandwidth, better signal quality, higher integration, and software reconfigurability, providing independent and controllable high-performance test solutions for cutting-edge fields including 6G terahertz communications, ultra-high-resolution radar, and quantum sensing.

In response to market demands and other application requirements, this paper focuses on the research of up-conversion modules operating in the 50~75 GHz frequency range [2]. By analyzing the specifications of existing up-conversion modules, it is found that improving the output frequency, power and spectrum purity of up-conversion modules is the research focus. In the signal generation chain of a signal source, the baseband or intermediate frequency signals to be synthesized must be up-converted and amplified by the RF front-end transmission chain before being converted into high-frequency RF signals. The performance of the RF front-end, especially the up-conversion module, directly determines the key indicators of the signal source such as the final output frequency, output power, spectrum purity and harmonic suppression. Therefore, integrating a high-performance up-conversion module into the system transmission chain is the main technical approach to extend the output frequency of the signal source to the millimeter-wave and even terahertz bands [3].

Accordingly, starting from the RF front-end of the signal generation chain, this paper aims to overcome the up-conversion technology of high-frequency broadband signals. The research will focus on three aspects: core device modeling, key circuit design and frequency conversion system construction, so as to make positive contributions to improving its high-frequency performance and spectrum purity [4].

II. BLOCK DIAGRAM AND SPECIFICATIONS OF THE FREQUENCY CONVERSION SYSTEM

A. Principle of Frequency Conversion System and Frequency Band Division

To achieve the up-conversion of broadband signals covering the frequency band of 50 GHz to 75 GHz, this paper proposes and verifies a scheme based on the feasibility analysis of key components, including the operating frequency band of mixers and the design complexity of filters. The system employs a local oscillator (LO) link based on frequency quadrupling to

up-convert the LO signal from 20 GHz to 26.25 GHz to the range of 80 GHz to 105 GHz. The LO frequency is boosted to 80 GHz–105 GHz mainly to avoid other high-order spurious components generated by mixing and to ensure the spectral purity of the radio frequency output. Subsequently, the up-converted LO signal is mixed with a 30 GHz intermediate frequency (IF) signal, and the desired radio frequency (RF) output ranging from 50 GHz to 75 GHz is obtained through frequency shifting. To improve the spectral purity of the RF output, a dedicated filter is integrated at the output port, which achieves a suppression level of more than 40 dBc for harmonics and other spurious components, thus ensuring the overall performance and stability of the system.

B. Maintaining the Integrity of the Specifications

As shown in Figure 1, for the spread spectrum system, the local oscillator (LO) signal (20 ~26.25 GHz) is input from the coaxial port, and first passes through a multi-stage frequency multiplication and filtering link to complete frequency spectrum shifting and suppress harmonic components. Subsequently, the power is adjusted to the optimal driving level of the mixer via a tunable attenuator and a post-stage amplifier, so as to prevent the mixer from overloading or entering the gain compression region. After the LO and intermediate frequency (IF) signals are frequency-converted by the mixer, an RF output of 50~75 GHz is generated. This output is then processed by an image rejection filter, an amplifier, and a tunable attenuator, which not only effectively suppresses spurious and image frequency interference, but also achieves precise regulation of the dynamic range of the output power, thereby fully realizing the up-conversion of broadband signals.

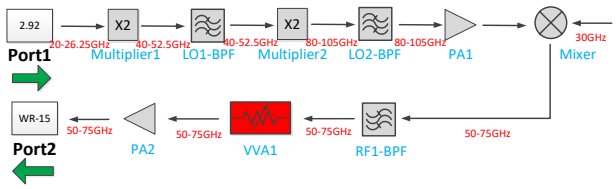


Fig. 1. Up-conversion process block diagram

The local oscillator (LO) signal is input through a 2.92mm (female) coaxial connector, the intermediate frequency (IF) signal is input through a 2.92 mm (female) connector, and the radio frequency (RF) output is delivered through a WR15 waveguide interface. The input signal power is limited to the range from DNAL to −10 dBm. In the LO link, the LO signal first undergoes frequency doubling processing, and then is mixed with the IF signal in a mixer; the generated RF signal is processed by filtering, amplification, and voltage-controlled attenuation before being output as the final RF signal.

C. Specification Requirements for the Frequency Conversion System

The up-conversion module imposes stringent requirements on the RF front-end devices, including wide bandwidth, flat output response, low spurious emissions, low local oscillator leakage, and high image rejection. The specifications of the frequency conversion module are listed as follows：

a) Output frequency: 50–75 GHz；
b) Output 1 dB compression point: > 0 dBm;
c) Spurious suppression: > 40 dBc;
d) Harmonic suppression: ≥ 40 dBc.

D. Filter Design Specifications

The local oscillator filter is used to suppress harmonics and spurious signals in the input signal, preventing them from being superimposed on the intermediate frequency (IF) signal after mixing and interfering with the radio frequency (RF) signal. The RF filter is employed to suppress image frequency signals and should also have a certain degree of suppression on the local oscillator (LO) signal, so as to improve the LO leakage suppression level.

The design specifications of the filter are listed as follows:

TABLE I
FILTER SPECIFICATIONS

Filter	Frequency	Insertion Loss	Out-of-band Rejection
LO1-BPF	40~52.5GHz	≤0.5dB	20~26.25GHz@≥45dBc 60~78.75GHz@≥45dBc
LO2-BPF	80~105GHz	≤0.5dB	40~52.5GHz @≥45dBc 120~157.5GHz@≥45dBc
RF1-BPF	50~75GHz	≤0.5dB	20~47GHz@≥45dBc 80~135GHz@≥45dBc

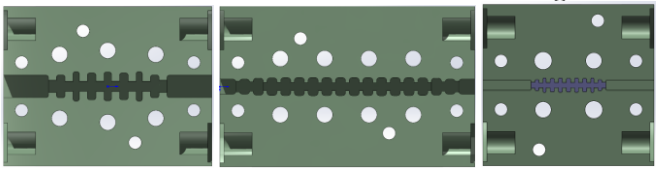


Fig. 2. Filter models operating at 40~52.5 GHz, 50~75 GHz, and 80~105 GHz

III. TEST DATA

The filter was tested using a Ceyear 3674E vector network analyzer equipped with a 1 mm coaxial extension module and a waveguide extension module, respectively. A 1 mm coaxial-to-waveguide adapter was required during the test.The test setup is shown in Fig. 3.A comparison between the measured results and the simulation results is presented in Fig. 4、Fig.5 and Fig.6.

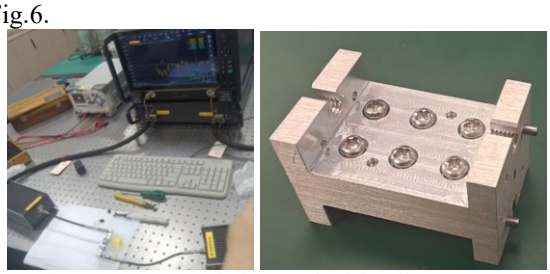


Fig. 3. Test Setup and Photograph of the Filter Prototype

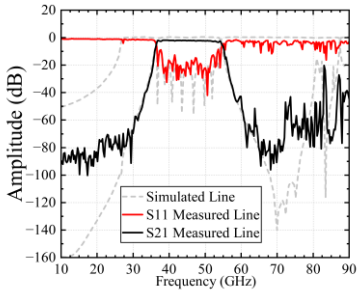


Fig. 4. Comparison of simulated and measured results for the 40~52.5 GHz filter.

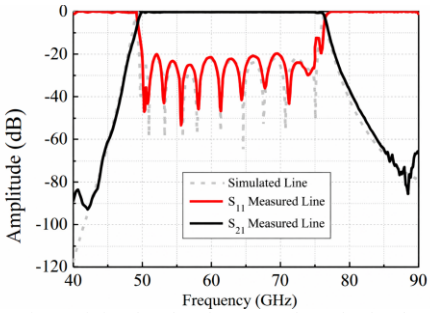


Fig. 5. Comparison of simulated and measured results for the 50~75 GHz filter.

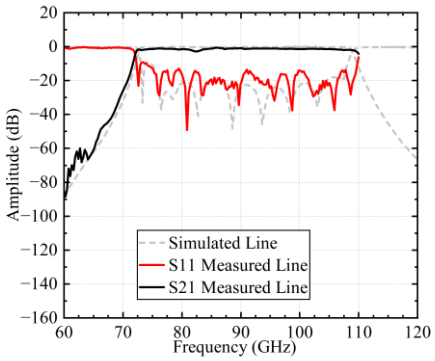


Fig. 6. Comparison of simulated and measured results for the 80~105 GHz filter.

According to the measured results, the return loss of the LO1-BPF is better than 18 dB, with an in-band insertion loss of less than 0.5 dB. Meanwhile, the filter exhibits an image rejection of greater than 50 dBc. For the LO2-BPF, the measured return loss is also better than 18 dB, and the in-band insertion loss is less than 0.5 dB. Similarly, the image rejection of this filter exceeds 50 dBc. With respect to the RF1-BPF, the measured return loss is better than 18 dB, and the rejection to local oscillator (LO) signals in the range of 80~105 GHz is higher than 50 dBc. The in-band insertion loss is less than 0.5 dB, which not only meets the design specifications but also shows good consistency with the simulation results.

The slight discrepancy between the simulation and measurement results is mainly attributed to non-ideal conductivity and surface roughness of the fabricated filter.

CONCLUSION

In this paper, three filters are designed by decomposing the filter specifications according to the project requirements.The filters adopt a waveguide Chebyshev structure with a centrally symmetric configuration. By adjusting the width and height of the resonant cavities, the dominant TE_{10} mode can be ensured to propagate in the cavities, while the higher-order modes such as TE_{20} and TE_{30} are pushed to higher frequencies, thereby improving the stopband rejection at high frequencies.The simulation results are basically consistent with the measured results. The relatively large insertion loss is mainly caused by the waveguide-to-coaxial transition loss and fabrication errors during the test.

ACKNOWLEDGMENT

This work is supported by the National Key Research and Development Program of China under Grant No. 2024YFE0200403. This work is supported by Zhejiang Provincial Natural Science Foundation LD25F040007. This work is supported by the Fundamental Research Funds for the Central Universities No. ZYGX2024Z012, No. ZYGX2024XJ009, ZYGX2024J006. This work is also supported by the Xinjiang Talent Development Fund Project No. XJRC-2025-KJ-YJ-CXPT-183. Key Scientific Research Project of Kashi University, No. 20242882.

REFERENCES

[1] MEINEL H H. Commercial applications of millimeterwaves: History, present status, and future trends [J]. IEEE Transactions on Microwave Theory and Techniques, 1995, 43(7): 1639-1653.

[2] APPLEBY R, ANDE R TON R N. Millimeter-wave and submillimeter-wave imaging for security and surveillance [J]. Proceedings of the IEEE, 2007, 95(8): 1683-1690.

[3] FENG Y N, XU K D, NIU Z Q, et al. W R-4 band wideband waveguide diplexer based on spoof surface plasmon polaritons and its application in terahertz communications [J]. IEEE Transactions on Microwave Theory and Techniques, 2024, PP(99): 1-11.

[4] DAI B L, ZHANG B, NIU Z Q, et al. A novel ultrawideband branch waveguide coupler with low amplitude imbalance [J]. IEEE Transactions on Microwave Theory and Techniques, 2022, 70(8): 3838-3846.

[5] A. A. Althuwayb, R. K. Barik, Q. S. Cheng, *et al.*, "Design and experimental verification of compact dual-band SIW power dividers with arbitrary power division," *Frequenz,* vol. 75, no. 7-8, pp. 313-318, 2021.

[6] J. Zheng, G. Zhang, X. Zhou, *et al.*, "Dual-band filtering power divider based on CSRRs loaded SIW cavity," *IEEE Transactions on Circuits and Systems II: Express Briefs,* vol. 69, no. 2, pp. 394-398, 2022.

[7] Z. Ou, Y. Zhong, J. Qiao, Z. Niu and H. Peng, "Design and Optimization of Metallic Cavity Packaging for Millimeter-Wave RF Chips," 2025 IEEE MTT-S International Microwave Workshop Series On Advanced Materials and Processes for RF and THz Applications (IMWS-AMP), Wuxi, China, 2025, pp. 1-3, doi: 10.1109/IMWS-AMP66175.2025.11136383.

Formula-Based Design of Bias Tees with Wide DC-Path Bandwidth and Transmission Zeros

1st Keebaek Lee
Dept. of Computer Science and Engineering
Korea University
Seoul, South Korea
kbstar27@korea.ac.kr

2nd Jongheun Lee
Wireless Semiconductor Division
Broadcom
Seoul, South Korea
jongheun2mml@gmail.com

3rd Juseop Lee
College of Informatics
Korea University
Seoul, South Korea
juseoplee@gmail.com

***Abstract*—This paper presents a formula-based synthesis and design method for bias tees capable of superimposing low-frequency AC signals onto a DC path while maintaining sharp frequency selectivity. By modeling the bias tee as a parallel connection of lowpass and highpass sections, closed-form expressions are derived to directly relate the element values of the RF path highpass section to those of the DC path lowpass section, allowing systematic circuit synthesis with reduced design complexity. The proposed approach enables the introduction of finite-frequency transmission zeros, resulting in a steep skirt response beyond those of conventional first-order bias tees. The fabricated prototype demonstrates an RF insertion loss better than 1 dB above 2.7 GHz and maintains acceptable matching.**

***Index Terms*—Bias tee, formula-based design, load-pull measurement, transmission zeros**

I. Introduction

Fig. 1 shows a traditional lumped-element bias tee prototype composed of three ports: a DC port, an RF port, and a DC+RF port. Between the DC and DC+RF ports, there is an inductor called RF choke that separates an RF signal from the DC port. The capacitor between the RF and DC+RF ports hinders the DC signal from flowing into the RF port. Bias tees designed based on this well-known prototype are suitable for applications to designs of active circuits such as amplifiers. In load-pull setups, commercially available bias tees are widely used to bias transistors under test, hereinafter referred to as DUTs. However, in some cases, it is necessary to superimpose low-frequency AC signals on DC bias when biasing DUTs [1], [2]. When a two-tone signal is applied, intermodulation distortion (IMD) products are generated. Those near DC appear on the supply line, modulating the supply voltage and degrading linearity. Although these IMD products cannot be eliminated, they can be controlled using an active baseband control system, which requires an appropriate bias tee to inject the control signal [2]. In this paper, we demonstrate a synthesis and design method for bias tees capable of superimposing AC signals to the DC bias and having steep skirt responses in both RF and DC paths.

This work was supported by Institute of Information and Communications Technology Planning and Evaluation grant funded by the Korea government (RS-2024-00395366, Development of RIS and NCR Component Technologies for Upper-Mid Band Smart Repeater).

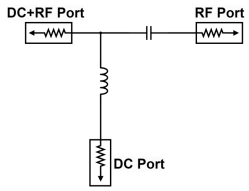


Fig. 1. Traditional lumped-element bias tee.

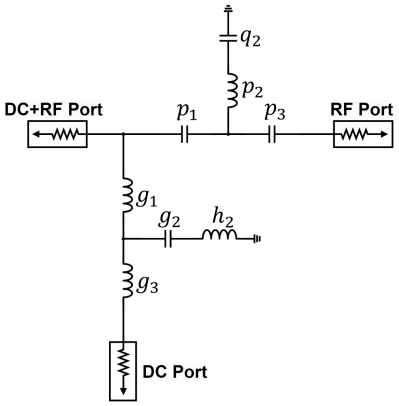


Fig. 2. Proposed bias tee prototype with lowpass and highpass sections.

II. Synthesis

The design starts with circuit synthesis. To achieve steep skirt responses in both the RF and DC paths, it is necessary to increase the circuit order. Conventional bias tees can be regarded as first-order circuits. In this paper, we first demonstrate a synthesis approach for the bias tee prototype in Fig. 2. The order of the prototype is three, and it is capable of producing a finite-frequency transmission zero in each of the DC and RF paths. DC and low-frequency signals propagate through the DC path, whereas high-frequency signals are routed through the RF path. Hence, the prototype comprises lowpass and highpass sections connected in parallel. Both sections can be synthesized using the concept of singly-terminated circuits [3]. For rapid and convenient design, this work derived closed-form formulas for the element values of the highpass section (p parameters) once those of lowpass section (g parameters)

are obtained. Hence, only half of the entire circuit needs to be synthesized. In the circuit of Fig. 2, all port impedances are assumed to be normalized to unity. The input admittances seen at the DC+RF port (port 1) toward the DC port (port 3) and the RF port (port 2) are denoted by Y_{DC} and Y_{RF}, respectively. The transmission responses of the DC path and the RF path are then determined by $\mathrm{Re}\{Y_{\mathrm{DC}}\}$ and $\mathrm{Re}\{Y_{\mathrm{RF}}\}$, respectively, where $\mathrm{Re}\{\cdot\}$ denotes the real-part operator. Once the RF passband is specified, the cutoff frequency of the DC-path lowpass response should be maximized without overlapping the RF band. Hence, in this design, the DC and RF paths are designed to be complementary, so that the power input to the DC+RF port is transmitted through one of the two paths, resulting in no reflection at the DC+RF port. Hence, the element values of the lowpass and highpass sections are related to each other by

$$Y_{\mathrm{DC}} + Y_{\mathrm{RF}} = 1. \tag{1}$$

Prior to finding the element values of the highpass section, it is necessary to ensure that the lowpass sections are synthesized such that the maximum value of $\mathrm{Re}\{Y_{\mathrm{DC}}\}$ is not larger than unity since $\mathrm{Re}\{Y_{\mathrm{RF}}\} \geq 0$ [4]. The transmission zero of the DC path transmission response is determined by g_2 and h_2 and is given by

$$\omega_2 = \frac{1}{\sqrt{g_2 h_2}}. \tag{2}$$

The lowpass section can be synthesized to exhibit transmission poles at $\omega = 0$ and $\omega = \omega_a$, where ω_a may be either zero or nonzero. In general, the value of ω_a determines the ripple characteristic of the transmission response. It is worth noting that the transmission zero of the RF path response coincides with the transmission pole of the DC path response. Hence, it follows that

$$\omega_a = \frac{1}{\sqrt{p_2 q_2}}. \tag{3}$$

Once Y_{DC} is obtained from the synthesis of the lowpass section, the element values of the highpass section, p_1, p_2, and p_3, can be extracted consecutively. All element values of the highpass section can be expressed in terms of those of the lowpass section as follows:

$$p_1 = \frac{g_2(g_1 - g_3)}{(g_1 + g_3) - \left(g_1 g_2 g_3 + \dfrac{g_1 + g_3}{\omega_2^2}\right)\omega_a^2} \tag{4}$$

$$p_2 = \frac{g_1 g_2 g_3 + \dfrac{g_1 + g_3}{\omega_2^2}}{g_2(g_1 - g_3)} \tag{5}$$

$$p_3 = \frac{g_1 g_2 g_3 + \dfrac{g_1 + g_3}{\omega_2^2}}{g_1 g_2 + \dfrac{1}{\omega_2^2} - \dfrac{g_1 g_2 g_3 + \dfrac{g_1 + g_3}{\omega_2^2}}{p_1}}. \tag{6}$$

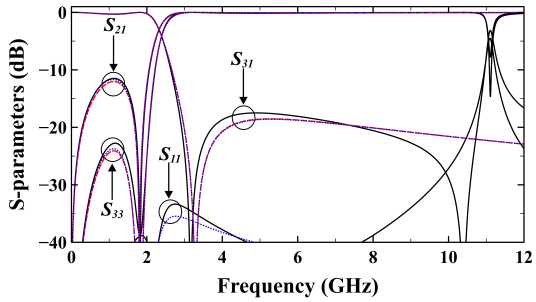


Fig. 3. Red dashed lines: Response of the bias tee schematic in Fig. 2 after frequency scaling without approximating the capacitor of p_3; Blue dotted lines: Response of the bias tee schematic in Fig. 2 after frequency scaling, with the capacitor of p_3 approximated as a short circuit; Black solid lines: Response of the bias tee schematic in Fig. 4.

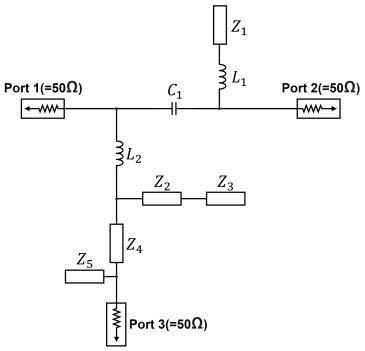


Fig. 4. Bias tee schematic with lumped elements and distributed elements. C_1 = 1.14 pF, L_1 = 5.88 nH, L_2 = 4.33 nH, Z_1 = 18.93 Ω, Z_2 = 99.89 Ω, Z_3 = 26.77 Ω, Z_4 = 105.29 Ω, and Z_5 = 95.22 Ω.

By virtue of (4)-(6), only one half of the entire circuit needs to be synthesized.

III. Design

A. Frequency scaling

We designed a bias tee based on the prototype in Fig. 2, following the specifications given in [2]. Specifically, the RF path is required to exhibit an insertion loss less than 1 dB in the frequency range from 2.7 GHz to 9.5 GHz, and the return loss greater than 15 dB. The DC path is required to maintain an insertion loss less than 3 dB for DC and low-frequency AC signals. The upper cutoff frequency of the DC path must be maximized while satisfying the requirements. Accordingly, this design employs normalized element values of g_1 = 1.0938, g_2 = 0.7502, h_2 = 0.4991, g_3 = 0.3503 which yield a 0.28 dB ripple in the DC path and introduce a transmission zero at 1.634 rad/s in the normalized frequency domain. These values place a transmission pole of the DC path at ω_a= 0.908 rad/s. Using (3)-(6), the normalized element values of the RF path are obtained as p_1 = 0.7174, p_2 = 1.4847, q_2 = 0.8368, p_3 = 20.4135. Frequency scaling is then applied, resulting in the frequency response depicted by red curves in Fig. 3. Due to the extremely large value of p_3, it can be approximated as a short circuit. The blue curves depict the frequency response

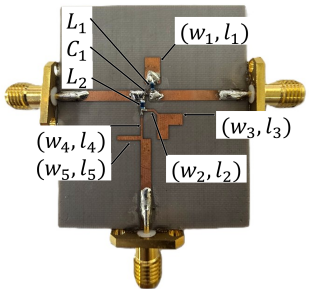


Fig. 5. Top-view of the fabricated bias tee. w and l denote the width and length of each line, respectively. w_1 = 3.5 mm, l_1 = 6 mm, w_2 = 0.39 mm, l_2 = 3.7 mm, w_3 = 2.5 mm, l_3 = 5.42 mm, w_4 = 0.43 mm, l_4 = 5.6 mm, w_5 = 0.95 mm, l_5 = 5.37 mm, L_1 = 5.1 nH, C_1= 1.0 pF, and L_2 = 3.9 nH

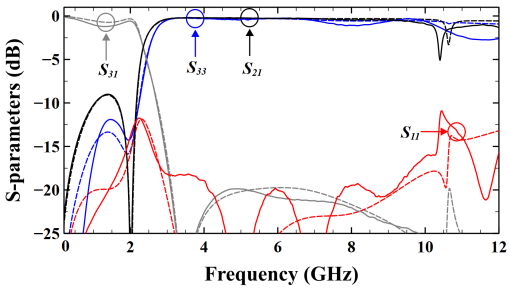


Fig. 6. Solid line : Measured response of the fabricated bias tee. Dashed line : EM-simulated response. (Red: S_{11}; Black: S_{21}; Gray: S_{31}; Blue: S_{33})

of the circuit in Fig. 2 with the capacitor of p_3 shorted, after applying the frequency scaling. As can be observed in Fig. 3, short-circuiting the capacitor of p_3 has a negligible effect on the frequency response. Therefore, it is not included in the proposed design.

B. Implementation

Using circuit transformations such as Kuroda's identities, some lumped elements can be converted into physically realizable transmission lines and were therefore replaced by distributed elements in this work. The inductors and capacitors can be implemented by short-circuited and open-circuited series stubs, respectively, with characteristic impedances Z_s and Z_o given by

$$Z_s = \frac{2\pi f_0 L}{\tan\theta} \tag{7}$$

$$Z_o = \frac{\tan\theta}{2\pi f_0 C} \tag{8}$$

where f_0 is the reference frequency and θ is the electrical length at f_0. There are multiple options for selecting the electrical length. In our design, the electrical length of the stubs was initially chosen to be 20° at 2.31 GHz, and fine-tuning of the length and width was executed. These series stubs were then transformed into physically realizable structures by applying Kuroda's identities [5]. The resulting schematic is shown in Fig. 4. The black curves in Fig. 3 show the frequency responses of the final schematic shown in Fig. 4.

IV. Fabrication and Measurement

The proposed bias tee was fabricated on a Taconic TLY-5 substrate (ϵ = 2.2) with a thickness of 0.762 mm. The component values were chosen by taking into account the parasitic effects of the landing pads used for mounting chip components, and fine-tuning was performed. Fig. 5 shows the photograph of the fabricated bias tee. The measured frequency response of the bias tee is presented in Fig. 6. The overall circuit performance is summarized in Table 1. Based on the measured performance, the design was awarded first place in APMC 2025 Student Design Competition.

TABLE I
Measured Performance Summary of the Proposed Bias Tee

Path	S-parameter	Requirement	Frequency Range
RF Path	S_{21}	≥ -1 dB	2.67 GHz – 10.05 GHz
DC Path	S_{31}	≥ -3 dB	DC – 2.31 GHz
DC Path	S_{33}	≤ -10 dB	DC – 2.24 GHz

Existing works (e.g. [6] and [7]) are not intended to maximize the cutoff frequency of the DC path while maintaining an insertion loss below 1 dB and a return loss at port 3 above 10 dB. In contrast, this design maximizes the DC-path cutoff frequency for a predetermined RF-path frequency range, which distinguishes it from existing designs.

V. Conclusion

This work presents a bias tee for load-pull systems with active baseband control. Closed-form equations enable synthesis of only half of the circuit, significantly reducing design complexity. The proposed topology enables steeper skirt responses compared to conventional first-order bias tees while maintaining low RF insertion loss over a wide frequency range. The measured result confirms that low-frequency AC signals can be effectively injected into the DC path.

References

[1] M. J. Pelk, L.C.N. de Vreede, M. Spirito and J. H. Jos, "Base-band impedance control and calibration for on-wafer linearity measurements," Accessed: Feb. 19, 2026, [Online], Available: maurymw.com/wp-content/uploads/5A-047.pdf?srsltid=AfmBOorcrQVPbB2GZfE0QKuRTX06Y3B9XiYQEm9-Wfg-eSKDoiRn9Cv5.

[2] "SDC2-Bias-Tee Design for Active Baseband Controlled Load-pull Applications," APMC 2025, Accessed: Feb. 19, 2026, [Online], Available: apmc2025.org/download/APMC2025-Bias-tee_Design_Competition_v1.1-rev20250916.pdf.

[3] A. I. Zverev, Handbook of Filter Synthesis, New York: John Wiley and Sons, 1967, pp. 137–151.

[4] J. Lee, J. Lee, and N. S. Barker, "Rigorous design of input-reflectionless filter with Chebyshev response and exact approach to increase reflectionless range," IEEE Trans. Microw. Theory Techn., vol. 69, no. 10, pp. 4460–4475, Oct. 2021.

[5] David M. Pozar, Microwave Engineering, 3rd ed., Hoboken, NJ: John Wiley and Sons, 2005, pp. 405–412.

[6] G. Bouisse and J. Gonzalez, "Load pull bias tee," 2019 92nd ARFTG Microwave Measurement Conference, Orlando, FL, USA, 2019, pp. 1-4.

[7] B. G. Panduang and K. Rawat, "Design of ultra-broadband (100 MHz to 8 GHz) bias-tee for the loadpull measurement," 2025 IEEE Microwaves, Antennas, and Propagation Conference (MAPCON), Kochi, India, 2025, pp. 1-4.

Electromagnetic–Thermal–Fluid Multiphysics Coupling Simulation of Electronic Packaging Based on the FDTD Method

Yan Peng, Guo Song, Tiancheng Zhang, Huaguang Bao, Dazhi Ding

Department of Integrated Circuit Engineering, Nanjing University of Science and Technology, Nanjing

{pppy, songguo, tczhang, hgbao, dzding}@njust.edu.cn

***Abstract*—This paper focuses on the transient electromagnetic-thermal-fluid coupling analysis of microchannel cooling in electronic packages using the finite difference method. Complex geometric models are comprehensively modeled and analyzed, with numerical discretization and iterative computation implemented through the finite difference scheme. The effectiveness and efficiency of the proposed method are validated through case studies and comparisons with the commercial software COMSOL.**

Keywords—Electronic device packaging; Electromagnetic-thermal-fluid coupling; Finite-difference time-domain algorithm; Simulation calculation

I. INTRODUCTION

The rapid advancement of integrated circuits and microsystems has brought increasing attention to the significant impact of temperature rise on the electrical characteristics of such systems [1][2]. Consequently, electromagnetic-thermal multiphysics simulation has emerged as a prominent research focus [3], with thermal management being one of the most critical challenges in the design of high-performance integrated packages and systems [4]. For the thermal simulation of liquid-cooled integrated circuits, the finite volume method (FVM) and the finite element method (FEM) are two widely adopted numerical approaches [5][6]. However, these methods typically require fine mesh resolutions to ensure accurate results, leading to substantially increased computational costs [7]. To address this issue, this paper proposes an electromagnetic-thermal-fluid coupling simulation method based on the Finite-Difference Time-Domain (FDTD) technique. The main contributions are as follows:

1) A finite-difference discretization scheme for the coupled electromagnetic-thermal-fluid governing equations is derived.

2) Numerical examples demonstrate that the proposed finite-difference method achieves accuracy comparable to that of COMSOL software, while offering significantly improved computational efficiency.

II. FORMULATION

Considering the Maxwell's equations in the time domain are as follows:

$$\nabla\times\vec{H}=\varepsilon\frac{\partial\vec{E}}{\partial t} \tag{1}$$

$$\nabla\times\vec{\mathrm{E}}=\mu\frac{\partial\vec{H}}{\partial t} \tag{2}$$

where $\vec{E}$ and $\vec{H}$ denote the electric field and magnetic field respectively, ε and μ respectively represent the permittivity and permeability of the medium.

In microchannels, the laminar Newtonian flow is assumed. The governing equation for fluid is expressed as

$$\rho C_p\frac{\partial T}{\partial t}+\rho C_p\boldsymbol{u}\cdot\nabla T=\nabla\cdot(k\nabla T)+Q \tag{3}$$

where ρ is the medium density, C_p is the specific heat of the medium, k is the thermal conductivity of the medium, Q is the thermal power density, and $\boldsymbol{u}$ is the flow velocity.

By discretizing Eq. (3) using the finite-difference time-domain (FDTD) method, the discrete expression for the spatial temperature can be obtained as follows:

$$\begin{aligned}T^{n+1}(i,j,k)=&\Delta t\frac{k_t(i,j,k)}{\rho(i,j,k)C_p(i,j,k)}\left(\frac{A_x}{\Delta x^2}+\frac{A_y}{\Delta y^2}+\frac{A_z}{\Delta z^2}\right)\\&-\Delta t\left(u_xB_x-u_yB_y-u_zB_z\right)\\&+\frac{\Delta t}{\rho(i,j,k)C_p(i,j,k)}Q_d(i,j,k)+T^n(i,j,k)\end{aligned} \tag{4}$$

where

$$\begin{cases}A_x=T^n(i+1,j,k)-2T^n(i,j,k)+T^n(i-1,j,k)\\A_y=T^n(i,j+1,k)-2T^n(i,j,k)+T^n(i,j-1,k)\\A_z=T^n(i,j,k+1)-2T^n(i,j,k)+T^n(i,j,k-1)\\B_x=T^n(i+1,j,k)-T^n(i,j,k)\\B_y=T^n(i,j+1,k)-T^n(i,j,k)\\B_z=T^n(i,j,k+1)-T^n(i,j,k)\end{cases} \tag{5}$$

Electromagnetic-thermal-fluid multiphysics coupling refers to the process in which the electromagnetic field, fluid field, and temperature field interact and co-evolve through energy transfer and parameter feedback. As previously described, the behavior of the electromagnetic field is governed by Maxwell's equations, which encompass the generation, propagation, and dissipation of electromagnetic energy. In conductive or lossy media, electromagnetic energy

979-8-3315-4544-4/26/$31.00 ©2026 IEEE

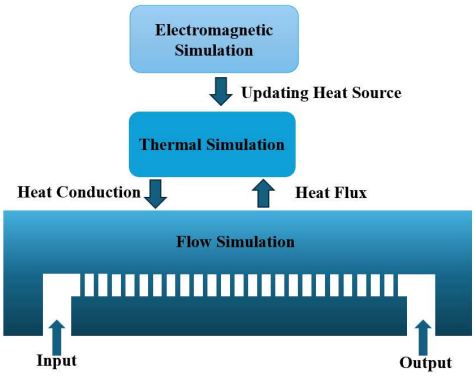


Fig. 1. Flowchart of the coupled electromagnetic-thermal-fluid analysis.

TABLE I. MATERIAL PARAMETER

Material	Density (kg/m^3)	Specific Heat Capacity (J/(kg.K))	Thermal Conductivity (W/(m.K))
Gold	19300	129	315
Water	997	4182	0.6
GaN	6150	600	200
TaN	16600	140	58
Silicon	2400	691	16
Thermal Conductive Adhesive	2000	1000	30
Diamond Copper	5000	450	650
Aluminum	2700	900	238

is converted into heat primarily via the Joule heating effect, thereby acting as an internal heat source for the temperature field. The fluid field is described by the Navier–Stokes equations and the continuity equation, which characterize momentum transfer and mass conservation. Fluid motion is driven by pressure gradients, viscous forces, and inertial forces, and its key role lies in convective heat transfer, which redistributes locally concentrated heat throughout the flow field, consequently modifying the spatial distribution of the temperature field.

III. RESULTS

In this section, the numerical computations are performed on an ASUS computer platform equipped with an Intel Core i5-10400F processor (with a main frequency of 2.90 GHz) and 32GB of memory.

The load chip serves as the heat-generating component, while the micro-scale silicon-based channels function as the heat dissipation structure. The dimensions of the entire structure are 70 mm in the x-direction, 70 mm in the y-direction, and 12 mm in the z-direction. The model geometry and material distribution are depicted in Fig. 2, and the corresponding material parameters are summarized in Table I.

To simulate periodic excitation, a sinusoidal source with a frequency of 15 GHz and an amplitude of 21.651 V is employed. The ambient temperature is set to 22 °C, and the entire system is initialized at the same temperature. A natural convection coefficient of 10 $W/(m^2 \cdot K)$ is applied at the interfaces between the system and the surrounding air. The

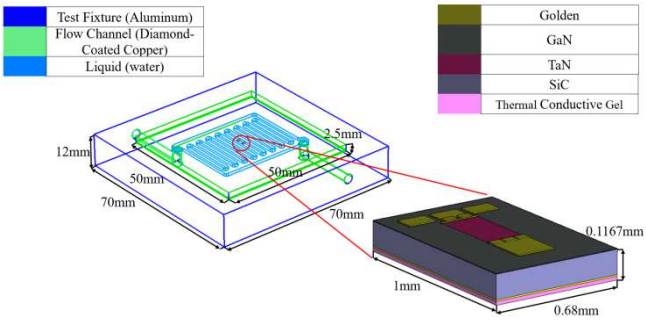
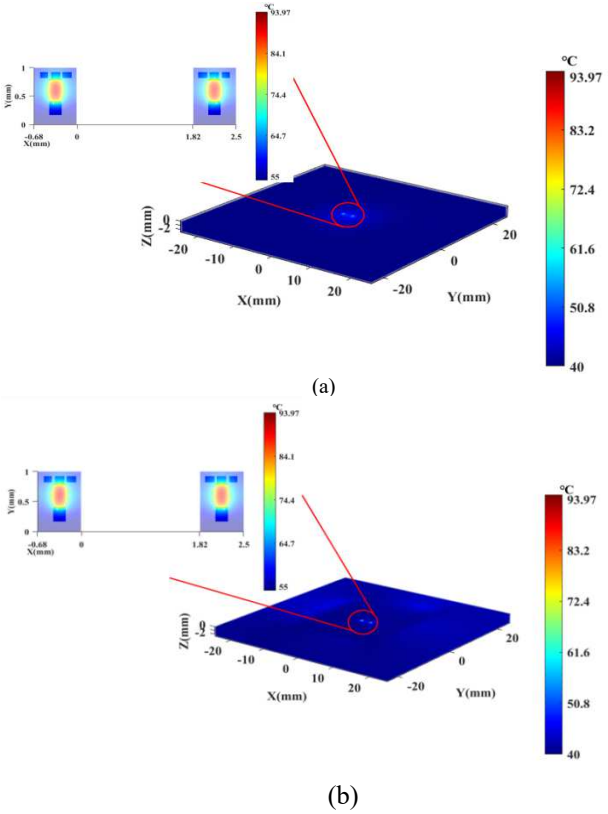


Fig. 2. Schematic of microchannel-integrated chip cooling structure.



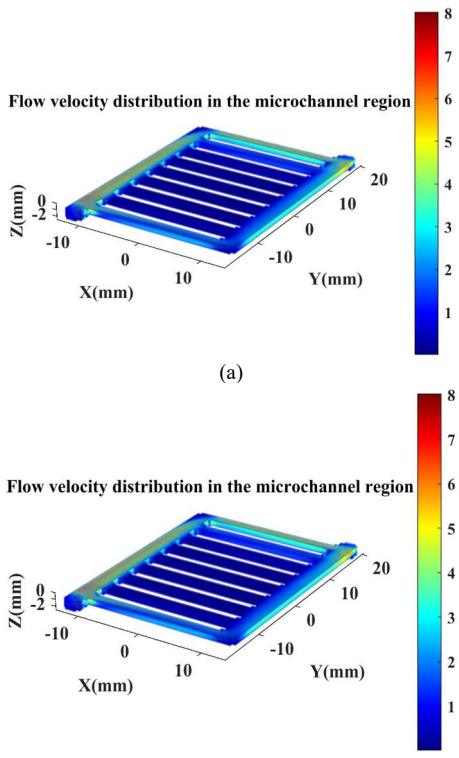
(a)

(b)

Fig. 3. Temperature distribution of overall region calculated using by (a) COMSOL and (b) FDTD.

time step is denoted as Δt, while the spatial discretization steps Δx, Δy, and Δz are set to 0.01 mm, 0.01 mm, and 0.01 mm, respectively.

First, the temperature distribution of the load chip model under no-flow conditions in the microchannel was simulated. The overall temperature distribution of the model is presented in Fig. 3, with the inset showing a detailed view of the load region. Subsequently, while keeping other parameters unchanged, the inlet flow rate of the microchannel was set to 0.58 L/min, and the outlet boundary condition was defined as static pressure. The velocity distribution within the microchannel was first obtained by solving the Navier–Stokes equations. As illustrated in Fig. 4, the velocity distributions calculated by COMSOL and the FDTD method are in good agreement. The computed flow field was then substituted into the heat transfer governing equations to determine the overall temperature distribution of the model. Fig. 5 compares the overall temperature distributions obtained from the FDTD method and COMSOL under flow conditions.

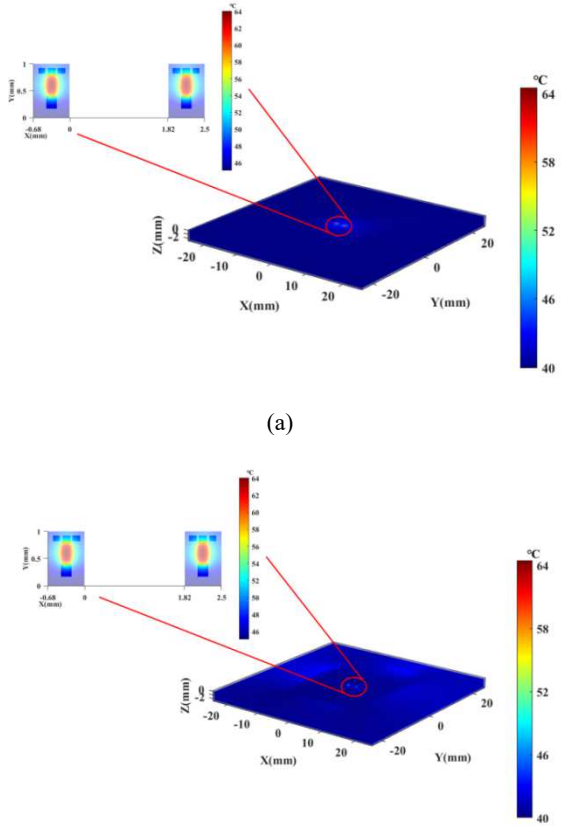


(a)

(b)

Fig. 4. Velocity distribution in the microchannel region calculated using by (a) COMSOL and (b) FDTD.

As illustrated in Figures 3 and 5, the highlighted region corresponds to the heating element. Under no-flow conditions, the maximum temperature in this region reaches 93.97 °C, which decreases to 64.35 °C upon the introduction of water circulation. For comparison, the COMSOL simulation yields maximum temperatures of 94.5 °C and 64.9 °C under no-flow and flow conditions, respectively. Taking the COMSOL results as a reference, the maximum relative errors of the proposed method are 0.56% under no-flow conditions and 0.85% at a flow rate of 0.58 L/min. Furthermore, the computational times of the FDTD method and COMSOL under both flow and no-flow conditions are summarized in Table II. In terms of computational efficiency, the FDTD method requires only half the time of COMSOL, demonstrating its good applicability in electromagnetic-fluid-thermal coupling analysis.



(a)

(b)

Fig. 5. Velocity distribution in the microchannel region calculated using by (a) COMSOL and (b) FDTD.

TABLE II. COMPARISON OF COMPUTATION TIME

Flow rate (L/min)	Solvers	CPU time(s)
0	FDTD	2330
	COMSOL	4685
0.58	FDTD	3726
	COMSOL	7564

IV. ACKNOWLEDGMENT

This work was supported in part by National Natural Science Foundation of China under Grant 92373108, 62571244, 62231016, 62431012, in part by Basic Research Program of Jiangsu under Grant BK20243020, and in part by the Fundamental Research Funds for the Central Universities under Grant 30924012003.

V. REFERENCES

[1] R. S. Patti, "Three-dimensional integrated circuits and the future of system-on-chip designs," *Proc. IEEE*, vol. 94, no. 6, pp. 1214–1224, Jun. 2006.

[2] S. S. Salvi and A. Jain, "A review of recent research on heat transfer in three-dimensional integrated circuits (3-D ICs)," *IEEE Trans. Compon., Package., Manuf. Technol.*, vol. 11, no. 5, pp. 802–821, Mar. 2021.

[3] K. Niu, W. Zhang, M. Li, X. Ren, Y. Li, and Z. Huang, "Transient Electromagnetic–Thermal Co-Simulation of Microwave/RF Integrated Circuits by the HIE-FDTD Method," *IEEE Trans. Microw. Theory Techn.*, vol. 72, no. 9, pp. 5228-5244, Sept. 2024.

[4] J. Li, M. Tang, and J. Mao, "An Efficient ADI Method for Transient Thermal Simulation of Liquid-Cooled 3-D ICs," *IEEE Trans. Compon., Package., Manuf. Technol*, vol.12, no.9, pp.1484-1491, Sept. 2022.

[5] J. Xie and M. Swaminathan, "Electrical-thermal co-simulationof 3D integrated systems with micro-fluidic cooling and Joule heating effects," *IEEE Trans. Compon., Package., Manuf. Technol.*, vol. 1, no. 2, pp. 234–246, Feb. 2011.

[6] B. Li, M. Tang, P. Li, and. J. Mao, "Efficient Thermal Analysis of Integrated Circuits and Packages With Microchannel Cooling Using Laguerre-Based Layered Finite Element Method," *IEEE J. Multiscale Multiphys. Comput. Techn.*, vol. 8, pp. 195-204, 2023.

[7] F. Wang, X. Wu, G. Shan and Y. Yang, "Electrothermal Coupling Optimization Method of a 3-D Microsystem Based on the Fast Dual-Cell Method," *IEEE Trans. Compon., Package., Manuf. Technol*, vol. 15, no. 2, pp. 263-271, Feb. 20

Rapid Analysis of Scattering Problem for LFPSs with Physics-informed Attention Network

Tian Liu
School of Information Science and Engineering, Southeast University
Nanjing, P.R.China
230258109@seu.edu.cn

Fei Guo
School of Information Science and Engineering, Southeast University
Nanjing, P.R.China
230248807@seu.edu.cn

Wenzhe Song
School of Cyber Science and Engineering, Southeast University
Nanjing, P.R.China
songwenzhe6662021@163.com

Yanzhe Luo
School of Information Science and Engineering, Southeast University
Nanjing, P.R.China
fcyxx4425@126.com

Wu Yang
School of Information Science and Engineering, Southeast University
Nanjing, P.R.China
yangwu@seu.edu.cn

Weibing Lu
Southeast University&Donghua University
Shanghai, P.R.China
wblu@seu.edu.cn

***Abstract*—In this work, a physics-informed attention network (PIAN) is proposed for the rapid analysis of scattering problems in large-scale finite periodic structures (LFPSs). The encoder captures the relationship between array features and global coupling with a self-attention mechanism, which guides the decoder to generate the final current coefficients of LFPSs based on the NASED initial current coefficients with a cross-attention mechanism. The introduction of initial current coefficients enables the characterization of cell structure for different cells. The well-trained network can generalize to larger-scale arrays, which significantly reduces the cost of dataset generation. Numerical experiments validate the accuracy, generalization capability, and efficiency of the proposed method.**

Keywords—physics-informed attention network (PIAN), large-scale finite periodic structures (LFPSs), self-attention mechanism, cross-attention mechanism

I. INTRODUCTION

Accurate and efficient electromagnetic (EM) analysis of large-scale finite periodic structures (LFPSs) is of great significance for research areas such as phased-array radar antenna arrays, frequency-selective surfaces [1], and novel artificial EM materials. Unlike infinite arrays, the boundary truncation effect renders the Floquet theorem inapplicable. When the array size becomes large, the method of moments (MoM) [2] using conventional basis functions (e.g., RWG [3]) generates a huge number of unknowns. The macro-basis-function method provides an effective approach to address such problems, such as characteristic basis functions (CBFs) [4] or new accurate sub-entire domain basis functions (NASED) [5,6]. However, with the increasing complexity of cell structure and the growing demand for larger array scales, filling and solving the impedance matrix equation still consume substantial computational resources and time. Data-driven Adaptive Artificial Neural Networks [7] can quickly obtain current coefficients by leveraging cell structures and spatial information, thereby accelerating computations by replacing part of the numerical solution process. However, this surrogate model only learns the relationships within the data, and their limited generalization capability prevents it from solving cell configurations outside the training dataset. Moreover, it requires the construction of repetitive network models based on the spatial distribution of the cells. A prior physics-driven graph neural network [8] has been proposed to analyze the scattering problems of composite LFPSs. The coupling interactions between cells and the current distribution of metallic elements are incorporated as prior physical information. Nevertheless, any change in the cell structure still necessitates the generation of new datasets and fine-tuning of the network parameters.

In this paper, we propose a rapid analysis method based on a physics-informed attention network (PIAN) for efficiently solving EM scattering problems in LFPSs. As shown in Fig. 1. The proposed method employs an encoder–decoder architecture integrated with an attention mechanism to modify the initial NASED current coefficients of 3×3 subarrays based on global coupling effects. The encoder captures the relationship between array features and global coupling, which guides the decoder to generate the final current coefficients of LFPSs from the initial estimates. The introduction of initial current coefficients serves to characterize the structural properties of different cells. The well-trained network can generalize to larger-scale arrays, offering a promising direction for reducing the cost associated with dataset generation.

II. PIAN MODEL

A. Obtaining NASED Basis Function

When solving large-scale finite periodic array problems using the full-wave NASED basis function method, 9 types of SED basis functions with physical spatial characteristics are first obtained by solving a small-scale 3×3 subarray problem, which can be expressed as

$$\mathbf{Z}^{sub} \cdot \mathbf{I}^{PWs} = \mathbf{V}^{PWs} \tag{1}$$

$$\mathbf{g}_n^k(\mathbf{r}) = \sum_{m=1}^{M} I_{n,m,k} \boldsymbol{f}_{n,m}(\mathbf{r}) \tag{2}$$

where $\mathbf{Z}^{sub}$, $\mathbf{I}^{PWs}$ and $\mathbf{V}^{PWs}$ are the impedance matrix, current coefficients and excitation matrix. $g_n^k(\mathbf{r})$ is the NASED Basis function. M is the number of the RWG basis functions of each cell, $I_{n,m,k}$ and $\boldsymbol{f}_{n,m}(\mathbf{r})$ is the m-th RWG basis function and the current coefficient of the n-th cell

B. Physics-informed Attention Network

In our research, the initial current coefficient of each cell from 3×3 subarray is considered as a type of feature associated with cell structure. Moreover, there exists a discrepancy between the initial current coefficient of each cell in the 3×3 subarray and the current coefficient of the corresponding cell in the large-scale finite periodic array, which arises from different coupling interactions. The role of the PIAN is to

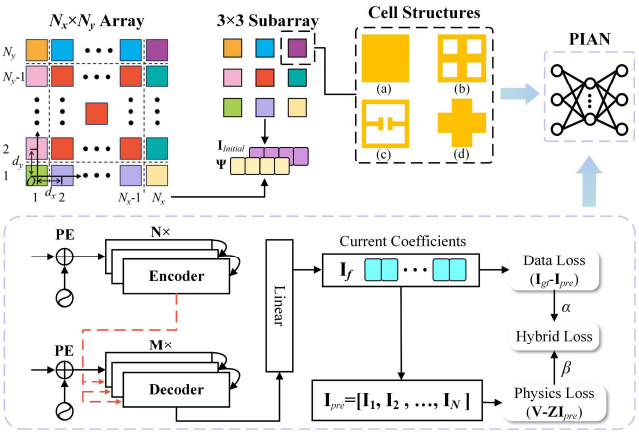


Fig. 1. The diagram of PIAN.

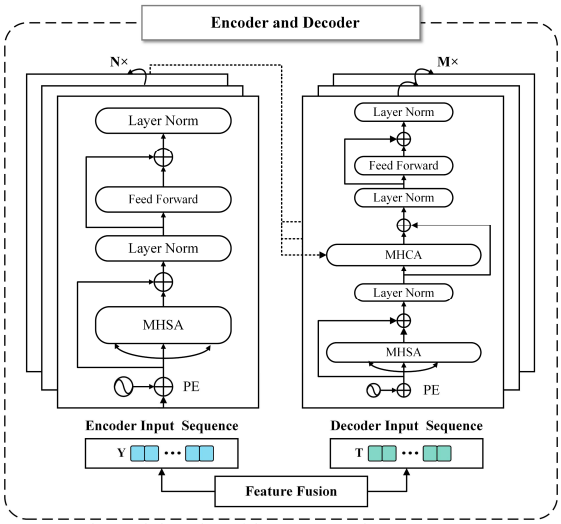


Fig. 2. Encoder and decoder with MHSA and MHCA.

learn the global coupling under various EM excitations, thereby replacing the complex process of solving the impedance matrix. Consequently, the function of the PIAN is expressed as

$$\mathbf{I}_{Final} = \mathbf{I}_{Initial} + \Delta = f(\mathbf{I}_{Initial} \oplus \Psi, \mathbf{\Theta}_{\mathrm{ENN}}) \tag{3}$$

where $\mathbf{I}_{Initial}$ and $\mathbf{I}_{Final}$ are the current coefficient of subarray and large-scale array, f is the role of the PIAN and the trainable parameters are expressed as $\mathbf{\Theta}_{\mathrm{ENN}}$, $\oplus$ denotes the fusion of $\mathbf{I}_{Initial}$ and Ψ. Ψ= [N_x, N_y, d_x, d_y x_i, y_i] are the structural parameters of LFPSs. N_x, N_y, d_x, d_y x_i, y_i represent array scales, periods and coordinates. As shown in Fig. 2, the PIAN consists of a feature fusion module, an encoder, and a decoder. The feature fusion module performs multi-scale feature fusion through linear layers to generate the feature sequence. The feature tokens are input into the encoder after being augmented with positional encoding. Based on the memory provided by the encoder, the decoder refines the initial current coefficients into the current coefficients. The multi-head self-attention (MHSA) [9] and multi-head cross-attention (MHCA) mechanisms are expressed as

$$Attention(\mathbf{Q}^i, \mathbf{K}^i, \mathbf{V}^i) = softmax(\frac{\mathbf{Q}^i \mathbf{K}^{iT}}{\sqrt{d_k}}) \times \mathbf{V}^i \tag{4}$$

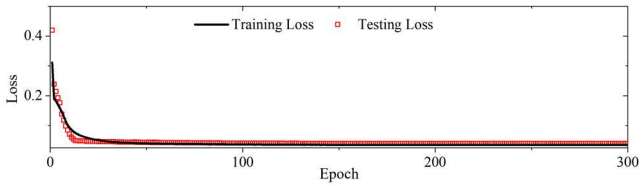


Fig. 3. Convergence process of PIAN.

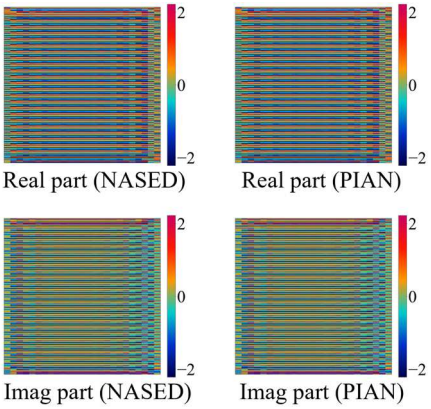


Fig. 4. Comparison of predicted real and imaginary current coefficients

$$Attention(\mathbf{Q}_{dec}, \mathbf{K}_{enc}, \mathbf{V}_{enc}) = softmax(\frac{\mathbf{Q}_{dec} \mathbf{K}_{enc}^T}{\sqrt{d_k}}) \times \mathbf{V}_{enc} \tag{5}$$

where $\mathbf{Q}^i = \mathbf{Q}\mathbf{W}_i^Q$, $\mathbf{K}^i = \mathbf{K}\mathbf{W}_i^K$, $\mathbf{V}^i = \mathbf{V}\mathbf{W}_i^V$. $d_k = d_m/h$. The $\mathbf{W}_i^Q$, $\mathbf{W}_i^K$ and $\mathbf{W}_i^V$ are weight matrices. $\mathbf{Q}_{dec}$ is from decoder, $\mathbf{K}_{enc}$ and $\mathbf{V}_{enc}$ are from encoder. The loss function is designed based on the impedance matrix equations and the ground truth labels, which are defined as

$$\mathrm{L} = \alpha \cdot \mathrm{L}_{data} + \beta \cdot \mathrm{L}_{phy} \tag{6}$$

$$\mathrm{L}_{data} = (\mathbf{I}_{pre}, \mathbf{I}_{gt})_{MSE} \tag{7}$$

$$\mathrm{L}_{phy} = \frac{\sum_{j=1}^{M} (\| \mathbf{V}_j^r - [\mathbf{Z}^{RED} \mathbf{I}_{pre}]^r \|_2^2 + \| \mathbf{V}_j^{im} - [\mathbf{Z}^{RED} \mathbf{I}_{pre}]^{im} \|_2^2)}{2M \sum_{v=1}^{M} d_v} \tag{8}$$

where α and β are weight factors. Λ is the hybrid loss function. $\mathbf{I}_{pre}$ and $\mathbf{I}_{gt}$ are the predicted and ground truth. M is number of the physics terms. d_v is the dimension of the $\mathbf{V}$. After obtaining the predicted current coefficients, the final surface current distribution $\mathbf{J}$ can be computed.

III. EXPERIMENTS

For constructing the dataset, we select four types of metallic cells with different structures (0.3λ×0.3λ) in normal incidence. The periods are sampled within the interval [0.4λ, 0.8λ] with a step size of 0.02λ, while the array dimensions are scaled from 10× 10 to 40×40 in increments of 5. The frequency is set as 300 MHz. All training samples are obtained by the NASED basis functions method. Following hyperparameter tuning, the model adopts a hidden dimension of 256, a learning rate of 0.0001, an encoder depth of 4 layers, a decoder depth of 3 layers, and a batch size of 512. The dataset is split into training and test sets in an 8:2 ratio. During training, the Adam optimizer updates all weight matrices

TABLE I
COMPARISON OF COMPUTING TIME

Array size/ Period/Shape	Unknowns	Computing time(s)			Saving
		FEKO	NASED	PIAN	
30×30/0.5λ/ Square Patch	18900	37	24	1.2	96.8%/95.0%
60×60/0.3λ/ Composite Cross	1742400	2259.4	524.7	20.2	98.5%/96.9%

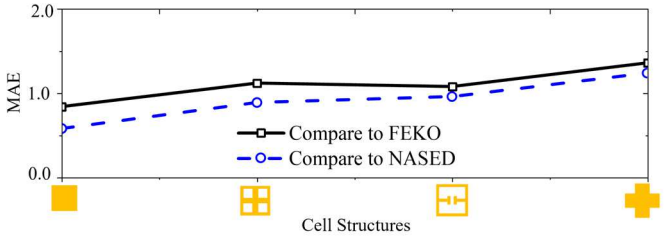


Fig. 5. The MAE of the bistatic RCS of 30×30 arrays of different cell structures.

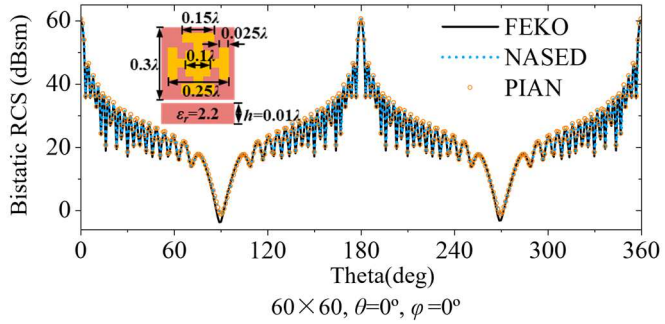


Fig. 6. The bistatic RCS of 60×60 composite cross array.

according to the hybrid loss function at each epoch. As shown in Fig. 3, the convergence curves of both training and testing losses follow a consistent trend. The computational environment consists of an NVIDIA GeForce RTX 4090 GPU.

First, we randomly select a sample from the test set to validate the accuracy of the proposed method. In this case, the cell shape is a patch, the array size is 30 × 30, and the period is 0.5λ. Fig. 4 shows the real and imaginary parts of the predicted current coefficients obtained by PIAN compared with those from the NASED basis function method, the relative error rates for the real and imaginary parts are 0.58% and 0.69%, respectively. Moreover, the MAE of samples with different cell structures are depicted in Fig. 5, with the error range ranging from 0.58dB to 1.36dB. Fig. 6 presents the bistatic RCS of composite LFPSs calculated via FEKO, NASED and PIAN methods. Even though the relevant sample was excluded from the training set, the PIAN model can accurately capture its electromagnetic characteristics by virtue of precise generalization on current coefficients with incremental learning. The predicted error of RCS is 1.23 dB compared to FEKO. Table I presents the computation time comparison, demonstrating the high efficiency of PIAN.

IV. CONCLUSION

In this paper, the proposed method employs an encoder–decoder network architecture integrated with an attention mechanism to correct the initial current coefficients based on global coupling. This approach replaces the complex and time-consuming process of solving the impedance matrix. Numerical experiments demonstrate that the well-trained model can be reused for different samples outside the training set, which offers a new perspective for reducing the cost of dataset generation.

ACKNOWLEDGMENT

This work was supported in part by the Key Program of the National Natural Science Foundation of China under Grant 62231001, the Special Fund for Key Basic Research in Jiangsu Province No. BK20243015, the Fundamental Research Funds for the Central Universities under Grant 2242022k60004, the National Natural Science Foundation of China under Grant 62101115, and Shanghai Science and Technology Plan Project No. 25DX1400200.

REFERENCES

[1] M. -Y. Geng *et al*., "Fabric Electromagnetic Energy Harvesting Platform Based on Absorbing Metasurface," *IEEE Trans. Antennas Propag*., vol. 73, no. 9, pp. 7021-7026, Sept. 2025.

[2] R. F. Harrington, Field Computation by Moment Method. New York, NY, USA: Macmillan, 1968.

[3] S. M. Rao, D. R. Wilton, and A. W. Glisson, "EM Scattering by Surfaces of Arbitrary Shape," *IEEE Trans. Antennas Propag*., vol. 30, no. 3, pp. 409-418, May 1982.

[4] E. Lucente, A. Monorchio, and R. Mittra, "An iteration-free MoM approach based on excitation independent characteristic basis functions for solving large multiscale EM scattering problems," *IEEE Trans. Antennas Propag*., vol. 56, no. 4, pp. 999-1007, Apr. 2008.

[5] W. B. Lu, T. J. Cui, Z. G. Qian, X. X. Yin and W. Hong, "Accurate Analysis of Large-Scale Periodic Structures Using an Efficient Subentire Domain Basis Function Method," *IEEE Trans. Antennas Propag*., vol. 52, no. 11, pp. 3078-3085, Nov. 2004.

[6] W. Xiang, W. Yang and B. W. Lu, "Fast Subentire-Domain Basis Functions Method for Analysis of Composite Finite Periodic Structures with Dielectric-Conductor Cells," *IEEE Antennas Wireless Propag.* Lett., vol. 22, no. 2, pp. 233-237, Feb. 2023.

[7] W. Xiang, Z. Zhang, W. Zheng, J. Li, W. Yang and W. Lu, "Rapid Subentire-Domain Basis Functions Method Based on Adaptive Artificial Neural Networks," *IEEE Trans. Antennas Propag*., vol. 70, no. 7, pp. 5156-5164, July. 2022.

[8] T. Liu, F. Guo, B. Song, Z. H. Chen, H. Chen, W. Yang, J. N. Zhang, J. W. You and W. B. Lu., "Efficient Analysis of EM Scattering from Composite Finite Periodic Structures by Prior Physics-Driven Graph Neural Network," *IEEE Antennas Wireless Propag. Lett.*, vol. 25, no. 1, pp. 319-323, Jan. 2026.

[9] N. Feng, C. Dong, J. Fu, F. Zheng and Z. Huang, "MVPTransformer: Long-Term Multivariate Time-Series Pattern for Plasma Array-Based Intelligent Protection Against HPM," *IEEE Trans. Microw*. Theory Tech., *Early Access*, 2025.

Characteristic Mode-Based Efficient Analysis Method for Electromagnetic Scattering of Complex Electromagnetic Structures with Lossy Dielectric Materials

Yutong Qiu
School of Microelectronics
Nanjing University of Science & Technology
Nanjing,China
qyt@njust.edu.cn

Jihong Gu
School of Microelectronics
Nanjing University of Science & Technology
Nanjing,China
gujihong@njust.edu.cn

Zhaoyuan Wang
School of Microelectronics
Nanjing University of Science & Technology
Nanjing,China
122104010545@njust.edu.cn

Zhou Cong
School of Microelectronics
Nanjing University of Science & Technology
Nanjing,China
congz@njust.edu.cn

Chao-fu Wang
School of Microelectronics
Nanjing University of Science & Technology
Nanjing,China
cfwang@ieee.org

Dazhi Ding
School of Microelectronics
Nanjing University of Science & Technology
Nanjing,China
dzding@njust.edu.cn

***Abstract*—This paper proposes a fast solution method to analysis the electromagnetic scattering characteristics of the complex electromagnetic structures with lossy dielectric materials. In this method, the characteristic mode (CM) formulation for complex electromagnetic structures with lossy dielectric materials is first established based on the energy theory and the surface integral equation. Utilizing the modal reconstruction property of the theory of characteristic mode (TCM), the surface induced electromagnetic currents of individual array elements are accurately solved, and the scattering fields are obtained. The scattering field of the array is then rapidly acquired through phase superposition, enabling the calculation of radar cross section (RCS). Numerical examples demonstrate that the proposed method significantly reduces computation time and memory overhead while maintaining accuracy.**

Keywords—Poggio–Miller–Chang–Harrington–Wu–Tsai (PMCHWT), The theory of characteristic mode (TCM), Lossy dielectric, Mode reconstruction, Scattering analysis , Array structure

I. INTRODUCTION

In the field of electromagnetic scattering analysis, repetitive structures composed of multiple identical or similar elements often exhibit superior performance compared to single elements. However, correspondingly, the scale of unknowns that need to be handled for repetitive structures is often very large, leading to an exponential increase in computational complexity. Therefore, proposing a more efficient method for analyzing the electromagnetic scattering characteristics of array structure is urgently needed. For the analysis of array structure electromagnetic scattering characteristics, current mainstream research methods include the multilevel fast multipole algorithm (MLFMA) [1], which reduces the computational complexity of the traditional method of moments (MoM) from $O(N^2)$ to $O(N\log N)$, significantly enhancing the capability to solve electrically large object. However, when processing large-scale arrays, the need to repeatedly compute nearly identical inter-element interaction matrices still leads to substantial redundancy in computational resources. The Equivalence Principle Algorithm (EPA) [2] can effectively reduce unknowns, but when elements are closely spaced, the equivalence surfaces may overlap, causing significant errors in field reconstruction on these surfaces, making this issue inconvenient to handle. Additionally, matrix dimensionality reduction methods based on the theory of characteristic modes (TCM) [3] offer fast solution speed and high accuracy. However, the existing Poggio–Miller–Chang–Harrington–Wu–Tsai (PMCHWT) eigenvalue equation does not effectively handle structures with lossy dielectric materials. Furthermore, there is currently a lack of efficient analysis methods for rapidly and accurately reconstructing the total scattering field of an array under various conditions based on the modal current distribution of a single element.

This paper proposes a characteristic mode formulation for handling structures with lossy dielectric materials. In this paper, the matrix obtained by testing the operator related to radiation energy in the PMCHWT equation is used as the weighting matrix of the generalized eigenvalue equation to extract the modes of structures with lossy dielectric materials. For array elements, with a certain element spacing, the coupling between elements is negligible. Based on this, considering the balance between accuracy and computational efficiency, we ignore the coupling between elements. The approach in this paper is to extract modes from a single element, replicate them to other elements in the array, and rapidly calculate the scattered field of each array element based on the mode reconstruction method. Finally, the total scattered field of the array is obtained by vector phase superposition.

979-8-3315-4544-4/26/$31.00 ©2026 IEEE

II. Theoretical Introduction

A. Lossy Dielectric-Metal Hybrid CM Method

Based on the PMCHWT equation and the VIE equation [4], the following generalized eigenvalue equation can be constructed:

$$\mathbf{Z}\cdot\mathbf{J}_n=(1+j\lambda_n)\mathrm{Re}\{\mathbf{Z}^0\}\cdot\mathbf{J}_n \tag{1}$$

where $\mathbf{Z}$ is the impedance matrix derived from PMCHWT, $\mathbf{Z}^0$ is the part of the $\mathbf{Z}$ matrix related to the background medium, and $\mathbf{J}_n$ represents the right eigenvector.

The characteristic modes obtained from equation (1) do not satisfy the orthogonality conditions in the conventional sense. Therefore, it is necessary to introduce bi-orthogonal mode theory. By simultaneously constructing the left eigenvectors and right eigenvectors corresponding to the original matrix equation, a set of characteristic mode systems satisfying the bi-orthogonal relationship is established[5]:

$$\mathbf{J}_n^H\cdot\mathbf{Z}=(1+j\lambda_n)\mathbf{J}_n^H\cdot\mathrm{Re}\{\mathbf{Z}^0\} \tag{2}$$

where $\mathbf{J}_n^H$ is the left eigenvector.

The induced electromagnetic current on a single element can be represented by a linear combination of modal currents:

$$\mathbf{J}=\sum_{n=1}^{N}\beta_n\mathbf{J}_n \tag{3}$$

where N is the number of truncated terms, and β_n is the modal weighting coefficient. The expression for β_n is:

$$\begin{aligned}\beta_n&=\frac{\langle\mathbf{J}_n^H,g_s\rangle}{1+j\lambda_n}\\&=\frac{\langle\mathbf{J}_d^H,\mathbf{E}^{inc}\rangle+\langle\mathbf{M}_d^H,\mathbf{H}^{inc}\rangle+\langle\mathbf{J}_m^H,\mathbf{E}^{inc}\rangle}{1+j\lambda_n}\end{aligned} \tag{4}$$

Here, g_s represents the excitation source, and $\frac{1}{1+j\lambda_n}$ is the modal significance (MS).

According to the generalized eigenvalue equation (2), the obtained eigenvalues are complex numbers. Among them, the real part of the eigenvalue represents the ratio of reactive power to radiated power. The imaginary part of the eigenvalue reflects the ratio of loss power to radiated power. When the medium loss approaches zero, the imaginary part of the eigenvalue correspondingly disappears, and the generalized eigenvalue equation degenerates into the eigenvalue problem for the lossless medium case. Therefore, this eigenvalue equation (2) is not only applicable to the characteristic mode analysis of lossy dielectric objects but can also be used for solving eigenvalues of lossless dielectric objects.

B. Efficient Calculation Method for Electromagnetic Scattering of Array Objects

The single-object scattering field $\mathbf{E}^{sca}$ is calculated using the electromagnetic current coefficients reconstructed by CM. Subsequently, the total scattering field is obtained through vector phase superposition . The principle of this method is that when the element spacing is much larger than the dimensions of the elements themselves, the multiple coupling effects between elements can be neglected, and the total scattering response of the array is approximately equal to the coherent superposition of the scattering responses of individual elements. The formula is as follows:

$$\begin{aligned}&\mathbf{E}_{total}^{sca}(\theta^{sca},\varphi^{sca},\theta^{inc},\varphi^{inc})\\&=\sum_{p=1}^{P}\mathbf{E}_p^{sca}(\theta^{sca},\varphi^{sca},\theta^{inc},\varphi^{inc})\exp\left[j(\mathbf{k}-\mathbf{k}^i)\cdot\mathbf{d}_p\right]\end{aligned} \tag{5}$$

where $\mathbf{k}$ is the scattering wave vector, $\mathbf{k}^i$ is the incident wave vector, and $\mathbf{d}_p$ is the position vector of the centroid of the p-th object. Finally, the Radar Cross Section (RCS) of the array object is calculated based on the total scattering field $\mathbf{E}_{total}^{sca}$.

This method allows for the rapid acquisition of RCS for array objects of arbitrary scale and arrangement, requiring only a single calculation of the scattering field for an individual element. Consequently, it significantly reduces computational complexity and memory overhead, enabling efficient analysis of the electromagnetic scattering characteristics of large-scale array objects.

III. Numerical Results

A frequency selective surface (FSS) array is taken as an example to verify the accuracy and efficiency of the proposed method. The unit cell structure of this 100×100 array is shown in Figure 1, where the purple part represents the lossy dielectric substrate with a relative permittivity of 4, $\tan\delta=0.02$ and the yellow part represents the metallic patch. And the distance between two adjacent units is 2mm. The simulation is carried out at a frequency of 30 GHz. For a single unit cell, the number of unknowns for the metallic part is 41, and for the dielectric part is 1068. The entire array, measuring 598mm×598mm×0.35mm, has 3,560,000 mesh elements, resulting in a total of 77,460,000 unknowns.

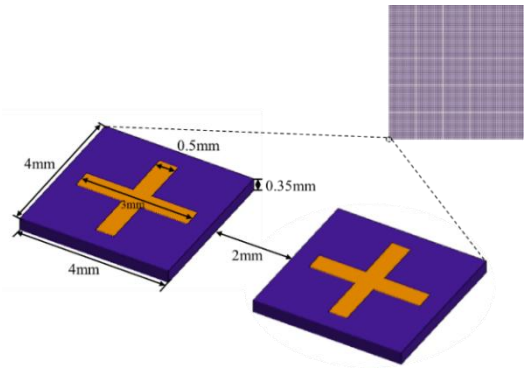


Figure 1. FSS model and 100×100 array.

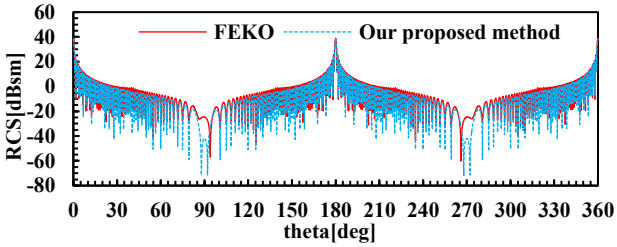


Figure 2. Comparison results between commercial software FEKO and the proposed method

The final RCS curves are shown in Figure 2. From Figure 2 and Table 1, the proposed method demonstrates good agreement compared with the full-wave simulation method, while significantly reducing computation time. The unfitted portions of the curves are negligible due to the small value discrepancy between the two methods.

TABLE I. COMPARISON OF COMPUTATIONAL RESOURCES BETWEEN FEKO AND OUR METHOD

	Solving time	**Memory overhead**
FEKO	7.637h	250.518GB
Our method	1.116h	0.797GB

IV. CONCLUSION

This paper proposes a fast computational method based on the combination of characteristic mode reconstruction and vector phase superposition to address the demand for efficient electromagnetic scattering analysis of complex electromagnetic array structures with lossy dielectric materials. By introducing the bi-orthogonal mode theory, a generalized eigenvalue equation suitable for lossy dielectric objects is established. To balance computational accuracy and efficiency, the coupling between array elements is neglected under the condition of a certain element spacing. A strategy employing mode reconstruction of a single array element combined with vector phase superposition is adopted to rapidly calculate the total scattered field of the array. This method fully leverages the repetitive nature of the array structure, avoids redundant computation of identical inter-element interactions, and significantly reduces computational complexity and memory consumption.

ACKNOWLEDGMENT

This work was supported in part by the Natural Science Foundation of China under Grant 62301258 and in part by the Natural Science Foundation of Jiangsu Province under Grants No. BK20230918. (Corresponding author: Jihong Gu.).

REFERENCES

[1] C. Wu, L. Guan, P. Gu and R. Chen, “Application of Parallel CM-MLFMA Method to the Analysis of Array Structures,” IEEE Trans. Antennas Propag., vol. 69, no. 9, pp. 6116-6121, Sept. 2021.

[2] L. Guan, C. Zhu, C. Dong, H. Yin, “Fast analysis of electromagnetic characteristics for UAV groups based on mode and domain decomposition”. Systems Engineering and Electronics, vol. 43,no. 10,pp. 2697-2705, Oct. 2021.

[3] Z. Wang, J. Gu, J. Shi, C. -F. Wang and D. Ding, “An Efficient Electromagnetic Scattering Analysis Method for Multiple Objects based on Characteristic Modes and MLFMA,” IEEE Trans. Antennas Propag., pp. 1-1, Jan. 2026.

[4] Ylä-Oijala P, Wallén H, “PMCHWT-based characteristic mode formulations for material bodies”. IEEE Trans. Antennas Propag., vol. 68, no. 3, pp. 2158-2165, Mar. 2020.

[5] Y. Chen, C. -F. Wang, “Characteristic Mode Theory for Antennas in Multilayered Medium,” in Characteristic Modes: Theory and Applications in Antenna Engineering, Wiley, 2015, pp.99-141.

Background Separation and Cancellation in Complex Indoor Testing Environments Based on the TTP Algorithm

1st Wei Gao
National Key Laboratory of Radar Detection and Sensing
Xidian University
Xi'an, China
174866160@qq.com

2nd Wen Jiang
National Key Laboratory of Radar Detection and Sensing
Xidian University
Xi'an, China
jw13@vip.qq.com

3rd Tao Hong
National Key Laboratory of Radar Detection and Sensing
Xidian University
Xi'an, China
thong@mail.xidian.edu.cn

4th Wei Hu
National Key Laboratory of Radar Detection and Sensing
Xidian University
Xi'an, China
whu@mail.xidian.edu.cn

5th Kun Wei
National Key Laboratory of Radar Detection and Sensing
Xidian University
Xi'an, China
weikun@xidian.edu.cn

6th Yuchen Gao
National Key Laboratory of Radar Detection and Sensing
Xidian University
Xi'an, China
gaoyuchen@xidian.edu.cn

***Abstract*—In indoor Radar Cross Section (RCS) test ranges, multipath signals generated by reflections from fixed structures such as walls and ceilings severely contaminate the true measured values of targets. This is particularly prominent in low-frequency band measurements and for low-RCS targets. Traditional background subtraction or time-gating methods often fail to isolate interference that is coherent or closely spaced with the target echo. To effectively suppress background clutter in indoor testing environments, this paper conducts an in-depth study on background separation and cancellation techniques. A target-background coupling model based on the Target Translation Processing (TTP) method is proposed. By utilizing a single translation of the target between two measurements, the phase of the multipath signal is actively altered, thereby achieving the separation of the target echo from the background multipath at the signal level. Simulation analysis determines that the optimal translation range is between 0.2λ and 0.3λ to minimize the ill-conditioning of the solution matrix. Experimental results on a flat plate demonstrate that the proposed algorithm can effectively suppress significant false interference peaks introduced by fixed wall reflections in the expected multipath directions, significantly improving the accuracy of target measurements and recovering the true RCS characteristics.**

Keywords—indoor testing, background cancellation, multipath interference, target translation processing (TTP), radar cross section (RCS)

I. Introduction

In indoor testing of radar target characteristics, background clutter in the testing environment is a critical factor affecting measurement accuracy [1]. In indoor test ranges, multipath signals reflected by structures such as walls, ceilings, and floors superimpose with the direct scattering echoes of targets, leading to severe distortion of measurement results [2], [3]. This multipath contamination is especially prominent during low-frequency band measurements and low-RCS target testing, where the target echo may be comparable in magnitude to the clutter. Traditional filtering techniques, such as time-domain gating, often struggle to completely eliminate clutter interference that is closely spaced with the target echo in the time domain [4]. Similarly, simple vector background subtraction requires a separate measurement of the empty room, which fails to account for the coupling between the target and the environment.

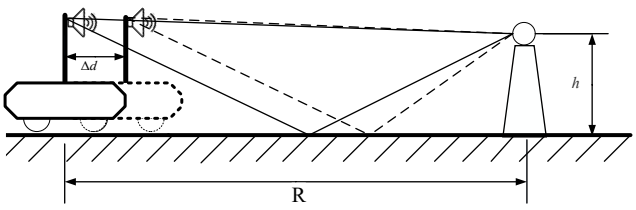


Fig. 1. Schematic of the TTP Algorithm.

To address the aforementioned issues, this paper investigates background separation and cancellation techniques in complex testing environments. The Target Translation Processing (TTP) algorithm is introduced to actively isolate multipath interference by altering the testing geometry. First, the mathematical model of the indoor received signal is constructed to analyze the coupling mechanism between the target and the background. Subsequently, the core parameters of the algorithm, specifically the optimal translation distance, are determined through numerical simulations. Finally, the effectiveness of the algorithm in background signal extraction and cancellation is verified using measured data from a flat plate, demonstrating a significant enhancement in the target-to-clutter ratio.

II. Coupling Model Construction Based on TTP

A. Indoor Received Signal Model

In conventional indoor testing, the signal received by the radar receiving antenna contains not only the direct scattering echo of the target but also multipath signals arriving at the antenna via environmental reflection paths. These paths may involve reflections off walls, floor, or ceiling before and after illuminating the target. To separate these components at the signal level, the TTP algorithm is employed as shown in Fig. 1.

The core idea of the TTP algorithm is to utilize a single translation of the target between two measurements to actively change the phase of the multipath signal relative to the direct signal. Since the direct backscatter and the multipath components have different angles of arrival relative to the translation vector, they experience distinct phase shifts. By solving the system of equations formed by these two

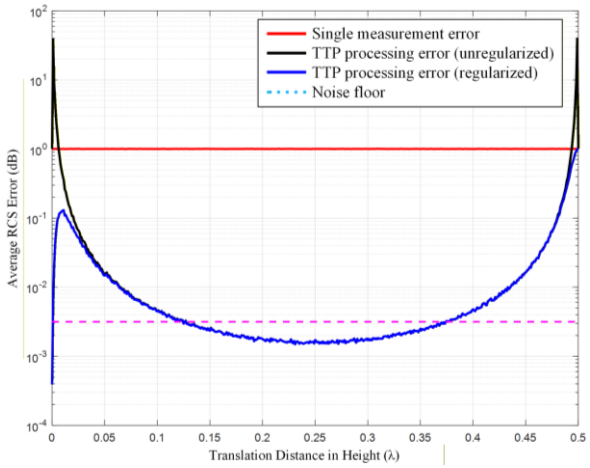


Fig. 2. Simulation Results of the Relationship Between Translation Distance and Error.

measurements, the true target response can be separated from the background multipath.

B. Mathematical Model Formulation

To simplify the problem and validate the fundamental feasibility of the TTP algorithm, this paper assumes that a single dominant multipath reflection (e.g., from a specific side wall) primarily contaminates the signal, thereby simplifying the coupling model to a dual-component system. Assuming the presence of both direct illumination and multipath illumination indoors, measurements are taken before and after the target moves along a specific translation direction. This allows the construction of the following indoor received signal matrix model:

$$\mathbf{s} = \begin{bmatrix} 1 & 1 \\ e^{-i2\mathbf{k}\cdot\Delta\mathbf{d}(\phi)} & e^{-i(\mathbf{k}+\mathbf{k}_m)\cdot\Delta\mathbf{d}(\phi)} \end{bmatrix} \begin{bmatrix} t \\ m \end{bmatrix} + \begin{bmatrix} n_1 \\ n_2 \end{bmatrix} = \mathbf{A}(\phi)\mathbf{x} + \mathbf{n} \quad (1)$$

where vector **s** represents the total received signal, t represents the true target signal, m represents the multipath signal, matrix $\mathbf{A}(\phi)$ is the coefficient matrix dependent on the azimuth angle ϕ, n_1 and n_2 denote system measurement noise.

In the phase term $e^{-i2\mathbf{k}\cdot\Delta\mathbf{d}(\phi)}$ and $e^{-i(\mathbf{k}+\mathbf{k}_m)\cdot\Delta\mathbf{d}(\phi)}$ of matrix **A**, the exponent part is the dot product of the wave vector and the translation vector. It is worth noting that the multipath direction function $\mathbf{k}_m$ changes dynamically with the rotation of the target (variation in azimuth angle). By solving the above system of equations, the decoupling and separation of the target signal t and the multipath clutter m can be achieved.

III. Background Signal Extraction And Cancellation

By solving the TTP-based coupling model, the background multipath signal can be extracted and cancelled from the total test data. To achieve optimal cancellation performance, the key parameter of translation distance must be optimized, and its performance verified through experiments.

A. Simulation and Analysis of Optimal Translation Distance

The selection of the translation distance **Δd** directly affects the condition number of matrix **A** and the final calculation error. This paper conducts a simulation study on the relationship between translation distance and average RCS error. As shown in Fig. 2, the simulation results indicate that

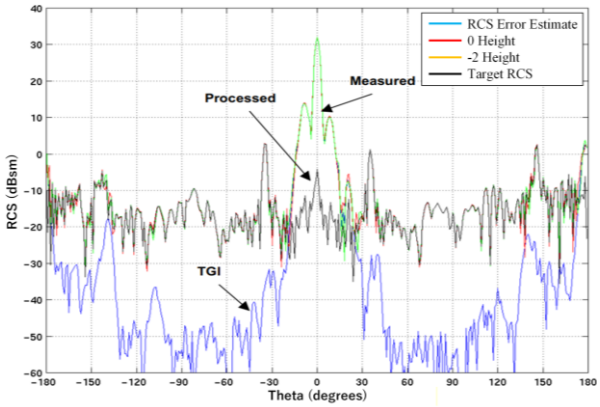


Fig. 3. Experimental results of flat plate cancellation before and after TTP processing. (TGI is the target-to-clutter/interference ratio.)

the average RCS error exhibits a non-linear "U-shaped" trend (first decreasing, then increasing) with respect to the longitudinal translation distance (measured in multiples of wavelength).

Through a comprehensive comparative analysis of single-measurement error, unregularized TTP processing error, and regularized TTP processing error, the error curve reaches its lowest level when the translation distance is between 0.15λ and 0.35λ. Based on this simulation result, this paper establishes that the optimal translation range for the TTP algorithm is 0.2λ ~ 0.3λ. Performing target translation within this interval maximizes the suppression of noise amplification effects, yielding optimal background cancellation results.

B. Flat Plate Cancellation Experiment Verification

To verify the aforementioned theory and simulation analysis, a flat plate target cancellation experiment was conducted in an indoor test range. The target was a metallic square plate, and measurements were taken across a range of azimuth angles (Theta). A background measurement with a high level of multipath interference was intentionally set up. The target was then translated along the radar line of sight by a distance of 0.25λ between two measurements, and the TTP algorithm was applied.

As shown in Fig. 3, by comparing the RCS curves varying with azimuth angle before processing (denoted as "Measured") and after TTP algorithm processing (denoted as "Processed"), the following observations can be made:

In the expected multipath directions (angles where specular reflections from side walls would reach the receiver), the original test data exhibit significant false interference peaks—ripples and lobes—introduced by reflections from fixed walls. These artifacts severely mask the true scattering behavior of the target, especially in the nulls and low-sidelobe regions.

After being processed by the TTP algorithm (using the optimized translation amount within the 0.2λ ~ 0.3λ range), these environmentally-induced false interference peaks are greatly suppressed. The ripple magnitude is reduced in the affected angular regions. The processed RCS curve more closely approximates the theoretical target RCS (labeled Target RCS), particularly in the low-scattering regions . The background clutter level is significantly reduced, and the Target-to-Clutter/Interference ratio (TGI) is notably improved, demonstrating the algorithm's efficacy in extracting the true coherent target response from a polluted signal.

IV. Conclusion

Targeting the severe multipath contamination issues inherent in complex indoor environmental testing, this paper thoroughly investigates background separation and cancellation techniques based on the TTP algorithm. By constructing mathematical coupling equations of the target and the multipath background, signal decoupling is successfully achieved using the phase difference generated by a single, precise target translation. Simulation and experimental results demonstrate that within the optimal translation range of 0.2λ–0.3λ, this method can effectively eliminate false interference peaks caused by fixed reflective surfaces indoors. This capability is particularly vital for improving measurement accuracy in low-frequency bands and for low-RCS targets, where traditional gating and subtraction methods fall short. The TTP algorithm thus provides a practical and feasible technical approach for achieving high-precision indoor microwave measurements and holds promise for application in anechoic chamber characterization and advanced imaging techniques.

References

[1] Q. Cui, C. Ji, Y. Yu, and J. Zhao, "Research on radar clutter simulation and background adaptive clutter map detection technique," in Proc. 2024 6th Int. Conf. Electron. Eng. Informatics (EEI), Chongqing, China, 2024, pp. 546–551.

[2] T. Peng, W. Huang, X. Zhou, and L. Yang, "Dual-frequency anechoic chamber constructed with the spatially arranged absorbing units," IEEE Antennas Wireless Propag. Lett., vol. 23, no. 10, pp. 2890–2894, Oct. 2024.

[3] R. P. S. Bhadoriya, V. Bajaj, and R. Panwar, "CGO-driven design of magnetic material and plasma integrated next-generation broadband pyramidal microwave absorber," IEEE Trans. Magn., vol. 60, no. 9, pp. 1–5, Sept. 2024, Art. no. 2200405.

[4] Y. He and C. Ding, "Automatic time-domain gating algorithm in freespace measurement system," in Proc. 2024 IEEE 10th Int. Symp. Microw., Antenna, Propag. EMC Technol. Wireless Commun. (MAPE), Guangzhou, China, 2024.

S Parameters Matrix Estimation for E-MIMO-based Beamforming

Qiaowei YUAN
Tohoku Institute of Technology
Sendai , Japan

***Abstract*— The Efficiency Maximum Multiple-Input Multiple-Output (E-MIMO) approach has recently been proposed as an effective beamforming technique for array antennas [1]. Practical implementation of E-MIMO requires accurate knowledge of the coupling matrix between transmitting and receiving elements, typically represented by the S-parameter or Z-parameter matrix. In realistic environments, however, direct measurement of the full multi-port matrix is time-consuming and often difficult, particularly when the receiving antennas are located far from the transmitting antennas. This paper proposes a method for estimating the coupling matrix using pilot signals. In the proposed approach, the mutual admittance or impedance matrix between the transmitting and receiving ports is derived from measured port voltages under known termination conditions at the transmitting side induced by pilot signal excitation. Numerical simulations are conducted to validate the proposed estimation method.**

Keywords—E-MIMO, S-parameters, Impedance Matrix, Admittance Matrix, Channel Estimation, Pilot Signal

I. INTRODUCTION

Our previous research demonstrated that the Efficiency Maximum Multiple-Input Multiple-Output (E-MIMO) approach achieves superior beamforming performance compared with conventional array factor (AF) and Retrodirective (RD) methods in both near-field and far-field regions [1].

Beamforming using array antennas is a fundamental technique in wireless communication systems. Conventional beamforming methods generally control the excitation phase of each array element based on array factor (AF) theory, assuming negligible mutual coupling between antenna elements. However, in practical antenna arrays, especially in compact or strongly coupled structures, electromagnetic coupling between elements cannot be neglected.

To address this issue, the E-MIMO approach has recently been proposed as a new beamforming framework that explicitly utilizes electromagnetic coupling between transmitting and receiving elements [1]. Unlike conventional array beamforming methods, the E-MIMO approach formulates the beamforming problem from the viewpoint of maximizing power transfer efficiency. It has been shown that the optimal excitation derived from the coupling matrix can significantly improve beamforming performance compared with conventional excitation schemes.

A key requirement for implementing the E-MIMO approach is accurate knowledge of the coupling matrix between transmitting and receiving elements. This matrix is typically represented by the S-parameter matrix or the Z-parameter matrix of the electromagnetic system. In many cases, these matrices can be obtained using full-wave electromagnetic simulations or multi-port measurements with a vector network analyzer. However, such measurements become increasingly difficult as the number of antenna elements increases or when the receiving antennas are located far from the transmitting antennas.

To overcome this difficulty, a previous study [2] proposed an estimation method of the coupling matrix when the receiving antenna is located far from the transmitting array. In that method, the magnitude of the coupling coefficients is estimated using the Friis transmission formula, while the phase of each element is estimated based on the array factor concept. Although the effectiveness of this method was verified, it requires prior estimation of the target receiving position when applying the array factor, which introduces additional processing steps.

In this paper, we propose a practical estimation method of the coupling matrix for the E-MIMO approach using pilot signals. By utilizing the Z-matrix formulation of the electromagnetic system and the known termination condition at the transmitting ports, the mutual impedance matrix between transmitting and receiving ports can be estimated from measured port voltages. The proposed method enables estimation of the required coupling matrix without performing full multi-port measurements. Numerical simulations are conducted to demonstrate the effectiveness of the proposed method and to confirm that the estimated matrix can be successfully applied to E-MIMO beamforming.

II. E-MIMO-BASED BEAMFORMING

A. Z or S-Matrix of MIMO sysytem

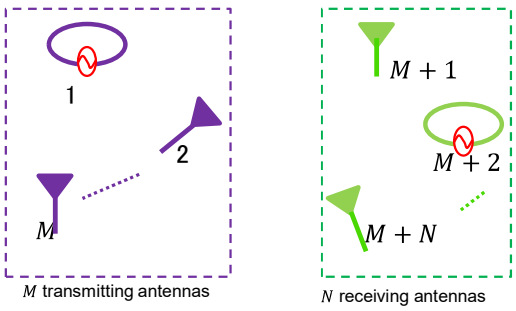


Fig.1 M transmitting antennas and N receiving antennas with arbitrary shapes and configurations

As shown in Fig. 1, consider a MIMO system consisting of M transmitting antennas and N receiving antennas. The electromagnetic interaction among the transmitting and receiving ports can be described using the impedance matrix (Z-matrix). The relationship between the port voltages and currents of the system can be expressed as

$$\begin{bmatrix}\mathbf{V}_T\\ \mathbf{V}_R\end{bmatrix}=\begin{bmatrix}\mathbf{Z}_{TT} & \mathbf{Z}_{TR}\\ \mathbf{Z}_{RT} & \mathbf{Z}_{RR}\end{bmatrix}\begin{bmatrix}\mathbf{I}_T\\ \mathbf{I}_R\end{bmatrix}, \quad (1)$$

where $\mathbf{V}_T$ and $\mathbf{I}_T$ denote the voltage and current vectors at the M transmitting ports, respectively, and $\mathbf{V}_R$ and $\mathbf{I}_R$ denote the voltage and current vectors at the N receiving ports.

The submatrices are defined as follows:

- $\mathbf{Z}_{TT}$: self-impedance matrix of the transmitting antennas ($M \times M$)
- $\mathbf{Z}_{RR}$: self-impedance matrix of the receiving antennas ($N \times N$)
- $\mathbf{Z}_{TR}$: mutual impedance matrix from transmitting antennas to receiving antennas ($M \times N$)
- $\mathbf{Z}_{RT}$: mutual impedance matrix from receiving antennas to transmitting antennas ($N \times M$)

For reciprocal electromagnetic systems, the following relationship generally holds:

$$\mathbf{Z}_{RT} = \mathbf{Z}_{TR}^{T}. \quad (2)$$

The same electromagnetic system can also be represented using the scattering matrix (S-matrix), which describes the relationship between the incident and reflected waves at each port. In the S-matrix representation, the relationship between the incident wave vector $\begin{bmatrix}\mathbf{A}_T\\ \mathbf{A}_R\end{bmatrix}$ and the reflected wave vector $\begin{bmatrix}\mathbf{B}_T\\ \mathbf{B}_R\end{bmatrix}$ is expressed as

$$\begin{bmatrix}\mathbf{B}_T\\ \mathbf{B}_R\end{bmatrix}=\begin{bmatrix}\mathbf{S}_{TT} & \mathbf{S}_{TR}\\ \mathbf{S}_{RT} & \mathbf{S}_{RR}\end{bmatrix}\begin{bmatrix}\mathbf{A}_T\\ \mathbf{A}_R\end{bmatrix}, \quad (3)$$

where $\mathbf{S}_{TT}$ and $\mathbf{S}_{RR}$ denote the reflection characteristics of the transmitting and receiving ports, respectively, while $\mathbf{S}_{TR}$ and $\mathbf{S}_{RT}$ represent the transmission characteristics between the transmitting and receiving ports.

The Z-matrix and S-matrix representations are related through the well-known transformation

$$\mathbf{S} = (\mathbf{Z} - Z_0\mathbf{U})(\mathbf{Z} + Z_0\mathbf{U})^{-1}, \quad (4)$$

where Z_0 is the reference impedance and $\mathbf{U}$ is the identity matrix.

Although the S-matrix representation is widely used in practical measurements with vector network analyzers, the proposed estimation method in this paper is derived based on the voltage–current relationship of the electromagnetic system.

B. Principle E-MIMO-Based Beamforming

The E-MIMO approach formulates the beamforming problem from the viewpoint of maximizing the power transfer efficiency between the transmitting and receiving antennas [1].

In the E-MIMO framework, the electromagnetic system consisting of the transmitting and receiving antennas is described using a multi-port network representation as explained in subsection A. The coupling between the transmitting and receiving ports is expressed by the Z-matrix. The power transfer efficiency is defined as the ratio between the total received power at the receiving antennas and the total input power supplied to the transmitting antennas,

$$\eta = \frac{P_{out}}{P_{in}} = \frac{\sum_{n=1}^{N} P_{M+n}}{\sum_{m=1}^{M} P_m} \quad (5)$$

where P_{out} and P_{in} denote the total received power at the N receiving antennas and the total transmitted power from the M transmitting antennas, respectively.

By solving the eigenvalue problem derived from the coupling matrix between the transmitting and receiving antennas, the optimal excitation voltages of the transmitting antennas that maximize the power transfer efficiency can be obtained [1]. In a MISO configuration, applying these optimal excitation voltages enables beamforming toward the desired receiving element with maximum efficiency.

III. Principle of Estimation Method of $\mathbf{S_{TR}}(\mathbf{S_{RT}})$

The proposed estimation method is based on a pilot-signal transmission scheme from the receiving antenna array to the transmitting antenna array. In this approach, the receiving antenna radiates a known pilot signal so that the excitation voltage vector at the receiving ports, denoted by $\mathbf{V}_R$, is known a priori. When the pilot signal is radiated, each transmitting antenna port receives an induced voltage generated by the electromagnetic coupling between the receiving and transmitting antennas. By measuring the received voltages $\mathbf{V}_T$ at the transmitting ports, the transfer admittance matrix between the two antenna groups can be estimated.

Assume a system composed of M transmitting antennas and N receiving antennas. The electromagnetic interaction of the system can be described using the network admittance matrix

$$\mathbf{Y}=\begin{bmatrix}\mathbf{Y}_{TT} & \mathbf{Y}_{TR}\\ \mathbf{Y}_{RT} & \mathbf{Y}_{RR}\end{bmatrix}, \quad (6)$$

where $\mathbf{Y}_{TT}$ and $\mathbf{Y}_{RR}$ represent the self-admittance matrices of the transmitting and receiving antennas, respectively, while $\mathbf{Y}_{TR}$ and $\mathbf{Y}_{RT}$ denote the transfer admittance matrices between them.

In the proposed scheme, the self-admittance matrices $\mathbf{Y}_{TT}$ and $\mathbf{Y}_{RR}$ are assumed to be known through either electromagnetic simulation or prior measurements of the individual antenna arrays. When the receiving antennas radiate the pilot signal, the transmitting ports observe induced voltages determined by the mutual electromagnetic coupling between the two antenna groups. Using the relationship between the equivalent transmitting voltage and the receiving

excitation voltage, the transfer admittance matrix can be estimated as

$$\mathbf{Y}_{TR} = \mathbf{V}_T^e \mathbf{V}_R^T (\mathbf{V}_R \mathbf{V}_R^T)^{-1}. \quad (7)$$

An assumption of the proposed method is that the transmitting and receiving antenna arrays are sufficiently separated so that they operate in the far-field region of each other. Under this condition, the self-admittance matrices of the two antenna arrays remain unchanged by the presence of the other array, and the mutual coupling is dominated by radiative coupling rather than strong near-field interactions. This assumption enables the independent characterization of $\mathbf{Y}_{TT}$ and $\mathbf{Y}_{RR}$ and allows the transfer admittance matrix $\mathbf{Y}_{TR}$ to be estimated accurately from the measured pilot-response voltages.

IV. Verification of the Proposed Estimation Method

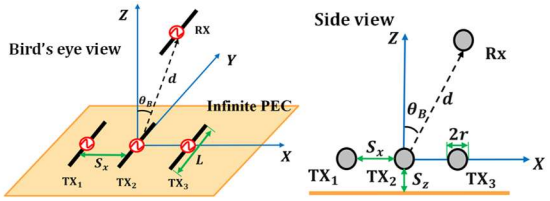


Fig. 2 3×1 dipole antenna array

To further investigate the validity of the proposed estimation method, numerical simulations were carried out using the antenna configuration shown in Fig. 2. The model consists of three transmitting dipole antennas (Tx1–Tx3) arranged on a PEC ground plane and one receiving dipole antenna located above the transmitting array. In this study, the element spacing of the transmitting array was fixed at $S_x = 0.5\lambda$, while the distance d between the transmitting array and the receiving antenna was varied from 0.1λ to 50λ. This distance variation enables the evaluation of the proposed estimation method under both near-field and far-field conditions.

The dipole length was set to $L = 0.5\lambda$, and the radius of each dipole element was $r = \lambda/100$. The operating frequency was 2.4 GHz. $\theta_B = 15$ [deg.]. The receiving antenna radiates a pilot signal with a known excitation voltage vector $\mathbf{V}_R$, and the induced voltages at the transmitting antenna ports are obtained through full-wave electromagnetic simulation. Using the proposed formulation, the transfer admittance matrix $\mathbf{Y}_{TR}$ is estimated from the measured pilot-response voltages, assuming that the self-admittance matrices $\mathbf{Y}_{TT}$ and $\mathbf{Y}_{RR}$ are known.

To evaluate the estimation accuracy, the reconstructed scattering matrix obtained from the proposed estimation approach was compared with the original transmission coefficients S_{14}, S_{24}, and S_{34} obtained from full-wave simulations. As shown in Fig. 3, when the distance between the transmitting and receiving antennas becomes moderately large (e.g., $d \geq 0.5\lambda$), the reconstructed transmission parameters agree very well with the original values, and both the amplitude and phase errors become almost negligible.

On the other hand, when the antennas are placed very close to each other (e.g., $d < 0.5\lambda$), strong near-field coupling occurs between the transmitting and receiving antennas. Even under this strong coupling condition, and assuming that the self-admittance matrices in (7) of the two antenna arrays remain unchanged by the presence of the other array, the relative amplitude error of the reconstructed parameters remains below approximately 2.5×10^{-4} [%], while the relative phase error is on the order of 10^{-4}[%]. These results indicate that the proposed estimation method maintains extremely high accuracy over a wide range of antenna separations.

V. Conclusion

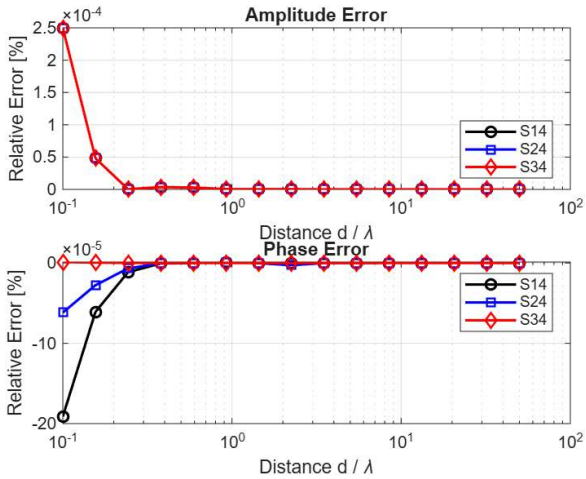


Fig. 3 Relative Estimation ERR for 3×1 System

This paper proposed a pilot-signal-based method for estimating the coupling matrix required for E-MIMO beamforming systems. The method derives the mutual admittance (or impedance) matrix between transmitting and receiving ports from measured port voltages under known termination conditions at the transmitting side. Using the estimated admittance matrix, the corresponding scattering parameters can be reconstructed without direct multi-port measurements. Numerical results showed that the reconstructed transmission coefficients closely match those obtained from full-wave simulations, with extremely small amplitude and phase errors even under strong near-field coupling conditions. Furthermore, the proposed framework can be extended to multi-receiver antenna systems and MIMO channel estimation, enabling efficient characterization of coupling or channel matrices for advanced wireless systems.

Acknowledgment

This work was partially supported by JSPS KAKENHI Grant Numbers 23K26102 and 25K07753.

References

[1] Q. Yuan, J. Wu, and H. Kato, "Beamforming of Array Antennas Using E-MIMO," IEICE Transactions on Communications, vol. J108-B, no. 11, pp. 511–519, Nov. 2025. doi:10.14923/transcomj.2025API0004..

[2] Jintai WU, Qiaowei YUAN, Takayuki OKADA and Bo YANG, "An Estimation Method of the 4-Port S-Parameters Used for the E-MIMO Approach," December 27, 2024, Space Solar Power and Wireless Transmission.

Modelling Clock Stability to Enabling Synchronisation for Multi-static Passive Radar

K.S. Bialkowski, The University of Queensland, Australia

Passive radar is a type of radar system that offers several advantages over traditional active radar systems. Unlike active radar, passive radar does not require a dedicated transmitter and instead uses existing signals from the environment, like radio or television signals as a source of illumination, making it low cost, low power and portable.

With advancements in receiver technology and computational power, passive radar has become an increasingly attractive option in many applications where active radar would have been used. However, the detection range and accuracy of passive radar are limited by the geometry of a single receiver scenario and the signal-to-noise ratio of the received signal. One way to overcome these limitations is to use multiple receivers to triangulate the position of a target, which provides increased coverage and the ability to detect smaller targets.

To fully make use of the signals, coherent detection provides the opportunity to maximally combine the signals from all of the receivers. However, this depends on accurate synchronisation between receivers. In practice, this is challenging, as differences in receivers caused by both manufacturing defects as well as temperature fluctuations, can degrade the level of synchronisation.

This work investigates the effect of synchronisation through experimental modelling of RF receivers and then looks at how these effect radar signal processing in terms of localisation performance in a virtual radar environment. Using the Generalised Canonical Correlation Analysis (GCCA) detector, a high-performance coherent detector is used. The key output of this work demonstrates that synchronization errors significantly affect localization performance, particularly where the detection performance is relying on coherent detection. However, when conditions, particularly temperature, remain stable, a calibration process can be used to mitigate most of the error.

Understanding the impact of synchronization errors is crucial for improving and developing future multi-receiver passive radar and distributed beamforming systems.

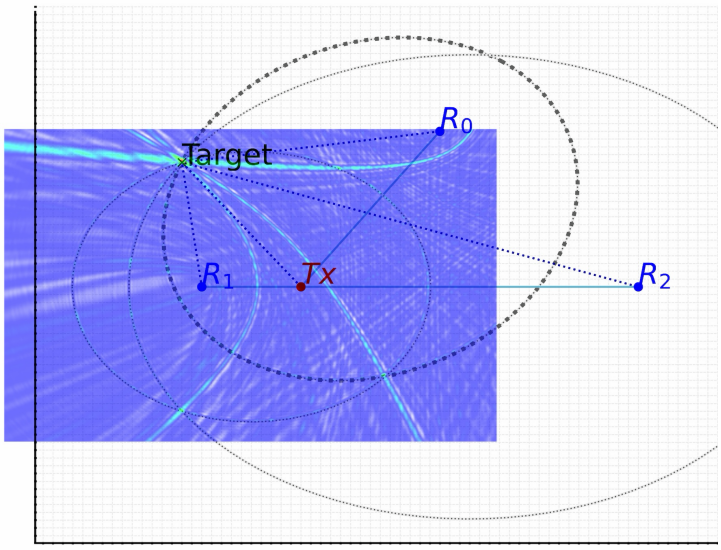


Fig 1. Multi-static radar detection using the Generalised Canonical Correlation Analysis Method, overlayed on a schematic of the transmitter and receiver configuration.

979-8-3315-4544-4/26/$31.00 ©2026 IEEE

Multi-Template Differential Correction for Subarray-Based Pattern Reconstruction of Large Phased Arrays

1st Yuqing Yang
School of Electronic Engineering
Beijing University of Posts and Telecommunications
Beijing, China
yuqing_yang@bupt.edu.cn

2nd Weimin Wang
School of Integrated Circuits
Beijing University of Posts and Telecommunications
Beijing, China
wangwm@bupt.edu.cn

3rd Yongle Wu
School of Integrated Circuits
Beijing University of Posts and Telecommunications
Beijing, China
wuyongle138@gmail.com

4th Yuanan Liu
School of Electronic Engineering
Beijing University of Posts and Telecommunications
Beijing, China
yuliu@bupt.edu.cn

***Abstract*—Electrically large phased arrays for satellite communications often exceed anechoic-chamber (AC) test-zone dimensions, motivating subarray-based pattern reconstruction realized through subarray stitching for over the air (OTA) characterization. However, conventional stitching tiles an isolated-subarray pattern and implicitly assumes identical embedded behavior across the aperture. This assumption produces systematic boundary-induced errors that accumulate in the reconstructed pattern, particularly at wide zenith angles. This paper proposes a multi-template differential correction method that uses one isolated subarray and four representative embedded templates (middle, two edges, and one corner). The method models template deviations as differential fields, propagates them across the aperture via symmetry mapping, and applies an angle-dependent least-squares weight for direction-selective compensation. Numerical simulations show up to a 53% reduction in full-angle gain Mean Squared Error (MSE) and a 65% reduction in wide-zenith MSE, validating improved wide-angle reconstruction under test-zone constraints.**

***Index Terms*—Pattern reconstruction, subarray stitching, OTA measurement, phased-array antennas, large antenna arrays.**

I. Introduction

Electrically large phased arrays have become a mainstream antenna solution in satellite communication systems, driven by the demand for high gain and agile beam steering [1]. From a measurement perspective, however, large apertures often exceed the finite test-zone dimensions available in practical AC, which makes direct full-aperture OTA pattern characterization difficult within existing facilities [2].

Subarray stitching provides a practical alternative by decomposing the aperture into smaller subarrays that can be characterized individually and then recombined through array-factor synthesis. Owing to its simplicity and low measurement burden, it has been widely adopted as an engineering baseline and is also outlined in 3GPP TR 38.803 for OTA evaluation of large arrays [3]. Nevertheless, the method implicitly assumes identical radiation behavior for all subarrays, which becomes inaccurate near array boundaries.

This work was supported by the National Natural Science Foundation of China (No. U22A2014).

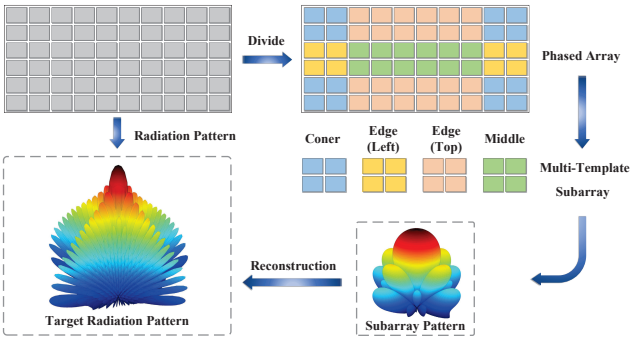


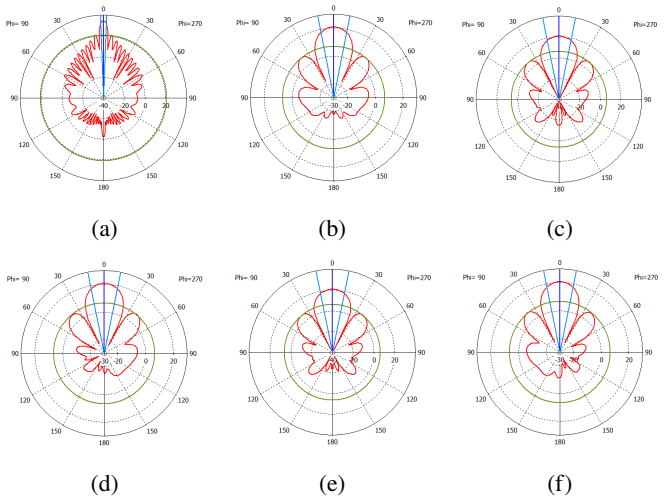
Fig. 1: Proposed multi-template subarray-stitching framework.

Edge and corner subarrays experience truncated coupling and asymmetric electromagnetic environments, which leads to systematic embedded-pattern deviations that accumulate in the reconstructed pattern, especially at wide zenith angles [4]. To mitigate this limitation, we propose an improved multi-template reconstruction approach that augments conventional stitching with representative embedded-subarray templates. Fig. 1 illustrates the workflow. We partition the aperture into regions with distinct electromagnetic environments, model location-dependent deviations using differential fields, propagate them across the aperture via symmetry mapping, and apply an angle-dependent least-squares weight for direction-selective compensation. The framework applies to both sub-6 GHz and mmWave phased arrays and is validated through full-wave simulations.

II. Subarray Stitching Method

A. Problem Formulation

Let $E_{\text{true}}(\theta, \varphi)$ denote the complex far field of the full finite planar array, whose direct OTA measurement is precluded by AC test zone limits. Standard stitching assumes that the same



(a) (b) (c)

(d) (e) (f)

Fig. 2: θ-cut patterns at $\varphi = 90°$: (a) full-array reference, (b) isolated subarray E_{iso} used in conventional stitching, and (c)–(f) embedded templates E_{mid}, E_{corner}, $E_{\text{edge-L}}$, and $E_{\text{edge-T}}$.

isolated-subarray pattern $E_{\text{iso}}(\theta,\varphi)$ applies at every subarray position. In practice, as shown in Fig. 2, embedded patterns vary with location due to truncated coupling and asymmetric neighborhoods. To capture this non-uniformity with minimal additional measurements, we measure four representative embedded templates: $E_{\text{mid}}, E_{\text{edge-L}}, E_{\text{edge-T}}, E_{\text{corner}}$, representing the array middle, a vertical edge, a horizontal edge, and a corner, respectively. The objective is to reconstruct the gain $G(\theta,\varphi)$ such that it best approximates $G_{\text{true}}(\theta,\varphi)$, especially at wide zenith angles.

B. Standard Subarray Stitching Baseline

Given $E_{\text{iso}}(\theta,\varphi)$, the standard reconstruction synthesizes the full-array field as

$$E_{\text{s}}(\theta,\varphi) = \sum_{m,n} \omega_{m,n}\, E_{\text{iso}}(\theta,\varphi)\, e^{\mathrm{j}k\,\mathbf{r}_{m,n}\cdot\hat{\mathbf{u}}(\theta,\varphi)}, \tag{1}$$

where $\omega_{m,n}$ denotes the beamforming weight and the exponential term accounts for spatial phase progression due to the subarray displacement [5]. k is the free-space wavenumber, $\mathbf{r}_{m,n}$ is the position vector, and $\hat{\mathbf{u}}(\theta,\varphi)$ is the unit vector. Although this approach is widely adopted due to its simplicity, it inherits the identical-subarray assumption and thus becomes increasingly biased when embedded behavior varies across the aperture, especially near array boundaries.

C. Multi-Template Differential Correction

The proposed method corrects E_{s} by modeling the embedded deviation using the template set defined in Section II-A. Each embedded template is phase-aligned to E_{iso}, and a differential field is formed as $D_p(\theta,\varphi) = E_p(\theta,\varphi) - E_{\text{iso}}(\theta,\varphi), p \in \{\text{mid, edge-L, edge-T, corner}\}$ [6].

The measured differentials are expanded over the full aperture via symmetry mapping (left/right edges, top/bottom edges, and four corners), which yields a location-dependent differential assignment $D_p^{m,n}(\theta,\varphi)$. We then synthesize a composite correction field as

$$D(\theta,\varphi) = \sum_{m,n,p} \omega_{m,n}\, D_p^{m,n}(\theta,\varphi)\, e^{\mathrm{j}k\,\mathbf{r}_{m,n}\cdot\hat{\mathbf{u}}(\theta,\varphi)}. \tag{2}$$

Finally, we obtain the reconstructed field by augmenting the baseline synthesis with an angular correction term

$$E_{\text{prop}}(\theta,\varphi) = E_{\text{s}}(\theta,\varphi) + \alpha(\theta,\varphi)\, D(\theta,\varphi), \tag{3}$$

where $\alpha(\theta,\varphi)$ is estimated by least squares to compensate direction-dependent mismatch.

The proposed formulation provides a first-order correction to isolated-subarray stitching. For a finite array, the embedded response at $[m,n]$ can be expressed as $E_{\text{iso}}(\theta,\varphi) + D_p^{m,n}(\theta,\varphi)$, where $D_p^{m,n}(\theta,\varphi)$ models boundary-induced perturbations from truncated coupling and asymmetric neighborhoods [7]. Unlike conventional stitching, the proposed method approximates the coherent accumulation of $D_p^{m,n}(\theta,\varphi)$ using symmetry-propagated middle/edge/corner differentials, yielding the largest benefit at wide-zenith angles.

D. Physical Interpretation and ESS Metric

We evaluate reconstruction discrepancy using the equivalent stray signal (ESS) metric [8]. In the preceding sections, the pattern is represented by the electric field $E(\theta,\varphi)$. For ESS evaluation, we use the corresponding gain patterns in dB, where $G(\theta,\varphi)$ denotes the reference pattern and $\tilde{G}(\theta,\varphi)$ denotes the reconstructed pattern. After normalizing two gain patterns G and $\tilde{G}$ to a 0 dB peak as G_{n} and $\tilde{G}_{\text{n}}$, we define $d_{\text{G}} = \max(G_{\text{n}}, \tilde{G}_{\text{n}})$ and $\Delta = |G_{\text{n}} - \tilde{G}_{\text{n}}|$. The ESS level is then computed as

$$\text{ESS}(\theta,\varphi) = d_{\text{G}} + 20\log_{10}\left(\frac{1-10^{-\Delta/20}}{2}\right), \tag{4}$$

and ESS_{max} is reported as the maximum over the sampled angular grid.

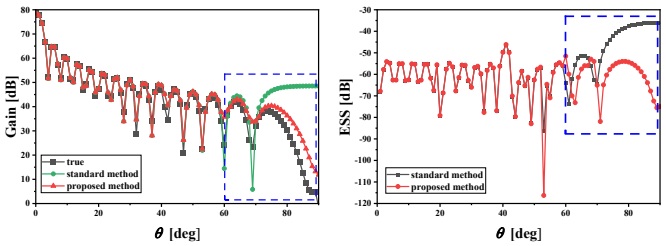
TABLE I: Simulation arrays and parameters

Parameters	Case A	Case B
Frequency band	Sub-6	mmWave
Center frequency	2.4 GHz	27.5 GHz
Array size	30×30	30×40
Subarray size	6×6	6×8

III. Numerical Analysis

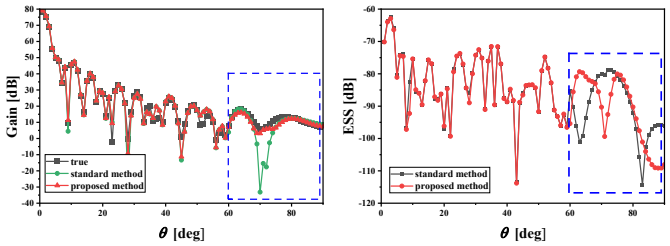
A. Simulation Setup

We evaluate the proposed method using two full-wave simulated planar phased arrays that represent S-band and mmWave operation, as summarized in Table I. Case A operates at 2.4 GHz with a 30×30 array composed of 6×6 subarrays, where boundary effects occupy a non-negligible portion of the aperture and embedded non-uniformity is expected to be pronounced. Case B operates at 27.5 GHz with a 30×40 array composed of 6×8 subarrays, serving as a compact mmWave baseline. For both cases, we sample far-field patterns with $\Delta\theta = \Delta\varphi = 1°$



(a) (b)

Fig. 3: Reconstruction results for the 30×30 array at 2.4 GHz: (a) gain-pattern comparison and (b) ESS comparison.



(a) (b)

Fig. 4: Reconstruction results for the 30×40 array at 27.5 GHz: (a) gain-pattern comparison and (b) ESS comparison.

over $\theta \in [0°, 90°]$, and we treat the full-array pattern as the reference G_{true}. We compare the reconstructed patterns G_{s} and G_{prop} using ESS_{max} and gain MSE. In particular, we compute the "wide-zenith" MSE over $\theta \in [60°, 90°]$, which captures the region where stitching errors typically amplify.

B. Simulation Results

We assess reconstruction performance by comparing the full-wave simulation results G_{true} with the baseline stitching result G_{s} and the proposed reconstruction G_{prop}. Figs. 3 and 4 show that the standard method exhibits noticeable mismatch at wide zenith angles, whereas the proposed method improves agreement by injecting a location-aware correction synthesized from embedded differential templates. Table II summarizes the numerical results.

For the 2.4 GHz 30×30 array, the proposed method reduces ESS_{max} from -36.21 dB to -46.17 dB, indicating substantial suppression of reconstruction-induced stray components. The gain MSE decreases from 45.14 to 21.03 dB^2 over the full angular range and from 100.77 to 35.46 dB^2 over $\theta \in [60°, 90°]$, which confirms that the improvement is most significant in the error-sensitive wide-zenith region. For the 27.5 GHz 30×40 array, ESS_{max} remains comparable, while the gain MSE decreases from 103.05 to 69.41 dB^2 (full angle) and from 168.77 to 101.23 dB^2 (wide zenith). The smaller improvement margin is consistent with reduced embedded diversity for a more compact aperture; nevertheless, the proposed method still yields measurable gain-fidelity improvement.

TABLE II: Performance comparison of reconstruction methods

Method		Brute force	[3]	This work
Case A	Tests	N^{*2}	1	5
	MSE	0	45.14	21.03
	MSE_L^{*1}	0	100.77	35.46
	ESS_{max}	-Inf	-36.21	-46.17
Case B	Tests	N^{*2}	1	5
	MSE	0	71.06	32.97
	MSE^{*1}	0	160.45	56.88
	ESS_{max}	-Inf	-62.44	-62.92

^{*1} wide-zenith MSE $\theta \in [60°, 90°]$. ^{*2} number of elements in the array.

IV. Conclusion

This paper proposes a multi-template differential correction to enhance conventional subarray stitching for electrically large phased arrays measured under anechoic-chamber test-zone constraints. The method measures representative embedded-subarray templates and propagates their deviations via symmetry mapping, which compensates the dominant boundary-induced bias neglected by isolated-subarray tiling. For a 30×30 array at 2.4 GHz, simulations show 53% lower full-angle gain MSE and 65% lower wide-zenith MSE, together with a 10 dB improvement in ESS_{max}. For a 30×40 array at 27.5 GHz, ESS_{max} remains comparable, while the gain MSE decreases by 33% (full angle) and 40% (wide zenith), confirming consistent wide-zenith fidelity gains across sub-6 and mmWave arrays. These results indicate that boundary-driven embedded non-uniformity constitutes the dominant bottleneck for wide-zenith reconstruction, and that a small set of representative templates provides a scalable path for chamber-limited OTA characterization of large arrays.

References

[1] Z. Yu, C. Chen, W.-D. Chen, X. Zhang, J.-G. Lu, X.-L. Zhang, B.-J. Che, and Q. Wang, "A Low-Profile LTCC Phased Array Antenna With Wideband and High-Gain for X-Band Satellite Communications," *IEEE Trans. Antennas Propag.*, vol. 73, no. 1, pp. 659-664, Jan. 2025.

[2] W. Fan, M. Li, Z. Wang, and F. Zhang, "Wireless Cable Testing for MIMO Radios: A Compact and Cost-effective 5G Radio Performance Test Solution," *IEEE Trans. Antennas Propag.*, vol. 71, no. 10, pp. 8239–8249, Oct. 2023.

[3] 3GPP, "Study on new radio access technology: Radio Frequency (RF) and co-existence aspects," *3GPP TR 38.803*, ver. 14.4.0 (Release 14), Jul. 2024.

[4] Q. Liu and L. Zhu, "Decoupling of 2-D Antenna Array Based on the Diagonal Mode of the Square Patch Resonator," *Proc. 2024 IEEE MTT-S Int. Microwave Workshop Series on Advanced Materials and Processes for RF and THz Applications (IMWS-AMP)*, Nanjing, China, Nov., 2024.

[5] Z. Wang, C. Pang, Y. Li and X. Wang, "A Method for Radiation Pattern Reconstruction of Phased-Array Antenna," *IEEE Antennas Wireless Propag. Lett.*, vol. 19, no. 1, pp. 168-172, Jan. 2020.

[6] F. Lisi, A. Michel, and P. Nepa, "Synthesis of near-field arrays based on electromagnetic inner products," *IEEE Trans. Antennas Propag.*, vol. 71, no. 6, pp. 4919-4931, Jun. 2023.

[7] Z. Wang, F. Zhang, and W. Fan, "In-Situ Calibration of Plane Wave Generator in an Aperture-Limited Multi-Probe Compact Setup," *IEEE Trans. Antennas Propag.*, vol. 73, no. 4, pp. 2204-2216, Apr. 2025.

[8] L. Yu, F. Zhang, Y. Zhang, X. Zhang, Z. Wang, Y. Jing, and W. Fan, "The Antenna Pattern Reconstruction Based on Mid-Field Phaseless Measured Data Using a Simplified Extrapolation Technique," *IEEE Trans. Antennas Propag.*, vol. 73, no. 6, pp. 3904-3916, Jun. 2025.

Multi-Material Additively Manufactured Wideband Dual-Linear Polarized Antenna with High Isolation

Zhichao Sun
School of Electrical and Data Engineering, University of Technology Sydney, Sydney, NSW 2019, Australia
Bryan.Sun@uts.edu.au

Xiaojing Lv
School of Electrical and Data Engineering, University of Technology Sydney, Sydney, NSW 2019, Australia
xiaojing.lv@uts.edu.au

Jiexin Lai
School of Electrical and Data Engineering, University of Technology Sydney, Sydney, NSW 2019, Australia
Jiexin.Lai@student.uts.edu.au

Yang Yang
School of Electrical and Data Engineering, University of Technology Sydney, Sydney, NSW 2019, Australia
yang.yang.au@ieee.org

***Abstract*—A multi-material additively manufactured wideband dual-linear polarized (dual-LP) antenna with high isolation is proposed in this paper. The structure integrates a magnetoelectric-dipole (ME-dipole) and a quasi-Yagi antenna. The ME-dipole utilizes a slot-coupled feed to produce horizontal polarization (HP), while the quasi-Yagi features two pairs of symmetrical dipoles with obliquely angled feed lines to realize vertical polarization (VP). The antenna is realized using multi-material additive manufacturing in a single integrated process, resulting in a highly compact design. Simulation results demonstrate that the antenna achieves a shared impedance bandwidth (IMBW) of 48.71% in the millimeter-wave (mm-wave) band, while maintaining an isolation level below −34.5 dB. Owing to its compact configuration, wide bandwidth, and high isolation, the proposed antenna is well-suited for a variety of modern communication and sensing applications.**

Keywords—dual-circularly polarized, high port isolation, millimeter-wave (mm-wave), wideband

I. Introduction

With the rapid development of mobile Internet, the Internet of Things (IoT), and next-generation wireless communication systems, antennas with enhanced performance are increasingly required to support higher data rates and improved spectral efficiency. Among various antenna technologies, dual-polarized antennas have attracted significant attention due to their ability to improve channel capacity and mitigate multipath fading and polarization mismatch between the transmitter and receiver [1].

For dual-polarized antennas, high port isolation is a critical requirement to ensure stable system performance. Insufficient isolation between the two orthogonal polarizations may lead to undesired mutual coupling, which degrades radiation performance and reduces polarization purity. Therefore, achieving high isolation while maintaining a compact antenna structure has become an important challenge in antenna design. Various dual- linear polarized (dual-LP) antenna configurations have been investigated in the literature [2-4], although these designs provide feasible solutions for realizing dual polarization, many of them still suffer from limited port isolation or relatively large structural dimensions, which restrict their application in highly integrated wireless systems.

Meanwhile, the rapid evolution of wireless communication technologies has driven the exploration of millimeter-wave

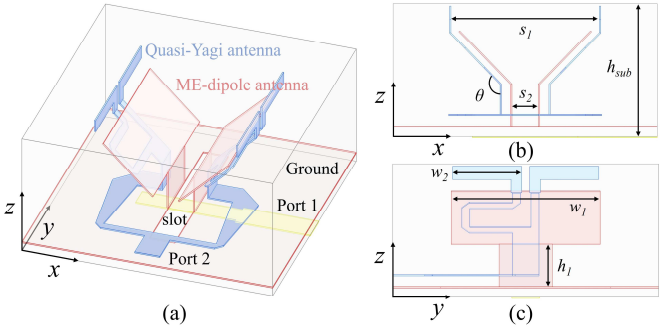


Fig. 1 Configuration of proposed dual-LP antenna. (a) 3-D view, (b) and (c) side view. (s_1=3.4mm, s_2=0.6mm, θ=135°, h_{sub}=3mm, w_1=3.36mm, w_2=1.56mm, h_1=0.96mm)

(mm-wave) frequency bands. Mm-wave systems offer abundant spectrum resources and enable high data-rate transmission, making them essential for emerging applications such as high-capacity wireless links, sensing, and integrated communication systems. However, mm-wave antennas generally require wide impedance bandwidth (IMBW) to accommodate high data throughput and support multiple communication standards. Consequently, the development of compact, wideband, and high-isolation dual-polarized antennas operating at mm-wave frequencies has become increasingly important.

In addition, the fabrication approach also plays a key role in the realization of advanced antenna structures. Traditional printed circuit board (PCB) manufacturing techniques impose limitations on structural complexity and integration capability. Recently, additive manufacturing has emerged as a promising technology for microwave and millimeter-wave applications. In particular, multi-material additive manufacturing enables the simultaneous deposition of metallic and dielectric materials, allowing the realization of complex three-dimensional structures that are difficult or impossible to achieve using conventional fabrication methods. Such capability provides new opportunities for designing highly integrated antenna architectures with enhanced electromagnetic performance [5-7].

Motivated by these advantages, this work presents a compact dual-LP antenna with high isolation based on multi-material additive manufacturing. The proposed antenna integrates a magnetoelectric-dipole (ME-dipole) radiator and a quasi-Yagi

XXX-X-XXXX-XXXX-X/XX/$XX.00 ©20XX IEEE

979-8-3315-4544-4/26/$31.00 ©2026 IEEE

structure within a unified architecture, enabling orthogonal polarizations with wide IMBW and excellent port isolation.

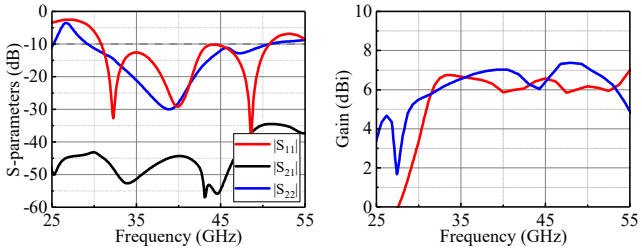


Fig. 2 Simulated (a) S-parameters and (b) realized gains of proposed dual-LP antenna.

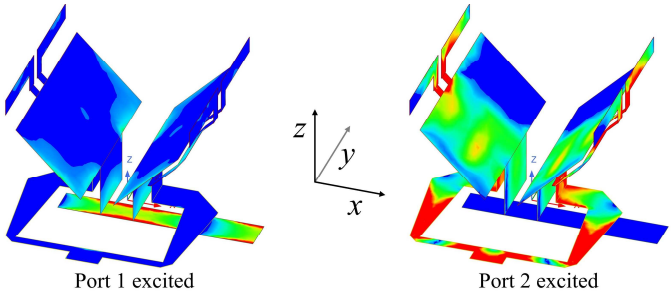


Fig. 3 Simulated current distributions of the proposed antenna when (a) port 1 excited, and (b) port 2 excited.

Benefiting from the integrated multi-material printing process, the antenna achieves a highly compact structure suitable for millimeter-wave communication and sensing applications.

II. Antenna Design

The configuration of the proposed dual-LP antenna is illustrated in Fig. 1. It comprises a ME-dipole antenna and a pair of quasi-Yagi antennas, and the *E*-dipole of the ME-dipole is reused as the ground of the quasi-Yagi antenna. Two microstrip feeding lines are located above and below the ground plane to excite the antenna. The entire antenna is designed in a single process using multi-material 3-D printing technology, where silver nanoparticles are used for the metallic parts and acrylate-based dielectric inks are used for the dielectric components. The overall height of the antenna is 3mm.

Fig. 2 (a) and (b) show the simulated S-parameters and realized gains of the proposed dual-LP antenna. The -10 dB shared impedance bandwidth (IMBW) is 48.71% (30.9-50.8 GHz) with a high isolation higher than 34.5 dB. The realized gain ranges from 5 dBic to 7.4 dBic within the operating bandwidth.

To more clearly illustrate the high isolation performance of the proposed design, Fig. 3 presents the current distribution on the metal part. It is observed that when one port is excited, negligible current is induced on the other port, owing to the two independent operating modes of the proposed design. Fig. 4 shows the simulated normalized radiation patterns of two polarizations in *xoz*- and *yoz*-planes. All patterns exhibit directional radiation characteristics, and the cross-polarization level in the main radiation direction is lower than −40 dB.

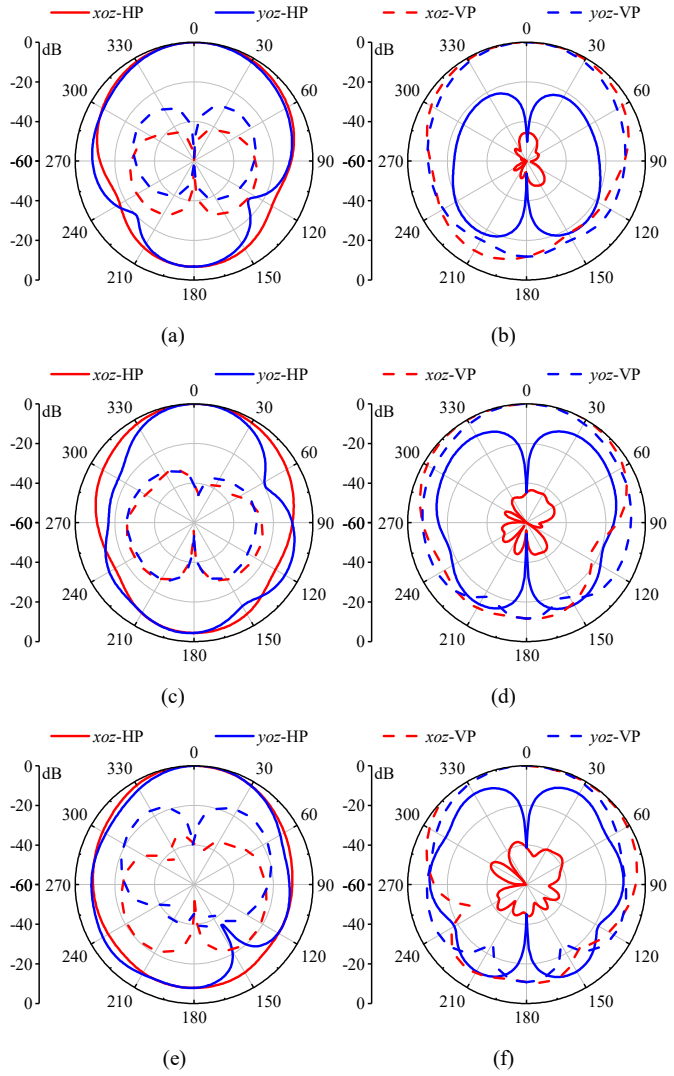


Fig. 4 Simulated radiation patterns of the proposed dual-LP antenna at (a) 35 GHz, (c) 40 GHz, and (e) 45 GHz when port 1 is excited, and (b) 35 GHz, (d) 40 GHz, and (f) 45 GHz when port 2 is excited.

III. Conclusion

This paper presents a wideband dual-LP antenna with high isolation based on multi-material 3-D printing technology. By integrating two different types of antennas within the same aperture through structural reuse, the proposed design achieves extremely high isolation between the two ports while maintaining a compact overall configuration. Benefiting from the integrated multi-material additive manufacturing process, the antenna can be fabricated in a single step, which simplifies the fabrication procedure and enables complex three-dimensional structures that are difficult to realize using conventional manufacturing techniques. Simulation results demonstrate that the proposed antenna achieves a shared impedance bandwidth of 48.71% in the mm-wave band while maintaining an isolation level better than −34.5 dB across the operating band. With the advantages of high isolation, compact structure, and wide operating bandwidth, the proposed antenna provides a promising solution for modern mm-wave communication and sensing applications that require highly integrated and high-performance antenna systems.

REFERENCES

[1] B. Li, Y. -Z. Yin, W. Hu, Y. Ding and Y. Zhao, "Wideband Dual-Polarized Patch Antenna With Low Cross Polarization and High Isolation," *IEEE Antennas Wireless Propag. Lett.*, vol. 11, pp. 427-430, 2012.

[2] W. Huang, X. -X. Yang and J. Du, "A Miniaturized Dual-Polarized Antenna With High Isolation and Low Cross Polarization," *IEEE Antennas Wireless Propag. Lett.*, vol. 24, no. 5, pp. 1075-1079, May 2025.

[3] X. Zhang, J. Li, C. Yang, T. Liang, W. Zhang and Y. Yang, "A Wideband Dual-Polarized Antenna-in-Package for 5G Millimeter-Wave User Equipment," IEEE Transactions on Components, Packaging and Manufacturing Technology, vol. 14, no. 10, pp. 1845-1853, Oct. 2024.

[4] F. Ge, H. Zhao, M. Yang, S. Li and X. Yin, "Ku-Band Small-Frequency-Ratio Self-Diplexing Vivaldi Antenna With High Isolation for High-Power Application," *IEEE Antennas Wireless Propag. Lett.*, vol. 24, no. 8, pp. 2682-2686, Aug. 2025.

[5] Z. Sun, J. Lai, X. Lv, M. A. I. Oni, S. Dey and Y. Yang, "Ultrawideband Low-Profile Metal–Dielectric Additively Manufactured Planar Vivaldi-Shaped Antenna Array for Millimeter-Wave Applications," *IEEE Transactions on Antennas and Propagation*, vol. 74, no. 1, pp. 1055-1060, Jan. 2026.

[6] J. Zhu, Y. Yang, J. Lai, and J. Nulman, "Additively manufactured polarization insensitive broadband transmissive metasurfaces for arbitrary polarization conversion and wavefront shaping," *Adv. Opt. Mater.*, vol. 10, no. 21, Nov. 2022, Art. no. 2200928.

[7] J. Zhu, Y. Yang, N. Hu, S. Liao, and J. Nulman, "Additively manufactured multi-material ultrathin metasurfaces for broadband circular polarization decoupled beams and orbital angular momentum generation," *ACS Appl. Mater. Interfaces*, vol. 13, no. 49, pp. 59460–59470, Dec. 2021.

General-purpose terahertz quasi-optics and mechanical beamformers enabled by 3D-printing

1st Bryce Chung
Terahertz Engineering Laboratory
Adelaide University
Adelaide, Australia
bryce.chung@adelaide.edu.au

2nd Daniel Headland
Terahertz Engineering Laboratory
Adelaide University
Adelaide, Australia
daniel.headland@adelaide.edu.au

3rd Withawat Withayachumnankul
Terahertz Engineering Laboratory
Adelaide University
Adelaide, Australia
withawat.withayachumnankul@adelaide.edu.au

***Abstract*—Owing to their short wavelength and light-like propagation behavior, terahertz waves require quasi-optical components to control the flow of radiation. To meet this need, 3D-printing has evolved over the past decade from a niche technique to a highly customizable, general-purpose methodology to produce terahertz quasi-optics, using consumer-grade hardware.**

***Index Terms*—Terahertz, Quasi-optics, 3D-printing.**

I. Introduction and background

The operation of terahertz systems is subtended upon the availability of suitable quasi-optics, and customizability thereof expands the functionality of terahertz systems. Thus, the freedom provided by manufacturing techniques such as 3D-printing is highly beneficial. Not only that, consumer-grade 3D-printers can produce feature sizes that are sub-millimeter, and hence compatible with a terahertz wavelength.

Initial demonstrations of terahertz 3D-printed quasi-optics utilized plastics such as polylactic acid which, although very suitable for printing, exhibit high loss in the terahertz range ($\sim$10 cm^{-1} at 500 GHz) [1], [2]. As a result, optically thick lenses produced in this way were too lossy to allow for characterization of their focusing functionality.

II. Selective laser sintering of metal

One approach to address propagation loss in the bulk material of quasi-optics is to switch from transmissive devices (e.g. lenses) to reflectors. This means that the conventional transmissive plastics that are typically employed in 3D printing must be replaced with reflective substances, such as metals. To this end, certain advanced 3D-printers can employ selective laser sintering in order to fuse particles of metal powder together with high accuracy, which we have previously employed to manufacture a terahertz reflective zone plate operating at 530 GHz [3]. However, this approach does have some drawbacks, as the metal's finish is somewhat rough, reflecting the grains of the powder, and there is also an oxide layer. This incurs nonnegligible losses. Moreover, this particular metal-printing technique requires prohibitively costly infrastructure, and so alternatives must be sought.

B. Chung acknowledges support received through the provision of an Australian Government research training program scholarship. This research was supported in-part by the Australian Government through the Australian Research Council's Discovery Projects funding scheme (project number DP240100162). D. Headland acknowledges support from the Australian Research Council's Discover Early Career Researcher Award (project number DE240100625) funded by the Australian government.

III. Fused deposition of cyclic olefin copolymer

The issues with reflective 3D-printed optics prompt renewed investigation into transmissive alternatives. Busch et. al. identified one highly promising candidate: cyclic olefin copolymer (COC) [4], which exhibits near-negligible loss across the terahertz range, and is amenable to fused-deposition printers; conventional, inexpensive, consumer-grade hardware. That said, these preliminary studies only detailed elementary optical components. Recent years have gone beyond, producing much needed systems such as a terahertz 2D beam-scanner containing an optical train of four 3D-printed optics [5]. The core beam-scanning component is a pair of independently rotating prisms, in an arrangement known as a Risley prism. Another noteworthy example is a novel terahertz dark-field imaging system, which combines various kinds of axicon and lens to allow for concurrent dark-field and bright-field acquisition [6].

IV. Conclusion

Over the past decade, 3D-printing has grown from a novel curiosity to a veritable workhorse, going beyond a wide range of quasi-optics to produce optical systems to control the flow of terahertz radiation, including broadband beamformers and dark-field imaging.

References

[1] A. Squires, E. Constable, and R. Lewis, "3D printing of aspherical terahertz lenses and diffraction gratings," in *Proc. IRMMW-THz*. IEEE, 2014.

[2] ——, "3D printed terahertz diffraction gratings and lenses," *Journal of infrared, millimeter, and terahertz waves*, vol. 36, no. 1, pp. 72–80, 2015.

[3] D. Headland, W. Withayachumnankul, M. Webb, H. Ebendorff-Heidepriem, A. Luiten, and D. Abbott, "Analysis of 3D-printed metal for rapid-prototyped reflective terahertz optics," *Opt. Express*, vol. 24, no. 15, pp. 17 384–17 396, 2016.

[4] S. F. Busch, M. Weidenbach, J. C. Balzer, and M. Koch, "THz optics 3D printed with TOPAS," *Journal of Infrared, Millimeter, and Terahertz Waves*, vol. 37, no. 4, pp. 303–307, 2016.

[5] B. Chung, D. Headland, and W. Withayachumnankul, "Terahertz imaging with 3D-printed Risley-prism and telecentric objective," *IEEE Trans. Terahertz Sci. Technol.*, vol. 14, no. 4, pp. 446–454, 2024.

[6] B. Chung, H. Lees, M. Ibrahim, D. Headland, and W. Withayachumnankul, "Highly efficient terahertz dark-field imaging system with 3D-printed components," *J. Phys. Photon.*, vol. 7, no. 2, p. 025012, 2025.

979-8-3315-4544-4/26/$31.00 ©2026 IEEE

Phase-Tapered Bus-Bar Combiner for Efficiency Enhancement in C-Band GaN MMIC Power Amplifier

Nupur Sood [1,2], Pinaki Sen[1], Dr. Karun Rawat[2]
[1]Defence Electronics Applications Laboratory (D.R.D.O)
[2]Indian Institute of Technology, IIT Roorkee, India
n_sood@ece.iitr.ac.in

***Abstract*- This work presents a layout-only phase-tapered bus-bar combiner for Gallium Nitride (GaN) MMIC power amplifiers (PAs) in foundry compatible form. The approach improves power-added efficiency (PAE) by introducing asymmetry in drain-feed without increasing circuit complexity or addition of extra components. A graded drain-feed taper is used to introduce controlled phase delays of 18.2° for the edge devices, 7.1° for second-edge devices and less than 1° for center devices at 4.65 GHz. This results in 12.5 percent reduction in DC current while maintaining excellent vector combining efficiency (η_{comb}= 99.2 percent). Second, a single output-per-four-transistor topology reduces the required impedance transformation thus lowering the matching loss as well as avoiding closed metal loops. EM co-simulations carried out using UMS GaN technology (0.25 µm) with eight GH25-10 HEMTs (total periphery of 20 mm) results in a PAE of (44.5–46.3) percent in CW mode (improved by 5-points over conventional bus-bar), an output power of 47.6W and (21–22.7) dB of gain with a negligible linearity degradation over (4.35-4.97) GHz.**

Keywords - GaN HEMT, power amplifiers (PAs), bus-bar combiner, phase tapering, efficiency, waveform engineering.

I. INTRODUCTION

GaN HEMT power amplifiers are widely used in radar and communication systems due to their high power density and efficiency [1],[2],[3]. Bus-bar combiners are a popular way to compactly combine many transistors on MMICs. However, conventional equal-length bus-bar feeds drive all devices into near-simultaneous Class-AB/B conduction, which leads to peak current crowding and elevated junction temperature, wasted DC power from overlapping current pulses with extra matching loss from dual or quadrature post-combining networks.

Various MMIC bus-bar implementations at X/Ka-band exploit bus-bar as a compact combiner and bias feed without intentional drain-current staggering [4],[5]. Newer GaN MMICs use asymmetrical or broadband output combiners to improve load distribution and bandwidth but rely on additional circuit structures [6]. Doherty, outphasing, and harmonic-tuned PAs achieve high power-added efficiency (PAE) and back-off through complex multi-stage matching, resonant networks, or dual-input combiners, incurring 20-40% area overhead and up to 0.5-1.2 dB extra insertion loss [7],[8],[9],[10]. This creates a gap for a simple, foundry-compatible bus-bar architecture directly improving efficiency through current waveform engineering at layout level.

This work presents a novel layout-only, foundry-compatible phase-tapered bus-bar combiner that enhances PAE using dual-side phase tapered architecture. It uses single-output-per-4-transistor topology thus avoiding closed metal loops problematic for foundry manufacturing.

II. DESIGN AND THEORETICAL FRAMEWORK

The proposed modification lengthens feeds asymmetrically for transistors in power stage using dual approach.

A. Modified Bus-Bar Architecture

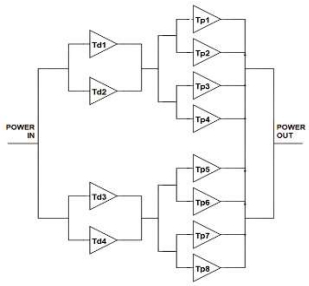


Fig. 1. Topology of proposed C-Band Power Amplifier

Fig. 1 shows the C-Band power amplifier (PA) architecture with 2 stages-driver stage (4 transistors, 180 µm, 10 fingers) and power stage (8 transistors, 250 µm, 10 fingers) using UMS GH25-10 HEMTs. Fig.2 shows the complete schematic of the proposed C-Band PA. The main features of this design include:

Gate-Side Asymmetry: i) Feed line length variation of 40 µm between edge and center branches ii) Differentiated capacitor values per branch (edge vs. inner transistor pairs) for input matching. Effect of this is the graded input phase offset for transistors in power stage.

Drain-Side Asymmetry: Drain-feed asymmetry is introduced for eight power-stage transistors (Tp1-Tp8) through graded physical lengths. Table I shows phase delays introduced because of these graded physical lengths. On 100 µm ceramic substrate (ε_r = 10.2, Z_0 = 50 Ω), with a wavelength, λg ≈ 20 mm, this graded taper staggers drain current peaks across the RF cycle, reducing peak overlap and I_{DC} crowding.

B. Vector Combining Efficiency

The total fundamental drain current is:

$$\mathbf{I_{Total}} = \sum_{i=1}^{8} I_i e^{j\phi_i} \quad (1)$$

For this design, ϕ_1=ϕ_8=18.2°, ϕ_2=ϕ_7=7.1°, ϕ_{3-6}=0°.

Total fundamental drain current (phasor sum) is $8.04I_0$. Vector combining efficiency (η_{comb}) for N transistors is:

$$\eta_{comb} = \left|\frac{\mathbf{I_{Total}}}{\mathbf{NI_0}}\right|^2 = 0.992 \quad (2)$$

This results in RF power loss ($P_{loss,RF}$) of 0.37W i.e., < 0.8 percent, which is negligible versus the 5% PAE gain.

Table I. Graded physical lengths with phase taper

Transistor Group	Position	Physical Length	Phase Delay @ 4.65 GHz
Edge pair	Tp1, Tp8	1.44 mm	18.2°
Second-edge pair	Tp2, Tp7	0.82 mm	7.1°
Inner pairs	Tp3–Tp6	0.42 mm	<1°

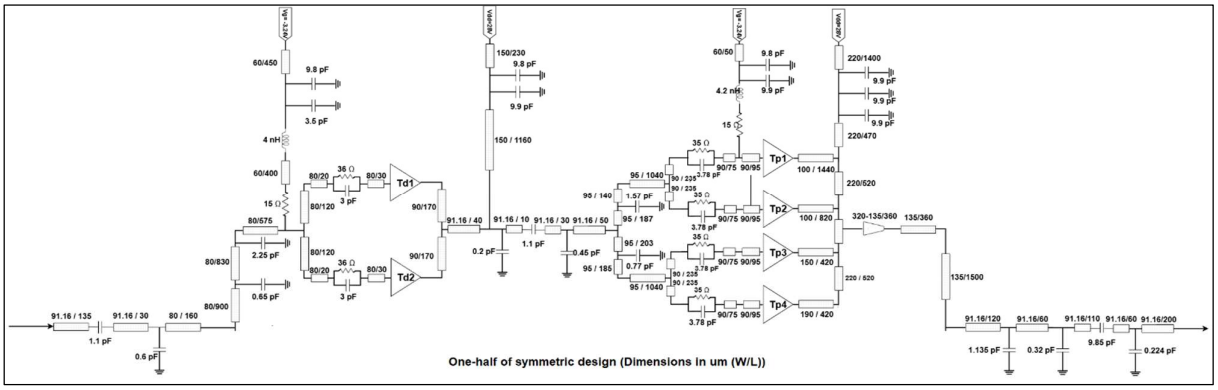


Fig.2. Schematic of proposed C-Band Power Amplifier (PA)

Phase taper thus preserves vector sum magnitude of waveform while reshaping drain current.

C. DC Current Reduction Mechanism

Time-domain instantaneous drain current (normalized, Class-AB) with staggered phases Φ_k is given as:

$$\boldsymbol{i_D}(t) = \sum_{k=1}^{8} I_0[1 - cos\,(\omega t - \Phi_k)]U(\theta_k) \quad (3)$$

where θ_k is conducting angle and $U(\theta_k)$ is the unit step.

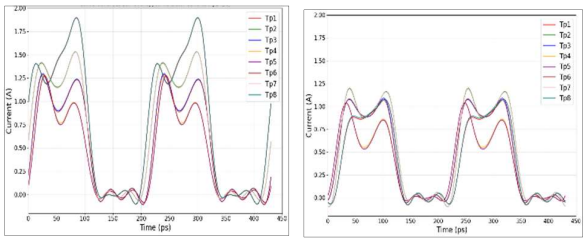
For conventional design, symmetric bus feeds all paths with Φ_k =0°. The peak overlap in Fig.3 (a) is thus given by:

$$\mathbf{i_{peak,conventional}} = 8\mathbf{I_o} \quad (4)$$

For the proposed design in this paper with graded Φ_1 =18.2°,Φ_2 =7.1° and Φ_3 =0°, peak reduction in staggered condition is given as in Fig.3 (b):

$\mathbf{i_{peak,taper}}$ = max [$2I_o\phi_1$(phase delayed) +$2I_o\phi_2$(phase delayed)+ $4I_o\phi_3$(no phase delay)] ≈ $5.7\mathbf{I_o}$ (5)

Reduction ratio (R_{Ratio}) of $i_{peak,taper}$ to $i_{peak,conventional}$ thus shows a 28.8% drop.



(a) (b)

Fig.3. (a) Drain Current waveforms for conventional Bus-bar (b) Drain Current waveforms for tapered Bus-bar

D. PAE Efficiency Gain Formula

At constant output power P_{out} and constant input power P_{in} (with same gain and input level), increase in PAE is given as 5.5 percent increase using given equation:

$$\Delta PAE \approx \frac{P_{out}-P_{in}}{V_{DD}*I_{DC,conventional}} \times \frac{\Delta I_{DC}}{I_{DC,conventional}} \quad (6)$$

III. Electromagnetic Validation and Layout

A. Drain Impedance Extraction & EM Validation

At each transistor drain (Tp1-Tp8) extracted Z_{int}=V/I over the frequency band are as shown in Fig.4. Smith Chart analysis shows magnitude variation of intrinsic Z_{drain} with 38 percent spread (45.4 Ω to 77.3 Ω) with a phase grading of 52° span (+25.5° to -26.6°). Measured intrinsic drain impedances (mag/phase) are summarized in Table II. This graded impedance trajectory precisely correlates with the intentional drain feed length taper confirming time staggered conduction reducing I_{DC}. The proposed phase-tapered bus-bar exhibits robust phase-delay control across process variations. Upto ±10 percent taper-length variation, results in PAE variation limited to ≤ 2.5 percent and within ± 0.3 point power output variation. Frequency robustness was validated by sweeping the operating frequency and confirming stable phase taper behavior and negligible PAE degradation across the band.

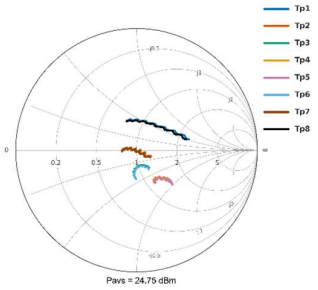


Fig.4. EM extracted Drain Impedances for phase tapered design

B. Single-Output-per-4-Transistor Design

In conventional bus-bar with single output for every two transistors, this gets transformed through drain feeds to Z_{group}≈11-12 Ω per 2-transistors branch. Then two-stage output matching network is required with intermediate impedance ~6 Ω which is be matched to 50 Ω resulting in approximately 0.7-1.0 dB loss. Whereas this work implements direct four-transistor star-point combining at Z_{star}=7.6 + j0.47 Ω per 4-transistors branch eliminating intermediate stage and requiring single-stage output matching network with approximately 0.23 dB loss. This further eliminates closed metal loops, which may otherwise pose foundry manufacturing issues.

C. Sensitivity Analysis of Phase Taper

Phase taper scales with frequency ($\Phi \propto f$). At 4.35 GHz,

Table II. EM Simulated Drain Impedances for present work

Transistor	Mag (Ω)	Phase (°)	Position	Length
Tp1	59.67	+25.5	Top edge	1.44 mm
Tp2	45.40	+2.6	2nd from top edge	0.82 mm
Tp3	50.21	-17.0	Inner	0.42 mm
Tp4	73.34	-26.6	Inner	0.42 mm

Table III. Performance Comparison (Phase Taper vs. Conventional)

Freq.(GHz)	Design	P_{out} (dBm)	Gain (dB)	PAE(%)
4.35	Conventional	47.2	22.2	39.3
	Present work	47.1	22.1	44.8
4.65	Conventional	48.0	23.0	41.4
	Present work	47.8	22.8	46.4
4.97	Conventional	46.3	21.3	39.9
	Present work	46	21	44.7

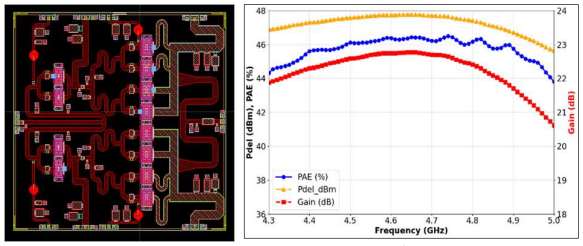
Table IV. Phase Tapered Bus-bar vs. Conventional Techniques

Technique	Phase Control	Foundry Yield	Extra Components	Area Overhead / Matching Loss
Doherty [7],[8]	λ/4 transformers (exact 90°)	<70% (±5° phase error kills efficiency)	Bias circuits and quarter-wave stubs	20-40% / 0.5-1.0 dB
Outphasing [9]	Variable phase shifters (0-90°)	<50% (needs calibration)	Control IC and phase detectors	25-35% /0.8-1.2 dB
Harmonic Tuning [10]	2nd and 3rd harmonic resonators (exact reactance required)	60-80% (±10% L/C tolerance leads to freq. shift)	On-chip LC networks and stubs	10-25%/ 0.3-0.8 dB
Phase-Taper (This work)	Fixed lengths (±5-10% tolerance)	>99%	None	0% / 0.2-0.3 dB

Φ_1=18.2°*(4.35/4.65) =17.02°, at 4.65 GHz Φ_1=18.2° and at 4.97 GHz Φ_1=18.2°*(4.97/4.65) =19.45°. Staggering remains effective across (4.35-4.97) GHz (i.e., 13.3% Fractional Bandwidth) limiting to ±1.25° variation with η_{comb} >98.3 percent.

IV. Simulation Results

The layout of proposed C-band PA (5.3 x 5.6) mm^2 is shown in Fig.5(a). 3D EM simulator of Keysight ADS Momentum has been used as simulation environment. The phase-tapered geometry is explicitly shown in the layout, where the progressive change in bus-bar length at drain side of transistors in power stage implements the required phase taper. For single transistor in power stage, source impedance, Z_{opt}=2.9+ 11.2 Ω was obtained from load-pull resulting in PAE > 65% and Pout=39 dBm. EM co-simulation was carried out with input power (CW) as 25 dBm, 28V supply voltage and gate bias of -3.24V. Fig.5(b) shows the results with a DE of 45-46.6 %, PAE of 44.7-46.3% and gain of 21-22.7 dB with power output of 46-47.7 dBm. Output power flatness is within ±0.85 dB variation. Across the entire 4.35-4.97 GHz band, the simulated PAE improvement (≈4.8-5.5%) closely matches the theoretically predicted improvement as discussed in Section II.D.



(a) (b)

Fig.5. (a) Layout of proposed C-Band PA (b) EM extracted PAE, Gain and Power delivered for phase tapered PA design

Harmonics were simulated and 2nd harmonic was found < -31 dBc and 3rd harmonic < -42 dBc over the band. Two-tone linearity test post-EM confirmed that phase taper preserves IMD performance at 6-dB back-off for each tone at output i.e., at total 3 dB back-off for output signal level. At 40 dBm CW power level at output, IMD3 suppression is better than -28 dBc while IMD5 suppression is better than -40 dBc across both low and high fundamental tones. Table III. summarizes the performance comparison of the phase tapered bus-bar design and the conventional bus bar design.

V. Novelty and Differentiation

As per the authors' knowledge, this work introduces the first layout-only phase-tapered bus-bar combiner that achieves an average of 5.3 point enhancement in PAE through feed asymmetry rather than complex matching networks or active control circuits. Unlike the conventional techniques like Doherty, outphasing or harmonic tuning by frequency-sensitive resonators requiring precise phase and amplitude tuning, our approach leverages the static phase gradients (18.2° to 7.1° to 0°) that tolerate upto ± 10 percent foundry variations while delivering efficiency and linearity improvements simultaneously in a 20 mm periphery C-band GaN MMIC. Table IV. summarizes the design limitations and performance comparison of this design with other conventional designs.

VI. Conclusion

A layout-only, foundry-compatible phase-tapered bus-bar combiner for GaN MMIC PAs is demonstrated. Graded drain-feed design (Φ_1 = 18.2°, Φ_2 = 7.1°) staggers 8-transistor conduction, yielding 28% peak and 12.5% average I_{DC} reduction while preserving vector combining efficiency(η_{comb}=99.2%). EM co-simulations from (4.35-4.97) GHz, using UMS 0.25 µm GaN, validate PAE of 46.3% with 47.6 W output power for CW mode, which is almost 5-point enhancement in PAE compared to the conventional design without compromising on gain or linearity. With increased process tolerance, nil overhead design increase along with no closed metal loops make this approach viable for production in MMIC foundries.

Acknowledgement

Authors would like to acknowledge UMS foundry for providing the GH25 PDK. We would also like to acknowledge Director, D.E.A.L (D.R.D.O) for his support.

References

[1] Ruizhe Zhang et al.," A GaN MMIC power amplifier using gain compensation and novel inter-stage matching method," Microelectronics Journal, vol. 169, 2026.

[2] Y. Noh et al., "Compact X-band 30 W power amplifier MMIC using 0.2 µm GaN HEMT technology," in Proc. 2025 IEEE MTT-S Int. Microw. Symp. (IMS), Jun. 2025, pp. 1-4.

[3] O. Silva et al., "Octave-band linear MMIC amplifier with +40-dBm OIP3 for high-reliability space applications," IEEE Trans. Microw. Theory Techn., vol. 64, no. 7, pp. 2059-2067, Jul. 2016..

[4] K. A. Lee et al., "A Ka-band MMIC power amplifier with bus-bar combiner," in Proceedings of Asia-Pacific. Microwave Conference (APMC), Dec.2004, pp. 1169-1172.

[5] S.P. Marsh et al.,"Design and analysis of an X-band MMIC bus-bar power comb.,"in Proc.34th Eur. Microw. conf.(EuMC), Oct.2004,pp. 1169-1172.

[6] Del Pino et al.,"A Ku-Band GaN-on-Si MMIC Power Amp. with an Asymmetrical Output Combiner. Sensors 2023,23, 6377

[7] D. K. Choi et al., "A modified Doherty power amplifier with high efficiency over an extended power range," IEEE Trans. Microwave Theory Tech., vol. 51, no. 4, pp. 986-993, Apr. 2003.

[8] Heng Zhang et al.," Design of Doherty power amplifier with power back-off extension based on harmonic tuning and output combining network optimization," Int.Jour. of Elec. & Comm.,vol. 187,Dec. 2024.

[9] Bai Hua Zeng et al,"An Efficient Asymmetric Outphasing Power Amplifier With Extended Back-Off Range for 5G Applications", IEEE Trans. on Circuits and Systems—I: Reg. Pprs., Vol. 72, No. 1, Jan 2025

[10] Caoyu Li et al.,"Internally Harmonic Matched Compact GaN Power Amplifier with 78.5% PAE for 2.45 GHz Wireless Power Transfer Systems", Micromachines 2024, 15, 13.

Design of Titanium SAW Phononic Crystal on Lithium Niobate $LiNbO_3$/Si Structure

Jingfu Bao*
School of Integrated Circuit Science and Engineering
University of Electronic Science and Technology of China
Chengdu, China
baojingfu@uestc.edu.cn

Mohammed Awad*
School of Integrated Circuit Science and Engineering
University of Electronic Science and Technology of China
Chengdu, China
mohadam494@uestc.edu.cn

Zijiang Yang
School of Integrated Circuit Science and Engineering
University of Electronic Science and Technology of China
Chengdu, China
yangzijiang1998@std.uestc.edu.cn

Taiyu Jiang
School of Integrated Circuit Science and Engineering
University of Electronic Science and Technology of China
Chengdu, China
202521311001@std.uestc.edu.cn

Kenya Hashimoto
School of Integrated Circuit Science and Engineering
University of Electronic Science and Technology of China
Chengdu, China
k.hashimoto@ieee.org

***Abstract*— This study explores the use of surface acoustic wave (SAW) phononic crystals (PnCs), specifically square pillar-based PnCs reflectors in SAW resonators. The PnC generates an acoustic band gap that reflects the wave onto the resonator body, thereby enhancing stored energy and reducing loss compared to a traditional reflector. The proposed square-shaped titanium PnC implemented on a 15 ° Y-X $LiNbO_3/SiO_2/Si$ layered substrate. To evaluate the practical impact of PnCs in SAW devices, two SAW resonators employing PnC and reflector designs are compared and analyzed. From the simulated frequency responses, it is shown that using the Square-PnC as a reflector reduces resonator energy loss and enhances the stored energy.**

Keywords—SAW resonators, Phononic Crystals, Stored Energy

I. INTRODUCTION

Recent progress in surface acoustic wave (SAW) design and fabrication has given SAW technology clear advantages over many alternatives, including compact form factor, strong performance, high stability, low cost, and relatively simple manufacturing. Consequently, SAW devices have become critical components in many RF and microwave systems, such as radar, wireless communications, satellite navigation, and sensing applications. In SAW resonators, metal reflective gratings are essential elements that strongly influence characteristics such as the quality factor (Bode-Q) and insertion loss (IL). Traditionally, achieving high performance relies on using a large number of metallic reflectors, which inevitably increases device size. Consequently, substantial research has focused on optimizing acoustic reflector designs to reduce SAW device dimensions while preserving performance [1–5].

In this setting, phononic-crystal (PnC) reflectors have gained attention as a compelling alternative because they can open elastic/acoustic band gaps. Such band gaps suppress acoustic-wave propagation along particular directions. Building on this concept, numerous studies have shown that PnCs can effectively manipulate SAW propagation, making. They are especially attractive as reflector elements in SAW devices [6–10]. Recent research on SAW-PnC shows performance improvements when PnC is applied to SAW resonators. In this regard, Bao J et al. introduced Analysis of Nano-Well Phononic Crystal on Si3N4/X-cut LiNbO3/SiC Heterostructure. The authors show that the PnC enhances the SAW resonator's performance compared to the reflector [11]. Also, Tang P et al. introduce Honeycomb-shaped phononic crystals on a 42° YX LiTaO3/SiO2/poly-Si/Si substrate to improve performance and enable miniaturization [12]. The authors show that using SAW-PnC improves performance while reducing size. In this work, we design a square-SAW PnC on LiNbO3/SiO_2/Si substrate. The results show enhanced stored energy and spurious-mode suppression compared with traditional reflectors.

.

II. DEVICE DESIGN

A. PnC Design

The PnC structure consisted of a 15° Y–X lithium Niobate (15° Y–X $LiNbO_3$) substrate with Titanium (Ti) pillars forming the PnC. A schematic of the square-PnC is provided in Fig. 1a. Dispersion curves were obtained with an eigenfrequency solver by sweeping the reduced wavevector (kx and ky), where (k) is the wavevector and (a) is the lattice constant along the Γ–X-M-Γ direction in the first irreducible Brillouin zone (IBZ) of the square lattice, as shown in Fig. 1a. The method used to calculate the dispersion curve is similar to the method used in [13].

The modeled Square-PnC employed a lattice constant (a = 1000nm) and a pillar height (h = 500nm). These parameters were selected to enhance the bandgap response. Figure 1b shows the 3-D view and the vibration mode of the designed PnC. We considered five metals widely used in acoustic-device fabrication: copper (Cu), aluminum (Al), gold (Au), platinum (Pt), and Titanium (Ti). The results show that aluminum and titanium have a wider band gap than the other materials due to their highest acoustic velocities (6420m/s, 6100m/s). While titanium shows a slightly wider band gap than aluminum due to additional impedance mismatch between the aluminum electrode and the titanium PnC.

979-8-3315-4544-4/26/$31.00 ©2026 IEEE

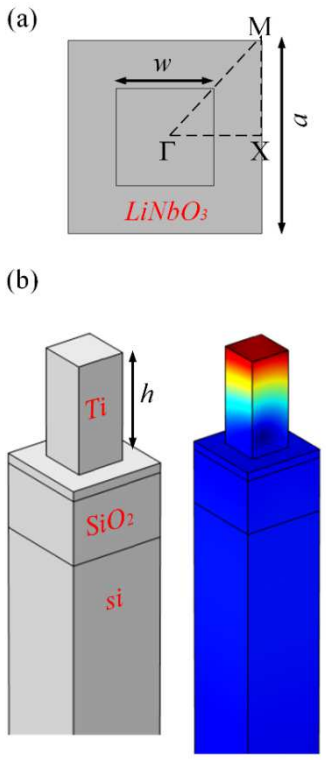


Figure 1. Illustration of The Square-PnC

B. *Bandgap and transmission*

To achieve a wide bandgap, the PnC dimensions (width and height) are swept to obtain maximum reflection. The optimized values are width equal to 0.5 µm and height equal to 1µm. Figure 2a reveals a partial bandgap shown in red spanning from a lower cutoff of 960 MHz to an upper cutoff of 1700 MHz. To quantify the acoustic attenuation provided by the proposed PnC, we simulated SAW transmission through the Square-PnC (colored in orange), using a finite array of unit cells along the x-direction. Figure 2b presents the transmission response of the Square-PnC reflector with 10 lattice periods. As seen in the Figure, there is strong attenuation at 1.25 GHz and 1.4 GHz.

III. RESONATOR DESIGN

As illustrated in Figure 3a, we developed a three-dimensional model of a SAW resonator. The IDT comprises 20 pairs of 100 nm-thick aluminum electrodes. The IDT period is λ = 2.65µm, the resonance frequency is 1.4 GHz, and the metallization ratio is 0.5. The piezoelectric layer thickness is 100nm. A perfectly matched layer (PML) width of 2*λ was applied at the bottom of the substrate to absorb waves leaking into the substrate and prevent artificial reflections. The width of the resonator (W) is equal to 2.65µm, and the length L = 32λ. The height of the resonator is H = 30 µm. For comparison, we also built a SAW resonator model using 10 pairs of conventional reflective gratings. The grating period is likewise λ = 2.65µm, ensuring that the overall reflector dimensions match those of the Square-PnC-based design exactly.

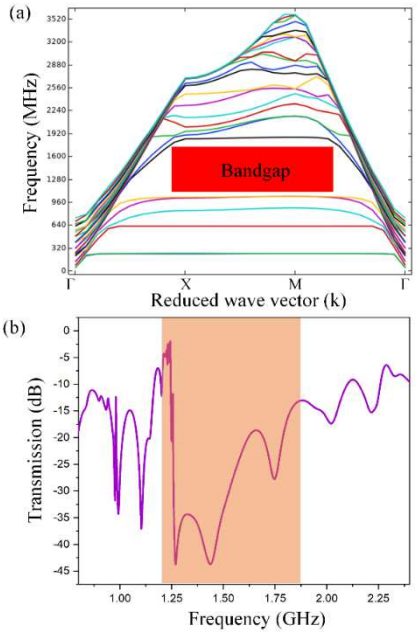


Figure 2. (a) Band gap of Square PnC (b) transmission attenuation of the proposed PnC

Figure 3b shows the vibration mode of the resonator. As seen from the figure, there is energy leakage in the resonator with a traditional reflector, while the resonator with the Square-PnC reflector shows more energy enhancement and lower loss at the PnC edges.

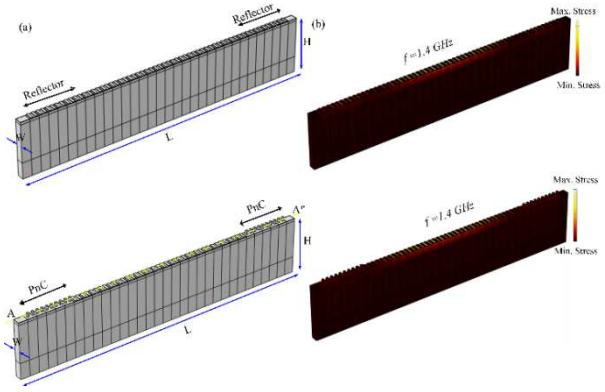


Figure 3. (a) 3- D representation of the resonator with PnC and reflector (b) Illustration of the resonator's vibration mode

A. *Displacement verification*

Figure 4 represents the resonator incorporating Square-PnC, which exhibits a substantially higher total displacement (10 nm) than the counterpart without PnC (1.3 nm). This increase confirms that the Square-PnC resonator stores more energy than the resonator with conventional reflectors. At the resonator edges, the displacement at the anchors is reduced for the resonator with Square-PnC, confirming the PnC's effectiveness in reducing loss compared to conventional reflectors. The displacement measured along the line A-À is illustrated in Figure 4.

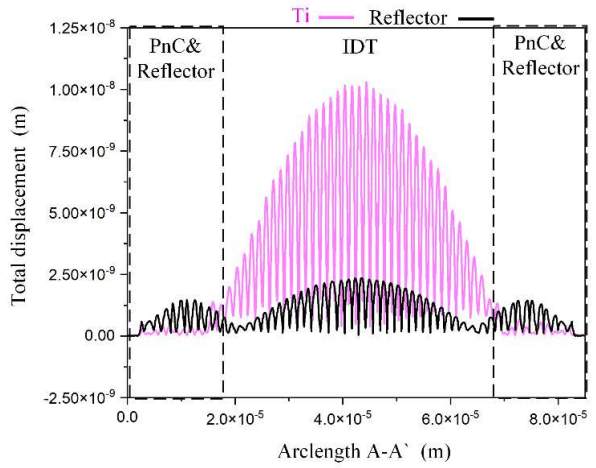


Figure 4. Illustration of displacement verification of the SAW resonator with reflector and Square-PnC

B. *Results*

Conventional SAW devices, metallic reflecting gratings, generate spurious modes that represent energy loss in the resonant body; the conductance curve shows a strong spurious mode in the resonator's passband around 1.25 GHz. When applying the square PnC, the resonator's stored energy is enhanced, and the spurious mode is suppressed, as shown in Figure 5. Table 1 compares the proposed PnC with that of some recent work.

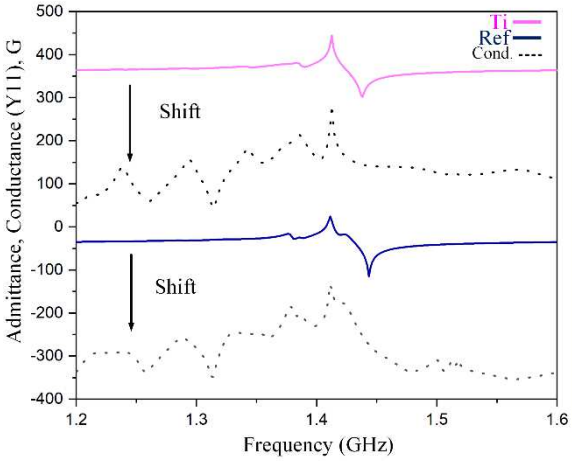


Figure 5. Admittance and conductance representation of the SAW resonator with Square-PnC and reflectors.

TABLE I. COMPARISON TO RECENT WORK

PnC shape	PnC material	Lattice constant *a*	Bandgap (GHz)
Nano-well [11]	$Si_3N4/LiNO_3$	0.7um	0.7-0.88
Honeycomb [12]	LT	5.4um	4.05-4.5
This work	Ti	1um	0.96-1.7

IV. CONCLUSION

In this study, we proposed a Square-PnC reflector for surface acoustic wave (SAW) resonators. The practicality of the approach was demonstrated by integrating the Square-PnC reflectors into SAW resonators. Resonator using Square-PnC arrays achieved higher resonant displacement amplitudes and greater spurious-mode suppression than resonators with conventional reflecting gratings.

ACKNOWLEDGMENT

This work is financially supported by a grant from the National Natural Science Foundation of China and the China Academy of Engineering Physics (Project No: U1430102) and 中央高校基本科研业务费专项资金资助（supported by the Fundamental Research Funds for the Central Universities） (No. A0920502052601-90).

REFERENCES

[1] Takai, Tsutomu, et al. "High-performance SAW resonator on new multilayered substrate using LiTaO 3 crystal." *IEEE transactions on ultrasonics, ferroelectrics, and frequency control* 64.9 (2017): 1382-1389J. Clerk Maxwell, A Treatise on Electricity and Magnetism, 3rd ed., vol. 2. Oxford: Clarendon, 1892, pp.68–73.

[2] Kent CK, Ramakrishnan N, Kesuma HP. Advancements in one-port surface acoustic wave (SAW) resonators for sensing applications: A review. IEEE Sensors Journal. 2024 Apr 16;24(11):17337-52.

[3] Zhgoon SA, Shvetsov AS, Sakharov SA, Elmazria O. High-temperature SAW resonator sensors: Electrode design specifics. IEEE transactions on ultrasonics, ferroelectrics, and frequency control. 2018 Jan 23;65(4):657-64.

[4] Karapetyan GY, Kaydashev VE, Kalinin VA. SAW resonators for temperature control of high-voltage equipment. Sensors and Actuators A: Physical. 2025 Oct 1; 392:116679.

[5] Fang X, Zheng P, Zhang S, Zhao J, Sun M, He J, Lin D, Ke X, Yao H, Xu Q, Ou X. Hybrid Integration of Dual-Mode SAW Resonators for High-Power and Wideband High-Frequency Filters. IEEE Transactions on Microwave Theory and Techniques. 2025 Aug 19.

[6] Awad M, Workie TB, Bao JF, Hashimoto KY. Reem-shape phononic crystal for Q anchor enhancement of thin-film-piezoelectric-on-Si MEMS resonator. Micromachines. 2023 Jul 31;14(8):1540.

[7] Wang Y, Wu SM, Yu SY, Wu Y, Hao X, Chen YF. Phononic crystals for Love waves based on thin-film lithium niobate. Journal of Physics D: Applied Physics. 2023 Nov 23;56(47):475103

[8] Awad M, Workie TB, Bao JF, Hashimoto KY. Three-channel acoustic wave filter in a phononic crystal-based slab. Microsystem Technologies. 2026 Jan;32(1):1.

[9] He YH, Qin ZH, Chen HY, Yu NX, Wang ZW, Yu SY, Chen YF. GHz Love-mode TF-SAW phononic crystals based on LiNbO3-on-SiC substrate. Applied Physics Letters. 2025 Apr 21;126(16).

[10] Xi Z, Thomas JG, Ji J, Wang D, Cen Z, Kravchenko II, Srijanto BR, Yao Y, Zhu Y, Shao L. Low-phase-noise surface-acoustic-wave oscillator using an edge mode of a phononic band gap. Physical Review Applied. 2025 Feb 1;23(2):024054.

[11] Bao J, Workie TB, Awad M, Yang Z, Hashimoto KY. 2P3-7 Analysis of Nano-Well Phononic Crystal on Si3N4/X-cut LiNbO3/SiC Heterostructure. In Proceedings of Symposium on Ultrasonic Electronics 2025 Nov 12 (Vol. 46, p. 112). Institute for Ultrasonic Electronics.

[12] Tang P, Pan H, Workie TB, Mi J, Bao J, Hashimoto KY. Honeycomb-shaped phononic crystals on 42° YX LiTaO3/SiO2/poly-Si/Si substrate for improved performance and miniaturization. Micromachines. 2024 Oct 14;15(10):1256.

[13] Awad M, Workie TB, Natalia K, Bao JF, Hashimoto KY. Enhancement of the quality factor of thin-film-piezoelectric-on-Si MEMS resonator using BOX shape phononic crystal. International Journal of Mechanics and Materials in Design. 2025 Jun 9:1-6.

High-Efficiency Broadband S-Shaped Thin-Film Lithium Niobate Electro-Optic Modulator

Xupeng Gu, Yafei Wu
IEEE IMWS-AMP 2026
University Of Electronic Science And Technology Of China, Chengdu, Sichuan, China
Email:17340152591@163.com

***Abstract*—In this work, we propose and demonstrate an S-shaped Mach-Zehnder modulator (MZM) on a silicon substrate. As global data traffic demands surge, thin-film lithium niobate on silicon has emerged as a premier platform due to its high electro-optic coefficient and seamless integration with CMOS-compatible processes. However, conventional straight-path traveling-wave electrodes are often limited by severe conductor losses and velocity mismatch at millimeter-wave frequencies. By utilizing an innovative S-shaped topological layout, we effectively mitigate microwave transmission loss by alleviating high-frequency current crowding at the electrode edges. This geometry also provides the added benefit of increasing the optical group index, thereby enhancing both velocity matching and modulation efficiency. We fabricated a prototype with a 5 mm interaction length, and experimental results—which align well with numerical simulations—show a 1 dB reduction in electrode loss compared to traditional straight-path designs of the same length. Consequently, the device achieves a record EO bandwidth exceeding 110 GHz. This silicon-based S-shaped MZM offers a high-performance and scalable solution for the next generation of ultra-broadband photonic integrated circuits.**

***Index Terms*—Mach-Zehnder modulator(MZM), thin-film lithium niobate (TFLN), S-shaped EO modulator, broadband**

I. Introduction

With the rapid expansion of global data communication, ultra-high-speed and energy-efficient electro-optic (EO) modulators have become fundamental building blocks for next-generation optical networks[1]. Thin-film lithium niobate on silicon platforms represent a promising frontier, combining the excellent Pockels effect of lithium niobate with the superior thermal dissipation and monolithic integration capabilities of silicon photonics[2]. Currently, traveling-wave electrode Mach-Zehnder modulators are preferred for high-fidelity signal transmission due to their superior linearity and bandwidth compared to resonant or lumped-electrode structures. However, conventional straight-path coplanar waveguide electrodes on silicon often face significant frequency-dependent conductor losses and velocity mismatch in the millimeter-wave regime, which severely limits the effective modulation bandwidth.

To address these challenges, we demonstrate an innovative S-shaped TFLN MZM featuring a periodic topological layout. This design effectively mitigates electrode transmission loss by alleviating high-frequency current crowding while simultaneously enabling precise engineering of the microwave phase velocity to match the optical group index. Experimental results for a 5 mm prototype achieve a 1 dB reduction in microwave loss and an EO bandwidth exceeding 110 GHz. This architecture provides a high-performance, scalable solution for future ultra-broadband photonic integrated circuits by successfully balancing modulation efficiency with extreme high-frequency performance.

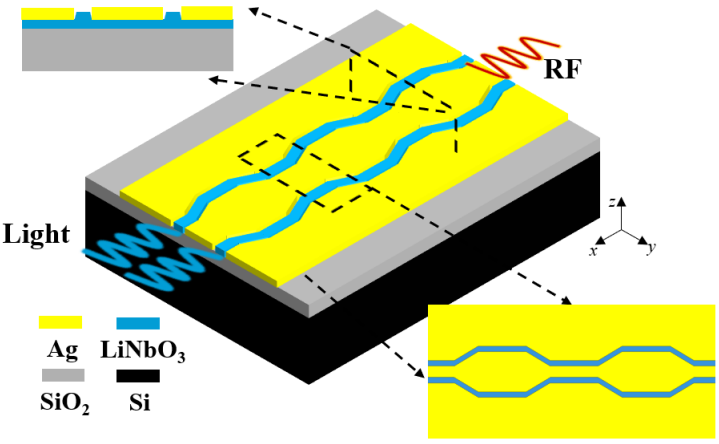


Fig. 1. Schematic diagram of the S-shaped electro-optic modulator.

II. Modulator Design

According to the theoretical formula for electro-optic (EO) bandwidth[3], the frequency response of the modulator is primarily governed by the microwave attenuation coefficient (alpha) and the mismatch between the microwave effective refractive index (n_e) and the optical group index (n_g).

$$m(f) = 20\lg\left(e^{-\frac{\alpha l}{2}}\left[\frac{\sinh^2\left(\frac{\alpha l}{2}\right)+\sin^2\left(\frac{\pi f(n_e-n_g)l}{c}\right)}{\left(\frac{\alpha l}{2}\right)^2+\left(\frac{\pi f(n_e-n_g)l}{c}\right)^2}\right]^{1/2}\right) \quad (1)$$

A detailed analysis reveals that microwave loss and electro-optic velocity matching are the two pivotal factors determining the upper limit of the EO bandwidth. In the high-frequency regime, particularly at millimeter-wave frequencies, conductor losses in the metal electrodes cause a significant attenuation of the microwave voltage along the transmission line[4], directly limiting the effective EO interaction length. Simultaneously,

velocity mismatch induces an accumulative phase shift between the microwave signal and the optical carrier as they propagate, leading to a rapid roll-off in the EO response[5]. Consequently, the subsequent design and optimization in this work are focused specifically on these two critical physical dimensions, aiming to achieve reduced microwave loss and precise velocity matching through the proposed S-shaped topological configuration.

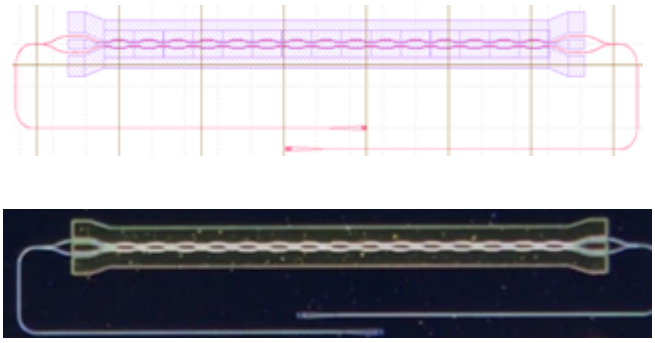


Fig. 2. Photograph of the S-shaped modulator.

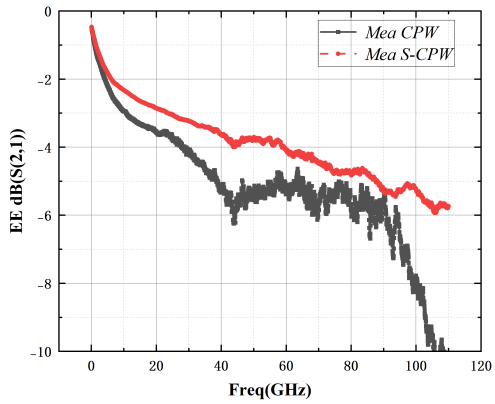


Fig. 3. Measured comparison of transmission loss between S-shaped and conventional CPWs.

III. Simulation and Measured Results

Figures [3-6] provide a comparative analysis of the microwave attenuation, effective refractive index, and electro-optic (EO) response for both the conventional and S-shaped CPW configurations.

The experimental results demonstrate that the S-shaped configuration significantly suppresses high-frequency roll-off, outperforming traditional straight-path designs. By successfully balancing microwave loss mitigation with precise velocity matching, the modulator achieves an ultra-broad EO bandwidth of 110 GHz on a silicon substrate. This performance enhancement confirms that the S-shaped topological layout is a highly effective solution for overcoming the bandwidth bottlenecks inherent in standard thin-film lithium niobate (TFLN) modulators.

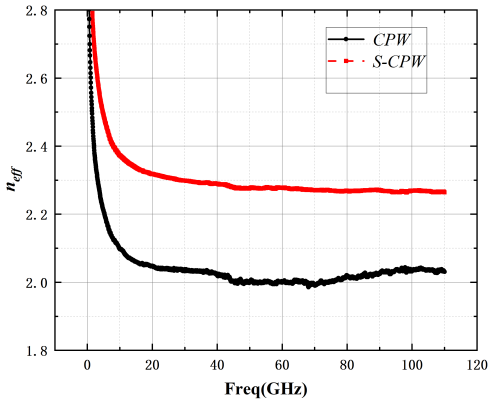


Fig. 4. Measured comparison of effective refractive index between S-shaped and conventional CPWs.

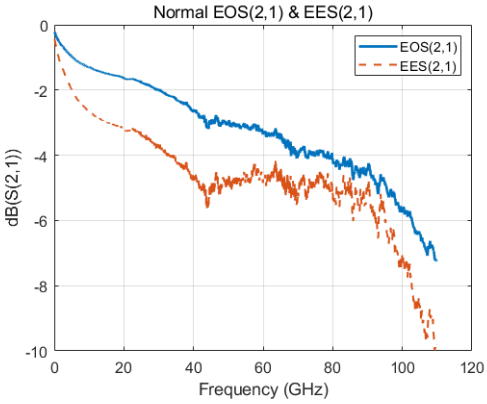


Fig. 5. Measured EOS_{21} of normal CPW.

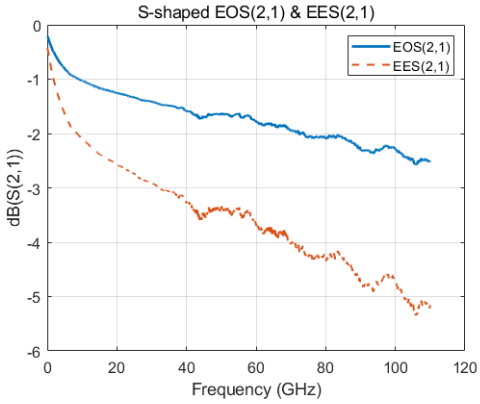


Fig. 6. Measured EOS_{21} of S-shaped CPW.

Conclusion

We demonstrate an S-shaped traveling-wave MZM on an TFLN platform. By leveraging periodic electrode topology, we achieved a 1 dB reduction in microwave loss and precise velocity matching over a 5 mm interaction length. Experimental results confirm an EO bandwidth exceeding 110 GHz, offering a high-performance and scalable solution for next-generation ultra-broadband photonic systems.

Acknowledgment

This work is supported in part by National Key Research and Development Plan of China under grant 2024YFB2807400, in part by the Xiaomi Young Scholar Program, and in part by Sichuan Province Engineering Research Center for Broadband Microwave Circuit High Density Integration.

References

[1] C. Wang, M. Zhang, B. Stern, M. Lipson, and M. Lončar, "Nanophotonic lithium niobate electro-optic modulators," Opt. Express, vol. 26, no. 2, p. 1547, Jan. 2018.

[2] P. Kharel, C. Reimer, K. Luke, L. He, and M. Zhang, "Breaking voltage–bandwidth limits in integrated lithium niobate modulators using micro-structured electrodes," Optica, vol. 8, no. 3, p. 357, Mar. 2021.

[3] M. Koshiba, Y. Tsuji, and M. Nishio, "Finite-element modeling of broad-band traveling-wave optical modulators," IEEE Trans. Microwave Theory Techn., vol. 47, no. 9, pp. 1627–1633, Sep. 1999.

[4] H. Liu et al., "Ultrahigh-Efficiency Dual-Band Thin-Film Lithium Niobate Modulator Incorporating Low-k Underfill for 390 Gbit s^{-1} PAM8 Transmission," Laser Photonics Rev, vol. 19, no. 14, p. 2402053, Jul. 2025.

[5] G. Chen et al., "Ultra-Compact and Ultra-High Speed Topological Photonic Crystal Modulator Based on Thin Film Lithium Niobate," Laser Photonics Rev, p. e00380, Aug. 2025.

Characterisation of Dynamic Particulate Media Using Broadband FMCW Spectrometry

James Elgy*, Stephan Reschke†, Edward Hoare*, Marina Gashinova*, and Fatemeh Norouzian*
*Electronic, Electrical and Systems Engineering, University of Birmingham, Birmingham, UK
†Toptica Photonics SE, Graefelfing, Germany
Email:j.elgy@bham.ac.uk

***Abstract*—There is a growing interest in spectrometer-based techniques to measure and characterise particulate media across diverse fields, including medicine, environmental monitoring, and manufacturing. Spectrometers provide broadband measurements in a non-destructive manner, potentially enabling the extraction of rich spectral information that can enhance the characterisation of the medium. In this paper, we present a new dataset of transmission measurements through dynamic dust clouds acquired using an optoelectronic frequency-modulated continuous-wave (FMCW) spectrometer. The experimental results demonstrate that simultaneous broadband magnitude and phase measurements enable the estimation of the effective refractive index of the particulate air–dust mixture. These findings highlight the potential of FMCW spectrometry for quantitative characterisation of dynamic mediums.**

***Index Terms*—Spectroscopy, dynamical systems, THz sensing, Airborne Particulates**

I. Introduction

Broadband terahertz (THz) spectroscopy offers significant potential in both scientific research and in industrial applications, particularly in material testing and development, see [1], [2] for examples. Typically, THz spectroscopy is performed either in frequency-domain (FDS) or, more commonly, time-domain (TDS). While both approaches offer broadband capability with good frequency resolution, FDS offers a finer frequency resolution, at the expense of a longer sweep time [3]. However, recent developments on an optoelectronic FDS system, as described by Liebermeister *et. al.* [3], has reduced minutes long sweep times to millisecond for a 4 THz bandwidth with their "T-Sweeper" system [3], [4].

Unlike prior TDS approaches which encase the particles in a resin or polymer matrix (e.g. [1], [5]), in this paper, we consider a free flowing stream of particles, which we model as a linear combination of air and dust. We present a unique dataset of THz transmission measurements using this T-Sweeper system and an initial analysis of the measurements to obtain the effective complex refractive index of the medium.

II. Methodology

We consider the measurement topology shown in Fig. 1 where two opposing antennas are separated by distance d to create a THz characterisation channel for particles to fall through. The medium is considered to be a homogeneous air-dust mixture, with the volume fraction of dust, v, defined as the ratio between the volume of dust and volume of air, influencing the effective refractive index of the medium.

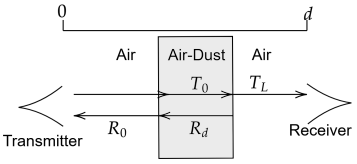


Fig. 1. Transmission measurement topology for propagation through a air-dust mixture of thickness d.

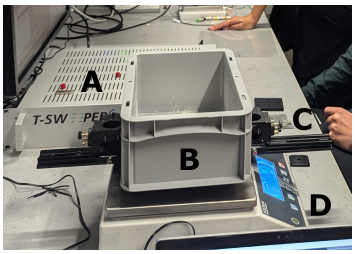


Fig. 2. Photograph of the measurement setup showing: A) the T-Sweeper, B) the polypropylene container, C) the linear guide rail, and D) the weighing scales

A. Measurement Setup

The T-Sweeper used in this paper operates analogous to a frequency modulated continuous wave (FMCW) system by leveraging the interference pattern generated by two offset C-band semiconductor lasers with frequency variation achieved by sweeping one of the laser sources. A THz beat frequency is generated with a 3 dB coupler which is then amplified and emitted using a PIN photodiode. Amplitude and phase are measured using a novel dual arm design where an additional 3 dB coupler splits the outgoing signal into a transmitted signal and a reference [3], [4]. The received wave is then mixed with the reference beat signal to produce a current in the receiver. The phase and amplitude of the transmitted signal are preserved by the mixing process [3] and can be recovered.

The measurements in this paper are conducted using a bandwidth of 4.4 THz with 1 GHz frequency resolution. The measurement topology is shown in Fig. 2 where the antennas are attached to a linear rail separated by 29 cm.

Dust is dispensed above the T-Sweeper system at varying speeds to generate different dust volume concentrations within the beam path. The particles are collected in a polypropylene container positioned on a Kern & Sohn FCB 6K-5 precision bench scale, which provides the ground-truth measurement of the accumulated dust mass with a resolution of 0.05 g at 50

979-8-3315-4544-4/26/$31.00 ©2026 IEEE

ms sample intervals. v is estimated from the measured dust mass accumulation using linear regression of the temporal mass data, yielding coefficients of determination >0.89 across all flow conditions. The resulting flow rates are combined with the known mineral density and particle size distribution of the dust sample [6] to estimate the particle concentration within the sensing region. Assuming approximately spherical particles, the total particle volume during the ~ 0.1 s sweep interval is calculated from the inferred particle number and size distribution, from which v is determined.

Based on visual observations during the measurements, the particles fall in a column volume of [100, 50, 150] mm^3. The particle cloud densities are calculated as ρ =183.9, 237.2, 303.2, 327.3, 342.2, 465.2, and 695.2 g/m^3. These densities correspond to $v = 6.8\times10^{-5}$, 8.7×10^{-5}, 1.1×10^{-4}, 1.2×10^{-4}, 1.3×10^{-4}, 1.7×10^{-4}, and 2.6×10^{-4}, respectively, for each flow rate. It should be noted that uncertainty in both the sweep time and column volume may contribute to errors in the calculated particle volume fractions.

B. Parameter Retrieval Methodology

In this section, the methodology employed to extract the effective refractive index, n_{eff}, is described. We use a phase difference approach by considering sample and reference signals using a propagation model for a homogeneous slab of thickness d: $S = |S|\cdot\exp(\mathrm{j}2\pi m f d/c) = |S|\cdot\exp(\mathrm{j}\phi)$ where $m = n+\mathrm{j}k$ is the complex refractive index, f is frequency and c is the free space speed of light. To compute the refractive index, a phase difference between the dust sample signal S (with phase ϕ) and the no dust reference signal S_{ref} (with phase ϕ_{ref}) is calculated. The real and imaginary refractive index is then related to the unwrapped phase difference [7] and the transmissivity by

$$n = \frac{c(\phi-\phi_{ref})}{2\pi f d} + n_{air}, \tag{1}$$

$$k = -\ln\left(\frac{|S|}{|S_{ref}|}\right)\frac{c}{2\pi f d}, \tag{2}$$

since $|\exp(\mathrm{j}\,\mathrm{Re}(\phi))| = 1$ and reference corresponds to propagation through air with a refractive index $n_{air} = 1.0003$. The calculated average particle separation is much bigger than the wavelength; hence multi-reflection between particles is considered negligible. The benefit of this approach is that since (1) is independent of power, it may operate in scenarios with high attenuation or where there is little difference in received power between samples.

In our measurements d is known approximately from the physical separation of the antennas. To compensate for uncertainty in the antenna phase centres we observe that $\phi_{ref} = 2\pi f n_{air} d/c$. Therefore the true antenna separation can be approximated by

$$d \approx \mathrm{mean}\left(\frac{\phi_{ref} c}{2\pi f n_{air}}\right). \tag{3}$$

Finally, since the true dust refractive index n_{dust} is independent of density, a linear effective medium approximation,

$$n_{eff} = (1-v)n_{air} + v n_{dust}, \tag{4}$$

is used to relate n_{eff} and volume fraction v for each measurement. Since $v \ll 1$ for our measurements, we cannot reasonably extract v or n_{dust} directly from measurements of n_{eff} without prior knowledge of the material. However, such an assumption would not be unreasonable in certain applications, e.g. medicine production. Assuming that a calibration measurement is performed with a known volume fraction v_0 such that an associated effective refractive index, $n_{eff,0}$, is also known, then the volume fraction for any subsequent measurements is estimated as

$$v = v_0\frac{(n_{eff}-n_{air})}{(n_{eff,0}-n_{air})}. \tag{5}$$

III. Results and Discussion

For all measurements, the signal becomes noise dominated above 2.2 THz; therefore the data processing is restricted to $f < 2.2$ THz. The measured power spectra $P(S)$ for the background (no dust) and for varying dust concentrations is shown in Fig. 3. The first observation is prominent water absorption peaks are observed at a number of frequencies along with variation in the received power due to changes in the density of dust, highlighted in Fig. 3b.

Due to the very small changes in amplitude, differentiating between densities based solely on power is limited and may require averaging over multiple frequencies. Instead the phase is examined, as detailed in Section II-B, where a greater sensitivity to the number of particles with respect to the reference measurement is expected. The analysis showed strong water absorption lines introduce rapid phase variations that can cause apparent 2π phase wraps, leading to jump discontinuities in the unwrapped phase. A correction is applied by excluding data for $f < 50$ GHz, and shifting the jumps to a linear fit. In addition, since the phase difference at $f = 50$ GHz is approximately zero for an air-dust mix, we shift the phase difference accordingly. This corrected phase is shown in Fig. 4 where a noticeable change in phase with respect to the reference is observed between the different densities, supporting the notion that there is an increased refractive index, indicating a greater volume fraction of dust in the medium.

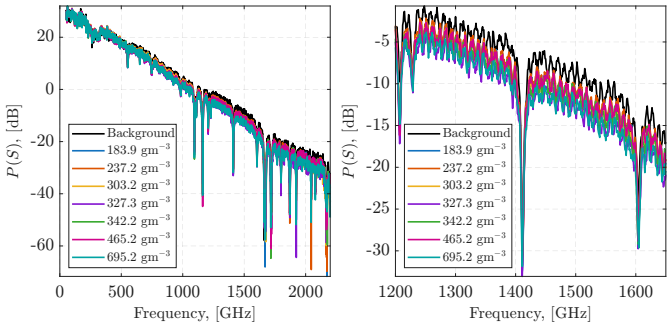


Fig. 3. Power spectrum for (a) full bandwidth and (b) cropped at $1.2 \leq f \leq 1.65$ THz.

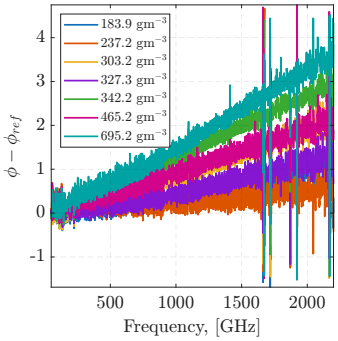


Fig. 4. Phase difference for the corrected phases.

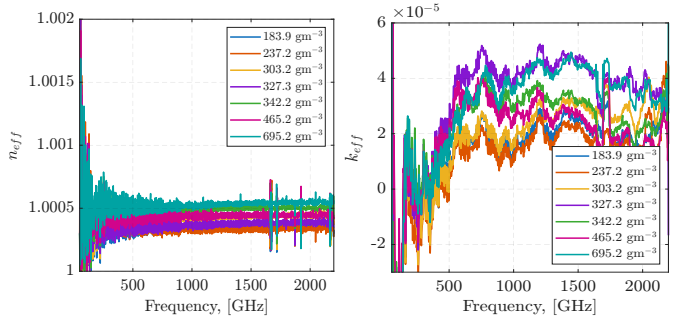


Fig. 5. (a) real and (b) imaginary components of the effective refractive index.

Using (1) and (2), the effective real and imaginary components of the refractive index are shown in Fig. 5. The imaginary, k_{eff}, component is highly oscillatory, therefore, to aid interpretation, a 50 point moving average is applied. From the figure, we see that the dust is non-dispersive, which is expected at these frequencies [8], and a small increase in both n_{eff} and k_{eff} as the quantity of dust increases.

From (4), a linear relationship between the n_{eff} and v, and by extension the density, is expected. To illustrate this relationship, the mean n_{eff} for each measurement is plotted in Fig. 6, where a linear trend is observed.

Finally, as noted earlier, it is not possible to convert from n_{eff} to v without additional information about the material. For our initial tests, we have assumed one known combination of v and n_{eff}, corresponding to $v_0 = 1.1 \times 10^{-4}$ and $n_{eff,0} = 1.00044$ for the measurement at $\rho = 303.2$ g/m^3. We substitute this value, along with the mean refractive index for each measurement, into (5) to obtain an estimate of the volume fraction directly from measurements. A comparison between the known volume fractions and the estimated values is shown in Fig. 6b, where a slight underestimation of v is observed, possibly because of a lightly skewed mean n_{eff}.

IV. Conclusion

The presented analysis details a data driven approach for retrieval of both the complex refractive index and the volume fraction of dust. To demonstrate this methodology, ultra-wideband THz transmission measurements were performed

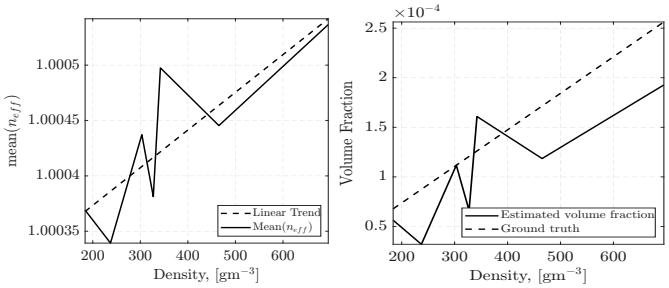


Fig. 6. (a) Mean n_{eff}, with a best fit trend defined by $n_{eff} = 3.8 \times 10^{-7}\rho + 1.0003$, and (b) the extracted v obtained using the mean n_{eff}.

for varying concentrations of a dust sample with known composition using an FMCW THz spectrometer.

A current limitation of the process is that prior knowledge is required for extrapolating other parameters of interest. For example, estimation of v in this study relies on pre-characterised material properties. Such assumptions are reasonable in controlled laboratory environments (e.g., pharmaceutical settings), where constituent properties are typically known a-priori.

Addressing this limitation requires the collection of a comprehensive particle-property library, which constitutes an important direction of our ongoing and future work. In addition, the current instrument configuration is transmission-based. The incorporation of reflection measurements and multi-polarimetric capabilities is expected to provide richer datasets for more independent medium characterisation.

V. Acknowledgements

This work has been supported by UK Research and Innovation (UKRI) under the project REPLENISH (10112182).

References

[1] P. Liu, X. Zhang, B. Pan, M. Wei, Z. Zhang, and P. B. Harrington, "Classification of sand grains by terahertz time-domain spectroscopy and chemometrics," *International Journal of Environmental Research*, vol. 13, no. 1, pp. 143–160, 2019.

[2] M. Zhai, A. Locquet, and D. S. Citrin, "Pulsed THz imaging for thickness characterization of plastic sheets," *NDT and E International*, vol. 116, no. July, pp. 1–12, 2020.

[3] L. Liebermeister, S. Nellen, R. B. Kohlhaas, S. Lauck, M. Deumer, S. Breuer, M. Schell, and B. Globisch, "Optoelectronic frequency-modulated continuous-wave terahertz spectroscopy with 4 THz bandwidth," *Nature Communications*, vol. 12, no. 1071, pp. 1–10, 2021.

[4] J. Kutz, L. Liebermeister, N. Vieweg, K. Wenzel, R. Kohlhaas, and M. Naftaly, "A terahertz fast-sweep optoelectronic frequency-domain spectrometer: Calibration, performance tests, and comparison with TDS and FDS," *Applied Sciences*, vol. 12, pp. 1–11, 2022.

[5] H. Huang, Z. Liu, M. T. Ruggiero, Z. Zheng, K. Qiu, and S. Li, "Terahertz Geoscience: THz Time-Domain Spectroscopy for Mineral Materials," *Crystal Growth and Design*, vol. 25, no. 10, pp. 3578–3594, 2025.

[6] J. Elms, A. Pawley, N. Bojdo, M. Jones, and R. Clarkson, "Formation of high-temperature minerals from an evaporite-rich dust in gas turbine engine ingestion tests," *Journal of Turbomachinery*, vol. 143, no. 6, pp. 1–9, 2021.

[7] P. U. Jepsen, "Phase retrieval in terahertz time-domain measurements: a "how to" Tutorial," *Journal of Infrared, Millimeter, and Terahertz Waves*, vol. 40, no. January, pp. 395–411, 2019.

[8] E. O. D. Group, "Aerosol refractive index archive." https://eodg.atm.ox.ac.uk/ARIA/data?Sand_and_Dust/Sand/Hematite_and_quartz_-_o-ray_(Longtin_et_al._1988)/sand_oray_longtin_1988.ri, 2012. Accessed: 2024-10-24.

From Language to Structure: Semantic-Guided Cross-Modal End-to-End Intelligent Design of High-Performance Metasurface Absorbers

1st Yihao Li
School of Microelectronics
Nanjing University of Science & Technology
Nanjing, China
avopears@outlook.com

2nd Shijie Wang
Dept. of Biomedical Engineering
National University of Singapore
Singapore, Singapore
e1499409@u.nus.edu

3rd Wen Lyu
School of Microelectronics
Nanjing University of Science & Technology
Nanjing, China
lyuwen@njust.edu.cn

4th Yanghui Wu
School of Microelectronics
Nanjing University of Science & Technology
Nanjing, China
YHWu@njust.edu.cn

5th HuanYu Yang
School of Automation
Nanjing University of Science and Technology
Nanjing, China
yhy@njust.edu.cn

***Abstract*—Metasurface inverse design usually relies on numerical targets and therefore cannot directly use natural-language requirements. The inverse mapping from spectra to structural parameters is also non-unique. To address these issues, we propose a semantics-guided cross-modal framework for intelligent design of high-performance metasurface absorbers. The framework combines vision-language alignment, forward surrogate modeling, and probabilistic inverse design in a unified pipeline built on a four-modal dataset. Specifically, we use a CLIP-based module for text-spectrum alignment, a spatially varying multi-channel attention Fourier neural operator for forward prediction, and a mixture density network for inverse design. The forward model achieves $R^2 = 0.9954$ on the test set and $R^2 = 0.9939$ on the validation set. The inverse model achieves MAE = 0.024855, RMSE = 0.046434, and $R^2 = 0.960359$, while the semantic alignment module reaches 88.24% Top-1 accuracy and 100.00% Top-5 accuracy.**

***Index Terms*—metasurface inverse design, vision-language alignment, Fourier neural operator, mixture density network, semantic-driven design**

I. Introduction

Metasurfaces are planar electromagnetic structures composed of subwavelength elements. By tuning the geometry and arrangement of these elements, one can control absorption, reflection, and phase response. Metasurface absorbers have therefore been used in radar cross-section reduction, electromagnetic compatibility, and wireless systems, where strong absorption and low profile are both required. Current design methods mainly rely on analytical models, full-wave parameter sweeps, or data-driven models [1], [2].

Each route has clear limitations. Analytical models often depend on simplifying assumptions and lose accuracy in strongly coupled structures. Full-wave optimization is accurate but computationally expensive. Data-driven methods reduce design time, but three issues remain. First, inverse design is inherently one-to-many [3]. Second, forward predictors often fail to resolve narrow resonances [4]. Third, many frameworks take only numerical targets and cannot directly use natural-language descriptions of absorber performance [5].

To address these issues, we propose a semantics-guided cross-modal end-to-end framework for intelligent design of high-performance metasurface absorbers, termed Semantics-Guided Cross-Modal End-to-End Intelligent Design (SGCM-ID). The framework uses a CLIP-based alignment module to connect language descriptions with spectral responses in a shared latent space, a spatially varying multi-channel attention Fourier neural operator for forward prediction, and a mixture density network for inverse design. We also introduce physics-based constraints to improve physical consistency and reduce ambiguity in the inverse solution space.

The main contributions are as follows. First, we develop a unified framework that links natural-language requirements, target spectra, and structural parameters for semantics-driven absorber design. Second, we introduce a spatially varying multi-channel attention Fourier neural operator to improve forward prediction for complex spectra. Third, we use a mixture density network to model the conditional distribution from spectra to structural parameters and capture the non-unique nature of inverse design. Fourth, we include physics-based constraints to improve the validity of the generated structures.

II. Methodology

A. Overall Framework

SGCM-ID links natural-language requirements, target spectra, and structural parameters in one pipeline. As shown in Fig. 1, it consists of semantic alignment, forward prediction, inverse design, and physics-based constraints.

979-8-3315-4544-4/26/$31.00 ©2026 IEEE

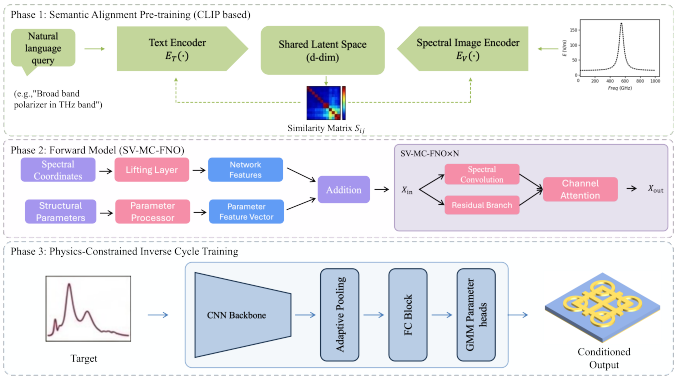


Fig. 1. Methodological roadmap of the proposed SGCM-ID framework.

B. Semantic Alignment

We use a CLIP-based module to align language targets with physical responses. A text encoder $E_T(\cdot)$ and a spectral-image encoder $E_V(\cdot)$ map paired descriptions and rendered spectra into a shared latent space.

The scaled cosine similarity is defined as

$$S_{ij} = \frac{z_v^i \cdot (z_t^j)^\top}{\tau}, \tag{1}$$

where τ is a learnable temperature parameter. The training loss is

$$L_{v\to t} = -\frac{1}{B}\sum_{i=1}^{B}\log\frac{\exp(S_{ii})}{\sum_{j=1}^{B}\exp(S_{ij})}, \tag{2}$$

$$L_{t\to v} = -\frac{1}{B}\sum_{i=1}^{B}\log\frac{\exp(S_{ii})}{\sum_{j=1}^{B}\exp(S_{ji})}, \tag{3}$$

$$L_{\text{align}} = \frac{1}{2}\left(L_{v\to t} + L_{t\to v}\right), \tag{4}$$

where B is the batch size. The learned representation is used in the downstream design stage.

C. Forward Modeling

The forward problem learns a surrogate operator $G_\theta : X \to Y$ that maps structural parameters $x \in X$ to spectra $y \in Y$. We use SV-MC-FNO for this task.

The backbone is an FNO. For the input function $v_l(x)$ at layer l, the update rule is

$$v_{l+1}(x) = \sigma\left(W v_l(x) + \mathcal{F}^{-1}\left(R \cdot \mathcal{F}(v_l)(k)\right)\right), \tag{5}$$

where $\mathcal{F}$ and $\mathcal{F}^{-1}$ denote the fast Fourier transform and its inverse, R is a learnable spectral weight matrix, W is a linear residual term, and σ is a nonlinear activation.

To better resolve narrow resonances, we add spatially varying channel attention after spectral convolution.

The network contains a lifting layer, four SV-MC-FNO blocks, and a projection layer. It is trained with a relative L_2 loss,

$$L_{\text{rel}} = \frac{1}{B}\sum_{i=1}^{B}\frac{\|\hat{y}_i - y_i\|_2}{\|y_i\|_2 + \epsilon}. \tag{6}$$

using Adam with a warmup cosine annealing schedule.

D. Inverse Design with MDN

The inverse mapping from a target spectrum $y \in Y$ to structural parameters $x \in X$ is non-unique. We therefore use an MDN for conditional density estimation.

The feature extractor is a 1D CNN with three convolutional layers, followed by adaptive average pooling and a fully connected block (hidden width $= 512$).

Instead of predicting a single vector x, the MDN outputs the parameters of a Gaussian mixture model for $p(x \mid y)$:

$$p(x \mid y) = \sum_{k=1}^{K}\pi_k(y)\,\mathcal{N}(x \mid \mu_k(y), \sigma_k(y)), \tag{7}$$

where $\pi_k(y)$, $\mu_k(y)$, and $\sigma_k(y)$ are the mixing coefficient, mean, and variance of the k-th component. We use $K = 32$.

The network is trained by minimizing the negative log-likelihood of the ground-truth parameters x_{gt}:

$$L_{\text{NLL}} = -\frac{1}{B}\sum_{i=1}^{B}\log\left(\sum_{k=1}^{K}\pi_k(y_i)\,\mathcal{N}(x_{\text{gt}}^{(i)} \mid \mu_k(y_i), \sigma_k(y_i))\right). \tag{8}$$

We also add an auxiliary term based on the highest-probability component. The final loss is

$$L_{\text{inv}} = L_{\text{NLL}} + \lambda L_{\text{aux}}. \tag{9}$$

This formulation yields multiple candidate structures for one target spectrum.

III. Dataset and Experimental Settings

A. Data Construction and Multimodal Representation

To support semantic-driven inverse design, we constructed a four-modal dataset. Each sample contains (1) geometric parameters, (2) numerical spectra from full-wave simulation, (3) rendered spectral images, and (4) semantic performance descriptions. Fig. 2 shows the data construction process.

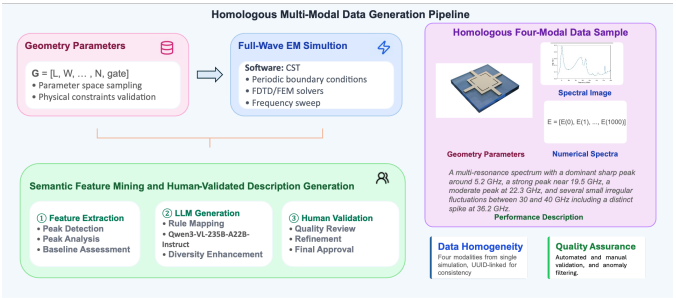


Fig. 2. Construction process of the multimodal dataset used for semantic-driven metasurface design.

The geometric parameters were sampled within a physically constrained design space. We then performed full-wave simulations in CST under periodic boundary conditions with an FDTD solver and frequency sweeping to obtain the corresponding spectra. Each response was stored as both a numerical vector for prediction tasks and a rendered image for vision-language alignment.

For the semantic modality, we extracted key spectral features, including peak position, peak shape, and baseline trend. Initial descriptions were generated by rule-based mapping and a large language model, then reviewed and revised manually. All four modalities were linked by a unified identifier to ensure consistent cross-modal pairing. We further applied automated inspection and manual checking to remove anomalous samples and low-quality annotations.

B. Experimental Settings

All models were implemented in PyTorch and trained on a single NVIDIA A100 GPU with 40 GB memory.

For the forward model, SV-MC-FNO, the channel width was 128, the depth was 4, and the number of Fourier modes was 48. Training used 1,200 epochs, a batch size of 32, Adam, an initial learning rate of 3.6×10^{-4}, and a weight decay of 1×10^{-5}.

For the inverse model, MDN, the feature extractor used three 1D convolutional layers with kernel sizes of 15, 11, and 7. The Gaussian mixture model used $K = 32$ components. Training used 600 epochs, a learning rate of 2×10^{-4}, and an auxiliary loss weight of $\lambda = 0.2$.

IV. Results and Discussion

The forward model achieved $R^2 = 0.9954$ on the test set and $R^2 = 0.9939$ on the validation set, which indicates accurate prediction of the mapping from geometric parameters to spectra. Visual comparison shows that the predicted curves agree well with the ground truth in global trend, resonance position, and peak amplitude, including samples with multiple resonances. The main errors appear near very narrow resonant peaks, where the response is highly sensitive to small parameter variations.

For inverse design, the MDN-based model achieved MAE = 0.024855, RMSE = 0.046434, and $R^2 = 0.960359$. These results show that the model can recover structural parameters from target spectra with good accuracy despite the one-to-many nature of the problem. In most cases, the reconstructed spectra remain close to the target responses, especially in the dominant resonances and overall profile. Representative results of the forward and inverse models are shown in Fig. 3.

For semantic alignment, the vision-language model achieved 88.24% Top-1 accuracy and 100.00% Top-5 accuracy. These results indicate that the model can retrieve the correct spectrum for most text queries and always place it within the top five candidates. This confirms effective alignment between natural-language descriptions and spectral responses.

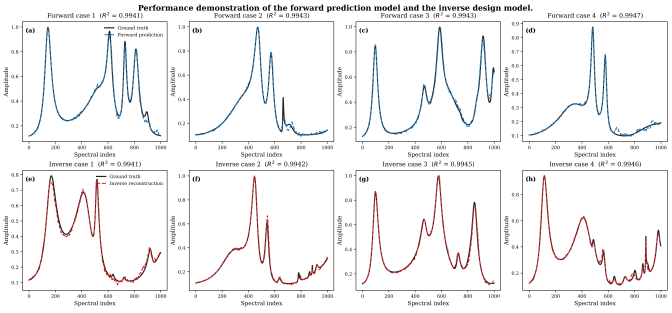


Fig. 3. Representative forward-prediction and inverse-design results.

Overall, the results support the proposed framework in three aspects: accurate forward prediction, reliable inverse reconstruction, and effective semantic alignment. Together, they show the feasibility of semantic-driven metasurface design.

V. Acknowledgment

We acknowledge funding by Key Technologies Research and Development Program (2023YFB3207800), Jiangsu Provincial Key Research and Development Program (No. BE2023818), the National Natural Science Foundation of China (Grant Nos.62271258, 62401261, 62404103), Basic Research Program of Jiangsu (Nos.BK20243046, BK20253062), Fundamental Research Funds for Central Universities (No. 30925010603), National Key Laboratory of Integrated Circuits and Microsystems (No: NICL2025KF2001).

References

[1] Y. Li, R. Chen, J. Sun, X. Deng, X. Li, Y. Xie, S. Wang, Z. You, C. Qin, and X. Zheng, "Deep-learning-driven design of multiplexed meta-array couplers for broadband hemt terahertz detection," *Photonics Research*, vol. 13, no. 5, pp. 1290–1301, 2025.

[2] Y. Li, Y. Zhai, J. Sun, S. Wang, H. Wang, X. Deng, X. Li, S. Wang, C. Lee, and X. Zheng, "Kan-empowered fano-resonant meta-array coupler for high-sensitivity terahertz detection in hemts," *Optics and Lasers in Engineering*, vol. 195, p. 109253, 2025.

[3] Q. Dai, Y. Wang, C. Xu, D. Li, P. Pitchappa, T. C. Tan, R. Singh, and C. Lee, "High-asymmetry metasurface: A new solution for terahertz resonance via active learning-augmented diffusion model," *Advanced Science*, vol. 13, no. 2, p. e08610, 2026.

[4] H. Chen, N. Li, Y. Zhao, H. Ou, Y. Wang, X. Jing, N. Zhang, Z. Su, and L. Huang, "Maximizing the chirality of bound states in the continuum by inverse design," *Photonics Research*, vol. 13, no. 8, pp. 2054–2064, 2025.

[5] Y. Yan, F. Li, J. Shen, M. Zhuang, Y. Gao, W. Chen, Y. Li, Z. Wu, Z. Dong, and J. Zhu, "Highly intelligent forward design of metamaterials empowered by circuit-physics-driven deep learning," *Laser & Photonics Reviews*, vol. 19, no. 5, p. 2400724, 2025.

Towards Fully Integrated Terahertz Frontends: Silicon Photonics Meets Resonant Tunneling Diodes

Weijie Gao, Nguyen H. Ngo, Daiki Ichikawa, Yuta Inose, and Masayuki Fujita
Graduate School of Engineering Science, The University of Osaka, Toyonaka, Japan

***Abstract*—The terahertz frequency band offers great potential for ultrahigh-speed wireless communications and high-resolution sensing in 6G and beyond systems. However, compact and scalable terahertz frontends are still limited by the lack of a unified integration platform that supports both low-loss propagation and efficient active devices. In this work, we present a photonic–electronic co-integration framework combining effective-medium silicon waveguides with resonant tunneling diodes. The platform enables low-loss, broadband propagation and compact nonlinear functionalities, including oscillation, detection, and phase control. Integrated transceivers and beam-steerable antennas at the 300-GHz band are demonstrated. This approach can be expected to promise fully integrated, reconfigurable terahertz frontends for next-generation communication and sensing systems.**

***Index Terms*—terahertz silicon photonics, resonant tunneling diodes, 6G communications**

I. Introduction

THE rapid evolution of wireless communications and sensing technologies has driven increasing interest in the terahertz frequency band. While individual terahertz components have demonstrated impressive performance, current systems still rely heavily on discrete implementations, including free-space optics, bulky packaging, and complex optical pumping schemes. These approaches fundamentally limit efficiency and system-level integration. At a fundamental level, these limitations stem from the lack of a unified integration platform that can simultaneously support low-loss signal propagation, efficient operation of active devices, and broadband system performance. Addressing these challenges requires a paradigm shift toward co-integrated platforms that combine photonic and electronic functionalities.

II. Methods

A. Silicon Effective-Medium Terahertz Platform

To address the propagation challenge, we establish a silicon-based terahertz integration platform based on effective-medium engineering [1]. By introducing deep-subwavelength perforations in high-resistivity silicon, the cladding is transformed into an anisotropic effective medium, enabling optical confinement through total internal reflection. This platform simultaneously achieves ultra-low loss, broadband operation, and reduced dispersion, providing a robust foundation for terahertz integration. By engineering the effective medium, this platform supports a wide range of passive functionalities, including filters, frequency-polarization multiplexers, hybrid couplers, phase shifters, and antennas, thereby enabling the systematic realization of complex terahertz integrated circuits.

This work was supported in part by JST CREST (No. JPMJCR21C4) and KAKENHI (24H00031).

B. RTD-based Active Device Integration

To enable active functionalities, we integrate resonant tunneling diodes (RTDs) into the silicon photonic platform. RTDs exploit quantum tunneling and exhibit negative differential conductance, enabling oscillation at terahertz frequencies as well as high-speed nonlinear response for mixing and detection [2]. In addition, it also enables efficient electronic terahertz phase tuning under injection locking condition. Unlike conventional approaches, the co-integration with silicon waveguides allows direct coupling between guided electromagnetic modes and RTD nonlinear dynamics, enabling efficient energy conversion within a compact footprint. This enables electrically driven terahertz oscillators, mixers, detectors, and phase shifters. The synergy between waveguide confinement and RTD nonlinear dynamics is critical for achieving efficient and scalable terahertz frontends. Building upon above fundamentals, we demonstrate two classes of RTD-enabled THz integrated devices operating at the 300-GHz band.

1) Terahertz transceiver: RTDs embedded within the waveguide core function as electrically driven sources or detectors. When integrated with 3D-printed lens antennas, they enable high-efficiency and broadband terahertz wireless transmission with a compact footprint.

2) Beam-steerable antennas: Phased-array architectures are realized by coupling RTDs to waveguide-fed antennas. Beam steering is achieved through bias control under injection locking of RTD array, enabling dynamic and electrically steerable radiation patterns.

These demonstrations highlight a transition from isolated devices to system-level integration, where signal generation, routing, and radiation are co-designed within a unified platform.

III. Conclusion

We have presented a unified approach to terahertz integrated devices based on silicon photonics and resonant tunneling diodes. By co-engineering electromagnetic propagation and nonlinear devices, the proposed method enables compact, efficient, and scalable terahertz frontends. The results highlight a transition from component-level innovation to architecture-level integration, paving the way toward practical and high-performance terahertz systems.

References

[1] W. Gao *et al.*, "Effective-medium-cladded dielectric waveguides for terahertz waves," *Optics Express*, vol. 27, no. 26, pp. 38 721–38 734, 2019.
[2] S. Suzuki *et al.*, "Fundamentals and recent advances of terahertz resonant tunneling diodes," *Applied Physics Express*, vol. 17, no. 7, p. 070101, 2024.

979-8-3315-4544-4/26/$31.00 ©2026 IEEE

2026 IMWS, Cairns, Australia
July 22-24, 2026

(invited talk)

Sources and Detectors for Space THz Communication Systems

Imran Mehdi
Jet Propulsion Laboratory, California Institute of Technology
Pasadena, CA 91109

Abstract:

THz applications have been increasing over the years. These applications include both space-based remote sensing as well as ground-based industrial applications such wireless communications. For communication systems, the THz frequency range is attractive as it provides larger bandwidth and smaller apertures. This talk will focus on the recent advancement in the development of room-temperature based wideband, compact sources and detectors in the THz range for space communication systems.

979-8-3315-4544-4/26/$31.00 ©2026 IEEE



Imran Mehdi (BSEE 1985, MSEE 1986 and Ph.D 1990, University of Michigan) is a Senior Research Scientist at the Jet Propulsion Laboratory, California Institute of Technology. He joined JPL in 1990 and is currently a Technical Group Supervisor leading research and development in submillimeter-wave/THz applications and instruments for space science. His responsibilities include developing THz components, technologies and subsystems for current and future NASA missions. These devices and components were implemented on the ozone-monitoring Microwave Limb Sounder (MLS) instrument which is still operational as well as the (Microwave Instrument on Rosetta Orbiter) MIRO instrument which represents the first submillimeter-wave receiver operational in deep-space. From 1999 he led the effort of developing broadband solid-state sources from 200 to 2500 GHz for the Heterodyne Instrument for Far Infrared (HIFI) on the Herschel Space Observatory, a cornerstone European Space Agency mission. He is an IEEE Fellow and served as the Editor in Chief for the IEEE Transactions on THz Science and Technology from 2019-2022. He is recipient of a number of NASA awards including the NASA Exceptional Technology Achievement Medal for developing advanced THz components and sub-systems. He currently leads the Submillimeter-Wave Advanced Technology group at JPL which is focused on developing space instruments for space exploration and discovery and have implemented complex instruments for airborne, balloon and space platforms. Dr. Mehdi has over 100 publications and is an elected member of the IEEE-Microwave Theory and Techniques Administrative Committee (AdCom, 2023-2028). He is the Chair of the Publication Committee of MTT-S overseeing the publication portfolio of the MTT-S. He also serves as a Senior Editor for IEEE Access as well as a board member for the Editorial Board of IEEE Access. His current interests include millimeter and submillimeter-wave devices and technology, nanotechnology, high-frequency space instrumentation, 3D Submm-wave systems, and development of compact, low-power heterodyne receiver arrays for deep-space missions.

High-Sensitivity Terahertz Sensing With Quadrature Self-Homodyne Detection

Bryce Chung, Nontiwat Amnuayphol, Harrison Lees, Withawat Withayachumnankul
Terahertz Engineering Laboratory, Adelaide University, Australia

Terahertz sensing is often cited as a transformative solution for non-destructive evaluation, offering millimeter-scale spatial resolution and unique see-through capabilities. Despite the availability of various photonic and electronic systems, significant challenges remain. Photonic-based systems are often hampered by inherent laser drift and phase noise, while electronic systems suffer from phase noise amplification through high-order frequency multiplier chains. These issues compromise sensitivity, which is typically improved through temporal averaging at the expense of measurement speed. Furthermore, high-performance components remain costly and delicate, whilst their limited output power often restricts the effective sensing range. Sensitivity can be dramatically enhanced by comparing the probe signal with a reference of the original carrier, a technique known as self-homodyning. In this presentation, we discuss two quadrature (I/Q) self-homodyne detection systems operating around 300 GHz, a strategic band for extended-range sensing due to minimal atmospheric absorption. One architecture utilizes I/Q interferometry, while the other employs I/Q mixing. Both systems achieve nanometer-scale vibration sensitivity with a theoretical measurement bandwidth reaching gigahertz rates. This detection scheme suppresses both external noise and source phase noise, enabling the use of high-power terahertz oscillators to further extend sensing range. We will demonstrate successful applications in acoustic eavesdropping, non-contact chip sensing, and vital-sign detection. assumption.

979-8-3315-4544-4/26/$31.00 ©2026 IEEE

Title:

Diverse Semiconductor Integrated Microelectronics in the Application-Oriented AI Era

Abstract:

Energy efficient materials, devices, technologies and systems will play a major role with the evolution of sensing and communication network architectures in the AI era. The progress in compound semiconductor devices combined with silicon technologies and 3D heterogeneous integration (3DHI) are defining the microelectronics future in the industry.

This talk will present the recent advancements in semiconductor and microelectronics integration technologies. The challenges and opportunities of the system-oriented compound semiconductor-based microelectronics in the Agentic AI era will also be discussed.

979-8-3315-4544-4/26/$31.00 ©2026 IEEE

Dr. Debabani Choudhury is the Founder and CEO of SeraTech-LLC, contributing to Technologies and system innovations spanning GHz to optical frequencies for the communication and sensing applications.
She led the strategy and vision for GHz to subTHz research and advancements for Intel systems and applications while serving as Senior Technologist and Research Director at Intel Research Labs.
She formerly developed technology for space, defense, and automotive applications at Hughes Research/HRL Labs, Millitech, and NASA Jet Propulsion Laboratories (JPL).
Dr. Choudhury is an IEEE Fellow with more than 150 patents and patent applications, as well as author of multiple publications. She received several Gordon Moore Awards from Intel for her outstanding research contributions. She also received several NASA recognition awards and is a recipient of the IEEE Solid State Society's JSSC Best Journal paper award.

Dr. Choudhury holds an elected ADCOM seat for IEEE MTT-Society. She chaired and served as member for several MTT-S ADCOM committees, plus four MTT-S technical committees (TCs). She served as the Chair of MTT-S Future Directions Committee and also currently Chairs the MTT-S Broadening Participation Committee (BPC). She is currently the member of IEEE TAB BP initiative. She guest-edited multiple IEEE journals, like T-MTT, Proceedings of IEEE. Dr. Choudhury sat on the IEEE 5G-Initiative Committee with ComSoc. She launched MTT-S and ComSoc teamwork for 5G Summits at IEEE IMS2017 as chair. She co-chaired TPCs for IEEE IMS2021 and RWS2013. She also co-chaired the IEEE 5G-World Forum TPCs in 2018 and 2019. She is the member of IEEE Antennas and Propagation AP-S technical committee and member of two IEEE TAB EIE committees also.

Millimeter-Wave and Sub-Terahertz Antenna and Metasurface Applications using Screen Printed Vanadium Dioxide Switches

Junghyeon Kim, Minjae Lee, Hyunwoo Koo, Duc Anh Pham, Eiyong Park, and Sungjoon Lim
School of Electrical and Electronics Engineering
Chung-Ang University, Seoul, 06974, Republic of Korea
E-mail: sungjoon@cau.ac.kr

Millimeter-wave (mm-wave) and sub-terahertz (sub-THz) frequencies are key technologies for future wireless systems such as 6G, enabling ultra-high data rates and massive connectivity. However, implementing reconfigurable RF components at these frequencies remains challenging because conventional semiconductor switches suffer from parasitic effects and performance degradation. Phase-change materials such as vanadium dioxide (VO_2) offer a promising alternative due to their reversible insulator–metal transition and large resistance change.

This work explores screen-printed VO_2 switches as a scalable platform for reconfigurable antenna and metasurface applications across microwave, mm-wave, and sub-THz frequencies.

First, a frequency-reconfigurable metasurface absorber is proposed using a large-area VO_2 layer integrated with a resistive metasurface pattern. Unlike conventional designs that require discrete RF components, the proposed structure achieves dynamic switching of absorption bands by modulating the sheet resistance of VO_2, demonstrating a simple and scalable approach for reconfigurable metasurfaces.

Second, a screen-printed VO_2-based intelligent reflective surface (IRS) operating at 100 GHz is demonstrated for sub-THz wireless communication. The IRS employs high phase-changing-ratio VO_2 switches to control the reflection phase and beam direction, enabling large-area beam steering while avoiding the parasitic limitations of conventional semiconductor switching devices.

Third, a VO_2-switched leaky-wave antenna operating in the V-band is presented to realize reconfigurable beam steering in mm-wave antenna systems. By switching the VO_2 elements between insulating and metallic states, the antenna dynamically alters its phase constant and radiation characteristics, enabling distinct beam-scanning behaviors within the operating band.

These three demonstrations collectively show that screen-printed VO_2 switches enable low-cost, large-area, and parasitic-free reconfigurable electromagnetic structures, highlighting their strong potential for adaptive antennas and metasurfaces in future mm-wave and sub-THz communication systems.

Acknowledgement
This research was supported by the National Research Foundation of Korea (NRF) grant funded by the Korea government (MSIT: Ministry of Science and ICT) (RS-2025-23323906, RS-2024-00396235).

979-8-3315-4544-4/26/$31.00 ©2026 IEEE

Meta-Screen: Full-Space EM Environment Reconfiguration for mmWave Communications

Jiatong Wu[1], Rui Pei[1], Zhao Wang[1], Jingchen Wang[1], Mark Leach[1], and Eng Gee Lim[1]
[1]School of Advanced Technology, Xi'an Jiaotong-Liverpool University, Jiangsu, China
Email: Zhao.Wang@xjtlu.edu.cn

***Abstract*—This paper presents the Meta-Screen, a novel reconfigurable indoor partition for full-space millimeter-wave environment control. Utilizing a highly integrated Rx-Gnd-Tx unit cell with only two PIN diodes, the proposed architecture achieves 1-bit phase quantization for both transmission and bi-directional reflection modes. Simulations show wide fractional bandwidths of 27.1%, 23.8%, and 8.3% for transmissive, +z-reflective, and -z-reflective modes, respectively, with a common operational bandwidth of 4.1%. System-level validation of a 14×14 array at 24 GHz confirms robust beam-scanning up to 60° and peak gains of 17.94 dBi. This design offers a low-complexity, high-efficiency solution for 360° coverage in future 6G smart radio environments.**

***Index Terms*—STAR-RIS, mmWave communication, reconfigurable intelligent surface, beam-scanning.**

I. Introduction

Millimeter-wave (mmWave) communications are vital for 6G networks but suffer from severe path loss and blockages. To address this, simultaneous transmitting and reflecting reconfigurable intelligent surfaces (STAR-RISs) [1], [2] have emerged to provide 360° omnidirectional coverage. We propose the "Meta-Screen" concept—an electromagnetic (EM) analogue to a physical room partition (or "screen" in interior design). Functioning as a reconfigurable EM divider, it bridges or isolates adjacent spaces via dynamic wavefront control on both sides. However, achieving independent dual-mode phase control with low hardware complexity remains a critical challenge for practical deployments.

STAR-RIS designs generally employ energy splitting or mode switching. While mode switching [3] yields higher gain by focusing power in a single direction, existing architectures often require numerous PIN diodes for phase and mode reconfiguration [4], [5]. Although simplified structures [6] or multi-layer designs [7], [8] have been explored, they are typically limited to single-side manipulation, suffer from unintended polarization rotation, or lack beam-scanning capabilities [9]. A low-complexity solution enabling independent, bi-directional, and full-space beam manipulation is highly desired.

To address these limitations, this article presents the Meta-Screen: a full-space reconfigurable metasurface with minimal hardware overhead. Utilizing a multi-layer Rx-Gnd-Tx topology and exactly two PIN diodes per cell, the proposed structure achieves a 180° phase difference for both full-transmission and bi-directional reflection modes (supporting incidence from both $+z$ and $-z$ directions) without additional lumped elements. Full-wave simulations of a 14×14 array at 24 GHz validate its robust beam-scanning performance across all operational modes. The design achieves a common operational bandwidth of 4.1% (23.3–24.3 GHz) for integrated full-space functionality, providing a low-complexity and high-efficiency solution for constructing smart radio environments.

The research is sponsored by XJTLU Research Development Fund under Grant RDF-24-01-079.

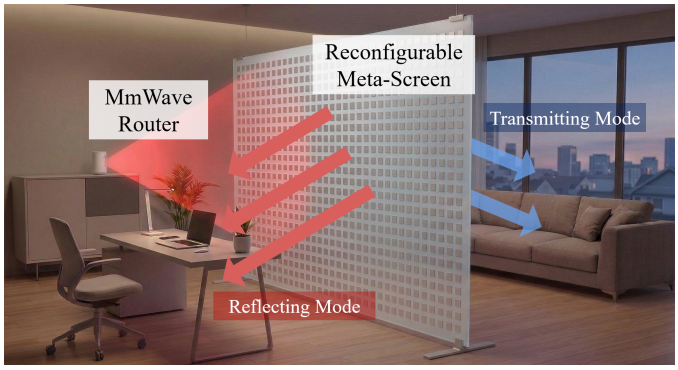


Fig. 1: Conceptual illustration of the proposed Meta-Screen for full-space EM environment reconfiguration.

II. Unit Cell Design

A. Topology of the unit cell

The proposed unit cell consists of 3 dielectric substrates and four metal layers, and the total thickness is about 2.1 mm ($0.168\lambda_0$ at 24 GHz) as demonstrated in Fig.2. The periodicity of the unit cell is 5.5 mm ($0.44\lambda_0$). The top and bottom layers are lightweight foams with a dielectric constant (ε_r) of 1.2 and extremely low loss tangent ($\tan\delta$) of 0.001. The middle prepreg is a thin PTFE film ($\varepsilon_r \approx 3.2$) of 100 um thickness, which is commonly used in flexible printed circuit (FPC) fabrication.

The design of the proposed meta-screen unit is based on the Rx-Gnd-Tx structure. The top layer is a patch loaded with two MACOM-MA4GP907 PIN diodes. The equivalent circuit of the diodes is a 5.2 Ohm resistor and 0.05 nH inductor in series for the ON state, and a 0.02 pF capacitor and 0.05 nH inductor in series for the OFF state. The bottom layer is an open-ended ring resonator and is connected to the top layer through the center via. Also, there is a via connected to the prepreg for DC biasing. The parameters are optimized with the Generic Algorithm (GA) to achieve the maximum bandwidth, and the geometries are shown in Fig.3.

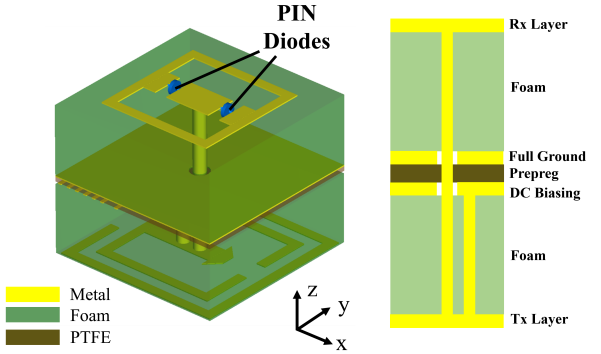
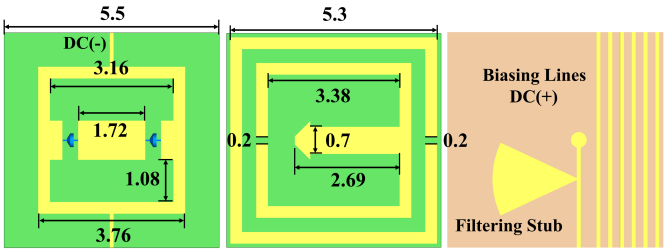


Fig. 2: Topology and side view of the proposed meta-screen unit.



(a) Rx Layer (b) Tx Layer (c) Prepreg

Fig. 3: Front view of the Rx layer, Tx layer and prepreg.

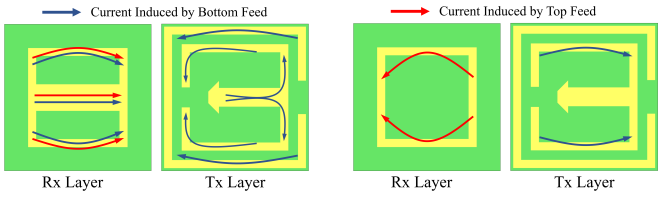
B. Operational Principle and Performance Analysis

The Meta-Screen unit cell's functionality is governed by four switching states, as defined in Table I. For $+z$-direction (top) incidence, the structure alternates between ring and patch resonance modes, yielding a stable 180° reflection phase shift. For $-z$-direction (bottom) incidence, State 1 utilizes the outer open ring for phase adjustment, while State 4 relies on inner ring resonance to generate the 1-bit phase difference. The surface current distributions in Fig. 4 illustrate these mechanisms. Notably, in transmission modes (States 2 and 3), switching the diodes induces anti-parallel current vectors, facilitating 1-bit phase quantization with near-unity magnitude.

TABLE I: Unit Cell Operational States

State	Diode 1	Diode 2	Mode	Phase (°)
1	ON	ON	Reflect	0
2	ON	OFF	Transmit	0
3	OFF	ON	Transmit	180
4	OFF	OFF	Reflect	180

Unit-cell simulation results with CST Studio Suite 2024 is shown in Fig. 5(a), the transmission mode achieves a 27.1% fractional bandwidth (FBW, 20.5–27 GHz) with a stable 180° phase response. For reflection, the structure maintains near-unity magnitude with $180\pm20^\circ$ phase difference across 23.3–29 GHz (23.8% FBW) under $+z$-illumination and 22.3–24.3 GHz (8.3% FBW) under $-z$-illumination.



(a) State 1 (b) State 4

Fig. 4: Surface current distributions on the equivalent Rx and Tx layers.

III. Full-Wave Validation of Meta-Screen

A. Coding Strategy Analysis

In light of reflect-array and transmit-array theory, the phase distribution across the metasurface must be synthesized to transform the incident spherical wavefront from the feed into a directional planar wave. For a configuration where the feed is positioned at a focal distance R from the array center, the required phase shift $\phi(m,n)$ at the $(m,n)^{th}$ element located at (x_m, y_n) to steer the beam toward the direction (θ, φ) is given by:

$$\begin{aligned}\phi(m,n) =& k\sqrt{x_m^2 + y_n^2 + R^2} \\ &- k(x_m \sin\theta\cos\varphi + y_n \sin\theta \sin\varphi) + \phi_0,\end{aligned} \tag{1}$$

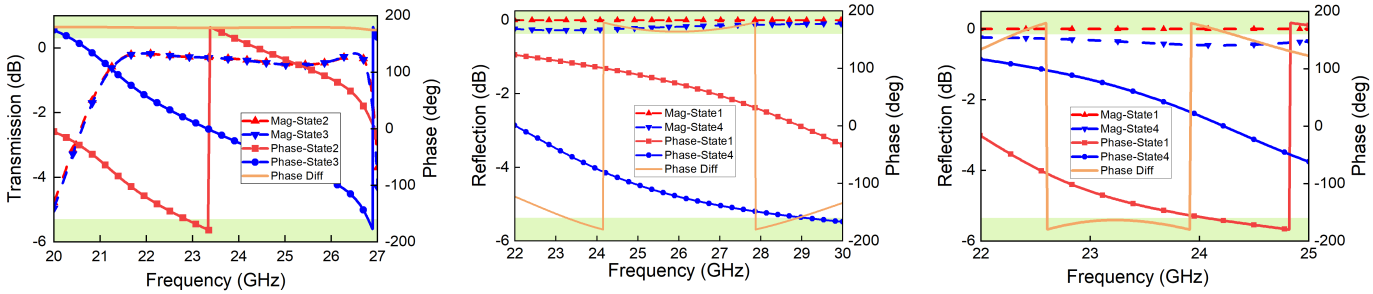
where k denotes the free-space wavenumber and ϕ_0 is an arbitrary constant phase offset. To realize a 1-bit digital coding metasurface, the continuous phase profile is subsequently quantized into binary states $\{0, \pi\}$. The optimal coding state for each element is determined by minimizing the local phase error, thereby ensuring an accurate wavefront reconstruction with suppressed quantization loss.

B. Beam Scanning Validation Simulation

The beam-steering performance of the 14×14 Meta-Screen was evaluated using a 24 GHz patch antenna feed positioned at a focal distance of 100 mm from the aperture. Optimal 1-bit coding patterns were synthesized according to (1). The system was characterized across three representative operational scenarios: transmissive mode, and bi-directional reflective modes under both $+z$- and $-z$-direction illumination (Figs. 6–8). Numerical results demonstrate robust beam-scanning coverage up to 60° for all modes at 24 GHz, with a maximum gain fluctuation of approximately 5 dB. Specifically, peak gains of 17.94 dBi, 16.91 dBi, and 17.84 dBi were achieved for the transmissive, $+z$-reflective, and $-z$-reflective modes, respectively. The observed gain variations are primarily attributed to 1-bit phase quantization loss and magnitude inconsistencies under oblique incidence.

IV. Conclusion

In conclusion, this article presents the design and validation of the Meta-Screen, a low-complexity reconfigurable metasurface tailored for full-space mmWave beam manipulation. By utilizing a multi-layer Rx-Gnd-Tx topology and optimizing



(a) Transmission (b) Top Reflection (+z) (c) Bottom Reflection (-z)

Fig. 5: Simulated S-parameters of the Meta-Screen unit cell showing magnitude and phase responses.

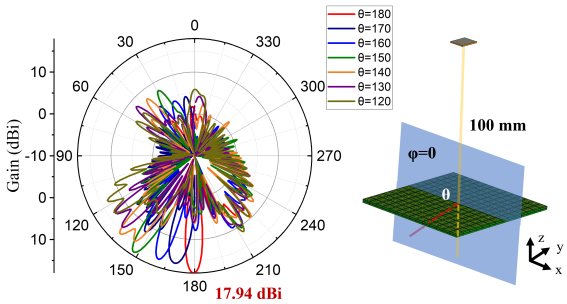


Fig. 6: Simulated transmissive beam-scanning radiation patterns under $+z$-direction illumination at 24 GHz.

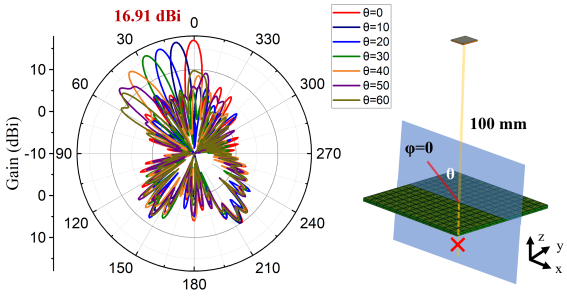


Fig. 7: Simulated reflective beam-scanning radiation patterns under $+z$-direction illumination at 24 GHz.

current paths with exactly two PIN diodes, we successfully achieved independent 1-bit phase control across all operational modes. The proposed unit cell exhibits wide fractional bandwidths of 27.1% for transmission, 23.8% for +z-direction reflection, 8.3% for -z-direction reflection, while maintaining a common operational bandwidth of 4.1% (23.3–24.3 GHz) for integrated full-space functionality. Full-wave simulations of a 14×14 Meta-Screen array at 24 GHz demonstrate robust beam-scanning performance up to 60° with a peak gain of 17.94 dBi and suppressed quantization loss. These characteristics, combined with minimal hardware overhead, position the Meta-Screen as a promising solution for overcoming blockages and constructing smart radio environments in next-generation wireless communication systems.

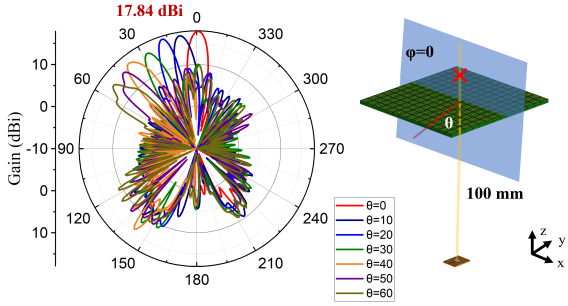


Fig. 8: Simulated reflective beam-scanning radiation patterns under $-z$-direction illumination at 24 GHz.

References

[1] M. Ahmed, A. Wahid, S. S. Laique, W. U. Khan, A. Ihsan, F. Xu, S. Chatzinotas, and Z. Han, "A Survey on STAR-RIS: Use Cases, Recent Advances, and Future Research Challenges," *IEEE Internet of Things Journal*, vol. 10, no. 16, pp. 14 689–14 711, Aug. 2023.

[2] X. Mu, Z. Wang, and Y. Liu, "Simultaneously Transmitting and Reflecting Surfaces (STARS) for Multi-Functional 6G," *IEEE Network*, vol. 39, no. 1, pp. 47–55, Jan. 2025.

[3] M. Wang, S. Xu, F. Yang, and M. Li, "A 1-Bit Bidirectional Reconfigurable Transmit-Reflect-Array Using a Single-Layer Slot Element With PIN Diodes," *IEEE Transactions on Antennas and Propagation*, vol. 67, no. 9, pp. 6205–6210, Sep. 2019.

[4] L. Bao, Q. Ma, R. Y. Wu, X. Fu, J. Wu, and T. J. Cui, "Programmable Reflection–Transmission Shared-Aperture Metasurface for Real-Time Control of Electromagnetic Waves in Full Space," *Advanced Science*, vol. 8, no. 15, p. 2100149, Aug. 2021.

[5] T. Yin, J. Ren, B. Zhang, P. Li, Y. Luan, and Y. Yin, "Reconfigurable Transmission-Reflection-Integrated Coding Metasurface for Full-Space Electromagnetic Wavefront Manipulation," *Advanced Optical Materials*, vol. 12, no. 2, p. 2301326, Jan. 2024.

[6] X. Cao, C. Deng, Y. Yin, Y. Hao, and K. Sarabandi, "1-Bit Reconfigurable Transmit- and Reflect-Array Antenna Using Patch-Ground-Patch Structure," *IEEE Antennas and Wireless Propagation Letters*, vol. 23, no. 1, pp. 434–438, Jan. 2024.

[7] H. Yu, P. Li, J. Su, Z. Li, S. Xu, and F. Yang, "Reconfigurable Bidirectional Beam-Steering Aperture With Transmitarray, Reflectarray, and Transmit-Reflect-Array Modes Switching," *IEEE Transactions on Antennas and Propagation*, vol. 71, no. 1, pp. 581–595, Jan. 2023.

[8] H. T. Shi, R. Y. Wu, L. Bao, and T. J. Cui, "Full-Space Programmable Metasurface for Controlling Both Reflected and Transmitted Waves Under the Same Polarization and in the Same Frequency Band," *Small*, vol. 21, no. 24, p. 2501218, Jun. 2025.

[9] F. Qin, J. Bi, J. Ma, C. Gu, H. Zhang, W. Cheng, and S. Gao, "A High-Efficiency Reconfigurable Bidirectional Array Antenna Based on Transmit–Reflect Switchable Metasurface," *IEEE Transactions on Antennas and Propagation*, vol. 73, no. 9, pp. 7051–7056, Sep. 2025.

A Low-Rate Digital Predistortion with Single Real Undersampling Feedback Using Switch-Estimated Method Excited by 400 MHz Sub-6 GHz Signals

Xiaoyu Lu
School of Information Science and Engineering
Southeast University
Nanjing, China
230239429@seu.edu.cn

Jianfeng Zhai
School of Information Science and Engineering
Southeast University
Nanjing, China
zhaijianfeng@seu.edu.cn

Zuofeng Zhang
ZTE Corporation
China
zhang.zuofeng@zte.com.cn

Dongfang Ning
ZTE Corporation
China
ning.dongfang@zte.com.cn

Yanru Cao
ZTE Corporation
China
cao.yanru30@zte.com.cn

PengChen
School of Information Science and Engineering
Southeast University
Nanjing, China
pchen@seu.edu.cn

Chao Yu*
School of Information Science and Engineering
Southeast University
Nanjing, China
chao.yu@seu.edu.cn

***Abstract*—This paper proposes a low-rate digital predistortion (DPD) technique. In this DPD technique, a switch-estimated method is applied to estimate the power amplifier (PA) output signal with low-complexity model extraction iteratively by a single real undersampling feedback signal. Furthermore, the band-limited DPD model is used to reduce the sampling rate of digital-to-analog converters (DACs). A 400 MHz 5G NR signal at the center frequency of 3.6 GHz is used to verify the proposed technique. The measurement results show that the proposed DPD technique can effectively reduce the hardware resources consumed during the model extraction process while maintain good linearization performance.**

Keywords—broadband, DAC/ADC, digital predistortion (DPD), power amplifier (PA)

I. INTRODUCTION

To meet the urgent demands of 5G/6G for high-speed data transmission, broadband signal transmission is gradually becoming an important support for modern communication systems [1]. Specifically, for Sub-6 GHz frequency spectrum, the modulated bandwidth is expected to be further increased, e.g. 400 MHz, makes it comparable with the one in millimeter wave (mmWave) band. The power amplifier (PA), as a core component in the communication system, whose nonlinearity and efficiency are contradictory, will face a huge challenge. Digital predistortion (DPD) technique is one of the most promising techniques to address that issue [2]. However, the new scenario to transmit 400 MHz bandwidth signal at Sub-6 GHz will face severe challenges, in which the sampling rates of digital-to-analog converters (DACs) and analog-to-digital converters (ADCs) of DPD usually require five times of the signal bandwidth [3], that is, 2 GSPS.

Some scholars have conducted research on reducing the sampling rates of DACs and ADCs in DPD systems [4], [5]. A DPD technique proposed in [6] has an ultra-low sampling rate of the ADCs in a feedback path. Based on [6], a direct-learning DPD scheme proposed in [7] can further save half of the hardware cost and avoid the problem of I/Q imbalance of the conventional Zero-IF feedback structure. However, PA has complex nonlinearity during such broadband transmission, which requires complex models and multiple iterations to achieve good linearization [8]. The modeling to estimate the feedback signal consumes large computing resources, and the error of the model itself is inevitable. In addition, very high sampling rates of DACs are still required to realize the linearization. For instance, a 400 MHz signal still requires 2 GSPS sampling rates of DACs. Therefore, it is urgent to propose a DPD technique to address the aforementioned problems encountered in broadband transmission.

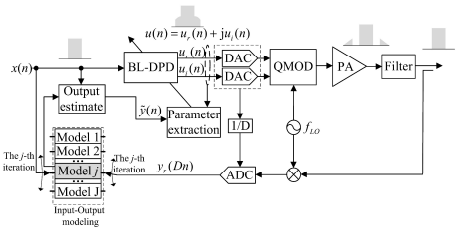


Fig. 1. The proposed DPD system.

This paper proposes a novel DPD technique for broadband signals, especially for transmitting 400 MHz 5G NR signals in a Sub-6 GHz GaN PA. This scheme adopts a switch-estimated method, which combines the baseband signals and the single real undersampling feedback signals to estimate the PA output signals through multiple iterations. In each iteration of estimation, the coefficients of model extraction are gradually reduced to significantly reduce the resource consumption. In addition, the band-limited DPD model based on Volterra series is employed to further reduce the sampling rate of DACs.

979-8-3315-4544-4/26/$31.00 ©2026 IEEE

II. Proposed Method

A. The Proposed DPD Technique

The structure of the proposed DPD system is shown in Fig. 1, which consists of a low-rate transmitter path and a low-rate feedback path. The baseband signal $x(n)$ is predistortion processed by a band-limited DPD model based on Volterra series. After passing through the transmitter path, it can obtain an amplified and linearized output signal. The single real undersampling feedback signals $y_r(Dn)$, which are $1/D$ sampling rates of the DACs, are collected by the feedback path. Then the PA output signals $\hat{y}(n)$ are estimated comparable to the sampling rate of the transmitter path by some iterations, in which the feedback signals and the baseband signals $x(n)$ are adopted to construct a model for the estimation. Finally, the parameters of a DPD model can be estimated by the PA output signals $\hat{y}(n)$ and the PA input signals $u(n)$.

B. The Switch-Estimated Method for Single Real Under-Sampling Feedback Signals

In [6], the high-rate estimated output signals are obtained by the PA modeling based on the input signals and the low-rate output signals of a PA. The error between the PA real output and the estimated output is ascribed to the errors of the model itself. Because the DPD model and the PA have opposite nonlinear characteristics, the cascade model of the DPD and the PA has a weaker nonlinear effect than the PA model. As shown in Fig.2, when the number of iterations increases, the nonlinearity of the PA output signals is gradually weakened. This paper proposes a switch-estimated method, which takes advantage of this feature and adopts the cascade model of DPD and PA to accurately estimate the output signal for better linearization.

In the switch-estimated method, different models from complex to simple are used in each iteration to estimate the PA output signal. When extracting the coefficients for the first time, this model is essentially the PA model without DPD, and the output signal estimation is carried out using the same parameters as the band-limited DPD model. When increasing the number of iterations, the nonlinearity of the DPD cascade PA model weakens, and therefore, a model with very few parameters can be adopted to estimate the output signals.

The process of estimating output signals is introduced below. In the j-th iteration, a Volterra series-based band-limited model j with few coefficients is selected. The band-limited basis function matrix $\mathbf{X}^{\boldsymbol{j}}$ of the model j can be constructed by the input signal $x(n)$. The estimated output of PA $\hat{y}^j(n)$ can be obtained by

$$\mathbf{X}^{\boldsymbol{j}} \cdot \mathbf{c}^j = \hat{y}^j(n) \tag{1}$$

where $\mathbf{c}^j$ is the coefficients matrix of the model j.

Equation (1) can be decomposed into the forms of real and imaginary parts, as shown in (2).

$$\begin{bmatrix} \mathbf{X}_r^j & -\mathbf{X}_i^j \\ \mathbf{X}_i^j & \mathbf{X}_r^j \end{bmatrix} \begin{bmatrix} c_r^j \\ c_i^j \end{bmatrix} = \begin{bmatrix} \hat{y}_r^j(n) \\ \hat{y}_i^j(n) \end{bmatrix} \tag{2}$$

where $\mathbf{X}_r^j$ and $\mathbf{X}_i^j$ are the real and imaginary parts of the band-limited basis function matrix $\mathbf{X}^{\boldsymbol{j}}$, respectively. c_r^j and c_i^j are the coefficients matrices of the real and imaginary parts of the model, respectively. $\hat{y}_r^j(n)$ and $\hat{y}_i^j(n)$ are the real and imaginary parts of estimated output of PA $\hat{y}^j(n)$, respectively.

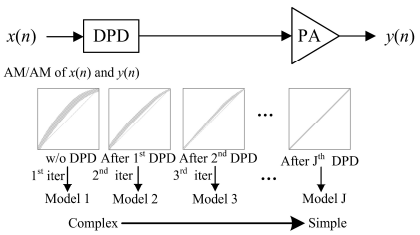


Fig. 2. The communication system tends to be linearized with continuous iterations.

Since the single real undersampling feedback signal $y_r^j(Dn)$ is known. Extracting some rows from the matrix in (2) and obtain (3),

$$\begin{bmatrix} \mathbf{X}_{l_r}^j & -\mathbf{X}_{l_i}^j \end{bmatrix} \begin{bmatrix} c_r^j \\ c_i^j \end{bmatrix} = \mathrm{Y}_{l_r} \tag{3}$$

where $\mathbf{X}_{l_r}^j$ and $\mathbf{X}_{l_i}^j$ are given in (4) and (5), and they are the real and imaginary parts of the low-rate band-limited basis function matrix $\mathbf{X}^{\boldsymbol{j}}$, respectively. As shown in (6), Y_{l_r} is the output matrix of the single real undersampling feedback signal $y_r^j(Dn)$.

$$\mathrm{X}_{l_r}^j = \begin{bmatrix} [\chi_1(0)]_r^j & \cdots & [\chi_K(0)]_r^j \\ [\chi_1(D)]_r^j & \cdots & [\chi_K(D)]_r^j \\ \vdots & \ddots & \vdots \\ [\chi_1(DN)]_r^j & \cdots & [\chi_K(DN)]_r^j \end{bmatrix} \tag{4}$$

$$\mathrm{X}_{l_i}^j = \begin{bmatrix} [\chi_1(0)]_i^j & \cdots & [\chi_K(0)]_i^j \\ [\chi_1(D)]_i^j & \cdots & [\chi_K(D)]_i^j \\ \vdots & \ddots & \vdots \\ [\chi_1(DN)]_i^j & \cdots & [\chi_K(DN)]_i^j \end{bmatrix} \tag{5}$$

where, χ_k is a basis function, and $k = 1,2,\cdots,K$.

$$\mathrm{Y}_{l_r} = [y_r(0), y_r(D), \cdots, y_r(DN)]^T \tag{6}$$

The least square (LS) algorithm can be used to estimate the model coefficients,

$$\begin{bmatrix} c_r^j \\ c_i^j \end{bmatrix} = \left(\mathbf{X}_l^{jT} \mathbf{X}_l^j\right)^{-1} \mathbf{X}_l^{jT} \mathrm{Y}_{l_r} \tag{7}$$

where $\mathbf{X}_l^j = \begin{bmatrix} \mathbf{X}_{l_r}^j & -\mathbf{X}_{l_i}^j \end{bmatrix}$.

Therefore, the complex coefficients of the model $\boldsymbol{c}^j$ can be obtained. And the estimated output $\hat{y}(n)$ can be calculated with using the coefficients $\boldsymbol{c}^j$ and the baseband signal $x(n)$.

III. Test Result

As shown in Fig. 3, the testbench was constructed to verify the proposed DPD technique. A 400 MHz 5G NR signal with 8.0 dB peaking average power ratio (PAPR) was generated in



Fig. 3. Testbench setup.

TABLE I. CONFIGURATION OF ESTIMATION MODEL FOR EACH TEST

Test	Input	Output	Type	Parameter settings*		
				Iterations	Parameters	Sum
Ref [6]	$u(n)$	$y(Dn)$	BL-GMP	j=1, …, 15	9,10,4,3	803
Proposed Method	$x(n)$	$y_r(Dn)$	BL-GMP	j=1, 2; j=3,4; j=5, …, 15	9,10,4,3 5,7,3,3 3,5,2,2	803 288 96

*The parameters in Table 1 are the order, the memory depth, the cross of lagging terms and the cross of leading terms of the band-limited GMP model.

TABLE II. TEST RESULTS

DPD Method	D	ADC (MSPS)	Type of feedback	NMSE* (dB)	ACPR* (dBc)
w/o DPD	1	737.28	complex	-17.16	-23.85/-22.18
Ref [6]	2	368.54	complex	-37.88	-43.64/-41.56
	5	147.28	complex	-37.58	-43.14/-41.36
	10	73.73	complex	-36.74	-41.86/-40.58
Proposed Method	2	368.54	real	-39.08	-43.93/-42.49
	5	147.28	real	-39.01	-43.68/-42.11
	10	73.73	real	-38.34	-41.60/-41.02

*The NMSE and ACPR are evaluated within 600MHz limited bandwidth range.

MATLAB from a personal computer (PC). The signal after DPD was fed into the signal generator (R&S SMW200A) and converted into the RF signal at 3.6 GHz. This signal was fed into a GaN PA operating at 3.4-3.8 GHz, and the output signal can be obtained by the signal analyzer (R&S FSW85) after passing through the attenuator.

The performance of the proposed DPD technique is verified by tests. The transmitter paths of these tests are all set same. The DPD models all adopt the band-limited (BL) GMP model [9] and the parameters are set as follows. The order is chosen as 9, and the memory depth is selected as 10. In addition, the cross of lagging terms is 4, the cross of leading terms is 3, and the order of the filtering function is 40. In addition, the bandwidth of the DACs and the filter are all set to 737.28 MHz in these tests. As shown in Table 1, the difference among these tests lies in the configuration of the output signal estimation models. The experimental results with using the method in [6] and the proposed method are compared. In [6], the PA input $u(n)$ and the complex undersampling feedback signals $y(Dn)$ are adopted to estimate the PA output, and the BL GMP model with the same parameter of the DPD model is used. In the proposed method, the estimation model varies with the number of iterations, and it adopts the single real undersampling feedback signals $y_r(Dn)$. The undersampling factors, $D = 2, 5, 10$, are set in sequence during the tests with the above configuration.

Fig. 4 shows the NMSE of the PA estimated output and the real output, and the number of coefficients of the output estimation model in each iteration is also given when $D = 10$ under the two test configurations. Initially, since the collected signals are real while those signals in [6] are complex, the accuracy of the output estimation is slightly lower. As the number of iterations increases, the feedback signal estimation accuracy of the proposed method in each iteration is better than that of [6], and the number of coefficients of the output estimation models decreases.

All the tests are evaluated using normalized mean square error (NMSE) and adjacent channel power ratio (ACPR) within 600 MHz to ignore the influence of the roll-off coefficient of the filter, as shown in Table 2. The test results show that the method proposed in this paper achieve better linearization performance than that in [6] under the same setting for the undersampling factor D, although the performance of the model slightly decreases when the undersampling factor D increases.

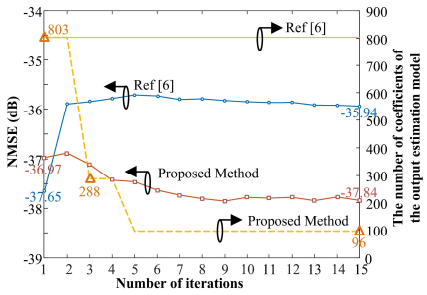


Fig. 4. The NMSE of the PA estimated and actual output, and the number of coefficients of the output estimation model at each iteration when D=10.

IV. CONCLUSION

A novel low-rate DPD technique is proposed under the condition in both low-rate DACs and ADCs. This scheme only requires small resources to accurately estimate the PA's low-rate output signals after multiple iterations, and it effectively reduces the consumption of hardware resources in a broadband and complex nonlinear scenario.

ACKNOWLEDGMENT

This work was supported in part by the Scientific Research Innovation Capability Support Project for Young Faculty under Grant No. SRICSPYF-ZY2025020, in part by the ZTE Industry-University-Institute Cooperation Funds under Grant No. IA20240723011-PO0010.

REFERENCES

[1] C. E. Shannon, "A mathematical theory of communication," The Bell System Technical Journal, vol. 27, no. 3, pp. 379–423, 1948.

[2] L. Guan and A. Zhu, "Green communications: digital predistortion for wideband rf power amplifiers," IEEE Microw. Mag., vol. 15, no. 7, pp. 84–99, 2014.

[3] F. M. Ghannouchi and O. Hammi, "Behavioral modeling and predistortion," IEEE Micro. Mag., vol. 10, no. 7, pp. 52–64, 2009.

[4] C. Yu, L. Guan, E. Zhu and A. Zhu, "Band-limited volterra series-based digital predistortion for wideband rf power amplifiers," IEEE Trans. Microw. Theory Techn., vol. 60, no. 12, pp. 4198-4208, Dec. 2012.

[5] Y. Ma, Y. Yamao, Y. Akaiwa, and K. Ishibashi, "Wideband digital predistortion using spectral extrapolation of band-limited feedback signal," IEEE Trans. Circuits Syst., vol. 61, no. 7, pp. 2088–2097, 2014.

[6] Z. Wang, W. Chen, G. Su, F. M. Ghannouchi, Z. Feng and Y. Liu, "Low feedback sampling rate digital predistortion for wideband wireless transmitters," IEEE Trans. Microw. Theory Techn., vol. 64, no. 11, pp. 3528-3539, Nov. 2016.

[7] N. Guan, N. Wu and H. Wang, "Digital predistortion of wideband power amplifier with single undersampling adc," IEEE Microw. Wireless Compo. Lett., vol. 27, no. 11, pp. 1016-1018, Nov. 2017.

[8] X. Liu, J. Zhai, Z. Zhang, D. Ning, P. Chen, and C. Yu, "High-precision digital predistortion for sub-6-GHz gan power amplifiers excited by a signal with 400-MHz modulation bandwidth," IEEE Microw. Wireless Technol. Lett., 2024.

[9] D. Morgan, Z. Ma, J. Kim, M. Zierdt, and J. Pastalan, "A generalized memory polynomial model for digital predistortion of rf power amplifiers," IEEE Trans. Signal Process., vol. 54, no. 10, pp. 3852–3860, 2006.

Ultra-Broadband 3D-Printed Metalens Using Height-Controlled Meta-Atoms

Xuyi Zhu
College of Electronics and Information Engineering
Sichuan University
Chengdu, China
zhuxuyi@stu.scu.edu.cn

Bing Zhang
College of Electronics and Information Engineering
Sichuan University
Chengdu, China
bing.zhang@scu.edu.cn

***Abstract*—This work presents a 15–40 GHz ultra-broadband metalens based on height-controlled meta-atoms and compatible with hybrid-material 3D printing fabrication. The proposed three-dimensional meta-atom introduces an additional vertical degree of freedom that governs multi-order mode evolution within the unit cell. By tuning the structural height, the evolution and interaction of higher-order modes are controlled, enabling effective phase control over a broad frequency range. Unlike conventional planar phase-shifting elements that rely primarily on two-dimensional geometric variations, the proposed 3D configuration leverages vertical structural modulation to extend the operational bandwidth while maintaining phase tunability. A prototype is fabricated and experimentally validated. Measured results demonstrate broadband operation from 15 to 40 GHz with a peak gain of 25.3 dBi at 25 GHz, corresponding to approximately 90% relative bandwidth. The proposed design provides a manufacturable route toward ultra-broadband metalenses.**

Keywords—Metalens, ultra-broadband, 3D meta-atoms, multi-order modes, 3D printing

979-8-3315-4544-4/26/$31.00 ©2026 IEEE

A Switchable Dual CP Array System for CubeSat Communications Based on Collocated RHCP/LHCP 4×4 Patch Arrays

Zihuan Lu
School of Electrical and Data Engineering
University of Technology Sydney,Sydney NSW 2019,Australia
zihuan.lu@foxmail.com

Zhichao Sun
School of Electrical and Data Engineering
University of Technology Sydney,Sydney NSW 2019,Australia
Bryan.Sun@uts.edu.au

Xiaojing lv
School of Electrical and Data Engineering
University of Technology Sydney,Sydney NSW 2019,Australia
xiaojing.lv@uts.edu.au

Yang Yang*
School of Electrical and Data Engineering
University of Technology Sydney,Sydney NSW 2019,Australia
*yang.yang.au@ieee.org

***Abstract*—This paper presents a switchable dual circularly polarized (CP) 4×4 patch array system for CubeSat communications. The CP element uses a slot-coupled feed to achieve wideband matching and a low axial ratio (AR). A mirror-transformed element is employed to realize right-hand circular polarization (RHCP) and left-hand circular polarization (LHCP) with similar performance. A sequential rotation feeding (SRF) network is used in the 4×4 arrays to improve the impedance and AR bandwidths. Simulation results show that the 4×4 RHCP and LHCP arrays achieve an overlapped bandwidth (|S11| < −10 dB, AR < 3 dB) of 48.7% (28.4–46.2 GHz), with realized peak gains above 16.6 dBic. Finally, the RHCP and LHCP arrays are collocated on the CubeSat top panel, providing a compact switchable dual CP antenna system for polarization diversity and reduced polarization mismatch.**

Keywords—Circularly polarized (CP), CubeSat， sequential rotated feeding (SRF), antenna array

I. INTRODUCTION

CubeSats have become an attractive platform for low-cost space missions and communication services, but the strict constraints on volume, mass, and available aperture make it challenging to integrate high-performance antennas on a 1U-class face [1]. Circular polarization (CP) is widely used in CubeSat communications because it reduces polarization mismatch and improves link robustness. Recent CP designs for CubeSats emphasize low profile, wide bandwidth, and high gain using array and feeding-network techniques [2][3]. Consequently, a large body of work has focused on compact and low-profile CP CubeSat antennas and arrays with wide impedance and axial ratio (AR) bandwidths [4]. Representative approaches include patch-array solutions using sequential rotation feeding (SRF) for broadband AR, shared-aperture concepts that leverage limited surface area for multi-band CP operation, and fully metallic waveguide-based antennas for high-frequency CubeSat data links [5][6].

Although these works show strong progress in compact CP CubeSat antennas, a practical gap remains for CubeSat payloads that benefit from dual CP capability, right-hand circular polarization (RHCP) and left-hand circular polarization (LHCP),

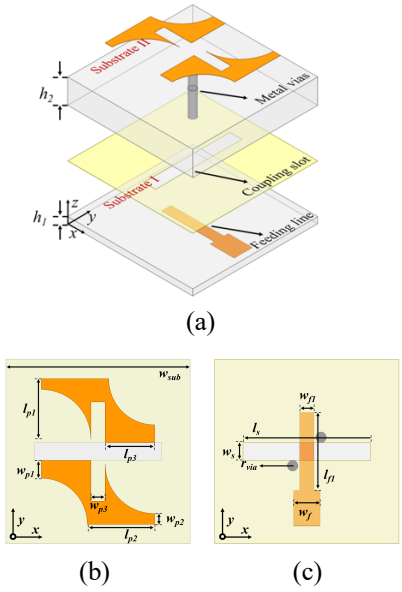


Fig. 1. Configuration of the proposed antenna element. (a) Exploded 3-D model, (b) top view, (c) bottom view. [l_{p1}=1.7, l_{p2}=1.9, l_{p3}=1.4, w_{p1}=0.5, w_{p2}=0.3, w_{p3}=0.4, w_f=0.75, w_{f1}=0.4, l_{f1}=2.2, l_s=3.6, w_s=0.5, r_{via}=0.15,w_{sub}=5.2. (unit: mm)].

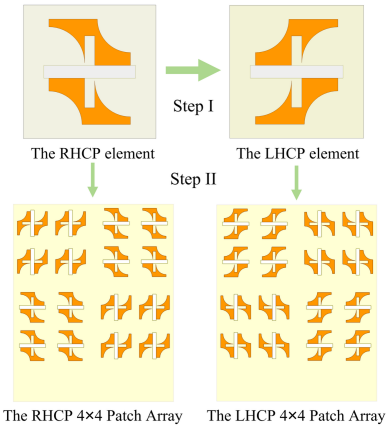


Fig. 2. Design process of the RHCP/LHCP 4×4 antenna Arrays.

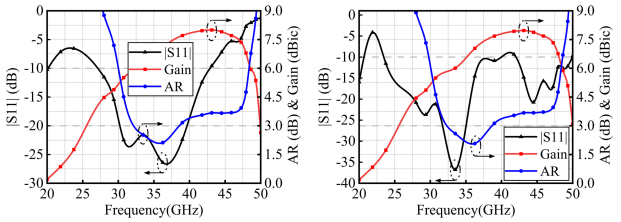


Fig. 3. Simulated |S11|, AR, and realized gain of the proposed antenna elements. (a) the RHCP element, (b) the LHCP element.

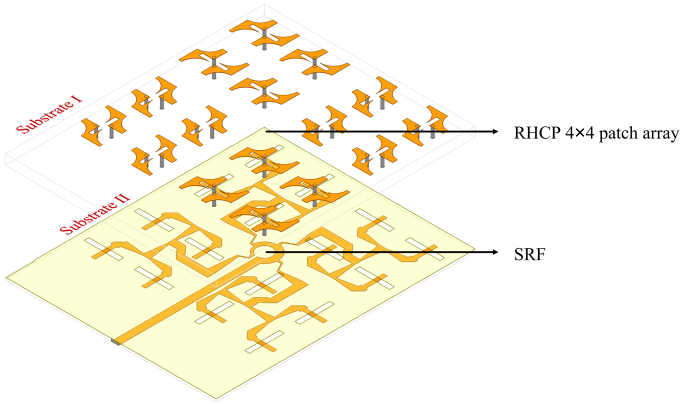


Fig. 4. Configuration of the proposed RHCP 4×4 antenna array.

on the same platform to support polarization diversity and reduce polarization-mismatch risk [7]. Dual CP antenna arrays have been designed using compact slot-based antennas (e.g., dual-feed dual CP slot structures), but such solutions are typically not presented as collocated high-gain array implementations integrated on a CubeSat face for communications [8][9].

To address the challenges, this paper presents a switchable dual CP 4×4 patch array system for CubeSat communications, combining slot-coupled feeding at the element level and an SRF network at the array level, and integrating the RHCP and LHCP arrays on the CubeSat top panel.

II. Antenna Element

Fig. 1 illustrates the proposed slot-coupled RHCP antenna element. The element is realized on two Taconic TLY-5 substrates with thicknesses of 0.254 mm and 1.016 mm, respectively, with copper cladding. The coupling slot is excited by a tapered microstrip-line feed. To account for inter-element mutual coupling, full-wave simulations are conducted under periodic boundary conditions (PBC). The key dimensional parameters are summarized in Fig. 1.

Fig. 2 (Step 1) shows the RHCP antenna element, and its mirror transformation is applied to obtain the LHCP antenna element. The simulated results of the RHCP/LHCP elements are presented in Fig. 3. The RHCP element exhibits an impedance-matching bandwidth (IMBW) of 39.5% (28–41.8 GHz) and an axial-ratio bandwidth (ARBW) of 13.6% (33.5–38.4 GHz), with a peak gain of 8.0 dBic. For the LHCP element, |S11| is −9.5 dB at 41 GHz, and it achieves an IMBW of approximately 70.1%

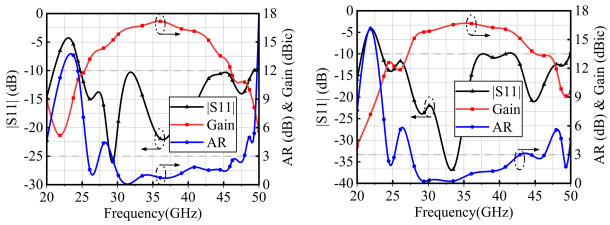


Fig. 5. Simulated |S11|, AR, and realized gain of the proposed 4×4 antenna arrays. (a) the RHCP array, (b) the LHCP array.

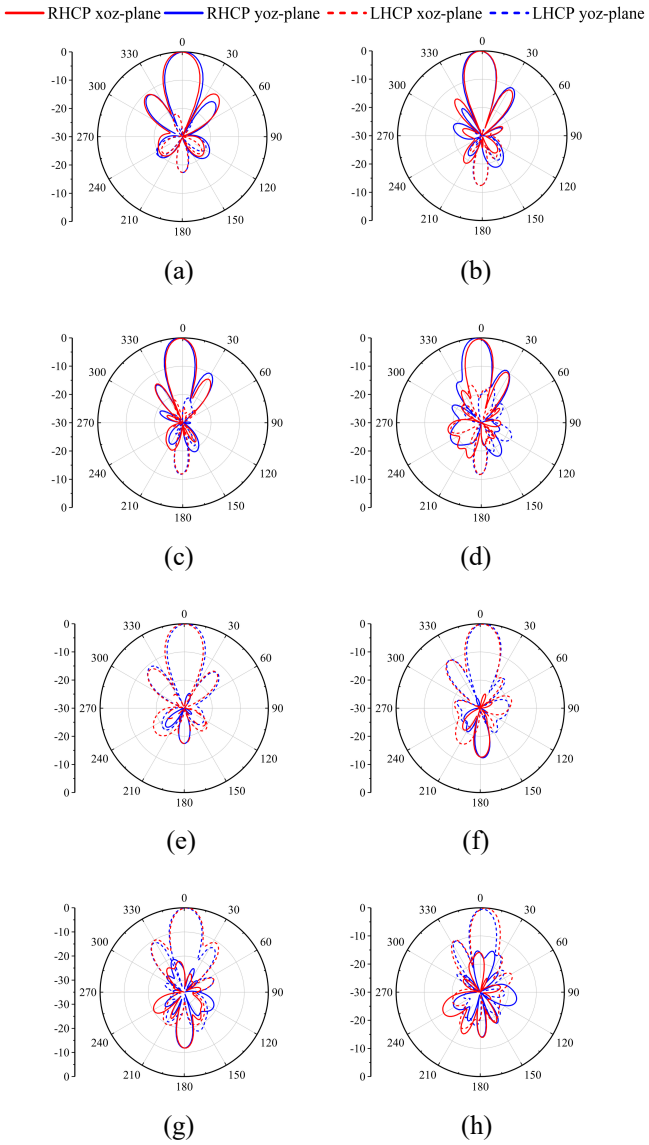


Fig. 6. Simulated radiation patterns of the proposed RHCP/LHCP 4×4 antenna arrays in the xoz-plane and yoz-plane. (a) RHCP array at 29 GHz, (b) RHCP array at 33 GHz, (c) RHCP array at 37 GHz, (d) RHCP array at 41GHz, (e) LHCP array at 29 GHz, (f) LHCP array at 33 GHz, (g) LHCP array at 37 GHz, (h) LHCP array at 41 GHz.

(23.7–49.3 GHz) and an ARBW of 13.6% (33.5–38.4 GHz), with a peak gain of 7.9 dBic.

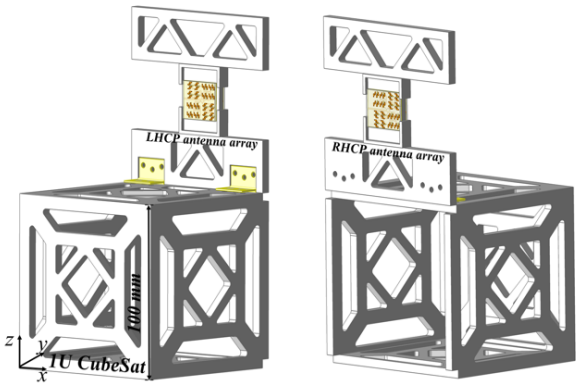


Fig. 7. Deployment of the proposed switchable dual CP array system on a 1U CubeSat. (a) LHCP 4×4 array on the CubeSat top panel, (b) RHCP 4×4 array on the CubeSat top panel.

III. RHCP/LHCP 4×4 Antenna Arrays

The RHCP/LHCP 4×4 patch arrays with an SRF network are implemented by arranging the RHCP/LHCP antenna elements with sequential rotations. Fig. 2 illustrates the rotation (Steps Ⅱ). Fig. 4 shows the configuration of the RHCP 4×4 patch array. To reserve space for the SRF network, the subarray spacing in the designed 4×4 array is a little larger than the element distance. In addition, transformers are introduced in the feed network to broaden the IMBW.

As shown in Fig. 5, the RHCP and LHCP 4×4 patch arrays achieve IMBWs of 72.2% (23.4–49 GHz) and 65.0% (25.1–49 GHz), respectively, while the simulated ARBW is 48.7% (28.4–46.2 GHz) and the realized peak gains are above 16.6 dBic. These performance metrics show a significant improvement compared with those of the antenna element. The radiation patterns at 29 GHz, 33 GHz, 37 GHz, and 41 GHz are depicted in Fig. 6. As observed, the patterns are stable, demonstrating good directivity.

IV. CubeSat Deployment of Switchable Dual-CP System

As shown in Fig. 7, the proposed switchable dual CP system is realized by deploying two 4×4 arrays with opposite handedness on a 1U CubeSat platform. Fig. 7(a) illustrates the installation of the LHCP antenna array on the CubeSat top deployable panel, while Fig. 7(b) shows the corresponding configuration for the RHCP antenna array. The two arrays use the same array size and mounting arrangement; the opposite CP is achieved by using the mirror-transformed element, enabling RHCP and LHCP operation within a 1U CubeSat.

V. Conclusion

This paper presented a switchable dual CP array system for CubeSat communications based on collocated RHCP/LHCP 4×4 patch arrays. A slot-coupled CP element was developed, and the opposite handedness was obtained through a mirror-transformed element. An SRF network was employed to improve the CP overlapped bandwidth at the array level. Simulation results show that the RHCP and LHCP arrays achieve IMBWs of 72.2% (23.4–49 GHz) and 65.0% (25.1–49 GHz), respectively, with an overlapped ARBW of 48.7% (28.4–46.2 GHz) and realized peak gains above 16.6 dBic. The simulated RHCP/LHCP radiation patterns at 29, 33, 37, and 41 GHz further verify the intended polarization, where the co-polarized component dominates, and the cross-polarized component is suppressed in the boresight direction.

References

[1] D. Hester, S. Han and M. Adams, “Design methodology for single-feed circularly polarized X-Band antenna arrays for CubeSats using multilevel sequential rotation,” *IEEE J. Miniaturization for Air Space Syst*., vol. 5, no. 1, pp. 42–50, Mar. 2024.

[2] Z. Sun et al., “C-/Ka-band low-profile circularly polarized shared-aperture antenna for CubeSat communications,” *IEEE Trans. Antennas Propag.,* vol. 73, no. 2, pp. 1221–1226, Feb. 2025.

[3] Z. Sun, X. Lv, X. Zhu, Z. Liang and Y. Yang, “A dual-band circularly polarized antenna with shared aperture for satellite-assisted Internet of Things communications,” *IEEE Internet Things J.*, vol. 12, no. 7, pp. 8461–8469, Apr. 2025.

[4] Z. Sun, X. Lv, Z. Liang and Y. Yang, “A compact 3-D printed wideband circularly polarized curl antenna for satellite communications,” *IEEE MTT-S Int. Microw. Symp.Dig.*, pp. 1–3, Jul. 2025.

[5] S. Singh, S. S. Chauhan and A. Basu, “A low profile wideband circularly polarized slotted waveguide antenna for W-band CubeSat data-links,” *IEEE J. Miniaturization for Air Space Syst.*, vol. 6, no. 1, pp. 19–26, Mar. 2025.

[6] C. Chen, “A dual-band circularly polarized shared-aperture antenna for 1U CubeSat applications,” in *IEEE Trans. Antennas Propag.*, vol. 70, no. 5, pp. 3818–3823, May. 2022.

[7] R. Hussain, M. Ikram, A. M. Algarni and S. S. Iqbal, “Dual sense circularly polarized compact slot antenna for CubeSat applications,” *IEEE Access*, vol. 10, pp. 111732–111737, Oct. 2022.

[8] C. D. Bui, N. Nguyen-Trong and T. K. Nguyen, “A planar dual-band and dual-sense circularly polarized microstrip patch leaky-wave antenna,” *IEEE Antennas Wireless Propag. Lett.*, vol. 19, no. 12, pp. 2162–2166, Dec. 2020.

[9] H. Wang, Y. B. Park and I. Park, “Low-profile wideband solar-cell-integrated circularly polarized CubeSat antenna for the internet of space things,” *IEEE Access*, vol. 10, pp. 61451–61462, Jun. 2022.

Pattern-Reconfigurable Metasurface for Dynamic Switching Between OAM Beam and Dual-Beam

Xiaoxuan Guo
School of Electrical and Data, Engineering, Tech Lab
University of Technology Sydney
Sydney, Australia
xiaoxuanguo02@hotmail.com

Yue Shi
Beijing Chenzhong Technology Electronics Division
Kuaishou Technology
Beijing, China
shiyue11@kuaishou.com

Yang Yang
School of Electrical and Data, Engineering, Tech Lab
University of Technology Sydney
Sydney, Australia
yang.yang-1@uts.edu.au

***Abstract*—A pattern-reconfigurable metasurface is proposed, which enables dynamic switching between Orbital Angular Momentum (OAM) vortex beams and dual-beam radiation patterns. The proposed metasurface is constructed using a multi-layer Printed Circuit Board (PCB), with its aperture phase distribution determining the radiation characteristics. The phase distribution for x-polarization consists of focusing phase and vortex OAM phase, while that for y-polarization comprises focusing phase and a periodically alternating phase of 0° and 180°. Simulation results demonstrate that the proposed metasurface can efficiently achieve dynamic switching between an OAM beam with a topological charge of 1 and dual-beam patterns.**

Keywords—Pattern-reconfigurable, metasurface, Orbital Angular Momentum, dual-beam, phase distribution

I. Introduction

Pattern-reconfigurable metasurfaces have been widely applied in communication systems due to their flexible radiation characteristics [1]-[2]. However, most existing metasurfaces can only switch between focused beams or among OAM beams with different topological charges, which imposes certain limitations in scenarios requiring both OAM beams for complex information transmission [3]-[4] and focused beams for high signal strength [2]-[]. To achieve broader applicability, a pattern-reconfigurable metasurface is proposed that enables dynamic switching between an OAM beam with a topological charge of 1 and dual-beam patterns. By adjusting the phase distributions under x-polarization and y-polarization, the proposed method can also be extended to achieve dynamic switching between OAM beams with arbitrary topological charges and arbitrary multi-beam patterns.

In terms of specific implementation, the proposed metasurface consists of 400 transmission unit cells, each of which is polarization-sensitive, with relatively independent phase responses under x-polarization and y-polarization at 25 GHz. The aperture phase distribution of the metasurface is composed of a focusing phase superimposed with a vortex phase of topological charge 1 under x-polarization, and a focusing phase superimposed with a periodically alternating phase of 0° and 180° under y-polarization. A Fermi antenna is utilized as the feed source to illuminate the metasurface. By rotating the Fermi feed, dynamic reconfiguration between an OAM beam with a topological charge of 1 and a dual-beam pattern is achieved.

II. Polarization-Sensitive Unit Cells

The metasurface unit cell employs an *F4B* dielectric substrate with a loss tangent of 0.0009, a relative permittivity of 2.2, a period of p = 5 mm, and a thickness of 0.8 mm. It is constructed by alternating five layers of PCB dielectric substrates and six layers of metal patches, with no gaps between any two adjacent layers, as illustrated in Fig. 1. The metal patch on each layer is identical and features a cross-shaped structure. The length of the metal branch in one direction (lx) determines the phase and amplitude characteristics of the unit under x-polarization, while the length of the metal branch in the orthogonal direction (ly) determines the phase and amplitude characteristics under y-polarization. The characteristics under x-polarization and y-polarization remain relatively independent of each other. The edge is designed as a 1 mm wide frame to enhance the isolation between adjacent unit cells.

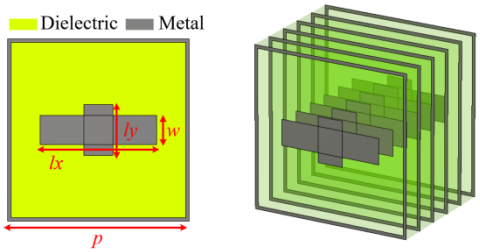


Fig. 1. View of the metasurface unit cell. (a) Front View. (b) Three-dimensional (3D) View.

The patch width w = 0.8mm of the metasurface unit cell is a fixed value. As *lx and ly* vary, the amplitude and phase responses of 3-bit unit cells under x-polarization and y-polarization are shown in Fig. 2. From Fig. 2(a), it can be observed that with *ly* held constant, the amplitude of the metasurface under x-polarization varies as *lx* changes, and all transmission amplitude values are greater than -2 dB, meeting the requirements for transmissive metasurfaces. From Fig. 2(b), it can be seen that with *ly* held constant, the phase of the metasurface under x-polarization varies as *lx* changes, and the transmission phase covers more than 315 degrees. Similarly, Figs. 2(c) and 2(d) demonstrate analogous results under y-polarization.

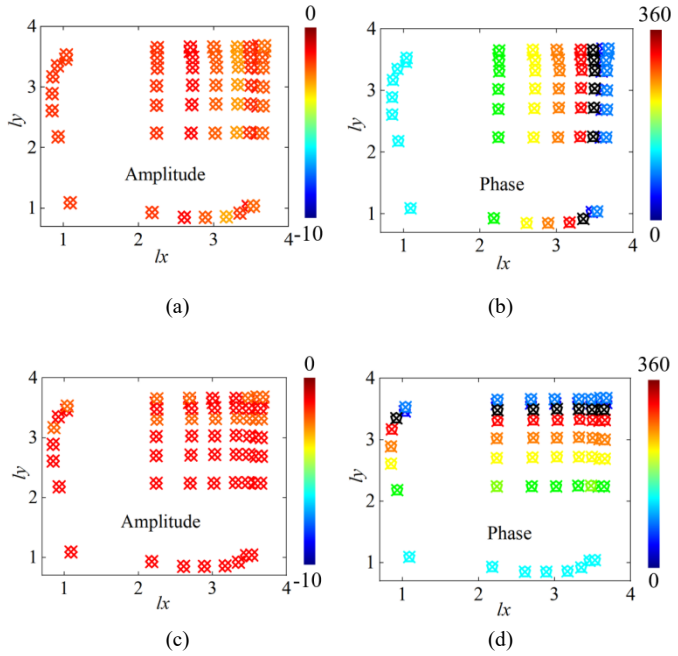


Fig. 2. Transmission amplitude and phase responses of the metasurface unit cell at the central frequency of 25 GHz. (a) Amplitude under x-polarization. (b) Phase under x-polarization. (c) Amplitude under y-polarization. (d) Phase under y-polarization.

III. Implementation of the Proposed Metasurface

Since this design requires high-performance radiation in both x-polarization and y-polarization, the feed source must also deliver high-performance radiation patterns under both polarizations. As feed source design is not the primary focus of this paper, a Fermi antenna from [11] is selected as the feed due to its ease of fixation, compact size, and ability to achieve high-performance radiation in both x-polarization and y-polarization.

Based on the half-power beamwidth of the radiation pattern of the feed antenna, the focal to diameter ratio is set to 1 for calculating the phase distribution across the metasurface aperture, as shown in Fig. 3. Fig. 3(a) shows the focusing phase distribution under x-polarization, Fig. 3(b) shows the focusing phase distribution under y-polarization, Fig. 3(c) shows the vortex OAM phase distribution with a topological charge of 1 under x-polarization, and Fig. 3(d) shows the periodic phase distribution alternating between 0° and 180° under y-polarization. Fig. 3(e) displays the overall phase distribution under x-polarization, which is the numerical superposition of the phase distributions in Figs. 3(a) and 3(c). Fig. 3(f) presents the overall phase distribution under y-polarization, which is the numerical superposition of the phase distributions in Figs. 3(b) and 3(d). All phase distributions under x-polarization and y-polarization are independent and exhibit no coupling between them.

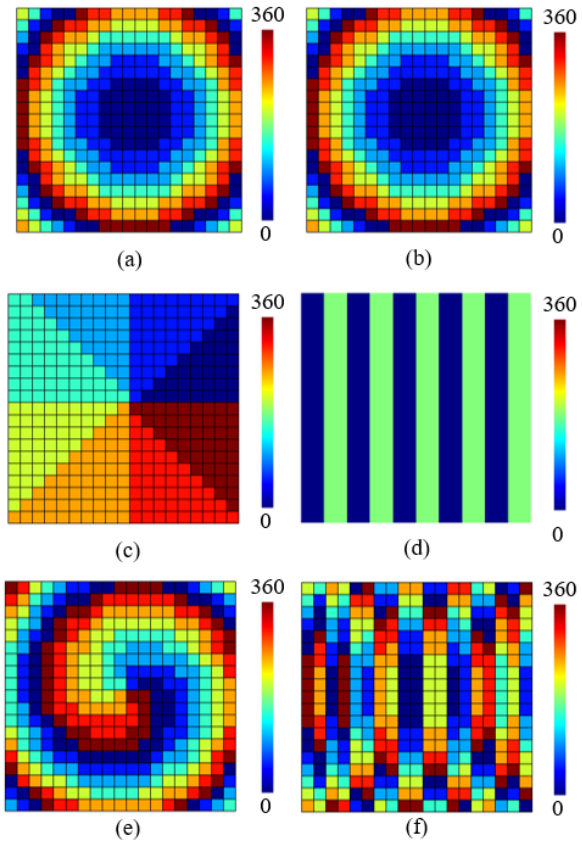


Fig. 3. Phase distribution of the metasurface aperture. (a) Focusing phase distribution under x-polarization. (b) Focusing phase distribution under y-polarization. (c) Vortex OAM phase distribution with a topological charge of 1 under x-polarization. (d) Periodic phase distribution alternating between 0° and 180° under y-polarization. (e) Overall phase distribution under x-polarization. (f) Overall phase distribution under y-polarization.

Based on the phase response curves of the unit in Fig. 2 and the phase distributions in Fig. 3, the physical dimensions of the metasurface can be derived, as illustrated in Fig. 4.

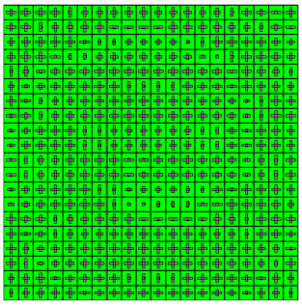
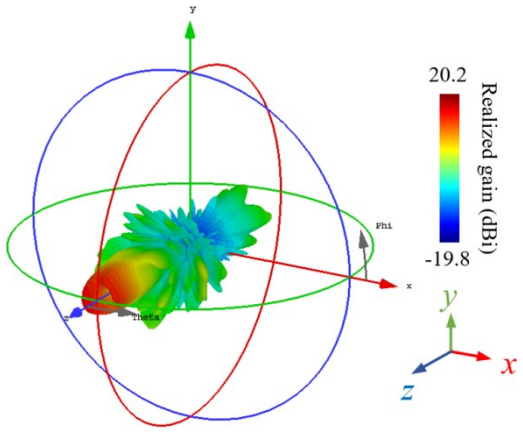
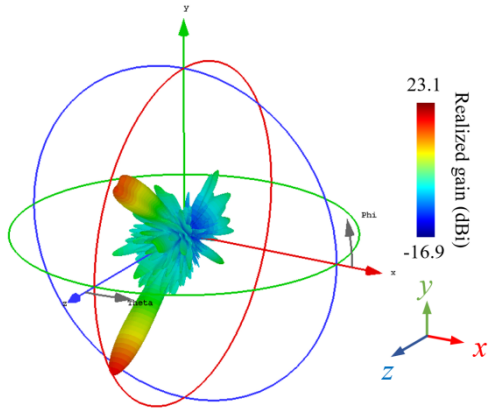


Fig. 4. Main view of the metasurface CST model.

Fig. 5 presents the 3D radiation patterns of the metasurface excited by a Fermi feed at the center frequency of 25 GHz. Fig. 5(a) shows the radiation pattern under x-polarization, indicating that the metasurface generates an OAM beam with a gain as high as 20.2 dBi. Fig. 5(b) displays the radiation pattern under y-polarization, demonstrating that the metasurface produces a dual-beam pattern with a gain as high as 20.2 dBi. These results confirm that the proposed metasurface can efficiently achieve pattern reconfiguration between an OAM beam with a topological charge of 1 and a dual-beam pattern. Furthermore, the proposed method is similarly applicable to dynamic switching between beams with arbitrary topological charges and multiple beams by adjusting the phase distribution of the metasurface.



(a)



(b)

Fig. 5. 3D radiation patterns of the metasurface at the center frequency of 25 GHz under different polarizations. (a) OAM beam under x-polarization. (b) Dual-beam pattern under y-polarization.

IV. Conclusion

Aiming at complex communication scenarios that require both OAM beams for high-capacity information transmission and focused beams for high signal strength, a pattern-reconfigurable transmissive metasurface is proposed. Simulation results demonstrate that by switching the excitation between x-polarization and y-polarization of the feed, the proposed metasurface can efficiently achieve dynamic reconfiguration between an OAM beam with a topological charge of 1 and dual-beam patterns.

References

[1] X. Guo and Y. Yang, "Polarization-multiplexed metasurface for dynamic reconfiguration between orbital angular momentum and focusing beams," *IEEE Trans. Microw. Theory Techn.*, early access, doi: 10.1109/TMTT.2025.3644340.

[2] C. Zhang, Y. Luo, N. Yan, X. Guo, Y. Guo, and K. Ma, "A reconfigurable metasurface with precise phase distribution for both transmission and reflection functions," *IEEE Trans. Antennas Propag.*, vol. 72, no. 9, pp. 7154-7163, Sept. 2024.

[3] X. Guo and Y. Yang, "Mm-wave high gain tri-OAM-beam reflective metasurface generator," *2024 IEEE Asia-Pacific Microwave Conference* (APMC), Bali, Indonesia, pp. 1-3, Nov, 2024. *(references)*

[4] X. Guo and Y. Yang, "Low-profile full-space transmission-reflection-integrated multiple focused and OAM beams metasurface for indoor communication," *IEEE Trans. Microw. Theory Techn.*, vol. 73, no. 6, pp. 3644-3654, Jun. 2025.

[5] X. Guo, Y. Guo, Y. Luo, and Y. Yang, "Full-space transmission-reflection-integrated metasurface for multibeam generation on orthogonal planes," *IEEE Trans. Microw. Theory Techn.*, vol. 73, no. 10, pp. 8199-8209, Oct. 2025.

[6] X. Guo and Y. Yang, "Low-profile transmissive metasurface for generating the butterfly-shaped beam," *2025 6th Australian Microwave Symposium* (AMS), Gold Coast, Australia, pp. 1-2, Feb. 2025. *(references)*

[7] X. Guo, Y. Luo, Z. N. Chen, N. Yan, W. An, and K. Ma, "Multiple tri-beam low scanning loss metasurface antenna for wide-angle coverage by superposing focusing and periodic phases," *IEEE Trans. Microw. Theory Techn.*, vol. 71, no. 8, pp. 3466-3478, Aug. 2023.

[8] X. Guo and Y. Yang, "Chessboard Distribution Transmission-Reflection-Integrated Bidirectional Dual-Beam Metasurface," *2025 IEEE MTT-S International Microwave Workshop Series On Advanced Materials and Processes for RF and THz Applications* (IMWS-AMP), Wuxi, China, pp. 1-3, Jul. 2025. *(references)*

[9] X. Guo, Y. Luo, Z. N. Chen, N. Yan, W. An, and K. Ma, "Interferometric Phase Transmitarray for Spatial Power Combining to Enhance EIRP of Millimeter-Wave Transmitters," *IEEE Trans. Antennas Propag.*, vol. 70, no. 11, pp. 10485-10493, Nov. 2022.

[10] X. Guo, Y. Luo, N. Yan, W. An, and K. Ma, "Multibeam transmit-reflect-array antenna using alternating transmission and reflection elements for space-air-ground-sea integrated network," *IEEE Trans. Antennas Propag.*, vol. 71, no. 11, pp. 8668-8676, Nov. 2023.

[11] W. Yang, K. Chen, and Y. Feng, "Multifunctional metasurface for broadband reflect-transmit-array antenna at 5G millimeter-wave band," *2022 16th European Conference on Antennas and Propagation (EuCAP)*, Madrid, Spain, pp. 1-5, Apr. 2022. *(references)*

A Textile Antenna for On-/Off-Body Communication

Yu-Fei Wang
Guangdong Provincial Mobile Terminal Microwave and Millimeter Wave Antenna Engineering Research Center
Shenzhen University
Shenzhen, 518060, China
1033619732@qq.com

Zhe Chen*
Guangdong Provincial Mobile Terminal Microwave and Millimeter Wave Antenna Engineering Research Center
Shenzhen University
Shenzhen, 518060, China
chenzhe@szu.edu.cn

Shuai Gao
Guangdong Provincial Mobile Terminal Microwave and Millimeter Wave Antenna Engineering Research Center
Shenzhen University
Shenzhen, 518060, China
shuaigao@szu.edu.cn

Yu-Xiang Sun
College of Electronics and Information Engineering
Shenzhen University
Shenzhen, 518060, China
eeyxsun@szu.edu.cn

Tao Yuan
Guangdong Provincial Mobile Terminal Microwave and Millimeter Wave Antenna Engineering Research Center
Shenzhen University
Shenzhen, 518060, China
yuantao@szu.edu.cn

***Abstract*—A textile antenna with dual-band dual-mode operation is proposed for on- and off-body communications. An omnidirectional radiation pattern is achieved by loading shorting pins to excite the TM_{00} mode at the 2.45-GHz band for on-body communication, while a broadside radiation pattern with high gain is realized by etching slots to modify the TM_{30} mode at the 5.8-GHz band for off-body communication. Both bands can be tuned independently. A prototype was fabricated using textile materials, allowing it to conform to the human body. The measured results indicate that the antenna can fully cover the 2.45- and 5.8-GHz WBAN bands, achieving measured peak gains of 1.31 dBi in free space and -1.09 dBi on a three-layer human tissue model for the 2.45-GHz band, as well as 9.97 dBi in free space and 9.62 dBi on the phantom for the 5.8-GHz band. The demonstrated properties confirm that the proposed antenna is suitable for wearable applications.**

***Keywords*—Dual-band dual-mode, high broadside gain, textile antenna, wearable antenna**

I. Introduction

According to the different types of wireless data transfer in body-centric communication, the wearable antennas need to realize on-body communication [1][1], between two wearable devices, or off-body communication [2], between wearable devices and the external wireless networks. Furthermore, the wearable antenna should also address requirements such as comfort in wear, structural simplicity, and seamless integration with garments. Therefore, the textile antenna with a simple structure and dual-band dual-mode (DBDM) operation becomes an ideal solution.

The design of DBDM antennas falls into three categories: multi-radiators [3], [4], loading metamaterials [5]-[7], and multi-mode technologies [8], [9]. These designs primarily focus on the excitation of diverse radiation modes, while demonstrating insufficient discussion regarding gain characteristics in practical scenarios. Considering the generally low input power of wearable devices, the impact of low gain is minimized in on-body communication, as the wearable devices are in close proximity; but off-body communication may require higher gain to ensure reliable performance, especially when an extended communication range is involved. Although high-gain techniques like multi-patch structures [10]-[12], loading artificial magnetic conductors (AMCs) [13], [14], loading shorting pins [15], [16] and etching slots [17], [18] have been widely used in conventional antennas, their application in textile antennas is limited by the inherent material and fabrication constraints. Combined with the requirements for independent frequency tuning and different radiation patterns, achieving a DBDM textile antenna with high broadside gain remains challenging.

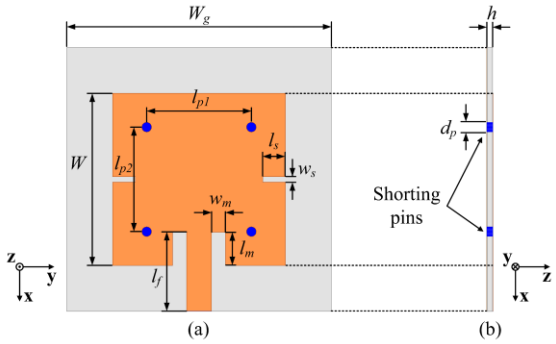


Fig. 1. Geometry of the proposed antenna: (a) top view and (b) lateral view.

In this paper, a DBDM textile antenna with enhanced broadside gain, operating in the 2.45- and 5.8-GHz WBAN bands, is presented. The proposed antenna employs shorting pins to excite the TM_{00} mode at the 2.45-GHz band for omnidirectional radiation. For the 5.8-GHz band, a pair of slots is etched to modify the TM_{30} mode, resulting in gain-enhanced broadside radiation. Both bands can be tuned independently. The antenna achieves measured peak gains of 9.97 dBi in free space and 9.62 dBi on phantom for off-body communication, respectively. In addition, the antenna is fabricated using textile materials to ensure optimal wearability.

II. Antenna Design

A. Antenna Configuration

The geometry of proposed antenna is depicted in Fig. 1. The antenna uses felt as the substrate, with a relative

permittivity of 1.2 and loss tangent of 0.03. The radiating patch, feedline, and the ground plane are constructed from conductive fabric, which has a surface resistivity of less than 0.05 Ω/sq and a thickness of 0.12 mm. The shorting pins are implemented using hollow copper rivets. All optimized parameters are listed as follows: $W = 62$ mm, $W_g = 95$ mm, $w_s = 2$ mm, $l_s = 8.1$ mm, $w_m = 5$ mm, $l_m = 12$ mm, $l_f = 28.5$ mm, $d_p = 3.5$ mm, $l_{p1} = 37.6$ mm, $l_{p2} = 37.6$ mm, $h = 2$ mm.

B. Design Process

The evolution process of the proposed antenna is illustrated in Fig. 2. Initially, ANT-I shows a traditional patch antenna fed by a microstrip line. Due to the reverse currents at the center of the patch, significant sidelobes are observed in the radiation pattern of the TM_{30} mode. To improve the directional radiation gain, ANT-II introduces a pair of rectangular slots etched symmetrically on both sides of ANT-I, exciting the modified TM_{30} mode at 5.80 GHz. Due to the narrow width of the slots, the radiation from the reverse currents on either side of the slots cancels out in the far field, effectively suppressing sidelobe levels in E-plane and compressing the main lobe in H-plane, thus improving the simulated peak realized gain by 3.63 dBi. Finally, ANT-III symmetrically loads four shorting pins on ANT-II to excite the TM_{00} mode at 2.45 GHz, achieving omnidirectional radiation. The currents flow to the shorting pins and generate an equivalent ring magnetic current at the edge of the patch, thereby achieving an omnidirectional radiation pattern. To minimize the impact of the shorting pins on the TM_{30} mode, they are positioned near the electric field nulls of the TM_{30} mode, as depicted in Fig. 3(a). Moreover, the currents of the

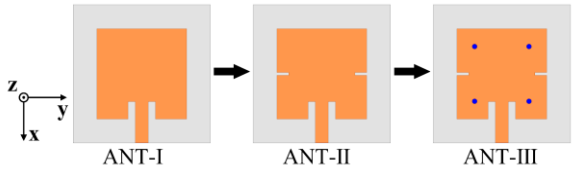


Fig. 2. Evolution of the proposed antenna.

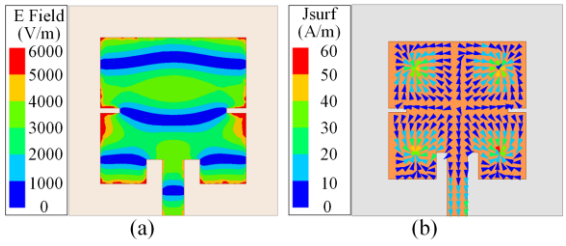


Fig. 3. Simulated (a) electric field distribution of TM_{30} mode for ANT-II and (b) current distribution of TM_{00} mode for ANT-III.

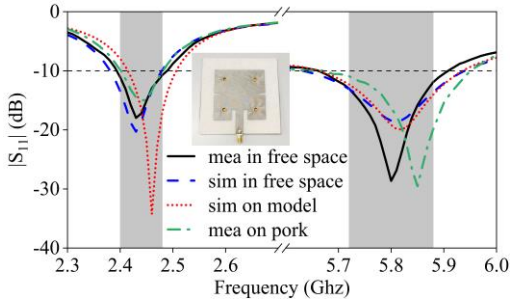


Fig. 4. Simulated and measured $|S_{11}|$ of proposed antenna in different scenarios.

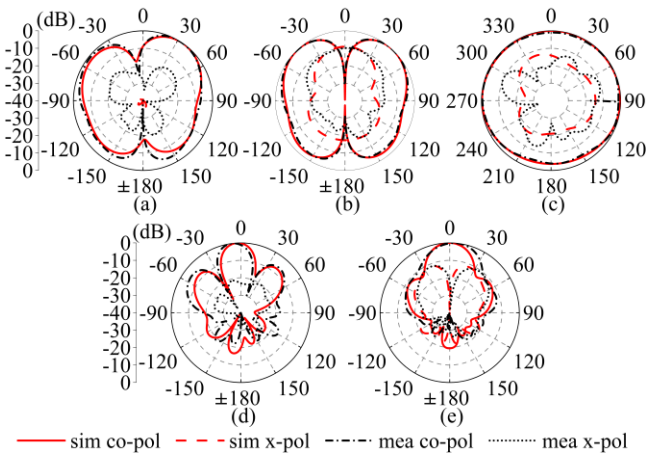


Fig. 5. Simulated and measured normalized Radiation Patterns of proposed antenna in free space: (a) XZ plane, (b) YZ plane, (c) XY plane (θ=34°) at 2.45GHz, and the (d) XZ plane, (e) YZ plane at 5.80GHz.

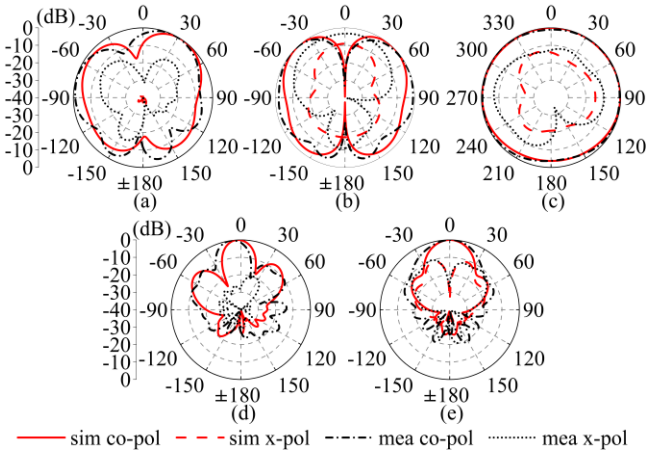


Fig. 6. Simulated and measured normalized Radiation Patterns of proposed antenna on human tissue model: (a) XZ plane, (b) YZ plane, (c) XY plane (θ=60°) at 2.45GHz, and the (d) XZ plane, (e) YZ plane at 5.80GHz.

TM_{00} mode flow parallel to the slots and thus minimize the impact of the slots on the TM_{00} mode, as depicted in Fig. 3(b).

III. Simulated and Measured Results

To validate the simulated results, a prototype was fabricated. Both the conductive fabric and felt were processed using laser cutting, with a precision of 0.05 mm. During assembly, the conductive fabric, which has the adhesive layer, was first adhered to the felt, using the pre-drilled rivet holes for alignment. And then, the hollow copper rivets were secured in place.

As shown in Fig. 4, the simulated and measured S-parameters of the proposed antenna exhibit good agreement, with discrepancies primarily attributed to manufacturing tolerances. The measured bandwidths where $|S_{11}| < -10$ dB are 2.40~2.49 GHz (3.7%) and 5.67~5.91 GHz (4.2%), respectively, fully covering the 2.45- and 5.8-GHz WBAN bands. Additionally, the performance of the antenna placed on the human body is evaluated through simulations utilizing a three-layer human tissue model and measurements using fresh pork. The antenna is placed 5 mm above the model, which measures 200 mm × 200 mm × 60 mm. Based on the simulation and measurement results, the model has little

influence on the S-parameters, and the antenna has a bandwidth of 3.3% and 4.6% in two bands.

The simulated and measured radiation patterns of the proposed antenna at 2.45 GHz and 5.80 GHz in free space, as shown in Fig. 5, indicate a good agreement. The asymmetry in the radiation patterns in the XZ plane at both bands is attributed to the microstrip feedline and the impedance matching slots. The maximum measured peak gain is 1.31 dBi at 2.45-GHz band and 9.97 dBi at 5.8-GHz band. When placed above the human tissue model, its influence on radiation performance of the antenna can be observed in Fig. 6. It can be observed that both modes have a slight tilt in the XZ plane and an increased beamwidth in the YZ plane. This results in a maximum measured gain reduction of the omnidirectional mode decreasing to -1.09 dBi, while the directional mode still maintains a maximum peak gain of 9.62 dBi. The difference between the simulated and measured results in free space and on human tissue model can be attributed to the environmental variations and fabrication inaccuracy, especially since the parameters of pork can hardly achieve an exact match with those of the model [19].

IV. Conclusion

A DBDM textile antenna with high broadside gain for on-/off-body communication is presented in this paper. The antenna has a simple structure and can fully cover the 2.45-/5.8-GHz WBAN bands. For the broadside mode, the antenna achieves a measured peak gain of 9.97 dBi in free space and 9.62 dBi on a three-layer human tissue model, respectively. As a result, the proposed antenna is highly suitable for wearable applications.

Acknowledgment

This work was supported in part by the National Key Research and Development Program of China under Grant 2021YFA0715303, in part by the National Natural Science Foundation of China under Grant 62471314, in part by the Guangdong Basic and Applied Basic Research Foundation under Grant 2025A1515011657.

References

[1] L. Akhoondzadeh-Asl, Y. Nechayev, P. S. Hall, and C. C. Constantinou, "Parasitic array antenna with enhanced surface wave launching for on-body communications," *IEEE Trans. Antennas Propag.*, vol. 61, no. 4, pp. 1976-1985, 2013.

[2] G. P. Gao, C. Yang, B. Hu, R. F. Zhang, and S. F. Wang, "A wearable pifa with an all-textile metasurface for 5 ghz wban applications," *IEEE Antennas Wireless Propag. Lett.*, vol. 18, no. 2, pp. 288-292, 2019.

[3] P. B. Samal, S. J. Chen, and C. Fumeaux, "Flexible hybrid-substrate dual-band dual-mode wearable antenna," *IEEE Trans. Antennas Propag.*, vol. 72, no. 2, pp. 1286-1296, 2024.

[4] G. P. Gao, Z. H. Dou, Z. Q. Yu, B. K. Zhang, J. H. Dong, and B. Hu, "Dual-mode patch antenna with capacitive coupling structure for on-/off-body applications," *IEEE Antennas Wireless Propag. Lett.*, vol. 21, no. 8, pp. 1512-1516, 2022.

[5] B. Zong, G. Wang, C. Zhou, and Y. Wang, "Compact low-profile dual-band patch antenna using novel tl-mtm structures," *IEEE Antennas Wireless Propag. Lett.*, vol. 14, pp. 567-570, 2015.

[6] J. Lin, Z. Qian, W. Cao, S. Shi, Q. Wang, and W. Zhong, "A low-profile dual-band dual-mode and dual-polarized antenna based on amc," *IEEE Antennas Wireless Propag. Lett.*, vol. 16, pp. 2473-2476, 2017.

[7] G. P. Gao, H. J. Meng, W. F. Geng, Z. H. Dou, B. K. Zhang, and B. Hu, "A wideband metasurface antenna with dual-band dual-mode for body-centric communications," *IEEE Antennas Wireless Propag. Lett.*, vol. 21, no. 1, pp. 149-153, 2022.

[8] R. B. V. B. Simorangkir, Y. Yang, L. Matekovits, and K. P. Esselle, "Dual-band dual-mode textile antenna on pdms substrate for body-centric communications," *IEEE Antennas Wireless Propag. Lett.*, vol. 16, pp. 677-680, 2017.

[9] H. Yang and X. Liu, "Wearable dual-band and dual-polarized textile antenna for on- and off-body communications," *IEEE Antennas Wireless Propag. Lett.*, vol. 19, no. 12, pp. 2324-2328, 2020.

[10] M. Zuo, J. Ren, and Y. Z. Yin, "Dual-band antenna with large frequency ratio based on dual-mode transmission line," *IEEE Antennas Wireless Propag. Lett.*, vol. 20, no. 10, pp. 2068-2072, 2021.

[11] C. X. Mao, D. H. Werner, Y. Zhang, and X. Y. Zhang, "Compact dual-band dual-mode antenna with omni-/unidirectional radiation characteristics," *IEEE Antennas Wireless Propag. Lett.*, vol. 18, no. 12, pp. 2657-2660, 2019.

[12] H. Yuan, F. C. Chen, and Q. X. Chu, "A wideband and high gain dual-polarized filtering antenna based on multiple patches," *IEEE Trans. Antennas Propag.*, vol. 70, no. 10, pp. 9843-9848, 2022.

[13] W. Yang, W. Che, and H. Wang, "High-gain design of a patch antenna using stub-loaded artificial magnetic conductor," *IEEE Antennas Wireless Propag. Lett.*, vol. 12, pp. 1172-1175, 2013.

[14] M. E. Atrash, M. A. Abdalla, and H. M. Elhennawy, "A wearable dual-band low profile high gain low sar antenna amc-backed for wban applications," *IEEE Trans. Antennas Propag.*, vol. 67, no. 10, pp. 6378-6388, 2019.

[15] Z. X. Liu, L. Zhu, and N. W. Liu, "Dual-band dual-mode patch antenna with high-gain and wide-beam radiations in two respective bands," *IEEE Trans. Antennas Propag.*, vol. 69, no. 12, pp. 8058-8068, 2021.

[16] X. Zhang and L. Zhu, "Gain-enhanced patch antennas with loading of shorting pins," *IEEE Trans. Antennas Propag.*, vol. 64, no. 8, pp. 3310-3318, 2016.

[17] P. Juyal and L. Shafai, "Sidelobe reduction of tm12 mode of circular patch via nonresonant narrow slot," *IEEE Trans. Antennas Propag.*, vol. 64, no. 8, pp. 3361-3369, 2016.

[18] X. Zhang, L. Zhu, and Q. S. Wu, "Sidelobe-reduced and gain-enhanced square patch antennas with adjustable beamwidth under tm03 mode operation," *IEEE Trans. Antennas Propag.*, vol. 66, no. 4, pp. 1704-1713, 2018.

[19] W. Zhu, X. Liu, Y. Fan, Z. Zhang, and X. Ma, "Transparent and flexible antenna with polarization reconfigurability using egain for wearable applications," *IEEE Trans. Antennas Propag.*, 2024.

A Compact Wideband Dual-Circularly Polarized Millimeter-wave Antenna with Isolation Enhancement

Zhichao Sun
School of Electrical and Data Engineering, University of Technology Sydney, Sydney, NSW 2019, Australia
Bryan.Sun@uts.edu.au

Xiaojing Lv
School of Electrical and Data Engineering, University of Technology Sydney, Sydney, NSW 2019, Australia
xiaojing.lv@uts.edu.au

Jiexin Lai
School of Electrical and Data Engineering, University of Technology Sydney, Sydney, NSW 2019, Australia
Jiexin.Lai@student.uts.edu.au

Yang Yang
School of Electrical and Data Engineering, University of Technology Sydney, Sydney, NSW 2019, Australia
yang.yang.au@ieee.org

***Abstract*—A compact wideband dual-circularly polarized (dual-CP) antenna with isolation enhancement is proposed in this paper. First, a compact antenna element is designed, exhibiting a 27.66% dual-CP bandwidth in the Ka-band. By employing a downward-folded electric-dipole (E-dipole), the footprint of the antenna is significantly reduced, leading to a highly compact structure. However, the isolation between the two ports is low, reaching only 6.5 dB across the operating bandwidth. To address this issue, two dielectric layers are introduced above the radiator, with a cavity etched in the center of the lower dielectric layer. With the cavity-loaded structure, the port isolation is improved by up to 15 dB. Owing to its wideband dual-CP, compact configuration, and high port isolation, the proposed antenna element is well suited for satellite communication antenna arrays.**

Keywords—dual-circularly polarized, high port isolation, millimeter-wave (mm-wave), wideband

I. Introduction

In recent years, satellite communication has become increasingly important with the rapid expansion of space technologies and the growing demand for global connectivity. However, the conventional microwave spectrum is becoming increasingly crowded due to the continuous growth of wireless communication services. Consequently, millimeter-wave (mm-wave) bands have attracted significant attention in satellite communication systems, owing to their abundant spectrum resources and capability to support extremely high data transmission rates.

As a key component of radio frequency (RF) front-end systems, antennas play a vital role in satellite communication links. Compared with linearly polarized (LP) antennas, circularly polarized (CP) antennas with wide bandwidth are more capable of mitigating polarization mismatch caused by satellite motion, atmospheric effects, and antenna orientation variations [1-3]. Meanwhile, wideband characteristics are essential for supporting multi-band satellite services and achieving high data-rate transmission. However, in various satellite communication scenarios, a single CP antenna may be insufficient because the polarization state of electromagnetic waves can change after propagation through the atmosphere or reflection from surrounding structures [4], [5]. To address this challenge, dual circularly polarized (dual-CP) antennas are more suitable for satellite terminals. In addition, dual-CP antennas can enhance link reliability and channel capacity while enabling simultaneous transmit-receive operations, which is highly beneficial for modern satellite communication systems [6], [7].

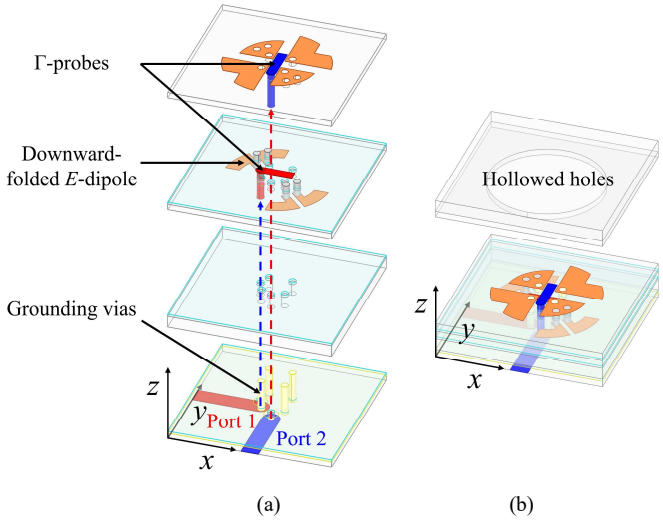


Fig. 1 Configuration of proposed dual-CP antenna (a) without and (b) with cavity-loaded.

Moreover, port isolation is another critical requirement for dual-polarized antenna systems. Insufficient isolation may lead to severe mutual coupling between the two polarization channels, which degrades polarization purity and reduces the overall system performance. Therefore, achieving high isolation between the two ports is essential for ensuring stable and reliable operation in practical satellite communication systems.

Motivated by the aforementioned requirements, a wideband dual-CP antenna element with high port isolation is proposed in this work. By employing folded E-dipoles, an extremely compact configuration is achieved. Furthermore, with the introduction of a cavity-loaded structure, the isolation between the two ports can reach up to 30 dB. Benefiting from its wideband dual-CP performance, high port isolation, and

XXX-X-XXXX-XXXX-X/XX/$XX.00 ©20XX IEEE

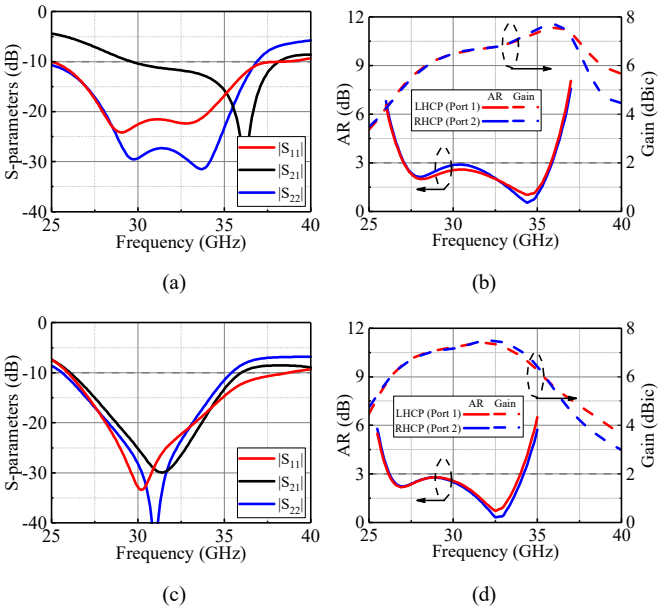


Fig. 2 Simulated S-parameters of proposed dual-CP antenna (a) without and (c) with cavity-loaded, ARs and Gains of proposed dual-CP antenna (b) without and (d) with cavity-loaded.

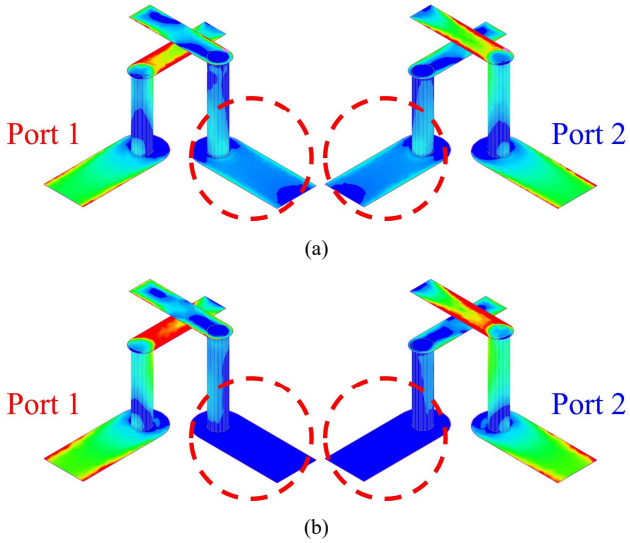


Fig. 3 Simulated current distributions on the two probes of the proposed antenna (a) without and (b) with cavity loading.

compact structure, the proposed antenna element is a promising candidate for satellite communication applications.

II. Antenna Design

The configuration of the proposed dual-CP antenna element is illustrated in Fig. 1(a). It consists of four dielectric substrates and three bonding layers. From bottom to top, these layers are denoted as Sub 1-4 (Rogers 5880, ε_r=2.2, $tan\delta$=0.0009) and Film 1-3 (Rogers 4450B, ε_r=3.52, $tan\delta$=0.004), respectively. The folded E-dipole is located on the top of Sub 4 and the bottom of Sub 3, which is connected with four vias. Two Γ-shaped probes are utilized to excite dual-CP performance and are connected to the microstrip feeding line on the bottom of Sub 1.

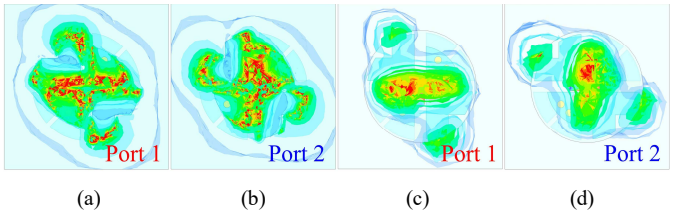


Fig. 4 Simulated electric field distributions of the proposed antenna without cavity loadiing when (a) port 1 is excited, and (b) port 2 is excited, with cavity loading when (a) port 1 and (b) port 2 is excited.

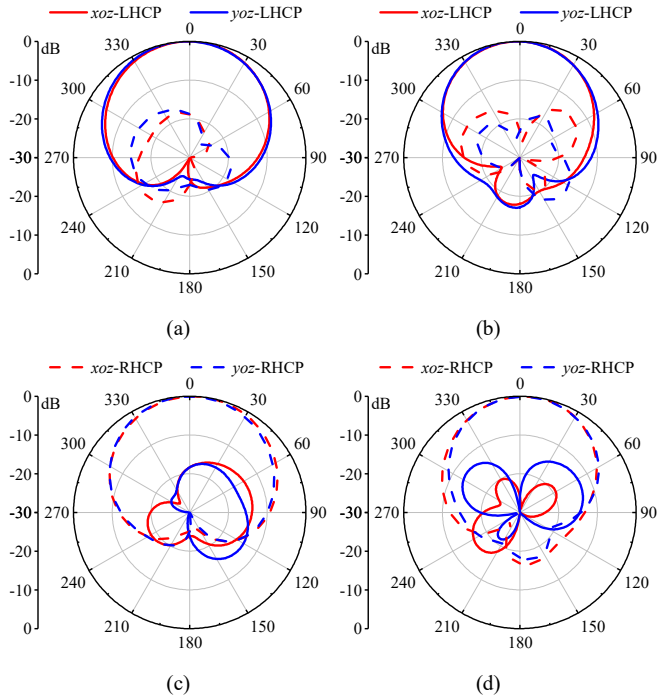


Fig. 5 Simulated normalized radiation patterns of the proposed antenna element without cavity-loaded in the *xoz*- and *yoz*-plane of port 1 at (a) 28 GHz, (b) 34 GHz, port 2 at (c) 28 GHz, (d) 34 GHz.

Fig. 2 (a) and (b) show the simulated S-parameters, ARs, and realized gains of the proposed antenna element. The -10 dB shared impedance bandwidth (IMBW) is 38.19% (25-36.8 GHz), and the shared 3 dB AR bandwidth (ARBW) is 27.66% from 27.1 GHz to 35.8 GHz which demonstrates that a wideband dual-CP performance is realized. The realized gain ranges from 5.15 dBic to 7.7 dBic within the operating bandwidth. However, the port isolation of the antenna is not satisfactory with the minimum value reaching only 6.5 dB at 27.1 GHz. This occurs because the excitation of one port generates two orthogonal current components on the E-dipole, leading to direct coupling into the other port.

To address that, we introduced a cavity-loaded structure, as shown in Fig. 1(b). It comprises two layers, where the bottom layer incorporates a central cylindrical hole, capped by a top substrate layer. After loading this structure, the simulated results of that are given in Fig. 2 (c) and (d). Compared with the antenna without cavity-loaded structure, the IMBW of the designed antenna decreases slightly to 30.62% (26-35.4 GHz) and the 3 dB ARBW is 25.91% (26.2-34 GHz). Meanwhile, the gain varies from 5.9 to 7.5 dBic. It is evident that the introduction of the cavity structure significantly enhances the isolation of the

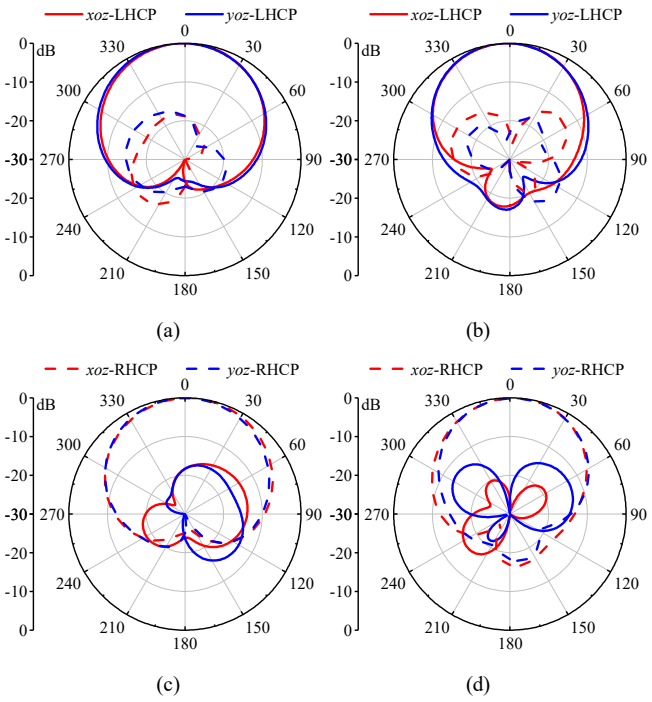


Fig. 5 Simulated normalized radiation patterns of the proposed antenna element with cavity-loaded in the *xoz*- and *yoz*-plane of port 1 at (a) 27 GHz, (b) 33 GHz, port 2 at (c) 27 GHz, (d) 33 GHz.

antenna element across the operating band, reaching a peak value of 30 dB.

To more clearly illustrate the improvement in port isolation after introducing the cavity-loaded structure, Fig, 3 and Fig. 4 present the current distribution on the Γ-shaped probes and the electric field distributions above the two antennas, respectively. Specifically, the noticeable current on the non-excited feedline in the conventional design disappears once the cavity-loaded structure is applied, confirming the suppression of direct coupling between the two ports. Furthermore, the electric distribution reveals that the field is predominantly confined within the cavity after its integration. This indicates a significant suppression of surface waves, which effectively minimizes the mutual coupling between the ports.

III. Conclusion

A wideband dual-CP antenna with high compactness and high isolation is presented in this paper. By employing folded E-dipoles, a significantly reduced footprint for the antenna element is achieved. Furthermore, the integration of a cavity-loaded structure effectively suppresses surface wave propagation and mitigates mutual coupling, thereby enhancing the isolation between the two ports. Given its wideband dual-CP performance, exceptional compactness, and high isolation, the proposed antenna is highly suitable for satellite communication applications.

References

[1] S. Gao, Q. Luo, and F. Zhu, *Circularly Polarized Antennas*. Hoboken, NJ, USA: Wiley, 2014.

[2] Q. Tan, K. Fan, W. Yu, Y. Yu and G. Q. Luo, "A Broadband Circularly Polarized Planar Antenna Array Using Magneto-Electric Dipole Element With Bent Strips for Ka-Band Applications," IEEE Antennas and Wireless Propagation Letters, vol. 22, no. 1, pp. 39-43, Jan. 2023.

[3] Q. Tan, K. Fan, W. Yu, W. Wang, L. Liu and G. Q. Luo, "A Circularly Polarized Magneto-Electric Dipole Antenna Array With Wide AR and Impedance Bandwidth for Millimeter-Wave Applications," IEEE Antennas and Wireless Propagation Letters, vol. 22, no. 9, pp. 2250-2254, Sept. 2023.

[4] Z. Sun, X. Lv and Y. Yang, "Wideband Sequential Rotation Dual-Circularly Polarized Magnetoelectric Dipole Array With Polarization Independent Control for Intelligent Vehicle Communications," IEEE Transactions on Antennas and Propagation, vol. 73, no. 4, pp. 2666-2671, April 2025.

[5] L. Ma, J. Lu, C. Gu, and J. Mao, "A wideband dual-circularly polarized, simultaneous transmit and receive (STAR) antenna array for integrated sensing and communication in IoT," *IEEE Internet Things J.*, vol. 10, no. 7, pp. 6367–6376, Apr. 2023.

[6] C. Zhu, G. Xu, A. Ren, W. Wang, Z. Huang and X. Wu, "A Compact Dual-Band Dual-Circularly Polarized SIW Cavity-Backed Antenna Array for Millimeter-Wave Applications," IEEE Antennas Wireless Propag. Lett., vol. 21, no. 8, pp. 1572-1576, Aug. 2022.

[7] J. Zhu, Y. Yang, S. Li, S. Liao and Q. Xue, "Dual-Band Dual Circularly Polarized Antenna Array Using FSS-Integrated Polarization Rotation AMC Ground for Vehicle Satellite Communications," IEEE Trans. Veh. Technol., vol. 68, no. 11, pp. 10742-10751, Nov. 2019.

Broadband Circularly Polarized Glass Antenna with Surface Wave Suppression

Xiaofeng Hou[1], Keying Huang[1], Zhipeng Zhang[1], Wenhai Zhang[1]*, Yilin Zheng[1], Chi-Hou Chio[2], Kam-Weng Tam[2], Zhixing Chen[3]
1School of Electronic and Information Engineering, Soochow University, Suzhou, 215006, China
2Faculty of Science and Technology, University of Macau, Macau 999078, China
3Fuyao Glass Industry Group Co., Ltd, Fujian 350300, China
*Corresponding author email: wenhaizhang@suda.edu.cn

***Abstract*—This paper presents a novel circularly polarized coplanar waveguide (CPW)-fed antenna designed for integration into vehicle roof glass for satellite navigation applications. The antenna utilizes an asymmetric ground plane to achieve broadband circular polarization. A key feature is the seamless integration of a coplanar frame structure within the blackout border region of the roof glass, which effectively suppresses surface wave propagation. Measurement results demonstrate that the prototype achieves an impedance bandwidth of 36.04% (1.16–1.67 GHz) and a 3-dB axial ratio (AR) bandwidth of 34.29% (1.16–1.64 GHz). Furthermore, the antenna exhibits a boresight right-hand circularly polarized (RHCP) gain exceeding 2 dBic across the B3 and L1 navigation bands. These characteristics satisfy the stringent requirements for modern automotive Global Navigation Satellite System (GNSS) antennas.**

Keywords—Broadband, circular polarization, CPW feed, surface wave suppression, GNSS application

I. Introduction

The rapid advancement of wireless communications is transforming vehicles into smart systems, driving the growth of automotive connectivity [1, 2]. This evolution has led to a substantial increase in the number of antennas integrated into modern intelligent vehicles to support a growing array of wireless services [3, 4]. For over a decade, antennas for essential services have typically been housed within a protruding "shark-fin" module on the vehicle roof. However, simply enlarging this module to accommodate more antennas is undesirable, as it would compromise the vehicle's aerodynamic performance and aesthetic design. Concurrently, a notable trend in automotive design is the replacement of metallic roof panels with glass structures, driven by the increasing popularity of panoramic sunroofs that offer passengers a spacious visual experience [5, 6]. This shift presents both a challenge and an opportunity: while the traditional shark-fin module becomes increasingly crowded, the expansive glass roof offers a new, large-aperture platform for antenna integration.

This paper addresses this opportunity by proposing a wideband circularly polarized antenna designed for direct integration into vehicle roof glass for GNSS applications. The proposed antenna is engineered to cover all major navigation frequency bands. A key challenge in such glass-integrated designs is the excitation of surface waves, which can significantly degrade radiation performance. To mitigate this, this paper introduces a novel surface wave suppression technique; by integrating a coplanar rectangular loop structure around the antenna, the deterioration of radiation patterns caused by surface waves is effectively minimized. This work not only provides a practical solution for antenna integration but also establishes a technical approach and feasibility reference for the future co-design of multifunctional vehicular antennas and automotive glazing.

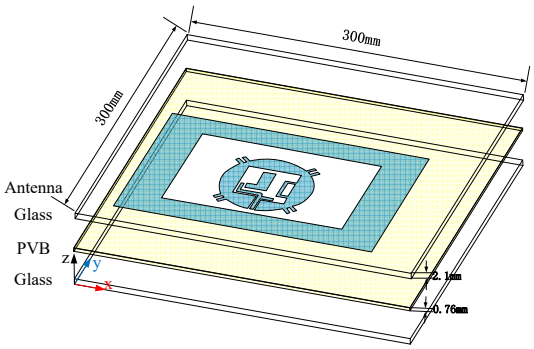


Fig. 1. The proposed wideband circularly polarized glass antenna.

II. Broadband Circularly Polarized Glass Antenna

A. Antenna Geometry

The geometry of the proposed wideband circularly polarized glass antenna with surface wave suppression is shown in Fig. 1. The basic structure is derived from the glass antenna design in [7]. Unlike a single-layer structure, the proposed antenna is integrated within laminated automotive glass, which consists of three layers: an inner glass layer, a polyvinyl butyral (PVB) interlayer, and an outer glass layer. The PVB interlayer, sandwiched between the two glass layers, significantly enhances the mechanical safety and security of the glazing [8]. It has a thickness of 0.76 mm, a relative permittivity of 2.96, and a loss tangent of 0.06. To effectively suppress the adverse effects of surface wave propagation, a rectangular loop structure is introduced, surrounding the proposed circularly polarized antenna. The entire antenna structure is strategically placed within the blackout border region on the roof glass to maintain aesthetic integration with the vehicle.

B. Surface Wave Suppression Analysis

Fig. 2 illustrates the simulated radiation patterns in the two principal planes, comparing the cases with and without the proposed frame structure. It is observed that the presence of surface waves significantly degrades the radiation patterns, particularly at the higher operating frequency of 1.575 GHz. Specifically, the surface waves reduce the broadside gain while increasing radiation towards the endfire direction, which in turn narrows the AR bandwidth of the antenna. This degradation is further elucidated by the electric field distributions shown in Fig. 3. Without the frame structure, the electric field is not confined to the radiator; instead, a significant portion of the energy propagates towards and concentrates along the edges of the glass substrate. As the substrate is electrically large, this leads to substantial power leakage via substrate-edge diffraction and surface wave

propagation. By introducing the rectangular loop structure, this power leakage is effectively suppressed. Consequently,

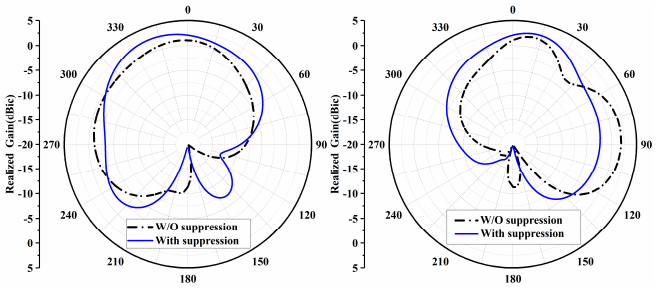


Fig. 2. Radiation patterns comparison with and without surface wave suppression at 1.575 GHz. (a) *xoz*-plane, and (b) *yoz*-plane.

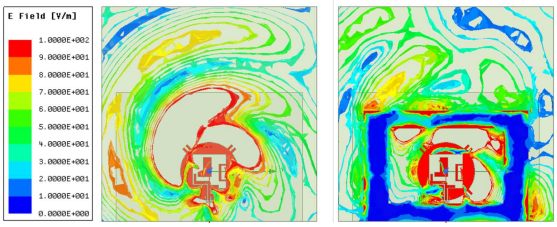


Fig. 3. Electric field distributions on the laminated glass at 1.575 GHz. (a) without, and (b) with the metallic frame structure.

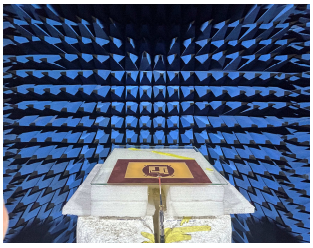


Fig. 4. Photo of glass antenna prototype measurement.

as demonstrated in Fig. 2, the radiation patterns are restored, with enhanced gain in the broadside direction and improved AR bandwidth.

C. Experimental Validation

Fig. 5(a) presents the simulated and measured reflection coefficients of the proposed antenna. The measured -10-dB impedance bandwidth reaches 36.04% (1.16–1.67 GHz), which agrees well with the simulated bandwidth of 36.82% (1.13–1.64 GHz). As shown in the same figure, the measured boresight gain varies from 1.1 to 3.2 dBic across the operating band, while the simulated gain ranges from 1.6 to 3.6 dBic, with a discrepancy of less than 0.4 dB. Fig. 5(b) compares the simulated and measured ARs and radiation efficiencies. The measured 3-dB AR bandwidth is 34.29% (1.16–1.64 GHz), closely matching the simulated one of 35.71% (1.15–1.65 GHz). Regarding radiation efficiency, the measured values remain around 65% within the 1.16–1.61 GHz range, which is effectively improved in the high frequency range, validating the surface wave suppression design.

III. Conclusion

This paper has presented a novel broadband circularly polarized antenna integrated into vehicle roof glass for GNSS applications. A rectangular loop structure is introduced to effectively suppress surface wave radiation. The fabricated prototype achieves a measured impedance bandwidth of 36.04% (1.16–1.67 GHz) and a 3-dB axial ratio bandwidth of 34.29%

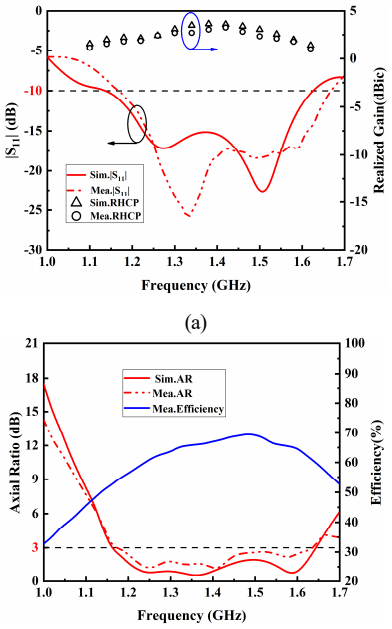


Fig. 5. Simulated and measured performances. (a) Reflection coefficients and gains, (b) ARs and radiation efficiencies.

(1.16–1.64 GHz), with boresight RHCP gain exceeding 2 dBic across the operating bands. Good agreement between simulation and measurement validates the proposed design, making it a promising candidate for vehicular GNSS applications.

IV. Acknowledgment

This work is supported by Gusu Youth Leading Talent Program under Grant ZXL2024371, Jiangsu Province Innovation Support Program Special Fund (File no. BZ2023061), and National Natural Science Foundation of China under Grant 61901178.

References

[1] D. Cao et al., “Future directions of intelligent vehicles: Potentials, possibilities, and perspectives,” *IEEE Trans. Intell. Veh.*, vol. 7, no. 1, pp. 7–10, Mar. 2022.

[2] W.-H. Zhang, Q. Xue, S. Liao, W. Che, and W. Yang, “Low-profile compact microstrip magnetic dipole antenna with large beamwidth and broad bandwidth for vehicular applications,” *IEEE Trans. Veh. Technol.*, vol. 70, no. 6, pp. 5445–5456, Jun. 2021.

[3] X.-Q. Xing, W.-J. Lu, F.-Y. Ji, L. Zhu, and H.-B. Zhu, “Low-profile dual-resonant wideband backfire antenna for vehicle-to-everything applications,” *IEEE Trans. Veh. Technol.*, vol. 71, no. 8, pp. 8330–8340, Aug. 2022.

[4] B. Feng, B. Yang, C.-Y.-D. Sim, L. Deng, Z. Zhou, and X. Ding, “A compact vehicle-mounted garden-themed artistic antenna with isolation improvement for 2G/3G/LTE/5G Sub-6-GHz/WiFi/Bluetooth communications,” *IEEE Trans. Veh. Technol.*, vol. 72, no. 4, pp. 4851–4862, Apr. 2023.

[5] K. K. Katare, I. M. Yousaf, and B. K. Lau, “Challenges and solutions for antennas in vehicle-to-everything services,” *IEEE Commun. Mag.*, vol. 60, no. 1, pp. 52–58, Jan. 2022.

[6] A. Kwoczek et al.,“Influence of car panorama glass roofs on Car2Car communication (Poster),” in *Proc. IEEE Veh. Netw. Conf.*, Nov. 2011, pp. 246–251.

[7] K. Huang et al., "A broadband transparent circularly polarized antenna for GNSS applications," *in Proc. IEEE Int. Workshop Wireless Sensing Technol. Appl. (IWSA)*, Nanjing, China, 2025, pp. 1–2.

A Low-Profile and High Front-to-Back Ratio Millimeter-Wave Array Based on Electromagnetic Band Gap Ground

Yu-Qi Ma, Zhi-Hong Tu, Huan-Bin Wang, Fu-Chang Chen
School of Electronic and Information Engineering
South China University of Technology
Guangzhou 510641, China

***Abstract*—This paper proposes a low profile and high front-to-back ratio (FBR) millimeter-wave array based on electromagnetic bandgap ground (EBGG). The proposed array consists of two SIW slot antenna elements operating in the 24 GHz ISM band. In order to enhance the gain and FBR, a π-shaped EBGG is introduced on both sides of the array, while maintaining an ultra-low profile of only 0.04λ_0. Compared with the original array, the proposed array achieves an enhancement in peak realized gain from 8.0 dBi to 9.0 dBi at 24.0 GHz, a reduction in the 3-dB beamwidth from 105° to 91°, and a significant enhancement in FBR from 17.34 dB to 30.17 dB. These results demonstrate that the proposed π-shaped EBGG is an effective solution for achieving gain and FBR enhancement in low-profile millimeter-wave antenna arrays.**

***Index Terms*—Low-profile, millimeter-wave antenna, gain enhancement, electromagnetic bandgap structure, front-to-back ratio**

I. Introduction

With the rapid development of wireless systems, increasing demands have been placed on antenna performance in applications such as identification, sensing, and millimeter-wave radar systems. In these systems, antennas are typically required to exhibit high gain, high FBR, and low profile [1], [2].

To meet these requirements, some techniques have been proposed. EBG structures have been widely employed either beneath the antennas as reflectors or above the antennas as metasurfaces to enhance radiation performance [3], [4], [5], [6], [7]. In [4], a gain-enhanced EBG reflector was introduced for dual-polarized antenna, achieving an increase in average broadside gain from 4.27 dBi to 8.03 dBi with a profile of 0.08λ_0. In [8], a low profile and high FBR antenna based on artificial magnetic conductor (AMC) was proposed, achieving a FBR of over 21.5 dB with a profile of 0.09λ_0. To enhance gain while maintaining low-profile, a cylindrical electromagnetic bandgap structure and an L-slotted mushroom EBG were proposed in [9] and [10], respectively. In [10], a microstrip patch with a single-layer L-slot mushroom EBG achieves a gain of 5.9 dBi, with 0.6 dB gain enhancement.

In this paper, a π-shaped EBGG is proposed to enhance the gain and FBR of a 1×2 SIW slot antenna array while maintaining a low profile of 0.04λ_0. The bandgap characteristic of π-shaped EBGG is first investigated using the direct transmission method. Then, the π-shaped EBGG is introduced into the array, achieving a peak gain of 10.7 dBi within the operating band, and 1.0 dB gain enhancement at 24.0 GHz compared with the original array. In addition, a high FBR of 30.17 dB is achieved, while the original array achieves a FBR of 17.34 dB.

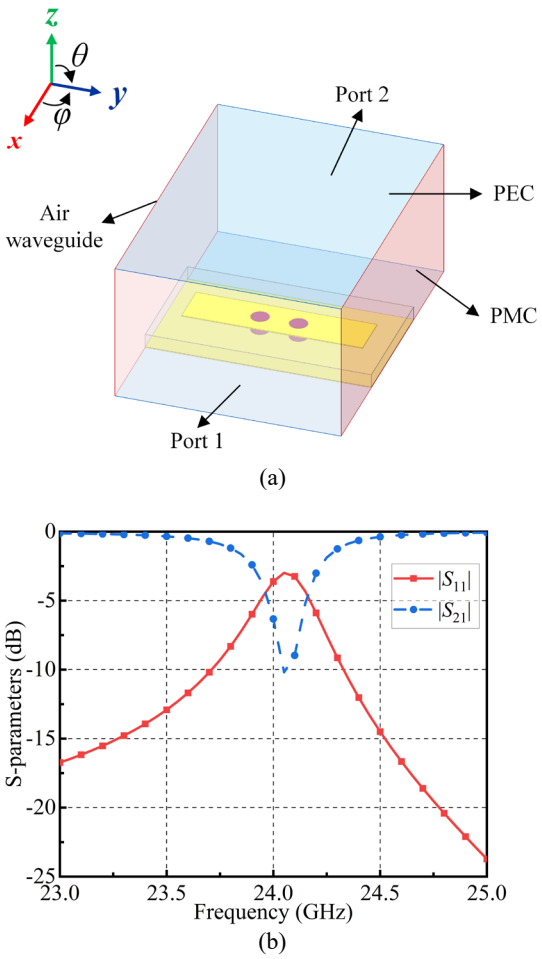
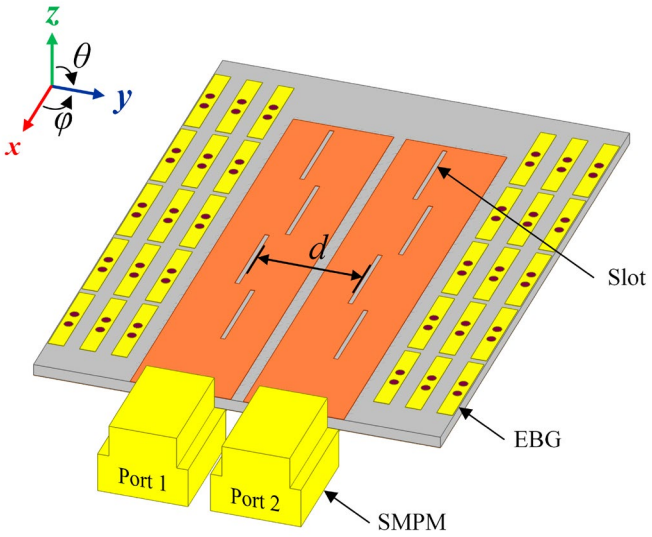
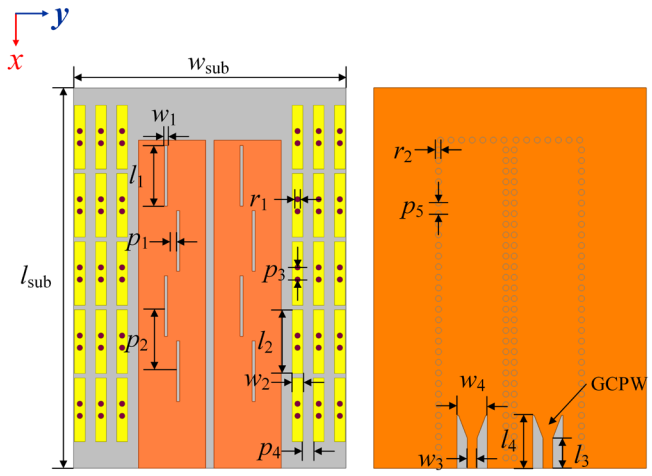


Fig. 1. (a) Simulation model of the proposed π-shaped EBGG structure using the direct transmission method. (b) S-parameters of the direct transmission model.



(a)



(b)

Fig. 2. Geometry of the 1×2-element subarray: (a) Isometric view. (b) Detailed configuration.

TABLE I
DIMENSIONS FOR THE ARRAY

Parameter	l_{sub}	w_{sub}	h_{sub}	l_1	w_1	l_2
Value(mm)	25.1	18.0	0.508	4.0	0.2	4.2
Parameter	w_2	l_3	w_3	l_4	w_4	p_1
Value(mm)	0.7	2.0	0.65	3.5	1.8	0.4
Parameter	p_2	p_3	p_4	p_5	r_1	r_2
Value(mm)	4.3	0.8	0.7	0.7	0.4	0.4

II. Design of Array With π-Shaped EBGG

A. Bandgap Characteristic of the π-Shaped EBGG

In order to analyze the bandgap characteristic of the π-shaped EBGG, the direct transmission method mentioned in [11] has been adopted. Fig. 1 shows the simulation model and S-parameters of the proposed π-shaped EBGG structure using the direct transmission method. With reference to Fig. 1(a), Port 1 and Port 2 are set according to the propagation direction of surface wave. The top and bottom surfaces of the air waveguide are set as perfect electric conductors (PECs). The left and right of the air waveguide are set as perfect magnetic conductor (PMC). With reference to Fig. 1(b), $|S_{21}|$ decreases to –10.2 dB and $|S_{11}|$ reaches –3.0 dB at 24.1 GHz, which indicates a bandgap characteristic of the π-shaped EBGG and effectively suppresses the propagation of the surface wave.

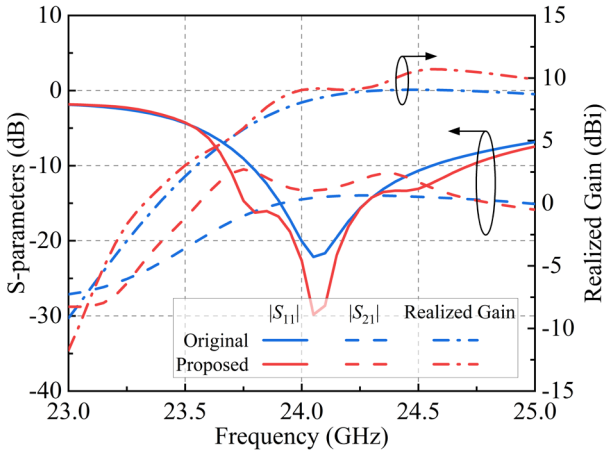


Fig. 3. Simulated S-parameters of the original and proposed array.

B. Structure of Array With π-Shaped EBGG

Fig. 2 shows the geometry of the 1×2-element array with π-shaped EBGG. The proposed array is composed of only one layer of dielectric substrate of Rogers 4003C (ε_r = 3.55, tan δ = 0.0027 at 10 GHz), with a thickness of 0.508 mm. The proposed array contains two SIW slot antenna elements, and each antenna element contains four radiation slots. Each antenna element is fed with grounded coplanar waveguide (GCPW). The interelement spacing d of the antenna element is 5.0 mm (0.40λ_0, where λ_0 is the free space wavelength at 24.0 GHz). In order to limit the propagation of the surface wave, three rows of π-shaped EBGG are introduced on each side of the array, and each row contains five π-shaped EBGG. The spacing of each row is p_4 = 0.4 mm. The overall size of the array is 25.1×18.0×0.508 mm^3 (2.0×1.4×0.04λ_0^3). The proposed array maintains a single-layer structure after introducing the π-shaped EBGG. The thickness of copper is 1.0 oz (0.035 mm). To feed the array, SMPM connectors are soldered to GCPW feed lines, and SMPM connectors are considered in the simulation. The detailed configurations are shown in Table I.

C. Performance of the Array

Fig. 3 compares the simulated performance of the original array and the proposed array with π-shaped EBGG. The original array achieves a –10-dB impedance bandwidth of 23.8-24.6 GHz (3.3%), whereas the proposed array achieves a bandwidth of 23.6-24.8 GHz (5.0%). Although the introduction of the EBGG slightly increases the mutual coupling, the mutual coupling remains below –11.0 dB. In addition, the original array achieves a realized gain varying from 6.5 to 9.0 dBi within the

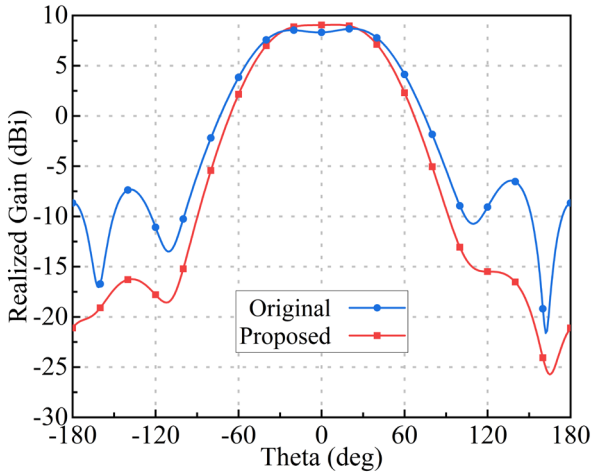


Fig. 4. Simulated *E*-plane radiation patterns at 24.0 GHz of the original and proposed array.

operating band, while the proposed array achieves a realized gain varying from 4.2 to 10.7 dBi within the operating band. Notably, the peak realized gain is improved from 8.0 dBi to 9.0 dBi at 24.0 GHz.

Fig. 4 compares the *E*-plane radiation patterns at 24.0 GHz of the original array and the proposed array. The original array achieves a radiation pattern with a peak realized gain of 8.68 dBi, and a 3-dB beamwidth of 105°. However, the proposed array achieves a radiation pattern with a peak realized gain of 9.07 dBi, and a 3-dB beamwidth of 91°. In particular, the radiation pattern of the original array shows a realized gain of -8.66 dBi in the back lobe direction, while the radiation pattern of the proposed array with π-shaped EBGG shows a realized gain of –21.1 dBi in the back lobe direction. Thus, the original array achieves a FBR of 17.34 dB, while the proposed array with π-shaped EBGG achieves a FBR of 30.17 dB.

III. Conclusion

In this paper, a 1×2 SIW slot antenna array based on π-shaped EBGG is proposed with gain and FBR enhancement, while maintaining a low profile of $0.04\lambda_0$. The proposed array achieves a peak realized gain of 10.7 dBi within the operating band and gain enhancement of 1.0 dB at 24.0 GHz compared with the original array. In addition, a high FBR of 30.17 dB is achieved, whereas the original array achieves a FBR of 17.34 dB.

Acknowledgment

This work was supported in part by the Science and Technology Planning Project of Guangdong Province under Grant 2025A1515011414, in part by the National Natural Science Foundation of China under Grant 62334005. (Corresponding author: Zhi-Hong Tu)

References

[1] Hashim, Fatimah Fawzi, et al. "Key factors in the implementation of wearable antennas for WBNs and ISM applications: A review WBNs and ISM applications: A review." Electronics 11.15 (2022): 2470.

[2] Jha U S. The millimeter Wave (mmW) radar characterization, testing, verification challenges and opportunities[J]. 2018 IEEE AUTOTESTCON, 2018: 1-5.

[3] Zhao, Luyu, et al. "Scanning angle extension of a millimeter-wave antenna array using electromagnetic band gap ground." *IEEE Transactions on Antennas and Propagation* 70.8 (2022): 7264-7269.

[4] Xiong, Huan Qian, Chen Jing Zhang, and Mei Song Tong. "Wideband low-profile dual-polarized antenna based on a gain-enhanced EBG reflector." IEEE Transactions on Components, Packaging and Manufacturing Technology 12.2 (2021): 391-394.

[5] Liu, Guanghong, et al. "Ultra - wideband Low - Detectable Coding Metasurface." Chinese Journal of Electronics 28.6 (2019): 1265-1270.

[6] Alnaiemy, Yahiea, and Lajos Nagy. "Improved antenna gain and efficiency using novel EBG layer." 2020 IEEE 15th International Conference of System of Systems Engineering (SoSE). IEEE, 2020.

[7] Leger, Ludovic, Thierry Monediere, and Bernard Jecko. "Enhancement of gain and radiation bandwidth for a planar 1-D EBG antenna." IEEE Microwave and Wireless Components Letters 15.9 (2005): 573-575.

[8] Gu, Zhengwei, Hui Li, and Tian-Xi Feng. "A Low-Profile and High Front-to-back Ratio Antenna Based on Artificial Magnetic Conductor." 2025 International Conference on Microwave and Millimeter Wave Technology (ICMMT). IEEE, 2025.

[9] Boutayeb, Halim, and Tayeb A. Denidni. "Gain enhancement of a microstrip patch antenna using a cylindrical electromagnetic crystal substrate." IEEE transactions on antennas and propagation 55.11 (2007): 3140-3145.

[10] Sravya, R. Venkata, and Runa Kumari. "Gain enhancement of patch antenna using L-slotted mushroom EBG." 2018 Conference on Signal Processing And Communication Engineering Systems (SPACES). IEEE, 2018.

[11] Yang, Fan, and Yahya Rahmat-Samii. Electromagnetic band gap structures in antenna engineering. Cambridge, UK: Cambridge university press, 2009.

A 19.3–23.7-GHz RTWO with Common-Mode Resonance and Distributed Varactors

Yuan Tian, Xiaosi Zhu, Pei Qin, Quan Xue*
South China University of Technology, Guangzhou, 510641, China
Email:eeqxue@scut.edu.cn

***Abstract*—This paper presents a millimeter-wave (mmW) rotary traveling-wave oscillator (RTWO) integrating distributed varactors and common-mode high-impedance techniques to mitigate dispersion-induced flicker noise upconversion. Fabricated in TSMC 65 nm CMOS, the 16-phase RTWO achieves a tuning range from 19.3 GHz to 23.7 GHz with phase noise of −130.2 dBc/Hz at 10-MHz offset. With a power consumption of 9.6 mW, peak Figure-of-Merit (FoM), FoM$_T$ and FoM$_P$ reach 187.8, 193.9, and 199.9 dBc/Hz, respectively.**

***Index Terms*—RTWO, Distributed Varactors, tail resonators, Multiphase**

I. Introduction

Millimeter-wave (mmW) systems require local oscillators (LOs) with low phase noise (PN), wide tuning range, multiphase outputs, and low power consumption. Rotary traveling-wave oscillators (RTWOs) naturally support multiphase generation with a compact layout but hindered by two primary constraints: limited transmission-line (TL) Q degrading thermal noise performance, and dispersion-induced phase shift between harmonics that upconverts flicker noise via AM–PM conversion [1], giving rise to a prominent $1/f^3$ phase noise region.

Recent works employ distributed stubs for phase compensation or extrinsic-Q enhancement [1] [2], yet face trade-offs between tuning range and noise suppression. Kumar et al. further link flicker noise upconversion to phase mismatches and differential INL-induced zero-crossing asymmetry [3]. This work presents an RTWO integrating distributed varactors with magnetically coupled second-harmonic tail resonators. A $2f_0$-resonant common-mode high-impedance network at cross-coupled amplifier tails prevents resonator loading, preserving Q [4], while distributed tuning capacitors compensate dispersion-induced phase shifts—synergistically suppressing flicker noise upconversion without sacrificing tuning range.

Fabricated in TSMC 65 nm CMOS, the prototype generates 16-phase outputs across a tuning range of 19.3–23.7 GHz. The peak FoM, FoM$_T$, and FoM$_P$ reach 187.8, 193.9, and 199.9 dBc/Hz, respectively, demonstrating competitive performance among mm-wave RTWOs.

II. Circuit Design

A. Common-mode high-impedance in RTWO

The schematic of the proposed RTWO is shown in Fig. 1. Conventional rotary traveling-wave oscillators typically employ complementary CMOS cross-coupled pairs to compensate transmission-line losses but lack active harmonic impedance control. When MOS transistors enter the triode region, their inherent flicker noise is upconverted to the frequency offsets near the carrier via AM–PM conversion, manifesting as a prominent $1/f^3$ phase noise region.

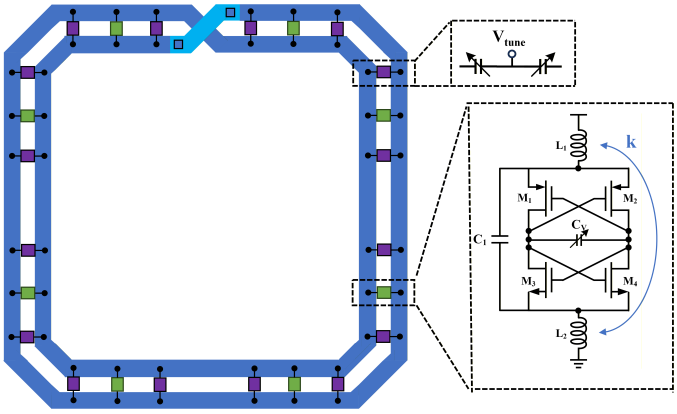


Fig. 1. Circuit schematic of the proposed RTWO.

To suppress this upconversion path, a $2f_0$-resonant common-mode high-impedance network is introduced at the tail node of each differential amplifier stage. Since the second harmonic manifests as a common-mode signal in an ideally symmetric differential pair, this network presents high impedance to $2f_0$ common-mode currents, effectively blocking their dissipation through the low-Q tail current source. Consequently, harmonic energy is confined within the high-Q main resonator, mitigating waveform asymmetry and suppressing flicker noise upconversion.

The implementation of this technique in a 16-phase RTWO faces significant layout challenges: the Möbius ring structure comprises eight differential cross-coupled cells, requiring a total of 16 tail inductors. These inductors must be compactly integrated without perturbing traveling-wave propagation while avoiding excessive area overhead. Therefore, this work adopts a scheme where two tail inductors are magnetically coupled outside the transmission line to reduce the overall footprint. By optimizing the mutual inductance M, the individual inductor value is reduced while preserving $2f_0$ resonance, thereby significantly minimizing the layout area.

Furthermore, this work adopts a topology where a tail capacitor C_1 bridges the source terminals of the NMOS and PMOS

979-8-3315-4544-4/26/$31.00 ©2026 IEEE

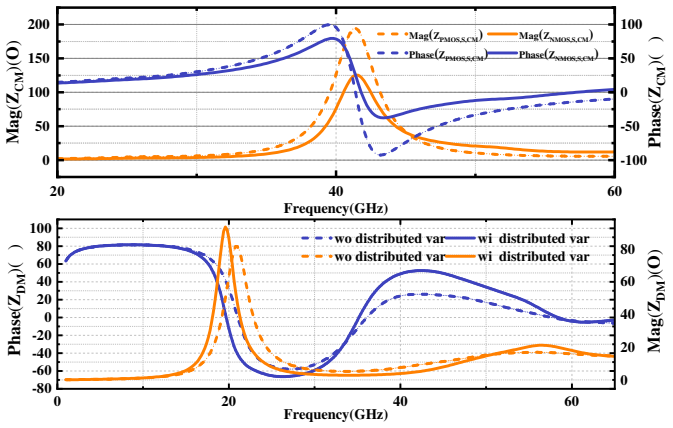


Fig. 2. (a) CM magnitude and phase curves.(b) DM magnitude and phase curves.

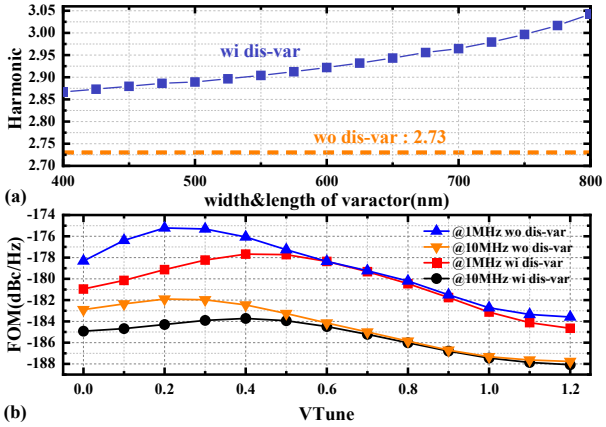


Fig. 3. (a) Harmonic Order verus the Length/Width of Distributed Varactors.(b) FOM wi/wo distributed varactors

transistors, rather than placing independent shunt capacitors across each tail inductor separately. In this configuration, the equivalent tail capacitance C_{tail} is jointly determined by C_1, the gate-source capacitances ($C_{\text{gs,n}}$, $C_{\text{gs,p}}$), and the drain-source capacitances ($C_{\text{ds,n}}$, $C_{\text{ds,p}}$), as expressed in (1).

$$C_{\text{T}} = C_1 + 2 \cdot \frac{(C_{\text{N,gs}} + C_{\text{N,ds}})(C_{\text{P,gs}} + C_{\text{P,ds}})}{(C_{\text{N,gs}} + C_{\text{N,ds}}) + (C_{\text{P,gs}} + C_{\text{P,ds}})} \tag{1}$$

Viewing from the source terminals of the PMOS and NMOS, the input impedances are respectively given by:

$$Z_{in,1} = -j\frac{\omega^2 L_1 L_2(k^2-1) + \frac{L_2}{C_T}}{\omega(L_1 + L_2 - 2k\sqrt{L_1 L_2}) - \frac{1}{\omega C_T}}, \tag{2}$$

$$Z_{in,2} = -j\frac{\omega^2 L_1 L_2(k^2-1) + \frac{L_1}{C_T}}{\omega(L_1 + L_2 - 2k\sqrt{L_1 L_2}) - \frac{1}{\omega C_T}} \tag{3}$$

where L_1 and L_2 denote the tail inductances connected to the PMOS and NMOS transistors, respectively. The common-mode resonance frequency is then derived as:

$$f_{cm} = \frac{1}{\sqrt{C_T(L_1 + L_2 - 2k\sqrt{L_1 L_2})}} \tag{4}$$

with k representing the mutual coupling coefficient between the magnetically coupled tail inductors. By contrast, the resonance frequency of the conventional shunt LC topology is:

$$f_{cm} = \frac{1}{\sqrt{C_1(L_1 - 2k\sqrt{L_1 L_2})}} \tag{5}$$

Consequently, under the identical target condition of $2f_0$ resonance, the bridging topology requires approximately half the inductance value compared to the conventional shunt configuration. This reduction significantly facilitates the layout integration of tail inductors alongside the RTWO transmission line while maintaining a compact footprint.

The two tail inductors are magnetically coupled with a positive coupling coefficient k, and their distal terminals are connected to VDD and GND, respectively. This configuration establishes a high-impedance path for common-mode signals at $2f_0$, as evidenced by the simulated common-mode impedance and phase response in Fig.2(a).

B. Distributed Varactors

Transmission line dispersion constitutes the fundamental mechanism of flicker noise upconversion in millimeter-wave rotary traveling-wave oscillators (RTWOs). To mitigate this dispersion effect, distributed varactors are placed along the transmission line. This configuration introduces additional harmonic phase shifts that scale with harmonic order. Simulations of the baseline structure without distributed varactors reveal that the resonant frequency of the third harmonic is merely 2.73 times that of the fundamental, substantially deviating from the ideal triple relationship and confirming dispersion-induced harmonic phase misalignment, as shown in Fig.2(b).

The distributed varactor length and width were subsequently swept from 300 to 900 nm. Fig. 3(a) demonstrates that the third-harmonic-to-fundamental frequency ratio increases monotonically with varactor width. At a width of 700 nm, this ratio precisely reaches 3.00, indicating complete compensation of dispersion-induced phase shift and restoration of the ideal integer-multiple frequency relationship for the third harmonic. Simulations further validate that harmonic phase compensation via distributed varactors yields significant FOM, as shown in Fig.3(b).

III. Simulation Results

Fig.4 shows the micrograph of the fabricated 16-phase RTWO. The core area occupies 0.128 mm^2. The oscillator achieves continuous tuning from 19.3 GHz to 23.7 GHz with a relative bandwidth of 20.5%. Figs.5 shows the simulated phase noise and FOM at representative frequencies, respectively. At 23.7 GHz, the measured phase noise reaches -104.8 dBc/Hz and -130.2 dBc/Hz at 1-MHz and 10-MHz offsets, corresponding to FoMs of 182.5 dBc/Hz and 187.8 dBc/Hz. The power consumption ranges from 9.6 mW to 11.7 mW from a 0.9-V supply. The measured results are summarized and compared with state-of-the-art oscillators in Table1. Compared with recently reported mm-wave multiphase oscillators, the proposed design demonstrates superior overall performance in FoM, FoM$_{\text{T}}$, and FoM$_{\text{P}}$.

TABLE I
COMPARISON WITH STATE-OF-THE-ART MMWAVE MULTI-PHASE OSCILLATORS

Reference	Topology	Process	Power (mW)	Frequency Range (GHz)	Phase Count	PN @10 MHz (dBc/Hz)	FOM @10 MHz (dBc/Hz)	FOM_T @10 MHz (dBc/Hz)	FOM_P @10 MHz (dBc/Hz)
JSSC'18 [5]	Dual RTWO	28 nm	75	16.1–19.8	16	−132.8	179.5	185.7	191.5
JSSC'18 [6]	Implicit PS	130 nm	35	74.8–79.0	8	−118.0	183.0	178.0	192.0
JSSC'21 [1]	Distribute RTWO	22 nm	20	26.2–30.0	16	−128.1	184.6	186.8	197.5
TCAS1'23 [2]	QRTWO	65 nm	5	28.3–32.9	16	−124.2	187.5	191.1	199.6
TCAS1'24 [7]	XFMR coupled	65 nm	21.8	21.2–25.5	4	−127.4	181.3	186.5	187.3
This work*	Distribute RTWO	65 nm	9.6	19.3–23.7	16	−130.2	187.8	193.9	199.9

FoM = PN - $20\log(\Delta f/f_0)$ + $10\log(P_{\text{diss}}/1\,\text{mW})$; FoM_T = FoM + $20\log(TR/10)$; FoM_P = FoM + $10\log(N_{\text{phases}})$; *Post-simulation results

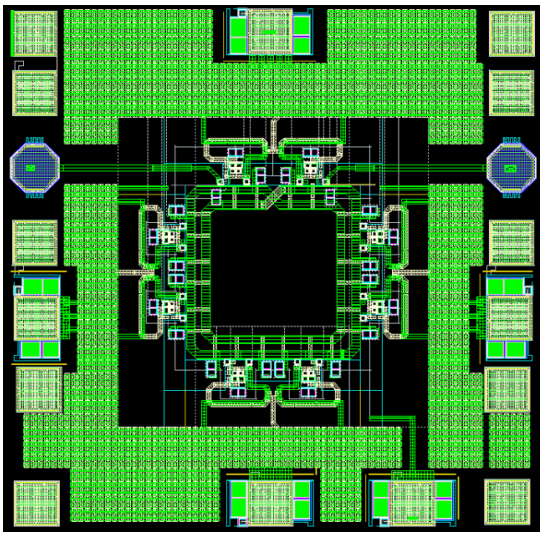


Fig. 4. Top layout of the proposed RTWO.

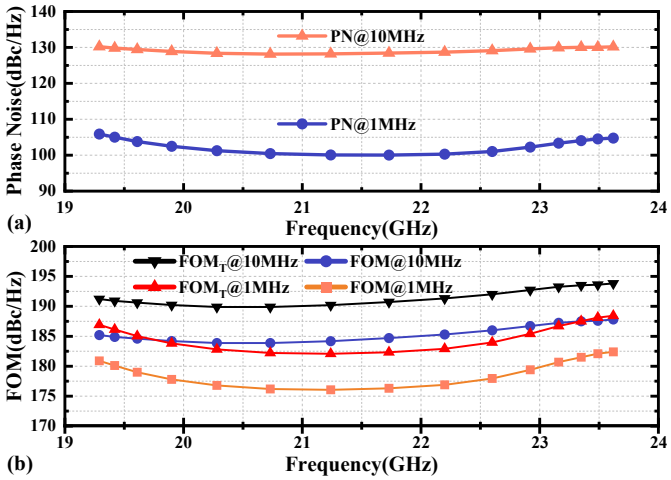


Fig. 5. Simulated (a)PN, and(b)FOM & FOMT.

IV. CONCLUSION

This paper presents a 16-phase rotary traveling-wave oscillator integrating distributed varactors and magnetically coupled second-harmonic tail resonators to suppress dispersion-induced flicker noise upconversion. Distributed tuning capacitors compensate harmonic phase shifts to restore ideal integer-multiple phase relationships, while the common-mode high-impedance tail network presents high impedance to second-harmonic common-mode currents at $2f_0$, preserving the high quality factor of the main resonator. Fabricated in TSMC 65 nm CMOS with a core area of merely 0.128 mm^2, the prototype achieves a 20.5% relative bandwidth from 19.3 GHz to 23.7 GHz, delivering −130.2 dBc/Hz phase noise at 10-MHz offset with 9.6 mW power consumption. The design demonstrates 187.8 dBc/Hz FoM, 193.9 dBc/Hz FoM_T, and 199.9 dBc/Hz FoM_P—making it highly attractive for low-phase-noise, low-power multiphase clock generation in millimeter-wave applications.

ACKNOWLEDGMENT

This work was supported in part by the National Natural Science Foundation of China under Grants 62301224, U23A20288, and 62271210, and by the Natural Science Foundation of Guangdong Province under Grants 2023B0303000008 and 2024A1515011982.*(Corresponding author: Quan Xue, Pei Qin)*

REFERENCES

[1] M. A. Shehata, M. Keaveney and R. B. Staszewski, "A Distributed Stubs Technique to Mitigate Flicker Noise Upconversion in a mm-Wave Rotary Traveling-Wave Oscillator," IEEE Journal of Solid-State Circuits, vol. 56, no. 6, pp. 1745-1760, June 2021.

[2] Z. Kang, M. Yang and L. Wu, "A 5-mW 30-GHz Quasi-Rotary Traveling-Wave Oscillator With Extrinsic-Q-Enhanced Transmission Line," in IEEE Transactions on Circuits and Systems I: Regular Papers, vol. 70, no. 10, pp. 3867-3878, Oct. 2023.

[3] S. Kumar et al., "Asymmetry Effects on Thermal and Flicker Phase Noise of Rotary Traveling-Wave Oscillators," in IEEE Transactions on Circuits and Systems II: Express Briefs, vol. 72, no. 12, pp. 1972-1976, Dec. 2025.

[4] M. Garampazzi, P. M. Mendes, N. Codega, D. Manstretta and R. Castello, "Analysis and Design of a 195.6 dBc/Hz Peak FoM P-N Class-B Oscillator With Transformer-Based Tail Filtering," in IEEE Journal of Solid-State Circuits, vol. 50, no. 7, pp. 1657-1668, July 2015.

[5] M. Vigilante and P. Reynaert, "A Coupled-RTWO-Based Subharmonic Receiver Front End for 5G E -Band Backhaul Links in 28-nm Bulk CMOS," in IEEE Journal of Solid-State Circuits, vol. 53, no. 10, pp. 2927-2938, Oct. 2018.

[6] L. Wu and Q. Xue, "E-Band Multi-Phase LC Oscillators With Rotated-Phase-Tuning Using Implicit Phase Shifters," in IEEE Journal of Solid-State Circuits, vol. 53, no. 9, pp. 2560-2571, Sept. 2018.

[7] Y. Zhao, C. Fan, J. Yin, P. -I. Mak and L. Geng, "Analysis and Design of a 21.2-to-25.5-GHz Triple-Coil Transformer-Coupled QVCO," in IEEE Transactions on Circuits and Systems I: Regular Papers, vol. 71, no. 10, pp. 4538-4549, Oct. 2024.

A 8.8-12.5 GHz Dual-Core Series Resonance VCO with 201.3-dBc/Hz FoM$_T$ in 28-nm CMOS Technology

Shuai Huang
School of Microelectronics
South China University of Technology
Guangzhou, China
202421062481@mail.scut.edu.cn

Li Gao*
School of Microelectronics
South China University of Technology
Guangzhou, China
State Key Laboratory of Integrated Chips and Systems, Shanghai, China
gaoliece@scut.edu.cn

Xiu Yin Zhang
School of Microelectronics
South China University of Technology
Guangzhou, China
eexyz@scut.edu.cn

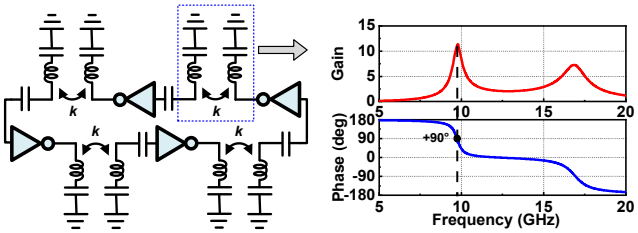
***Abstract*—This paper proposes a dual-core series resonance voltage-controlled oscillator (SRVCO) designed for wideband communication applications. The dual-core SRVCO topology is utilized to achieve a wide tuning range (TR), significantly lower the power consumption of SRVCO while still maintaining a decent PN and FoM performance. By manipulating the coupling coefficient between the primary and secondary coils of the transformer, mode ambiguity is eliminated. Implemented in TSMC 28-nm bulk CMOS process, the VCO achieves a simulated continuous oscillation frequency range of 8.8 to 12.5 GHz (tuning range of 34.7%). This SRVCO operates at a 0.7 V supply with a power consumption of 13.1 mW. The simulated results demonstrate a best phase noise of -137.8 dBc/Hz at 10-MHz offset, corresponding to a figure-of-merit (FoM) of 190.5 dBc/Hz and a FOM of tuning range (FoM$_T$) of 201.3 dBc/Hz.**

Index Terms*—Series resonance, phase noise (PN), wideband tuning range (TR), voltage-controlled oscillator (VCO)

I. Introduction

With the rapid development of technologies such as 5G communication, millimeter-wave radar, high-speed data conversion and high-performance computing, systems have put forward higher requirements for the frequency accuracy, stability and protocol compatibility. Therefore, local oscillators (LOs) are critical to achieve extremely pure signal (i.e., ultra-low phase noise (PN)) and wide frequency tuning range (FTR). A widely adopted approach for achieving wide FTR is the utilization of multi-mode techniques. However, mode-switching parallel-resonance (PR) based oscillators cannot achieve very low phase noise. Moreover, achieving wide FTR is limited by the parasitic capacitance of mode switch and systems complexity arises. Recently, the series resonance VCO(SRVCO) presents the potential to achieve low phase noise without introducing structural complexity [1]. With the same inductance and capacitance, the equivalent resistance at the parallel-LC tank is Q^2 times that of the series-LC tank. Hence, the series-LC tank possesses a phase noise reduction of 20log$Q$ [1], which means Q^2 times power consumption than that of the parallel-LC tank. However, due to the single-core structure of the series resonant oscillator [2], low phase noise is accessible but the tuning range is challenging to be further expanded. To achieve an ultra-low PN, the multi-core oscillator topology is employed [5], with high power consumption budget and limited FTR improvement. Hence, achieving very low power consumption and wide FTR simultaneously turns out a serious challenge.

This work was supported in part by Guangzhou Applied Basic Research Program under Grant 2025A04J3531, in part by open project of State Key Laboratory of Integrated Chips and Systems under Grant SKLICS-K202509.



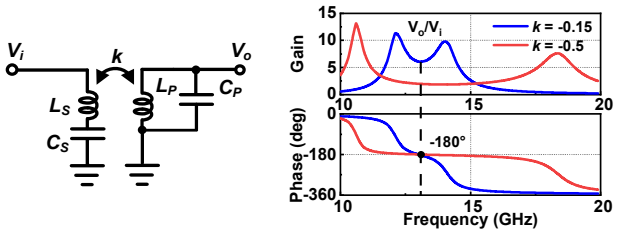
(a) (b)

Fig. 1. (a) A four-stage transformer-based SRVCO; (b) simulated transformer characteristic of gain and phase.

To optimize the tradeoff between FTR, PN and power for SRVCOs, this paper proposes a dual-core series resonance oscillator that leverages an innovative transformer-based SR tank with PR compensation to achieve a wide FTR and low power consumption. This structure allows the SRVCO to works without mode ambiguity and widens the tuning range. The proposed SRVCO is simulated in 28-nm bulk CMOS process, with the tuning range of 34.7% from 8.8 to 12.5 GHz. The best PN at a 10-MHz offset is -137.8 dBc/Hz, corresponding to a FoM of 190.5 dBc/Hz and a FoMT of 201.3 dBc/Hz with the power consumption of 13.1 mW under a 0.7V supply.

II. Design of Proposed SRVCO

Fig. 1 (a) shows the traditional transformer-based SRVCO proposed in [2], which is driven by a four-stage inverter. Fig.1(b) shows the magnitude response of a second-order series resonant transformer, which exhibits two peaks as expected. The two resonant peaks correspond to a 90° advancing or lagging phase shift in the output voltage, leading to the satisfying of the Barkhausen's criterion at both frequencies. By choosing a sufficiently strong coupling coefficient k (k = 0.5), the two



(a) (b)

Fig. 2. (a) Simplified LC SR-PR tank model; (b) simulated SR-PR tank characteristic of gain and phase.

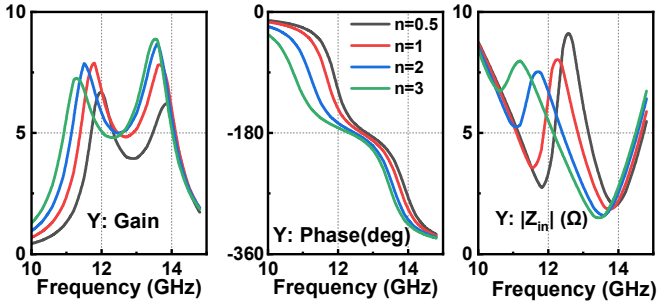


Fig. 3. Simulated frequency response curves for different n (n= L_P/L_S) of gain; phase and Z_{in}.

peaks are separated away from each other and the high frequency peak is mildly suppressed. Thus, the low resonant frequency can be used as the oscillation frequency of the four stage SRVCO. However, the problem of oscillation mode ambiguity still exists as the high resonant frequency still satisfies the oscillation condition. Moreover, as four active stages are used, it consumes high power. To significantly reduce power consumption, it is necessary to simplify the active circuit (i.e., reduce the number of inverters). Therefore, reselecting the oscillating point is necessary.

Fig. 2 (a) shows a simplified circuit model of the SR-PR transformer tank. As shown in Fig. 2 (b), compared to a strong coupled transformer, by choosing a sufficiently small coupling coefficient k, the magnitude response of the transformer at phase shift of -180° will be enhanced. By setting the corresponding frequency as the oscillating frequency, the number of inverters required to maintain oscillation will be greatly reduced to one, and only this frequency can maintain oscillation, the problem of mode ambiguity is avoided and power consumption is significantly reduced and the single-core SRVCO topology is formed. At the oscillating frequency ω_0, the input impedance Z_{in} at ω_0 can be expressed as

$$Z_{in} = R_S + k^2 Q_P \omega_0 L_S \quad (1)$$

Here, L_S is the series inductance, R_S is the loss of L_S caused by its limited quality factors and Q_P is the quality factors of the parallel inductor at ω_0. If k decreases, the input impedance drops significantly, resulting in lower phase noise and higher power consumption. The oscillating gain $|A_v|$ at ω_0 can be expressed as

$$|A_v| = \frac{\sqrt{L_P/L_S}\,Q_S Q_P}{\frac{1}{k} + kQ_S Q_P} \quad (2)$$

where L_P is the parallel inductance, Q_S is the quality factors of L_S at ω_0, respectively. When k is sufficiently small, A_V will

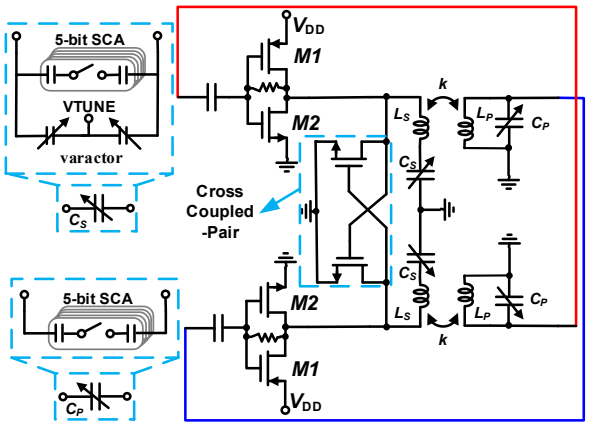
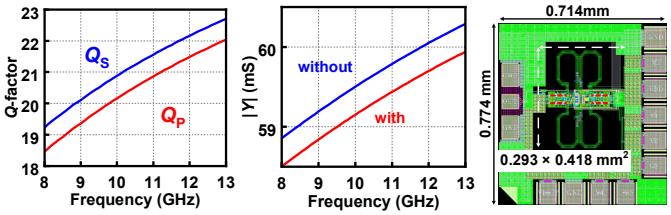


Fig. 4. Schematic of proposed SRVCO.



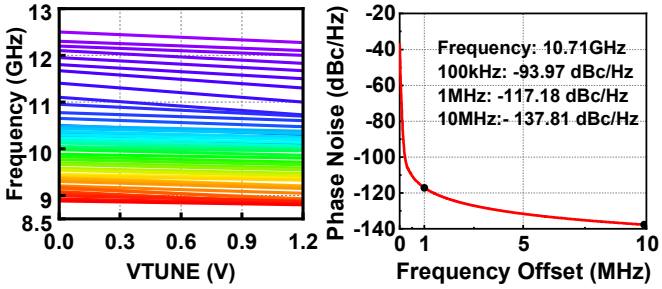
(a) (b) (c)

Fig. 5. (a) Simulated Q-factor of inductors; (b) simulated output characteristic of active circuit (with or without a cross coupled-pair); (c)the complete layout.

decrease, resulting in phase noise degradation. Therefore, an appropriate coupling coefficient k (k = -0.15) should be set to maintain oscillation and optimize the tradeoff between phase noise performance and power consumption.

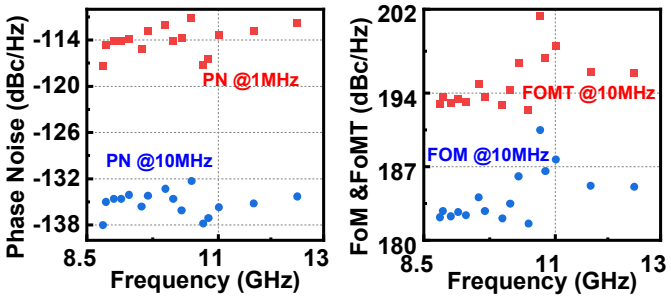
Since k is chosen as -0.15 for analysis, to further reduce phase noise, we set the series tank and the parallel tank to oscillate at the same frequency. By varying the ratio n ($n = L_P/L_S$, L_S=300 pH, $Q_P = Q_S$ =20, $C_P = C_S$ =500 fF) and maintaining the same oscillating frequency, Fig. 3 illustrates the frequency response characteristic of the SR-PR tank. It is evident that the input impedance and the voltage gain at the oscillating frequency will increase first and then decrease when n increases. A relatively large ratio n of 2 to 3 has been proven to be applicable for achieving ultra-low phase noise [4]-[6], but it simultaneously leads to high power consumption and is more sensitive to the loss of the switching capacitor arrays, resulting in a limited bandwidth. As mentioned above, a large voltage gain and a small input impedance will increase the output voltage and the DC current of MOSFETs, which leads to a descended phase noise and higher power consumption. Moreover, an appropriate Z_{in} can suppress the performance degradation caused by the loss of switching capacitance arrays, which is conducive to a wider FTR.

Fig. 4 shows the schematic of proposed SRVCO, which is composed of two cascaded single-core SRVCOs. This dual-core structure is designed to ensure that the oscillator operate normally under low power consumption and maintain the consistent PN performance over FTR. Considering the implementation of inductors and the performance optimization of the proposed SRVCO, n =1 (i.e., $L_S = L_P$ =300pH) is chosen to achieve the balance between phase noise performance and power consumption. As shown in equation (1), the Q of the inductors affect the input impedance, which need to be designed



(a) (b)

Fig. 6. (a) Simulated oscillating frequency range; (b) simulated phase noise at 10.71GHz.



(a) (b)

Fig. 7. (a) Summarized simulated phase noise; (b) summarized simulated FoM and FoM_T at 10-MHz offset frequency.

carefully. Fig. 5(a) shows the *Q*-factor of inductors over the FTR, with an exceptional low loss and symmetrical characteristic. To meet the Barkhausen's criterion, a two-stage P-N inverter with M1/2 width of 336µm/168µm is utilized to obtain a small R_{on} that maintains oscillation while reducing the influence of active noise. As shown in Fig. 5 (b), an appropriate -*G*m (i.e., a cross coupled-pair) was introduced to provide greater negative resistance seen by the resonance without introducing extra DC power consumption (< 0.1 mW), while compensating for the loss of the switching capacitor arrays.

III. Simulation Results

The proposed SRVCO is implemented in TSMC 28-nm bulk CMOS process. Fig. 5(c) shows its complete layout with an area of 0.55mm^2. All transformers and important connects are EM simulated by EMX. The active transistors and caps/resistors are extracted by Calibre. The SRVCO consumes the DC power of 13.1 mW from a 0.7 V supply.

The simulated oscillating frequency of each state are shown in Fig. 6(a). The results exhibit a continuous frequency range from 8.8 to 12.5 GHz (34.7% tuning range) and frequency overlap is observed between adjacent mode. The PN performance of the whole band is summarized as Fig. 7(a). The PN at 10-MHz offset ranges from -132 to -137.8 dBc/Hz, with a best PN performance of -137.8 dBc/Hz at 10.71GHz, as shown in Fig. 6(b). Fig. 7(b) shows the best FoM at 10-MHz Offset is 190.5 dBc/Hz, corresponding to the peak FoM_T of 201.3 dBc/Hz at 10.71 GHz.

The detailed comparison of other recently reported VCOs is shown in Table I. The proposed design achieves low power consumption, with a wide FTR, resulting in a competitive FoM_T of 201.3 dBc/Hz.

TABLE I. Comparison with Other VCOs

Ref.	[4]	[5]	[6]	[7]	This work
Technology	65-nm CMOS	65-nm CMOS	65-nm CMOS	28-nm CMOS	**28-nm CMOS**
f (GHz)	10.3 to 11.1	11 to 12.2	7.65 to 9.135	8.1 to 9.9	**8.8 to 12.5**
Tuning Range (%)	7.4	10.3	17.7	20	**34.7**
Power (mW)	224 to 330	1200	159 to 164	33.5 to 36.3	**13.1**
PN@10MHz (dBc/Hz)	-151.9	-155.4	-152.9	-146*	**-137.8**
FoM @10MHz (dBc/Hz)	187.26	188.27	190	191.4	**190.5**
FoM_T @10MHz (dBc/Hz)	184.6	188.5	195	197.4	**201.3**
Area (mm^2)	0.45	3.4	0.192	0.19	**0.55**

FoM= -PN+ $20\log_{10}(f_o/\Delta f)$- $10\log_{10}(P_{DC}/1mW)$; FoM_T= FoM+ $20\log_{10}(TR/10)$; *Read from plot

IV. Conclusion

In this paper, a dual-core transformer-based SRVCO is proposed. The PR tank is introduced and the coupling coefficient *k* is reselected to better adjust the phase shift of the SR-PR resonance. As a result, a 34.7% tuning range is achieved with power consumption of 13.1 mW. The low power consumption, wide FTR and decent phase noise makes it suitable for high quality communication.

References

[1] F. Pepe, A. Bevilacqua and P. Andreani, "On the remarkable performance of the series-resonance CMOS oscillator," *IEEE Trans. Circuits Syst. I: Reg. Papers*, vol. 65, no. 2, pp. 531-542, Feb. 2018.

[2] S. Zhang et al., "A transformer-based series-resonance CMOS VCO," *IEEE J. Solid-State Circuits*, vol. 60, no. 2, pp. 529–542, Feb. 2025

[3] A. Franceschin, D. Riccardi and A. Mazzanti, "Series-resonance BiCMOS VCO with phase noise of -138dBc/Hz at 1MHz offset from 10GHz and -190dBc/Hz FoM," in *IEEE International Solid-State Circuits Conference (ISSCC)*, San Francisco, CA, USA, 2022, pp. 1-3.

[4] S. Zhang et al., "A 100 MHz-reference, 10.3-to-11.1 GHz quadrature PLL with 33.7-fsrms jitter and -83.9 dBc reference spur level using a -130.8 dBc/Hz phase noise at 1MHz offset folded series-resonance VCO in 65nm CMOS," in *Proc. IEEE Custom Integr. Circuits Conf. (CICC)*, San Antonio, TX, USA, 2023, pp. 1-2.

[5] S. Zhang et al., "An 11GHz 8-core series resonance CMOS VCO with scalable ring-coupling scheme achieving phase noise of -136.8dBc/Hz at 1 MHz offset," in *Proc. IEEE Radio Freq. Integr. Circuits (RFIC)*, pp. 95–98, Jun. 2024.

[6] J. Guo et al., "A differential series-resonance CMOS VCO with pole-convergence technique achieving 202.1 dBc/Hz FoM_{TA} at 10MHz offset," *2025 IEEE International Solid-State Circuits Conference (ISSCC)*, San Francisco, CA, USA, 2025, pp. 332-334.

[7] J. Chen, K. Xu, T. Siriburanon and R. B. Staszewski, "An 8.1-to-9.9GHz single-core pseudo-series-resonance oscillator achieving -128.7dBc/Hz PN at 1MHz," *2025 IEEE International Solid-State Circuits Conference (ISSCC)*, San Francisco, CA, USA, 2025, pp. 1-3.

[8] O. El-Aassar and G. M. Rebeiz, "Octave-tuning dual-core folded VCO leveraging a triple-mode switch-less tertiary magnetic loop," *IEEE J. Solid-State Circuits*, vol. 56, no. 5, pp. 1475-1486, May 2021.

[9] L. Tomasin et al., "A 12-GHz reconfigurable multicore CMOS DCO, with a time-variant analysis of the impact of reconfiguration switches on phase noise," *IEEE J. Solid-State Circuits*, vol. 57, no. 9, pp. 2802–2811, Sep. 2022.

Super-Mode-Group Based Reduced-Order Analysis of Multi-Mode Antenna Decoupling

Yuqi Wang[1], Hao Jiang[2], Yinglu Wan[3]
[1]*School of Electronic and Information Engineering*, *South China University of Technology*, Guangzhou, China
[2]*Department of Electrical Engineering*, *City University of Hong Kong*, Hong Kong, China
[3]*School of Computer and Electronic Information*, *Guangxi University*, Nanning, China
[1]eeyqwang@mail.scut.edu.cn

***Abstract*—Broadband and multiband antenna decoupling is often associated with the joint contribution of multiple characteristic modes. This paper presents a super-mode-group (SMG) framework for reduced-order analysis of symmetric multi-mode antennas. Starting from the characteristic-mode expansion of the port admittance matrix, the relevant modes are grouped into odd and even groups according to structural symmetry. Two grouped descriptors, namely the total excitation weight and the weighted modal eigenvalue, are introduced to describe the overall contribution of each group. The formulation shows that decoupling is favored when the odd and even groups remain balanced in grouped-power/conductance contribution and synchronized in near-resonant behavior. Numerical parametric results support this interpretation. The framework provides a reduced-order view for symmetric multi-mode antenna analysis.**

***Index Terms*—Antenna decoupling, characteristic modes, odd and even modes, multi-port antennas, symmetry.**

I. Introduction

Broadband and multiband decoupling remains an important issue in compact multi-mode antennas [1]–[5]. For symmetric structures, odd/even-mode decomposition gives an exact network condition for matching and isolation. However, when several characteristic modes participate simultaneously, a direct mode-by-mode interpretation becomes cumbersome and does not clearly indicate which grouped modal interactions dominate the response.

Characteristic mode theory describes the port response as the superposition of structure-dependent eigencurrents weighted by their modal contributions [6]–[8]. This paper develops a super-mode-group (SMG) framework for symmetric multi-mode antennas. The participating modes are grouped into odd and even groups, and two grouped descriptors are introduced to describe their collective contribution. The resulting formulation provides a compact physical interpretation of multi-mode decoupling while remaining consistent with the exact odd/even admittance criterion.

The present work focuses on the reduced-order formulation and its parametric interpretation. In practical antenna design, the proposed SMG descriptors can serve as intermediate indicators before detailed modal and geometry optimization.

II. Admittance-Based Modal Representation

For a multi-port antenna, the conducting-surface current can be expanded as a superposition of orthogonal characteristic modes [6]. For port p and mode n, the modal excitation coefficient (MEC) is [9]

$$V_{pn} = \oint_S \mathbf{E}_p^{\mathrm{inc}} \cdot \mathbf{J}_n \, dS \tag{1}$$

where $\mathbf{E}_p^{\mathrm{inc}}$ is the normalized incident field at port p, $\mathbf{J}_n$ is the normalized current of the nth characteristic mode, and S is the metallic surface supporting the characteristic current.

Under the usual power normalization, the corresponding modal weighting coefficient (MWC) is

$$I_{pn} = \frac{V_{pn}}{1 + j\lambda_n} \tag{2}$$

where λ_n is the eigenvalue of the nth mode. Under modal orthogonality, the generalized admittance between ports p and q is [8]

$$Y_{pq} = \sum_{n=1}^{N} \frac{V_{pn} V_{qn}}{1 + j\lambda_n}. \tag{3}$$

Equation (3) shows that the port response is jointly determined by all participating modes. For a symmetric two-port antenna, the exact matching and decoupling condition is [10], [11]

$$Y_{in}^{odd}(\omega) = Y_{in}^{even}(\omega) = Y_0 \tag{4}$$

where Y_{in}^{odd} and Y_{in}^{even} are the odd- and even-mode input admittances, and Y_0 is the reference port admittance. The purpose here is not to replace (4), but to reinterpret how it may be approached in a multi-mode system.

III. Super-Mode-Group Formulation

Consider a symmetric two-port antenna in which the two ports are mirror images with respect to the structural symmetry plane. The dominant modes can then be divided into an odd group $\mathcal{O}$ and an even group $\mathcal{E}$, as illustrated in Fig. 1. By symmetry, the MECs satisfy

$$V_{pn} = s_n V_{qn}, \qquad s_n = \begin{cases} -1, & n \in \mathcal{O} \\ 1, & n \in \mathcal{E}. \end{cases} \tag{5}$$

Substituting (5) into (3) gives

$$Y_{pp} = \sum_{n \in \mathcal{E}} \frac{|V_{pn}|^2}{1 + j\lambda_n} + \sum_{n \in \mathcal{O}} \frac{|V_{pn}|^2}{1 + j\lambda_n} \tag{6}$$

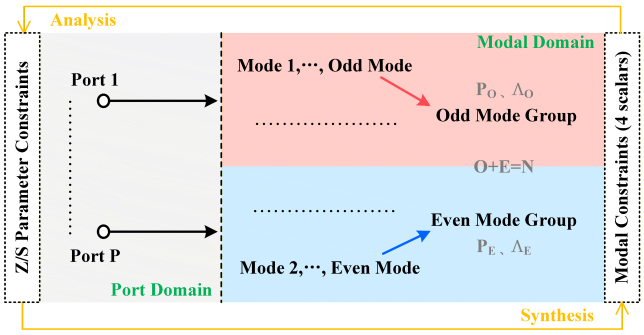


Fig. 1: Reduced-order modal analysis and synthesis framework for symmetric multi-port antennas.

$$Y_{pq} = \sum_{n\in\mathcal{E}} \frac{|V_{pn}|^2}{1+j\lambda_n} - \sum_{n\in\mathcal{O}} \frac{|V_{pn}|^2}{1+j\lambda_n}. \tag{7}$$

To obtain a reduced-order description, define the total excitation weights

$$P_{\mathcal{E}} = \sum_{n\in\mathcal{E}} |V_{pn}|^2, \qquad P_{\mathcal{O}} = \sum_{n\in\mathcal{O}} |V_{pn}|^2 \tag{8}$$

and the weighted eigenvalues

$$\Lambda_{\mathcal{E}} = \frac{\sum_{n\in\mathcal{E}} \lambda_n |V_{pn}|^2}{P_{\mathcal{E}}}, \qquad \Lambda_{\mathcal{O}} = \frac{\sum_{n\in\mathcal{O}} \lambda_n |V_{pn}|^2}{P_{\mathcal{O}}}. \tag{9}$$

In general, the exact grouped admittances in (6) and (7) cannot be rewritten exactly using only $P_{\mathcal{E}/\mathcal{O}}$ and $\Lambda_{\mathcal{E}/\mathcal{O}}$ since

$$\sum_n \frac{|V_{pn}|^2}{1+j\lambda_n} \neq \frac{\sum_n |V_{pn}|^2}{1+j\left(\sum_n \lambda_n |V_{pn}|^2 / \sum_n |V_{pn}|^2\right)} \tag{10}$$

The SMG description is a reduced-order approximation rather than an exact regrouping identity. With (8) and (9), (6) and (7) are approximated as

$$Y_{pp} \approx \frac{P_{\mathcal{E}}}{1+j\Lambda_{\mathcal{E}}} + \frac{P_{\mathcal{O}}}{1+j\Lambda_{\mathcal{O}}} \tag{11}$$

$$Y_{pq} \approx \frac{P_{\mathcal{E}}}{1+j\Lambda_{\mathcal{E}}} - \frac{P_{\mathcal{O}}}{1+j\Lambda_{\mathcal{O}}}. \tag{12}$$

These expressions are useful when the dominant weighted detuning states within each group are not excessively spread. A simple measure of the approximation error is

$$\varepsilon_{\mathcal{G}} = \frac{\left|\sum_{n\in\mathcal{G}} \frac{|V_{pn}|^2}{1+j\lambda_n} - \frac{P_{\mathcal{G}}}{1+j\Lambda_{\mathcal{G}}}\right|}{\left|\sum_{n\in\mathcal{G}} \frac{|V_{pn}|^2}{1+j\lambda_n}\right|}, \qquad \mathcal{G}\in\{\mathcal{E},\mathcal{O}\} \tag{13}$$

with the corresponding weighted detuning variance

$$\sigma^2_{\lambda,\mathcal{G}} = \frac{\sum_{n\in\mathcal{G}} |V_{pn}|^2 (\lambda_n - \Lambda_{\mathcal{G}})^2}{\sum_{n\in\mathcal{G}} |V_{pn}|^2}. \tag{14}$$

A small $\varepsilon_{\mathcal{G}}$, or equivalently a limited $\sigma_{\lambda,\mathcal{G}}$, indicates that the modes in the same group can be approximately described by one effective detuning factor. In practical full-wave analysis, the MWCs are first used to identify the modes that effectively participate in the operating band, while modes with negligible contribution can be excluded. The selected modes are then classified into odd and even groups according to structural symmetry. For each group, $P_{\mathcal{G}}$ and $\Lambda_{\mathcal{G}}$ are calculated from the corresponding MECs and eigenvalues, and $\sigma_{\lambda,\mathcal{G}}$ is used to check the eigenvalue spread within the group. A small $\sigma_{\lambda,\mathcal{G}}$ means that the grouped average detuning is meaningful, whereas a large value means that the modes in the group are too dispersed in detuning and should not be over-interpreted as a single SMG.

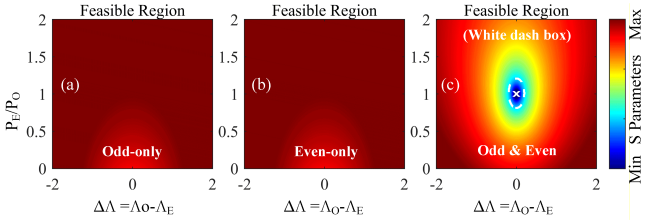


Fig. 2: Feasible regions predicted by the SMG model under different modal participation strategies. The color map denotes the minimum S-parameter level, and the dashed contour marks the overlap satisfying $|S_{11}| < -10$ dB and $|S_{21}| < -20$ dB. (a) Odd-group-only case. (b) Even-group-only case. (c) Cooperative odd/even-group case.

For matching and decoupling, the port self-admittance should approach the reference value while the mutual admittance should vanish. Substituting (11) and (12) into these port conditions gives, for the ideal near-resonant case,

$$P_{\mathcal{E}} = P_{\mathcal{O}} = \frac{Y_0}{2} \tag{15}$$

$$\Lambda_{\mathcal{E}} = \Lambda_{\mathcal{O}} = 0. \tag{16}$$

Equation (15) indicates that the odd and even groups should contribute balanced grouped power near resonance, whereas (16) requires synchronized average detuning. Together, they provide a reduced-order interpretation of (4).

IV. Numerical Parametric Analysis

Using (11) and (12), the odd- and even-group parameters are mapped to approximate port responses. The purpose is to reveal the dominant grouped trends rather than replace the exact modal criterion.

We first compare three modal strategies: odd-group only, even-group only, and cooperative odd/even grouping. The engineering targets are defined as $|S_{11}| < -10$ dB and $|S_{21}| < -20$ dB. As shown in Fig. 2, no clear overlap region is obtained when only one group participates. When both groups are included, a feasible region appears around $\Delta\Lambda = \Lambda_{\mathcal{O}} - \Lambda_{\mathcal{E}} = 0$ and $P_{\mathcal{E}}/P_{\mathcal{O}} = 1$, with the center corresponding to (15) and (16). This indicates that odd/even cooperation is required for simultaneously approaching matching and decoupling.

Fig. 3 shows the grouped sensitivity. In the balanced near-resonant case, the feasible region is centered near

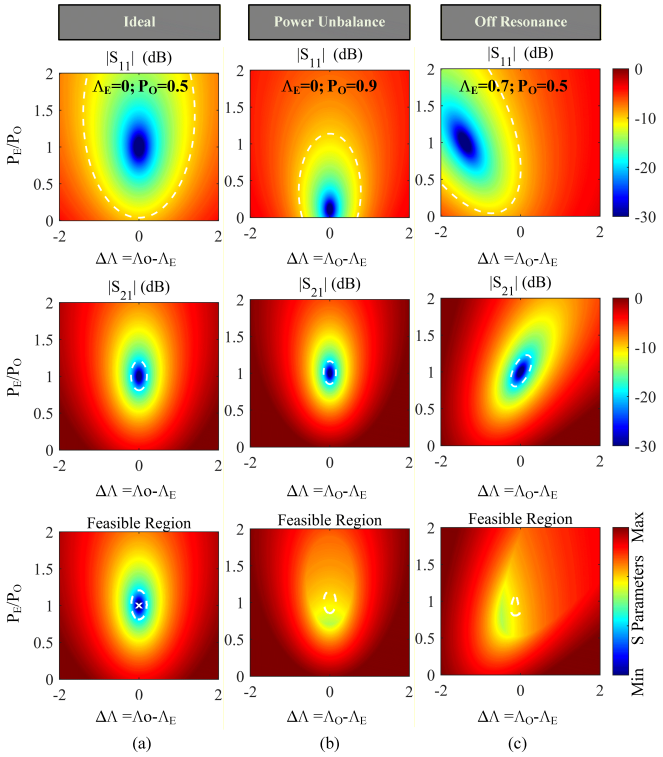


Fig. 3: SMG-predicted sensitivity to grouped-power balance and grouped-detuning synchronization. Top row: $|S_{11}|$. Middle row: $|S_{21}|$. Bottom row: feasible overlap satisfying $|S_{11}| < -10$ dB and $|S_{21}| < -20$ dB. (a) Balanced case. (b) Power/conductance imbalance. (c) Detuning mismatch.

equal grouped contribution and synchronized detuning. In the grouped power/conductance imbalance case, the feasible region shrinks mainly along the matching dimension. Here, "power imbalance" refers to unequal total grouped participation, while "conductance imbalance" refers to unequal real-admittance contribution near resonance; the two are equivalent in the present reduced-order model. In the grouped detuning-mismatch case, the feasible region shifts and contracts in both dimensions, showing that matching and decoupling both depend on synchronized near-resonant evolution of the groups.

A global view is given in Fig. 4. The valid solutions cluster around the balanced and synchronized region described by (15) and (16). This confirms that the reduced-order decoupling tendency is mainly controlled by grouped balance and grouped detuning synchronization. Thus, the SMG framework can be used to examine the grouped modal condition before detailed modal tuning and geometry optimization.

V. Conclusion

An SMG-based reduced-order framework has been proposed for the decoupling analysis of symmetric multi-mode antennas. By regrouping the participating characteristic modes into odd and even groups, the multi-mode problem is reduced to a compact grouped description. The results show that decoupling is favored when the two groups have balanced

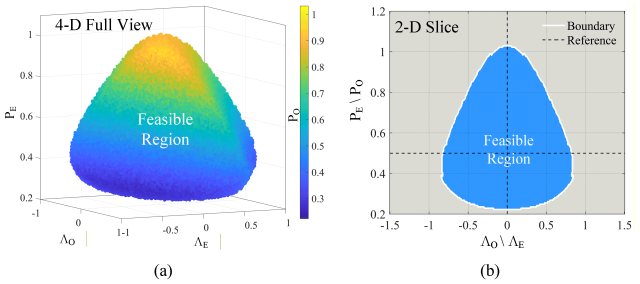


Fig. 4: Global feasible SMG region satisfying $|S_{11}| < -10$ dB and $|S_{21}| < -20$ dB under mode grouping. (a) Four-dimensional view. (b) Two-dimensional slice.

grouped contribution and synchronized detuning. The framework provides a concise physical interpretation consistent with the exact odd/even admittance criterion.

References

[1] N. Peitzmeier and D. Manteuffel, "Upper bounds and design guidelines for realizing uncorrelated ports on multimode antennas based on symmetry analysis of characteristic modes," *IEEE Trans. Antennas Propag.*, vol. 67, no. 6, pp. 3902–3914, Jun. 2019.

[2] L. Sun, Y. Li, and Z. Zhang, "Decoupling between extremely closely spaced patch antennas by mode cancellation method," *IEEE Trans. Antennas Propag.*, vol. 69, no. 6, pp. 3074–3083, Jun. 2021.

[3] Y. Wang, Q. Xue, and H. Xie, "Wideband decoupled asynchronously coupled patch antennas," *IEEE Trans. Antennas Propag.*, vol. 73, no. 2, pp. 906–919, Feb. 2025.

[4] Y. Wang, Q. Xue, H. Xie, Y. Wan, and X. Liu, "Modal-driven decoupling and modal-mapping beamforming antennas," *IEEE Trans. Antennas Propag.*, vol. 73, no. 12, pp. 10847–10852, Dec. 2025.

[5] Y. Wang, Q. Xue, and Y. Wan, "Element-level polarization-switchable beamforming empowering three-stage phased array antennas," *IEEE Trans. Antennas Propag.*, vol. 73, no. 6, pp. 3680–3691, Jun. 2025, doi: 10.1109/TAP.2025.3564735.

[6] R. F. Harrington and J. R. Mautz, "Theory of characteristic modes for conducting bodies," *IEEE Trans. Antennas Propag.*, vol. 19, no. 5, pp. 622–628, Sep. 1971.

[7] Y. Chen and C.-F. Wang, *Characteristic Modes: Theory and Applications in Antenna Engineering*. Hoboken, NJ, USA: Wiley, 2015.

[8] M. Cabedo-Fabrés, "Systematic design of antennas using the theory of characteristic modes," Ph.D. dissertation, Universidad Politécnica de Valencia, Valencia, Spain, 2008.

[9] V. H. Rumsey, "Reaction concept in electromagnetic theory," *Phys. Rev.*, vol. 94, no. 6, pp. 1483–1491, Jun. 1954.

[10] C. A. Balanis, *Antenna Theory: Analysis and Design*, 2nd ed. New York, NY, USA: Wiley, 1997.

[11] D. M. Pozar, *Microwave Engineering*, 4th ed. Hoboken, NJ, USA: Wiley, 2011.

A V-band LNA with Pole-Tuning and g_m-boosting Technique in 40-nm CMOS

Xiangjie Li, Hetai Zhang, Pei Qin, Quan Xue*
Guangdong Provincial Key Laboratory of Millimeter-Wave and Terahertz, School of Electronic and Information Engineering
South China University of Technology, Guangzhou, 510641, China
Email: eeqxue@scut.edu.cn

***Abstract*—For millimeter-wave applications in short-range wireless communication, this paper proposes an LNA based on a three-stage cascode. To expand the input-matching bandwidth, the input-matching network introduces another pole at a higher frequency, thereby achieving a wider S_{11} bandwidth. Moreover, two transformers were used to connect the transistor drain in the previous stage to the transistor source in the subsequent stage. This enables the transistor to exhibit enhanced conductivity in the latter stage, thereby increasing its gain. The increase in gain suppresses noise. Under a 1 V power supply, the power consumption is 17.6 mW. This low-noise amplifier has a peak gain of 21.1 dB at 61.1 GHz within a 3-dB bandwidth of 45.7–68.9 GHz and achieves the lowest noise of 3.67 dB at 55.9 GHz. Meanwhile, this LNA is unconditionally stable across the entire frequency range. The area of this LNA is 0.17 mm^2.**

***Index Terms*—CMOS, LNA, pole-tuning, transformer, gm-boosting**

I. Introduction

As the primary active stage in a receiver front-end, the Low-Noise Amplifier (LNA) must provide sufficient power gain to suppress downstream noise while establishing a minimal noise figure (NF) for the entire system. At V-band frequencies, however, the intrinsic gain of CMOS devices degrades significantly, while pervasive interconnect parasitics further compromise the gain-bandwidth trade-off and stability. To mitigate these constraints, transformer-based feedback and dual-resonant networks have been reported to broaden the operating bandwidth [1]. Moreover, integrating transformer-based matching with pole-tuning techniques provides a robust mechanism for optimizing the gain-bandwidth product and mitigating gate-induced noise [2]. For millimeter-wave applications, leveraging transformer-assisted G_m-boosting alongside independent pole control is instrumental for achieving flat, wideband gain and superior noise performance [3].

In this work, we present a high-gain wideband V-band LNA implemented in 40-nm CMOS. To counteract the high-frequency gain roll-off and enhance sensitivity, a three-stage cascaded cascode architecture is employed, incorporating transformer-based G_m-boosting and optimized inter-stage matching. This topology enables precise pole-tuning to ensure a flat frequency response across the V-band. The proposed LNA, shown in Fig.1, achieves a peak gain of 21.1 dB and a minimum NF of 3.67 dB. It exhibits a 3-dB bandwidth of 23.2 GHz (45.7–68.9 GHz), demonstrating its suitability for next-generation V-band wireless communication.

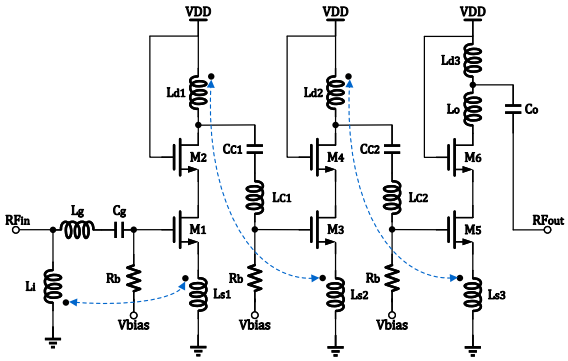


Fig. 1. Schematic of the proposed LNA

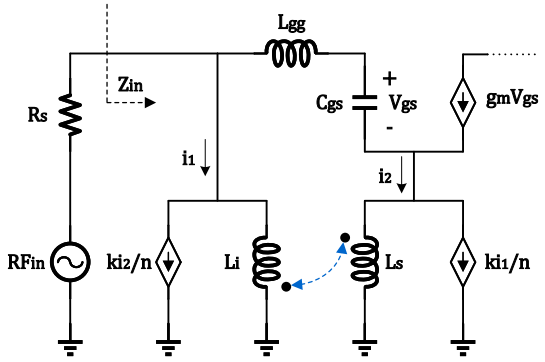


Fig. 2. The small-signal diagram of the input network

II. Theoretical Analysis Of The LNA

A. Wideband Input Matching

In a conventional common-source (CS) topology, the input impedance is predominantly capacitive at millimeter-wave frequencies, lacking the necessary real part to achieve a broadband match to 50 Ω. Consequently, extending the bandwidth requires the synthesis of a higher-order matching network to compensate for the frequency-dependent nature of the transistor's input. Inspired by [2], the proposed LNA incorporates a transformer-based input network that introduces an additional high-frequency pole through L_{gg}, effectively creating a dual-resonance response. By leveraging leakage inductance and coupling, a stable resistive component is synthesized at the gate terminal over a wide frequency range. This approach not only facilitates broadband S_{11} but also optimizes noise matching (Γ_{opt}), ensuring consistent performance across the V-band.

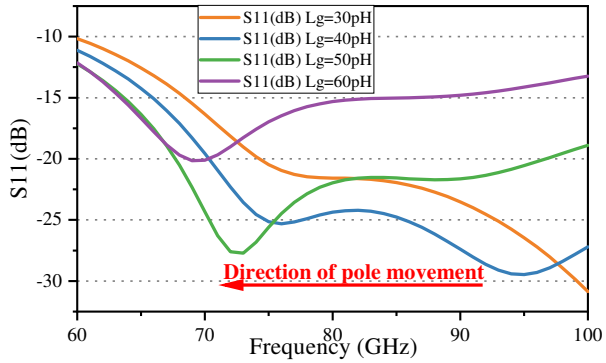


Fig. 3. S_{11} as L_{gg} varies from 30 to 60 pH

Applying KVL/KCL to the small-signal model in Fig.2 and neglecting second-order effects, the input impedance $Z_{\text{in}}(s)$ can be derived as a function of component parameters and the transformer turns ratio ($n_1 = \sqrt{L_i/L_s}$).

$$Z_{\text{in}}(s) = \frac{s^3 L_i L_{gg} C_{gs} + s^2 L_i L_s g_m (1+k) + s L_i}{s^2 C_{gs}(L_i + L_{gg}) + s g_m L_s (1+k) + 1} \tag{1}$$

Here, g_m and C_{gs} represent the transconductance of transistor M_1 and the parasitic gate-source capacitance, respectively. At the same time, we can also obtain the expressions for the real parts of the input impedance.

$$\text{Re}\{Z_{\text{in}}\} = \frac{\omega^2 g_m L_2 L_g \left[k - \omega^2 C_{gs}\left(k L_{gg} - L_s(1-k^2)\right)\right]}{\left(1 - \omega^2 C_{gs} L_1\right)^2 + \left(\omega g_m L_2\right)^2} \tag{2}$$

Where:

$$L_1 = L_i + L_{gg}, \quad L_2 = L_s(1+k) \tag{3}$$

According to $Z_{\text{in}}(s)$, the poles of the input-matching network can be obtained as:

$$s_{p1,p2} = \frac{-g_m L_2 \pm \sqrt{(g_m L_2)^2 - 4 L_1 C_{gs}}}{2 L_1 C_{gs}} \tag{4}$$

Analysis of the pole expressions reveals that L_{gg} in (2) more significantly influences the input impedance than the numerator terms. Increasing L_{gg} shifts the pole frequencies downward, facilitating a second resonance peak in the impedance profile. This pole migration directly determines the secondary S_{11} notch; thus, by optimizing L_i and L_s, a dual-resonance characteristic is synthesized for broadband matching. Fig.3 illustrates S_{11} trajectories versus L_{gg} with L_i and L_s fixed at 175 pH and 100 pH.

Furthermore, ensuring a positive real part of the input impedance ($\text{Re}\{Z_{\text{in}}\} > 0$) is a fundamental requirement for maintaining input-stage stability [4]. However, (4) implies that an excessively large L_{gg} may drive $\text{Re}\{Z_{\text{in}}\}$ into a negative regime, compromising the stability margin. Consequently, the selection of L_{gg} involves a fundamental trade-off between broadband coverage and robust stability.

To maintain a safe operating region, L_{gg} must satisfy the following boundary condition:

$$L_{gg} < \frac{1+k^2}{k} n_1 L_s \tag{5}$$

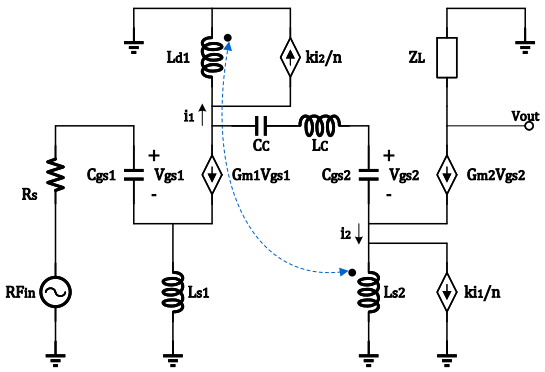


Fig. 4. Equivalent small-signal model of the proposed topology

B. G_m-Boosting Technique

To mitigate the Miller effect at high frequencies, a cascode topology is adopted. Considering the finite output resistance (r_{o1}) of the input transistor, the equivalent transconductance (G_m) is:

$$G_m = \frac{(g_{m2} + g_{mb2}) r_{o1}}{(g_{m2} + g_{mb2}) r_{o1} + 1} \cdot g_{m1} \tag{6}$$

To optimize the trade-off between input matching and gain, source-degeneration inductors are typically employed [3]. In this design, a transformer-based coupling technique replaces conventional discrete inductors, thereby enhancing voltage gain while reducing silicon area. Based on the small-signal model in Fig.4, the equivalent inductances for the interstage and source branches, accounting for mutual coupling, are expressed as:

$$L_{d1,\text{eq}} = L_{d1}\left(1 + \frac{k}{n_2} \cdot \frac{i_2}{i_1}\right) \tag{7}$$

$$L_{s2,\text{eq}} = L_{s2}\left(1 + n_2 k \cdot \frac{i_1}{i_2}\right) \tag{8}$$

The turns ratio of the inter-stage transformer is defined as $n_2 = \sqrt{L_{d1}/L_{s2}}$, where L_{d1} and L_{s2} denote the drain inductance of the previous stage and the source inductance of the next stage, respectively. To evaluate the impact of transformer coupling on the stage's transconductance, the effective transconductance ($G_{m,\text{eff}}$) is derived based on the small-signal equivalent circuit in Fig.4.

In the absence of magnetic coupling ($k = 0$), the $G_{m,\text{eff}}$ suffers from source degeneration and is expressed as:

$$G_{m,\text{eff}} = \frac{G_{m2}}{1 + j\omega L_{s2}(G_{m2} + j\omega C_{gs2})} \tag{9}$$

When the mutual inductance is considered ($k \neq 0$), an additional feedback path is established. By defining a feedback coefficient $\beta = i_1/V_{gs2}$, which characterizes the current distribution between the stages, the augmented $G_{m,\text{eff}}$ is given by:

$$G_{m,\text{eff}} = \frac{G_{m2}}{1 + j\omega L_{s2}(G_{m2} + j\omega C_{gs2}) + j\omega L_{s2} \cdot k\left(n_2 + \frac{1}{n_2}\right)\beta} \tag{10}$$

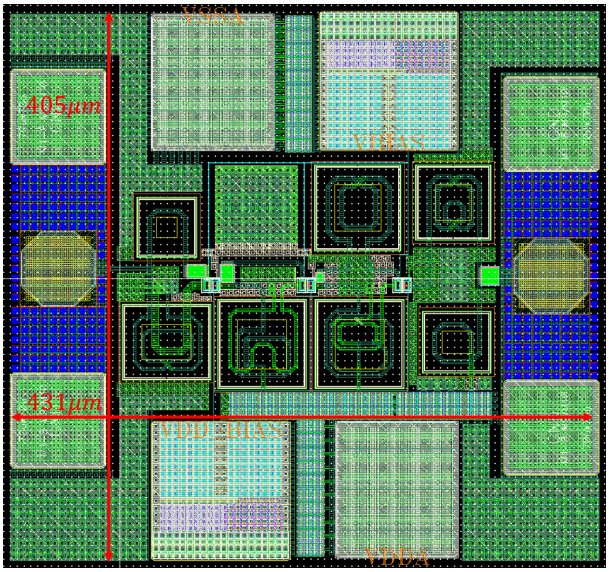


Fig. 5. Layout of the proposed LNA

The introduction of mutual inductance manifests as a controllable feedback term in the denominator. Specifically, the induced voltage at the source of M_2 can be engineered to counteract the inherent negative feedback caused by L_{s2}. By precisely tuning the inter-stage matching network and the coupling coefficient k, the current distribution is optimized to compensate for the gain degradation. This mechanism not only enhances the mid-band transconductance but also extends the bandwidth by mitigating the roll-off associated with the parasitic capacitance C_{gs2}.

III. Post-Layout Simulation

The proposed V-band LNA is fabricated using a TSMC 40-nm CMOS process. As shown in Fig.5, the chip occupies a total area of $431\,\mu\text{m} \times 405\,\mu\text{m}$ including the testing pads. Operating under a 1-V supply voltage, the LNA consumes a total power of 17.63 mW. The post-simulation S-parameters and Noise Figure (NF) are plotted in Fig.6. The design achieves a peak gain S_{21} of 21.1 dB at 61.1 GHz, with a 3-dB bandwidth spanning from 45.7 GHz to 68.9 GHz. Throughout the entire operating band (starting from 43.7 GHz), the input return loss (S_{11}) remains consistently below -10 dB. Furthermore, the LNA exhibits a minimum NF of 3.67 dB at 55.9 GHz, with the NF ranging between 3.67 dB and 4.18 dB across the designated 3-dB bandwidth. The post-simulated $IP_{1\text{dB}}$ is from -18.8 to -1.7 dBm in the bandwidth. A comprehensive performance comparison between this work and state-of-the-art CMOS LNAs is summarized in Table I.

IV. Conclusion

In this paper, a V-band LNA that employs Pole-Tuning and g_m-boosting Technique and is fabricated under the TSMC 40-nm CMOS process is introduced. This study demonstrates the excellent gain and input-matching performance of this LNA, and its noise performance also meets the requirements of the receiver system, enabling high-quality signal transmission at high frequencies.

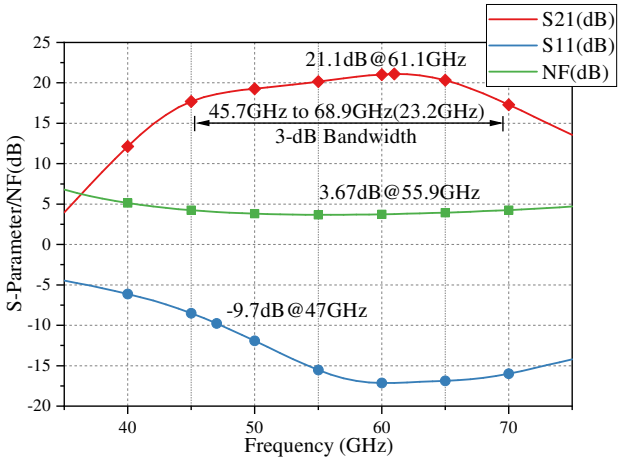


Fig. 6. Post-layout simulation results of S_{21}, S_{11} and NF

TABLE I. COMPARISON WITH PREVIOUS LNAS

References	JSSC 2017[3]	MWCL 2022[5]	JSSC 2024[6]	This Work
Technology	65-nm CMOS	90-nm CMOS	40-nm CMOS	**40-nm CMOS**
Frequency(GHz)	54.4∼90	50∼67	51.6∼73.7	**45.7∼68.9***
Peak Gain(dB)	17.7	16.8	22.4	**21.1***
NF(dB)	5.4∼7.4	5.4∼8	3.78∼6	**3.67∼4.18***
$\|S_{11}\|$ BW(GHz)	61∼76	-	48.6∼71.8	**47.3∼68.9***
$IP_{1\text{dB}}$(dBm)^	-15.4∼11.7	-26$	-14.2∼-10	**-18.8∼-1.7**
Power(mW)	19	5.7	26	**17.63***
Area(mm^2)	0.37	0.6	0.12#	**0.174**

*Post-simulation #Core area ^In 3-dB gain bandwidth $At 60GHz

Acknowledgment

This work was supported in part by the National Natural Science Foundation of China under Grants 62301224, U23A20288, and 62271210, and by the Natural Science Foundation of Guangdong Province under Grants 2023B0303000008 and 2024A1515011982.*(Corresponding author: Quan Xue, Pei Qin)*

References

[1] P. Qin and Q. Xue, "Compact Wideband LNA With Gain and Input Matching Bandwidth Extensions by Transformer," *IEEE Microw. Wirel. Compon. Lett.*, vol. 27, no. 7, pp. 657–659, Jul. 2017.

[2] H. Chen, H. Zhu, L. Wu, W. Che, and Q. Xue, "A Wideband CMOS LNA Using Transformer-Based Input Matching and Pole-Tuning Technique," *IEEE Trans. Microw. Theory Tech.*, vol. 69, no. 7, pp. 3335–3347, Jul. 2021.

[3] Y. Yu, H. Liu, Y. Wu, and K. Kang, "A 54.4–90 GHz Low-Noise Amplifier in 65-nm CMOS," *IEEE J. Solid-State Circuits*, vol. 52, no. 11, pp. 2892–2904, Nov. 2017.

[4] J. H. Jiang, L. Gao, and X. Y. Zhang, "A 0.5–44-GHz LNA With 23-dB Peak Gain and 3-dB Average NF in 28-nm CMOS Technology," *IEEE Trans. Microw. Theory Tech.*, vol. 73, no. 12, pp. 10855–10864, Dec. 2025.

[5] M.-H. Li, Y. Wang, and H. Wang, "A 50–67-GHz Ultralow-Power LNA Using Double-Transformer-Coupling Technique and Self-Resonant Matching in 90-nm CMOS," *IEEE Microw. Wirel. Compon. Lett.*, vol. 32, no. 1, pp. 68–71, Jan. 2022.

[6] J. Ke, Z. Lin, G. Feng, and Y. Wang, "A 52–73-GHz LNA With Tri-Coupled Transformer for Gm Boosting and Enhanced Noise Canceling," *IEEE J. Solid-State Circuits*, vol. 59, no. 3, pp. 668–676, Mar. 2024.

A High-Sensitivity Rectifier Employing a Low-ESR Distributed Spiral Inductor

Pai-Dong Lin
School of Integrated Circuits
Guangdong University of Technology
Guangzhou, China

Jun-Hui Ou
Future Tech
South Chnia University of technology
Guangzhou, China

Zhi-Xia Du*
School of Integrated Circuits
Guangdong University of Technology
Guangzhou, China
duzhixia@gdut.edu.cn

***Abstract*—As the input power of rectifiers decreases to below -30 dBm, the rectifier exhibits a highly capacitive complex impedance, leading to a dramatic increase in power loss within the impedance matching network during energy transmission. To minimize the equivalent series resistance (ESR) of the matching structure, this paper proposes a low-ESR distributed spiral inductor, which is synergistically integrated with a T-junction microstrip structure to construct the matching network. Compared to the conventional impedance matching networks, this structure effectively minimizes parasitic ohmic losses within the matching network, achieving higher power conversion efficiency. Simulation results demonstrate that at an operating frequency of 900 MHz and an input power of -35 dBm, the rectifier circuit utilizing the proposed matching network achieves a power conversion efficiency (PCE) of approximately 10.97%.**

Keywords—Inductor, low-ESR, nanowatt level, rectifier.

I. INTRODUCTION

In recent years, radio frequency energy harvesting (RFEH) technology has achieved significant progress for input power levels above -20 dBm [1]. However, substantial challenges remain in enhancing rectification efficiency when the input power drops to below -30 dBm [2]. In this power regime, the rectifying diode exhibits a n extremely high equivalent impedance. To achieve impedance matching, the matching network must provide a vast amount of impedance compensation, which significantly increases the proportion of parasitic loss from the matching structure within the overall system power budget [2], [3]. Under nanowatt-level weak signal conditions, the RF energy suffers severe attenuation before reaching the diode junction if the ohmic loss of the matching structure is not effectively suppressed, thereby limiting the improvement of power conversion efficiency (PCE).

To address the challenges of ultra-low power rectification, various topology optimization techniques have been explored to enhance system performance. Regarding matching networks, multi-segment microstrip lines [3] have been employed to facilitate high impedance transformation ratios. Similarly, compact L-section matching topologies utilizing commercial lumped inductors and multiple stubs [4] have been investigated to refine the impedance matching trajectory. On a system level, a dual-port quad-band rectenna [5] incorporating multiple lumped components has been developed to maximize energy capture from diverse ambient sources. However, under standard printed circuit board (PCB) processes, these structures often introduce additional distributed losses due to excessive physical lengths of distributed lines or the inherent high equivalent series resistance (ESR) of lumped components. As characterized in [6], such matching network losses will severely degrade the overall PCE, a phenomenon that becomes even more critical in the ultra-low power regime.

To reduce matching network losses, this paper proposes a low-ESR distributed spiral inductor structure implemented via a standard PCB process for ultra-low power rectification circuits operating at 900 MHz. By leveraging the mutual inductance enhancement effect of spiral lines, the inductor achieves a high inductance compensation of approximately 62.23 nH with a physical footprint of 20.18 mm × 20.1 mm, while effectively minimizing its ESR. The designed inductor features an ESR of 1.47 Ω and a quality factor (Q) of 239.68 at 900 MHz. By synergistically constructing an impedance matching network with this low-ESR inductor and a T-junction microstrip structure, a conversion efficiency of approximately 10.97% is achieved at an input power of -35 dBm, providing a novel impedance matching solution for efficient energy harvesting in weak signal environments.

II. DESIGN AND SIMULATION ANALYSIS

The schematic of the rectifier circuit is illustrated in Fig. 1. In this design, a distributed spiral inductor is incorporated between the rectifying diode and the T-junction microstrip matching network to provide the primary inductive compensation. By leveraging the spiral topology, a high inductance is achieved within a limited layout area, while maintaining a low ESR and a high Q. This configuration effectively reduces the matching network losses and enhances the overall PCE.

A. Distributed Spiral Inductor

According to the circuit-level efficiency model, the total PCE is expressed as

$$PCE = \eta_m \cdot \eta_{rect}, \tag{1}$$

where η_m denotes the transmission efficiency of the impedance matching network, and η_{rect} represents the combined rectification efficiency of the diode stage.

Based on impedance transformation theory, the η_m is

$$\eta_m = \frac{1}{1+\frac{Q_L}{Q_u}}, \tag{2}$$

where Q_L and Q_u are the loaded and unloaded quality factors. For the proposed hybrid network, the unloaded quality factors Q_u is modeled using a stored energy-weighting method:

$$\frac{1}{Q_u} = \frac{k_{ind}}{Q_{ind}} + \frac{1-k_{ind}}{Q_{TL}}, \tag{3}$$

979-8-3315-4544-4/26/$31.00 ©2026 IEEE

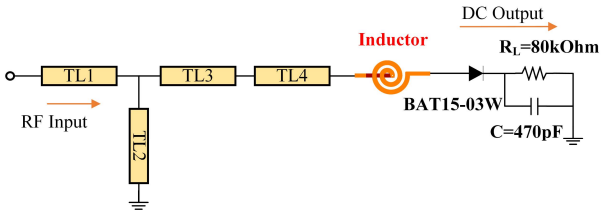
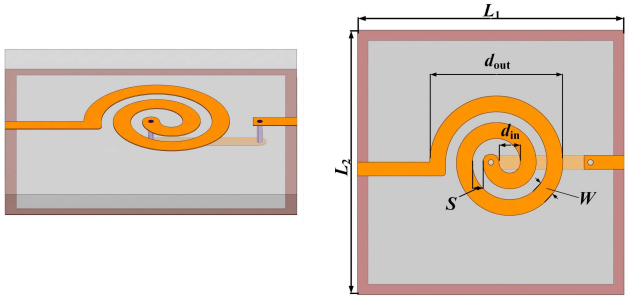
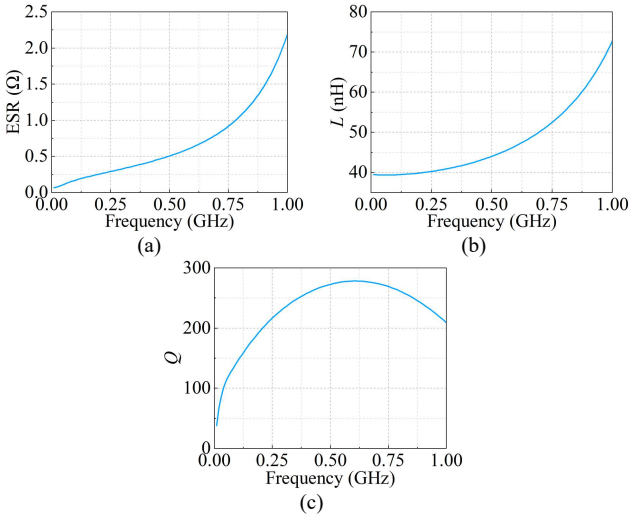


Fig. 1. Schematic of the rectifier circuit.



(a) (b)

Fig. 2. Structure of the distributed spiral inductor: (a) 3D simulation model; (b) layout with physical dimensions (L_1 = 20.18 mm, L_2 = 20.1 mm, W = 1.22 mm, S = 0.8 mm, d_{in}=1.6 mm and d_{out} = 10.15 mm).



(a) (b) (c)

Fig. 3. Simulated results of the proposed distributed spiral inductor versus frequency: (a) ESR, (b) L, and (c) Q.

where Q_{ind} and Q_{TL} are the intrinsic Q of the spiral inductor and T-junction network, and $k_{ind} = L_{ind}/L_{TL}$ is the inductive reactance weight. Since the spiral inductor provides the dominant reactance compensation (k_{ind} is close to 1), the overall Q_u is governed by the proposed inductor.

To further analyze the matching network loss, the intrinsic quality factor of the component, Q_{ind} is defined as:

$$Q_{\text{ind}} = \frac{\omega L}{ESR}, \tag{4}$$

where ω is the angular frequency and L is the inductance. This relationship indicates that at a given inductance and frequency, Q_{ind} is inversely proportional to ESR. It indicates that lower internal resistance directly corresponds to a higher Q, which serves as the core rationale for the proposed low-ESR distributed spiral inductor.

Guided by this theory, a distributed spiral inductor was designed, whose layout is shown in Fig. 2.

The equivalent inductance (L) of a spiral inductor can be expressed as:

$$L = K_1 \mu_0 \frac{N^2 d_{avg}}{1 + K_2 \rho}, \tag{5}$$

$$d_{avg} = 0.5 \cdot (d_{out} + d_{in}), \tag{6}$$

$$\rho = \frac{d_{out} - d_{in}}{d_{out} + d_{in}}, \tag{7}$$

where N is the number of turns, d_{avg} denotes the average diameter, μ_0 stands for the magnetic constant and ρ represents the fill factor. The coefficients are set as K_1 = 2.23, K_2 = 3.45. d_{out} and d_{in} refer to the outer and inner diameters of the inductor, respectively. The ESR is given by:

$$ESR = \frac{l_{total}}{W \cdot \sigma \cdot \delta \left(1 - e^{-\frac{t}{\delta}}\right)}, \tag{8}$$

where l_{total} is the total trace length, W is the trace width, σ is the conductor conductivity, δ is the skin depth and t is the thickness of the trace. It should be noted that the analytical models above are intended to guide the initial parameter design of the inductor's core region, not to precisely predict final performance. In an actual layout, factors such as distributed feedlines and complex substrate effects will inevitably lead to discrepancies between these analytical calculations and the results of full-wave electromagnetic simulations. However, the value of these expressions lies in establishing the fundamental design trade-offs: they clearly show that while increasing the N enhances inductance, it also lengthens the current path, leading to a higher ESR.

Based on the above analysis, a configuration with N=2 is selected in this design to balance the inductive reactance requirements and ohmic losses. By further optimizing the geometric parameters (including W, S, and d_{avg}), a superior Q is achieved at 900 MHz.

To quantitatively evaluate the losses within the matching network, an equivalent electrical model based on Y-parameters is established in this paper. In full-wave electromagnetic (EM) simulation, the equivalent inductance, ESR, and Q of the inductor at the operating frequency can be accurately derived by extracting the Y_{11} parameters of the inductor port. The calculation formulas are defined as:

$$ESR = Re\left(\frac{1}{Y_{11}}\right), \tag{9}$$

$$L = \frac{10^9 \cdot Im\left(\frac{1}{Y_{11}}\right)}{2\pi \cdot freq}, \tag{10}$$

$$Q = \frac{Im\left(\frac{1}{Y_{11}}\right)}{Re\left(\frac{1}{Y_{11}}\right)}. \tag{11}$$

The simulated ESR, L, and Q of the inductor are illustrated in Fig. 3. At the operating frequency of 900 MHz, the inductor achieves an inductance of 62.23 nH with an ESR of only 1.47 Ω, resulting in a high Q of 239.68.

B. Circuit Co-simulation and Performance Comparison

To evaluate the performance of the proposed distributed spiral inductor, the proposed rectifier is designed as shown in Fig. 1. The circuit utilizes Rogers 5880 as the dielectric with a relative permittivity of 2.2, a loss tangent of 0.0009, a

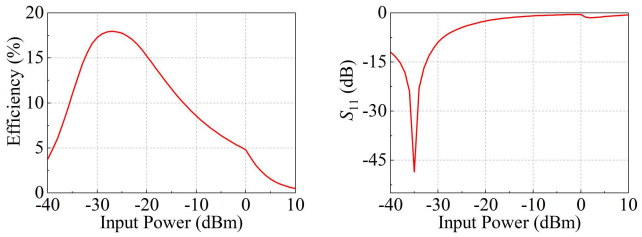


Fig. 4. EM layout simulation results of the rectifier: (a) PCE versus input power; (b) S_{11} versus input power.

TABLE I
SUMMARY OF RECTIFICATION PERFORMANCE BASED ON THIS WORK AND CONVENTIONAL MATCHING SCHEMES.

Inductor	ESR (Ω)	L (nH)	Q	PCE (%)
Without	-	-	-	3.01
Ideal	0	62.23	-	19.44
Ideal	1.47	62.23	239.72	11.65
LQW18AN	5.75	65.17	64.1	4.66
LQW15AN	7.48	62.37	47.14	3.18
LQP03TN	23.22	66.5	16.2	0.53
This Work	**1.47**	**62.23**	**239.68**	**10.97**

substrate thickness of 62 mil, and a microstrip conductor thickness of 0.035 mm. Based on these physical parameters, an EM full-wave layout co-simulation was performed. The simulated return loss (S_{11}) and PCE are illustrated in Fig. 4. As observed, the rectifier achieves excellent impedance matching with an ultra-low input power of -35 dBm at 900 MHz. It achieves a PCE of 10.97% with the S_{11} of -48.5 dB.

Based on the aforementioned Y-parameter extraction formulas, an EM full-wave layout co-simulation was performed to compare four matching configurations: pure microstrip lines (Without inductor), ideal inductors (Ideal), commercial lumped inductors (LQW/LQP series), and the proposed distributed spiral inductor. As summarized in Table I, all configurations are well-matched at 900 MHz, with S_{11} for all cases consistently below -30 dB at -35 dBm. The PCE for pure microstrip matching is only 3.01%. When an ESR of 1.47 Ω is introduced to the ideal inductor, the efficiency drops sharply from a theoretical upper limit of 19.44% to 11.65%. This demonstrates that even slight ohmic losses have a significant impact on energy transfer at nanowatt power levels. In comparison, common commercial inductors such as the LQW18AN and LQP03TN yield efficiencies of only 4.66% and 0.53%, respectively, due to their high ESR (up to 23.22 Ω).

The proposed distributed spiral inductor achieves a PCE of 10.97% in the layout co-simulation. Although this result is lower than the 11.65% achieved by the ideal inductor scheme with an equivalent ESR, the discrepancy primarily stems from the differences in physical boundary conditions between the ideal model and the actual layout. While the ideal model only characterizes lumped impedance, the distributed spiral structure, as an integral part of the physical layout, allows the full-wave simulation to more comprehensively account for spatial coupling, substrate dielectric losses, and subtle parasitic effects induced by microstrip discontinuities. These distributed effects, which are difficult to fully parameterize in analytical formulas, lead to minor physical losses before the energy is transmitted to the diode. Nevertheless, by virtue of its extremely low ESR, the proposed design significantly outperforms commercial lumped inductor configurations in terms of overall performance.

III. CONCLUSION

To address the bottleneck of significantly increased losses in impedance matching networks caused by the large capacitive reactance of rectifiers at nanowatt-level (below -30 dBm) input power, this paper proposes and designs a low-ESR distributed spiral inductor structure. Through the optimization of geometric parameters such as the number of turns and trace width, a high-performance inductor is achieved with an inductance of 62.23 nH, an ESR of 1.47 Ω, and a superior Q of 239.68. EM co-simulation results demonstrate that at 900 MHz and -35 dBm input power, the rectifier achieves a PCE of 10.97%, which is significantly superior to that of impedance matching network schemes composed of conventional microstrip line matching and lumped inductors. This study proves that the distributed spiral low-ESR inductor can effectively suppress matching network losses and substantially enhance the rectification performance of nanowatt-level energy harvesting systems.

ACKNOWLEDGMENT

This work was supported by the Key Research and Development Program of the Guangzhou Science and Technology Plan under Grant 2025B03J0109.

REFERENCES

[1] V. Palazzi et al., "Radiative wireless power transfer: Where we are and where we want to go," *IEEE Microw. Mag.*, vol. 24, no. 2, pp. 57–79, Feb. 2023.

[2] X. Gu, S. Hemour, and K. Wu, "Far-field wireless power harvesting: Nonlinear modeling, rectenna design, and emerging applications,"*Proc. IEEE.*, vol. 110, no. 1, pp. 56–73, Jan. 2022.

[3] P. M. Wang, J.-H. Ou, S. Fei Bo, H. Jiang, M. Huang, and X. Y. Zhang, "A method for designing efficient rectifier with Schottky diodes at Ultra-Low input power Level," *IEEE Trans. Circuits Syst. I, Reg. Papers*., pp. 1–10, 2025.

[4] S. Muhammad, O. Abuajwa, S. Mitani, and J. J. Tiang, "A high-efficiency compact rectifier circuit design for harvesting RF signals in low-powered wireless communication systems," in *2024 IEEE Symp. Wirel. Technol. Appl.*, pp. 23–28, Jul. 2024.

[5] S. Roy, J. J. Tiang, M. B. Roslee, M. T. Ahmed, A. Z. Kouzani, and M. A. P. Mahmud, "Quad-Band Rectenna for Ambient Radio Frequency (RF) Energy Harvesting," *Sensors.*, vol. 21, no. 23, p. 7838, Jan. 2021.

[6] Y.-S. Chen and C.-W. Chiu, "Characterization of the lossyness of matching networks for RF energy-harvesting rectennas," in *2017 11th Eur. Conf. Antennas Propag.*, pp. 2053–2056, Mar. 2017.

A Continuously Tunable Silicon-Based 3D Matching Network for Heterogeneous RF Transceiver

Yanwen Zheng, Guangban Shan*, Xiang Fan , Chunyu Yang, and Pan Zhang
Faculty of Integrated Circuit
Xidian University
Xi'an, China
gbshan@xidian.edu.cn

***Abstract*—The wideband impedance mismatch is main critical challenge to improve the efficiency. This paper presents a multi-mode tunable matching network. The matching performance can be improved with the flexible combination of tuning excitation modulus and phase. Across the 0.1–10 GHz range, the return loss is less than 10 dB. The prototype occupies an area of only 200×140μm².**

Keywords—Tunable; matching network, wide load impedance range; Through-silicon via (TSV)

I. INTRODUCTION

With the maturation of 5G communication technology and the ongoing development of 6G, fixed frequency radio frequency (RF) transceivers cannot meet the demands of wideband and multi-task communication [1]. Tunable matching networks have emerged as key components to support flexible combinations of Chiplets to construct reconfigurable RF transceivers [2], [3]. The energy transmission efficiency is improved by dynamically tuning the network. Tunable matching networks can dynamically adapt to load variations, decoupling the design of individual Chiplets and providing greater flexibility for the modular design of reconfigurable RF transceivers. Thus, the design constraint in the heterogeneous reconfigurable RF transceivers is obviously alleviated. By adding tunable matching network, the significant reconfiguration power efficiency and design flexibility are improved in multi-Chiplet RF transceivers. The efforts primarily focus on cost, integration level, and matching performance under the drive by size, weigh, power, and cost. The typical tunable matching network can be classified into the following three categories.

The first is the switched capacitors or inductor-based tunable matching network. It has an excellent matching capacity by tunable digital programmable capacitors or inductor. However, the discontinuity tuned characteristic hinders its application in finer continuous tuning mode [4], [5], [6]. The second is varactor-based matching network. The matching performance can be tuned with the bias voltage. The low matching band and extra area of the bias circuit is main concern [7], [8]. Another type is the microstrip tunable matching network. The impedance between the input and output ports by incorporating switch-controlled stubs. It has merits of low cost, but high loss and large size [9], [10].

To further cut down the size, the IPD integration technologies based on Through-Silicon Via (TSV) offer a promising pathway for the miniaturization of matching networks. The area is significantly reduced compared to monolithic technology by mounting the RF Chiplet on the two sides of the TSVs.

II. BASIC THEORY OF THE MATCHING NETWORK

A. The Principle of The Tunable Matching Network

The simplified circuit of the tuning matching network is shown in Fig. 1(a). The branch containing L_1 is defined as the control circuit, while the branch containing L_2 is denoted as the main circuit. Here, V_c represents the signal transmitted between Chiplets, R_s is output impedance of the preceding Chiplet , and Z_L is the load impedance of the Chiplet. When V_{in} is applied to the control circuit, the decoupled circuit is shown in Fig. 1(b).

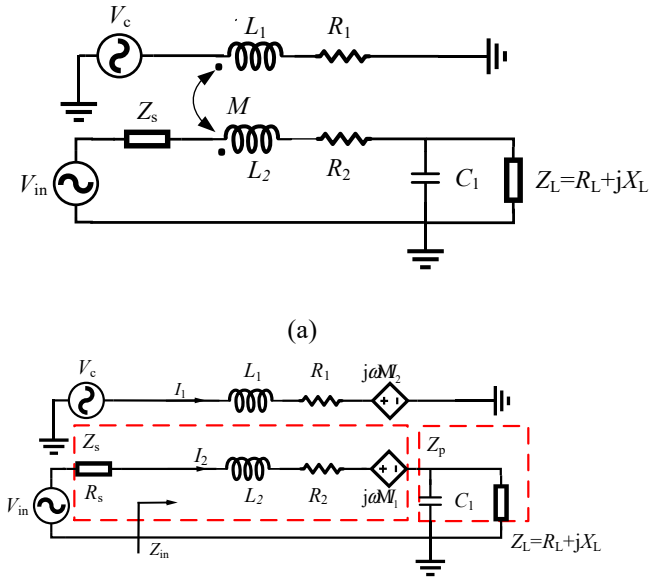


Fig. 1. Schematic of the tunable matching network. (a) simplified circuit. (b) decoupled circuit.

The relationship between I_1 and I_1 expressed by (1):

$$\begin{bmatrix} V_c \\ V_{in} \end{bmatrix} = \begin{bmatrix} R_1 + j\omega L_1 & j\omega M \\ j\omega M & R_s + R_2 + j\omega L_2 + Z_p \end{bmatrix} \begin{bmatrix} I_1 \\ I_2 \end{bmatrix} \quad (1)$$

where M is mutual inductance, Z_p is show in (2):

$$Z_P = \frac{Z_L(1/j\omega C)}{Z_L + (1/j\omega C)} \quad (2)$$

α is defined as the current ratio coefficient of I_1 and I_2, as shown in (3):

$$\alpha = \frac{I_1}{I_2} = \frac{(R_s + R_2 + j\omega L_2 + Z_p)V_c - j\omega M V_{in}}{R_1 V_{in} + j\omega(L_1 V_{in} - M V_c)} \quad (3)$$

β is defined as the voltage ratio coefficient of V_c and V_{in}, as shown in (4):

$$\beta = \frac{|V_c|}{|V_{in}|} \angle(\phi_1 - \phi_2) \quad (4)$$

The equivalent inductance(L_{eq}) in main circuit can be rewritten as (5):

$$L_{eq} = L_2 + M|\alpha| e^{j\phi_\alpha} \quad (5)$$

When $Z_p = Z_s^*$, the L_{eq} is shown in (6):

$$L_{eq} = \frac{\omega C\left(R_L^2 + X_L^2\right) - X_L}{\omega^3 C^2\left(R_L^2 + \left(X_L - \frac{1}{\omega C}\right)^2\right)} - M\alpha \quad (6)$$

The matching performance can be optimized by tuning the L_{eq}. The relationship between β and Z_L is shown in (7):

$$\beta = \frac{j\left(\frac{\left(\omega C\left(R_L^2 + X_L^2\right) - X_L\right)L_2}{(1-\omega C X_L)^2 + (\omega C R_L)^2} + \omega\left(2M^2 - L_1 L_2\right)\right)}{2M\left(R_s + \frac{R_L}{(1-\omega C X_L)^2 + (\omega C R_L)^2}\right) - jM\left(\frac{\omega C\left(R_L^2 + X_L^2\right) - X_L}{(1-\omega C X_L)^2 + (\omega C R_L)^2} - \omega L_1\right)} \quad (7)$$

III. Design and Fabrication of the Silicon-based Tunable Matching Network

A. Models of the Silicon-based Tunable Matching Network

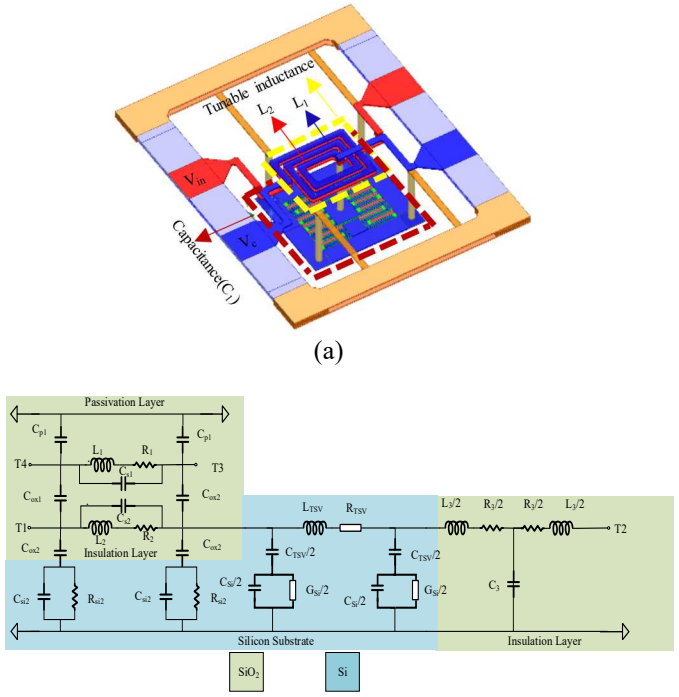
The proposed tunable matching network consists of two spiral inductors and an interdigital capacitor, and the electrical interconnections are achieved through Through-Silicon Vias (TSVs). A silicon wafer with a resistivity of 2500 Ω·cm is used. The key model parameters are show in Table I.

TABLE I. Model Parameters

unit: μm

	Value
RDL width	10
RDL Spacing	5
RDL thickness	2
TSV diameter	10
TSV height	100
Insulation thickness	3
Substrate thickness	100
Inductor spacing	0.5

As the geometric model shown in Fig. 2(a), The tunable inductor is implemented on the top layer using a double-layer redistribution layer (RDL), while the interdigital capacitor is fabricated on the bottom layer with a single-layer RDL. Multiple grounded Through-Silicon Vias (TSVs) provide vertical electrical interconnections between the tunable inductor and the interdigital capacitor. After the geometric model is given, as shown in Fig. 2(b), the lumped RLGC circuit model can be established for the dimensions of the matching network is being orders of magnitude smaller than the millimeter wavelengths. The parasitic RLGC in the inductor and capacitor can be extracted with two-port method [11], [12].



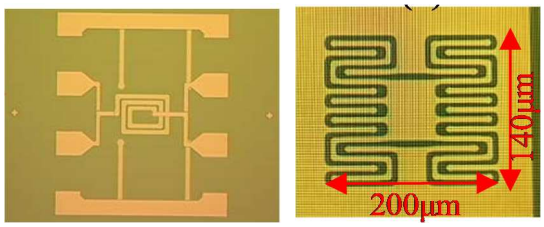
(a)

(b)

Fig. 2. Models of the tunable matching network. (a) geometrical model. (b) circuit model.

IV. Verfication and Dissussion

The tunable matching network is fabricated with the wafer with a diameter of 20 cm. The front and backside of the tunable matching network is shown in Fig. 3(a) and Fig. 3(b), respectively.



(a) (b)

Fig. 3. Photos of the porotypes. (a) front side. (b) backside.

The return loss(RL) and insertion loss(IL) of the tunable matching network are shown in Fig. 4. The results demonstrate a good agreement between the models and porotype.

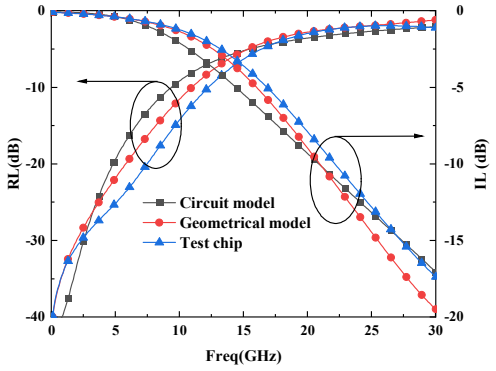
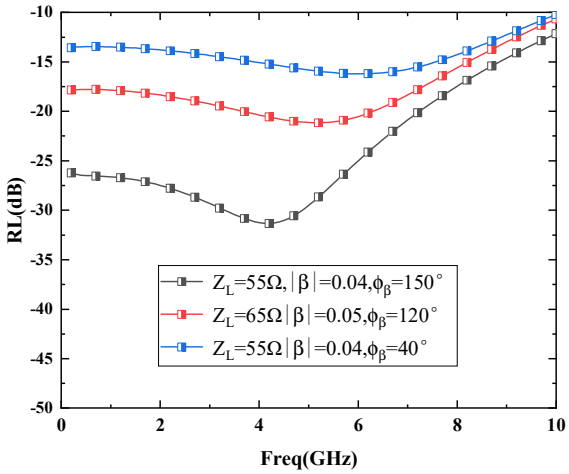
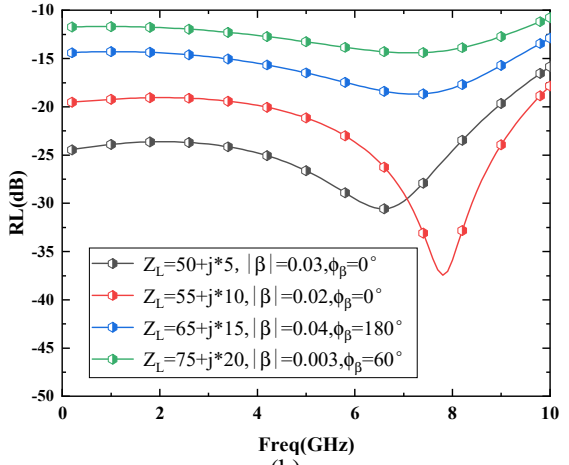


Fig. 4. S-parameters of the tunable matching network.

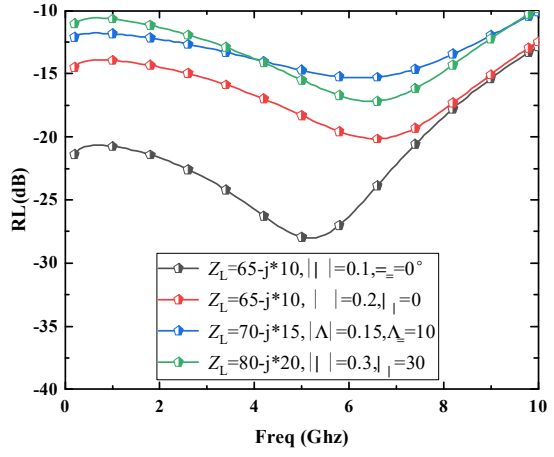
When $Z_L = R_L$, as shown in Fig. 5(a), with the load impedance increase with the step of 10 Ω, the RL below 10.21 dB under different tuning excitations. When $Z_L = R_L - jX_L$, the RL remains below 10.29 dB, as Fig. 5(b) depicted. When $Z_L = R_L + jX_L$, with R_L and X_L increasing with the step of 5Ω. As shown in Fig. 5(c), the RL remains below 10.76 dB.



(a)



(b)



(c)

Fig. 5. RL of the tunable matching network. (a) $Z_L = R_L$. (b) ZL= $R_L + jX_L$. (c) $Z_L = R_L - jX_L$.

SUMMARY

This paper present a miniaturization silicon-based tunable network. A tunable matching principle is proposed. The tuning principle is deviated in detail. The geometric model and equivalent circuit model are established. The results demonstrate a strong agreement between the geometric model and the equivalent circuit model. The network expresses a good tunable impedance matching characteristic under the different load condition. Compared with the existing tunable matching networks, it demonstrates excellent continuous tunability under the wide load and frequency range.

ACKNOWLEDGMENT

This work was supported in part by the National Key Research and Development Program of China under Grant 2022YFB4401303, in part by the Science Fund for Creative Research Groups of the National Natural Science Foundation of China under Grant 62021004, and in part by the State Key Program of National Natural Science of China under Grant 62134005.

REFERENCES

[1] S. Wang, Y. Liu, Q. F. Zhang et al., "Hierarchical Reinforcement Learning-Guided Framework for Impedance Matching Network Design of RFIC Application[J]. *IEEE Microw. Wireless Compon. Lett.*,.

[2] C. Moran Guizan, P. Baumgartner, S. Heinen and M. Lauritano. Millimeter-Wave Tunable Impedance Matching Network in an Advanced CMOS Process[J]. *IEEE Trans. Microw. Theory Techn.*, vol. 72, no. 8, pp. 4590-4596, Aug. 2024.

[3] P. Stärke, D. Fritsche, C. Carta and F. Ellinger. A Passive Tunable Matching Filter for Multiband RF Applications Demonstrated at 7 to 14 GHz[J]. *IEEE Microw. Wireless Compon. Lett.*, vol. 27, no. 8, pp. 703-705, Aug. 2017.

[4] J. Lee, J. -S. Paek and S. Hong. Millimeter-Wave Frequency Reconfigurable Dual-Band CMOS Power Amplifier for 5G Communication Radios[J]. *IEEE Trans. Microw. Theory Techn.*, vol. 70, no. 1, pp. 801-812, Jan. 2022.

[5] B. Liu, X. Quan, C. C. Boon, D. Khanna, P. Choi and X. Yi. Reconfigurable 2.4-/5-GHz Dual-Band Transmitter Front-End Supporting 1024-QAM for WLAN 802.11ax Application in 40-nm CMOS[J]. *IEEE Trans. Microw. Theory Techn.*, vol. 68, no. 9, pp. 4018-4030, Sept. 2020.

[6] M. Gilasgar, A. Barlabé and L. Pradell. A 2.4 GHz CMOS Class-F Power Amplifier With Reconfigurable Load-Impedance Matching[J]. *IEEE Trans. Circuits Syst. I, Reg. Papers*, vol. 66, no. 1, pp. 31-42, Jan. 2019.

[7] J. A. Estrada, S. Johannes, D. Psychogiou and Z. Popović. Tunable Impedance-Matching Filters[J]. *IEEE Microw. Wireless Compon. Lett.*, vol. 31, no. 8, pp. 993-996, Aug. 2021.

[8] T. Zhang, W. Che and H. Chen, "A Wideband Reconfigurable Impedance Matching Network for Complex Loads[J]. *IEEE Trans. Compon., Packag., Manuf. Technol.*, vol. 8, no. 6, pp. 1073-1081, June 2018.

[9] S. Rabbani, S. Narayana and Y. K. Singh. A Novel Concurrent Dual Band Matching Network for Complex to Real Impedance Matching for RF Applications[J]. *IEEE Trans. Circuits Syst. II, Exp. Briefs*, vol. 70, no. 1, pp. 66-70, Jan. 2023.

[10] Y. Zheng, G. Shan, X. Fan, Z. Yang and G. Li. An 0.04–10.32 nH Ultracompact Tunable Inductor Based on Flexible Magnetic Coupling Tuning Technique[J]. *IEEE Trans. Electron Devices*, vol. 71, no. 8, pp. 4945-4951, Aug. 2024.

[11] Z. Xu, X. Gu and J. Q. Lu. Parasitics extraction, wideband modeling and sensitivity analysis of through-strata-via (TSV) in 3D integration/packaging[C] *IEEE/SEMI Advanced Semiconductor Manufacturing Conference*, Saratoga Springs, NY, USA, 2011, pp. 1-6.

A Broadband Tunable Matching Network based on Magnetic Coupling

Fangqian Wang, Guangbao Shan, Yanwen Zheng*.
Faculty of Integrated Circuit
Xidian University
Xi'an, China
zhengyanwen@xidian.edu.cn

***Abstract*—To address the limitations of conventional lumped-element matching networks in broadband applications, this paper investigates the broadband mechanism and tuning characteristics of magnetically coupled matching networks. Based on a tunable transformer structure, a matching network with adjustable bandwidth and ripple is proposed. The frequency and impedance tuning mechanisms of in-phase and out-of-phase configurations are systematically analyzed, thereby extending the theoretical framework of magnetically coupled matching networks.**

***Index Terms*—matching network, tunable, magnetic coupling, reconfigurable**

I. Introduction

Traditional lumped-element matching networks exhibit significant limitations in broadband scenarios. Higher-order matching networks utilize magnetic coupling to split poles, whose superposition enables broadband characteristics. Broadband matching techniques mainly fall into three categories: capacitive, inductive, and magnetic coupling. Among these, magnetic coupling offers advantages such as low in-band ripple, compact layout, and DC isolation, presenting outstanding overall benefits. Capacitive coupling suffers from the highest loss and ripple, while inductive coupling requires additional DC-blocking capacitors and occupies a larger area. Although magnetic coupling is affected by the quality factor (Q) of the transformer, it remains widely adopted.

In recent years, matching networks based on magnetic coupling structures have attracted extensive attention. Numerous researchers have investigated their equivalent circuits [1], [2], frequency responses of input/output impedance [3], and variation patterns of in-band flatness [4], [5], [6]. Studies indicate that the circuit performance of matching networks is primarily influenced by fixed component values, coupling factor (k), and quality factor (Q). A larger k leads to greater pole splitting and broader bandwidth, but also results in degraded flatness. To maintain high flatness, k and Q exhibit a negative correlation. To meet the requirements of tunable circuits, tunable matching networks employ varactors [7], MOS transistors [8], or switches [9] to switch the component values and k of the matching network, thereby achieving frequency band tuning. However, existing methods lack research on the flatness during band switching, and the tunable frequency range remains quite limited.

This paper proposes a matching network with tunable bandwidth and ripple based on a tunable transformer structure [10], and provides an in-depth analysis of the circuit characteristics of both inverting and non-inverting matching networks, aiming to refine the theoretical framework of magnetically coupled matching networks. The variation patterns of the frequency and impedance characteristics of the tunable matching network are investigated. The principles of bandwidth tuning for inverting/non-inverting matching networks and the factors affecting impedance peaks are analyzed. Finally, the distinct effects of voltage amplitude ratio and phase difference on bandwidth and impedance are summarized.

II. The Tuning Principle

The principle of the tunable matching network is shown in the Fig. 1. In Fig. 1(a), the effects of L_1 on L_2 and L_3 are coupled by (1) and (2), and the coupled circuit is expressed in Fig. 1(b). L_i denotes the intrinsic inductance of the inductor, and k_{ij} represents the mutual inductance coefficient between inductor L_i and L_j. L_{eff} is the equivalent inductance of inductor L_i after coupling with L_1, while k_{eff} is the equivalent value of the mutual inductance coefficients k_{23} and k_{1j}. Let $L_2 = L_3$:

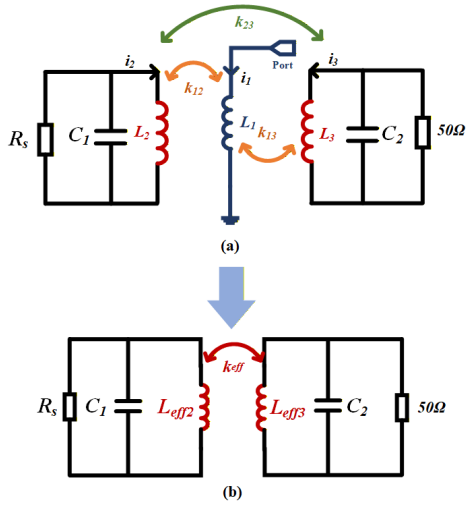


Fig. 1. Schematic diagram (a) equivalent model of the tunable transformer and (b) equivalent conventional transformer model.

$$L_{\text{eff}} = L + M\frac{i_1}{i_2 + i_3} \tag{1}$$

$$M_{\text{eff}} = M_{23} + M\frac{i_1}{i_2 + i_3} \tag{2}$$

$$k_{\text{eff}} = \frac{M_{\text{eff}}}{L_{\text{eff}}} \tag{3}$$

Next, the relationship between the pole frequencies of the transformer and the signal source is analyzed. In a transformer-based matching network, the impedance poles split due to the effect of the transformer coupling factor. The two pole frequencies are given in (4).

$$\begin{aligned}\omega_{L,H}^2 &= \frac{\omega_{\text{eff0}}^2}{1 \pm |k_{\text{eff}}|} \\ &= \frac{1}{L_{\text{eff}}C}\frac{\sqrt{L_{\text{eff2}}L_{\text{eff3}}}}{\sqrt{L_{\text{eff2}}L_{\text{eff3}}} \pm M_{\text{eff}}}\end{aligned} \tag{4}$$

When $L_{\text{eff2}} = L_{\text{eff3}} = L_{\text{eff}}$, $\omega_{L,H}^2$ is simplified to (5).

$$\omega_{L,H}^2 = \frac{1}{C}\frac{1}{|L_{\text{eff}}| \pm |M_{\text{eff}}|} \tag{5}$$

Therefore, the relationship between $\omega_{L,H}^2$ and the signal source are expressed by (6) and (7).

$${\omega_L}^2 = \frac{1}{C}\frac{1}{\left|L + M_{23} + 2M\frac{i_1}{i_2+i_3}\right|} \tag{6}$$

$${\omega_H}^2 = \frac{1}{C}\frac{1}{L - M_{23}} \tag{7}$$

Note that in the reverse matching network, $M_{\text{eff}} < 0$. Consequently, the expressions for $\omega_{L,H}^2$ become those given in (8), (9), and (10).

$$\begin{aligned}\omega_{L,H}^2 &= \frac{\omega_{\text{eff0}}^2}{1 \pm |k_{\text{eff}}|} \\ &= \frac{1}{L_{\text{eff}}C}\frac{|L_{\text{eff}}|}{|L_{\text{eff}}| \mp |M_{\text{eff}}|}\end{aligned} \tag{8}$$

$${\omega_L}^2 = \frac{1}{C}\frac{1}{L - M_{23}} \tag{9}$$

$${\omega_H}^2 = \frac{1}{C}\frac{1}{\left|L + M_{23} - 2M\frac{i_1}{i_2+i_3}\right|} \tag{10}$$

As can be seen from (6), (7), (9), and (10), the bandwidth of the tunable matching network can be adjusted by varying the current ratio. When the current ratio increases, the lower-frequency point in the in-phase mode decreases, leading to an increased bandwidth; while in the out-of-phase mode, the higher-frequency point increases, which also results in a broader bandwidth.

According to (6), (10), (11) and (12), the variation of ω_H is determined by the voltage ratio of the signal source.

$$\left|\frac{i_1}{i_2 + i_3}\right| = \left|\frac{(\alpha + \beta)M - (M_{23} + L)}{2M - (\alpha + \beta)L}\right| \tag{11}$$

$$\begin{aligned}|\alpha + \beta| &= 2\left|\frac{V_2}{V_1}\right|\sqrt{[\cos^2(\angle V_2 - \angle V_1) + \sin^2(\angle V_2 - \angle V_1)]} \\ &= 2\left|\frac{V_2}{V_1}\right|\end{aligned} \tag{12}$$

As for the in-band impedance of the matching network, it primarily depends on the phase of the signal source. The detailed derivation process is as follows. The equivalent circuit of matching network is shown in Fig. 2.

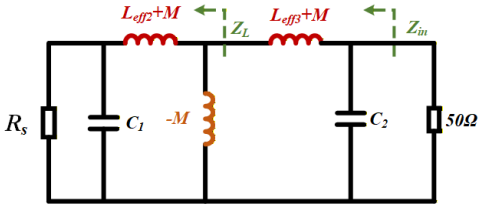


Fig. 2. The equivalent circuit of matching network

The load impedance Z_L and input impedance Z_{in} are given by (13) and (14), respectively.

$$\begin{aligned}Z_L &= [j\omega(L_{\text{eff}} + M_{\text{eff}}) + (\frac{1}{j\omega C_1} \parallel R_s)] \parallel -j\omega M_{\text{eff}} \\ &= \frac{\omega^2 M_{\text{eff}}(L_{\text{eff}} + M_{\text{eff}})(1 + j\omega C_1 R_s) - j\omega M_{\text{eff}} R_s}{j\omega L_{\text{eff}}(1 + j\omega C_1 R_s) + R_s}\end{aligned} \tag{13}$$

$$\begin{aligned}Z_{in} &= [j\omega(L_{\text{eff}} + M_{\text{eff}}) + Z_L] \parallel \frac{1}{j\omega C_2} \\ &= \frac{j\omega(L_{\text{eff}} + M_{\text{eff}}) + Z_L}{j\omega C_2[j\omega(L_{\text{eff}} + M_{\text{eff}}) + Z_L] + 1}\end{aligned} \tag{14}$$

Z_L at ω_H is express as:

$$Z_L(\omega_H) = \frac{\frac{M_{\text{eff}}}{C}}{j\omega L_{\text{eff}}(1 + j\omega C_1 R_s) + R_s} \tag{15}$$

During phase tuning, ω_H is held constant, whereas the parameters L_{eff} and M_{eff} are adjusted. Consequently, the impedance can be regulated through phase tuning.

III. Simulation Verification

The simulation results of the voltage-ratio-tuned matching network are shown in Fig.3. According to the current direction of $i_{1,2,3}$, the network is divided into in-phase and anti-phase configurations.It is in-phase when i_1 has the same direction as $i_{2,3}$; otherwise, it is out-of-phase.

For the in-phase matching network, ω_L decreases as the voltage ratio increases, while the bandwidth expands by 2.5 GHz. For the out-of-phase matching network, ω_H increases with the voltage ratio, and the bandwidth also widens by 5.5 GHz. In summary, increasing the voltage ratio leads to an enhanced bandwidth of the matching network.

As shown in Fig. 4, adjusting the voltage phase can effectively modify the in-band impedance characteristics of the matching network. In the in-phase matching network shown in Fig. 4(a), as the phase increases from 0° to 10°, the real

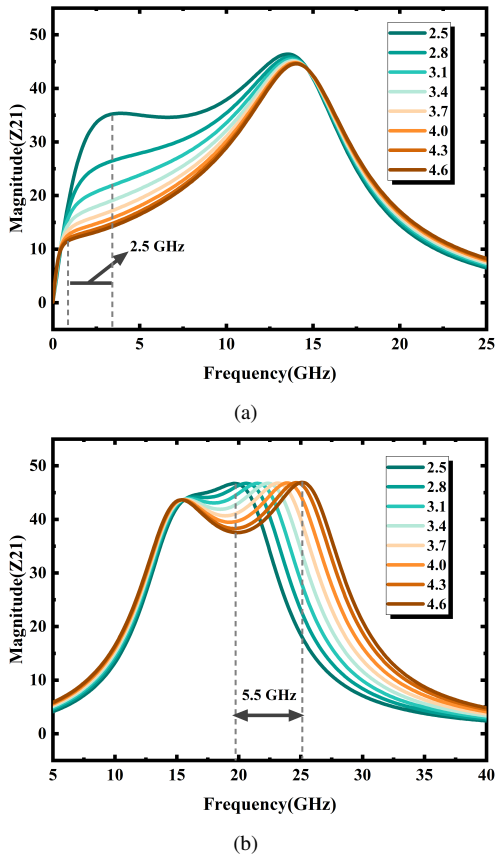


Fig. 3. The variation of $\omega_{L,H}$ with voltage ratio (a) in-phase matching network and (b) anti-phase matching network

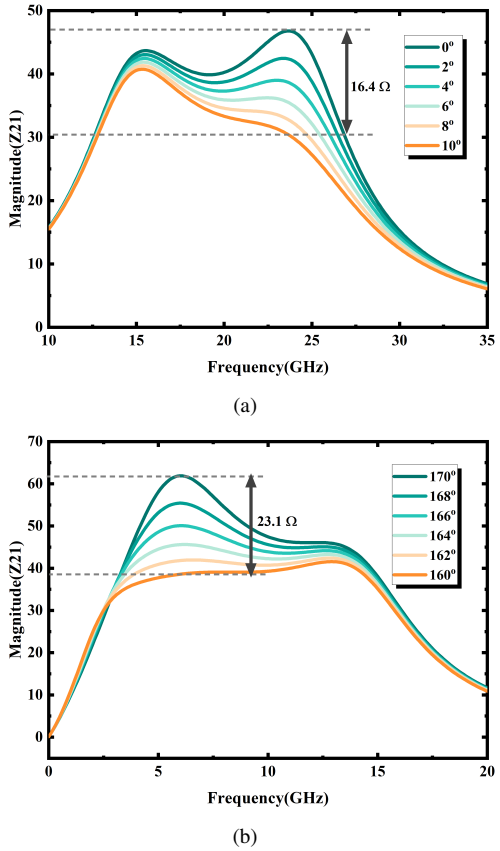


Fig. 4. The variation of $\omega_{L,H}$ with voltage phase (a) in-phase matching network and (b) anti-phase matching network

part of the impedance at the corresponding frequency point decreases from 16.4 Ω. In the anti-phase matching network shown in Fig. 4(b), when the phase varies within the range of 160° to 170°, the impedance increases correspondingly from 23.1 Ω. These results provide an effective design guideline for realizing low-loss tunable matching networks.

IV. CONCLUSION

Measurement and analysis results demonstrate the effectiveness of the proposed approach. Compared with the conventional configuration, the in-phase matching network achieves a bandwidth extension of 2.5 GHz, while the out-of-phase configuration further extends the bandwidth by 5.5 GHz. Meanwhile, the in-band impedance variation is limited to 16.4 Ω for the in-phase case and 23.1 Ω for the out-of-phase case, validating the proposed network's capability to balance bandwidth enhancement and impedance flatness.

REFERENCES

[1] R. Wang, C. Li, K. Qiu, Y. Liu, S. Yin, and Y. Wang, "A ka-band broadband power amplifier with transformer-based lossy magnetically coupled resonator network: Analysis and design," *IEEE Transactions on Microwave Theory and Techniques*, vol. 72, no. 12, pp. 6857–6870, 2024.

[2] A. Mazzanti and A. Bevilacqua, "Second-order equivalent circuits for the design of doubly-tuned transformer matching networks," *IEEE Transactions on Circuits and Systems I: Regular Papers*, vol. 65, no. 12, pp. 4157–4168, 2018.

[3] C. Zhao, X. Zhang, H. Liu, Y. Yu, Y. Wu, and K. Kang, "A sige power amplifier with double gain peaks based on the control of stationary points of impedance transformation," *IEEE Transactions on Microwave Theory and Techniques*, vol. 69, no. 4, pp. 2279–2290, 2021.

[4] J. Zhang, D. Zhao, and X. You, "A 20-ghz 1.9-mw lna using gm-boost and current-reuse techniques in 65-nm cmos for satellite communications," *IEEE Journal of Solid-State Circuits*, vol. 55, no. 10, pp. 2714–2723, 2020.

[5] H. Jia, C. C. Prawoto, B. Chi, Z. Wang, and C. P. Yue, "A full ka-band power amplifier with 32.9% pae and 15.3-dbm power in 65-nm cmos," *IEEE Transactions on Circuits and Systems I: Regular Papers*, vol. 65, no. 9, pp. 2657–2668, 2018.

[6] J. Zhang, T. Wu, L. Nie, S. Ma, Y. Chen, and J. Ren, "A 120–150 ghz power amplifier in 28-nm cmos achieving 21.9-db gain and 11.8-dbm psat for sub-thz imaging system," *IEEE Access*, vol. 9, pp. 74 752–74 762, 2021.

[7] B. Liu, R. Zhou, and Z. Zhu, "Reconfigurable 2.4/5.0-ghz dual-band cmos power amplifier for wlan 802.11ax," *IEEE Transactions on Circuits and Systems I: Regular Papers*, vol. 71, no. 7, pp. 3120–3133, 2024.

[8] N.-Z. Sun, L. Gao, H.-Y. Li, J.-X. Xu, and X. Zhang, "A compact millimeter-wave reconfigurable dual-band lna with image-rejection in 28-nm bulk cmos for 5g applications," *IEEE Journal of Solid-State Circuits*, vol. 59, no. 10, pp. 3406–3416, 2024.

[9] B. Bae, E. Kim, S. Kim, and J. Han, "Dual-band cmos low-noise amplifier employing transformer-based band-switchable load for 5g nr fr2 applications," *IEEE Microwave and Wireless Technology Letters*, vol. 33, no. 3, pp. 319–322, 2023.

[10] G. Shan, F. Wang, Y. Zheng, G. Li, B. Meng, X. Fan, and R. Wang, "A broadband tunable on-chip transformer based on magnetic coupling technique," *IEEE Transactions on Microwave Theory and Techniques*, pp. 1–11, 2026.

Wideband High-Precision Resonator-Based Phase Shifters via Lossy Electric and Magnetic Coupling

Na Ji
Guangdong Provincial Key Laboratory of Millimeter-Wave and Terahertz
South China University of Technology
Guangzhou, China
eegina@scut.edu.cn

Guangxu Shen
Department of Electronic and Optical Engineering
Nanjing University of Posts and Telecommunications
Nanjing, China
shenguangxu@njupt.edu.cn

Wenquan Che
Guangdong Provincial Key Laboratory of Millimeter-Wave and Terahertz
South China University of Technology
Guangzhou, China
eewqche@scut.edu.cn

***Abstract*—This paper presents a novel dual-branch switchable architecture for wideband millimeter-wave phase shifters. By alternating between lossy electric and magnetic coupling paths, the desired phase shift can be accurately obtained. In this architecture, the transistors are not only utilized as switches for path selection but are also reused to form the resonators by leveraging their parasitic components. This co-design strategy ensures that a multi-resonator topology is consistently maintained across both states, resulting in stable wideband performance. A representative 90° phase shifter (PS) targeting the 22–32 GHz band was implemented in a 0.25-µm GaAs process to validate the design. Post-layout EM simulations show a differential phase shift of 91.5° ± 1.5°, with a maximum insertion loss of 3 dB and an amplitude imbalance of less than 1 dB. The proposed architecture offers a compact and robust solution for millimeter-wave phased-array systems.**

***Keywords*——wideband, phase shifter, lossy electric and magnetic coupling path, GaAs process.**

I. Introduction

Phased array systems for mm-wave communications and radar demand precise phase control to enable accurate beam steering and system calibration[1]. As core components, on-chip phase shifters (PSs) are expected to simultaneously achieve wide bandwidth and high precision.

Conventionally, wideband on-chip phase shifters are implemented using high-pass/low-pass (HP/LP) networks due to their inherently flat phase responses. To achieve larger phase-shift values, higher-order networks are typically required. For instance, a 6-bit PS reported in [2] utilizes a third-order HP/LP network for the 90° bit and a fifth-order network for the 180° bit. Although this approach achieves a fractional bandwidth (FBW) of 66.7%, it comes at the expense of significantly increased insertion loss (IL) and a larger physical footprint. In [3], an improved HP/LP network is employed for the 90° bit by reusing transistors to enhance integration. Nevertheless, a series-shunt SPDT topology is required to ensure sufficient isolation between the HP and LP states, which degrades the IL by approximately 1.2 dB.

This paper presents a novel phase shifter architecture featuring a dual-branch structure that is switchable between lossy electric and magnetic coupling paths. By reusing transistor parasitics, multi-resonator topologies are formed in both states. Benefit from the reusing mechanism, the design removes the need for extra isolation structures, ensuring wideband high precision with low insertion loss. For validation, a representative 90° phase shifter targeting the 22–32 GHz range is implemented in a 0.25-µm GaAs process.

II. Theoretical Analysis and Circuit Design

This section details the dual-branch switchable architecture, phase shift mechanism, circuit implementation, and nodal phase analysis. It is noted that GaAs pHEMT transistors are utilized throughout the design.

A. Dual-Branch Switchable Architecture

The block diagram and the corresponding state-evolution of the proposed dual-branch switchable architecture are illustrated in Fig. 1. The source and load are denoted as S and L, respectively, while R_i represents the resonators. The architecture integrates lossy electric (E) and magnetic (M) coupling paths, a fixed resonator R_1, and two switchable resonators R_2 and R_2'.

The two states are achieved by alternating the switches integrated into the resonators. In the reference state, the switch in R_2' is turned off, allowing R_2' to remain in resonance. Simultaneously, the switch in R_2 is turned on; thus, R_2 combines with the E-coupling path and the load to constrcut a new equivalent resonator R_3'. By effectively reusing transistor parasitics, a third-order inline topology dominated by M-coupling is generated.

Similarly, in the shift state, the switch in R_2 is turned off while the switch in R_2' is turned on, resulting in a third-order inline topology with E-coupling. This consistent multi-resonator configuration across both states is instrumental in maintaining a stable phase response and enhancing the fractional bandwidth.

B. Phase Shift Mechanism Via Lossy Coupling

To theoretically explain the wideband phase-shifting mechanism, two generalized three-pole coupled-resonator models using admittance inverters (J-inverters) are presented in Fig. 2, where the J-inverters correspond to the transformer magnetic coupling discussed later.

Defining the network that incorporates a positive admittance inverter ($+J_{12}$) alongside a lossy magnetic coupling path as the reference state. Given that the $+J_{12}$ inverter ideally provides a +90° phase shift and the lossy magnetic coupling introduces a phase shift φ_1, the total transmission phase in this state (assuming all resonators are at resonance) is $\Phi_1 = +90° + \varphi_1$. In addition, defining the network utilizing a negative admittance inverter ($-J_{12}$) combined with a lossy electric coupling path as the phase-shift state. Since the $-J_{12}$ inverter ideally provides a −90° phase shift and the lossy electric coupling introduces a phase

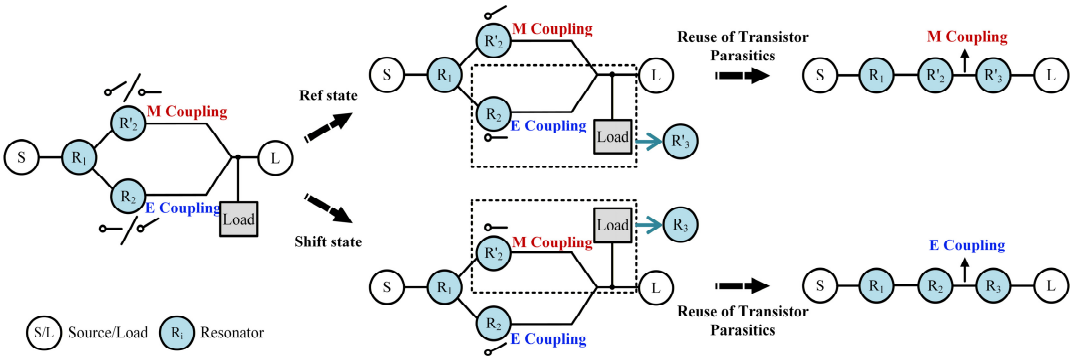


Fig. 1 Block diagram of the proposed dual-branch switchable architecture.

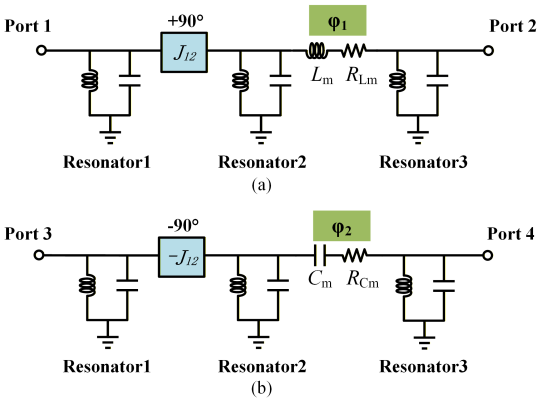


Fig. 2 Generalized three-pole coupled-resonator models using J-inverter: (a) $+J_{12}$ with lossy magnetic coupling, and (b) $-J_{12}$ with lossy electric coupling.

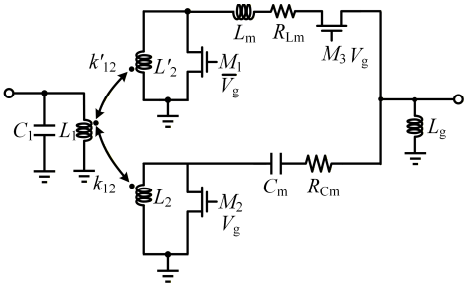


Fig. 3 Circuit schematic of the 90° phase shifter. (C_1=96 fF, L_1=883 pH, L_2=295 pH, L'_2=700 pH, C_m=150 fF, L_m=160 pH, L_g=380 pH, k_{12}=0.51, k'_{12}=0.73, M_1=75*6, M_2=75*6, M_3=50*2)

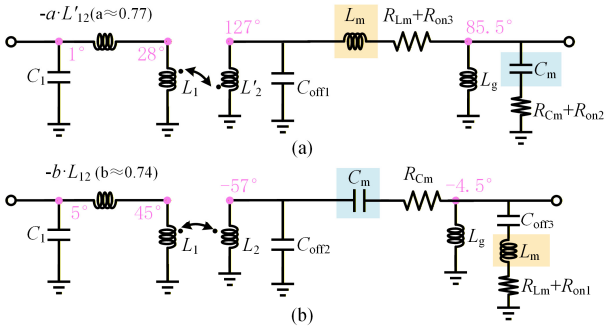


Fig. 4 Extracted internal node phases at the center frequency for the (a) reference state, and (b) phase-shift state.

shift φ_2, the total transmission phase is yielded as $\Phi_2 = -90° + \varphi$. The total phase difference $\Delta\Phi$ between the two states is thus expressed as $\Delta\Phi=\Phi_1-\Phi_2=180°+(\varphi_1-\varphi_2)$.

Moreover, to maintain a consistent phase slope and high linearity across the operating bandwidth, it is essential to satisfy the condition $C_1L_1 - C_mL_m = 0$ [4], assuming all coupled resonators are composed of a shunt capacitance C_1 and an inductance L_1. By strategically tuning the ratio of electric and magnetic coupling strengths, the desired phase shift can be realized accurately over a wide bandwidth.

C. Circuit Implementation

The circuit schematic of the 90° PS design is illustrated in Fig. 3. A transformer network consisting of three coupled inductors is employed to construct the dual branches and realize the *J*-inverter function. Additionally, a series capacitor C_m and an inductor L_m are separately employed to provide the lossy electric and magnetic coupling paths. Three transistors (M_1, M_2, and M_3) are employed for path switching and multi-resonator construction, with their gate biases controlled between V_g = 0 V and -5 V. Transistors M_2 and M_3 share the same control signal, while M_1 is driven by the complementary control.

In the reference state (V_g = 0V), the signal propagates through the upper branch via a lossy magnetic coupling path. Simultaneously, the lower branch is deactivated, and the lossy electric coupling element C_m is reused to form a new resonator with the shunt load L_g. The three resonators are constructed as follows: Resonator 1 is formed by the shunt capacitor C_1 and inductor L_1; Resonator 2 is composed of the off-state transistor M_1 and inductor L'_2; and resonator 3 is realized by C_m in resonance with L_g. These three resonators form a third-order in-line topology, in which Resonator 1 and Resonator 2 are coupled through the out-of-phase magnetic coupling k_{12}', while Resonator 2 and Resonator 3 are coupled via the lossy magnetic coupling L_m.

In the phase-shifting state (V_g = -5V), the signal propagates through the lower branch via a lossy electric coupling path. Simultaneously, the upper branch is deactivated, and the lossy magnetic coupling element L_m associated with the off-state transistor M_3 is reused to form a new resonator with the shunt load L_g. Specifically, Resonator 1 remains the shunt C_1L_1 structure; Resonator 2 is constructed by the off-state transistor M_2 and inductor L_2; and resonator 3 is formed by the series combination of L_m and the off-state transistor M_3, which together resonate with L_g. These three resonators form a third-order in-line topology, in which Resonator 1 and Resonator 2 are coupled through the in-phase magnetic coupling k_{12}, while Resonator 2 and Resonator 3 are coupled via the lossy electric coupling C_m.

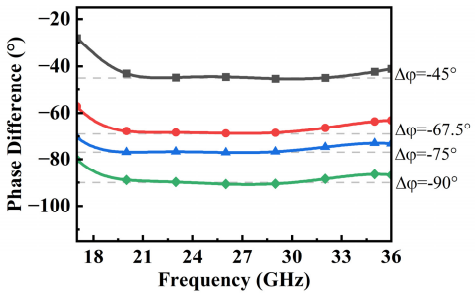


Fig. 5 Simulated phase responses of the designed phase shifters for 45°, 67.5°, 75°, and 90° targets.

D. Nodal Phase Analysis and Model Verification

To validate the proposed design approach, an internal node phase progression analysis is conducted at the center frequency, with the simulated nodal phases extracted and presented in Fig. 4.

In the reference state, the RF signal first propagates through the shunt capacitor C_1 and mutual inductance $-a \cdot L'_{12}$ (where $a \approx 0.77$), exhibiting a phase transition from 1° to 28°. The phase then transitions from 28° to 127°, resulting in a 99° phase advance that physically approximates an ideal $+J_{12}$ inverter. Subsequently, the cascaded lossy magnetic coupling (L_m) introduces a specific phase delay. This delay is associated with the combined effect of the shunt elements, including the off-state capacitance C_{off1}, the inductor L_g, and the capacitor C_m, which together establish a final output phase of 85.5°.

In the phase-shift state, the signal is first routed through the shunt capacitor C_1 and the mutual inductance $-b \cdot L_{12}$ (where $b \approx 0.74$), exhibiting a phase transition from 5° to 45°. The phase then transitions from 45° to −57°, resulting in a 102° phase delay that physically approximates an ideal $-J_{12}$ inverter. The lossy electric coupling (C_m) then provides a necessary phase advance. This advance is associated with the combined effect of the shunt elements, establishing a final output phase of -4.5°.

The total differential phase shift between the two states is calculated as 85.5° − (−4.5°) = 90.0°.

III. Simulation Results and Conclusion

To demonstrate the scalability of the proposed dual-branch switchable topology, phase shifters targeting 45°, 67.5°, 75°, and 90° are presented, as illustrated in Fig. 5. The results show that all designs exhibit stable wideband phase-shifting characteristics across the 22–32 GHz range.

To further validate the layout implementation, a 90° phase shifter implemented in a 0.25-μm GaAs process is presented in Fig. 6. EM simulations were conducted in ADS Momentum RF with a 20-cells/wavelength mesh density and edge mesh enabled. The post-layout EM simulation results for this specific design are plotted in Fig. 7, where P0 and P1 denote the reference and phase-shifting states, respectively. The results exhibit multi-resonator characteristics within the passband for both states, with the return loss remaining greater than 10 dB. Moreover, the insertion loss for both states is well-maintained below 3 dB, while the amplitude

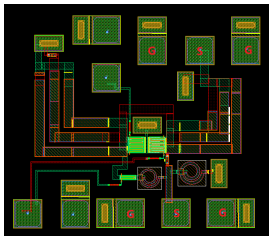


Fig. 6 Layout of the designed 90° PS.

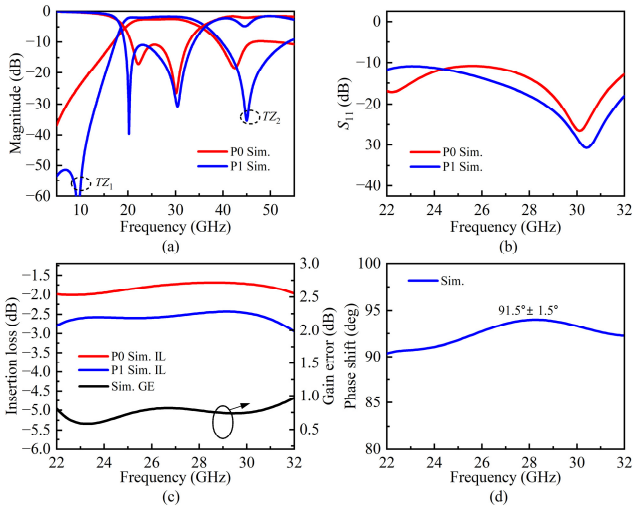


Fig. 7 Post-layout EM simulation results of the 90° PS: (a) magnitude responses, (b) return loss (S_{11}), (c) insertion loss and gain error, and (d) phase shift.

imbalance (gain error) is strictly kept under 1 dB across the entire target band. Furthermore, an excellent flat phase response of 91.5° ± 1.5° is achieved, corresponding to a precise phase error of less than 1.5°.

In conclusion, a novel phase shifter architecture featuring a dual-branch structure has been presented. By reusing transistor parasitic, multi-resonator topologies are successfully formed in both states, ensuring inherent wideband characteristics. By tuning the ratio of lossy electric-to-magnetic coupling strengths, the desired phase shift is accurately realized across a broad frequency range. Implemented in a 0.25-μm GaAs process, the 90° phase shifter prototype demonstrates precise phase control and stable wideband performance, providing a high-precision solution for millimeter-wave phased-array systems.

References

[1] K. Kibaroglu, M. Sayginer and G. M. Rebeiz, "A Low-Cost Scalable 32-Element 28-GHz Phased Array Transceiver for 5G Communication Links Based on a 2×2 Beamformer Flip-Chip Unit Cell," *IEEE J. Solid-State Circuit*, vol. 53, no. 5, pp. 1260-1274, May 2018.

[2] J. Chen, S. Mou, K. Ma and F. Meng, "A 3–6-GHz Wideband Compact 6-Bit Phase Shifter in 0.5-μm GaAs Technology," *IEEE Microw. Wireless Compon. Lett.*, vol. 30, no. 8, pp. 794-797, Aug. 2020.

[3] U. Kodak and G. M. Rebeiz, "A 5G 28-GHz Common-Leg T/R Front-End in 45-nm CMOS SOI With 3.7-dB NF and −30-dBc EVM With 64-QAM/500-MBaud Modulation," *IEEE Trans. Microw. Theory Techn.*, vol. 67, no. 1, pp. 318-331, Jan. 2019.

[4] N. Ji, G. Shen, D. Zeng, W. Feng and W. Che, "45°/90° Broadband Phase Shifter MMICs Using Switchable Electric–Magnetic Coupling Path Architecture," *IEEE Trans. Microw. Theory Techn.*, vol. 74, no. 2, pp. 1342-1352, Feb. 2026.

Ultra-Wideband RCS Reduction Metasurface with Tunable Transmission Window

1st Cong Zhang
National Key Laboratory of Radar Detection and Sensing
Xidian University
Xi'an, China
15243146618@163.com

2nd Yuchen Gao
National Key Laboratory of Radar Detection and Sensing
Xidian University
Xi'an, China
gaoyuchen@xidian.edu.cn

3rd Hui Xin
National Key Laboratory of Radar Detection and Sensing
Xidian University
Xi'an, China
2582833627@qq.com

4th Tao Hong
National Key Laboratory of Radar Detection and Sensing
Xidian University
Xi'an, China
thong@mail.xidian.edu.cn

***Abstract*—This paper presents a metasurface design that integrates polarization conversion and reconfigurable frequency selective surface (FSS) technologies to achieve ultra-wideband radar cross section (RCS) reduction with a continuously tunable transmission window. The structure comprises a tunable low-frequency polarization conversion metasurface (PCM) loaded with varactors and resistors, a high-frequency PCM orthogonally stacked to avoid Fano resonance, and a reconfigurable FSS. By adjusting varactor capacitance, the transmission window can be tuned from 4.6 GHz to 7.1 GHz with insertion loss <1 dB, while maintaining polarization conversion absorption ratio (PCAR) >0.9 in stopbands. A checkerboard array achieves >10 dB RCS reduction from 5 GHz to 26 GHz (135.5% bandwidth). This design offers unique flexibility for adaptive stealth antennas.**

Keywords—Radar Cross Section Reduction, Polarization Con version Metasurface, Tunable Transmission Window, FSS

I. INTRODUCTION

Radar cross section (RCS) reduction is essential for stealth platforms. Conventional methods using absorbers or reflective metasurfaces suffer from fixed operational bands and lack transmission capability, limiting their integration with antennas requiring transparent windows. Polarization conversion metasurfaces (PCMs) effectively reduce RCS via phase cancellation [1], [2], but most designs neglect adaptively tunable transmission bands.

Frequency selective surfaces (FSS) provide bandpass filtering [3]. Combining FSS with PCM achieves low-scattering surfaces with fixed transmission windows [4]–[6]. However, these windows cannot be reconfigured. While reconfigurable metasurfaces with active components enable dynamic control [7], [8], a design offering both ultra-wideband RCS reduction and a continuously tunable transmission window remains unreported.

This paper proposes a multilayer metasurface combining a tunable low-frequency PCM, a high-frequency PCM, and a reconfigurable FSS. Varactor-loaded PCM creates a tunable transmission band, while orthogonal stacking suppresses Fano resonance. The checkerboard array achieves 10-dB RCS reduction from 5 GHz to 26 GHz and a transmission window tunable from 4.6 GHz to 7.1 GHz.

II. DESIGN METHOD

A. Ultra-Wideband PCM Unit

Low-frequency (LF) and high-frequency (HF) PCM units are designed separately. The LF unit consists of a cross-shaped patch with multiple stubs on a 0.5-mm Rogers 5880 substrate ($\varepsilon r = 2.2$, $\tan\delta = 0.0009$), backed by a 9.8-mm air layer and a ground plane. The HF unit uses a curved cross-stub geometry on a 2.5-mm substrate with a 1.7-mm air layer. Chip resistors (110 Ω and 145 Ω) are loaded at the stub ends of the LF unit to suppress higher-order harmonics above 14 GHz, which otherwise would interfere with the HF unit's operation.

If the two units were simply stacked vertically, anti-parallel surface currents would appear at certain frequencies (e.g., around 10 GHz) due to Fano resonance, severely degrading the polarization conversion efficiency. To eliminate this, the HF units are rotated by 90° and placed orthogonally within the gaps of the LF unit. This orthogonal arrangement ensures that currents in both layers remain either co-directional (at 8 GHz and 24 GHz) or orthogonal (at 10 GHz), thereby avoiding destructive interference. As a result, the combined ultra-wideband unit achieves a polarization conversion absorption ratio (PCAR) greater than 0.9 across an ultra-wide frequency range from 4.2 GHz to 28 GHz, effectively merging the operating bands of the two constituent units.

B. Tunable Transmission Window

To introduce a tunable transmission window, the LF PCM is modified by adding two capacitors (0.7 pF each) and a varactor diode in series with the stubs. The capacitors block DC bias while allowing RF current, and the varactor provides capacitance tunability. By varying the varactor's capacitance, the resonance condition of the LF unit shifts, creating a frequency band where polarization conversion is suppressed and incident waves can transmit through with minimal loss. This band serves as a tunable transmission window.

A reconfigurable FSS is designed using circuit model mapping. The equivalent circuit is a parallel LC resonator; varactors are incorporated to make the resonant frequency tunable. The physical FSS is implemented on a 0.5-mm Rogers 5880 substrate with square ring patches on both sides and four metallic vias connecting the layers. Varactors are

placed at strategic locations to realize the tunable capacitance. The FSS provides a –1 dB passband that can be tuned from 5 GHz to 8 GHz, matching the tunable range of the modified LF PCM.

The final unit cell stacks (from top to bottom): tunable LF PCM layer, HF PCM layer (with orthogonal orientation), reconfigurable FSS layer, and ground plane, separated by air gaps of optimized heights (t1 = 0.5 mm, t2 = 2.5 mm, t3 = 0.5 mm, t4 = 3.4 mm, t5 = 4.1 mm). Fig. 1 shows the complete structure. The period of the LF PCM is 18 mm, while the HF PCM and FSS have periods of 6 mm and 9 mm, respectively.

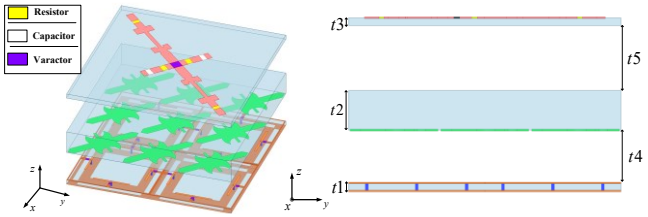


Fig. 1. Combined metasurface unit.

III. Results and Analysis

A. Tunable Transmission Performance

Full-wave simulations are conducted using periodic boundary conditions. Six representative capacitance states (C1 to C6) are selected to cover the intended tuning range. Fig.2 shows the simulated co-polarized transmission coefficient (S21). As capacitance increases, the transmission window shifts continuously from 4.6 GHz to 7.1 GHz. Within each passband, S21 exceeds –1 dB, indicating low insertion loss. The seamless transition between adjacent states confirms the continuous tunability of the design.

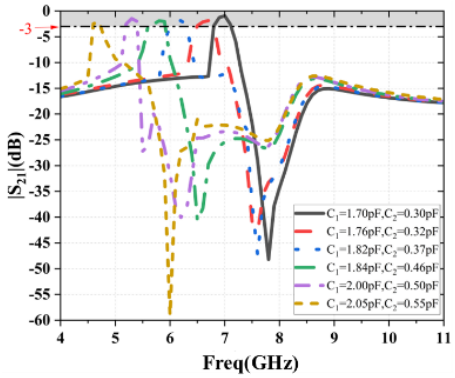


Fig. 2. Co-polarized transmission coefficient (|S_{21}|).

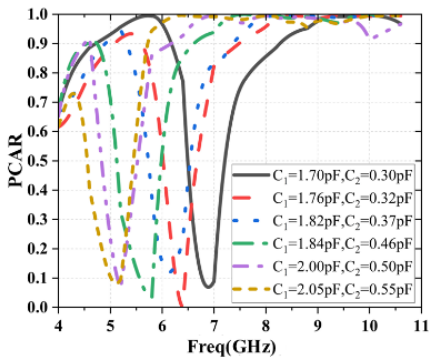


Fig. 3. Polarization conversion absorption ratio.

Fig.3 presents the corresponding PCAR. In the transmission band, PCAR drops below 0.2, confirming that negligible polarization conversion occurs. Outside the passband, PCAR remains above 0.9, ensuring efficient polarization conversion for RCS reduction. The sharp transition between transmission and reflection modes demonstrates good frequency selectivity.

B. RCS Reduction Performance

To evaluate RCS reduction, a 180 mm × 180 mm checkerboard array is constructed by arranging the unit cells in a 10×10 supercell pattern, which contains 10×10 LF units, 30×30 HF units, and 20×20 FSS units. Fig. 4 illustrates the schematic of the proposed metasurface array, showing the arrangement of the three functional layers in a checkerboard configuration.

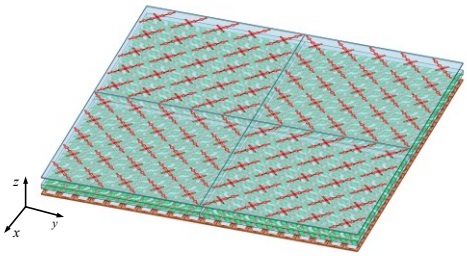


Fig. 4. Schematic of the proposed metasurface array with checkerboard layout.

Fig. 5 compares the simulated monostatic RCS of the metasurface array with that of a same-sized metallic plate under normal incidence for x-polarization (similar results for y-polarization due to symmetry). The metasurface exhibits significantly lower RCS over a broad frequency range.

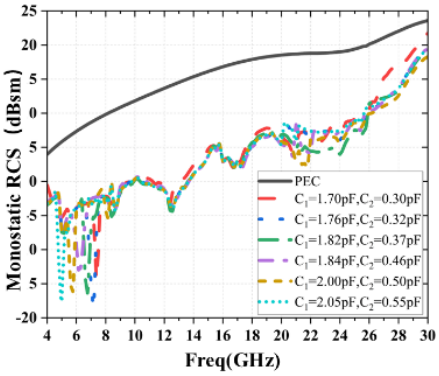


Fig. 5. Simulated monostatic RCS.

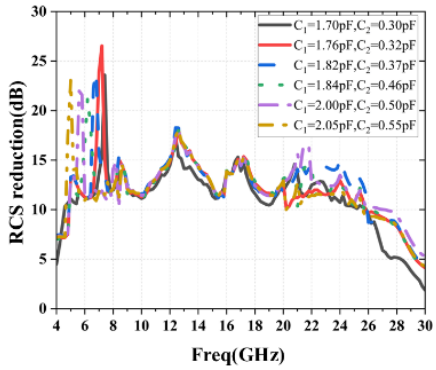


Fig. 6. RCS reduction relative to the metal plate.

Fig. 6 shows the RCS reduction relative to the metal plate. The reduction exceeds 10 dB from 5 GHz to 26 GHz, corresponding to a relative bandwidth of 135.5%. The slight narrowing compared to the unit-cell bandwidth is attributed to edge truncation effects in the finite array. The ultra-wideband performance is attributed to the successful merging of the LF and HF PCM bands via orthogonal stacking and harmonic suppression.

Table I compares the RCS reduction performance of the proposed design with previously reported works. This work achieves an ultra-wideband 10-dB RCS reduction from 5 GHz to 26 GHz (135.5% bandwidth), which is among the widest reported to date.

Table II summarizes the transmission window characteristics and reconfigurability of different designs. Unlike prior works with fixed or switchable passbands, this design offers a continuously tunable transmission window from 4.6 GHz to 7.1 GHz (43.5% tuning range).

The combination of ultra-wideband RCS reduction and dynamic passband tunability makes this metasurface highly attractive for adaptive stealth antennas and multifunctional radomes.

TABLE I. COMPARISON OF RCS REDUCTION PERFORMANCE

Design	Mechanism	RCS Red. (>10 dB)
[9]	Absorption	2.3 - 14.6 GHz (143.5%)
[4]	Polarization Conversion	6 - 15 GHz (85.7%)
[5]	Polarization Conversion & Absorption	2.2 - 18 GHz (156.4%)
[6]	Polarization Conversion	3 - 10.8 GHz (113%)
This Work	Polarization Conversion & Absorption	5 - 26 GHz (135.5%)

TABLE II. COMPARISON OF TRANSMISSION WINDOW PERFORMANCE

Design	Transmission Band (>-3 dB)	Reconfigurability
[9]	5.3–7.8 GHz (38.2%)	None
[4]	8.5–11.1 GHz (25.6%)	None
[5]	6.8–12.6 GHz (59.8%)	None
[6]	2.6–4.4 GHz (51.4%)	Switchable
This Work	4.6–7.1 GHz (43.5%)	Tunable

IV. CONCLUSION

A metasurface with ultra-wideband RCS reduction and a continuously tunable transmission window is proposed and numerically demonstrated. Orthogonal stacking of dual-band PCMs eliminates Fano resonance, enabling seamless merging of their operating bands. Varactor-tuned PCM and FSS provide a transmission window tunable from 4.6 GHz to 7.1 GHz with low insertion loss. The checkerboard array achieves >10 dB RCS reduction over 5–26 GHz (135.5% bandwidth). This design offers unprecedented flexibility for adaptive antenna systems and multifunctional radomes. Future work will focus on experimental validation and angular stability analysis.

REFERENCES

[1] Y. Jia, Y. Liu, Y. J. Guo, K. Li, and S. Gong, "Broadband polarization rotation reflective surfaces and their application on RCS reduction," IEEE Trans. Antennas Propag., vol. 64, no. 1, pp. 179–188, Jan. 2016.

[2] S. Sun, W. Jiang, P. Liu, and S. Gong, "Ultra-wideband high-efficiency 2.5-dimensional polarization conversion metasurface and its application in RCS reduction of antenna," IEEE Antennas Wireless Propag. Lett., vol. 18, no. 5, pp. 881–885, May 2019.

[3] B. A. Munk, Frequency Selective Surfaces: Theory and Design. New York: Wiley, 2000.

[4] L. Wang, S. Liu, X. Kong, H. Zhang, and Y. Li, "A multifunctional frequency-selective polarization converter for broadband backward-scattering reduction," IEEE Trans. Antennas Propag., vol. 69, no. 5, pp. 2833–2841, May 2021.

[5] Q. Lv, C. Jin, B. Zhang, and R. Mittra, "Hybrid absorptive-diffusive frequency selective radome," IEEE Trans. Antennas Propag., vol. 69, no. 6, pp. 3312–3321, Jun. 2021.

[6] Y. Zhu, W. Yang, K. Duan, and Q. Chen, "Wideband low-scattering metasurface with an in-band reconfigurable transparent window," Chin. Phys. B, vol. 33, no. 2, p. 024102, 2024.

[7] H. Yang, S. Wang, P. Li, and Y. Li, "A broadband multifunctional reconfigurable polarization conversion metasurface," IEEE Trans. Antennas Propag., vol. 71, no. 7, pp. 5759–5767, Jul. 2023.

[8] F. Costa, A. Monorchio, and G. Manara, "An overview of equivalent circuit modeling techniques of frequency selective surfaces and metasurfaces," Appl. Comput. Electromagn. Soc. J., vol. 29, no. 12, pp. 960–976, Dec. 2014.

[9] J. Xia, J. Wei, Y. Liu, et al., "Design of a wideband absorption frequency selective rasorber based on double lossy layers," IEEE Trans. Antennas Propag., vol. 68, no. 7, pp. 5718–5723, Jul. 2020.

3D-Printed Copper Waveguide Bandpass Filter for Q-Band Ground Station Application

Lu Qian
School of Engineering
University of Birmingham
Birmingham, United Kingdom
L.Qian.1@bham.ac.uk

John Robinson
School of Engineering
University of Wolverhampton
Wolverhampton, United Kingdom
J.Robinson12@wlv.ac.uk

Arun Arjunan
School of Engineering
University of Wolverhampton
Wolverhampton, United Kingdom
A.Arjunan@wlv.ac.uk

Yi Wang
School of Engineering
University of Birmingham
Birmingham, United Kingdom
Y.Wang.1@bham.ac.uk

***Abstract*—Metal additive manufacturing has emerged as a transformative fabrication technique for microwave and millimetre-wave waveguide components, yet challenges persist due to degrading surface conductivity from high surface roughness, particularly in low-conductivity metals and alloys. Copper is one of the most electrically conductive metals. Its nominal bulk conductivity is 53% higher than aluminium. However, copper printing is not as well developed and utilised due to process difficulties that arise from the poor absorption of infrared laser commonly used in Laser Powder Bed Fusion (L-PBF) Additive Manufacturing (AM). This work investigates the application of pure copper printing to waveguide devices. A monolithic copper waveguide bandpass filter is fabricated using L-PBF technology, leveraging copper's superior electrical and thermal properties for high-power microwave applications. This filter employs a step-impedance low-pass design and exploits waveguide cut-off characteristics for passband frequency selectivity. The filter is designed for Q-band ground segment network applications, with a passband from 37.5 to 42.5 GHz. Optimized L-PBF processing parameters overcome copper's high reflectivity to infrared laser. RF measurements show excellent agreement with simulations, yielding a 0.45 dB insertion loss and an 19 dB worst-case return loss, with minimal frequency shift confirming high manufacturing accuracy. This study demonstrates the potential of copper 3D printing for waveguide filters.**

Keywords—Additive manufacturing (AM), Copper high-power filter, millimetre-wave components, novel materials, waveguide.

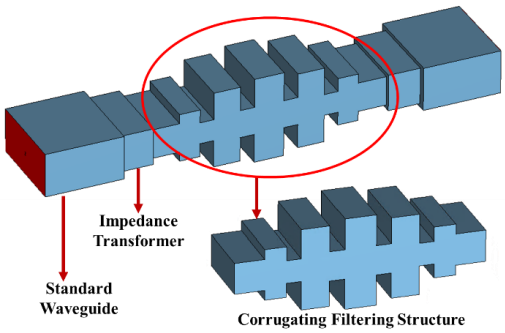
I. INTRODUCTION

The advancement of satellite communication technology has driven the space industry to explore higher frequency bands for commercial applications [1]. The Q-/V-band is of particular interest, primarily facilitating communication between ground station gateways and satellites. Waveguide filters are essential RF components in these high-frequency communication systems due to their low-loss characteristics and high-power capacity. Conventional waveguide bandpass filter (BPF) for Q-band typically employs coupled resonant cavities through rectangular waveguide sections and inductive/capacitive irises [2]. However, the increasing frequency (and therefore decreasing geometry features) of the filters introduces new challenges to manufacturing, as they require higher precision, making the fabrication process more expensive and time-consuming. Additionally, the need for assembly of separately machined parts increases insertion loss and risk of leakage.

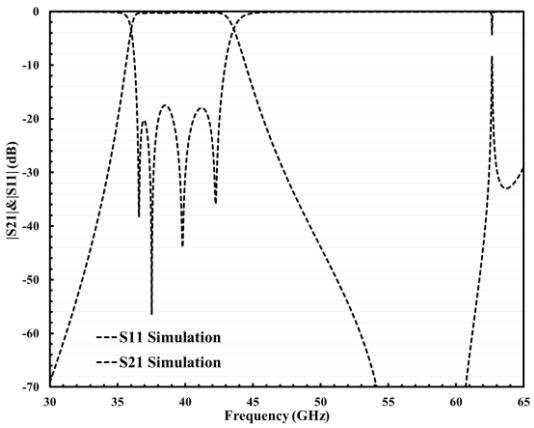
Additive manufacturing (AM), particularly metallic AM, has emerged as a new fabrication solution for microwave and millimetre-wave waveguide components due to its capability for rapid prototyping and monolithic construction of complex geometries [3], [4]. Among metallic AM technologies, L-PBF is the most widely used approach in the microwave community. Numerous 3D-printed microwave and mm-wave waveguide filters have been reported [5], [6], [7]. However, a common drawback of 3D-printed devices is their poor surface conductivity largely due to higher surface roughness than those machined counterparts [8]. One solution is the direct fabrication using high-conductivity metals, such as copper or silver. Pure copper has one of the highest electrical conductivities, 53% higher than aluminium. It is more affordable than silver. Copper also has lower coefficient of thermal expansion (CTE) and higher thermal conductivity than aluminium. Its electrical and thermal properties are excellent for high-power microwave applications. However, pure copper is not easy to machine for its softness and ductility. It is not easy to print either, due to its high reflectivity and conductivity, which hinder laser-material interaction [9], [10], [11]. Additionally, its tendency to oxidize further complicates the process. This work developed and applied optimised laser processing parameter for copper printing using an industrial-grade EOS M290 L-PBF system (EOS GmbH, Krailling, Germany).

To mitigate the high sensitivity to geometrical dimensions associated with coupled cavity waveguide filters, a corrugated waveguide bandpass filter is proposed. Stepped-impedance corrugated waveguide filter is a classical low-pass filter commonly used in satellite transponders as a harmonic rejection filter [12]. Compared to conventional coupled resonant cavity filters, it exhibits greater robustness to fabrication tolerances by eliminating sensitive coupling irises. Despite its high fabrication yield, the application of corrugated waveguide filters has traditionally been limited to low-pass filtering. To achieve a BPF response, one approach is to

979-8-3315-4544-4/26/$31.00 ©2026 IEEE



(a)



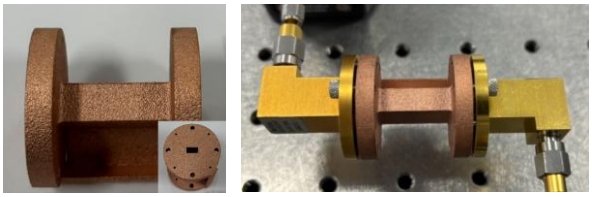
(b)

Fig. 1. (a) Air model of the corrugate waveguide bandpass filter. (b) Simulation results.

leverage the first passband replica of the commensurate-line stepped-impedance low-pass structure [13]. In this work, we adopt a different approach by adjusting the broadside of the corrugated waveguide structure to align the fundamental cutoff frequency with the lower passband edge. Additionally, an impedance transformer is incorporated at both ports of the block filter to ensure compatibility with standard waveguide interfaces.

II. Design of Corrugate Waveguide Bandpass Filter

The proposed bandpass filter employs a stepped-impedance corrugated waveguide structure to mitigate fabrication sensitivity. Fig. 1(a) illustrates the air model of the filter. The primary structure consists of the corrugate waveguide structure that provide the required filtering characteristics. Impedance transformers are used at both ends of the filter block to match the input and output dimensions to the standard waveguide. To achieve the bandpass characteristics, the width of the central cascaded step-impedance waveguide sections is determined to ensure the cutoff frequency aligns with the lower passband edge. For the 37.5–42.5 GHz passband, the waveguide width is set to 4.2 mm, corresponding to a cutoff frequency of 35.7 GHz. Heights of individual waveguide sections are optimized based on classical stepped-impedance lowpass filter design principles. A single-stage impedance transformer is used to ensure optimal matching with WR-22. Full-wave electromagnetic (EM) simulations are performed to fine-tune the filter dimensions. Fig. 1(b) presents the simulated S-parameters after optimization, demonstrating a return loss of better than 17 dB and out-of-band rejection exceeding 40 dB up to 62 GHz.



(a) (b)

Fig. 2. (a) Photograph of the as-printed copper waveguide filter; (b) Measurement setup

III. Manufacture

The L-PBF process constructs the part layer by layer using selective laser melting, where fine metal powder is melted and fused onto previously solidified layers. The effectiveness of L-PBF depends heavily on the interaction between the laser and the metal powder. Critical factors affecting this process include the composition of the metal powder feedstock, its Particle Size Distribution (PSD), as well as laser power, scan speed, spot size, and layer thickness. These elements collectively impact phase transformations, molten metal dynamics, cooling rates, and laser-related phenomena such as diffusion, absorption, reflection, and scattering. Infrared laser wavelengths (1060–1090 nm) are commonly used in L-PBF systems because they are efficiently absorbed by metals like steel, which typically reflects only ~40% of thermal energy. However, copper has very high reflectivity. Solid Cu reflects up to ~98% of infrared laser energy while Cu powder still reflects approximately 71%. To address these processing challenges, a laser parametric study was conducted to optimize laser-material interaction and enhance the electrical and thermal performance of printed copper samples. Table I presents the developed laser processing parameters. The study utilized an industrial-grade EOS M290 L-PBF system equipped with a 400 W infrared laser source and a 100 µm spot size. The process was conducted under an argon atmosphere with oxygen levels maintained below 0.1% to mitigate oxidation. Based on experimental material characterization, the highest achieved density and electrical conductivity for printed copper samples were 88% and 73% of the International Annealed Copper Standard (IACS), respectively, significantly higher than commonly used AlSi10Mg alloy.

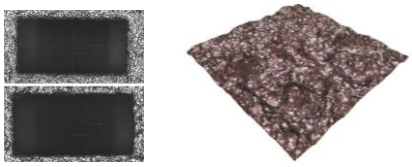
TABLE I. Summary of Laser Processing Parameter

Laser Power (W)	Laser Spot Size (µm)	Scan Speed (mm/s)	Hatch Distance (mm)	Layer Thickness (µm)
370	100	400	0.14	30

For printing, the filter was tilted at 45° to avoid overhang structures inside the filter. The as-printed filter was detached from the build platform using non-contact electrical discharge machining. Bead blasting was applied but is not expected to work on the internal surfaces. Fig. 2 shows a photograph of the monolithically as-printed filter.

IV. Measurement

The mechanical properties of the as-printed copper filter, including dimensions and surface roughness, were evaluated using an Alicona G4 InfiniteFocus Optical system. Figure 3(a) provides a zoomed view of the waveguide (WG) openings of



(a) (b)

Fig. 5. (a) Photograph of waveguide cross section of the as-printed copper filter. (b) Surface morphology.

the as-printed copper filter, showing that the average measured opening size is 5.63 mm × 2.84 mm, which closely matches the standard WR-22 waveguide (5.6896 mm × 2.8448 mm). Figure 3(b) illustrates the surface morphology of the as-printed filter after bead blasting. Multiple points were measured, with test results revealing an average surface roughness of Sa = 3.45 µm. Using this surface roughness, the effective electrical conductivity was calculated based on the Hammerstad-Bekkadal (HB) model, assuming a copper conductivity of 4.52×10^7 S/m (73% IACS), resulting in an effective electric conductivity of 1.14×10^7 S/m. This effective conductivity was then incorporated into simulations for comparison with measurement results. It should be noted that the internal surface roughness is expected to be higher than 3.45 µm but this was not measured due to limited availability of samples.

Following the mechanical assessment, the flange surfaces were machined for flatness and good contact with test ports. RF measurements were conducted using a Keysight N53478B PNA-X network analyser covering the entire Q-band (33–50 GHz). No tuning was applied during testing. Figure 4 presents the measured and simulated responses of the copper filter, including an EM simulation that accounts for the effective conductivity of 1.14×10^7 S/m the for comparison. The results demonstrate good agreement between measured and simulated responses. The measured centre frequency is 40.2 GHz, with a slight up shift of only 0.5%. Within the passband, the measured minimum return loss is approximately 19 dB, while the average insertion loss is around 0.45 dB. There is a minor discrepancy of 0.2 dB in insertion loss, compared to simulations. As mentioned early, the effective conductivity is likely an underestimation as the internal surface roughness was not obtained. So, the discrepancy will be investigated with more comparison study. Broadly, the measured results validate the theoretical predictions, confirming the feasibility of the proposed design and fabrication approach.

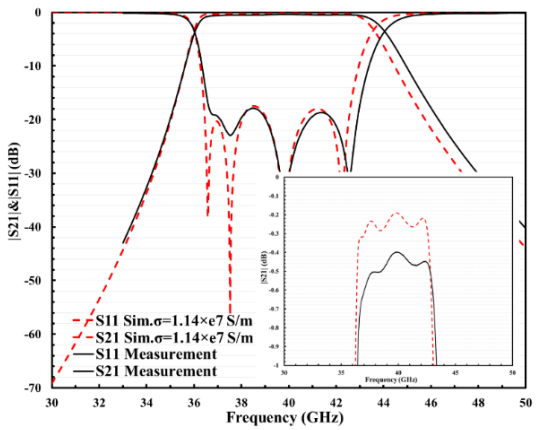


Fig. 4. Measurement results in comparison with simulations considering the effective conductivity.

V. Conclusion

A Q-band 3D-printed copper waveguide filter has been experimentally demonstrated. RF measurement results showed excellent agreement with simulations, showing the feasibility of using copper 3D printing technology for waveguide filter fabrication. Further performance improvements may be achievable by applying post-processing techniques such as surface treatment and enhancements in copper powder quality. The proposed design and manufacturing approach can be extended to develop more complex passive microwave devices and antennas for space applications.

References

[1] T. Rossi, M. De Sanctis, E. Cianca, G. Codispoti, G. Parca, and M. Ruggieri, "A decade of EHF scientific research: Unveiling insights from Alphasat Q/V-band satellite communication experiments," *International Journal of Satellite Communications and Networking*, 2024, doi: 10.1002/SAT.1532.

[2] V. E. Boria and B. Gimeno, "Waveguide filters for satellites," *IEEE Microw. Mag.*, vol. 8, no. 5, pp. 60–70, Oct. 2007, doi: 10.1109/MMM.2007.903649.

[3] O. A. Peverini, M. Lumia, G. Addamo, G. Virone, and N. J. G. Fonseca, "How 3D-Printing Is Changing RF Front-End Design for Space Applications," *IEEE Journal of Microwaves*, vol. 3, no. 2, pp. 1–15, Apr. 2023, doi: 10.1109/jmw.2023.3250343.

[4] M. D. Nguyen, Z. Yin, R. Del Rey, F. Iacopi, and Y. Yang, "Additive Manufacturing Materials and Processes for Passive Electronics in Wireless Communication," *IEEE Transactions on Materials for Electron Devices*, pp. 1–9, Aug. 2024, doi: 10.1109/tmat.2024.3440889.

[5] L. Qian *et al.*, "A Narrowband 3-D Printed Invar Spherical Dual-Mode Filter With High Thermal Stability for OMUXs," *IEEE Trans. Microw. Theory Tech.*, vol. 70, no. 4, pp. 2165–2173, Apr. 2022, doi: 10.1109/TMTT.2022.3152795.

[6] L. Qian, R. Martinez, M. Salek, M. Attallah, Y. Wang, and M. J. Lancaster, "Compact Monolithic SLM 3D-Printed Filters using Pole-Generating Resonant Irises," in *2021 51st European Microwave Conference (EuMC)*, IEEE, Apr. 2022, pp. 118–121. doi: 10.23919/EuMC50147.2022.9784337.

[7] P. Booth and E. V. Lluch, "Enhancing the Performance of Waveguide Filters Using Additive Manufacturing," *Proceedings of the IEEE*, vol. 105, no. 4, pp. 613–619, Nov. 2016, doi: 10.1109/jproc.2016.2616494.

[8] J. Sorocki *et al.*, "Low-Cost Method for Internal Surface Roughness Reduction of Additively Manufactured All-Metal Waveguide Components," *IEEE Trans. Microw. Theory Tech.*, vol. 72, no. 8, pp. 4519–4529, 2024, doi: 10.1109/TMTT.2024.3361976.

[9] L. Gargalis *et al.*, "Determining processing behaviour of pure Cu in laser powder bed fusion using direct micro-calorimetry," *J. Mater. Process. Technol.*, vol. 294, Aug. 2021, doi: 10.1016/j.jmatprotec.2021.117130.

[10] S. W. Britten, L. Schmid, T. Molitor, and M. Rütering, "Blue high-power laser sources for processing solutions in e-mobility and beyond," in *Procedia CIRP*, Elsevier B.V., 2020, pp. 592–595. doi: 10.1016/j.procir.2020.09.082.

[11] J. Robinson *et al.*, "Electrical Conductivity of Additively Manufactured Copper and Silver for Electrical Winding Applications," *Materials*, vol. 15, no. 21, Nov. 2022, doi: 10.3390/ma15217563.

[12] E. M. T. Jones, George Matthaei, and Leo Young, *Microwave Filters, Impedance-Matching Networks, and Coupling Structures*, vol. 5. New York, USA: McGraw-Hill, 1964.

[13] A. Sami *et al.*, "Robust Tolerance Design of Bandpass Filter with Improved Frequency Response for Q-Band Satellite Applications," *IEEE Microwave and Wireless Components Letters*, vol. 31, no. 11, pp. 1183–1186, Nov. 2021, doi: 10.1109/LMWC.2021.3090218.

A Broadband Unequal Power Divider Based on an H-Plane Height-Reduced Waveguide T-Junction

Bo Li

Chengdu Polaris Information and Communication Technology Co.,Ltd

Chengdu, China

polarixis.cd@gmail.com

***Abstract* —This paper presents a method for designing a broadband unequal power divider to achieve an arbitrary power-dividing ratio. The divider is realized by reducing the height of the narrow edge of a waveguide, without affecting the phase consistency between the two output ports. Formulas for determining the power ratio and a design methodology to compensate for discontinuities in the waveguide—using irises, a septum, and a matching section—are introduced. Moreover, a 2:1 unequal power divider operating in the frequency range of 25–31 GHz is designed and fabricated. The measured bandwidth is approximately 21%, featuring an input return loss exceeding 25 dB, an insertion loss below 0.15 dB, and a phase difference between the output ports of less than 5°.**

Keywords — reduced height waveguide T-Junction, unequal power divider, arbitrary power-dividing ratio.

I. INTRODUCTION

Power dividers with an unequal output dividing ratio are fundamental components and widely used in microwave circuits, such as power amplifier, antenna arrays. As discussed in previous studies [1], [2], [3], [4], H-plane waveguide T-junction, which has the characteristics of low loss and easy fabrication is the most widely used structure of the unequal power divider. Wedges and inductive windows were used to design a 2:1 power divider operating at 12.2-12.7 GHz, with 0.2 dB insertion loss and 2 degree phase-difference as in [1]. A T-junction operating at a normalized frequency of 1.374 achieves a maximum magnitude and phase variation of 0.4 dB and 2.8º at the output ports, designed by optimizing irises and septum to control dividing power ratio as in [2]. An unequal power divider was realized by an offset septum and a matching window, which achieved 8º phase difference in 14-17 GHz with return loss better than 23 dB as in [3]. Two rectangular waveguide power dividers, featuring straight and slanted septa respectively, were designed to facilitate a high power-division ratio of 1:11.6 in the H-plane as in [4]. However, most of these studies need to adjust the length of output ports to obtain in-phase performance caused by the different length of transmission path between two output ports.

In this study, an unequal power divider realized by reduced height waveguide T-junction is presented, which could easily alter the power-dividing ratio by varying the ‘b’ dimension of the waveguide, as shown in Fig.2(a). This novel design features a septum inserted in the center of output waveguides, two inductive iris loaded on the joint of waveguides and a rectangular matching-section placed in one of output reduced-height waveguide, connecting the septum. With this unique design, the discontinuity of waveguide can be compensated, as while as, the effective bandwidth can be extended as stepped impedance matching.

II. THEORETICAL ANALYSIS AND DESIGN OF UNEQUAL POWER DIVIDER

When electromagnetic waves are transmitted in rectangular waveguides, the theoretical phase velocity is given by

$$v_p = \frac{\omega}{\beta} = \frac{v}{\sqrt{1-(\lambda/\lambda_c)^2}} \tag{1}$$

where $\lambda = 1/\sqrt{\mu\varepsilon}$, $\lambda_c = 2a$. According to (1), the phase velocity only depends on the ‘a’ dimension, and has nothing to do with the ‘b’ dimension. In order to get some physical insight on the relationship between the phase velocity and ‘a’, ’b’ dimension, an analysis model is established as shown in Fig.1. Two section rectangular waveguides are placed on the workspace of simulation software. Firstly, only ‘a’ dimension is varied, assumed $\Delta = a_2/a_1$, the electric field intensity and phase of two waveguides are both different as shown in Fig.1(a) and Fig.1(b). Then, only ‘b’ dimension is varied, assumed $\Delta = b_2/b_1$, the electric field intensity is changed, but the phase of two waveguides are the same as shown in Fig.1(c) and Fig.1 (d). Therefore, unequal power divider based on H-plane reduced height waveguide T-junction has a great advantage in phase consistency between two output ports.

To figure out the relationship between power-dividing ratio and ‘b’ dimension, an equivalent circuit was developed as shown in Fig.2(b). In theroy, if port1 is matched, the characteristic impedance of three waveguide branches has the following relationship:

$$Y_{in} = \frac{1}{Z_1} = j\beta + \frac{1}{Z_2} + \frac{1}{Z_3} \tag{2}$$

Where jβ is the equivalent lumped susceptance of waveguid discontinuity. By compensating waveguide discontinuity with irises, septum and matching-section, jβ can be treated as 0, then there is

$$\frac{1}{Z_1} = \frac{1}{Z_2} + \frac{1}{Z_3} \tag{3}$$

As we all kown, the transmission power and equivalent characteristic impedance of rectangular waveguide TE10 mode is defined as

$$P_{TE10} = \frac{E_0^2 ab}{4Z_{TEM}}\sqrt{1-(\lambda/2a)^2} \tag{4}$$

$$Z_0 = \frac{U}{I} = \frac{\pi b}{2a}\cdot\frac{Z_{TEM}}{\sqrt{1-(\lambda/2a)^2}} \tag{5}$$

By inserting (5) into (3), 'b' dimensions of three waveguide branches can be expressed as (6), meanwhile, based on (4) and (5), the power ratio of port2 and port3 can be derived as (7).

$$\frac{1}{b_1} = \frac{1}{b_2} + \frac{1}{b_3} \tag{6}$$

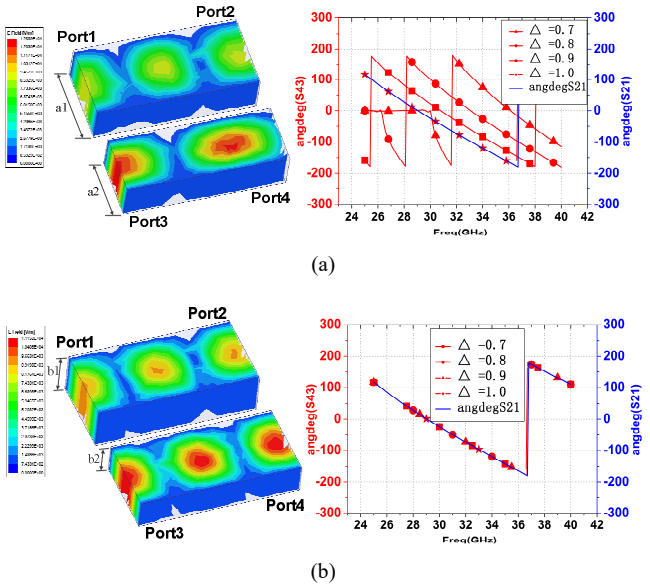
$$\frac{P_{port2}}{P_{port3}} = \frac{U_2^2}{Z_2}\times\frac{Z_3}{U_3^2} \tag{7}$$

From Fig.2(b) we can kown that the equivalent voltage of three ports could be expressed as (8), by inserting (8) into (7), the power ratio of port2 and port3 can be restated as (9), where $m = b_3/b_2$.

$$U = \frac{U_1}{2} = \frac{\frac{Z_1Z_3}{Z_1+Z_3}}{\frac{Z_1Z_3}{Z_1+Z_3}+Z_2}\times U_2 = \frac{\frac{Z_1Z_2}{Z_1+Z_2}}{\frac{Z_1Z_2}{Z_1+Z_2}+Z_3}\times U_3 \tag{8}$$

$$\frac{P_{port2}}{P_{port3}} = m\left(\frac{m^2+m}{m^2+m^3}\right)^2 = 1/m \tag{9}$$

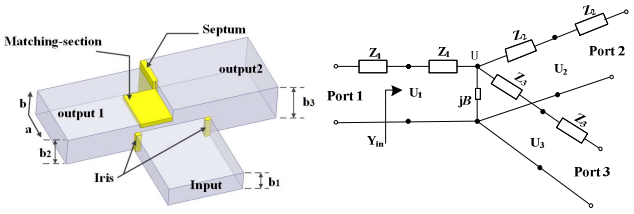
According to the above analysis, power-dividing ratio between two output ports can be easily obtained by adjusting the ratio of 'b' dimension of three rectangular waveguide branches, what needs to do is to optimize matching-structure.



(a)

(b)

Fig.1. Analysis model and simulated results of the electric field intensity and phase. (a) Changing 'a' dimension. (b) Changing 'b' dimension.

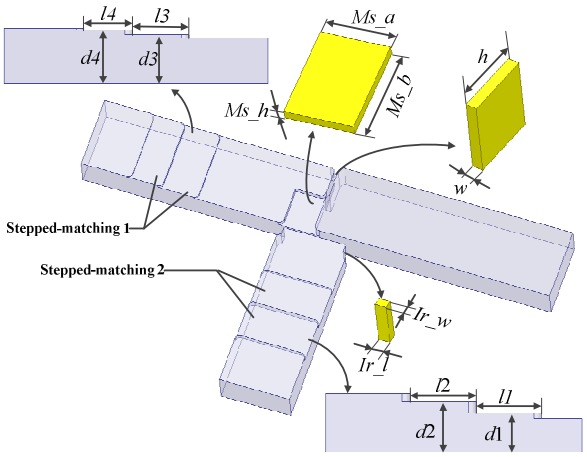


(a) (b)

Fig.2. Unequal power divider based on H-plane reduced height waveguide T-junction. (a) Artificial model. (b) Equivalent circuit.

III. Simulation and Measurement

In this work, one 2:1 unequal power divider operating at Ka band is designed and fabricated as shown in Fig.3. Make the 'b' dimension of one output waveguide equal to the 3.56 mm, which is the standard size of WR28, the other output waveguide and input waveguide are matched to standard waveguide by stepped-matching, respectively. The key parameters of the 2:1 unequal power divider and detailed values are given in Fig.3.

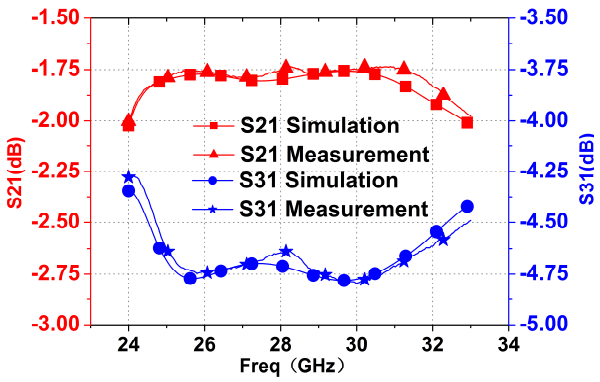


(a)

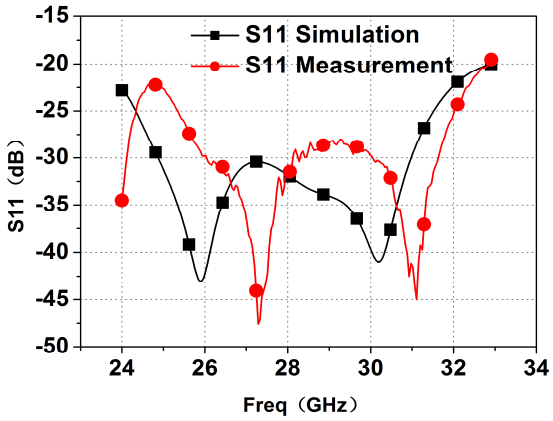


(b)

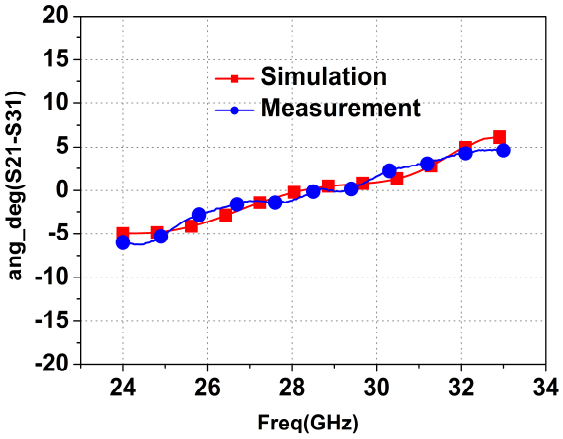
Fig.3. 3-D model and Physical drawing of the 2:1 unequal power divider: (a) 3-D model with detailed parameters; (b) Physical drawing. (w=0.5,h=3.21,Ms_a=3.22,Ms_b=3.91,Ir_w=0.74,Ir_l=0.42,l1=3.96,l2=4.03, l3=3.6,l4=3.14,d1=2.39,d2=3.07,d3=3.12,d4=3.44,unit:mm)



(a)



(b)



(c)

Fig.4. Simulated and measured results of the 2:1 unequal power divider prototype: (a) Insertion loss; (b) Return loss at the input; (c) Phase difference of the two output ports.

TABLE I. COMPARISONS WITH PREVIOUSLY REPORTED REFERENCES

Ref.	*Freq (GHz)*	*IRL*[a] *(dB)*	*IL*[b] *(dB)*	*FB*[c] *(%)*	*PI*[d] *(°)*
[1]	12.2-12.7	21	0.2	4	1
[3]	14-17	23	-	19	8
[4]	$0.95*F_c$-$1.05*F_c$	31	1.0	10	65
This work	25-31	25	0.15	21	5

[a] Input return loss

[b] Insertion loss

[c] Fractional bandwidth

[d] Phase imbalance

As shown in Fig.4, the simulated and measured S-parameters exhibit excellent agreement. The bandwidth which return loss is better than 25 dB at the input port is from 25 to 31 GHz, with an insertion loss less than 0.15 dB. Within this range, the maximum imbalance of the phase is less than 5 degree.

IV. CONCLUSION

In this study, a novel broadband unequal power divider based on H-plane reduced height waveguide T-junction has been presented. And a 2:1 unequal power divider has been designed and measured. The advantages of this design include wide band, low cost, inherent phase consistency. Furthermore, the design approach is applicable across any frequency band.

ACKNOWLEDGMENT

The author would like to thank the organizers of IMWS-AMP for providing an excellent platform to present my work. Special thanks go to my colleagues at Chengdu Polaris Information and Communication Technology Co.,Ltd for their insightful discussions, technical assistance and invaluable suggestions during the course of this research. I appreciate the constructive comments from reviewers and the support from all those who contributed to the success of this project.

REFERENCES

[1] Songnan Yang et al., “Synthesis of a Compound T-Junction for a Two-Way Splitter with Arbitrary Power Ratio” IEEE MTT-S International Microwave Symposium Digest, IEEE MTT-S International Microwave Symposium Digest, 2005., Long Beach, CA, USA, 2005, pp. 985-988.

[2] Sang Heun Lee et al., “Six-Way Power Divider For Series Feed Using H-plane T-junctions” Microwave and OPtical Technology Letters., 2016, 58, (7), pp.1622-1626.

[3] Guan-Long Huang et al., “Design of a Symmetric Rectangular Waveguide T-junction with In-phase and Unequal Power Split Characteristics” IEEE Antennas and Propagation Society International Symposium, 2013 IEEE, vol. 47, no. 10, pp. 2119–2120, Oct. 2013.

[4] S. C. A, M. Tamang and B. K.S, "High Power Ratio Waveguide Power Divider," 2022 IEEE Microwaves, Antennas, and Propagation Conference (MAPCON), Bangalore, India, 2022, pp. 780-785.

Low-loss Millimeter-Wave Wideband Bandpass Filter in InP Technology with Cryogenic Performance Analysis

Hongliang Tian
the State Key Laboratory of Radio Frequency Heterogeneous Integration
Shenzhen University
Shenzhen, China
thl2026@szu.edu.cn

Haiwen Liu
School of Information Engineering
Dalian University
Dalian, China
haiwen_liu@hotmail.com

Junfa Mao
the State Key Laboratory of Radio Frequency Heterogeneous Integration
Shenzhen University
Shenzhen, China
jfmao@sjtu.edu.cn

***Abstract*—The design and cryogenic characterization of millimeter-wave ultra-wideband (UWB) bandpass filters (BPF) in InP technology are presented. First, an on-chip mm-wave UWB BPF is designed based on five LC stages, which are implemented using spiral inductors and MIM capacitors. Measurement results reveal a 0.12 dB reduction in insertion loss (IL) and a 0.3 GHz frequency shift as the device is cooled from 300 K to 77 K. To interpret these thermal effects, the GWO is employed to globally extract the equivalent circuit model parameters of the filter at both temperatures, providing quantitative insights into the parameter variations across this cryogenic temperature range. Second, a flip-chip balanced UWB BPF is proposed, incorporating an electromagnetic-circuit co-optimization strategy driven by the GWO. The filter chip is flip-chip mounted onto an alumina substrate, exhibiting stable differential-mode performance across 300 K, 70 K, and 5 K, characterized by a center frequency of 15.45 GHz, a fractional bandwidth of 101.9%, and a common-mode rejection exceeding 20 dB over the 0–24.5 GHz range. Notably, the minimum IL decreases from 1.02 dB to 0.72 dB upon cooling from 300 K to 70 K, with improvements of 0.3–0.8 dB observed across the passband. Further analysis reveals that the enhancement of gold conductivity at cryogenic temperatures constitutes the primary mechanism driving IL reduction, whose beneficial effect substantially outweighs the adverse contributions of dielectric loss and structural deformation.**

Keywords—Bandpass filter, cryogenic characterization, InP technology, grey wolf optimization (GWO), ultra-wideband.

979-8-3315-4544-4/26/$31.00 ©2026 IEEE

A Broadband High-Selectivity Bandpass Filter Branch-Line Coupler Operating in the C-Band

1st Yiyang Han
National Key Laboratory of Radar Detection and Sensing, Xidian University
Xi'an, China
hanyiyang330@163.com

2nd Kun Wei
National Key Laboratory of Radar Detection and Sensing, Xidian University
Xi'an, China
weikun@xidian.edu.cn

3rd Wei Hu
National Key Laboratory of Radar Detection and Sensing, Xidian University
Xi'an, China
whu@mail.xidian.edu.cn

4th Wen Jiang
National Key Laboratory of Radar Detection and Sensing, Xidian University
Xi'an, China
jw13@vip.qq.com

***Abstract*—This paper proposes a design scheme for a broadband, highly selective bandpass filter branch-line coupler (BHFC) for the C-band. By integrating a broadband coupling structure—comprising parallel coupling lines, high-impedance transmission lines, and parallel open-circuit branch lines—at each port of a single-section branch-line coupler, the coupler achieves bandpass filtering characteristics with excellent selectivity and a wide operating bandwidth. The circuit design has been validated through electromagnetic simulation. Experimental results demonstrate an operating frequency range of 4.02 GHz to 7.88 GHz, with a relative bandwidth reaching 64.9%. The power imbalance is ±0.6 dB, return loss exceeds 13 dB, phase imbalance is ±6.6° and selectivity exceeding 73.2%.**

Keywords—Branch-line coupler, bandpass filter, highly-selective.

I. INTRODUCTION

In recent years, with the rapid advancement of wireless communication technology, the branch-line coupler (BLC) has become an indispensable key component in numerous microwave systems. A 3dB branch-line coupler achieves equal power distribution and a 90° phase shift, making it widely applicable in devices such as power amplifiers, modulators, array antennas, and filters. However, traditional single-section BLCs constructed from transmission lines suffer from issues such as narrow bandwidth and poor passband selectivity. Therefore, designing high-performance couplers with integrated filtering response and wide operating bandwidth holds significant importance. To achieve broader bandwidth and enhanced filtering response, the industry has developed multiple technical solutions.

For instance, connecting impedance transformers [1]-[2] to each port of a single-stage BLC and employing a multi-stage cascaded topology [3]-[6] can both effectively enhance bandwidth. However, while this approach increases the overall passband filter bandwidth, it also results in an excessively large overall circuit size, making further integration with other components challenging. Reference [7] proposes a four-segment branch line topology, while Reference [8] introduces a λ/4 transmission line for a three-segment branch line coupler that replaces conventional wavelength transmission lines with meander technology. Although both structures exhibit excellent broadband coupling performance, their selectivity remains limited. Reference [9] proposed a branch line coupler employing an improved radial stub-loaded resonator. Although compact in design, it suffers from poor broadband performance and selectivity.

In modern wireless system design, beyond broadband passband performance, the suppression of signals outside the passband is another critical consideration. A novel filtering branch line coupler is proposed in [10]. This device achieves both broadband performance and filtering characteristics by cascading λ/4-length parallel coupled microstrip lines and open-circuit branch lines across the four ports of a single-section branch line coupler. However, the relatively fixed coupling bandwidth provided by the λ/4 parallel coupled lines and the transmission zeros at $(2k+1)f_0$ (k = 0, 1, 2, ...; where f_0 is the selected transmission zero frequency), this design can only achieve fixed octave bandwidth and selectivity. It cannot be applied to provide specific frequency passbands and out-of-band suppression.

This paper proposes a novel design scheme for a broadband high-selectivity bandpass filter branch coupler (BHFC). By integrating a structure comprising parallel-coupled microstrip lines, high-impedance microstrip lines, and parallel open-circuit branch lines at each port of a single-section branch coupler, it achieves bandpass filtering characteristics with excellent selectivity and a wide operating bandwidth from 4.02 GHz to 7.88 GHz. This circuit structure features a simple and compact design, facilitating manufacturing and integration with other functional devices. It holds significant application value in C-band satellite communications, WLAN wireless networks, and phased array antennas.

II. DESIGN PROCEDURE

A. Circuit Structure Analysis of Broadband Bandpass Transmission Line Unit

Figure 1(a) shows the schematic diagram of the proposed BHFC. First, a conventional single-section BLC is constructed using a λ/4-length microstrip transmission line, with branch line impedances Z_1 and Z_2 in the coupler. Subsequently, adding a broadband bandpass transmission line unit (BBLU) centered on a parallel coupled line to each of the four ports of this BLC improves the performance of the conventional BLC.

979-8-3315-4544-4/26/$31.00 ©2026 IEEE

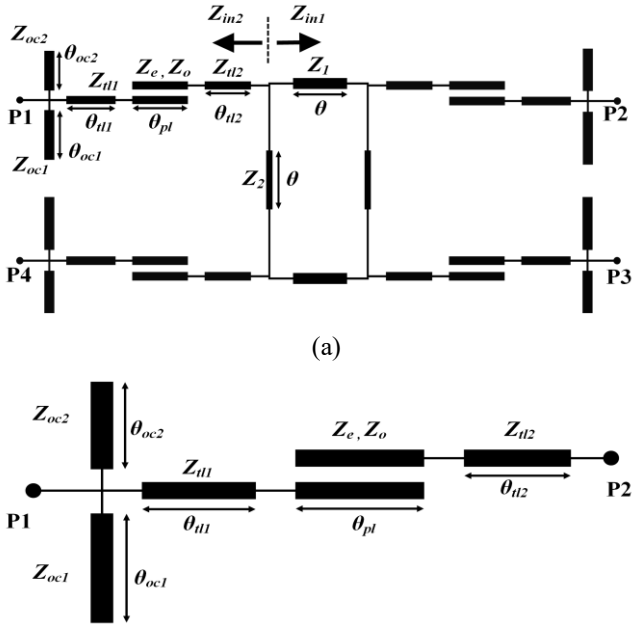


Fig. 1. Proposed structure of BHFC: (a) overall design schematic, (b) structure of BBLU.

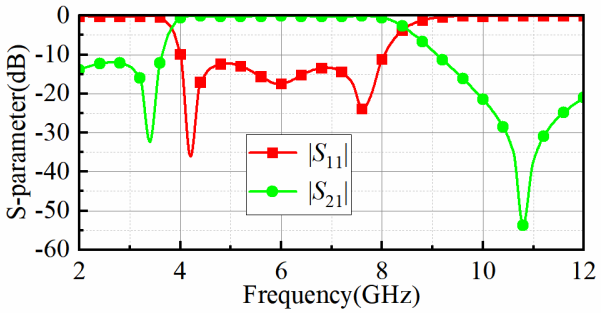


Fig. 2. ADS simulation S-parameter response of the BBLU.

Figure 1(b) illustrates the schematic of the proposed BBLU structure, which comprises parallel coupled lines (Z_e, Z_o, and θ_{pl}), open-circuit branch lines (Z_{oc1}, Z_{oc2}, θ_{oc1}, and θ_{oc2}), and high-impedance transmission lines (Z_{tl1}, Z_{tl2}, θ_{tl1}, and θ_{tl2}). The open-circuit branch lines provide transmission zeros to enhance the passband suppression level and selectivity of the filter response. Meanwhile, the parallel coupled lines, in conjunction with the high-impedance transmission lines, enable flexible control by achieving a broadband coupled passband while simultaneously regulating its relative bandwidth. Here, the A-parameter matrix is used to analyze the design theory of BBLU.

$$[A]_{BBLU} = [A]_{OC}[A]_{TL1}[A]_{PL}[A]_{TL2} \tag{1}$$

$$[Y]_{OC} = [Y]_{OC1} + [Y]_{OC2} \tag{2}$$

During design, $Z_{oc1} = Z_{oc2} = Z_{oc}$ can be assumed. Substituting this into equations (2), (3), and (4) yields $[Y]_{OC}$. Subsequently, converting the Y-parameter matrix to the A-parameter matrix results in:

$$[A]_{OC} = \begin{bmatrix} 1 & 0 \\ \dfrac{j(\tan\theta_{oc1} + \tan\theta_{oc2})}{Z_{oc}} & 1 \end{bmatrix} \tag{3}$$

$$[A]_{TL1} = \begin{bmatrix} 1 & Z_{tl1} \\ 0 & 1 \end{bmatrix} \tag{4}$$

$$[A]_{PL} = \begin{bmatrix} \dfrac{k_1}{k_2}\cos\theta_{pl} & j\dfrac{k_2^2 - k_1^2\cos^2\theta_{pl}}{2k_2\sin\theta_{pl}} \\ j\dfrac{2\sin\theta_{pl}}{k_2} & \dfrac{k_1}{k_2}\cos\theta_{pl} \end{bmatrix} \tag{5}$$

Here, $k_1 = Z_e + Z_o$, $k_2 = Z_e - Z_o$,

$$[A]_{TL2} = \begin{bmatrix} 1 & Z_{tl2} \\ 0 & 1 \end{bmatrix} \tag{6}$$

Substituting equations (3), (4), (5), and (6) into (1) yields $[A]_{BBLU}$. Subsequently, based on the transformation relationship between the A-parameter matrix and the S-parameter matrix, $[A]_{BBLU}$ can be converted to $[S]_{BBLU}$, thereby obtaining S_{11} and S_{21}.

B. Matching of BBLU with Single-Section BLC

In the circuit structure design of traditional single-section branch line couplers, to achieve impedance matching between the single-section loop coupler and the BBLU, so Zin1 = Zin2. During design, $\theta = \pi/4$, it can be concluded that Z_{oc}, Z_{tl1}, Z_{tl2}, Z_e, Z_o. Figure 2 shows the ADS simulation S-parameter response of the BBLU. As shown, this BBLU operates at a center frequency of 6 GHz with a passband range of 4 to 8 GHz, achieving a relative passband bandwidth of 66.7%. Its return loss exceeds 13 dB.

III. Simulation Results and Discussion

To validate the proposed bandpass filter circuit structure, we designed and fabricated a broadband bandpass coupler centered at 5.95 GHz using Rogers 4350 substrate (ε_r = 3.66, thickness T = 0.762 mm). The optimized layout is shown in Figure 3.

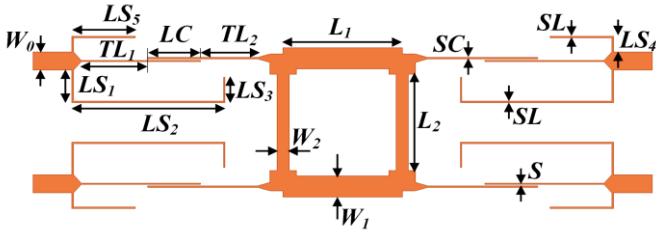


Fig. 3. Proposed BHFC diagram and optimized dimensions: W_0=1.3, W_1=1.5, W_2=0.8, LS_1=2.3, LS_2=9.9, LS_3=1.8, LS_4=1.1, LS_5=4.1, TL_1=4.3, TL_2=3.7, LC=3.4, L_1=7.7, L_2=6.8 *and* SC=SL=S=0.1, unit: mm.

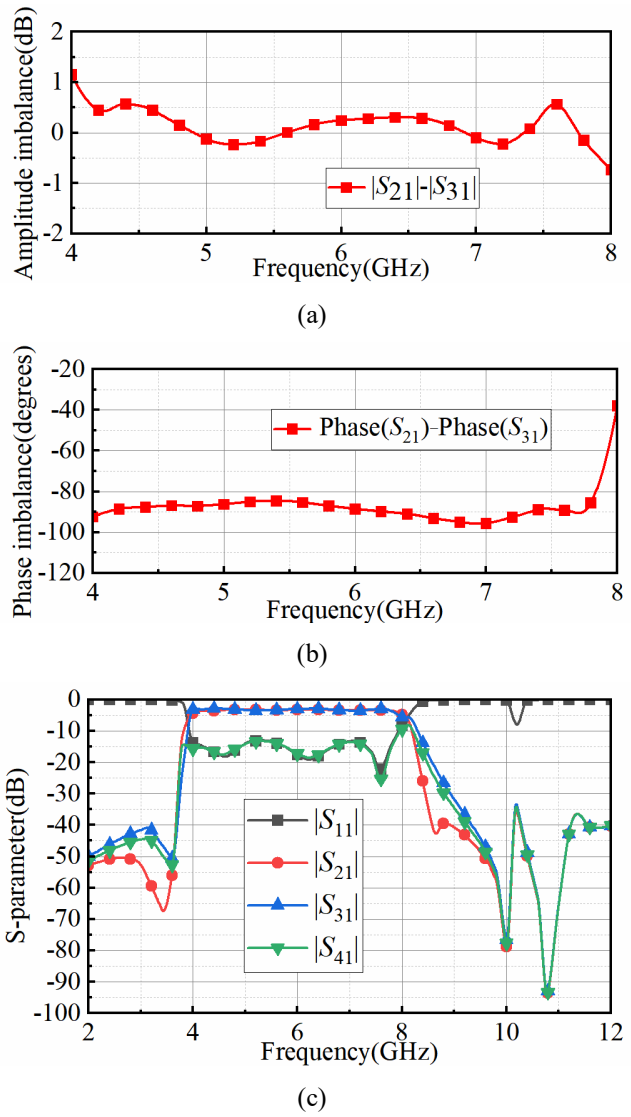


Fig. 4. The proposed BHFC's S-parameters: (a) amplitude imbalance, (b) phase difference, (c) BHFC's S-parameters.

Figure 4(a) shows the amplitude-frequency response curve of this circuit structure. The results indicate that within the range of 3.99 GHz to 7.86 GHz, both the return loss ($|S_{11}|$) and isolation ($|S_{41}|$) consistently remain below 13 dB. Within the frequency range of 4.02 GHz to 7.88 GHz, the amplitude imbalance ($|S_{21}|$ - $|S_{31}|$) between the coupler's direct path (Port 2) and the coupled path (Port 3) is shown in Figure 4b. It can be observed that the amplitude imbalance of this circuit is less than 0.6 dB, with a relative bandwidth of 64.9%. The Selectivity Factor of Bandpass Filter Response(SFBR) is calculated using formula (7):

$$SFBR = \frac{BW_{3dB}}{BW_{30dB}} \times 100\% \quad (7)$$

Here, BW_{3dB} and BW_{30dB} represent the 3dB bandwidth and 30dB bandwidth, respectively. The SFBR can be calculated as 73.2%. The phase difference between the through port and the coupled port (Phase(S_{21}) - Phase(S_{31})), as shown in Figure 4(b), indicates that the phase difference of this structure remains less than 6.6° across the frequency range from 4.02 GHz to 7.88 GHz.

IV. Conclusion

This paper proposes a novel bandpass coupler with high selectivity and broadband characteristics. In this design, a parallel-coupled microstrip line, an open-circuit branch line, and a high-impedance transmission line are added to each port of a single-section BLC to form a BBLU, thereby achieving broadband bandpass and filtering response. Subsequently, the operating principle is analyzed, and the design process of the BFHC is described. Simulation analysis is performed on the prototype circuit designed for a center frequency of 5.95 GHz and operating within the 4.02 GHz ~ 7.88 GHz band. The results demonstrate a relative bandwidth of 64.9%, return loss and isolation loss exceeding 13 dB, amplitude imbalance below 0.6 dB, phase imbalance below 6.6°, and selectivity exceeding 73.2%.

References

[1] H. Ahn and M. M. Tentzeris, ‘‘Arbitrary power-division branch-line hybrids for high-performance, wideband, and selective harmonic suppressions from 2f0,’’ IEEE Trans. Microw. Theory Techn., vol. 67, no. 3, pp. 978–987, Mar. 2019.

[2] R. K. Barik, K. V. Phani Kumar, and S. S. Karthikeyan, ‘‘A compact wideband harmonic suppressed 10 dB branch line coupler using cascaded symmetric PI sections,’’ Microw. Opt. Technol. Lett., vol. 58, no. 7, pp. 1610–1613, Jul. 2016.

[3] H.-J. Yoon and B.-W. Min, ‘‘Two section wideband 90◦ hybrid coupler using parallel-coupled three-line,’’ IEEE Microw. Wireless Compon. Lett., vol. 27, no. 6, pp. 548–550, Jun. 2017.

[4] Z. Qamar, W. S. Chan, and H. Derek, ‘‘Wide bandwidth arbitrary phase difference branch line coupler,’’ Microw. Opt. Technol. Lett., vol. 59, no. 9, pp. 2241–2245, Jun. 2017.

[5] Z. Qamar, S. Y. Zheng, W. S. Chan, and D. Ho, ‘‘Coupling coefficient reconfigurable wideband branch-line coupler topology with harmonic suppression,’’ IEEE Trans. Microw. Theory Techn., vol. 66, no. 4, pp. 1912–1920, Apr. 2018.

[6] Q. Wu, Y. Yang, Y. Wang, X. Shi, and M. Yu, ‘‘Characteristic impedance control for branch-line coupler design,’’ IEEE Microw. Wireless Compon. Lett., vol. 28, no. 2, pp. 123–125, Feb. 2018.

[7] R. K. Barik, Q. S. Cheng, N. C. Pradhan, and K. S. Subramanian, ‘‘Highly miniaturized wideband 3-dB branch-line hybrid with second harmonic-suppression,’’ Microw. Opt. Technol. Lett., vol. 62, no. 6, pp. 2248–2256, Jun. 2020.

[8] K. V. P. Kumar and A. J. Alazemi, "A Flexible Miniaturized Wideband Branch-Line Coupler Using Shunt Open-Stubs and Meandering Technique," in IEEE Access, vol. 9, pp. 158241-158246, 2021.

[9] J. Zhao, S. Wang, X. Chen, W. Lv, Z. Li and H. Jiang, "Miniaturized Microstrip Branch-Line Coupler with Wideband Harmonic Suppression Using Modified Radial Stub Loaded Resonators," 2023 15th International Conference on Communication Software and Networks (ICCSN), Shenyang, China, pp. 358-360, 2023.

[10] R. K. Barik, S. Koziel and S. Szczepanski, "Wideband Highly-Selective Bandpass Filtering Branch-Line Coupler," IEEE Access, vol. 10, pp. 20832-20838, 2022.

Ultrahigh-Sensitivity Microwave Biosensor Based on a CPW Loaded with a Modified Complementary Electric-LC Resonator

Shaghayegh Chamani
School of Electrical and Data Engineering
University of Technology Sydney
Sydney, Australia
shaghayegh.chamani@student.uts.edu.au

Xiaojing Lv
School of Electrical and Data Engineering
University of Technology Sydney
Sydney, Australia
xiaojing.lv@uts.edu.au

Trevor S. Bird
Antengenuity
Sydney, Australia
ts.bird@ieee.org

Yang Yang
School of Electrical and Data Engineering
University of Technology Sydney
Sydney, Australia
yang.yang.au@ieee.org

***Abstract*—This paper presents an ultra-high-sensitivity microwave planar sensor for biological permittivity sensing based on a conductor-backed coplanar waveguide (CPW) integrated with a modified complementary electric-LC (CELC) resonator. The proposed structure incorporates meandered frames and an interdigital capacitor (IDC) into the CELC resonator etched on the bottom ground plane to enhance the effective inductance and capacitance of the resonant structure. The proposed sensor achieves peak and average sensitivities of 3.58% and 2.58%, respectively, demonstrating its potential for biological permittivity sensing applications..**

***Index Terms*—Planar microwave sensing, coplanar waveguide (CPW), complementary electric–LC (CELC) resonator.**

I. Introduction

Microwave resonant sensors have attracted considerable interest because of their capability to characterize materials in a wide range of applications, including the food industry, agriculture, biomedical systems, and healthcare. In recent years, metamaterial-based resonators such as the electric–LC (ELC), split-ring resonator (SRR), and complementary split-ring resonator (CSRR) have been extensively employed in sensing platforms owing to their compact size, low fabrication cost, structural robustness, and high measurement accuracy [1]. When a material under test (MUT) is loaded on the resonator, the scattering parameters change, thereby establishing a relationship between the variations in the reflection and/or transmission coefficients and the material properties.

Recent studies have reported a variety of microwave resonant sensors for material characterization. For instance, a differential microstrip sensor based on complementary split-ring resonators (CSRRs) was introduced in [2] to mitigate environmental perturbations. In another approach, a microstrip transmission line incorporating an open-ended step-impedance section was presented in [3] to enhance the sensitivity of the sensing structure. Recently, a structure employing negative-refractive-index transmission-line metamaterials was introduced in [4] to enhance the coupling and exploit the resonant properties of the structure. In [5], a modified CSRR-based structure was developed for retrieving the complex permittivity of liquid samples.

In this article, a microwave sensor based on a coplanar waveguide (CPW) coupled with a meandered-frame and an interdigital capacitor (IDC) complementary ELC resonator etched on the bottom ground plane is proposed for dielectric sensing applications. Compared with a conventional complementary ELC resonator, the proposed sensor improves sensitivity without increasing the sensor dimensions. The rest of the paper is structured as follows. Section II explains the working principle of the proposed sensor. Section III presents the results and discussion. Section IV concludes the paper.

II. Methodology

Fig. 1(a) shows the schematic of a conductor-backed CPW integrated with a complementary ELC (CELC) resonator etched on the bottom ground plane. The CELC resonator is symmetrically aligned with respect to the CPW signal conductor to ensure a uniform field distribution. To increase the effective inductance and electrical length, meandered frames are incorporated into the CELC structure, forming the meandered CELC (M-CELC) resonator, as illustrated in Fig. 1(b). In the next step, to further improve the sensitivity and enhance electric-field confinement in the central region, an IDC is incorporated, as shown in Fig. 1(c), resulting in the IDC-M-CELC configuration. The IDC contributes to a higher effective capacitance in the resonator and consequently enhances its electromagnetic interaction with the MUT.

Two 50 Ω connectors are placed at both ends of the sensor. A Rogers 4350B substrate ($\varepsilon_r = 3.66$, $\tan\delta = 0.0031$)

979-8-3315-4544-4/26/$31.00 ©2026 IEEE

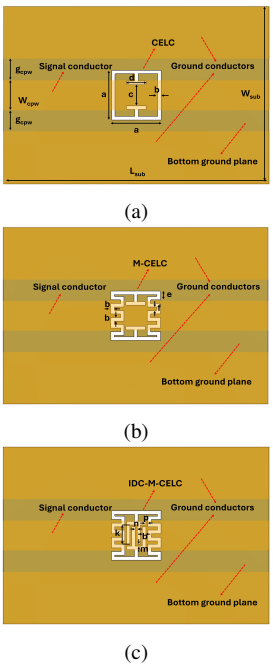


Fig. 1: Schematic of the CPW microwave sensor loaded with (a) CELC, (b) M-CELC, and (c) IDC-M-CELC resonators. The geometrical parameters are $L_{sub} = 15$, $W_{sub} = 10$, $W_{cpw} = 1.67$, $g_{cpw} = 1.21$, $a = 2.8$, $b = 0.2$, $c = 1.2$, $d = 1.1$, $e = 0.5$, $f = 0.2$, $k = 1.1$, $m = 0.1$, $n = 0.1$, $p = 0.1$, all in mm.

with 0.035-mm copper cladding on both the top and bottom layers is used. The dimensions of the different parts of the structure are provided in the caption of Fig. 1. Fig. 2 shows the transmission coefficients obtained from full-wave electromagnetic simulations performed in CST. As can be observed, the CELC resonator exhibits a resonance around 20 GHz. After introducing the meandered frames, the resonance shifts to a lower frequency due to the increased electrical length of the structure. When the IDC is incorporated, the resonance further shifts to a lower frequency and becomes deeper as a result of the increased effective capacitance. The IDC-M-CELC also exhibits a second resonance around 27 GHz, which corresponds to a higher-order mode that is not used due to its low resonance strength and Q-factor. The electric field distributions of the CELC, M-CELC, and IDC-M-CELC resonators at their resonance frequencies are shown in Fig. 3. It can be observed that the electric field intensity is significantly enhanced and becomes more strongly concentrated when the CELC structure is modified by introducing meandered frames and IDC elements on the ground plane of the CPW.

III. Results and Discussion

Fig. 4 shows the 3D model of the proposed sensor loaded with MUT. In the sensing analysis, biological materials with different complex permittivities are used. A series of simulations is conducted in which the relative permittivity (ε_r) varies from 5 to 40 in steps of 5, and the loss tangent ($\tan\delta$) varies from 0.1 to 1.2 in steps of 0.1. The corresponding relative permittivity and loss tangent values are obtained from

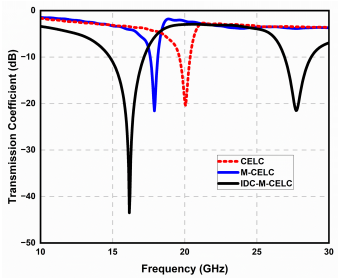


Fig. 2: Transmission coefficient of the CPW coupled with CELC, M-CELC, and IDC-M-CELC resonators.

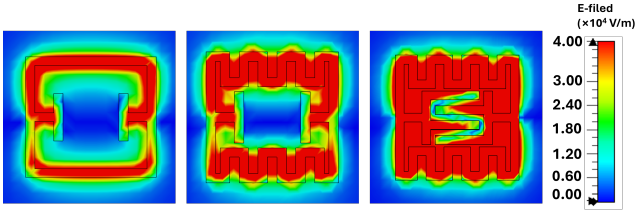


Fig. 3: Electric field distribution of the CELC, M-CELC, and IDC-M-CELC resonators at the resonant frequencies of 20 GHz, 17.8 GHz, and 16.1 GHz, respectively, shown from left to right.

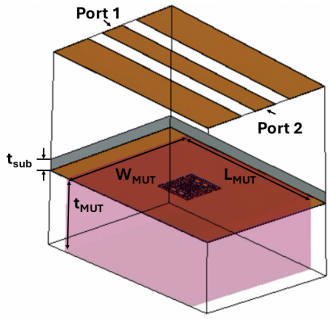


Fig. 4: 3D model of the proposed sensor loaded with the material under test (MUT). The geometrical parameters are $t_{sub} = 0.762$, $L_{MUT} = 11$, $W_{MUT} = 10$, $t_{MUT} = 5$, all in mm.

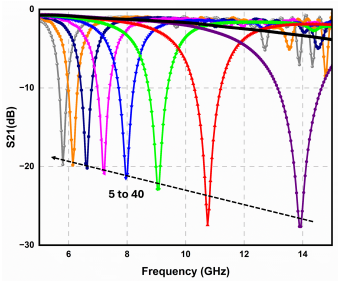


Fig. 5: Resonant frequency variation of the proposed IDC-M-CELC-based CPW sensor with MUTs having different relative permittivities. The relative permittivity is varied from 5 to 40 with a step of 5.

[6], based on the reported dielectric properties of skin over the frequency range of interest. For the proposed IDC-M-CELC sensor, as indicated in Fig. 5, the resonant frequency decreases from approximately 14 GHz to 5 GHz as the relative permittivity increases from 5 to 40. It is worth noting that the small dips appearing at the right-hand side of the spectrum correspond to higher-order-mode resonances.

To investigate the influence of the MUT thickness on sensor performance, the resonant frequency shift as a function of the relative permittivity and MUT thickness is plotted in Fig. 6(a). The resonant frequency shift is defined as

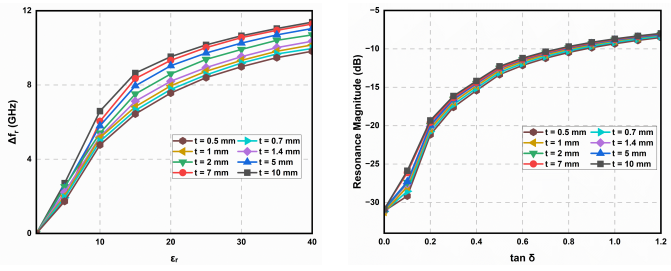
$$\Delta f_r = |f_{r,\varepsilon_r} - f_{r,\text{unloaded}}| \tag{1}$$

where f_{r,ε_r} and $f_{r,\text{unloaded}}$ are the sensor's resonant frequencies with and without the MUT placed beneath it, respectively. For a fixed relative permittivity, the frequency shift increases with increasing MUT thickness; however, this increase becomes less pronounced for larger thickness values, suggesting that the electric field interaction between the sensor and the MUT approaches a saturation state. In addition, the variation of the peak attenuation with respect to the loss tangent and MUT thickness is illustrated in Fig. 6(b). The peak attenuation gradually decreases as the loss tangent increases due to the higher losses introduced by the MUT. Moreover, the peak attenuation exhibits a slight dependence on the MUT thickness.

The sensitivity of a microwave resonator sensor is defined as below [5].

$$S_{\varepsilon_r} = \left| \frac{f_{r,\varepsilon_r} - f_{r,\text{unloaded}}}{f_{r,\text{unloaded}}} \right| \cdot \frac{1}{\varepsilon_r - 1} \times 100\%. \tag{2}$$

Fig. 7 shows a comparison between the proposed sensor and recently reported planar sensors. The sensitivity decreases as the relative permittivity increases from 5 to 40. The incorporation of a meandered-slot frame together with IDC slots into the CELC structure leads to stronger electric-field confinement, which consequently enhances the sensitivity of the sensor. The IDC–M–CELC configuration therefore achieves a maximum sensitivity of 3.58% and an average sensitivity of 2.58%. The proposed sensor enables ultrahigh-sensitivity measurement of the complex permittivity of the MUT.



(a) (b)

Fig. 6: (a) Variation of resonant frequency shift with the changes of relative permittivity and thickness of MUTs. (b) Variation of attenuation peak with the changes of loss tangent and thickness of MUTs

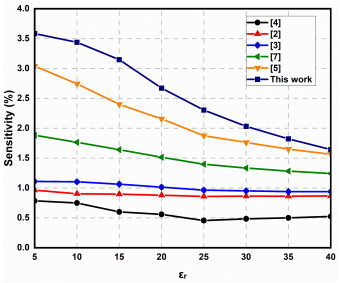


Fig. 7: Comparison of the sensitivity of the proposed sensor with reported designs in [2], [3], [4], [5], and [7]

IV. Conclusion

This paper proposed an ultrahigh-sensitivity microwave planar sensor for complex permittivity sensing. The sensor is realized by incorporating a meandered-frame slot together with an interdigital capacitor (IDC) slot into the CELC resonator. The resulting resonant structure is etched in the ground plane of a coplanar waveguide (CPW). When the sensor is brought into contact with a material under test (MUT), variations occur in both the resonance frequency and the peak attenuation. The obtained results indicate that the proposed sensor offers competitive performance in terms of ultrahigh sensitivity, structural miniaturization, low fabrication cost, and ease of implementation, making it a suitable candidate for biological sensing applications.

Acknowledgment

This work was supported by the University of Technology Sydney for Prof. Yang Yang's ARC Future Fellow Near Miss Support.

References

[1] S. Chamani, M. Esfandiari, X. Lv, Y. Yang, and T. S. Bird, "A survey of antennas for skin cancer detection: From microwave to terahertz technologies." *IEEE Antennas and Propagation Magazine*, pp. 2–16, 2025.

[2] H.-Y. Gan, W.-S. Zhao, Q. Liu, D. Wang, L. Dong, G. Wang, and W.-Y. Yin, "Differential microwave microfluidic sensor based on microstrip complementary split-ring resonator (mcsrr) structure," *IEEE Sensors Journal*, vol. 20, pp. 5876–5884, 02 2020.

[3] A. Ebrahimi, J. Scott, and K. Ghorbani, "Ultrahigh-sensitivity microwave sensor for microfluidic complex permittivity measurement," *IEEE Transactions on Microwave Theory and Techniques*, vol. 67, no. 10, pp. 4269–4277, 2019.

[4] M. Abdolrazzaghi, M. Daneshmand, and A. K. Iyer, "Strongly enhanced sensitivity in planar microwave sensors based on metamaterial coupling," *IEEE Transactions on Microwave Theory and Techniques*, vol. 66, no. 4, pp. 1843–1855, 2018.

[5] W.-J. Wu, W.-S. Zhao, D. Wang, B. Yuan, and G. Wang, "Ultrahigh-sensitivity microwave microfluidic sensors based on modified complementary electric-lc and split-ring resonator structures," *IEEE Sensors Journal*, vol. 21, pp. 18 756–18 763, 06 2021.

[6] D. Andreuccetti, R. Fossi, and C. Petrucci. (2024) Dielectric Properties of Body Tissues. IFAC-CNR. Florence, Italy. 1997–2024. [Online]. Available: http://niremf.ifac.cnr.it/tissprop/htmlclie/htmlclie.php

[7] L.-C. Fan, W.-S. Zhao, D.-W. Wang, Q. Liu, S. Chen, and G. Wang, "An ultrahigh sensitivity microwave sensor for microfluidic applications," *IEEE Microwave and Wireless Components Letters*, vol. 30, no. 12, pp. 1201–1204, 2020.

Reconfigurable Millimetre-Waves and Terahertz Devices Using Phase Change Materials

Aurelian Crunteanu[1], Wilfrid Renkanga Mbatchi[1], E.-N. Sirjita[1], Cyril Decroze[1], Georges Humbert[1], A. Boulle[2], J.C. Orlianges[1]

[1]XLIM Research Institute, UMR 7252 CNRS/ University of Limoges, 123 Avenue Albert Thomas 87060, Limoges, France, [2] Institute of Ceramic Research (IRCer), CNRS UMR 7315, 12 rue Atlantis, Limoges, France

We present the integration of phase transition materials -PTM (e.g. VO_2) with volatile metal-insulator transition (MIT) and of chalcogenides (GeTe, $Ge_2Sb_2Te_5$…) phase change materials (PCM)- showing a non-volatile, reversible structural and electrical state changes, as agile elements for switching, frequency reconfiguration and amplitude modulation of devices operating at millimeter-waves and THz frequencies. Usually designated as “phase change materials” albeit their distinct state modification mechanisms and volatile/ non-volatile behavior, both class of materials show remarkable performances in the high frequency range - microwaves, millimeter waves and terahertz, due to the ability to modify their electrical and optical properties under thermal, electrical or optical excitations, changing between an insulating/ low-loss state, and a conductive state which is blocking the propagation of electromagnetic waves [1- 4].

Thus, the MIT in vanadium dioxide is accompanied by drastic changes in the material’s electrical and optical properties (e.g. electrical resistivity decreases by 5 orders of magnitude) with broadband frequency response (from DC to microwaves and THz domains) and triggered a diversity of interesting applications (switching, THz modulators, reconfigurable filters and antennas etc.). We present here our investigations on VO_2 and W-doped VO_2 epitaxial films and demonstrate that tungsten doping allows not only to tune the MIT temperature, but also to control the topology of the electrically activated transition. This feature was exploited to fabricate VO_2– based devices whose MIT can be triggered either thermally or electrically over areas as large as 3.8×10 mm^2, hence allowing the development of efficient THz amplitude modulators operating over a large spectral range (0.2– 2 THz) with modulation depths reaching 96% [2]. On the other hand, the non-volatile or bi-stable nature of chalcogenides PCMs such as GeTe is a key advantage over conventional switching solutions, as the devices incorporating PCMs do not require a permanent bias or optical stimulus to maintain a device in a specifically prepared state. We present our researches on the elaboration of GeTe thin films and their integration in high frequency devices and the evaluation of their electrical and THz properties during the amorphous/insulator to -crystalline/ metallic phase change. We have developed several approaches enabling fast, reversible optical control with short UV and visible laser pulses over large areas of the two different states of GeTe and have evaluated the phase change performance of these thin films in the terahertz domain using time domain spectroscopy (THz-TDS). The excellent contrast in THz properties of GeTe between the two states, was also used to demonstrate the integration of the material as agile elements in frequency reconfigurable metasurfaces or all-GeTe THz polarizers with broadband responses and very good performance [3].

By combining THz device design techniques with the unique properties of these materials, we have experimentally confirmed the feasibility of chalcogenide PCMs integration for reconfigurable THz metamaterials or spatially- coded metasurfaces allowing frequency or propagation direction control of incident THz waves [4]. This versatile and flexible approach based on non-volatile, optically controlled and multi-operational devices incorporating chalcogenides is expected to generate exciting developments in the millimeter wave and THz domains and anticipates novel programmable (meta)surfaces with multifunctional capabilities for electromagnetic wave manipulation.

1. S. Raoux, F. Xiong, M. Wuttig, E. Pop, MRS Bull. 39, 8, (2014) 703-710.
2. E.-N. Sirjita, A. Boulle, J.C. Orlianges, R. Mayet, A. Debelle, L. Thomé, M. Colas, J. Cornette, A. Crunteanu, "Electrically activated W-doped VO2 films for reliable, large-area, broadband THz waves modulators", *ACS Applied Materials & Interfaces*, v. 17(16), p. 24564 -24577, 2025, https://doi.org/10.1021/acsami.5c00777
3. M. Pinaud, G. Humbert, S. Engelbrecht, L. Merlat, B. Fischer, A. Crunteanu, *ACS Photonics*, 8, 11 (2021) 3272.
4. Y.-S. To, J. Du, C. Decroze, L. Huitema, A. Crunteanu, and H. Wong, “Phase Change Material-Driven Tunable Metasurface for Adaptive Terahertz Sensing and Communication in 6G Perceptive Networks.” *Adv. Funct. Mater.* 36, no. 12 (2026): e15085. https://doi.org/10.1002/adfm.202515085

979-8-3315-4544-4/26/$31.00 ©2026 IEEE

Design of a Pattern Reconfigurable Amplifier Antenna with Gain Amplification Using Transistors

Minghuan Wang, Hao Wang, Yan Wang, and Jianyin Cao
Nanjing University of Science and Technology, Nanjing 210094, China
haowang@njust.edu.cn

***Abstract*—This letter proposes an amplifier antenna that integrates gain amplification and pattern reconfigurability. Using two transistors not only amplifies the antenna gain but also enables pattern switching among three states. The antenna and the microstrip-to-slotline transition serve as the input and output matching networks of the amplifier, respectively, which reduces the circuit size. This design achieves the highly efficient integration of the antenna and the amplifier. Two integrated antenna elements placed on the same dielectric substrate form a pattern reconfigurable antenna. Simulation results show that the designed pattern reconfigurable amplifier antenna operates over the frequency band 5.8 GHz to 10.3 GHz. The gain varies from 11.38 dBi to 16.88 dBi. The gain amplification over a wide operating frequency band and the radiation patterns in three states demonstrate the feasibility of the integrated design.**

***Index Terms*—Pattern reconfigurability, amplifier antenna, gain amplification.**

I. Introduction

Reconfigurable antennas are widely used due to their ability to switch between different operating states on a single dielectric substrate or platform. Pattern reconfigurable antennas capable of changing the beam pointing direction can enhance the coverage range of radiated energy [1]-[4]. In [5], eight radiation patterns with different pointing directions are achieved by controlling twelve PIN diodes loaded on the microstrip line. The results indicate that the pattern reconfigurable antenna operates over the frequency range of 3.16 GHz to 6.42 GHz, with a gain range of 3 dBi to 5.2 dBi. Transistors, also serving as tunable devices, are widely used in the design of active circuits such as amplifiers. With the ongoing improvement in system integration, the integrated design of amplifiers and antennas has evolved into a unified integration approach [6]. In [7], the impedance characteristics of rectangular patch antennas with different feeding positions are analyzed. The unified integrated design is achieved by loading the gate and drain of the transistor at their optimal physical positions. This method enhances antenna gain without additional matching networks, thereby reducing system size and losses. Inspired by this, transistors can be used simultaneously for gain amplification and pattern reconfigurable design. This method realizes a pattern reconfigurable amplifier antenna with gain amplification.

To achieve this objective, this letter proposes a pattern reconfigurable amplifier antenna based on the Vivaldi antenna. The antenna serves as the input matching network, and the microstrip-to-slotline transition is used as the output matching network. The designed amplifier antenna is equipped with signal reception capability. This structure not only achieves gain amplification over a wide operating frequency band, but also realizes three directional radiation patterns by controlling the on-off states of the two transistors. The favorable isolation between the two amplifier antenna units ensures reliable communication. To better adapt the proposed amplifier antenna for practical communication system applications, an in-phase power divider is employed at the two input feeding ports to ensure equal-amplitude, in-phase signals are excited.

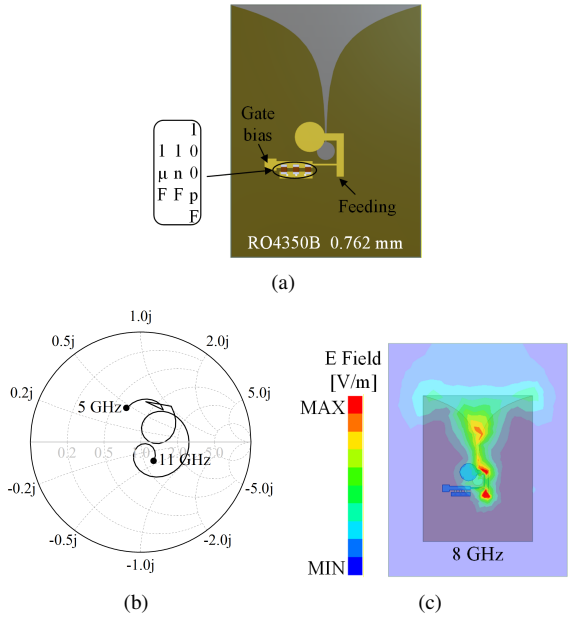


Fig. 1. Vivaldi antenna integrated with bias circuit. (a) Structure. (b) Input impedance. (c) Surface current distribution at 8 GHz.

II. Amplifier Antenna Design

When a traditional Vivaldi antenna is used as the input matching network of an amplifier, its input impedance may not be 50 Ω. During the integration process, the input impedance of the antenna's feeding port needs to be maintained within the stable region of the transistor. Since transistors require a bias circuit to supply direct voltage for operation, the Vivaldi antenna integrated with the bias circuit is shown in Fig. 1(a). To further verify the feasibility of the bias circuit integration position, Fig. 1(b) presents the input impedance at the feeding port and the surface current distribution at

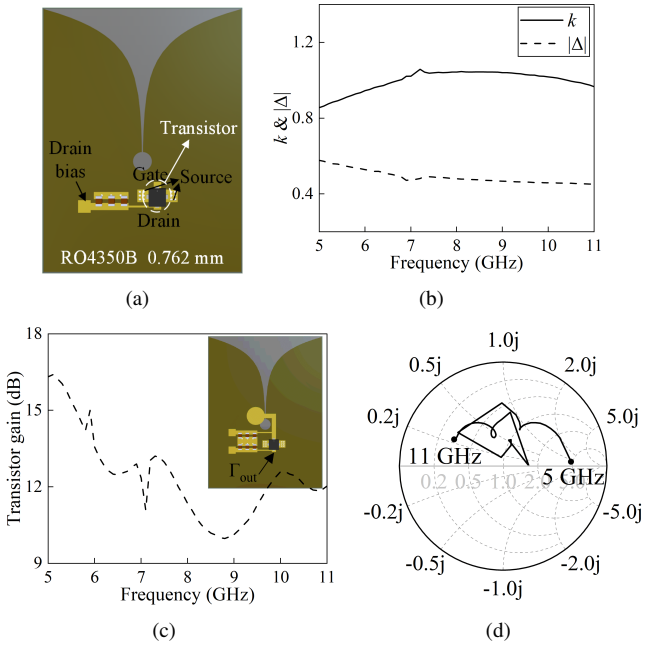


Fig. 2. Transistor analysis. (a) Structure. (b) Stability. (c) Transistor amplification gain with Vivaldi antenna input impedance. (d) Load reflection coefficient.

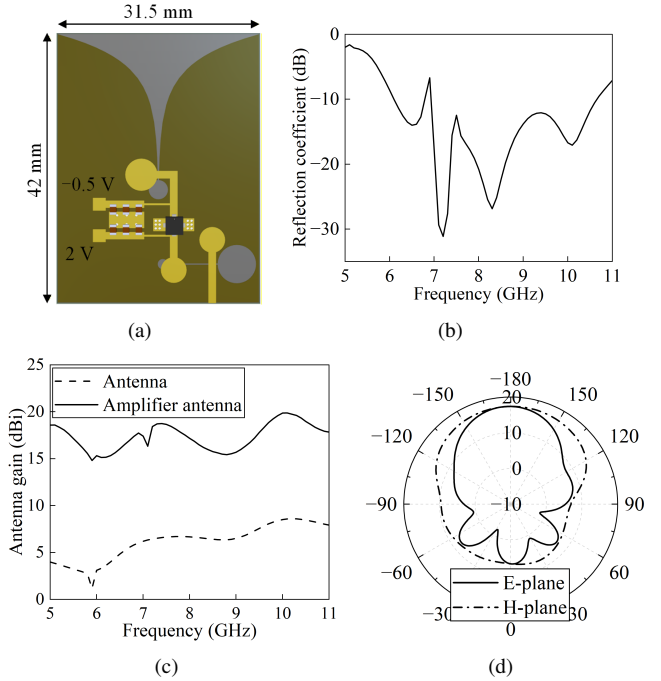


Fig. 3. Simulation results of the proposed amplifier antenna. (a) Structure. (b) Reflection coefficient. (c) Gain and gain of the passive antenna. (d) Radiation patterns at 8 GHz.

8 GHz. The favorable impedance distribution on the Smith chart confirms the feasibility of using the antenna as the amplifier's input matching network. The favorable surface current distribution indicates that the integration position of the bias circuit minimizes its impact on the antenna's radiation performance.

To determine the gain amplification at different frequencies, we analyzed the transistor's performance. The field effect transistor model CE3512K2 is selected. The structure of the transistor attached to the RO4350B dielectric substrate is shown in Fig. 2(a). The two source terminals are connected to the ground via microstrip vias with a length and width of 2 mm each. The same bias circuit as that used for the gate is integrated with the drain. The operating point of the transistor is set at 2 V and 10 mA. Based on the stability factor k and $|\Delta|$ in Fig. 2(b), the transistor is potentially unstable at specific frequencies. The amplification gain, derived from the constant available power-gain circles of the transistor at different operating frequencies, is shown in Fig. 2(c). The Vivaldi antenna, integrated with a bias circuit, is connected to the transistor's gate terminal as the input matching network. The resulting load impedance at the drain terminal is shown in Fig. 2(d), and the structure diagram after connection is also provided.

The input matching network of the amplifier employs a microstrip-to-slotline transition. The drain terminal in Fig. 2(c) is integrated with the proposed two-port microstrip-to-slotline transition. The integrated structure is presented in Fig. 3(a). Based on the simulation, the designed amplifier antenna operates over the frequency range of 7 GHz to 10.6 GHz. The gain varies from 15.43 dBi to 19.88 dBi, which is significantly higher than that of the passive antenna integrated with the bias circuit. Fig. 3(d) presents the radiation pattern of the amplifier antenna at 8 GHz.

III. Design of the Pattern Reconfigurable Amplifier Antenna

The amplifier antenna units designed above are orthogonally arranged to form a two-port pattern reconfigurable amplifier antenna. The E-plane radiation pattern in Fig. 3(d) shows that the energy from the designed amplifier antenna propagates outward along the tapered slot of the Vivaldi antenna. Therefore, the arrangement method shown in Fig. 4(a) can generate at least two radiation patterns. Fig. 4(c) presents the E-plane radiation patterns of the designed pattern reconfigurable amplifier antenna under three operating states. The beam pointing angle of the radiation pattern can be steered to –180° and –90°, respectively, by turning on transistors T1 and T2 individually. Turning on both transistors simultaneously yields a radiation pattern pointing at –135°. Therefore, the amplifier antenna's pattern reconfigurability can be achieved by controlling the on-off states of the two transistors.

Meanwhile, the gain of the reconfigurable antenna has been enhanced. Fig. 4(d) shows the operating frequency bands of the two ports of the designed pattern reconfigurable amplifier antenna. They are 5.8 GHz to 10.3 GHz and 6.7 GHz to 10.2 GHz, respectively. The isolation between the ports is less than –10 dB, ensuring the quality of wireless communication.

Table I compares the performance of the proposed pattern reconfigurable amplifier antenna with that of existing

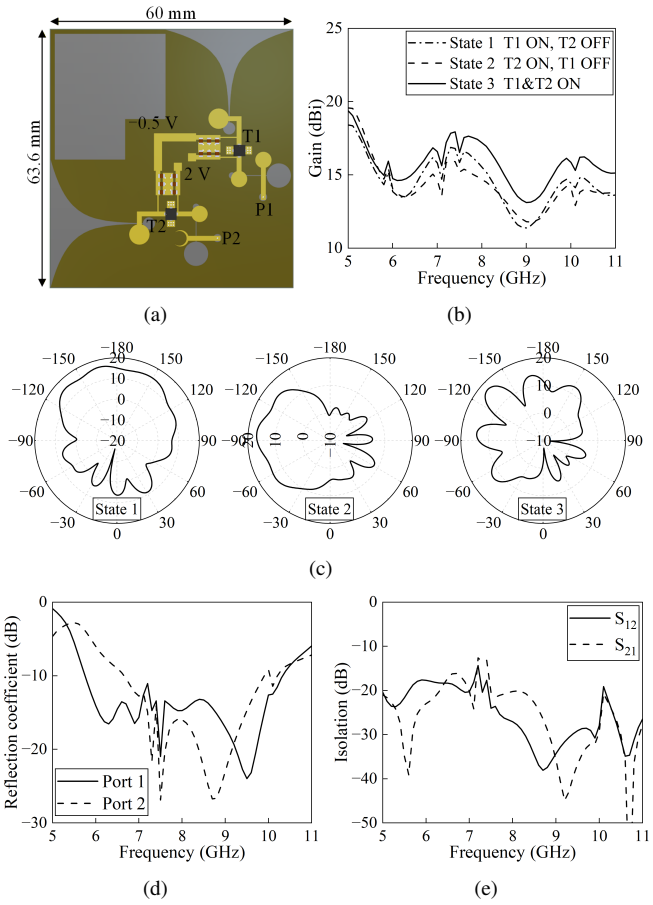


Fig. 4. Simulation results of the proposed pattern reconfigurable amplifier antenna. (a) Structure. (b) Gain. (c) E-plane radiation patterns for the three states at 8 GHz. (d) Reflection coefficient. (e) Isolation.

TABLE I
COMPARISON OF THE PROPOSED STRUCTURE WITH REPORTED PATTERN RECONFIGURABLE ANTENNAS

Ref.	Num. of switches	States	Bandwidth (GHz)	Min. Gain (dBi)
[1]	2 diodes	2	3.24–3.65 (11.9%)	6.5
[2]	4 diodes	10	2.38–2.59 (8.4%)	2.8
[4]	13 diodes	7	3.41–3.61 (5.7%)	5.5
[5]	12 diodes	8	3.16–6.42 (68%)	3.2
Prop.	**2 transistors**	**3**	**5.8–10.3 (58.2%)**	**11.38**

pattern reconfigurable antennas. The comparative analysis demonstrates that the proposed structure not only provides a wide operating frequency band and multi-state radiation patterns, but also achieves a significant gain improvement with fewer tunable components.

IV. CONCLUSION

A pattern reconfigurable amplifier antenna is proposed. The Vivaldi antenna and microstrip-to-slotline transition are integrated into the amplifier, with the two passive components serving as its matching network. Two amplifier antenna units are fabricated on a single dielectric substrate. By controlling the on-off states of the two transistors, three radiation pattern states are achieved. Compared with conventional pattern reconfigurable antennas, this design achieves higher gain without adding diodes. The high integration and high gain demonstrate its suitability for application in communication systems.

ACKNOWLEDGMENT

This work was supported by the Youth Foundation of Jiangsu Province under Grant BK20230919.

REFERENCES

[1] Z. Wang and Y. Dong, "High-order-mode antenna with pattern reconfigurability for intelligent IoT applications," *IEEE Antennas Wireless Propag. Lett.*, vol. 24, no. 5, pp. 1258–1262, May 2025.

[2] Y. Liu and Y. Dong, "Pattern-reconfigurable planar antenna based on Vivaldi structure," *IEEE Antennas Wireless Propag. Lett.*, vol. 23, no. 8, pp. 2516–2520, Aug. 2024.

[3] S. Lin, Y. Cao, F. Chen, Q. Xue, and W. Che, "Dual-band antenna with 2.4 GHz omnidirectional and 5.8 GHz pattern-reconfigurable radiation modes," *IEEE Antennas Wireless Propag. Lett.*, vol. 24, no. 5, pp. 1238–1242, May 2025.

[4] Z. Wang, and Y. Dong, "Novel pattern reconfigurable epsilon-near-zero (ENZ) antenna for intelligent IoT communication applications," *IEEE Internet Things J.*, vol. 11, no. 12, pp. 22364–22375, Jun. 2024.

[5] F. Zhang, L. Liu, Y. Zhang, and F. Zhang, "Compact ultrathin wideband pattern-reconfigurable antenna with enhanced operating bandwidth," *IEEE Antennas Wireless Propag. Lett.*, vol. 23, no. 12, pp. 4443–4447, Dec. 2024.

[6] S. N. Nallandhigal and K. Wu, "Unified and integrated circuit antenna in front end—A proof of concept," *IEEE Trans. Microw. Theory Techn.*, vol. 67, no. 1, pp. 347–364, Jan. 2019.

[7] S. N. Nallandhigal, F. Ghorbani, and K. Wu, "A unified architecture for integrated circuit and radiation function using co-located active device and multimode antenna," *IEEE Trans. Microw. Theory Techn.*, vol. 73, no. 9, pp. 6931–6943, Sept. 2025.

Characterization of 32 GT/s UCIe-Compatible Package Interconnects for Reconfigurable RF Chiplet Integration

Baoping Meng, Guanbao Shan*, Guoliang Li, Yanwen Zheng, Wenbin Wei, Jiaxu Cao
Faculty of Integrated Circuit
Xidian University
Xi'an, China
gbshan@xidian.edu.cn

***Abstract*—To address the critical need for modular and flexible integration in reconfigurable RF integrated systems, a substrate interconnect model based on standard packaging is designed and validated for the 32 GT/s Universal Chiplet Interconnect Express (UCIe) standard. In reconfigurable architectures, the bandwidth consistency and electromagnetic isolation of the underlying interconnects are essential for enabling dynamic functional scheduling. This work establishes a full-link model incorporating pillars, vias, and traces on an organic substrate. Frequency response simulations demonstrate that at the 16 GHz Nyquist frequency, Voltage Transfer Function (VTF) loss remains above -7.5 dB and crosstalk is suppressed below -26 dB, satisfying UCIe specifications for standard packages. Furthermore, system robustness is verified via statistical eye diagram analysis, achieving an eye width of 0.925 UI at a low Bit Error Rate (BER). This study validates the feasibility of utilizing mature standard packaging processes to build high-performance, cost-effective communication platforms for reconfigurable RF chiplet integration.**

Keywords—reconfigurable, RF integrated systems, substrate interconnect, standard package, UCIe, VTF.

I. INTRODUCTION (*HEADING 1*)

The escalating demand for multi-band and multi-mode operation in modern wireless systems has positioned reconfigurable RF integrated circuits as a cornerstone for flexible system integration [1]. To incorporate diverse RF front-end modules within a unified architecture, chiplet-based modular designs are increasingly favored over traditional monolithic integration. The Universal Chiplet Interconnect Express (UCIe) standard has emerged as a pivotal open protocol [2], providing standardized interfaces for RF functional blocks across varying process nodes. However, in reconfigurable environments, the concurrent transmission of RF signal flows and high-speed control data imposes stringent requirements on the bandwidth consistency and phase stability of the underlying physical interconnects.

While advanced packaging technologies like silicon interposers offer exceptional interconnect density [3, 4], standard organic substrate packaging remains highly attractive for cost-sensitive and mass-produced reconfigurable RF systems due to its superior manufacturing efficiency. Nevertheless, as operational frequencies reach 32 GT/s with a 16 GHz Nyquist frequency, standard packages encounter significant frequency-dependent losses and inter-channel electromagnetic interference. These physical phenomena directly degrade the signal integrity of reconfigurable links, thereby constraining the functional scheduling range across RF modules. Consequently, a rigorous analysis of the compliance and electromagnetic characteristics of standard packaging in the microwave frequency range is fundamental to realizing high-performance RF reconfiguration.

This manuscript proposes a high-performance standard package substrate design meeting 32 GT/s requirements. Impedance continuity is verified via Time-Domain Reflectometry (TDR), and compliance at the Nyquist frequency is analyzed in detail. Finally, by considering transmitter jitter and adjacent channel interference, the timing margins are validated through statistical eye diagrams, providing a valuable reference for the low-cost, high-bandwidth integration of dynamic reconfigurable RF architectures.

II. CHANNEL MODELING & SIMULATION METHODOLOGY

A. Layout and Stackup Design

According to the UCIe protocol, a total of 44 signal lines are included in a standard package module. Among these, 40 high-speed signal lines constitute the mainband for clock and data transmission, while the remaining 4 lines serve as the sideband for link training and tracking. To optimize routing efficiency, a staggered bump arrangement is adopted. The bump pitch is designed to be 128.7 μm, which meets the UCIe requirement of being less than 130 μm. Additionally, a dual-layer routing scheme is implemented for the 40 signal lines. The trace width is set to 18 μm with a spacing of 1x width, satisfying the design specification of a trace width under 25 μm.

To ensure uniform impedance distribution and suppress signal reflections, a complete return path must be provided for the signal transmission. In the stackup design, signal layers are positioned between adjacent power and ground planes. Effective connections between signal lines and reference planes are established through return vias and power vias placed near the signal traces. Interconnections between chips are primarily completed within the CON_3 and CON_5 layers, while fan-out operations are executed through the SURFACE and BASE layers. The detailed layout design and stackup structure are illustrated in Fig. 1 and Fig. 2, respectively. In the simulation model, FR-4 is utilized as the dielectric material for the organic substrate. At the Nyquist frequency of 16 GHz, the relative dielectric constant D_k and the loss tangent D_f of FR-4 are set to 4.2 and 0.02, respectively [5].

979-8-3315-4544-4/26/$31.00 ©2026 IEEE

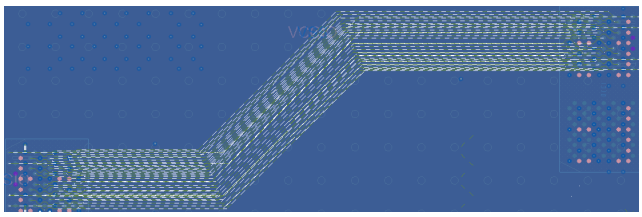


Fig. 1. Interconnect layout of the UCIe interface.

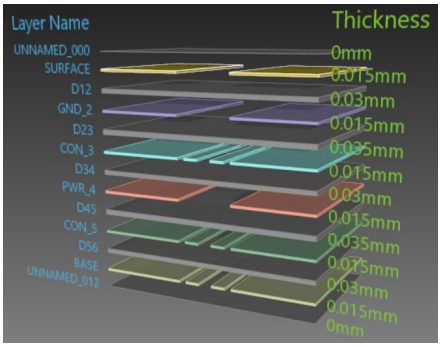


Fig. 2. Stackup structure of the layout.

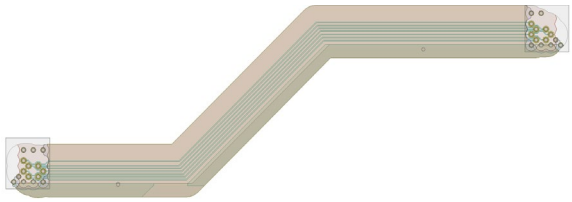


Fig. 3. Clipped model for simulation.

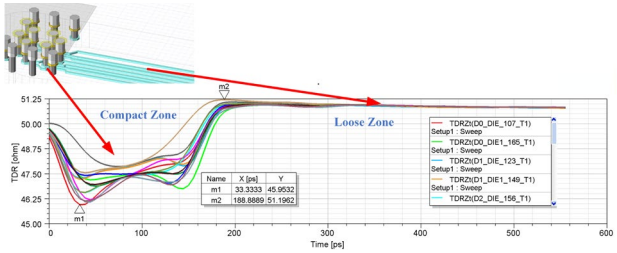


Fig. 4. TDR simulation results of the interconnection link.

B. Simulation Methodology

Due to the large number of interconnects on the substrate, the computational cost for a full-model simulation is extremely high. To improve simulation efficiency, the substrate model is appropriately clipped. Considering the high consistency of the data signal environments and the fact that two adjacent aggressors can capture over 98% of the coupling noise [6], the model is simplified to include 7 data signals and one differential clock pair. The clipped 3D model is shown in Fig. 3.

A hierarchical simulation strategy is adopted in this study. First, electromagnetic characteristics are extracted from the clipped substrate model using a 3D Electromagnetic full-wave simulation tool to generate a high-precision S-parameter model, with a frequency coverage from DC to 40 GHz. In our system, the typical signal rise time (20%-80%) is estimated to be approximately 0.2 to 0.3 UI, a bandwidth of 40 GHz is sufficient to capture up to the 2.5th harmonic of the 16 GHz Nyquist frequency, containing the vast majority of the signal's spectral energy. During the EM simulation, input ports are assigned at the copper pillars on the die side, using a 50 Ω ideal impedance as a reference for all signal ports. To simulate a realistic electrical environment, the power and ground planes within the stackup are designated as reference planes, and radiation boundary conditions are applied around the 3D model. Impedance continuity is verified via TDR analysis. As illustrated in Fig. 4, a noticeable capacitive dip occurs in the "Compact Zone" due to the dense bump arrangement, with the minimum impedance (m1) recorded at approximately 45.95 Ω. As the signal enters the "Loose Zone" with sparser routing, the impedance gradually recovers and stabilizes at approximately 51.20 Ω (m2). The overall link impedance fluctuation is maintained within the 50 Ω ± 10% range, effectively suppressing signal reflections.

Subsequently, the extracted S-parameters are imported into the Advanced Design System (ADS) for channel simulation. To evaluate the link performance at 32 GT/s, AC simulation is utilized for frequency-domain analysis, while channel simulation is employed for time-domain statistical eye diagram analysis. In the ADS channel simulation, the transmitter output impedance is configured to 30 Ω to comply with the UCIe Voltage Transfer Function (VTF) loss definition, and the receiver utilizes a 50 Ω matched load.

III. Results and Discussion

A. Frequency-Domain Characteristics and Compliance Analysis

To verify the transmission performance of the channel within a reconfigurable RF environment, the Voltage Transfer Function (VTF) loss and electromagnetic isolation (crosstalk) are evaluated. The VTF is defined as the complex ratio of the voltage at the receiver input V_{rx} to the internal source voltage at the transmitter V_{src}. Unlike traditional scattering parameters, VTF accurately captures the impact of impedance mismatch on the voltage swing between different nodes in an RF system. Its mathematical definition is given by (1):

$$L(f) = 20\log_{10}\frac{V_{rx}(f)}{V_{src}(f)} \quad (1)$$

In this model, following the UCIe specification, the transmitter driver load line is set to 30 Ω and the receiver termination to 50 Ω. The reflection losses induced by this impedance mismatch are directly incorporated into the VTF metric.

As shown in Fig. 5 and Fig. 6, the simulated VTF loss at the 16 GHz Nyquist frequency is −5.914 dB. According to the UCIe specification for standard packages, $L(f_N)$ at a data rate of 32 GT/s should be greater than −7.5 dB. The simulation results demonstrate a margin of approximately 1.58 dB. Meanwhile, the low-frequency loss $L(0)$ is maintained above −4.5 dB, satisfying the specification requirements.:

Regarding crosstalk characteristics, the integrated VTF crosstalk is measured as −27.075 dB at 16 GHz. Based on the specification formula $XT(f_N) < -26$ dB and $XT(f_N) < 2.5 \times L(f_N) - 10$, the design is at the compliance margin but still satisfies the standard. This indicates that electromagnetic coupling between high-density traces is effectively suppressed through the staggered bump arrangement and optimized trace spacing, providing adequate isolation for reconfigurable RF signal paths.

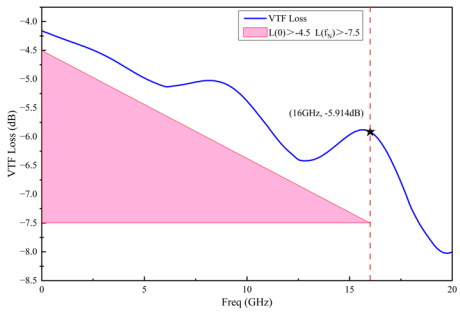


Fig. 5. Simulated VTF-based loss result.

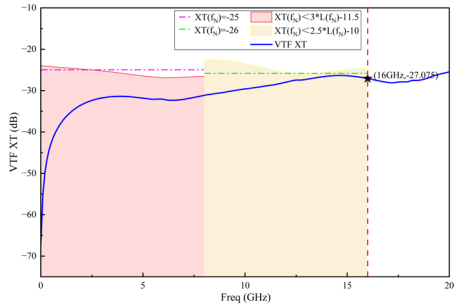


Fig. 6. Simulated VTF-based crosstalk result.

B. *Time-Domain Eye Diagram Analysis*

To verify the link reliability under extreme operating conditions, a statistical analysis of the 32 GT/s signal is performed at a Bit Error Rate (BER) of 10^{-15}. The simulation results are presented Fig. 7. After considering deterministic jitter and integrated crosstalk, the statistical eye width (WidthAtBER) is measured at 28.91 ps, with a statistical eye height (HeightAtBER) of 78 mV.

The results of this study are compared with the UCIe interconnect simulation results based on standard packaging from the literature [6]. As shown in Table I, its eye width (28.91 ps) outperforms the 27.85 ps reported for the scheme in the literature. At a data rate of 32 GT/s (where 1 UI = 31.25 ps), the eye width of this design reaches 0.925 UI, significantly exceeding the minimum requirement of 0.7 UI specified by UCIe. This demonstrates that by optimizing staggered routing and impedance control, the standard packaging scheme can still provide superior timing margins.

IV. CONCLUSION

This study evaluates the physical-layer performance of standard package interconnects up to 32 GT/s (16 GHz), addressing the critical demand for high-bandwidth, low-loss connectivity in reconfigurable RF integrated systems. Simulation results reveal that the insertion loss remains within -7.5 dB at 16 GHz, complemented by channel isolation exceeding -26 dB. Such broadband response characteristics ensure that the physical link maintains high signal linearity and phase consistency during the functional switching and reconfiguration of RF modules. Moreover, a statistical eye width margin of 0.925 UI provides ample timing tolerance for the concurrent transmission of complex RF control logic and high-speed data streams. This work confirms that mature organic substrate packaging is fully capable of meeting the requirements for high-performance, cost-effective reconfigurable RF chiplet integration, offering essential

TABLE I. PERFORMANCE COMPARISON OF 32 GT/S INTERCONNECTS

Parameter	UCIe	[6]	Our work
Data Rate	32 GT/S	32 GT/S	32 GT/S
BER	10^{-15}	-	10^{-15}
Eye Width	0.7 UI	0.891 UI	0.925 UI
Eye Height	40 mV	-	78 mV

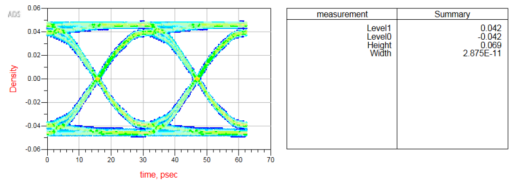


Fig. 7. Simulated eye diagram result.

physical-layer criteria for the engineering of next-generation modular RF front-ends. In the future, we will further enhance and refine the dynamic scheduling based on RF reconfigurability, and will systematically implement this work into actual devices.

ACKNOWLEDGMENT

This work was supported in part by the National Key Research and Development Program of China under Grant 2022YFB4401301 and Grant 2022YFB4401302; in part by the Science Fund for Creative Research Groups of the National Natural Science Foundation of China under Grant 62021004; and in part by the State Key Program of National Natural Science of China under Grant 62134005.

REFERENCES

[1] Y. Zheng, G. Shan, L. Yang, X. Fan, H. Cao, "A DC-5 GHz TSV-Based 3-D Network for Multichiplet Wireless System Reconfiguration", IEEE Internet of Things Journal, Vol.15, no.2, pp.263-271, Feb. 2025.

[2] D. Das Sharma, G. Pasdast, Z. Qian, and K. Aygun, "Universal chiplet interconnect express (UCIe): An open industry standard for innovations with chiplets at package level," IEEE Transactions on Components, Packaging and Manufacturing Technology, vol. 12, no. 9, pp. 1423–1431, Sept. 2022.

[3] D. T. Melek, J. Vandersand, R. N. Kumar, P. M. Sarkar, P. BS, A. Leuciuc, K. Geary, S. Ma, C. M. Mehta, B. Bothra, S. Jain, P. Sabharwal, R. Vaish, K. Bhanushali, Y. Ding, C. Frost, J. Annunziata, K. Sadhu, D. Kyritsis, J. Bostak, M. Li, S. Williams, and K. Chang, "A 0.29 pJ/b 5.27 Tb/s/mm UCIe advanced package link with 2.5-D CoWoS interposer and a 0.52 pJ/b 0.448 Tb/s/mm UCIe standard package link with organic substrate in 3 nm FinFET," IEEE Journal of Solid-State Circuits, pp. 1–13, 2026.

[4] T. Shin, K. Kim, H. Park, B. Sim, S. Kim, J. Kim, S. Choi, J. Park, J. Song, J. Kim, J. W. Park, D. Kang, and J. Kim, "Signal integrity design and analysis of universal chiplet interconnect express (UCIe) channel in silicon interposer for advanced package," in 2023 IEEE Electrical Design of Advanced Packaging and Systems (EDAPS), pp. 1–3, Dec. 2023.

[5] T. Kitazawa, T. Yamagiwa, R. Kitahara, Y. Kim, J. Chakarothai, Y. Hayashi, and T. Kasuga, "A novel FDTD approach considering frequency dispersion of FR-4 substrates for signal transmission analyses at GHz band," IEEE Transactions on Electromagnetic Compatibility, vol. 64, no. 5, pp. 1522–1532, Oct. 2022.

[6] Y. Fan, H. Gan, Y. Zhou, B. Lei, G. Song, and Q. Wang, "Signal integrity simulation and analysis for 2.5D advanced package interconnect based on universal chiplet interconnect express (UCIe)," in 2024 IEEE 26th Electronics Packaging Technology Conference (EPTC), pp. 401–406, Dec. 2024.

A Sub-THz Conductive-Bridging Memristive Switch for Reconfigurable RF Front-Ends

Zong-Rui Xu[1, 2], Yongxin Guo[1, 2]

1 State Key Laboratory of Terahertz and Millimeter Waves, City University of Hong Kong, Hong Kong, China
2 Department of Electronic Engineering, City University of Hong Kong, Hong Kong, China
yongxin.guo@cityu.edu.hk

***Abstract*—This paper proposes a sub-THz conductive-bridging memristive switch implemented on high-resistivity silicon for reconfigurable RF front-end applications. Driven by the increasing demand for low-power, compact, and non-volatile reconfigurable hardware in beyond-5G/6G systems, the proposed device explores the feasibility of extending conductive-bridging memristive switching mechanisms toward the sub-THz frequency range. The switch is developed based on a parasitic-aware compact model, in which the ON/OFF-state resistance transition is jointly considered with the intrinsic shunt capacitance and series inductance introduced by the device geometry and interconnect layout. To suppress high-frequency degradation, the structural design is optimized to minimize OFF-state capacitive coupling and parasitic inductive effects while maintaining a compact footprint compatible with high-density integration on silicon platforms. Compared with conventional semiconductor or volatile switching technologies, the proposed conductive-bridging memristive switch is expected to offer near-zero static power consumption, non-volatile state retention, and enhanced scalability for large-scale reconfigurable front-ends. The proposed concept provides a promising device-level solution for future sub-THz switches, switch matrices, and programmable passive networks in reconfigurable transceivers and intelligent RF systems.**

979-8-3315-4544-4/26/$31.00 ©2026 IEEE

On-Body Characterization of a Planar Horseshoe-Slot MXene Microstrip Antenna with an Elevated Ground Plane for Wearable Applications

Purna B. Samal[1], Shengjian Jammy Chen[2,4], and Christophe Fumeaux[3,4]
[1]Faculty of Engineering and Information Technology, University of Technology, NSW, Australia
[2]College of Science and Engineering, Flinders University, Tonsley, Australia
[3]School of Electrical Engineering and Computer Science, The University of Queensland, Brisbane, Australia
[4]School of Electrical & Mechanical Engineering, The University of Adelaide, Adelaide, Australia
purna.samal@uts.edu.au

***Abstract*—This paper presents the on-body characterization of a horseshoe-slot microstrip antenna with an elevated ground plane fabricated using flexible MXene conductors and a PDMS substrate. The design incorporates two previously developed efficiency-enhancement techniques: radiator optimization to reduce conductor loss and an elevated ground plane to mitigate dielectric loss. These methods improve radiation efficiency by approximately 14% without altering the antenna size or bandwidth. In this work, the optimized antenna is evaluated under on-body conditions to assess its suitability for wearable applications. The results show close agreement between simulation and measurement, with stable impedance characteristics, preserved broadside radiation patterns, and minimal gain degradation when placed on the body. These findings confirm the robustness of the efficiency-driven design for wearable applications.**

***Index Terms*—Wearable antenna, non-conventional conductor, non-metallic antennas, flexible antennas, microstrip patch antennas, radiation efficiency, wideband, wireless body area network, wireless local area network.**

I. Introduction

Wearable antennas, in addition to being flexible, lightweight, and compact to ensure conformability and good ergonomics, are also required to exhibit relatively high radiation efficiency even in close proximity to the wearer's body [1]. These characteristics enable seamless integration into clothing or flexible platforms while maintaining efficient radiation performance in the presence of nearby lossy human tissues. Low radiation efficiency can lead to reduced communication range, weak signal strength, and degraded overall system performance. A conventional approach to improving radiation efficiency is to reduce conductor and dielectric losses by employing low-loss materials. Nevertheless, advances in material engineering have introduced various non-conventional materials that offer attractive physical characteristics such as environmental friendliness, corrosion resistance, low weight, flexibility, and low cost, making them appealing for wearable antenna design [2], [3]. While these materials exhibit significant potential for wearable applications, their relatively low electrical conductivity and higher dielectric losses often result in reduced radiation efficiency.

Therefore, to better exploit the potential of such non-conventional materials for wearable antenna design, several techniques have been proposed in the literature to reduce conductor and dielectric losses. One approach involves employing either thicker conductors or laminating multiple thin conductive layers to reduce ohmic loss, as demonstrated in [4], [5]. Another method introduces metallic layer deposition along the radiating edges or radiator regions to reduce conductor loss, for example through silver paste coating or gold deposition [6]. Similarly, several techniques have been proposed to reduce dielectric losses in lossy substrates. These included micromachining to create a localized low-dielectric-constant region by drilling closely spaced holes beneath the microstrip antenna [7], and partially removing the substrate surrounding the patch to suppress surface waves and reduce dielectric loss [8]. A hybrid-substrate method for minimizing dielectric loss was proposed in our previous work [9]. This method preserves the attractive physical properties of the dielectric material, such as flexibility and biocompatibility, while selectively replacing regions of high power density with a lower-loss material.

To develop additional strategies to mitigate these losses, we previously proposed techniques to improve the efficiency of a standard microstrip antenna fabricated using non-conventional materials for wearable applications, where the conductor consisted of a moderately conductive MXene film and the substrate was a flexible but lossy PDMS slab [10]. The first technique is a radiator optimization method that reduces conductor ohmic loss by minimizing the maximum surface current density over the conductor area, thereby progressively equalizing the current distribution across the radiator surface. The second technique introduces an elevated ground plane, which reduces dielectric loss by minimizing the power density within the lossy substrate by moving the field concentration near the patch edges from the substrate into the air through partial replacement with a low-loss material. The design procedure is presented in detail in [10], supported by surface current distribution and power-loss density analysis. Compared to existing approaches, the proposed method does not require physical modification of the dielectric substrate and offers a

979-8-3315-4544-4/26/$31.00 ©2026 IEEE

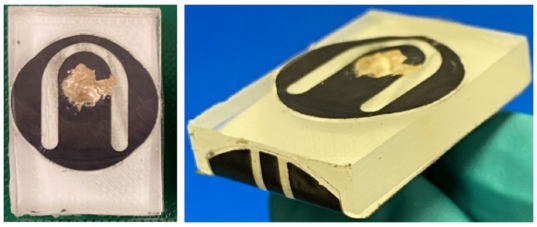


Fig. 1. (a) Top view and (b) the perspective view of the fabricated prototype.

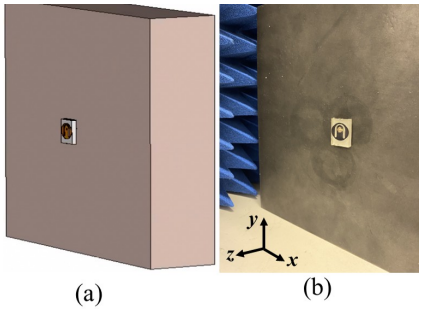


Fig. 2. (a) Full-wave simulation and (b) experimental validation of the antenna under investigation.

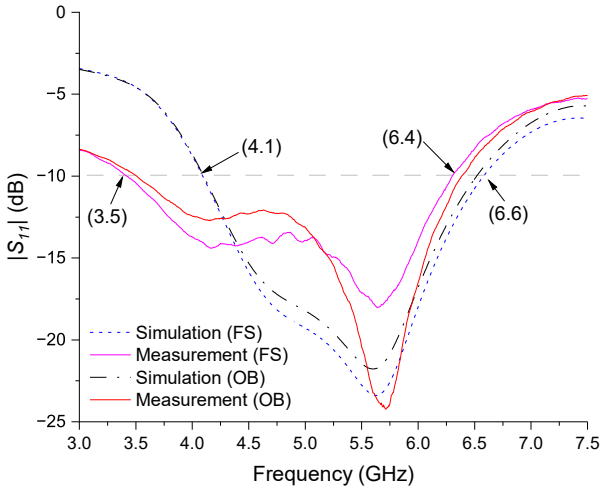


Fig. 3. The free space (FS) and on-body (OB) simulated and measured reflection coefficients of the horseshoe slot microstrip antenna with elevated ground plane.

simple fabrication process. The work demonstrated a total radiation efficiency improvement of approximately 14%. In addition, the technique preserves the operating bandwidth, and shows potential for improving the efficiency of antennas based on other unconventional lossy materials.

In this paper, we extend our previous work [10] by characterizing the on-body performance of the proposed horseshoe-slot Mxene microstrip antenna with an elevated ground plane fabricated using non-conventional materials for wearable applications. While the earlier study reported only free-space performance, this work presents on-body experimental results to validate the antenna for wearable communications scenarios.

II. Antenna Structure

The fabricated horseshoe-slot microstrip antenna with an elevated ground plane is shown in Fig. 1. The conductor consists of a single MXene film with a thickness of 20 μm and a predefined sheet resistance of 2 Ω/square. The substrate is a flexible PDMS layer with a relative permittivity ε_r of 2.7 and a loss tangent tan δ of 0.022 at 6 GHz. The overall dimensions of the antenna are 24×18×4.2 mm^3. Detailed antenna dimensions and fabrication steps are provided in [10]. The shapes of the radiator and the ground plane, which resulted from the application of the efficiency-improvement technique, are also described in [10].

III. On-Body Results

To validate the proposed antenna for WBAN applications, its on-body performance is evaluated by placing the horseshoe-slot microstrip antenna directly on the body model, with no gap between the ground plane and the body surface. This worst-case configuration is adopted to assess robustness under realistic wearable conditions. A tissue-equivalent phantom block from SPEAG, representing a homogeneous human body tissue with relative permittivity $\varepsilon_r = 26$ and loss tangent $\tan\delta = 0.3$, is used for on-body evaluations. The phantom has overall dimensions of $4.8\lambda_0 \times 4.8\lambda_0 \times 1.2\lambda_0$ at 5.8 GHz. The simulation and measurement setups are shown in Fig. 2.

A. Reflection Coefficient

The on-body simulated and measured reflection coefficients are shown in Fig. 3. The results indicate a reasonable agreement between simulation and measurement. The measured reflection coefficient shows that the operational bandwidth is well preserved, primarily due to the isolation provided by the full ground plane. The antenna prototype maintains a wide impedance bandwidth ranging from 3.5 to 6.5 GHz. The free-space results are also included in Fig. 3 for comparison. A downward shift of around 600 MHz in the measured operating band is observed, likely caused by the blunt vertical folding of the elevated ground plane compared to the sharp 90^0 fold used in simulation (Fig. 1(b)). These results demonstrate that the proposed antenna is capable of preserving its impedance characteristics even in an on-body environment.

B. Radiation Pattern and Gain

Similarly, the radiation pattern and antenna gain in the on-body environment are evaluated using the direct placement setup described earlier. The normalized simulated and measured radiation patterns at 5 and 6 GHz are shown in Fig. 4 (a) and (b), respectively. The measured patterns show good agreement with the simulated results. The antenna preserves a directional radiation pattern with maximum radiation in the broadside direction. The measured patterns exhibit relatively low back radiation, which can be attributed to the large size of the phantom model.

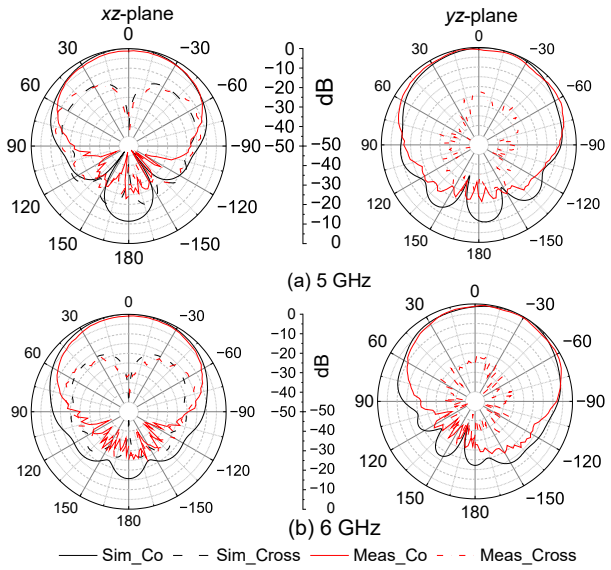


Fig. 4. On-body normalized radiation patterns of the horse-shoe slot microstrip antenna in the *xz*- plane and *yz* plane at (a) 5 GHz and (b) 6 GHz.

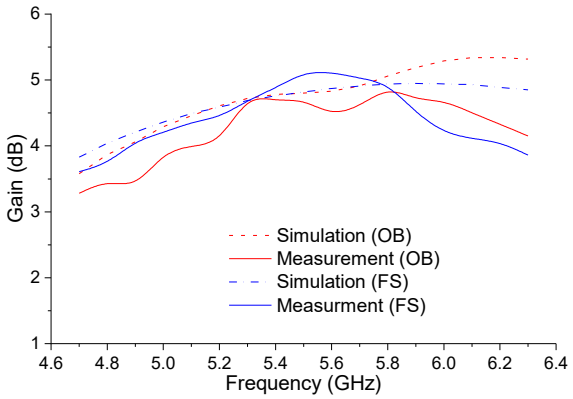


Fig. 5. Comparison of the simulated and measured maximum realized gain in-free-space and on the phantom.

The maximum simulated and measured realized gains are presented in Fig. 5. The simulated results agree well with the measurements. For comparison, the simulated and measured free-space gains are also included in the figure. As observed, the maximum free-space gain is not significantly affected when the antenna operates in the on-body environment. These results demonstrate that the proposed horseshoe-slot antenna maintains stable performance in close proximity to the human body, making it suitable for WBAN applications.

The specific absorption rate (SAR) performance is investigated through simulations using a three-layer body model consisting of skin, fat, and muscle tissues [11], with overall dimensions similar to the phantom model. The corresponding layer thicknesses are 3 mm (skin), 7 mm (fat), and 40 mm (muscle). The SAR is evaluated in accordance with the IEEE C95.3 standard, averaged over 10 g of tissue, with an input power of 0.5 W [11]. The worst-case SAR, obtained when the antenna ground plane is placed directly on the body model, is 1.3 W/kg at 5.8 GHz. This value is within the permissible limit of 2 W/kg [12], thereby confirming the suitability of the proposed antenna for wearable applications.

IV. Conclusion

This paper has presented an on-body evaluation of a horseshoe-slot microstrip antenna fabricated using non-conventional conductive and dielectric materials. The results demonstrate stable impedance characteristics with measured bandwidth of 2.9 GHz, preserved broadside radiation patterns, and minimal gain degradation in close-body proximity. Extending previously published efficiency-driven design techniques validated under free-space conditions, the on-body measurements confirm that such methods remain effective for wearable antennas employing lossy materials. These findings demonstrate that efficiency-driven design approaches can be successfully extended to wearable antenna applications using unconventional lossy conductors, thereby supporting their broader adoption in practical wearable systems.

Acknowledgment

The authors acknowledge the support provided by the ARC Research Hub for Graphene Enabled Industry Transformation at The University of Adelaide for producing the non-conventional conductor materials.

References

[1] P. J. Soh, G. A. E. Vandenbosch, S. L. Ooi, and N. H. M. Rais, "Design of a broadband all-textile slotted PIFA," *IEEE Trans. Antennas Propag.,* vol. 60, no. 1, pp. 379–384, 2012.

[2] S. J. Chen and C. Fumeaux, "Wearable antennas based on graphite paper and conductive polymer," in 12th European Conference on Antennas and Propagation (EuCAP 2018), 2018, pp. 1–4.

[3] S. H. Kang and C. W. Jung, "Transparent patch antenna using metal mesh," *IEEE Trans. Antennas Propag.,* vol. 66, no. 4, pp. 2095–2100, 2018.

[4] T. Kaufmann, T. V. Verma, A., R. Weng B., Shepherd, and C. Fumeaux, "Efficiency of a compact elliptical planar ultra-wideband antenna based on conductive polymers," *Int. J. Antennas Propag.,* vol. 2012, April 2012.

[5] S. I. Latif, L. Shafai, and C. Shafai, "An engineered conductor for gain and efficiency improvement of miniaturized microstrip antennas," *IEEE Antennas Propag. Mag.,* vol. 55, no. 2, pp. 77–90, 2013.

[6] M. R. Haraty, M. Naser-Moghadasi, A. A. Lotfi-Neyestanak, and A. Nikfarjam, "Improving the efficiency of transparent antenna using gold nanolayer deposition," *IEEE Antennas Wireless Propag. Lett.,* vol. 15, pp. 4–7, 2016.

[7] G. Gauthier, A. Courtay, and G. Rebeiz, "Microstrip antennas on synthesized low dielectric constant substrates," *IEEE Trans. Antennas Propag.,* vol. 45, no. 8, pp. 1310–1314, 1997.

[8] S. B. Yeap and Z. N. Chen, "Microstrip patch antennas with enhanced gain by partial substrate removal," *IEEE Trans. Antennas Propag.,* vol. 58, no. 9, pp. 2811–2816, 2010.

[9] P. B. Samal, S. J. Chen and C. Fumeaux, "Flexible hybrid-substrate dual-band dual-mode wearable antenna," *IEEE Trans. Antennas Propag.,* vol. 72, no. 2, pp. 1286-1296, Feb. 2024.

[10] P. B. Samal, S. J. Chen, T. T. Tung, D. Losic and C. Fumeaux, "Efficiency-driven design for planar antennas with lossy materials," *IEEE Open Journal of Antennas and Propagation,* vol. 4, pp. 23-33, 2023.

[11] P. B. Samal, S. J. Chen and C. Fumeaux, "Wearable textile multiband antenna for WBAN applications," *IEEE Trans. Antennas Propag.,* vol. 71, no. 2, pp. 1391-1402, Feb. 2023.

[12] *IEEE Standard for Safety Levels with Respect to Human Exposure to Radio Frequency Electromagnetic Fields 3 kHz to 300 GHz, 2005.*

THz Material Characterization of Rough Samples

Miguel Navarro-Cía
School of Physics and Astronomy & Dept. Electronic, Electrical and Systems Engineering
University of Birmingham
Birmingham, UK
m.navarro-cia@bham.ac.uk

***Abstract*—The accurate extraction of material properties from free-space methods is dependent on several assumptions, including that the sample has parallel, flat surfaces, and constant thickness, and that the material is homogeneous. In reality, none of these are satisfied for standard samples probed with THz due to the usual non-negligible surface roughness in the range of tens of microns. This invited talk will give an overview on the work done at the University of Birmingham to develop methodologies that pivot around quasi-optical time- and frequency-domain spectroscopy systems to deal with rough samples.**

***Index Terms*—quasi-optics, terahertz, frequency-domain spectroscopy, time-domain spectroscopy**

I. Introduction

Quasi-optical spectroscopy setups based on time- or frequency-domain systems are the preferred methods for material characterization in the TeraHertz (THz) range because of simplicity, broadband capability, and low-insertion loss associated with free-space propagation [1]. They rely strongly on several key assumptions to accurately determine the complex electric permittivity such as planarity and homogeneity of the material under test, as well as plane wave illumination assumption [2]. When operating with collimated beams or focused beams when the sample is much smaller than the Rayleigh range (also known as confocal distance), the latter is an acceptable approximation. However, sample's planarity and homogeneity are unlikely to be fulfilled since untreated samples are expected to have surface roughness characteristics (i.e., spatial correlation length and height) from few to hundreds of microns [3] while THz probing beams carry sub-mm wavelengths and expand from few to several mm across.

II. Methods

A. Quasi-optical Systems

The experimental campaigns covered in this invited talk utilized the Midlands mm-Wave and THz Measurement Facility. The material characterization suites include:

- a vector analyzer Keysight N5247B PNA-X equipped with VDI frequency extenders and integrated into a four off-axis parabolic mirror quasi-optical bench system from Thomas Keating Instruments.
- two commercial time-domain spectrometers, the Menlo Systems Tera K15 Mark II and the Toptica Photonics TeraFlash Pro Dual, integrated into quasi-optical bench systems based on off-the-shelf lenses or mirrors.

EPSRC [Grant Nos. EP/X014118/1 and Grant EP/P020615/1], and the Royal Society [Grant No. IES\R1\241009].

B. Samples

A wide range of samples were investigated. They included controlled samples fabricated through 3D printing, commercial and experimental high-frequency laminate substrates, building materials procured locally, etc.

Samples' surface roughness characterization is performed using a Filmetrics Profilm3D optical profilometer and a Dektak 3ST stylus profilometer.

C. Extraction Algorithms

Two different approaches were followed to develop surface scattering-aware material extraction algorithms:

- a geometrical optics based approach suitable for low to moderate surface roughness characteristics that was adopted for vector network analyzer and time-domain spectrometer measurements [4].
- a machine learning based approach suitable for any type of surface roughness characteristic that was adopted only for time-domain spectrometer measurements [5].

III. Conclusion

Scattering-aware material extraction algorithms have been successfully developed for quasi-optical measurements. The physics-based approach inherits the limitations of geometrical optics and its range of validity includes low to moderate rough samples. The machine-learning approach is only limited to the diversity of the training set while there is signal detected at the receiver end.

Acknowledgment

The author thanks past and current group members working on the topic, specially Alperen Sari and Yeganeh Farahi.

References

[1] D. Feng *et al.*, "Building a Comprehensive Complex Permittivity Library for THz Radio Planning Using Quasi-Optical Measurements," IEEE Trans. Terahertz Sci. Techn., vol. 15, no. 3, pp. 307–318, May 2025.
[2] M. Naftaly, Terahertz Metrology. Norwood, MA, USA: Artech House, 2015.
[3] L. Azpilicueta *et al.*, "Diffuse-scattering-Informed geometric channel modeling for THz wireless communications systems," IEEE Trans. Antennas Propag., vol. 71, no. 10, pp. 8226–8238, Oct. 2023.
[4] A. Sari *et al.*, "Interlaboratory mmWave and THz Quasi-Optical Characterization of Commercial Conventional and 3-D Printable Substrates," *Early Access*, 10.1109/TTHZ.2026.3674230.
[5] Y. Farahi, N. Hadjiantoni, N. Klokkou, V. Apostolopoulos and M. Navarro-Cía, "Deep Learning for Scattering Robust TeraHertz Time Domain Spectroscopy," IEEE Trans. Terahertz Sci. Techn., vol. 16, no.3, pp. 247–257, March 2026.

A Branch-Independent Computational Method for Dielectric Material Characterization

Yunhao Fu
School of Electrical Engineering and Telecommunications
the University of New South Wales
Sydney, Australia
yunhao.fu@unsw.edu.au

Rodica Ramer
School of Electrical Engineering and Telecommunications
the University of New South Wales
Sydney, Australia
ror@unsw.edu.au

***Abstract*—A branch-independent computational method is proposed, permitting dielectric material characterization by extracting its real relative permittivity ε_r from a propagation factor. The propagation factor, which describes the interaction between a dielectric and an electromagnetic wave, is widely employed in material characterization. However, ε_r extracted from the propagation factor suffers from phase ambiguity due to the multi-valued nature of the logarithm operation. The resulting multiple phase branches correspond to different ε_r, making it difficult to determine the correct value. A computational method based on the first derivative of the phase branch is developed with closed-form formulas, producing the correct ε_r. Simulation validation in the 12-18 GHz band is conducted to demonstrate the method under ideal conditions; an experimental measurement on PTFE samples follows. Unlike traditional wideband characterization methods, which focus solely on a single frequency, the branch-independent method considers the propagation factor's overall behavior in wideband dielectric material characterization.**

Keywords—dielectrics, material characterization, multi-value branches, permittivity extraction, phase ambiguity

I. Introduction

Dielectric materials that affect electromagnetic wave propagation are extensively employed in microwave and millimeter-wave applications. Dielectrics generally serve as substrates for microwave circuits and components [1], [2]. Based on printed circuit boards, substrate-integrated waveguide technologies [3] permit the planar realization of bulky waveguide components. Dielectric materials can also be constructed to increase antenna efficiency or to guide wave transmission [4]. As additive manufacturing techniques advance, dielectrics can be easily customized into complex structures to meet specific functional requirements [5]. The real relative permittivity ε_r, as a parameter describing the electromagnetic wave's response to dielectrics, affects the quality and dimensions of devices, and characterizing ε_r of a material is essential for practical use.

The material characterization methods can be classified into two types: resonant methods [6] and non-resonant methods [7]. The resonant method typically focuses on material properties at a single frequency by processing data across a frequency band; in contrast, the non-resonant method reveals the broadband behavior of ε_r, but the calculation of ε_r at each frequency relies only on the data at that frequency. In non-resonant methods, the propagation factor can be used to extract ε_r over a frequency band, as it contains information on the phase delay. However, the practice of obtaining the phase delay via the natural logarithm results in an infinite number of phase branches, known as phase ambiguity. Such a non-resonant method is considered in [8] for characterizing several materials, but the proper selection of the correct branch is not addressed. The solution to the ambiguity issue in [9] is to compute ε_r for all branches and choose the one with a constant value over the band, which is under the assumption of ε_r being independent of frequency, but the practice relies on the prior knowledge of the material and neglects the potential of an infinite number of branches. The multiple solutions of the propagation factor also occur in [10], with the correct solution at each frequency determined by comparison with other measured parameters, while an undefined solution range may yield a result valid only locally and deviating from the correct value. The ambiguity arising from multiple phase branches fundamentally limits the broadband material characterization methods that extract ε_r from the propagation factor.

This paper proposes a practically implementable method of dielectric material characterization. The contribution of the work lies in addressing the phase ambiguity by skipping the identification of the correct branch, allowing the method to be applied to any branch and thus making it branch-independent. With the propagation factor obtained, the branch-independent method is explained, detailing the case of rectangular waveguides (RWGs) as the transmission line (TL) and including explicit formulas. The proposed method is initially validated in the Ku-band simulation under ideal conditions, and experimental measurements of PTFE demonstrate its practical applications. Rather than focusing on a single frequency, the overall phase branch behavior across frequencies is taken into account.

II. Branch-Independent Computational Method

The branch-independent method handles the multiple branches generated when applying the natural logarithm to the propagation factor, which must first be obtained. Fig. 1 illustrates the measurement setup to get the propagation factor in a TL section. The measurement procedure is known as the line-line (LL) method [8], and RWGs are adopted as the holding structure with the material under test (MUT) fully filled. The LL method consists of two steps, in which RWG#1 and RWG#2 are measured sequentially. Both MUT-filled RWGs have the same cross-sectional dimensions of $w \times h$ circled in Face A, and the MUT is a dielectric material with ε_r, which is the unknown parameter to be extracted. The only difference between RWG#1 and RWG#2 is their longitudinal lengths, being l_1 and l_2, and the differential length is defined as $\Delta l = l_2 - l_1$. The LL method produces the propagation factor $e^{-\gamma\Delta l}$ of the differential MUT-filled RWG section, where $\gamma = \alpha + \mathrm{j}\beta$ is the propagation constant including the attenuation constant α and the phase constant β. The product $\beta\Delta l$ indicates the phase delay when the wave transmits through a distance of Δl in the MUT-filled RWG, and it can be expressed as

$$\beta\Delta l = -\mathrm{Im}(\ln(e^{-\gamma\Delta l})) + 2\pi n, \tag{1}$$

where operator Im() extracts the imaginary parts and n is an integer. Applying the function ln() on $e^{-\gamma\Delta l}$ mathematically generates infinite roots, while the practical computation only

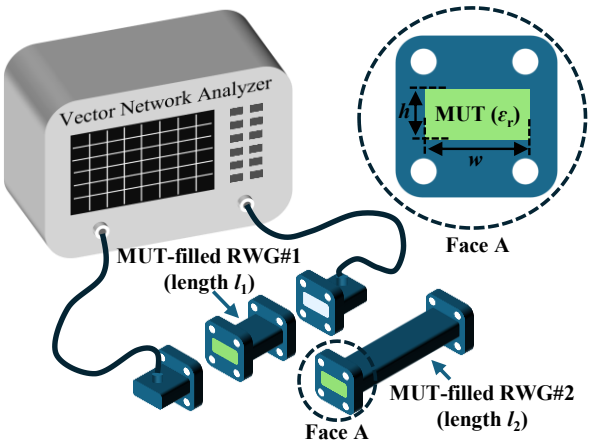


Fig. 1. The measurement setup of the LL method to obtain the propagation factor of the differential section between the two MUT-filled RWGs.

produces a single result in the principal value range (-π, +π], introducing n in (1) for correction. Each value of n corresponds to a phase branch, indicating a unique variation of ε_r, and the unknown n in (1) leads to phase ambiguity. In the proposed branch-independent method, the n = 0 phase branch is utilized; it increases monotonically with frequency f and can be fitted using polynomial techniques as $M(f)$.

RWGs are the structure that accommodates the MUT, and the TE_{10} mode dominants, with its β expressed as

$$\beta(f) = \sqrt{Af^2\varepsilon_r - B}\,, \tag{2}$$

where

$$A = \frac{4\pi^2}{c^2}\,, \tag{3}$$

$$B = \left(\frac{\pi}{w}\right)^2, \tag{4}$$

c is the speed of light in vacuum, and w is the width in Fig. 1.

The actual β in (2) and the fitted phase branch $M(f)$ follow

$$\beta(f) = \frac{M(f)}{\Delta l} + \frac{2\pi n}{\Delta l}\,. \tag{5}$$

Taking the first derivative of both sides of (5) with respect to f eliminates the unknown constant item of $2\pi n/\Delta l$, yielding

$$D \overset{\text{def}}{=} \frac{1}{\Delta l} \times \frac{dM}{df}\,. \tag{6}$$

Since the function $M(f)$ is obtained with the fitting technique, the value of D at each f in (6) can be directly computed.

At each f, a quadratic equation for ε_r exists, as follows

$$A^2f^2\varepsilon_r^2 + (-Af^2D^2)\varepsilon_r + BD^2 = 0\,. \tag{7}$$

The physical meanings of the involved parameters constrain their values. By maintaining the continuity of the root across frequencies, the practical solution of ε_r at each f is given as

$$\varepsilon_r = \frac{fD^2 + D\sqrt{f^2D^2 - 4B}}{2Af}\,. \tag{8}$$

III. Simulation Validation

Validation from 12 to 18 GHz is conducted in ANSYS HFSS. Simulations follow the measurement setup as in Fig. 1. The RWGs have cross-sectional dimensions w = 15.8 mm and h = 7.9 mm, with lengths l_1 = 10 mm for RWG#1 and l_2 = 30 mm for RWG#2. The MUT is constructed with tanδ = 0.001, and its ε_r is denoted as $\varepsilon_{r,set}$, = 2. To account for the impedance mismatch introduced by the material discontinuity, a 6-mm air-filled RWG is added at both ends of the MUT-filled RWG in simulation, while the reference planes are de-embedded to the air-MUT interfaces, aligning with the calibrated ports at the RWG adaptors in the measurements. The transverse boundaries of the MUT and air sections are defined by RWG set as perfect electric conductors. The LL method processes the simulated data to obtain $e^{-\gamma\Delta l}$ in the differential MUT-filled RWG of Δl = 20 mm. Then, the branch-independent computational method is applied to extract ε_r in the frequency band of interest. A fifth-order polynomial is adopted to fit the n = 0 phase branch, and the fitting range is extended by one-sixth of the bandwidth beyond both the lower and upper frequencies. By comparing the calculated ε_r from (8) with the set value $\varepsilon_{r,set}$, and the error is defined as

$$\text{Error_}\varepsilon_r(\%) = \frac{\left|\varepsilon_r - \varepsilon_{r,set}\right|}{\varepsilon_{r,set}} \times 100\%\,. \tag{9}$$

Fig. 2 illustrates the ε_r extracted over the Ku-band by applying the proposed branch-independent computational method, along with a comparison to $\varepsilon_{r,set}$ = 2 and the associated error. In the upper region of Fig. 2, the dashed curve represents the extracted ε_r, and the solid line is the reference $\varepsilon_{r,set}$ = 2. Although the extracted ε_r shows a slight downward trend with frequency, it closely matches $\varepsilon_{r,set}$ = 2 in the frequency band. The lower region of Fig. 2 shows the in-band error calculated from (9). Error_ε_r is larger at the frequency ends and smaller in the interval, reaching the maximum value of 0.22% at 18 GHz. The tiny discrepancy between the extracted ε_r and $\varepsilon_{r,set}$ = 2 validates the branch-independent method. Unlike the Nicholson Ross method [11], Fig. 2 shows that the ε_r calculated using the proposed method does not diverge in a wide frequency range.

IV. Experimental Measurement

An experimental demonstration of the branch-independent method is further conducted by characterizing PTFE, a stable dielectric material with typical properties of tanδ = 0.0002 and ε_r = 2.06. Fig. 3 captures the photograph of the measurements, and its setup aligns with the simulation validation in terms of frequency range and structural dimensions. A Keysight PNA-L Network Analyzer (N5235B) with the IFBW of 10 kHz measures S-parameters for the propagation factor calculation. The two PNA ports are connected to identical coaxial cables

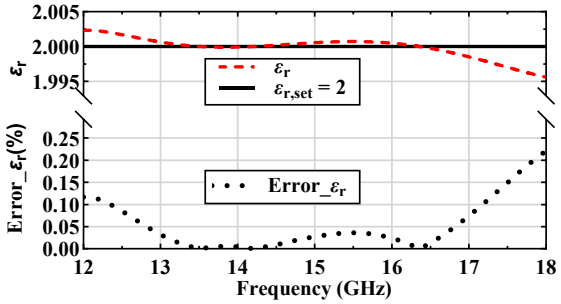


Fig. 2. Comparison between the ε_r calculated by the branch-independent computational method and $\varepsilon_{r,set}$ = 2, with Error_ε_r in the Ku-band.

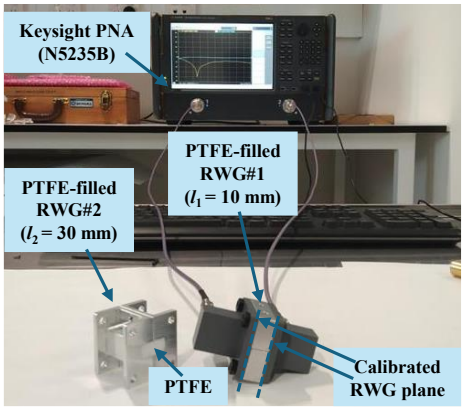


Fig. 3. Photograph of the measurements.

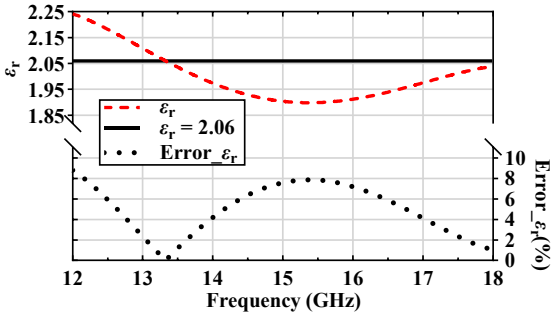


Fig. 4. The calculated ε_r for PTFE using the branch-independent computational method, compared to the typical ε_r = 2.06 and with Error_ε_r in the Ku-band.

and adaptors with WR62 waveguide ports, which are calibrated as the reference plane using a thru-reflect-line calibration. The 10-mm PTFE-filled RWG#1 is under measurement, and the 30-mm PTFE-filled RWG#2 is prepared aside, with the white PTFE visible at the port.

Fig. 4 compares the extracted ε_r of the measured PTFE using the branch-independent method (a dashed line) and the typical reference value ε_r = 2.06 (a flat solid line), with the variation of the Error_ε_r from 12 to 18 GHz. Regarding the dashed line for ε_r, it starts at 2.24 at 12 GHz, corresponding to the maximum Error_ε_r of 8.74%. Then, ε_r decreases with frequency, crossing the ε_r = 2.06 at 13.33 GHz and reaching the minimum of 1.90 at 15.38 GHz; after that, it rises gradually and approaches the reference line, reaching 2.04 at 18 GHz with the Error_ε_r of 1.02%. The fluctuating Error_ε_r is mainly due to the measurement noise and the polynomial-fitting limitation. Although the calibration is conducted, the measurement noise can be amplified when the phase branch is obtained from the logarithm of the propagation factor $e^{-\gamma\Delta l}$ in (1), causing a small phase deviation. In fitting the n = 0 phase branch, the boundary effects on the polynomials make the fitting error more pronounced at the band edge than in the interval. Although the n = 0 phase branch increases from -0.38 to 3.62 rad over 12-18 GHz, making the branch appear almost linear, the polynomial tends to follow the phase pattern with the noise and captures the fine variation. With the derivative operation in (6), the phase deviation is further magnified as a frequency-dependent variation in the extracted ε_r. Moreover, the possible density discrepancy between the short and long PTFE samples and the fixture-related uncertainties could lead to a slight offset of the overall ε_r. Overall, the extracted ε_r fluctuates around the reference ε_r = 2.06, and the in-band error based on simulated data under ideal conditions is small for ε_r = 2, confirming that the underlying branch-independent method is fundamentally valid. The use of PTFE is for proof-of-concept demonstration and does not imply limitation of the proposed method to other materials.

V. Conclusion

In this paper, we address the ambiguity in phase branch selection when extracting ε_r from the propagation factor. The branch-independent computational method allows the n = 0 phase branch to serve as a valid input in material characterization. The method is initially validated through simulations and demonstrated by measuring PTFE samples experimentally. The proposed method enables the extraction of ε_r over a wide frequency range, while the loss tangent extraction is beyond the scope and will be addressed in future work. Unlike conventional non-resonant methods that process each frequency point independently, the proposed branch-independent computational method introduces a broadband perspective that considers the overall frequency behavior, incorporating the resonant methods' practice of evaluating the wideband performance into the non-resonant methods.

Acknowledgment

The authors would like to thank Dr. J. Kot and Prof. M. Bozzi for constructive discussions.

References

[1] M. Li, Y. Liu, S. -L. Chen, J. Hu, and Y. J. Guo, "Synthesizing shaped-beam cylindrical conformal array considering mutual coupling using refined rotation/phase optimization," IEEE Trans. Antennas Propag., vol. 70, no. 11, pp. 10543-10553, 2022.

[2] X. Guo, Y. Guo, Y. Luo, and Y. Yang, "Full-space transmission–reflection-integrated metasurface for multibeam generation on orthogonal planes," IEEE Trans. Microw. Theory Techn., vol. 73, no. 10, pp. 8199-8209, 2025.

[3] Z. Luo, K. Zhou, and K. Wu, "A compact planar quad-channel SIW filtering crossover with flexibly allocated channel frequencies and bandwidths," Proc. IEEE/MTT-S Int. Microw. Symp., San Francisco, CA, USA, 2025, pp. 394-397.

[4] A. Di Serio et al., "Flexible testbed at 300 GHz for performance assessment of 1-D and 2-D antenna arrays for MIMO radar applications," IEEE Trans. Microw. Theory Techn., vol. 72, no. 1, pp. 435-445, 2024.

[5] Y. Fu, K. Y. Chan, M. Bozzi, and R. Ramer, "3-D-printed monolithically integrated waveguide polarizer," IEEE Trans. Microw. Theory Techn., vol. 73, no. 9, pp. 5696-5710, 2025.

[6] A. Paghi et al., "Estimation of the FR4 microwave dielectric properties at cryogenic temperature for quantum-chip-interface PCBs design," IEEE Trans. Instrum. Meas., vol. 73, pp. 1-7, 2024.

[7] P. Kůrka, D. Havelka, and M. Cifra, "Broadband extraction of sample permittivity from microwave planar transmission lines," IEEE Trans. Microw. Theory Techn., vol. 73, no. 9, pp. 6707-6718, 2025.

[8] I. Huynen, C. Steukers, and F. Duhamel, "A wideband line-line dielectrometric method for liquids, soils, and planar substrates," IEEE Trans. Instrum. Meas., vol. 50, no. 5, pp. 1343-1348, 2001.

[9] Y. Ozturk, B. Paul, A. Arage, N. K. Nahar, and K. Sertel, "Characterization of automotive paint permittivity for mmwave radar applications," IEEE Trans. Microw. Theory Techn., vol. 72, no. 4, pp. 2477-2485, 2024.

[10] C. Yang, K. Ma, and J. -G. Ma, "A noniterative and efficient technique to extract complex permittivity of low-loss dielectric materials at terahertz frequencies," IEEE Antennas Wireless Propag. Lett., vol. 18, no. 10, pp. 1971-1975, 2019.

[11] A. M. Nicolson and G. F. Ross, "Measurement of the intrinsic properties of materials by time-domain techniques," IEEE Trans. Instrum. Meas., vol. 19, no. 4, pp. 377-382, 1970.

Application of Q-Chokes for Enhanced Characterization of Materials in FR3 Band

Malgorzata Celuch
QWED Sp. z o.o.
Warsaaw, Poland
mceluch@qwed.eu

Wojciech Gwarek
QWED Sp. z o.o.
Warsaw, Poland
wgwarek@qwed.eu

Lukasz Nowicki
QWED Sp. z o.o. and Warsaw Univ. Tech.
Warsaw, Poland
lukasznowicki@qwed.com.pl

Marzena Olszewska-Placha
QWED Sp. z o.o.
Warsaw, Poland
molszewska@qwed.com.pl
…

***Abstract*—This contribution concerns resonator-based characterization of materials. First, the relevant physical principles are discussed and illustrated with EM modeling. Then, industrial round-robin results are summarized, assessing the commercially available techniques from the viewpoint of 5G/mmWave applications. The presentation then focuses on the novel Q-Choked resonators and their advantages for materials' characterization in the forthcoming FR3 frequency band.**

Keywords—materials characterization, nondestructive testing, chokes, resonators, microwave sensors, EM modeling, FR3, 5G-A

SUMMARY

Resonator-based techniques are well recognized for their precision and ease-of-use in material measurements. A review paper [1] discussed resonator topologies suitable for the characterization of various dielectric, magnetic, and conducting materials. Industrial round-robin experiments [2] provided estimates for repeatability and reproducibility of most popular techniques based on SCR, SPDR, BCDR, and FPOR instruments from popular vendors.

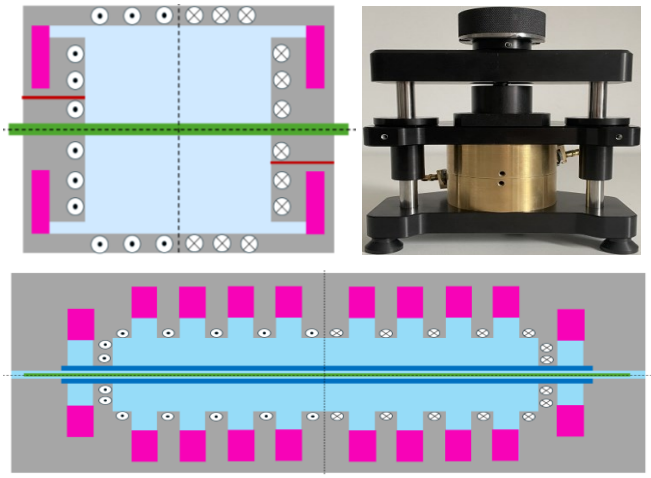


Fig. 1. Upper: Q-SCR cross-section [4] and product photo https://qwed.eu/measurement-setups/q-choke-split-cylinder-resonator/. Lower: Q-SSR cross-section [5], grey – metal (dots / crosses mark currents), blue – air, navy blue – sapphire, magenta – lossy material, green – sample.

Our workshop talk will summarize the above works and then focus on a recent invention of Q-Choke [3] and its embodiments in Q-SCR [4] and Q-SSR [5] instruments (Fig. 1). Q-Chokes create an artifical electromagnetic boundary condition at a cavity walls, such that:

- the axisymmetrical TE modes, which are the desired measurement modes in many practical applications [2], remain unperturbed,
- other modes have their energy dissipated in the lossy pockets (magenta regions in Fig. 1) of the choke.

This allows measurements with larger frequency shifts, without the risk of confusing the desired mode with undesired ones. Thereby, higher-permittivity or thicker samples can be characterized, which is important for novel materials in different form-factors. With respect to clasiscal SCR or SPDR units, Q-SCR ensures higher sensitivity in low-loss / high-resistivity measurements, while Q-SSR enables multi-modal characterization. Q-SCR (which has reached a product form) and Q-SSR (prototype) have been validated with respect to earlier benchmarks [2], [6]. Both are specifically suitable for emerging applications in the FR3 frequency band.

ACKNOWLEDGMENT

This work was supported by the Polish National Centre for Research and Development under contracts M-ERA.NET3/2021/83/I4BAGS/2022 and InnovativeSMEs/4/100/5G_Foil/2023. The authors also thank the iNEMI project partners for benchmarking collaborations.

REFERENCES

[1] J. Krupka, "Microwave measurements of electromagnetic properties of materials," Materials, vol. 14, no. 17, p. 5097, 2021, doi: 10.3390/ma14175097.

[2] Int. Electron. Manuf. Initiative. (2024). 5G/mmWave Materials Assessment and Characterization [Online]. Available: https://www.inemi.org/iNEMI/Projects/Completed/5GmmWave%20Materials%20Assessment%20and%20Characterization.aspx

[3] W .K. Gwarek, European Patent Application no. EP23461651.4, of 2023-09-18, published as EP4524554A1, EP Bulletin 2025/12; Intl. Patent Application no. PCT/IB2024/056934, of 2024-07-17, published as WO 2025/062194A1.

[4] M. Celuch, M. Olszewska-Placha, L. Nowicki, and W. Gwarek, "A novel Q-Choked resonator for microwave material measurements alleviating sample thickness limitations of existing techniques," IEEE Microw. Wireless Techn. Lett., vol. 34, no. 6, pp. 845-848, June 2024, doi: 10.1109/LMWT.2024.3397912.

[5] W. Gwarek, M. Celuch and L. Nowicki, "A novel Q-Choked Sapphire Sandwiched Resonator for wideband measurements of flat dielectric samples," IEEE Microw. Wireless Techn. Lett., vol. 35, no. 6, pp. 900-903, June 2025, doi: 10.1109/LMWT.2025.3568534.

[6] M. Celuch et al., "Benchmarking of GHz resonator techniques for thecharacterisation of 5G / mmWave materials," in Proc. 51st Eur. Microw.Conf. (EuMC), Apr. 2022, pp. 568–571, doi: 10.23919/EuMC50147.2022.9784292.

[7] FR3: https://www.everythingrf.com/community/fr3-frequency-bands

XXX-X-XXXX-XXXX-X/XX/$XX.00 ©20XX IEEE

Microwave Probe with Enhanced Sensitivity for Wideband Dielectric Characterizations

Amir Ebrahimi
School of Engineering
RMIT University
Melbourne, Australia
amir.ebrahimi@rmit.edu.au

Syed Akbar Raza Naqvi
School of Inform. Tech. and Electrical Eng.
The University of Queensland
Brisbane, Australia
s.naqvi@uq.edu.au

Amin Abbosh
School of Inform. Tech. and Electrical Eng.
The University of Queensland
Brisbane, Australia
a.abbosh@uq.edu.au

***Abstract*— This paper presents a high-sensitivity microwave probe for broadband dielectric characterization, achieving improved accuracy compared to conventional open-ended coaxial probes based on RG405 coaxial cable. The proposed design employs a series inductive loading at the probe tip, implemented using a via-connected circular patch structure, to enhance electromagnetic interaction with the material under test. An analytical circuit model is developed to quantify amplitude and phase sensitivities, confirming significant improvement over standard probes. A fabricated prototype demonstrates superior performance across 1–7 GHz, validated through measurements of water–ethanol mixtures with up to 15% water content.**

Keywords—Coaxial probe, dielectric characterization, sensitivity enhancement

I. Introduction

Microwave dielectric characterization plays a critical role in a wide range of applications, including biomedical sensing, chemical analysis, and material inspection. Among available techniques, open-ended coaxial probes are widely adopted due to their broadband capability, non-destructive nature, and ease of implementation [1]. However, their sensitivity is fundamentally limited by the probe geometry and weak fringing-field interaction with the material under test. This limitation becomes more pronounced when tracking small dielectric variations in samples arising from compositional changes or similar effects. In this work, a high-sensitivity probe based on a modified tip structure with series inductive loading is proposed to enhance the electromagnetic interaction at the sensing interface without compromising broadband performance. The proposed design is analytically modeled, experimentally validated, and shown to significantly outperform a conventional RG405 coaxial cable-based probe over a wide frequency range.

II. The Proposed Probe

The proposed high-sensitivity probe is based on a modified open-ended coaxial structure incorporating a series inductive loading at the tip. As illustrated in Fig. 1(a), the probe tip is formed by extending the coaxial line onto a dielectric substrate, where the exposed metallization creates a circular patch capacitance surrounded by a grounded ring connected to the outer conductor through metallic vias. The center conductor is connected to the patch via a vertical via, which introduces a controlled series inductance. This configuration enhances the local electromagnetic field confinement and strengthens the interaction with the material under test (MUT). An equivalent circuit model, shown in Fig. 1(b), represents the probe as a combination of the intrinsic coaxial line impedance, the fringing capacitance at the probe–MUT interface (C_p), and the added series inductance (L_p).

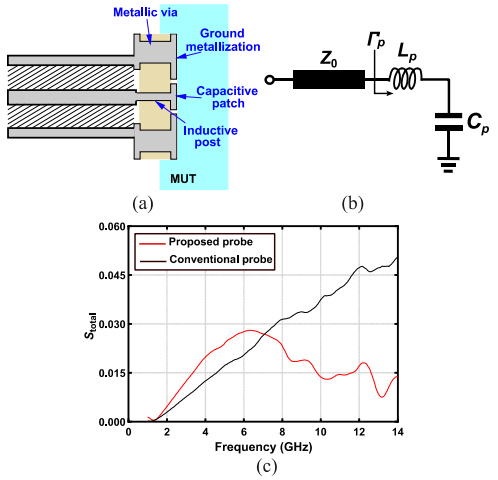


Fig. 1. (a) Cross-sectional view of the proposed probe. (b) Equivalent circuit model. (c) Measured sensitivity comparison between the proposed probe and the conventional RG405 coaxial probe.

Compared to a conventional RG405 coaxial cable-based probe, the introduced inductive element effectively increases the sensitivity of the reflection response to variations in complex permittivity, particularly by amplifying both amplitude and phase perturbations.

The proposed probe was fabricated and experimentally validated. Fig. 1(c) compares the measured total sensitivity with a conventional RG405 coaxial cable-based probe, showing clear improvement across 1–7 GHz. The results confirm that the introduced series inductive loading enhances the response to variations in complex permittivity, increasing both amplitude and phase sensitivity. The performance is further verified through measurements of representative liquid samples, demonstrating consistent and repeatable behavior. Full design details and validation will be presented at the conference.

III. Conclusions

The proposed inductively loaded open-ended coaxial probe enables significantly enhanced sensitivity for broadband dielectric characterization, overcoming key limitations of conventional RG405 coaxial cable-based designs. This approach provides a powerful platform for accurate detection of subtle permittivity variations, with strong potential for advanced sensing applications in biomedical and material analysis.

References

[1] P. M. Meaney, A. P. Gregory, J. Seppl, and T. Lahtinen, "Open-ended coaxial dielectric probe effective penetration depth determination," *IEEE Trans. Microw. Theory Techn.*, vol. 64, no. 3, pp. 915-923, 2016.

A High-Sensitivity Dielectric Characterization Method for Thin-Film Materials Using Ridge Gap Waveguide Resonator

Jia Min He, Gang Zhuang, Ya Fei Wu*, and Yu Jian Cheng
University of Electronic Science and Technology of China, Chengdu 611731, China
wuyafei@uestc.edu.cn

***Abstract*—This paper presents a high-sensitivity dielectric characterization method for thin-film materials using a ridge gap waveguide resonator. The ridge structure enhances the electric field interaction with the material under test (MUT), achieving a 20.5% improvement in sensitivity. The method requires no vias or metal plating, offering reusability and broadband operation. It is verified in Ka-band with RO4350B and in W-band with quartz film, showing good agreement with manufacturer data and simulations.**

Keywords—Ridge gap waveguide; high sensitivity; dielectric characterization; thin-film materials

I. INTRODUCTION

With the rapid development of millimeter-wave technologies including 5G, satellite internet, and automotive radar, the demand for higher operating frequency bands, particularly the W-band, has been continuously increasing [1]. As frequencies extend into the millimeter-wave and terahertz regimes, the electromagnetic properties of materials become strongly frequency-dependent. However, most PCB manufacturers only provide material parameters measured at 10 GHz, which often causes unexpected frequency shifts in high-frequency circuit designs [2]. Consequently, accurate characterization of packaging materials in W-band is critically important.

Resonant methods offer high accuracy, but conventional approaches have limitations when characterizing thin films. SIW resonators require metal vias, increasing sample complexity and preventing reuse. Microstrip-based sensors eliminate vias and are reusable, but the electric field is mostly confined within the substrate, limiting interaction with the MUT, resulting in weak interaction and limited sensitivity for thin materials [3]. Gap waveguide resonators enable via-less measurement, yet their standard configuration still provides insufficient field confinement for ultra-thin films.

To address these issues, this paper proposes a ridge gap waveguide resonator that concentrates the electric field above the ridge, significantly enhancing field-MUT interaction and increasing sensitivity from 8% to 20.5%. The method is verified by Ka-band tests on RO4350B, showing good agreement with manufacturer data, and W-band measurements on quartz films, where the extracted complex permittivity matches simulations. The approach offers via-less, reusable, and high-sensitivity measurement for thin-film materials.

II. PRINCIPLE AND DESIGN

A. A. Design of Ridge Gap Waveguide Resonant Cavity

Fig. 1 illustrates the proposed ridge gap waveguide resonator structure. It consists of WR-10 waveguide ports, coupling slots, the cavity, and the MUT. Energy is coupled into and out of the cavity via coupling slots, exciting quasi-TE10k modes. An EBG structure with periodic metal posts confines energy in the W-band. A ridge at the cavity bottom enhances field-MUT interaction. The cavity length supports multiple resonant modes, and coupling slots are optimized for weak coupling. Key design parameters are given in Table I.

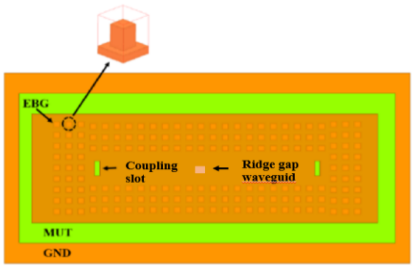


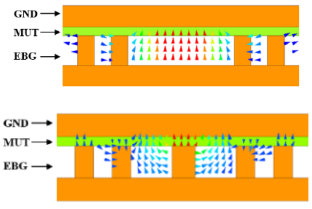
Fig. 1. Top view of the ridge gap waveguide multi-mode resonator measurement structure.

TABLE I

GEOMETRICAL PARAMETERS OF THE STRUCTURE

Parameter	EBG width	EBG height	EBG spacing	Ridge width	Coupling slot length
Values	0.4mm	0.7mm	0.4mm	0.5mm	1.1mm
Parameter	Coupling slot width	Cavity length	Cavity width	Waveguid eoffset	Air gap height
Values	0.35mm	26mm	2.54mm	3mm	0.1mm

B. Sensitivity enhancement mechanism



(a) (b)

Fig. 2. Field distribution of two types of gap waveguides. (a) Conventional gap waveguide; (b) Ridge gap waveguide

Conventional gap waveguides have dispersive fields, limiting sensitivity. The ridge compresses and concentrates the field above the MUT, as shown in Fig. 2. This improvement is quantified by the normalized resonant frequency shift:

$$\Delta f_0 = \left(f_0^{unloaded} - f_0^{loaded} \right) / f_0^{unloaded} \quad (1)$$

where $f_0^{unloaded}$ and f_0^{loaded} are the resonant frequencies without and with the MUT, respectively. A larger Δf_0 indicates higher sensitivity to changes in the material's permittivity.

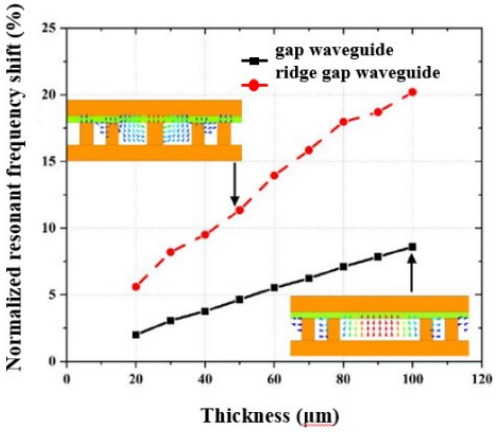


Fig. 3. Graph of sensitivity versus thickness for two types of gap waveguides.

Simulation results in Fig. 3 show that the ridge structure increases the normalized frequency shift from 8% to 20.5%, substantially improving the sensor's sensitivity to changes in the material's permittivity.

III. Results And Discussion

The proposed method is validated through both simulation and experiment. In simulation, the ridge gap waveguide resonator is modeled and the extraction method is verified using materials with known permittivity.

Experimentally, we followed the approach described in [3] to collect data, which was first validated in the Ka-band using a gap waveguide resonator fabricated with RO4350B. The extracted results agree well with the manufacturer's specifications. In W-band, the ridge gap waveguide resonator is used to measure quartz films. The measured S21 curve shows good agreement with simulations in Fig. 4, and the extracted permittivity and loss tangent of quartz are shown in Fig. 5, demonstrating broadband capability. Compared to the conventional design, the ridge resonator offers enhanced sensitivity while maintaining via-less operation and reusability for thin-film characterization.

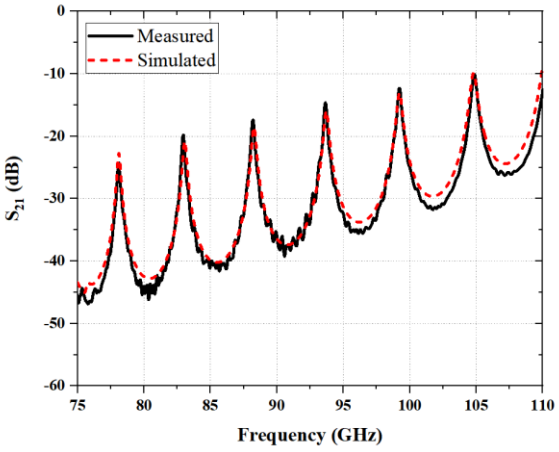


Fig. 4. Measured and simulated transmission coefficients of the ridge gap waveguide resonator in the W-band.

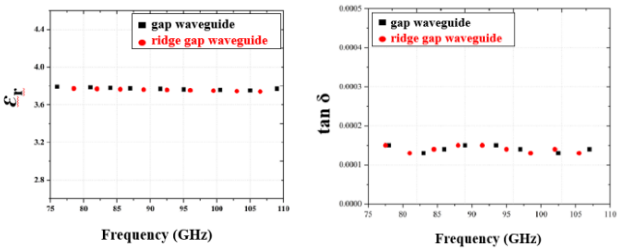


Fig. 5. Measured results of the quartz substrate in the W-band. (a) Dielectric constant; (b) Loss tangent

IV. Conclusion

This paper presents a ridge gap waveguide resonator that improves sensitivity from 8% to 20.5% via electric field concentration, with via-less and broadband operation. Ka-band RO4350B and W-band quartz measurements validate the method for thin-film material characterization. Future work will extend it to higher frequencies or on-chip sensing integration.

V. Acknowledgment

This work was supported in part by National Key Research and Development Plan of China under Grant 2024YFB2807400; in part by National Natural Science Foundation of China (NSFC) under Grant 62101109; in part by Young Elite Scientists Sponsorship Program by CAST under Grant 2023QNRC001, in part by the Xiaomi Young Scholar Program; in part by Sichuan Province Engineering Research Center for Broadband Microwave Circuit High Density Integration; and in part by the Fundamental Research Funds for the Central Universities

References

[1] M. S. Arunima, S. Bhuvana Nair and K. A. Unnikrishna Menon, "An Overview of Millimeter-wave Antennas," *2020 5th International Conference on Communication and Electronics Systems (ICCES)*, Coimbatore, India, 2020, pp. 395-400.

[2] L. X. Zhao, Y. F. Wu, Z. R. He, Y. Chai and Y. J. Cheng, "Terahertz Broadband Characterization of Wafer-Level Packaging Materials Based on SIW Multimode Cavities," *2024 IEEE 12th Asia-Pacific Conference on Antennas and Propagation (APCAP)*, Nanjing, China, 2024, pp. 1-2.

[3] X. X. Song, Y. F. Wu, Y. Guo and Y. J. Cheng, "A Broadband, Via-Less, and Reusable Characterization Method for Advanced Packaging Materials with Multimode Gap Waveguide Resonator," *2022 IEEE MTT-S International Microwave Workshop Series on Advanced Materials and Processes for RF and THz Applications (IMWS-AMP)*, Guangzhou, China, 2022, pp. 1-3.

Radiative Wireless Power Transfer with Advanced Materials

Naoki Shinohara
Research Institute for Sustainable Humanosphere,
Kyoto University, Kyoto, Japan
shino@rish.kyoto-ua.c.jp

Radiative wireless power transfer (WPT) via microwaves and millimeter waves is considered a promising technology to expand the application of electricity. A lot of historical excellent research and development of the WPT via microwaves were carried out in 1960s and in 1970s[1]. Recently, advanced WPT business has started in the world based on the WPT radio wave regulations. Especially in Japan, new legal WPT radio wave regulations at 920MHz, at 2.4GHz, and at 5.8GHz was published in 2022[2]. After the 2022, over 800 WPT base stations has already installed and are working in Japanese buildings mainly for battery-free Billing Energy Management System (BEMS). In Japan in 2026, we will update the Japanese WPT regulation for more conveniency. In 2026 in IEEE, discussion for new IEEE WPT regulation has already started as IEEE Standard WG3735 originally supported by MTT-S.

Current WPT business is based on the wide beam WPT technology, in which wireless power is provided widely to multi-users without beam forming like conventional wireless communication system. Key technology in the wide beam WPT is a high efficiency rectenna, rectifying antenna with diode or CMOS. For the wide beam WPT, advanced diode or CMOS with high efficiency is required. In the next step of the WPT, novel beam forming technology with a phased array antenna is expected. In this talk, current R&D and business of the WPT via microwaves and millimeter waves are introduced. The expectation for the advanced materials for next step WPT is also explained in this talk.

References

[1] Brown, W. C., “The History of Power Transmission by Radio Waves”, IEEE Trans. MTT, Vol. 32, No. 9, pp.1230-1242, 1984

[2] Shinohara, N., “History and Innovation of Wireless Power Transfer via Microwaves”, Journal of Microwaves, Vol.1, No.1, pp.218-228, 2021

979-8-3315-4544-4/26/$31.00 ©2026 IEEE

Microwave Sensors Exploiting Nonlinear Dynamics

Almudena Suárez, Universidad de Cantabria, Santander, Spain

Oscillator-based sensing offers compact implementations, with autonomous operation, simple readout mechanisms, and the possibility of exploiting nonlinear dynamical phenomena. These phenomena can significantly enhance sensitivity and provide new sensing modalities that go beyond conventional frequency-shift measurements. The central idea is to deliberately operate oscillators in specific nonlinear regimes in which measurable quantities—such as oscillation frequency, locking bandwidth, beat frequency, spectral structure, or switching thresholds—exhibit a strong dependence on the properties of the material under test. The presentation will first provide an insightful study of how the sensing behavior of a resonant structure is affected when it is incorporated into a loop containing an active nonlinear block. We then address oscillator sensors based on injection locking, using the boundaries of the locking band as the sensing observables. We additionally investigate the high sensitivity of the beat frequency near the locking edges, which is compared with that of the original free-running oscillator. In a different configuration, we synthesize a low-frequency self-oscillation that, through its coupling to the main one, enables sensing based on multiple spectral lines. Using self-injected configurations, we demonstrate extremely sensitive operation near the hysteresis limit, as well as the deliberate use of hysteresis to trigger a state change only when the measurand crosses specific thresholds. A key aspect is the use of rigorous nonlinear analysis and design methodologies that combine analytical modeling, bifurcation theory, describing-function techniques, and harmonic-balance simulations, enabling a systematic understanding of the various dynamical behaviors on which these sensors are based. Experimental implementations based on transistor oscillators operating in the microwave range demonstrate the practical feasibility of these concepts. They illustrate how nonlinear dynamical phenomena, often regarded as undesired effects, can instead provide powerful sensing mechanisms and open new opportunities for the design of compact, highly sensitive microwave sensors.

979-8-3315-4544-4/26/$31.00 ©2026 IEEE

Design of Filtering Power Amplifier Based on TGV-IPD Filtering Matching Network

Shi-Yu Zhu, Jin-Xu Xu*, Xiu Yin Zhang
School of Microelectronics, South China University of Technology, Guangzhou 511442, China.
E-mail: xjinxu@126.com

***Abstract*—This paper presents a 6.425-7.125 GHz filtering power amplifier (FPA) implemented using a 0.1-um GaAs pHEMT process integrated with glass-substrate integrated passive device (IPD) technology. A two-stage architecture is adopted, where multiple transmission zeros are introduced to realize a bandpass filtering response. To minimize insertion loss, the output matching network (OMN) is fabricated using high-Q through glass via (TGV) IPD technology. Simulation results show that the proposed PA achieves a gain of 20.5–21 dB over the frequency range of 6.425–7.125 GHz with a strong out-of-band rejection. The output power reaches 32.2–32.9 dBm with a saturated power-added efficiency (PAE) of 46.5–49.5%.**

***Keywords*— Filtering power amplifier, GaAs, TGV IPD, transmission zeros.**

I. Introduction

In recent years, the U6G (6.425-7.125 GHz) band has attracted significant attention as a potential spectrum resource for next-generation wireless communication systems [1]. Owing to its mid-band characteristics, this frequency range provides a favorable balance between coverage and capacity, making it attractive for emerging applications such as 5G and further applications. Therefore, higher integration and improved power efficiency have become increasingly important requirements for RF front-end circuits.

In conventional RF front-end designs, the power amplifiers [2], [3] and filters are usually implemented separately, which increases system size and insertion loss. Therefore, filtering power amplifiers (FPAs) have attracted significant attention as an effective solution for achieving compact and high-performance RF front-end modules[4], [5]. Filtering power amplifiers based on PCB implementations have been extensively studied in recent years [6], [7]. Furthermore, fully integrated filtering power amplifiers based on chip technologies have been reported to improve circuit integration. In [8], a co-design approach of filtering matching networks for power amplifiers with arbitrary complex impedances was presented. In [9], a bandpass differential PA employing a distributed-active-transformer (DAT) filtering combiner was proposed to introduce transmission zeros for harmonic suppression. In [10], a bandpass filtering PA using a coupled-line-based filtering impedance transformer was developed to generate transmission zeros and achieve sharp roll-off characteristics.

In this paper, a 6.425–7.125 GHz filtering power amplifier is implemented using a 0.1-μm GaAs pHEMT process. The OMN is implemented using TGV IPD technology to achieve higher Q-factor passive components and reduced insertion loss. In addition, transmission zeros are introduced in the matching networks to improve out-of-band suppression and enhance filtering selectivity. The simulation results demonstrates a gain of 20.5-21 dB and a output power of 32.2-32.9 dBm with a saturated power-added efficiency (PAE) of 46.5–49.5%.

II. Design of the Proposed Filtering PA

A. Circuit Configuration

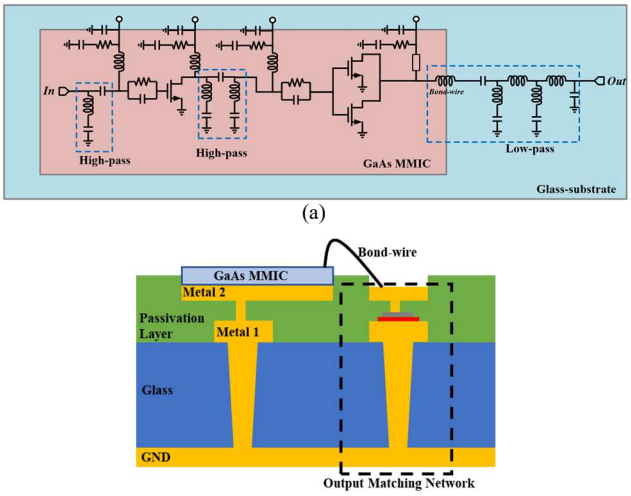


Fig. 1 (a)The overall schematic of the proposed filtering PA. (b) Integration scheme of the glass substrate and GaAs MMIC

The proposed filtering PA is implemented using transistors in WIN 0.1-um GaAs pHEMT process. The overall topology of proposed circuit is shown in Fig. 1(a), where a two-stage architecture is employed. To obtain bandpass characteristics, high-pass networks are implemented in the input and inter-stage matching networks, while a low-pass network is implemented in the output matching network.

The loss of the output matching network has a significant impact on the performance of the PA. Therefore, passive components with higher Q factors are preferred to reduce insertion loss. In the GaAs process, on-chip inductors typically exhibit Q factors of lower than 30, whereas inductors implemented on glass substrates can achieve Q factors of 60–70. Hence, the glass substrate is adopted to implement the output matching network, and the integration scheme of the glass substrate and GaAs MMIC is shown in Fig. 1(b)

B. Design of the Filtering Matching Network

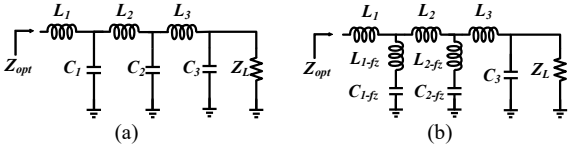
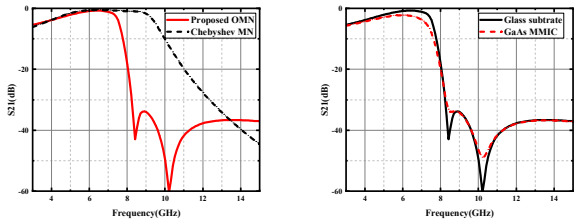


Fig. 2 (a) Chebyshev LPF OMN (b) The proposed OMN.



(a) (b)

Fig. 3 (a) Simulated S-parameters with and without the introduced transmission zeros (b) Comparison of the OMNs implemented in the GaAs process and on a glass substrate.

In this work, to achieve an output power of 32 dBm in the frequency range of 6.425-7.125 GHz, a 4 × 150 μm device is used for the driver stage, while two 8 × 150 μm devices are adopted in the power stage.

Based on load-pull analysis, the optimum load impedance of the power stage is determined to be 3.8+j8 Ω. A Chebyshev low-pass stepped-impedance matching network is employed to realize the OMN. Due to the high impedance transformation ratio of about 13.2 (50/3.8), a third-order LC matching network is adopted to achieve low loss and sufficient bandwidth. The required Chebyshev prototype parameters can be estimated according to the table in [12]: g_1=1.11, g_2=0.75, g_3=3.95, g_4=0.30, g_5=9.9, g_6=0.08, g_7=13.2. And the values of the lumped components can be calculated as follows, where L_n', C_n', R' are represented the normalized parameters, and $\omega' = 1$:

$$L_n = L_n' \frac{\omega_0'}{\omega_0} \frac{R'}{R} = g_{2n-1} \frac{1}{\omega_0} \frac{50}{g_7} \tag{1}$$

$$C_n = C_n' \frac{\omega_0'}{\omega_0} \frac{R}{R'} = g_{2n} \frac{1}{\omega_0} \frac{g_7}{50} \tag{2}$$

Thus, a real-to-real matching network is designed. In order to realize a real-to-complex low-pass matching network, the value of L_1 is increased to compensate for the reactive part of the impedance.

$$imag(Z_{opt}) = j\omega L_{1,add} \tag{3}$$

The values are shown in Table I.

TABLE I PARAMETERS OF THE CHEBYSHEV OMN

L_1	C_1	L_2	C_2	L_3	C_3
268.6pH	4.65pF	351pH	1.8pF	880.9pH	0.496pF

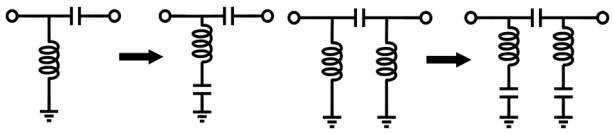
The conventional Chebyshev network provides insufficient roll-off. To enhance the selectivity, two of the shunt capacitors are replaced by series LC resonant branches, as shown in Fig. 2(b), in order to introduce transmission zeros. The corresponding design equations are given as follows, where f_z denotes the resonant frequency of the series LC branch:

$$C_{n-f_z} = \frac{f_z^2 - f_0^2}{f_z^2} C_n \tag{4}$$

$$L_{n-f_z} = \frac{1}{C_{n-f_0}(2\pi f_z)^2} \tag{5}$$

The resonant frequencies of the two series LC branches are designed at 8.4 GHz and 10.2 GHz respectively, to enhance the out-of-band suppression with minimal impact on the insertion loss in the passband. The calculated values are: $C_{1-f_{z1}} = 1.625\text{pF}$, $L_{1-f_{z1}} = 220.9\text{pH}$, $C_{2-f_{z2}} = 1.01\text{pF}$, $L_{2-f_{z2}} = 243\text{pH}$. The comparison of the simulated S-parameters with and without the introduced transmission zeros is shown in Fig. 3(a). The proposed network provides better roll-off while maintaining the desired impedance transformation and insertion loss within the passband.

As discussed in Section II-A, the passive components in the GaAs MMIC process typically exhibit low Q factors, leading to significant loss in the on-chip matching networks and thus limiting the overall efficiency of the PA. To mitigate this issue, the output matching network is implemented based on glass-substrate IPD technology. Owing to the low dielectric loss and high Q-factor passive components achievable on the glass substrate, the insertion loss of the matching network can be significantly reduced, which benefits the overall efficiency of the PA. A comparison between the OMNs implemented in the GaAs process and on the glass-substrate is shown in Fig. 3(b). The glass-substrate implementation exhibits significantly lower insertion loss and deeper transmission zeros.



(a) (b)

Fig. 4 The schematic of the (a) IMN (b) the inter-stage MN.

Since the transistor exhibits higher gain at lower frequencies, high-pass matching networks are employed both in the input and inter-stage matching networks to suppress the low-frequency gain. An L-type high-pass network and a π-type high-pass network are employed in the input matching network and the inter-stage matching network, respectively. The π-type topology in the inter-stage matching network provides additional flexibility for impedance transformation and facilitates the introduction of transmission zeros. Similarly, the shunt inductors are replaced by series LC resonant branches to introduce transmission zeros, which further sharpens the out-of-band rejection and improves the overall filtering selectivity of the PA. The corresponding equations are given as follows:

$$L' = \frac{f_0^2 - f_z^2}{f_0^2} L \tag{6}$$

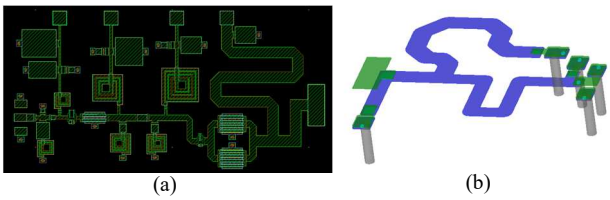
$$C' = \frac{1}{L'(2\pi f_z)^2} \tag{7}$$

The input matching network introduces a transmission zero at 4.2 GHz, while two transmission zeros at 3.3 GHz and 4.0 GHz are generated by the inter-stage matching network.

Based on the above matching network design, multiple transmission zeros are introduced outside the passband, enabling the PA to achieve a band-pass filtering response. The introduced transmission zeros significantly improve the

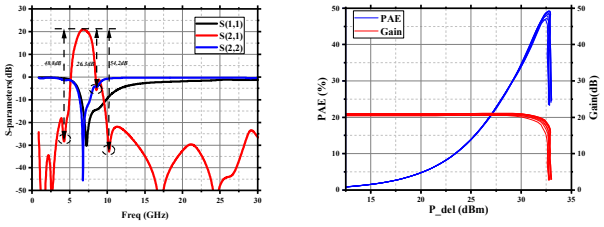
out-of-band suppression while maintaining the desired impedance transformation and low insertion loss within the passband.

III. Simulation Results And Comparison



(a) (b)

Fig. 5 The layout of the (a) GaAs MMIC and (b) OMN on glass-substrate.



(a) (b)

Fig. 6 The simulated results of (a) S-parameters (b) PAE and gain versus output power.

TABLE II Comparison with Other PAs

Ref.	Tech.	Freq (GHz)	P_{out} (dBm)	PAE (%)	Gain (dB)	Filtering @TZ(GHz)
[2]	GaAs HBT	5.15-7.125	33	34	24	No
[3]	0.5um GaAs	4.4-6	35	41	32.6	No
[7]	0.5um GaAs	5.1-5.9	33.3	30.6	26.0-26.8	Yes @9.5
[8]	0.25um GaAs	9-11	27.1-27.6	37-48	7.7-9.0	Yes @7.5&13.5
T.W.	0.1um GaAs	6.425-7.125	32.2-32.9	46.5-49.5	20.4-21	Yes @4.2&8.2

Based on the matching networks above, a 6.425-7.125 GHz filtering power amplifier is designed and the layout of the proposed circuit is shown in Fig. 5. The size of the GaAs MMIC is 2.2 × 1.1 mm^2, while the OMN implemented on the glass substrate occupies an area of 1.2 × 1.1 mm^2. Fig. 6(a) shows the simulated S-parameters. The proposed PA achieves a gain of 20.5–21dB over the frequency range of 6.425–7.125 GHz. The rejection levels at 4.2 GHz, 8.2 GHz, and 10.1 GHz are 48.8 dB, 26.3 dB, and 54.2 dB, respectively, indicating high selectivity. Fig. 6(b) shows gain and PAE versus P_{out}. The output power is 32.2-32.9 dBm and the saturated PAE is 46.5-49.5%. Table II compares the proposed filtering PA with other PAs. As observed, the proposed design achieves better selectivity while remains good large signal performance.

IV. Conclusion

In this work, a 6.425–7.125 GHz filtering power amplifier is designed in a 0.1-μm GaAs pHEMT process and glass-substrate IPD technology. The proposed PA achieves a gain of 20.5–21 dB over the 6.425–7.125 GHz frequency range while providing the desired filtering response, with an output power of 32.2–32.9 dBm and a saturated PAE of 46.5–49.5%.

Acknowledgment

This work was supported in part by the National Natural Science Foundation of China under Grant 62522111 and 62371193, in part by the Guangdong Talent Program under Grant 2023QN10X451, and in part by the Guangzhou Program under Grant 2024D01J0086.

References

[1] A. Pastukh, E. Deviatkin, V. Tikhvinskiy, and A. Kulakaeva, "Compatibility Studies between 5G IoT Networks and Fixed Service in the 6425-7125 MHz Band," in *2021 International Conference on Engineering Management of Communication and Technology (EMCTECH)*, Vienna, Austria: IEEE, Oct. 2021, pp. 1–4.

[2] S. Hwang, J. Jeon, S. Bae, B. Yoon, S. Kang, and J. Kim, "A 5.15–7.125-GHz Differential Power Amplifier With Enhanced Linearity of Average Power Region Using Dynamic Cross-Coupled Capacitor," *IEEE Trans. Microw. Theory Tech.*, pp. 1–14, 2023.

[3] Z. Ma, Z. Ma, and K. Ma, "A 35 dBm P_{SAT} and 41% PAE GaAs Power Amplifier With Series Distributed-Balun," *IEEE Trans. Circuits Syst. II Express Briefs*, vol. 70, no. 2, pp. 461–465, Feb. 2023.

[4] J.-X. Xu, X. Y. Zhang, and X.-Q. Song, "High-Efficiency Filter-Integrated Class-F Power Amplifier Based on Dielectric Resonator," *IEEE Microw. Wirel. Compon. Lett.*, vol. 27, no. 9, pp. 827–829, Sep. 2017.

[5] J.-X. Xu and X. Y. Zhang, "Dual-Channel Dielectric Resonator Filter and Its Application to Doherty Power Amplifier for 5G Massive MIMO System," *IEEE Trans. Microw. Theory Tech.*, vol. 66, no. 7, pp. 3297–3305, Jul. 2018.

[6] Q.-Y. Guo, X. Y. Zhang, J.-X. Xu, Y. C. Li, and Q. Xue, "Bandpass Class-F Power Amplifier Based on Multifunction Hybrid Cavity–Microstrip Filter," *IEEE Trans. Circuits Syst. II Express Briefs*, vol. 64, no. 7, pp. 742–746, Jul. 2017.

[7] M. F. Haider, F. You, T. Qi, C. Li, and S. Ahmad, "Co-Design of Second Harmonic-Tuned Power Amplifier and a Parallel-Coupled Stub Loaded Resonator," *IEEE Trans. Circuits Syst. II Express Briefs*, vol. 67, no. 12, pp. 3013–3017, Dec. 2020.

[8] J. A. Estrada, J. R. Montejo-Garai, P. De Paco, D. Psychogiou, and Z. Popovic, "Power Amplifiers With Frequency-Selective Matching Networks," *IEEE Trans. Microw. Theory Tech.*, vol. 69, no. 1, pp. 697–708, Jan. 2021.

[9] J. Li, Y. Zhang, K. Ma, Z. Ma, and H. Fu, "A Bandpass Power Amplifier Applying Transformer-Based Filtering Combiner in 0.5-μm GaAs pHEMT," *IEEE Microw. Wirel. Technol. Lett.*, vol. 33, no. 7, pp. 1023–1026, Jul. 2023.

[10] X. Chen, Y. Wu, Z. Chen, M. Yang, S. Zhen, and W. Wang, "Fully Integrated GaAs MMIC Bandpass Filtering Power Amplifier Chip With Compact Couple-Line-Based Matching Network," *IEEE Microw. Wirel. Technol. Lett.*, vol. 35, no. 9, pp. 1416–1419, Sep. 2025.

[11] G. L. Matthaei, "Tables of Chebyshev impedance–transforming networks of low-pass filter form," in Proceedings of the IEEE, vol. 52, no. 8, pp. 939-963, Aug. 1964.

Machine Learning-Assisted End-to-End Synthesis of RF Transformer-Based Matching Networks

Tao Wang
South China University of Technology
Guangzhou, China
miwtao@mail.scut.edu.cn

Li Gao*
South China University of Technology
Guangzhou, China
State Key Laboratory of Integrated Chips and Systems,
Shanghai, China
gaoliece@scut.edu.cn

Yao Fo Chen
South China University of Technology
Guangzhou, China
chenyaofo@scut.edu.cn

Xiu Yin Zhang
South China University of Technology
Guangzhou, China
eexyz@scut.edu.cn

***Abstract*—This paper proposes a learning-driven synthesis framework for RF transformer-based matching networks with three-dimensional electromagnetic (EM) structures. Unlike conventional methods that derive EM structures from target circuit element values and topologies, the proposed method directly synthesizes passive networks from desired performance metrics and given topologies. Using on-chip transformer impedance matching networks as a case study, the model first extracts key features from input impedance and load capacitance via neural networks to predict initial geometric parameters of the transformer's 3D EM structure in 28-nm TSMC CMOS technology. Subsequently, Bayesian optimization (BO) refines these geometric parameters for precise performance tuning. The resulting structures achieve arbitrary impedance matching while simultaneously accommodating two load capacitances. As a proof of concept, multiple transformer designs were synthesized and validated by Cadence simulations, confirming their compliance with the targeted impedance characteristics.**

Keywords—EM optimization, machine learning, inverse design, end-to-end synthesis.

I. Introduction

Passive matching networks are essential in RF systems to ensure maximum power transfer, noise matching, and impedance transformation [1], [2]. Despite the diversity of available topologies, their design still heavily relies on full-wave EM simulations. This makes the process time-consuming, resource-intensive, and dependent on expert experience [3]-[5]. Typically, designers must build and simulate the EM structure before evaluating key metrics such as S-parameters, impedance, loss, and bandwidth. As network complexity grows, simulation time can extend to several hours, and multiple optimization iterations are often required [6]-[8]. An end-to-end synthesis tool that generates EM geometry directly from the network topology and target specifications would significantly streamline this process, reducing design time and manual effort.

Many recent advances rely heavily on high-fidelity surrogate models, which shift the cost from full-wave simulations to large-scale data collection. However, training such models for EM tasks often requires tens of thousands to millions of labeled samples, demanding months or even years of simulation time. This makes them impractical for time- and resource-constrained industrial applications.

To address these challenges, we propose a data-efficient end-to-end synthesis framework that directly generates transformer-based impedance matching networks operating at 28 GHz. Given circuit-level specifications, including the source and load impedances (Z_1, Z_2) and target S-parameters,

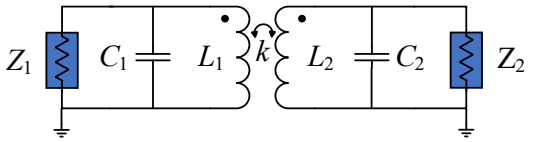


Fig. 1. Schematic of transformer-based impedance matching network.

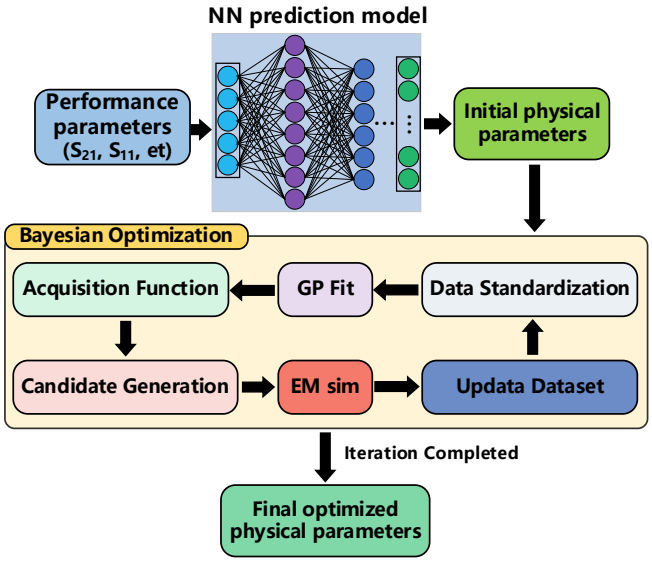


Fig. 2. End-to-end inverse design framework combining neural network and BO.

the framework predicts the EM structure and corresponding shunt capacitors. As illustrated in Fig. 1, the network incorporates non-ideal magnetic coupling and shunt capacitors (C_1, C_2) at both ports. By synthesizing the EM geometry directly from performance targets, the proposed method significantly reduces design iterations and computational overhead compared with conventional EM-driven optimization workflows.

II. End-to-End Synthesis Model

The proposed framework automates the synthesis process through two sequential modules, as illustrated in Fig. 2. A neural network first extracts features from the target impedance and S-parameters to generate a coarse prediction of the transformer geometry and shunt capacitance in a 28 nm CMOS process [9]. This prediction is then refined by a BO module that searches within a constrained design space to further improve performance.

979-8-3315-4544-4/26/$31.00 ©2026 IEEE

A. *Initial Prediction with Neural Network*

While neural networks (NNs) have demonstrated outstanding performance in various domains, their architectures must be carefully tailored to specific tasks. In this end-to-end synthesis problem, one key challenge lies in predicting a high-dimensional physical parameter set (11 variables) from a low-dimensional input (5 performance metrics). This mapping is inherently ill-posed due to information loss: physical parameters determine performance through deterministic physical laws, but the reverse is not uniquely defined. According to the data processing inequality, performance metrics may contain less information than the full set of physical variables, making inverse prediction fundamentally difficult. Therefore, the neural network is employed to provide a coarse estimate of the transformer geometry and shunt capacitance based on a 28-nm TSMC CMOS process. Fig. 3 illustrates the synthesized transformer structure along with the input and output parameters of the neural network.

A total of 22k samples were generated using Cadence EM simulations. After shuffling, 20k samples were randomly selected for training and the remaining 2k were reserved for testing. To mitigate overfitting, weight regularization was applied to all trainable parameters. The input and output layers consist of 5 and 11 elements, corresponding to the target circuit performance parameters and the predicted transformer design parameters including the shunt capacitances, respectively. As shown in Fig. 4, by properly selecting the network depth, a robust predictive model can be constructed. Experimental results indicate that a 6-layer fully connected network achieves lower absolute errors and a smaller gap in RMSE between training and testing datasets, suggesting improved generalization and reduced overfitting compared to shallower or deeper architectures.

B. *Refinement with Bayesian Optimization*

To further enhance the accuracy of transformer-based impedance matching network synthesis, a second-stage refinement process is applied to the geometry parameters predicted by the neural network. Specifically, the predicted transformer three-dimensional EM structure and the associated capacitance values are used as the initialization for a constrained optimization procedure. The neural network achieves an average Mean Squared Error (MSE) of approximately 0.7 on the test set, corresponding to an average per-parameter error of roughly 0.06 across the 11 design variables. Based on this analysis, a ±20% search range is defined around each predicted parameter to construct a feasible design space for further optimization. This range is sufficiently wide to include potentially better-performing configurations, while remaining close enough to the initial estimates to maintain physical feasibility and ensure stable convergence during the optimization process.

To efficiently explore this design space, BO is adopted as the refinement strategy. BO is a sample-efficient global optimization method that is particularly well suited for problems where objective function evaluations are expensive, such as full-wave EM simulations. In this framework, a Gaussian Process (GP) surrogate model is first constructed to approximate the relationship between the design parameters and the circuit performance. An acquisition function, specifically the Expected Improvement (EI), is then employed to balance exploration and exploitation when selecting new candidate solutions. These candidates are subsequently evaluated using EM simulations, and the resulting data are iteratively incorporated into the surrogate model to progressively improve its accuracy. The optimization objective is to minimize a performance metric that jointly reflects transmission efficiency and impedance matching characteristics, thereby guiding the search toward high-performance transformer-based matching network designs.

To evaluate the performance of BO, we compare it against several commonly used optimization algorithms, including Random Search and Genetic Algorithm (GA). All algorithms are initialized from the same set of starting samples and are allowed to run for the same number of iterations to ensure fairness in comparison. To mitigate the effects of randomness inherent in stochastic optimization methods, each algorithm is independently repeated ten times. Table I presents the comparative results among the three methods. The

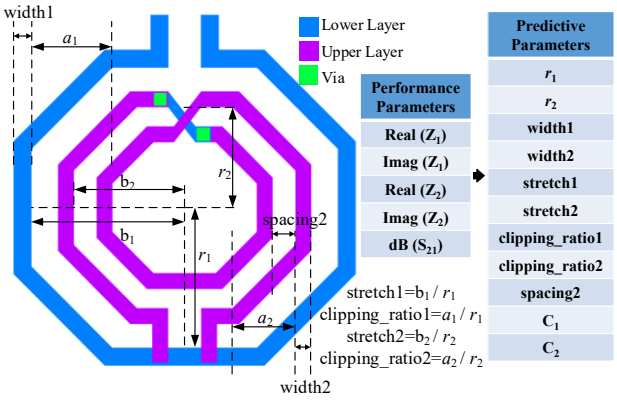


Fig. 3. Synthesized transformer structure and neural network input-output parameters.

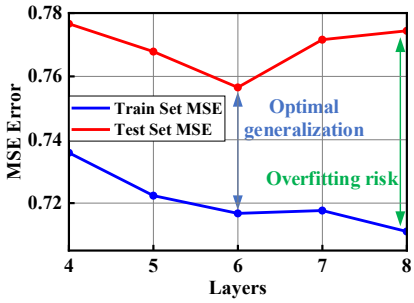


Fig. 4. RMSE versus number of fully connected layers for overfitting prevention.

TABLE I. PERFORMANCE COMPARISON OF OPTIMIZATION ALGORITHMS. (10 RUNS)

Method	Best S_{21} (dB)	Std. Dev. of Best S_{21}	Top-10 S_{21} Mean (dB)	Std. Dev. of All S_{21}
Random Search	-1.29	0.1815	-2.5086	6.4390
Genetic Algorithm	-1.30	0.2349	-1.9868	**6.0234**
BO(Ours)	**-1.13**	**0.1385**	**-1.8383**	6.1178

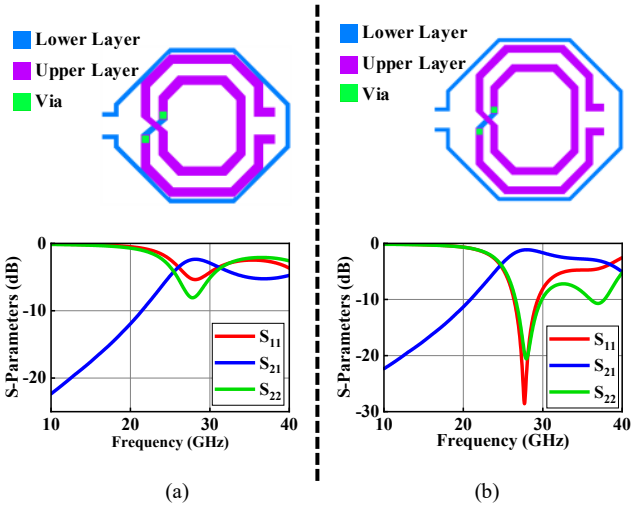


Fig. 5. (a) Neural network prediction and (b) BO refinement of transformer geometry and S-parameters.

performance is evaluated using four metrics: the best S_{21} value obtained across all iterations, the standard deviation of the best S_{21} over the ten repeated runs to reflect consistency, the average S_{21} value of the top 10 candidates in each run as an indicator of overall solution quality, and the standard deviation of all S_{21} values produced during optimization to characterize the exploration behavior of each algorithm. As shown in the table, BO achieves the best transmission performance with the lowest variability, demonstrating superior accuracy and robustness compared to Random Search and GA. This underscores the advantage of combining deep learning-based initialization with probabilistic optimization, resulting in a practical and scalable framework for RF passive component synthesis.

III. Matching Network Design and Verification

The inverse design of matching networks essentially enables end-to-end circuit synthesis through algorithmic automation, eliminating the need for manual tuning during the optimization process. To demonstrate the potential of the transformer-based design methodology, we evaluate the entire optimization process. First, specific port impedances—Z_1 for Port 1 and Z_2 for Port 2—as well as S-parameter targets are fed into a neural network prediction model. The model provides a coarse estimation of the transformer's 3D EM structural parameters along with the associated parallel capacitances. The resulting predicted transformer geometry and corresponding S-parameters of the matching network are shown in Fig. 5(a). Next, based on the predicted geometrical parameters and capacitance values, we define a ±20% search range and apply BO to iteratively refine the parameters. As shown in Fig. 5(b), the performance of the matching network is significantly improved after optimization—for example, the S_{21} is enhanced from -2.4 dB to -1.3 dB. This integrated framework enables direct synthesis of transformer geometry and associated capacitance values, achieving end-to-end synthesis of transformer-based impedance matching networks.

IV. Conclusion

In this work, we proposed a machine learning-assisted framework for the inverse synthesis of transformer-based impedance matching networks operating at frequencies. The proposed framework integrates a neural network for coarse prediction of 3D transformer geometry and parasitic capacitance based on port impedance and desired S-parameters. This is followed by BO within a constrained design range to refine the geometric parameters and enhance matching performance. Experimental results demonstrate that the synthesized structures can achieve precise impedance matching, with the final S_{21} performance significantly improved. Validated through EM simulations on a 28nm CMOS process, our inverse design methodology reduces the need for manual tuning and significantly accelerates the design cycle. This study highlights the potential of data-driven techniques in synthesizing RF passive structures, paving the way for efficient, automated circuit-level design solutions.

V. Acknowledgement

This work was supported by National Natural Science Foundation of China under Grant 62401208, Guangzhou Applied Basic Research Program under Grant 2025A04J3531 and by open project of State Key Laboratory of Integrated Chips and Systems under Grant SKLICS-K202509.

References

[1] F. Feng, W. Na, J. Jin, J. Zhang, W. Zhang and Q. -J. Zhang, "Artificial Neural Networks for Microwave Computer-Aided Design: The State of the Art," *IEEE Trans. Microw. Theory Techn.*, vol. 70, no. 11, pp. 4597-4619, Nov. 2022.

[2] Z. Zhou, Z. H. Wei, A. Tahir, J. Ren, Y. Z. Yin, G. F. Pedersen M. Shen, "A High-Quality Data Acquisition Method for Machine-Learning-Based Design and Analysis of Electromagnetic Structures," *IEEE Trans. on Microw. Theory Techn.*, vol. 71, no. 10, pp. 4295-4306, Oct. 2023.

[3] E. A. Karahan, Z. Liu and K. Sengupta, "Deep-Learning-Based Inverse-Designed Millimeter-Wave Passives and Power Amplifiers," *IEEE J. Solid-State Circuits*, vol. 58, no. 11, pp. 3074-3088, Nov. 2023.

[4] B. Shen, P. Wang, R. Polson, and R. Menon, "An integrated-nanophotonics polarization beamsplitter with 2.4 × 2.4 μm2 footprint," *Nat. Photon.*, vol. 9, no. 6, pp. 378–382, Jun. 2015.

[5] T. Zhang, C. Y. Kee, Y. S. Ang, and L. K. Ang, "Deep learning-based design of broadband GHz complex and random metasurfaces," arXiv: 2110.12999, Oct. 2021.

[6] Y. Wang, C. Zhang, T. Zhang, Y. Luo, and H. Lu, "Deep learning-enhanced inverse modeling of terahertz metasurface based on a convolutional neural network technique," *Photonics*, vol. 11, no. 5, pp. 424, May 2024.

[7] R. Palmeri, A. Y. Ruiz, R. Scapaticci, T. Isernia, and L. Crocco, "Deep learning procedures for the inverse design of electromagnetic devices," in *Proc. 2024 Int.l Conf. Electromagn. Adv. Appl.(ICEAA)*, Lisbon, Portugal, 2024, pp. 682-682.

[8] V. Chenna and H. Hashemi, "Topology-Optimized Nonintuitive Multilayered mm-Wave Power Amplifiers," in *Proc. IEEE Radio Freq. Integr. Circuits Symp.(RFIC)*, Jun. 2025, pp. 279-282.

[9] Y. Wei, J. Li, D. Cai, F. Meng, N. Kim, Y. Wu, C. Wang, "A Flexible Automated Design Method for Broadband Matching Networks in Power Amplifiers," *IEEE Trans. Microw. Theory Techn.*, vol. 73, no. 8, pp. 4779-4790, Aug. 2025.

A Wideband Terahertz Interconnection Between Microstrip Line and Waveguide Using Novel Short-Circuited Stub

Juncheng Min[1,2], Peng Wu[1,2*], Kaiyuan Du[1,2], and Chao Xue[1,2]
[1]*Aerospace Information Research Institute, Chinese Academy of Sciences,* Beijing 100190, China
[2]*School of Electronic, Electrical and Communication Engineering, University of Chinese Academy of Sciences,* Beijing 100190, China

***Abstract*—A novel wideband terahertz interconnection between microstrip line and waveguide is proposed for full-band applications, addressing the requirements of high-frequency test equipment, radar modules, and communication systems. A short-circuited stub is newly introduced to enhance the performance of the microstrip-to-waveguide transition. The short-circuited stub adjacent to the probe provides additional inductive loading, generating multiple resonant matching frequencies and thereby improving impedance matching across a wider bandwidth. With the proposed interconnection scheme, the D-band is entirely covered. A back-to-back probe transition is fabricated and measured. The measured return loss and insertion loss of the back-to-back transition are better than 13 dB and 2.5 dB from 103 GHz to 177 GHz. After the back-to-back microstrip-line loss is de-embed, the measured insertion loss of the proposed single interconnection is about 0.583 dB around the operation frequency band. The proposed interconnection exhibits not only broad operational bandwidth but also potential applications for compact integration in high-frequency systems.**

***Keywords*—Microstrip-to-waveguide transition; microstrip probe; short-circuited stub; full-band coverage; broadband matching**

I. Introduction

Millimeter-wave systems, including high-frequency test instruments, radar modules, and communication systems, increasingly rely on hybrid interconnections between planar transmission lines and standard rectangular waveguides. Microstrip lines are widely used due to their compact size, ease of integration, and compatibility with hybrid microwave integrated circuits (HMICs) and monolithic microwave integrated circuits (MMICs). Measurement systems and transceiver modules still require waveguide integration to ensure low-loss power transmission and high signal integrity. In these applications, a wideband microstrip-to-waveguide transition with impedance matching is essential to maintain efficient performance across the whole frequency range.

To meet these requirements, various microstrip-to-waveguide transitions have been developed, such as E-plane probe transitions, H-plane probe transitions, coaxial probe transitions, and quasi-radial probe structures [1]. Techniques to enhance bandwidth include quasi-Yagi antenna probes, U-slot and stepped matching structures, and multi-layer LTCC implementations for high-frequency integration. Tunable waveguide back-short designs have also been proposed to compensate for fabrication and substrate tolerances. These studies demonstrate the potential to achieve compact, low-loss, and broadband transitions [2]-[5]. In particular, achieving full-band coverage with low reflection and insertion loss while maintaining a manufacturable compact structure remains difficult [6]. In this work, a short-circuited stub is explored to enhance the performance of the microstrip-to-waveguide transition. The short-circuited stub adjacent to the probe provides additional inductive loading, generating multiple resonant matching frequencies and thereby improving impedance matching across a wider bandwidth. The D-band frequency range is entirely covered. A back-to-back probe interconnection is fabricated and measured with excellent wideband performance.

II. Proposed Interconnection Design

A. Probe Transition Model with Short-Circuited Stub

The original microstrip-to-waveguide probe interconnection is shown in Figs. 1(a1) and (b1). The probe extends into the

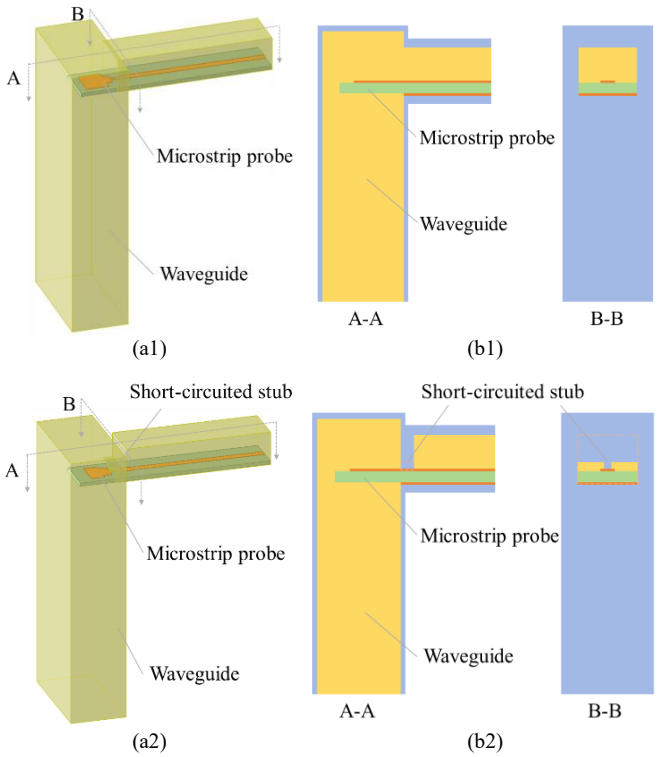


Fig. 1. Microstrip-to-waveguide interconnection models: (a1) 3-D view without stub, (b1) Cross-section view without stub, (a2) 3D view with stub, (b2) Cross-section view with stub

waveguide aperture and couples the quasi-TEM mode of the microstrip line to the dominant TE_{10} mode of the rectangular waveguide. The bandwidth can be improved by multiple step impedance matching, and it is still limited by the inherently inductive or capacitive effects. As shown in Fig. 1(a2) and (b2), a short-circuited stub is proposed to enhance the performance of the microstrip-to-waveguide transition. The short-circuited stub adjacent to the probe provides additional inductive loading, generating multiple resonant matching frequencies and thereby improving impedance matching across a wider bandwidth. The broadband performance of the proposed interconnection between microstrip line and waveguide can be analyzed from electromagnetic and circuit perspectives. Electromagnetically, the microstrip probe excites a quasi-TEM mode that must be efficiently converted into the dominant TE_{10} mode of the waveguide. The presence of the short-circuited stub mitigates electric field perturbations around the probe and stabilizes mode conversion across a wide frequency range. This structural feature effectively reduces reflection and improves energy coupling, contributing to enhanced transmission efficiency.

In the original probe interconnection shown in Fig. 1(a1), a microstrip prob is inserted inside the waveguide and couples the electromagnetic field from microstrip line to waveguide. The coupling metallic aperture is required traditionally and coaxial strip line is realized. In this paper, a short-circuited structure is newly introduced. The short-circuited stub adds a shunt reactive component at the end of the probe to improve the matching impedance. By properly optimizing the stub dimensions, this additional susceptance partially compensates the probe-related reactance over a broad frequency range, producing two matching minima instead of a single narrow resonance. This is verified and the improved performance is shown in Fig. 2.

B. Simulation Results

Both the original and proposed microstrip-to-waveguide interconnections are designed. The simulation results are shown and compared in Fig. 2. With the proposed interconnection scheme, the D-band is entirely covered, and the interconnection bandwidth with the short-circuited stub is about twice compared with the original interconnection. For the original microstrip-to-waveguide interconnection, the return loss S_{11} is better than -15 dB and the insertion loss S_{21} is better than -0.75 dB across 115-165 GHz. For the proposed interconnection, S_{11} remains below –15 dB and S_{21} remains above –0.75 dB from 95 GHz to 200 GHz, indicating a substantially wider band than that of the original structure. This result confirms that the novel stub significantly enhances impedance matching and extends the operational bandwidth.

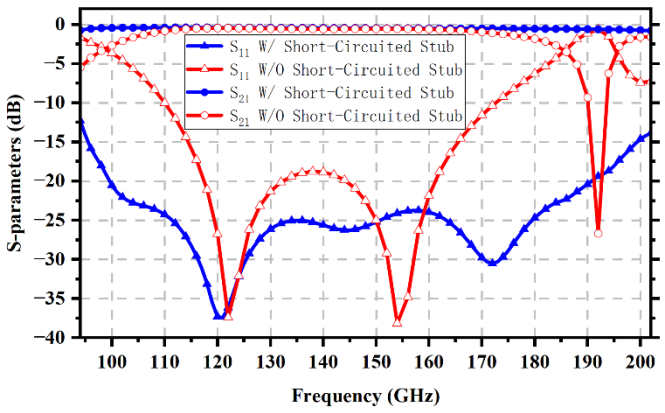


Fig. 2. Simulated S-parameters of single interconnection with/without short-circuited stub

III. Fabrication And Measurement

To validate the proposed interconnection with short-circuited stub, a back-to-back interconnection is designed and fabricated, as shown in Fig. 3. Standard WR-7 waveguides are used at both input and output ports. The microstrip line is fabricated on a quartz substrate with ε_r of 3.78 and tanδ of 0.005. The substrate thickness is 50 μm. 50 Ω microstrip line is applied and the microstrip width is 106 μm. The length of the microstrip line is 6 mm.

As shown in Fig. 4, the back-to-back interconnection simulated results exhibit $S_{11} < -15$ dB and $S_{21} > -1.25$ dB over the frequency range from 100 GHz to 180 GHz. The slightly increased reflection and reduced transmission compared with the single transition can be attributed to the cumulative effect of cascaded probes and internal reflections. The back-to-back configuration maintains excellent broadband performance. The measured S_{11} and S_{21} are better than –13 dB and –2.5 dB, respectively, from 103 GHz to 177 GHz. The difference between the measured and simulated results are as the results of substrate dielectric and waveguide loss, the fabrication and micro assembly tolerances, and additional losses from connectors and measurement fixtures. Despite these factors, the results confirm broadband operation and demonstrate the robustness and practical feasibility of the proposed design for high-frequency D-band applications.



Fig. 3. Photograph of the fabricated microstrip-to-waveguide interconnection: (a) prototype, (b) measurement setup.

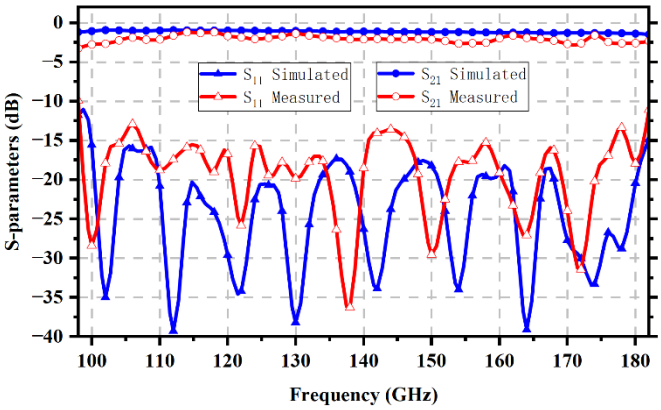


Fig. 4. Back-to-back S-parameter comparison: simulation vs. measurement.

Since the test results are obtained based on the back-to-back configuration and the microstrip line on the quartz substrate also introduces non-negligible losses, the insertion loss of this transition structure needs to be further corrected by subtracting the microstrip line loss from the measured data. In our previous work [9], the transmission loss of the microstrip line fabricated on the same quartz substrate was determined to be 0.71 dB/mm over 185–229 GHz. Therefore, the transmission loss of the microstrip line over 103–177 GHz can be reasonably estimated to be about 0.6 dB/mm. Considering the additional 2-mm microstrip-line length in the test setup, the corresponding microstrip-line loss is estimated to be about 1.2 dB. Meanwhile, based on the rectangular metallic waveguide attenuation model derived in [10], the transmission loss of a standard WR-7 waveguide over 103–177 GHz is estimated to be 0.0045–0.0088 dB/mm. In this work, the lower value of 0.0045 dB/mm is used for the calculation. Considering the additional 30 mm waveguide length in the test setup, the corresponding waveguide loss is approximately 0.135 dB. Therefore, the actual insertion loss S_{21} of the proposed single transition structure is about 0.583 dB in the operation frequency range.

This work is compared with representative microstrip-to-waveguide structures in TABLE I. The table lists different structures and compares their operational frequency ranges, relative bandwidths, and measured S-parameter results. It is evident that the proposed single short-circuited stub probe achieves broadband operation with measured return loss better than 13 dB and insertion loss about 0.583 dB across 103–177 GHz. In contrast, the conventional single probes and slot-fed transitions generally exhibit narrower operational bands or higher reflection and insertion loss.

IV. Conclusion

In this work, a wideband terahertz microstrip-to-waveguide interconnection based on a novel short-circuited stub is presented. The short-circuited stub is introduced to enhance the performance of the microstrip-to-waveguide transition. The short-circuited stub adjacent to the probe provides additional inductive loading, generating multiple resonant matching frequencies and thereby improving impedance matching across a wider bandwidth. The proposed interconnection scheme is demonstrated and a back-to-back interconnection is fabricated and measured. The novel wideband terahertz interconnection between microstrip line and waveguide is suitable for applications, e.g. high-frequency test equipment, radar modules, and communication integration systems.

TABLE I. Measured Performance Comparison Of The Proposed Structure And Representative Microstrip-To-Waveguide Structures

TABLE EF.	Type	Single/ Double	Freq. (GHz)	Insertion loss (dB)	Return loss (dB)
[2]	E-plane probe	Double (B2B)	70–110 (40%)	< 2.5	> 13
[7]	Vertical probe	Single	95–106 (10.4%)	< 2	> 8
[3]	Slot antenna	Single	110–138 (22%)	< 2.25	> 10
[8]	Slot-fed probe	Double (B2B)	198–244 (20.65%)	< 6	> 10
This work	**Short-circuited stub probe**	**Double (B2B)**	**103-177 (52.8%)**	**< 2.5 (0.583)***	**> 13**

(* The single interconnection loss with microstrip and waveguide calibrated)

Acknowledgment

This work was supported by the Foundations of Chinese Academy of Sciences under Grants E33321010D and E1Z2D10500, and also supported by the International Partnership Program of the Chinese Academy of Sciences, Grant No. 313GJHZ2023096FN.

References

[1] L. Li, J. Li, X. Wei, A. Zhang, and H. Ma, "A Ka band microstrip to waveguide transition using a quasi-triangle probe," Int. J. RF Microw. Comput. Aided Eng., vol. 27, no. 7, p. e21124, Jul. 2017.

[2] M. Han, C. Wang, C. Liu, S. Xiao, J. Ma, and H. Sun, "A wideband microstrip-to-waveguide transition using E-plane probe with parasitic patch for W-band application," Appl. Sci., vol. 12, no. 23, p. 12162, 2022, doi: 10.3390/app122312162.

[3] A. Hassona, Z. S. He, C. Mariotti, F. Dielacher, V. Vassilev, Y. Li, J. Oberhammer, and H. Zirath, "A non-galvanic D-band MMIC-to-waveguide transition using eWLB packaging technology," in Proc. IEEE MTT-S Int. Microw. Symp. Dig., Honolulu, HI, USA, 2017, pp. 510–512.

[4] A. Navarrini, T. Pisanu, S. Mariotti, and T. Idda, "A simple K-band waveguide-to-microstrip probe transition," Microw. Opt. Technol. Lett., vol. 49, no. 7, pp. 1597–1600, Jul. 2007.

[5] A. Dewantari, J. Kim, S.-Y. Jeon, S. Kim, and M.-H. Ka, "Tunable waveguide-to-microstrip transition for W-band antenna," IET Microw. Antennas Propag., vol. 13, no. 8, pp. 1174–1180, Aug. 2019.

[6] P. Wu, Y. Zhang, Z. Wang, S. Sun, and R. Xu, "Waveguide to microstrip probe transition for millimetre wave applications using LTCC technology," in Proc. Asia-Pacific Int. Symp. Electromagn. Compat., Beijing, China, 2010, pp. 1387–1389.

[7] B. Yu, Z. Wang, and R. Xu, "A HTCC-based hermetically sealed transition from stripline to vertical waveguide for sub-THz SiPs," in Proc. Int. Conf. Microw. Millim. Wave Technol. (ICMMT), 2025, pp. 1–4, doi: 10.1109/ICMMT65948.2025.11187906.

[8] H. Chang, Z. S. He, and H. Zirath, "Design of chip-to-waveguide transition centered at 220 GHz for sub-THz packaging," in Proc. 53rd Eur. Microw. Conf., Berlin, Germany, 2023, pp. 126–129.

[9] B. Yuan, P. Wu, Z. Yu, Z. Zhu, and L. Teng, "A novel end-wall waveguide excitation with wide bandwidth and simple structure for millimeter-wave/terahertz application," IEEE Microw. Wireless Compon. Lett., vol. 32, no. 7, pp. 831–834, Jul. 2022, doi: 10.1109/LMWC.2022.3153674.

[10] J. Skinner, D. Koller, H.-U. Nickel, N. M. Ridler, and S. Lucyszyn, "Derivation of rectangular metallic waveguide attenuation constant for IEC 60153-2 and IEEE 1785.1 international standards," IEEE Transactions on Terahertz Science and Technology, vol. 15, no. 4, pp. 734–737, Jul. 2025.

A 300-GHz Broadband Power-Reconfigurable Load-Modulated Balanced Amplifier

Kaiyuan Du[1,2], Peng Wu[1,2], Juncheng Min[1,2], and Zhongjun Yu[1,2]
[1]*Aerospace Information Research Institute, Chinese Academy of Sciences,* Beijing 100190, China
[2]*School of Electronic, Electrical and Communication Engineering, University of Chinese Academy of Sciences* Beijing 101408, China

***Abstract*—This paper presents a 300 GHz broadband power-reconfigurable load-modulated balanced amplifier (PR-LMBA) for broadband sub-terahertz applications. The implemented architecture leverages intrinsic load modulation within a balanced topology to realize dual-mode power operation without employing RF switches or reconfigurable matching networks. Implemented in a 0.13-µm SiGe BiCMOS technology, the PR-LMBA achieves a peak small-signal gain of 19.4 dB with a 3-dB bandwidth of 62 GHz (246–308 GHz). In high-power mode, a maximum output power of 11.4 dBm and a peak power-added efficiency (PAE) of 2.3% are obtained. In low-power mode, the amplifier provides 4.7 dBm output power with 1.89% PAE, corresponding to a 6.3 dB reconfigurable power range.**

***Index Terms*—sub-terahertz, broadband, SiGe BiCMOS, power-reconfigurable, high output power.**

I. Introduction

The rapid development of sub-terahertz (sub-THz) communication and sensing systems has intensified the demand for power amplifiers (PAs) operating beyond 200 GHz. In practical sub-THz links, dynamic power control is essential due to link adaptation, beamforming gain variation, and distance-dependent propagation loss [1]. Power-reconfigurable PAs have been widely investigated at millimeter-wave frequencies, typically employing RF switches, reconfigurable output matching networks, or load-modulated architectures such as Doherty PAs [2]. However, these approaches become increasingly impractical at sub-THz frequencies due to the high insertion loss of RF switches, the strong sensitivity of matching networks, and the limited feasibility of quarter-wavelength impedance inverters. Consequently, achieving wideband and efficient power reconfiguration at sub-THz band remains challenging.

At RF and microwave frequencies, load-Modulated Balanced Amplifiers (LMBAs) have recently emerged as an attractive alternative for wideband load modulation [3] [4]. By embedding a control amplifier within a balanced structure, the effective load impedance of the main amplifier can be modulated in a broadband manner while maintaining inherent port isolation and stability.

In this work, a 300 GHz power-reconfigurable LMBA (PR-LMBA) is presented to realize broadband dual-mode power operation without RF switches or complex output networks. Implemented in 0.13-µm SiGe BiCMOS technology, the PR-LMBA achieves a 62 GHz 3-dB bandwidth from 246 to 308 GHz. In high-power mode, it delivers 11.4 dBm maximum output power with 2.3% peak PAE, while in low-power mode it provides 4.7 dBm output power with 1.89% PAE, corresponding to a 6.3 dB reconfigurable power range.

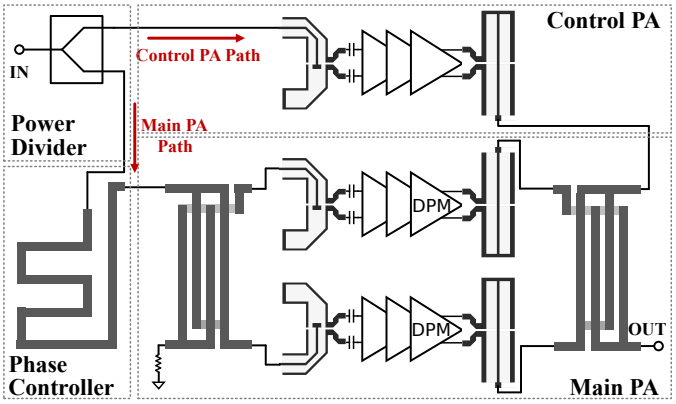


Fig. 1. The architecture of the proposed PR-LMBA.

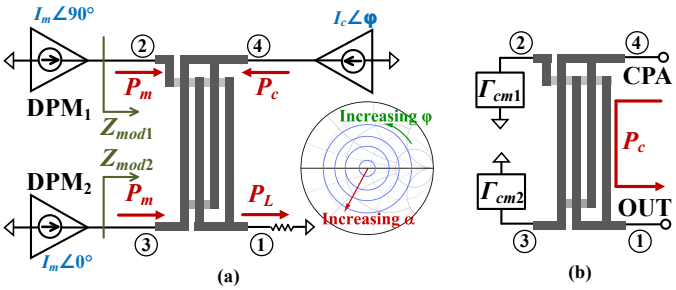


Fig. 2. The operating principle of the PR-LMBA in (a) HP mode. (b) LP mode.

II. Circuit Implementation

A. Architecture and Operating Principle of the PR-LMBA

The architecture of the PR-LMBA is shown in Fig. 1, which consists of a main power amplifier (MPA), a control power amplifier (CPA), a power distribution network, and a phase controller. The MPA employs a balanced topology composed of two identical three-stage differential power modules (DPMs). The CPA output is injected into the isolated port of the output Lange coupler. A phase controller regulates the relative phase between the MPA and CPA paths, enabling frequency-dependent load modulation.

The operating principle in high-power (HP) mode is illustrated in Fig. 2(a) [3]. Both MPA and CPA operating in

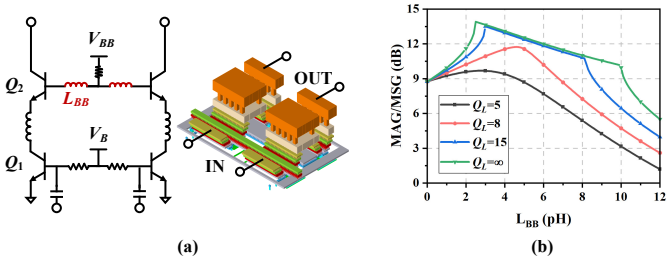


Fig. 3. (a) The schematic of the PA core in the three-stage DPM. (b) MAG/MSG of the PA core with various L_{BB}.

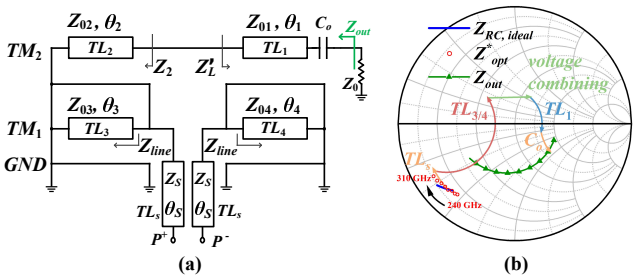


Fig. 4. (a) The schematic of the power combiner based on three-conductor balun. (b) Impedance transformation trajectory.

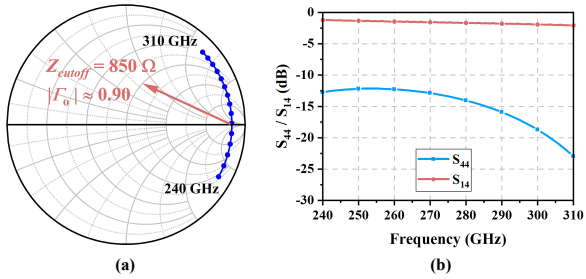


Fig. 5. (a) The output reflection coefficient of the DPM in LP mode. (b) The reflection and transmission coefficient of the Lange coupler in LP mode.

saturation are equivalently modeled as current sources. The two DPM branches have initial phases of 0 and 90 degree respectively, while the CPA has a phase difference of φ. Under this condition, the input impedances at ports 2 and 3 of the output coupler, Z_{mod1} and Z_{mod2}, are given by [3]

$$Z_{mod1} = Z_{mod2} = Z_0(1 + \sqrt{2}\frac{I_c e^{j\varphi}}{I_m}) \tag{1}$$

The effective load impedance seen by each DPM is therefore determined by the amplitude and phase of the CPA current.

Let the powers associated with currents I_m and I_c be P_m and P_c, respectively. Defining the power ratio of P_c and P_m as α, the output power and the corresponding load reflection coefficients at ports 2 and 3 satisfy [3]

$$P_L = 2P_m + P_c, \quad |\Gamma_m| = \sqrt{\frac{\alpha}{\alpha + 2}} \tag{2}$$

The reflection coefficient traces a family of circles in the Smith chart, governed by the power ratio α and phase φ, as shown in Fig. 2(a). Increasing α enlarges the magnitude of the reflection coefficient, while increasing φ rotates it counter-clockwise along the circle. By transforming the intrinsic DPM output impedance onto a frequency-dependent arc in the Smith chart and designing the phase controller to provide a tailored phase response, broadband load matching is achieved without reconfigurable matching networks [4].

In low-power (LP) mode, with the MPA biased in cutoff, the DPM output can be modeled as a predominantly reactive impedance jX_{cm}, as shown in Fig. 2(b). The transmission coefficient from port 4 to port 1 is $j/2(\Gamma_{cm1} + \Gamma_{cm2})$; therefore, $|S_{14}| \approx 1$ when $\Gamma_{cm1} = \Gamma_{cm2}$. Consequently, the CPA alone operates in saturation and delivers its output power to the load, enabling low-power operation with high efficiency.

B. Circuit Design of the PR-LMBA

To ensure closely matched gain and phase characteristics between the main power amplifier (MPA) and the control power amplifier (CPA), both paths employ identical three-stage stagger-tuned differential amplifier architectures. The schematic of the PA core unit is shown in Fig. 3(a). Each stage is based on a cascode topology with inductive positive feedback for gain enhancement [4]. The simulated MAG/MSG under different inductance values and quality factors are shown in Fig. 3(b). The inductance of L_{BB} is selected as 5 pH, resulting in approximately 3 dB gain improvement compared to the non-feedback case.

To maximize output power, the MPA output transistors adopt a size of $6 \times 0.07 \times 0.9$ μm^2. Load-pull simulations of the output stage are performed across the operating frequency band, and the extracted optimal load impedances are shown in Fig. 4(b).

For broadband load modulation and differential-to-single-ended conversion, a sub-quarter-wavelength three-conductor transmission-line balun-based power combiner is employed. This network transforms the optimal load impedance onto a frequency-dependent arc in the Smith chart, as illustrated in Fig. 4. The corresponding reflection coefficient magnitude is approximately 0.44, which yields a power ratio $\alpha = 0.5$ according to 2. Accordingly, the CPA output transistor size is chosen as $4 \times 0.07 \times 0.9$ μm^2. The CPA output stage adopts the same three-conductor balun structure and is matched to 50 Ω.

Based on the impedance trajectory shown in Fig. 4(b), the required phase difference φ varies from 22.8° at 240 GHz to 144.2° at 310 GHz. This phase compensation is implemented by inserting a microstrip phase-shifting line in the MPA input path. The line has a characteristic impedance of 50 Ω and an electrical length of 382° at 240 GHz, with approximately 0.9 dB insertion loss. Since the phase shifter is placed before the amplifying stage, it does not degrade the saturated output power.

In low-power (LP) mode, the MPA base bias is set to −2 V to fully turn off the output transistors. The resulting DPM output impedance is shown in Fig. 5(a), with a reflection

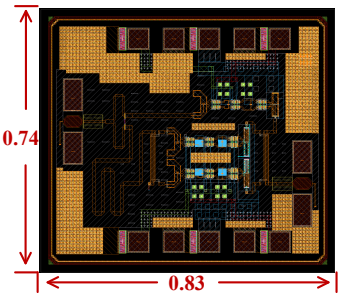


Fig. 6. The layout of the proposed PR-LMBA.

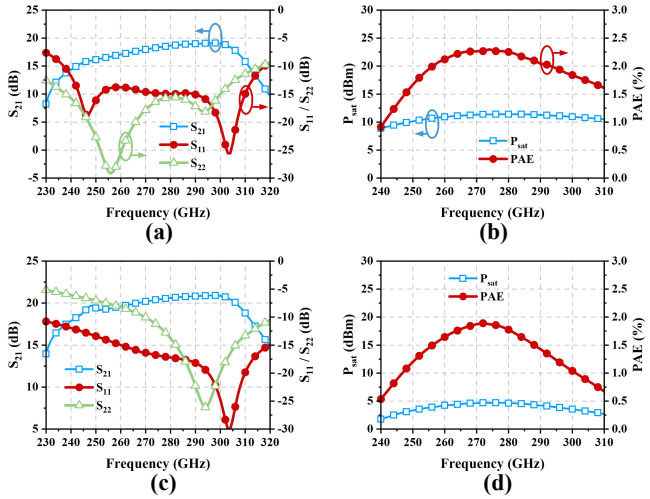


Fig. 7. Simulated results of PR-LMBA in HP mode (a) Small signal. (b) Large signal. Results in LP mode (c) Small signal and (d) Large signal.

coefficient magnitude close to unity. The output Lange coupler and DPMs can therefore be treated as a two-port network, through which the CPA signal is transferred from port 4 to port 1. The corresponding reflection coefficient and insertion loss are shown in Fig. 5(b). The intrinsic insertion loss of the Lange coupler is approximately 0.8 dB, while incomplete cutoff of the DPM introduces an additional 1 dB loss.

III. EM-Simulated Results

The PR-LMBA is implemented in a 0.13-µm SiGe BiCMOS technology. The chip layout is shown in Fig. 6, occupying an area of 0.83×0.74 mm^2. In HP mode, simulated results in Fig. 7(a) and (b) show a peak gain of 19.4 dB with a 3-dB bandwidth of 62 GHz (246–308 GHz). A maximum output power of 11.4 dBm and a peak PAE of 2.3% are achieved. In LP mode, as shown in Fig. 7(c) and (d), the amplifier provides a peak gain of 20.9 dB and a maximum output power of 4.7 dBm, corresponding to a 6.3 dB power back-off from HP mode, while maintaining 1.89% PAE.

The PAE is mainly limited by the device performance roll-off at 300 GHz and the insertion losses of the passive circuits. In LP mode, the nonideal cutoff impedance of the MPA also introduces additional loss. Nevertheless, the PR-LMBA maintains comparable PAE in both power modes while providing a 6.3 dB reconfigurable power range.

TABLE I
Comparison with Other SiGe-Based THz PAs

Ref.	f_0 (GHz)	BW (GHz)	Gain (GHz)	P_{sat} (dBm)	PAE (%)
[5]	280	67	20	6	1.4
[6]	286	56	17	6.3	1.5
[7]	235	58	16	12.5	1.75
[8]	279	60	25	10.2	3.0
This work	**277**	**62**	**19.4/20.9**	**11.4/4.7**	**2.3/1.89**

The simulated performance of recently-reported SiGe-based sub-THz PAs is summarized in Table I. The PR-LMBA demonstrates a competitive combination of bandwidth, output power, efficiency, and power reconfigurability.

IV. Conclusion

A 300 GHz power-reconfigurable load-modulated balanced amplifier (PR-LMBA) with broadband dual-mode operation, requiring no RF switches or tunable matching networks, is presented in this paper. Implemented in 0.13-µm SiGe BiCMOS, the PR-LMBA maintains comparable efficiency over a 6.3 dB power reconfiguration range, providing a compact solution for power-adaptive sub-THz transmitters.

Acknowledgment

This work was supported by the Foundations of Chinese Academy of Sciences under Grants E44621010T, and also supported by the International Partnership Program of the Chinese Academy of Sciences, Grant No. 313GJHZ2023096FN.

References

[1] K. Du, P. Wu, and Z. Yu, "A 300-GHz broadband high-output-power terahertz source based on low-Q colpitts injection-locked oscillator," in *2025 IEEE MTT-S International Wireless Symposium (IWS)*, 2025, pp. 1–3.

[2] X. Li, W. Chen, H. Wu, S. Li, X. Yi, R. Han, and Z. Feng, "A 110-to-130 GHz SiGe BiCMOS doherty power amplifier with a slotline-based power combiner," *IEEE J. Solid-State Circuits*, vol. 57, no. 12, pp. 3567–3581, 2022.

[3] D. J. Shepphard, J. Powell, and S. C. Cripps, "An efficient broadband reconfigurable power amplifier using active load modulation," *IEEE Microw. Wireless Compon. Lett.*, vol. 26, no. 6, pp. 443–445, 2016.

[4] A. Der and T. Barton, "An 18–44 GHz power amplifier in 90-nm GaN using active impedance matching," *IEEE Journal of Microwaves*, vol. 5, no. 3, pp. 702–710, 2025.

[5] X. Li, W. Chen, P. Zhou, Y. Wang, F. Huang, S. Li, J. Chen, and Z. Feng, "A 250–310 GHz power amplifier with 15-dB peak gain in 130-nm SiGe BiCMOS process for terahertz wireless system," *IEEE Transactions on Terahertz Science and Technology*, vol. 12, no. 1, pp. 1–12, 2022.

[6] S. Fu, S. Li, X. Li, and W. Chen, "A 6.3 dBm 258-314 GHz power amplifier using a broadband 8-way SQWL power combiner in 130-nm SiGe BiCMOS technology," in *2024 IEEE European Solid-State Electronics Research Conference (ESSERC)*, 2024, pp. 713–716.

[7] Z. Li, J. Chen, Z. Wang, and W. Hong, "A 206–264 GHz power amplifier based on a high-linearity cascode core with 15 dB gain and 12.2-dBm Psat in 130-nm SiGe BiCMOS," *IEEE Transactions on Terahertz Science and Technology*, vol. 14, no. 2, pp. 293–297, 2024.

[8] S. Fu, S. Li, H. Wu, X. Liu, X. Li, Q. Liao, S. Hu, and W. Chen, "A compact 249–309 GHz power amplifier using a four-conductor transmission line balun," *IEEE Transactions on Terahertz Science and Technology*, vol. 16, no. 3, pp. 272–285, 2026.

A Low-Loss Tunable Bandpass Filter Based on Boundary-Reconfigurable Patch Resonators

1st Huihui Fei
School of Information Science and Engineering
Southeast University
Nanjing, China
feihuihui@seu.edu.cn

2nd Ren-Rong Zhao
School of Information Science and Engineering
Southeast University
Nanjing, China
phdzhao@ seu.edu.cn

3rd Peng Chen
School of Information Science and Engineering
Southeast University
Nanjing, China
pchen@ seu.edu.cn

4th Chao Yu
School of Information Science and Engineering
Southeast University
Nanjing, China
chao.yu@seu.edu.cn

***Abstract*—This paper presents a low-loss tunable bandpass filter (BPF) based on a boundary-reconfigurable patch resonator. Frequency tuning is realized by reconfiguring the resonator boundary conditions without using conventional lumped elements such as varactor diodes, thereby maintaining low insertion loss. The fabricated filter demonstrates a center-frequency tuning range from 0.45 to 1.15 GHz, corresponding to a tuning ratio of 2.56. Across the entire CF tuning range, the measured minimal insertion loss is maintained below 1.35 dB. In addition, bandwidth reconfigurability is realized, with the fractional bandwidth adjustable from 20.5% to 32.0%. Moreover, transmission zeros are generated at both sides of the passband which enhance the BPF's selectivity. Therefore, the proposed filter provides a practical solution for low-loss tunable filtering applications.**

Keywords—bandpass filter, boundary condition, LC mode, patch resonator, reconfigurability

I. Introduction

With the rapid development of 6G flexible-spectrum technologies, wireless signal transmission is evolving toward multi-band operation, dynamic bandwidth allocation, and spectrum reconfigurability [1], [2]. This trend places increasingly stringent requirements on the frequency-selective capability of RF front-end systems, making tunable filters indispensable components for flexible spectrum access and interference suppression. In addition to a wide tuning range and fine frequency agility, modern RF front ends demand tunable filters with low insertion loss, high linearity, and stable performance across the tuning range.

In recent years, various types of tunable filters have been extensively investigated. Varactor-based tunable filters have attracted considerable attention due to their compact size and fast tuning capability [3]–[6]; however, the intrinsic nonlinearity and additional loss introduced by the varactor diodes significantly limit their performance in high-power and high-linearity applications. MEMS-based tunable filters offer low loss and high quality factors, yet challenges such as high actuation voltage, tuning speed, and long-term reliability remain [7], [8]. In addition, several emerging tuning approaches, including those based on liquid metals, ferroelectric materials, phase-change materials, and reconfigurable resonant structures, have been proposed to enable frequency agility through alter-native physical mechanisms [9], [10].

Despite their diverse operating principles, most existing tunable filters suffer from a fundamental tradeoff between tuning range and insertion loss. As the tuning range increases, the insertion loss and performance robustness often degrade markedly, which restricts their applicability in 6G flexible-spectrum RF front-end systems.

In this paper, we propose a novel tunable filter based on re-configurable boundary conditions. By manipulating the boundary conditions of the resonator, a continuously tunable filtering response over the frequency range of 0.45–1.15 GHz is achieved without relying on conventional tuning elements. Both simulated and measured results demonstrate good agreement, validating the proposed filter in terms of good tunability performance and low insertion loss, which makes it a promising candidate for 6G flexible-spectrum applications.

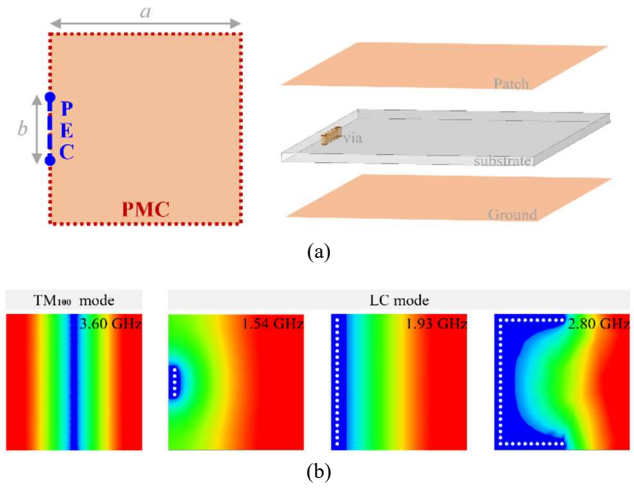


Fig.1. (a) Structure of the proposed boundary-reconfigurable grounded patch resonator. (b) Electric-field distributions of the fundamental mode of the unperturbed patch resonator and the proposed boundary-reconfigurable grounded patch resonator.

II. Analysis and Design

A. Grounded Patch Resonator with Reconfigurable Boundary

Fig. 1(a) illustrates the structure of the proposed boundary-reconfigurable grounded patch resonator. The resonator consists of a square patch and several metallic vias that connect the patch to the ground plane. For conventional square patch resonator, the patch edges can be approximately modeled as perfect magnetic conductor (PMC) boundary conditions. However, the introduced metallic vias locally transform the boundary condition from PMC to perfect electric conductor (PEC) along a segment of the patch edge. This modification of the boundary condition significantly alters the electromagnetic behavior of the resonator and gives rise to a new resonance, referred to as the LC mode. The patch and metallic vias together form an effective LC resonant unit, where the patch provides capacitance and the vias act as inductance. As illustrated in Fig. 1(b), the fundamental resonance shifts from the conventional TM_{100} mode to a lower-frequency LC mode, enabling more compact size.

From a circuit-model perspective, as the number of metallic vias increases, the resonant frequency shifts toward higher frequencies, which can be attributed to the reduction of the effective inductance provided by the parallel vias. From a field-based perspective, since the metallic vias are used to construct the boundary conditions, the loss remains relatively low across different operating frequencies, which enables low-loss reconfigurable CF operation. Therefore, the resonant frequency of the LC mode shown in Fig. 2 shifts toward higher frequencies with increasing N_{via}, while the insertion loss remains nearly unchanged.

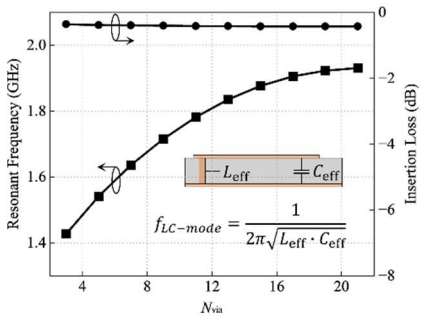


Fig.2. Tunable LC-mode resonance with low insertion loss achieved by varying the number of metallic vias Nvia.

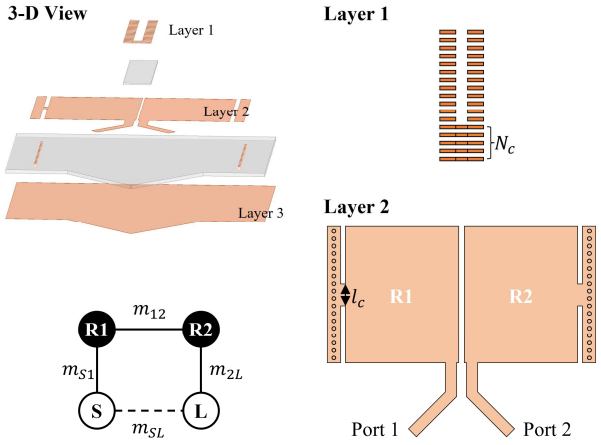


Fig.3. Design schematic of the proposed two-stage tunable filter and its coupling scheme.

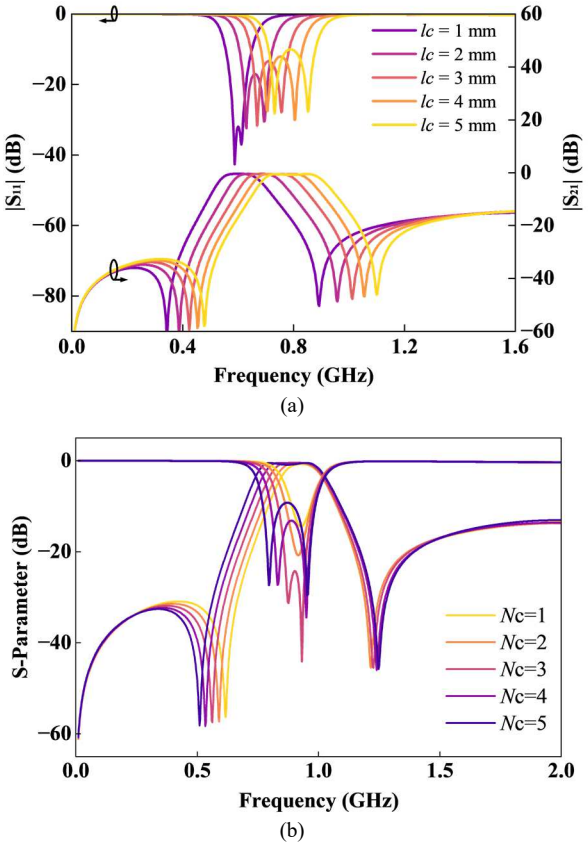
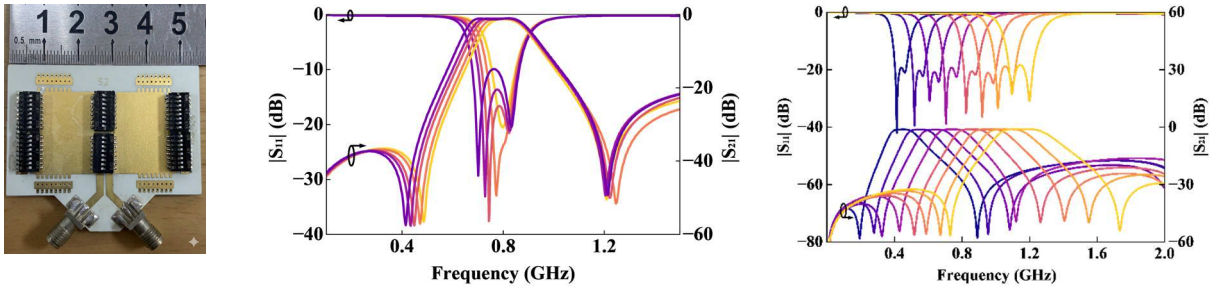


Fig.4. Simulated S-Parameter versus (a) l_c and (b) N_c

B. Passband Realization and Filter Design

Based on the proposed boundary-reconfigurable grounded patch resonator, a two-stage resonator configuration is employed to extend the achievable bandwidth, thereby realizing a tunable bandpass filter. Fig. 3 illustrates the overall structure of the proposed filter along with its corresponding coupling configuration. The center frequency of the filter can be reconfigured by adjusting the parameter lc, which effectively modifies the boundary conditions of each resonator. The coupling between R_1 and R_2 can be controlled by the coupling structure implemented in Layer 1. Here, N_c denotes the number of interconnected metallic segments, which directly determines the coupling coefficient and thus the resulting bandwidth. Moreover, the introduced source–load coupling facilitates the generation of transmission zeros near the passband, thereby improving the selectivity of the proposed filter. Fig. 4(a) shows that the center frequency can be tuned by varying l_c, with insertion loss about 0.85 dB across the tuning range. As shown in Fig. 4(b), adjusting N_c allows bandwidth control. The results demonstrate independent frequency and bandwidth tuning with stable passband responses. In the practical implementation, frequency tuning is accomplished through surface-mounted switches positioned between the grounding via array and the patch edge. Similarly, bandwidth tuning is realized by



(a) (b) (c)

Fig. 5 (a) Fabricated prototype of the proposed tunable bandpass filter. (b) Measured S-Parameter for different bandwidth tuning states. (c) Measured S-Parameter for different center-frequency states.

integrating dual in-line package (DIP) switches into the coupling structure in Layer 1.

III. Fabrication and Measurement

To verify the design concept, the proposed tunable filter is fabricated and measured. Fig. 5 shows the fabricated filter and its measurement results. The filter is implemented on a single-layer Rogers RO4350B substrate with a dielectric constant of 3.66 and a thickness of 0.508 mm. Besides, DIP switches are integrated to enable boundary reconfiguration and coupling adjustment. By configuring the switch states, the effective boundary conditions of the resonators as well as the coupling strength can be modified during measurement. Fig. 5(b) presents the measured bandwidth tuning performance of the proposed filter. The fractional bandwidth is adjusted from 20.5% to 32.0%, while the measured return loss remains better than 10 dB and the minimum insertion loss is maintained below 1.35 dB throughout the tuning process. As further illustrated in Fig. 5(b), the proposed filter provides a wide tuning range from 0.45 to 1.15 GHz. Throughout this range, the measured return loss is better than 20 dB, and the minimum insertion loss is measured to be 0.95–1.25 dB. Furthermore, transmission zeros located at both sides of the passband improve the selectivity of the filter. Compared with existing tunable filters summarized in Table I, the proposed design achieves low insertion loss while maintaining a competitive tuning ratio of 2.6.

IV. Conclusion

In this paper, a boundary-reconfigurable patch resonator is proposed and applied to realize a tunable bandpass filter. The reconfigurability is achieved by modifying the resonators' boundary conditions, avoiding conventional tuning elements such as varactors. As a result, low insertion loss is maintained across the tuning range. Therefore, the proposed approach provides an effective solution for low-loss reconfigurable BPF design, making it suitable for emerging 6G flexible-spectrum systems.

Table I Performance Comparison with Other Tunable Bandpass Filters

Ref.	Method	Range (GHz)	Tuning Ratio	BW Tuning	IL (dB)	Num of TZs
[11]	varactor	1.58–1.88	1.2	No	<1.9	2
[4]	varactor	1.4–2.0	1.4	No	<4.0	2
[5]	varactor	1.5–2.2	1.5	Yes	<5.1	2
[6]	varactor	0.55–1.9	3.5	No	<4.4	1
[7]	MEMS	0.6–1.0	1.7	No	<3.6	0
[8]	MEMS	0.4–0.56	1.4	No	<2.3	0
[10]	liquid metal	1.24–2.75	2.2	No	<5.5	0
[9]	liquid metal	4.5–5.5	1.2	Yes	<2.0	0
This Work	boundary reconfiguration	0.45–1.15	2.6	Yes	<1.4	2

Acknowledgments

This work was supported by the Scientific Research Innovation Capability Support Project for Young Faculty (SRICSPYF-ZY2025020).

References

[1] M. Matinmikko-Blue, S. Yrjölä, and P. Ahokangas, "Spectrum Management in the 6G Era: The Role of Regulation and Spectrum Sharing," in *2020 2nd 6G Wireless Summit (6G SUMMIT)*, Mar. 2020, pp. 1–5.

[2] W. K. Alsaedi, H. Ahmadi, Z. Khan, and D. Grace, "Spectrum Options and Allocations for 6G: A Regulatory and Standardization Review," *IEEE Open Journal of the Communications Society*, vol. 4, pp. 1787–1812, 2023.

[3] J. Hong, "Reconfigurable planar filters," *IEEE Microwave Magazine*, vol. 10, no. 6, pp. 73–83, Oct. 2009.

[4] J. Long, C. Li, W. Cui, J. Huangfu, and L. Ran, "A Tunable Microstrip Bandpass Filter With Two Independently Adjustable Transmission Zeros," *IEEE Microwave and Wireless Components Letters*, vol. 21, no. 2, pp. 74–76, Feb. 2011.

[5] Y.-C. Chiou and G. M. Rebeiz, "A Tunable Three-Pole 1.5–2.2-GHz Bandpass Filter With Bandwidth and Transmission Zero Control," *IEEE Transactions on Microwave Theory and Techniques*, vol. 59, no. 11, pp. 2872–2878, Nov. 2011.

[6] F. Lin and M. Rais-Zadeh, "Continuously Tunable 0.55–1.9-GHz Bandpass Filter With a Constant Bandwidth Using Switchable Varactor-Tuned Resonators," *IEEE Transactions on Microwave Theory and Techniques*, vol. 65, no. 3, pp. 792–803, Mar. 2017.

[7] Y. Shim, Z. Wu, and M. Rais-Zadeh, "A High-Performance Continuously Tunable MEMS Bandpass Filter at 1 GHz," *IEEE Transactions on Microwave Theory and Techniques*, vol. 60, no. 8, pp. 2439–2447, Aug. 2012.

[8] T.-W. Lin, L. Gao, R. Gaddi, and G. M. Rebeiz, "400–560 MHz Tunable 2-Pole RF MEMS Bandpass Filter with Improved Stopband Rejection," in *2018 IEEE/MTT-S International Microwave Symposium - IMS*, Jun. 2018, pp. 510–513.

[9] A. Pham and H. H. Sigmarsson, "Full Bandpass Filter Reconfigurability Through Liquid Metal Tuning and a Novel External Coupling Technique," *IEEE Microwave and Wireless Technology Letters*, vol. 34, no. 11, pp. 1231–1234, Nov. 2024.

[10] A. Widaa, F. Kamrath, and M. Höft, "Reconfigurable TM-Mode Dielectric Bandpass Filter Using Liquid Metals," in *2024 IEEE International Microwave Filter Workshop (IMFW)*, Feb. 2024, pp. 173–175.

[11] A. Widaa, C. J. You, and M. Awad, "High Selectivity Low-Loss Tunable Bandpass Filter with Transmission Zeros Control Using Staircase Resonators," in *2021 IEEE 21st Annual Wireless and Microwave Technology Conference (WAMICON)*, Apr. 2021, pp. 1–4.

A multi-mode tunable bandpass filter with the continuous transmission zero

Guangbao Shan, Chunyu Yang, and Yanwen Zheng*
Faculty of Integrated Circuit
Xidian University
Xi'an, China
zhengyanwen@xidian.edu.cn

***Abstract*—This paper presents a compact tunable bandpass filter (TBPF) realized using Through-Silicon Via (TSV) technology. The controlled tunable transmission zeros (TZs) are introduced to achieve bandwidth tuning. The area of the filter is $720 \times 510\ \mu\mathrm{m}^2$. The result demonstrates a wide continuous bandwidth tuning range from 8.09 GHz to 13.5 GHz, with a minimum insertion loss of 0.069 dB.**

***Index Terms*—Tunable, BPF, RF front-end, 3d integration**

I. Introduction

There is an increasing demand for micro-unmanned aerial vehicles (UAVs) capable of integrated reconnaissance, detection, and communication. The RF front-end serves as the core module for realizing these functions. Since reconnaissance, detection, and communication typically operate across distinct frequency bands, traditional RF front-end designs often rely on stacking multiple fixed-frequency modules on printed circuit boards (PCBs). However, this approach suffers from significant drawbacks, namely large volume and excessive weight. This limitation stems primarily from the fixed passbands of traditional filters, which fail to meet the diverse frequency requirements of multi-functional applications.

Tunable filter technology has emerged to address the demand for dynamic passband control in RF front-ends. Among these, reconfigurable bandpass filters, serving as core frequency-selective components, have attracted significant research attention. In existing reconfiguration techniques, electrical tuning represents the mainstream approach. Varactor diodes are widely adopted due to their continuous tuning capabilities and high integration potential; however, their tuning range is often constrained by the inherent capacitance tuning ratio of the device. For instance, Wójcik et al. proposed a filter based on dual capacitively coupled resonators, where the bandwidth tuning range was limited to 35–75 MHz due to varactor constraints [1]. Saad et al. introduced a highly tunable, fully integrated bandpass filter based on a novel differential active inductor architecture, achieving a wide tuning range from 280 MHz to 2.246 GHz [2]. Nevertheless, tuning methods based on active inductors typically suffer from inherent drawbacks, such as high noise figure and significant static power consumption. Furthermore, switching mechanisms represent another common approach. Zhang et al. presented a switchable bandpass filter, capable of switching its center frequency between 7.81 GHz and 8.35 GHz [3]. However, despite their high linearity, such MEMS-based designs typically suffer from slow switching speeds and the inability to achieve continuous frequency tunability.

This work was supported in part by the National Key Research and Development Program of China under Grant 2022YFB4401300 and Grant 2022YFB4401301, and in part by the National Natural Science Foundation of China under Grant 61934006, Grant 62090040, and Grant 62090043. (Corresponding author: Yanwen Zheng.)

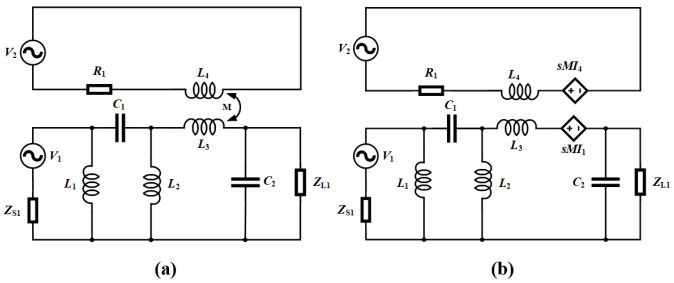


Fig. 1. Equivalent circuit model of the proposed TBPF. (a) Circuit topology with magnetic coupling. (b) Decoupled equivalent circuit model.

In summary, existing bandpass filters are limited by a lack of continuous bandwidth tunability, narrow tuning ranges, and poor integration capabilities [4] [5]. As the bandpass filter is the core component of the RF front-end, it acts as a critical bottleneck restricting functional reconfiguration [6]. Therefore, it is imperative to develop miniaturized, reconfigurable, and continuously tunable bandpass filter structures along with their tuning methods. These advancements will provide a technological foundation for the design and development of micro-scale equipment.

II. Filter Design and Performance Analysis

To illustrate the structure and working principle of the proposed filter, a simplified equivalent circuit is presented in Fig. 1(a). This design is realized by cascading a fixed High-Pass Filter with a Tunable Low-Pass Filter. The fixed HPF stage comprises the elements L_1, L_2, and C_1, while the TLPF stage consists of L_3, L_4, and C_2.

Based on the decoupled equivalent circuit model in Fig. 1(b) [7] [8], the voltage transfer function $H(s)$ is obtained as:

$$H(s) = \frac{V_{out}}{V_1} = A + B\beta \tag{1}$$

$$A = \frac{1}{\left(sC_2+\frac{1}{Z_{L1}}\right)\left[Z_{S1}+\frac{Z_{S1}+sL_1}{s^2C_1L_1}\right]+\frac{1}{sL_2}\left[Z_{S1}+\frac{Z_{S1}+sL_1}{sL_1}\left(\frac{1}{sC_1}+sL_2\right)\right]\left[1+\left(sC_2+\frac{1}{Z_{L1}}\right)\left(sL_3-\frac{s^2M^2}{sL_4+R_1}\right)\right]} \tag{3}$$

$$B = \frac{\frac{sM}{sL_2(sL_4+R_1)}\left[Z_{S1}+\frac{Z_{S1}+sL_1}{sL_1}\left(\frac{1}{sC_1}+sL_2\right)\right]}{\left(sC_2+\frac{1}{Z_{L1}}\right)\left[Z_{S1}+\frac{Z_{S1}+sL_1}{s^2C_1L_1}\right]+\frac{1}{sL_2}\left[Z_{S1}+\frac{Z_{S1}+sL_1}{sL_1}\left(\frac{1}{sC_1}+sL_2\right)\right]\left[1+\left(sC_2+\frac{1}{Z_{L1}}\right)\left(sL_3-\frac{s^2M^2}{sL_4+R_1}\right)\right]} \tag{4}$$

Here, the voltage ratio β is defined as the complex ratio of V_2 to V_1, where φ_1 and φ_2 represent the phases of V_1 and V_2, respectively.

$$\beta = \frac{V_2}{V_1} = \left|\frac{V_2}{V_1}\right| \angle(\varphi_2 - \varphi_1) = |\beta| e^{j\varphi_\beta} \tag{2}$$

where the coefficients A and B, which depend on the circuit parameters, are given by (3) and (4) at the top of the next page.

To facilitate the observation of the zero-pole distribution, the numerator $Z(s)$ and denominator $P(s)$ of the transfer function are simplified and expanded in powers of s. Setting them to zero yields the following characteristic equations:

$$a_1 s^3 + a_2 s^2 + a_3 s + a_4 = 0 \tag{5}$$

$$b_5 s^5 + b_4 s^4 + b_3 s^3 + b_2 s^2 + b_1 s + b_0 = 0 \tag{6}$$

Where

$$a_1 = \left(\frac{L_4}{\beta M} - 1\right) \tag{7}$$

Note that a_1 is the coefficient dependent on β, while all others are constants. Consequently, the transmission zeros can be flexibly tuned, whereas the poles remain invariant.

The equations shows that the filter possesses three zeros and five poles. Crucially, the zeros can be tuned with β, whereas the poles remain fixed. The corresponding pole-zero distribution is illustrated in Fig. 2.

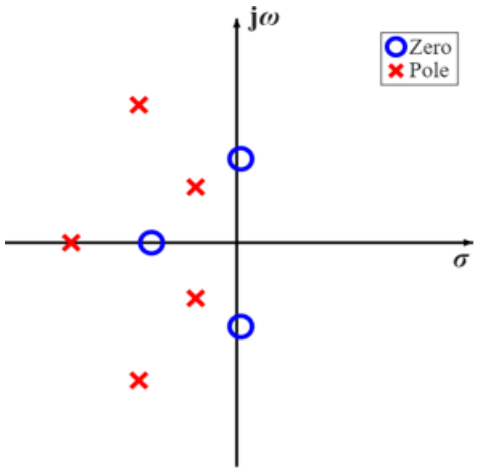


Fig. 2. Pole-zero distribution of the proposed tunable bandpass filter.

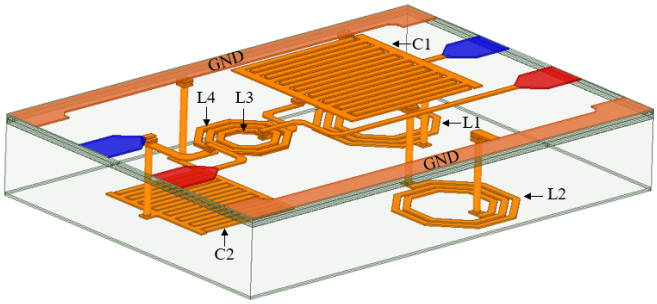


Fig. 3. Geometrical model of the silicon-based BPF.

III. Geometric Model and Simulation Results

A. Geometric Model and Simulation Results

The 3D geometrical model of the proposed tunable bandpass filter is illustrated in Fig. 3. Consistent with the fabrication flow, the inductors (L_3, L_4) and capacitor (C_1) are located on the top surface of the high-resistivity silicon substrate, while the inductors (L_1, L_2) and capacitor (C_2) are positioned on the bottom. The vertical electrical connection between the front-side and back-side layers is achieved through copper-filled TSVs. The device is manufactured using the aforementioned silicon-based TSV technology.

Following the physical modeling, an electromagnetic (EM) simulation was conducted in HFSS. To specifically validate the proposed bandwidth tuning technique, the SNP files extracted from the EM simulation were imported into Advanced Design System (ADS) for circuit-level co-simulation. At this theoretical stage, the dynamic adjustment of the excitation voltage's relative amplitude ($|\beta|$) and phase difference (φ_β) was conceptually verified using ideal tunable voltage sources in ADS. This approach effectively validates the core tuning mechanism while abstracting away the complexities of practical tuning elements and external biasing circuits. By systematically varying these ideal parameters, the dynamic frequency response of the filter was obtained, as plotted in Fig. 4. As illustrated, the tunable bandpass filter exhibits a wide tuning range, with its 3-dB bandwidth being continuously tunable from 8.09 GHz to 13.5 GHz. Correspondingly, the simulated reflection response S_{11} is presented in Fig. 5.

Table I presents a performance comparison between the previous works and proposed TBPF. It can be observed that the proposed filter achieves a high tuning ratio while maintaining an extremely compact footprint.

TABLE I
COMPARISON OF THE TUNABLE BANDPASS FILTER

Ref.	Filter type	Tuning devices	Tuning range (GHz)	Continuous adjustability	Process	Size (μm^2)
[1]	Microstrip Filter	Varactors	0.035 - 0.075	Yes	PCB	30000 × 35000*
[2]	Active Filter	Active Inductor	0.28-2.426	Yes	130 nm CMOS	-
[9]	Microstrip Filter	PIN diode	2.8 / 9.03	No	PCB	2170 × 1140
[10]	Microstrip Filter	Tunable Capacitor	1.5-3	Yes	PCB	14000 × 16000
This work	**Silicon 3D**	**Tunable Inductor**	**8.09-13.5**	**Yes**	**3D IPD**	**720×510**

* Estimation from prototype image.

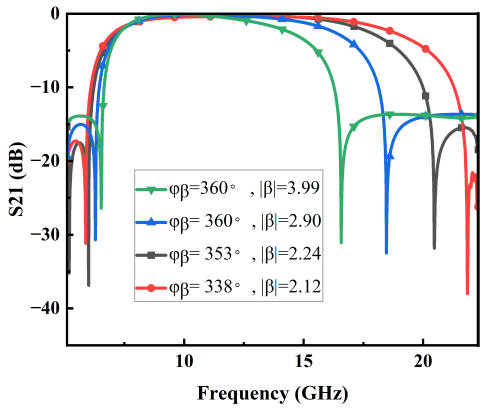


Fig. 4. Simulated S_{21} response under varying excitation parameters $|\beta|$ and φ_β.

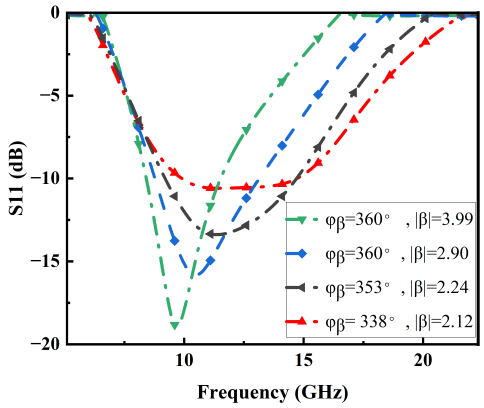


Fig. 5. Simulated S_{11} response under varying excitation parameters $|\beta|$ and φ_β.

IV. CONCLUSION

In this work, a compact tunable bandpass filter is proposed and comprehensively analyzed utilizing a silicon-based 3D fabrication process with Through-Silicon Vias. The proposed filter achieves continuous bandwidth tuning, demonstrating low in-band insertion loss and high out-of-band rejection. Furthermore, the architecture facilitates the direct 3D heterogeneous integration of RF front-end bare dies onto the filter surface, offering a promising solution to address the size and weight constraints of traditional RF front-end modules. Future work will focus on the experimental tape-out validation of the proposed architecture and the implementation of practical peripheral control circuitry.

REFERENCES

[1] D. Wójcik, M. Surma, and M. Magnuski, "Variable bandwidth double-coupled double-tuned filter with capacitive couplings," *Electronics*, vol. 14, no. 2, p. 252, 2025.

[2] S. Saad *et al.*, "A compact and tunable active inductor-based bandpass filter with high dynamic range for UHF band applications," *Sensors*, vol. 25, no. 10, 2025.

[3] N. Zhang, L. Mei, C. Wang, Z. Deng, J. Yang, and Q. Guo, "A switchable bandpass filter employing RF MEMS switches and open-ring resonators," *IEEE Trans. Electron Devices*, vol. 64, no. 8, pp. 3377–3383, Aug. 2017.

[4] D. Jung, M. Jung, and B.-W. Min, "Compact tunable filter based on dual-mode resonators with 1.5-octave tuning range wide stopband and single bias control," *IEEE Trans. Microw. Theory Techn.*, vol. 66, no. 1, pp. 240–248, 2018.

[5] C. J. You, S. H. Hu, and R. F. Xie, "Independent reconfigurable dual-band filter based on stub-loaded multimode resonators," in *Proc. Int. Conf. Microw. Millimeter Wave Technol. (ICMMT)*, Beijing, China, 2024, pp. 1–3.

[6] H.-R. Zhu, X.-Y. Ning, Z.-X. Huang, and X.-L. Wu, "An ultra-compact on-chip reconfigurable bandpass filter with semi-lumped topology by using GaAs pHEMT technology," *IEEE Access*, vol. 8, pp. 31606–31613, 2020.

[7] Y. Zheng, G. Shan and G. Li, "A Wide Range Tunable Inductor Based on Magnetic Coupling Techniques for RF Communication," in *Proc. IEEE MTT-S Int. Microw. Workshop Ser. Adv. Mater. Process. RF THz Appl. (IMWS-AMP)*, Chengdu, China, 2023, pp. 1–3.

[8] Y. Zheng, G. Shan, L. Yang, X. Fan, and H. Cao, "A DC-5 GHz TSV-Based 3-D Network for Multichiplet Wireless System Reconfiguration," *IEEE Internet of Things J.*, vol. 12, no. 4, pp. 3512–3520, Feb. 15, 2025.

[9] A. Bandyopadhyay, P. Sarkar, and R. Ghatak, "A Bandwidth Reconfigurable Bandpass Filter for Ultrawideband and Wideband Applications," *IEEE Trans. Circuits Syst. II, Exp. Briefs*, vol. 69, no. 6, pp. 2747–2751, Jun. 2022.

[10] M. Fan, K. Song, and Y. Fan, "Reconfigurable bandpass filter with wide-range bandwidth and frequency control," *IEEE Trans. Circuits Syst. II, Exp. Briefs*, vol. 68, no. 6, pp. 1758–1762, Jun. 2021.

Wideband Phased-Array Meta-Antenna without Air Cavity for Ku-Band Satellite Communication

Qing You[1], Dianxin Luan[2], Pui-In Mak[1], Rui P. Martins[1], Jun Yin[1*]
[1]University of Macau, Macau, China
[2]University of Edinburgh, Edinburgh, UK
qingyou@ieee.org, *junyin@um.edu.mo

***Abstract*- This paper presents a wideband dual-linear polarization Ku-Band phased-array meta-antenna that eliminates the need for an air cavity. By incorporating a metasurface, the proposed antenna achieves a broad operational bandwidth from 10.7 GHz to 14.5 GHz with a realized gain exceeding 1.7 dBi. The wideband performance is realized without an air cavity, thereby simplifying the fabrication process. By leveraging this antenna design, a method for achieving both dual-linear and dual-circular polarization is demonstrated. Implemented on a cost-effective PCB platform, the proposed phased array offers a low-cost solution well-suited for satellite communication applications.**

I. Introduction

The Internet of Things (IoT) holds significant promise for a wide range of large-scale, data-intensive, computation-heavy, and delay-sensitive applications, including smart cities, industrial automation, smart homes, and autonomous driving [1] [2]. However, existing wireless communication systems often fall short of meeting the stringent requirements posed by such massive IoT deployments, which has recently sparked growing interest in mobile satellite communication (SATCOM) as a complementary solution [3].

SATCOM offers broad coverage, making it highly suitable for deployment on moving platforms, including ground, maritime, and airborne platforms [4] [5]. Early SATCOM ground terminals predominantly relied on mechanically steered systems driven by motors, which are typically bulky and require frequent maintenance [6] [7] [8]. With advancements in silicon integrated circuit technologies, low-cost active electronically scanned phased arrays integrated with silicon-based beamformer chips have been adopted in SATCOM systems [9]. Recent developments include a Ku-band dual-linear-polarized phased-array receiver [10] and a Ku-band single-polarization phased-array transmitter [11], both reported in 2021 for SATCOM applications. To further enhance integration, a wideband phased-array antenna enabling both receiver and transmitter functions within a single phased-array system has been proposed [12]. However, this antenna employs an air cavity to enhance bandwidth, which necessitates an additional processing step, thereby increasing fabrication time and cost.

In this paper, we present a wideband dual-linear-polarization Ku-band phased-array meta-antenna for satellite communication that eliminates the need for an air cavity. By integrating a metasurface into a conventional antenna design, the proposed meta-antenna achieves wideband operation from 10.7 GHz to 14.5 GHz with a gain exceeding 1.7 dBi. Unlike conventional approaches, the proposed design does not require an air cavity, thereby reducing fabrication complexity and cost. The entire system is implemented on a low-cost PCB platform, making it well-suited for satellite communication applications.

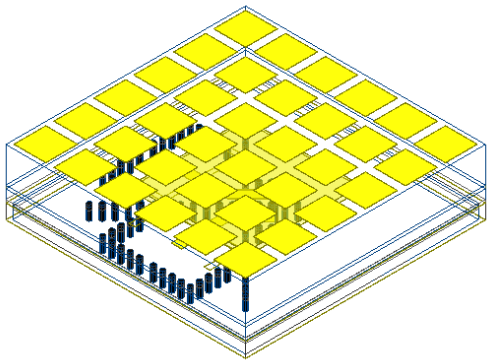


Fig. 1. Structure of the presented meta-antenna.

II. Wideband Meta-Antenna Design

A. Wideband Meta-Antenna Design

The presented meta-antenna consists of a meta-surface, a radiation patch and a parasitic patch to enhance the bandwidth, as shown in Fig. 1. The parasitic patch is introduced to broaden the impedance bandwidth by generating an additional resonant frequency.

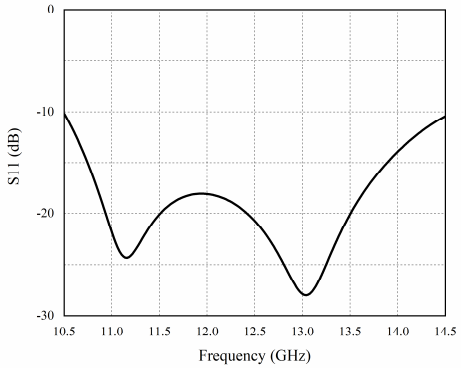


Fig. 2. Simulated S parameter of the proposed wideband meta-antenna.

The size of the meta-antenna is 10.4 mm × 10.4 mm, and the $\lambda_0/2$ of the highest frequency is 10.3 mm. The size of the

radiation patch is 5.1 mm × 5.1 mm while the size of the parasitic patch is 5 mm × 5 mm. The meta-surface is placed on the top layer of the proposed antenna to further extend the operating bandwidth. The simulated S-parameter is shown in Fig. 2, where the results indicate that S11 remains below -10 dB from 10.5 GHz to 14.5 GHz. In other words, the proposed meta-antenna can cover both the receive and transmit bands for Ku-band satellite communication.

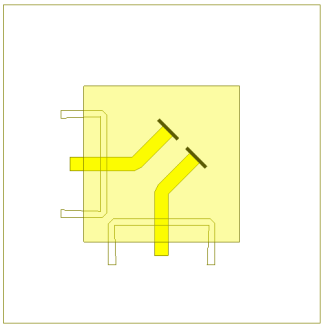


Fig. 3. Structure of the orthogonal coupling slot.

To realize dual-linear polarization, two orthogonal coupling slots are utilized, as shown in Fig. 3. Vias are placed between the two ports to enhance isolation, and the simulated S-parameters are shown in Fig. 4. The simulated results show that the S12 remains below -23 dB from 10.5 GHz to 14.5 GHz, demonstrating good isolation between the two linear polarizations.

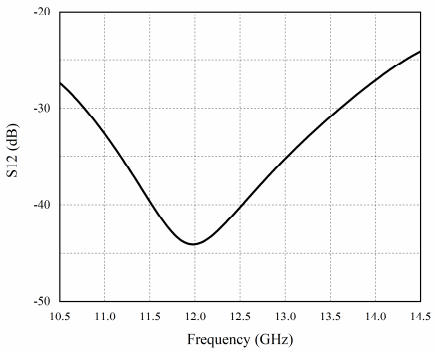


Fig. 4. S12 of the presented meta-antenna.

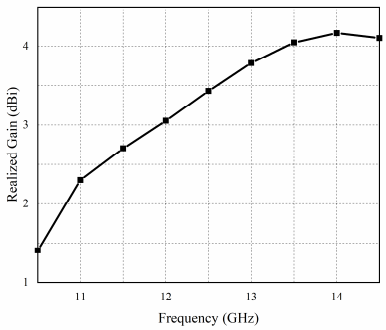


Fig. 5. Simulated realized gain of the presented meta-antenna.

The simulated realized gain and radiation efficiency are presented in Fig. 5 and Fig. 6, respectively. The results show that the realized gain exceeds 1.77 dBi from 10.5 GHz to 14.5 GHz and increases with frequency. It reaches a maximum of 4.17 dBi at 14.0 GHz, before slightly decreasing to 4.10 dBi at 14.5 GHz. The radiation efficiency remains over 90 % from 10.5 GHz to 14.43 GHz, with a minimum value of 89.3 % at 14.5 GHz. These results demonstrate that the proposed meta-antenna exhibits favorable radiation performance across the targeted frequency range.

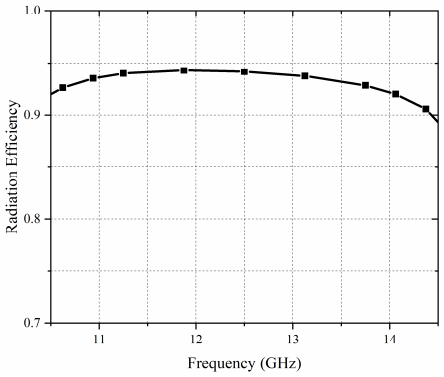


Fig. 6. Simulated radiation efficiency of the presented meta-antenna.

B. Meta-Antenna Subarray Design

In the phased-array system, the beamforming chip features eight channels and is connected to four meta-antennas. These four meta-antennas are arranged in a rotated configuration to form a subarray, with the chip placed at the center to ensure equal feed line lengths. This topology enhances the consistency among antenna elements, thereby mitigating efficiency degradation caused by phase and amplitude mismatches.

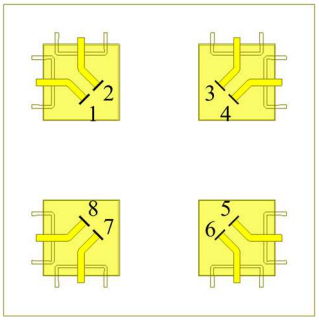


Fig. 7. Subarray of the presented meta-antenna.

The rotated subarray offers considerable flexibility in polarization control and can be configured to support both dual-linear and dual-circular polarization. Table I lists the required amplitude and phase settings for each port to achieve the desired polarization states. It is worth noting that only one of the two linearly polarized feeding ports per antenna is activated at a time, which helps reduce the power consumption of the beamforming chip and alleviate heat dissipation.

Table I
Amplitude and Phase Configuration for Different Polarization States

Port	H-Pol.	V-Pol.	LHCP	RHCP
1	1 (0 °)	0	1 (0 °)	0
2	0	1 (0 °)	0	1 (0 °)
3	0	1 (0 °)	1 (90 °)	0
4	1 (180 °)	0	0	1 (-90 °)
5	1 (180 °)	0	1 (180 °)	0
6	0	1 (180 °)	0	1 (-180 °)
7	0	1 (180 °)	1 (270 °)	0
8	1 (0 °)	0	0	1 (-270 °)

Fig. 8 presents the simulated radiation pattern of the subarray for both linear and circular polarization. The peak realized gain is 9.15 dBi for linear polarization and 6.19 dBi for circular polarization. The 3 dB lower gain observed for circular polarization is attributed to polarization loss, which is consistent with theoretical expectations.

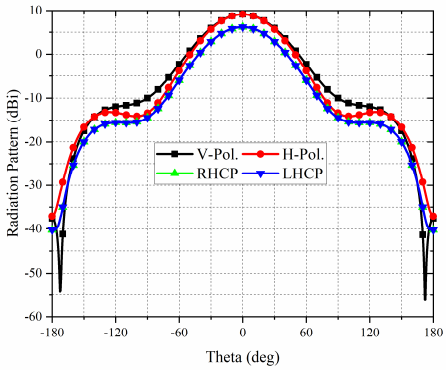


Fig. 8. Radiation pattern of the subarray with different polarizations.

IV. Conclusion

This paper presents the design of a wideband dual-linear polarized Ku-band meta-antenna without an air cavity. The proposed meta-antenna achieves broad frequency coverage from 10.7 GHz to 14.5 GHz, with a realized gain exceeding 1.7 dBi and radiation efficiency above 89.3 % across the operation band.

Based on this element, a method for realizing both dual-linear and dual-circular polarization is demonstrated. By eliminating the air cavity and leveraging a fully low-cost PCB implementation, the proposed design offers reduced fabrication complexity and cost compared to conventional approaches. This work provides a promising foundation for the development of cost-effective, high-performance phased-array technologies for emerging wireless communication applications.

Acknowledgement

The work is funded by the Macau Science and Technology Development Fund (FDCT) - 0109/2025/RIB2, - 0001/2025/NRP, and the University of Macau Research Fund - MYRG-GRG2024-00298-IME

References

[1] D. C. Nguyen *et al.*, "6G Internet of Things: A comprehensive survey," *IEEE Internet Things J.*, vol. 9, no. 1, pp. 359 - 383, Jan. 2022.

[2] T. R. Wanasinghe, R. G. Gosine, L. A. James, G. K. I. Mann, O. de Silva and P. J. Warrian, "The Internet of Things in the oil and gas industry: A systematic review," *IEEE Internet Things J.*, vol. 7, no. 9, pp. 8654 - 8673, Sep. 2020.

[3] D. Wilcoxson, B. Sleight, J. O'Neill, and D. Chester, "Helicopter Ku-band SATCOM On-the-move," in *Proc. IEEE Mil. Commun. Conf.* (MILCOM), Washington, DC, USA, Oct. 2006, pp. 1–7.

[4] S. Vaccaro, F. Tiezzi, D. Llorens, M. F. Rua, and C. D. G. de Oro, "Ku-band low profile antennas for mobile SATCOM," in *Proc. 4th Adv. Satell. Mobile Syst.*, Bologna, Italy, Aug. 2008, pp. 24–28.

[5] G. Gultepe, S. Zihir, T. Kanar, and G. M. Rebeiz, "A dual-polarized 1024-element Ku-band SATCOM transmit phased-array with ±70◦ scan and 43.5 dBW EIRP," in *IEEE MTT-S Int. Microw. Symp. Dig.*, Los Angeles, CA, USA, Aug. 2020, pp. 837–840.

[6] R. S. Wexler, D. Ho, and D. N. Jones, "Medium data rate (MDR) satellite communications (SATCOM) on the move (SOTM) prototype terminal for the army warfighters," in *Proc. IEEE Mil. Commun. Conf.* (MILCOM), Atlantic City, NJ, USA, vol. 3, Oct. 2005, pp. 1734–1739.

[7] A. R. Weily and N. Nikolic, "Dual-polarized planar feed for low-profile hemispherical luneburg lens antennas," *IEEE Trans. Antennas Propag.*, vol. 60, no. 1, pp. 402–407, Jan. 2012.

[8] F. Tiezzi and S. Vaccaro, "Hybrid phased array antenna for mobile Ku-band DVB-S services," in *Proc. 1st Eur. Conf. Antennas Propag.*, Nice, France, Nov. 2006, pp. 1–4.

[9] K. Kibaroglu, M. Sayginer, T. Phelps, and G. M. Rebeiz, "A 64-element 28-GHz phased-array transceiver with 52-dBm EIRP and 8–12-Gb/s 5G link at 300 meters without any calibration," *IEEE Trans. Microw. Theory Techn.*, vol. 66, no. 12, pp. 5796–5811, Dec. 2018.

[10] G. Gültepe and Gabriel M. Rebeiz, "A 256-Element Dual-Beam Polarization-Agile SATCOM Ku-Band Phased-Array With 5-dB/K G/T," *IEEE Trans. Microw. Theory Techn.*, vol. 69, no. 11, pp. 4986–4994, Nov. 2021.

[11] Gökhan Gültepe, Tumay Kanar, Samet Zihir and Gabriel M. Rebeiz, "A 1024-Element Ku-Band SATCOM Phased-Array Transmitter With 45-dBW Single-Polarization EIRP," *IEEE Trans. Microw. Theory Techn.*, vol. 69, no. 9, pp. 4157–4168, Sep. 2021.

[12] Q. You *et al.*, "Wideband Dual-Circular Polarization Phased-Array Antenna for Ku-Band Satellite Communication," in *Proc. IEEE MTT-S Int. Microw. Workshop Ser. Adv. Mater. Processes for RF THz Appl.* (*IMWS-AMP*), Wuxi, China, Jul. 2025, pp. 1 – 3.

A Hexagonal Six-Port Hybrid Coupler for Beamforming Applications

Zhiwei Yin
School of Electrical and Data Engineering
University of Technology Sydney
Sydney, Australia
zhiwei.yin@student.uts.edu.au

He Zhu
Manufacturing, Commonwealth Scientific and Industrial Research Organisation (CSIRO)
Sydney, Australia
He.Zhu@csiro.au

Xiaojing Lv
School of Electrical and Data Engineering
University of Technology Sydney
Sydney, Australia
Xiaojing.Lv@uts.edu.au

Yang Yang
School of Electrical and Data Engineering
University of Technology Sydney
Sydney, Australia
yang.yang-1@uts.edu.au

***Abstract*—Multibeam scanning capabilities are essential for modern wireless communication systems, including 5G/6G MIMO and satellite technology. This paper presents a novel approach to implementing a 3-beam feeding network using a compact planar six-port regular hexagonal hybrid coupler. Compared to conventional Nolen matrix (NM) designs that rely on a cascaded arrangement of multiple couplers and phase shifters, the proposed design integrates these functionalities into a single planar component. This approach achieves a significant size reduction of over 70% while maintaining excellent RF performance. To verify the concept, a prototype operating at 2.45 GHz was designed and fabricated. The measured results demonstrate an equal power division of 5 ± 0.9 dB and phase differences of $\pm 120^\circ$ and 0° across the 2.28–2.61 GHz band. The simplicity and effectiveness of this approach make it highly suitable for compact, scalable beamforming systems.**

***Keywords*—Beam-forming network, hexagonal coupler, six-port, Nolen matrix, compact.**

I. Introduction

Multibeam scanning antennas have become a pivotal technology for various applications, ranging from mobile terminals and satellite communications to massive MIMO and automotive radar systems [1]. Within the Internet of Things (IoT) ecosystem, passive beamforming networks (BFNs) are particularly advantageous due to their low energy consumption, structural simplicity, and cost-effective mass production. Traditional BFNs, such as the Butler matrix (BM), Blass matrix, and NM, are widely utilized to synthesize desired beam patterns [2], [3]. Among these, the NM provides superior design flexibility, especially in terms of the number of input and output ports, making it ideal for asymmetric beam-forming and pattern synthesis.

Despite these advantages, conventional NM implementations often suffer from high circuit complexity and significant footprints [4]. A typical uniplanar 3×3 NM requires multiple cascaded directional couplers and discrete phase shifters [5]. This cascaded arrangement not only increases the physical size but also introduces cumulative insertion losses and phase fluctuations across the operating bandwidth. Previous research has explored several miniaturization techniques, including vertically installed planar couplers and substrate-integrated waveguide (SIW) technology. However, many of these approaches result in non-planar structures or high fabrication complexities, which limits its scalability and practicality in space-constrained applications.

In this article, we propose a novel compact planar six-port regular hexagonal coupler to replace the traditional third-order 3×3 NM. By integrating all functionalities—including three couplers and three phase shifters—into a single hexagonal transmission-line structure, we achieve a substantial size reduction of over 70%. The proposed design is realized on a single-layer PCB, maintaining a fully uniplanar configuration without the need for jump lines or multi-layer structures. This represents a significant advancement in miniaturization while ensuring high-precision electromagnetic performance.

II. Proposed Hexagonal Six-Port Coupler

A. Topology and Design Principle

The proposed BFN utilizes a centrally symmetric regular hexagonal structure to achieve compact integration. As illustrated in Fig. 1, the coupler is composed of two concentric regular hexagons—an outermost ring and an inner ring—connected by a series of intermediate transmission-line branches.

The electrical parameters of the outermost hexagon ring are defined as unilateral impedance Z_1 and electrical length θ_1. Similarly, the inner hexagon ring is characterized by Z_2 and θ_2, while the connecting branches are denoted by Z_3 and θ_3. By utilizing the network's symmetry and combinatorial excitation characteristics, the six-port structure can be decomposed into several subnetworks in Fig. 2. According to the modal analysis [6], the input reflection coefficients Γ_i (where $i \in \{ooo, eee, oe, ee\}$) represent the input reflection for odd-odd-odd, even-even-even, odd-even, and even-even excitation

979-8-3315-4544-4/26/$31.00 ©2026 IEEE

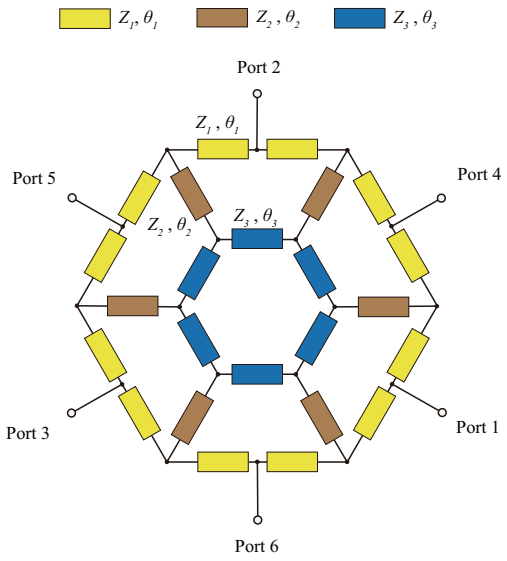


Fig. 1. Schematic of the proposed six-port hexagonal coupler.

modes, respectively. The S-parameters from Port 1 to all other ports can be expressed as:

$$S_{11} = \frac{1}{6}(\Gamma_{ooo} + 2\Gamma_{oe} + 2\Gamma_{ee} + \Gamma_{eee}) \quad (1)$$

$$S_{21} = S_{31} = \frac{1}{6}(\Gamma_{ooo} - \Gamma_{oe} - \Gamma_{ee} + \Gamma_{eee}) \quad (2)$$

$$S_{41} = S_{61} = \frac{1}{6}(\Gamma_{ooo} - \Gamma_{oe} + \Gamma_{ee} - \Gamma_{eee}) \quad (3)$$

$$S_{51} = \frac{1}{6}(\Gamma_{ooo} - 2\Gamma_{oe} + 2\Gamma_{ee} - \Gamma_{eee}) \quad (4)$$

By solving these equations, the characteristic impedances Z_1, Z_2, Z_3 can be determined to satisfy the desired power division ratio and phase differences.

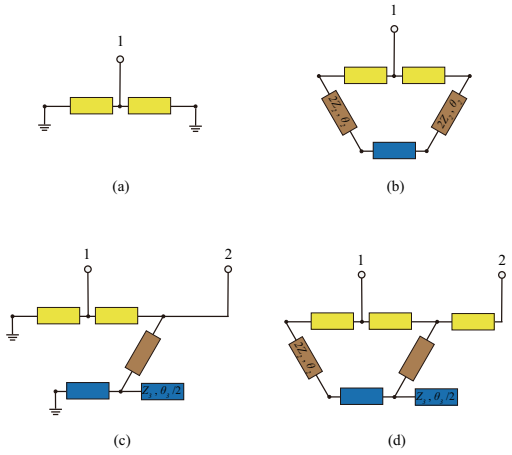


Fig. 2. Equivalent circuits of the six-port hexagonal coupler with different excitation: (a) Odd-odd-odd, (b) Even-even-even, (c) Odd-even, and (d) Even-even.

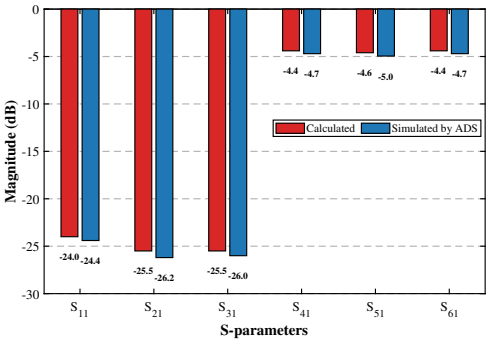


Fig. 3. Comparison results between calculated and ADS of the proposed coupler with equal power division.

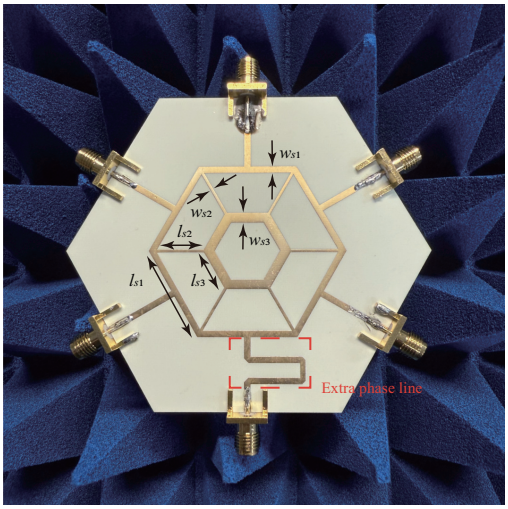


Fig. 4. The prototype of the six-port regular hexagonal coupler with extra phase delay line. (ls1= 24.26 mm, ls2= 11.64 mm, ls3= 10 mm, ws1= 1.56 mm, ws2= 0.7 mm and ws3= 2.38 mm.)

B. Theoretical Equation and Optimization

The scattering matrix of the 3×3 BFN, which maps input Ports 1–3 to output Ports 4–6, must satisfy the lossless condition $U = S \cdot S^H$. Using the mode-analysis [6], the power division ratio at the output ports can be precisely controlled by adjusting the characteristic impedances.

For the equal power division (1:1:1) case operating at 2.45 GHz, initial values were predetermined to constrain the design space: $\theta_1 = 55°$ and $Z_1 = 60\ \Omega$ were chosen based on conventional ring coupler designs. Through node-analysis and mapping of the $|S_{11}|$ and transmission coefficient curves, the optimal required impedances for the NM matrix functionality were identified as $Z_2 = 70\ \Omega$ and $Z_3 = 30\ \Omega$. To rapidly validate the design, the derived parameters were imported into ADS for simulation. As shown in Fig. 3, the comparison between the calculated values and ADS simulations at 2.45 GHz shows excellent agreement. For the equal power division target, S_{11}, S_{21}, and S_{31} are effectively suppressed below -23 dB, while the transmission coefficients S_{41}, S_{51}, and S_{61} are precisely maintained at approximately -4.77 dB, validating the accuracy of the proposed modal analysis equations. Based

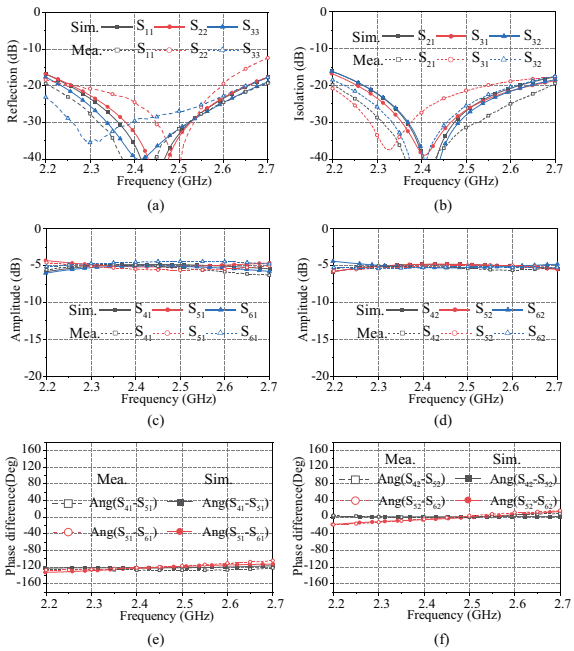


Fig. 5. The simulated and measured results of the proposed coupler. (a) Reflection coefficient. (b)Isolation. (c)-(d) Transmission coefficient.(e)-(f) Output phase difference.

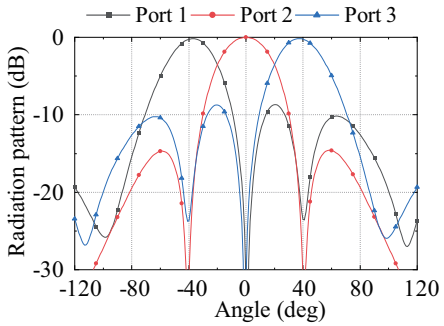


Fig. 6. The simulated normalized radiation patterns of a 1 × 3 array at 2.45 GHz with element spacing of half wavelength fed by the proposed six-port coupler.

on the calculated electrical parameters and RO4350B substrate properties, the physical dimensions were derived for full-wave electromagnetic simulation in CST Studio Suite. To account for practical discontinuities and parasitic effects at the T-junctions, the hexagonal layout was further optimized.

III. Measurement Results

The prototype of the proposed six-port hexagonal hybrid coupler was fabricated on a Rogers 4350B substrate ($\epsilon_r = 3.48$, $\tan\delta = 0.0037$), as shown in Fig. 4. The design includes an integrated extra phase delay line at the output section to provide the required phase compensation. The measured and simulated S-parameters and output phase differences are comprehensively evaluated and presented in Fig. 5.

As shown in Fig. 5(a), the measured reflection coefficients (S_{11}, S_{22}, S_{33}) demonstrate excellent matching performance, with values below -20 dB across the operating band and reaching approximately -30 dB at the center frequency of 2.45 GHz. The isolation between the input ports (S_{21}, S_{31}, S_{32}) is also maintained below -20 dB, as depicted in Fig. 5(b), indicating minimal crosstalk. Figs. 5(c) and 5(d) illustrate the transmission coefficients when Port 1 and Port 2 are excited, respectively. The measured magnitudes of S_{41}, S_{51}, and S_{61} are approximately -5.5 ± 0.88 dB, which aligns well with the simulated -5 ± 0.4 dB, with the slight deviation attributed to the insertion loss of SMA connectors and cables.

The phase characteristics are critical for beamforming accuracy. As shown in Fig. 5(e), when Port 1 is excited, the measured phase differences $Ang(S_{41} - S_{51})$ and $Ang(S_{51} - S_{61})$ are approximately $-120° \pm 10°$. Conversely, when Port 2 is excited, Fig. 5(f) shows that the phase differences $Ang(S_{42} - S_{52})$ and $Ang(S_{52} - S_{62})$ remain close to $0° \pm 14°$. These results confirm that the proposed coupler can effectively generate the required phase distributions for multiple beams. To validate its beam-steering capability, the coupler was used to feed a 1×3 antenna array, producing simulated scan angles of $-37°, 0°$, and $37°$ for individual port excitations, as shown in Fig. 6.

Conclusion

A novel, compact six-port hexagonal hybrid coupler for 3-beam array feeding is presented. By integrating multiple couplers and phase shifters into a single planar structure, the proposed design significantly simplifies the traditional Nolen matrix while reducing the footprint by over 70%. The measured RF performance and scanning patterns confirm its effectiveness, making it a promising candidate for modern compact multibeam antenna systems.

Acknowledgment

This project was supported by UTS's ARC Future Fellow Near Miss Support for Yang Yang, and Nano Dimension's Ph.D. Scholarship, partially supported by the ARC Linkage Project LP210300004.

References

[1] W. Hong, Z. H. Jiang, C. Yu, et al., "The role of millimeter-wave technologies in 5G/6G wireless communications," *IEEE J. Microw.*, vol. 1, no. 1, pp. 101–122, Jan. 2021.

[2] F. Silva, P. Pinho, and N. B. Carvalho, "Multibeam beamforming technology in microwave power transfer and harvesting," *IEEE Journal of Microwaves*, vol. 5, no. 4, pp. 918–938, Jul. 2025.

[3] Z. Yin, H. Zhu, X. Lv, J. Lai, and Y. Yang, "3-D-printed ultra-compact Butler matrix for wideband millimeter-wave beamforming," *IEEE Trans. Microwave Theory Techn.*, vol. 73, no. 9, pp. 5953–5965, Sep. 2025.

[4] Q. Li, J. Hirokawa, T. Tomura, and N. J. G. Fonseca, "Two-dimensional one-body 3 × 3-way hollow-waveguide Nolen matrix using a two-plane unequal division coupler," *IEEE Trans. Microwave Theory Techn.*, vol. 72, no. 1, pp. 376–390, Jan. 2024.

[5] Y. Xu, H. Zhu, and Y. J. Guo, "Compact wideband 3 × 3 Nolen matrix with couplers integrated with phase shifters," *IEEE Microw. Wireless Tech. Lett.*, vol. 34, no. 2, pp. 159–162, Feb. 2024.

[6] Z. Yin, H. Zhu, X. Lv, J. Lai, and Y. Yang, "Novel regular hexagonal six-port hybrid couplers for multibeam applications," *IEEE Trans. Microwave Theory Techn.*, pp. 1–10, 2025.

Short-Circuit Ring Patch Bandpass Filter on Glass Substrate with MLP-Based Optimization

Xin Chen
Xiamen University
School of Electronic Science and Engineering
Xiamen, China
34320240156427@stu.xmu.edu.cn

Sicheng An
Xiamen University
School of Electronic Science and Engineering
Xiamen, China
34320251150255@stu.xmu.edu.cn

Jingyu Lin*
University of Birmingham
School of Engineering
Birmingham, UK
L.J.2014@ieee.org

Yi Wang
University of Birmingham
School of Engineering
Birmingham, UK
y.wang.1@bham.ac.uk

Tian Yu
Jiangnan University
School of Integrated Circuits
Wuxi, China
yutian@jiangnan.edu.cn

Daquan Yu
Xiamen University
School of Electronic Science and Engineering
Xiamen Sky Semiconductor
Xiamen, China
yudaquan@xmu.edu.cn

***Abstract*—This paper presents a novel design framework for 3rd-order on-chip bandpass filters based on short-circuited ring patch resonators fabricated using through-glass via technology on fused silica substrates. The filter units are implemented using 1/n-mode SCRP resonators. To achieve efficient and precise structural optimization, a multilayer perceptron-based model is employed, trained on electromagnetic simulation data to map geometric parameters to S-parameter responses. The optimized design, targeting 5G n257/n258 bands, and filter prototypes are designed, fabricated, and experimentally characterized. Both filters exhibit excellent performance, with measured insertion loss below 1.5 dB and return loss exceeding 15 dB. The measured results show strong agreement with simulations, validating the effectiveness of the proposed MLP-assisted design methodology.**

Keywords—on-chip, short-circuited ring patch, bandpass filter, through-glass via, multilayer perceptron.

I. INTRODUCTION

As essential passive components in RF front-end modules, bandpass filters (BPFs) with high selectivity, low loss, deep stopband rejection, and compact footprints are increasingly demanded in modern wireless communication systems [1]-[2].

While conventional microelectronic integration technologies such as LTCC, HTCC, and silicon substrates are hindered by high loss, limited precision, and cost, glass-based 3D integration has emerged as a compelling alternative due to its superior high-frequency performance, low substrate loss, and stable dielectric constant [3]-[4].

In parallel, the evolution of neural networks and deep learning has emerged as a powerful enabler for the design and optimization of microwave filters. Prior studies have leveraged neural network-based learning techniques for microwave filter synthesis [5], and have also integrated neural networks with coupling matrix representations to facilitate filter design [6]-[7]. Building upon these advances, this work employs a multilayer perceptron (MLP) to optimize the structural parameters of the proposed bandpass filter. The MLP model is trained on a dataset derived from full-wave electromagnetic simulations, learning the nonlinear mapping between geometric variables and the corresponding filter responses. This data-driven approach enables efficient parameter prediction and rapid performance optimization, significantly reducing the need for iterative manual tuning.

The proposed filter architecture is based on the short-circuited ring patch (SCRP). By incorporating equivalent magnetic wall cutting techniques, the 1/n-mode SCRP configuration preserves a centrosymmetric electromagnetic (EM) field distribution while achieving a compact footprint. The integration of MLP-based optimization allows precise adjustment of the TGV array distribution to achieve the desired center frequency while maintaining high selectivity and low insertion loss. A filter prototype is designed, fabricated, and experimentally characterized to validate the proposed approach.

II. THE THEORY OF THE 1/*N* MODE SCRP

This section presents an analysis of the SCRP resonator and introduces the proposed equivalent magnetic wall cutting technique.

Fig. 1 illustrates the geometry of a conventional SCRP model, consisting of a circular patch with a radius of R positioned on top of the glass substrate with a thickness of h. The top patch is connected to the ground plane through a shorted circular via with a radius of r.

Assuming the region between the patch and the ground plane behaves as a cavity, the top and bottom boundaries, along with the inner sidewall, are treated as electric walls, whereas the outer periphery is approximated as a magnetic wall. Based on this assumption and following the formulation in [8], the resonant frequencies can be expressed as:

$$f_{mn} = \frac{k_{mn} \cdot c}{2\pi R \cdot \sqrt{\varepsilon_r}} \tag{1}$$

where the indices m, n denote the corresponding transverse magnetic (TM) mode, c is the light velocity in free space, and ε_r represents relative permittivity of the substrate. The wavenumbers k_{mn} are obtained as roots of the following characteristic equation:

$$J'_{mn}(k_{mn})N_m(k_{mn}\frac{r}{R}) - J_m(k_{mn}\frac{r}{R})N'_m(k_{mn}) = 0 \tag{2}$$

where $J_m(x)$ and $N_m(x)$ are the Bessel functions of the first and second kind of order m, and the prime denotes the first derivative with respect to the argument.

By solving the characteristic equations (1) and (2), the

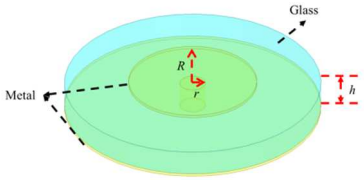


Fig. 1 The geometrical structure of the SCRP resonator on glass interposer

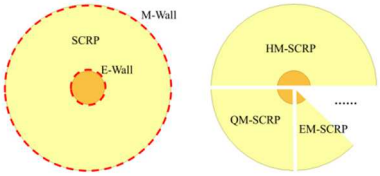


Fig. 2 The equivalent magnetic wall cutting technology

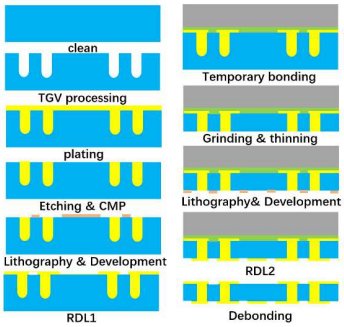


Fig. 3 Process Flow Diagram

resonant frequencies for the relevant TM modes are obtained. The resonant frequency of the SCRP filter is mainly governed by the ratio *R/r*. Combined with the low-loss property of the fused silica, this provides the basis for realizing flexible, low-loss filter designs.

Extensive research has been conducted on substrate-integrated waveguide (SIW) filters [9], and SCRP-based filters exhibit analogous characteristics [8]. Leveraging the equivalent magnetic wall cutting technique, size reduction of the SCRP resonator can be achieved, as illustrated in Fig. 2. When operating in the fundamental mode, a half-mode SCRP resonator can be obtained by bisecting the magnetic wall along the symmetry axis, thereby reducing the footprint by half. Further miniaturization can be realized through quarter-mode and eighth-mode configurations, which are obtained by successive bisections along the resonator centerlines. These topologies enable substantial area reduction while preserving the key filtering characteristics.

III. Process Flow

The filters designed in this work are both fabricated based on the 8-inch fused silica glass interposer. The corresponding process flow is illustrated in Fig. 3 as follows:

First, the fused silica is cleaned, and a picosecond laser is employed to induce modification. Then, the hydrofluoric (HF) acid solution is used to form the through glass vias (TGVs) with designed arrays. Second, Physical Vapor Deposition (PVD) is used and the full-surface electroplating is adopted to metalize TGVs. Third, the surface metal layer produced during the full-surface electroplating process is removed by etching. Fourth, photolithography, development, and electroplating are performed on the front side of the wafer to define the top-layer pattern. The glass wafer is then temporarily bonded to provide support and protection for the existing structure, so as to facilitate grinding and thinning the back side of the wafer. Finally, the backside of wafer is also patterned. After debonding the temporary bonding carrier (TBC), the sample is obtained.

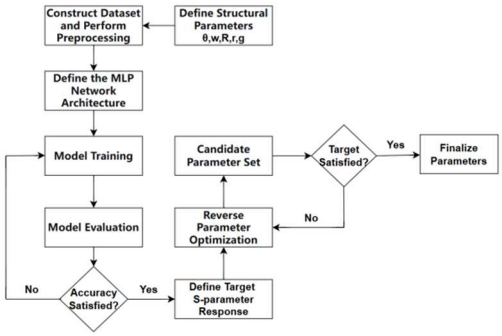


Fig.4 Flowchart of MLP-Based Structural Parameter Optimization

IV. MLP-Based Structural Parameter Optimization

To achieve efficient optimization of filter structural parameters, this work introduces an MLP as an auxiliary optimization tool. A forward prediction model is established to map structural parameters—namely, the sector angle θ, coupling width w, inner and outer radii R/r, and the gap g between the sector and the input/output ports—to the corresponding S-parameters. Concurrently, a reverse optimization model is developed to derive structural parameters from target S-parameters. This approach constructs a nonlinear mapping between structural parameters and S-parameters, enabling efficient exploration and rapid optimization of the design space.

The training process of the MLP-based model is depicted in the flowchart of Fig. 4, and the detailed procedure is summarized as follows:

(1) Dataset Generation: A reasonable parameter space is defined, and CST electromagnetic simulation software is employed to perform parametric sweeps across different combinations of structural parameters. The corresponding S-parameter curves are obtained, forming a training dataset that undergoes preprocessing.

(2) Model Training: An MLP network comprising multiple hidden layers is trained via supervised learning, enabling it to accurately predict the S-parameter response for a given filter structure.

(3) Parameter Optimization: Upon completion of model training, the trained model is embedded into an optimization loop. Using the target S-parameters as input, a genetic algorithm is employed to rapidly identify candidate sets of structural parameters that satisfy the performance requirements.

Based on the optimization results and considering factors such as physical realizability, the optimal solution is selected from multiple recommended parameter sets. A corresponding physical model is then established for validation.

V. Third-Order 1/*N* Mode SCRP Filters in a Semi-Circular Geometry

This section proposes a 3rd-order filter consisting of three 1/7.2 mode SCRP resonators based on 1/n-mode SCRP resonators, by integrating the fundamental analysis of such resonators with MLP-based structural parameter optimization.

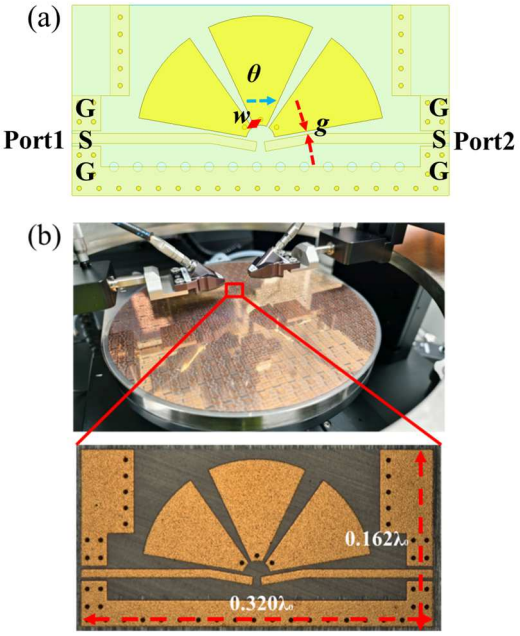


Fig.5 3rd-order SCRP filter: (a) the layout of the simulated structure, (b) the photograph of the sample.

As illustrated in Fig. 5 (a), three 1/7.2 mode SCRPs are laterally arranged. The input (Port1) and output (Port2) are implemented using Ground-Signal-Ground (G-S-G) pads.

The inter-resonator coupling is governed by the hybrid electromagnetic coupling mechanism. The coupling strength is dominantly controlled by the width of the shared boundary between the two resonator sectors. Also, this parameter serves as a key factor in controlling the frequency of TZ generated by hybrid EM coupling.

The proposed third-order filter, targeting a center frequency (CF) of 25 GHz with 20% fractional bandwidth (FBW), is optimized using the MLP-based framework described previously. Structural parameters refined through simulation-driven iterative optimization—considering both electromagnetic performance and physical constraints—resulted in an outer radius R of 1.3 mm, an inner via radius r of 0.15 mm, the coupling width w of 26 μm, the port gap g of 33 μm, and the sector angle θ of 45°. The test environment and the fabricated prototype are shown in Fig. 5(b).

Fig. 6 illustrates the frequency response, demonstrating excellent agreement between the measured results and full-wave EM simulations. The filter exhibits a CF of 24.23 GHz, with a measured insertion loss (IL) of 1.15 dB, return loss (RL) exceeding 15 dB across the passband, and a 3dB FBW of 21.48%. Occupying a compact footprint of only $0.320\lambda_g$ * $0.162\lambda_g$, the proposed 1/n mode SCRP filter effectively mitigates the inherent trade-off between electrical performance and physical size, simultaneously offering wide bandwidth, low IL, and significant miniaturization.

CONCLUSION

This paper presents a novel and highly competitive approach for designing compact, low-loss on-chip bandpass filters tailored for millimeter-wave applications, with a focus on the 5G n257/n258 bands. The core innovation lies in the development of 1/n-mode SCRP resonators, fabricated using

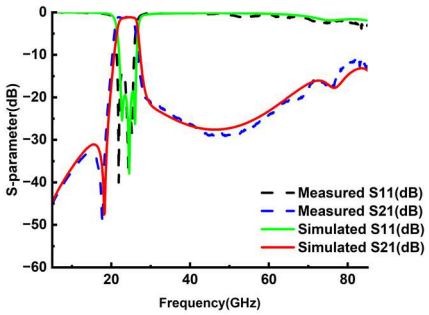


Fig.6 The S-parameter comparison between simulated and measured results of the 3rd-order SCRP filter

a high-precision TGV process on fused silica substrates. This architecture offers a low-cost, miniaturized solution well-suited for next-generation mobile communication systems. Furthermore, neural network-assisted optimization is employed to efficiently determine the structural parameters, significantly enhancing design efficiency. The demonstrated design flexibility across various geometries and coupling topologies offers valuable design flexibility, paving the way for further advancements in advanced RF front-end modules.

ACKNOWLEDGEMENT

This work was supported by the Open Research Fund of the State Key Laboratory of Millimeter Waves, Southeast University, under Grant No. K202519. The authors would like to thank the laboratory for its financial support and for providing valuable academic resources that contributed to this research.

REFERENCES

[1] J. Corsi *et al.*, "A Millimeter-Wave Substrate Integrated Waveguide Filter in Si-BCB Technology," in *2021 51st European Microwave Conference (EuMC)*, London, United Kingdom: IEEE, Apr. 2022, pp. 849–852.

[2] C. Fan, X. Liu, N. Liu, and Z. Zhu, "Compact Bandpass Filters With Low Loss and TZs Based on 1/ *n* Mode Circle-SIW in Through Silicon Vias (TSVs) Technology," *IEEE Trans. Microwave Theory Techn.*, vol. 72, no. 9, pp. 5095–5105, Sep. 2024,.

[3] X. Chen, J.-Y. Lin, L. Yan, T. Yu, M. Zhang, and D. Yu, "High- *Q* Dual-Mode On-Chip Filter Based on Through Glass Via Technology," *IEEE Microw. Wireless Tech. Lett.*, vol. 35, no. 11, pp. 1712–1715, Nov. 2025.

[4] W. Li *et al.*, "Glass-Based Single-Layer Slow Wave SIW Filter With Embedded Composite Right-/ Left-Handed Resonator," *IEEE Trans. Microwave Theory Techn.*, vol. 73, no. 2, pp. 1105–1116, Feb. 2025.

[5] Y. Wu, G. Pan, D. Lu, and M. Yu, "Artificial Neural Network for Dimensionality Reduction and Its Application to Microwave Filters Inverse Modeling," *IEEE Trans. Microwave Theory Techn.*, vol. 70, no. 11, pp. 4683–4693, Nov. 2022.

[6] S. Liu *et al.*, "Novel Neuro-Coupling Matrix Technique for Parametric Modeling of Microwave Filters," *IEEE Microw. Wireless Tech. Lett.*, vol. 34, no. 7, pp. 871–874, Jul. 2024.

[7] X. Lu, S. Shang, L. Zhou, S. Zhou, and B. Wei, "High Order Narrow Band Superconducting Filter Design Based on Neural Networks and Extracted Coupling Matrix," *IEEE Trans. Appl. Supercond.*, vol. 33, no. 9, pp. 1–10, Dec. 2023.

[8] J.-Y. Lin *et al.*, "Compact On-Chip Bandpass Filters Based on 1/ *n* Mode Short-Circuited Ring Patch in Through Glass Via Technology," *IEEE Trans. Microwave Theory Techn.*, pp. 1–11, 2026.

[9] T. Yu, X. Chen, M. Wang, J.-Y. Lin, and D. Yu, "W-Band Substrate Integrated Waveguide IPD Bandpass Filters Using Through Glass via Technology," *IEEE Trans. Microwave Theory Techn.*, vol. 73, no. 9, pp. 5929–5940, Sep. 2025.